

SPRINGER  
REFERENCE

Deren Yang  
*Editor*

# Handbook of Photovoltaic Silicon

 Springer

---

# Handbook of Photovoltaic Silicon



---

Deren Yang  
Editor

# Handbook of Photovoltaic Silicon

With 578 Figures and 71 Tables

 Springer

*Editor*

Deren Yang  
State Key Laboratory of Silicon Materials and  
School of Materials Science and Engineering  
Zhejiang University  
Hangzhou, China

ISBN 978-3-662-56471-4                      ISBN 978-3-662-56472-1 (eBook)

ISBN 978-3-662-56473-8 (print and electronic bundle)

<https://doi.org/10.1007/978-3-662-56472-1>

© Springer-Verlag GmbH Germany, part of Springer Nature 2019

This work is subject to copyright. All rights are reserved by the Publisher, whether the whole or part of the material is concerned, specifically the rights of translation, reprinting, reuse of illustrations, recitation, broadcasting, reproduction on microfilms or in any other physical way, and transmission or information storage and retrieval, electronic adaptation, computer software, or by similar or dissimilar methodology now known or hereafter developed.

The use of general descriptive names, registered names, trademarks, service marks, etc. in this publication does not imply, even in the absence of a specific statement, that such names are exempt from the relevant protective laws and regulations and therefore free for general use.

The publisher, the authors, and the editors are safe to assume that the advice and information in this book are believed to be true and accurate at the date of publication. Neither the publisher nor the authors or the editors give a warranty, express or implied, with respect to the material contained herein or for any errors or omissions that may have been made. The publisher remains neutral with regard to jurisdictional claims in published maps and institutional affiliations.

This Springer imprint is published by the registered company Springer-Verlag GmbH, DE, part of Springer Nature

The registered company address is: Heidelberger Platz 3, 14197 Berlin, Germany

---

## Preface

At present, resource shortage, environmental pollution, and ecological deterioration of the earth have become the main challenges for humanity. To protect resources and the environment, people all over the world make arduous efforts. Among them, the use of solar energy has attracted much attention in the last few decades. It is obvious that this clean and renewable form of energy, available in abundance, will be the main energy source for human beings in the future. Solar photovoltaic (PV) effect was discovered by a French scientist, A. E. Becquerel, in 1839, and his device could directly transform solar energy into electrical energy. A century later, in 1954, D. M. Chapin et al., at the Bell Labs in the USA, invented the first solar cell with an efficiency of about 6%. Since then, research and application of modern photovoltaic solar cells have been booming. Solar cells have been mounted on satellites, space stations, remote prairies, mountains, and islands to offer off-grid electricity, and on the roofs of houses, apartments, and public buildings to generate in-grid electricity. In most cases, solar cells have been installed together to form large photovoltaic power stations to produce mega-watt (MW) or even giga-watt (GW) electricity. Up to 2017, more than 405 GW solar cells were installed all over the world. It is clear that the photovoltaic industry has become one of the most important renewable energy industries, which influences the future direction of energy consumption of human beings.

Silicon, a semiconducting material, has widely been used in the microelectronic industry for more than 60 years as the basic material. Currently, silicon, including Czochralski (CZ) and multicrystalline (mc) silicon, is also the main material for the photovoltaic industry, and the related solar cells occupy more than 90% market shares. In fact, the first solar cell was produced using *n*-type silicon. It is clear that silicon is the key material for the photovoltaic industry. At first, in the production chain of the silicon photovoltaic industry, polycrystalline silicon with high purity should be manufactured. Second, crystalline silicon based on Czochralski, controlled directional solidification techniques, and other technologies is obtained. After wafer processes, silicon solar cells will be fabricated on the basis of *pn* junction. Finally, those solar cells are assembled as modules for further installation. Therefore, this handbook will depict the properties, structures, fabrications, and applications of those silicon materials used in the photovoltaic industry.

This handbook provides a comprehensive summary of the state of the art of photovoltaic silicon science and technology. It is divided into six parts, which are Polycrystalline Silicon, Crystalline Silicon Growth, Silicon Wafer Preparing, Impurity and Defect in Crystalline Silicon, Thin Film Silicon, and Nano-structure Silicon Materials and Solar Cells. Every part contains several self-contained and accessible chapters that are connected to each other and are also independent for new comers. Totally, there are about 26 chapters in this handbook. Forty-seven world class scholars and industrial experts from 27 institutes/universities/research centers (companies) in China, France, Germany, Japan, Russia, and the USA have contributed their valuable knowledge to the handbook. As the editor in chief, I would like to express my great appreciation to the authors for their contributions.

This handbook opens with an introduction in which I describe the importance of photovoltaic power for humanity and the research and application of silicon photovoltaics. In Chapter 1, I also introduce the developmental history of silicon photovoltaics in the last 60 years, the silicon materials which are used, and current investigations. Finally, I describe the part contents in the handbook so that readers can have an overview of the topics.

Part 1 is about polycrystalline silicon, co-edited by Dr. Yupeng Wan, the CTO of GCL-poly Energy Holdings Limited in China, as the part editor. This part consisting of four chapters discusses higher purity polycrystalline silicon materials that work as raw materials for silicon solar cells. The contents include the basic properties of polysilicon and its characterization methods, written by X. Liu, P. Payra, and Y. Wan; Siemens process, written by D. Yan; fluidized bed process, written by L. Jiang, B. Fiesemann, L. Chen, and D. Mixon; and upgrade metallurgical grade silicon, written by W. Ma, J. Wu, K. Wei, and Y. Lei.

Part 2 describes crystalline silicon, co-edited by Prof. Kazuo Nakajima from Tohoku University in Japan as the part editor. This part is divided into five chapters and discusses the different techniques for the growth of crystalline silicon ingots and their properties. The contents include Czochralski single crystal silicon, contributed by X. Yu and D. Yang; high-performance cast multicrystalline silicon, contributed by C. Lan; dendritic cast multicrystalline silicon, contributed by K. Fujiwara; mono-like crystalline silicon, contributed by K. Kutsukake; and noncontact crucible crystalline silicon, contributed by K. Nakajima.

Part 3 depicts wafer processes of crystalline silicon, co-edited by Prof. Hans Möller from Fraunhofer Technology Center for Semiconductor Materials in Germany as the part editor. This part contains three chapters and discusses how to prepare wafers from crystalline silicon ingots. The chapter about general wafer processing and the chapter characterization of wafer and supply materials during cutting are written by H. Möller, and the chapter about the wafer cleaning, etching, and texturization are written by A. Stapf, C. Gondek, E. Kroke, and G. Roewer.

Part 4 is about impurities and defects in crystalline silicon that have seriously affected the efficiency of solar cells. This part consists of six chapters and is co-edited by Prof. Michael Seibt from Göttingen University as the part editor. This part first depicts the important impurities in crystalline silicon, including oxygen impurity, contributed by G. Kissinger; carbon impurity, contributed by B. Gao and

K. Kakimoto; and nitrogen impurity, contributed by S. Yuan and D. Yang. Furthermore, the chapter on metal impurity and gettering processes is contributed by E. Yakimov. Finally, dislocations in crystalline silicon, written by I. Yonenaga, and grain boundary, written by M. Trempa, G. Müller, J. Friedrich, and C. Reimann, are discussed in detail.

Part 5 consisting of three chapters is about thin film silicon materials, co-edited by Prof. Y. Zhao from Nankai University in China as the part editor. This part describes hydrogenated amorphous silicon thin films and hydrogenated microcrystalline silicon thin films, written by Y. Zhao, X. Zhang, B. Yan, and L. Bai, and polycrystalline silicon thin films, written by F. Liu and Y. Zhou.

Part 6 is the last part which mainly describes nanocrystalline silicon and their application in solar cells. This part consists of four chapters, which are co-edited by Prof. J. Xu from Nanjing University in China. This part discusses nanocrystalline silicon, written by D. Wei, S. Xu, and I. Levchenko; nanocrystalline silicon-based multilayers, written by Y. Cao and J. Xu; polymorphous nano-Si and radial junction solar cells, written by L. Yu and P. Roca i Cabarrocas; and colloidal silicon quantum dots, written by S. Zhao and X. Pi.

The handbook provides the most comprehensive, authoritative, and updated reference on photovoltaic silicon from material fabrication, physical structures, and processing techniques to their applications in solar cells. I believe all the readers from universities, institutes, and industries in silicon photovoltaic field will benefit from this handbook.

November 2019

Deren Yang  
Editor

---

# Contents

<b>1 Introduction</b> .....	<b>1</b>
Deren Yang	
<b>Part I Polycrystalline Silicon</b> .....	<b>7</b>
<b>2 Polysilicon and Its Characterization Methods</b> .....	<b>9</b>
Xiaoxia Liu, Pramatha Payra, and Yuepeng Wan	
<b>3 Siemens Process</b> .....	<b>37</b>
Dazhou Yan	
<b>4 Fluidized Bed Process with Silane</b> .....	<b>69</b>
Limin Jiang, Benjamin F. Fieselmann, Liguo Chen, and David Mixon	
<b>5 Upgrade Metallurgical Grade Silicon</b> .....	<b>109</b>
Wen-hui Ma, Ji-Jun Wu, Kui-xian Wei, and Yun Lei	
<b>Part II Crystalline Silicon Growth</b> .....	<b>127</b>
<b>6 Growth of Crystalline Silicon for Solar Cells: Czochralski Si</b> ....	<b>129</b>
Xuegong Yu and Deren Yang	
<b>7 Growth of Multicrystalline Silicon for Solar Cells: The High-Performance Casting Method</b> .....	<b>175</b>
C. W. Lan	
<b>8 Growth of Multicrystalline Silicon for Solar Cells: Dendritic Cast Method</b> .....	<b>193</b>
Kozo Fujiwara	
<b>9 Growth of Crystalline Silicon for Solar Cells: Mono-Like Method</b> .....	<b>215</b>
Kentaro Kutsukake	

<b>10</b>	<b>Growth of Crystalline Silicon for Solar Cells: Noncontact Crucible Method</b> .....	<b>235</b>
	Kazuo Nakajima	
<b>Part III</b>	<b>Silicon Wafer Preparing</b> .....	<b>267</b>
<b>11</b>	<b>Wafer Processing</b> .....	<b>269</b>
	Hans Joachim Möller	
<b>12</b>	<b>Wafer Cleaning, Etching, and Texturization</b> .....	<b>311</b>
	André Stapf, Christoph Gondek, Edwin Kroke, and Gerhard Roewer	
<b>13</b>	<b>Characterization of Wafers and Supply Materials</b> .....	<b>359</b>
	Hans Joachim Möller	
<b>Part IV</b>	<b>Impurity and Defect in Crystalline Silicon</b> .....	<b>397</b>
<b>14</b>	<b>Oxygen Impurity in Crystalline Silicon</b> .....	<b>399</b>
	G. Kissinger	
<b>15</b>	<b>Carbon Impurity in Crystalline Silicon</b> .....	<b>437</b>
	Bing Gao and Koichi Kakimoto	
<b>16</b>	<b>Nitrogen Impurity in Crystalline Silicon</b> .....	<b>463</b>
	Shuai Yuan and Deren Yang	
<b>17</b>	<b>Metal Impurities and Gettering in Crystalline Silicon</b> .....	<b>495</b>
	Eugene B. Yakimov	
<b>18</b>	<b>Defects in Crystalline Silicon: Dislocations</b> .....	<b>541</b>
	Ichiro Yonenaga	
<b>19</b>	<b>Grain Boundaries in Multicrystalline Silicon</b> .....	<b>589</b>
	Matthias Trempa, Georg Müller, Jochen Friedrich, and Christian Reimann	
<b>Part V</b>	<b>Thin Film Silicon</b> .....	<b>637</b>
<b>20</b>	<b>Hydrogenated Amorphous Silicon Thin Film</b> .....	<b>639</b>
	Ying Zhao, Xiaodan Zhang, and Baojie Yan	
<b>21</b>	<b>Hydrogenated Microcrystalline Silicon Thin Films</b> .....	<b>693</b>
	Ying Zhao, Xiaodan Zhang, Lisha Bai, and Baojie Yan	
<b>22</b>	<b>Polycrystalline Silicon Thin Film</b> .....	<b>757</b>
	Fengzhen Liu and Yurong Zhou	

---

<b>Part VI Nano-structure Silicon Materials and Solar Cells</b> . . . . .	<b>791</b>
<b>23 Nanocrystalline Silicon and Solar Cells</b> . . . . .	<b>793</b>
Deyuan Wei, Shuyan Xu, and Igor Levchenko	
<b>24 Nanocrystalline Silicon-Based Multilayers and Solar Cells</b> . . . . .	<b>843</b>
Yunqing Cao and Jun Xu	
<b>25 Polymorphous Nano-Si and Radial Junction Solar Cells</b> . . . . .	<b>879</b>
Linwei Yu and Pere Roca i Cabarocas	
<b>26 Colloidal Silicon Quantum Dots and Solar Cells</b> . . . . .	<b>933</b>
Shuangyi Zhao and Xiaodong Pi	
<b>Index</b> . . . . .	<b>959</b>



---

## About the Editor



**Prof. Dr. Deren Yang** was born in 1964 in China. He is an academician of the Chinese Academy of Sciences and a Cheung Kong Professor at Zhejiang University in China. He is the dean of Faculty of Engineering at Zhejiang University. He is also the director of the State Key Lab of Silicon Materials and the director of Semiconductor Materials Institute at Zhejiang University. Dr. Yang received his bachelor's degree in 1985 and his Ph.D. in 1991 from Zhejiang University and then worked there. He worked as a visiting researcher in Japan in 1993, in Germany from 1995 to 1997, and in Sweden in 1999. In 1997, he was promoted to be a full professor by Zhejiang University and then promoted to be the Cheung Kong Professor in 2000 by the Ministry of Education of China. Dr. Yang received the National Science Fund for Distinguished Young Scholars in China in 2002, won the Award of National Nature Science in 2005 and 2013, as well as the Award of Chinese Young Science and Technology in 2006. He got elected as an academician of the Chinese Academy of Sciences in 2017.

Dr. Yang has engaged in the research of silicon materials used for microelectronic devices, solar cells, and opto-electric and nano devices. He has authored/co-authored 14 books, including 6 books in English, and edited 6 proceedings of the international conference. He has published over 780 research papers in international peer-reviewed journals, such as *Nature Communications*, *Advanced Materials*, *Nano Letters*, *Journal of the American Chemical Society*, *Applied Physics Letter*, and *Physics Review B*, with the total number of over 14,200 citations by SCI cited papers published by other groups. His *h* index is 63. He also holds 152 Chinese

patents. In the past, he chaired or co-chaired 18 international conferences/symposia and was appointed as the member of international committee of more than 50 international conferences. Dr. Yang also presented more than 53 invited talks in international conferences. He is the editor-in-chief of *Superlattices and Microstructures* and also the member of editorial advisory board of eight journals, including three international journals, such as *Physica Status Solidi* and *Silicon*.

Dr. Yang is vice director of China Photovoltaic Association, member of Expert Team of Chinese Keystone Special Projects, member of Board of Chinese Renewable Energy Association, member of Board of Chinese Crystal Association, member of SEMI China PV Committee, and chief scientist of a national key project for basic research of China.

---

## Contributors

**Lisha Bai** Institute of Photoelectronic Thin Film Devices and Technology, Nankai University, Tianjin, P. R. China

**Yunqing Cao** National Laboratory of Solid State Microstructures and School of Electronic Science and Engineering, The Collaborative Innovation Center of Advanced Microstructures, Nanjing University, Nanjing, China

College of Physics Science and Technology, Yangzhou University, Yangzhou, China

**Liguo Chen** GCL Technology Research Center, LLC, Princeton, NJ, USA

**Benjamin F. Fiesemann** GCL Technology Research Center, LLC, Princeton, NJ, USA

**Jochen Friedrich** Fraunhofer Technology Center Semiconductor Materials (THM), Freiberg, Germany

Fraunhofer Institute for Integrated Systems and Device Technology (IISB), Erlangen, Germany

**Kozo Fujiwara** Institute for Materials Research, Tohoku University, Sendai, Japan

**Bing Gao** The Institute of Technological Sciences, Wuhan University, Wuhan, China

**Christoph Gondek** Institute of Inorganic Chemistry, TU Bergakademie Freiberg, Freiberg, Germany

**Limin Jiang** GCL Solar Energy Trading Limited, Suzhou, Hong Kong

Jiangsu Zhongneng Polysilicon Technology Development Co., Ltd., (GCL), Xuzhou, Jiangsu, P. R. China

**Koichi Kakimoto** RIAM, Kyushu University, Fukuoka, Japan

**G. Kissinger** IHP – Leibniz-Institut für innovative Mikroelektronik, Frankfurt (Oder), Germany

**Edwin Kroke** Institute of Inorganic Chemistry, TU Bergakademie Freiberg, Freiberg, Germany

**Kentaro Kutsukake** Center for Advanced Intelligence Project, RIKEN, Tokyo, Japan

**C. W. Lan** Department of Chemical Engineering, National Taiwan University (NTU), Taipei, Taiwan

**Yun Lei** National Engineering Laboratory for Vacuum Metallurgy, Faculty of Materials and Metallurgical Engineering, Kunming University of Science and Technology, Kunming, Yunnan, China

**Igor Levchenko** Plasma Sources and Application Center, NIE, Nanyang Technological University, Singapore, Republic of Singapore

School of Chemistry, Physics and Mechanical Engineering, Queensland University of Technology, Brisbane, QLD, Australia

**Fengzhen Liu** College of Materials Science and Opto-Electronic Technology, University of Chinese Academy of Sciences, Beijing, China

**Xiaoxia Liu** Jiangsu Zhongneng Polysilicon Technology Development Co. Ltd., Jiangsu Province, China

**Wen-hui Ma** National Engineering Laboratory for Vacuum Metallurgy, Faculty of Materials and Metallurgical Engineering, Kunming University of Science and Technology, Kunming, Yunnan, China

**Hans Joachim Möller** Fraunhofer Technology Center for Semiconductor Materials, Freiberg, Germany

**Georg Müller** Crystal Consulting, Langensendelbach, Germany

**David Mixon** GCL Technology Research Center, LLC, Princeton, NJ, USA

**Kazuo Nakajima** Tohoku University, Sendai, Miyagi, Japan

**Pramatha Payra** GCL Solar Materials US LLC, Pasadena, TX, USA

**Xiaodong Pi** State Key Laboratory of Silicon Materials and School of Materials Science and Engineering, Zhejiang University, Zhejiang, Hangzhou, China

**Christian Reimann** Fraunhofer Technology Center Semiconductor Materials (THM), Freiberg, Germany

Fraunhofer Institute for Integrated Systems and Device Technology (IISB), Erlangen, Germany

**Pere Roca i Cabarrocas** Laboratoire de Physique des Interfaces et Couches Minces (LPICM), CNRS, Ecole Polytechnique, Palaiseau, France

**Gerhard Roewer** Institute of Inorganic Chemistry, TU Bergakademie Freiberg, Freiberg, Germany

**André Stapf** Institute of Inorganic Chemistry, TU Bergakademie Freiberg, Freiberg, Germany

**Matthias Trempa** Fraunhofer Institute for Integrated Systems and Device Technology (IISB), Erlangen, Germany

**Yuepeng Wan** GCL-Poly Energy Holdings Ltd., Jiangsu Province, China

**Deyuan Wei** Plasma Sources and Application Center, NIE, Nanyang Technological University, Singapore, Republic of Singapore

Micromachines Lab 1, School of Mechanical and Aerospace Engineering, Nanyang Technological University, Singapore, Republic of Singapore

**Kui-xian Wei** National Engineering Laboratory for Vacuum Metallurgy, Faculty of Materials and Metallurgical Engineering, Kunming University of Science and Technology, Kunming, Yunnan, China

**Ji-Jun Wu** National Engineering Laboratory for Vacuum Metallurgy, Faculty of Materials and Metallurgical Engineering, Kunming University of Science and Technology, Kunming, Yunnan, China

**Jun Xu** National Laboratory of Solid State Microstructures and School of Electronic Science and Engineering, The Collaborative Innovation Center of Advanced Microstructures, Nanjing University, Nanjing, China

**Shuyan Xu** Plasma Sources and Application Center, NIE, Nanyang Technological University, Singapore, Republic of Singapore

**Eugene B. Yakimov** Institute of Microelectronics Technology, Russian Academy of Science, Chernogolovka, Russia

National University of Science and Technology, MISiS, Moscow, Russia

**Dazhou Yan** China ENFI Engineering Corp, Beijing, China

China Silicon Corporation Ltd., Luoyang, Henan, China

**Baojie Yan** Institute of Photoelectronic Thin Film Devices and Technology, Nankai University, Tianjin, P. R. China

**Deren Yang** State Key Laboratory of Silicon Materials and School of Materials Science and Engineering, Zhejiang University, Hangzhou, China

**Ichiro Yonenaga** Tohoku University, Sendai, Japan

**Linwei Yu** School of Electronics Science and Engineering/National Laboratory of Solid State Microstructures, Nanjing University, Nanjing, China

Laboratoire de Physique des Interfaces et Couches Minces (LPICM), CNRS, Ecole Polytechnique, Palaiseau, France

**Xuegong Yu** State Key Lab of Silicon Materials and School of Materials Science and Engineering, Zhejiang University, Zhejiang, Hangzhou, China

**Shuai Yuan** State Key Laboratory of Silicon Materials and school of Materials Science and Engineering, Zhejiang University, Zhejiang, Hangzhou, China

---

**Xiaodan Zhang** Institute of Photoelectronic Thin Film Devices and Technology, Nankai University, Tianjin, P. R. China

**Shuangyi Zhao** State Key Laboratory of Silicon Materials and School of Materials Science and Engineering, Zhejiang University, Zhejiang, Hangzhou, China

**Ying Zhao** Institute of Photoelectronic Thin Film Devices and Technology, Nankai University, Tianjin, P. R. China

**Yurong Zhou** University of Chinese Academy of Sciences, Beijing, China



# Introduction

# 1

Deren Yang

Earth is the home of human beings. However, resource shortage, environmental pollution, and ecological deterioration of the earth have become the main challenges for humanity. To protect resources and the environment, people all over the world make arduous efforts. Among them, one of the main tasks is to change the energy sources of modern industries, which have seriously deteriorated earth's environment. It is well-known that modern industries are driven chiefly by fuel-combustion power generation, hydroelectric power generation, and nuclear power generation, which conflict with environmental protection. Therefore, people are now devoted to clean and renewable energies.

The sun, producing huge amounts of energy, is an important star for humanity. It is a continuous source of energy and light for people on earth, which maintains human life. While sunlight shines on earth, one part of this light is absorbed by the atmospheric layer and the other reaches the earth's surface, which is absorbed or reflected by earth. Once the sunlight is absorbed by earth, it can be either directly used or transformed into other forms of energy. Therefore, it is believed that solar energy is one of the most important renewable energies that can support the development of human economy.

There are several ways in which humans can use solar energy, e.g., photosynthesis, photochemical reaction, solar thermal, and solar photovoltaic. Among them, solar photovoltaic directly transforms solar energy into electrical energy by photovoltaic effect, which is the primary usage mode of solar energy. Dating back to 1839, A. E. Becquerel, a French physicist, found that under the illumination of sunlight, electrical voltage could be detected on two metal pieces in dilute hydrochloric acid, so-called photovoltaic (PV) effect. In the 1950s, the first silicon solar cell was invented by Bell Labs in the USA, which triggered off its research and application in the modern PV

---

D. Yang (✉)

State Key Laboratory of Silicon Materials and School of Materials Science and Engineering,  
Zhejiang University, Hangzhou, China  
e-mail: [mseyang@zju.edu.cn](mailto:mseyang@zju.edu.cn)

industry. Nowadays, solar cells have been widely used in different fields all over the world. Solar cells have been mounted on satellites and space stations for electric power. They have been installed in remote prairies, mountains, and islands to provide off-grid electricity. They have also been installed on the roofs of houses, apartments, and public buildings to generate in-grid electricity. In most of the cases, solar cells have been installed together to form large PV power stations to produce megawatt (MW) or even gigawatt (GW) electricity.

Since the invention of the first solar cell, with about 6% conversion efficiency, in 1954, by D. M. Chapin, C. S. Fuller, and G. L. Pearson at Bell Labs in the USA, the PV industry has gradually developed due to the support by governments of the USA, Japan, Europe, China, India, etc. Solar cells were first installed on spacecrafts to provide electric power. Then, people used them to support the powering of electronic counters, electronic watches, electronic toys, and so on. However, solar cells were expensive and their cost was largely higher than that of conventional electrical power. Therefore, solar cells were not used widely. In the 1970s and 1980s, the efficiency of solar cells increased gradually, and their cost decreased due to the support of different projects by governments of the USA, Germany, and Japan, such as “Sunshine Project,” “100,000 Roofs Project,” etc. Solar cells were installed in remote areas such as grasslands, deserts, mountains, and islands to provide electric power. They were also installed in light towers, communication bases, and oil pipelines. People also started to install solar cells on the roofs of buildings to generate electricity. In the 2000s, PV industry was booming and developed very fast. Many countries made laws and policies to enhance the application of solar cells and nurture the PV industry. In 2017, about 98.9 GW of solar power capacity was installed all over the world, which was an increase of more than 60 times in comparison with the installation of 1.5 GW of solar power capacity in 2006. The growth rate of PV industry per year was more than 40% during the last decade and even higher than that of microelectronic industry. Meanwhile, the cost or price of solar cells and modules has continuously dropped and in 2017, by comparison, is only about 15% of that in 2006. Figure 1 shows the PV installation amount per year in the world, indicating rapid increase in the last decade. Of the 98.9 GW of solar power capacity installed all over the world in 2017, China added 53 GW, which is the largest PV market. Moreover, it is expected that more PV panels will be installed in the future. It is predicted that PV power all over the world in 2040 will be more than 1 terawatt (TW). Therefore, it is obvious that PV industry is one of the most promising industries in the world.

Silicon (Si) is the main material for PV industry and occupies more than 90% market shares in the last decades while other thin film solar cells including amorphous Si, CdTe, and CuInGaSe occupy less than 10%. On the basis of high purity polycrystalline Si as raw materials, crystalline Si including Czochralski (CZ), multicrystalline (mc) Si, ribbon Si, etc., have been used for fabricating solar cells. In the initial stage of PV industry, leftover Si materials or fragments of Si wafers in microelectronic industry were used as raw materials. Since the beginning of this century, polycrystalline Si became scarce in the market because PV industry bloomed. More and more polycrystalline Si is being manufactured in Europe, the



**Fig. 1** PV installation amount per year in the world

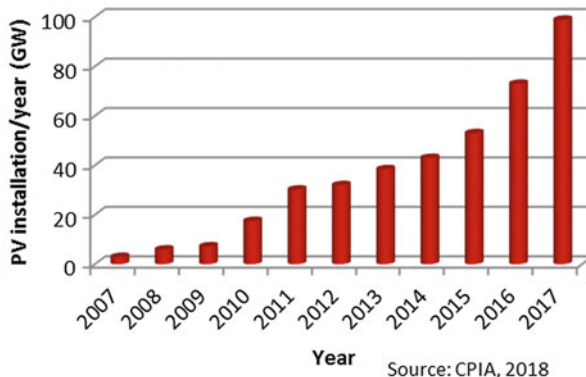
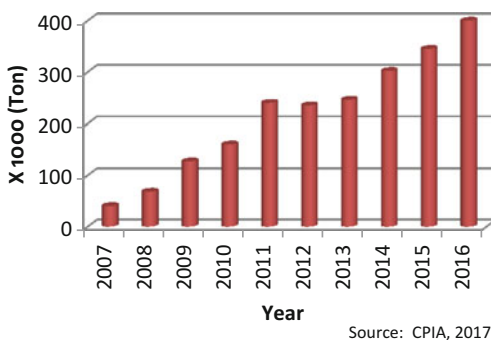


**Fig. 2** Polycrystalline Si production in the world



USA Asia, and the USA, especially in China. For example, GCL-Poly Energy Holdings Limited in China, built in 2006, has become the largest manufacturer of polycrystalline Si in the world and produced ~75,000 ton polycrystalline Si in 2017, which is about ~20% of world market share. Similar to Si solar cells, production of polycrystalline Si increased very much in the last decade and has satisfied market demands. Figure 2 shows the polycrystalline Si production as a function of time. It can be seen that in 2016 more than ~400,000 tons polycrystalline Si were produced to support the production of 77 GW Si solar cells.

Silicon is one of the most important materials in the world and was discovered in 1824 by Swedish scientist Jons Jakob Berzelius (1779–1948). In modern industry, Si is made from silica sand (SiO<sub>2</sub>). After the reaction of SiO<sub>2</sub> and carbon, metallurgic Si with purity of 95~98% can be fabricated. It is mainly used as an additive in steel and organosilicon production or as a component to produce Si-Al alloy. It is also used in the areas of medicine, biomaterials, etc. After the purification by means of Siemens and other technologies, metallurgic Si becomes high purity Si with a content larger than Si 99.99999% (7 N) and is so called PV grade polycrystalline Si or semiconductor grade polycrystalline Si. In this process, the main target is how to reduce the concentration of boron, phosphorous, and metal impurities and how to decrease cost including energy consumption.

And then, man melts high purity Si in a quartz crucible and grows the molten Si into single crystalline Si by means of Czochralski (CZ) technology. This method was first used to produce Si wafers for the microelectronic industry and later was also used to fabricate Si solar cells. From the 1950s to 1980s, all Si solar cells were made of CZ Si wafers. CZ Si possesses perfect crystal lattices and little impurities, which is of higher quality fit for higher efficiency solar cells, but however consumes more energy and is produced by scarce raw materials, which increases cost. At present, CZ Si occupies about 25% market share and will increase its share in the near future. In addition, the higher quality single crystalline Si fabricated by float zone (FZ) technology can be used to produce Si solar cells with higher efficiency. In 2017, 26.6% efficiency of Si solar cells was reported, which is the highest efficiency for Si single junction solar cells in the world. However, due to higher cost, FZ Si has not been widely used in PV industry, but only in the manufacture of higher efficiency solar cells in which cost is not sensitive.

Multicrystalline Si (mc-Si) is another important Si material used in PV industry and occupies more than 60% market share. It is fabricated by melting Si raw materials in a square quartz crucible and then is casted by directional solidification technology. It was developed in the 1970s and has been mass-produced since the 1990s. Recently, Si slugs or other particles at the bottom of crucibles are used as seeds to grow mc-Si, so called high-performance mc-Si. Based on cast solidification technology, mono-cast Si is developed by means of single crystal Si seeds at the bottom of crucibles. However, multicrystalline grains around the edges and corners of mc-Si ingots, higher density dislocations and dislocation clusters in the ingots, and higher cost of seeds used for the ingots are hindering its application in PV. Moreover, several kinds of Si ribbon materials, which can be directly cut and used for the fabrication of solar cells, have been explored and even have been produced.

Amorphous thin film Si (a-Si) and solar cells have been widely investigated for more than 40 years and currently have little market share even if their efficiency was above 10% in the past. Single-junction, bi-junction, and tri-junction a-Si thin films and solar cells have been fabricated, and, SiGe, SiC, etc., are also investigated as layers in the thin film solar cells. At the moment, nano-Si materials including micro-/nanocrystal Si combined of a-Si thin films, nano-Si wires, nano-Si core-shell structures, etc., are focused.

This handbook covers the photovoltaics of silicon materials, providing a comprehensive summary of the state of the art of photovoltaic silicon science and technology. It is divided into various areas including, but not limited to, fundamental principles, design methodologies, wafering techniques/fabrications, characterizations, applications, current research trends, and challenges. The handbook includes six sections, which are Polycrystalline Silicon, Crystalline Silicon Growth, Silicon Wafer Preparing, Impurity and Defect in Crystalline Silicon, Thin Film Silicon, and Nano-structure Silicon Materials and Solar Cells, respectively.

Higher purity polycrystalline Si is the raw material for crystal Si and solar cells. Therefore, Section 1 first discusses the polycrystalline behaviors and its characterization methods and then describes three main technologies to produce

polycrystalline Si, including Siemens process, fluidized bed process with silane, and upgrade metallurgical grade silicon. Currently, Siemens process is the main technology while fluidized bed process is slowly increasing its market share. However, the application of upgrade metallurgical grade silicon in PV industry is still controversial due to its purity and costs, even if a great deal of research has been done in the last decade.

Section 2 is mainly describes the growth technology of crystalline Si and its behaviors. CZ Si as the main technology for single crystal Si solar cells is introduced. And then, the growth and characterization of mc-Si, known also as high-performance mc-Si, is discussed. Moreover, the recently developed new technologies related to mono-like cast Si and noncontact crucible cast Si are introduced.

Section 3 is related to wafer preparing. This section is first dedicated to wafer cutting process, which is divided into slurry wire sawing and diamond wire sawing. Later, wafer cleaning, etching, and texturization related to solar cell fabrication are discussed. Finally, the characterization of Si wafers and supply materials during wafer preparing is depicted.

Section 4 describes impurities and defects in crystal Si, which have significantly influenced the efficiency of solar cells. The behaviors, measurements, and effects of oxygen, carbon, nitrogen, and metal impurities are reported. Finally, gettering technology, which reduces the deteriorate effects of metal impurities, is discussed. Moreover, the defects including dislocations and grain boundaries in mc-Si are also focused.

Section 5 introduces the behavior and fabrication of thin film Si and its solar cells. At first, hydrogenated amorphous Si thin films, which are basic amorphous Si thin films, are elaborated. Later, hydrogenated microcrystalline silicon thin films, which have less light degradation, of solar cells are discussed. Even if polycrystalline silicon thin films are not used to produce solar cells due to lower efficiency, its behavior, characteristics, and fabrication are also mentioned in this section.

Section 6 describes the properties and manufacture of nanostructure Si and solar cells, which have been widely investigated and are expected to have the advantage of structures for the improvement of solar cell efficiency. Several concepts, including nanocrystalline Si and solar cells, size-controllable nanocrystalline Si-based multilayers and solar cells, silicon nano-wires and radical junction solar cells, and colloidal Si quantum dots and their PV applications, are expounded in this section.

Finally, I would like to thank all the section editors and co-authors of this handbook for their valuable contributions. I am also grateful to Rebecca Urban, Karin Bartsch, and Stephen Yeung from Springer for their help.

---

**Part I**

**Polycrystalline Silicon**



# Polysilicon and Its Characterization Methods

# 2

Xiaoxia Liu, Pramatha Payra, and Yuepeng Wan

## Contents

Introduction .....	10
Float Zone (FZ) Method for Polysilicon Characterization .....	13
Float Zone for Acceptors (Boron, Aluminum) and Donors (Phosphorous, Arsenic) Determination .....	14
Polysilicon Donor and Acceptor Test Methods .....	16
Sample Wafer Preparation .....	16
Procedure .....	16
Calculation .....	17
Measuring Polycrystalline Silicon Conductivity .....	17
Hot Probe, Thermoelectric Conductivity Type Test Method .....	17
Rectifier Conductivity Type Test Method .....	18
Test Methods for Measuring the Resistivity of Polysilicon .....	19
Method for Determining Interstitial Oxygen and Substitutional Atomic Carbon Content in Polysilicon .....	19
The Method of Determining Interstitial Oxygen Content in Silicon Infrared Absorption .....	19
Test Method for Substitutional Atomic Carbon Content of Silicon by Infrared Absorption .....	22
Polysilicon Minority Carrier Lifetime Detection .....	24
Apparatus for Pulsed Light Method .....	24

---

X. Liu (✉)

Jiangsu Zhongneng Polysilicon Technology Development Co. Ltd., Jiangsu Province, China  
e-mail: [liuxiaoxia@gcl-power.com](mailto:liuxiaoxia@gcl-power.com)

P. Payra

GCL Solar Materials US LLC, Pasadena, TX, USA  
e-mail: [ppayra@gclsolarmaterials.com](mailto:ppayra@gclsolarmaterials.com)

Y. Wan

GCL-Poly Energy Holdings Ltd., Jiangsu Province, China  
e-mail: [wanyuepeng@gcl-power.com](mailto:wanyuepeng@gcl-power.com)

Sample Preparation .....	25
Procedure .....	26
Calculation .....	28
Test Methods for Measuring Metallic Impurities and Surface Metallic Contamination in Polysilicon .....	29
Test Method for Measuring Metallic Impurity Contamination in Polysilicon .....	30
Test Method for Measuring Surface Metallic Contamination in Polysilicon .....	32
Raw Materials and Other Test Methods .....	34
Metallurgical-Grade Silicon Test Methods .....	34
Trichlorosilane Test Methods .....	34
High-Purity Gas Test Method .....	35
High-Purity Water Test Method .....	35
Ambient Air Test Method .....	35
Packing Material Test Methods .....	35
Conclusion .....	35
References .....	36

### Abstract

The purity of polysilicon is usually between 6 N (99.9999%) and 9 N (99.9999999%). This chapter describes the test methods for measuring physical characteristics as well as quantification of elemental impurities in polysilicon materials. Float zone (FZ) process is an important method for converting granular polysilicon and polycrystalline chunk materials to monocrystalline silicon. A monocrystalline silicon rod is used to test the resistivity (n-type or p-type), minority carrier lifetime, carbon, oxygen, donors, and acceptor impurities in the polysilicon materials. Due to technological advancement, the analytical instrument detection limit (IDL) has improved in recent years allowing parts per billion atomic (ppba) to parts per trillion atomic (pptp) impurity detection in polysilicon. Donors (P, As, Sb), acceptors (B, Al), carbon, and oxygen can be measured by low-temperature FT-IR. The concentration of bulk and surface metal impurities (iron, chromium, nickel, copper, zinc, etc.) can be measured using ICP-MS.

### Keywords

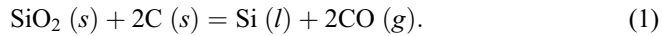
Polysilicon · Characterization · Analytical methods · Float zone (FZ) · Conductivity · Resistivity · Minority carrier lifetime · Donors · Acceptors · Metallic impurities

## Introduction

Ultrapure polycrystalline silicon (polysilicon) is the major material used for crystalline silicon-based solar cells. The silicon purity required is generally more than 99.99999%, or called 7-nines, or 7 Ns. Theoretically, the higher the purity of the silicon material, the better is the quality of the solar cell that is produced. The effect

of the polysilicon purity on the cost and quality of the resulting solar cells is an important factor that needs to be considered.

Ultrapure polysilicon is manufactured by the purification of metallurgical-grade silicon (MG silicon). MG silicon is produced from high-purity silicon dioxide using an electric arc furnace process and is typically about 98.5% pure. The feed materials silica and carbon (such as high-purity coals, charcoals, wood chips, cokes, etc.) are reacted in a furnace according to the following high temperature reduction:



Metallurgical-grade silicon is widely used in the metallurgical, chemical, and electrical industries. About 55% of MG silicon production is consumed by the metallurgical industry for aluminum production. Another 35% of the MG silicon manufactured is consumed by the chemical industry, mainly for the use in silicone-related polymers and other materials. Only a small portion of the MG silicon produced is consumed for the semiconductor and photovoltaic applications which require further purification to form ultrapure polysilicon. For semiconductor and solar applications, ultrapure silicon is separated into electronic-grade silicon (EG silicon) and solar-grade silicon (SG silicon).

In the past 15 years, there has been a rapid growth in the demand for solar-grade silicon, as shown in Fig. 1. Before 2005 ultrapure polysilicon was mainly consumed by the semiconductor industry. The source of silicon feedstock for solar cells at that time was the scrap leftovers from the semiconductor industry. After the rapid growth of the photovoltaic industry started around 2006, the demand on silicon for solar applications exceeded the amount of SG silicon that could be obtained from the semiconductor industry. Much polysilicon production capacity was added to meet the needs from the PV industry. By 2016 the quantity of polysilicon consumed by the PV industry was about 326,000 metric tons, which was more than 11 times the amount of polysilicon required for semiconductor needs.

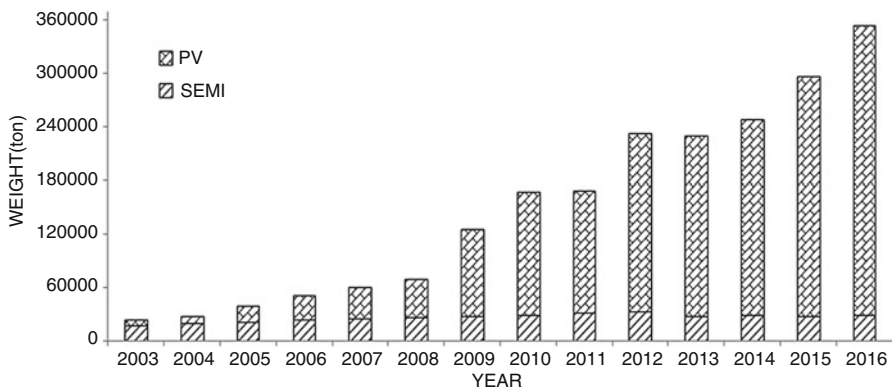


**Fig. 1** Market demand for polysilicon in the semiconductor and photovoltaic industries. (Source: CPIA reports, Bloomberg new energy, and GCL research data)

Solar grade silicon (SG silicon) is a term used to describe the silicon feedstock that can be directly utilized to produce solar cell material. This term is similar to the electronic-grade silicon (EG silicon) or semiconductor-grade silicon. Under the current main processes for solar cells, the purity requirement for SG silicon is not as high as that for EG silicon. Therefore, the sources of SG silicon may include virgin silicon (directly produced from Siemens reactors or fluidized bed reactors), pot scraps, and recycled silicon. SG silicon may also include MG silicon material purified with physical processes (called as upgraded metallurgical silicon, UMG).

The quality of SG silicon is determined by its purity. The purity of silicon is characterized by the amount of impurities, such as the concentration of donors, acceptors, metals, oxygen, carbon, and other impurities. This chapter outlines the accepted analytical methods for determining the concentration of the major impurities in SG polysilicon.

There are several standards for the specifications of SG polysilicon. The Chinese national standard for solar-grade polysilicon was issued in 2010 by the General Administration of Quality Supervision, Inspection and Quarantine of the People's Republic of China (AQSIQ) and the National Standardization Management Committee. The code is GB/T25074-2010 (Yang et al. 2010). This is the first version of the SG polysilicon national standard in China. The quality of the SG polysilicon is divided into three categories. Compared to the national standard for the EG polysilicon where only one grade is defined, it also implied that the purity requirement for polysilicon in solar applications is so far relatively less strict. The detailed requirements are cited in Table 1.

The SEMI (Semiconductor Equipment and Materials International) standard committee also issued a standard on the polysilicon for solar cell in 2011 (new approved edition published on Aug 30, 2012), SEMI PV 17-1012 (2012). In this standard, polysilicon is categorized into four grades. The purity requirements for the III and IV grade levels of polysilicon in the SEMI (SEMI PV17-1012 2012)

**Table 1** Specifications for the solar-grade polysilicon (Yang et al. 2010)

Parameters	Specifications		
	Grade I	Grade II	Grade III
Resistivity (P, As, Sb): ( $\Omega$ .cm)	$\geq 100$	$\geq 40$	$\geq 20$
Resistivity (B, Al): ( $\Omega$ .cm)	$\geq 500$	$\geq 200$	$\geq 100$
Donors (P, As, Sb): ppba	$\leq 1.5$	$\leq 3.76$	$\leq 7.74$
Acceptors (B, Al): ppba	$\leq 0.5$	$\leq 1.3$	$\leq 2.7$
Minority lifetime: $\mu$ s	$\geq 100$	$\geq 50$	$\geq 30$
Oxygen: (atoms/cm <sup>3</sup> )	$\leq 1.0 \times 10^{17}$	$\leq 1.0 \times 10^{17}$	$\leq 1.5 \times 10^{17}$
Carbon: (atoms/cm <sup>3</sup> )	$\leq 2.5 \times 10^{16}$	$\leq 4.0 \times 10^{16}$	$\leq 4.5 \times 10^{16}$
Total metal impurities (Fe, Cr, Ni, Cu, Zn, etc.)	$\leq 0.05$	$\leq 0.1$	$\leq 0.2$

Note: Bulk metal impurity requirement is optional



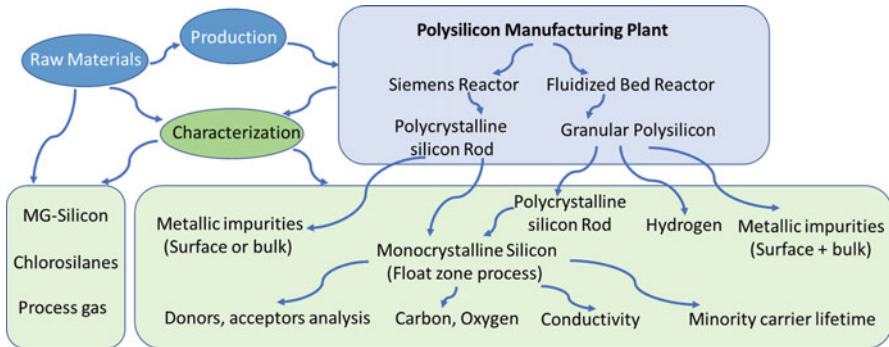


**Fig. 2** Process flow diagram of polysilicon production and materials characterization

specification guidelines are much lower than that in the GB/T25074-2010 (Yang et al. 2010).

In fact, it is difficult to specify the polysilicon purity that is acceptable for the manufacturing of solar cells because of the changing requirements. The topic of polysilicon purity is getting even more difficult to define as the impurity concentrations may change during crystallization and other processing steps. In general, the solar cell conversion efficiency will increase as the impurity concentration (mainly metallic impurities) decreases, until the minority lifetime of the wafer does not show significant effect on the efficiency. As the solar cell manufacturing process improves, the requirement on the minority lifetime of wafers will be increased for the enhancement of the solar efficiency. The need to improve solar cell operating efficiency will impose new and higher requirements on the purity of polysilicon.

With advances in the solar cell processing, the conversion efficiency of solar cell has been improved significantly in the past decade. The requirements for virgin polysilicon for the PV applications are getting more stringent. The standards for SG polysilicon will be upgraded, and the different specifications of various organizations will likely approach each other.

In addition to the purity of polysilicon, the requirements for particle size, size distribution, and the surface impurities will be adjusted. The standards will apply to both polysilicon chunks produced by Siemens process and polysilicon beads produced by fluidized bed reactors (FBR) (Fig. 2).

Specific methods that can be used to characterize polysilicon for semiconductor and/or solar applications are discussed in this chapter.

## Float Zone (FZ) Method for Polysilicon Characterization

The float zone process converts polycrystalline silicon (e.g., polysilicon or poly-Si) to monocrystalline silicon for impurity analysis. A rod (diameter  $\approx 20$ mm) is drilled through the polysilicon produced in the Chemical Vapor Deposition

(CVD) reactor. This sample polysilicon rod is then heated with an induction heating ring to form melt zone. The melt crystallizes into monocrystalline silicon, while the polysilicon rod is continuously melted by moving through the heating zone. Through this zone-melting process, many of the metal impurities in the polysilicon remain in the liquid phase as it moves down the polysilicon rod.

The float zone process can also convert granular polysilicon to monocrystalline silicon as described in SEMI MF1708-1104 (2004). Granular polysilicon to single-crystal conversion is a two-step process. The silicon granule consolidation into a polysilicon rod by melting fluidized granules into the molten end of a silicon pedestal during the downward pass is the first step. A single-crystal silicon seed is then melted into the bottom end of the poly rod during a single zone pass in the upward direction to convert to a single crystal in the second step. The single-crystal rod is used to measure trace impurities such as acceptor and donor components (typically boron, aluminum, phosphorous, arsenic, and antimony) and even substitutional carbon in the polysilicon.

## **Float Zone for Acceptors (Boron, Aluminum) and Donors (Phosphorous, Arsenic) Determination**

### **Procedure**

- (a) Seed preparation: N-type single crystal, resistivity  $>500\Omega$  cm, carbon content  $<0.2 \times 10^{-6}$ , no dislocation, crystallographic orientation deviation  $<5^\circ$ , crystal orientation  $<111>$ . To avoid surface contamination, the seed crystal must be stored properly and recommended to use within 36 h after decontamination, pickling, cleaning, and drying.
- (b) Sample preparation: All operations should be performed in the clean room. HF and  $\text{HNO}_3$  are mixed into an etching fluid in the volume ratio of 1:4–1:8. Polysilicon rod obtained from the core drill (core samples) is polished to remove 100  $\mu\text{m}$  surface damage in the process of coring and then cleaned with deionized water of 18 Megohm-cm. The cleaned core sample must then be float-zoned as soon as possible to reduce the possibility of contamination. If the sample is beyond the maximum period, the previous process must be repeated. The core sample may be sealed with appropriate clean material and stored in a clean room. Granular polysilicon may be used for float zone without prior cleaning of granules.
- (c) Device preparation: Float zone apparatus with radio-frequency (RF) generator is used for RF coupling to the silicon. The apparatus is set up inside an ISO 6 (class 1000) clean room. Carefully clean all parts and thoroughly dry in the clean room environment.
- (d) Ingot growth: Through zone-melting process, the core sample from Siemens polysilicon was drawn as a single-crystal ingot with a diameter of 10–20 mm.

## (e) Ingot evaluation:

- (i) Visual inspection. Check the uniformity of the crystal ingot diameter and the continuity of the growth plate ridge and the ingot color to ascertain whether the ingot is a dislocation-free single crystal and free of oxide deposition caused by air leak or other reasons.
- (ii) Testing of crystal structure and electrical parameters.
- (iii) Test the orientation of the single crystal according to GB/T 1555 (Yang et al. 2009).
- (iv) Test the integrity of the ingot crystal according to GB/T 1554 (He et al. 2009).
- (v) Detect minority carrier lifetime of the single-crystal ingot according to SEMI MF28-0707 (SEMI MF28-0317 2017).
- (vi) Cut coupons on the position where it was eight times the single-crystal ingot melting zone length to measure its phosphorus content. Detect the phosphorus content using low-temperature Fourier transform infrared (LT FT-IR) spectroscopy or fluorescence spectroscopy. Detect longitudinal resistivity of single crystal according to the method of GB/T 1551 DC two probe (Li et al. 2009). Read the data in the appropriate space based on the segregated coefficient of phosphorus, get N resistivity, and calculate the phosphorus content. Float zone method for boron determination may be found in GB/T 4060 (Luo et al. 2007).

**Calculation**

After measuring the donors, acceptors, and carbon impurities in cut wafers, the values can be related to the impurity level present in the polysilicon by following Eq. (2). For parallel core sample where the silicon may have doped or may have different composition compared to deposition layer, Eq. (2) can be used to determine the values for the total rod product.

$$C_p = \frac{A_f \times C_f + (A_1 - A_f) \times C_d}{A_1} \quad (2)$$

where:

$C_p$  = concentration (total rod product)

$A_f$  = cross-sectional area of silicon core,  $\text{cm}^2$

$C_f$  = concentration of impurity in the silicon core, in ppba for donor or acceptor and ppma for carbon

$A_1$  = cross-sectional area of polycrystalline silicon rods,  $\text{cm}^2$

$C_d$  = concentration of impurity in deposition layer in ppba for donor or acceptor and ppma for carbon

## Polysilicon Donor and Acceptor Test Methods

Polysilicon producers and users rely on the impurity (donors and acceptors) data obtained from low-temperature Fourier transform infrared (LT FT-IR) spectroscopy, SEMI MF 1630-1107 (2012).

Donor impurities refer to elements in Group V of the periodic table, including P, As, etc. The donor impurity acts as a substitution replacement for a silicon atom. Acceptor impurities refer to elements located in Group IIIA in the periodic table and include B, Al, etc. Likewise, the acceptor impurity is a substitution replacement for a silicon atom and is measured using LT FT-IR or photoluminescence.

The boron (n-type) or phosphorous (p-type) impurity content is an important index to evaluate the quality of the polysilicon. The instrumental sensitivity and reproducibility for phosphorus and boron remain to be improved.

## Sample Wafer Preparation

- (a) Samples must be cut and polished to fit the LT FT-IR sample holder. The sample surface can be mechanically or chemically polished so that the thickness variation of each sample should be less than 1% of the thickness.
- (b) Measuring electronically active impurity content, according to the thickness of the following samples:  
samples of high purity (greater than 2000  $\Omega\cdot\text{cm}$ ) should have a thickness of 3–5 mm, to achieve a lower detection limit. Samples with the thickness of 5–20 mm can be used to measure the impurities below  $0.01 \times 10^{-9}$  atoms (0.01 ppba).

Note: For heavily doped silicon (less than 10  $\Omega\text{ cm}$ ), the thickness of the sample should be 1–2 mm, to obtain adequate infrared light transmission.

## Procedure

- (a) The thickness of sample should be measured accurate to 0.02mm. Measure all the samples by the instrument, meanwhile, the reference sample should be measured at the same time to check the device performance.
- (b) Mount samples in cryostat and cool down below 15 K.
- (c) Set the instrument parameters with resolution of  $1.0\text{ cm}^{-1}$  or higher.
- (d) Take reference sample as the first test sample.
- (e) A total of 1000 scans were collected for the empty sample chamber as a background.
- (f) Move the sample to the measurement position.
- (g) Turn on the continuous source of incandescent lamp; make sure that the samples are completely in the beam and aligned relative to the infrared beam.
- (h) Take 300 times scans of the sample at least; get all the maps collected.

- (i) The blank, the apodization, and then the interferogram are converted to the spectrogram and the background spectrum.
- (j) Convert to an absorbance spectrum as a sample.
- (k) Store the spectrum for further processing and calculation of the absorption peak areas.
- (l) Steps of (e–k) should be repeated for each sample.

## Calculation

Calculate the concentration of active impurities/dopants at each point in the sample measured according to Eq. (3):

$$C_{ij} = (I_{ij}/t_j) \times f_i \quad (3)$$

where:

$C_{ij}$  = concentration of impurity/dopant element  $i$ , in sample  $j$

$I_{ij}$  = integral area of component  $i$

$t_j$  = thickness of sample  $j$  in millimeters (mm)

$f_i$  = the calibration factor for component  $i$ , in millimeters (mm-cm)

Concentration can also be expressed as density,  $D_{ij}$  (atoms/cm<sup>3</sup>), shown in Eq. (4):

$$D_{ij} = 5.0 \times 10^{13} \times C_{ij} \quad (4)$$

---

## Measuring Polycrystalline Silicon Conductivity

The conductivity is determined by the nature of the majority carrier in the semiconductor materials for electrical conductivity, generally  $n$ - and  $p$ -type. A conductivity type tester is used to directly measure the conductivity. There are several basic methods that can be used, such as “rectifier method,” “thermoelectric emfs,” “double-current dynamic conductance method,” and “Hall effect method.” This chapter mainly introduces “thermoelectric emfs” and “rectifier method.” One can choose a suitable measurement instrument according to the value of the resistivity.

### Hot Probe, Thermoelectric Conductivity Type Test Method

Two metal probes with different temperatures are contacted with the sample; the thermoelectric potential signal is generated between the two probes. Silicon acts as a semiconductor. Conductivity can arise from either a  $p$ - or  $n$ - type of doping.

### Measurement Equipment

- (a) Two probes are made of stainless steel and nickel; each probe tip is a  $60^\circ$  cone. One of the probes' rod is wrapped with a 10–20 W heating coil. For the resistivity of germanium materials greater than  $40 \Omega \text{ cm}$  at room temperature, the probe is made of lead or graphite; the temperature of the probe is  $5^\circ\text{C}$  higher than the room temperature.
- (b) The power supply can bring the temperature of the hot probe to  $40\text{--}60^\circ\text{C}$ .
- (c) The null indicator is adjusted to make the deflection sensitivity less than  $1 \times 10^{-9} \text{ A/mm}$ .
- (d) The temperature sensor is used to measure the temperature of the hot probe.

### Procedure

- (a) Verify that the thermal probe is connected on the negative pole zero indicator.
- (b) The material (stainless steel wool and other equivalent materials) is used to polish the thermal probe tip to remove the surface oxide layer.
- (c) The hot probe is heated to  $40\text{--}60^\circ\text{C}$ , and use a temperature measuring device to measure temperature.
- (d) The distance between two probes is brought to within a few millimeters, and the sample is pressed by the two probes firmly without damage to the thin silicon.
- (e) Observe the deflection of the pointer of null indicator. If the pointer is deflected to the positive direction, the sample is *p*-type. If the is deflected to the negative direction, the sample is *n*-type.
- (f) Determine the conductivity type through moving the probe on the test area of the specimen surface.

### Rectifier Conductivity Type Test Method

In this method, the conductivity of the sample is determined by the polarity of the voltage of the point contact reverse bias required. An alternating voltage is added to two contacts of the sample contacted. In the first half cycle, one of the contacts will be inversely biased and will suffer most of the voltage drop. In the second half of next period, the contact will be a positive bias; compared with the first half cycle, the voltage drop on the contact will be much smaller; there is a DC component in the mutual fluctuation voltage drop, which can be detected by a third contact.

### Measurement Equipment

- (a) For three probes in GB/T 1551 (Li jing et al. 2009), a collinear four-probe array can be used.
- (b) The voltage using AC power is 6-24V; and the general using of 12.6V is to make sure the maximum current is not greater than 1.0A.
- (c) The sensitivity of the zero indicator should be better than  $10\text{--}7 \text{ A/mm}$ , and the  $1 \text{ M}\Omega$  resistor series should be at least  $0.1 \text{ V/mm}$  resolution or polarity of the digital voltmeter (DVM); the resolution is better than the  $0.1 \text{ V/unit}$  scale.

**Procedure**

- (a) The probe is contacted with the sample, and the silicon wafer is supported by the thin silicon wafer without damage.
- (b) Observe the deflection of the zero-indicator pointer or the digital gauge reading.
- (c) Move the probe on the test area of the specimen surface to determine the conductivity type of the material.

---

**Test Methods for Measuring the Resistivity of Polysilicon**

Resistivity reflects the electrical properties of single-crystal silicon rod. A resistivity analyzer test uses a two-point probe or a four-probe method. For monocrystalline silicon resistivity measurements, the four-probe method is the most commonly used. The four-probe method has the advantage of requiring simple equipment, of providing ease of operation, and of giving high-precision measurements.

---

**Method for Determining Interstitial Oxygen and Substitutional Atomic Carbon Content in Polysilicon**

Polysilicon oxygen exists in the form of interstitial oxygen or oxygen precipitation, and the carbon is present as a substitution for a silicon atom. Infrared absorption is the most common method for the determination of oxygen and carbon.

**The Method of Determining Interstitial Oxygen Content in Silicon Infrared Absorption**

Use a corrected infrared spectrometer and appropriate reference materials, and record the infrared transmission spectrum of a double-sided polishing oxygen-containing silicon chip by a reference method. The thickness of the oxygen-free reference sample should be similar to the test sample to eliminate the effects of absorption caused by the silicon lattice vibration. Using the absorption coefficient of the silicon-oxygen absorption band at  $1107\text{ cm}^{-1}$ , calculate the concentration of interstitial oxygen in silicon wafer.

**Apparatus**

- (a) Infrared spectrometer: The resolution of Fourier transform infrared spectrophotometer should be  $4\text{ cm}^{-1}$  or better and that of dispersive infrared spectrophotometer should be  $5\text{ cm}^{-1}$  or better.
- (b) Sample holder: Sample should be loaded on a holder with tiny holes to prevent the passage of any infrared light beside the sample when testing smaller samples. The sample should be perpendicular (or substantially perpendicular) to the axial direction of the infrared beam.

- (c) Micrometer: Micrometers or other devices applicable to the measurement of the thickness of the sample and the error should be less than  $\pm 0.2\%$ .
- (d) The thermocouple millivolt meter or other measuring systems applicable to measure the temperature of the sample during the test.

### Sample Preparation

- (a) The thickness of the sample in this method ranges from 0.04 cm to 0.4 cm.
- (b) Cut the monocrystalline silicon sample; measure the thickness of the sample by a micrometer or other devices after sided grinding and polishing. Both sides of the sample after processing should be parallel and the angle should be less than  $5^\circ$ . The difference value of the thickness should be less than or equal to 0.5%, and the surface evenness should be less than the 1/4 of that at the maximum absorption wavelength of the measured impurity band.
- (c) Choose monocrystalline silicon wafers with their concentration of oxygen as low as possible. Compare these wafers by using them as reference to each other, and choose the one with lowest absorption coefficient as the reference sample.

### Procedure

- (a) The spectrometer: Fourier transform infrared (FT-IR) spectrometer should be equipped with optics and detector to be used in the region  $250\text{--}1300\text{ cm}^{-1}$ .
- (b) Equipment inspection: Determine the noise level at 100% baseline by measurement. During the measurement, record the transmission spectrum with both the sample and reference optical path being empty when using double-beam spectrometer. For single-beam spectrometers, record the transmittance spectrum as a ratio of two spectra keeping the sample optical beam empty. Draw the 100% baseline of the spectrum with the wave number within  $900\text{ cm}^{-1}$  and  $1300\text{ cm}^{-1}$ . Increase the testing time until transmittance line reaches  $(100 \pm 5)\%$ . If the problem persists, the equipment needs to be repaired.  
Determine 0% transmittance line only when using dispersive equipment (DIR). Block the sample optical path, and record the zero of the device at the wave number ranging from  $900\text{ cm}^{-1}$  to  $1300\text{ cm}^{-1}$ . If there is a larger non-zero signal in this range, it should be checked if there is stray light on the detector. If the problem persists, the equipment needs to be repaired.

Record the characteristic curve of luminous flux of the spectrometer only when using Fourier transform infrared spectrophotometer (FT-IR). Leave the sample optical path empty and draw the single-beam spectrum with its wave number ranging from  $450\text{ cm}^{-1}$  to  $4000\text{ cm}^{-1}$ . Record the spectrum as the reference spectrum to assess the equipment performance after adjusting the equipment according to the equipment specification. It should be readjusted when there's larger difference between the sample spectrum and the reference spectrum.

Measure the spectrum of the sided and polished single-crystal silicon slice with its resistivity greater than  $0.5\ \Omega\cdot\text{cm}$  and its wave number ranging from  $1600\text{ cm}^{-1}$  to  $2000\text{ cm}^{-1}$  by air reference method to check the mid-scale linearity of the spectrometer. If the value of the transmittance is not  $(53.8 \pm 2)\%$  in this wavenumber



range, it should be adjusted by placing the sample perpendicular to the axial direction of the incident light, and the tilt angle should be no more than  $10^\circ$ .

Determine the measuring time of the spectra, and keep a sided and polished single-crystal silicon slice with its resistivity greater than  $0.5 \Omega\text{-cm}$ , thickness ranging from  $0.04 \text{ cm}$  to  $0.065 \text{ cm}$  and content of oxygen ranging from  $6 \times 10^{17} \text{ atoms/cm}^3$  to  $9 \times 10^{17} \text{ atoms/cm}^3$ , through Fourier transform infrared spectrophotometer (FT-IR) at the speed of 64 times a minute or through dispersive infrared spectrophotometer (DIR) at a certain speed, and scan to get the transmission spectrum with the record of full peak height. If the ratio of the net amplitude ( $T_{\text{base}} - T_{\text{peak}}$ ) of the oxygen absorption band to the standard deviation does not exceed 100, increase the number of sweeps (FT-IR) or reduce the sweep rate (DIR) until the indicator is reached.

- (c) Surface treatment: Prior to each laboratory measurement, all samples, including the reference sample, are first etched with HF to remove oxide from the surface.
- (d) Thickness measurement: When measuring the thickness of the test samples and the reference sample, the difference in thickness should be less than  $\pm 0.2\%$ . It is necessary to separately prepare a reference sample of appropriate thickness if it is more than  $\pm 0.2\%$ .
- (e) Temperature: Measure and record the temperature of the spectrometer sample chamber.
- (f) The infrared transmission spectra measurement: Obtain the spectra. It should be checked that the infrared beam passes through the center of the test sample and the reference sample. The spectra are obtained by putting the oxygen-free reference sample in the reference optical path and putting the testing sample in the sample optical path when using double-beam dispersive equipment and by calculating with reference spectrum and sample spectrum when using single-beam equipment.
- (g) Transmission spectra plotting: The wave number from  $900 \text{ cm}^{-1}$  to  $1300 \text{ cm}^{-1}$  should be covered during the scanning of the transmission spectrum. Draw a line as the baseline within  $900 \text{ cm}^{-1}$  and  $1300 \text{ cm}^{-1}$ , and take the average transmittance of  $900 \text{ cm}^{-1}$  to  $1000 \text{ cm}^{-1}$  and  $1200 \text{ cm}^{-1}$  to  $1300 \text{ cm}^{-1}$  as the two sides of the line. Find the wave number corresponding to the minimum transmittance within  $1102 \text{ cm}^{-1}$  and  $1112 \text{ cm}^{-1}$ , and record the value as  $W_p$  (given 5 significant digits). Record the minimum transmittance as  $T_p$  as the peak absorbance.
- (h) Record: Determine and record the full width at half maximum height (FWHM) of the absorption peak.

### Calculation

Calculate the interstitial oxygen content in silicon,  $N[O]$  in absolute units of atoms/ $\text{cm}^3$ . Absolute units can be divided by  $5 \times 10^{16}$  to convert it to the relative units in ppm.

$$N[O] = 3.14 \times 10^{17} \alpha_o \text{ (atoms/cm}^3\text{)} \quad (5)$$

where  $\alpha_o$  = absorption coefficient.

## Test Method for Substitutional Atomic Carbon Content of Silicon by Infrared Absorption

This test method is suitable for production control, quality assurance, and research on polysilicon materials, SEMI MF1391-1107 (2012). This method measures the substitutional atomic carbon content of silicon depending on its absorption coefficient of infrared absorption peak at the wave number of  $607.3\text{ cm}^{-1}$  ( $16.47\text{ }\mu\text{m}$ ) at cryogenic temperature (below 80 K). For room temperature ( $\sim 300\text{ K}$ ), the absorption band at  $605\text{ cm}^{-1}$  ( $16.53\text{ }\mu\text{m}$ ) can also be used.

### Apparatus

- (a) Fourier transform infrared (FT-IR) spectrometer: The spectrum range is  $500\text{--}700\text{ cm}^{-1}$  ( $14\text{--}20\text{ }\mu\text{m}$ ), and the resolution of spectrometer must be above  $2\text{ cm}^{-1}$  at room temperature and above  $1\text{ cm}^{-1}$  at 77 K.
- (b) Thickness measuring instrument: Thickness tolerance should be 0.005 mm or less.
- (c) Sample stand: The sample should be placed into the holder with hole to avoid any infrared crossing beside the sample if the sample is too small, and the sample stand should be perpendicular to or fundamentally perpendicular to the axis of infrared.
- (d) Window materials: The cryostat and proper window materials should maintain the sample and reference sample at 77 K.
- (e) Thermometer: Use a thermometer that can test the temperature of sample chamber at room-temperature measurements and the temperature of sample holder at low-temperature measurements. The thermometer tolerance should be  $< \pm 2^\circ\text{C}$ .

### Sample Preparation

- (a) Due to carbon segregation coefficient that is  $< 1$  ( $\sim 7 \times 10^{-2}$ ), the carbon test sample should be taken from the end of single crystal (when single crystals are obtained from the core-drilled polysilicon) because of high carbon content.
- (b) Reference sample must be the silicon which substitutional atomic carbon content is  $< 1 \times 10^{15}\text{ atoms/cm}^{-3}$  (0.02 ppma).
- (c) It can be applied for testing the substitutional atomic content of p-silicon and n-silicon with resistivity above  $3\text{ }\Omega\text{-cm}$  and  $1\text{ }\Omega\text{-cm}$ , respectively, as well as other non-highly precise silicon whose resistivity is above  $0.1\text{ }\Omega\text{-cm}$ .
- (d) Take the center of the silicon as the measure area, and utilize GB/T 6618 to measure the sample thickness except for any special regulations. The center should be the same as original silicon slice, ensuring the sufficient sample area, to avoid incident beam bypassing the sample.
- (e) The test sample and reference sample should be grinded in both sides and then polished to 2 mm or even less.
- (f) The thickness tolerance should be less than 0.005 mm.
- (g) The difference between test sample and reference sample should be less than 0.01 mm.

## Procedure

- (a) Instrument examination: To measure the stability and noise level, establish 100% transmittance line. For double-beam instrument, record the transmittance spectra with both test and reference sample beams empty. For single-beam instrument, record the transmittance spectra as the ratio of two spectra when sample beam is empty. Draw the 100% baseline of the transmittance spectra from  $500\text{ cm}^{-1}$  to  $700\text{ cm}^{-1}$ . If the baseline is still not up to  $100\% \pm 0.5\%$  range, then increase the test time to achieve the range; otherwise, adjust or repair the instrument.

Establish 0% transmittance line. For dispersive (DIR) instrument, block the sample beam, and record the transmittance spectrum from  $500\text{ cm}^{-1}$  to  $700\text{ cm}^{-1}$ . In getting a relative high non-zero signal among the range, check whether there is stray light cast onto the detector. If not, adjust or repair the instrument. Use the air reference ratio method to test the spectrogram of double-sided polished silicon single-crystal slice which has a resistivity of  $>5\ \Omega\cdot\text{cm}$ . Test the linearity of the instrument from the spectrum over the wavenumber (WN) range of  $1600\text{--}2000\text{ cm}^{-1}$ . If the transmittance of these WN range is not  $53.8\% \pm 2\%$ , adjust the orientation of sample vertical to the axis of incident beam, and keep the inclined angle below  $10^\circ$ .

- (b) Test the difference sample spectrum between room temperature and 77 K. Use a resolution of  $\leq 2\text{ cm}^{-1}$  to test the sample at  $607.2\text{ cm}^{-1}$  at room temperature, and use a resolution of  $1\text{ cm}^{-1}$  to test the sample at  $607.5\text{ cm}^{-1}$  at 77 K.

Acquire spectrum: Make sure that infrared beam passing through the center of the test sample and reference sample. For double-beam instrument, put the sample onto the sample beam and the reference sample onto the reference beam, and test the absorption spectrum from  $500\text{ cm}^{-1}$  to  $700\text{ cm}^{-1}$ , and for single-beam instrument, use the test sample spectrum and reference sample spectrum to calculate the absorption spectrum.

Use the nitrogen and dry air to fully blow the instrument beam, and keep the relative humidity  $< 20\%$ . Sweep repeatedly no less than 64 times. In the above condition, measure the absorption spectrum test sample and reference sample, respectively, from  $500\text{ cm}^{-1}$  to  $700\text{ cm}^{-1}$ .

## Calculation

Carbon content  $N[C]$  is calculated as formula (6):

$$N[C] = F \times \alpha \quad (6)$$

where:

$\alpha$  = absorption coefficient.

$N[C]$  = carbon content; unit, atoms per cubic centimeter (atoms/cm<sup>3</sup>).

$F$  = calibration factor; unit, atoms per square centimeter (atoms/cm<sup>2</sup>).  $F$  is  $8.2 \times 10^{16}$  (atoms/cm<sup>2</sup>) at 300 K and is  $3.7 \times 10^{16}$  (atoms/cm<sup>2</sup>) at 77 K.

The absorption coefficient  $\alpha$  can be calculated by Eq. (7):

$$\alpha = (23.03/X) \times (Sp - Sb) \quad (7)$$

where:

$X$  = thickness of the test sample (mm)

$Sp$  = peak value of carbon absorbance spectrum

$Sb$  = baseline value of the carbon absorbance spectrum

---

## Polysilicon Minority Carrier Lifetime Detection

Minority carrier lifetime is one of the most important characteristics of semiconductor materials to understand the device performance and can be measured using pulsed light method or chopped light method, SEMI MF28-0707 (SEMI MF28-0317 2017).

### Apparatus for Pulsed Light Method

- (a) Light source: The turnoff time of the pulsed light source should be such a way that the light intensity decreases to  $\leq 10\%$  of its maximum value in  $< 0.2$  times of the filament lifetime of the silicon sample to be measured. For silicon sample measurement, the maximum of the spectral distribution of the light source should be in the wavelength range within 1.0–1.1  $\mu\text{m}$ . Xenon light tube or discharge tube is equipped with 0.01  $\mu\text{F}$  capacitor and can provide the frequency of 2–60 Hz pulse high-voltage power supply. The maximum light intensity can be reached in  $< 0.3 \mu\text{s}$ , and the light intensity decreases to less than 5% of its maximum value in  $< 0.5 \mu\text{s}$ . The smaller capacitor can achieve shorter pulse width, which may be suitable for measuring filament lifetimes  $< 0.5 \mu\text{s}$ .
- (b) Power supply: Power should be stable after filtering at 5 V DC voltage. The current supply may act as a constant current or voltage source along with a nonreactive series resistance ( $R_s$ ), which is around 20 times as large as combining the values of sample resistance ( $R$ ) and contact resistances ( $R_c$ ).
- (c) Sample holder and thermostat: Heat insulation sample clamp and thermostat should be able to keep the sample at a constant temperature of  $27^\circ\text{C} \pm 1^\circ\text{C}$ . The sample holder should maintain Ohmic contact with the sample's whole surfaces, and at least one side of the sample's four sides should be lightened.  
Note: There are many procedures to make Ohmic contacts to the sample surface, but it is recommended to use pressure contacts of metal braid or fiber. Indium and thick lead plate can also be used for this purpose.
- (d) Filter is typically 1 mm thick and of the same material as the sample, and it should be double-sided polished, placed directly above the rectangle opening or diaphragm.

- (e) The rectangle opening diaphragm: The diaphragm should be placed close to the sample, part area of the sample is lighted by the light through the diaphragm.  $L_i = L/2$  is the length of the lighted area of the sample and width  $W_i = W/2$ . Typically, lighted area is in the middle of the sample.
- (f) Electrical signal measuring circuit:
- (i) The preamplifier, with an adjustable range of high and low-frequency, and the low-frequency cutoff should be adjustable from 0.3 Hz to 30 Hz.
  - (ii) The oscilloscope, scanning time and the sensitivity should be appropriate. Oscilloscope may have a continuously calibrated time sweep with accuracy and linearity that is better than 3% and triggering capability by test signals or external signals. For the oscilloscope with a 10 cm × 10 cm screen size, the screen is ruled in cm<sup>2</sup> to help reduce parallax. For the attenuation curve of the transparent screen, the height above the baseline decays exponentially following Eq. (8):

$$y = 6 \exp(-x/2.5) \quad (8)$$

where the  $x$  and  $y$  are the scale divisions of the graph.

- (g) The electronic circuit general requirements: (i) Vertical scanning deflection sensitivity correction to 0.1 mV/cm or less; (ii) correction gain and vertical scanning deflection linearity within 3%; (iii) for the response time, if the input signal changes in a stepwise manner, the output signal's rise or fall time be <1/5 of the smallest filament lifetime; (iv) pulse had no obvious failure, such as the overshoot or damping effect.

## Sample Preparation

- (a) Sample size measuring: Record all size, accuracy to 0.1 mm. Micrometer or Vernier calipers can be used. Pulsed light method is suitable for bar-shaped samples: Type A (length × width × thickness = 15 mm × 2.5 mm × 2.5 mm), Type B (length × width × thickness = 25 mm × 5.0 mm × 5.0 mm), and Type C (length × width × thickness = 25 mm × 10.0 mm × 10.0 mm). Smaller samples are suitable for lower lifetime values. Type B is recommended for Czochralski silicon and Type C for float zone silicon.
- (b) Grinding: Before the test, polish the sample with alumina powder until the six surfaces of the sample is smooth enough. Typically, the aluminum oxide particle sizes are 5–12 μm.
- (c) Cleaning: Clean the sample with ultrasonic water bath or rinse with ultrapure water, and dry with nitrogen, and make sure the sample surfaces are clean enough for circuit formation.
- (d) Ohmic contact: (i) Use the entire surfaces of the sample's two ends to make Ohmic contacts. For germanium sample it is suggested to be plated with nickel, rhodium, or gold, and copper should be avoided in the coating process. For silicon samples, the best way is to heat the samples at 35 °C, while rubbing the

sample's end face at the same time, to prevent drip on gallium from gallium blot emery cloth. N-type silicon samples two ends with nickel plated, or p-type silicon samples with rhodium plated can also be used.

- (e) The contact point test: Place the sample in the clamp, then the current is switched on in one direction of the sample to produce voltage of 2–5 V, and record the voltage drop as V1. Change the direction of current, and record the voltage drop V2. If the difference of V1 and V2 is less than 5%, accept the sample.
- (f) Measure and record: According to GB/T 1551 (Li et al. 2009), measure and record and correct the resistivity to 27 °C. If the sample conductive type is unknown, follow GB/T 1550 (Chen et al. 1997).

## Procedure

- (a) With the sample fixture clamping and positioning in the diaphragm of the rectangular hole, the middle section of the sample is lighted. Measure and record the temperature of the sample clamp (accuracy  $\pm 1$  °C).
- (b) Open the light source and, at the same time, preamplifier and oscilloscope to be connected.
- (c) Turn on the power, and adjust the current to generate 2–5 V of potential difference across the sample.
- (d) Make observed decay curve, occurring together with the reference exponential curve, as drawn on the oscilloscope's transparent screen by the method as follows: (i) for vertical displacement adjustment knob, observe the attenuation curve of the baseline overlap with standard index curve. Adjust the time benchmark scanning speed to the lower end; make multiple attenuation curve appear on the screen orientation.  
Extend the time reference signal to produce a single cycle pattern; adjust the horizontal displacement, vertical amplification, and time benchmark scanning speed, as much as possible until the observed decay curve matches the standard index curve (exponential curve) closely with the pulse amplitude peak value consistent with standard non-traumatic line on the upper left point.
- (e) Test samples for inhomogeneity: shut off the current, keep light and other knobs unchanged, and observe whether the oscilloscope detects a voltage signal light. If detected signal is more than 1% of signal pulse peak, the sample should not be used for testing due to the inhomogeneities.
- (f) If no voltage signal is observed and the decay (light attenuation curve) is exponential, then the time constant of the decay can be determined as the filament lifetime  $\tau_F$  ( $\mu\text{s}$ ):

$$\tau_F = 2.5S_1 \quad (9)$$

where  $S_1$  is the time benchmark scanning speed (sweep speed) and the unit is microseconds per cm ( $\mu\text{s}/\text{cm}$ ).

- (g) If the oscilloscope doesn't have time benchmark calibration, standard index curve is not applicable, but the filament lifetime can be determined as follows: rotate the time benchmark scanning speed to a suitable degree value  $S_2$  ( $\mu\text{s}/\text{cm}$ ); test on any two points on the decay curve of 2:1 oscillation ratio of the horizontal distance  $M$  (cm), the filament lifetime:

$$\tau_F = 1.44 \times MS_2 \quad (10)$$

When the screen does not have the standard curve, this step may be used.

- (h) When observed screen decay curve is not pure index curve but close to exponential curve, the apparent lifetime can be determined at the lower end of the curve.
1. When sample's half or less width is already affected by light, the filament lifetime can be determined from signal attenuation to the peak after the voltage has decayed to 60% of the peak value.
  2. When more than half of the sample width has been affected by light, the filament lifetime can be determined from signal attenuation to the peak after the voltage has decayed to 25% of the peak value.
  3. During the above two cases, the vertical gain attenuation strip are increased to extend the decay curve, in this case, some specify part of a decay curve on the screen vertical full scale, by adjusting the time reference, a suitable value of  $S_2$  ( $\mu\text{s}/\text{cm}$ ) can be scanned, to make a specified part of a decay curve up to the level of the screen full horizontal scale as far as possible, measure decay curve of the amplitude ratio of 2:1, measure distance between any two points as  $M$  (cm), and calculate the filament lifetime in Eq. (10).
  4. Repeat the process two times; identify and record the average filament lifetime  $\tau_F$ . If the values differ more than 10%, then the sample is not appropriate for the method.
- Note: Especially in the case of p-type silicon, the lifetime may change rapidly with the density of carrier, so for the wide range of lifetime, the mean value may deviate from the true values.
- (i) Check whether there is a trapping effect, which can be determined by the changes in the filament lifetime value from points on the decay curve below 25% of the decay curve peak ( $\Delta V_0$ ). If lifetime value increases along the lower part of the curve, then there is a trap. Trapping effect can be eliminated by heating the sample to 50–70°C or with a stable background light. If trapping causes > 5% to the decay curve, the sample cannot be measured by this method.
- (j) Check whether the carriers meet the sweep-out conditions at the ends of the sample, shut off the light source, and measure the DC voltage  $V_{dc}$  on the sample. Calculate the product of  $V_{dc}$  and  $\sqrt{\tau_F}$  if the value is not greater than the corresponding constant provided in Table 2; sweep-out effect is not significant. Table 2 shows the constant of the recommended length of the sample. For other sample lengths, the condition is given in Eq. (11):

**Table 2** Minority carrier mobility,  $\text{cm}^2/\text{Vs}$ , and sweep-out condition constants for suggested sample lengths (SEMI MF28-0317 2017)

Material	Mobility	Type A	Type B and type C
N-type Germanium	3800	7.3	12
N-type Germanium	1800	11	18
P-type silicon	1400	12	20
N-type silicon	470	20	35

$$V_{dc}\sqrt{\tau_F} \leq (30 L/\sqrt{\mu}) \quad (11)$$

where:

$L$  = sample length; the unit is millimeter (mm).

$\mu$  = minority carrier mobility; the unit is square centimeter per volt seconds ( $\text{cm}^2/\text{Vs}$ ) (Table 2).

$\tau_F$  = filament lifetime; the unit is microseconds ( $\mu\text{s}$ ).

If the sweep-out conditions are not met, this can reduce the sample current  $V_{dc}$ , this will change the curve shape, and the  $\tau_F$  value will change as well.

(k) Check whether the low injection level conditions are met.

Use the same current value which can satisfy the sweep-out conditions, switch on the light, and measure the pulse amplitude's peak value ( $\Delta V_0$ ).

If  $\Delta V_0/V_{dc} \leq 0.01$  injection level is low for this method.

If  $\Delta V_0/V_{dc} > 0.01$  filament lifetime correction is needed according to Eq. (12):

$$\tau_F = \tau_{Fmeas} [1 - (\Delta V_0/V_{dc})] \quad (12)$$

where:

$\tau_{Fmeas}$  = value of the filament lifetime as measured in the above item #f or calculated in item #h-(4)

$\tau_F$  = corrected value of the filament lifetime

## Calculation

(a) Low injection level bulk minority carrier lifetime can be calculated by Eq. (13):

$$\tau_b = (\tau_F^{-1} - R_{SF})^{-1} \quad (13)$$

where:

$\tau_b$  = bulk minority carrier lifetime, the unit is microseconds ( $\mu\text{s}$ ).

$\tau_F$  = filament lifetime, the unit is microseconds ( $\mu\text{s}$ ).



**Table 3** Surface recombination rate,  $R_{SF}$  ( $\mu\text{s}^{-1}$ ), (SEMI MF28-0317 2017)

Material	Type A	Type B	Type C
P-type germanium	0.3230	0.00813	0.00215
N-type germanium	0.01575	0.00396	0.00105
P-type silicon	0.01120	0.00282	0.00075
N-type silicon	0.00420	0.00105	0.00028

$R_{SF}$  = surface recombination rate. Standard samples  $R_{SF}$  are given in Table 3; unit is microseconds<sup>-1</sup> ( $\mu\text{s}^{-1}$ ).

(b) When samples are rectangular,  $R_{SF}$  can be obtained by Eq. (14):

$$R_{SF} = \pi^2 D [L^{-2} + W^{-2} + T^{-2}] \quad (14)$$

where  $L$  = sample length,  $W$  = sample width, and  $T$  = sample thickness.

(c) For right circular samples, the sample length is  $L$ , sample radius is  $r$ , and then the  $R_{SF}$  can be obtained by Eq. (15):

$$R_{SF} = \pi^2 D [L^{-2} + (9/16 r^2)] \quad (15)$$

where  $D$  = minority carrier diffusion coefficient and the unit is square centimeters per second ( $\text{cm}^2/\text{s}$ ).

---

## Test Methods for Measuring Metallic Impurities and Surface Metallic Contamination in Polysilicon

Metal impurities can be present in silicon in two forms. Metals can be present as substitutions for a silicon atom where it is surrounded by silicon atoms and/or as small samples of precipitate in the bulk of silicon. The concentration of silicon metal impurities can be measured by neutron activation analysis, mass spectrometry, atomic absorption spectrometry, and X-ray fluorescence measurement.

Neutron activation method can measure almost all metal impurities, but it requires a neutron radiation sources. Secondary ion mass spectroscopy (SIMS) is used to measure impurities in silicon. SIMS requires calibration standards to accurately quantify the metal concentration in silicon. SIMS has a lower detection limit of 1 ppb. Presently inductively coupled plasma mass spectroscopy (ICP-MS) is used to measure low levels of metals in silicon. ICP-MS requires that the silicon be dissolved in a solution before analysis.

## Test Method for Measuring Metallic Impurity Contamination in Polysilicon

Metal impurities can be determined by dry processes such as secondary ion mass spectrometry or neutron activation analysis. Wet methods of silicon analysis involved digesting silicon samples with a mixture of hydrofluoric acid and nitric acid and then carrying out the analysis with ICP-MS.

### Apparatus

- (a) Inductively coupled plasma mass spectrometry (ICP-MS).
- (b) Analytical balance: sensitivity 0.1 mg.
- (c) Fume hood.
- (d) Containers: All containers shall be made of materials which are resistant to hydrofluoric acid, such as polytetrafluoroethylene (PTFE) or perfluoroalkoxy resin (PFA).
- (e) Electrically heated plate.

### Sample Preparation

- (a) Pulverize the chunk or chip polysilicon samples without introducing contaminants.
- (b) Treat the sample in a suitable concentration of hydrofluoric acid solution. If necessary, add the appropriate concentration of nitric acid solution, and then rinse with ultrapure water (surface cleaning is recommended for the bulk metal analysis).
- (c) Dry the sample at 100 °C–110 °C.
- (d) Granular polysilicon can be used without grinding to fine particles.

### Procedure

- (a) Sample amount: It is recommended to take samples according to Table 4, accurately to 0.1 mg; different experiments can be adjusted according to the actual situation.
- (b) Measurement times: Take the measurement three times independently for each sample, and choose the arithmetic mean of these three measurement results.
- (c) Blank test: Do blank test with the sample.
- (d) Standard solution preparation: For the mixed element standard solution, prepare it by mixing the standard storage solution of iron, chromium, nickel, copper, and zinc, then diluting the standard storage solution step-by-step (from mg/mL to ng/mL, the proper acidity shall be maintained during the process of dilution). The concentration of each element in this mixed element standard solution is 1 µg/mL.

Standard series of working solution (or calibration standards) preparation: A 1000 µg/mL standard must be available for the analyte element and should be less than 1 year old. Respectively, add 0 µL, 50 µL, 100 µL, 300 µL, and 500 µL of mixed element standard solution into five clean 100 mL volumetric flasks, then add 40 mL nitric acid solution separately, and use ultrapure DI water to fill

the volumetric flask to the mark. The concentrations of iron, chromium, nickel, copper, and zinc in these standard series of solutions are 0  $\mu\text{g/L}$ , 0.50  $\mu\text{g/L}$ , 1.00  $\mu\text{g/L}$ , 3.00  $\mu\text{g/L}$ , and 5.00  $\mu\text{g/L}$ , respectively. The concentrations of the standard series of working solutions should be as close as possible to the concentrations of the elements to be measured in the sample solution. For the yttrium standard solution preparation, take 100  $\mu\text{L}$  of yttrium standard storage solution, place into a 100 mL volumetric flask, add 40 mL nitric acid solution, dilute with ultrapure water to the mark, and shake. The concentration of this standard solution is 1  $\mu\text{g/mL}$ . For the yttrium standard working solution preparation, take 200  $\mu\text{L}$  of yttrium standard solution, place into a 100 mL volumetric flask, add 40 mL nitric acid solution, dilute with ultrapure water to the mark, and shake. The concentration of this standard working solution is 2  $\mu\text{g/mL}$ .

- (e) Sample solution preparation: Place the sample into an open container, which should be clean and with a suitable volume. Add the suitable amount of nitric acid-hydrofluoric acid mixed solution according to Table 4, and dissolve the sample by heating. Evaporate the solution to dryness at 160–170  $^{\circ}\text{C}$ . After cooling at room temperature, add 4 mL mixture of nitric acid and hydrofluoric acid to dissolve the residues, and then evaporate the solution to dryness at 160–170  $^{\circ}\text{C}$  again. Add 4 mL nitric acid solution, fully shake, and ensure the residues are completely dissolved. Then transfer the solution to a 10 mL volumetric flask, using the ultrapure water for volume constant, shake, and wait for ICP-MS measurement.
- (f) Instrumental analysis: Prior to testing, the inductively coupled plasma mass spectrometry (ICP-MS) needs to be set in appropriate operating conditions and tuned to achieve the best test conditions. The elements to be analyzed in the sample and the internal standard element's isotopes should be selected according to Table 5. Analyze the blank solution, the sample solution, and the standard series of working solutions using the inductively coupled plasma mass spectrometry (ICP-MS). Take the yttrium standard working solution as the internal standard, and use internal standard method for calibration.

Make the calibration curves by using the ratios of the metal element contents to that of internal standard element in the standard series working solutions as the ordinate and using the concentrations of each element in the standard working solution as abscissa. The mass concentrations of each analyte in the blank solution and the sample solution will be automatically given by the ICP-MS. Other methods of quantitative analysis also can be used according to the situation.

**Table 4** Volume (mL) of acid mixture recommended to digest the amount of polysilicon sample (g)

Single element impurity content (ng/g)	Sample amount (g)	Nitric acid-hydrofluoric acid mixed solution dosage (mL)
1–10	2	40
10–100	1	20
100–500	0.5	10
500–2000	0.2	8

**Table 5** Isotope selection summary table for ICP-MS

Metal elements to be measured				Internal standard element <sup>a</sup>	
Element name	Isotope	Element name	Isotope	Element name	Isotope
Sodium	<sup>23</sup> Na	Chromium	<sup>53</sup> Cr	(A)(A)(A)(A)(A)	(A)(A)(A)(A)
Magnesium	<sup>24</sup> Mg	Iron	<sup>56</sup> Fe	Yttrium	(A) <sup>89</sup> Y
Aluminum	<sup>27</sup> Al	Nickel	<sup>60</sup> Ni		
Potassium	<sup>39</sup> K	Copper	<sup>63</sup> Cu		
Calcium	<sup>40</sup> Ca	Zinc	<sup>66</sup> Zn		
Titanium	<sup>49</sup> Ti	Molybdenum	<sup>96</sup> Mo		

<sup>a</sup>Other elements cannot be used as internal standard except yttrium due to matrix compatibility

### Calculation

Calculate the mass fractions of the metallic impurities in the sample according to Eq. (16):

$$w_x = \frac{C_2 - C_1 \times V}{m} \quad (16)$$

where:

$w_x$  = mass fractions of Fe, Cr, Ni, Cu, and Zn in the sample; the unit is ng per gram (ng/g).

$C_1$  = concentrations of the elements to be measured in the blank solution; the unit is ng per milliliter (ng/mL).

$C_2$  = concentrations of the element to be measured in the sample solution; the unit is nanograms per milliliter (ng/mL).

$V$  = volume of the sample solution; the unit is milliliter (mL).

$m$  = mass of the sample; the unit is gram (g).

### Test Method for Measuring Surface Metallic Contamination in Polysilicon

This test method is used to measure surface metal contamination on polysilicon chunks, SEMI MF1724-1104 (2004). Surface contamination can be used to monitor polysilicon production process. This method is the quantitative analysis of surface trace metals by using acid extraction of metals from the polysilicon surface. Metal content is analyzed by inductively coupled plasma mass spectrometry (ICP-MS). This method can be used for polysilicon rod, chunk, granule, or single-crystal silicon. Due to the irregularity in shapes of chunks, granules, or chips, the quantitative analytical values are based on the sample weight. Typically, 50–300 gm samples may be needed to achieve the detection limit around 0.01 parts per billion weight (ppbw). The temperature, exposure time, composition, or acid strength is the determining factor for the depth of surface etched or efficiency of the extraction process. It is recommended that <1% of the sample weight may be removed in this

test method. This method is suitable for silicon surface trace metal impurities, such as sodium, magnesium, aluminum, potassium, calcium, titanium, chromium, iron, nickel, copper, zinc, molybdenum, etc. The detection limit of the instrument is dependent on the dilution factor, spectral response to analyte, instrument sensitivity, acid recovery efficiency, blank data, and method interferences.

### Apparatus

Follow the details as described in Section 2.8.1 (A).

### Sample Preparation

- (a) The sample preparation is carried out in a Class 6 clean room. Around 5 Kg polysilicon sample may be selected from a batch of products (or production lot) for the analysis.
- (b) To ensure the consistency of sample analysis and interlaboratory comparison of analytical values for bulk samples, a standard weight and volume are recommended. Select six chunk samples, each size is about 3 cm × 3 cm × 3 cm, and the weight is about 50 g each. The total weight of the sample is about 300 g.

### Procedure

- (a) In the clean room, transfer the chunks to a clean PTFE bottle. Weigh the samples (if sample size allowed, take about 50 g), measurement accuracy to 0.01 g.
- (b) Three measurements were carried out independently, at least one sample with an external surface, and the arithmetic mean of the three measurements was taken.
- (c) Blank test: Standard blank should be prepared with the sample.
- (d) Preparation of mixed element standard solution: Follow the details as described in Section 2.8.1 (C)-d. Use the standard storage solution of Na, Mg, Al, K, Ca, Ti, Cr, Fe, Ni, Cu, Zn, and Mo, and mix into a standard solution of mixed elements, where each element concentration is 1 µg/mL. Prepare the series working solutions for the calibration standards, control standards and blanks.
- (e) Preparation of sample solution: After weighing the sample, add 250 mL of acid etching mixture to cover the chunk samples, and close the lids. Place the bottles onto the electric heating plate at 70°C for about 60 min constant temperature heating. Remove the heat, cool it to room temperature, remove the chunks, and rinse the surface with ultrapure DI water into the bottle. The bottle with the leaching solution is heated on a hot plate at 120–150°C to dryness. Remove the bottle from the hot plate; cover the surface of the dish, after cooling at room temperature; and add 4 mL of 5% nitric acid solution. Transfer the solution to a 10 mL volumetric flask, use ultrapure water to make the volume to the mark, shake, and the solution is ready for the ICP-MS analysis.
- (f) Instrumental analysis: Follow the details as described in Section 2.8.1 (C)-f.

### Calculation

Follow the details as described in Section 2.8.1 (D).

## Raw Materials and Other Test Methods

### Metallurgical-Grade Silicon Test Methods

The feedstock for polysilicon production is metallurgical-grade (MG) silicon, with certain requirement of purity, usually more than 99% of silicon. The impurities in the metallurgical-grade silicon mainly include silica, carbonaceous reactants, and metallic impurities such as iron, aluminum, calcium, carbon, etc. Metallic impurities of iron, aluminum, and calcium can be measured with two of the following methods. One is ICP-OES testing method, in which the sample is dissolved with acid and the solution is then analyzed with ICP-OES. The other method is fluorescence spectroscopy.

Dry process using compression pressure prototype test method, the X-ray spectrum emitted by secondary excitation wavelength, and its intensity can be used for qualitative and quantitative analyses. Activated by the primary X-ray beam in the light tube on the sample, each element in the sample generates respective characteristics of secondary radiation. This secondary radiation passes through the collimator to the spectral crystal, only the radiation with special wavelength which satisfies the diffraction condition is strengthened, while the rest with different wavelength radiation are weakened.

Carbon content in the metallurgical silicon can be determined under the action of propellants and the sample with the oxygen flow inside a high-frequency induction furnace heating combustion method. Carbon is converted to carbon dioxide ( $\text{CO}_2$ ) and carbon monoxide ( $\text{CO}$ ), carried by the oxygen to the measuring chamber, and the intensity of special wavelength is detected by infrared detector. The absorption is proportional to the concentration of total carbon content in the sample.

### Trichlorosilane Test Methods

Trichlorosilane (TCS or  $\text{SiHCl}_3$ ) purification is an important part of silicon manufacturing process. TCS and silane are produced from MG-Si and HCl reaction followed by distillation process to purify them from volatile compounds. During distillation process the impurities can be reduced from  $10^{-7}$  to  $10^{-10}$  orders of magnitude.

Using gas chromatographic, various chlorosilane components (dichlorosilane, silicon tetrachloride, etc.) and HCl can be separated in the chromatographic column. The quantitative measurements of these components can be performed by using external known standard and by area normalization method. P content can be tested by gas chromatography using flame photometric detector (FPD).

Trace element analysis is an important means of monitoring the distillation efficiency. TCS monitoring after the purification can be done in two ways: (i) by growing polysilicon rod in a small reduction furnace to test the polysilicon, (ii) by collecting TCS impurities as acid soluble and using ICP-OES or ICP-MS for metallic impurity analysis.

## High-Purity Gas Test Method

In polysilicon production process, the main use of high-purity gas is hydrogen. High-purity gas may have trace impurities such as oxygen, carbon monoxide, argon, nitrogen, etc. Trace impurities can be quantitatively measured using gas chromatography (GC). Moisture content can be monitored using the dew-point meter or moisture analyzer.

GB/T 3634.2-2011 (Wang et al. 2011) standards can be followed for pure hydrogen, high-purity hydrogen, and super pure hydrogen analysis. GB/T 8979-2008 (He et al. 2008) standards can be followed for pure nitrogen, high-purity nitrogen, and ultrapure nitrogen analysis. These two standards specify how to analyze the physical parameters of high-purity gases and impurities.

## High-Purity Water Test Method

Ultrapure deionized water is used in the solar and semiconductor industries. Impurity content in water can be divided into two types: conductive impurities and non-conductive impurities. To make high-purity water, remove the non-conductive impurities and then conductive impurities. The impurity content in pure water can be analyzed by ICP-MS.

## Ambient Air Test Method

The handling and manipulation of polysilicon materials needs to be done in a clean environment. The clean room air should be monitored routinely, and the classification is dependent on the number of particles measured with method ISO 14644-1 (2015).

## Packing Material Test Methods

Polysilicon is a very high-purity material. Polysilicon manufacturer is very strict with its packaging materials. High-quality and clean packaging materials are critical to reduce or eliminate impurities. Packaging materials and their impacts on surface contamination of polysilicon should be monitored using ICP-MS or ICP-OES for trace-level impurities. The details can be referenced to SEMI-PV74-0216 (2016).

---

## Conclusion

This chapter introduces the characterization methods of polysilicon materials. Float zone (FZ) process is used to obtain monocrystalline silicon from polycrystalline chunk and granular silicon materials. The analytical detection principles and

processes including the type of analytical equipment used for impurity analysis are described. Donor and acceptor quantification; conductivity and resistivity measurements; determination of interstitial oxygen and substitutional atomic carbon content; minority carrier lifetime; measurements of bulk and surface metallic impurities, etc.; and various analytical methodologies are described. Detection technologies for raw materials such as MG silicon and trichlorosilanes are also introduced in this chapter.

---

## References

- Y. Chen, W. Liu, F. Wu, GB/T 1550-1997 Standard methods for measuring conductivity type of extrinsic semiconducting material (1997)
- D. He, Y. Chen, M. Tian, H. Li, GB/T 8979-2008 Pure nitrogen and high purity nitrogen and ultra-pure nitrogen (2008)
- I. He, Y. Wang, H. Zhang, Y. Liu, GB/T 1554-2009 Testing method for crystallographic perfection of silicon by preferential etch techniques (2009)
- ISO 14644-1:2015 Clean rooms and associated controlled environments – part 1: classification of air cleanliness by particle concentration (2015). <https://www.iso.org/standard/53394.html>
- J. Li, X. He, J. Zhang, S. Duan, GB/T1551-2009 Test method for measuring resistivity of monocrystalline silicon (2009)
- L. Luo, H. Liang, R. Tan, Y. Wang, X. Wang, GB/T 4060-2007 Polycrystalline silicon – examination method -vacuum zone-melting on boron (2007)
- SEMI MF1391-1107 (reapproved 0912) Test method for substitutional atomic carbon content of silicon by infrared absorption (2012)
- SEMI MF1630-1107 Test method for low temperature FT-IR analysis of single crystal silicon for III-V impurities (2012)
- SEMI MF1708-1104 Practice for evaluation of granular polysilicon by Melter-Zoner spectroscopies (2004)
- SEMI MF1724-1104 Test method for measuring surface metal contamination of polycrystalline silicon by acid extraction-atomic absorption spectroscopy (2004)
- SEMI MF28-0317 Test methods for minority carrier lifetime in bulk germanium and silicon by measurement of photoconductivity decay (2017)
- SEMI PV17-1012 Specification for virgin silicon feedstock materials for photovoltaic applications (2012)
- SEMI PV74-0216 Test method for the measurement of chlorine in silicon by ion chromatography (2016)
- S. Wang, T. Cai, T. Shen, W. Shen, J. Chen, H. Fang, J. Zhang, GB/T 3634.2-2011 Hydrogen-Part 2: pure hydrogen, high pure hydrogen and ultrapure hydrogen (2011)
- X. Yang, I. He, GB/T 1555-2009 Testing methods for determining the orientation of a semiconductor single crystal (2009)
- Y. Yang, J. Yuan, S. Sun, J. Liu, D. He, Y. Wang, J. Liu, Y. Cao, H. Liang, GB/T25074-2010 Solar grade polysilicon (2010)





Dazhou Yan

## Contents

Introduction .....	38
Process Overview .....	38
Synthesis of Trichlorosilane (TCS) .....	39
Distillation and Purification of TCS .....	42
TCS Decomposition and Reduction .....	47
Vent Gas Recovery .....	58
STC Hydrogenation .....	60
Recycling of By-product Dichlorosilane (DCS) .....	64
Filament Preparation .....	65
Comprehensive Utilization of By-produced Energy .....	66
Conclusion .....	67
References .....	67

## Abstract

Polysilicon is the elementary raw material for integrated circuits and photovoltaic products. In recent years, the technology of polysilicon made great progress, its cost dramatically reduced, and it provided ideal conditions for photovoltaic energy power to meet the state-set price. This chapter summarizes the achievements of Siemens process, including the technology process, the technical principle, main equipment, technological operations, polysilicon quality control, energy-saving feature, and cost reduction. This could be used as a reference for the production of polysilicon.

---

D. Yan (✉)  
China ENFI Engineering Corp, Beijing, China  
China Silicon Corporation Ltd., Luoyang, Henan, China  
e-mail: [yandz@enfi.com.cn](mailto:yandz@enfi.com.cn)

---

**Keywords**

Polysilicon · Siemens process · TCS synthesis · TCS distillation and purification · CVD reactor · Vent gas recovery · STC hydrogenation · Comprehensive utilization of by-product

---

**Introduction**

This chapter describes the process of preparation of high-purity polysilicon. Metal-grade silicon as the raw material reacts with hydrogen chloride to produce trichlorosilane (TCS); after distillation and purification, trichlorosilane deposits on the filament of high-purity silicon to obtain polysilicon at the temperature of 1050 °C in a high-purity hydrogen environment. The sections of this chapter discuss TCS synthesis, TCS distillation and purification, TCS decomposition and hydrogen reduction in CVD reactor, vent gas recovery, STC hydrogenation, comprehensive utilization of other by-products, filament preparation, and comprehensive utilization of by-produced energy.

Technical contents including the principles, reaction conditions, major equipment, materials, energy consumption, and so on are the reference for scholars and engineers engaged in teaching, research, and production of polysilicon.

**Process Overview**

The global polysilicon output was 370,000 t (Bohua Wang 2017) in 2016, of which the output by using Siemens process (trichlorosilane process) accounts for more than 90%. Siemens process is still the mainstream of polysilicon production process in the world today.

Siemens process uses metallic silicon powder containing approximately 98.5% of silicon and 1.5% of B, P, C, Fe, Al, Ca, Cu, Ni, Zn, and other metal impurities as the feed, which reacts with HCl to produce TCS, STC, and various impurity chlorides. By taking advantage of the difference in boiling point between TCS and impurity chlorides, the process then separates the impurity chlorides from TCS through distillation and purification to ultimately obtain high-purity TCS, which is then subjected to reduction and decomposition reactions in high-purity hydrogen environment, and deposits on the filament to obtain high-purity polysilicon. See Fig. 1 for the process flow.

The main processes include TCS synthesis, TCS distillation and purification, TCS decomposition and hydrogen reduction, vent gas recovery, STC hydrogenation, comprehensive utilization of other by-products (dichlorosilane, hydrogen chloride, and hydrogen), filament preparation, and comprehensive utilization of by-produced energy.

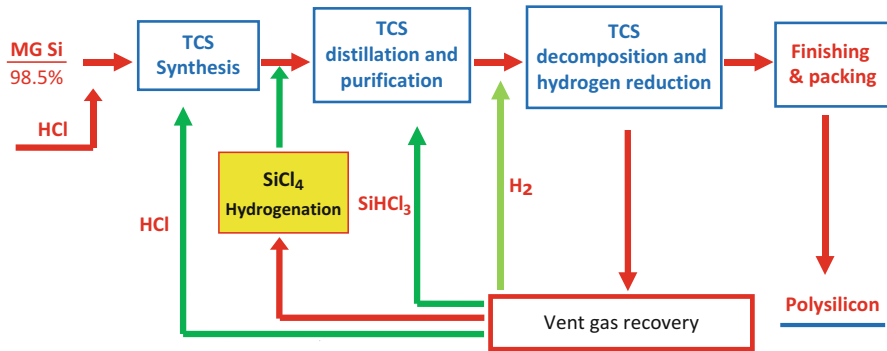


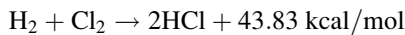
**Fig. 1** Improved Siemens process flow

## Synthesis of Trichlorosilane (TCS)

### Preparation of Hydrogen Chloride (HCL)

Hydrogen chloride (HCL), with a molecular weight of 36.5, is a pungent odor gas, and it is water-soluble to generate hydrochloric acid, having strong corrosivity upon contact with water.

Hydrogen chloride can be generated through burning chlorine with hydrogen and the reaction equation is as follows:



The produced hydrogen chloride contains a small amount of water, which shall be separated and removed through dehydrofrosting methods.

Preparation conditions:

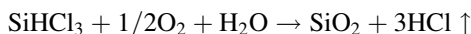
1. Application pressure of  $\text{H}_2$  and  $\text{Cl}_2$  shall be lower than  $0.8 \text{ Kg/cm}^2$
2.  $\text{H}_2\text{Cl}_2$  equals to 1.1:1 (volume ratio), and the volume of  $\text{H}_2$  slightly exceeds that of  $\text{Cl}_2$  for its full reaction, so as to prevent generation of free chlorine
3. Purity requirements:  $\text{H}_2 \geq 98\%$ ,  $\text{Cl}_2 \geq 96\%$ ,  $\text{HCl} \geq 96\%$ , moisture in  $\text{HCl} \leq 0.05\text{--}0.1\%$ , and free chlorine  $< 0.02\%$
4. The temperature of synthesis reactor outlet shall be within  $280\text{--}450 \text{ }^\circ\text{C}$ ; otherwise, the excess temperature will exacerbate the reaction in reactor even causing an explosion. Besides, it will exacerbate corrosiveness of the synthesis reactor.

### Synthesis of TCS

#### 1. Properties of TCS

At normal temperature, purified trichlorosilane ( $\text{SiHCl}_3$ ) is a colorless, transparent, volatile, and flammable liquid, with strong pungent odor, and its chemical characteristics are as follows:

- (a) Easily hydrolyzable, deliquescent, and forms intensive fumes in the air. Hydrolysis reaction is as below:



Highly volatile and easily gasified with a low boiling point

- (b) Easily prepared and reduced  
 (c) Highly combustible and explosive, with ignition point of 28 °C and ignition temperature of 220 °C, producing hydrogen chloride and chlorine while burning; its chemical reaction equation is as below:



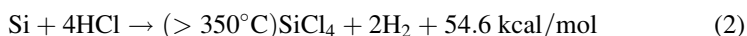
- (d) Extremely steady to metals, even not reacting with sodium  
 (e) Its vapor is hypotoxic

## 2. TCS synthesis process

Silicon powder reacts with hydrogen chloride in the fluidized bed reactor to produce  $\text{SiHCl}_3$  and its reaction equation is as below:

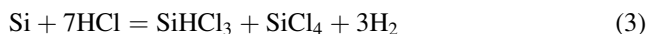


The reaction is exothermic and the reaction heat shall be extracted in real time, so as to maintain reaction temperature in the reactor between 280 °C and 320 °C and improve product quality and actual recovery. As the temperature rises, the quantity of produced  $\text{SiCl}_4$  will increase and massive  $\text{SiCl}_4$  will be produced while it exceeds 350 °C, with its reaction equation as following:



If the temperature is improperly controlled, there may be more than 50% of  $\text{SiCl}_4$  produced, as well as various chlorosilane and polyethylene halide compounds.

The predominant reaction in the reactor is



The mole ratio of  $\text{SiHCl}_3$  (TCS) to  $\text{SiCl}_4$  (STC) can be varied by controlling the reactor temperature.

## 3. TCS synthesis process and main equipment

The fluidized bed reactor is generally used for TCS synthesis reactor. See Fig. 2 for its process flow.

The chlorinator is a fluidized bed reactor. Metallurgical grade Si powder is fed to the middle of the reactor. HCl gas and some recycled gas from the hydrogen recycle plant and the distillation towers are also introduced to the bottom of the reactor through a gas distributor plate.

Since the reaction is exothermic, the reaction zone must be cooled by an external cooling media. The condenser pipe, with circulation cooling medium, used to regulate the temperature.

#### 4. Separation of synthetic product and recycling of tail gas

The reaction products containing TCS, STC, HCl, and H<sub>2</sub> with entrained solid particles first go through a cyclone, where most of the unreacted solids and some condensed metallic chlorides are removed. The collected dust from the cyclone is treated as solid waste.

Synthetic products are firstly condensed through  $-35\text{ }^{\circ}\text{C}$  refrigerants to obtain mixtures of TCS and STC, and then they are sent for crude distillation, separation, and purification. The rest gas is collected for recovery. See Table 1 for components of the typical tail gas.

Upon process requirements, components shall be separated and recycled without any intervention from foreign ingredients. The separation process mainly relies on the difference of boiling point, the performance, and the molecular polarity. Chlorosilane is recycled through compression and condensation, using the adsorption characteristics of activated carbon, control adsorption conditions, and H<sub>2</sub> and HCl in tail gas. After adsorption reaches a certain extent, chlorosilane is desorbed

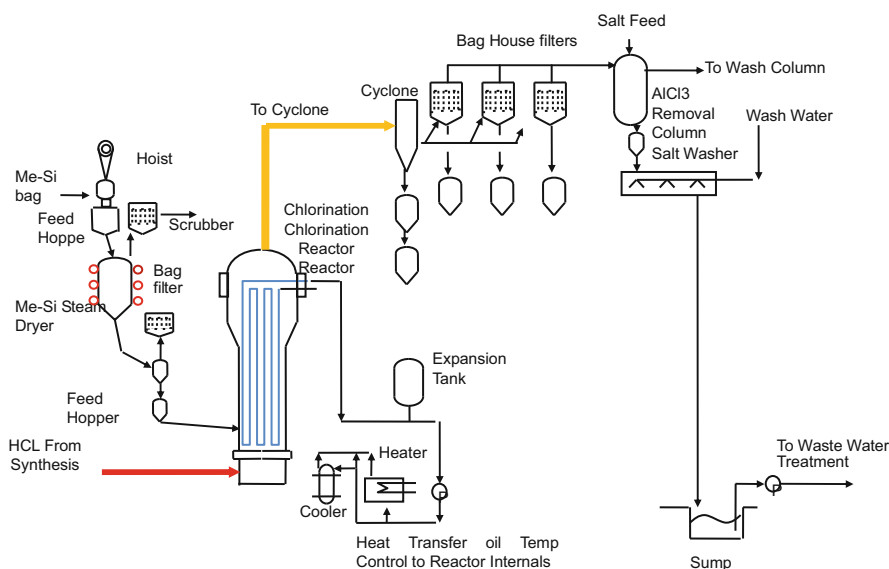


**Fig. 2** Chlorination process flow

**Table 1** Typical chemical analysis of synthesis tail gas

Component	H <sub>2</sub>	HCl	SiHCl <sub>3</sub>	SiCl <sub>4</sub>	Total
Content (%)	53.97	43.49	1.39	1.15	100

and recycled. At last, recycle chlorosilane through compression, condensation, and separation. Purified  $H_2$  and  $HCl$  either can be sent to  $HCl$  synthesis system or TCS synthesis system, or be absorbed by water for acid preparation. The entire process is free of materials discharged to the outside, which fundamentally solves environmental issues.

## Distillation and Purification of TCS

### Requirements of Polysilicon for TCS Quality

In the production process of polysilicon, its raw material TCS may be extracted from composite materials, hydride materials, dry recovered materials with tail gas reduction, and so on. These materials may contain chlorides and complexes as shown in Table 2, with contents from level ppm to level ppb, and they shall be purified to appropriate contents, ensuring polysilicon quality. According to polysilicon quality requirements, presume and calculate the corresponding relation among B&P impurities concentration in final high-purity TCS and polysilicon quality index under reaction atmosphere, temperature, and pressure in the reactor. See Table 3 (Standardization administration of the people's republic of China 2014, 2016).

Moreover, metallic contamination in polysilicon is closely related to the material, mainly including TCS and hydrogen. Given the low probability of introduced metallic impurities in hydrogen, impurities in TCS consequently become the main contamination sources in polycrystalline substrates. The corresponding relation, as

**Table 2** Properties of impurity halides and complexes in TCS

Complex	Boiling point °C	Complex	Boiling point °C	Complex	Boiling point °C
$SiH_3Cl$	-10.0	$CHCl:$ $CHCl$	48.4	$PSCl_3$	125
$SiH_2Cl_2$	8.2	$C_3H_7PH_2$	50-53	$TiCl_4$	135.8
$CH_3BCl_2$	11.2	$P_2H_4$	56	$PCl_5$	160 (sublimation)
$BCl_3$	12.1	$(CH_3)_3SiCl$	57	$SbCl_5$	172
$PFCl_2$	13.9	$SiCl_4$	57	$PH_3 \cdot BCl_3$	180
$B_2H$	18.0	$CH_3Cl$	61.2	$AlCl_3$	180 (sublimation)
$PO_2F_6Cl$	21-23	$B_2Cl_4$	65.5	$SbCl_3$	216
$(CH_3)_2PH$	21.5-25	$CH_3SiCl_3$	66.4	$FeCl_3$	315
$SiHCl_3$	31.5	$PCl_3$	76	$ZnCl_2$	732
$CH_3 \cdot CCl_2$	37	$CCl_4$	76.8	$CuCl_2$	1359
$(CH_3)_3P$	37.8	$CH_3PCl_3$	77-79	$MgCl_2$	
$CH_3SiHCl_3$	41	$POCl_3$	105.8		
$B_5H_9$	48	$CrO_2Cl_2$	116.3		

**Table 3** Relation between polysilicon quality and TCS quality

Item	Relation between boron impurity and raw material			Relation between phosphorus impurity and raw material		
	Polysilicon ppba	Polysilicon ppbw	TCS ppbw	Polysilicon ppba	Polysilicon ppbw	TCS ppbw
Polysilicon quality level						
Electronic grade level I	0.05	0.020	0.004	0.15	0.166	0.034
Electronic grade level II	0.08	0.031	0.006	0.25	0.277	0.057
Electronic grade level III	0.10	0.039	0.008	0.30	0.332	0.069
Super PV level	0.18	0.07	0.03	0.75	0.830	0.17
PV level I	0.26	0.102	0.021	1.24	1.373	0.284
PV level II	0.54	0.212	0.044	3.00	3.321	0.686
PV level III	1.32	0.519	0.107	6.32	6.997	1.446

**Table 4** Relation between polysilicon metal impurity and TCS quality

Item	Total metallic contamination of Fe, Cr, Ni, Cu, and Zn					
	10	20	30	50	100	200
Total metals of polysilicon (ng/g)	2.07	4.13	6.20	10.33	20.66	41.32
Total metals of TCS (ng/g)						

shown in Table 4, between TCS and polycrystalline base metal is determined through theoretical calculation and practical operation.

Impurities in TCS are mainly removed through distillation and impurity contents vary with TCS sources. Therefore, separation and purification conditions differ from one another and multiple systems are set accordingly to meet separation, crude distillation, distillation, and purification requirements.

### Typical TCS Distillation and Purification System

Typical TCS purification tower consists of synthetic crude distillation, hydrogenated crude distillation, recovery tower, dry separating tower, and distillation tower. Select sieve-plate tower or filled tower according to material whether containing solid particles or substances with high boiling points. Generally, crude distillation chooses sieve-plate tower, distillation chooses packed tower.

#### 1. Synthetic and hydrogenated crude distillation purification system

TCS in synthetic materials is with content between 80% and 85% and that in hydrogenated condensed materials between 20% and 25%; the others include STC and various chloride impurities, and it may include solid particles. Consequently, the sieve-plate tower is applicable to crude distillation. See Fig. 3 for separation and purification process:

The crude distillation tower, processing condensed materials for synthesis and hydrogenation reaction, commonly consists of two towers to separate  $\text{SiHCl}_3$  from  $\text{SiCl}_4$ , and to distill off TCS (crude distillation product) at top of Tower 2#,

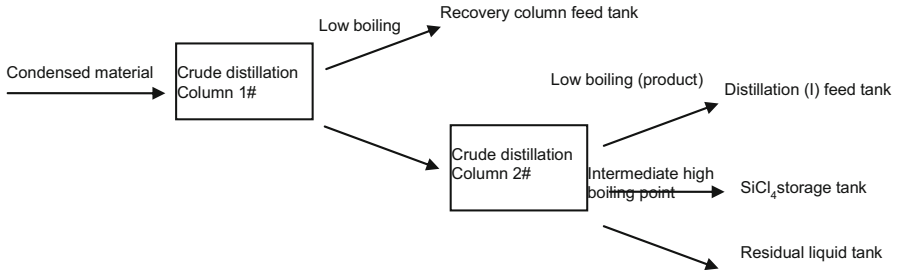


**Fig. 3** Synthesis and hydrogenated crude distillation flow

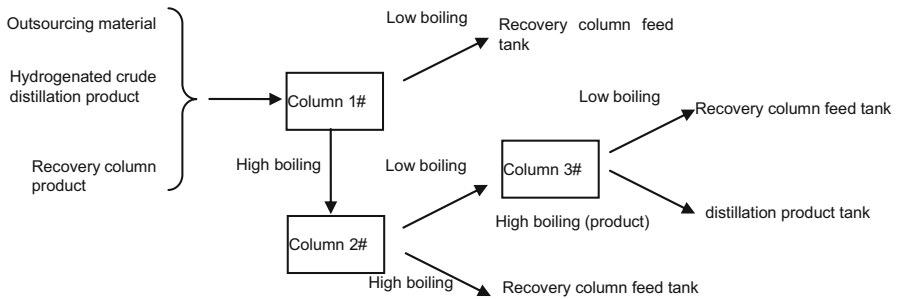


**Fig. 4** Distillation flow

with the content of  $\text{SiHCl}_3 \geq 99\%$ . The rest  $\text{HCl}$  and  $\text{SiCl}_4$ , as the materials, are sent to distillation feed tank for further purification.

## 2. Distillation tower

The distillation tower consists of three packed towers and its rectifying materials mainly include outsourcing materials, hydrogenated crude distillation products, and recovery tower products. Main components of the materials include  $\text{SiHCl}_3 \geq 98\%$ , a small amount of  $\text{SiCl}_4$ , and  $\text{HCl}$ .  $\text{SiHCl}_3$  in products from the bottom of Tower 3# reaches 99.95% after distillation, and it also includes a minor amount of  $\text{HCl}$  and other impurities. The products, as raw materials, are sent to distillation product tank for storage and the flow diagram is as shown in Fig. 4

## 3. Vent gas recovery material distillation tower

Vent gas recovery material distillation tower consists of two packed towers mainly used for processing vent gas recovery material recycling materials in the raw material plant. The purity of  $\text{SiHCl}_3$  in product almost reaches 100% after vent gas recovery material distillation while it also contains a small amount of dichlorosilane, which may be used as the raw material of reduction plant.  $\text{SiCl}_4$  in high boiling point material of Tower 2#, with content  $\geq 99.9\%$ , maybe as the hydrogenation material. See Fig. 5 for vent gas recovery material distillation tower:

## 4. Recovery tower

Recovery tower consists of three towers mainly used for processing materials with low purity, typical components include  $\text{HCl}$  0.05%,  $\text{SiH}_2\text{Cl}_2$  1.6%,  $\text{SiHCl}_3$



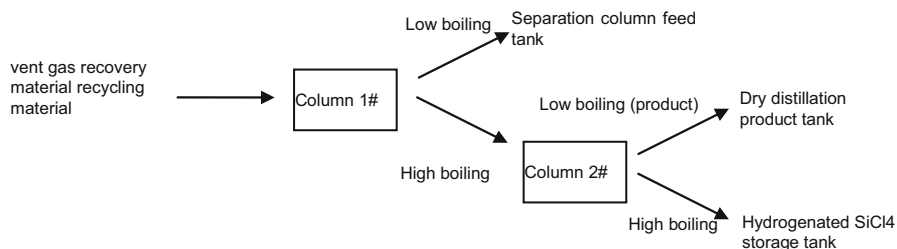


**Fig. 5** Vent gas recovery material distillation tower flow

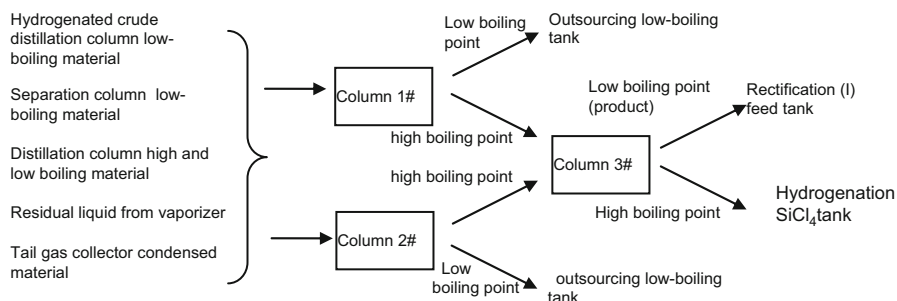


**Fig. 6** Recovery tower process flow

70.0%, and  $\text{SiCl}_4$ . Tower 1# and 2#, with a feed of high boiling point material recycled, are sieve-plate towers and Tower 3# is packed tower. Distilled product from the top of Tower 3# includes  $\text{SiHCl}_3 \geq 99.9\%$  and a small amount of  $\text{HCl}$ , and the product is sent to the distillation tower for further  $\text{SiHCl}_3$  purification. Distilled product from the tower bottom contains  $\text{SiCl}_4 \geq 99.8\%$  and a small amount of  $\text{SiHCl}_3$ , which will be sent for dehydrogenation reaction. See Fig. 6 for recovery tower flow

##### 5. Differential pressure thermal coupling distillation technology

For the differential pressure thermal coupling distillation technology, pinch technology is adopted to adjust pressure of two towers and to use overhead vapor from the high-pressure tower as the heat source for liquid at bottom of the low-pressure tower through technical optimization and matching, so as to complete cooling and heating load exchange inside of tower groups for full energy utilization. Overhead vapors from the high-pressure tower will not directly enter condenser but shell side of condensation reboiler, and condensated materials will enter auxiliary condenser for further condensation, so as to ensure that materials are fully condensed to liquids or to subcooled substances; liquid in bottom of the low-pressure tower will be vaporized through tube side of condenser reboiler, and the cold source required for the condensation of overhead vapor from high-pressure tower and the heat source necessary for vaporization of

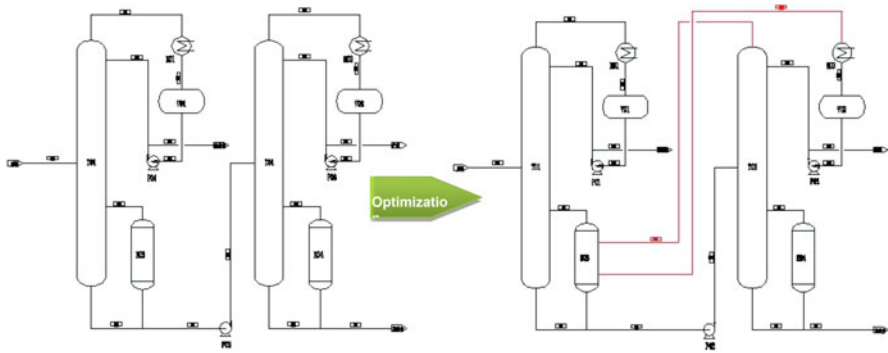


**Fig. 7** Differential pressure thermal coupling distillation and purification process

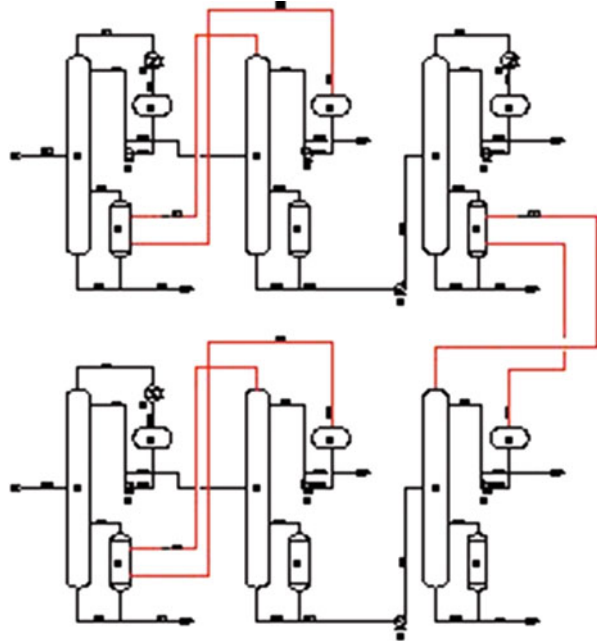
liquid in bottom of the low-pressure tower are neither needed in the process. Consequently, 40–50% energy consumption is reduced (Jiang et al. 2010). It is shown in Fig. 7.

In order to recycle heat quantity of reduction system and further reduce energy consumption, pressure of the first distillation tower is adjusted to ensure overhead vapors' temperature within 50–70 °C, enabling the common circulating water used as cold source for condenser; pressure of the second distillation tower is adjusted to ensure the average temperature difference, between temperature of overhead vapor from the second distillation tower and the bottom of the first distillation tower, is within 15–30 °C, so as to meet heat exchange temperature difference requirements between them. Moreover, it shall be ensured that the high-temperature water, cooling medium of reduction process, can be used as the heat source for the second distillation tower, so as to enable cooling and heating load exchange between purification process and reduction process and reduce polysilicon costs as many as possible.

Multi-tower-system differential pressure thermal coupling distillation technology integrates single-tower-group differential pressure thermal coupling technology with interelement two-tower parallel differential pressure thermal coupling technology and continuous differential pressure thermal coupling among tower groups of towers and multi-group tower differential pressure thermal coupling among different towers of different tower groups are achieved through optimization of technology, equipment configuration, and pipings. See Fig. 8 for the process of differential pressure thermal coupling technology used for two groups of tower systems:

As shown in the flow diagram, two groups of distillation towers consist of three towers respectively, in which differential pressure thermal coupling technology is all adopted between Tower 1 and 2 in the first distillation tower group, Tower 1 and 2 in the second distillation tower group, Tower 3 in the first distillation tower group and

**Fig. 8** Process of multi-tower-system thermal coupling distillation and purification



Tower 3 in the second distillation tower group. Namely, the cold source is applicable to Tower 1 and 3 in the first distillation tower group as well as Tower 1 in the second distillation tower group while the heat source is used for Tower 2 in the first distillation tower group as well as Tower 2 and 3 in the second distillation tower group. This will minimize energy consumption of the entire distillation and purification system, with reduced energy consumption between 50% and 80%, and will reduce polysilicon costs as many as possible.

## TCS Decomposition and Reduction

### Overview of Polysilicon Deposition Process

High-purity hydrogen and high-purity gaseous chlorosilane (TCS, DCS) are introduced into the CVD reactor in a certain proportion, and chemical vapor deposition reaction takes place on the surface of high-temperature filament carrier (about 1050 °C) to obtain high-purity polysilicon products; meanwhile, the by-product vent gas in the reactor is discharged out of the system and then enters the follow-up process for material recovery. See Fig. 9 for a sketch showing the specific deposition process.

The reactions in the reduction reactor are very complicated during the operation. TCS's hydrogen reduction reaction and thermal decomposition reaction are the main reactions, and others are side reactions.

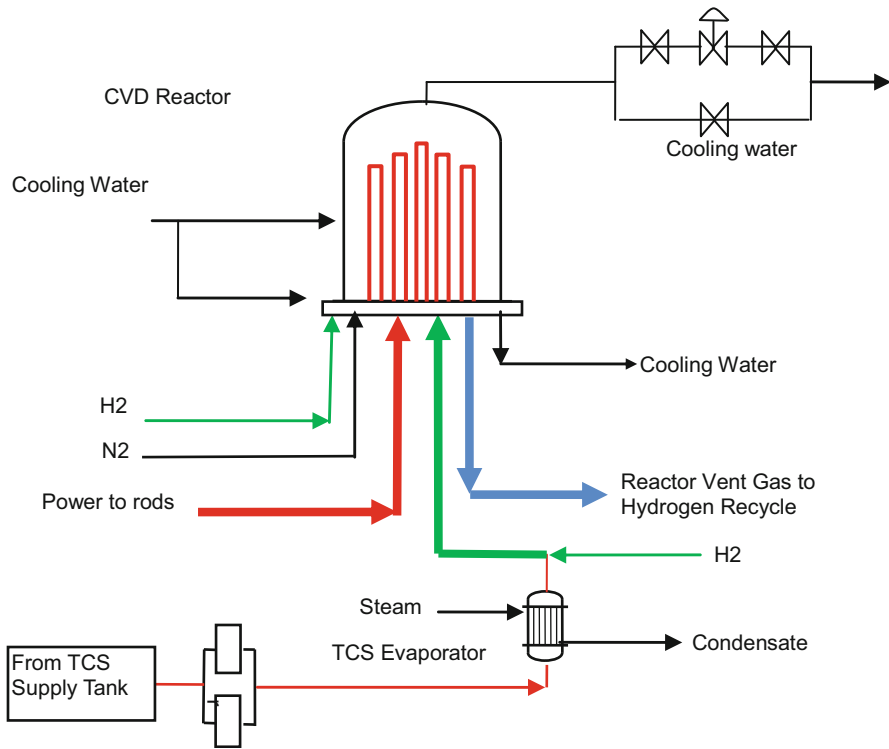
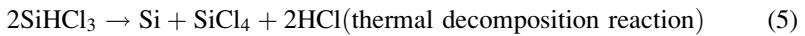
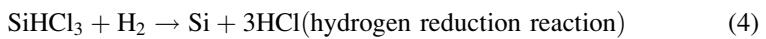
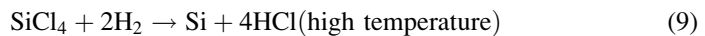
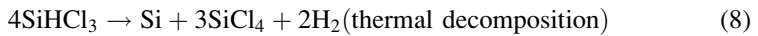
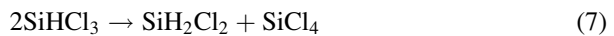
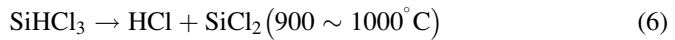


**Fig. 9** CVD reduction process

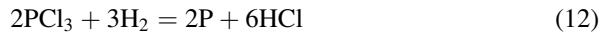
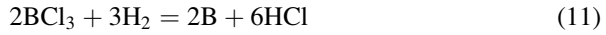
The main reaction equations are as follows:



The side reaction equations are as follows:



Reduction reaction of impurities:



### Analysis of Factors Affecting Polysilicon Deposition

Polysilicon deposition in the reactor is a sophisticated physicochemical process and its effective deposition is closely related to structure and type of the reactor, feed ratio, reactor temperature, reactor pressure, structure and type of nozzle, and current-voltage curve, and those factors are inter-conditioned and interactive; theoretical research of polycrystalline silicon deposition indicates that high-efficiency polysilicon deposition will not be realized unless above factors are controlled under the optimal matching state. See Figs. 10 and 11 (Yan et al. 2016) for the reaction process:

#### 1. Feed ratio

The feed gas ratio refers to the mole ratio of hydrogen to TCS in materials entering the reactor. During polysilicon deposition, TCS concentration directly depends on the feed gas ratio. Namely, higher the feed ratio is, more hydrogen is. It tends to form a strong reducing atmosphere, contributing to the reduction of material consumption (TCS) costs. The increase of the feed gas ratio means the presence of more hydrogen, and more hydrogen means more adequate reduction reaction of  $\text{SiHCl}_3$  and restrained generation of  $\text{SiCl}_4$ . However, excessive ratio will dilute concentration of the reaction mass (TCS) and reduce the growth rate of silicon rod, and will increase power consumption and also cause waste of hydrogen. Therefore, feed gas ratio is limited in a certain range of practical processes and the optimum ratio shall be adopted during reactions.

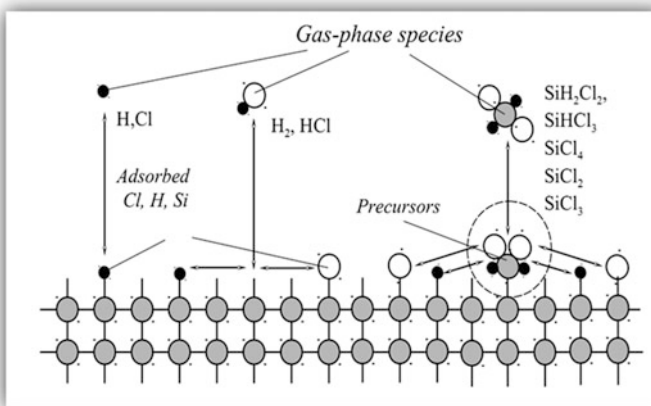


**Fig. 10** Vapor deposition on silicon rod surface

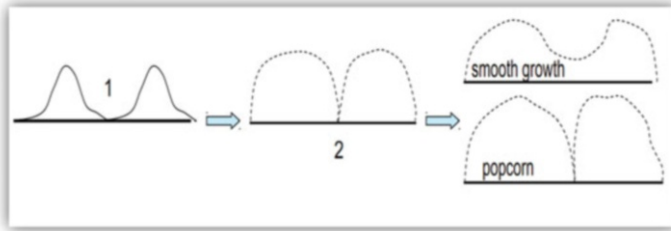


Fig. 11 Polysilicon rod surface growth schematic diagram

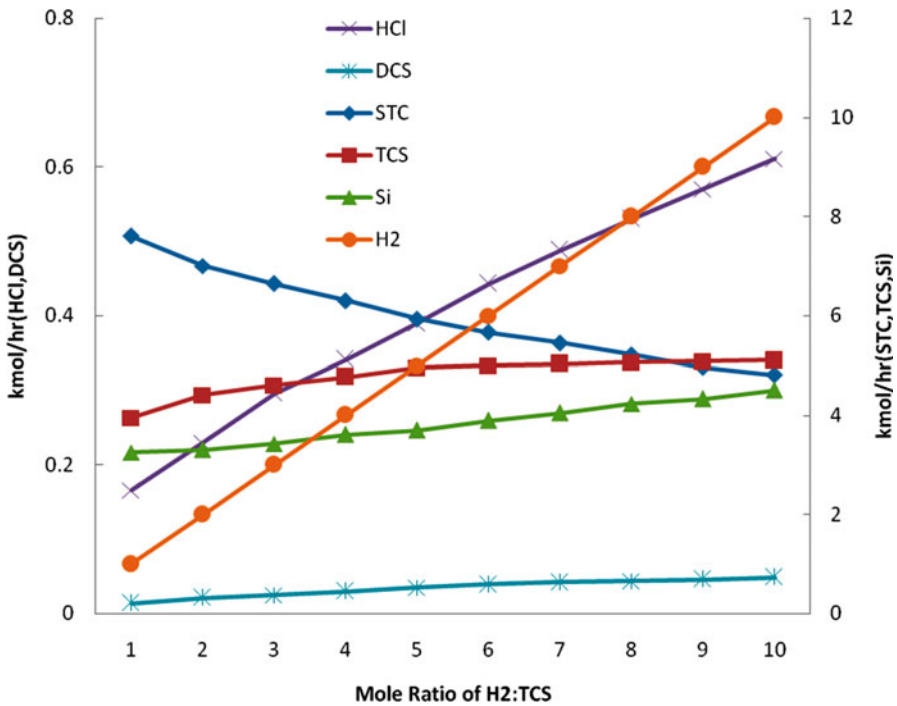
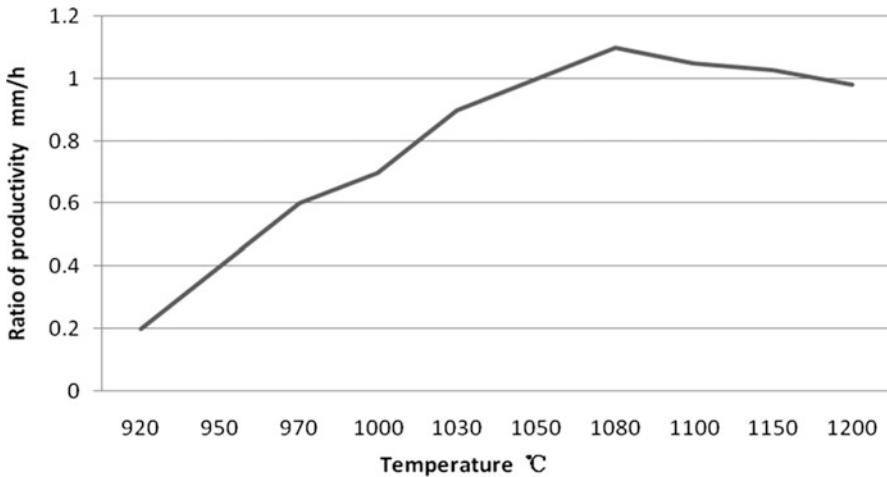


Fig. 12 Product components under different feed ratios

Through analog computation, material components in products will vary with different feed ratio (the mole ratio of hydrogen to TCS) in the reactor if the TCS in the feed is 1 kmol/h as shown in Fig. 12.

As shown in the above figure, hydrogen concentration in the reactor increases as the feed ratio rises, which restrains the thermal decomposition reaction and the hydrogen reduction reaction prevails. Consequently, the primary conversion rate of chlorosilane improves. Even so, the feed ratio shall not be too high, and main reasons include:



**Fig. 13** Deposition rate of polysilicon over temperature

- (a) Excessive hydrogen will dilute chlorosilane and reduce reactant concentration, which will reduce the probability that chlorosilane molecule impacts silicon rod surface as well as polysilicon deposition velocity. Namely, the polysilicon output is reduced due to that.
- (b) High hydrogen ratio will increase the load of the subsequent tail-gas treatment system and it is negative for energy conservation of the entire system. In practical production, the determined mole ratio of hydrogen to TCS is between 1.5 and 3.5, and the ratio may be adjusted accordingly as the polysilicon diameter varies in production process.

In feeding process, dichlorosilane (DCS) may also be added to facilitate polysilicon deposition in the reactor, so as to restrain the side reaction in the reactor and to reduce power consumption and material consumption.

## 2. Reaction temperature

TCS reduction and decomposition reaction are both endothermic, as a result, increased reaction temperature will accelerate the reaction and will also improve deposition rate of silicon. However, silicon deposition is a physical crystallization process, and when the reaction temperature is higher than the crystallization temperature, the deposition and crystallization rate decreases on the contrary as the reaction temperature increases. Therefore, the temperature of silicon rod carrier in the reactor is controlled by reaction equilibrium temperature to the maximum temperature, with optimum deposition temperature between 1050 and 1080 °C. The deposition rate will increase as the temperature rises within the temperature range. See Fig. 13 for the process.

## 3. Reaction pressure

Vapor deposition occurs in the reactor, and the chemical vapor deposition reaction may come to an end after the feed gas stays in the reactor for 5–20 s. Molecular collision probability will be improved by boosting pressure, so as to

accelerate the deposition rate. As shown in chemical reactions (4), (5), (6), (7), (8), (9) in the reactor, the equilibrium tends to be adverse to polysilicon deposition with the increase of pressure, while low pressure, resulting in a decrease of molecular collision probability, is also adverse to polysilicon deposition. Therefore, operating pressure of the reactor shall be controlled and the industrially proven pressure, facilitating polysilicon deposition, is between 0.5 MPa to 0.6 MPa.

#### 4. Gas flow field

During polysilicon production, its diameter constantly changes in the reactor, requiring feed gas to vary accordingly, so as to ensure the optimum polysilicon growth rate, the maximum output, and the minimum energy consumption, including gas flow control and gas flow rate control.

##### (a) Gas flow control

Given constant reactor volume, an increase of gas mixture in the reactor will also improve collision probability between TCS gas and silicon rod. Meanwhile, rapid deposition of silicon particles on the surface of silicon filament carrier increases silicon rod diameter and also enlarges carrier deposition area that provides spaces for deposition of silicon particles and so repeated. Consequently, silicon rod growth is accelerated, its growth cycle is shortened and polysilicon output in a single reactor is improved. Besides, intensified gas turbulence, caused by gas disturbance in the reactor after increasing feed, enables removing HCl gas blanket above silicon rod surface.

According to practical production, increased gas feed results in reduced unit power consumption, shortened deposition time, prolonged operation cycle of reactor, increased operation time, and improved annual output capacity. However, when the feed rate is increased to a very high level, this will result in increased reaction intensity in reactor and accelerated deposition rate of silicon particle, when the silicon rod surface is unable to receive excessive silicon particles, as a result, atomization appears in the reactor and amorphous product is produced. Moreover, unreacted gas mixture enters the subsequent vent gas recovery material system with vent gas, resulting in increased loads in vent gas recovery material recovery process, increased costs, and waste of gas mixture. As suggested by production, the maximum material is proportional to silicon rod surface and larger reactor body requires more polysilicon rods and more feeds. See Fig. 14 for common feed curve, and see Fig. 15 (Yao et al. 2011) for the overall flow field vector diagram, simulated through computer, inside the reactor

##### (b) Vector inside reactor

The gas containing TCS and hydrogen in the reactor, with a flow rate between 1 m/s and 2 m/s above silicon rod surface, will facilitate polysilicon deposition on silicon rod surface and will help hydrogen chloride, the byproduct material, being timely separated from the silicon rod. Laminar flow shall be prevented to keep the gas flow in turbulence state.



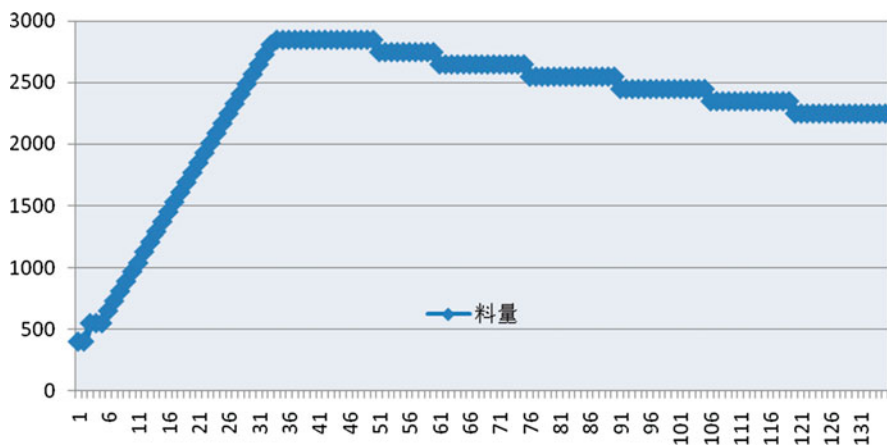


Fig. 14 CVD reactor feed curve

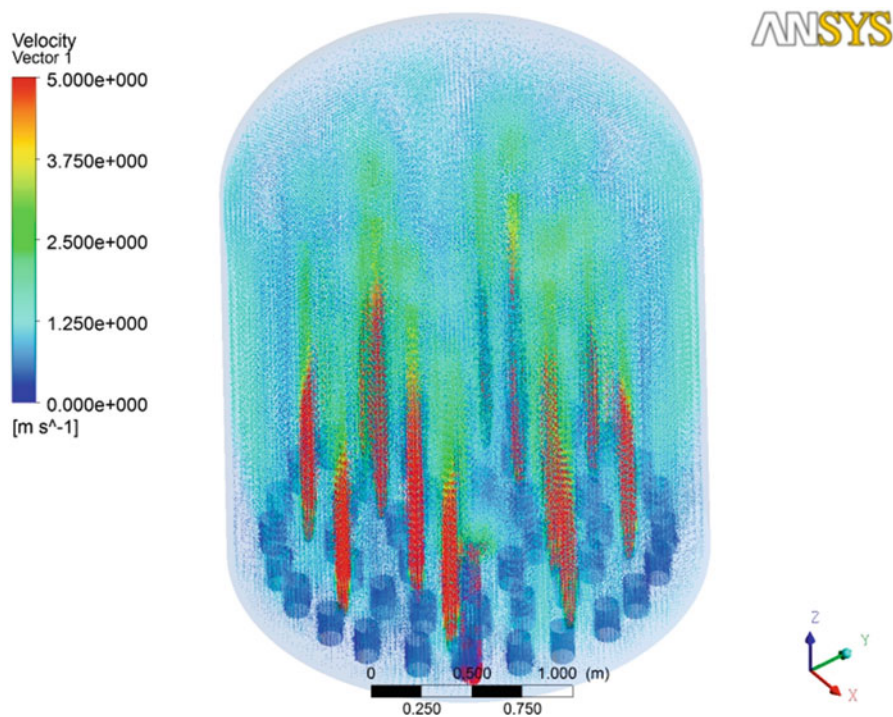
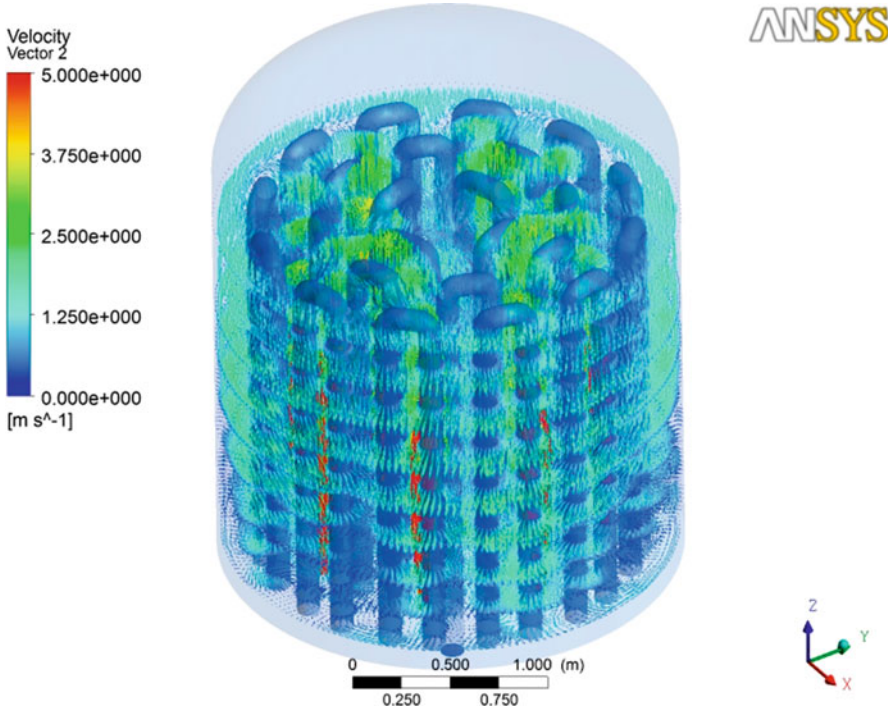


Fig. 15 Diagram of overall flow field

Generally, the gas flow is controlled by nozzles. Nozzle's location on base plate of reactor, nozzle openings, and its control during operation are relied on to enable feed gas to form the optimal flow field in the reactor, thus, gas velocity shall also remain high at the nozzles, normally at 70–90 m/s or



**Fig. 16** Velocity vector on the reactor vertical section

so in order to produce an intensive turbulence, allowing an ideal concentration distribution for mixed gas flow in the entire reactor during gas flow ascending, which is conducive to gas-phase concentration renewal over silicon rod surface.

According to production practice, nozzle opening makes a significant difference on gas flow distribution. For instance, under the condition with same feeding pressure, constant temperature and amount, the bigger the opening is, the lower the flow rate is, with low feed lifting height, low top gas concentration, and high crossbeam temperature, easily resulting in rod crack. Coral-like and popcorn-like polysilicon can be easily formed if local rod surface temperature is too high. The smaller nozzle aperture is, the higher the flow rate is, as a result, material may be taken out from the reactor and sent to the vent gas system before depositing on silicon rod surface. Besides, filament fall, caused by filament vibration, may occur in the reactor with high-silicon filament. Therefore, it is very important to select proper nozzle aperture and nozzle structure and the opening type shall be determined on the basis of repeated trials in production. See Fig. 16 for the velocity vector on the reactor vertical section in the computer simulation model. See Fig. 17 for vertical sections' temperatures of the furnace (Yan et al. 2014b).

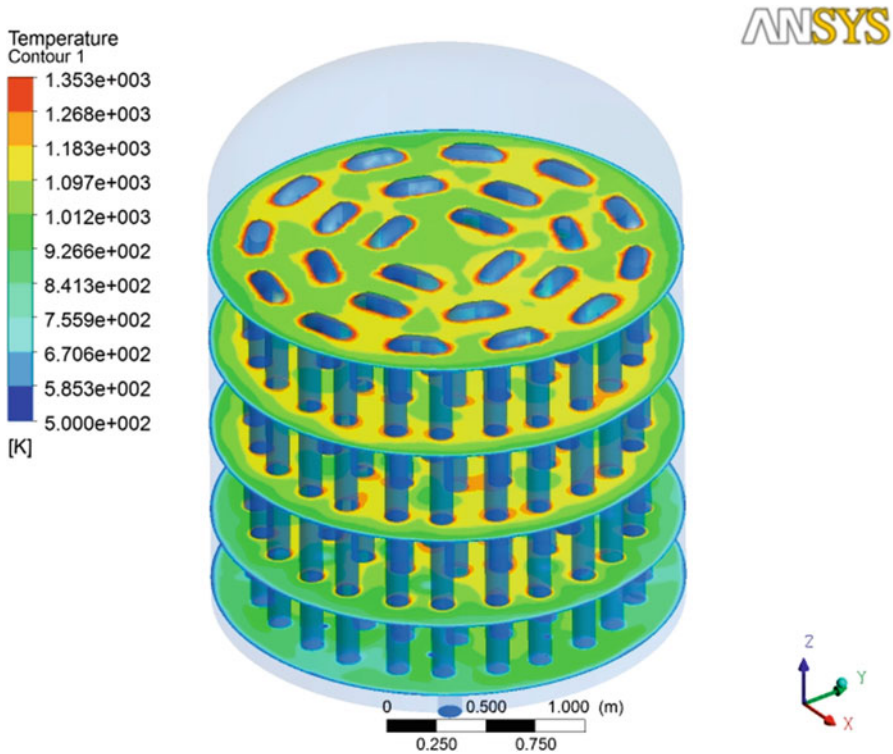


**Fig. 17** Furnace vertical sections' temperatures

### 5. Current–voltage curve

The resistance of silicon rod with high-purity polysilicon is high at normal temperature and would decline with the increasing of the temperature and reduction of the rod's diameter. For the production of polysilicon at 1050~1080 °C, it is required to keep the silicon rod in the reactor at a constant temperature and to keep the heating power constant while the silicon rod volume and materials increasing. With the result of that the reduction, electrical system's power design and regulation are responsible for providing the condition of polysilicon production. In the case, the current and voltage shall be regulated and controlled as per the curve shown in Fig. 18 without disturbance.

The charging of current such as its amount and duration plays a decisive role in reduction reaction. Therefore, reasonable current/voltage curves should be developed based on production experience to maintain a stable polysilicon production.

### 6. Adding of dichlorosilane (DCS)

Adding 1–2% of dichlorosilane into TCS has little impact on the reduction power consumption, which slightly declines. It can be deduced that a few dichlorosilane slightly influences the consumption because it is the by-product of gas reaction in the reactor, also involving in the reaction.

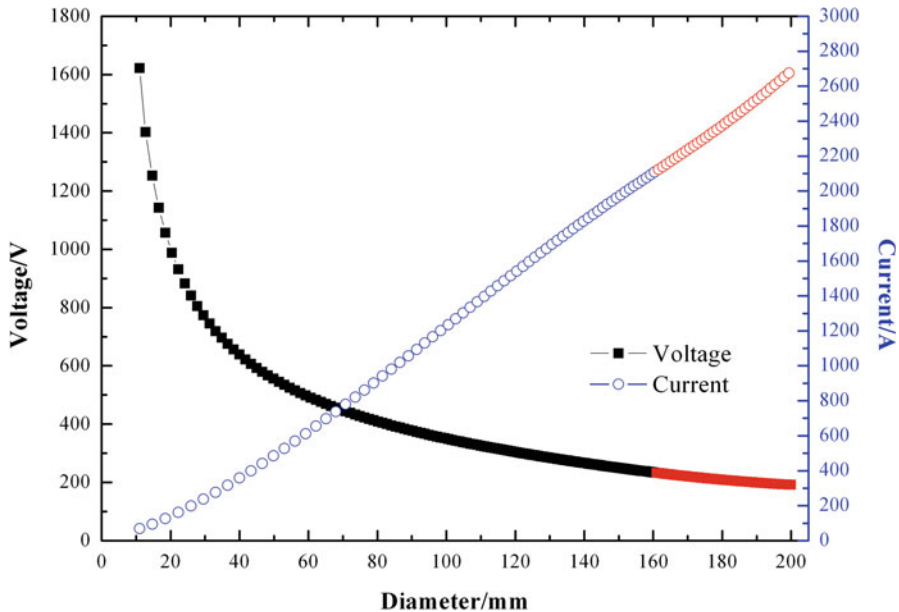


**Fig. 18** U/I curve for the CVD-reactor

Adding 3–5% of dichlorosilane into TCS significantly reduces the power consumption, by about 3–6 kWh/kg-Si, and the adding proportion is in direct proportion to the reduction power consumption.

When adding more than 7% of dichlorosilane into TCS, it will react intensely, which is hard to control causing atomization a large amount of amorphous silicon dust in the reactor and product with coralline or popcorn appearance. Default phase tends to occur in the reactor operation. The polysilicon rod fails to stop operating at normal cycle. As a result, the production of a single reactor drops with the material consumption going up. Although the power consumption descends greatly, it is not efficient in the terms of balance of economic benefit. Therefore, it is advised to add 3–5% of dichlorosilane into TCS in actual production.

## 7. Parameter calculation during polysilicon deposition

### (a) Feed gas ratio

The ratio of hydrogen to TCS is in mole. The ratio of hydrogen to TCS can be deduced from the mole flow, which is calculated from the mass flow rate of TCS or hydrogen. The computational formula is:

1st step: Mole number  $n_1 = \frac{m_1}{M_1} n_1$  of  $H_2$  in the gas mixture

$$n_1 = m_1/M_1$$

Wherein  $m_1$  refers to the mass of hydrogen in kg or  $Nm^3$  in the gas mixture,

and  $M_1$  stands for the molar mass of hydrogen, 2 kg/kmol or 22.4 Nm<sup>3</sup>/kmol.

2nd step: mole number  $n_2$  of TCS in the gas mixture

$$n_2 = m_2/M_2$$

Wherein,  $m_2$  refers to the mass of TCS in kg in the gas mixture, and  $M_2$  stands for the molar mass of TCS, 135 kg/kmol.

3rd step: gas mixture ratio  $N$

$$N = n_1/n_2$$

(b) Deposition rate

Deposition rate: the weight of polysilicon sediments in unit time in the reactor. The computational formula is:

$$V = M/T$$

Wherein

$V$  represents the deposition rate,

$M$  stands for the weight of polysilicon in a single reactor,

and  $T$  represents the running time (h) of a single reactor, beginning from the charging of gas until the stoppage of such charging.

(c) Primary reduction conversion rate

Primary reduction conversion rate is the proportion of polysilicon generated as a result of reactions between the materials fed into the reactor. The magnitude of primary conversion rate greatly influences the material and energy consumption of the reactor. A higher primary conversion rate means a higher single reactor's production as well as a lower consumption of both material and energy.

The amount of TCS in the vent gas changes with the generation of STC, which can be used to reduce the load of the following vent gas recovery material system, reducing the general energy consumption of the production system. The computational formula is:

$$W = 100\% \frac{m_1}{m_2 \times (M_{Si}/M_{Si} + M_{SiHCl_3})}$$

Wherein  $W$  represents the primary reduction conversion rate,

$m_1$  the product weight in a single reactor,

$m_2$  the gross weight (kg) of the gas mixture charged into a single reactor,

$M_{Si}$  the silicon molecular weight,

and  $M_{TCS}$  the TCS molecular weight.

(d) Reduction power consumption

(e) Reduction power consumption defines how much power is needed to produce one kilo polysilicon (unit: kWh/kg-Si). The computational formula is:

$$P = E/M$$

Wherein

$P$  refers to the power consumed by a single reactor (kWh/kg-Si),

$E$  the total power consumption of a single reactor (kWh),

and  $M$  the weight of product polysilicon (kg-Si) in a single reactor.

8. Comprehensive utilization of heat energy, reducing power consumption

Based on the computer simulation, feed distribution are optimized, and various inlet nozzles designed, allowing for even distributed thermal and flow field and material concentration, as well as lower power and material consumption, further facilitating the growth of dense polysilicon rod with a smooth surface, uniform diameter, and high quality.

The mainstream polysilicon reactors include reactors with 24, 27, 36, 40, or 48 pairs of rods. A single reactor could produce 5–13 tons product with a reduction reaction power consumption of polysilicon dropping from 120 kWh/kg-Si in 2009 to 550 kWh/kg-Si or below. Under given optimal operating conditions and less strict appearance requirements for the polysilicon, the power consumption would drop to 40 kWh/kg-Si. SIEMENS reactor normally uses such mediums as high-temperature water and conduction oil for cooling purpose, recovers such portion of heat, and uses it for purification and activated carbon regeneration. It also recovers the reduction power consumption in the form of heat for use. Leading companies could make the waste heat recovery rate reach above 75% (Yan et al. 2014a). Overall power consumption of the whole polysilicon production process drops from 200 kWh/kg-Si in 2009 to about 85 kWh/kg-Si today, including 75% of power consumption by reduction reaction converted to heat for recycling ( $55 \times 75\% = 41.25$  kWh/kg-Si). Therefore, it is calculated that the actual modified SIEMENS polysilicon production process achieves an overall power consumption of 43.75 kWh/kg-Si ( $85 - 41.25$  kWh/kg-Si). With further optimization, modified Siemens process is expected to make the figure drop to below 70 kWh/kg-Si (Photovoltaic Industry Association of China 2017).

## Vent Gas Recovery

### Principle of Vent Gas Recovery Process

The vent gas from the polysilicon reactor contains  $H_2$ ,  $HCl$ ,  $SiHCl_3$ ,  $SiCl_4$ , and  $SiH_2Cl_2$ . The gas mixture compressed and cooled to a certain degree produces condensed  $SiHCl_3$  and  $SiCl_4$ , which then can be separated by distillation tower.  $SiHCl_3$  can be directly delivered into the reduction system to produce polysilicon.  $SiCl_4$  can be delivered to the hydrogenation process to produce  $SiHCl_3$ , which can be separated through the distillation tower and then delivered into the reduction system to produce polysilicon. The noncondensable gas after the compression and cooling mainly consists of  $H_2$  and  $HCl$ . Under pressure and low temperature, the  $H_2$  and  $HCl$  can be separated from the gas mixture by special separation process (activated carbon adsorption method or cold  $SiCl_4$  and  $HCl$  solution method for recovering  $HCl$ ).  $H_2$  without water and impurities could be reused in the reduction process. On the other hand,  $HCl$  can charge into the synthesis process for producing  $SiHCl_3$ . The dry recovery is able to protect the vent gas from any water and to separate its constituents from each other. All constituents will be free of pollution and be reused by the system.

### 1. Cooling before compressing vent gas

0.5–0.6 MPag vent gas from the reduction process will go through the vent gas water cooler, gas-gas heat exchanger for vent gas, and vent gas chilled water cooler in order. Then the gas will enter the elution tower for further cooling under  $-20\text{ }^{\circ}\text{C} \sim -25\text{ }^{\circ}\text{C}$ . After this step, chlorosilane is basically separated from the vent gas;

### 2. Compression and condensation of vent gas

The condensed vent gas will be processed to gas with pressure of 1.1~1.5 Mpag (compressed air) by the compressor. The chlorosilane can be cooled and separated by the multistage heat exchanger where the gas goes through primary compressed gas heat exchanger, compressed air chilled water cooler, secondary compressed gas heat exchanger, compressed gas cooler, tertiary compressed gas heat exchanger, and compressed gas chiller in order. And then the gas will be cooled to  $-50\text{ }^{\circ}\text{C}$  and charged into the absorption tower.

The gas processed by the tower, namely the gas after absorption, will go through the tertiary, secondary, and primary compressed gas heat exchangers in order and then the absorber. Some low-temperature chlorosilane condensate occurs during cooling of the compressed air. The condensate can be fed into the elution tower with the leachate for recovering the cold capability of low-temperature condensate.

### 3. Absorption and desorption

After the deep cooling, the hydrogen chloride, for the most part, still exists in the hydrogen, which can be absorbed in the absorption tower by chlorosilanes. Then the hydrogen chloride can be separated from the chlorosilane by the desorption tower.

As absorption requires low temperature but desorption high temperature, heat exchanger multistage dual purpose heat exchanger is adopted for the rich and lean solution heat transfer to reduce the amount of  $-55\text{ }^{\circ}\text{C}$  refrigerants used so as to cut the cost.

Low-pressure desorption technology is used in the desorption process, allowing low-temperature gas products to be discharged at the top of the tower. After heat exchange by higher temperature leachate, the low-temperature hydrogen chloride is fed to the recovery process.

### 4. Hydrogen purification

Gas after absorption still contains a trace of chlorosilane and hydrogen chloride. Activated carbon temperature and pressure swing adsorption method will be adopted to process the gas and produce high purity hydrogen, which can meet the production requirements of polysilicon production. At the same time, the hydrogen can be recycled, reducing the demand for original hydrogen production and saving operation cost.

The hydrogen after adsorption can be directly used in the reduction reaction. Gas generated during the activated carbon desorption and regeneration processes can be compressed by the compressor for the hydrogenation process. All the rest gas can return the absorption tower for following separation after deep cooling.



The above processes can recover 98% of each constituent of the vent gas from the polysilicon production. The recycled and separated  $H_2$ ,  $HCl$ , chlorosilane, etc., can satisfy the demands of the polysilicon production by completely being recovered and reused in the system, which substantially reduces discharge and emission of waste gas, wastewater, and waste solid as well as material consumption.

## STC Hydrogenation

### STC Hydrogenation Overview

The Siemens process can produce 1 t polysilicon and 15–20 t  $SiCl_4$ , which at room temperature is liquid and not good for storage and transportation. With consideration of its characteristics, the STC is converted into TCS by hydrogenation and returned to the system as a raw material. In this way, a clean production is achieved.

STC hydrogenation can be mainly realized by low- and high- temperature hydrogenation, hydrochlorination, and plasma hydrogenation technologies (Wan et al. 2010). Hydrochlorination refers to adding the hydrogen chloride (2~5%) recovered by the system to the low-temperature hydrogenation process, in which the hydrogen chloride is mainly involved in the synthesis reaction with Si powder. The reaction mainly produces STC and a few amount of TCS. The hydrochlorination shares the equipment and operating conditions with the low-temperature hydrogenation process.

High-temperature hydrogenation process is named for its high temperature reaction requirements. It requires 1200~1300 °C temperatures and 0.6 MPa pressure. Under such conditions, the STC directly reacts with hydrogen.  $SiCl_4$  conversion rate is 15–17 mol%. The power consumption, however, is high. The reaction products contain high carbon content because of the graphite or carbon heating pieces.

The low-temperature hydrogenation process, opposite to the high-temperature one, requires low reaction temperature. In the process, such reaction materials as STC, hydrogen, and Si powder react under 450~600 °C and 1.6~3.5 MPa. The process consumes low power. Primary  $SiCl_4$  conversion rate can be up to 23~28 mol % back. Moreover, the equipment is suitable for enlargement.

Plasma hydrogenation (Zhijun Huang et.al. 2011) belongs to a new technology. It is characterized by high conversion rate and simple equipment. The technology is still under development, for it is limited by its requirement for radio-frequency power supply, high power consumption, and small processing capacity of  $SiCl_4$  (Gusev et al. 2006).

Based on the trend of the polysilicon industry, high-quality, large-scale, low-energy consumption, and low cost are widely pursued during the industrial development and in the market competition. Therefore, the low-temperature hydrogenation process has grown into a prevailing processing for possessing the above-mentioned features. In the low-temperature hydrogenation, main raw materials including  $SiCl_4$ ,  $H_2$ , and Si powder react in the hydrogenation reactor under a certain temperature and pressure with cuprous chloride, copper chloride, copper alloy, and

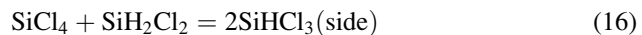
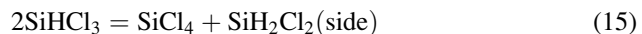
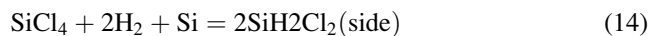
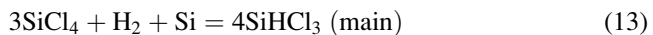


nickel alloy as catalysts. The reaction involving gas and solid materials generates  $\text{SiHCl}_3$ . Low-temperature hydrogenation reactor mainly includes fixed bed and fluidized-bed.

## Low-Temperature Hydrogenation

### Principle of Low-Temperature Hydrogenation

Raw materials  $\text{SiCl}_4$ ,  $\text{H}_2$ , and silicon powder mixed by a certain ratio mainly take the following reaction in the hydrogenation reactor under a certain temperature and pressure:



### Low-Temperature Hydrogenation Process

The process mainly refers Si powder preparation and feeding, STC-hydrogen mixed heating system, hydrogenation system, rapid cooling system, condensate separation system, and auxiliary systems, which consist of nitrogen, hydrogen, refrigeration, air pressure, and circulating water. See Fig. 19.

### Main Factors Affecting the Low-Temperature Hydrogenation

According to the chemical equilibrium, the reaction is taking place toward the positive direction, conducive to the conversion of STC to the TCS. The main reaction factors include temperature, pressure, material ratio, and catalyst. Analysis is as follows:

#### 1. Effect of hydrogen and STC ratio on the conversion rate

The chemical equilibrium indicates that the material ratio, especially the ratio of hydrogen and STC, largely influences the conversion. With the ratio increasing,



**Fig. 19** Low-temperature hydrogenation process

the conversion rate climbs up, showing the chemical equilibrium principle. With the ratio increasing, reduction of STC under a certain flow rate directly affects the production capacity of the system. It shows that the best ratio of hydrogen and STC should be maintained, normally between 2.2 and 3.5.

## 2. Effect of reaction temperature on the conversion rate

When the system pressure, differential pressure of reactant material level and material ratio are fixed, with temperature rising, the conversion rate rises. It is because that the increasing temperature will fuel the reaction dynamic, resulting in increase of the conversion rates of materials per unit time. On the other hand, the low-temperature hydrogenation is to a slight endothermic reaction. Thus, the temperature increase is good for accelerating the hydrogenation reaction rate. The further increasing temperature, however, will propel TCS decomposition reaction, reducing its yield. As a result of that, the temperature for low-temperature hydrogenation should not be too high. Usually, the reaction temperature is optimally controlled at 500–550 °C.

## 3. Effect of reaction pressure on the conversion rate

In terms of chemical equilibrium and the reaction equations, the product volumes of the main reaction (13) and side reaction (15) are the same as their reactants; the product volume of the side reaction (14) is smaller than its reactants. In this case, increased pressure will propel the side reaction (14), producing more dichlorosilane, and the side reaction (16), causing the TCS to increase slightly. In general, the reaction pressure has a little impact on the conversion rate. Increased pressure will improve the gas concentration per unit volume. When other reaction conditions are kept unchanged, the STC molar conversion will increase with the pressure increase in the reactor. But when the pressure increases to 2.5 MPa or higher, the conversion rate is increased steadily. In the event, the increased pressure rarely improves the conversion rate. But higher pressure will enlarge the feed rate and processing capacity of the system, increasing the system's economic benefit.

## 4. Effect of the Si powder layer height on the conversion rate

For the fixed bed, the higher layer in the hydrogenation reactor, the higher conversion rate, namely the better reaction of STC and Si powder. The equipment design will limit the layer height.

For the fluidized bed reactor, the fluidized Si powder brings large difficulty in detecting the layer level. For low-temperature hydrogenation,  $\gamma$ -ray level gauge is used to detect the level. The gauge, however, is not enough for detection accuracy and its radioactive source causes management difficulties. Therefore, the differential pressure between the top and bottom of the Si powder layer is used to determine the layer height. And the gauge can be used as an auxiliary tool. When other parameters are kept unchanged, the conversion rate increases as the layer height increasing, for that the contact time of Si powder with STC and hydrogen rises leads to longer reaction time. But at the later stage, the increment of the conversion rate is limited because the Si powder moves to the top of the reactor and leaves with partial gas produced by the reactions in the reactor. Higher

content of Si powder in such gas will cause difficulties for the following disposal process. In this case, the differential pressure of the Si powder layer is normally at 70–90 kPa.

#### 5. Effect of catalyst on the conversion rate

The main catalysts used in the low-temperature hydrogenation system are such copper-based catalysts as copper chloride, cuprous chloride, and copper powder. The catalyst can increase the conversion rate by 1–3%.

### Hydrochlorination

Hydrochlorination, in the industry, refers to the low-temperature hydrogenation of adding of hydrogen chloride from the dry vent gas recovery. It aims to dispose of the by-product hydrogen chloride of polysilicon reduction and the chlorine element equilibrium in the polysilicon production system.

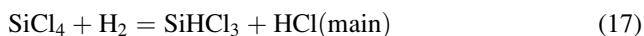
The relevant experiments and studies at early stages show that under the synthesis reaction conditions of increased pressure or atmospheric pressure and temperature 220 °C or above, HCl reacts with Si powder. With temperature increasing, the TCS production rate is dropping greatly. Reaction temperature at 260~290 °C, cross-linked silicon hydrogen generation rate can reach 85~90%; when the reaction temperature at 360 °C, cross-linked silicon hydrogen generation rate down to 62%; when the reaction temperature at 450 °C, cross-linked silicon hydrogen generation rate dropped to 10~20%; when the reaction temperature above 500 °C, low silicon chemical hydrogen generation rate mainly produces SiCl<sub>4</sub> and a small amount of SiHCl<sub>3</sub>, SiH<sub>2</sub>Cl<sub>2</sub>, SiH<sub>3</sub>Cl, SiH<sub>4</sub>, and polymer chlorosilane.

The result comparison of the low-temperature hydrogenation and hydrochlorination shows that the two processes have the similar conversion rate, generally around 25%. In terms of production balance of the whole plant, the hydrochlorination has the following advantages:

1. No additional devices are required. The hydrochlorination could directly recovery the by-product hydrogen chloride in the reduction reaction.
2. Addition of hydrogen chloride makes up chlorine needed in the production, achieving chlorine equilibrium in polysilicon production system.
3. The reaction of silicon with hydrogen chloride is an exothermic reaction, low-temperature hydrogenation endothermic reaction. The hydrochlorination will help the heat balance and utilization in the low-temperature hydrogenation reactor reducing external heat demand.

### High-Temperature Hydrogenation

Process principle is that when the electrical graphite heat exchanger produces heat with temperature reaching above 1250 °C, the STC and hydrogen are heated and react. The TCS is produced. The equations are as follows



The side reaction:



After leaving the reactor, the reactant gas is rapidly cooled by the quench cooler where TCS, STC, etc. is generated. After the processing of separating tower, STC returns to the high-temperature hydrogenation system, the TCS be delivered to the distillation and purification system for separation and purification.

### Comparison of Low- and High-Temperature Hydrogenation

For the comparison of low- and high-temperature hydrogenation, see Table 5.

### Recycling of By-product Dichlorosilane (DCS)

#### TCS Generation by Comproportionation

With the catalyst of resin, dichlorosilane takes reaction with STC to produce TCS. Exchange resin with alkalescence and anions can be used. The functional groups are amino radical. The reaction equation is:

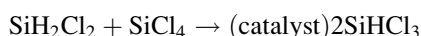


**Table 5** Comparison of low- and high-temperature hydrogenation

S/N	Item	Low-temperature hydrogenation	High-temperature hydrogenation
1	SiCl <sub>4</sub> processing capacity (kg/h) per set	12500~30000	500~1500
2	Primary conversion rate (%)	23~28	17~22
3	Reaction temperature (°C)	400~600	1200~1300
4	Power consumption (kWh/kg-TCS)	0.4~0.7	2.0~3.5
5	Continuous running time (days)	150~330	120~
6	Running condition	1. It is hard to feed the solid Si powder under sealing condition 2. The equipment should be sophisticated for its large size and internal high pressure	1. Graphite electrodes and carbon fiber should be changed regularly 2. Carbon is involved in the reaction under high-temperature reaction, affecting the production quality

Process: a certain ratio (1:4~6 mole ratio) of dichlorosilane and STC enter the stabilization tank after being blended by the mixer. The material is charged into the preheat exchanger when the shield pump pressurizes. After heated to 50~60 °C by the preheat exchanger, the material is fed to the reactor for the catalytic reaction. Then the products are fed to the tank area for separation and purification after cooled by the cooler. The purified TCS returns the system for use. The conversion is typically >95%, and the TCS recovered can be recycled within the plant.

### **Take Part in CVD Reaction and Low-Temperature Hydrogenation**

Both the reduction reaction and low-temperature hydrogenation continuously generate a certain concentration of dichlorosilane. After distillation and purification or adsorption purification, the dichlorosilane can be fed into the reduction process together with hydrogen and TCS, which is favorable for improving the primary conversion rate of TCS to polysilicon by reduction and sedimentation.

The dichlorosilane with a high content of impurities can be fed into the low-temperature hydrogenation reactor to raise the primary conversion rate of hydrogenation system, lower the system's Si powder consumption, and recycle the dichlorosilane.

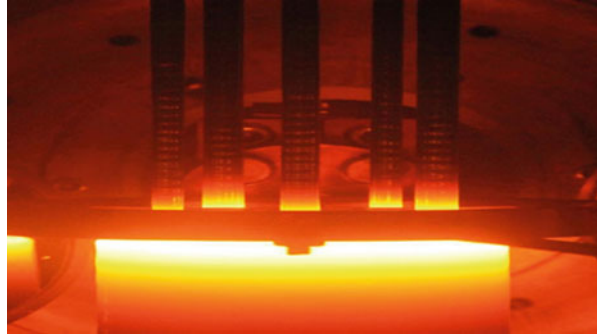
In this process configuration, DCS will build up an equilibrium condition of approximately 6~9% DCS in the TCS feed. The recycle of DCS has a significant effect at decreasing the manufacturing cost of silicon. Higher DCS concentrations in the TCS translate to faster deposition rates and correspondingly lower power consumption. The only disadvantage is slightly higher rates of homogeneous nucleation of silicon (powder formation). Powder formation can be mitigated in GTs CVD reactors when operated at proper conditions, and the GT plant design addresses particulate problems in downstream equipment. The advantages of greater deposition rates and material efficiency far outweigh the single disadvantage of the particulate formation.

In this process configuration, DCS will build up an equilibrium condition of approximately 6~9% DCS in the TCS feed. The recycle of DCS has a significant effect at decreasing the manufacturing cost of silicon. Higher DCS concentrations in the TCS translate to faster deposition rates and correspondingly lower power consumption. The only disadvantage is slightly higher rates of homogeneous nucleation of silicon (powder formation). Powder formation can be mitigated in GT's CVD reactors when operated at proper conditions and the GT plant design addresses particulate problems in downstream equipment. The advantages of greater deposition rates and material efficiency far outweigh the single disadvantage of the particulate formation.

### **Filament Preparation**

Today, there are two mainly technologies available for the production of filaments for CVD reactors: float zone and wire saw. As for the zoning melting method, five pieces can be made from one campaign, seen in Fig. 20. As for the wire saw

**Fig. 20** Filaments making by float zone method



method, the raw polysilicon is melted in the monosilicon reactor and drawn into rods with a respective diameter of about 200 mm and length of 2.5–3.5 m, which are cut by multiwire sawing machine into  $10 \times 10$  mm~ $15 \times 15$  mm filaments at one time.

### **Float Zone Process**

Pros: High purity filament, filaments are easily doped allowing for low voltage power starts, and easier for cleaning of etching.

Cons: Requires large capital investments, personnel required to operate are 5–10 times the requirement for wire saw, high maintenance, requires specially grown polysilicon source rod, high energy consumption, and affecting polysilicon production capacity by reduction reactor.

### **Wire Saw Process**

Wire saws use a wire coated with diamonds to cut silicon. It is an efficient and cost-effective process used in a new application cutting CZ grown rods into filaments more than 3 m in length.

Pros: Silicon loss from the knife is the lowest of the sawing processes. Low manpower and investment requirements when compared to float zone process.

Cons: Requires additional etching for semiconductor use. The Si loss is about 5% more than that by float zone.

## **Comprehensive Utilization of By-produced Energy**

Around 60–70% of power would be consumed in the reduction reaction in the polysilicon production. Heat transfer oil or high-temperature water is used in the reaction to recover the by-produced energy. Such energy can be used in TCS purification, vent gas dry recovery system, and other links in the polysilicon production. By experience, up to 75% of recovery energy can be used in the above links to reduce the overall power consumption in the polysilicon production.

There are refrigeration systems with a temperature of  $-55\text{ }^{\circ}\text{C}$ ,  $-35\text{ }^{\circ}\text{C}$ , and  $7\text{ }^{\circ}\text{C}$  in the polysilicon production system. The idea of materials at varied temperatures exchanging heat is adopted in the project design to reduce cold energy consumption. This gradient temperature method makes the maximized utilization of cold energy in the systems possible. About 30% or above refrigeration power consumption is saved.

---

## Conclusion

Polysilicon is the basic material of integrated circuits and photovoltaic solar cells. Today, the global polysilicon output by using Siemens process (trichlorosilane process) accounts for more than 90% in the world. Siemens process is still expected to be the mainstream of polysilicon production process in the future.

This chapter describes the details of Siemens process. The processes include TCS synthesis, TCS distillation and purification, TCS decomposition and hydrogen reduction in CVD reactor, vent gas recovery, STC hydrogenation, comprehensive utilization of other by-products, filament preparation, and comprehensive utilization of by-produced energy. In each section, the technology principles, reaction conditions, major equipment, operation conditions, materials and energy consumption, and so on are all described.

**Acknowledgments** This chapter is grateful for the help of Zheng Ning, Shi Hewu, Zhang Chao, China ENFI Engineering Technology Co., Ltd., Secretary-General of China Photovoltaic Industry Association Wang Bohua, and my wife Dr. Li Rong.

---

## References

- A.V. Gusev et al., Preparation of trichlorosilane by plasma hydrogenation of silicon tetrachloride. *Inorg. Mater.* **42**, 1123–1126 (2006)
- Bohua Wang, Review of 2016 China PV and expectation of 2017, Photovoltaic Industry Association of China, (2017) pp 1–6
- D. Yan et al., Polycrystalline silicon energy consumption analysis and energy-saving practice. *Electron Sci. Technol* **02**(01), 224–230 (2014a)
- Dazhou Yan et al., Polysilicon production theory and practice of comprehensive utilization of byproduct of Silicon tetrachloride, Chinese Academy of engineering, chemical, metallurgical and materials engineering, in *Proceedings of the 10th Conference* ed. by Hongxiang Cao (Chemical industry press, Beijing, 2014b), p. 274
- Dazhou Yan et al., The theory research and production practice for polysilicon high efficiency deposition, Chinese Academy of engineering, chemical, metallurgical and materials engineering, in *Proceedings of the 11th Conference* ed. by Hongxiang Cao (Chemical Industry Press, Beijing, 2016), p. 392
- Lixia Jiang et al., Application of energy saving technology in silicon purification, Energy saving of nonferrous metallurgy, December, 6 (2010)
- Photovoltaic Industry Association of China, China PV industry development road ap, 6–8 (2017)

- 
- Standardization administration of the people's republic of China, GB/T 12963-2014 Electronic-grade polycrystalline silicon, National standard of people's Republic of China (2014)
- Standardization administration of the people's republic of China, GB/T 25074-2016 Solar-grade polycrystalline silicon, National standard of people's Republic of China (2016)
- X. Yao et al., Polysilicon reactor based on Fluent numerical simulating and optimization. *Energy Saving Nonfer Metallurg* **4**(8), 48–56 (2011)
- Y. Wan et al., Trichlorosilane production of Silicon tetrachloride silicon technology. *Energy Saving Nonfer Metallurg* **12**(6), 30–32 (2010)
- Z. Huang et al., Hydrogen plasma reduction preparation of trichlorosilane Silicon tetrachloride consumption analysis. *J. Portland* **39**(5), 769–772 (2011)





# Fluidized Bed Process with Silane

# 4

Limin Jiang, Benjamin F. Fieselmann, Liguochan Chen, and David Mixon

## Contents

Introduction .....	70
Commercial Production of Polysilicon .....	71
Fluidized-Bed Process for Producing Silicon from Silane .....	73
Background on Fluidized-Bed Engineering .....	74
Industrial Applications of Fluidized-Bed Technology .....	77
Applying Fluidized-Bed Technology to the Production of Polysilicon .....	79
Commercial Production of Silane .....	80
Total Silane-Based Process for Converting MGS to Granular Polysilicon .....	80
Siemens Process for Producing Polysilicon Rods from Trichlorosilane .....	81
Comparison of the Fluidized-Bed Process and the Siemens Process for Making Polysilicon .....	83
Process of Polycrystalline Silicon Fabrication .....	85
Downside to the Use of Silane-Based Fluidized-Bed Technology .....	85
Alternate Technologies for the Production of Polysilicon .....	86
Alternate Approaches to Polysilicon Production .....	87
Silane Reactions in a Fluidized-Bed Reactor .....	87
Chemical Reaction of Silane in a Fluidized-Bed Reactor .....	87
Homogeneous, Heterogenous, and Scavenging Reactions of Silicon Particles .....	87
Modeling of Silane Fluidized-Bed Reactors .....	89
Operation of a Silane-Based Fluidized-Bed Reactor to Make Silicon .....	95
Feed Gas to the Fluidized-Bed Reactor .....	95
Preheating the Feed Gas .....	95

---

L. Jiang  
GCL Solar Energy Trading Limited, Suzhou, Hong Kong

Jiangsu Zhongneng Polysilicon Technology Development Co., Ltd., (GCL), Xuzhou, Jiangsu,  
P. R. China  
e-mail: [jianglimin@gclsolarenergy.com](mailto:jianglimin@gclsolarenergy.com)

B. F. Fieselmann (✉) · L. Chen · D. Mixon  
GCL Technology Research Center, LLC, Princeton, NJ, USA  
e-mail: [benfieselmann@gclsolarenergy.com](mailto:benfieselmann@gclsolarenergy.com); [liguochen@gclsolarenergy.com](mailto:liguochen@gclsolarenergy.com);  
[davidmixon@gclsolarenergy.com](mailto:davidmixon@gclsolarenergy.com)

Distributor and Jet Nozzles to Introduce the Feed Gas .....	96
Different Designs for Heating Silane-Based Fluidized-Bed Reactors .....	97
Reactor Dimensions, Pressure, and Silicon Production Rate .....	99
Agglomeration of Silicon Particles .....	99
Control of the Silicon Particle Size Distribution in the Reactor .....	100
Factors to Consider When Optimizing Silicon Particle Size Distribution .....	101
Silicon Powder Formation and Handling in a Fluidized-Bed Reactor .....	101
Removing the Silicon Deposited on the Reactor Wall .....	102
Safety Issue with Silane and Hydrogen .....	103
Atmospheric Contamination of Silicon .....	103
Current Status of Commercial Research and Development of Silane Fluidized-Bed Reactors .....	103
Specifications for Polycrystalline Silicon for PV Applications .....	105
Improving FB Technology with Modeling .....	106
Summary and Conclusions .....	106
References .....	107

---

### Abstract

Silane-based fluidized-bed technology is used to produce polysilicon for solar cells by decomposing silane onto silicon particles suspended in a heated stream of silane and hydrogen. Silane-based fluidized-bed reactors potentially provide a lower cost method to produce polysilicon than the current Siemens reactors that dominate the silicon market. Production of silicon in a fluidized bed requires 80–90% less electrical energy than the currently favored Siemens process and converts a batch process into a more economical continuous process. The spherical granular silicon product from fluidized-bed reactors is preferred to the polysilicon rods produced by the Siemens process for downstream processing. Production of silicon by fluidized beds has been carried on for over 20 years, but the simpler Siemens process has dominated polysilicon production because of the high purity of its polysilicon product and the availability of low-cost electricity. The economics of the silane-based fluidized-bed technology has improved significantly due to advances in reactor design, process modeling, and operational experience. Fluidized-bed technology is the leading candidate to eventually provide less expensive polysilicon for solar cells.

---

### Keywords

Silicon fluidized-bed · Silicon production with silane · Silane-based fluidized-bed · Fluidized bed and Siemens silicon · FBR polysilicon · Granular silicon

---

## Introduction

The market price for purified polysilicon for solar applications has reached a critical point such that new technology is needed to further reduce the production costs for polysilicon. The price of polysilicon has decreased significantly over the last decade with over building of Siemens production capacity (Bemreuter 2016). Further major

cost reductions using the current Siemens process are unlikely. In order for the price of electricity from solar cells to achieve grid parity with other sources of electricity in more markets, the price of polysilicon must continue to drop. Silane ( $\text{SiH}_4$ )-based fluidized-bed (FB) technology is now the leading candidate to provide a significant reduction in the price of polysilicon chiefly because FB reactors use 10–20% as much electrical power as a Siemens reactor.

Fluidized-bed technology using silane has been applied to silicon preparation since the early 1980s by Ethyl Corporation and MEMC (now SunEdison) (Roselund 2015). REC has produced FB silicon for many years (REC 2017). Despite the decades of commercial experience, the silane-based fluidized-bed technology has failed to achieve its expected production efficiencies and anticipated cost savings. Currently silane-based fluidized-bed technology accounts for less than 10% of world production of polysilicon (IHS 2014). The development of the silane-based fluidized-bed process for silicon production still remains a major engineering challenge to reach its full potential.

This chapter reviews the state of technology for polysilicon production from silane-based fluidized-bed reactors. The presentation is industrially oriented with an emphasis on the practical issues that are encountered when operating a fluidized-bed reactor with silane. Much of the research and development on silane-based fluidized-bed reactors has been carried out by industry. The result is that there are few published articles on polysilicon production technology by those working with the technology. There are a large number of patents on the subject and a few third-party news reports. Two useful reviews on various aspects of silicon production using silane in a fluidized bed are the articles by Filtvedt et al. (2010) and Jianlong et al. (2011).

This review also provides a brief background on the current Siemens technology for producing polysilicon. This chapter outlines why the Siemens process is currently the preferred method for polysilicon production and presents the engineering challenges that must be overcome before FB technology can reach the point where it can replace the Siemens process.

---

## Commercial Production of Polysilicon

As the demand for polysilicon for photovoltaic applications increases, there has been a search for more economical methods for producing polysilicon. Many competing technologies have been examined over the last 50 years, but the Siemens process has emerged as the most cost-effective method for producing polysilicon, despite its many deficiencies. Of all the alternative methods for polysilicon production, the silane fluidized-bed process has shown the greatest potential for replacing the Siemens process (Filtvedt et al. 2010).

In order to understand how FB technology could eventually become the dominant method for polysilicon production, one needs to understand how polysilicon is currently produced. Although the Siemens process and fluidized-bed technology appear to be different, they both produce high purity polysilicon and deal with many

of the same technical challenges. The chemistry of the two methods is shown in the chart below:

## Two Favored Commercial Routes to Polysilicon

<u>Process</u>	<u>Silicon Source</u>	<u>Overall Deposition Reaction</u>	
Siemens Reactor	$\text{HSiCl}_3$	$n \text{HSiCl}_3 \rightleftharpoons \text{Si} + \text{HCl} + \text{SiCl}_4 + \text{H}_2$ (equilibrium reaction)	(1)
Silane Fluidized Bed	$\text{SiH}_4$	$\text{SiH}_4 \rightarrow \text{Si} + 2\text{H}_2$ (reaction goes to completion)	(2)

Most of the commercial silicon purification methods start with metallurgical grade silicon (MGS) (Mazumder 2000). High purity silicon dioxide ore is reduced with carbon in an electric arc furnace at 1900 °C as follows:



Liquid silicon (melting point 1414 °C) is drained out of the furnace and collected. This arc furnace process produces metallurgical grade silicon that is 98.5–99.5% pure.

For photovoltaic and semiconductor applications, further purification of the silicon is needed to reduce impurity levels to the part per million (ppm) or to the part per billion (ppb) by mass level. (These levels of impurity are referred to as 6 N (99.9999%) or 9 N (99.999999%), respectively.) Roughly photovoltaic grade silicon must be at or purer than the 6 N level. Semiconductor grade silicon is typically in the 9 N or better range of purity. For photovoltaic applications, the highest purity of polysilicon possible is favored because it yields more efficient solar cells. Industrially, one is continually faced with the tradeoff between producing higher efficient solar cells with the increased cost of higher purity polysilicon.

The most common method for purification of silicon requires conversion of the MGS to trichlorosilane ( $\text{HSiCl}_3$ ). Purification occurs by two sequential steps. Under reaction conditions to produce  $\text{HSiCl}_3$  from silicon most other elements present as impurities are removed because others elements do not form volatile compounds under the conditions where trichlorosilane is formed. Secondly, the  $\text{HSiCl}_3$  that is produced can be further purified by distillation to remove residual impurities with different vapor pressures.

The highly purified trichlorosilane can be directly converted back to polysilicon by the Siemens process, or it can be reacted to form silane. The silane can be thermally decomposed to polysilicon by a FB process. In both cases, metallurgical grade silicon forms a volatile compound or compounds which are purified

and then decomposed back to silicon for further processing. This conversion through multiple steps makes possible the production of ultrapure silicon necessary for photovoltaic and semiconductor applications. In the purification process to form polysilicon the critical steps are the conversion of either trichlorosilane or silane back to silicon.

In the following sections the operation of a fluidized-bed process with silane to form polysilicon will be presented. The use of trichlorosilane in the Siemens process will be presented later for contrast.

### Fluidized-Bed Process for Producing Silicon from Silane

Fluidized-bed technology works well with silane as the feed gas to make silicon. The FB reaction involves the deposition of silicon from silane onto small, heated particles of silicon that are suspended in a flow of feed gas as shown in Fig. 1.

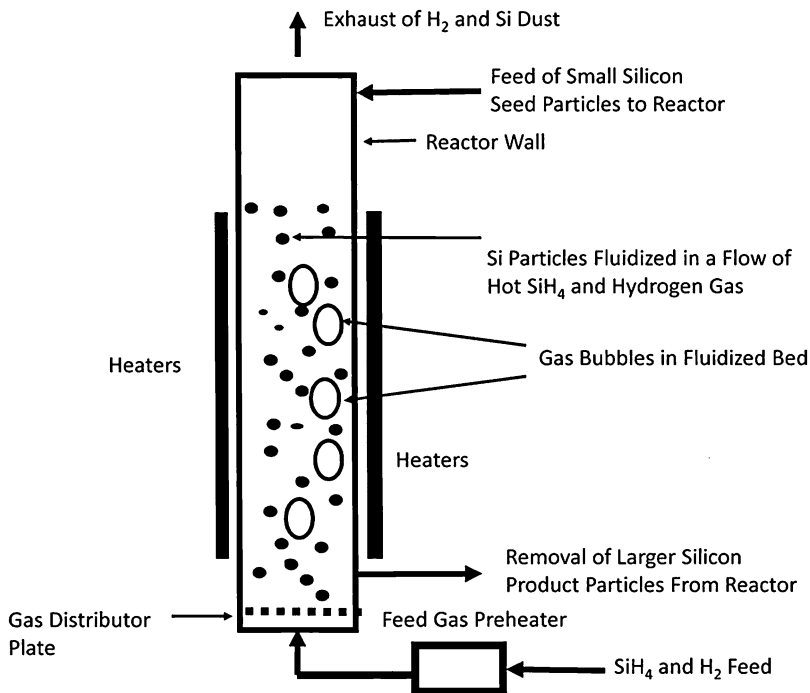


**Fig. 1** Simplified basic fluidized-bed reactor with silicon particles suspended in a stream of silane and hydrogen. The reactor is heated to 650–850 °C so that the silane decomposes and deposits silicon onto the suspended particles. Over time larger particles of silicon are removed as product and smaller silicon particles are added to maintain the particle size distribution of the suspended silicon particles. Hydrogen, unreacted silane, and silicon dust are removed from the top of the reactor

When describing the environment in a fluidized-bed reactor, it has become common to refer to the bubble phase and the emulsion phase. The bubble phase is the gas contained within a bubble. For a silane-based reactor the emulsion phase refers to the dense mixture of silicon particles and the surrounding gas.

The reactor presented above is a simple type of fluidized bed presented as an introduction. Later in this review, more modern and sophisticated reactors will be discussed. In the simple model, the reactor is heated through the walls. The feed gas enters the reactor from the bottom with sufficient flow gas to fluidize the silicon particles. During the course of the fluidized-bed operation, small seed particles of silicon are periodically added and larger particles are removed permitting continuous production of silicon. The silane decomposes on the silicon particles and deposits silicon.

## Background on Fluidized-Bed Engineering

It is worthwhile to cover some of the basics of fluidized-bed engineering since they are vital to the understanding of the process that produces silicon in a fluidized bed. For a complete discussion of fluidized-bed engineering, please refer to the books by Kunii and Levenspiel (1991) and by Yang (2003).

### Minimum Fluidization Gas Velocity

The minimum fluidization velocity is the gas superficial fluid velocity at the onset of fluidization during which the drag force on the particles by the upward moving fluid is balanced by the weight of the particles. The minimum fluidization velocity can normally be calculated by the Ergun equation as below

$$\frac{1.75}{\varepsilon_{mf}^3 \phi_s} \text{Re}_{mf}^2 + \frac{150(1 - \varepsilon_{mf})}{\varepsilon_{mf}^3 \phi_s^2} \text{Re}_{mf} = \frac{d_p^3 \rho_g (\rho_s - \rho_g) g}{\mu^2} \quad (4)$$

and

$$\text{Re}_{mf} = \frac{\rho_g u_{mf} d_p}{\mu}, \quad (5)$$

where  $\varepsilon_{mf}$  is void fraction at minimum fluidizations,  $\phi_s$  is the sphericity of the particles,  $\rho_s$  is the particle density,  $\rho_g$  is the gas density,  $d_p$  is the diameter of the particle,  $\mu$  is the viscosity of the gas and  $g$  is the acceleration of gravity.

### Minimum Bubbling Gas Velocity

The minimum bubbling velocity is the superficial fluid velocity at which bubbles start to form. This bubbling behavior normally occurs after the onset of the fluidization, so the minimum bubbling velocity should be at least equal to or larger than the minimum fluidization velocity.

### Geldart Classification of Particles

By studying the fluidization behavior of different solids, Geldart (1986), classified them into four distinguishable groups with clearly recognizable fluidization behavior. The classification is described as follows:

- Geldart C: The particles are small (<100 microns) and cohesive. They are very difficult to fluidize because the interparticle forces are large and the particles tend to agglomerate together.
- Geldart A: The particles fluidize easily. They exhibit smooth fluidization behavior after minimum fluidization velocity. They have controlled bubbling behavior with recognizable minimum bubbling velocity.
- Geldart B: The particles fluidize well with bubbling action and gas bubbles appear right after minimum fluidization velocity.
- Geldart B and D: The particles are very hard to fluidize, since they normally are large, dense solids. Stable spouted bed can be formed for this type of solids.

Geldart's classification has since become the standard and can be readily displayed by Fig. 2:

### Bed Pressure Drop

Once the bed reaches the minimum fluidization state, the pressure drop across the bed is equal to the weight of the bed per unit area. Therefore,

$$\Delta P = \frac{Wg}{A}, \quad (6)$$

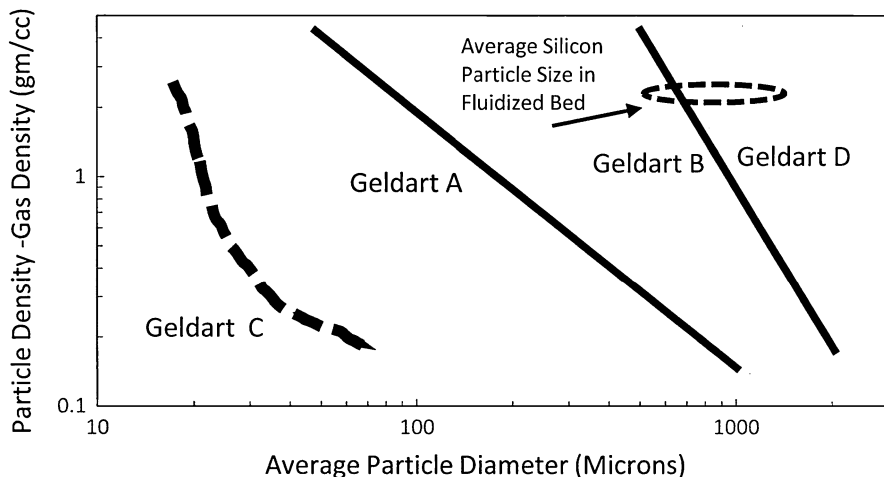


**Fig. 2** Geldart classification of particles for fluidization based on particle size and density. Geldart B and D group are those encountered in a silane-based fluidized-bed reactor. The approximate location of the silicon particles is noted in the chart (Geldart 1986)

where  $\Delta P$  is the pressure drop across the bed,  $Wg$  is the total weight of the bed,  $A$  is the cross-sectional area of the bed.

We can conclude that once the bed is in the fluidization state, varying the gas flow rate will not change the total pressure drop across the bed as long as the total weight of the particles is fixed. The pressure drop across the bed can also be formulated as follows:

$$\frac{\Delta P}{H} = (1 - \varepsilon)(\rho_s - \rho_g)g, \quad (7)$$

where  $H$  is the bed height, and  $\varepsilon$  is the void fraction of the bed. For gas fluidized bed, since  $\rho_s \gg \rho_g$ , so

$$\frac{\Delta P}{H} = (1 - \varepsilon)\rho_s g. \quad (8)$$

The fluidized bed density  $\rho_b = (1 - \varepsilon)\rho_s$  can be estimated from the bed pressure drop

$$\rho_b = \frac{\Delta P}{gH}. \quad (9)$$

### Slugging Beds

In fluidized beds, with increasing gas velocity the bubbles can increase in size to the bed diameter and form slugging beds. The gas slugs rise at regular intervals and cause large pressure fluctuations inside the beds. The pressure fluctuation inside the bed can result in severe vibration of the reactor and its associated piping, hence causing damage. Slugging should be avoided in those cases if possible. The following correlation (Baeyens and Geldart 1974) can be used to calculate the minimum slugging velocity  $U_{ms}$

$$U_{ms} = U_{mf} + 0.07\sqrt{gD}, \quad (10)$$

where  $D$  is the reactor diameter.

### Heat Transfer in Fluidized Beds

One of the major advantages of using fluidized-bed reactors is its capacity for heat transfer features. Due to the rapid mixing of the fluidized particles, the entire bed is nearly isothermal. Since hot spots can be minimized, the process operations can be well controlled.

Heat transfer between particles and gas in a fluidized bed is very fast and they can be regarded as being at the same temperature in most cases. In rare transient cases, the following correlation (Yang 2003) can be used to calculate the heat transfer coefficient:

$$\text{For } 0.1 \leq \text{Re}_p \leq 50$$



$$Nu_p = \frac{h_p d_p}{k_g} = 0.0282 Re_p^{1.4} Pr_g^{0.33} \quad (11)$$

For  $50 \leq Re_p \leq 10^4$

$$Nu_p = \frac{h_p d_p}{k_g} = 0.0282 Re_p^{1.4} Pr_g^{0.33}, \quad (12)$$

where  $h_p$  is the heat transfer coefficient between the particles and the gas,  $d_p$  is the particle diameter,  $k_g$  is the gas thermal conductivity, and  $Pr_g$  is the Prandtl number of the gas.

$Re_p$  is the particle Reynolds number

$$Re_p = \frac{\rho_g d_p u_0}{\mu_g}. \quad (13)$$

There are many correlations in the literature for calculating the wall-to-bed heat transfer coefficient  $h_w$ . Leva's formula (Yang 2003) has been used extensively for large particle bubbling fluidized beds

$$Nu_w = \frac{h_w d_p}{k_g} = 0.525 Re_p^{0.75}. \quad (14)$$

Heat transfer between the fluidized bed and a gas feeding distributor plate has been studied by Zhang and Quyang (1985):

$$Nu_d = \frac{h_d d_p}{k_g} = 0.09 \left( \frac{\rho_s C_{ps}}{\rho_g C_{pg}} \right)^{0.4} \left( \frac{d_p \rho_g u_0}{\mu_g} \right)^{0.4}. \quad (15)$$

With the condition,

$$0.3 < \frac{d_p \rho_g u_0}{\mu_g} < 40, \quad (16)$$

where  $\mu_g$  is the gas viscosity,  $u_0$  is the superficial gas velocity,  $C_{ps}$  is the specific heat of the solid,  $C_{pg}$  is the specific heat of the gas.

## Industrial Applications of Fluidized-Bed Technology

There are a wide range of commercial processes that use fluidized-bed technology in multiphase reactions where solids are reacted with gases. The basic concept of fluidized-bed technology is that solids are suspended in a high velocity stream of gas. A major advantage of fluidized-bed technology is the good heat and mass

transfer between materials in the solid phase and gas phase. Good heat transfer is especially useful with very exothermic reactions where over heating can result in “hot spots” in a fixed bed reactor. A second major advantage with fluidized-bed reactors is that the processes can be made continuous by adding and removing solid and gaseous reactants from the reactor.

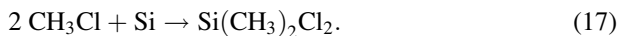
There are several negative aspects to the use of FB technology. Fluidized-bed reactors can be challenging to control. Parameters such as feed gas make up, temperature, flow rate, and particle size have to be held within a small range of settings. The bed level must be carefully monitored. The possibilities of collapsing the bed or elutriating bed particles out of the top of the reactor continually exist. Temperature, pressure, concentration, and many other parameters vary throughout the reactor at any given moment. Understanding what is going on in a FB reactor is difficult. Reaction process modeling may be required to interpret the behavior in a reactor and to correctly respond to changing reactor conditions.

Scalability is difficult to achieve with a fluidized bed (Howard 1989). It is not easy to predict the conditions in the reactor as the diameter and height of the unit increase. As the diameter of the reactor increases the bed volume increases faster than the wall heating surface area.

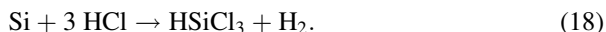
Fluidized beds are used extensively in the petrochemical and energy industries. Catalytic cracking of high molecular weight petroleum is accomplished by passing gaseous hydrocarbons over a suspended bed of catalyst. Catalytic reforming is another process where fluidized-bed technology is used to upgrade petroleum.

In many fluidized-bed processes the contents of the reactor bed either do not change, as when catalyst particles make up the bed, or decrease over time, as when the suspended particles are consumed in a reaction. In contrast, in the silane-based FB process the particles grow in diameter as silicon is deposited. The industrial process that is superficially similar to the fluidized-bed deposition of silane on silicon particles is the growth of polymer beads. The growth of silicon particles and the growth of polymer beads in a FB reactor are similar in that the suspended particles increase in size as the process is operated. Polymer beads are introduced into the fluidized-bed reactor. The product beads are suspended and grow as monomer vapor is added. The product beads are periodically screened and the larger beads are removed and the small beads are returned to the reactor. Fluidized-bed technology is used with ethylene, propylene, styrene, and other monomer feedstock to generate flowable beads that can later be processed into plastics.

Fluidized beds are widely used in the silicon industry in many processes. Many reactions involving silicon tend to be very exothermic and make use of the excellent heat transfer characteristics of fluidized-bed reactors. The preparation of silicones depends on the highly efficient production of the monomer dimethyldichlorosilane ( $\text{Si}(\text{CH}_3)_2\text{Cl}_2$ ) by the reaction of methyl chloride with silicon in a fluidized-bed reactor. The reaction is referred as the Direct Process. Particles of silicon and a copper catalyst are suspended in a stream of methyl chloride to carry out the following high yield reaction:



Some of the trichlorosilane used in the silicon industry is prepared in fluidized beds using the following highly exothermic direct chlorination process:



It is not surprising that the fluidized-bed hydrochlorination process reaction shown below was developed to convert the Siemens byproduct silicon tetrachloride back to trichlorosilane, for recycle back to the Siemens process and for the production of silane.

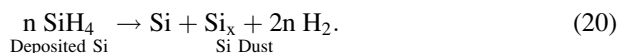


It is clear that the silicon industry makes use of fluidized-bed technology to carry out many of the key reactions. Most of the silicon-based reactions that use a fluidized-bed technology have been optimized and are routinely run to prepare numerous chlorosilane and organosilane compounds. Despite decades of experience optimizing and working successfully with silicon-based fluidized beds to make chlorosilanes and organosilicones, it has remained a challenge to achieve the same level of success with the deposition reaction to produce silicon. The potential benefits of fluidized beds such as high selectivity, good yield, and increased throughput have been achieved with many silicon and organosilicon reactions. Difficulties remain in optimizing the process to deposit silane on fluidizedsilicon particles. The next section presents the specifics of how FB technology is applied to the case of silane deposition on suspended silicon particles.

## Applying Fluidized-Bed Technology to the Production of Polysilicon

Polysilicon is produced in a fluidized bed by suspending a bed of granular silicon particles in a flow of silane bearing gas that is usually diluted with hydrogen. The hot reactor walls heat the silicon particles which then transfer heat to the silane and hydrogen feed gases. The silane is decomposed in the FB reactor and deposits silicon on the granular silicon particles. As indicated in Fig. 1, bubbles of feed gas can form. The silane in the bubbles may have little opportunity to react with the silicon particles. The rapidly moving and often violent actions of the silicon particles in the bed lead to a wide range of differing conditions in the reactor over time.

The overall chemical reaction behind the silane-based FB reactor is the following thermal decomposition:



This reaction can go to completion and is not limited by equilibrium (Walch and Dateo 2001). The silane decomposition reaction yields two main silicon products. The desired process is the deposition of silicon onto the fluidized particles in the emulsion phase to increase the size of the polysilicon granules. The silane also decomposes to form fine silicon dust by the homogeneous thermal decomposition in the bubble phase.

## Commercial Production of Silane

The most economical method for silane production for use in a FB uses disproportionation of trichlorosilane (Breneman 1987, 2016). In this well-established route trichlorosilane is converted to silane by using staged amine catalyzed reactions and multiple distillations. In silane plants anion exchange styrene resins with amine functional groups are used as the disproportionation catalyst, and the chlorosilanes in the liquid phase are passed through several heated resin beds, equilibrated, and distilled. The net reaction to produce silane is the following:



In the disproportionation process, there is no net stoichiometric consumption of silicon or any element. There is only a rearrangement of hydrogen and chloride bonded to silicon.

## Total Silane-Based Process for Converting MGS to Granular Polysilicon

In order to make the silane-based fluidized-bed process possible, three chemical units described below are required. The first two reactions are well understood equilibrium processes that have been optimized for high performance. The third reaction used to deposit silane on silicon in a FB reactor is just the final step in the overall process to produce a highly purified granular silicon product.

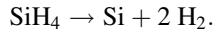
1. Metallurgical grade silicon (MGS) is converted to trichlorosilane by hydrochlorination with silicon tetrachloride and hydrogen



2. Trichlorosilane is disproportionated to silane and silicon tetrachloride



3. Silane is deposited in a fluidized bed onto granular silicon seed particles and releases hydrogen



When the three chemical reactions are added, the net result is the following:



There is theoretically no net consumption of hydrogen and chloride in the three-step process. In reality small amounts of hydrogen (as  $\text{H}_2$ ) and chlorine (as  $\text{HSiCl}_3$  or  $\text{SiCl}_4$ ) must be added to replace process losses due to required purification steps.

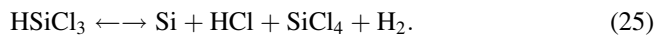
To understand how silane-based fluidized-bed technology can compete with the Siemens process, it is important to understand how the Siemens process operates. Both technologies produce polysilicon and have many characteristics in common.

### Siemens Process for Producing Polysilicon Rods from Trichlorosilane

The Siemens process depends on converting metallurgical grade silicon to trichlorosilane ( $\text{HSiCl}_3$ ). After one has obtained highly purified trichlorosilane by distillation, the final purification step is the conversion to polysilicon by thermal decomposition.

#### The Siemens Process

Siemens Process deposits trichlorosilane onto a seed rod of polysilicon via the following reaction (H. Gutschel 1962):



Equation 25 is not a balanced chemical equation but instead represents an equilibrium. This Siemens reaction is a chemical equilibrium process that does not go to completion but produces a number of compounds. The reaction produces hydrogen, silicon tetrachloride, and hydrogen chloride. Depending on reaction conditions the Siemens process typically deposits less than 25% of the trichlorosilane feed in a given pass through the reactor (Filtvedt et al. 2012). Extensive recycling of feed gases is required during the operation of the Siemens process. The Siemens reactor is schematically shown in Fig. 3.

The Siemens process involves feeding a gas mixture of hydrogen and trichlorosilane into a bell jar-shaped chamber containing U-shaped silicon rods and depositing silicon on the hot silicon surfaces. An electric current is passed through the rods to bring the silicon rods to a temperature near 1150 C. The trichlorosilane is heated to the reaction temperature as it approaches the hot silicon rods. The trichlorosilane reacts on the hot

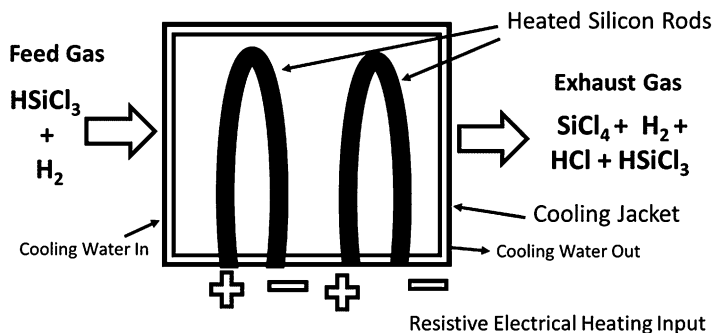


**Fig. 3** Schematic diagram of a Siemens reactor showing how silicon is deposited via thermal deposition of trichlorosilane on heated, shaped silicon rods. The reaction is run in a bell jar where the reactor walls are water cooled to prevent silicon deposition

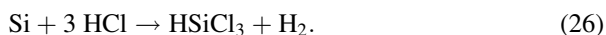
silicon surface to deposit silicon and to release silicon tetrachloride, hydrogen, and unreacted trichlorosilane. The diameter of the rods increases as silicon is deposited.

The Siemens process has several operational difficulties that were of little concern when the price of polysilicon was high and the price of electricity to power the Siemens reactors was low. As a cold wall reactor process, much of the heat generated to deposit silicon is removed by cooling of the reactor walls resulting in low energy efficiency. Furthermore, the Siemens process is a batch process that must be shut down in each production cycle when the rods have grown sufficiently large. The thick product rods are replaced with new seed rods and the deposition process is repeated.

The success of the Siemens reactors has been largely credited to the decoupling of the heating of the silicon rods from the heating of the feed gas (Filtvedt et al. 2010). The feed gas is only heated when the trichlorosilane and hydrogen are near the hot silicon rods where the deposition reaction occurs. The walls of the Siemens reactor are vigorously cooled to prevent silicon deposition on the walls and to hold down the temperature of the feed gas throughout the bell jar except near the heated silicon rods.

The major advantage of the Siemens process is that it is a mature technology that can produce high purity silicon (often greater than 9 N). The Siemens process is relatively easy to operate and has become very reliable. Siemens reactors are run worldwide by many companies. The Siemens process is made commercially viable by a separate fluidized-bed hydrochlorination process shown in the summary below. In the hydrochlorination process metallurgical grade silicon is reacted with the Siemens by-product silicon tetrachloride ( $\text{SiCl}_4$ ) and hydrogen to produce trichlorosilane feed for the Siemens reactor.

Almost all commercial Siemens reactors use trichlorosilane as the feed material. The process produces very little silicon powder, as the reaction intermediate hydrogen chloride reacts with silicon powder to produce more trichlorosilane according to the following reaction:

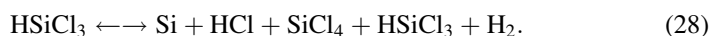


In summary, the chemistry involved in the Siemens process is based on the following two reactions:

1. Metallurgical grade silicon, silicon tetrachloride, and hydrogen are converted to trichlorosilane in a heated hydrochlorination equilibrium reaction



2. In a Siemens reactor trichlorosilane undergoes an equilibration reaction to deposit silicon and produce silicon tetrachloride, hydrogen chloride, and hydrogen



Over the last 50 years the Siemens process has been optimized by using increasingly larger reactors and achieving high conversion rates (Fu et al. 2015). The Siemens reactors are readily scalable for commercial operation. Production levels are increased by adding more reactors. The economics of the Siemens process depends on the recycling of all forms of the off-gas products or their use in other processes within a chemical complex. One needs to reduce losses of silicon or chloride from the process. Even though Siemens technology has been brought to a high level of development, the major deficiency remains that the process is a batch process that is a high consumer of electric power.

The Siemens process remains the dominant process for the production of polysilicon due to the high purity of the product silicon and the high reliability of reactor operations. As the demand for polysilicon continues to increase, the question remains whether the rising cost of electricity and the added costs for running a batch process will make the FB route to make polysilicon production more cost-effective.

## Comparison of the Fluidized-Bed Process and the Siemens Process for Making Polysilicon

There are both advantages and disadvantages to the operation of each type of polysilicon production process. With increasing demand for polysilicon and with the high electrical power consumption of the Siemens process, there are renewed incentives to investigate new production techniques. Fluidized-bed technology has the potential to bring significant cost reduction specifically to polysilicon production as it has done in many other industrial processes.

The following table compares various aspects of the silane-based FB production of polysilicon with the Siemens process:

Based on Table 1, the comparison between the Siemens and FB processes is quite complex. Each technology has advantages and disadvantages. The following discussion expands on the information presented in the chart.

**Table 1** Comparison of several factors between Siemens reactors and fluidized-bed reactors in the production of polysilicon

Fluidized-bed process (Based on $\text{SiH}_4$ Feed)	Siemens process (Based on $\text{HSiCl}_3$ Feed)
Potential for reduced Si cost	Limited future cost reduction likely
Continuous operation	Batch process
Flowable, spherical Si product	Crushing step required to convert rods to chunk Si
Noncorrosive feed gas	Corrosive feed gas
Reaction goes to completion	Limited equilibrium reaction producing HCl and $\text{SiCl}_4$
Produces higher amounts of powder	Minimal Si powder produced
80–90% less energy required	High electric power consumption
Minimal cooling required (hot wall)	Large cooling load to cool reactor walls (cold wall)
Developing technology	Mature optimized technology
Reactor operates at 650–850 °C	High temperature reactor operates near 1150 C
Chloride-free feed product	Residual chloride in product from $\text{HSiCl}_3$ feed
Violent fluidized-bed environment	Stable, fixed reactor environment

There are several key issues encountered when comparing the two silicon production methods. As a batch process, there is extensive time and effort required to remove the silicon product rods from a Siemens reactor and set up the reactor for each new cycle. Because silicon is harvested from a Siemens reactor as a thick rod that is broken into large chunks, there is little surface contamination from the environment. In contrast the production and handling of granular silicon from a fluidized-bed reactor is prone to contamination. Both during production and during handling of the final granular polysilicon product the vastly larger surface area of the silicon granules can lead to contamination from other elements that come into contact with the product. In general, silicon from Siemens reactors tends to have higher purity than silicon from fluidized-bed reactors, even when considering the crushing process to reduce the size of Siemens rods (Bernreuter 2014). Solar cell efficiency is dependent on the purity of the silicon going into the solar cell. Even though FB silicon does not normally have the purity found in silicon produced by the Siemens process, it has been argued that FB reactors offer a viable, low-cost source of polysilicon to manufacture solar cells (Stemann et al. 2012).

One of the major differences between FB reactors and the Siemens process is the feed gases. These differences in chemical and reaction properties result in many of the differences in the two types of processes. The fluidized-bed reactor uses silane, which is a chloride-free silicon hydride gas. Silane can decompose completely under the reaction conditions in a noncorrosive environment. With a silane feed another advantage is that the reaction can be run at a lower temperature because of silane's lower decomposition temperature (see section "Chemical Reaction of Silane in a Fluidized-Bed Reactor"). The main downside consideration with silane as a feed gas is that a disproportionation plant is required to convert trichlorosilane to silane.



A major industrial factor is that the Siemens process produces only rods of polysilicon that have to be crushed into smaller particles for downstream crystallization processing.

## Process of Polycrystalline Silicon Fabrication

Spherical silicon particles are the favored form for handling polysilicon for downstream continuous crystallization processing (Filtvedt et al. 2010). Round particles of silicon have greater flowability for feeding polysilicon. The spherical, granular product silicon from a fluidized-bed reactor is uniquely suited as feed for continuous Czochralski (Cz) crystal pullers in the manufacture of monocrystalline silicon. The specific need for flowability in polysilicon is yet another cost-reducing factor encouraging the development of fluidized-bed technology.

Research continues on fluidized-bed reactors to improve their benefits. As mentioned fluidized-bed reactors can be run in a continuous mode with far less electrical power demands. On the down side, fluidized-bed silicon reactors must be periodically cleaned and repaired.

As mentioned above, there are many industrial processes that successfully utilize fluidized beds in various chemical processes. Typically, such processes are developed and optimized over a number of years to reach a stage where the process is stable in commercial operation. The use of fluidized-bed technology for the deposition of silane to silicon has been slow to follow this pattern. Even though the theoretical advantages of fluidized bed for silane production are well recognized, the actual development of the technology in commercial-sized plants has proven to be challenging. The difficulties result from the nature of the reaction that is being carried out and the need to resolve conflicting factors. Many of these issues will be expanded later in this chapter.

## Downside to the Use of Silane-Based Fluidized-Bed Technology

Table 1 points out the main advantages and disadvantages of fluidized-bed technology to produce polysilicon, but it does not prioritize them. One major disadvantage of FB reactors is that they may produce less pure polysilicon than the Siemens rods at this time, but the potential exists for improvement in the purity of FB polysilicon product. Another disadvantage is that FB process is more complicated to operate. Problems typically encountered with all FB reactors such as defluidization and plugging may occur. The possibility of slugging, wall deposition, and agglomeration all complicate the operation of a FB reactor. The production of silane alone requires the operation of a disproportionation plant before the actual silane deposition unit can be run. The production of silicon dust as a by-product of using silane in a FB reactor is a disadvantage because of product loss and because of the need to remove the silicon dust. The numerous disadvantages of the FB process have allowed the Siemens process to dominate as the preferred method for polysilicon production.

Progress has been made in overcoming or reducing many of the current disadvantages encountered with the FB silane process. A more systematic review of the challenges of the silane-based FB process will be presented later.

## **Alternate Technologies for the Production of Polysilicon**

Although this chapter focuses on fluidized silane-bed technology to produce polysilicon, it is useful to briefly mention other related methods currently being studied to produce polysilicon. By recognizing other methods for silicon purification, it is possible to put some context into why the silane-based fluidized-bed method is currently considered as the most likely to succeed and to replace the Siemens process.

### **Use of Trichlorosilane in Fluidized-Bed Production of Polysilicon**

The use of silane in a fluidized bed has been mentioned above as the most favored alternative for fluidized-bed production of silicon. Industry has explored many other feed compounds for deposition to produce polysilicon. In 1961 DuPont patented the use of trichlorosilane in a fluidized-bed reactor to purify silicon (Bertrand and Olsen 1961). Wacker has operated a plant and has developed fluidized-bed technology using trichlorosilane directly as the feed material (Wacker 2016). Wacker claims to have eliminated silicon dust formation and to have produced high purity polysilicon (Weidhaus et al. 2005).

The trichlorosilane-based FB process produces spherical polysilicon but the plants have so far proven not to be economical. The major difficulty is that the deposition reaction has to be run at the higher temperature range of 850–1000 °C, which is far above that of a silane-based FB reactor. The reactor has to withstand a corrosive chloride environment at high temperatures. One encounters difficulties with materials of construction that can withstand the highly corrosive environment and can achieve high levels of purity in the product polysilicon. There is also the problem of chloride incorporation into the silicon. As with the Siemens process, deposition with trichlorosilane runs as an equilibrium reaction that does not go to completion so that extensive recycling is required. Silane remains the favored silicon compound for use in a FB reactor for polysilicon production.

### **Use of Silane in Siemens Reactors to Make Polysilicon**

One novel approach to silicon production uses a Siemens type reactor, with silane replacing trichlorosilane as the feed gas (Revankar and Lohoti 2014). With silane feed the Siemens reactors can be run at a lower temperature. The major problem using a Siemens reactor with silane appears to be excessive silicon powder formation. To reduce the powder problem the Siemens reactors have to be run with lower silane conversions. A high proportion of the silane must be recovered from the off gas and recycled.

## Alternate Approaches to Polysilicon Production

There are many other approaches to polysilicon production that have been explored in the patent literature. One interesting approach deals with the problem of creating silicon dust. The technique is to convert all of the silane directly to silicon powder in a free space reactor. The silicon powder is compressed into briquets and melted to form an ingot (Iya 1987).

---

## Silane Reactions in a Fluidized-Bed Reactor

The reaction of silane in a FB reactor consists of a complex series of chemical steps. The thermal decomposition of silane has been extensively studied (Walch and Dateo 2001). The low pressure (often far below one atmosphere) epitaxial deposition of silicon from silane plays a major part in the semiconductor industry and is well understood. The higher-pressure deposition of silicon at above one atmosphere encountered in the preparation of polysilicon from silane has had much more limited study. A high-pressure (well above one atmosphere) FB silane-based fluidized-bed silicon plant has been constructed and operated in a joint venture between SunEdison and Samsung (Roselund 2015). After a startup and initial operation, this plant has not restarted due to business conditions. GCL has also developed high pressure FB technology using silane feedstock.

## Chemical Reaction of Silane in a Fluidized-Bed Reactor

The decomposition of silane is known to occur between 350 °C and 480 °C depending on conditions such as hydrogen pressure and the availability of surfaces that can support the deposition reaction (Filtvedt et al. 2010). In a free space reaction in the absence of silicon particles it is known that the pyrolysis of silane produces mostly silicon dust and not crystalline silicon. It is also well known that silicon particles must be heated to the range of 650–850 °C for the deposition of silicon compounds to form polysilicon on silicon particles. Several attempts have been made to combine the information on the lower temperature decomposition and the higher temperature deposition reaction to provide a coherent mechanism that explains the operating chemistry of a silane fluidized-bed reactor (Lai et al. 1986).

## Homogeneous, Heterogenous, and Scavenging Reactions of Silicon Particles

To understand the mechanism of how a silane-based fluidized bed converts silane to silicon one needs to consider the two phases present in the reactor. The bubble phase

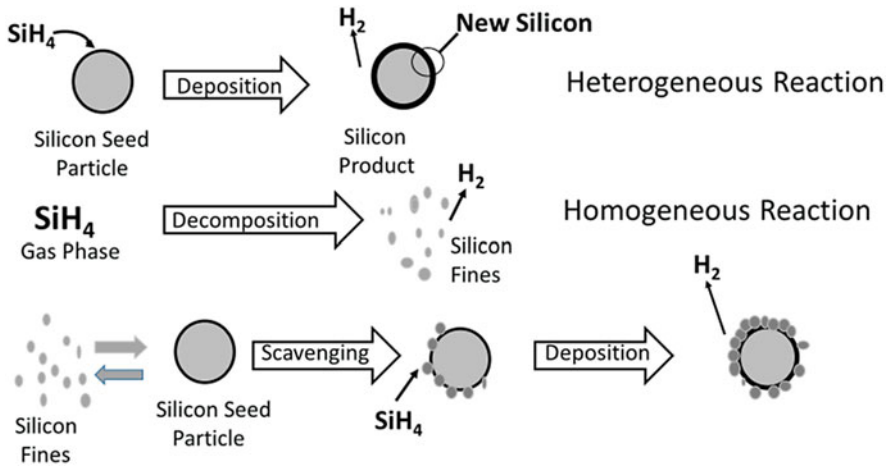


**Fig. 4** Three main types of processes found in a silane-based fluidized-bed reactor. They include (1) a heterogenous reaction on the surface of a silicon particle, (2) a homogeneous reaction in the gas phase forming silicon powder, and (3) surface scavenging of silicon powder on a silicon particle followed by deposition

consists of the space between the silicon particles existing as bubbles. The emulsion phase is made up of the silicon particles and the nearby gases. The small silicon particles provide a large surface area for reaction with the gas phase.

The three main types of reactions taking place in a silane-based fluidized bed are shown in Fig. 4.

The chemistry of the bed can be broken down into three types of reactions. The preferred reaction is the heterogenous decomposition of silane on a silicon particle. The undesirable reaction occurs with the homogeneous thermal decomposition of silane to produce fine silicon dust (Kerner et al. 2003). The favorable scavenging mechanism removes some of the silicon dust by the accretion of dust in the submicron size range onto fluidized silicon particles. The silicon dust then chemically sinters onto the granular particles aided by the heterogeneous reaction.

It is possible to understand how this proposed mechanism can explain the observed FB reactor behavior. The heterogeneous reaction benefits from the large surface area provided by the silicon particles. The bubbles and space occupied by the hot gas phase provide a place where the homogeneous reaction produces silicon dust. Some of the dust could migrate to the surface of hot silicon particles that then scavenge the silicon dust.

A typical silane fluidized-bed reactor is run at a temperature between 650 °C and 850 °C to allow the growth of silicon particles by deposition. The ultimate goal is to find operating conditions where powder production is limited so that the rate of granular silicon preparation is commercially viable. Powder formation cannot be completely suppressed and some silicon is always formed as a fine dust by-product at the current level of silane FB reactor development.

The nature of the fluidized-bed reactor further complicates the optimization of granular silicon production. Fluidized-bed reactors provide a highly variable reaction environment. Temperature, pressure, concentration, silicon surface area, and many other parameters vary throughout the reactor in a complex way that has to be modeled analytically. There are a large number of physical parameters that must be optimized to control the complex reactions involved in the operation of a fluidized bed to convert silane to polysilicon.

## Modeling of Silane Fluidized-Bed Reactors

The complexity of designing and operating a silane-based fluidized-bed reactor is a daunting task. There are so many challenging issues and complex factors in play that simple intuition and engineering tools have not proven sufficient to solve the problems. One area that shows promise in improving understanding of the process involved is computational fluid dynamics (CFD) modeling (Kunii and Levenspiel 1991). The silane fluidized-bed system represents a complex case that is being developed.

### Advantages of Using Numerical Simulation

The steady improvement in the speed and memory capacity of computers has led to the wide spread use of numerical simulation. This branch of physics and engineering complements experimental and theoretical work by providing an alternative cost-effective means of solving problems. As such it offers the means of testing theoretical advances for conditions unavailable experimentally. By using numerical simulation, the lead time in design and development is significantly reduced. Simulation can provide more detailed and comprehensive information. More importantly, numerical simulation is much cheaper than real-time experimental testing and will become even more so in the future.

### Classification of Models for Fluid Bed

Generally speaking, there are two main categories of models for fluid beds: 1D phenomenological models and detailed CFD models (Filtvedt et al. 2010).

Historically, two classes of phenomenological models have been proposed to model fluid beds: the pseudo homogeneous approach and the two-phase approach (Yang 2003). The conventional pseudo homogeneous model, where only one phase is taken into account, may include ideal flow models, dispersion models, and residence time distribution models. Due to lack of accuracy, the use of this approach has been slowly dropped.

The two-phase model assumes that the bed can be divided into a bubble phase and an emulsion phase. The bubble phase contains a large gas voidance and very little solids. The emulsion phase contains most of the bed particles. The two-phase model was originally proposed by Toomy (1952).

Detailed CFD models solve the mass, momentum, and energy equations on a point-to-point approach to compute local variables. There are several approaches

used in detailed CFD models, each making a tradeoff between the modeling effort and the computational cost. Greater physical resolution reduces the modeling effort, but increases the computational cost. Generally speaking, there are two main categories: the Euler-Euler model and the Euler Lagrangian model. In the Euler-Euler model, both the gas phase and solid phase are treated as an interpenetrating continuum. The conservation equations are solved for each phase with phase interaction terms and constitutive relations. In the Euler-Lagrangian model, the solids are treated as a discrete phase. This model is more realistic, but is computationally more intensive and assumptions are made (Pannala et al. 2010).

### Modeling of a Silane Fluid Bed

Several research groups have investigated modeling of a silane-based FBR for silicon production. The main models are reviewed below:

Historically, there are many variations of two-phase models for fluidized bed and the Kunii and Levenspiel (1991) model has wide spread use for the bubbling fluidized bed. In this model, the bubble diameter can be kept invariant through the bed and is treated as a fitting parameter. An alternative is to allow the bubble size to vary along the bed axis. The initial bubble diameter formed at the surface of a perforated and of a porous gas distribution plate can be calculated from the following equations, respectively:

$$d_{b0} = \frac{1.3}{g^{0.2}} \left[ \frac{u_0 - u_{mf}}{N_{or}} \right] \quad (29)$$

$$d_{b0} = \frac{2.78}{g} (u_0 - u_{mf})^2, \quad (30)$$

where  $u_{mf}$  is the fluidization velocity of the bed,  $u_0$  is the superficial gas velocity,  $g$  is the gravity acceleration,  $N_{or}$  is the number of orifices per unit area. The bubble growth at any level  $z$  in the bed can be correlated as:

$$d_b = 0.0085 [1 + 27(u_0 - u_{mf})]^{1/3} (1 + 6.8z)^{1.2}. \quad (31)$$

The rise velocity of the bubbles can be calculated as

$$U_b = 0.71 \sqrt{gd_b} + u_0 - u_{mf}. \quad (32)$$

The volume fraction occupied by bubbles can be calculated as

$$\delta = \frac{u_0 - u_{mf}}{u_b}. \quad (33)$$

The interchange coefficient of gas between bubble and the emulsion can be calculated as

$$k_{be} = 4.5 \frac{u_{mf}}{d_b}. \quad (34)$$

$u_{mf}$  can be calculated by the Ergun equation as below

$$\frac{1.75}{\varepsilon_{mf}^3 \phi_s} \text{Re}_{mf}^2 + \frac{150(1 - \varepsilon_{mf})}{\varepsilon_{mf}^3 \phi_s^2} \text{Re}_{mf} = \frac{d_p^3 \rho_g (\rho_s - \rho_g) g}{\mu^2} \quad (35)$$

and

$$\text{Re}_{mf} = \frac{\rho_g u_{mf} d_p}{\mu}, \quad (36)$$

where  $\varepsilon_{mf}$  is void fraction of the fluidized bed at a minimum fluidization,  $\phi_s$  is the sphericity of the particles,  $\rho_s$  is the particle density,  $\rho_g$  is the gas density,  $d_p$  is the diameter of the particle, and  $\mu$  is the viscosity of the gas.

By making a simple mass balance and noting the reactant gas A (in our case silane), we only consider the homogenous reaction in the bubble phase

$$-\delta U_b^* \frac{dC_{Ab}}{dz} = \delta k_{hom} C_{Ab} + k_{be} (C_{Ab} - C_{Ae}). \quad (37)$$

And in the emulsion phase, only the heterogeneous reaction is considered

$$-(1 - \delta) u_{mf} \frac{dC_{Ae}}{dz} = (1 - \delta) (1 - \varepsilon_{mf}) k_{het} C_{Ae} - \delta k_{be} (C_{Ab} - C_{Ae}), \quad (38)$$

where  $C_{Ab}$  means the concentration of reactant A in the bubble phase and  $C_{Ae}$  means the concentration of reactant A in the emulsion phase.

Where the rise velocity of the bubble gas, not just the bubble is

$$U_b^* = u_b + 3u_{mf}. \quad (39)$$

Several researchers have used the two-phase model to study silane pyrolysis in a fluidized bed. Caussat et al. (1995) used four different models to compare with his experiment data. He concluded that the fines are mainly formed by wall deposition rather than homogeneous decomposition in the bed, which is in disagreement with other studies (Hsu et al. 1987), but he used nitrogen as carrying gas, rather than hydrogen, which can be responsible for the different results.

Lai et al. (1986) applied both an ideal back mix reactor model and the two-phase fluidized model to simulate a silane FBR. In his model, similar to Hsu's proposal, there are nine different reaction pathways. He also used the method of moments to count the population balance for fines. His model predictions show reasonable agreement with experimental results. The continuous stirred tank reactor (CSTR) model yields an upper estimate on the production rate and the fluidized-bed bubbling

reactor (FBBR) model overpredicts the formation of fines. It concludes that in order to suppress fines formation, a reactor needs to have good gas-solid contacting in the gas inlet distributor region and suppress bubbles formation.

Later Pina et al. (2006) used the two-phase model approach to simulate a spouted fluidized-bed reactor. In a spouted fluidized bed, the inlet gas is introduced through a spout nozzle at the bottom of the bed rather than a distributor plate. In his model, two regions in series are taken into account, a spout zone in the bottom followed by a fluidized-bed region. A new set of equations is used to model the spout region exchanging gas between the spout and surrounding dense emulsion. He also used a detailed population balance equation to model particle size distribution in the reactor. Two adjustable parameters, a scavenging coefficient and an agglomeration constant, have to be fitted to the experimental data for each case and then correlated as a function of the silane concentration. Then the model was tested for longer experimental runs and found to have good agreement with the data.

Kimura and Kojima (1991) used a simplified two-phase model for a silane FBR, where the bubble diameter is invariant throughout the bed and is treated as a fitting parameter. They only considered two reaction pathways: the homogenous reaction to form fines and the heterogeneous reaction to deposit on the particles. Their simulation results are compared with experimental data by Hsu et al. (1987). The experimental tendency of increasing of fines elutriation with increasing silane concentration or increasing bed temperature can be explained well. However, at higher bed temperature, the numerical results of fines elutriation are much higher than the experimental data. As the author pointed out, it can be due to the lack of a scavenging effect in their model.

### Eulerian-Eulerian CFD Model

Eulerian-Eulerian modeling is the most commonly used approach for fluidized-bed simulations because it can handle large industrial-scale geometries. The general idea is to formulate a multifluid model to treat both solid phase and gas phase as an interpenetrating continuum and therefore to construct integral balances of mass, momentum, and energy for both phases. Appropriate boundary conditions and jump conditions will be applied at the interfaces to account for the discontinuity effect.

Mass conservation equations of gas and solid phases:

$$\frac{\partial}{\partial t} (\alpha_g \rho_g) + \nabla \cdot (\alpha_g \rho_g \overline{V}_g) = 0 \quad (40)$$

$$\frac{\partial}{\partial t} (\alpha_s \rho_s) + \nabla \cdot (\alpha_s \rho_s \overline{V}_s) = 0. \quad (41)$$

Momentum conservation equations of gas and solid phases:



$$\frac{\partial}{\partial t} (\alpha_g \rho_g \vec{V}_g) + \nabla \cdot \frac{\partial}{\partial t} (\alpha_g \rho_g \vec{V}_g \vec{V}_g) = -\alpha_g \nabla p + \nabla \cdot \bar{\bar{\tau}} + \alpha_g \rho_g \vec{g} + K_{gs} (\vec{V}_g - \vec{V}_s) \quad (42)$$

$$\frac{\partial}{\partial t} (\alpha_s \rho_s \vec{V}_s) + \nabla \cdot \frac{\partial}{\partial t} (\alpha_s \rho_s \vec{V}_s \vec{V}_s) = -\alpha_s \nabla p - \nabla P_s + \nabla \cdot \bar{\bar{\tau}} + \alpha_s \rho_s \vec{g} - K_{gs} (\vec{V}_g - \vec{V}_s). \quad (43)$$

The drag between gas and solid phase is one of the dominant forces in gas-solid fluidized-bed applications. There are many correlations in the literature for calculating the momentum exchange coefficient  $K_{gs}$  which may have different ranges of application. The solid phase momentum equation contains an additional term called solid pressure,  $P_s$  to account for particle-particle collisions. The stress term in solid phase momentum transfer is normally computed by using kinetic theory.

MFIX (Multiphase Flow with Interphase Exchange) is an open-source CFD (computational fluid dynamics) code developed and maintained by NETL (National Energy Technology Laboratory), and it is a powerful tool for the simulation of fluidized beds using the Eulerian-Eulerian method. Cadoret et al. (2007) performed silane FBR experiments, and the MFIX code was used for simulation. They used nitrogen as carrier gas and dense alumina powders as deposition seeds, both of which are rarely used in industry. They did both 2D and 3D simulations and found that 2D simulation results are very inaccurate and that 2D simulations were not suitable for fluidized-bed modeling. Later, they performed another group of 3D simulations (Reuge et al. 2009), in which they used detailed silane reaction kinetics. Besides determining which kinetic model is more appropriate, they concluded that there is a strong interaction between bed hydrodynamics and reaction chemistry. Also, silicon deposition from silane mainly occurs in the dense zones of the bed where silylene ( $\text{SiH}_2$ ) does much of the work within the bubble phase and at its periphery.

### Particle-in-Cell Method

The Eulerian-Eulerian approach has trouble modeling flows with a distribution of particle types and sizes because separate governing equations must be solved for each of them and it can be too computationally intensive. The traditional Eulerian-Lagrangian approach will treat each particle as a tracking element and resolve the fluid flow around each particle with a no-slip condition. This saves the efforts of developing closure models, but is so computationally intense that only a small number of particles and a small domain of fluid can be realistically done.

The particle-in-cell (PIC) method is based on the Eulerian-Lagrangian approach, but also combines the good features of the Eulerian-Eulerian approach to make it computationally affordable. Like the regular Eulerian-Lagrangian model, PIC employs a fixed Eulerian grid and Lagrangian particles, but rather than resolving fluid flow around each particle, it averages the fluid flow over a spatial region

containing a number of particles. Also, the particles are not tracked one by one, but a collection of particles called “numerical particles” are solved together, and both the interactions of the particles and fluid-particle momentum transfer are calculated through closure models on the Eulerian grid. Particle properties are interpolated to the grid and the flow field on the grid is interpolated back to the particles.

Solid Phase Equation:

$$\frac{du_s}{dt} = D_s(u_g - u_s) - \frac{1}{\rho_s} \nabla p + g - \frac{1}{\alpha_s \rho_s} \nabla \tau_s = 0, \quad (44)$$

where  $D_s$  is the drag function and  $\tau_s$  is the particle normal stress due to collisions,  $\alpha_s$  is the particle volume fraction.

Mass and momentum conservation equations For the gas:

$$\frac{\partial}{\partial t} (\alpha_g \rho_g) + \nabla \cdot (\alpha_g \rho_g \vec{V}_g) = 0 \quad (45)$$

$$\frac{\partial}{\partial t} (\alpha_g \rho_g \vec{V}_g) + \nabla \cdot \left( \alpha_g \rho_g \vec{V}_g \vec{V}_g \right) = -\nabla p + \nabla \cdot (\alpha_g \vec{\tau}) + \alpha_g \rho_g \vec{g} + F, \quad (46)$$

where  $F$  is the rate of momentum exchange between the fluid and particles per unit volume.

Barracuda is a commercial software owned by CPFDF, (<https://cpfd-software.com>) that successfully implemented the PIC method to solve particle fluid interaction problems, which has more and more wide spread use in industry. Parker (2011) simulated JPL silane FBR experiments (Hsu et al. 1987) by using Barracuda. A simple empirical first order silane reaction mechanism is adopted in his simulation and both homogenous and heterogenous reaction rate data are taken from the literature. A constant scavenging coefficient is used to capture the scavenging effect and was found to reasonably capture the trend of the experiments. The simulation results can predict the temperature gradient inside the bed fairly well in comparison with experimental measurements. The simulation can also reproduce the fines production rate with changing silane concentration in the feed gas. The effect of the distributor type was examined and found that a nozzle type inlet would create a spouted bed and a screen mesh inlet would result in much more uniform gas distribution and a much better performing bubbling bed, which is also consistent with the experimental results.

## Multiscale Modeling

There are different time scales in the complicated physics of silane fluidized-bed reactors. The chemical reaction is almost instantaneous, and the hydrodynamics can take few seconds to gain equilibrium, while the particle size growth may take hours and days to reach steady state. In order to capture all the time scales, Balaji et al. (2010) developed a multiscale model for a silane FBR by coupling the CFD solver COMSOL and the equation solver MATLAB. The hydrodynamics are solved by the CFD module in COMSOL, which provides information to a CVD module in MATLAB. The CVD module calculates the overall production rate and feeds it to

population balance module in MATLAB. The population balance module calculates the particle size distribution and gives an average particle diameter to feed the CFD module to start another round of computation. The simulation results were validated by experiments.

---

## **Operation of a Silane-Based Fluidized-Bed Reactor to Make Silicon**

The operation of a silane-based fluidized bed reactor is relatively complex and provides unique difficulties when compared to the operation of most other industrial FB reactors. In order to understand the state of this technology it is necessary to review many of the operation steps that are encountered in a FB plant to make silicon from silane.

### **Feed Gas to the Fluidized-Bed Reactor**

One of the key factors in optimizing silicon deposition and reactor production rate is the  $\text{SiH}_4/\text{H}_2$  mole ratio of the feed gas. Ideally one would prefer to use 100% silane as the feed gas in order to maximize reaction productivity, but this would result in the formation of a large amount of silicon dust. Powder formation can be reduced by diluting the silane feed gas with hydrogen. The optimum feed gas concentration has been found to be between 10% to 30% silane in hydrogen depending on the reactor operating conditions and geometry (Filtvedt 2013). This amount of hydrogen does not eliminate powder formation, but reduces it to acceptable levels. The hydrogen acts primarily as a diluent to reduce the concentration of silane and thereby reduce the reaction rate. As the major component in the fluidizing gas, the viscosity, thermal conductivity, heat capacity, and other physical properties of hydrogen play a vital part in maintaining the fluidization and reactions in the fluidized bed.

The hydrogen is recycled after passing through the fluidized-bed reactor. The hydrogen, unreacted silane, and other reaction by-products can be cryogenically separated. The hydrogen is returned to the reactor and mixed with silane to continue the operation of the fluidized bed. The unreacted silane is purified and recycled back to the reactor.

### **Preheating the Feed Gas**

One of the most challenging aspects of operating a silane-based fluidized-bed reactor is the control of heat and temperature. It is difficult to introduce enough heat through the reactor walls into the reactor interior to achieve the optimum reaction temperature. In a typical reactor one would increase the temperature of the reactor walls to obtain the desired amount of heat transfer to the reactants. This option must be approached with caution for a silane-based process because it would greatly increase

silicon deposition on the reactor walls. The fluidized silicon particles need to be heated from the reactor wall so that they can then heat the feed gas to the reaction temperature. This heat transfer has to be accomplished in such a way as to minimize the temperature of the reactor wall.

The use of a preheater to increase the temperature of the of the feed gas has proved useful. The temperature of the preheater is limited by the reactivity of silane. It is undesirable to decompose the silane in the preheater to form silicon dust or to deposit silicon. Given the decomposition temperature of silane, the feed gas is typically heated to less than 400 °C depending on the operating conditions and structure of the preheater (Filtvedt et al. 2012). The remainder of the heat energy to bring the feed gases up reaction temperature of over 700 C must come from the heated walls and heated fluidized silicon particles.

Many different arrangements have been studied for introducing heated feed gases into the reactor. One patented approach involves heating hydrogen to over 1000 °C and using this hot hydrogen as the sole source of heat for the reactor. As the hydrogen is mixed with the silane, the reaction gas is brought quickly to reaction temperature (Spangler and Stucki 2015).

## Distributor and Jet Nozzles to Introduce the Feed Gas

The feed gas is typically introduced into the bottom of the reactor through a distributor or jet nozzles. The distributor consists of many orifices that spread the feed gas out over the bottom surface of the reactor to make uniform fluidization of the silicon particles possible. Jetnozzles consist of tubes with designed shapes and diameters that can inject the feed gas stream further into the reactor bed. Jets offer the ability to direct the flow of gases and increase the gas velocity into the bed of granular silicon. One approach in the patent literature, which makes use of the ability to aim the flow from the distributor proposes directing hydrogen towards the wall of the reactor to reduce the amount of silicon deposition on the reactor wall. (Kulkarni et al. 2013).

One major challenge is to ensure that the temperature of the distributor or jets is kept below the reaction temperature of silane as feed gas passes through the distributor to the reactor. Much of the heat that warms the distributor comes from the heated silicon particles that migrate from hot parts of the reactor. The granular particles can be at the reaction temperature which is well above the decomposition temperature for silane. The objective is to keep the bottom of the reactor with the distributor or jet nozzles cool enough to prevent the premature decomposition of silane to silicon deposits or dust that will plug the jet nozzles or the distributor orifices.

There have been several approaches in the patent literature for cooling of the distributor. Most of the methods use cooling fluids to reduce the temperature of the distributor to below the decomposition temperature of silane. The major differences between the many distributor and jet designs are in the placement of holes for the feed gases and channels for the cooling fluids.

The plugging of the distributor and jets is a significant problem for the long-term operation of a fluidized bed. Dust can easily plug the narrow gas orifices and disrupt the flow of feed gas and the fluidization of the bed. Large chunks of silicon from agglomeration of silicon particles or from the walls of the reactor can drop to the bottom of the reactor and plug the gas inlets. The only way to clear such blockages is to empty the reactor and remove the silicon responsible for stopping the gas flow.

## Different Designs for Heating Silane-Based Fluidized-Bed Reactors

The main source of heat that brings the silicon particles and feed gas up to reaction temperature comes from the heated reactor walls, which conduct thermal energy to the silicon particles that come in contact with the wall. The heat is distributed to the gas throughout the reactor by the movement of the fluidized particles.

There are several different types of reactor designs that have been proposed. The simplest design is a common hot wall metal reactor structure (Type 1), as shown in Fig. 5a. The Type 1 reactor is typical of many fluidized-bed reactors where the heated metal walls of the reactor come in contact with the feed gases and fluidized silicon particles (Gautreaux and Allen 1988).

At the reaction temperature of over 600 °C the diffusion rate of metals such as iron throughout the silicon deposited on the wall is sufficiently rapid that metals are spread to the fluidized silicon particles by contact with the silicon deposited on the reactor wall. More recent designs to improve product purity included the use of an inert liner (Type 2) for the inside of the reactor (see Fig. 5b). The liner is typically constructed with a hard-ceramic material to reduce the wall erosion by the fluidized silicon particles.

A more recent approach has the placement of the heating elements inside the metal pressure containment vessel as shown in Fig. 6 (Kim et al. 2010). An inert liner is placed next to the heating elements as shown below:

Heat to bring the fluidized bed up to reactor temperature comes from two sources. As mentioned above a preheater brings the reactants from low temperature to above

**Fig. 5** Reactor designs using resistive heaters to provide thermal energy to the reactor. Type 1 reactor (Fig. 5a) has a metal wall. In Type 2 (Fig. 5b) the reactor has a liner that helps to reduce metal contamination to the fluidized silicon particles

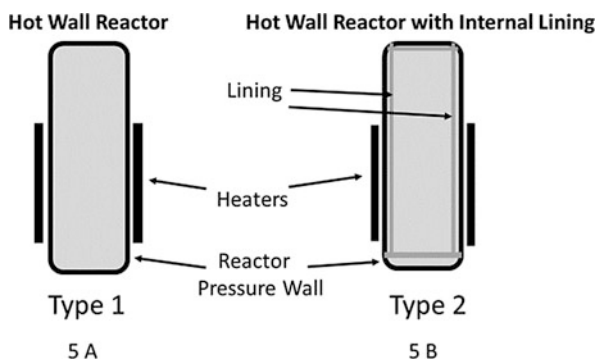


**Fig. 6** Cold wall reactor. Going from outside of the reactor toward the inner reactor chamber, which holds the granular silicon, one encounters the following: (1) outer reactor pressure wall, (2) a layer of insulation, (3) a heating element, (4) the reactor liner, (5) the inner reactor chamber

**Cold Wall Pressure Vessel with Internal Heating**

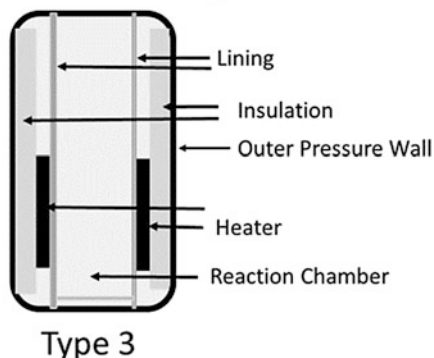
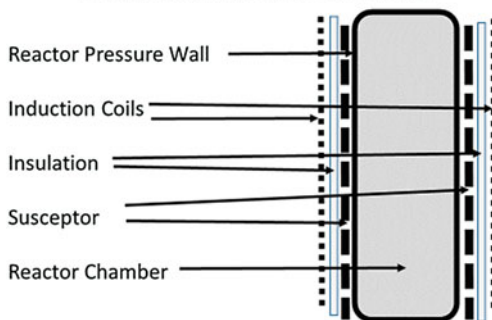


**Fig. 7** Reactor with external induction heating (Clary and Wikman 1993). Going from outside to the heating unit includes the following: induction coils on the outside followed by a layer of insulation. Next comes a susceptor that is next to the pressure wall of the reactor. The heated susceptor conducts heat to the reactor wall

**Reactor with Induction Heating**



300 C. The final heat source is the heated reactor walls which supply the bulk of the thermal energy and which brings the fluidized-bed reactor temperature to above 600 C.

In addition to electrical resistance heating, induction heating has proven to be a useful method for introducing the necessary amount of heat energy into a silane-based fluidized-bed reactor (Clary and Wikman 1993). One of the advantages of induction heating is that it can bring a large amount of thermal energy uniformly into a large area of the reactor wall. Below is a diagram showing one of many patented reactor designs that utilize induction heating (Fig. 7):

This unit consists of a reaction chamber that is surrounded by the induction unit. Next to the chamber is a susceptor that is heated by the induction coils. After the susceptor is heated by the induction coils the susceptor brings that reactor wall up to reaction temperature. Between the induction coils and the susceptor is insulation that holds most of the heat within the reactor.

Another approach to reactor design for silane FB reactors involves separating the FB reactor into zones (Iya 1989). It has been mentioned that the distributor can be

cooled to prevent silicon deposition while the reactor is heated to create two temperature zones. Another approach is to try to heat different parts of the reactor to different temperatures. The idea is to limit the locations where silane decomposition and the deposition can occur to specific areas in a reactor. Given the violent nature of mixing in a fluidized-bed reactor, the ability to control the temperature at specific zones in a reactor is limited.

Reactor design remains one of the areas that holds the most promise for improving the efficiency of a silane fluidized-bed reactor's operation. Companies continue to build commercial scale reactors with innovative designs. Modeling of the FB reactors remains an important tool for evaluating different thermal designs before they are built and for operating the reactors after they have been constructed.

## **Reactor Dimensions, Pressure, and Silicon Production Rate**

Factors such as reactor height and diameter are critical to the operation of a fluidized-bed reactor (Filtvedt et al. 2012). The height of the fluidized-bed reactor can affect the residence time of the feed gas, the silane conversion and the residence time for scavenging of powders.

Pressure is an important variable when optimizing a silane FB reactor. With greater pressure one is able to increase the production rate due to increased mass feed rate. Building a reactor to operate at greater pressure at high temperatures involves greater design complexity and a reduced safety margin. Working with a feed gas at higher pressure means that silane will be at a higher concentration and the fluidization properties of the gas phase will be different than at lower pressures.

The diameter of the reactor is a major factor in determining the FB reactor bed capacity. Since the heating of the silicon particles to the reaction temperature typically occurs through the walls of the reactor, the amount of wall heating surface area is important. The surface to volume ratio of the reactor decreases with increasing diameter. A larger diameter reactor may allow the processing of more silane, but it becomes more difficult to heat the contents uniformly.

## **Agglomeration of Silicon Particles**

One area of practical concern in operating a FB reactor is the agglomeration of silicon particles. Chunks of agglomerated silicon particles can form in the reactor where fluidization may be reduced due to particle segregation or dead flow zones. In underfluidized areas within the FB reactor chemical sintering of particles can form agglomerates which settle to the bottom of the reactor and block the distributor or the jet nozzles. Agglomeration can become a problem that slowly develops for a FB

campaign lasting several months. Such blockages necessitate the shutdown of the reaction.

Filtvedt et al. (2012) discuss the relationship between the Tamman temperature and the agglomeration of silicon particles. The Tamman temperature is the temperature at which mobility of molecules in a solid becomes appreciable. Above the Tamman temperature the surface reactivity and wetting properties of a material become strong enough to allow powder to stick to the surface. For silicon, the Tamman temperature is 610 C. In a FB reactor run at 650–850 °C the sticking of silicon powder onto the surface of a silicon particle as shown in the earlier scavenging mechanism is favorable for the growth of silicon particles. Unfortunately, the adhering together of several larger silicon particles presents a problem if chunks of silicon form and fall to the bottom of the reactor. At the bottom of the reactor the heavier chunks of silicon have limited motion but continue to grow as they interact with the silane feed gas. Similarly, when pieces of silicon detach from the wall, they drop to the bottom of the reactor and continue to increase in size. It is necessary to find flow conditions such that scavenging of silicon dust on granular silicon particles can occur, but agglomeration of bigger particles is minimized.

## Control of the Silicon Particle Size Distribution in the Reactor

In order to operate the fluidized-bed reactor in a continuous mode it is necessary to maintain the size distribution of silicon particles nearly constant while the particles grow. This can be accomplished by periodically feeding smaller silicon seed particles and removing particles that have grown larger. To keep the FB operating continuously, a portion of the product needs to be reduced in size and returned to the reactor as seed particles so that the particle size distribution is maintained in a favorable range for fluidization and silicon growth.

The content of the fluidized bed has a distribution of particle sizes because of the constant mixing and motion from the normal fluidizing action within the bed. The favored method for monitoring the granular particle size distribution is by commercial instruments which use digital photography to measure a stream of silicon particles passing in front of a camera. The digital image can be analyzed by computer to determine particle size and shape. A plot of particle size distribution of a statistically significant number of particles can be used to monitor the particle size distribution in the FB reactor. The digital image method for monitoring the particle size distribution is used because it is both rapid and accurate compared to screening the particle using a sieve.

The size reduction of the silicon particles needs to be accomplished in such a way as to minimize contamination of the silicon with metals. Contamination must be reduced by using equipment that is coated with hard, nonmetallic materials. The grinding of silicon is especially challenging because silicon is such a hard substance with a Mohr hardness of 7 (Lide 2008).



## Factors to Consider When Optimizing Silicon Particle Size Distribution

Particle size distribution determines the flow rates of feed hydrogen and silane gas that are required to maintain fluidization. Larger particles require a greater flow rate to suspend particles. At some point as the velocity of feed gas increases the conversion rate will decrease due to reduced gas residence time. Controlling particle size is a major factor in optimizing a stable reacting bed.

It is most important to maintain stable reactor bed and fluidization state during reactor operation. Without a stable bed, a commercial process would not be feasible. One needs dependable reactors that can run for weeks or months in a predictable and controllable fashion. Based on experience with fluidized bed operated with many particle size distributions, it has been possible to determine the range of particles sizes that offer the best chance for long-term stability. For most silane-based FB reactors the mean particle size ranges from 500 to 1500 microns in diameter (Filtvedt et al. 2013).

The relationship between particle size and ease of fluidization is presented earlier in the discussion on the Geldart classification of particles. Because of their ease of handling and of fluidization, larger particles in Geldart Groups B and D are favored for silicon fluidized beds, see Fig. 2.

From this discussion on fluidization, heat transfer, and reactivity of silicon particles as a function of particle size distribution, it is clear why modeling of the complex reaction bed is vital. All of the above factors can be calculated and introduced into a model that can describe the physical state of the fluidized bed.

## Silicon Powder Formation and Handling in a Fluidized-Bed Reactor

One of the major deficiencies of silane base fluidized-bed production of silicon is the production of silicon dust (Hsu et al. 1984). As discussed earlier, powder formation is the result of homogeneous decomposition of silane trapped in bubbles between silicon particles and any silane present in the free space above the reactor bed. Several techniques have been considered to reduce powder formation. One approach is to increase the residence time in the bed by reducing the particle size and the feed gas flow rate (Gautreaux and Allen 1988). Under this condition the amount of silicon dust is significantly reduced because there is more time for the silane gas to react. The silicon powder is more likely to be captured on the surface of a silicon particle. The downside to reducing the flow rate of silane is that the output of polysilicon is reduced. Another approach to reduce powder formation is to inject cool hydrogen into the top of the reactor above the fluidized bed of silicon to lower the temperature of silane in the off gas below its reaction temperature (Allen 1988). Hwang (1999) looked at injecting hydrogen chloride into the FB reactor to eliminate silicon dust. Hydrogen chloride reacts with silicon particles to form trichlorosilane and to eliminate silicon powder as observed in Siemens reactor operation. There has been a

patent issued for equipment to reduce the size of bubbles in the FB reactor in an attempt to limit the homogeneous reaction that produces dust within the bubbles (Spangler and Miller 2016). Currently silicon dust formation appears to be inevitable during the operation of the FB reactor with silane. One approach that has been patented is to collect the silicon powder and pelletize it for use in other applications (Hariharan et al. 2007). The formation of silicon dust from silane remains an area of active research (Wyller et al. 2016). The preferred option is to find reactor conditions that minimize silicon dust formation.

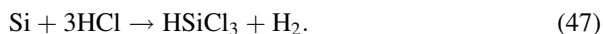
## Removing the Silicon Deposited on the Reactor Wall

Another downside to the use of silane-based FB reactors is silicon deposition on the inside reactor wall that must be periodically removed. Because the hottest part of the reactor is its walls, the space near the walls is the most chemically active part of the reactor. As the thickness of deposited silicon on the reactor wall increases over time the heating characteristics of the wall change. Eventually the silicon producing fluidized-bed reactor must be shut down to remove the reactor wall deposits.

Several techniques have been developed for lengthening the time between reactor shut downs for silicon removal from the walls. One obvious method is to minimize the temperature on the walls to reduce silicon deposition. Another approach mentioned earlier is to flow hydrogen or an inert gas along the wall surface to reduce the concentration of silane on the reactor wall (Kulkarni et al. 2013). Proposals to install baffles in the reactor have been made to dilute silane next to the wall and to reduce the exposure of the reactor wall to silane (Bhusarapu et al. 2015).

Despite all efforts to minimize the deposition of silicon on the walls of the reactor, a point is reached where it is necessary to remove the silicon layer that has formed on the reactor walls. The buildup of silicon on the reactor walls leads to several problems. As the layer of silicon becomes thicker, the transfer of heat from the wall and through the silicon layer becomes less efficient. As the silicon deposits become thicker, the probability of chunks of silicon breaking off the wall and falling to the bottom of the reactor increases.

The primary method for removing silicon deposited on the reactor wall is to chemically remove the silicon. The reactor can be emptied of granular silicon and then a gas mixture containing hydrogen chloride (HCl) is passed over the deposited silicon to convert the deposited silicon to chlorosilanes. The reactor walls have to be heated to achieve an acceptable silicon etch rate:



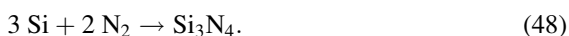
By using dry hydrogen chloride with a very low water content and diluting the hydrogen chloride with hydrogen, it has proven possible to etch off the silicon from the reactor wall and to minimize corrosion of the metal parts of the reactor (Chung and Sturm 2007).

## Safety Issue with Silane and Hydrogen

Although it is often not stated, safety is one of the major concerns when operating a fluidized-bed reactor to produce silicon. Both silane and hydrogen can form explosive mixtures when combined with air. In addition, silane is pyrophoric and combusts spontaneously in contact with air. One is faced with the possibility that any leaks or failures in parts of the plant piping containing hydrogen and silane could result in fires or explosions. The risk factor is increased because the reactor is operated at such a high temperature. All parts of plant design must take into consideration the inherent dangers encountered with hydrogen and silane-based processes.

## Atmospheric Contamination of Silicon

Unlike many chemical processes, nitrogen cannot be used as an inert gas for high temperature silicon processes such as the fluidized bed. The safety issue arrives from the fact that at elevated temperatures above 900 °C silicon reacts with nitrogen to form silicon nitride (Riley 2000):



The reaction of silicon and nitrogen is quite exothermic so that there is a danger of thermal runaway. The reaction between silicon and nitrogen may start slowly but if the heat generated is not dispersed, the temperature of the silicon will rise and further increase the reaction rate. Often argon is required as a blanket gas when dealing with high-purity silicon. Since hydrogen is used as a reaction gas and is available, it is often used as the blanket gas above hot silicon.

In addition to considering the reaction of nitrogen and silicon at elevated temperatures, the interaction between silicon and oxygen is an issue. Any silicon surface exposed to air or other source of oxygen at room temperature or above will instantaneously form multiple atomic layers of silicon oxide. This formation of an oxide outer layer becomes more of an issue when dealing with granular silicon because of the greater surface area provided by the small particles of silicon. In the fluidized-bed reactor and the silicon handling lines, it is preferred to eliminate oxygen and keep the silicon covered with an inert gas or hydrogen.

---

## Current Status of Commercial Research and Development of Silane Fluidized-Bed Reactors

As noted above, there are many industrial processes that have successfully used fluidized-bed technology in chemical processes. Such processes are developed and optimized over a number of years and reach a stage where the process is predictable and stable on the commercial scale. The use of a fluidized bed for the

deposition of silane to produce high purity silicon has not followed this pattern. Even though the theoretical advantages of fluidized bed for silane deposition are well recognized, the actual development of the technology has proven to be difficult. Over the last few years REC, GCL, and SunEdison have all operated commercial scale silicon production plants and have gained experience with silane-based fluidized-bed silane units (Bernreuter 2014). There are several FB reactor projects currently under construction in China (Roselund 2015). Despite decades of experience with the silane-based FB technology, challenges still remain before the technology can compete with the Siemens process. The difficulties result from the nature of the reaction that is being carried out and the need to resolve conflicting factors.

The optimization of the silane-based fluidized-bed technology has proven to be complex and has not reached its theoretical potential. Most of the issues found when designing and running a FB silicon plant have been discussed above. The following is an organized list of five largely unique, complex, and interrelated issues that are encountered while operating a silane deposition FB reactor:

1. Silicon particle deposition versus powder formation: In a silane fluidized-bed reactor, there are competing reactions between the desired deposition of silane onto silicon particles and the undesirable formation of very fine silicon powder. In practice one cannot eliminate powder formation. It is important to develop techniques for minimizing the amount of silicon powder produced. Reactor design and operating regime is critical in minimizing powder formation in a FB reactor. The goal is to minimize the volume of silane that is heated above its reaction temperatures when the silane is not in contact with a silicon surface. For a fluidized-bed reactor, this means limiting slugging and reducing the size of bubbles.
2. Agglomeration of silicon particles: At the high temperature that a silane-based FB reactor operates, agglomeration of silicon particles can become a problem. Large chunks of silicon particles made up of many attached silicon particles can disrupt the flow of feed gas and silicon particles in the reactor. One must find reactor conditions such that silicon particles will not interact sufficiently to allow agglomeration to occur. At the same time, it is important to encourage the scavenging reaction where silicon dust adheres to silicon particles and adds to the growth of individual silicon particles.
3. Depositing silicon on the reactor walls: By design, silicon is mostly deposited on the silicon particles in the reactor, but it is inevitable that some silicon deposition occurs on the reactor walls. Deposition on the vessel walls becomes a significant issue if the reactor is heated through the walls and the walls are the hottest points in the reactor where silicon will preferentially be deposited. Much effort in reactor design has been expended to reduce wall deposition. Approaches using the bottom distributor or jets to blanket the walls with hydrogen or inert gas have been patented (Kulkarni et al. 2013). Other approaches using baffles have been suggested (Osborne et al. 2011). The ultimate answer to

minimizing wall deposition may be found in developing novel approaches to heating the reactor.

4. Heating the reactor bed to a high reaction temperature: By its nature, a fluidized-bed reactor requires extensive heating. There is a large, continuous energy demand to heat the incoming gas and maintain fluidization of the silicon particles at the reaction temperature. Several different heating designs have been presented.

Reactor design has centered around using electrical resistance or induction heating to supply the necessary thermal energy to the reactor. The problem is to find a reactor design such that sufficient heat can be introduced while minimizing silicon wall deposition and dust formation and optimize growth of granular silicon.

5. Achieving high purity in the product silicon: Operating cost and product purity are the most important factors in evaluating FB silicon.

## Specifications for Polycrystalline Silicon for PV Applications

Polysilicon with higher purity yields solar cells with higher efficiencies. Even with the use of high-purity silane and high-purity silicon particles, processing of materials in the fluidized-bed reactor requires special techniques and materials to prevent contamination. Materials of construction and environmental elements such as oxygen and carbon in the plant can contaminate the silicon product. It is challenging to build and operate a silicon plant where contamination in the product silicon is maintained below the ppm (6 N) level.

Because the main purpose for producing polysilicon using FB technology or the Siemens process is to obtain silicon sufficiently pure for photovoltaic and semiconductor applications, it is worth discussing how high-purity polysilicon is obtained and analyzed. Handling of polysilicon has to be done in such a way that the silicon does not come in contact with any metal or material that could cause contamination. At low temperatures, the polysilicon particles can be handled in plastic lined containers or tubes. At high temperatures, inert liners and hard coatings are necessary to protect fluidized silicon from contamination.

The determination of metals in polysilicon down to the 6 N and 9 N levels has been revolutionized by the use of the analytical technique of inductively coupled plasma mass spectroscopy (ICP-MS). Silicon samples can be dissolved in a hydrofluoric acid/nitric acid solution, vaporized in a plasma, and analyzed by mass spectroscopy after sample workup. Metals and other impurities can be monitored in silicon down to the ppb level or below using ICP-MS. Analysis for dopants such as boron and phosphorous can be carried out by low temperature infrared (IR) analysis. It is necessary to prepare an appropriate silicon sample for IR analysis by growing single crystal rods of the granular silicon product. The organization SEMI (Semiconductor Equipment and Materials International) and other international organizations provides approved analytical methods and standards for the analysis of polysilicon. (SEMI 2013).

---

## Improving FB Technology with Modeling

These five problem areas listed above form the basis for improving silane FB reactor technology. The issues are interrelated in complex ways. With such complicated interactions occurring simultaneously, optimizing silane-based FB technology can be a complex task. Reactor modeling offers a way to evaluate several of the issues at the same time. Using simulation methods differing reactor configurations and operating conditions can be tested before building a reactor. The effects of changing parameters such as temperature, flow rate, concentration, and pressure while operating a FB reactor can be difficult to anticipate. Reactor modeling can provide insights into trends and fundamental chemical and fluid mechanical mechanisms.

---

## Summary and Conclusions

There is renewed interest in the use of the fluidized-bed process for commercial production of polysilicon for solar applications. Fluidized-bed technology and its continuous processing shows promise as a means to significantly reduce the price of polysilicon. The process uses considerably less electrical energy than the competing Siemens process. Silane-based fluidized-bed reactors produce granular polysilicon, this reduces the cost of downstream crystallization processing. There has been a gradual improvement in silane technology but there remains a large difference between the commercial state of the process and the theoretical potential for improvement. The developing photovoltaic market for silicon has prompted several companies to further investigate the fluidized-bed route to high-purity polysilicon.

The downside to the use of the silane-based fluidized-bed process is that the installed capital cost is higher and it is more difficult to operate than a Siemens plant. As with all fluidized-bed units, the reactor operation is very dynamic and prone to upsets. Silicon powder formation is a constant problem along with agglomeration of silicon. Cleaning the walls of deposited silicon is a periodic maintenance task.

The issue of scalability remains. If FB silicon is to overtake silicon produced by the Siemens process, FB plants will have to be able to produce ever larger amounts of polysilicon. This means that larger and more productive FB reactors will have to be designed and operated. Because of the unpredictability of scale up in FB plants, it is difficult to predict if scaled up FB reactor will operate successfully.

The one overriding issue that ultimately could determine the success of silicon FB technology is the purity of the silicon can be produced. Roughly, optimized FB silicon plants of today can produce material which has impurities in the 6 N to 9 N level (IHS 2014). Siemens product is often in the 9 N to 11 N range. Higher solar cell efficiencies require higher purity silicon. FB silicon will eventually have to be superior to Siemens product not only in cost but also nearly equal in purity.

## References

- R.H. Allen, U.S. Patent 4,748,052, 1988
- J. Baeyens, D. Geldart, *Chem. Eng. Sci.* **29**, 255–265 (1974)
- S. Balaji, J. Du, C.M. White, E. Ydstie, *Powder Technol.* **199**, 23 (2010)
- J. Bernreuter, *FBR Polysilicon Technology – Promise or Hype?* (PV-Tech, 2014.) [www.pv-tech.org/guest-blog/fbr\\_polysilicon\\_technology\\_promise\\_or\\_hype](http://www.pv-tech.org/guest-blog/fbr_polysilicon_technology_promise_or_hype). Accessed 2 March 2017
- J. Bernreuter, *Cut-throat Competition on the Polysilicon Market* (World News, 2016.) [https://eresearch.fidelity.com/eresearch/markets\\_sectors/news/story.jhtml?storyid=201611240400PR\\_NEWS\\_USPR\\_\\_\\_\\_\\_enUK201611224068&provider=PR\\_NEWS\\_&product=USPR\\_\\_\\_\\_\\_&category=sectorNews&gic=453010](https://eresearch.fidelity.com/eresearch/markets_sectors/news/story.jhtml?storyid=201611240400PR_NEWS_USPR_____enUK201611224068&provider=PR_NEWS_&product=USPR_____&category=sectorNews&gic=453010). Accessed 3 March 2017
- L. Bertrand, C.M Olsen, U.S. Patent 3,012,862, 1961
- S. Bhusarapu, P. Gupta, Y. Huang, U.S. Patents 9,114,996, 2015 and 9,114,997, 2015
- W.C. Breneman, U.S. Patent 4,676,967, 1987
- W.C. Breneman, U.S. Patent 9,352,971, 2016
- L. Cadoret, N. Reuge, S. Pannala, M. Syamlal, C. Coufort, B. Caussat, *Surf. Coat. Technol.* **201**, 8919 (2007)
- B. Caussat, M. Hemati, J.P. Couderc, *Chem. Eng. Sci.* **50**, 3625 (1995)
- K.H. Chung and J.C. Sturm, [https://pdfs.semanticscholar.org/2ff4/3f7680437746363\\_fap33038725145\\_eee607\\_pdf](https://pdfs.semanticscholar.org/2ff4/3f7680437746363_fap33038725145_eee607_pdf), 2007
- D.W. Clary, A.O. Wikman, U.S. Patent 5,260,538, 1993
- W.O. Filtvedt, Production of Polysilicon from Silane Pyrolysis in a Fluidized bed, thesis, Telemark University College, 2013. Available from <https://teora.hit.no/handle/2282/1453>
- W.O. Filtvedt, M. Javidi, A. Holt, M.C. Melaaen, E. Marstein, H. Tathgar, P.A. Ramachandran, *Sol. Energy Mater. Sol. Cells* **94**, 1890 (2010)
- W.O. Filtvedt, A. Holt, P.A. Ramachandran, M.C. Melaaen, *Sol. Energy Mater. Sol. Cells* **107**, 188 (2012)
- W.O. Filtvedt, T. Mongstad, A. Holt, M. Melaaen, H. Klette, *Int. J. Chem. React. Eng.* **11**(1) (2013)
- R. Fu, T.L. James, M. Woodhouse, *IEEE J Photovoltaics* **5**, 515 (2015)
- M.F. Gautreaux, R.H. Allen, U.S. Patent 4,784,840, 1988
- D. Geldart, Characterization of fluidized powders, in *Gas Fluidization Technology*, ed. by D. Geldart (Wiley, Chichester, 1986)
- H. Gutschel, U.S. Patent 3,042,494, 1962
- A.V. Hariharan, M. Chandra, K.P. Gupta, U.S. Patent 7,175,685, 2007
- J.R. Howard, *Fluidized Bed Technology: Principles and Applications* (Adam Hilger, Bristol/New York, 1989), p. 30, p. 202
- G. Hsu, R. Hogle, N. Rohtagi, A. Morrison, *J. Electrochem. Soc.* **131**, 660 (1984)
- G. Hsu, N. Rohatgi, J. Houseman, *AIChE J.* **33**(5), 784 (1987)
- N.W. Hwang, *J. Cryst. Growth* **205**, 59 (1999)
- IHS, Technology: Fluidized Bed Reactor Technology Stakes its claim in solar Polysilicon Manufacturing. <http://news.ihsmarket.com/press-release/design-supply-chain-media/fluidized-bed-reactor-technology-stakes-its-claim-solar-poly>, 2014
- S.K. Iya, U.S. Patent 4,684,513, 1987
- S.K. Iya, U.S. Patent 4,818,496, 1989
- L. Jianlong, C. Guanghui, Z. Pan, W. Weiwen, D. Jihai, *Chin. J. Chem. Eng.* **19**, 747 (2011)
- D.K. Kerner, R.W. Davis, E.F. Moore, S.H. Ehrman, *J. Cryst. Growth* **247**, 333 (2003)
- H.Y. Kim, K.K. Yoon, Y.K. Park, W.C. Choi, U.S. Patent 7,771,687, 2010
- T. Kimura, T. Kojima, *Journal de Physique IV Colloque*, 1991, 02 (C2), pp. C2-103–C2-110
- M.S. Kulkarni, P. Gupta, B. Devulapalli, J. Ibrahim, V. Revankar, K. Foli, U.S. Patent 8,404,206, 2013
- D. Kunii, O. Levenspiel, *Fluidization Engineering*, 2nd edn. (Butterworth-Heinemann, Newton, 1991), p. 35, p. 52, and p. 78
- S. Lai, M.P. Dudukovic, P.A. Ramachandran, *Chem. Eng. Sci.* **41**, 633 (1986)

- D. R. Lide (ed.), *CRC Handbook of Chemistry and Physics*, 89th edn. (CRC Press, Boca Raton, 2008), pp. 12–217
- B. Mazumder, *Silicon and Its Compounds* (Science Publishers, Plymouth, 2000), p. 7  
NETL, <https://mfix.netl.doe.gov/>
- R.I Newman, W.E. Watson, U.S. Patent 3,370,938, 1968
- E.W. Osborne, M.V Spangler, L.C. Allen, R.J Geertsen, P.E. Ege, W.J. Stupin, G. Zeininger, U.S. Patent 8,075,692, 2011
- S. Pannala, M. Syamlal, T. O'Brien, *Computational Gas-Solid Flows and Reacting Systems* (Engineering Science Reference, Hersey, New York, 2010)
- J.M. Parker, Int. J. Chem. React. Eng. **9**(A40) (2011)
- J. Pina, V. Bacala, N.S. Schbib, P. Ege, H. Ignacio, I. Lasa, Int. J. Chem. React. Eng. **4**, A9 (2006) REC, <https://www.recsilicon.com/products/solar-grade-polysilicon>. (2017)
- N. Reuge, L. Cadoret, B. Caussat, Chem. Eng. J. **148**, 509 (2009)
- V. Revankar, S. Lohoti, U.S. Patent 8,657,958, 2014
- F.L. Riley, J. Am. Ceram. Soc. **83**, 245 (2000)
- C. Roselund, The slow grind of FBR polysilicon, (pv magazine, 2015). [www.http://www.bernreuter.com/fileadmin/user\\_upload/library/Slow-grind-of-FBR-polysilicon-pv-magazine-9-2015.pdf](http://www.bernreuter.com/fileadmin/user_upload/library/Slow-grind-of-FBR-polysilicon-pv-magazine-9-2015.pdf). Accessed 2 Mar 2017
- SEMI, <http://ams.semi.org/ebusiness/standards/semistandard.aspx?volumeid=12>, (see methods SEMI PV49-0613 2013 and SEMI PV 17–1012, 2012)
- M.V. Spangler, M.J. Miller, U.S. Patent 9,404,177, 2016
- M.V Spangler, Glen Stucki, U.S. Patent 8,926,929, 2015
- R. Steemann, J. Yong, O. Mjos, A. Song, Energy Procedia **15**, 20 (2012)
- R.D. Toomy, Chem. Eng. Process. **48**, 220 (1952)
- Wacker, [https://www.wacker.com/cms/media/documents/investor-relations/cmd16/cmd16\\_polysilicon.pdf](https://www.wacker.com/cms/media/documents/investor-relations/cmd16/cmd16_polysilicon.pdf). 2016
- S.P. Walch, C.E. Dateo, J. Phys. Chem. **105**, 2015 (2001)
- D. Weidhaus, I. Crossmann, F. Schreieder, U.S. Patent Application 2005/0135986, 2005
- G.M. Wyller, T.J. Preston, H. Klette, O. Nordseth, T.T. Mongstad, W.O. Filtvedt, E.S. Marstein, Energy Procedia **92**, 904 (2016)
- Yang (ed.), *Handbook of Fluidization and Fluid-Particle Systems* (CRC Press/Taylor & Francis Group, Boca Raton, 2003), p. 261
- G. Zhang, F. Quyang, Ind. Eng. Chem. Process. Des. Dev. **24**, 430 (1985)





# Upgrade Metallurgical Grade Silicon

# 5

Wen-hui Ma, Ji-Jun Wu, Kui-xian Wei, and Yun Lei

## Contents

Introduction .....	110
Smelting of Metallurgical-Grade Silicon .....	110
Secondary Refining of MG-Si .....	112
Boron Removal by Gas-Blowing Refining .....	112
Boron Removal by Slag Treatment .....	114
Acid Leaching Treatment .....	116
Solvent Refining .....	116
Vacuum Treatment .....	117
Theoretical Basis of Vacuum Refining .....	117
Vacuum Refining .....	118
Experimental Measurements of the Volatilization Rate of Si .....	119
Plasma Refining .....	120
Electron Beam Treatment .....	121
Purification by Solidification .....	123
Traditional Directional Solidification Technology .....	123
Conclusion .....	125
References .....	125

## Abstract

Producing upgraded metallurgical-grade silicon may be the most promising method to replace the modified Siemens process to produce solar-grade silicon, which has many advantages such as no pollution and low cost in the production process. The main process is described in detail, including smelting and secondary refining of metallurgical-grade silicon and acid leaching treatment. Other

W.-h. Ma (✉) · J.-J. Wu · K.-x. Wei · Y. Lei

National Engineering Laboratory for Vacuum Metallurgy, Faculty of Materials and Metallurgical Engineering, Kunming University of Science and Technology, Kunming, Yunnan, China

e-mail: [mwhsilicon@126.com](mailto:mwhsilicon@126.com); [dragon\\_wu213@126.com](mailto:dragon_wu213@126.com); [kxwei2008@hotmail.com](mailto:kxwei2008@hotmail.com); [leiyn2008@163.com](mailto:leiyn2008@163.com)

technologies also are introduced and discussed: solvent refining, vacuum treatment, plasma refining, and electron beam treatment; these technologies are used to refine metallurgical-grade silicon. Purification is also very important in the production process; a solidification process is used in purification to obtain highly pure silicon.

---

**Keywords**

Metallurgical-grade silicon · Impurity removal · Solar-grade silicon · Refining · Purification

---

## Introduction

The production of solar cells has increased significantly in response to a growing demand for clean energy worldwide. However, solar-grade silicon (SOG-Si) is expensive and the supply is limited. For this reason, many researchers have developed successful processing methods to use metallurgy to produce SOG-Si, including refining, removing impurities, and acid leaching treatment, which have their own advantages; these have been used to remove all kinds of impurities. Vacuum melting, plasma refining, and electron beam treatment have also been used to refine silicon (Si) and remove impurities. In addition, solidification has been used to purify Si to obtain different segregation coefficients between liquids and solids. The entire process and various methods to produce SOG-Si using metallurgical methods are discussed and described here.

---

## Smelting of Metallurgical-Grade Silicon

Metallurgical-grade Si (MG-Si), with a typical purity higher than 98.5%, is produced in a submerged electric arc furnace at a temperature higher than 1,900 °C. The electric furnace consists essentially of charge (silica, a carbonaceous reducing agent) and a carbon/graphite electrode. The high-class silica lump with lumpiness of 10–100 mm is mixed with a carbonaceous reducing agent such as petroleum coke, bitumite, carbocoal, wood chips, and/or charcoal and then charged into the furnace. The electrodes are submerged in raw materials and the Si is smelted.

MG-Si is produced by the carbothermic reduction of silica according to the overall reaction:



In a practical electric furnace, the reduction of silica is very complicated. The raw materials ( $\text{SiO}_2$  and carbon), after being put into the furnace, move down continuously, away from the pre-reaction zone, and their temperature continually increases

as they are heated by the ascending furnace gases. The gaseous SiO will be decomposed into Si and SiO<sub>2</sub>.



Most products are deposited in the pore of the reducing agent and some escape from the furnace. The raw materials continue to move down. The following reactions take place when the temperature reaches 1,820 °C:



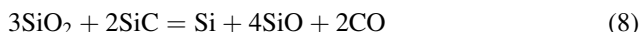
When the temperature rises again, other reactions occur:



Below the electrodes, the reactions to produce Si include:



and



In the process of sinking the furnace charge, reactions (5) and (6) take place in reverse:



At the same time, waste heat is recovered as energy. Figure 1 shows a schematic description of the MG-Si production process in an electric furnace.

MG-Si contains 1–3% impurities, depending on the raw materials and the type of electrodes. Impurities in MG-Si come mainly from silica, the reducing agent, and the carbon electrode. Iron, aluminum, and calcium account for the largest numbers of impurities in MG-Si. Among the oxides in silica and in ash of the reducing agent, nearly 100% Fe<sub>2</sub>O<sub>3</sub>, 50–55% Al<sub>2</sub>O<sub>3</sub>, 35–40% CaO, and 30% MgO are reduced after smelting. A small amount of nonmetallic impurities (boron, phosphorus, carbon, etc.) enters the MG-Si melt (Schei et al. 1992). In general, MG-Si includes different amounts of impurities: 0.2–1% iron, 0.4–0.7% aluminum, 0.2–0.6% calcium, 0.1–0.02% titanium, 0.1–0.15% carbon, ~80 ppmw boron, and ~150 ppmw phosphorus.

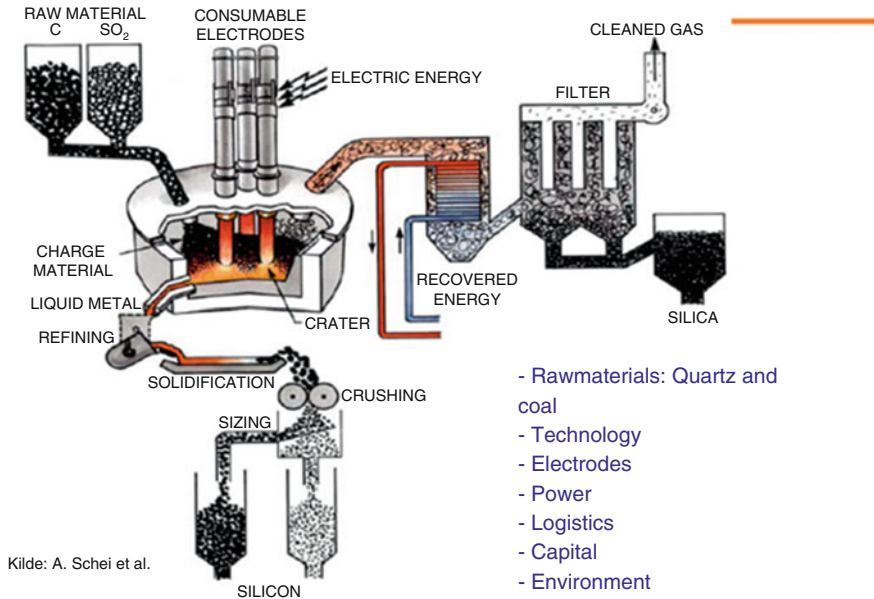


**Fig. 1** Production process of MG-Si smelting in an electric furnace

## Secondary Refining of MG-Si

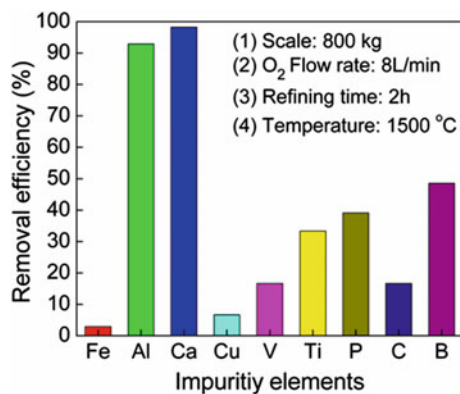
### Boron Removal by Gas-Blowing Refining

During production, MG-Si melt is tapped into a ladle from the electric furnace for a secondary refining treatment, which is similar to secondary refining in steelmaking. Some oxidizing media, such as air and oxygen or synthetic slag ( $\text{CaO-SiO}_2$ ,  $\text{CaO-Al}_2\text{O}_3\text{-SiO}_2$ ), are usually blown or added to the ladle for secondary refining.

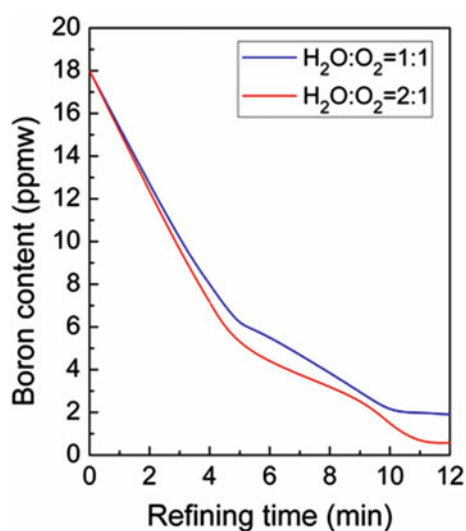
Figure 2 shows the removal efficiencies of impurities (Wu et al. 2014a). Calcium and aluminum are reduced from 18400 ppmw to 320 ppmw and 124000 to 880 ppmw, respectively. Their removal efficiencies are both higher than 90%, which is enough to meet the requirements for the next refining step. Boron is reduced from 35 to 18 ppmw; its removal efficiency is about 50%. However, removal efficiencies are lower than 17% for iron, copper, vanadium, and carbon. Phosphorus is reduced from 184 to 112 ppmw.

Figure 3 shows the efficiency of boron removal using the different compositions of  $\text{Ar-H}_2\text{O-O}_2$  and refining time in a direct current arc furnace. When the composition of  $\text{H}_2\text{O-O}_2$  is 1:1, the boron content is reduced from 18 to 2.0 ppmw; when the composition is changed into 2:1, it is reduced to 0.6 ppmw.

**Fig. 2** Removal efficiency of impure elements in MG-Si using O<sub>2</sub> gas blowing

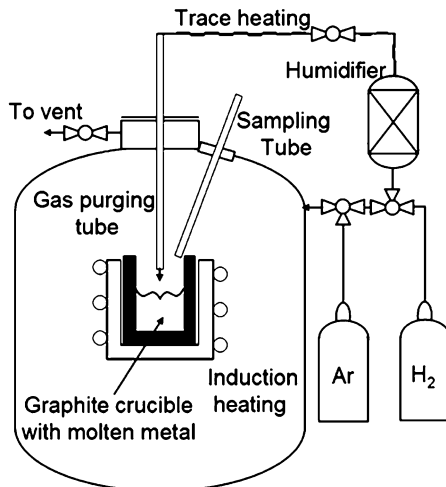


**Fig. 3** Effects of H<sub>2</sub>O–O<sub>2</sub> composition and refining time on boron removal



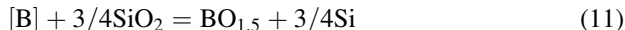
Different compositions of the gases argon, H<sub>2</sub>, and H<sub>2</sub>O were blown into an induction furnace, as shown in Fig. 4, to remove boron under different refining temperatures. At the range of 1723–1872 K, the removal efficiency of boron was better at a lower temperature. Boron could barely be removed from Si when blowing pure H<sub>2</sub> gas; however, the removal efficiency was greatly improved with the addition of H<sub>2</sub>O to the H<sub>2</sub> gas. The results indicate that boron removal was very different when blowing 3.2% compared with 7.4% H<sub>2</sub>O–H<sub>2</sub> at 1,500 °C for 2 h. The latter had a better effect. The boron in Si could be reduced from 52 ppm to 3.4 and 0.7 ppm at 1,450 °C and 1,500 °C, respectively, using 3.2% H<sub>2</sub>O–H<sub>2</sub> gas-blowing refining (Tang et al. 2012).

**Fig. 4** Schematic drawing of a vacuum-induction furnace equipped with a gas purging unit



## Boron Removal by Slag Treatment

The reaction to remove boron from MG-Si using slag refining containing  $\text{SiO}_2$  can be expressed as:



Aluminum, calcium, titanium, boron, and phosphorus impurities in MG-Si can be oxidized and absorbed by a flux of  $\text{CaO-SiO}_2$  (Wu et al. 2014b). The reaction for boron to enter the slag through oxidation, with silica as the oxidizing agent, can be represented by the ionic reaction:



Oxygen ions are provided by basic oxides such as lime:



And the partial pressure of oxygen that results from the equilibrium between Si and  $\text{SiO}_2$  is expressed as:



The maximal value of the distribution coefficient of boron ( $L_B$ ) reached 1.57 with slag comprising 60%  $\text{CaO}$ –40%  $\text{SiO}_2$  (mass). The boron content in refined silicon was reduced from 18 to 1.8 ppmw with a  $\text{CaO-SiO}_2$  slag-to-MG-Si ratio of 2.5 at 1,600 °C for 3 h, and the removal efficiency of boron reached 90%. As shown in Fig. 5, the results of both calculations and experiments suggest that the distribution

coefficient of boron is strongly affected by the basicity of slag. When using CaO–SiO<sub>2</sub> slag,  $L_B$  varies from a low basicity of 0.83 to a high basicity of 1.46; it reaches a maximal value of 1.58 with a slag basicity of 0.78. The addition of K<sub>2</sub>CO<sub>3</sub> to calcium silicate slag obviously plays an important role to the increase of  $L_B$ , which reaches 2.08 using a high-basicity slag of 40% CaO–40% SiO<sub>2</sub>–20% K<sub>2</sub>CO<sub>3</sub> (Wu et al. 2016).

A mixed gas (H<sub>2</sub>O–O<sub>2</sub>) and a chloric CaCl<sub>2</sub>–CaO–SiO<sub>2</sub> slag are combined to separated boron from MG-Si (Wu et al. 2017). As shown in Fig. 6, the efficiency of

**Fig. 5** Distribution coefficient of boron ( $L_B$ ) with different basicities of calcium silicate slags

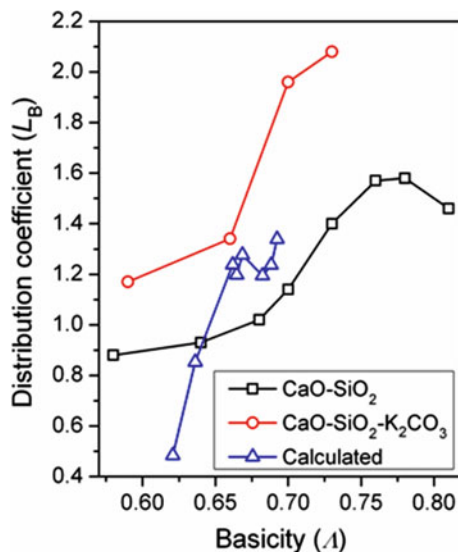
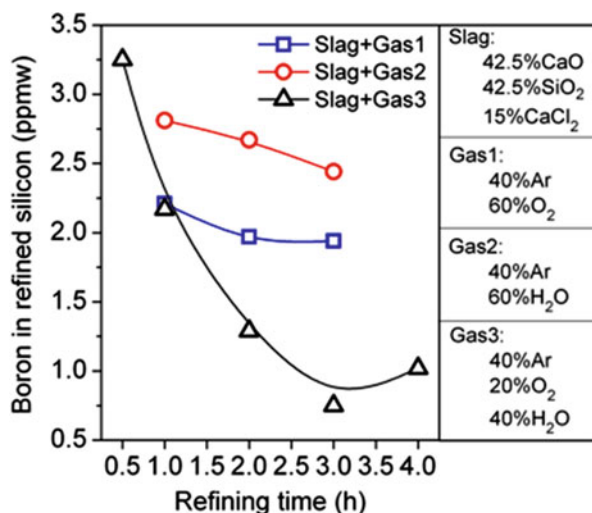


**Fig. 6** Boron removal using combined slagging and gas-blowing refining



boron removal was greatly improved by combining the slagging and gas-blowing refining techniques. When 40% Ar–60% O<sub>2</sub> and 40% Ar–60% H<sub>2</sub>O gases were combined with 42.5% CaO–42.5% SiO<sub>2</sub>–15% CaCl<sub>2</sub> slag and refined at 1,823 K for 3 h, the boron concentration in refined Si was reduced from 22 to approximately 2 ppmw. However, it was reduced to 0.75 ppmw when combining 40% Ar–20% O<sub>2</sub>–40% H<sub>2</sub>O gas blowing with the 42.5% CaO–42.5% SiO<sub>2</sub>–15% CaCl<sub>2</sub> slag refining for 3 h, at which point the efficiency of boron removal reached 96.6%.

---

## Acid Leaching Treatment

Acid leaching treatment can purify Si because of the segregation of impurities between Si solid and liquid phases among grain boundaries of Si crystals. A smaller segregation coefficient of an impurity occurs before the precipitate among the grain boundaries compared with those with a larger segregation coefficient. The segregation coefficients of impurities at the melting point of Si are shown in section “[Purification by Solidification.](#)” Metallic impurities normally have smaller segregation coefficients than nonmetallic impurities. Therefore, acid leaching treatment can efficiently eliminate metallic impurities, whereas further work needs to be done to enhance the extraction of nonmetallic impurities.

Because impurities precipitate among the boundaries of Si crystals, the bulk Si must be crushed and ground to a powder in order to make the acid solution completely touch the impurity-containing phases. If the powder size is not small enough, some of impurities will become entrapped in the Si particles; extraction of these impurities is not efficient because of the poor contact between the acid solution and the impurities. Therefore, the size of Si powder is an important factor that influences the extraction of impurities. Other influential factors are the conditions of acid leaching, such as leaching time, lixiviant, leaching temperature, and stirring technology. An efficient lixiviant can be chosen using thermodynamic Eh–pH diagrams. A high leaching temperature, good stirring technology, and enough leaching time often improve the kinetic conditions of the leaching process.

---

## Solvent Refining

Unlike other refining methods, solvent refining is a technology that can refine MG-Si at temperatures below the melting point of Si. Low-temperature refining is a typical advantage of this technology, indicating it consumes low amounts of energy. Solvent refining includes some basic steps:

- (a) One or more elements are melted together with MG-Si to form a molten Si-rich solvent or alloy.
- (b) Si crystals with a high purity will be precipitated first by lowering the temperature of the solvent, such as cooling the solvent in the heating zone or pulling the



solvent from the heating zone. The Si crystals will gradually precipitate until the temperature reaches the eutectic point of the alloy.

- (c) After eliminating the eutectic phases that contain impurities by acid leaching, the high-purity Si can be collected.

Solvent refining works based on the segregation behaviors of impurities between liquid and solid phases. In step (b), the impurities enrich within the liquid phase because of their segregation behaviors, rather than stay in the precipitated Si. An ideal element that can be selected to form a solvent with Si should meet these requirements:

- (a) Its solubility in solid Si and its segregation coefficient between the liquid and solid phases should be extremely low.
- (b) It must have a low cost and be environmental friendly.
- (c) It can form a solvent such that the yield of Si can achieve the economic purpose; that is, Si has high solubility in the solvent.
- (d) It can form a solvent that decreases the segregation coefficients of impurities, especially boron and phosphorus.
- (e) Si is the only precipitated phase in the solidification process.

According to these basic requirements, many researchers have tried to use different solvents to refine MG-Si; examples of solvent systems include Si–Al, Si–Fe, Si–Sn, Si–Na, Si–Cu, Si–Ga, and combinations thereof.

---

## Vacuum Treatment

### Theoretical Basis of Vacuum Refining

Based on the different properties of elements available when vaporizing and condensing, crude metal can be separated from impurities by vacuum distillation refining. The difference in the vapor pressure of each metal at different temperatures is the basic principle of crude metal vacuum distillation. The relation between the saturated pressure and temperature is shown in Eq. 15 (Dai and Yang 2009; Zhang 1988):

$$\lg p^* = AT^{-1} + B \lg T + CT + D \quad (15)$$

The coefficients  $A$ ,  $B$ ,  $C$ , and  $D$  for different substances can be obtained from Kubaschewski et al. (1985), Kubaschewski and Alcock (1979), Bharadwaj et al. (1990), Juneja et al. (1986), and Liang and Che (1993). Then, according to Eq. 15, the relation between saturated vapor pressure ( $p^*$ , pascal) of impurities in the MG-Si and temperature ( $T$ , Kelvin) is obtained.

The saturated vapor pressures of several typical impurities in MG-Si are shown in Fig. 7. We can see that the saturated vapor pressures of Si and of impurities in MG-Si

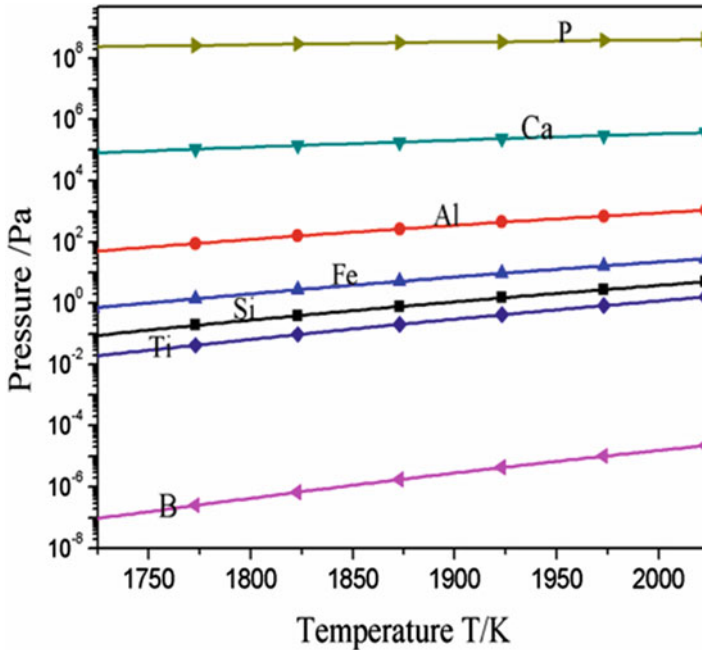


**Fig. 7** Relation between the saturated vapor pressure of the pure component and temperature

both increase as the temperature increases. The saturated vapor pressures of impurities of phosphorous, calcium, and aluminum are higher than that of the Si (the main part), which means that these elements volatilize earlier than Si in the same condition. So, the main part and the impurities can be segregated under a vacuum, in which impurities with a higher saturated vapor pressure volatilize, leaving impurities and Si with lower saturated vapor pressures.

## Vacuum Refining

### Vacuum Refining by Resistance Heating

Research on vacuum evaporation refining was conducted in a resistance heating vacuum furnace. The removal effects of phosphorus, aluminum, and calcium at 1,823 K were investigated by vacuum evaporation at 30, 60, 90, 120, and 150 min. The impure elements in the samples were analyzed by inductively coupled plasma atomic emission spectroscopy. With an increasing temperature, the amounts of phosphorus, aluminum, and calcium in the samples become lower. That is, the removal efficiency of impurities can be improved by increasing the volatilization temperature in the process of vacuum evaporation refining for

MG-Si, but this temperature increase also enhances the volatilization of the primary metal, leading to a more volatilization of the main part and a decrease in the metal recovered.

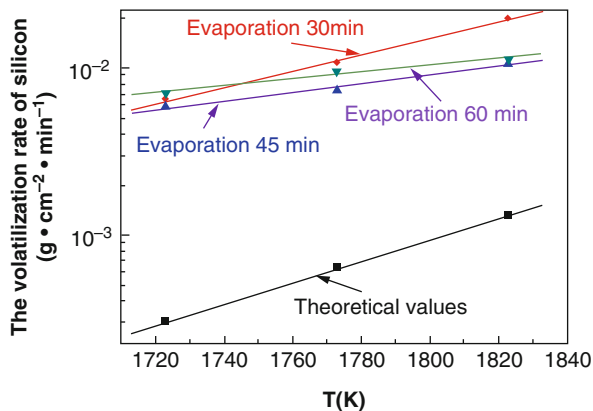
### Vacuum Induction Refining

The induction device is the induction melting furnace part of a 10 t/a vacuum oxygen decarburization solidification (VODS) type SOG-Si furnace, which is designed according to patented technology to prepare SOG-Si through metallurgy and is consigned processing. Because the induction melting temperature cannot be automatically controlled, the experimental temperature is measured by adjusting the induction melting power and using an infrared thermometer. The samples obtained after induction melting treatment were analyzed by inductively coupled plasma mass spectrometry. The impure element phosphorus can easily be reduced from 12 to below 1 ppmw, and the smallest amount (0.11 ppmw) can be achieved by induction-heating refining treatment. This amount fully meets the requirement for phosphorus content in SOG-Si.

### Experimental Measurements of the Volatilization Rate of Si

Based on Fig. 8, we found that the slope of the theoretical volatilization rate was invariable. On the other hand, the slope of the experimental volatilization rate decreases as evaporation time increases. This indicates that experimental values will be closer to the theoretical values when evaporation time is increased as a result of the formation of vapor–liquid equilibrium in the vacuum furnace in the early stages of the experiment, which may favor Si evaporation. Vapor–liquid equilibrium is generally established in a vacuum furnace when evaporation time is long. Because no effective technology is included in our experimental setup to detect when vapor–liquid equilibrium forms, we cannot easily assess the impact of the process of achieving vapor–liquid equilibrium on the volatilization rate of Si during the

**Fig. 8** Comparison of the volatilization rate of Si based on theoretical and experimental data (Wei et al. 2011)



experiment. The results and analysis show that a major discrepancy exists between the experimental and theoretical volatilization rates of Si. Three possible reasons are advanced to explain this discrepancy; that is, the vapor–liquid equilibrium is destroyed by (1) carbon/graphite, (2) oxygen, or (3) the water-cooling system.

## Plasma Refining

Similar to gas-blowing refining, plasma refining is a high-efficiency metallurgical method to remove impurities. Figure 9 displays the operating principle of plasma refining to remove impurities. The reactive gases comprise  $O_2$ ,  $H_2$ , and  $H_2O$  molecules, which plasma gas then decomposes into O, H, OH,  $O^+$ , and/or  $OH^+$  atoms or ions. Using plasma refining with  $O_2$ ,  $H_2$ , or  $H_2O$  reactive gases, boron impurities in MG-Si change into gaseous borides such as BO,  $B_2O$ , HBO, and  $BH_2$ .

A mixed reaction gas comprising  $O_2$  and  $H_2$  (or water vapor) was added to a high-temperature plasma flame to volatilize impurities on the surface of the Si melt. Boron was volatilized mainly in the form of gaseous BOH. After refining, the boron concentration in Si decreased from 15 to 2 ppmw.

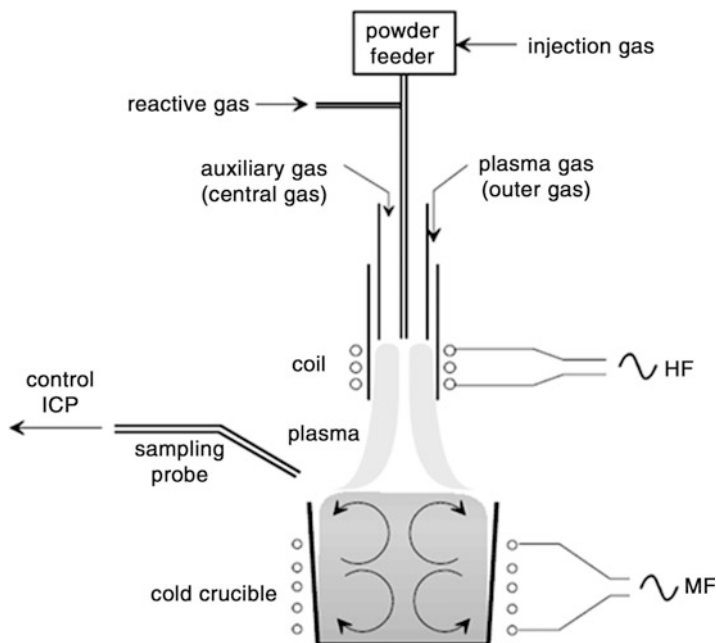
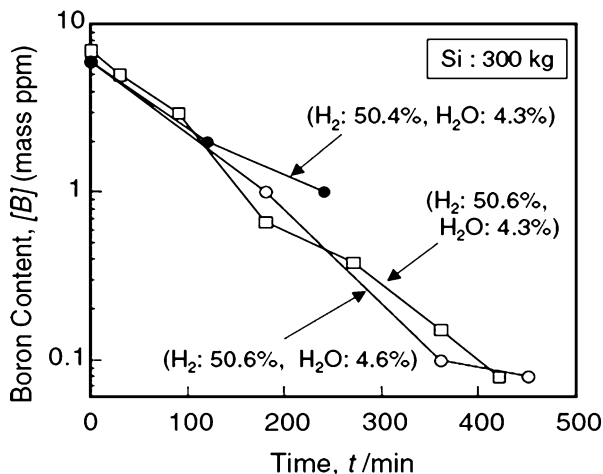


**Fig. 9** Schematic diagram of the volatilization rate experiment

**Fig. 10** Time dependence of boron content for 300 kg/ch-scale experiments



Nakamura et al. (2004) blew plasmas containing 4.3–4.6 vol% H<sub>2</sub> and 50.4–50.6 vol% H<sub>2</sub>O into MG-Si with boron content of 5–10 ppmw, as shown in Fig. 10. The boron content in refined Si decreased to below 0.1 ppmw after refining for 400 min, and the weight reached 300 kg. In addition, they found that the rate of boron removal was proportional to water vapor content, according to the reaction kinetics.

## Electron Beam Treatment

Electron beam melting technology has the following characteristics: (1) It is maintained at a vacuum level of  $10^{-2}$ – $10^{-3}$  Pa using a water-cooled copper crucible or no crucible to avoid contamination from the outside. (2) It uses a high energy density (up to  $10^3$ – $10^6$  W/cm<sup>2</sup>), an electron beam spot diameter up to  $10^{-7}$  cm, and a melting rate that can effectively remove volatile impure elements. (3) Melting power and speed can be adjusted individually, and control is easily automated, safe, and reliable. (4) The chemical composition of the melt can be precisely controlled to obtain highly pure rare and refractory metal materials and to meet certain performance requirements. (5) High-quality ingots can be prepared in different shapes, dimensions, and masses. (6) The requirements to achieve particular shapes, sizes, and qualities are lower. The morphologies of electron beam-melted Si ingots are shown in Fig. 11.

Tan et al. (2013) have done much work in Si purification through electron beam melting, and they investigated the influence of beam power, refining time, and solidification mode on impurity removal efficiency. Phosphorus content was decreased steadily to less than  $0.1 \times 10^{-4}$  wt.% with laboratory-scale electron beam melting equipment. The removal efficiencies of aluminum and calcium are up to 98%, which can meet the requirements for SOG-Si. The results are shown in Fig. 12.

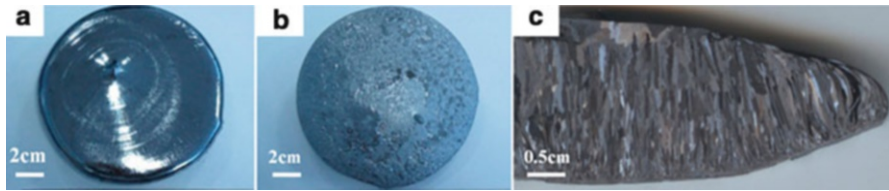
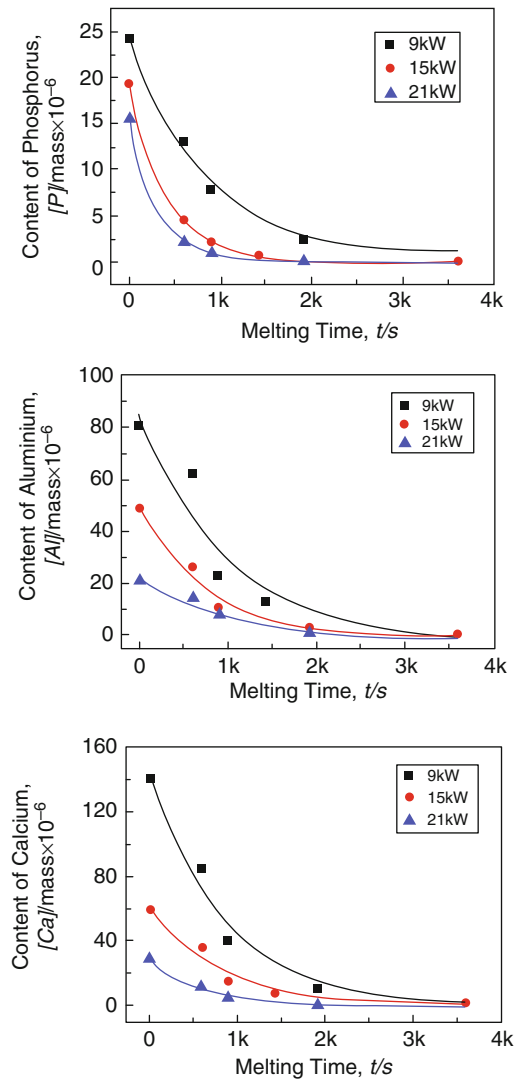


**Fig. 11** Morphologies of electron beam-melted Si ingots: (a) surface, (b) bottom, (c) cross section

**Fig. 12** Phosphorus, aluminum, and calcium contents as a function of time at different powers



## Purification by Solidification

### Traditional Directional Solidification Technology

Segregation behaviors of impurities between solid and liquid Si are significantly different because of their different solubilities in each phase. A segregation coefficient is calculated as the concentration of an impurity in solid Si/the concentration of an impurity in the liquid phase. Therefore, a smaller segregation coefficient indicates extraction of more of the impurity in the liquid phase, indicating impurities prefer to enrich in the liquid phase rather than stay in the solid purified Si. High-purity Si can be collected after the impurity-containing liquid phase is eliminated. The solubility of an impurity in solid Si is another important factor influencing the efficiency of Si refining. To obtain high-purity Si, the solubility of an impurity in solid Si should be as small as possible. The segregation coefficients of evaluated impurities are listed in Table 1 (Hu et al. 2013; Hopkins and Rohatgi 1986; Lei et al. 2016), and the solubilities of impurities in solid Si are shown in Fig. 13 (Tang et al. 2010). According to Table 1, metallic impurities have smaller segregation coefficients than nonmetallic impurities, which is the main reason why nonmetallic impurities cannot be efficiently eliminated by solidification, acid leaching treatment, solvent refining, or other metallurgical technologies.

Several solidification methods exist, including common solidification technology, directional solidification technology, zone melting technology, and Czochralski technology.

**Table 1** Evaluated segregation coefficients of impure elements between solid and liquid silicon at the melting point of silicon (1,687 K) (Hopkins and Rohatgi 1986; Lei et al. 2016; Tang et al. 2010)

Element	Segregation coefficient	Element	Segregation coefficient
Fe	$6.4 \times 10^{-6}$	Sb	$2.3 \times 10^{-2}$
Ti	$2.0 \times 10^{-6}$	Pb	$2.0 \times 10^{-3}$
Cr	$1.1 \times 10^{-5}$	Bi	$7.0 \times 10^{-4}$
Mn	$1.3 \times 10^{-5}$	Zr	$1.6 \times 10^{-8}$
Ni	$1.3 \times 10^{-4}$	W	$1.7 \times 10^{-8}$
Cu	$8.0 \times 10^{-4}$	Mo	$4.5 \times 10^{-8}$
Zn	$1.0 \times 10^{-5}$	Nb	$4.4 \times 10^{-7}$
Ag	$1.7 \times 10^{-5}$	Sn	$3.2 \times 10^{-2}$
Au	$2.5 \times 10^{-5}$	Ta	$2.1 \times 10^{-8}$
Ga	$8.0 \times 10^{-3}$	V	$4.0 \times 10^{-6}$
In	$4.0 \times 10^{-4}$	Pd	$5.0 \times 10^{-5}$
P	$3.5 \times 10^{-1}$	Co	$2.0 \times 10^{-5}$
B	$8.0 \times 10^{-1}$	O	$5.0 \times 10^{-1}$
Al	$8.0 \times 10^{-2}$	C	$5.0 \times 10^{-2}$
Hf	$4.9 \times 10^{-6}$	As	$3.0 \times 10^{-1}$
Mg	$3.2 \times 10^{-6}$	Ca	$8.0 \times 10^{-3}$

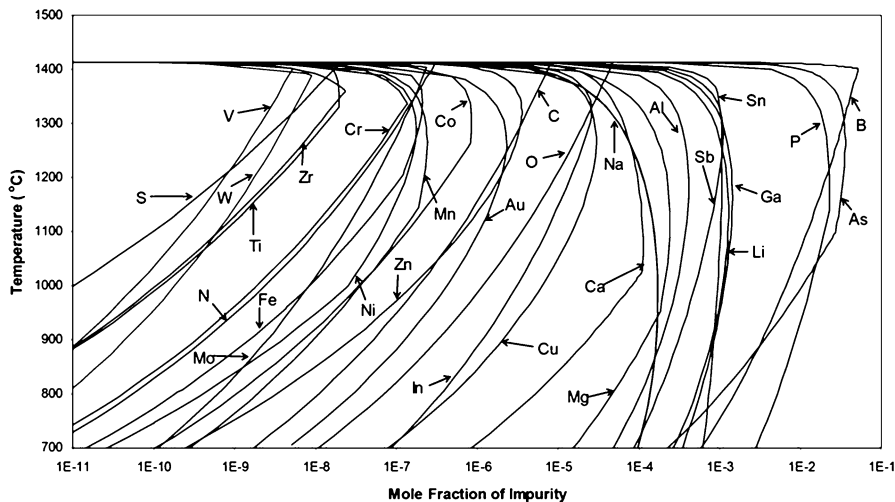


**Fig. 13** Solubilities of impurities in solid silicon (Tang et al. 2010)

For common solidification technology, Si is first melted above its melting point and then solidified with a cooling rate. Impurities precipitate among the grain boundaries of Si crystals. After grinding and acid leaching, the precipitated impurities are eliminated.

For directional solidification technology, Si is first melted in a heating zone and then solidified when the sample is gradually pulled from the heating zone vertically. For example, when the sample is pulled from the heating zone, Si first solidifies at the bottom of the sample and the upper end of the sample stays as a melted liquid until directional solidification finishes. In this case, the impurities are enriched in the final liquid melt (the top of the sample). After removing the top of sample, purified Si can be obtained. In addition, directional solidification with electromagnetic force was proposed to separate Si crystals from Si-rich solvents. Si crystals can agglomerate well at one end of the solvent, and they can be separated easily from the residual solvent by mechanical cutting and then purified by hydrometallurgical treatment.

The mechanism of zone melting technology is similar to that of directional solidification technology. The main difference is that a heating ring (normally induction coils) is used to melt only a small part of the sample. After moving the sample (or the heating ring) up (or down), the impurities enrich in the final liquid phase because of their different segregation behaviors between solid and liquid Si.

Czochralski technology is currently used to grow monocrystalline Si in industrial processes. When the seed is immersed into the liquid Si melt, Si crystals grow on the seed. After pulling the seed and the monocrystalline Si from the Si melt, the impurities stay in the Si melt and monocrystalline Si with an extremely high purity can be obtained.



## Conclusion

1. Researchers have done much work using metallurgy because of its outstanding advantages such as low cost and low pollution.
2. Metallurgical Si production technology has been introduced, and impurities should be removed. Gas blowing refining and slag treatment to remove purities have been discussed.
3. Acid leaching treatment is used to purify Si. It works on both nonmetallic and metallic impurities.
4. Solvent refining and vacuum treatment have been investigated by many researchers because of their low cost and low pollution.
5. Plasma refining is a high-efficiency metallurgical method to remove impurities. Some researchers also use electron treatment.
6. Purification by solidification is an efficient process. Segregation behaviors of impurities are significantly different in solid and liquid Si because of their different solubilities in the solid the liquid Si.

---

## References

- S.R. Bharadwaj, A.S. Kerker, S.N. Tripathi, et al., *J. Chem. Thermodyn.* **22**, 453–461 (1990)
- Y. Dai, B. Yang (eds.), *Nonferrous Metal Vacuum Metallurgy*, 2nd edn. (Metallurgical Industry Press, Beijing, 2009)
- R.H. Hopkins, A. Rohatgi, Impurity effects in silicon for high efficiency solar cells. *J. Cryst. Growth* **75**, 67–79 (1986)
- L. Hu, Z. Wang, X. Gong, Z. Guo, H. Zhang, Purification of metallurgical-grade silicon by Sn–Si refining system with calcium addition. *Sep. Purif. Technol.* **118**, 699–703 (2013)
- J.M. Juneja, G.N.K. Iyengar, K.P. Abraham, *J. Chem. Thermodyn.* **18**, 1025–1035 (1986)
- O. Kubaschewski, C.B. Alcock, *Metallurgical Thermochemistry*, 5th edn. (Pergamon Press, Oxford, 1979)
- O. Kubaschewski, C.B. Alcock, wrote. Z. Qiu, Y. Liang, X. Li, et al., trans. *Metallurgical Thermochemistry* (Metallurgical Industry Press, Beijing, 1985), pp. 486–513.
- Y. Lei, W. Ma, L. Sun, J. Wu, Y. Dai, K. Morita, Removal of B from Si by Hf addition during Al–Si solvent refining process. *Sci. Technol. Adv. Mater.* **17**, 12–19 (2016)
- Y. Liang, Y. Che (eds.), *Inorganic Thermodynamics Data Sheet* (Northeastern University Press, Shenyang, 1993)
- N. Nakamura, H. Baba, Y. Sakaguchi, Y. Kato, Boron removal in molten silicon by a steam-added plasma melting method. *Mater. Trans.* **45**(3), 858 (2004)
- A. Schei, H. Rong, A.G. Forwald, *Impurity distribution in silicon* (Silicon for Chemical Industry, Geiranger, 1992), pp. 16–18
- Y. Tan, X. Guo, S. Shi, W. Dong, D. Jiang, Study on the removal process of phosphorus from silicon by electron beam melting. *Vacuum* **93**, 65–70 (2013)
- K. Tang, E.J. Øvrelid, G. Tranell, M. Tangstad, Thermochemical and kinetic databases for the solar cell silicon materials, in *The Twelfth International Ferroalloys Congress, Sustainable Future*, Helsinki, 6–9 June 2010
- K. Tang, S. Andersson, E. Nordstrand, M. Tangstad, Removal of boron in silicon by H<sub>2</sub>–H<sub>2</sub>O gas mixtures. *J. Miner. Met. Mater. Soc.* **64**(8), 952–956 (2012)
- K. Wei, W. Ma, B. Yang, D. Liu, Y. Dai, K. Morita, Study on volatilization rate of silicon in multicrystalline silicon preparation from metallurgical grade silicon. *Vacuum* **85**, 749–754 (2011)

- J. Wu, Y. Li, W. Ma, K. Liu, K. Wei, K. Xie, B. Yang, Y. Dai, Impurities removal from metallurgical grade silicon using gas blowing refining techniques. *Silicon* **6**, 79–85 (2014a)
- J. Wu, Y. Li, W. Ma, K. Wei, B. Yang, Y. Dai, Boron removal in purifying metallurgical grade silicon by CaO–SiO<sub>2</sub> slag refining. *Trans. Nonferrous Metals Soc. Chin.* **24**, 1231–1236 (2014b.) <http://www.sciencedirect.com/science/article/pii/S1003632614631836>
- J. Wu, F. Wang, W. Ma, Y. Lei, B. Yang, Thermodynamics and kinetics of boron removal from metallurgical grade silicon by addition of high basic potassium carbonate to calcium silicate. *Metall. Mater. Trans. B* **47B**, 1796–1803 (2016.) <https://link.springer.com/article/10.1007/s11663-016-0615-z>
- J. Wu, Y. Zhou, W. Ma, M. Xu, B. Yang, Synergistic separation behavior of boron in metallurgical grade silicon using a combined slagging and gas blowing refining technique. *Metall. Mater. Trans. B* **48**(1), 22–26 (2017.) <https://link.springer.com/article/10.1007/s11663-016-0860-1>
- S. Zhang (ed.), *Vacuum Technology Physical Basis* (Northeast Institute of Technology Press, Shenyang, 1988)

---

## Part II

# Crystalline Silicon Growth



# Growth of Crystalline Silicon for Solar Cells: Czochralski Si

# 6

Xuegong Yu and Deren Yang

## Contents

Introduction .....	130
Fundamentals of CZ Silicon Crystal Puller .....	131
Crystal Puller .....	131
Pulling Procedure .....	135
Dislocation-Free Growth .....	137
Thermal Control .....	138
Melt Flow in Crucible .....	140
Incorporation of Impurities .....	142
Segregation Theory .....	142
Dopant Distribution Inhomogeneity .....	144
Oxygen Impurity .....	146
Light-Induced Degradation of CZ Silicon .....	148
Oxygen Control .....	150
Novel CZ Silicon Crystal Growth .....	151
Magnetic Field Assisted Growth .....	151
Continuous Growth .....	153
Square Ingot Growth .....	156
Germanium-Doped CZ Silicon Crystal Growth .....	157
Germanium Doping Method .....	157
Germanium Property in Silicon .....	158
Suppression of Ge Doping on Thermal Donors .....	160
Enhancement of Ge Doping on Silicon Mechanical Strength .....	161
Anti-irradiation Effect of Ge-Doped CZ Silicon Crystal .....	163

---

X. Yu (✉)

State Key Lab of Silicon Materials and School of Materials Science and Engineering, Zhejiang University, Zhejiang, Hangzhou, China

e-mail: [yuxuegong@zju.edu.cn](mailto:yuxuegong@zju.edu.cn)

D. Yang

State Key Laboratory of Silicon Materials and School of Materials Science and Engineering, Zhejiang University, Hangzhou, China

e-mail: [mseyang@zju.edu.cn](mailto:mseyang@zju.edu.cn)

---

LID Effect of Ge-Doped CZ Silicon Crystal .....	166
Conclusion .....	169
References .....	170

---

### Abstract

Czochralski (CZ) silicon is widely used in the fabrication of high-efficiency solar cells in photovoltaic industry. It requires strict control of defects and impurities, which are harmful for the performances of solar cells. Therefore, the CZ silicon crystal growth aims at achieving defect-free single crystals for advanced solar cell wafers. Meanwhile, attention must be paid to the low cost of CZ silicon crystal growth. Therefore, it is necessary to develop novel crystal growth techniques suitable for practical application of photovoltaics. This chapter will review the fundamentals of CZ silicon and recent developments. The oxygen-related defects and control technologies are emphasized. Meanwhile, the novel crystal growth methods are introduced. The Ge doping in CZ silicon can not only improve the material's mechanical strength, but also suppress the generation of boron–oxygen complexes. This will enable thinner solar cells at reduced cost and benefit the fabrication of high efficiency solar cells with low light-induced degradation effects.

---

### Keywords

Czochralski silicon · Crystal growth · Photovoltaic · Solar cell · Low cost · Defect · Light induced degradation

---

## Introduction

The growth of silicon crystals from high-purity polycrystalline silicon (>99.9999%) is a critical step for the fabrication of solar cells in photovoltaic industry. About 90% of the world's solar cells in photovoltaic (PV) industry are currently fabricated using crystalline silicon. Various techniques have been developed to grow photovoltaic silicon crystals. Among them, two techniques are dominant and meet the requirements of photovoltaic device technology. One is a casting method to produce multicrystalline (mc) silicon crystals, and the other is a Czochralski (CZ) method to produce single crystals. Compared to mc silicon, CZ silicon wafer has the advantages of low defect density and the well-textured surface with low reflectance, which is important for high performance solar cells. However, CZ silicon crystal growth is less productive than mc silicon crystal. The high cost of CZ silicon material causes a barrier for the worldwide application of solar cells (Watanabe et al. 1981). One strategy is to reduce the thickness of silicon wafers, which is strongly dependent on the mechanic strength of materials. Moreover, the round CZ silicon crystals have to be cut into pseudo-squares with round corners for the sake of solar modules, leading to not only the loss of materials but also the coverage loss of the final module. More important, boron-doped *p*-type CZ silicon solar cells widely used in photovoltaics nowadays are unavoidably suffering from the serious light-induced degradation (LID) of

efficiency under the sunlight due to boron–oxygen defects, further decreasing the cost-effectiveness of this material.

In this chapter, the major topics in the science and engineering of CZ silicon crystal growth technology are first discussed, including crystal puller, hot field, thermal control, melt flow, and so on. Then, the impurity incorporation and novel CZ silicon crystal growth techniques are presented. The impurity incorporation is mainly concerning oxygen contamination, which cause the generation of electrically recombination active defects. The novel CZ techniques aim at the control of oxygen level and the low cost of crystal growth. Finally, it will focus on the crystal growth of germanium (Ge)-doped CZ silicon for impurity engineering.

---

## Fundamentals of CZ Silicon Crystal Puller

### Crystal Puller

A typical CZ silicon crystal puller is shown in Fig. 1. It mainly consists of an air-tight, water-cooled growth chamber and a crystal harvesting chamber. An optional isolation gate valve is placed between the growth and harvesting chambers for the crystal transferring. The growth chamber is usually made of stainless steel.

**Fig. 1** A CZ silicon crystal puller



**Fig. 2** A graphite heater used in a CZ silicon crystal puller



The most important component in the growth chamber is the hot field, which includes a heater and a graphite cup. The graphite cup is used to support a quartz crucible that contains polysilicon charges. During crystal growth, the puller chamber is purged with an inert gas like argon or nitrogen with a reduced pressure. The purging gas flows from the top to the bottom of the puller, which can effectively remove the evaporated SiO particles and CO gas from the melt surface. The graphite cup is put on a graphite pedestal which is rotatable. The seed used for the single crystal growth is held by a seed holder which is controlled to rotate in the opposition direction of the graphite pedestal rotation.

The heater is made of molded graphite cylinders, which have a higher density and smoother surfaces. Slots are cut out of the cylinder to form a zigzag conductive path as shown in Fig. 2. The cross-section area of the conductive paths is usually kept constant in order to obtain a uniform radial temperature distribution. Arcing in the furnace using a RF coil heater can effectively be avoided by the highly conductive graphite. The typical voltage between two terminals of a heater is less than 100 volts (DC). The height to the diameter ratio of a heater is an important parameter that affects the temperature profile in the furnace, which is usually in the range of 1–1.4. A small ratio can cause a large value of temperature gradient along the crystal growth direction. Changing the cross-section area of the conductive paths can also be used to modify the temperature gradient at some positions in the crucible.

The graphite cup usually consists of two parts. One is a shallow and thick graphite dish at the bottom and the other is a graphite cylinder on the graphite dish. The thick bottom is for the purpose of thermal insulation, which can insure a positive temperature gradient for the solidification of melt from the bottom. It is known that the volume of silicon will expand approximately 9% by solidification. After crystal growth, the melt silicon remaining in the crucible will expand in volume during solidification and therefore can make the graphite cup break. In order to avoid this phenomenon, the graphite cylinder on the graphite dish has a slit in the sidewall to compensate the expanding of silicon phase change and crucible.

**Fig. 3** A quartz crucible for CZ silicon crystal growth



However, it should be noted that the graphite usually contains certain concentration of iron in ppm, which can diffuse into the crystal and decrease the minority carrier lifetime. The iron concentration in the crystal is strongly dependent on the iron content in the hot field graphite. To reduce the iron contamination from the graphite, the technology of coating protective layers can be used, including an initial protective layer of silicon carbide and a second protective layer of silicon by the chemical vapor deposition process. The coating layers can cause a barrier for the iron diffusion by sealing the graphite surface. Meanwhile, the silicon coating layer can also work as a gettering center for iron and form stable iron silicide phases. Experimental study has been performed to evaluate the impact of graphite furnace parts on radial impurity distributions for the crystals. When silicon carbide-coated graphite is used, the minority carrier lifetime of CZ silicon crystal gets significantly improved, as a result of the silicon carbide film acting as an effective seal against iron diffusion from the graphite parts. Further experiments have evaluated the iron contamination of silicon wafers in different graphite heaters. It is found that the wafers exposed to silicon carbide-coated graphite have higher iron concentrations than to the graphite coated with silicon and silicon carbide (O'Mara et al. 2007).

The crucible used for CZ silicon crystal growth is made of high purity fused quartz, as shown in Fig. 3. The quartz usually softens at 1,670 °C and fuses at 1,800 °C. Two types of quartz crucibles are commercially used nowadays. One is transparent and bubble-free, made of completely fused quartz. The other is opaque, made of partially fused quartz. However, the inner surfaces of the opaque crucibles are fused by fire-polishing and are also smooth. Both types of crucibles are made of semiconductor-grade quartz and have no significant difference on impurity contents in crystals. The crucible bottom profile and its aspect ratio can affect the convection flow pattern of the melt. The crucibles with semi-flat bottom can produce a better



radial resistivity in the crystals. During crystal growth at high temperatures, the devitrification of silica forms cristobalite, which is often detached from the crucible surface and cause structural defects in the crystals. Therefore, a dense barium silicate-coated layer on the crucible inner walls is necessary since barium oxide is a good devitrification promoter that helps forming a uniform dissolution layer on the crucible inner surface during crystal growth. Nevertheless, the CZ silicon crystal grown in these crucibles unavoidably contains a substantial amount of interstitial oxygen impurity since oxygen is inherently present in the crucible material.

Recently, silicon nitride-based crucibles are attractive because of the absence of oxygen. For such crucibles, the pressed  $\text{Si}_3\text{N}_4$  or carbon crucibles are used as substrates, and meanwhile, a pure  $\text{Si}_3\text{N}_4$  film without cracks is deposited on the substrates by chemical vapor deposition. However, it is found that silicon nitride performs well as a crucible material during a short time since silicon melt does not wet the silicon nitride crucible. It is attributed to the protective silicon dioxide films on the surface of the nitride. Late on, the silicon melt can penetrate into the silicon nitride matrix and finally leads to the decomposition of the crucible. The decomposition of silicon nitride follows the reaction:  $\text{Si}_3\text{N}_4 = 3 \text{Si} + 2 \text{N}_2$ . Experimental results have shown that the CZ silicon crystals grown from silicon nitride crucibles contain the oxygen concentration below  $2 \times 10^{16}$  atoms/cm<sup>3</sup>. However, a nitrogen concentration of  $4 \times 10^{15}$  atoms/cm<sup>3</sup> in the CZ silicon is found (Watanabe et al. 1981).

Aluminum oxide is another choice for crucible material. However, the dissolution of the aluminum oxide material releases aluminum impurities into the silicon melt, which can be incorporated into the silicon crystal by segregation effect. Since aluminum is a *p*-type dopant material for silicon, the incorporation of aluminum impurities may lead to unexpected deviation of dopant concentration in the as-grown silicon.

During silicon growth, silicon monoxide (SiO) will be formed due to the reaction of melt silicon and oxygen dissolved from the crucible into the melt. It is very important to remove SiO gas and particles from the chamber since too much deposition of SiO particles on cooler surfaces, such as the chamber wall, crucible inner wall, and ingot surface, could cause serious problems when the particles fall down to the melt. The dislocations or grain boundaries will generate and make structure integrity lost if the particles get into the growing crystal. By applying a cone structure component on the crucible, the argon flow rate and its path can be tailed to resolve this problem. Both molybdenum (Mo) and graphite with coating have been considered for the cone material. Figure 4 shows the photographs of both cones. With the cone, the argon flow consumption could be significantly reduced. The major reason is that the flow space between the cone and the melt is small and the argon flow across the melt surface becomes faster. Accordingly, the removal of SiO from the melt surface is more effective. With the cone, near the melt surface, no flow circulation is found, which is believed to be useful for reducing the falling-back of SiO particles from the upper cooler surfaces. Nevertheless, the upper part of the cone still has significant SiO deposition. With the top-wall insulation or a composite cone, the deposition is reduced and its position is higher due to the increase of cone temperature. Besides the argon consumption, the original argon flow path has to run

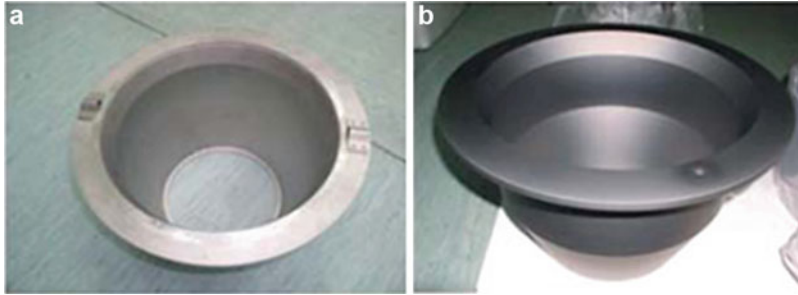


**Fig. 4** Photographs of the molybdenum (a) and the graphite (b) cones

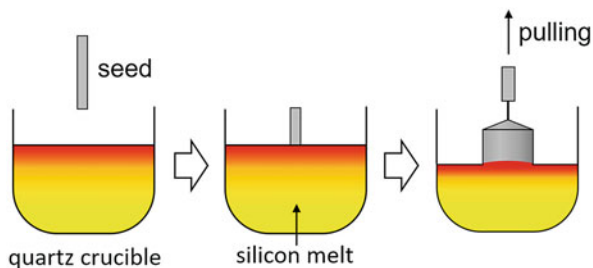
through the graphite heater and SiO reacts with graphite forming silicon carbide. This deteriorates the heater and shortens heater's lifetime. The same is true for graphic susceptor. By redirecting argon to the side insulation, it is found that the heater lifetime, as well as that of the graphite susceptor, could be significantly elongated. The heater lifetime can be increased to about 4,500 h from the original lifetime of 3,000 h. The lifetime of the graphite crucible (susceptor) is increased to 1,500 h, which is almost double that of the original one (880 h). As argon is redirected to the side wall, the deposition of SiO on the heater is significantly reduced after crystal growth, and the grown crystal surface is very shining, without any surface oxidation. If the cone is not used, the colorful oxidation rings generally appear on the crystal surface. Furthermore, with the cone, the melt leftover in the crucible could be significantly reduced because silicon remains molten near the end of the growth easily due to the less radiation heat loss. As a result, the wastage of material is reduced significantly.

## Pulling Procedure

The basic process of CZ silicon crystal pulling procedure is schematically shown in Fig. 5. Polycrystalline silicon raw materials are melted in the crucible under the inert gas protection. The inert gas has to flow permanently downwards through the pulling chamber to carry off the reaction by-products from melt. After the polycrystalline silicon is completely molten, the temperature of the melt will continue to rise for a short time due to the fusion heat transmission. In order to suppress the thermal shocking, the heater power is reduced to about the value which is needed for the crystal growth shortly before completely melting. For crystal growth, the whole furnace should be in thermal equilibrium. There is no further temperature variation at any point of the furnace. In this case, the supply and release of heat are in equilibrium. The heating can be controlled by measuring the temperature at a suitable position by a thermal couple. The empirical method is to dip the seed and observe its melting behavior.

After the silicon melt is thermally stable, the seed is dipped into the melt. When the seed starts to melt, the temperature is tuned down slightly. The seed is then

**Fig. 5** A schematic of a CZ silicon crystal growth



withdrawn from the melt so that it begins to grow but no increase in its diameter. By applying the Dash necking technology, the dislocations in the seed can be eliminated. For the dislocation elimination, the neck diameter needs to be reduced to 2–5 mm, and meanwhile the growth velocity is usually raised to  $\sim 6$  mm/min. After the neck reach a few centimeters in length by combining growth velocity and crystal diameter, the crystal becomes dislocation-free. Afterwards, the pulling rate of crystal needs to be reduced and the diameter of the crystal can be enlarged until it reaches the desired value. The transition part between the seed end and the silicon cylinder has a shape of cone, which is usually called the seed cone. Once the desired diameter is about to achieve, the pulling rate of crystal needs to be increased rapidly. In this case, the crystal can start to grow with the required diameter. Usually, the growth of the crystal cylindrical part is automatically controlled. The crystal radius at the solid/melt interface is the most important. The usual way is optical capturing of the meniscus shape, typically by detecting the bright meniscus ring. Optical imaging of the bright meniscus ring, which results from reflections of light emitted by the heaters, is an important measuring technique for CZ silicon crystal growth. It should be noted that the measured object is the diameter of the meniscus at a certain height, not the crystal diameter at the three-phase boundary. When the crystal radius begins to decrease the meniscus height will increase first. This means that the measured diameter of the bright meniscus ring will increase, which might result in incorrect reactions of the controller if it is not adapted to this behavior. The pulling rate of crystal growth should be reduced towards the bottom end of the crystal with the melt surface lowering, which is caused by the increase of heat radiation from the crucible wall. Meanwhile, the removal of the heat of crystallization is more difficult and the crystal growth needs more time. After the crystal cylinder is finished, the crystal diameter has to be reduced gradually to a small size and an end-cone is formed. For this purpose, the pulling rate is raised and the crystal diameter decreases. When the diameter is small enough, the crystal can be separated from the melt without dislocation generation. Noted that the withdrawal of the crystal from the melt surface cannot be very fast, otherwise the thermal shocking would cause plastic deformation in the lower part of the crystal. After finishing the growth of whole crystal, some silicon melt has to be remained in the crucible. This is because the high surface tension of liquid silicon makes it difficult to empty the crucible completely. The melt tends to diminish this surface and therefore flows away from the crystal.

Additionally, the melt residues contain high concentration of impurities, which will be harmful for the crystal quality.

## Dislocation-Free Growth

The seeds used for the growth of CZ silicon crystals are seldom dislocation-free. The thermal shocking dislocations have to be generated when the seed is dipped into the melt. Meanwhile, the strain that occurs as a result of different cooling rates between the inner and outer parts of the crystal is also one cause for dislocation generation. These dislocations will be propagated at high temperatures, or move into the grown crystal, which is more pronounced in the large diameter crystals. During the dislocation movement, the dislocations are not only movable in their glide planes, but also can spread into adjacent glide planes by cross slip, multiplication processes, and climb.

The dislocations in silicon crystals with diamond structure are preferable to propagate in a  $\{111\}$  plane. When a silicon crystal is pulled in a  $[100]$  direction, all  $\{111\}$  planes are oblique to the pull axis. Therefore, all the dislocations with Burgers vectors of  $(a/2) [110]$  will grow out and terminate at the crystal surface provided that the crystal diameter is reduced to a small value and no new dislocations are generated at the interface. This principle is first utilized by Dash to eliminate all the dislocations during the seeding process, which are called “Dash necking technology.” Nowadays, the Dash necking technology has been widely used in the crystal growth of CZ silicon. Figure 6 shows the basic process of Dash necking in the practical application. One need first melt back the seed to remove surface damages and to create a clean substrate surface. Then, a higher pull rates up to 6 mm/min is needed for the growth of the neck with a small diameter. This can allow the dislocations to emerge and terminate at the ingot surface and let the dislocations propagate behind the growth interface so that they will be eliminated by pairing or bending to form complete loops. Meanwhile, the temperature gradients for the neck growth must be controlled to keep the facet growing in the flat interface, which can provide thermal requirements for the two-dimensional growth with less thermal stress.

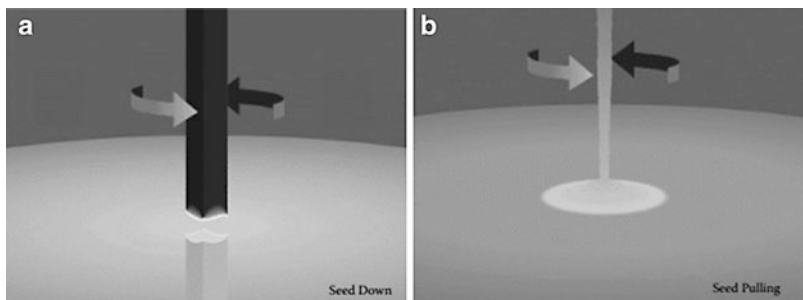
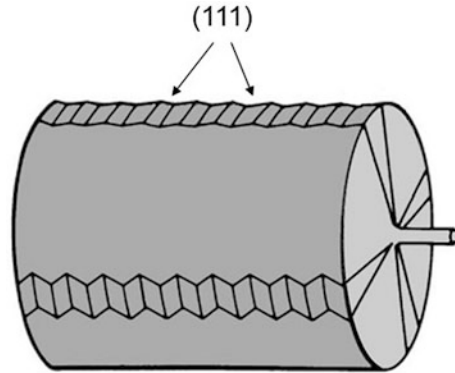


**Fig. 6** (a) Seed melting back in the molten silicon, (b) fast pulling to reduce the crystal diameter to implement the Dash process

**Fig. 7** A sketch of side facets in a [100] CZ silicon crystal without dislocations

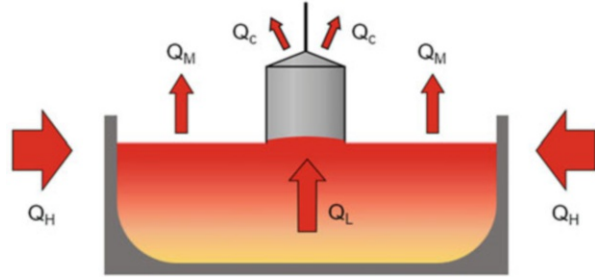


Generally, the dislocation generation is difficult to occur during the CZ silicon crystal growth if the growth parameters are stable. However, if a first dislocation is formed, it will multiply rapidly and move into the crystal. This will result in that the whole cross section at this position and a considerable part of the grown crystal are dislocated. The length of dislocated part is approximately equal to the diameter of CZ silicon crystal. It is important to recognize whether or not the dislocations are generated for the growing crystal, which can save the cost of crystal growth. The growth of dislocation-free crystal requires the existence of singular or faceted surfaces at the interface for two-dimensional nucleation. In a [100] CZ silicon crystal, four side-facets that are  $90^\circ$  apart are present in the interface. The facets form four ridges that are uninterrupted from the top to the side surface of the ingot, as shown by Fig. 7. The side facets in a [100] CZ silicon crystal are usually the  $\{111\}$  planes, which are  $54.5^\circ$  from the melt surface. The facets protrude beyond the circular circumference of the crystal. Thus, these four facets can be clearly identified in the meniscus during the crystal growth and the reflect light that irradiates from the heater through the crucible with a greater intensity than the nonfaceted regions. If one or more facets are not present at the interface, the dislocations must be generated in the CZ silicon crystal.

## Thermal Control

The crystal growth of CZ silicon is a phase transition from liquid to solid with the decrease of melt temperature, which corresponds to a decrease in entropy and Gibbs free energy. At the silicon melting temperature, the liquid and solid phases can co-exist in equilibrium, which have the same Gibbs free energies. When the melt is cooled below the melting point for crystal growth, the variation in Gibbs free energy is directly proportional to the undercooling ( $\Delta T$ ). Therefore, the undercooling can be considered as the only driving force for phase transition and determine the crystal growth rate.

**Fig. 8** A heat flow pattern in the furnace during crystal pulling



For the practical CZ silicon crystal growth, thermal insulation is usually applied at the bottom of the crucible and outside surfaces of the heater, which causes vertical and radial temperature gradients in the melt. The lowest temperature part of the melt is located at the center of the melt surface. For crystal growth, the melt temperature needs to be reduced so that the center of the melt surface reaches the melting point. At this moment, the seed can be dipped into the melt and initiate the crystal pulling by further lowering the melt temperature. Once the crystallization occurs on the seed, it can be gradually withdrawn from the melt and grows as an ingot. The crystallization of molten silicon is accompanied by generating the latent heat of solidification. The latent heat needs to be removed because it can suppress the further solidification of molten silicon. The latent heat is usually dissipated into the crystal by thermal conduction and then released to the ambient through thermal radiation and convection.

Under equilibrium state, the heat input to the whole system should be equal to the heat output, as shown by Fig. 8. The heat input consists of heat supply by the heater ( $Q_H$ ) and latent heat ( $Q_L$ ) of solidification. The heat output consists of heat loss from the melt ( $Q_M$ ) and heat loss from the crystal ( $Q_C$ ). Heat loss of the melt occurs primarily from its free surface to the ambient gas and from the melt/crystal interface to the crystal. The latent heat generated at the interface mainly dissipates to the crystal by conduction. The heat transfer behavior through the crystal/melt interface is a critical parameter to determine the crystal growth rate and crystal perfection, which can be expressed as,

$$\sigma_s \left( \frac{dT}{dx} \right)_s - \sigma_L \left( \frac{dT}{dx} \right)_L = \frac{Q_L v}{A} \quad (1)$$

where  $\sigma_s$  and  $\sigma_L$  are the thermal conductivity of silicon crystal and melt, respectively,  $v$  is the crystal pull rate in the unit of mass per unit time,  $A$  is the area of the solid–liquid interface, and  $\left( \frac{dT}{dx} \right)_s$  and  $\left( \frac{dT}{dx} \right)_L$  are the vertical temperature gradient in the solid and liquid silicon, respectively. The Eq. (1) suggests that the pull rate of CZ silicon crystal is determined by the two variables  $\left( \frac{dT}{dx} \right)_s$  and  $\left( \frac{dT}{dx} \right)_L$ . Note that the value of  $\left( \frac{dT}{dx} \right)_L$  cannot be negative, or else the solidification could occur below the solid–melt interface and interrupt the growth of a single crystal. When  $\left( \frac{dT}{dx} \right)_L$  is

equal to zero, the growth rate of CZ silicon reaches a maximum value, which is directly proportional to  $\left(\frac{dT}{dx}\right)_s$ .

Theoretically, the value of  $\left(\frac{dT}{dx}\right)_s$  can be evaluated by the following differential equation (Runyan 1965):

$$\frac{d^2T}{dx^2} = BT^4 \quad (2)$$

where  $B = \frac{2\sigma_r e}{\sigma_s R}$ . Here  $e$  is the thermal emissivity,  $\sigma_r$  the radiation constant,  $\sigma_s$  the conduction constant, and  $R$  the radius of the crystal. The ratio of radiation to conduction heat loss  $\left(\frac{\sigma_r}{\sigma_s}\right)$  is referred as the emission power of the ingot and is a constant for a given material. The Eq. (2) can be solved under the boundary conditions in which one end of the crystal is at the melting point and the other end is at zero, as expressed below,

$$\left(\frac{dT}{dx}\right)_s = CB^{\frac{1}{2}}T_m^{\frac{5}{2}} \quad (3)$$

where  $T_m^{\frac{5}{2}}$  is the melt temperature of the crystal and  $C$  is a constant. It can be seen that the magnitude of  $\left(\frac{dT}{dx}\right)_s$  depends only upon the emission power of the ingot. If assuming  $\left(\frac{dT}{dx}\right)_L = 0$ , the maximum growth rate can be calculated by

$$V_{\max} = \frac{CA}{Q_L} \left( \frac{2\sigma_s \sigma_r e T_m^5}{R} \right)^{\frac{1}{2}} \quad (4)$$

The interface shape can be qualitatively predicted by considering whether there is any deviation from the heat balance at the interface. When the heat dissipation term  $\left(\sigma_s \left(\frac{dT}{dx}\right)_s\right)$  is greater than the receiving term  $\left(\sigma_L \left(\frac{dT}{dx}\right)_L + \frac{Q_L v}{A}\right)$  in the Eq. (1), the interface shape will become convex toward the melt. The interface shape will become concave if the heat dissipation term is smaller than the receiving term. When the crystal pull rate and axial temperature gradient in the melt are constant, the rate of heat receiving will be constant. However, the rate of heat dissipation will be progressively reduced as the crystal length increases. Therefore, the interface shape will change during the course of the crystal growth process.

## Melt Flow in Crucible

The convection in the silicon melt can be classified into two categories. One is related to temperature gradients, and the other is related to the movements of crystal and crucible. The silicon melt flow is barely visible because of the metallic character of the melt (nontransparent, low emissivity). To make such flow visible, a melt of transparent  $\text{CaF}_2$  with the same melting point as silicon is sometimes used. Due to

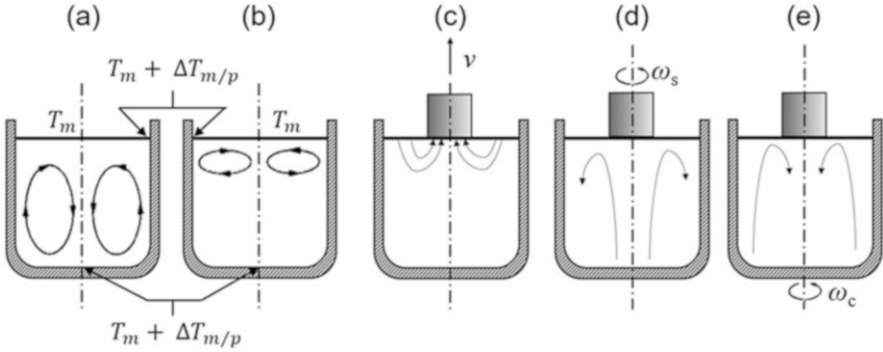


**Fig. 9** Patterns of melt convection in the crucible during CZ silicon crystal growth

the temperature differences in the melt, the emission of light occurs at distinctly different intensities and thus the flow pattern can be easily seen.

The large temperature differences lead to considerable differences in the density of the silicon melt. Due to the low viscosity of the silicon melt, the buoyant force causes strong convection currents develop, as shown in Fig. 9a. Meanwhile, since the surface tension is associated with melt temperature, it will cause the Marangoni convection or the thermocapillary convection, as shown in Fig. 9b. The basic flow pattern is determined by the crucible geometry, melt height, and thermal boundary conditions. The driving force for the melt flowing can be represented by Grashof number ( $Gr$ ) (Carruthers et al. 1977),

$$Gr = g\beta\Delta TmL^3/v_k \quad (5)$$

where  $g$  is the gravity acceleration,  $\beta$  is the melt thermal expansion coefficient,  $\Delta Tm$  the temperature difference in the melt over a specific length ( $L$ ), and  $v_k$  the kinematic viscosity of the silicon melt. The thermal convection of the melt is suppressed by decreasing the value of  $Gr$ . In the CZ silicon crystal growth process, heat is supplied to the crucible laterally by the heater, and the temperature difference between the periphery and the center regions of the melt ( $\Delta T_{m/p}$ ) becomes larger than the difference between the surface and bottom of the melt. Thus, a large-diameter crucible will cause a strong thermal convection according to the dependence of  $Gr$  on  $L$  in Eq. (5). During the crystal growth, the forced convection will be caused by crystal pulling, crystal rotation, and crucible rotation, as shown in Fig. 9c–e. The crystal rotation plays like a pump, which makes the melt move upward and radially outward near the surface. The crucible rotation brings about melt convection from the crucible wall toward the center, which can reduce the thermal asymmetry and decrease the thickness of the growth interface diffusion boundary layer. The degree of melt convection can be expressed by Reynolds number ( $Re$ ),

$$Re = \omega R^2/v_k \quad (6)$$



where  $R$  is the crystal radius. The thermal convection is dominant in the melt for a low value, while the forced convection becomes dominant for a high value. The critical ratio for the melt flow changing from thermal convection dominance to forced convection dominance is on the order of ten. Here, it should be mentioned that the melt convections can accelerate temperature variations in the melt, which usually causes the re-melting and super cooling at the growth interface, and therefore might introduce crystal disorder and inhomogeneous impurity distribution.

In practical CZ crystal growth, the convections caused by different reasons are mixed with each other, and the melt flow becomes more complex. With the crystal growing, the melt level and the length of the grown crystal are changed, which significantly affects the melt flow. For a deep melt, the forced convection caused by crystal rotation affects only the upper region of the melt in the crucible and the rest is controlled by thermal convection. For a shallow melt, the forced convection affects the whole melt in the crucible, and the vertical flow extends from the crucible bottom to the melt surface.

---

## Incorporation of Impurities

Generally speaking, impurities in silicon crystal can be classified as two categories: dopants and contaminants. Dopants are intentionally incorporated to modulate the resistivity of silicon crystal, while contaminants are unintentionally incorporated. The incorporation of impurities into silicon crystal during growth is mainly determined by segregation effect. As a result, during silicon crystal growth, impurities are mainly segregated along the axial direction, which can be described by the normal freezing equation.

## Segregation Theory

A true equilibrium system means that impurity distributions in both melt and crystal are uniform, without concentration gradients in each phase. The impurity segregation effect in CZ silicon can be defined by the impurity concentration ratio of the solid and melt silicon. It can be described by the equilibrium segregation coefficient,  $k_{eq}$ , as

$$k_{eq} = \frac{C_S}{C_L} \quad (7)$$

where  $C_s$  is the impurity concentration in the crystal silicon at the crystal/melt interface and  $C_L$  the impurity concentration in the melt silicon. The impurity concentrations in the solid and melt silicon can be obtained by the binary phase diagrams of impurity-silicon systems. Table 1 shows the equilibrium segregation coefficients  $k_{eq}$  of various impurities in silicon (Hull 1999). Note that among all the impurities, oxygen is the unique element which has a segregation coefficient of

**Table 1** Equilibrium segregation coefficients of main impurities in silicon

<b>B</b>	0.8	<b>O</b>	1.25	<b>Fe</b>	$8 \times 10^{-6}$
<b>Al</b>	0.002	<b>C</b>	0.07	<b>Ni</b>	$8 \times 10^{-6}$
<b>Ga</b>	0.008	<b>N</b>	0.0007	<b>Au</b>	$2.5 \times 10^{-5}$
<b>In</b>	0.0004	<b>Sn</b>	0.016	<b>Zn</b>	0.001
<b>P</b>	0.35	<b>Cu</b>	0.0004	<b>Mn</b>	$1 \times 10^{-5}$
<b>As</b>	0.8	<b>Cd</b>	$1 \times 10^{-6}$	<b>Li</b>	0.01
<b>Sb</b>	0.023	<b>Ti</b>	$3.6 \times 10^{-4}$	<b>Ag</b>	$1 \times 10^{-6}$
<b>Ge</b>	0.56	<b>Cr</b>	$1.1 \times 10^{-5}$		

larger than 1.0. Furthermore, our recent work has clarified that the segregation coefficient of germanium in silicon should be 0.56 (Wang et al. 2011), instead of 0.33 which was generally accepted.

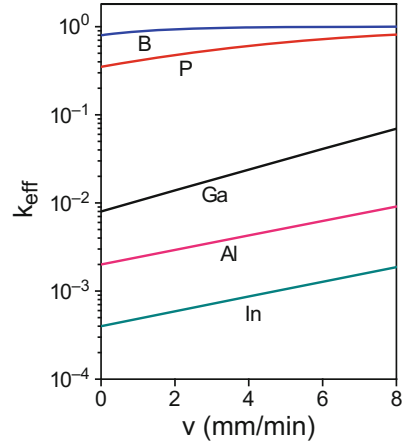
According to the phase diagram, the equilibrium segregation of impurities must be dependent on their solubility in silicon. However, the impurity solubility is strongly influenced by their atom sizes. With an increase of impurity atom sizes, their solubility in silicon usually decreases. Therefore, the large impurity atoms are generally difficult to incorporate into silicon crystal, causing small equilibrium segregation coefficients.

In the practical CZ silicon crystal growth, the melt convection should also be considered for the impurity segregation effect. Usually, an effective segregation coefficient ( $k_{eff}$ ) is used to define the practical segregation behavior of impurities during silicon crystal growth. It is assumed that there is a boundary layer with the thickness of  $\delta$  at the crystal/melt interface within which the impurities transport by diffusion, and meanwhile the impurity concentration in the melt beyond this boundary layer is uniform due to the convection. The effective segregation coefficient can be written as

$$k_{eff} = \frac{1}{1 + \left(\frac{1}{k_{eq}} - 1\right) \exp\left(-\frac{v\delta}{D}\right)} \quad (8)$$

The value of  $k_{eff}$  depends strongly on  $\delta$ . In practice,  $\delta$  is difficult to estimate, which depends on the convection strength in the melt silicon. This means that there is no simple way to predict  $k_{eff}$ . It can be noticed that for  $\delta = 0$ ,  $k_{eff} = k_{eq}$  and for  $\delta = \infty$ ,  $k_{eff} = 1$ . From the Eq. (8), it can also be noted that with an increase of crystal growth rate, the value of  $k_{eff}$  increases. Figure 10 shows the effective segregation coefficients of different impurities as a function of crystal growth rate. Note that the effective segregation coefficients always tend towards one with an increase of crystal growth rate. In the practical crystal growth of CZ silicon, the growth rate is usually less than 1 mm/min, so the effective segregation coefficients of impurities are close to the equilibrium one, which can be seen in Fig. 10. This allows us to often predict the impurity distribution in a silicon crystal using the equilibrium segregation coefficient according to the Eq. (8).

**Fig. 10** Effective impurity segregation coefficients in silicon as a function of crystal growth rate



If assuming that the impurity concentration in the melt is uniform throughout, the local impurity concentration in the crystal can be given by  $C_S = k_{eff}C_L$ . The sum of impurities in the crystal and in the melt should keep constant, which can be written as,

$$\int_0^g C_S dx + (1 - g)C_L = C_0 \quad (9)$$

where  $C_0$  is the start concentration of impurity in the melt silicon as defined above and  $g$  the solidified fraction. Considering  $C_S = kC_L$  and  $C_L = C_0$  at  $g = 0$ , the Eq. (9) can be solved to be,

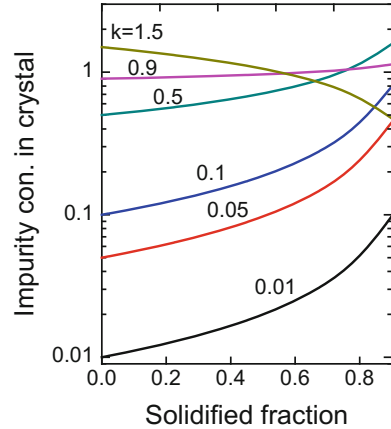
$$C_S = k_{eff}C_0(1 - g)^{k_{eff}-1} \quad (10)$$

This expression is so-called “normal freezing equation” describing the distribution of impurity concentration along the axial direction of silicon crystal.

### Dopant Distribution Inhomogeneity

Figure 11 shows the distribution of impurities with different  $k$  along the axial direction of silicon crystal. For  $k_{eff} < 1$ , the solidified crystal part contains less of impurity. This will cause more and more impurity remaining in the melt, so the impurity concentration in the silicon melt increases with crystal growth proceeding. For  $k_{eff} > 1$ , the solidified crystal part contains more impurity and the impurity concentration in the melt will reduce, which decreases with crystal growth proceeding. It should be noticed that when the value of  $g$  is closing to one, the impurity concentrations in the crystal and melt both go to infinity for  $k_{eff} < 1$ , and they go to

**Fig. 11** Distribution of impurities with different  $k$  along the axial direction of silicon crystal ( $\delta = 0.8$  mm)

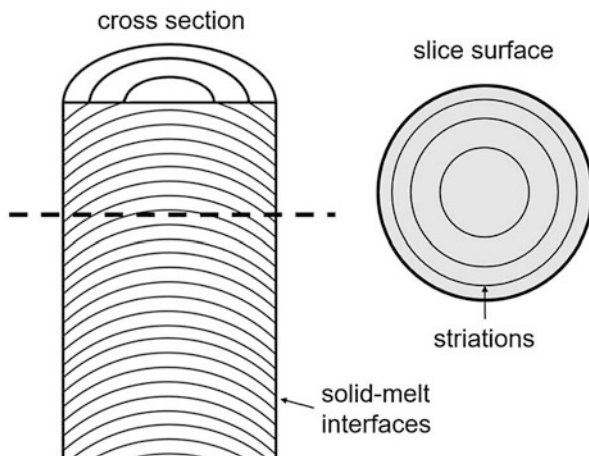


zero for  $k_{eff} > 1$ . For all the dopants, the value of  $k_{eff}$  is smaller than one. The experimentally obtained results for boron-doping generally fit the calculated ones well, while in the phosphorus-doping case, the measured resistivity is higher than the calculated ones due partially to the evaporation of phosphorus during the crystal growth process. It can be understood that the segregation phenomenon of dopants causes a low production yield of silicon crystal that meets the resistivity tolerance required by solar cell producers. This problem becomes even more serious for crystal growth using a dopant with a smaller segregation coefficient.

Dopant compensation technology can be used to modulate the resistivity distribution along the crystal axial direction. For instance, the resistivity in the tail part of gallium-doped CZ silicon crystal can be effectively enhanced by phosphorus codoping. Experimental results have clarified that both majority and minority carrier mobility in CZ silicon are reduced due to the Ga and P compensation. However, the reduction of carrier mobility is not as severe as expected by Klaassen's model (Chen et al. 2011). The infrared absorption spectra for the compensated CZ samples show that the Ga- and P-related bands significantly get broadened. A portion of P atoms are possibly trapped by Ga atoms to form the Ga-P pairs, resulting in the reduction of carrier scattering centers. The solar cells based on the compensated silicon have comparable efficiencies with the reference silicon solar cells, implying that the Ga and P compensation in the level of  $<10^{17}/\text{cm}^3$  has no problem for its photovoltaic application (Xiao et al. 2012).

In the CZ crystal growth processes, the changes of the growth parameters like growth rate and the diffusion boundary layer thickness can result in variations of the effective segregation coefficient  $k_{eff}$ . This gives rise to microscopic impurity distribution inhomogeneities at the solid/liquid interface. As a result, the impurity striations can be found by preferential chemical etching and X-ray topography. The impurity striation usually shows long-range periodicity. The major causes of striations are temperature fluctuations near the crystal-melt interface induced by unstable thermal convection in the melt and crystal rotation in an asymmetric thermal

**Fig. 12** The formation of impurity striations in a CZ silicon crystal



environment. The higher thermal gradients and the more pronounced thermal convection are observed in melts with higher melting points. Therefore, the extent of thermal asymmetry is great and re-melting is common during rotation and pulling of a silicon crystal because of the high melting point of silicon. With high thermal asymmetry in a crystal growth system, the microscopic growth rate will assume negative values with each rotation cycle, which causes more or less partial re-melting. Consequently, rotational striations are caused by localized regions of decreased microscopic growth rate, which result in a decreased concentration for impurities with an equilibrium segregation coefficient  $k_0 < 1$ . Accordingly, the periodicity  $d_{rs}$  of rotational striations is given by  $v/\omega$ .

Figure 12 schematically illustrates a CZ silicon crystal cross section containing a curved crystal–melt interface, which results in inhomogeneities on a slice surface. As each planar wafer is sliced, it contains different portions of several curved striations, which are referred to as swirl. Radial impurity concentration gradients are known to affect the local electrical properties of solar cells. Therefore, it is important to minimize radial fluctuations in dopant concentration for high performance solar cells.

## Oxygen Impurity

Oxygen is one of the main impurities in silicon crystals for solar cells, which originates from the contamination of silica crucibles. During silicon crystal growth, the melt will interact with silica crucibles to form SiO. Most of SiO will come to the melt surface to evaporate as gas and only a small portion of SiO remains in the melt, which finally are segregated into silicon crystal. The concentrations of oxygen in CZ silicon are about  $\sim 10^{18}/\text{cm}^3$ . They generally stay at the interstitial sites to form covalent bonds with two silicon atoms and therefore are electrically neutral. However, the interstitial oxygen in silicon can form various microdefects, giving detrimental influence on the performance of solar cells. The diffusion rate of oxygen in

silicon is determined by its existence forms. An oxygen dimer diffuses much more rapidly than an interstitial oxygen ( $O_i$ ). Oxygen atoms can form thermal donors (TDs) by annealing CZ silicon in the temperature range 300–500 °C (Capper et al. 1977). The generation of thermal donors will result in that the resistivity of  $n$ -type CZ silicon samples decreases, while the resistivity of  $p$ -type samples increases. In a more serious case, the  $p$ -type silicon which is the basic material for silicon solar cells will be transformed into  $n$ -type. Obviously, a high concentration of thermal donors definitely affects the electrical performance of solar cells. The most effective temperature for the formation of thermal donors is 450 °C (Ruiz and Pollack 1978), and an annealing at 650 °C for 30 min can remove grown-in thermal donors formed during crystal growth. The experiments have verified that the generation rate of thermal donors in the beginning is proportional to the oxygen concentrations to the fourth power and their maximum concentration is proportional to the oxygen concentration to the third power (Londos et al. 1993). Furthermore, the existence of other impurities can significantly affect their formation, e.g., their formation is suppressed by nitrogen and carbon, but is enhanced by hydrogen.

Oxygen in silicon can also induce another kind of donors, so-called “new donors,” whose formation temperature is in the range of 550–850 °C, but their formation needs a relatively long time, above 10 h (Gaworzewski and Schmalz 1983). For the crystal growth of silicon used for solar cells, the 550–850 °C period of its thermal history is much short than 10 h, so new donors cannot have enough time to form. Therefore, the new donor effect has never been seriously considered in photovoltaic industry.

Since oxygen exists as super-saturation states in silicon crystal, some interstitial oxygen atoms can form precipitates in a wide temperature range while silicon is annealed. In general, oxygen precipitates consist of amorphous or crystalline  $SiO_x$  ( $x < 2$ ) with a volume  $V$  which is 1.25 times larger than the silicon atomic volume in the lattice. Accordingly, the process of oxygen precipitation is accompanied with the emission of considerable self-interstitial atoms, forming extended defects such as dislocation loops or stacking faults. For the silicon crystal used for solar cells, the formation of grown-in oxygen precipitates during crystal growth is very important, due to the thermal history. It can cause different behaviors of subsequent oxygen precipitation for the wafers cut from the different crystals with equal initial oxygen concentrations and subjected to the same heat treatments. The thermal history is generally understood as the in situ annealing silicon crystals after solidification.

On the other hand, carbon is often found as an impurity in silicon crystal used for solar cells in amounts varying with the growth techniques. In photovoltaic CZ silicon, the carbon concentrations are in general  $\sim 10^{17} \text{ cm}^{-3}$ . The carbon atoms in crystalline silicon usually occupy the substitutional sites, as labeled  $C_s$ . It can easily form C–O complexes with oxygen, which can become the heterogeneous nucleation sites for oxygen precipitates and promote their formation. Experiments have clarified that carbon in silicon can enhance oxygen precipitation during both crystal growth and following heat treatments.

The electrical properties of solar cell devices are strongly influenced by the presence of oxygen precipitates in crystalline silicon. They can increase the current

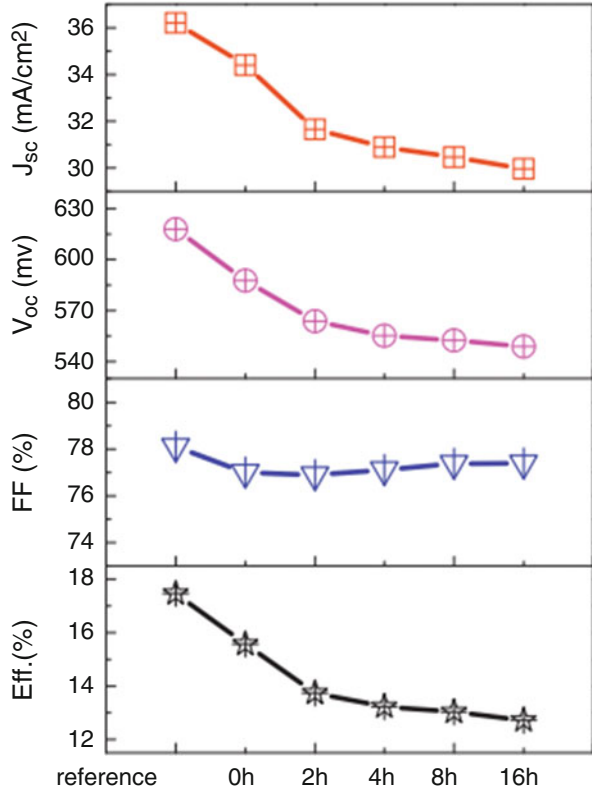
in reverse-biased  $p$ - $n$  junctions and therefore reduce open-circuit voltage of solar cells (Chakravarti et al. 1982). The leakage current could be related to oxygen precipitates themselves or their induced dislocations and stacking faults. Furthermore, the formation of oxygen precipitates within the bulk of silicon wafers can affect both the recombination and the generation lifetimes since they can cause deep energy levels in band gap and become the recombination centers for minority carriers (Vanhellemont et al. 1995). Hwang and Schroder (1986) studied the recombination properties of oxygen-precipitated silicon and found that once interstitial oxygen precipitated in silicon bulk, the minority carrier recombination lifetime reduced dramatically, and meanwhile, the degree of lifetime degradation was more pronounced in  $p$ -type silicon than in  $n$ -type silicon. They believed that the recombination at oxygen precipitates took place through their interface states. Moreover, the existence of positive fixed charges in oxygen precipitates will also help the lifetime degradation in  $p$ -type silicon. Experiments have clarified that a high concentration of initial oxygen will not help the improvement of solar cell efficiency due to oxygen precipitation during device thermal recycles. The reduction of cell out-put power and efficiency along with its short-circuit current, fill factor, and open-circuit voltage could take place with an increase of oxygen precipitates, see Fig. 13 (Chen et al. 2011).

## Light-Induced Degradation of CZ Silicon

P-type boron-doped CZ silicon solar cells are suffering a light-induced-degradation (LID) in efficiency up to 1–2% absolutely, due to a CZ-specific defect formation. These defects are readily to form once silicon crystal simultaneously contains the dopant B and the inevitable impurity O incorporated by dissolving of silica crucibles. The complexes can form in the case of excess carrier injection under light illumination (Schmidt et al. 1997) or application of forward bias (Hashigami et al. 2002) and can be fully annealed out at elevated temperatures in dark. However, the recovery process is reversible and the degradation will take place once again under illumination. The generation of B–O complexes consists of a fast- and a slow-forming process (Dhamrin and Saitoh 2003), corresponding to activation energies of about 0.2 and 0.4 eV, respectively. The recovery at elevated temperatures in dark is a thermal activation process with an activation energy of 1.3 eV (Schmidt and Bothe 2004). Advanced carrier-lifetime spectroscopic studies have revealed that the slow-forming defect causes a deep level at  $E_c - 0.41$  eV with capture cross-section ratio  $\sigma_n/\sigma_p$  of 10 and a shallow level at  $E_c - 0.15$  eV with uncertain  $\sigma_n/\sigma_p$  value, while the fast-forming defect is also a deep center with energy level lying between  $E_c - 0.35$  and  $E_c - 0.85$  eV and with a much larger  $\sigma_n/\sigma_p$  of 100 (Rein and Glunz 2003).

Glunz et al. firstly reported that the saturated concentration of B–O complexes ( $N_t^*$ ) is proportional to the B concentration ( $N_B$ ) in exclusively B-doped Si (Glunz et al. 1998), but later it was clarified to be dependent on the hole concentration ( $p_0$ ) in B and P compensated Si (Macdonald et al. 2009). However, a recent result reported by Forster et al. reconfirmed that the proportionality of  $N_t^*$  is related to

**Fig. 13** Characteristic parameters of the solar cells from the reference sample and the samples subjected to preannealing for different durations at 750 °C followed by 1,050 °C/16 h annealing which contains different oxygen precipitate concentrations (Reprinted with pending permission, Chen et al. 2011)



$N_B$  in a special B and Ga co-doped silicon crystal, instead of the  $p_0$  (Monkhorst and Pack 1976), indicating that the relation between  $N_i^*$  and  $N_B$  or  $p_0$  is still controversial. Meanwhile, studies in the three cases above all have shown that the generation rate constants ( $R_{gen}$ ) of B–O complexes exhibit a dependence on  $p_0^2$ , instead of  $p_0 \times N_B$ . Moreover, it has been clarified that the value of  $N_i^*$  is precisely proportional to the square of  $O_i$  concentration ( $[O_i]^2$ ) (Bosomworth et al. 1970), suggesting that the oxygen dimers ( $O_{2i}$ ) are important components of the B–O complexes.

Schmidt and Bothe (2004) and Palmer et al. (2007) (proposed a  $B_sO_{2i}$  model as a good explanation of LID behaviors in exclusively B-doped silicon). In this model, the randomly distributed  $O_{2i}$  diffuse quickly by the assistance of excess carriers towards  $B_s$  atoms to form recombination centers (Voronkov and Falster 2010). This model will naturally lead to a relation  $R_{gen} \propto p_0 \times N_B$  since the reaction probability increases with the  $N_B$ , which is not in accordance with the experimental result that the  $R_{gen}$  actually depends on the  $p_0^2$ . Moreover, Voronkov and Falster (2010) put forward a  $B_iO_{2i}$  model in which the positively charged interstitial boron atoms ( $B_i$ ) are assumed to be captured by the  $O_{2i}$  to form latent centers in as-grown silicon and then the LID occurs via the transformation of latent centers into recombination centers. However, this model cannot account for the



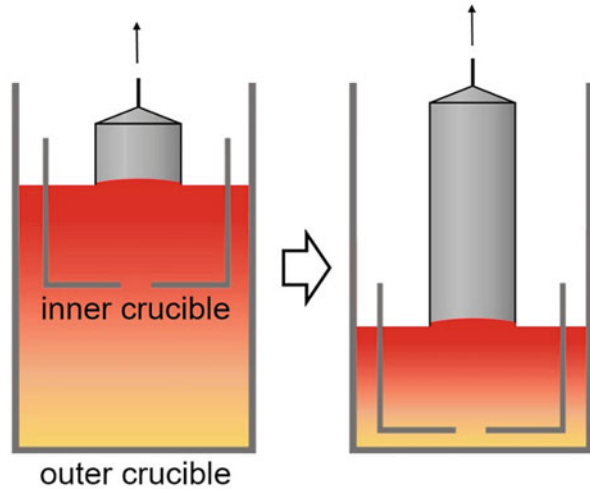
occurrence of LID phenomenon in *n*-type compensated Si which seems to be in the same nature with the case in *p*-type silicon. Recently, a new “hybrid” model that combines the advantages of previous two models is proposed. The latent centers are first formed by the  $B_s$  atoms, instead of  $B_i$  atoms, capturing  $O_{2i}$ , and then transform into the recombination centers (Bosomworth et al. 1970). More importantly, the combination of temperature and illumination with hydrogen passivation can permanently deactivate B–O complexes, which is named as regeneration process. The distinguish between thermal annealing and regeneration process is dominantly due to the different electronic properties of varied hydrogen charged species passivating B–O complexes.

Replacing boron by other III group dopants (Al, Ga, In) can effectively avoid the B–O defect generation during CZ silicon crystal growth. However, Ga has a small segregation efficient in silicon, which will reduce the effective length of crystal utilization for the solar cell fabrication. The Al dopant can also form the Al–O complexes with oxygen and reduce the minority carrier lifetime. It is found that the open-circuit voltages ( $U_{oc}$ ), short-circuit currents ( $I_{sc}$ ), and photo-electrical conversion efficiency of the Al-containing solar cells decrease with the increase of Al concentrations because of Al-related deep level recombination centers. The average absolute efficiency of Al-doped silicon solar cells is 0.34% lower than that of Ga-doped-only cells, even though Al-doped silicon solar cells show no light-induced efficiency degradation (Yuan et al. 2016). But the Al-doped silicon solar cells are comparable at the final state to that of normal B-doped silicon solar cells. The evaporation of indium is rather severe during the CZ silicon crystal growth, which makes the accurate control of desired resistivity in the crystal difficult. With an increase of doping concentrations, the electrical activity of indium dopants in silicon is found to become smaller. Moreover, the In solubility in silicon is very small. Beyond a critical doping concentration, the cellular growth of indium-doped CZ silicon crystal generally occurs (Yu et al. 2012).

## Oxygen Control

The total oxygen atoms incorporated into a crystal through the crystal–melt interface are balanced by the oxygen dissolved into the melt through silica crucible dissolution and the oxygen evaporated from the melt free surface. Therefore, the oxygen incorporation into a growing silicon crystal involves three diffusion boundary layers and three interface areas: crucible–melt, melt–ambient, and crystal–melt. The thickness of boundary layers depends on the melt convection flows, while the interface areas are determined by the melt charge weight, size, and shape of the crucible and crystal diameter. Under these circumstances, the ratio of the crucible–melt interface area to the free melt surface area is the primary factor that determines the oxygen concentration incorporated into CZ silicon. Since the large silica crucibles used in current CZ growth system are of approximately cylindrical shape, the crucible–melt interface area constantly decreases during growth as the melt volume decreases, while the free melt surface area remains unchanged because the crystal diameter is constant over most of the growth. As a result, the oxygen dissolved into the melt

**Fig. 14** Double-crucible CZ silicon crystal growth



through silica crucible dissolution decreases, but the oxygen evaporated from the melt free surface remains constant during growth. This phenomenon, together with the segregation coefficient of oxygen, which is larger than one, leads to a gradual decrease in the oxygen concentration toward the tail end of a CZ crystal. Therefore, in order to obtain an axially uniform distribution of oxygen, the ratio of oxygen from crucible dissolution and the evaporated oxygen must be kept constant by controlling silicon melt flows, usually by controlling crystal/crucible rotation rates.

If the ratio of the crucible–melt interface area to the free melt surface area can be maintained constant during crystal growth, a more uniform axial oxygen distribution will be obtained. This has been realized in the crystal growth using a crucible with truncated cone. However, this method cannot meet the requirement of high production throughput. Figure 14 shows the method of double crucible CZ silicon crystal growth (Shimura and Kimura 1981). A smaller silica crucible is submerged in the melt held by a larger crucible. This method enables the ratio to remain constant and in turn may grow a silicon crystal with a uniform axial oxygen distribution at a desired concentration. However, this method has not been realized yet because of its complex operating mechanism and expensive cost. More practical solutions to control oxygen concentration are the continuous CZ crystal growth or magnetic field assisted crystal growth technique.

---

## Novel CZ Silicon Crystal Growth

### Magnetic Field Assisted Growth

The electrical conductivity of silicon increases with the temperatures. The conductivity of silicon increases to  $12,300 \text{ ohm}^{-1} \text{ cm}^{-1}$  when it transforms into a molten state at its melting temperature. This number is within the same range of conductivity

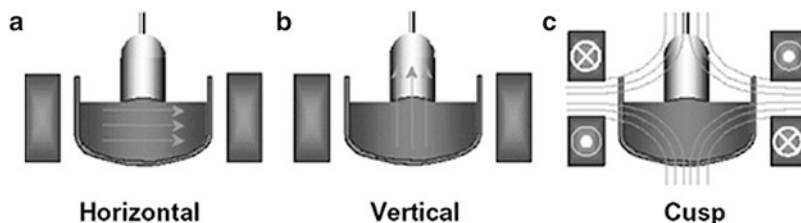


**Fig. 15** Magnet flux lines for (a) HMCZ, (b) VMCZ, and (c) CMCZ cases

values for many metals. Electrically, the molten silicon can be considered as a metal. Since the molten silicon flows in the crucible due to the thermal-driven convection, the application of a magnetic field into the silicon melt can cause a force that retards its flow (i.e., Lenz law). An increase in the melt viscosity brings about suppression of the thermal convection and results in a decrease in temperature fluctuations at the growth interface.

Silicon crystal growth by the magnetic-field applied CZ (MCZ) method was reported for the first time in 1980s (Hoshi et al. 1980). Various types of magnetic field configurations have been developed. The direction of magnetic field can be perpendicular (horizontal or transverse) or parallel (vertical or axial) to the growth axis, which are referred to as HMCZ and VMCZ, respectively (Shimura 1989). Figure 15a, b shows the magnetic flux lines for VMCZ and HMCZ cases. A vertical magnetic field can be applied to the melt, by surrounding the growth chamber with a solenoid coil, and is much easier and less costly than a horizontal magnetic field, which requires heavy electromagnets. Moreover, a magnetic field parallel to the crystal growth axis offers the advantage that the axial symmetry of the configuration is not disturbed, thus minimizing azimuthal variations in the crystal.

From a practical point of view, the HMCZ method seems to be more successful than the VMCZ in growing high-quality silicon crystal with both an axial and radial uniformity of oxygen at a desired level. By applying a horizontal magnetic field larger than a critical value, the surface vibration of silicon melt can be eliminated and the temperature fluctuations in a silicon melt close to the surface are suppressed (Ohwa et al. 1986). Temperature fluctuations of about 1–2 °C usually appear in the melt at zero magnetic field, and as the field increases, the fluctuations can be decreased to less than 0.1 °C. This is attributed to the reduced vibration of the melt surface due to the suppression of thermal convection. Since a magnetic field suppresses thermal convection, the temperature depth profile in the melt is significantly affected by applying a magnetic field. It has been known that the horizontal and vertical magnetic fields influence temperature profiles differently. The radial temperature gradient and the average melt temperature increase with application of a vertical field, while they decrease with a horizontal magnetic field. It has been observed that HMCZ silicon can be grown at a rate about twice the usual rate at zero magnetic field, which is attributed to the larger temperature gradients in a growing crystal and smaller temperature gradients in the melt. The value of

HMCZ silicon lies in its high quality and controlled oxygen concentration over a wide range. Experimental results have suggested that a horizontal magnetic field is effective in reducing growth striations, particularly nonrotational striations. The oxygen concentration in silicon can be controlled in the range of 5–25 ppm by HMCZ method (Hoshi et al. 1985).

CZ silicon crystal growth in the presence of an axially symmetric cusp magnetic field was reported for the first time by Hirata and Hoshikawa (1989). The free surface of the melt is centered between two superconducting coils. In this way, the oxygen concentration was successfully controlled from  $1.0 \times 10^{18}$  to  $2.0 \times 10^{17}$  atoms/cm<sup>3</sup>, while keeping the crystal rotation rate at 30 rpm and crucible rotation rate at –10 rpm. Both the oxygen and dopant concentrations were homogenized by the presence of the magnetic field. The controllability of oxygen concentration is due to the advantageous characteristics of the cusp magnetic field to realize localized control of thermal convection at the melt–crucible interface, independent of that at the melt free surface. Good crystal homogeneity results because there is no need to change the crystal and crucible rotations adequately to control the oxygen concentration, in contrast to the previous use of a transverse or vertical magnetic field in which extreme changes in the crucible or crystal rotation rate are required.

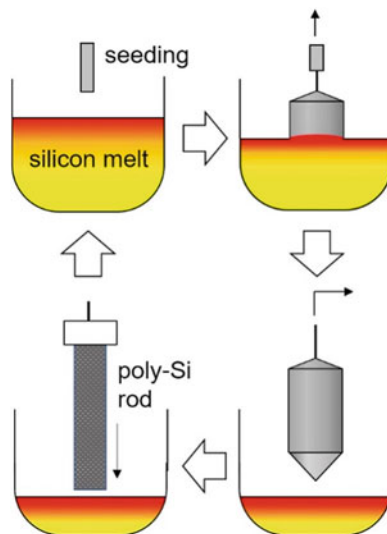
The MCZ technology can achieve the possibility of a high pulling rate and easy control of oxygen transfer, but it has some disadvantages, such as an inconvenient apparatus and its limitation on process variability.

## Continuous Growth

Several schemes have been proposed to make the CZ growth process continuous and keep the silicon melt height constant by continuously recharging the melt externally. In such processes, the buoyancy effects can be reduced significantly by maintaining a shallow layer of the melt region. By keeping the melt height fixed, many kinds of inhomogeneities, unsteady kinetics, and instabilities can be suppressed. The oxygen impurity will also be decreased, since the wetted surface area will remain at a constant location. By continuously charging the melt, the crystal quality can be tightly controlled; the dopants can be added continuously to the desired concentration levels.

The conventional CZ crystal growth has the following pitfalls: (a) It consumes one quartz crucible per run since the crucible cracks during cooling off the furnace for crystal harvesting, (b) it produces crystals with a large difference in doping concentration between the seed and tang ends of ingots, and (c) it requires a long machine idle time to dismantle and set-up of furnace for each crystal growth run. These pitfalls can be reduced or eliminated if the crystal growth is converted to a semi-continuous or continuous process. These new processes are particularly appealing to the photovoltaic industry. It requires low cost silicon wafers for the fabrication of terrestrial solar cells. The semi-continuous process can use a conventional CZ puller. However, a gate valve is required between the growth and harvesting

**Fig. 16** Operation outline of multiple CZ silicon crystal growth



chambers. Figure 16 schematically shows the operational procedure for multiple CZ silicon crystal growth. The growth of the first ingot by this process is identical to that by the batch process. After the grown ingot is separated from the melt and raised to the harvest chamber, the melt should be kept molten and the gate valve is closed. The crystal is then removed from the puller and is replaced with a polysilicon charge. After a few minutes of purging, the gate valve can be open and the re-charged polysilicon is loaded into the crucible. After the recharging of the crucible with the polysilicon, the growth of the second ingot can be initiated. The process can continue to alternate growth and recharging for several times from a single crucible without cooling the furnace. Another recharge system was developed which transforms standard CZ growth into a semi-continuous process. Now when the charge is depleted, the crucible can be refilled in situ as the grown ingot is being removed from the furnace. The continuous growth process of CZ silicon crystal has many advantages, such as significant cost reduction, increased yield, increased throughput, reduced energy consumption, improved process capability, reduced material handling requirements, and reduced labor. The recharge system also enables the use of granular silicon, which requires less than 30% of the energy required when manufacturing silicon-starting materials.

Several methods have been developed for the recharging of the polysilicon. Lane and Kachare used a long polysilicon rod which was about a one-half section of the U-shaped polysilicon rod harvested from a Siemens reactor (Lane and Kachare 1980). The polysilicon rod is attached to the recharging mechanism which they are added to the puller. The recharging mechanism was incorporated with a weighting device so that the amount of each recharging from this rod could be controlled. Helda et al. (1985) used a charge container to hold the preweighed polysilicon cylinders. The dopant can be placed between two poly cylinders for

addition into the melt. The bottom of the container consists of heat deformable support members. At low temperatures, the support members rigidly hold the polysilicon cylinders in the container. When the container is lowered to about 1–2 inches above the melt, the heat of the furnace and the weight of the polysilicon force the support member to deform. This opens the bottom of the container and allows the polysilicon to descend into the crucible. During the melting of the polysilicon, the container is gradually withdrawn from the furnace and removed from the puller. One concern about the recharging technique is increase of impurity concentration in the melts with the number of recharging. The impurity concentrations can be calculated by the repeated application of Eq. (9). At the beginning of the  $n$ th pull, the concentration of impurity in the melt  $[C]_L^n$  can be expressed as

$$\begin{aligned} [C]_L^n &= [C]_0 P^{n-1} + [C]_0 g (P^{n-2} + P^{n-3} + \dots + 1) \\ &= [C]_0 \{ P^{n-1} + g [(P^{n-1} - 1)/(P - 1)] \} \end{aligned} \quad (11)$$

where  $P = (1 - g)^{k_0}$ . If  $k_0 \ll 1$ , then  $P \approx 1$  and Eq. (9) can be approximated by,

$$[C]_L^n = [C]_0 [1 + ng(1 - g)] \quad (12)$$

Thus, this impurity buildup in the residual melt may limit multiple growth of high-quality CZ crystals.

Continuous Czochralski growth of silicon crystals has been developed by Lorenzini et al. (1977). The puller that they used is schematically shown in Fig. 17. This continuous crystal puller consists of two separated furnaces connected by a continuous liquid feed quartz tube. One furnace is for crystal pulling and the other for the melting of polysilicon. The silicon melt is transferred by siphon action. The crucible in the growth chamber contains a quartz baffle which dampens the melt vibration caused by the melt feeding. The melt is fed at such a rate that a constant melt level in the growth chamber is maintained. One advantage of this method is the uniform impurity distribution in the axial direction of the grown crystals. Drawbacks

**Fig. 17** Continuous liquid-seed CZ silicon growth furnace

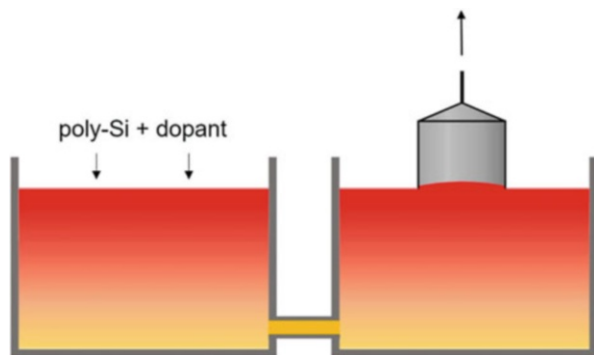
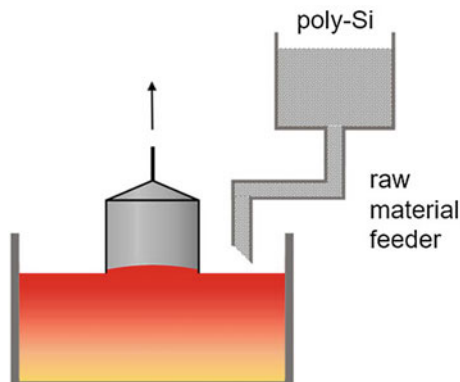


**Fig. 18** Continuous solid-feed CZ silicon growth furnace



of the continuous growth process are the complexities in equipment and processing. The major process problems are the transfer of the melt from one chamber to another and the control of equality between the feed and pull rates. A continuous solid feed system is shown in Fig. 18. This system consists basically of a hopper for storing the polysilicon raw materials and a vibratory feeder that transfers polysilicon chunks to the crucible. In the crucible that contains the silicon melt, a quartz baffle may be required in order to prevent melt turbulence, caused by feeding solid chunks, around the growth interface.

## Square Ingot Growth

Two approaches have been used to grow square silicon ingots from a CZ silicon puller. One approach is to enhance the formation of natural crystal habits. This requires a melt with an extremely good radial symmetry and stable temperatures. Under these conditions, the fast growth portions (or directions) of the ingot will not be melted back during the crystal rotation and the ingot will maintain a natural crystal habit. Kuroda et al. (1980) have demonstrated the growth of  $[100]$  square ingots. Continuous seed and crucible rotations both at 10 rpm were applied in opposite directions. The temperature fluctuation at a given point was kept below  $22\text{ }^{\circ}\text{C}$ . They have found that a square ingot was obtained when the temperature variations along a circular contour in the melt were less than  $2\text{ }^{\circ}\text{C}$  and that a circular ingot was grown when the variations were  $10\text{--}15\text{ }^{\circ}\text{C}$ . The square ingots exhibited such a crystal habit that the diagonals of the square were along  $\langle 100 \rangle$  directions and four edges of the square were perpendicular to  $\langle 110 \rangle$ . They have been able to maintain square cross-sections throughout the length of the ingots. Resistivity measurements on the wafers showed that the iso-resistivity contours were parallel to the edges of the wafers.

Another approach is to shape the temperature profile of the melt into a square configuration. Liaw (1980) used a thermal insulation plate suspended above the melt surface. The gap between the melt and the plate was approximately 2 cm or less. The

**Fig. 19** The cross-section of square silicon ingots



center of the plate was cut in a square opening. A single crystal seed was dipped into the center of melt surface through this opening. During the crown portion of the crystal growth, a high supercooling was applied to the melt. The high supercooling forces the crystal to grow faster in  $\langle 110 \rangle$  direction than in  $\langle 100 \rangle$ . Thus, the crystal crown will grow into a square with diagonals in  $\langle 110 \rangle$  and edges in  $\langle 100 \rangle$ . Once the size of the crystal crown was approaching that of the opening, the crystal rotation was paused in such a way that the four edges of the crystal crown were parallel to the four sides of the opening. Then the crystal was pulled with a discontinuous rotation during the growth of main crystal body. Each rotation applied a  $90^\circ$  turn of the crystal. The purpose of pause rotation was to keep the ingot growing straight since the temperature of the melt was not perfectly symmetrical with respect to the pull axis. The time interval between each rotation was determined by the symmetry of the melt. The poorer symmetry in the melt, the shorter the pause time was needed between each rotation and the less square would be in the ingot. Figure 19 shows the cross-section of square ingots grown by this technique.

---

## Germanium-Doped CZ Silicon Crystal Growth

### Germanium Doping Method

The doping of Ge in silicon is based on the addition of either high purity Ge raw material or the high purity SiGe alloy. High purity Ge-containing dopants are very easy to fabricate, and they are not required to have uniform and small size.



Ge-containing solid source cannot be powder-like because Ge or SiGe alloy is very easily oxidized. According to the SiGe binary phase diagram, Ge has unlimited solubility in silicon melt and a melting point lower than Si. In this sense, if high purity Ge is applied as the doping source, it will completely melt when silicon raw materials are all solid, and after the complete transformation from solid silicon to molten Si, Ge can completely dissolve in silicon solvent, where there will be few small un-molten Ge particles that may cause imperfection of silicon lattices. As for SiGe, the melting mechanism is the same as for pure Ge so that it should play the same role in the crystal growth process of Ge particle-doped CZ (GCZ) silicon.

## Germanium Property in Silicon

Ge, as one of the isovalent elements with silicon, usually occupies substitutional sites in the silicon lattice. Due to its larger radius, Ge can cause a volume expansion ( $\Delta V/V_{\text{Si}}$ ) of ~4%. It is completely miscible with silicon to form GeSi alloy with any ratio. Since Ge atoms form bonds with silicon atoms in the lattice, they can cause an absorption band of  $710 \text{ cm}^{-1}$  in the infrared absorption spectrum at room temperature (Niu et al. 2004). The Ge concentrations in CZ silicon can be calculated by the following formula,

$$[\text{Ge}] = k \times 10^{20} \alpha_{\text{max}} W_{1/2} (\text{/cm}^3) \quad (13)$$

where  $k = 1.211$  is the conversion factor,  $\alpha_{\text{max}}$  the absorption coefficient, and  $W_{1/2}$  the band width of half maximum (BWHM).

The segregation of Ge in silicon has been investigated for many years, but the results are not consistent because of different calculating methods. Trumbore firstly reported that the segregation coefficient of Ge is 0.33 (Thurmond et al. 1956), obtained from crystal pulling experiments and an analysis of the Ge–Si phase diagram. However, the evaluation of Ge concentrations in the silicon melt was difficult in their experiment, which could cause a big error in the value of the segregation coefficient. Later on, Rea et al. acquired an effective segregation coefficient of 0.68 by designing an experiment to avoid this error (Rea et al. 1987). Zhang et al. further clarified that the effective segregation coefficient of Ge in silicon is 0.69 and the equilibrium segregation coefficient is 0.63 (Zhang et al. 1996). The Ge equilibrium segregation coefficient has been modified into 0.62 by Niu et al. (2004). Recently the research group in Zhejiang University has grown a series of GCZ silicon crystals with the Ge concentrations ranging from  $10^{16}$  to  $10^{20}/\text{cm}^3$ . Based on both the experimental results and theoretical calculations, they obtained an effective segregation coefficient of 0.56 for the Ge in silicon, and the equilibrium segregation coefficient should be 0.5 (Wang et al. 2011). Nevertheless, even though the accurate segregation coefficient of Ge is still controversial, it is no doubt that this value must be smaller than 1.0. Thus, the Ge concentration increases along the CZ silicon crystal axis from seed-end to tail-end.

The Ge diffusion in silicon was first investigated by radioactive tracer experiments, in which the isotope  $^{71}\text{Ge}$  with a half-life of 11 days was utilized. Petrov et al. (1957) acquired the diffusion coefficient of Ge in the temperature range of 1,150–1,350 °C as follows:

$$D = 6.26 \times 10^5 \exp\left(-\frac{5.28\text{eV}}{kT}\right) \text{ (cm}^2/\text{s)} \quad (14)$$

However, Mcvay and Ducharme (1973) reported a different result by the same method as shown below,

$$D = 1.54 \times 10^3 \exp\left(-\frac{4.7 \pm 0.2\text{eV}}{kT}\right) \text{ (cm}^2/\text{s)} \quad (15)$$

By combining the SIMS measurements and the fitting of the Ge diffusion profiles with a complementary error function, Ogino et al. obtained the Ge diffusion coefficient as follows (Ogino et al. 1982):

$$D = 7.55 \times 10^3 \exp\left(-\frac{5.08\text{eV}}{kT}\right) \text{ (cm}^2/\text{s)} \quad (16)$$

Later on, Pichler (2004) claimed that the Ge diffusion coefficient in silicon should be expressed as,

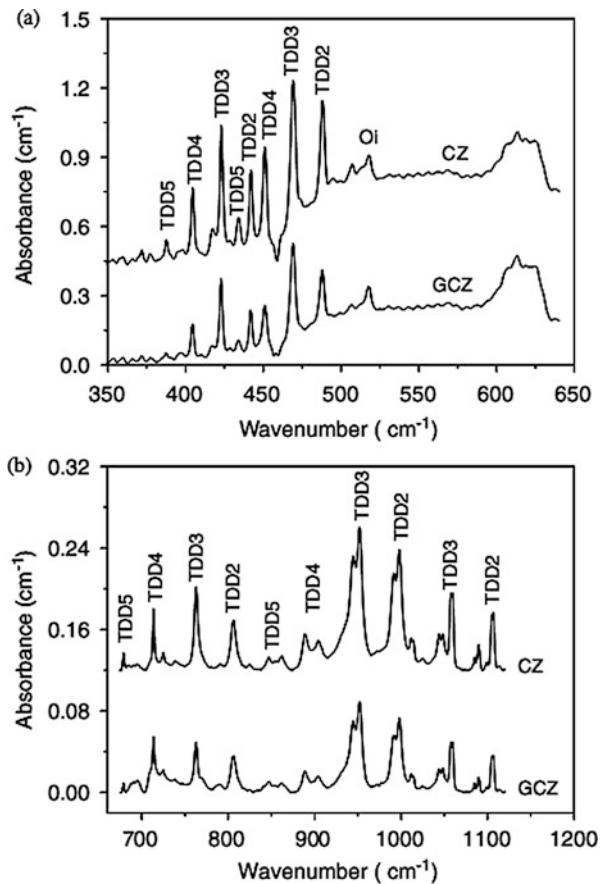
$$D = 1.72 \times 10^3 \exp\left(-\frac{4.830\text{eV}}{kT}\right) \text{ (cm}^2/\text{s)} \quad (17)$$

Hettich and Mehrer (1978) have investigated the behaviors of Ge diffusion in an extended temperature range. They reported a non-Arrhenius behavior of Ge diffusivity with a kink at the temperature of 1,050 °C. Therefore, the characteristics of Ge diffusion in silicon could be separated into regimes, i.e., a high-temperature regime (1,100–1,300 °C) with the activation energy of 5.3 eV and a low-temperature regime (850–1,000 °C) with the significantly lower activation energy of 4.1 eV. This kink point has been attributed to the evolution in the mechanism of Ge diffusion at different temperature ranges. The impurity diffusion in silicon is generally based on either interstitial or vacancy mechanisms. The temperature dependence of Ge diffusion in silicon is related to a change from an interstitial mechanism at high temperatures to a vacancy mechanism at low temperatures. Fahey et al. (1989) investigated the effect of vacancy and interstitial injection on the Ge diffusion in silicon. They estimated that under the 1,050 °C equilibrium conditions, 30–40% Ge atoms diffuse by an interstitial-assisted mechanism and the other 60–70% by a vacancy mechanism if assuming vacancy-interstitial interchange to take place by a kick-out reaction.

## Suppression of Ge Doping on Thermal Donors

Oxygen-related TDs are electrically active microdefects in CZ silicon. They are usually generated in the temperature range of 350–500 °C, with the energy levels close to the conduction band edge. It has been reported that the TD formation is retarded in oxygen-rich SiGe alloy with more than 1% Ge content (Hild et al. 1998). In GCZ silicon, the Ge concentration is usually below  $10^{20} \text{ cm}^{-3}$ , much lower than that in the SiGe alloy. In this case, however, the Ge-doping still suppresses the formation of TDs in CZ silicon. Li et al. (2004) found that the generation rate of TDs in the CZ silicon co-doped with  $10^{18} \text{ cm}^{-3}$  Ge atoms was much smaller than that in the conventional CZ silicon during the annealing at 450 °C. Low temperature far- and medium-IR spectra as shown in Fig. 20 indicate that although the Ge doping suppresses the formation of TDs, it does not change the wavenumbers of the TD-related absorption bands. This result implies that the Ge doping does not affect the configuration of TDs (Cui et al. 2006). The retardation effect of Ge on TDs has

**Fig. 20** Low temperature far- and medium-IR spectra in CZ and GCZ silicon (Reprinted with pending permission, Cui et al. 2006)



been tentatively explained in terms of interactions between Ge atoms with vacancies and oxygen atoms. The Ge doping introduces compressive stress into silicon matrix, which can be relieved by attraction of vacancies. The consequent Ge–V complexes can further combine with oxygen atoms during the TD formation annealing. Therefore, the number of oxygen atoms available for TDs is decreased, thus leading to the retarded TD formation.

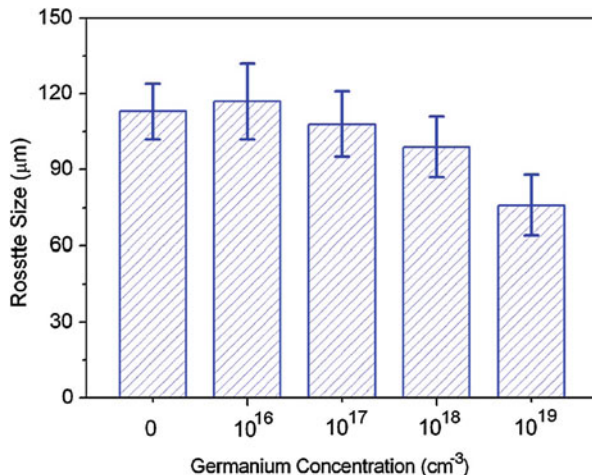
## Enhancement of Ge Doping on Silicon Mechanical Strength

The mechanical properties of CZ silicon wafers are crucial for ensuring manufacturing yield of ICs and solar cells. Silicon is a brittle material at room temperature, thus being susceptible to breakage or fracture during device manufacturing due to either localized stress at sharp contacts during handling, chemical–mechanical polishing, back–face grinding and dicing, or global stress during robot handling, down force during chemical mechanical polishing, etc. (Cook 2006). Silicon turns into a ductile material when annealed at temperatures beyond the brittle–ductile transition (BDT) point (Hirsch et al. 1989). In this case, the mechanical properties of silicon are dictated by dislocation generation and motion. The stress in the silicon wafer generated at high temperatures may result in warpage, which is detrimental for alignment in the lithography process, and even worse, may lead to slip lines which are the disastrous killer of device manufacturing yield. In a word, the mechanical properties of silicon at room and elevated temperatures are of great importance for crystal cutting and device manufacturing. For CZ silicon, the primary impurity of oxygen exerts significant effects on the mechanical properties. Moreover, it has been verified that Ge doping also affects the mechanical properties of CZ silicon in different manners.

The mechanical behavior of GCZ silicon has also been investigated by nano-indentation (Zeng et al. 2011). The GCZ silicon with a Ge concentration of  $8 \times 10^{19} \text{ cm}^{-3}$  shows a stiffer mechanical behavior under contact loading with sharper slopes for both loading and unloading segments, smaller maximum indentation depth and smaller residual indentation depth. It is derived from nano-indentation experiments that GCZ silicon has higher Young's modulus and hardness of than ordinary CZ silicon. The improvement in the elastic module of GCZ silicon is supposed to be caused by the promotion effect of Ge doping on metallic phase transformation (Si-I to Si-II phase) during the indentation, which has been confirmed by micro-Raman spectroscopy measurements (Xu et al. 2011).

High concentration Ge doping can also suppress dislocation generation in silicon. Generally, a so-called Dash necking process is necessary in CZ silicon crystal growth in order to grow a dislocation-free silicon ingot. However, using an appropriately Ge doped silicon seed, dislocation-free GCZ silicon can be grown successfully without the Dash necking process. The generation of dislocations due to thermal shock was found to be suppressed in a seed with a cross-section of  $7 \times 7 \text{ mm}^2$  when the doped Ge concentration exceeded  $9 \times 10^{19} \text{ cm}^{-3}$  (Taishi et al. 2002). Heavy Ge and boron co-doping (e.g. [Ge]:  $4 \times 10^{19} \text{ cm}^{-3}$ , [B]:

**Fig. 21** Rosette sizes in the CZ silicon wafer and the GCZ silicon wafers with different Ge concentrations subjected to 1,100 °C/2 h annealing after the 200 g indentation



$9 \times 10^{18} \text{ cm}^{-3}$ ) in silicon can also suppress dislocation generation significantly due to the increase of critical resolved shear stress for dislocation generation (Yonenaga et al. 2005). Moreover, the  $\text{Si}_{1-x}\text{Ge}_x$  alloy also shows higher yield strength than pure silicon due to higher concentration of Ge in silicon, and the yield strength of the alloy increases with increasing Ge concentrations in the region  $0 < x < 0.1$  (Yonenaga et al. 2005).

Ge doping can also retard dislocation motion in silicon. The sizes of dislocation-motion-induced rosettes in Ge doped CZ silicon are smaller than those in conventional CZ silicon (Fukuda and Ohsawa 1992). Moreover, the rosette size decreases with increasing Ge concentrations, as shown in Fig. 21. The influence of Ge doping on dislocation moving velocity depends on the doping concentrations. The dislocation velocity is not significantly reduced in the GCZ silicon with the Ge concentrations between  $10^{19}$  and  $10^{20} \text{ cm}^{-3}$ , compared to that in Ge-free CZ silicon (Yonenaga et al. 2005). With a higher Ge concentration, such as 2.2% ( $\sim 1.1 \times 10^{21} \text{ cm}^{-3}$ ) and 5.4% ( $2.7 \times 10^{21} \text{ cm}^{-3}$ ), the dislocation movement can be obviously lower than that in conventional CZ silicon (Yonenaga 1999).

As a substitutional impurity in silicon, Ge cannot lock dislocations as strongly as oxygen. The interaction energy between Ge atoms and dislocations is  $0.34 \text{ eV}/\text{\AA}$ , much lower than those for oxygen ( $1.80 \text{ eV}/\text{\AA}$ ). Moreover, the diffusion coefficient of Ge in silicon is several orders of magnitude lower than that of oxygen. Therefore, the dislocation locking by Ge can be ignored when oxygen is present in silicon even if the Ge concentration is one to two orders of magnitude higher than the typical oxygen concentration in CZ silicon ( $\sim 10^{18} \text{ cm}^{-3}$ ). In addition to the direct interaction with dislocations, Ge can affect dislocation locking indirectly by influencing oxygen diffusion. It is found that the dislocation unlocking stress in Ge-doped CZ silicon ([Ge]:  $8 \times 10^{19} \text{ cm}^{-3}$ ) is lower than that in conventional CZ silicon. The strain introduced by Ge doping may retard oxygen diffusion in silicon, resulting in a lower unlocking stress (Zeng et al. 2011). Moreover, the enhancement of tiny

oxygen precipitates in GCZ silicon also plays an important role in the locking effect of dislocation movement.

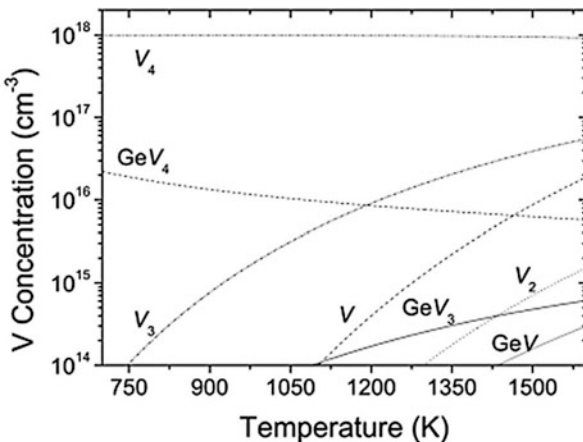
## Anti-irradiation Effect of Ge-Doped CZ Silicon Crystal

Radiation-induced defects in GCZ silicon have been widely studied and it is found that Ge atoms tend to interact with vacancies to form Ge–V centers (Khirunen et al. 2003). The Ge–V pair in CZ silicon has been studied by electron paramagnetic resonance (EPR) (Watkins 1969), IR (Brelot and Charlemagne 1971) and deep level transient spectroscopy (DLTS) (Budtz-Jørgensen et al. 1998) techniques. The EPR measurements show the spectrum of a vacancy in GCZ silicon is roughly similar to that of an isolated vacancy (V) except in the hyperfine structure with several satellites (Watkins 1969). Vacancies are trapped next to substitutional Ge. By selective illumination, charge states can be generated. The electronic structures of  $\text{GeV}^+$  and  $\text{GeV}^-$  were found to be slightly perturbed from that for  $\text{V}^+$  and  $\text{V}^-$  in silicon crystal, and their distortions and level positions appear very similar to those for the isolated vacancy.

The binding energy of Ge–V is about  $\sim 0.27$  eV (Chroneos et al. 2009). The equilibrium concentration of vacancies in GCZ silicon with irradiation is significantly higher than that in conventional CZ silicon (Vanhellemont et al. 2010). The vacancies can be released from Ge atoms in the irradiated silicon by annealing (Brelot and Charlemagne 1971; Budtz-Jørgensen et al. 1998; Vanhellemont et al. 2010). Watkins (1975) reported that the consequent release of vacancies could be observed as a growth in the  $12 \mu\text{m}$  band when the vacancies in turn were trapped by oxygen atoms to form O–V (A-centers). Brelot et al. (1971) also studied the stability of Ge–V in *n*-type silicon containing  $3 \times 10^{20}$  Ge atoms/cm<sup>3</sup> by IR technique. There was no  $12 \mu\text{m}$  absorption line related to V–O after a 90 K electron irradiation. The A-centers appear only after annealing between 200 and 280 K. This means that the Ge acts as an efficient trap for vacancies at low temperatures, and the trapped vacancies can be released from the Ge–V centers by thermal activation in the range of 200–280 K. The electrical levels of Ge–V pairs in GCZ silicon have not been directly measured. The dangling bond reconstructions reveal an only slightly perturbed vacancy, and its general behavior vs. electrical properties, such as Fermi level, optical excitation, appears identical to that of the isolated vacancy (George 2000). The DLTS results of the *n*-type Ge–Si alloy after electron radiation (Budtz-Jørgensen et al. 1998) show that the energy level of Ge–V complexes is about  $E_c - 0.29$  eV, with a capture cross section of  $5 \times 10^{-16}$  cm<sup>2</sup> for electrons.

Chroneos et al. found that the total energy of the configurations for the multi-vacancies involved GCZ silicon super-cells would follow the bond-length-related rules by first principles simulation. Vacancies tend to bind with Ge atoms and relax the local lattice deformation stresses in silicon. Therefore, it seems that Ge atoms in CZ silicon crystals act as nuclei sites for Ge–V pairs. In this way, it is therefore proposed that the vacancy could transfer to the surroundings of the generated Ge–V

**Fig. 22** The temperature dependence of the concentration of  $V_n$  clusters in comparison to the concentration of  $GeV_n$  clusters for a Ge concentration of  $10^{19} \text{ cm}^{-3}$ , an initial V supersaturation of  $10^{18} \text{ cm}^{-3}$  (Reprinted with pending permission, Chroneos et al. 2009)



pairs with a probable routing of  $Ge \rightarrow GeV \rightarrow GeV_2 \rightarrow GeV_3 \rightarrow GeV_m$  ( $m = 4, 5, 6, \dots$ ) transformation. Using the law of mass action, the relative concentrations of defect clusters can be expressed as follows,

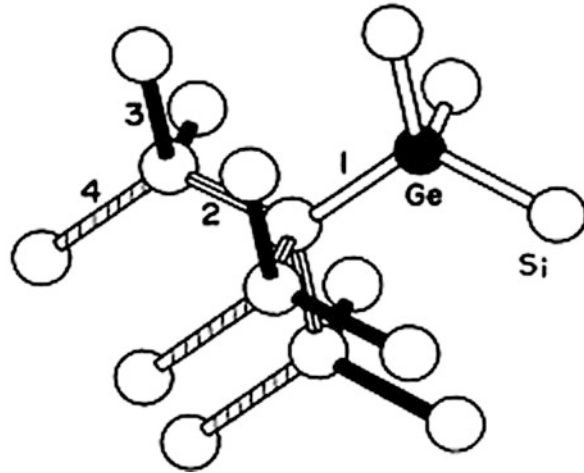
$$[Ge_m V_n] / [Ge]^m [V]^n = \exp(-E_b / k_B T) \quad (18)$$

where  $E_b$  is the binding energy of the clusters,  $[Ge_m V_n]$  the concentration of a  $Ge_m V_n$  cluster,  $[Ge]$  the concentration of unbound Ge atoms,  $[V]$  the concentration of unbound V,  $k_B$  Boltzmann's constant, and  $T$  the temperature. Figure 22 shows the variation of the concentration of  $GeV_n$  clusters and  $V_n$  clusters with temperatures (Chroneos and Londos 2010). It can be seen that  $[GeV_n]$  is lower than  $[V_n]$  at the whole temperature range. The binding energies of  $GeV_n$  clusters are higher than that of  $V_n$  clusters by a value of 0.35 eV. It indicates that Ge cannot act as a site to trap a significant proportion of vacancies.

Interstitial oxygen atoms can also be captured by Ge atoms to form stable Ge–O complexes, but the oxygen atom should be located at the third-nearest-neighbor site to the Ge atom (Chroneos and Londos 2010). The interstitial oxygen occupies the bridging position between two silicon atoms, forming the  $Si_2O$  molecule, which causes IR absorption bands at 30, 1,100, and 1,200  $\text{cm}^{-1}$ , and which benefit different local vibration modes (LVMS) of  $Si_2O$  quasi-molecule (Yang and Chen 2005). In heavily doped GCZ silicon, the oscillator strength of the 1,200  $\text{cm}^{-1}$  band absorption and the peak separations between the 1,100  $\text{cm}^{-1}$  band absorptions are largely reduced, which are attributed to the perturbation of Si–O–Si centers by the nearby Ge atoms. Furthermore, three additional low-frequency IR absorption lines located at 1,130, 1,127, and 1,184  $\text{cm}^{-1}$  are detected in GCZ silicon with a Ge concentration of  $2 \times 10^{20} \text{ cm}^{-3}$  (Khirunen et al. 1999). The shifted positions of other bands are ascribed to the weakened harmonic coupling between the rotational and asymmetric vibration modes of the Si–O–Si molecule (Khirunen et al. 1999). For higher values of the Ge content, a broad, low-frequency band is found (Humlíček et al.



**Fig. 23** Part of the silicon crystal lattice around a substitutional Ge atom, showing the first-, second-, third-, and fourth-neighbor bonds to the Ge atom (Reprinted with pending permission, Khirunen et al. 2001)



2006), attributed to the vibrations of the  $\text{Si}_2\text{O}$  units with several nearest-neighbor lattice sites occupied by Ge atoms. The observed absorption bands can be described as the vibration of interstitial oxygen disturbed by Ge atoms located in the nearest second, third, and fourth coordination spheres relative to an oxygen atom (Khirunen et al. 2001), seeing Fig. 23.

Theoretical calculations also demonstrate the stability and the configurations of different possible Ge–O complexes in CZ silicon (Chroneos and Lontos 2010). The oxygen atom is preferable to stay away from the Ge atom and most likely to form  $\text{Si}_2\text{O}$  molecules. However, these molecules may have Ge atoms in their neighborhood. This is supported by the much lower formation enthalpy ( $-910.7$  kJ/mol) of  $\text{SiO}_2$  ( $\alpha$ -quartz), than that ( $-580.0$  kJ/mol) of  $\text{GeO}_2$  (rutile) (Markevich et al. 2004). But it is possible to form Si–O–Ge molecules (Hao et al. 2004). Note that the effect of the Ge atoms on the geometry and vibration properties of the  $\text{Si}_2\text{O}$  molecules is not significant.

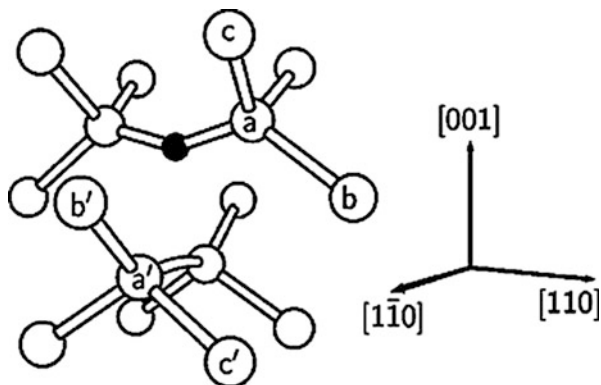
In order to relieve the lattice stress, Ge atoms incline to react with vacancies and interstitial oxygen to form related complexes (Yang and Chen 2005). VO defects containing a core Ge atom (one of the neighbors or next neighbors of the vacancy) are referred as GeVO complexes (Lontos et al. 2009). The following equation illustrates the formation of GeVO by the VO defect diffusing toward Ge (Yang and Chen 2005),



The structure of VO in the  $\text{Si}_{1-x}\text{Ge}_x$  crystals has been studied by DLTS and *ab initio* modeling. Figure 24 shows the considered structures of the GeVO complex. The formation energy of GeVO at sites of  $b$ ,  $a'$ , and  $b'$  are 0.07, 0.19, and 0.09 eV, respectively, by *ab initio* modeling (Markevich et al. 2004). The binding energy of the deeper GeVO complex is found to be about 0.18 eV from the DLTS studies.



**Fig. 24** The VO–Ge complex considered here results from substituting first- or second-neighboring silicon atoms by Ge. These structures are labeled with letters from  $a$  to  $c$  and  $a'$  to  $c'$  (Reprinted with pending permission, Markevich et al. 2004)



From the FTIR measurements, it is known that the  $839.2\text{ cm}^{-1}$  band grows at the expense of the  $834.6\text{ cm}^{-1}$  band, both of them lying above the main band of VO at  $830\text{ cm}^{-1}$  (Markevich et al. 2004). Therefore, the  $839.2\text{ cm}^{-1}$  band to VO–Ge<sub>a</sub> and the  $834.6\text{ cm}^{-1}$  band are assigned to VO–Ge<sub>b</sub> and/or VO–Ge<sub>c</sub> defect forms. This assignment is also supported by the relative defect stability and respective electric levels. Most of stable GeVO complexes produce an acceptor state very close to that of VO, but VO–Ge<sub>a</sub> has a deeper level, i.e., 20 meV deeper than VO (2/0). The acceptor state of GeVO is more localized than that of VO. Markevich et al. found from the DLTS studies at least three configurations of VO centers with distinct levels and the energy level shifted upward from the level of the dominant configuration in as-irradiated GCZ Si material. On isochronal annealing in the temperature range of 200–300 °C, the dominant VO defect transforms into another one whose level is about 25 meV deeper (Markevich et al. 2004).

Ge atoms in silicon can effectively compete with oxygen in trapping vacancies (Chroneos and Londos 2010), and therefore, a gradual increase in the concentration of VO defects is observed versus Ge content (Londos et al. 2009). Taking into account a noticeable fraction of oxygen atoms with nearby Ge atoms in CZ silicon, it is believed that such defects may be more effective traps for vacancies than isolated oxygen atoms due to a larger cross-section for vacancy capture (Schmalz and Emtsev 1994). After vacancy capture by Ge, the electronic properties and thermal stability of GeVO are expected to differ from those of the A-centers, and their annealing via vacancy dissociation gives rise to A-center formation (Schmalz and Emtsev 1994).

### LID Effect of Ge-Doped CZ Silicon Crystal

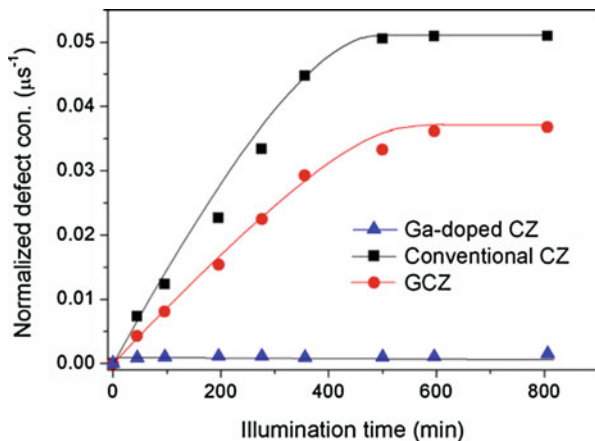
It is well known that the LID effect of CZ silicon solar cells is related to the boron and oxygen impurities. However, the exact form of boron and oxygen existing in the

defects has kept as a puzzle for a long time. Voronkov and Falster (2010) have proposed a new  $B_iO_{2i}$  model for the structure of B–O defects, in which the  $O_{2i}$  is not mobile at room temperature, but bound with an interstitial boron atom. However, the density functional theory calculation has clarified that the most stable configuration of  $B_iO_{2i}$  keeps constant in various charge states, in which the  $B_i$ , one  $O_i$ , and two Si atoms form a four membered ring in the  $\{101\}$  plane (Chen et al. 2013). The result is apparently against the formation mechanism of the  $B_iO_{2i}$  complex.

The  $B_sO_{2i}$  model is more acceptable for most researchers, which is composed of a substitutional boron atom ( $B_s$ ) and an interstitial oxygen dimer ( $O_{2i}$ ). However, Murin et al. (2011) reported that they found no clue of the existence of the doubly positively charged oxygen dimer ( $O_{2i}^{++}$ ) and doubted whether the  $O_{2i}$  can play the central role in the formation of B–O complexes. By choosing a series of samples with different oxygen concentrations, Chen et al. (2013) have investigated the correlation of B–O complexes with the  $O_{2i}$  in silicon. It is found that the LID defect concentration and the stagger type  $[O_{2i}]$  in CZ silicon have the similar dependence on the annealing temperatures, with quite close binding energies, meaning that the LID defect concentration is proportional to the concentration of stagger type  $O_{2i}$ . Moreover, even though the value of  $[O_{2i}^{st}]/[O_i]^2$  is influenced by the oxygen content level, the proportionality between the LID defect concentration and  $[O_{2i}^{st}]$  is still established. These finding suggests that the  $O_{2i}^{st}$  is one ingredient of B–O complexes. Hence, the method of reducing the  $[O_{2i}^{st}]$  should be effective to suppress the generation of B–O complexes.

Ge doping in CZ silicon is a strategy of suppressing the B–O defects (Yu et al. 2010). Figure 25 shows the evolution of the normalized B–O defect concentrations under one sun illumination at 50 °C for the conventional CZ silicon and GCZ silicon containing a Ge concentration of  $8 \times 10^{19}/\text{cm}^3$  as well as the referenced Ga-doped sample. Note that the concentration of B–O defects keeps almost zero for the referenced sample during the illumination, indicating that the wafer surface passivation is quite stable under illumination, and meanwhile no carrier lifetime degradation takes place in the bulk. For both the conventional CZ and GCZ samples, the

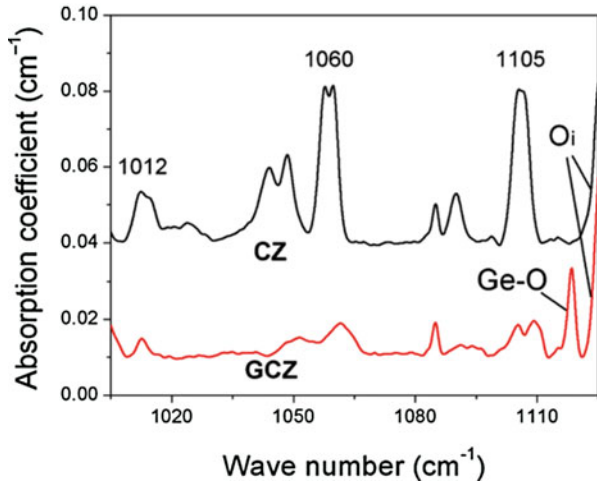
**Fig. 25** The normalized concentration of B–O defects as a function of illumination time at 50 °C for the conventional CZ silicon and the GCZ silicon containing the Ge concentration of  $8 \times 10^{19}/\text{cm}^3$  as well as the referenced Ga-doped CZ silicon (Reprinted with pending permission, Yu et al. 2010)



B–O defect concentration increases with an increase in illumination time and then reaches a stable value in hundreds of minutes. More importantly, one can see that the saturated concentration of B–O defects in the GCZ sample is obviously lower than that in the CZ silicon. Since these two samples with similar thermal history almost contain the same concentration of boron and interstitial oxygen, the present result strongly evidences that Ge doping can reduce the saturated concentration of B–O defects in CZ silicon. The study on the defect kinetics shows that the activation energies for the B–O defect generation and dissociation in the GCZ silicon are around 0.63 and 1.52 eV, respectively, both larger than those in the conventional CZ silicon. The corresponding pre-exponential factors also are enhanced by two orders of magnitude due to Ge doping. It is believed that the Ge cannot only cause a higher energy barrier for oxygen-dimer  $O_{2i}$  diffusion, due to its modulation on the crystal field in silicon lattice, but also enhance the capture cross-section of  $B_s$  for  $O_{2i}$ , as predicted by first-principle calculation. However, it should be noted that a relatively low concentration of Ge cannot effectively suppress the formation of B–O defects. When the Ge concentration is beyond  $10^{19}/\text{cm}^3$ , the reduction in B–O defects can be effectively triggered, whose percentage increases with an increase in Ge concentrations. So, a higher concentration of Ge will benefit for the suppression of the B–O defects in CZ silicon. However, it should be mentioned that Ge doping in CZ silicon with extremely high concentrations like  $10^{20}/\text{cm}^3$  could not be practically used for PV industry, since it will not only increase the cost of crystal, but also easily cause the cellular growth. Based on this consideration, Ge doping in CZ silicon with a concentration in the order of  $10^{19}/\text{cm}^3$  is more interesting for us. After fabricating hundreds of solar cells based on the conventional CZ silicon wafers and the GCZ silicon wafers containing the Ge concentration in the order of  $10^{19}/\text{cm}^3$ , an average 2% loss in efficiency can be found for the conventional CZ silicon solar cells after 2-week sun light illumination, while a smaller efficiency loss of 1.75% for the GCZ silicon solar cells. Likewise, the evolutions of power outputs of PV modules based on the conventional CZ and GCZ silicon exhibit the same trend. The power output loss of GCZ module can be saved by a value of 5%, compared to the conventional one. Based on these results, it is believed that the GCZ silicon can be practically used in PV industry for reducing the LID effect of solar cells.

The lower concentration of  $B_sO_{2i}$  in GCZ silicon might be attributed to the reduction in  $O_{2i}$  concentration due to Ge doping. Figure 26 shows the typical absorption spectra measured at 10 K of the conventional CZ silicon and GCZ silicon with a Ge concentration of  $8 \times 10^{19}/\text{cm}^3$ . One can see that three vibrational IR absorption bands associated with  $O_{2i}$  at 1,012, 1,060, and 1,105  $\text{cm}^{-1}$ , respectively, appear in the low-temperature FTIR spectra for both the samples (Murin et al. 1998). More importantly, the intensities of all these three absorption bands in the GCZ silicon are significantly lower than those in the conventional CZ silicon, suggesting that a lower concentration of  $O_{2i}$  indeed exists in the GCZ sample. The  $O_{2i}$  in CZ silicon forms from two  $O_i$  atoms based on diffusion mechanism via  $O_i + O_i \rightarrow O_{2i}$ . The concentration of  $O_{2i}$  is actually determined by the  $O_i$  concentration and the  $O_i$  diffusion energy barrier. Since our conventional CZ and GCZ silicon contain

**Fig. 26** Typical FTIR spectra measured at 10 K for the conventional CZ and GCZ silicon with a Ge concentration of  $8 \times 10^{19}/\text{cm}^3$  (Reprinted with pending permission, Yu et al. 2010)



the same concentration of  $O_i$ , the only reason for the reduction in  $O_{2i}$  in GCZ silicon is that the Ge doping increases the energy barrier of  $O_i$  diffusion. In fact, Ge, as a substitutional impurity with the atom size larger than silicon, can essentially give rise to considerable local perturbation of silicon lattice. Therefore, it is believed that Ge doping must necessarily increase the crystal fields of silicon lattice. This consequently causes a large energy barrier for  $O_i$  diffusion to form the  $O_{2i}$ . Furthermore, it is worthy to mention that an infrared absorption band associated with the local vibrational mode of Ge–O bond has also been found in GCZ silicon, which is close the signal of  $O_i$ . This indicates that the substitutional Ge atoms in silicon lattice tend to bind with  $O_i$  and form Ge–O complexes, which has been predicted by our previous experiments and first-principle theoretical calculations (Wang and Yang 2009). The binding of Ge with  $O_i$  in silicon lattice will reduce the concentration of free  $O_i$ , contributing to the formation of  $O_{2i}$ . This should also finally result in a decrease in  $O_{2i}$  concentration and therefore suppress the  $B_sO_{2i}$  defects.

## Conclusion

The CZ pulling method is the main technique used at present to grow single crystals of silicon in photovoltaic industry. Polysilicon feed is used as a raw material, and the entire charge is kept inside the quartz crucible supported by graphite. By using the graphite heater, the charge is melted at the desired temperature and dopant species are added at this stage to the silicon melt to get the desired resistivity values. When using a seed crystal, it is first allowed to touch the molten silicon and then is slowly pulled up, allowing the molten silicon to solidify according to the seed crystal. In this process, the crucible and graphite heaters become the source of oxygen and carbon contamination for the growing silicon crystal, respectively. We have reviewed recent advances in the understanding of some of the science and engineering aspects of CZ

silicon growth. A better understanding of the control mechanisms and their interactions has facilitated the development of growth processes for more uniform oxygen distribution at desired incorporation levels. We have analyzed the causes of defects in CZ crystals and discussed their effects on solar cell performances. The impurity incorporation behavior under the influence of applied magnetic field is introduced. Crystal growth from small melts and constant melt volume provided by double-crucible arrangements yields improved axial and radial uniformity. The double-crucible methodology can be extended to a generalized two-container, continuous “feed and pull” growth system with the benefit of the double crucibles. The availability of recently developed granular polysilicon simplifies the development of a crystal growth process using continuous “feed and pull.” Pseudo-square ingot growth can effectively avoid the loss that the round CZ silicon crystals are cut into pseudo-squares for the sake of solar modules. The Ge doping during crystal growth can improve the CZ silicon mechanical strength and suppress the boron–oxygen complexes. This will not only enable thinner solar cells for the reduction of cost, but also benefit for the fabrication of high efficiency solar cells with low LID effects.

In the future, the main development goals will be to improve the economy of the CZ silicon crystal production, in particular by growing longer crystals from large melts. At the same time, the quality of the crystals must be continuously improved, especially in respect to oxygen impurities and defects.

---

## References

- D.R. Bosomworth, W. Hayes, A.R.L. Spray, G.D. Watkins, Absorption of oxygen in silicon in the near and the far infrared. *Proc. R. Soc. Lond. A Math. Phys. and Eng. Sci.* **317**(1528), 133–152 (1970)
- A. BreLOT, J. Charlemagne, Infrared studies of low temperature electron irradiated silicon containing germanium oxygen and carbon. *Radiat. Eff.* **9**(1-2), 65–73 (1971)
- A. BreLOT, J. Charlemagne, *Radiat. Eff.* **9**, 65 (1971)
- C.V. Budtz-Jørgensen, P. Kringhøj, A.N. Larsen, N.V. Abrosimov, Deep-level transient spectroscopy of the Ge-vacancy pair in Ge-doped n-type silicon. *Phys. Rev. B* **58**(3), 1110 (1998)
- P. Capper, A.W. Jones, E.J. Wallhouse, J.G. Wilkes, The effects of heat treatment on dislocation-free oxygen-containing silicon crystals. *J. Appl. Phys.* **48**(4), 1646–1655 (1977)
- J.R. Carruthers, A.F. Witt, R.E. Reusser, Czochralski growth of large diameter silicon crystals – convection and segregation. *Semicond. Silicon* **3**, 61 (1977)
- S.N. Chakravarti, P.L. Garbarino, K. Murty, Oxygen precipitation effects on Si n<sup>+</sup>-p junction leakage behavior. *Appl. Phys. Lett.* **40**(7), 581–583 (1982)
- L. Chen, X. Yu, P. Chen, P. Wang, X. Gu, J. Lu, D. Yang, Effect of oxygen precipitation on the performance of Czochralski silicon solar cells. *Sol. Energy Mater. Sol. Cells* **95**(11), 3148–3151 (2011a)
- P. Chen, X. Yu, L. Chen, D. Yang, Formation of shallow junctions in gallium and phosphorus compensated silicon for cell performance improvement. *Scr. Mater.* **65**(10), 871–874 (2011b)
- P. Chen, X. Yu, X. Liu, X. Chen, Y. Wu, D. Yang, Experimental evidence of staggered oxygen dimers as a component of boron–oxygen complexes in silicon. *Appl. Phys. Lett.* **102**(8), 082107 (2013a)
- X. Chen, X. Yu, X. Zhu, P. Chen, D. Yang, First-principles study of interstitial boron and oxygen dimer complex in silicon. *Appl. Phys. Express* **6**, 041301 (2013b)

- A. Chroneos, C.A. Londos, Interaction of A-centers with isovalent impurities in silicon. *J. Appl. Phys.* **107**(9), 093518 (2010)
- A. Chroneos, R.W. Grimes, H. Bracht, Impact of germanium on vacancy clustering in germanium-doped silicon. *J. Appl. Phys.* **105**(1), 016102 (2009)
- R.F. Cook, Strength and sharp contact fracture of silicon. *J. Mater. Sci.* **41**(3), 841–872 (2006)
- C. Cui, D. Yang, X. Ma, M. Li, D. Que, Effect of light germanium doping on thermal donors in Czochralski silicon wafers. *Mater. Sci. Semicond. Process.* **9**(1), 110–113 (2006)
- M. Dhamrin, T. Saitoh, Characterization of the initial rapid decay on light-induced carrier lifetime and cell performance degradation of Czochralski-grown silicon. *Jpn. J. Appl. Phys.* **42**(5R), 2564 (2003)
- P. Fahey, S.S. Iyer, G.J. Scilla, Experimental evidence of both interstitial- and vacancy-assisted diffusion of Ge in Si. *Appl. Phys. Lett.* **54**(9), 843–845 (1989)
- T. Fukuda, A. Ohsawa, Mechanical strength of silicon crystals with oxygen and/or germanium impurities. *Appl. Phys. Lett.* **60**(10), 1184–1186 (1992)
- P. Gaworzewski, K. Schmalz, Oxygen-related donors formed at 600°C in silicon in dependence on oxygen and carbon content. *Phys. Status Solidi A* **77**(2), 571–582 (1983)
- D. W. George, *Mater. Sci. Semi. Proc.* **3**, 227 (2000)
- S. W. Glunz, S. Rein, W. Warta, J. Knobloch, W. Wettling, In Proceedings of the 2nd World Conference on Photovoltaic Solar Energy Conversion, Vienna, 1343 (1998)
- S. Hao, L. Kantorovich, G. Davies, Interstitial oxygen in Si and Si 1-x Ge x. *Phys. Rev. B* **69**(15), 155204 (2004)
- H. Hashigami, M. Dhamrin, T. Saitoh, Performance degradation of Czochralski-grown silicon solar cells by means of current injection. *Jpn. J. Appl. Phys.* **41**(11A), L1191 (2002)
- D. Helda, W. Robert, M. Liaw, Melt recharge method, U.S. Patent No. 4557795, U.S. Patent and Trademark Office, Washington, DC, 1985
- G. Hettich, H.K. Mehrer, in *Maier in Defects and Radiation Effects in Semiconductors*, ed. by J.H. Albany. Institute of Physics Conference Series, vol 46 (Institute of Physics, London, 1978), p. 500
- E. Hild, P. Gaworzewski, M. Franz, K. Pressel, Thermal donors in silicon-rich SiGe. *Appl. Phys. Lett.* **72**(11), 1362–1364 (1998)
- H. Hirata, K. Hoshikawa, Silicon crystal growth in a cusp magnetic field. *J. Cryst. Growth* **96**(4), 747–755 (1989)
- P.B. Hirsch, S.G. Roberts, J. Samuels, The brittle–ductile transition in silicon. II. Interpretation. *Proc. R. Soc. Lond. A Mat. Phys. Eng. Sci.* **421**(1860), 25–53 (1989)
- K. Hoshi, T. Suzuki, Y. Okubo, N. Isawa, Cz silicon crystal grown in transverse magnetic-fields. *J. Electrochem. Soc.* **127**(3), C113–C113 (1980)
- K. Hoshi, N. Isawa, T. Suzuki, Y. Ohkubo, Czochralski silicon crystals grown in a transverse magnetic field. *J. Electrochem. Soc.* **132**(3), 693–700 (1985)
- R. Hull, Properties of crystalline silicon, INSPEC, The institution of electrical engineers, London, United Kindom (1999)
- J. Humlíček, R. Štoudek, A. Dubroka, Infrared vibrations of interstitial oxygen in silicon-rich SiGe alloys. *Phys. B Condens. Matter* **376**, 212–215 (2006)
- J.M. Hwang, D.K. Schroder, Recombination properties of oxygen-precipitated silicon. *J. Appl. Phys.* **59**(7), 2476–2487 (1986)
- L.I. Khirunenko, Y.V. Pomezov, M.G. Sosnin, V.K. Shinkarenko, Oxygen in silicon doped with isovalent impurities. *Phys. B Condens. Matter* **273**, 317–321 (1999)
- L.I. Khirunenko, V.A. Zasuha, Y.V. Pomezov, M.G. Sosnin, Disturbance of oxygen by isovalent impurity atoms in silicon. *Phys. B Condens. Matter* **308**, 301–304 (2001)
- L.I. Khirunenko, O.O. Kobzar, Y.V. Pomezov, M.G. Sosnin, G. Weyer, Interstitial-related reactions in silicon doped with isovalent impurities. *Phys. B Condens. Matter* **340–342**, 546–550 (2003)
- E. Kuroda, S. Matsubara, T. Saitoh, Czochralski growth of square silicon single crystals. *Jpn. J. Appl. Phys.* **19**(7), L361 (1980)
- R.L. Lane, A.H. Kachare, Multiple Czochralski growth of silicon crystals from a single crucible. *J. Cryst. Growth* **50**(2), 437–444 (1980)

- H. Li, D. Yang, X. Yu, X. Ma, D. Tian, L. Li, D. Que, The effect of germanium doping on oxygen donors in Czochralski-grown silicon. *J. Phys. Condens. Matter* **16**(32), 5745 (2004)
- H.M. Liaw, Growth of single crystal silicon square ingots. *Electrochem. Soc. Meet. Extended Abstract*, **80-1**, 806–807 (1980)
- C.A. Londos, M.J. Binns, A.R. Brown, S.A. McQuaid, R.C. Newman, Effect of oxygen concentration on the kinetics of thermal donor formation in silicon at temperatures between 350 and 500°C. *Appl. Phys. Lett.* **62**(13), 1525–1526 (1993)
- C.A. Londos, A. Andrianakis, V. Emtsev, H. Ohyama, Radiation effects on the behavior of carbon and oxygen impurities and the role of Ge in Czochralski grown Si upon annealing. *J. Appl. Phys.* **105**(12), 123508 (2009)
- R.E. Lorenzini, A. Iwata, K. Lorenz, U.S. Patent No. 4,036,595, U.S. Patent and Trademark Office, Washington, DC, 1977
- D. Macdonald, F. Rougieux, A. Cuevas, B. Lim, J. Schmidt, M. Di Sabatino, L.J. Geerligs, Light-induced boron–oxygen defect generation in compensated p-type Czochralski silicon. *J. Appl. Phys.* **105**(9), 093704 (2009)
- V.P. Markevich, A.R. Peaker, J. Coutinho, R. Jones, V.J.B. Torres, S. Öberg, et al., Structure and properties of vacancy-oxygen complexes in Si 1-x Ge x alloys. *Phys. Rev. B* **69**(12), 125218 (2004)
- G.L. McVay, A.R. DuCharme, The diffusion of germanium in silicon. *J. Appl. Phys.* **44**(3), 1409–1410 (1973)
- H.J. Monkhorst, J.D. Pack, Special points for Brillouin-zone integrations. *Phys. Rev. B* **13**(12), 5188 (1976)
- L.I. Murin, T. Hallberg, V.P. Markevich, J.L. Lindström, Experimental evidence of the oxygen dimer in silicon. *Phys. Rev. Lett.* **80**(1), 93 (1998)
- L.I. Murin, E.A. Tolkacheva, V.P. Markevich, A.R. Peaker, B. Hamilton, E. Monakhov, et al., The oxygen dimer in Si: Its relationship to the light-induced degradation of Si solar cells? *Appl. Phys. Lett.* **98**(18), 182101 (2011)
- X. Niu, W. Zhang, G. Lu, Z. Jiang, Distribution of Ge in high concentration Ge-doped Czochralski-Si crystal. *J. Cryst. Growth* **267**(3), 424–428 (2004a)
- X. Niu, W. Zhang, E. Zhang, J. Sun, G. Lu, FTIR spectroscopy of high concentration Ge-doped Czochralski-Si. *J. Cryst. Growth* **263**(1), 167–170 (2004b)
- W. O'Mara, R.B. Herring, L.P. Hunt, *Handbook of Semiconductor Silicon Technology* (Crest Publishing House, Norwich, 2007)
- M. Ogino, Y. Oana, M. Watanabe, The diffusion coefficient of germanium in silicon. *Phys. Status Solidi A* **72**(2), 535–541 (1982)
- M. Ohwa, T. Higuchi, E. Toji, M. Watanabe, K. Homma, S. Takasu, Growth of large diameter silicon single crystal under horizontal or vertical magnetic field, In *Semiconductor Silicon*, The Electrochemical Society, Princeton, 117–128 (1986)
- D.W. Palmer, K. Bothe, J. Schmidt, Kinetics of the electronically stimulated formation of a boron–oxygen complex in crystalline silicon. *Phys. Rev. B* **76**(3), 035210 (2007)
- A.D. Petrov, L.L. Shchukovskaya, S.I. Sadykhzade, Y.P. Egorov, The synthesis and dehydration of unsaturated silicon containing alcohols. *Dokl. Akad. Nauk SSSR* **115**(3), 522–525 (1957)
- P. Pichler, *Intrinsic Point Defects, Impurities, and Their Diffusion in Silicon* (Springer, Wien, 2004)
- S.N. Rea, J.D. Lawrence, J.M. Anthony, Effective segregation coefficient of germanium in Czochralski silicon. *J. Electrochem. Soc.* **134**(3), 752–753 (1987)
- S. Rein, S.W. Glunz, Electronic properties of the metastable defect in boron-doped Czochralski silicon: Unambiguous determination by advanced lifetime spectroscopy. *Appl. Phys. Lett.* **82**(7), 1054–1056 (2003)
- H.J. Ruiz, G.P. Pollack, High temperature annealing behavior of oxygen in silicon. *J. Electrochem. Soc.* **125**(1), 128–130 (1978)

- W.R. Runyan, *Silicon Semiconductor Technology* (McGraw-Hill, New York, 1965)
- K. Schmalz, V.V. Emtsev, Radiation-induced defects in Czochralski-grown silicon doped with germanium. *Appl. Phys. Lett.* **65**(12), 1575–1577 (1994)
- J. Schmidt, K. Bothe, Structure and transformation of the metastable boron and oxygen-related defect center in crystalline silicon. *Phys. Rev. B* **69**(2), 024107 (2004)
- J. Schmidt, A. G. Aberle, R. Hezel, in *Proceedings of the 26th IEEE Photovoltaic Specialists Conference*, IEEE, Anaheim, 13 (1997)
- F. Shimura, *Semiconductor Silicon Crystal Technology* (Academic, San Diego, 1989), pp. 69–71
- F. Shimura, M. Kimura, Growth method and equipment of semiconductor single crystals, Japanese Patent 56-190318, 1981
- T. Taishi, X. Huang, I. Yonenaga, K. Hoshikawa, Dislocation behavior in heavily germanium-doped silicon crystal. *Mater. Sci. Semicond. Process.* **5**(4), 409–412 (2002)
- C.D. Thurmond, F.A. Trumbore, M. Kowalchik, Germanium solidus curves. *J. Chem. Phys.* **25**(4), 799–800 (1956)
- J. Vanhellemont, E. Simoen, A. Kaniava, M. Libezny, C. Claeys, Impact of oxygen related extended defects on silicon diode characteristics. *J. Appl. Phys.* **77**(11), 5669–5676 (1995)
- J. Vanhellemont, M. Suezawa, I. Yonenaga, On the impact of germanium doping on the vacancy formation energy in Czochralski-grown silicon. *J. Appl. Phys.* **108**, 016105 (2010)
- V.V. Voronkov, R. Falster, Latent complexes of interstitial boron and oxygen dimers as a reason for degradation of silicon-based solar cells. *J. Appl. Phys.* **107**(5), 053509 (2010)
- L. Wang, D. Yang, Structure of Ge–O complexes in Czochralski silicon. *Phys. B Condens. Matter* **404**(1), 58–60 (2009)
- P. Wang, X. Yu, P. Chen, X. Li, D. Yang, X. Chen, Z. Huang, Germanium-doped Czochralski silicon for photovoltaic applications. *Sol. Energy Mater. Sol. Cells* **95**(8), 2466–2470 (2011)
- M. Watanabe, T. Usami, H. Muraoka, S. Matsuo, Y. Imanishi, H. Nagashima, Oxygen-free silicon single crystal grown from silicon nitride crucible. *Semicond. Silicon* **4**, 126 (1981)
- G.D. Watkins, A microscopic view of radiation damage in semiconductors using EPR as a probe invited paper. *IEEE Trans. Nucl. Sci.* **16**(6), 13–18 (1969)
- G.D. Watkins, Defects in irradiated silicon: EPR of the tin-vacancy pair. *Phys. Rev. B* **12**(10), 4383 (1975)
- C. Xiao, D. Yang, X. Yu, X. Gu, D. Que, Influence of the compensation level on the performance of p-type crystalline silicon solar cells: Theoretical calculations and experimental study. *Sol. Energy Mater. Sol. Cells* **107**, 263–271 (2012a)
- C. Xiao, D. Yang, X. Yu, P. Wang, P. Chen, D. Que, Effect of dopant compensation on the performance of Czochralski silicon solar cells. *Sol. Energy Mater. Sol. Cells* **101**, 102–106 (2012b)
- W. Xu, J. Chen, X. Ma, D. Yang, L. Gong, D. Tian, Characterization of a Czochralski grown silicon crystal doped with  $1020^{20}\text{cm}^{-3}$  germanium. *Cryst. Res. Technol.* **46**(1), 10–13 (2011)
- D. Yang, J. Chen, Defects and Diffusion in Ceramics: An Annual Retrospective **Vii** **242–244**, 169 (2005)
- I. Yonenaga, Growth and mechanical properties of GeSi bulk crystals. *J. Mater. Sci. Mater. Electron.* **10**(5), 329–333 (1999)
- I. Yonenaga, T. Taishi, X. Huang, K. Hoshikawa, Dislocation–impurity interaction in Czochralski-grown Si heavily doped with B and Ge. *J. Cryst. Growth* **275**(1), e501–e505 (2005)
- X. Yu, P. Wang, P. Chen, X. Li, D. Yang, Suppression of boron–oxygen defects in p-type Czochralski silicon by germanium doping. *Appl. Phys. Lett.* **97**(5), 051903 (2010)
- X. Yu, X. Zheng, K. Hoshikawa, D. Yang, Crystal growth of indium-doped Czochralski silicon for photovoltaic application. *Jpn. J. Appl. Phys.* **51**(10R), 105501 (2012)
- S. Yuan, X. Yu, X. Gu, Y. Feng, J. Lu, D. Yang, Aluminum-doped crystalline silicon and its photovoltaic application. *Superlattice. Microst.* **99**, 158–164 (2016)



- 
- Z. Zeng, J.D. Murphy, R.J. Falster, X. Ma, D. Yang, P.R. Wilshaw, The effect of impurity-induced lattice strain and Fermi level position on low temperature oxygen diffusion in silicon. *J. Appl. Phys.* **109**(6), 063532 (2011a)
- Z. Zeng, L. Wang, X. Ma, S. Qu, J. Chen, Y. Liu, D. Yang, Improvement in the mechanical performance of Czochralski silicon under indentation by germanium doping. *Scr. Mater.* **64**(9), 832–835 (2011b)
- W. Zhang, S. Yan, Z. Ji, Effective segregation coefficient and steady state segregation coefficient of germanium in Czochralski silicon. *J. Cryst. Growth* **169**(3), 598–599 (1996)



# Growth of Multicrystalline Silicon for Solar Cells: The High-Performance Casting Method

# 7

C. W. Lan

## Contents

Introduction .....	176
The Emergence of HP mc-Si .....	177
The Growth of HP mc-Si .....	178
The Performance of HP mc-Si .....	181
Growth of HP mc-Si Without Seeding .....	183
The Properties of HP mc-Si .....	186
Outlook for HP mc-Si .....	187
Conclusion .....	190
Cross-References .....	190
References .....	190

## Abstract

The emergence of high-performance multicrystalline silicon (HP mc-Si) in 2011 has made a significant impact to photovoltaic (PV) industry. In addition to the much better ingot uniformity and production yield, HP mc-Si also has better material quality for solar cells. As a result, the average efficiency of solar cells made from HP mc-Si in production increased from 16.6% in 2011 to 18.5% or beyond in 2016. With an advanced cell structure, an average efficiency of more than 20% has also been reported. More importantly, the efficiency distribution became much narrower; the difference even from various wafer producers became smaller as well. Unlike the conventional way of having large grains and electrically inactive twin boundaries, the crystal growth of HP mc-Si by directional solidification is initiated from uniform small grains having a high fraction of random grain boundaries (GBs). The grains developed from such grain structures significantly relax thermal stress and suppress the massive generation

---

C. W. Lan (✉)

Department of Chemical Engineering, National Taiwan University (NTU), Taipei, Taiwan

e-mail: [cwlan@ntu.edu.tw](mailto:cwlan@ntu.edu.tw)

and propagation of dislocation clusters. The gettering efficacy of HP mc-Si is also superior to the conventional one, which also increases solar cell efficiency. Nowadays, most of commercial mc-Si is grown by this approach, which could be implemented by either seeded with silicon particles or controlled nucleation, e.g., through nucleation agent coating. The future improvement of this technology is also discussed in this chapter.

### Keywords

A2: High-performance · B2: Multicrystalline Si · A1: Directional solidification · A1: Casting · A1: Dislocation cluster · A1: Grain boundary · A1: Lifetime · A1: Gettering

## Introduction

In 2015, the annual PV production was about 57 GW, and the solar cells made from mc-Si shared the production of 68% (Fraunhofer Institute for Solar Energy Systems 2016). The mc-Si has been grown by the directional solidification (DS) or casting since late 1970s due to its high throughput and low cost (Lan et al. 2015; Khattak and Schmid 1987). Although DS is a matured technology, as discussed in the previous chapters, due to the higher structure defects and impurities, the ingot quality of mc-Si has been much inferior to the dislocation-free single-crystalline Si (sc-Si) grown by the Cz method. To mimic sc-Si, over the past 30 years, tremendous effort has been focused on the growth of large grains with more electrically inactive GBs, especially the  $\Sigma 3$  twin boundaries. Among these efforts, the mono-like (Stoddard 2007; Stoddard et al. 2008) and dendritic casting techniques (Fujiwara et al. 2006; Li et al. 2011, 2012; Nakajima et al. 2010a, b; Wang et al. 2009; Yeh et al. 2010) are the most typical ones, and their schematics are shown in Fig. 1a, b, respectively. For the mono-like techniques, due to the limited size of the seeds from the Cz ingot, the splitting seeds are usually used as illustrated in Fig. 1a. The seed orientation is usually in (100) for the ease of alkaline texturing during solar cell production; the

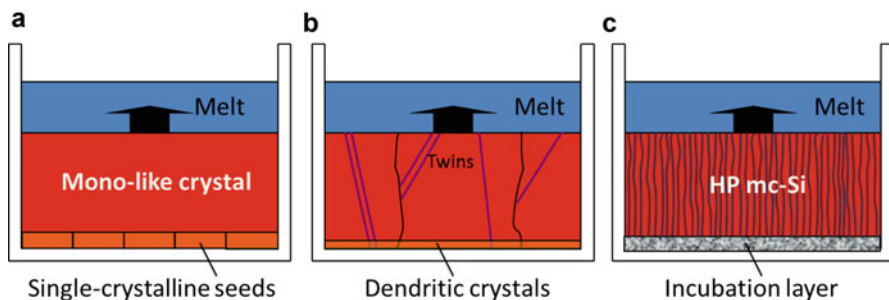


**Fig. 1** Schematics of different DS technologies: (a) mono-like casting using splitting seeds; (b) dendritic casting; (c) HP mc-Si (Lan et al. (2016b) with permission of Elsevier)

textures on the silicon wafer enhance light trapping, which is crucial for solar cell efficiency. On the other hand, instead of using the seeds, the dendritic casting technique, as illustrated in Fig. 1b, is to use the growth habit of silicon faceted dendrites to initiate a dendritic layer by high undercooling. Because the dendritic growth in the lateral direction at high undercooling ( $>10$  K) is preferred in  $\langle 110 \rangle$ , the grains in the ingot growth direction could then be controlled in  $\langle 112 \rangle$  (Fujiwara et al. 2006; Nakajima et al. 2010a, b). Both approaches are effective in the growth of large grains having fewer GBs, and the GBs are mainly coherent  $\Sigma 3$  in the dendritic casting. The details could be found in other chapters. Since 2006, Lan's group at NTU also has worked with Sino-American Silicon Products Inc. (SAS) to develop the dendrite casting method for mass production. For small ingots, they could reach a very high percentage of  $\Sigma 3$  GBs, up to 80%, with very high minority lifetime (Yeh et al. 2010). Even in industry-scale wafers, the twinning area had rather low defects and high lifetime (Li et al. 2012; Lan 2011a). With this belief, they continued to develop the dendritic casting technique for several years until 2010; however, the progress was slow. During this period of time, most companies, including SAS, started to shift their effort to the mono-like technique, especially after the Mono2™ wafers of BP Solar appeared in the market in 2006 (Stoddard et al. 2008). Afterward, a few companies announced the success of mono-like production, such as the U-grade wafers from SAS, Virtus wafers from Renasolar, S2 wafers from GCL, and Maple wafers from JA Solar. SAS also branded its  $\langle 110 \rangle$  mono-like wafers as E-wafers, which were found to have a better lifetime uniformity in the ingot production. Although the mono-like technology attracted much attention since 2006, it stayed in the market only for a short period of time (PV Magazine 2012). As the HP mc-Si emerged in late 2011 (Lan 2011a, b; Lan et al. 2012a, b, 2013, 2014; Stoddard et al. 2008; Wong et al. 2014; Yang et al. 2015), the mono-like wafers essentially disappeared from the market after 2012.

---

## The Emergence of HP mc-Si

Although high-quality ingots have been demonstrated for both mono-like and dendritic casting techniques, the multiplication and propagation of dislocation clusters due to thermal stress are still very difficult to control during crystal growth, especially for industrial-scale production. As a result, the solar cells fabricated from the wafers grown by both techniques have a very wide distribution in the conversion efficiency, and the low-efficiency tail in the distribution causes significant yield loss in the cell production. During the development of the dendritic casting technique, Lan's group found that the control of undercooling was also not trivial. The thick quartz crucible wall ( $>30$  mm) in production made the heat extraction from the crucible bottom much less effective. Moreover, the undercooling was sensitive to the silicon nitride coating as well. On the other hand, even large dendrites could be induced, massive dislocation clusters still appeared afterward due to thermal stress (Lan et al. 2012a, b; Yang et al. 2015). As the defect clusters appeared, they multiplied and propagated, so that the upper part of the ingot still had poor quality,

i.e., low minority lifetime. Surprisingly, they occasionally induced small grains by controlling the undercooling, and the ingot grown from the small grains turned out to have a much better uniformity (Yang et al. 2015). The defect multiplication and propagation were significantly mitigated. For the wafers without massive dislocation clusters, they also noticed that the correlation between efficiency and grain size was small. This indicated that the GBs were not crucial to the wafer performance.

---

## The Growth of HP mc-Si

To implement the small grain growth, at the beginning Lan's group cut off the bottom part of the small-grain ingot and reused it as the seeds for the next run. However, the bottom red zone increased as the seed plates were reused; in addition, the seed preparation was also tedious. Accidentally, they found that using small silicon particles as the seeds for ingot growth turned out to have a much better quality for the grown ingot (Lan et al. 2014). Especially, during that period of time, low-cost granular silicon was available from the downgrade product of the fluidized-bed polysilicon. Different particle sizes were tested, but the size ranging from 2 to 5 mm was considered for production; the smaller particles could be easily contaminated due to the larger specific surface area. They referred this seed layer for small grains as the incubation layer, as illustrated in Fig. 1c, and the growth of such small-grain ingots as the HP mc-Si technology. The use of nucleation agents was also found useful, and it will be discussed shortly. Using silicon particles was very robust in production in terms of ingot quality, but the melting stage required more care to keep a flat melting interface and a thin remaining seed layer. The red zone, the low-lifetime area due to the impurity diffusion from the crucible and the contaminated seeds, above the seed layer was found to be proportional to the remaining thickness of the seed layer. Surprisingly, in the HP mc-Si wafers, the percentage of noncoherent or random GBs was unprecedentedly high, more than 70%. However, the solar cell performance was significantly improved, especially the efficiency distribution was very narrow. The appearance of the conventional and HP mc-Si wafers are shown in Fig. 2a, b, respectively. As shown in Fig. 2a, the conventional one has large but nonuniform grains, and more importantly it contains many twins. On the other hand, the HP mc-Si wafer has uniform and small grains with many random GBs. Nevertheless, the grain structure is hardly visible from the appearance of the solar cell due to the isotropic acid texturing and antireflection coating, as shown in Fig. 2c. The adoption of HP mc-Si using silicon particles as the seeds was rather quick in industry. One of the major reasons was that the switch from the growth of mono-like to mc-Si ingots was straightforward; both required the control of seed melting.

The experimental results of HP mc-Si were first presented by Prof. Lan in the 5th International Workshop on Crystal Growth Technology in June of 2011 (Lan 2011a; Lan et al. 2013), and later in the 5th International Workshop on Crystalline Silicon Solar Cells held in Boston in October (Lan 2011b). The sample wafers were also sent to Solarworld for testing right after the Boston conference, and the feedback was

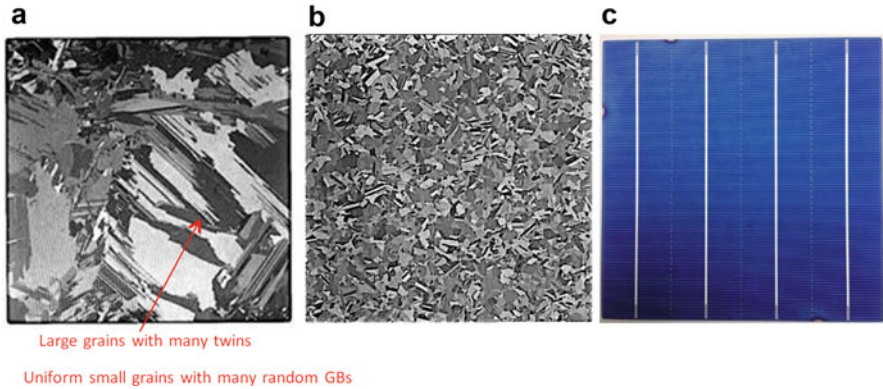


**Fig. 2** (a) A typical conventional multicrystalline silicon wafer ( $156 \times 156$  mm) having large grains and twin boundaries; (b) a typical high-performance multicrystalline silicon wafer having uniform small grains and many random GBs; (c) a typical multicrystalline silicon solar cell with four bus bars

excellent. The patent for such grain structures in the ingot and the wafer was filed in 2011 and first granted in 2014 (Lan et al. 2014); both silicon and nonsilicon particle seeds were used for ingot growth in the illustrated examples. After this finding, different approaches for getting such a grain structure have been explored and reported (Zhu et al. 2014; Wong et al. 2014a; Lan et al. 2016a, b; Zhang et al. 2016).

Figure 3a shows the comparison of HP mc-Si and conventional mc-Si. The lifetime mappings of both ingots are shown in Fig. 3a, where the HP mc-Si ingot was grown from small silicon particles ( $3 \sim 5$  mm in size) (Lan et al. 2016b). The effect of particle size will be discussed shortly; however, the grains nucleated from the silicon particles depended on the microstructure of the seed materials, not the apparent size of the seeds. As shown, as compared with the conventional mc-Si ingot, the lifetime of HP mc-Si was very uniform; the low-lifetime areas due to the dislocation clusters were significantly reduced. Figure 3b shows the comparison of grain structures of the wafers at the top and bottom portions of the ingots. For HP mc-Si, the grains near the bottom part of the ingot were small and uniform. On the contrary, the grains were large but un-uniform in the conventional mc-Si. In general, during ingot growth the grain size increased with the increasing ingot height for both growth, but sometimes the grain size decreased in the conventional mc-Si due to the nucleation of new grains from grits, subgrains, or twinning (Lan et al. 2013; Wong et al. 2014a). More importantly, as shown by the EPD mappings in Fig. 3c, in contrast to the conventional mc-Si, the high-EPD areas ( $\text{EPD} > 10^5/\text{cm}^2$ ) in HP mc-Si were much smaller and they were confined in the small grains. Because the columnar grain growth in HP mc-Si, the propagation of dislocation clusters from the bottom to the top was easily blocked by the random GBs. Furthermore, the defected grains tended to be softer, due to the plastic deformation assisted by dislocations, and they were easily overgrown or squeezed by others (Lan et al. 2012b; Yang et al. 2015). As will be discussed shortly, the large amount of random GBs seems to be quite effective in relaxing the thermal stress, presumably due

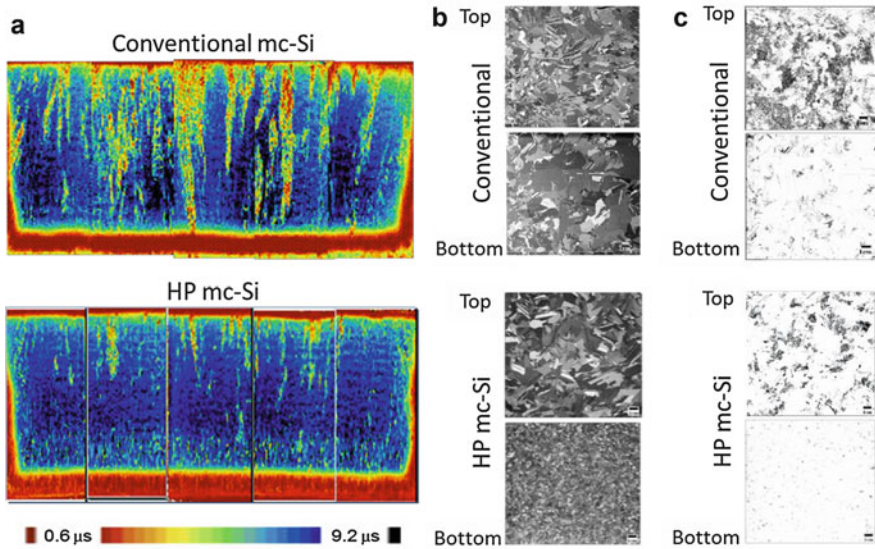


**Fig. 3** Comparison of (a) ingot lifetime mapping; (b) grains and (c) EPD mapping at ingot *bottom* and *top* for conventional (*top*) and HP mc-Si; the ingot width in (a) is 780 mm and wafer size in (b) and (c) is  $156 \times 156$  mm (Lan et al. (2016b) with permission of Elsevier)

to the sliding nature of the amorphous layer on the GBs (Lan et al. 2012b; Stokkan et al. 2014; Yang et al. 2015).

The grain size indeed plays a key factor in the growth of the defects. Lan's group also conducted a G5 experiment by putting several sc-Si chunks at different positions of the crucible along with the small silicon particles as the seeds, as shown in Fig. 4 (Lan et al. 2016b). The bricks were numbered by alphabets row by row as shown on the left of Fig. 4a, so that bricks C and F were next to the crucible wall and brick I was one brick away from the wall. The grain structures are shown in Fig. 4a. As shown in all cases, the big grains were gradually overgrown by the small grains from different directions; the areas of the chunk seeds are indicated by the red dashed-boxes. For silicon, it expands as it solidifies, so that the grains from the big chunks could be easily overgrown by the small grains. However, for brick F, some grains were grown from the crucible wall due to the slightly concave growth front near the wall. The resulted EPD mappings corresponding to the grain structure are shown in Fig. 4b. Interestingly, as shown, even though the grain size became uniform near the top of the ingot, the high EPD areas, inside the red dashed-boxes, seemed to correspond to the initial chunk seeds very well. The case for brick F was slightly affected by the grains grown from the wall. Because the new born grains from the wall had the lower EPD than the old grains, the high EPD area for brick F was slightly smaller than the original chunk size. The big grains from the chunk seeds being overgrown by the neighbor grains is often observed in mono-like growth. Again, it is presumed that during grain growth each grain expands as it



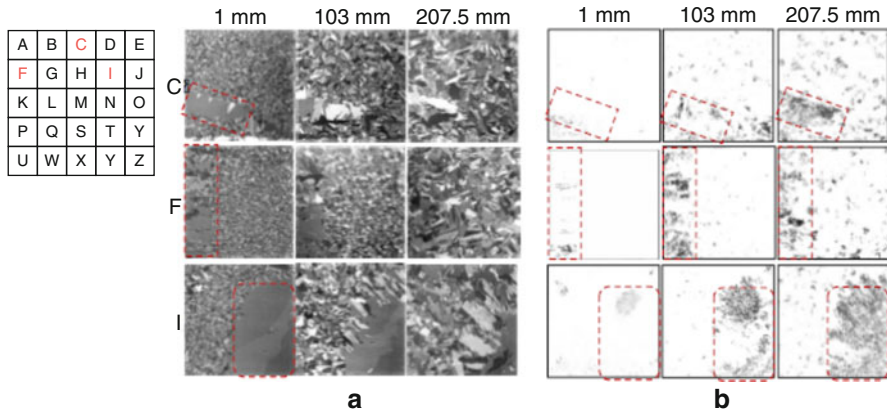


**Fig. 4** (a) Grain growth from different seeds; (b) EPD mapping of the wafers from different ingot positions; the *red dashed-boxes* indicate the area of the chunk seeds at the crucible bottom (Lan et al. (2016b) with permission of Elsevier). The positions of bricks C, F, and I are indicated on the *left of (a)*. The numbers on the *top* of the figures indicate the positions of the wafers in the bricks from the *bottom* to the *top*

solidifies; the more crowded columnar grains tend to grow outwards because they have more random orientations. Similarly, the weaker grains due to more dislocations for plastic deformation are overgrown by the stronger ones.

## The Performance of HP mc-Si

With the emergence of HP mc-Si in 2011, the solar cell efficiency has increased dramatically. As shown in Fig. 5, the biggest jump was from A+ to A3+; in fact, there was A2+ wafers in between that were the first generation of HP mc-Si using undercooling control and reused seed plates (Lan 2011a, b); the brand name for A+-series wafers was used by SAS since 2009. Interestingly, A2+ wafers appeared in the market only for a short period time due to the lower production yield. On the other hand, A3+ wafers were from the ingot grown from silicon particle seeds (Lan et al. 2012a, 2014), and this made the crystal growth much more robust both on the yield and quality. The progress to A4+ and A5+ required much better growth control including the hot zone, as well as the improvement of crucible/coating purity (Lan et al. 2016a, b; Yang et al. 2015). Nowadays, the average efficiency in production is about 18.3%, and the best could reach 18.5%, based on the back surface field (BSF) cell structure. If the passivated emitter and rear cell (PERC) structure is used, using alumina back surface passivation, an average efficiency up to 19.6% in production has been reached (Lan et al. 2016b). Some companies, such as REC and Trina, also reported an efficiency of more than 20% in their production line, while the champion cell recently reported by Jinko Solar was up to 21.63% using HP mc-Si wafers (156 × 156 mm). For these cells, reactive ion etching (RIE) was used for texturing,



**Fig. 5** Progress of solar cell efficiency using HP-mc Si wafers for BSF and PERC cells; A+ is not HP mc-Si

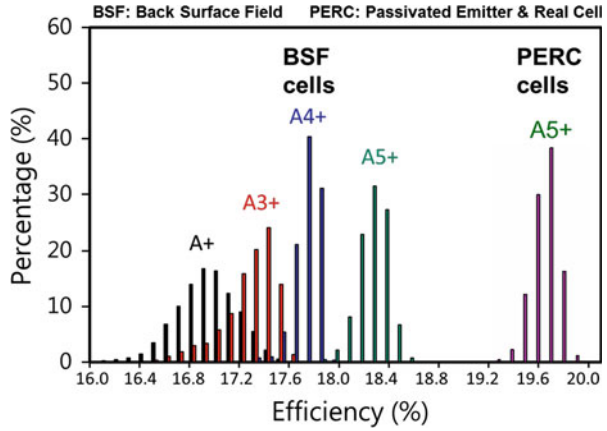
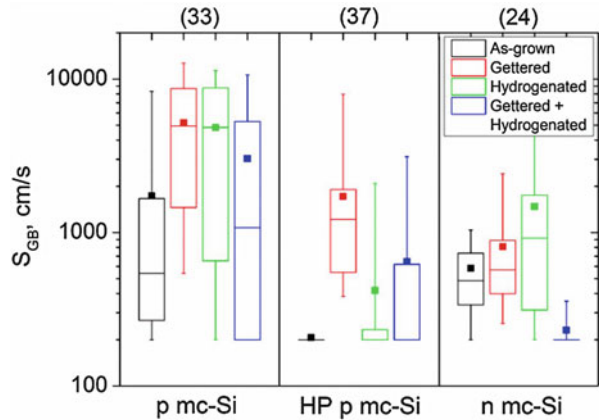


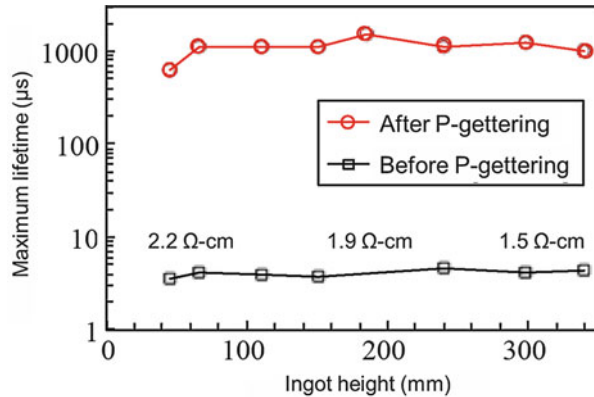
**Fig. 6** Variation of surface recombination activity of p-type mc-Si, p-type HP mc-Si, and n-type mc-Si wafers after gettingter, hydrogenation, and both treatments (Sio and Macdonald (2016) with permission of Elsevier)



i.e., the so-called black silicon, instead of the traditional isotropic acidic etching. In addition, these wafers were also cut by diamond wire, so that the cutting damage was much less and the backside polishing was much easier for passivation.

Furthermore, from the recent investigation by Sio and Macdonald (2016), as shown in Fig. 6, the recombination activity of the GBs in HP mc-Si wafers turned out to be very low (the recombination velocity was about 200 cm/s) as compared with that in the traditional mc-Si wafers (~1000 cm/s). The reason for the low recombination activity at the GBs for HP mc-Si remains unknown and needs further investigation. Moreover, the gettering efficacy of the HP mc-Si wafers was much higher than the convectional mc-Si wafers as well (Castellanos et al. 2016). In general, the lifetime could be easily enhanced by gettering for HP mc-Si wafers, but the lifetime often deteriorated for the conventional ones. The main reason was believed to be the lower dislocation clusters to trap the metals in the HP mc-Si, so that the gettering could be more efficient. The gettering efficacy is very important to

**Fig. 7** Maximum minority lifetime distribution of n-type HP mc-Si wafers from a G6 ingot (P/Ga co-doped) before and after P-gettering (Lan et al. (2016b) with permission of Elsevier)



enhance the lifetime of the wafer in the emitter formation during solar cell production. The higher wafer lifetime gives the higher solar cell efficiency. Therefore, HP mc-Si has not only the better uniformity and production yield, but also the better solar cell performance owing to its better gettering efficacy and lower GB activities. Recently, Lan et al. (2016b) also grew G6 n-type HP mc-Si, and the lifetime of the wafers before and after phosphorous gettering from the center brick was shown in Fig. 7. As shown, the best lifetime could be increased to 1 ms after gettering. In fact, after hydrogenation, the best lifetime was further increased to above 2 ms (Phang et al. 2016). Although boron-gettering was found not effective, the additional phosphorous gettering and hydrogen passivation were found effective in gaining the lifetime. This indicates that N-type HP mc-Si is also a potential material for high-efficiency solar cells based on the lifetime results (Phang et al. 2016). Recently, Schubert et al. (2016) further reported that the simulated solar cell efficiency was up to 22% for this material.

## Growth of HP mc-Si Without Seeding

In addition to the use of silicon particles for seeding, using nucleation agent for getting small grains could be useful as well (Lan et al. 2016a, b; Wong et al. 2014b; Zhang et al. 2016). A few nucleation coatings have been considered including silica, silicon nitride, and their mixtures with silicon particles (Lan et al. 2016a), and some have been adopted in production. Figure 8a shows an example of using a  $\text{Si}_3\text{N}_4/\text{Si}$  nucleation agent; the agent was paint on the left part of a  $\text{Si}_3\text{N}_4$ -coated quartz crucible. The grain structures grown from the coating are shown in Fig. 8b. As shown, uniform small grains could be early nucleated from the nucleation agent. Because the thickness of the nucleation agent coating was only 500  $\mu\text{m}$ , the thermal condition in the crucible bottom for different coatings should be similar. The roughness due to the voids occupied by silicon might be key factor for the nucleation of small grains. Recently, Kupka et al. (2016) used  $\text{SiO}_2$  and  $\text{SiC}$  particles with different particle sizes for the nucleation agents. They also had a similar observation

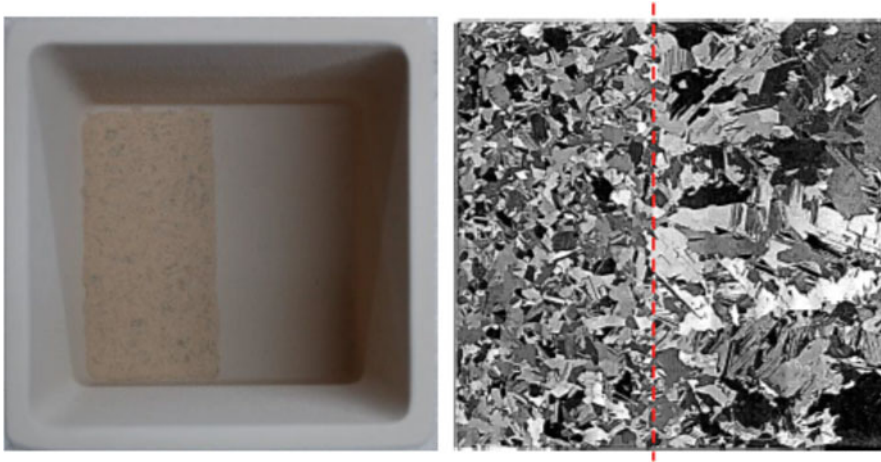


**Fig. 8** An example of nucleation agent for grain control: (a) the additional  $\text{Si}_3\text{N}_4/\text{Si}$  coating on the left bottom of the  $\text{Si}_3\text{N}_4$ -coated quartz crucible; (b) the grain structures; the dashed-line indicates the boundary of the nucleation agent coating

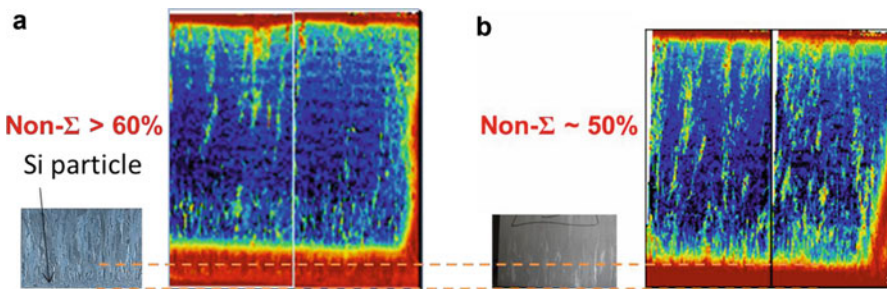


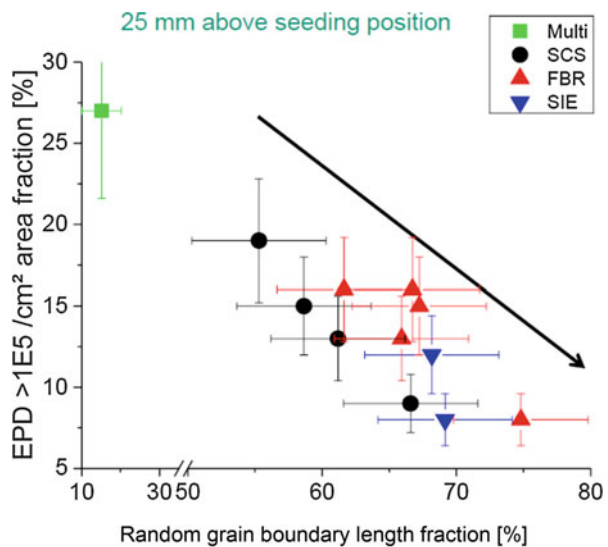
**Fig. 9** Grains and lifetime time of the ingots from (a) seeded growth; (b) the silica nucleation agent; the thinner bottom red zone in (b) could be seen (Lan et al. (2016b) with permission of Elsevier)

that the grains nucleated from the coating decreased with the increasing roughness. Therefore, the small and uniform grains could be induced by the nucleation agent; however, the portion of the random GBs usually was not as high as that from the silicon particle seeding. Figure 9 shows the comparison of the columnar growth and the lifetime mapping of a brick in a G5 growth obtained by from two different seeding approaches; silica (0.1 mm in size) was used as the nucleation agent for Fig. 9b. As shown, the columnar grains from both seeding methods were very similar. Both methods had good uniformity in the lifetime mappings. The major difference was in the thickness of the bottom red zone. Using the nucleation agent significantly reduced the red zone thickness. As a result, the growth yield was increased. Nevertheless, as compared with the silicon seeding, the initial percentage

of non- $\Sigma$  or random GBs ( $\sim 50\%$ ) of the ingot was found lower for using the silica nucleation agent. Kupka et al. (2016) also observed similar results, especially for SiC particles. They observed that although small grains could be initiated from SiC particles, the fraction of random GBs was not high; still many  $\Sigma 3$  GBs appeared during nucleation. On the other hand, the silica nucleation layer gave the grain structures much closer to HP mc-Si, i.e., small grains with a high fraction of random GBs. In addition, the silica particles used previously were presumed to be in the  $\beta$ -cristobalite phase during nucleation.

Moreover, increasing temperature gradients was found easier to get smaller grains from the nucleation; however, the fraction of  $\Sigma 3$  GBs depended on the coatings. Magnetic stirring could also be used, e.g., by REC Inc. in Singapore. Nowadays, the quality and thus the solar cell performance of the ingot grown from the nucleation agent were still found slightly inferior to that from the silicon particles, even through several companies claimed that they could grow high quality HP mc-Si without using silicon particle seeds. Therefore, this indicated that the amount of “random GBs” would be more crucial for stress relaxation and thus defect reduction, instead of just the small grains. This observation was further confirmed by Reimann et al. in their recent experiments (2016). They conducted small ingot growth using different seeding materials. As shown in Fig. 10, the longer random GB length fraction from the seeds led to the smaller area of high EPD clusters in the grown ingot. More importantly, the seed materials played a crucial role. For example, if the seeds were from Siemen’s feedstock or fluidized-bed-reactor, which was mc-Si with very small grains, the seed size had little effect on the grown grain size and the length fraction of random GBs (Reimann et al. 2016). In other words, to initial the grain structures for

**Fig. 10** Area fraction of EPD  $> 10^5 \text{ cm}^{-2}$  versus the random grain boundary length fraction for all performed experiments for the 25 mm cut; seeds were from single crystalline crushed (SCC), fluidized-bed-reactor (FBR) and Siemens (SIE) feedstock; the conventional mc-Si was included for comparison (Reimann et al. (2016) with permission of Elsevier)



HP mc-Si, the grain structures were more important than the apparent size for the seed materials.

## The Properties of HP mc-Si

Figure 11 summarizes the typical grain structures (a), crystallographic orientations and GB types (c) of the wafers taken from different positions of a HP mc-Si ingot seeded by silicon particles (Lan et al. 2016c). The statistics in Figs. 11b and 6c was obtained from Fig. 11a. As shown in Fig. 11b, the grain orientations were mainly located in the low-energy planes, such as (111) and (112). Other orientations such as (115) and (313) had nontrivial portions and this might be generated due to twinning (Wong et al. 2014a). More importantly, as shown in Fig. 11c, the percentage of the non- $\Sigma$  or random GBs at the lower part of the ingot was greater than 70%. Even in the top portion of the ingot, the percentage of the random GBs was also more than 60%.

Wong et al. (2014a) did a detailed analysis of the grain structures developed from small silicon beads (0.9 mm in diameter), and they also found that the lowest-energy orientation, i.e., (111) tended to dominate during grain competition. However, the twinning from the tri-junctions generated new grains with different orientations (Wong et al. 2014a); this might be the reason for more (112) orientation at the top ingot. Indeed, the (111)- or (112)-dominated orientations and the high fraction of

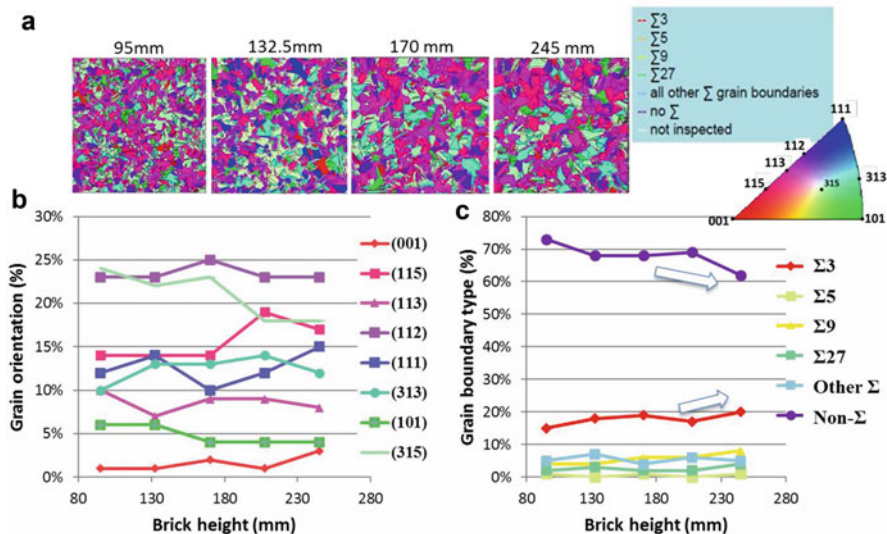


**Fig. 11** Development of (a) grain structures; (b) crystallographic orientations; and (c) GB types along the height of an HP mc-Si ingot. The orientations and GB types were obtained from the wafers at different heights of the central brick of the ingot (Lan et al. (2016b) with permission of Elsevier)

random GBs are the typical characteristics nowadays in commercial HP mc-Si wafers. The high-percentage of the random GBs shown in Fig. 11c upsets the previous understanding for high quality mc-Si wafers; however, they played a crucial role in the reduction of dislocation clusters, especially for industrial production. Before Lan's group reported this finding (Lan et al. 2012a, b, 2014; Yang et al. 2015), most people believed that twins or  $\Sigma 3$  GBs were needed for better lifetime (Fujiwara et al. 2006; Li et al. 2011, 2012; Nakajima et al. 2010a, b; Wang et al. 2009; Yeh et al. 2010), which was the core concept of the dendritic casting approach. In fact, if the wafers from the dendritic casting are carefully examined, one could find that the twin areas often have very few defects (Li et al. 2012; Rynningen et al. 2011); however, this is based on the condition without massive dislocation clusters. During the growth of large ingot, the relaxation of thermal stress for reducing the multiplication of dislocation clusters is crucial, and the large amount of random GBs in HP mc-Si plays a critical role.

## Outlook for HP mc-Si

Although the growth of HP mc-Si having low defects and good uniformity is rather robust, especially seeded with silicon particles, the random GBs decrease and defects increase during crystal growth. The defect growth is strongly affected by the evolution of grain structures, and the grain growth, which leads to the reduction of random GBs, is very important. Lehmann et al. (2016) analyzed HP and conventional mc-Si wafers from various companies, as shown in Fig. 12. They found that indeed the GB types were very different as shown in Fig. 12a. The HP mc-Si in general had more than 60% of random GBs, while the conventional one had high percentage of  $\Sigma 3$  GBs. However, as shown in Fig. 12b, their difference became smaller near the top of the ingots due to grain growth and the decrease of random

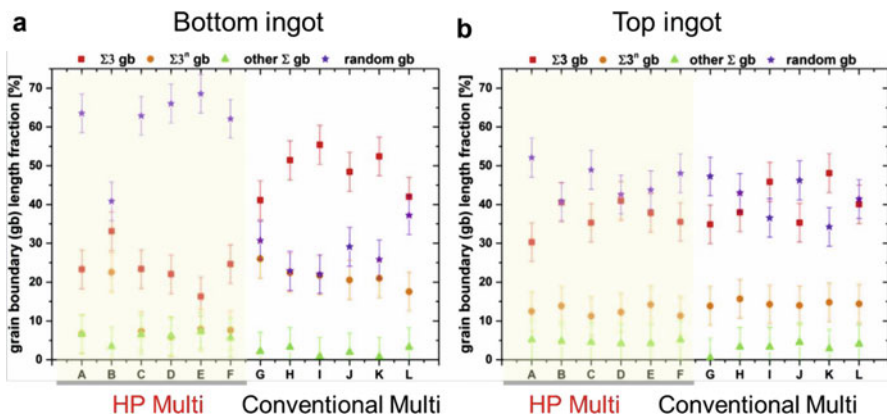


**Fig. 12** Comparison of GB types in HP and conventional mc-Si at the *bottom* (a) and the *top* (b) of the ingots from different suppliers (Lehmann et al. (2016) with permission of Elsevier)

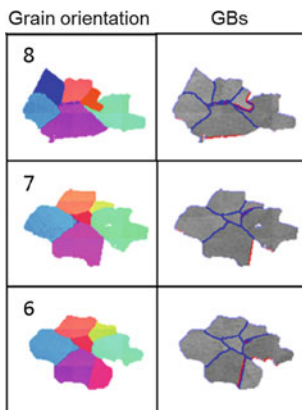


GBs, as well as the increase of  $\Sigma 3$  GBs. As a result, if the ingot grows taller, there are less random GBs for stress relaxation, so that the dislocation clusters even in HP mc-Si will become more problematic.

In fact, Wong et al. (2014a) was the first to perform detailed experiments to investigate the structure evolution of HP mc-Si in a lab-scale furnace for different growth speeds ranging from 10 to 200 mm/h. They analyzed the grain structures of the wafers cut from the ingot by using electron backscattered diffraction (EBSD). For grain growth, some of their results are shown in Fig. 13a for illustration. In general, the low-energy (111) grain became dominant during grain coarsening due to the reduction of overall interfacial energy. The random GBs decreased as grains coarsened. On the other hand, as shown in Fig. 13b, they also found that  $\Sigma 3$  GBs increased due to twinning (Wong et al. 2014a; Duffar and Nadri 2010) and decreased due to the blocking by the random GBs. As shown, the new grain nucleated from the tri-junction, and this twinning process could repeat based on the twinning probability (Duffar and Nadri 2010). Lin and Lan (2017) recently found that the GB type at the faceted groove, i.e., tri-junction, between grains played a crucial role in reducing the nucleation barrier of twinning. With a random GB, the twinning probability could be greater than  $10^{-6}$  at an undercooling of 0.5 K, which gave a twin spacing about 300  $\mu\text{m}$ . The reduction of random GBs and the generation of twin boundaries eventually tended to be close. As a result, near the top of the small ingots, the fraction of both GBs became comparable. Nevertheless, because twinning became

### a Grain Coarsening

Minimizing energy  $\Rightarrow$  (111)  
**Non- $\Sigma$  GBs decrease**



### b Twinning from Tri-junction

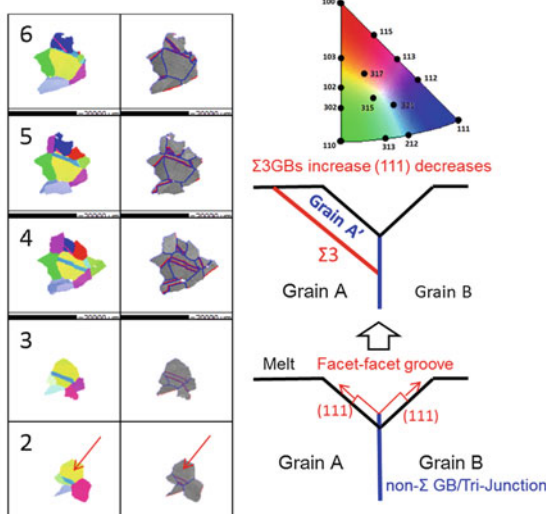


**Fig. 13** (a) Grain coarsening (*left* figures are EBSD and *right* figure are GBs); (b) nucleation of twins and their movement; twin boundary was blocked by the random GBs (from wafers 4 to 6). The twin nucleation from the faceted groove at tri-junction is illustrated on the *right* (Wong et al. (2014a) with permission of Elsevier)

more frequent with the increasing speed or undercooling, the generation of  $\Sigma 3$  GBs and the reduction of random GBs became faster as the growth speed increased. Therefore, the control of grain growth and twining is crucial to HP mc-Si for taller ingots. Nowadays, even for the normal ingot height, e.g., 35 cm in G6, the high defect density near the top of the ingot for HP mc-Si is still problematic due to the reduction of random GBs. In fact, if one carefully examines the amount of random GBs near the top ingots in (Lehmann et al. 2016), it is clear that some ingots could still keep a high percentage of random GBs. This indicates that the growth conditions could be optimized for HP mc-Si in practice. Recently, Trempa et al. (2017) compared the grain structures and defects of the conventional and HP mc-Si ingots from eight successive growths to simulate the extraordinary ingot height of 710 mm. They found that the grain structures and the defects of both ingots became similar after 350 mm. Especially, as shown in Fig. 14 for the comparison of defects and recombination area fraction for convectional and HP mc-Si in their study (Trempa et al. 2017). In other words, the advantage of HP mc-Si is limited to the first grown 350 mm of the ingot.

In addition to the dislocation clusters, the control of impurities is also important to ingot quality. The back diffusion of the metals from the silicon seeds increases the red zone and deteriorates the quality of bottom ingot, even though the EPD is the lowest there. Therefore, to further improve HP mc-Si, the reduction of seed layer thickness and the improvement of crucible/coating purity would be important. Recently, the crucibles coated with high purity silica are available in the market;

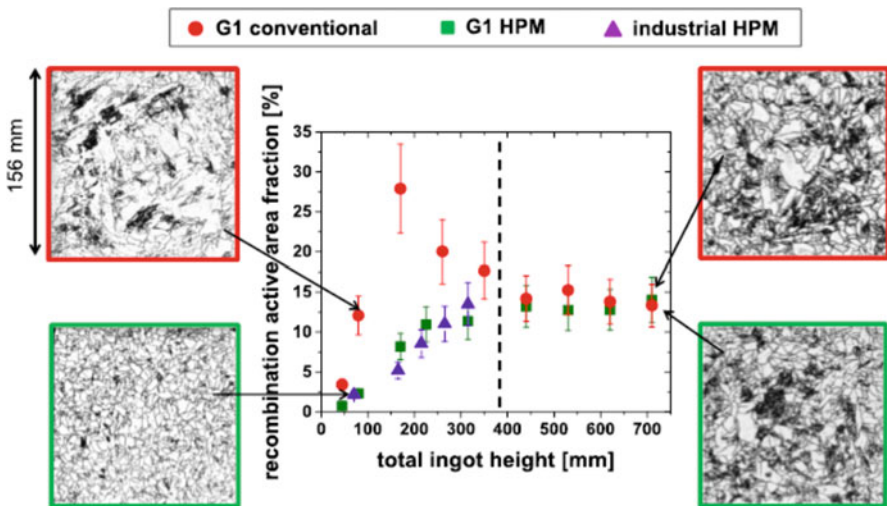


**Fig. 14** Recombination active area fraction versus total ingot height for the 710 mm G1 conventional ingot (*red circles*) and the 710 mm G1 HP mc-Si (HPM) ingot (*green squares*). Additionally, the values for a 300 mm industrial HPM ingot (*violet triangles*) are shown. On the sides, PL images of both 710 mm G1 ingots are shown for 80 mm and 710 mm total ingot height (Trempa et al. (2017) with permission of Elsevier)



using a diffusion barrier could also be feasible (Hsieh et al. 2014). Eventually, if the seeding layer is replaced by simple coating, while keeping small grains and high fraction of random GBs after nucleation, both quality and yield of HP mc-Si could be improved.

---

## Conclusion

Nowadays, nearly 70% of solar cells are made from mc-Si wafers, and most of them are produced from the HP casting method. The method is very robust, so that it has been widely adopted by industry. In addition to the excellent ingot quality, the yield of the HP casting is also very high due to the much less massive propagation of dislocation clusters. The excellent quality of the HP mc-Si has been reflected on the significant progress of the solar cell efficiency in the recent years. Besides the p-type champion cell with an efficiency higher than 21.23% reported by Trina Solar Inc., the very recent world record (21.9%) on the n-type HP mc-Si solar cell has been made by Fraunhofer ISE in early 2007. Nevertheless, to compete with the mono-crystalline silicon solar cells, further improvement of the ingot quality by HP casting can be expected.

---

## Cross-References

- [Growth of Multicrystalline Silicon for Solar Cells: Dendritic Cast Method](#)

**Acknowledgments** CWL is grateful for the generous support by the Ministry of Science and Technology of Taiwan, National Taiwan University, and SAS.

---

## References

- S. Castellanos, K.E. Ekström, A. Autruffe, M.A. Jensen, A.E. Morishige, J. Hofstetter, P. Yen, B. Lai, G. Stokkan, C. del Canizo, T. Buonassisi, *IEEE J. Photovolt.* **6**, 632 (2016)
- T. Duffar, A. Nadri, *Scr. Mater.* **62**, 955 (2010)
- Fraunhofer Institute for Solar Energy Systems, ISE, Freiburg, Photovoltaics Report. <http://www.ise.fraunhofer.de>. Accessed 17 Nov 2016
- K. Fujiwara, W. Pan, K. Sawada, M. Tokairin, N. Usami, Y. Nose, A. Nomura, T. Shishido, K. Nakajima, *J. Cryst. Growth* **292**, 282 (2006)
- C.C. Hsieh, A. Lan, C. Hsu, C.W. Lan, *J. Cryst. Growth* **401**, 727 (2014)
- C.P. Khattak, F. Schmid, in *Silicon Processing for Photovoltaics II*, ed. by C. P. Khattak, K. V. Ravi (Elsevier Science Publishers, North Holland, 1987), p. 153
- I. Kupka, C. Reimann, T. Lehmann, D. Oriwol, F. Kropfgans, J. Friedrich, in *Abstracts of Technical Digest of the 18th International Conference on Crystal Growth and Epitaxy*, Nogyoya, 7–12 Aug 2016
- C.W. Lan, in *Abstracts of the 5th International Workshop on Crystal Growth Technology*, Berlin, 26–30 June 2011a
- C. W. Lan, in *Abstracts of the 5th International Workshop on Crystalline Silicon Solar Cells*, Boston, 1–3 Nov 2011b

- C.W. Lan, W.C. Lan, T.F. Li, A. Yu, Y.M. Yang, C. Hsu, B. Hsu, A. Yang, From A+ to A+++, in *Abstracts of the 22nd Workshop on Crystalline Silicon Solar Cells & Modules: Materials and Processes*, Vail, 22–25 July 2012a
- C.W. Lan, Y.M. Yang, A. Yu, B. Hsu, A. Yang, in *Abstracts of the 27th European Photovoltaic Solar Energy Conference (27th EU PVSEC)*, Frankfurt, 24–28 Sept 2012b
- C.W. Lan, W.C. Lan, T.F. Li, A. Yu, Y.M. Yang, C. Hsu, B. Hsu, A. Yang, *J. Cryst. Growth* **360**, 68 (2013)
- C.W. Lan, W.H. Yu, Y.M. Yang, H.S. Chou, C.L. Hsu, W.C. Hsu, TW Patent I452185(B), 11 Sept 2014
- C.W. Lan, C. Chuck, K. Nakajima, in *Handbook of Crystal Growth 2A: Bulk Crystal Growth: Basic Techniques*, 2nd edn., ed. by P. Rudolph (Elsevier Science Publishers, Amsterdam, 2015), p. 373
- C.W. Lan, Y.M. Yang, A. Yu, Y.C. Wu, B. Hsu, W.C. Hsu, A. Yang, *Solid State Phenom.* **242**, 21 (2016a)
- C.W. Lan, A. Lan, C.F. Yang, H.P. Hsu, M. Yang, A. Yu, B. Hsu, W.C. Hsu, A. Yang, *J. Cryst. Growth*, in press (2016b), <http://www.sciencedirect.com/science/article/pii/S0022024816306728>. Accessed 28 Oct 2016
- C.W. Lan, C.F. Yang, A. Lan, M. Yang, A. Yu, H.P. Hsu, B. Hsu, C. Hsu, *Cryst. Eng. Comm.* **18**, 1474 (2016c)
- T. Lehmann, C. Reimann, E. Meissner, J. Friedrich, *Acta Mater.* **106**, 98 (2016)
- T.F. Li, K.M. Yeh, W.C. Hsu, C.W. Lan, *J. Cryst. Growth* **318**, 219 (2011)
- T.F. Li, H.C. Huang, H.W. Tsai, A. Lan, C. Hsu, C.W. Lan, *J. Cryst. Growth* **340**, 202 (2012)
- H.K. Lin, C.W. Lan, *Acta Mater.* **131**, 1 (2017)
- P.V. Magazine, Sep 2012, pp. 94–99. <http://www.pv-magazine.com>
- K. Nakajima, K. Kutsukake, K. Fujiwara, N. Usami, S. Ono, I. Yamasaki, in *Abstracts of the 35th IEEE Photovoltaic Specialists Conference*, Honolulu, 20–25 June 2010a
- K. Nakajima, K. Kutsukake, K. Fujiwara, N. Usami, S. Ono, I. Yamasaki, in *Abstracts of the 25th European Photovoltaic Solar Energy Conference and Exhibition (25th EU PVSEC), The 5th World Conference on Photovoltaic Energy Conversion (WCPEC-5)*, Spain, 6–9 Sep 2010b
- S. P. Phang, H. C. Sio, C.F. Yang, C.W. Lan, Y.M. Yang, A. Yu, B. Hsu, C. Hsu, D. Macdonald, in *Abstracts of the 26th Photovoltaics Science and Engineering Conference (PVSEC-26)*, Singapore, 24–28 Oct 2016
- C. Reimann, M. Trempa, T. Lehmann, K. Rosshirt, J. Stenzenberger, J. Friedrich, K. Hesse, E. Dornberger, *J. Cryst. Growth* **434**, 88 (2016)
- B. Ryningen, G. Stokkan, M. Kivambe, T. Ervik, O. Lohne, *Acta Mater.* **59**, 7703 (2011)
- M. Schubert, F. Schindler, J. Schön, W. Kwapil, B. Michl, J. Benick, in *Abstracts of the 9th International Workshop on Crystalline Silicon Solar Cells*, Tempe, Arizona, 10–12 Oct 2016
- H.C. Sio, D. Macdonald, *Sol. Energ. Mat. Sol. Cells* **144**, 339 (2016)
- N. Stoddard, BP Corp., WO Patent 2007084936, A2 July 2007
- N. Stoddard, B. Wu, I. Witting, M. Wagener, Y. Park, G. Rozgonyi, R. Clark, *Solid State Phenom.* **1**, 131 (2008)
- G. Stokkan, Y. Hu, O. Mjos, M. Juel, *Sol. Energ. Mat. Sol. Cells* **130**, 679 (2014)
- M. Trempa, I. Kupka, C. Kranert, T. Lehmann, C. Reimann, J. Friedrich, *J. Cryst. Growth* **459**, 67–75 (2017)
- T.Y. Wang, S.L. Hsu, C.C. Fei, K.M. Yei, W.C. Hsu, C.W. Lan, *J. Cryst. Growth* **311**, 263 (2009)
- Y.T. Wong, C. Hsu, C.W. Lan, *J. Cryst. Growth* **387**, 59 (2014a)
- Y.T. Wong, C.T. Hsieh, A. Lan, C. Hsu, C.W. Lan, *J. Cryst. Growth* **404**, 59 (2014b)
- Y.M. Yang, A. Yu, B. Hsu, W.C. Hsu, A. Yang, C.W. Lan, *Prog. Photovolt. Res. Appl.* **23**, 340 (2015)
- K.M. Yeh, C.K. Hsieh, W.C. Hsu, C.W. Lan, *Prog. Photovolt. Res. Appl.* **18**, 265 (2010)
- H. Zhang, D. You, C. Huang, Y. Wu, Y. Xu, P. Wu, *J. Cryst. Growth* **435**, 91 (2016)
- D. Zhu, L. Ming, M. Huang, Z. Zhang, X. Huang, *J. Cryst. Growth* **386**, 52 (2014)



# Growth of Multicrystalline Silicon for Solar Cells: Dendritic Cast Method

# 8

Kozo Fujiwara

## Contents

Introduction .....	194
Development of the Dendritic Cast Method .....	195
In Situ Observation of the Growth of the Si Dendrite Crystal .....	195
Growth Concept of the Dendritic Cast Method .....	197
Conditions for Growing a Dendrite Crystal in Si Melt .....	198
Mc-Si Ingot Grown by the Dendritic Cast Method .....	203
Growth of a Small Size mc-Si Ingot .....	203
Improvement of the Dendritic Cast Method .....	205
Problems and Future Developments of the Dendritic Cast Method .....	208
Concluding Remarks .....	213
Cross-References .....	213
References .....	214

## Abstract

This chapter introduces the dendritic cast method which allows us to obtain multicrystalline silicon ingot containing large-size crystal grains with specific orientations. The growth of dendrite crystals along the bottom wall of crucible in the initial stage of casting is crucial in this method. First, the features of Si dendrite crystals including the conditions for initiating dendrite growth will be explained following the concept of the dendritic cast method. The parallel twin formation and undercooling, those are prerequisites for the growth of the dendrite crystal, will be considered fundamentally. Next, experimental results of the growth of multicrystalline silicon ingots by the dendritic cast method will be summarized. The idea to control the dendrite growth will be described. Finally, problems and the future development of this method will be

---

K. Fujiwara (✉)

Institute for Materials Research, Tohoku University, Sendai, Japan

e-mail: [kozo@imr.tohoku.ac.jp](mailto:kozo@imr.tohoku.ac.jp)

considered. A nonwetting dendritic cast method, which is a growth concept for the reduction of generation of dislocation and impurity during casting, will be introduced.

---

**Keywords**

Cast method · Silicon · Dendrite growth · Crystal/melt interface · Undercooling · Twin boundary

---

## Introduction

At present, control of grain structures including grain size, grain orientation, grain boundary (see ► [Chap. 19, “Grain Boundaries in Multicrystalline Silicon”](#)), twin boundary, dislocation (see ► [Chap. 18, “Defects in Crystalline Silicon: Dislocations”](#)), subgrain boundary, and impurity (see ► [Chaps. 14, “Oxygen Impurity in Crystalline Silicon,”](#) and ► [15, “Carbon Impurity in Crystalline Silicon”](#)) is the common recognition in the field of crystal growth of multicrystalline silicon (mc-Si) ingot for solar cells. The proposal of the dendritic cast method became the trigger to share this recognition in researchers widely. In this chapter, the concept and features of dendritic cast method will be described.

The dendritic cast method was proposed in 2006 on publications (Fujiwara et al. [2006a, b](#)). Since the late 1970s (Ciszek et al. [1979](#)), a mc-Si ingot for solar cells is grown by directional solidification method, which is usually called cast method. The quality of the ingot has been improved until now although there is still room for further improvement. Before the proposal of the dendritic cast method, researchers attempted to improve the quality of mc-Si ingot by the control of growth conditions, such as thermal history, growth rate, purity of feedstock, or materials of crucible. In the dendritic cast method, the quality of mc-Si ingot is improved by controlling grain structures. The key point is the control of dendrite crystals in the initial stage of casting, which will play a role of “seed” crystal during directional solidification. The concept of the dendritic cast method was born from the fundamental study of the crystal growth mechanisms of Si, as explained below.

In the early 2000s, Nakajima’s group started to develop a crystal growth technology for obtaining a structure-controlled mc-Si ingot, aiming to realize an ideal mc-Si ingot for solar cells, as schematically shown in [Fig. 1](#). However, it was not well understood how to control the complicated grain structure in mc-Si ingot which contains variety types of defects including grain boundary, twin boundary, dislocation, subgrain boundary, and metallic impurity. Therefore, the study of crystal growth mechanisms for obtaining fundamental understandings was started by the development of an in situ observation technique (Fujiwara et al. [2002, 2004](#)). It was found that the dendrite growth was promoted in a melt even at a low degree of undercooling, and also found that the growth velocity of the dendrite crystal was much faster than that of the normal crystal grain (Fujiwara et al. [2006a](#)). Furthermore, it was well known that the growth orientation of the dendrite was limited to

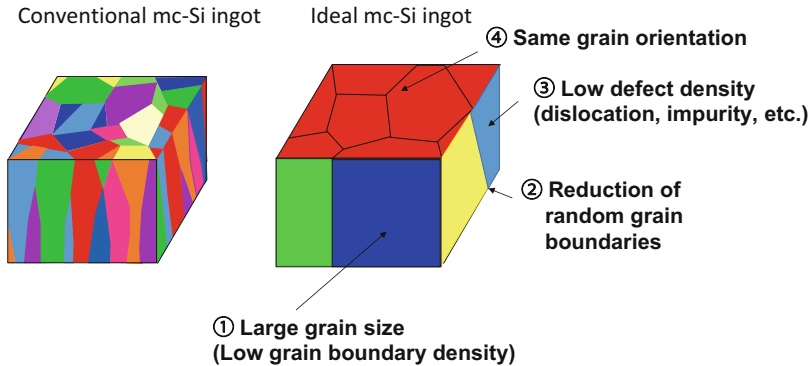


**Fig. 1** Schematic image of ideal mc-Si ingot (*right*)

specific orientations (Billig 1955; Bennett and Longini 1959; Hamilton and Seidensticker 1960; Wagner 1960; Albon and Owen 1963; O'Hara and Bennett 1964; Barrett et al. 1971; Lau and Kui 1991; Li and Herlach 1996; Nagashio and Kuribayashi 2005). From those fundamental understanding of the dendrite growth of Si, it was considered that if one could control the dendrite growth at the initial stage of casting, a mc-Si ingot with large-size oriented crystal grains would be produced.

In this chapter, first, the concept of the dendritic cast method and the features of dendrite crystal of Si will be explained. Next, mc-Si ingots grown by this method will be shown. Finally, the remained problems and future development of the dendritic cast method will be discussed.

## Development of the Dendritic Cast Method

### In Situ Observation of the Growth of the Si Dendrite Crystal

Here, the features of dendrite crystals of Si will be explained. An in situ observation system consisting of a furnace and a microscope (Fig. 2) was developed for the observations of crystal/melt interface of Si (Fujiwara et al. 2004). Si raw materials were set in a fused silica crucible with the size of  $10 \times 20 \times 10$  mm and melted in the furnace. The temperature gradient in the furnace could be controlled by controlling the power of two zone heaters. A water cooled tube was inserted from one side of the sample, and thus, the temperature gradient in the sample can be reached around 9 K/mm. Such a temperature gradient was kept during a cooling process to observe a crystal/melt interface during directional solidification. The growth velocity was changed by controlling the cooling rate.

When the crystal grows at low growth velocity, the crystal melt interface was kept planar shape, as shown in Fig. 3a. On the other hand, dendrite growth was initiated from a zigzag faceted interface at higher growth velocity, as shown in Fig. 3b. The undercooling at the initiation of the dendrite growth was estimated to

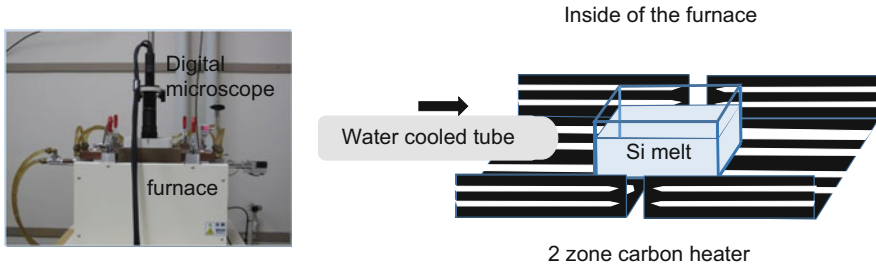


**Fig. 2** In situ observation system

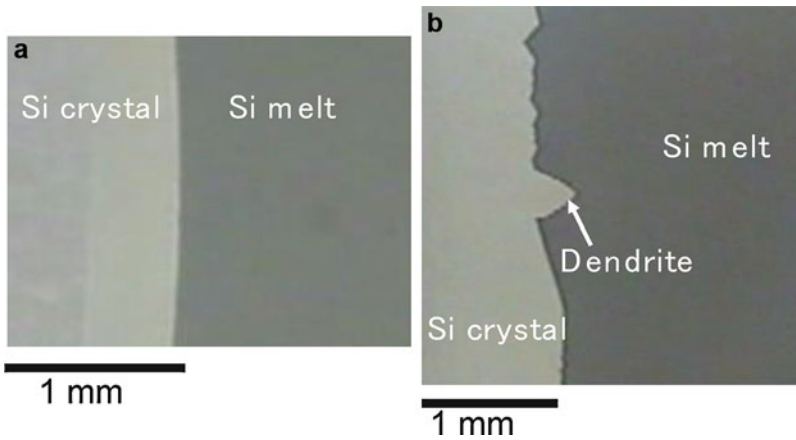


**Fig. 3** (a) Planar crystal/melt interface and (b) appearance of a dendrite growth

be  $\Delta T \approx 10$  K (Fujiwara et al. 2008). The typical structure of dendrite crystal is shown in Fig. 4 (Fujiwara et al. 2007). The most important feature of the dendrite crystals of Si is the existence of parallel twin boundaries at the center part, as shown in Fig. 4.

The features of dendrite crystal of Si are summarized as following (Fujiwara 2015):

1. The surface is bounded by  $\{111\}$  facet planes.
2. At least two parallel  $\{111\}$  twin boundaries exist at its center.
3. The preferential growth direction is  $\langle 112 \rangle$  or  $\langle 110 \rangle$  (hereafter, dendrites with these growth directions will be expressed as  $\langle 112 \rangle$  and  $\langle 110 \rangle$  dendrites, respectively).

Nagashio and Kuribayashi reported that twin-free dendrite, which preferentially grows to the  $\langle 100 \rangle$  direction, appeared in the highly undercooled melt,  $\Delta T > 100$  K (Nagashio and Kuribayashi 2005). In the casting process of mc-Si ingot, the

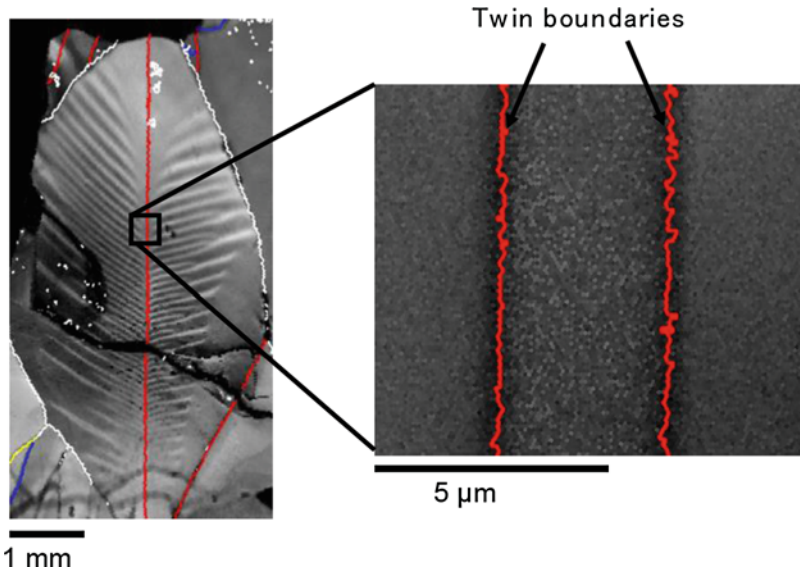


**Fig. 4** Structure of a dendrite crystal (Fujiwara et al. 2007)

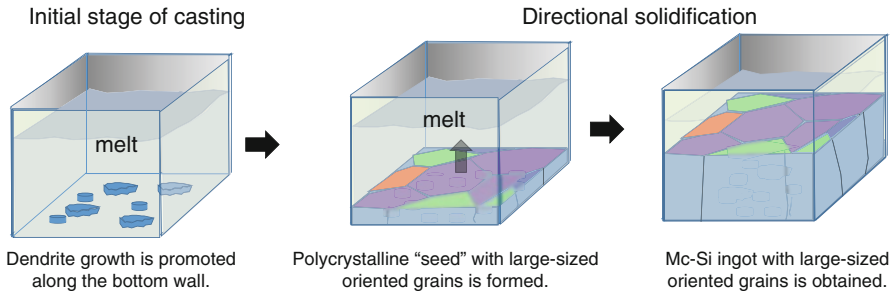


**Fig. 5** The growth concept of the dendritic cast method

undercooling at the crystal growth is not so high, and thus the  $\langle 112 \rangle$  and  $\langle 110 \rangle$  dendrites usually appear.

## Growth Concept of the Dendritic Cast Method

From the above features of dendrite crystals, it was considered that if one could control this growth mechanism in the casting, it would be able to obtain a mc-Si ingot with large-oriented crystal grains. Figure 5 shows a concept of growing a mc-Si ingot using dendrite growth in the casting. The dendrite growth is induced along the bottom wall of a crucible in the initial stage of casting by controlling the cooling conditions. To realize this process, the temperature field in the furnace should be controlled carefully.

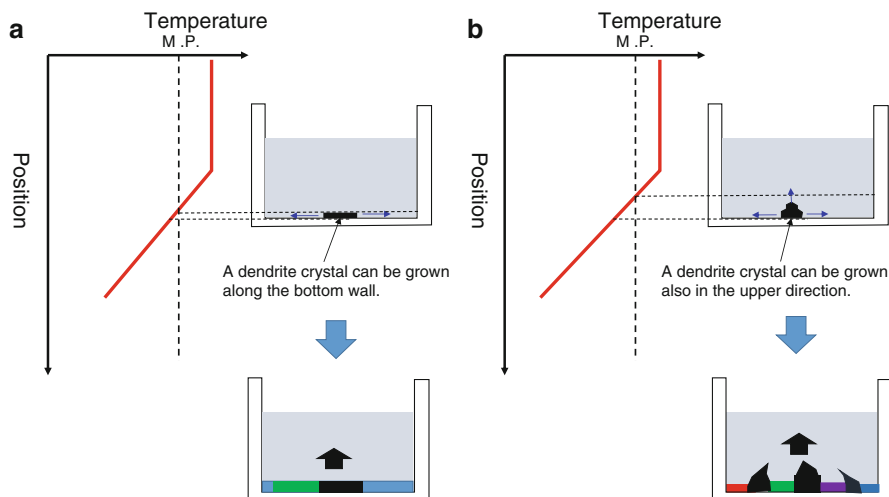


**Fig. 6** Schematic images of the growth of dendrite crystals in the initial stage of casting

Dendrite crystals can be grown only along the bottom wall of the crucible when the melt only at the bottom wall is undercooled, as shown in Fig. 6a. However, if the upper part of the melt is also in the undercooled state, the dendrite crystals can be grown not only along the bottom wall but also in the upper direction, as shown in Fig. 6b. The growth velocity of the dendrite crystal is very fast, and thus the crystal grains become very large. And, when the dendrite grows along the bottom wall of the crucible, the upper orientation of the dendrite crystal is limited to  $\{112\}$  or  $\{110\}$  ideally, and thus the oriented grain structures will be obtained in the initial stage of casting. If the dendrite crystals grew also in the upper direction in this initial stage, the grain size at the bottom part of the ingot becomes small and the grain boundary density increases. Moreover, the dendrite crystals grown in the upper direction will make a rough crystal/melt interface, as shown in Fig. 6b, which will cause the defect generation at the crystal/melt interface. Therefore, to obtain a high quality mc-Si ingot, the control of the dendrite growth in the initial stage is crucial. Subsequently, crystallization will be promoted in the upper direction from this bottom structure with large-size oriented grains. The concept shown in Fig. 5, which is called the dendritic cast method, does not require the use of any seeds and it was expected to be available for the growth of a large ingot by a commercial casting furnace. Needless to say, the enhancement and control of the dendrite growth at the bottom of the crucible is crucial in this method. In the next section, the conditions for promoting dendrite growth in the Si melt will be considered.

### Conditions for Growing a Dendrite Crystal in Si Melt

Here, let us consider the conditions for the initiation of the dendrite growth. As shown in Fig. 4, a dendrite crystal of Si contains at least two parallel  $\{111\}$  twin



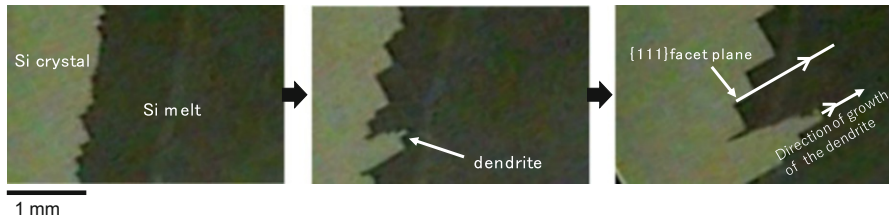


**Fig. 7** Dendrite growth initiated from a part of zigzag faceted interface (Fujiwara et al. 2007)

boundaries at its center part. This means that the crystal must contain two parallel twin boundaries for the initiation of the dendrite growth. It is well known that the formation energy of Si  $\{111\}$  twin boundary is quite low, such as  $30 \text{ mJ/m}^2$  (Kohyama et al. 1986). Therefore, twin boundaries are often observed in a mc-Si ingot after solidification. It seems that a twin boundary is formed by many reasons, such as the stress from the crucible and/or the thermal stress during cooling process and so on. However, here, the consideration of the parallel twin formation in a crystal during melt growth process is required.

To obtain information on the parallel twin formation during melt growth process, the crystal growth behavior of dendrites was directly observed by using an in situ observation system (Fujiwara et al. 2007). In that study, morphological change of the crystal/melt interface was observed. A planar crystal/melt interface changed to a zigzag faceted interface with decreasing melt temperature, and then, a dendrite crystal grew from a part of the faceted interface, as shown in Fig. 7. It was noted that the direction of growth of the dendrite crystal was parallel to the  $\{111\}$  facet plane on a zigzag faceted interface, as shown in Fig. 6 (the right image). This means that the parallel twins at the center of the dendrite crystal were formed parallel to the  $\{111\}$  facet plane on the zigzag faceted interface.

From this experimental facts, one model for the parallel twin formation was considered, as shown in Fig. 8 (Fujiwara et al. 2007). Since the growth interface is faceted (zigzag shape) at a high growth velocity, crystal growth is always promoted on the  $\{111\}$  facet planes. If an atom attaches on a facet plane with a twin relationship, a layer that maintains the twin relationship is formed on the facet plane after lateral growth, and then one twin boundary is generated on the layer, as shown in Fig. 8(2). It is expected that the atoms are often attached on the  $\{111\}$  growth plane with twin relationship because the grain boundary energy of Si  $\{111\}$  twin boundary is close to zero ( $\sim 30 \text{ mJ/m}^2$ ). Such twin configuration of adatoms may be rearranged so that adatoms obey the epitaxial configuration at the crystal surface to minimize the Gibbs free energy of the system when the driving force for crystallization is very low at near equilibrium condition. On the other hand, when the driving force is large, high undercooling, the growth of the layer with twin relationship should be promoted because of the faster growth kinetics and the larger energy gain due to the crystallization. Continuing the crystal growth in the lateral-growth mode (Fig. 8(3)), the another twin boundary will form parallel to the previous twin, as shown in Fig. 8(4). In this model, the formation of two parallel twins is

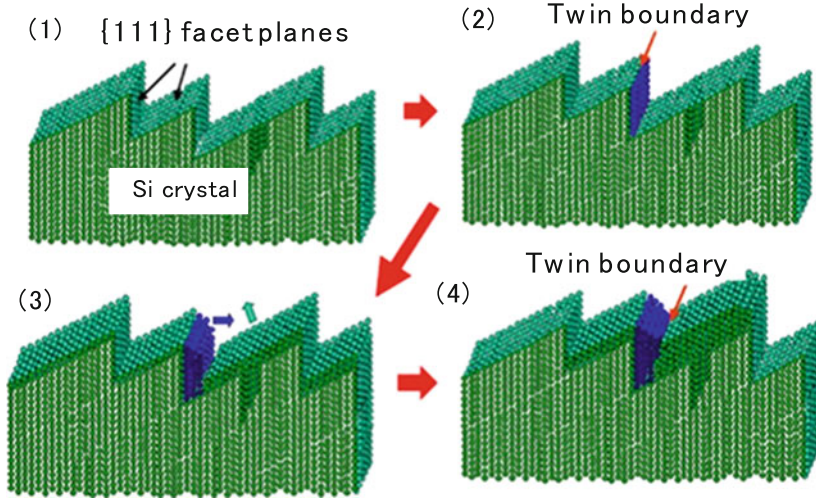


**Fig. 8** Model for parallel twin formation on the zigzag faceted crystal/melt interface

certain when one twin is formed on a facet plane at the growth surface. Here, it is found that the distance between the two parallel twin boundaries is dependent on the wavelength of the zigzag faceted interface. According to the theoretical treatment for the interface instability by Mullins and Sekerka (Mullins and Sekerka 1964), the wavelength of zigzag faceted interface decreases with increase in the growth velocity, and that was confirmed for the crystal/melt interface of Si by experiments (Tokairin et al. 2009; Fujiwara et al. 2011).

Next, the undercooling for the growth of the dendrite crystal should be considered. From the in situ observation experiments, the undercooling ( $\Delta T$ ) at the initiation of the growth of the dendrite crystal was estimated as  $\Delta T \approx 10$  K (Fujiwara et al. 2008). This value of the undercooling might be changed by the design of the furnace and the temperature field in the furnace. Now, the temperature field at the initiation of the dendrite growth is discussed below. First, the case that the parallel twin boundaries are generated into a crystal by the model shown in Fig. 8 is considered. In that model, the morphological transformation of the crystal/melt interface from a planar shape to a zigzag faceted shape is required for the parallel twin formation. A crystal grain born at the bottom of the crucible will grow along the bottom wall of the crucible, as schematically shown in Fig. 9 (Fujiwara et al. 2011). The crystal grain does not contain twin boundaries. It seems that a fluctuation is often generated on the planar crystal/melt interface during growth. When the temperature gradient in the melt at the crystal/melt interface is positive, the crystal grows with a planar crystal/melt interface because the temperature at the top of the fluctuation is higher than that at the bottom of the fluctuation, that is, the growth velocity at the bottom of the fluctuation is faster than that at the top part. Therefore, a zigzag faceted interface will not be established, as shown in Fig. 9a. On the other hand, under the negative

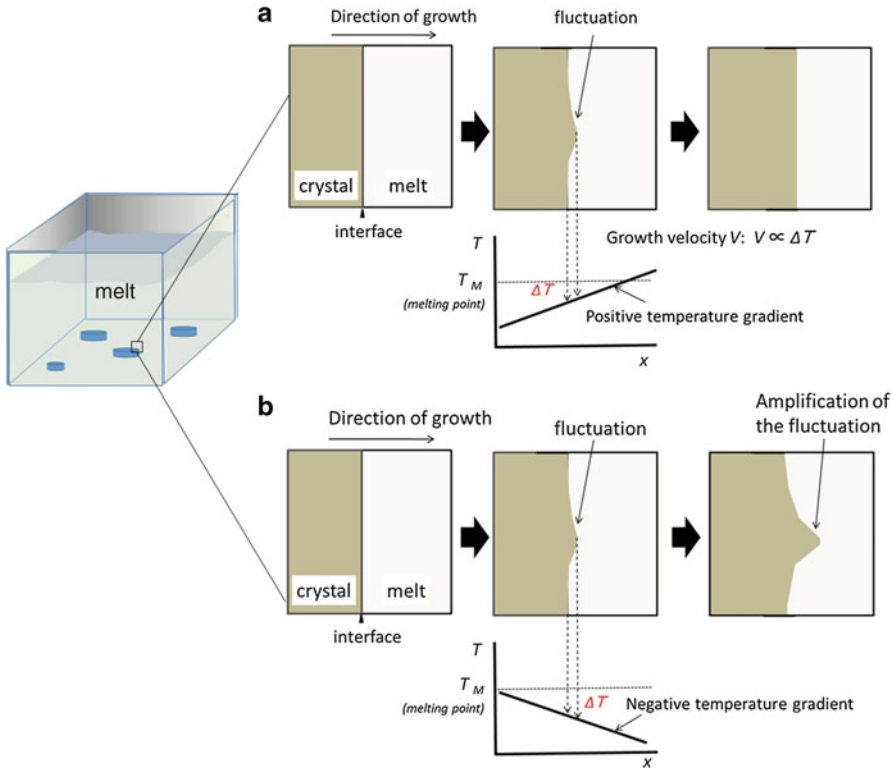


**Fig. 9** Crystal/melt interface under (a) positive temperature gradient and (b) negative temperature gradient when the crystal grain contains no twin boundaries (Fujiwara et al. 2011)

temperature gradient, the fluctuation will be amplified, which leads to the formation of zigzag faceted interface, as shown in Fig. 9b. In this case, the parallel twin boundaries could be formed based on the model of Fig. 8, and then, the dendrite growth will be initiated after the parallel twin formation. The temperature gradient in the melt at the crystal/melt interface is affected by the thermal field in the ambient surrounding the crystal and the growth velocity which is related to the amount of the latent heat of crystallization. A smaller temperature gradient in the ambient requires a lower growth velocity to change the temperature gradient in the melt at the crystal/melt interface from positive to negative. Usually, in the casting furnace, the temperature gradient in the growth direction of the ingot is positive, as shown in Fig. 6. On the other hand, the temperature field vertical to the growth direction is almost homogeneous. Therefore, when a crystal grain is born in the undercooled melt at the bottom wall of the crucible, it seems that the negative temperature gradient is easily formed in front of the crystal/melt interface because the temperature at the crystal/melt interface reaches melting temperature due to the latent heat and the melt surrounding the crystal grain is undercooled. One can easily imagine that if the melt of the upper part of the crystal grain is also

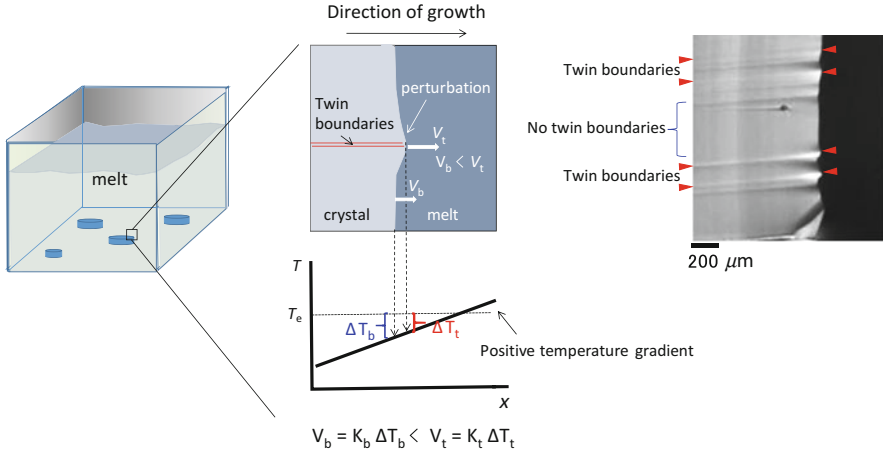


**Fig. 10** The explanation for the initiation of the dendrite growth even under the positive temperature gradient when the crystal grain contains twin boundaries (Fujiwara et al. 2014)

undercooled, dendrite crystals is possible to grow to upper direction, as explained in Fig. 6b, which is not suitable for obtaining a high quality ingot.

Next, in Fig. 10, we consider the case that the crystal grain originally contains parallel twin boundaries, those were formed by some kind of mechanisms except the model in Fig. 8 (Fujiwara et al. 2014). The growth velocity is roughly expressed as  $V \approx K\Delta T$ , where  $K$  and  $\Delta T$  are the kinetic constant and undercooling, respectively. When the temperature gradient is positive, the undercooling at the bottom part ( $\Delta T_b$ ) is larger than that at the top part ( $\Delta T_t$ ) of the fluctuation,  $\Delta T_t < \Delta T_b$ , as shown in Fig. 10. Therefore, the kinetic constant at the twin boundaries ( $K_t$ ) must be larger than that in the area without twin boundaries ( $K_b$ ),  $K_t > K_b$ , to amplify the fluctuation. Actually, it seems that the crystallization is easier at the twin boundary than at the  $\{111\}$  flat plane, as shown by atomic models in Fig. 11. When the atoms in the melt crystallize on the  $\{111\}$  plane, a trio of atoms is required to connect half of their bonds with each other, as shown in the left image of Fig. 11. On the other hand, a pair of atoms can satisfy this condition, as shown in the right image of Fig. 11. When the condition  $K_t\Delta T_t/K_b\Delta T_b > 1$  is satisfied, the dendrite growth is initiated at the parallel twin boundaries. The difference between  $\Delta T_t$  and  $\Delta T_b$  is dependent on the temperature gradient at the interface. One can predict that when the positive temperature gradient is steep,  $\Delta T_t \ll \Delta T_b$ , a planar interface will be maintained because the growth velocity at the bottom of the fluctuation ( $V_b$ ) will be larger than that at the top of the fluctuation ( $V_t$ ). On the other hand, under a low positive temperature gradient, the fluctuation at the twin boundaries is amplified owing to the larger  $K_t$ . In this case, dendrite growth will appear at lower undercooling than in the case that crystal originally does not contain the twin boundaries (Fig. 9).

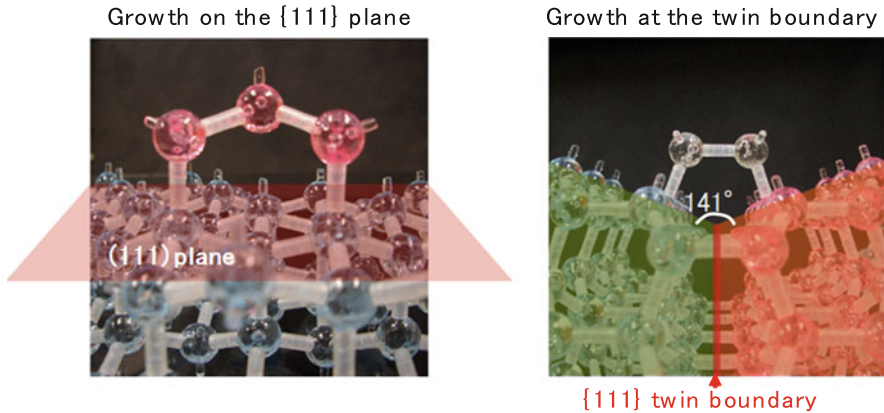


**Fig. 11** Atomic models of crystal/melt interface of  $\{111\}$  plane (*left*) and at twin boundary

## Mc-Si Ingot Grown by the Dendritic Cast Method

### Growth of a Small Size mc-Si Ingot

In the earlier experiments of the dendritic cast method, mc-Si ingots were grown with a 50-mm-diameter silica crucible with  $\text{Si}_3\text{N}_4$  coating. As mentioned above, the undercooling of  $\Delta T \approx 10$  K seemed to be required to induce dendrite growth in the initial stage of directional growth (Fujiwara et al. 2006a). Therefore, the bottom of the crucible was cooled fast to induce the dendrite growth and then the crucible was pulled down at 0.2 mm/min in the temperature gradient zone of 20 K/cm. In the fast cooling process for promoting dendrite growth along the bottom wall of the crucible, the steep temperature gradient in the direction of growth of the ingot is required, as explained in Fig. 6. In addition, generally, a fixed time is required until the dendrite crystals grow to cover the whole bottom wall. Another ingot was grown by simply pulling the crucible down at 0.2 mm/min in the same temperature gradient, for comparison. Figure 12a, b show the orientation maps of 15 mm<sup>2</sup> wafers cut from the bottom, middle, and top parts of ingots grown by (a) a dendritic cast method and (b) a conventional cast method (Fujiwara et al. 2006a). Near the (112) plane was seen to occupy almost the entire surface of the wafers and large grains were observed in the bottom part to top part in wafers cut from the ingot grown by a dendritic cast method, as shown in Fig. 12a, because  $\langle 110 \rangle$  dendrites grew along the bottom wall of the crucible in the initial stage. On the other hand, many equiaxed grains with random orientations were observed in wafers cut from the ingot grown by a conventional cast method, as shown in Fig. 12b. Figure 13a, b shows the typical properties of solar cells based on mc-Si wafers cut from the two ingots (Fujiwara et al. 2006a). A higher energy conversion efficiency was obtained for the Si wafer obtained by the dendritic cast method. The results in Figs. 12 and 13 show that the



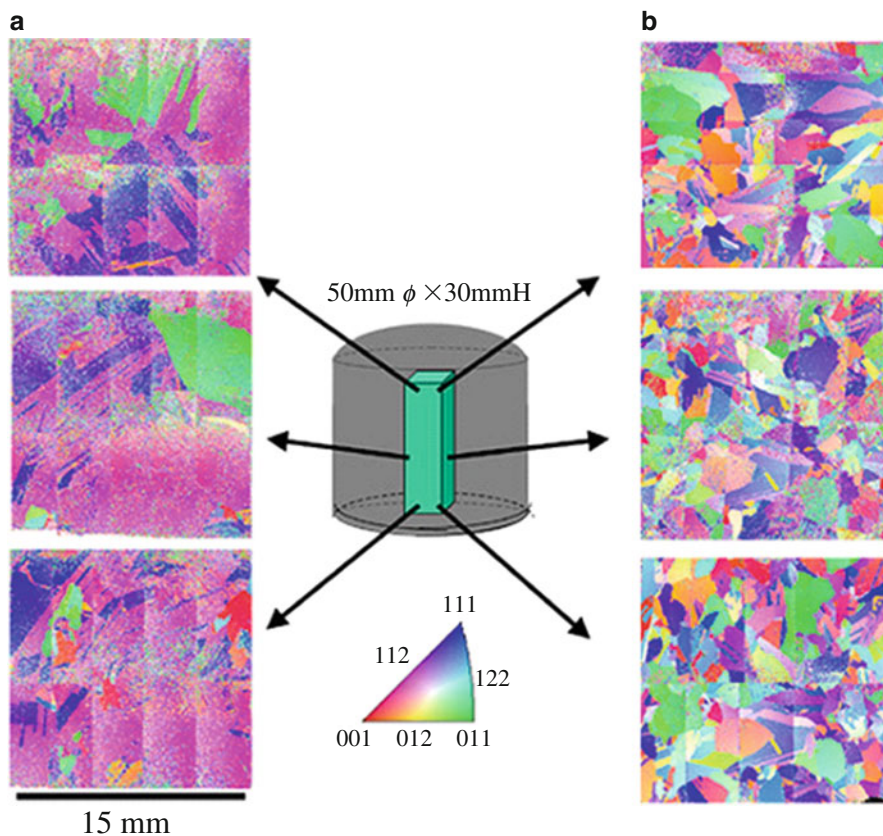


**Fig. 12** Orientation maps in Si wafers cut from the ingot grown by (a) a dendritic cast method and (b) a conventional cast method (Fujiwara et al. 2006a)

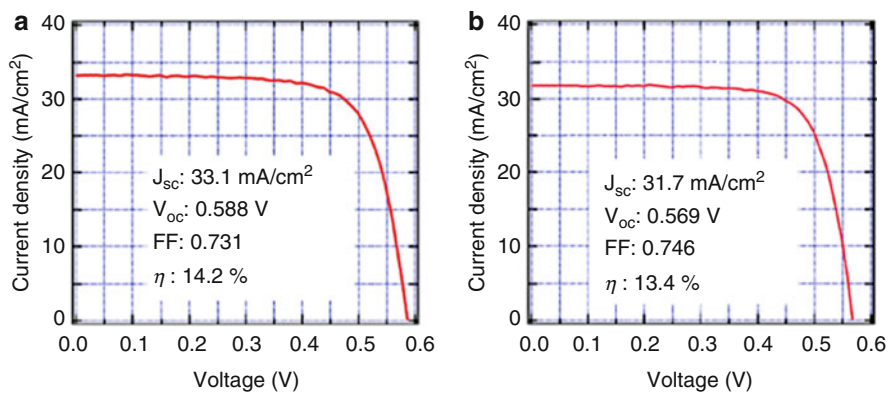


**Fig. 13** I-V curves of wafers cut from the ingot grown by (a) a dendritic cast method and (b) a conventional cast method (Fujiwara et al. 2006a)

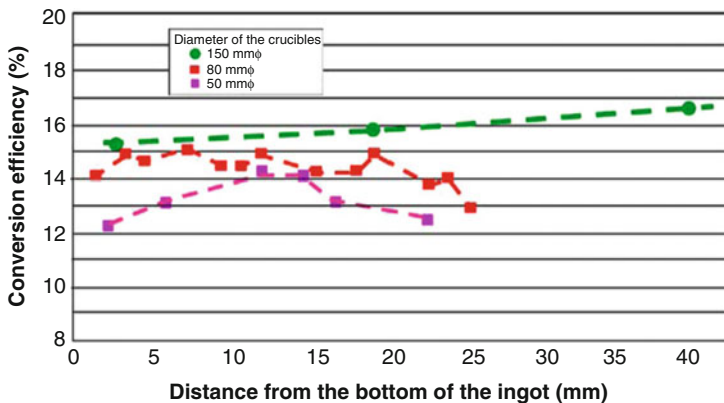


**Fig. 14** Solar cell efficiencies of the wafers cut from mc-Si ingots grown by dendritic cast method. The diameters of the crucible were 50 mmφ, 80 mmφ, and 150 mmφ (Fujiwara et al. 2006a)

growth concept of the dendritic cast method is promising for obtaining a mc-Si ingot suitable for solar cells. We also investigated the effect of crucible size on solar cell properties. Figure 14 shows the energy conversion efficiencies of solar cells based on the mc-Si wafers cut from the ingot grown by a dendritic cast method. The diameters of the crucible used were 50 mmφ, 80 mmφ, and 150 mmφ (Fujiwara et al. 2006a). Conversion efficiency increased with increasing crucible size. The highest efficiency of the solar cells was more than 16% even without a surface textural structure or hydrogen passivation during solar cell processes. For comparison, we also fabricated a solar cell based on an sc-Si wafer grown by the Czochralski method using the same solar cell process as above and obtained a conversion efficiency of 17%.

## Improvement of the Dendritic Cast Method

Researchers made an effort for the improvement of the dendritic cast method for the sake of use in practical (Nakajima et al. 2009, 2010a, b, 2011; Yang et al. 2015). Solar cells based on mc-Si wafers obtained from ingots grown by the dendritic cast method were fabricated by SHARP Co (Nakajima et al. 2009, 2010a, b, 2011), and the top values of the energy conversion efficiency were 18.2% for Si wafer of  $10 \times 10 \text{ cm}^2$  and 17.7% for Si wafer of  $15.6 \times 15.6 \text{ cm}^2$ . Dendritic cast method has a potential to control not only grain size and grain orientation but also grain boundary characteristics. As shown in Fig. 15, when the dendrite crystals grow to random direction at the bottom of the crucible, the grain boundaries formed by the impingement of dendrite crystals will become random grain boundaries. On the other hand, if the direction of the growth of dendrite crystals would be controlled to one direction, the formed grain boundary would be  $\{111\}\Sigma 3$  twin boundary, because the side surface of the dendrite crystal is  $\{111\}$  plane owing to the existence of two parallel  $\{111\}$  twin boundaries at the center of the dendrite crystal. Actually, it was reported that the angle of the impingement of two dendrite crystals affected the

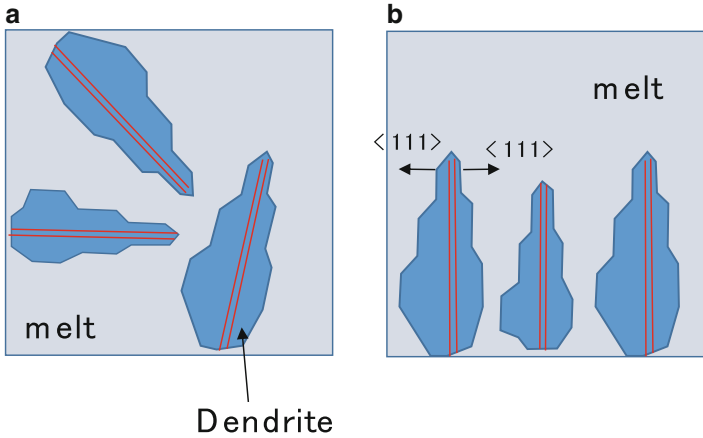


**Fig. 15** Schematic image of the control of dendrite growth at the *bottom* of the crucible. (a) In case that dendrites grow to random direction. Random grain boundaries will be formed at the impingement of the dendrites. (b) In case that dendrites grow to the same direction,  $\Sigma 3$  twin boundaries will be formed at the impingement of the dendrites

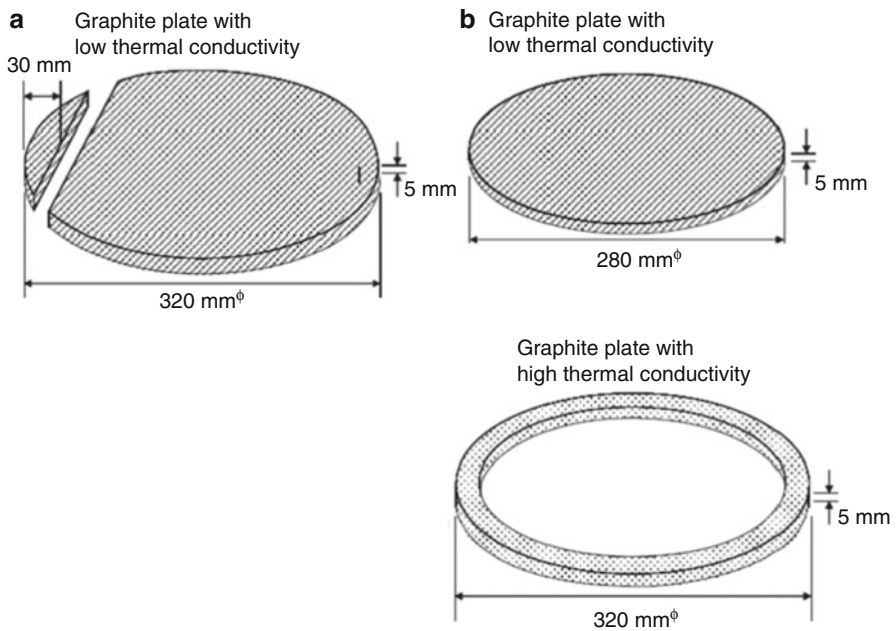


**Fig. 16** Graphite plates set under the crucible to control the dendrite growth (Nakajima et al. 2011)

dislocation density at the formed grain boundaries (Takahashi et al. 2015). It was shown that the parallel arrangement of dendrite crystals beneficially decreased dislocation density.



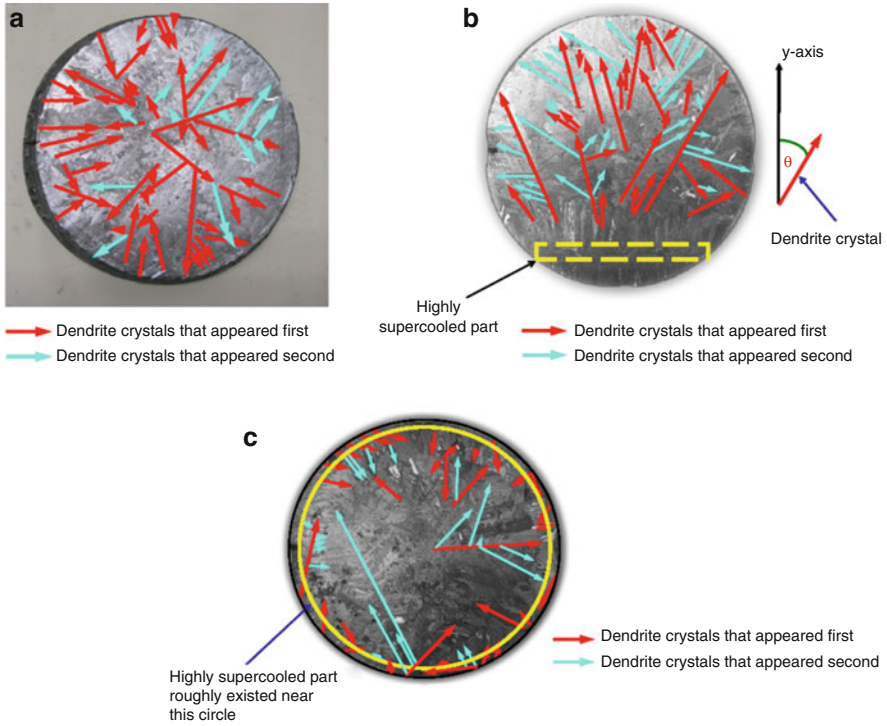


**Fig. 17** Bottom structures of mc-Si ingot grown by a dendritic cast method using (a) no graphite plates, (b) a graphite plate with a line-shaped highly cooled part, and (c) two kinds of graphite plates with a ring-shaped highly cooled part (Nakajima et al. 2011)

Nakajima et al. attempted to control the direction of growth of the dendrite crystals at the bottom wall of crucible by using graphite plates with different thermal conductivity (Nakajima et al. 2011). They set carbon plates under the crucible (Fig. 16). In case of Fig. 16a, there was a line-shaped highly cooled part by making a gap in a circular graphite plate. In case of Fig. 16b, there was a ring-shaped highly cooled part, which were made by combining graphite plates with high and low thermal conductivities of 40 and 0.35 W/m K, respectively.

Figure 17 shows bottom structures of mc-Si ingot grown by dendritic cast method with (a) no graphite plates, (b) a graphite plate with a line-shaped highly cooled part, and (c) a ring-shaped highly cooled part combining two kinds of graphite plates. When the dendrite growth was promoted by cooling all over the bottom part in the initial stage of casting, dendrite crystals grew to random direction, as indicated by arrows. On the other hand, in the ingot grown using a graphite plate with a line-shaped highly cooled part, most of dendrite crystals initiated to grow at the line-shaped highly cooled part. Also, in the ingot grown using two kinds of graphite plates with a ring-shaped highly cooled part, dendrite crystals initiated to grow at the edge part due to the existence of a ring shape high-thermal conductivity graphite. In this way, the direction of the growth of the dendrite could be controlled by the

generation of a local cooling system at the bottom of the crucible. Wang et al. attempted to control the nucleation site and initial grain growth by using a spot cooling (Wang et al. 2009). They also obtained large size grains due to the promotion of the dendrite growth.

## Problems and Future Developments of the Dendritic Cast Method

The dendritic cast method was attempted to use in the industrial-scale furnace. Yang et al. grew mc-Si ingots by changing the undercooling at the bottom of the crucible (Yang et al. 2015). Figure 18 shows bottom structures of three typical ingots obtained by controlling undercooling. It was shown that dendrite structures were obtained at highly undercooled region. They reported that “the control of undercooling in the industrial-scale furnace became much more difficult due to the much higher thermal resistance of the crucible and the heat exchanger block, as well as the coating uniformity in large area for nucleation” (Yang et al. 2015). Actually, the undercooling and the direction of heat releasing at the bottom of the crucible have to be controlled for controlling the dendrite growth in the initial stage of casting. Some kind of devices, such as the combining graphite plates with high and low thermal conductivities, which was attempted by Nakajima et al., will be required to control the dendrite growth.

Generation of dislocations is also the problem. In the dendritic cast method, dislocation densities decreased in comparison with a conventional casting method. However, the dislocations generated in the initial stage of casting, generally at the grain boundary, will develop during directional solidification, as shown in Fig. 19 (Ryningen et al. 2011). Larger sized crystal grains obtained by the dendritic cast method leads to decrease in the grain boundary density; however, this means that

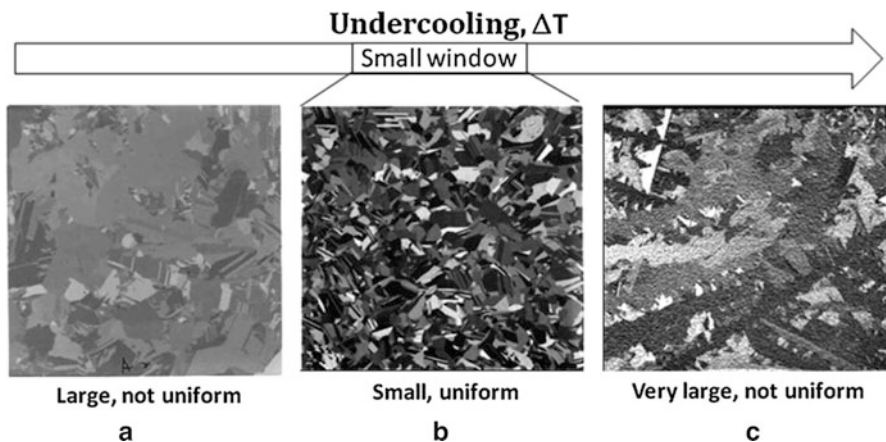
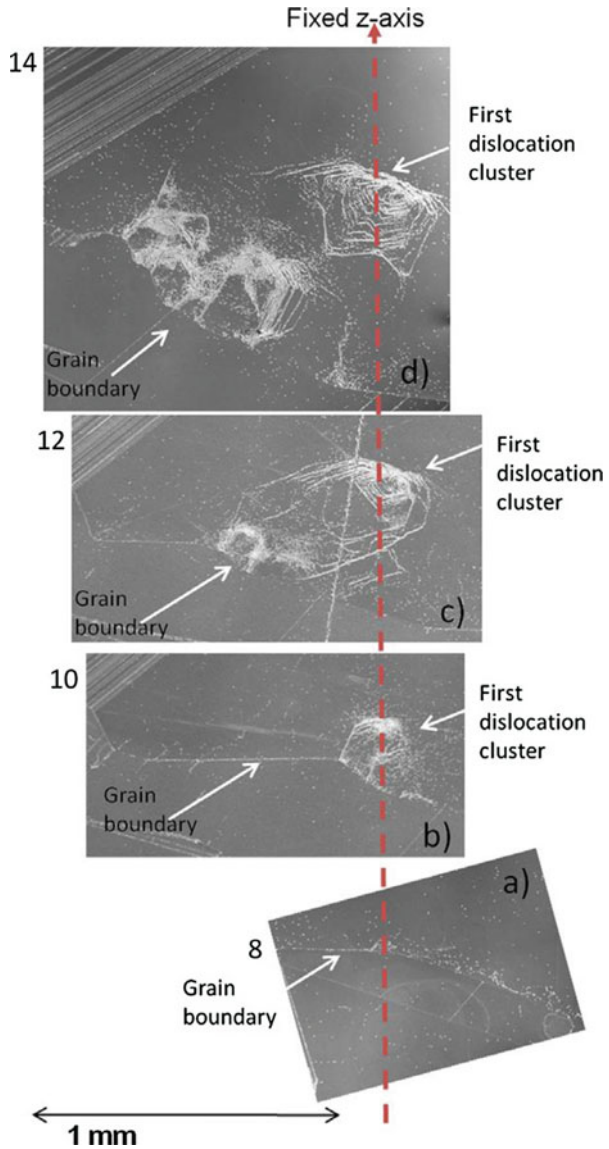


**Fig. 18** Bottom structures of mc-Si ingots by controlling undercooling (Yang et al. 2015)

**Fig. 19** Development of dislocation clusters during directional solidification (Ryningen et al. 2011)



dislocations are difficult to be absorbed in grain boundaries during directional solidification due to the low density of random grain boundary. To decrease the dislocation density at the initial stage of casting, first, the density of dendrite crystal should be decreased to reduce the density of grain boundary which becomes the source of dislocations. In addition, it is necessary not only to control the direction of growth of the dendrite crystals, but also to disturb the impurity contamination and

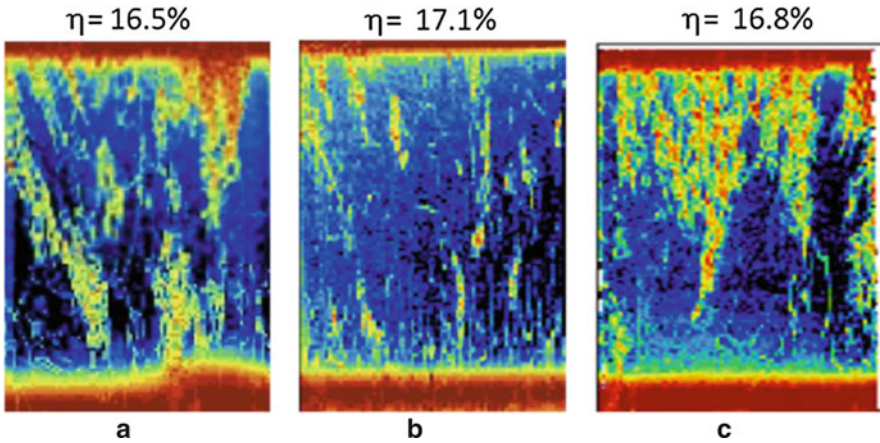


**Fig. 20** Life time mapping and average conversion efficiency of the bricks and wafers obtained by (a) a conventional cast method, (b) Hp Mc-Si, and (c) a dendritic cast method (Yang et al. 2015)

the stress generation from the crucible wall coated with  $\text{Si}_3\text{N}_4$  powders, which is the common problem in all kinds of casting methods.

Recently, the high-performance mc-Si (HP mc-Si) is widely used in industry (Yang et al. 2015), as described in Chapter 10 in this book (see ► [Chap. 7, “Growth of Multicrystalline Silicon for Solar Cells: The High-Performance Casting Method”](#)). HP mc-Si ingots include uniform small sized (a few millimeters) crystal grains and high density of random grain boundaries. It seems that dislocations will be absorbed into the random grain boundaries during directional solidification, and thus the dislocation density in the ingot decreases. Therefore, at present, the minority carrier lifetime of HP mc-Si is higher than that of mc-Si grown by a conventional casting method and a dendritic cast method, as shown in Fig. 20 (Yang et al. 2015).

In future, if the densities of dislocation and impurities (carbon and oxygen) are reduced in the mc-Si ingot with larger sized crystal grains, the order will be changed like Fig. 21, because the grain boundary is the defect itself which acts as a recombination center of photocarriers. Further, in the process of solar cells, a solar cell based on mc-Si wafer loses about 1% of energy conversion efficiency because of their inefficient surface textural structure. If a mc-Si wafer with large-size oriented grains would be obtained, a better surface textural structure will be obtained, which leads to a higher energy conversion efficiency of solar cells.

As one of the future developments, a nonwetting cast method combining the dendritic cast method was proposed (Fujiwara et al. 2015). The growth concept is shown in Fig. 22. In this method, the purities of atmosphere and raw Si materials, and the material for crucible should be taken care to realize a state that a Si melt is nonwetting and nonreactive with a crucible at high temperature (Fig. 22a). The impurity contamination and stress generation into Si crystal from the crucible or

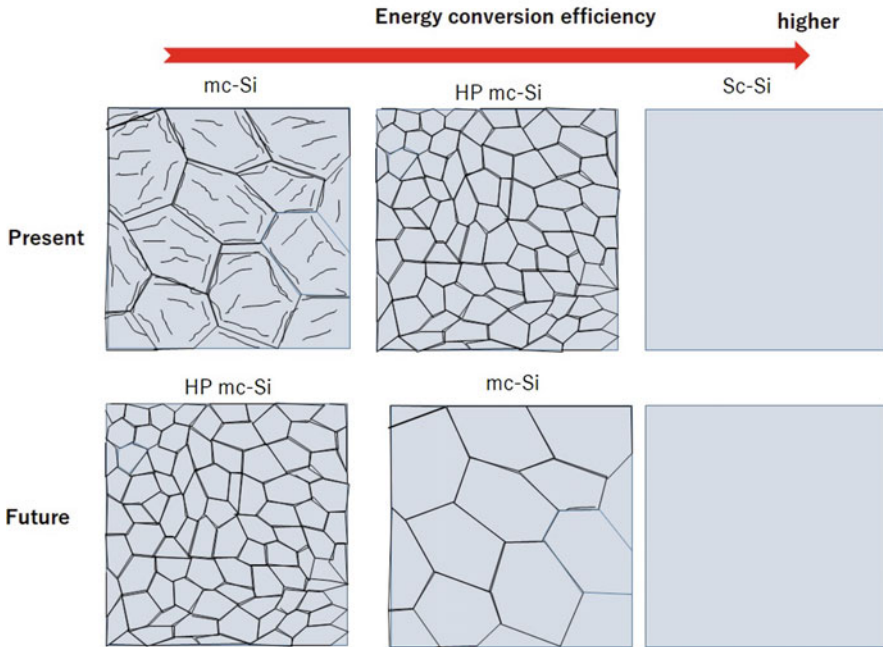


**Fig. 21** Grain structures and energy conversion efficiency of solar cells

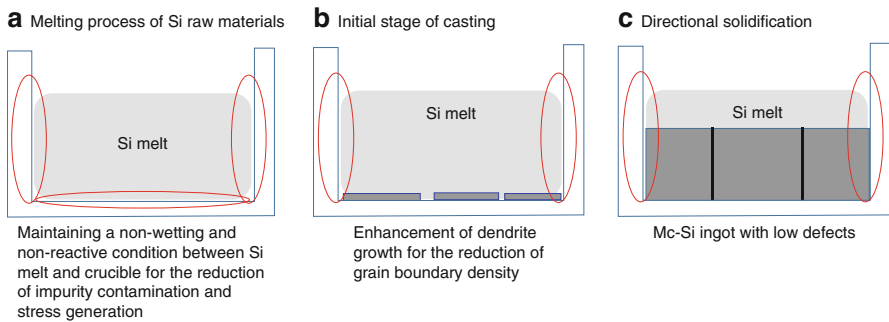


**Fig. 22** Growth concept combining a non-wetting and a dendritic cast methods

coating materials will be disturbed when the ingot is grown from the Si melt maintaining the state that nonwetting and nonreactive with a crucible. The dendritic cast method, enhancing the dendrite growth in the initial stage of casting, will be useful for obtaining larger-sized oriented crystal grains to reduce the grain boundary density (Fig. 22b). The nonwetting and nonreactive condition should be maintained during directional solidification process.



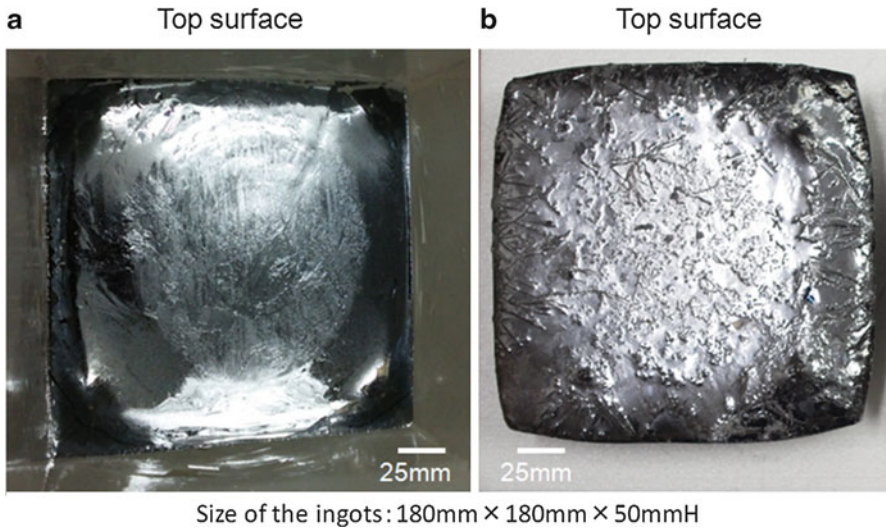


**Fig. 23** Top surface of as grown mc-Si ingots grown by (a) nonwetting dendritic cast method and (b) conventional cast method (Fujiwara et al. 2015)

Based on this growth concept, it was attempted to grow a mc-Si ingot (Fujiwara et al. 2015). Barium hydroxide was spread all over the inner surface of a quartz crucible, instead of  $\text{Si}_3\text{N}_4$  coating, and fired it. For comparison, a similar quartz crucible (GE214) with  $\text{Si}_3\text{N}_4$  coating was used for growing mc-Si ingot. Figure 23 shows the top surfaces of as-grown mc-Si ingots grown by the method of Fig. 22 (hereafter, nonwetting dendritic cast method) and the conventional method. The surface of the ingot grown by the nonwetting dendritic cast method was much shinier. Figure 24 shows the side and bottom surfaces of both as-grown mc-Si ingots. The surfaces of the ingot grown by the nonwetting dendritic cast method were very smooth and shiny, so that the grain structures were not visible, while the surfaces of the ingot grown by the conventional method were rough and the grain structures were visible. Those results indicated that wetting and reaction between the Si melt and crucible were restrained.

The minority carrier lifetime of the wafers with a size of  $125 \times 125 \times 0.2 \text{ mm}^3$  cut from the middle part of both ingots was measured. The average values of minority carrier lifetime of the wafer cut from the ingot grown in a nonwetting cast method was about three times higher than that of the wafer taken from the ingot grown by the conventional method. These results indicate that the mc-Si ingot grown by a nonwetting dendritic cast method has the potential for the production of high-quality mc-Si ingot for solar cells.

The development of this technology was just started and should be improved more and more. However, if this technology will be completely established, the mc-Si ingot with low densities of impurity, dislocation, and grain boundary will be realized.

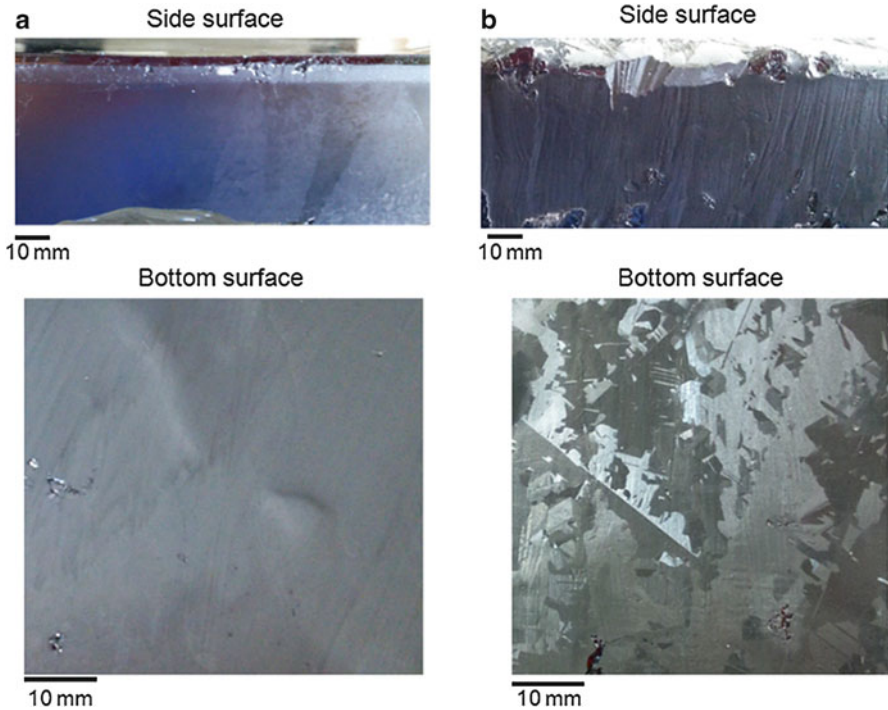


**Fig. 24** Side and bottom surfaces of as grown mc-Si ingots grown by (a) nonwetting dendritic cast method and (b) conventional cast method (Fujiwara et al. 2015)

---

## Concluding Remarks

The dendritic cast method is a unique method for controlling grain structures in mc-Si ingots. Large-sized oriented grain structure is obtained by this method. On the other hand, the control of undercooling in the initial stage of casting and decrease of dislocation density during directional solidification process in the industrial scale furnace are the main problems. However, the ideas to overcome these problems have been proposed, which suggested us the direction for the improvement of this method. The continuous efforts by the researchers will lead to the establishment of this technology for producing high-quality mc-Si ingots.

---

## Cross-References

- ▶ [Growth of Crystalline Silicon for Solar Cells: Czochralski Si](#)
- ▶ [Growth of Crystalline Silicon for Solar Cells: Mono-Like Method](#)

- ▶ [Growth of Crystalline Silicon for Solar Cells: Noncontact Crucible Method](#)
- ▶ [Growth of Multicrystalline Silicon for Solar Cells: The High-Performance Casting Method](#)

---

## References

- N. Albon, A.E. Owen, *J. Phys. Chem. Solids* **24**, 899 (1963)
- D.L. Barrett, E.H. Myers, D.R. Hamilton, A.I. Bennett, *J. Electrochem. Soc.* **118**, 952 (1971)
- A.I. Bennett, R.L. Longini, *Phys. Rev.* **116**, 53 (1959)
- E. Billig, *Proc. R. Soc. A* **229**, 346 (1955)
- T.F. Cizsek, G.H. Schwuttke, K.H. Yang, *J. Cryst. Growth* **46**, 527 (1979)
- K. Fujiwara, in *Handbook of Crystal Growth*, vol. 1B, 2nd edn., ed. by T. Nishinaga (Elsevier, Amsterdam, 2015), p. 723
- K. Fujiwara, K. Nakajima, T. Ujihara, N. Usami, G. Sazaki, H. Hasegawa, S. Mizoguchi, K. Nakajima, *J. Cryst. Growth* **243**, 275 (2002)
- K. Fujiwara, Y. Obinata, T. Ujihara, N. Usami, G. Sazaki, K. Nakajima, *J. Cryst. Growth* **262**, 124 (2004)
- K. Fujiwara, W. Pan, N. Usami, K. Sawada, M. Tokairin, Y. Nose, A. Nomura, T. Shishido, K. Nakajima, *Acta Mater.* **54**, 3191 (2006a)
- K. Fujiwara, W. Pan, K. Sawada, M. Tokairin, N. Usami, Y. Nose, A. Nomura, T. Shishido, K. Nakajima, *J. Cryst. Growth* **292**, 282 (2006b)
- K. Fujiwara, K. Maeda, N. Usami, G. Sazaki, Y. Nose, K. Nakajima, *Scr. Mater.* **57**, 81 (2007)
- K. Fujiwara, K. Maeda, N. Usami, G. Sazaki, Y. Nose, A. Nomura, T. Shishido, K. Nakajima, *Acta Mater.* **56**, 2663 (2008)
- K. Fujiwara, R. Gotoh, X. Yang, H. Koizumi, J. Nozawa, S. Uda, *Acta Mater.* **59**, 4700 (2011)
- K. Fujiwara, M. Tokairin, W. Pan, H. Koizumi, J. Nozawa, S. Uda, *Appl. Phys. Lett.* **104**, 182110 (2014)
- K. Fujiwara, Y. Horioka, S. Sakuragi, *Energy Sci. Eng.* **3**, 419 (2015)
- D.R. Hamilton, R.G. Seidensticker, *J. Appl. Phys.* **31**, 1165 (1960)
- M. Kohyama, R. Yamamoto, M. Doyama, *Phys. Stat. Sol. B* **138**, 387 (1986)
- C.F. Lau, H.W. Kui, *Acta Metall. Mater.* **39**, 323 (1991)
- D. Li, D.M. Herlach, *Phys. Rev. Lett.* **77**, 1801 (1996)
- W.W. Mullins, R.F. Sekerka, *J. Appl. Phys.* **35**, 444 (1964)
- K. Nagashio, K. Kuribayashi, *Acta Mater.* **53**, 3021 (2005)
- K. Nakajima, N. Usami, K. Fujiwara, K. Kutsukake, S. Okamoto, in *Proceedings of the 24th European Photovoltaic Solar Energy Conference*, 2009, p. 1219
- K. Nakajima, K. Kutsukake, K. Fujiwara, N. Usami, S. Ono, I. Yamasaki, in *Proceedings of the 35th IEEE Photovoltaic Specialists Conference*, 2010a, p. 817
- K. Nakajima, K. Kutsukake, K. Fujiwara, N. Usami, S. Ono, I. Yamasaki, in *Proceedings of the 25th European Photovoltaic Solar Energy Conference and Exhibition (25th EU PVSEC); the 5th World Conference on Photovoltaic Energy Conversion (WCPEC-5)*, 2010b, p. 1299
- K. Nakajima, K. Kutsukake, K. Fujiwara, K. Morishita, S. Ono, *J. Cryst. Growth* **319**, 13 (2011)
- S. O'Hara, A.I. Bennett, *J. Appl. Phys.* **35**, 686 (1964)
- B. Rynningen, G. Stokkan, M. Kivambe, T. Ervik, O. Lohne, *Acta Mater.* **59**, 7703 (2011)
- I. Takahashi, S. Joonwichien, S. Matsushima, N. Usami, *J. Appl. Phys.* **117**, 095701 (2015)
- M. Tokairin, K. Fujiwara, K. Kutsukake, N. Usami, K. Nakajima, *Phys. Rev. B* **80**, 174108 (2009)
- R.S. Wagner, *Acta Metall.* **8**, 57 (1960)
- Y. Wang, Y. Hsu, C.C. Fei, K.M. Yei, W.C. Hsu, C.W. Lan, *J. Cryst. Growth* **311**, 263 (2009)
- Y.M. Yang, A. Yu, B. Hsu, W.C. Hsu, A. Yang, C.W. Lan, *Prog. Photovolt. Res. Appl.* **23**, 340 (2015)





# Growth of Crystalline Silicon for Solar Cells: Mono-Like Method

# 9

Kentaro Kutsukake

## Contents

Introduction .....	216
Fundamentals of the Mono-Like Method .....	217
Seed Growth .....	217
Advantages and Disadvantages of the Mono-Like Method .....	219
Dislocation Generation .....	221
Influence of Grain Boundary Microstructure .....	221
Influence of Stress Distribution .....	223
Advanced Mono-Like Methods .....	225
Functional Grain Boundaries .....	225
Seed Manipulation for Artificially Controlled Defects Technique (SMART) .....	228
Control of Seed Joint Structure: Special Grain Boundaries and Seed Partitions .....	230
Mono-Like Growth Without Seed Joints: Large Seed and Mushroom-Type Interface Growth .....	232
Conclusions .....	232
Cross-References .....	233
References .....	233

## Abstract

The mono-like method, also known as the mono cast, seed cast, and quasi-mono methods, is a candidate next-generation method of casting Si ingots for solar cell applications, replacing conventional casting methods. The mono-like method provides single crystalline Si ingots with the use of almost the same facilities as those used for growth of multicrystalline Si ingots. Hence, the mono-like method has potential to achieve Si ingots with both high quality and low cost. However, the mono-like method faces challenges owing to its crystal growth processes,

---

K. Kutsukake (✉)

Center for Advanced Intelligence Project, RIKEN, Tokyo, Japan

e-mail: [kentaro.kutsukake@riken.jp](mailto:kentaro.kutsukake@riken.jp)

© Springer-Verlag GmbH Germany, part of Springer Nature 2019

D. Yang (ed.), *Handbook of Photovoltaic Silicon*,

[https://doi.org/10.1007/978-3-662-56472-1\\_35](https://doi.org/10.1007/978-3-662-56472-1_35)

215

such as multicrystallization, dislocation generation, and impurity contamination. To address these problems, advanced mono-like methods have been developed. In this chapter, advanced mono-like methods are reviewed from the viewpoint of crystal growth and the fundamentals of the mono-like method.

---

**Keywords**

Silicon · Crystal growth · Mono-like · Seed growth · Seed cast · Quasi-mono · Dislocations · Dislocation generation · Grain boundaries · Defect engineering · Artificial grain boundaries · Functional defects

---

## Introduction

The mono-like method is a growth method for single crystalline Si ingots based on a casting method. Almost the same growth furnace and procedures as those for multicrystalline silicon (mc-Si) can be used. The similarity with the mc-Si casting process leads to advantages in terms of low cost and high throughput. The main difference with mc-Si processes is that single crystalline Si ingots can be obtained with the use of single crystalline seeds. Generally, single crystalline Si solar cells show higher performance than those based on mc-Si, and this is also true for single crystalline Si grown by the mono-like method (e.g., Mrcarica 2013, Jay et al. 2014, and Jouini 2018). Thus, mono-like Si has both the advantages of single crystalline and multicrystalline Si and represents a potential high-quality low cost-material for solar cells.

The development of mono-like methods for solar cell applications started following the BP solar report (Stoddard et al. 2008). The idea of growing single crystalline Si in a crucible together with seed crystals had been suggested for a long time (e.g., Ciszek et al. 1979). The BP solar breakthrough was to demonstrate that a single crystalline ingot could be obtained with a practically useful size. Considerable research and development followed this initial report; however, the market share of the mono-like method remains low at present. The reasons for this low-market share are related to the ingot cost and quality, which are in turn controlled by the crystal growth process and crystal defects in mono-like ingots. Thus, further research to address these issues is necessary for developing and practically applying the mono-like method.

In this chapter, first the fundamentals of the mono-like method are described from the viewpoint of crystal growth. Then, advanced mono-like methods such as functional grain boundaries, functional defects, and mushroom-type interface growth are presented. Most of these advanced methods aim to control the generation and propagation of crystal defects during the crystal growth processes. Finally, future developments of the mono-like method are discussed.

Note that the growth method and single crystalline Si ingots grown in a crucible by the casting method are also described by the terms as seed cast, mono cast, and quasi-mono. In this chapter, the term “mono-like” is used collectively.

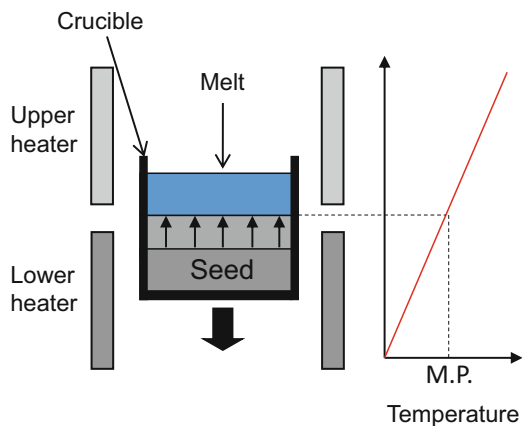
## Fundamentals of the Mono-Like Method

### Seed Growth

The Czochralski (CZ) method is well known for growing single bulk crystals by drawing seed crystals over the Si melt (see ► Chap. 6, “Growth of Crystalline Silicon for Solar Cells: Czochralski Si”). Seed crystals are also used directly inside the crucible in the Bridgman method. Figure 1 shows a schematic illustration of the vertical Bridgeman method. In the method, crystal growth is performed by slowly pulling the crucible down in a temperature gradient formed by separated heaters in the furnace. The crystal directionally grows from the melt as the materials move across the position corresponding to the melting point. In this process, if a seed crystal is placed at the bottom of the crucible, crystals with the same crystal orientation as the seed grow on the seed epitaxially. The mono-like method to produce single crystalline Si ingots for solar cells is basically same as the vertical Bridgman method in terms of the following technical features: it involves directional growth in a crucible from the bottom to the top and the use of single crystalline seeds.

From another point of view, the mono-like method is similar to the casting method used to produce mc-Si for solar cells (see ► Chaps. 8, “Growth of Multicrystalline Silicon for Solar Cells: Dendritic Cast Method,” and ► 7, “Growth of Multicrystalline Silicon for Solar Cells: The High-Performance Casting Method”). Figures 2 and 3 show schematic illustrations of the casting method and mono-like method, respectively. In the case of the casting method, first, all the Si raw materials in a crucible are completely melted at a high temperature above the melting point. Then, the furnace is cooled down, and crystals grow directionally from the bottom to the top of the crucible. At the initial stage of this process, crystal grains randomly nucleate on the bottom surface of the crucible with various crystal orientations. These initial crystal grains act as a template for the following directional growth. As

**Fig. 1** Schematic illustration of vertical Bridgeman method



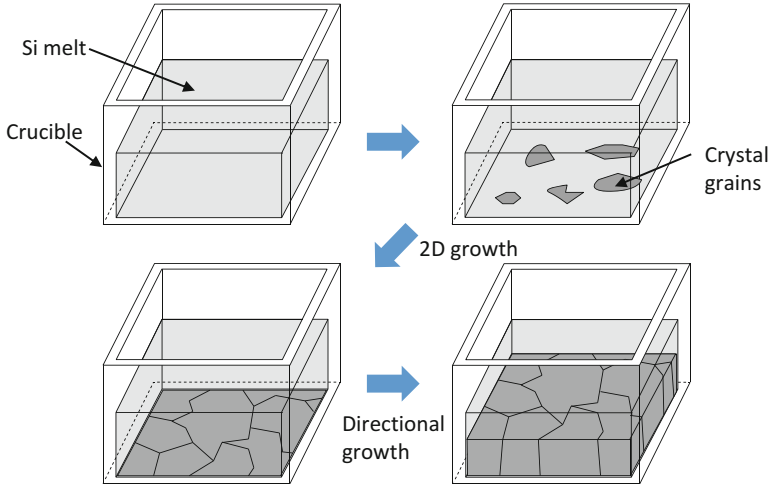


**Fig. 2** Schematic illustration of mc-Si growth of the casting method

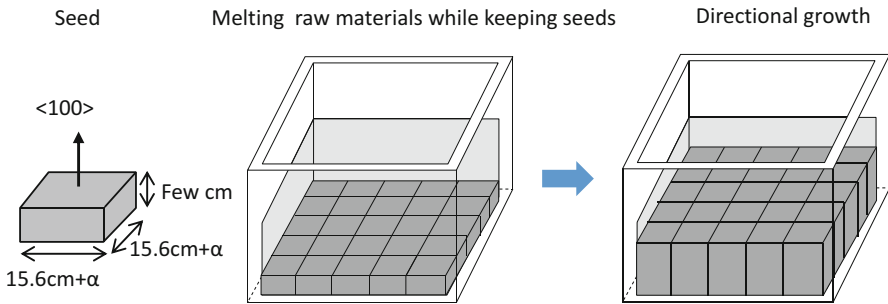


**Fig. 3** Schematic illustration of seed and single crystalline growth of the mono-like method

a result, the grown ingot becomes a columnar multicrystal and inherits the initial grain structure.

However, in the case of the mono-like method, single crystalline seeds are used as a template for directional growth. Generally, the  $\langle 100 \rangle$  orientation is selected for the crystal orientation of the seed in the growth direction in consideration of solar cell applications. These seed bricks are prepared from single crystalline CZ ingots. In the practical mono-like method, a typical seed size is similar to the size of solar cell wafers, i.e.,  $(15.6 + \alpha) \times (15.6 + \alpha) \times \text{few cm}^3$ . Here,  $\alpha$  is the kerf for cutting ingots to bricks. For example, in the case of the growth of G5 size mono-like ingots,  $5 \times 5 = 25$  seed bricks are needed as shown in Fig. 3. As in this example, multiple seed crystals are required for practical mono-like growth because a large seed crystal covering the whole area of the bottom of the crucible cannot be made from CZ ingots. Thus, boundaries between seed crystals are introduced into the ingot. These seed joints are a source of dislocation generation during crystal growth. This

problem will be discussed in the next section together with the other problems associated with the mono-like method. Except for the seed crystals, the same materials as the growth of mc-Si ingots can be used for the crucible, its coating, the Si raw materials, and flow gases.

For the ingot growth, a mc-Si crystal growth furnace can be used. In the growth procedure, to keeping the seed crystals solid during the melting process of the Si raw materials, the processing conditions and temperature profile require some modifications from those used to grow mc-Si ingots. These modifications lead to a slight increase of the processing time, typically less than few hours. There are almost no differences in the following growth processes: directional solidification, and cooling.

In the cutting process from ingots to bricks and the slicing process from bricks to wafers, almost the same facilities and sequences used for mc-Si can be applied to mono-like ingots (see ► Chap. 11, “Wafer Processing”). Additionally, for slicing, multiwire sawing using fixed diamond abrasive grains is applicable. This is a considerable advantage of the mono-like method and will be explained in the next section.

---

## Advantages and Disadvantages of the Mono-Like Method

As described in the above section, the production facilities and processes for the mono-like method are similar to those used in the casting method for growth of mc-Si ingots. Therefore, the mono-like method has almost the same advantages as the casting method in terms of ingot production. Namely, it provides a high production throughput owing to the huge size of the ingots and the greater material yield owing to the square shape of ingots, comparing with the CZ method. Furthermore, mono-like and casting growth can be conducted with automatic operation; however, the CZ method needs human checking of the process when the seed touches the Si melt surface. These processing features reduce the production costs. Furthermore, the similarity with the casting method also lowers the barrier to introducing this method on a practical manufacturing line. Existing facilities for producing mc-Si ingots can also be effectively used for mono-like ingots.

Mono-like Si also has advantages in terms of its crystal quality. Mono-like Si ingots are single crystalline although these are sometimes termed “single-crystal-like” or “quasi-crystalline.” Mono-like Si wafers share many of the advantages of single crystalline wafers made from CZ ingots. In mono-like Si wafers, there are no grain boundaries which operate as recombination sites for photogenerated carriers. Therefore, the conversion efficiency of solar cells based on mono-like Si wafers is potentially higher than that of mc-Si wafers containing electrically active grain boundaries.

Another advantage of single crystals is the uniform {100} crystal orientation of the wafer surface, which is beneficial for surface texturing in alkaline solution. This feature also contributes to better optical confinement by texturing and can be adapted to cost-effective multiwire sawing by fixed diamond abrasive grains. In the case of mc-Si, surface texturing is generally performed in acid solution owing to the

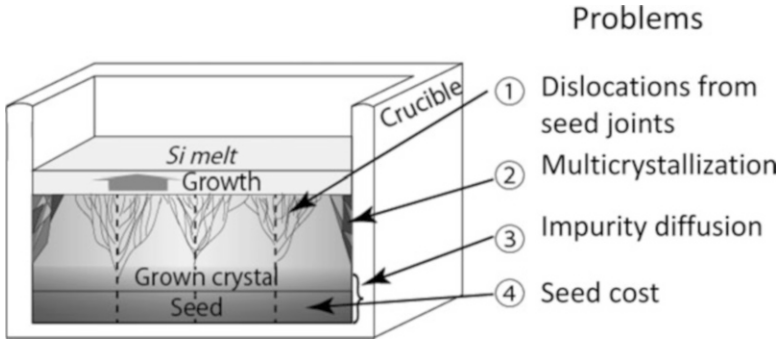


**Fig. 4** Schematic illustration of the problems associated with the mono-like method

random crystal orientation of the wafer surface. Such acid texturing requires the formation of a surface damage layer formed by multiwire sawing with loose grains. However, multiwire sawing by fixed diamond abrasive grains forms a layer with little damage present. For these reasons, it is difficult to adapt cost-effective multiwire sawing by fixed-diamond abrasives to mc-Si. However, texturing of the {100} surface of single-crystalline Si in alkaline solution does not need a surface damage layer; therefore, mono-like Si is suitable for multiwire sawing by fixed-diamond abrasives.

As discussed above, mono-like Si shares many of the advantages of CZ-Si and mc-Si; however, these advantages can become limitations in certain cases. The crystal quality of mono-like Si is slightly worse than that of CZ-Si and mono-like Si has a slightly higher cost than that of mc-Si.

These crystal quality and cost issues are mainly related to the problems of growing crystals of mono-like Si ingots, as shown in Fig. 4. (1) Dislocation generation: a large number of dislocations are generated from grain boundaries formed at seed-crystal joints. These dislocations form clusters, which degrade solar cell performance. (2) Multicrystallization: crystal grains nucleate at the inner side walls of the crucible during directional crystal growth in the same way that grains nucleate on mc-Si at the bottom surface of the crucible. These crystal grains extend inside the ingot with directional growth. As a result, the obtained wafers become partially multicrystalline. (3) Impurity diffusion: the periphery region of an mc-Si ingot, a so-called red zone, typically shows low carrier lifetimes owing to solid phase diffusion of metallic impurities, such as iron, from the crucible and its coating materials. In the case of the mono-like method, the seed crystals remain solid in the high-temperature process of melting the raw materials. During the process, metallic impurities diffuse into the seed crystals from the bottom of the crucible. This diffusion results in a thicker bottom red zone for mono-like Si ingots than that of mc-Si ingots. (4) Seed cost: single crystalline seeds are made from CZ-Si ingots. This raises the cost of mono-like Si because, of course, CZ-Si is more expensive than the Si raw materials.

All these disadvantages are related to the crystal growth of mono-like Si, although each factor has a different influence. Thus, further fundamental studies of the crystal growth of mono-like crystals are needed. Investigations have been performed to try to resolve the issues related to the mono-like method. In the following sections, the mechanism of dislocation generation is discussed and advanced mono-like methods are described.

## Dislocation Generation

As described in the above section, dislocations generated from grain boundaries formed by seed joints are a serious problem in mono-like Si. The problem of dislocation generation at grain boundaries is also common in the growth of mc-Si ingots (see ► Chaps. 18, “Defects in Crystalline Silicon: Dislocations,” and ► 19, “Grain Boundaries in Multicrystalline Silicon”). Thus, many studies have been conducted to reveal the mechanism of dislocation generation during ingot growth. The studies can be roughly categorized into two types of investigations from different viewpoints: the influence of the grain boundary microstructure and the influence of the stress distribution. This section reviews studies on the mechanism of dislocation generation from grain boundaries from these two viewpoints.

## Influence of Grain Boundary Microstructure

Grain boundaries can be categorized into three types by their misorientation angle,  $\theta_R$ , as illustrated in Fig. 5. Grain boundaries with  $\theta_R$  less than or equal to the critical angle,  $\theta_C$ , are categorized as small angle boundaries (sub-grain boundary). The microstructure of small angle boundaries is described by aligned dislocations, as shown in Fig. 6. The distance between adjacent dislocations is inversely proportional

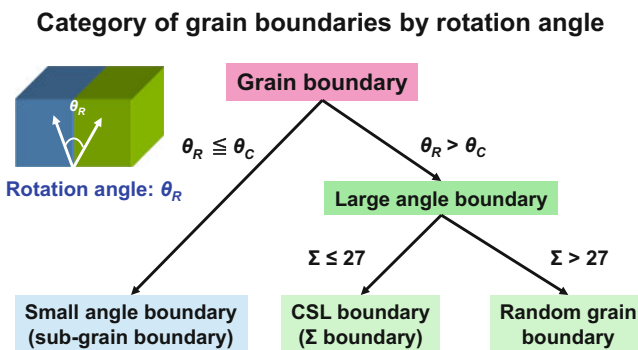


**Fig. 5** Categories of grain boundaries based on rotation angle, where  $\theta_C$  is the critical angle and  $\Sigma$  is determined by coincidence site lattice theory

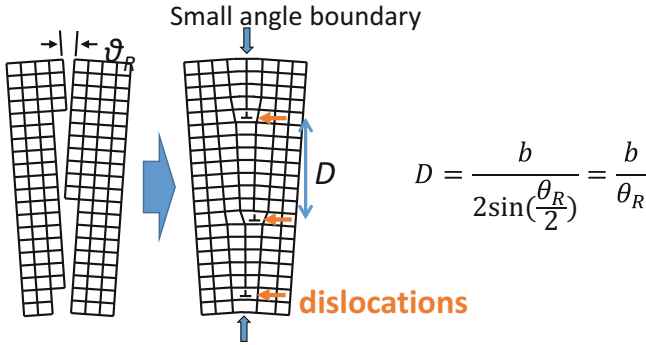


**Fig. 6** Schematic illustration of the microstructure of small angle boundaries. In the equation,  $b$  is the length of the Burgers vector of the dislocations

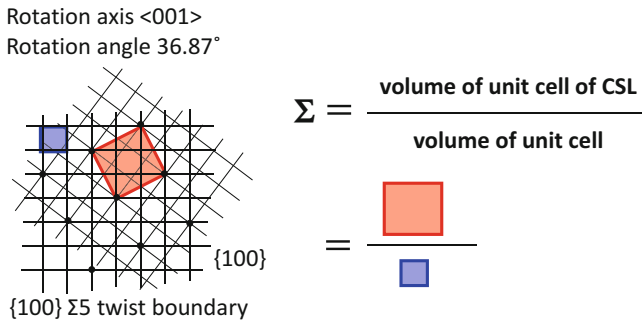


**Fig. 7** Schematic illustration of the calculation of the  $\Sigma$  value. The displayed grain boundary is a  $\{100\} \Sigma 5$  twist boundary for a simple cubic lattice. The value of  $\Sigma$  is defined by the volume ratio of the unit cell of the CSL and volume of the unit cell

to  $\theta_R$ . The type of dislocations introduced at the boundary plane depends on the component of  $\theta_R$ : edge dislocations and screw dislocations are introduced to relax tilt and twist components of  $\theta_R$ , respectively. Thus, the microstructure of small angle boundaries changes markedly with the angle and component of  $\theta_R$ . The critical angle between small and large angle boundaries,  $\theta_C$ , approximately corresponds to the angle at which the microstructure of the grain boundaries changes from that consisting of aligned dislocations to a random structure. In the case of Si crystals, an angle in the range of  $10^\circ$  to  $15^\circ$  is typically expected for  $\theta_C$ .

Grain boundaries with  $\theta_R$  larger than  $\theta_C$  are considered to be large angle boundaries and these can be further divided into two groups based on their  $\Sigma$  value, which is determined by coincidence site lattice (CSL) theory (see Fig. 7). The  $\Sigma$  value shows the coherency of the two crystal lattices at both sides of the grain boundary. A smaller  $\Sigma$  value indicates a higher density of coincidence lattice points at the grain boundary surface, i.e., a more stable grain boundary structure. In the case of Si, large angle boundaries with  $\Sigma$  values less than or equal to 27 are considered to be CSL



boundaries, and other large angle boundaries with  $\Sigma$  values greater than 27 are considered to be random grain boundaries.

Deviation from the misorientation angle of a perfect CSL boundary is relaxed by insertion of grain boundary dislocations at the grain boundary plane, as for the case of small angle boundaries. Thus, the microstructures of CSL boundary are sensitive to change in the misorientation angle and its components. However, the microstructure of random grain boundaries is insensitive to small changes in the misorientation angle and its components. For these reasons, the influence of the grain boundary microstructure on dislocation generation is crucial for small angle and CSL boundaries in terms of the deviation angle from the perfect crystal and the perfect CSL misorientation, respectively. Experimentally, Wu et al. showed that a  $0^\circ$ -tilt boundary (note that in this paper there was no definition of small misorientation angle) generates dislocations more easily than large-angle tilt boundaries during the growth of mono-like Si ingots (Wu et al. 2016). Their results also support the above idea that dislocation generation from a small angle boundary is more sensitive to the microstructure than that from large angle random grain boundaries.

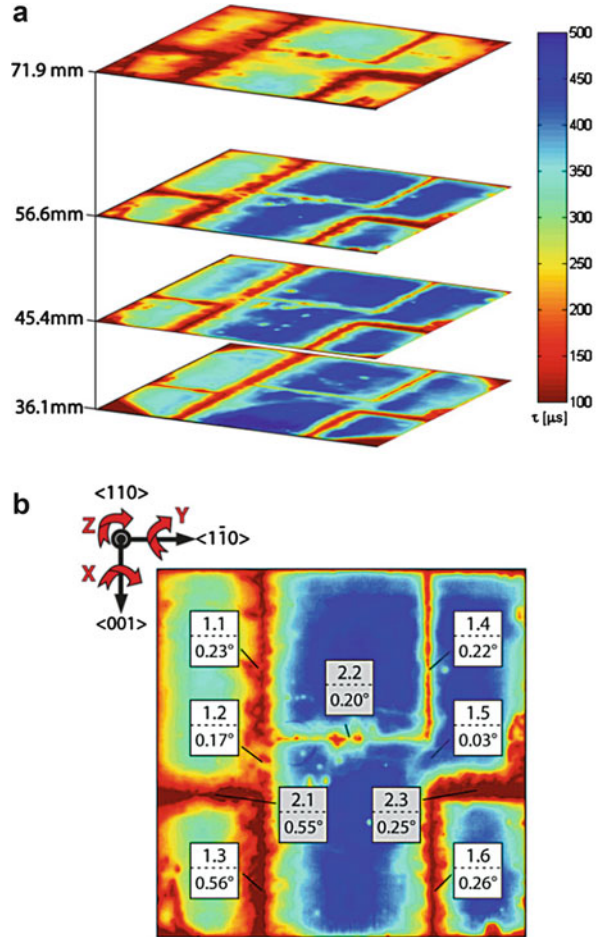
The influence of the misorientation angle of a small angle boundary on the dislocation generation was investigated in a mono-like Si ingot with  $\langle 110 \rangle$  crystal orientations in the growth direction (Ekström et al. 2015). They formed nine small angle boundaries in an ingot with boundary planes of  $\{100\}/\{100\}$  or  $\{110\}/\{110\}$  having different misorientations less than  $0.6^\circ$  using designed seed crystals. The dislocation generation from the boundaries was evaluated through photoluminescence imaging of horizontal cross sections of the ingot, as shown in Fig. 8. In the junctions containing no or small gaps, the amount of generated dislocations mainly depends on the misorientation between the adjacent seeds. High bulk lifetimes are retained for sufficiently low misorientations.

The gap between adjacent seeds is another parameter that determines the microstructure of grain boundaries formed by seed joints. Dislocation generation inside and above seed gaps during the growth of mono-like ingots has also been investigated (Trempe et al. 2014), by testing the influence of various parameters of the seeds joints, including: crystal orientation in the growth direction, crystal orientation of the gap plane, surface treatment of the gap surface, and the space of the gaps. Dislocations generated above the gaps were smaller for the  $\langle 100 \rangle$  growth direction than those for the  $\langle 110 \rangle$  and  $\langle 111 \rangle$  directions.

## Influence of Stress Distribution

As described above, dislocation generation from a random grain boundary is insensitive to the microstructure. Thus, in the case of random grain boundaries, the influence of stress around the boundary has a greater influence on dislocation generation. Si crystals have an anisotropic elastic constant. Therefore, the macroscopic stress distribution in an ingot during the crystal growth process depends on the combination of crystal orientation of grains at both sides of the grain boundary as well as growth conditions, such as the temperature distribution and cooling speed.

**Fig. 8** (a) Carrier lifetime distribution evaluated by quantitative photoluminescence imaging. Junctions from 1.1 to 1.6 and from 2.1 and 2.3 in (b) are  $\{110\}/\{110\}$  and  $\{100\}/\{100\}$  junctions, respectively. The angle of each junction shows the misorientation angle of the boundaries. (From Ekstrøm et al. 2015)



The distribution of shear stress produced by isotropic deformation was calculated for various combinations of crystal grain orientation grains by a finite element method and the calculation results were compared with experimental results for the growth of small mono-like ingots (Takahashi et al. 2010). The amount of observed dislocations generated from a random grain boundary showed a positive correlation with the magnitude of the numerically calculated shear stress, as calculated for the crystal orientations of the grain boundary.

The dislocation behavior in mono-like Si with a seed junction and single crystalline Si without a seed junction has been investigated from the view point of the stress distribution during crystal growth processes (Jiptner et al. 2016). Single crystalline Si results have shown that dislocation motion has a considerable influence on the dislocation distribution in the (111) system. Long slip lines were observed in (111)-oriented ingots but not in (100)-oriented ingots. Experimental results and

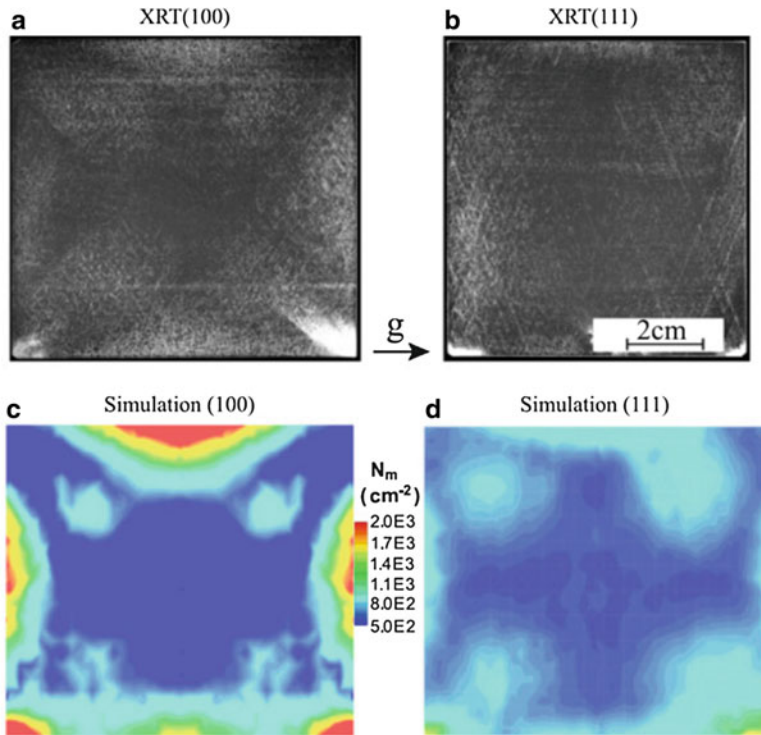


**Fig. 9** X-ray topography images of (a)  $\langle 100 \rangle$  and (b)  $\langle 111 \rangle$  single crystalline Si ingots after annealing experiments and the distribution of dislocation density of (c)  $\langle 100 \rangle$  and (d)  $\langle 111 \rangle$  ingots predicted by numerical simulation. (From Jiptner et al. 2016)

numerical simulations using the Hasen–Alexander–Sumino model showed good correlation; however, simulations cannot correctly predict such long dislocation motion, as shown in Fig. 9.

---

## Advanced Mono-Like Methods

### Functional Grain Boundaries

Generally, grain boundaries have a negative impact on solar cell performance, acting as carrier recombination sites and a source of dislocations. In the early 2000s, the concept of controlling multicrystalline structures was proposed by Nakajima’s group (see Fig. 1 in ► Chap. 8, “Growth of Multicrystalline Silicon for Solar Cells: Dendritic Cast Method”). An ideal grain boundary is described as electrically inactive with the ability to act as a sink for other defects, such as point defects, impurities, and dislocations. Thus, the positive features of grain boundaries can be used to improve solar cell performance.

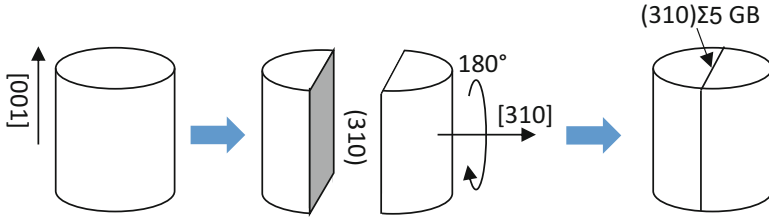


**Fig. 10** Seed design for forming a  $\{310\}\Sigma 5$  grain boundary

The idea of a functional grain boundary was conceived based on the above concept (Kutsukake et al. 2013). Furthermore, in addition to the taking advantage of the positive features of grain boundaries, the idea of controlling grain boundary structures in multi-seed crystals has been adapted.

The growth of artificial grain boundaries in bulk Si crystals based on multi-seed crystals has been developed to investigate microstructure, growth phenomena, and electrical properties of the grain boundaries, before the BP solar report on mono-like Si in 2008. In particular, coincidence site lattice (CSL) grain boundaries have been well investigated, including:  $\{111\}\Sigma 3$  and  $\{221\}\Sigma 9$  grain boundaries grown by the CZ method (Endrös 2002);  $\{111\}\Sigma 3$  grain boundaries grown by floating zone (FZ) method (Kitamura et al. 2005);  $\{310\}\Sigma 5$  grain boundaries grown by the vertical Bridgman method (Kutsukake et al. 2007a);  $\{310\}\Sigma 5$  grain boundaries grown by the FZ method (Kutsukake et al. 2007b); and random grain boundaries grown by the CZ method (Hoshikawa et al. 2007). Among the various CSL boundaries,  $\Sigma 5$  grain boundaries are notable as potential functional grain boundary candidates because they have the lowest sigma value in the CSL grain boundary family parallel to the  $\langle 100 \rangle$  crystal orientation, which is a useful orientation for solar cell applications. Figure 10 shows the seed design for forming a  $\{310\}\Sigma 5$  grain boundary grown by the vertical Bridgman method. A columnar single crystalline Si with a  $[001]$  crystal orientation in the growth direction was cut along the  $(310)$  plane perpendicular to the growth direction. Then, one crystal piece was rotated  $180^\circ$  around the  $[310]$  axis perpendicular to the cutting plane. Through this operation, a  $\Sigma 5$  relationship was formed between the two crystal pieces. A  $\{310\}\Sigma 5$  grain boundary can be artificially formed by epitaxial growth on these multi-seed crystals in the vertical Bridgman method.

The  $\{310\}\Sigma 5$  grain boundaries formed by such designed multi-seed crystals have been used as functional grain boundaries to suppress multicrystallization, which is a crystal growth issue associated with the mono-like method, as mentioned in the previous section. Figure 11 shows a schematic illustration and photographs of vertical cross sections of mono-like Si ingots with and without functional grain boundaries to suppress multicrystallization (Kutsukake et al. 2014). The ingot without functional grain boundaries corresponds to a conventional mono-like Si ingot.

During directional growth of mono-like Si ingots,  $\{111\}\Sigma 3$  grain boundaries frequently form at the crucible side walls accompanied by nucleation of multicrystalline grains. The  $\{111\}$  grain boundary plane of the formed  $\{111\}\Sigma 3$  grain

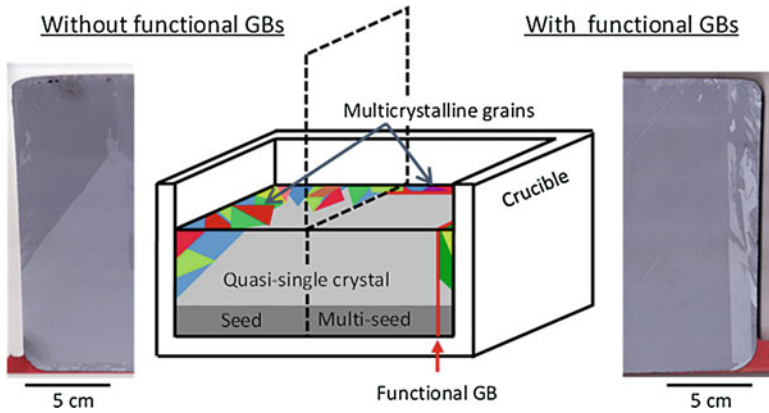
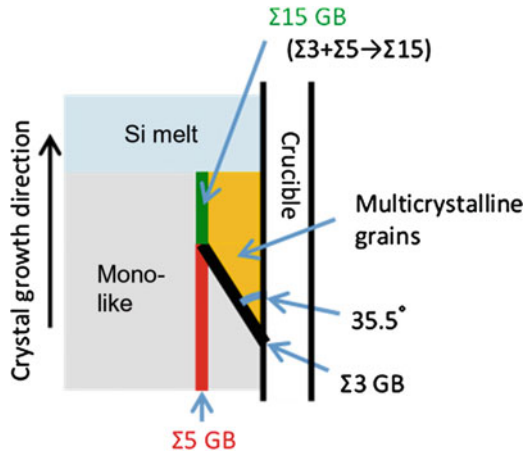


**Fig. 11** Schematic illustration and photographs of vertical cross sections of mono-like Si ingots with and without functional grain boundaries to suppress multicrystallization

**Fig. 12** Schematic illustration of the mechanism by which multicrystallization is suppressed



boundaries inclines from the [001] crystal orientation in the growth direction of the mono-like ingots. The area of multicrystalline grains consequently increases with the crystal growth direction. As a result, conventional mono-like wafers along the crucible side walls contain a large multicrystalline area.

In the case of a mono-like Si ingot with functional grain boundaries,  $\{310\}\Sigma5$  grain boundaries form near the crucible side walls for multi-seed crystals. Figure 12 shows a schematic illustration of the mechanism by which multicrystallization is suppressed. The  $\{310\}\Sigma5$  grain boundaries have a stable configuration in the [001] crystal orientation, and therefore extend straight in the growth direction of the mono-like Si ingot. The  $\{111\}\Sigma3$  grain boundaries formed on the crucible side walls were converted into  $\{310\}\Sigma15$  grain boundaries by interaction with  $\{310\}\Sigma5$  grain boundaries. The  $\{310\}\Sigma15$  grain boundaries have a stable configuration in the [001] crystal orientation, and therefore extend straight in the growth direction of

the mono-like Si ingot as  $\{310\}\Sigma 5$  grain boundaries. As a result, extension of multicrystalline grains inside the ingot was prevented and the multicrystalline regions were confined to the periphery of the ingot. As mentioned in the previous section, such periphery regions correspond to the red zone, which is a highly contaminated area and not used for solar cell wafers. Therefore, the material yield is not impaired by the functional grain boundary method.

Moreover, the functional grain boundary method also has the advantage of a wide processing window. The grain boundary interaction is determined only by the crystallographic geometry and does not depend on the crystal growth conditions, such as growth rate, magnitude of the temperature gradient, and crystal size. Therefore, multicrystallization of mono-like Si can be suppressed by replacing conventional seeds with functional grain boundary seeds without changing growth conditions.

### Seed Manipulation for Artificially Controlled Defects Technique (SMART)

Takahashi et al. extended the idea of functional grain boundaries to functional defects and proposed the seed manipulation for artificially controlled defects technique (SMART). Figure 13 shows a schematic illustration of SMART. This method used two types of functional grain boundaries to generate dislocations and block dislocation propagation. Dislocations make positive contributions to impurity gettering and stress relaxation with plastic deformation in the crystal growth process; however, dislocations also have considerable negative effects, acting as carrier recombination sites in solar cell wafers. To take advantage of their positive effects, dislocations are intentionally and locally introduced as functional defects in functional grain boundaries formed from multiple seed crystals. However, introduced dislocations normally propagate to a large area in the ingot with directional growth

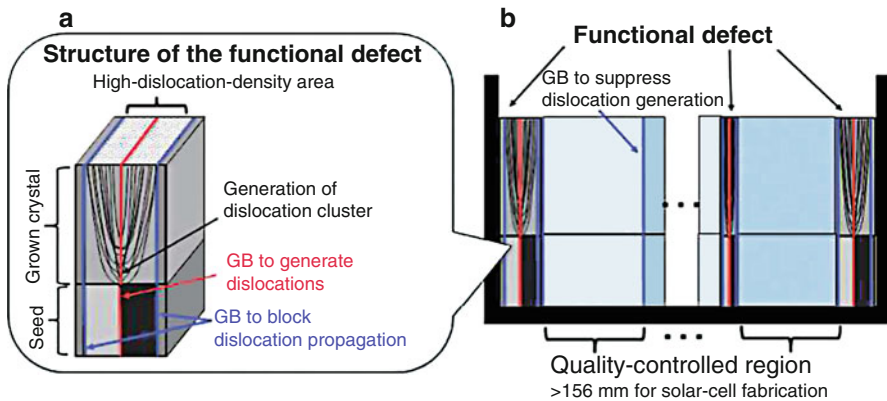


**Fig. 13** Concept of SMART. (a) Structure of functional defects and (b) arrangement of seeds and grown crystals in a crucible. (From Takahashi et al. 2015)

as in the case of dislocations generated at seed joints. Thus, to block propagation of the dislocations, another type of functional grain boundary is also formed along the functional grain boundary used to generate dislocations. As a result, a high-density group of dislocations is confined in a thin region of the ingot. In addition, it is possible to make functional grain boundaries with the ability to both block propagation of dislocations and extension of multicrystalline grains. Therefore, by controlling the configuration of these thin dislocation regions overlapping with the ingot portion not used for solar cells, i.e., the red zones and cutting kerfs, high-quality ingots with a high yield ratio are achieved.

The effectiveness of SMART has been demonstrated through growth of laboratory scale ingots. Figure 14 shows a crystal orientation image map and an etch pit image of the vertical cross section of an ingot grown by SMART. Functional grain boundaries having the ability to generate dislocations were formed at the periphery of the ingot along the crucible side walls accompanied by those having the ability to block dislocation propagation inside them. In addition, at the center of the ingot, a grain boundary was formed as a model of that which forms at a seed joint. The etch pit image clearly shows that propagation of the dislocations generated by the functional grain boundaries was blocked by other functional grain boundaries. Inside the

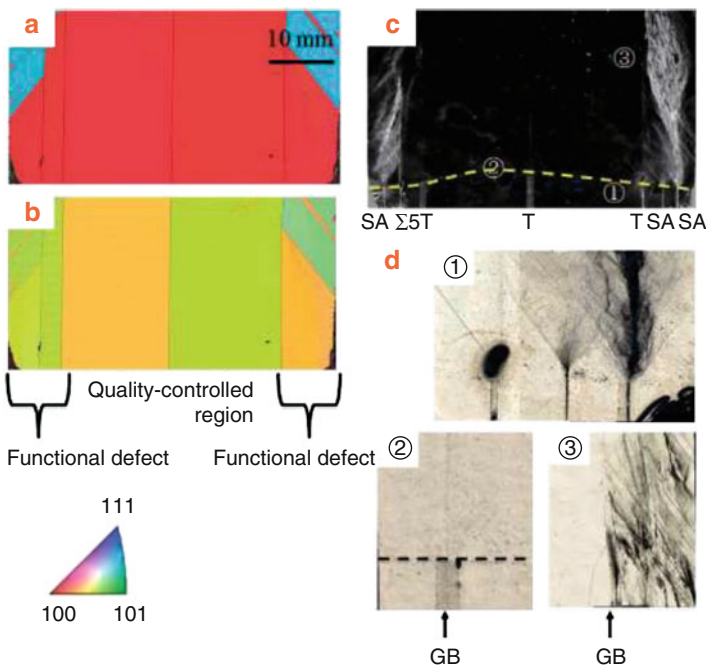


**Fig. 14** (a) Orientation maps of growth direction, (b) the GB plane, (c) an etch pit image, and (d) magnified images taken by an optical microscope. In the orientation maps, the GBs – except for the SA GB – are separated by lines. The number in (d) corresponds to the observed area in (c). The dashed lines show the interface between the unmelted seeds and grown crystals. (From Takahashi et al. 2015)



functional grain boundaries, there were no clear etch pits from dislocation clusters. In particular, no dislocation clusters were generated at the grain boundary in the center of the ingot. This result suggests that dislocations intentionally introduced contribute to reduced stress during the thermal process of the crystal growth. Thus, the dislocations acted as functional defects.

### Control of Seed Joint Structure: Special Grain Boundaries and Seed Partitions

Suppression of dislocation generation from grain boundaries formed at seed joints is a serious issue for mono-like Si. Dislocation generation from grain boundaries also affects the growth of mc-Si. Therefore, a number of studies have examined the mechanism of dislocation generation, as discussed in the previous section. In this chapter, two methods of using seed joint structures are addressed as candidates for next-generation mono-like methods.

Hu et al. reported the growth of high-quality mono-like Si with special grain boundaries (Hu et al. 2015). Two  $870 \times 870 \times 300 \text{ mm}^3$  ingots were grown. One conventional (100)-oriented mono-like Si with small-angle grain boundaries at the seed joints. The other with special grain boundaries between the adjacent (100)-oriented seed crystals with a twisted angular deviation of  $10^\circ\text{--}45^\circ$ . Figure 15 shows photoluminescence images of the wafers (a1–3) with small-angle grain boundaries

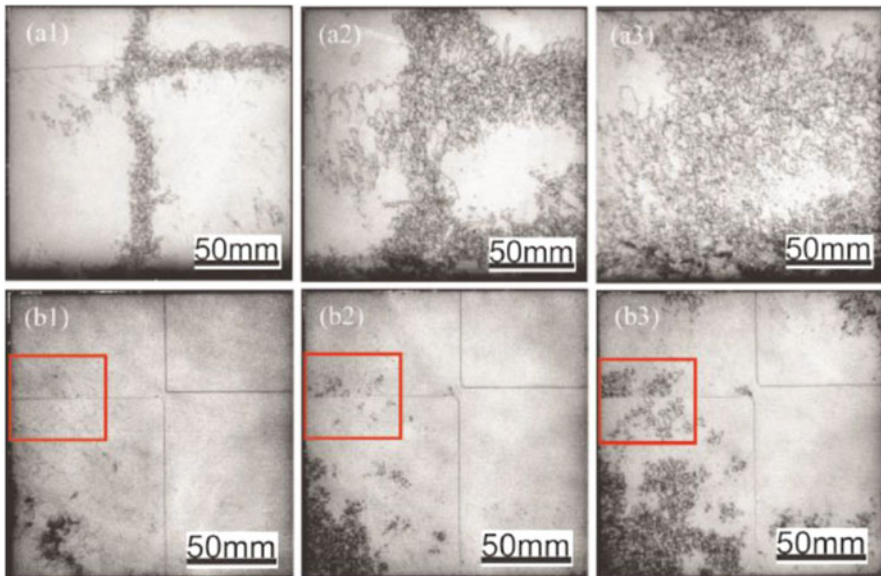


**Fig. 15** Photoluminescence images of the wafers from the bottom (a1,b1), middle (a2,b2), and top (a3,b3) of the block of (a) ingot with small angle grain boundaries and (b) ingot with special grain boundaries. (From Hu et al. 2015)



and (b1–3) shows that with the special grain boundaries. Considerably fewer dislocation clusters were generated from the special grain boundaries than those from the small angle grain boundaries. As a result, the average conversion efficiency of the solar cells was reported to be 18.1%, which is 0.6% higher than the efficiency of conventional cells. Although these results are promising, the details of the seed orientation and configuration have not been disclosed.

Lan et al. proposed a simple approach using seed partitions (Lan et al. 2017). Between the seed crystals with the same crystal orientation, thin Si plate seeds with a  $30^\circ$  or  $-30^\circ$  tilt angle from both sides of the seed crystals were inserted. As a result, two parallel grain boundaries with  $30^\circ$  or  $-30^\circ$  tilt angles were formed at both sides of the thin seed crystals in the grown mono-like Si ingot. Etch pit observations showed that these grain boundaries effectively suppressed dislocation generation. Furthermore, two advantages are emphasized: the ease of seed preparation and the lack of color mismatch. By this method, the main seed crystals have the same three-dimensional crystal orientation. Therefore, the seed preparation is much easier than that for combination seeds with special crystal orientations. Moreover, the same crystal orientation mitigates mismatch of the color of the solar cell surface, which appears after application of an anti-reflection coating, as shown in Fig. 16.

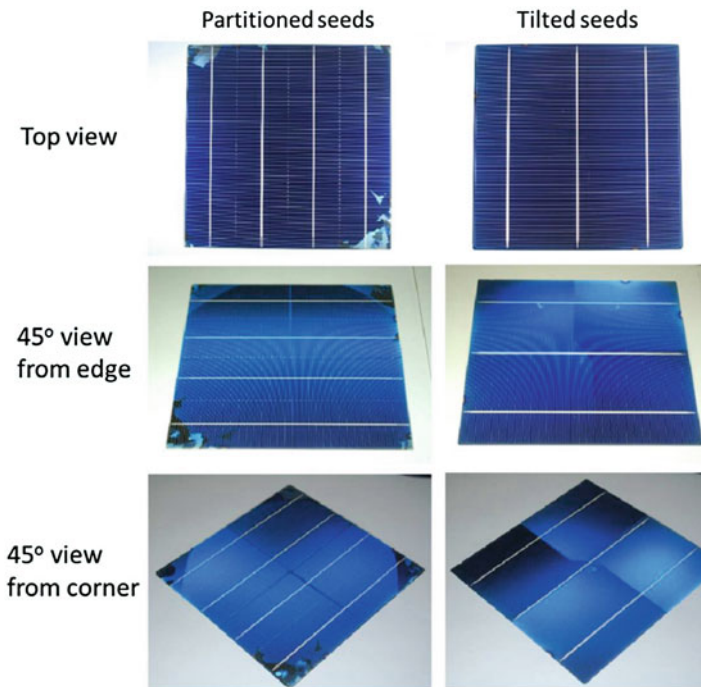


**Fig. 16** Appearances at different view angles for the solar cells made from: (a) partitioned seeds; (b) tilted seeds. (From Lan et al. 2017)

## Mono-Like Growth Without Seed Joints: Large Seed and Mushroom-Type Interface Growth

Another idea to suppress dislocation generation from seed joints is simply to rid the seed crystals of dislocation sources, i.e., seed joints. Two methods have been proposed: the use of large seed crystals and growth from small seed crystals.

As mentioned previously, the typical size of a seed crystal is almost the same as that of a solar cell wafer, i.e.,  $(15.6 + \alpha) \times (15.6 + \alpha) \text{ cm}^2$ . These seed crystals are prepared from slices perpendicular to the growth direction of the CZ ingots. Gu et al. used rectangular plates cut along the axial direction of CZ columnar ingots as seed crystals for mono-like Si (Gu et al. 2012). The seed crystals were prepared to have a  $\langle 100 \rangle$  crystal orientation in the growth direction. Dislocation generation was successfully suppressed in the vertical cross-section of the ingot along the longitudinal direction of the rectangular seeds. However, in another cross-section perpendicular to the longitudinal direction of the rectangular seeds seed joints existed as in the case of seed joints from conventional mono-like ingots.

Zhang et al. also proposed the use of large rectangular seed crystals; however, they used the  $\langle 110 \rangle$  crystal orientation as the growth direction of the mono-like ingots (Zhang et al. 2018). They suggested that multiplication of dislocations in the ingot with the  $\langle 110 \rangle$  growth direction was milder than that with  $\langle 100 \rangle$  growth direction. Therefore, although the dislocation density at the bottom of the ingot was higher in the ingot with the  $\langle 110 \rangle$  growth direction than that with  $\langle 100 \rangle$  growth direction, the total dislocation density in the ingot was reduced by using  $\langle 110 \rangle$  seed crystals. Furthermore, for applications to solar cell wafers, square column bricks are cut along the  $\langle 100 \rangle$  crystal orientation, which is perpendicular to both the growth direction of the ingot and the longitudinal direction of the rectangular seeds.

Another idea to rid seed crystals of seed joints is to grow the ingot from one small seed crystal. Kakimoto's group developed this growth method, so-called mushroom-type interface growth. Numerical simulation modeling of the conditions inside the growth furnace revealed characteristics of the mushroom-type interface growth, as well as details of the thermal condition of the growth (Gao et al. 2012). On the basis of the results of this numerical study, the method was applied to growth of a  $50\text{-cm}^2$  mono-like ingot (Miyamura et al. 2014). By controlling the shape of the liquid-solid interface, a mono-like crystal was grown from a small seed 20 cm in diameter. A dislocation density of  $3 \times 10^4 \text{ cm}^{-2}$  was achieved.

---

## Conclusions

The mono-like method can provide single crystalline Si ingots using the same facilities currently used for production of mc-Si ingots. Thus, this method has advantages of mc-Si in terms of low cost and high production throughput, and the uniform crystal orientation and high crystalline quality of CZ-Si. However, current

mono-like Si is intermediate between mc-Si and CZ-Si in terms of crystalline quality and production cost. Many of the issues associated with crystalline quality are related to the crystal growth process of mono-like ingots, such as multicrystallization, dislocation generation, and impurity contamination. To resolve these problems, advanced mono-like methods have been proposed based on fundamental studies of crystal growth and defect generation in mono-like Si. Control of crystal orientation and the configuration of the seed crystals show promise as methods for addressing the issues of crystallinity. This chapter reviews functional grain boundaries, SMART, special grain boundaries, seed partitions, large seeds, and one-small seed. In addition to these methods considerable research has been done to develop mono-like Si methods. Although these methods are promising, further investigations of mono-like Si will be necessary. For instance, in the near future, the average dislocation density will become a problem for super-high efficiency solar cell application. To address this issue, further studies on seed preparation and optimization of thermal process are needed.

---

## Cross-References

- ▶ [Defects in Crystalline Silicon: Dislocations](#)
- ▶ [Grain Boundaries in Multicrystalline Silicon](#)
- ▶ [Growth of Crystalline Silicon for Solar Cells: Czochralski Si](#)
- ▶ [Growth of Crystalline Silicon for Solar Cells: Noncontact Crucible Method](#)
- ▶ [Growth of Multicrystalline Silicon for Solar Cells: Dendritic Cast Method](#)
- ▶ [Growth of Multicrystalline Silicon for Solar Cells: The High-Performance Casting Method](#)

**Acknowledgment** The author is very grateful to Professor Kazuo Nakajima from Tohoku University for fruitful discussions about the fundamentals of crystal growth and defects generation of mono-like Si.

---

## References

- M. Mrcarica, *Photo-Dermatology* **19**, 28 (2013)
- F. Jay, D. Muñoz, T. Desrues, E. Pihan, V. Amaral de Oliveira, N. Enjalbert, A. Jouini, *Solar Energ. Mater. Solar Cells* **130**, 690 (2014)
- A. Jouini, in *Abstract of the 10th International Workshop on Crystalline Silicon for Solar Cells (CSCS-10)* (2018), p. 9
- N. Stoddard, B. Wu, L. Witting, M. Wagener, Y. Park, G. Rozgonyi, R. Clark, *Solid State Phenom.* **1**, 131–133 (2008)
- T.F. Ciszek, G.H. Schwuttke, K.H. Yang, *J. Cryst. Growth* **46**, 527 (1979)
- K.E. Ekstrøm, G. Stokkan, R. Søndena, H. Dalaker, T. Lehmann, L. Arnberg, M. Di Sabation, *Phys. Status Solidi A* **212**, 2278 (2015)
- Y.C. Wu, A. Lan, C.F. Yang, C.W. Hsu, C.M. Lu, A. Yang, C.W. Lan, *Cryst. Growth Des.* **16**, 6641 (2016)

- M. Trempa, C. Reimann, J. Friedrich, G. Mueller, A. Krause, L. Sylla, T. Richter, *J. Cryst. Growth* **405**, 131 (2014)
- I. Takahashi, N. Usami, K. Kutsukake, G. Stokkan, K. Morishita, K. Nakajima, *J. Cryst. Growth* **312**, 897 (2010)
- K. Jiptner, Y. Miyamura, H. Harada, B. Gao, K. Kakimoto, T. Sekiguchi, *Prog. Photovolt. Res. Appl.* **24**, 1513 (2016)
- K. Kutsukake, N. Usami, Y. Ohno, Y. Tokumoto, I. Yonenaga, *Appl. Phys. Express* **6**, 025505 (2013)
- A.L. Endrös, *Sol. Energ. Mater. Sol. Cells* **72**, 109 (2002)
- M. Kitamura, N. Usami, T. Sugawara, K. Kutsukake, K. Fujiwara, Y. Nose, T. Shishido, K. Nakajima, *J. Cryst. Growth* **280**, 419 (2005)
- K. Kutsukake, N. Usami, K. Fujiwara, Y. Nose, K. Nakajima, *J. Appl. Phys.* **101**, 063509 (2007a)
- K. Kutsukake, N. Usami, K. Fujiwara, Y. Nose, T. Sugawara, T. Shishido, K. Nakajima, *Mater. Trans.* **481**, 143 (2007b)
- T. Hoshikawa, T. Taishi, X. Huang, S. Uda, M. Yamatani, K. Shirasawa, K. Hoshikawa, *J. Cryst. Growth* **307**, 466 (2007)
- K. Kutsukake, N. Usami, Y. Ohno, Y. Tokumoto, I. Yonenaga, *IEEE J. Photovolt.* **4**, 84 (2014)
- I. Takahashi, S. Joonwichien, T. Iwata, N. Usami, *Appl. Phys. Express* **8**, 105501 (2015)
- D. Hu, S. Yuan, L. He, H. Chen, Y. Wan, X. Yu, D. Yang, *Solar Energ. Mater Solar Cells* **140**, 121 (2015)
- C.Y. Lan, Y.C. Wu, A. Lan, C.F. Yang, C. Hsu, C.M. Lu, A. Yang, C.W. Lan, *J. Cryst. Growth* **475**, 136 (2017)
- X. Gu, X. Yu, K. Guo, L. Chen, D. Wang, D. Yang, *Solar Energ. Mater. Solar Cells* **101**, 95 (2012)
- F. Zhang, X. Yu, S. Yuan, L. He, H. Chen, R. Hu, and D. Yang, in *Abstract of the 10th International Workshop on Crystalline Silicon for Solar Cells (CSSC-10)* (2018), p. 19
- B. Gao, S. Nakano, H. Harada, Y. Miyamura, T. Sekiguchi, K. Kakimoto, *J. Cryst. Growth* **352**, 47 (2012)
- Y. Miyamura, H. Harada, K. Jiptner, J. Chen, R.R. Prakash, S. Nakano, B. Gao, K. Kakimoto, T. Sekiguchi, *J. Cryst. Growth* **401**, 133 (2014)



# Growth of Crystalline Silicon for Solar Cells: Noncontact Crucible Method 10

Kazuo Nakajima

## Contents

Introduction .....	236
Growth Mechanism of the NOC Method .....	236
Design of a Furnace with Two Zone Heaters .....	238
Characteristics and Merits of the NOC Method .....	241
Effect of $\Delta T$ and $\Delta T_d$ on the Size of the Low-Temperature Region in the Si Melt .....	241
Growth Rate of Si Ingots Inside Si Melts .....	242
Growth of Square-Shaped Si Single Bulk Crystals with Large Side-Face Widths .....	247
Growth of Si Single Ingots with the Large Diameter and Diameter Ratio Using the Cast Furnace .....	250
Quality of Si Single Ingots Grown Using the Cast Furnace .....	252
Distribution of Conversion Efficiency of n- and p-Type Solar Cells Prepared by the NOC Method After Furnace Cleaning .....	258
Applications of the NOC Method .....	261
Conclusion .....	264
Cross-References .....	265
References .....	265

## Abstract

The noncontact crucible (NOC) method has the potential to be an advanced cast method. It is effective in obtaining Si single ingots with large diameter and volume using cast furnace, and solar cells manufactured with Si obtained this way have high yield and high conversion efficiency. Several novel characteristics of this method are explained based on the existence of a large low-temperature region in a Si melt, which is key to realize its enclosing potential as follows. The largest diameter ratio of 0.9 was obtained by expanding the low-temperature region in the Si melt. For *p*-type solar

---

K. Nakajima (✉)  
Tohoku University, Sendai, Miyagi, Japan  
e-mail: [nakasisc@imr.tohoku.ac.jp](mailto:nakasisc@imr.tohoku.ac.jp)

cells, the highest of 19.14% and the average conversion efficiencies of 19.0% were obtained for the NOC wafers, using the same solar cell structure and process to obtain the conversion efficiency of 19.1% for a *p*-type Czochralski (CZ) wafers. The present method realized solar cells with conversion efficiency and yield as high as those of CZ solar cells using cast furnace for the first time. The latest information about the growth of Si ingots using the NOC method is explained.

---

**Keywords**

Melt growth · NOC method · Solar cells · Si single crystals · Growth method · Large diameter · Cast furnace · Conversion efficiency · Yield · Low-temperature region

---

## Introduction

The noncontact crucible (NOC) method was proposed to obtain Si single ingots with large diameter and volume using the cast furnace and resulted in solar cells with high yield and high conversion efficiency. This method has several novel characteristics based on the core point that ingots can be grown inside Si melt without contact to crucible wall. A large low-temperature region is intentionally created in the upper-central part of the Si melt to allow natural crystal growth inside of it. As the size of the ingots can be controlled by the low-temperature region, large ingots with a large diameter ratio can be grown using small crucibles. The diameter ratio means the maximum diameter of the ingot divided by the crucible diameter. The largest diameter ratio of 0.9 was obtained by expanding the low-temperature region in the Si melt. *p*- and *n*-type Si single ingots were grown for solar cells utilizing merits created by these characteristics. To confirm the quality of the ingots, the etch-pit density (EPD) of dislocations, oxygen concentration of the ingots, and minority carrier lifetime were measured and the conversion efficiency of solar cells was determined whether solar cells with the conversion efficiency and yield as high as those of Czochralski (CZ) solar cells were obtained by the NOC method. The goal of the NOC method is to obtain uniform large Si single ingots with sufficient quality to build solar cells with high conversion efficiency and high yield using a cast furnace. For *p*-type solar cells prepared using wafers cut from the ingot grown by this method, the highest of 19.14% and the average conversion efficiencies of 19.0% were obtained, using the same solar cell structure and process to obtain the conversion efficiency of 19.1% for a *p*-type CZ wafers. Using the cast furnace, solar cells with the conversion efficiency and yield as high as those of the CZ solar cells can be obtained by the NOC method for the first time.

---

## Growth Mechanism of the NOC Method

In the NOC method (Nakajima et al. 2012a, b, 2013, 2014a, b, c; Kivambe et al. 2014; Nakajima et al. 2015, 2016a), the Si melt has a large low-temperature region in its upper central part to allow natural crystal growth inside it as shown in Fig. 1

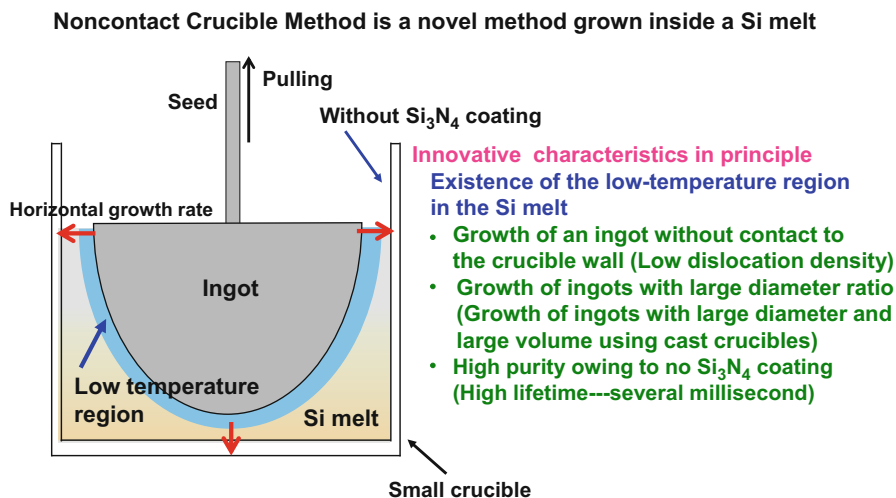


**Fig. 1** Schematic illustration of the NOC method with novel characteristics that originate from its key feature that ingots can be grown inside Si melt without contact to crucible wall owing to a low-temperature region (From Nakajima et al. (2017))

(Nakajima et al. 2017). The low-temperature region means the region in which the melt temperature is kept lower than that of the surrounded melt. It can be established mainly by designing the distribution of heaters in the furnace. Nucleation occurs on the surface of the Si melt by touching a seed crystal on the melt, and an ingot grows inside the Si melt without contact with the crucible wall during cooling the melt. Then, the growing ingot is slowly pulled upward while the ingot grows inside the low-temperature region. As the size of the ingots can be controlled by that of the low-temperature region, large ingots with a large diameter ratio can be grown using small crucibles by expanding the low-temperature region in the Si melt.

The NOC method has been defined as a growth method by which a distinct low-temperature region is intentionally established in a Si melt, under the seed. The melt surrounding the low-temperature region prevents the contact and bonding between the crystal and the relatively hot crucible wall. Since the crucible wall is basically above the freezing point, there is not spurious nucleation from the crucible wall. The present method has the below novel characteristics because of the existence of the low-temperature region in the Si melt: (1) An single ingot can be grown inside the Si melt without contact to the crucible wall. The dislocation density in the ingot is low because of low residual stress. (2) An ingot with a large diameter ratio of 0.9 can be realized by expanding the low-temperature region in the Si melt. The single ingot with a large diameter and a large volume can be grown using a cast furnace. (3) Millisecond lifetime can be obtained after getting because the purity of the ingot is high not to use  $\text{Si}_3\text{N}_4$  coating on the crucible wall.

This method is similar to the Kyropoulos method, in which crystals are mainly grown by the removal of heat from a Si melt through a seed holder (Bliss 2004). The Kyropoulos method has mainly been used for the growth of oxide crystals such

as sapphire (Demina et al. 2007). Ravishankar attempted to grow Si ingots using the Kyropoulos method, but the growing ingots came in contact with the crucible wall because a low-temperature region was not clearly established in the Si melt (Ravishankar 1985). The clear low-temperature region is especially required for the growth of a Si ingot inside the Si melt. The definition of the Kyropoulos method in a broad sense is generally used as a growth method to grow an ingot inside a melt. In this broad sense, the present method belongs to the Kyropoulos method. In contrast to the CZ method (Czochralski 1917), the NOC method grows an ingot inside the Si melt and enables the control of the ingot shape by regulating the degree and distribution of undercooling in the melt or the shape and size of the low-temperature region in the melt. In this method, the shape of the growing interface in the Si deep melt was generally convex in the growth direction.

## Design of a Furnace with Two Zone Heaters

For this method, a furnace with three zone heaters were usually used as shown in Fig. 2a (Nakajima et al. 2016a). In the furnace with three zone heaters, the first heater is mainly used to cool the Si melt in the crucible to grow an ingot by controlling. The second heater is mainly used to heat the crucible wall and maintain its heat. The third heater is used to supply more thermal energy to the Si melt to keep its temperature higher than the melting point of Si. The three zone heaters have each role to obtain a large low-temperature region in a Si melt. For practical use, a furnace with two zone heaters (NOC Furnace 600: Dai-ich Kiden Corporation Limit.) was developed to design as a simple furnace as shown in Fig. 2b (Nakajima et al. 2016a). The first zone heater is a cylindrical carbon heater and the second zone heater is a disk-shaped carbon heater, which is set horizontally and below the first zone heater. The inner diameter of the first

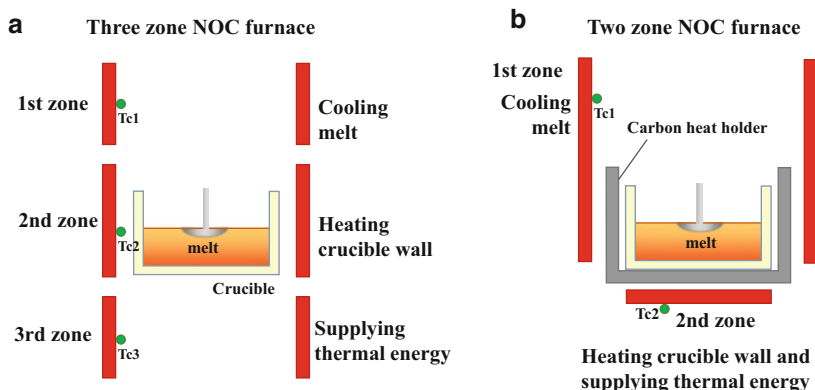


**Fig. 2** (a) NOC furnace with three zone heaters, (b) NOC furnace with two zone heaters which has a carbon heat holder to maintain the heat of the crucible wall. These NOC furnaces have three roles such as cooling the Si melt, heating the crucible wall and supplying thermal energy to the Si melt assigned for each zone-heater (From Nakajima et al. (2016a))



heater is 89 cm and the diameter of the second heater is 65 cm. The power of the first and second heaters is 140 and 60 kW, respectively. To satisfy the three roles using the furnace with only two zone heaters, a carbon heat holder was applied to keep the temperature of the crucible wall high as shown in Fig. 2b. In Fig. 2, Tc1, Tc2, and Tc3 are the thermocouples of the first, second, and third heaters, respectively.

Figure 3 shows a schematic illustration of the relationship between  $\Delta T$  (K) and  $\Delta T_d$  (K) for the system with two zone heaters (Nakajima et al. 2016a).  $\Delta T$  is the temperature reduction of a Si melt defined as the difference between the starting temperature at which an initial crystal is first observed to start growing from the seed crystal and the final temperature at the end of the cooling.  $\Delta T_d$  is the temperature reduction of a Si melt defined as the difference between the initial temperature before cooling near the crucible wall and the melting point of Si. In the initial stage before cooling the Si melt, the melt temperature is equal to the melting point of Si near the center of the Si melt and it has a steep slope near the crucible wall. After cooling using only the first zone heater by  $\Delta T_1$ , a low temperature region is created in the Si melt and an ingot simultaneously grows inside the region. In the second stage, the Si melt is cooled using only the second zone heater, and the melt temperature near the crucible wall is also reduced owing to the carbon heat holder.  $T_{w2}$  is the melt temperature close to the crucible wall after cooling by  $\Delta T_2$ .  $\Delta T$  is estimated as the sum of  $\Delta T_1$  and  $\Delta T_2$  as follows,

$$\Delta T = \Delta T_1 + \Delta T_2, \quad (1)$$

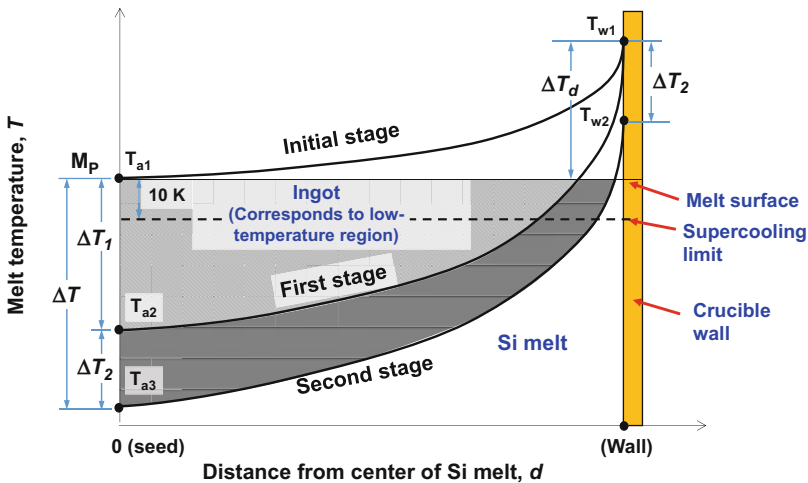


**Fig. 3** Schematic illustration of the relationship between  $\Delta T$  and  $\Delta T_d$ . In the initial stage, the Si melt was cooled from  $T_{a1}$  to  $T_{a2}$  ( $\Delta T_1 = T_{a1} - T_{a2}$ ) using only the first heater, and the melt temperature near the crucible wall remained at  $T_{w1}$ . In the second stage, the Si melt was cooled from  $T_{a2}$  to  $T_{a3}$  ( $\Delta T_2 = T_{a2} - T_{a3}$ ) using only the second heater, and the melt temperature near the crucible wall was also reduced from  $T_{w1}$  to  $T_{w2}$  owing to the carbon heat holder.  $\Delta T$  is estimated as the sum of  $\Delta T_1$  and  $\Delta T_2$  ( $\Delta T = \Delta T_1 + \Delta T_2$ ).  $\Delta T_d$  is defined as the temperature difference between  $T_{w1}$  and  $T_{a1}$  ( $\Delta T_d = T_{w1} - T_{a1} = T_{w1} - M_p$ ) (From Nakajima et al. (2016a))

where  $\Delta T_1$  is defined as the difference between the starting temperature, at which the initial crystal is first observed to start growing from the seed crystal just after reducing the temperature of the first heater, and the final temperature at the end of the cooling, and  $\Delta T_2$  is defined as the difference between the initial temperature at the start of cooling by reducing the temperature of the second heater near the crucible wall and the final temperature at the end of the cooling using the second heater.  $\Delta T$  and  $\Delta T_d$  are the most important parameters determining the size of the low-temperature region.

For the furnace with two zone heaters shown in Fig. 2b, the carbon heat holder was used to keep the temperature near the crucible wall much higher than the melting point of Si. The heat holder can contain an entire growth crucible. The heat holder has an outer diameter of 55 cm and a height of 21 cm. The heat holders with inner diameters of 35, 42, and 52 cm are used for crucibles with diameters of 33, 40, and 50 cm, respectively. The wall of the heat holder is very thick (5.5–10.0 cm) to retain the thermal energy from the second heater and prevent the cooling of the crucible wall. This heat holder is necessary for the NOC method when the furnace with two zone heaters is used. Owing to the existence of the heat holder, both the Si melt and the crucible wall are simultaneously cooled by reducing the temperature of the second heater. This cooling promotes dendrite growth from the crucible wall when  $\Delta T_2$  largely increases, as discussed in detail later.

Figure 4 shows the power (kW) of the first and second heaters as a function of growth time (min) (Nakajima et al. 2016a). First, the temperature of the first heater was reduced to obtain a cooling rate of 0.2 K/min and to start the growth of an ingot. The power of the first heater was gradually decreased. The second heater was used

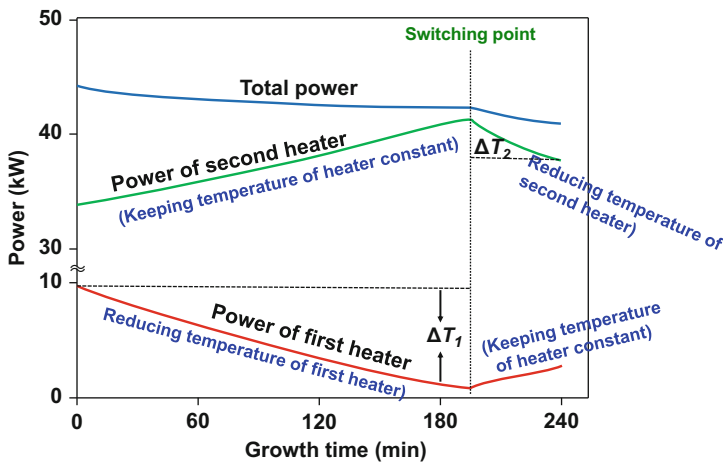


**Fig. 4** Power (kW) of the first and second zone heaters as a function of growth time (min) (From Nakajima et al. (2016a))

constantly to keep the temperature of the crucible wall higher than the melting point of Si. Therefore, at that time, the power of the second heater was gradually increased to supply thermal energy to the crucible wall and the Si melt as the power of the first heater was decreased. However, the temperature of the second heater was kept constant when that of the first heater was reduced. The total power was also gradually decreased during crystal growth. At the switching point, the temperature of the first heater was kept constant and the temperature of the second heater was reduced to keep the diameter of the ingot constant. At that time, the power of the first heater was gradually increased to maintain the supply of thermal energy to the crucible wall and the Si melt as the power of the second heater was decreased.  $\Delta T_1$  and  $\Delta T_2$  correspond to the temperature reductions caused by the power reduction of the first and second heaters, respectively.  $\Delta T_1$  and  $\Delta T_2$  also correspond to those defined in Fig. 3.

---

## Characteristics and Merits of the NOC Method

The present method has several novel characteristics because of existence of a low-temperature region in the Si melt. Figure 1 shows the characteristics and merits pulled out from them. The NOC method has the following characteristics in principle. (1) Single ingots with low stress can be grown without contact to the crucible wall. (2) Single ingots with large diameter ratio can be grown inside the Si melt. (3) Single ingots with high purity can be grown in the exquisite environment of the furnace. Then, several merits are derived from these characteristics. (1) Low dislocation density can be realized under low stress without necking technique (Dash 1959) because the growth interface is convex in the growth direction and dislocations move to the periphery from the center of the ingots during growth (Nakajima et al. 2016a). (2) Single ingots with the large diameter and volume can be grown because the high buoyancy from the Si melt helps the large ingot to remain in the Si melt (Nakajima et al. 2016a). (3) Single ingots with minority carrier lifetime on the order of several ms can be grown owing to high purity growth (Nakajima et al. 2015, 2016b). (4) Single ingots with low oxygen concentration can be obtained because of small convection in the Si melt (Nakajima et al. 2016a). These merits can be effectively applied as an advanced cast method to obtain large single ingots with sufficient quality to prepare *p*-type solar cells with the yield and conversion efficiency as high as those of CZ solar cells.

---

## Effect of $\Delta T$ and $\Delta T_d$ on the Size of the Low-Temperature Region in the Si Melt

The diameter of ingots grown by the NOC method is determined by the size of the low-temperature region in the Si melt, which is mainly determined by  $\Delta T$  during crystal growth and the temperature slope in the Si melt. In the NOC furnace, the melt temperature near the crucible wall must be kept higher than that in the

low-temperature region to prevent crystal growth from the wall as shown in Fig. 3 (Nakajima et al. 2016a). In the initial stage before cooling the Si melt, the melt temperature is equal to the melting point of Si,  $M_p$  (1414 °C), near the center of the Si melt immediately below the seed crystal. It has a steep slope near the crucible wall which has much higher temperature than  $M_p$ . The slope becomes much steeper near the crucible wall as  $\Delta T_d$  increases. Therefore,  $\Delta T_d$  is a key parameter determining the temperature gradient in the Si melt and obtaining a large ingot inside the crucible because we can use a larger  $\Delta T$  with a larger  $\Delta T_d$ . The most important point to design the furnace is to devise the method to enlarge  $\Delta T_d$ .

In the first stage, the Si melt was cooled from  $T_{a1}$  ( $=M_p$ ) to  $T_{a2}$  ( $\Delta T_1 = T_{a1} - T_{a2}$ ) using only the first zone heater, and the melt temperature near the wall remained at  $T_{w1}$  during cooling. Here,  $T_{a1}$  is the initial melt temperature immediately below the seed set on the central axis, and it corresponds to the starting growth temperature from the seed or the melting point of Si.  $T_{a2}$  is the melt temperature after cooling by  $\Delta T_1$ .  $T_{a1}$  and  $T_{a2}$  were monitored using Tc1 for the first zone heater.  $T_{w1}$  is the initial melt temperature close to the crucible wall. A low-temperature region was created in the Si melt by this cooling and an ingot simultaneously grew inside the region. In the second stage, the Si melt was cooled from  $T_{a2}$  to  $T_{a3}$  ( $\Delta T_2 = T_{a2} - T_{a3}$ ) using only the second zone heater, and the melt temperature near the crucible wall was also reduced from  $T_{w1}$  to  $T_{w2}$  owing to the effect of the carbon heat holder.  $T_{w2}$  is the melt temperature close to the crucible wall after cooling by  $\Delta T_2$  ( $\Delta T_2 \cong T_{w1} - T_{w2}$ ).  $\Delta T_d$  is defined as the temperature difference between  $T_{w1}$  and  $T_{a1}$  ( $\Delta T_d = T_{w1} - T_{a1} = T_{w1} - M_p$ ). When sufficient large  $\Delta T_d$  can be established to obtain a large  $\Delta T_2$ , the large  $\Delta T_2$  and  $\Delta T$  can be used before  $\Delta T_2$  reaches the supercooling limit of 10 K below  $M_p$  (Fujiwara et al. 2008). When  $\Delta T_2$  becomes larger than the sum of ( $\Delta T_d + 10$  K), dendrite crystals appear from the crucible wall.

## Growth Rate of Si Ingots Inside Si Melts

For expanding the present method for practical use, a high-speed growth is required for obtaining large ingots with a constant diameter. The horizontal and vertical growth rates of the NOC method are determined by the expanding rate of the low-temperature region in a Si melt, as shown in Figs. 1 and 3. The expanding rate is mainly determined by the cooling rate of the Si melt. Therefore, it is very important to experimentally determine the growth rate that can be attained by increasing the cooling rate. The horizontal growth rate along the melt surface was determined in the  $\langle 110 \rangle$  and  $\langle 100 \rangle$  directions as a function of the cooling rate (Nakajima et al. 2014c). In this work, the cooling rates of 0.2, 0.3 and 0.4 K/min were used. At first for several cooling rates, the growth length was determined as a function of the growth time during cooling by  $\Delta T$ . The growth time increases as  $\Delta T$  increases.

The growth length on the top surface of an ingot was determined by making marks in it (Nakajima et al. 2014c). Figure 5a shows an *n*-type ingot with a size of  $20.3 \times 20.3$  cm<sup>2</sup>, a diagonal length of 25.0 cm, a mass of 2960 g (solidification ratio:

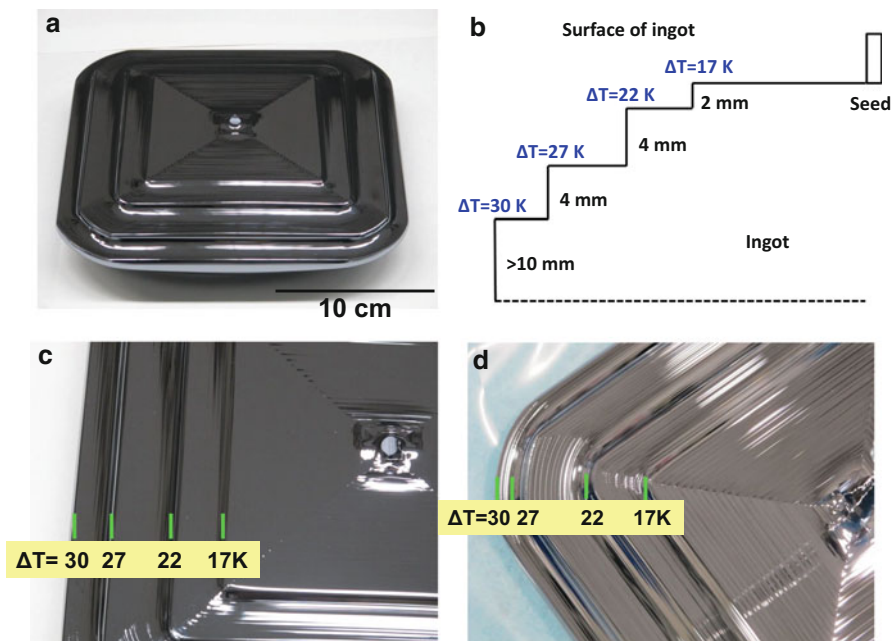


**Fig. 5** (a) n-Type ingot with a square-like shape of size  $20.3 \times 20.3 \text{ cm}^2$ . The top surface has four steps corresponding to the growth process. (b) Growth process of this ingot for the purpose of making marks to determine the growth length. (c) Top surface of the ingot in the  $\langle 110 \rangle$  direction. (d) Top surface of the ingot in the  $\langle 100 \rangle$  direction (From Nakajima et al. (2014c))

41%), and a thickness of 4.0 cm. The ingot was grown using a crucible with 28 cm diameter. The thickness of the Si melt was 5.0 cm and the cooling rate was 0.3 K/min. The growth process of this ingot is shown in Fig. 5b. The ingot was pulled upward by 0.3, 0.4, 0.4, and 0.2 cm at  $\Delta T = 17, 22, 27,$  and  $30 \text{ K}$  with a pulling rate of 2 mm/min, respectively. The purpose of making marks is to determine the growth length as a function of  $\Delta T$  or the growth time. The growth rate was determined by the ratio between the growth length and the growth time. The top surface of the ingot had four steps, which were located at distances of 5.2, 6.8, 9.0, and 10.0 cm in the  $\langle 110 \rangle$  direction and at distances of 7.1, 8.0, 11.6, and 12.3 cm in the  $\langle 100 \rangle$  direction from the center of the seed. The growth times for these growth lengths were 57, 73, 90, and 100 min, respectively. At  $\Delta T = 30 \text{ K}$ , the ingot was continuously pulled upward with a pulling rate of 0.4 mm/min without cooling the melt. The ingot had a square-like shape because the growth rate in the  $\langle 100 \rangle$  direction was larger than that in the  $\langle 110 \rangle$  direction. Figures 5c, d shows the top surface of the ingot in the  $\langle 110 \rangle$  and  $\langle 100 \rangle$  directions, respectively. The top surface has four steps corresponding to the growth process shown in Fig. 5b. The side face in the  $\langle 110 \rangle$  direction was flat, but the  $\langle 100 \rangle$  corner had a fan-shaped face (Nakajima et al. 2014a). The side-face widths were 10.3 and 10.7 cm for this ingot, which were the side lengths corresponded to the step at  $\Delta T = 17 \text{ K}$  shown in Fig. 5c, d.

**Fig. 6** Surface or horizontal growth length in the  $\langle 110 \rangle$  direction as a function of the growth time. The growth rate was determined from the slope (From Nakajima et al. (2014c))

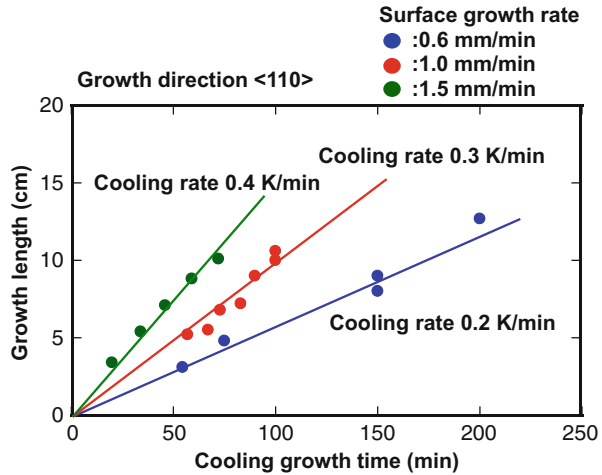
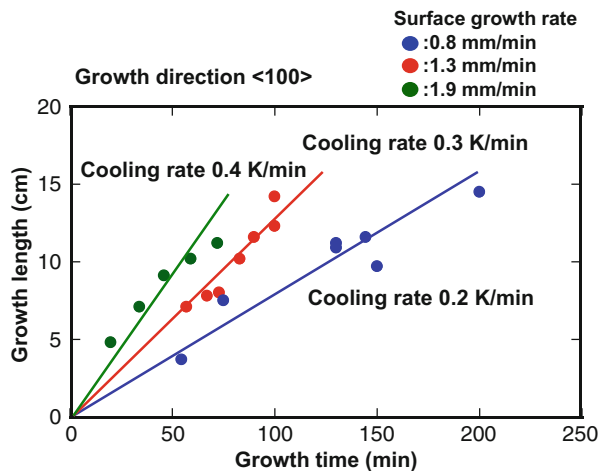


**Fig. 7** Surface or horizontal grown length in the  $\langle 100 \rangle$  direction as a function of the growth time. The growth rate was determined from the slope (From Nakajima et al. (2014c))



The side-face width was defined as the side length of the largest square in the four-cornered pattern on the top surface of the ingots (Nakajima et al. 2014a).

Figure 6 shows the growth length as a function of the growth time in the  $\langle 110 \rangle$  direction (Nakajima et al. 2014c). The growth length almost linearly increased with the growth time, and the growth rate, given by the slope, increased with the cooling rate. From these results, the growth rate was determined to be 0.6, 1.0, and 1.5 mm/min for the cooling rates of 0.2, 0.3, and 0.4 K/min, respectively. Figure 7 shows the growth length as a function of the growth time in the  $\langle 100 \rangle$  direction (Nakajima et al. 2014c). The growth rate was determined to be 0.8, 1.3, and 1.9 mm/min for the cooling rates of 0.2, 0.3, and 0.4 K/min, respectively. The growth rate in the  $\langle 100 \rangle$  direction was about 1.3 times higher than that in the  $\langle 110 \rangle$  direction. The horizontal growth rates in the  $\langle 110 \rangle$  and  $\langle 100 \rangle$

directions increased with the cooling rate. A high growth rate of about 2 mm/min was obtained in the  $\langle 100 \rangle$  direction for the cooling rate of 0.4 K/min. This growth rate is much higher than that of the cast method and is as high as that of the CZ method. The relationship between the growth length and  $\Delta T$  was determined in the  $\langle 110 \rangle$  direction. The growth length almost linearly depended on  $\Delta T$  regardless of the cooling rate, so it was simply determined by only  $\Delta T$ . A higher cooling rate can shorten the growth time required for cooling the same  $\Delta T$ . Therefore, the size of ingot can be obtained using the shorter growth time.

In the NOC method, the vertical growth rate toward the bottom of the crucible does not depend on the pulling rate like the CZ method. The vertical growth rate depends on the vertically expanding rate of the low-temperature region in the melt. It almost corresponds to the maximum pulling rate at which an ingot can be pulled upward above the surface of the Si melt. During the growth of a crystal along the surface of the Si melt, the crystal also grew inside the melt in the vertical direction. Just when the ingot came in contact with the bottom of the crucible, the ingot swung in the melt, which could be directly observed through the windows of the furnace chamber. The vertical growth rate was determined by observation of the first swing of the ingots at the initial stage of growth, and it was estimated from the depth of the melt and the growth time between the start time of the surface growth from the seed crystal and the collision time at which the ingot swung. Figure 8 shows the vertical growth rate as a function of the depth of the Si melt used for the growth of the ingots when the cooling rate was 0.2 K/min (Nakajima et al. 2014c). The vertical growth rate tended to increase with the depth of the Si melt even though the data were scattered, and it was determined to be 0.3–0.6 mm/min.

It is desirable to clarify the maximum growth rate for the present method. The growth rate can be expressed as

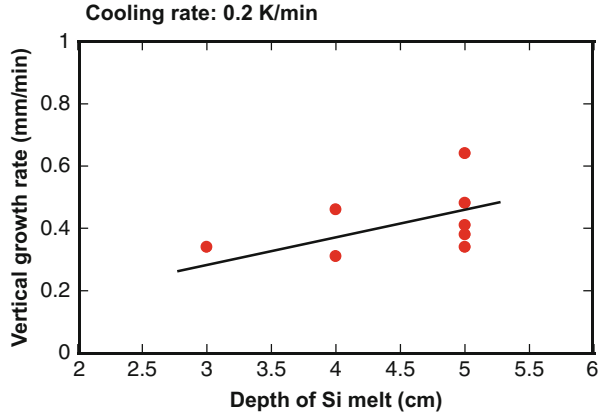
$$\begin{aligned} V(\text{cm/min}) &= dr/dt \\ &= (d\Delta T/dt)/(d\Delta T/dr) \\ &= (d\Delta T/dt)/G_T^s. \end{aligned} \quad (2)$$

Here,  $V$  (cm/min) is the growth rate,  $r$  (cm) is the grown length at  $\Delta T$ , and  $t$  (min) is the growth time required to obtain the growth length.  $d\Delta T/dt$  is the cooling rate, which is expressed in terms of the temperature reduction, and  $d\Delta T/dr$  is the temperature gradient near the surface of the melt on the growth interface when expanding crystal along the surface of the Si melt, which is expressed by  $G_T^s$  (K/cm).

In the NOC method, the temperature gradient across the crucible near the surface of the Si melt was almost constant when the low-temperature region was expanding because the side-face width (10–12 cm) was almost constant for  $\Delta T = 30$  K regardless the cooling rate. As Kuroda et al. 1980a reported, the side-face width,  $d$  (cm), of a square-shaped crystal can be expressed as (Nakajima et al. 2014a; Kuroda et al. 1980a),

$$d \propto \Delta T/G_T^s. \quad (3)$$

**Fig. 8** Vertical growth rate as a function of the depth of the Si melt used for the growth of ingots when the cooling rate was 0.2 K/min. The *solid line* was inserted as a linear least squares fit for equally weighted data (From Nakajima et al. (2014c))



The result that the side-face width was almost constant at the same  $\Delta T$  means that  $G_T^s$  was also almost constant regardless of the cooling rate. Therefore, as indicated by Eq. 2, the growth rate is almost proportional to the cooling rate.

For the practical use of ingots for solar cells, it is important to keep the initial size of the ingot constant during crystal growth and to grow the long ingot with a constant diameter. Figure 9a shows an *n*-type Si single ingot with a diagonal length of 23 cm, a mass of 6440 g (solidification ratio: 64%), and a thickness of 7.0 cm (Nakajima et al. 2014c). The ingot was grown using a crucible with 33 cm diameter, a Si melt depth of 5 cm, and a cooling rate of 0.4 K/min. The ingot was grown while cooling the melt by  $\Delta T = 30$  K without pulling. To determine the horizontal growth rate, the ingot was rapidly pulled upward by 0.5 cm at  $\Delta T = 25$  K with a pulling rate of 2 mm/min for the purpose of making marks. The top surface of the ingot had a step located at distances of 8.0 cm in the  $\langle 110 \rangle$  direction and 8.5 cm in the  $\langle 100 \rangle$  direction from the center of the seed crystal. The growth time for these growth lengths was 58 min. The growth rates were 1.4 and 1.5 mm/min in the  $\langle 110 \rangle$  and  $\langle 100 \rangle$  directions, respectively. At  $\Delta T = 30$  K, the ingot was grown while pulling it upward with a pulling rate of 0.4 mm/min. The ingot was circular because the side-face width was very short (4.8–5.1 cm) as shown in Fig. 9b. A fan-shaped face appeared in the  $\langle 100 \rangle$  direction at the point shown by the red arrow; thus, the top surface of the ingot has circular corners in the  $\langle 100 \rangle$  direction. As shown in Fig. 9c, the diameter of the ingot remained constant during pulling with a high cooling rate of 0.4 K/min. The high cooling rate increases the horizontal growth rate because the melt temperature markedly decreased by it, and prevents the reduction of the diameter. The same diagonal length of the top surface of ingots was obtained for cooling rates between 0.2 and 0.4 K/min. Therefore, we can use a larger cooling rate to obtain ingots with the same diameter.

The growth rate of the present method increases with the cooling rate. The limit of the cooling rate depends on the heat capacity of the furnace. For the present furnace, the high cooling rate sometimes caused overcooling below the setting temperature. For example, during the surface growth of the ingot shown in Fig. 9a, the cooling was occasionally



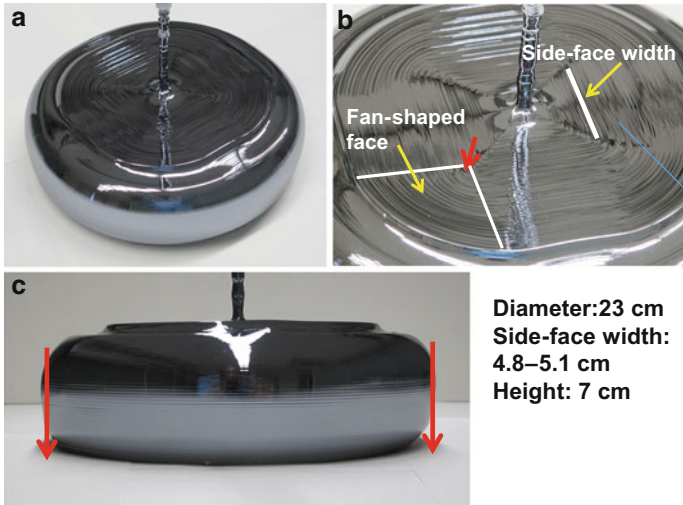


**Fig. 9** (a) *n*-Type ingot with a circular shape. (b) Top surface of the ingot with short side-face widths and fan-shaped faces in the  $\langle 100 \rangle$  direction. A fan-shaped face appeared at the point shown by the red arrow. (c) Ingot with a diameter that remained constant during pulling with a high cooling rate of 0.4 K/min because the horizontal growth rate increased with increasing cooling rate and the melt temperature markedly decreased (From Nakajima et al. (2014c))

stopped at  $\Delta T = 10, 15, 20, 25,$  and  $30$  K to prevent the overcooling of the furnace. The control of the overcooling of the furnace was also effective for keeping the initial diameter constant during crystal growth as shown in Fig. 9c. Therefore, the diameter of the ingot remained constant during pulling with a high cooling rate of 0.4 K/min. From these results, this furnace has suitable heat capacity to increase the cooling rate to above 0.4 K/min, at which the horizontal growth rate will be higher than 2 mm/min.

In the case that  $G_T^s$  is not constant, the growth rate strongly depends on the temperature gradient in the Si melt as indicated by Eq. 2. When the temperature gradient is larger, the melt temperature has a steep slope near the crucible wall as shown in Fig. 3. Therefore, it is more difficult to significantly expand the low-temperature region in the Si melt. The growth rate is also lower for a larger temperature gradient in the Si melt. To obtain ingots with a diameter as large as the crucible diameter, it is important to select a low temperature gradient in the Si melt because a low-temperature region can largely expand in it.

## Growth of Square-Shaped Si Single Bulk Crystals with Large Side-Face Widths

The growth of square-shaped or rectangular Si single crystals by the CZ method and the floating zone (FZ) method (Ratnieks et al. 2003) has been reported by several researchers (Muiznieks et al. 2006; Kuroda et al. 1980b; Rudolph et al. 2011;

Rudolph 2012; Miller et al. 2012). Rudolph and coworkers prepared rectangular Si single bulk crystals using a traveling magnetic field (TMF) to stabilize the radial temperature gradient in the Si melt (Rudolph et al. 2011; Rudolph 2012).

The square wafers are effective for solar cells because the cutting loss from a circular cross section is 36% larger than that from a square-shaped cross section. The square-shaped single ingots are effective to reduce wafer cost and increase yield of materials.

The growth of square-shaped Si single ingots was demonstrated using the NOC method. To obtain large square-shaped single ingots, the side-face width of the four-cornered pattern (Rudolph 2012) appearing on the top surface of the ingots should be much largely increased. Rudolph et al. named the side-facet width (Rudolph et al. 2011) as the side-face width. For the CZ growth method, Kuroda et al. reported that the growth of square-shaped crystals could be explained by supercooling occurring in the radial direction of the ingots and the radial temperature gradient near the growing interface (Kuroda et al. 1980b). Using numerical modeling, Miller et al. reported that a small radial temperature gradient near the melt surface and a large vertical temperature gradient below the crystals are both important for the growth of square-shaped crystals by forming  $\{110\}$  faces (Miller et al. 2012). Rudolph and coworkers used a TMF to obtain a small radial temperature gradient for the growth of Si bulk crystals with a quadratic cross section, and they obtained an ingot with a maximum area of  $9.1 \times 9.1 \text{ cm}^2$  and a side-face width of 5.6 cm (Rudolph et al. 2011; Rudolph 2012). This side-face width was not long enough to obtain significantly large ingots with a square shape, even though a 15-cm fused silica crucible and 2 kg of Si feedstock were used for their growth. Factors that affect the side-face width may include the radial temperature gradient, the degree of supercooling, the quality of crystals, the size of crucibles, and so forth.

These factors were experimentally studied by growing Si single ingots with a four-cornered pattern using the NOC method without the use of a TMF. The ingots were grown in a low-temperature region in Si melts. Figure 10a, b shows a circular  $n$ -type ingot grown using a crucible with a diameter of 33 cm and the four-cornered pattern on its top surface, respectively, when  $\Delta T$  was 45 K (Nakajima et al. 2014a). The ingot weighed 5,320 g and had a diameter of 19.5 cm and a height of 8.2 cm. Figure 10c shows a crystallographic image of a four-cornered pattern grown from a Si (100) seed crystal, along with the top surface of a circular Si ingot. The top surface of the ingot clearly showed a four-cornered pattern with four  $\{111\}$  faces with macrosteps (ms  $\{111\}$ ) and four  $\{110\}$  side faces (Zulehner 1983; Borle et al. 1971). The size of the square-shaped ingots was basically determined by the side-face width. As shown in Fig. 10b, the growth in the  $\langle 100 \rangle$  direction stopped at the point shown by the red arrow, but the  $\{110\}$  side faces of the four-cornered pattern continued to grow from this point. From this point, fan-shaped  $\{110\}$  faces with macrosteps (ms  $\{110\}$ ) appeared on the four corners of the four-cornered pattern, which bordered on two  $\{111\}$  faces with macrosteps, as shown by the yellow lines. The  $\{110\}$  side-face width of the four-cornered pattern was determined at this point as shown in Fig. 10c. The side-face width of the ingot was 6.2–6.5 cm. Figure 10d shows an as-cut cross section cut from 1.4 cm below the top surface. No grain boundaries were observed in the cross section, and the surface orientation of the entire cross section was found to be (100).



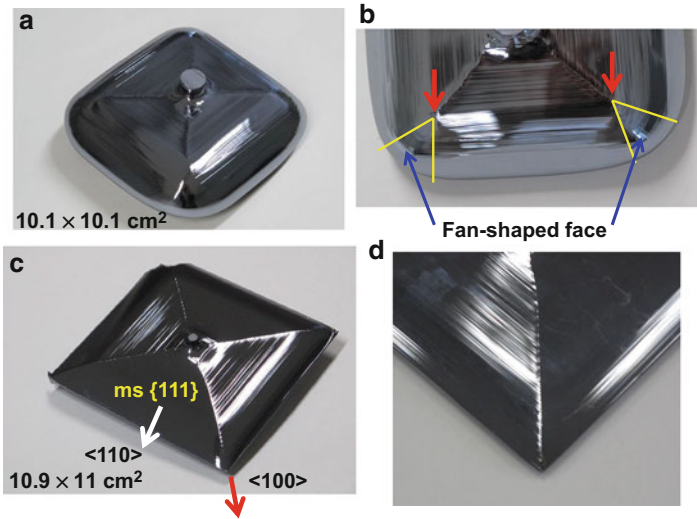


**Fig. 11** (a) *n*-Type square-shaped single bulk crystal grown using a crucible with a diameter of 17 cm. It had a size of  $10.1 \times 10.1 \text{ cm}^2$  (with a diagonal length of 14.3 cm) and a height of 2.5 cm. The (110) side-face width was 6.2 cm. (b)  $\langle 100 \rangle$  corners of the ingot with fan-shaped faces. (c) *n*-Type single bulk crystal with a perfect square shape grown using a crucible with a diameter of 17 cm. The dimensions of the square were  $10.9 \times 11.0 \text{ cm}^2$  (with a (110) side-face width of 11 cm and a diagonal length of 15.5 cm). (d)  $\langle 100 \rangle$  corner of the ingot that had a perfect square shape without any fan-shaped faces (From Nakajima et al. (2014a))

side-face width, it is very important to obtain a perfect  $\langle 100 \rangle$  corner. The maximum diagonal length of the present square-shaped ingots was as large as 91% of the crucible diameter. The side-face width depended on the temperature reduction  $\Delta T$  and increased with  $1/\Delta T$  (Nakajima et al. 2014a). The present method has the potential to grow large square-shaped Si single bulk crystals with long side-face widths when a large low-temperature region is maintained while  $\Delta T$  is kept small.

## Growth of Si Single Ingots with the Large Diameter and Diameter Ratio Using the Cast Furnace

For the reduction of production cost of Si ingots, it is effective to grow large ingots using small crucibles. To confirm the possibility of growing ingots with, a diameter as large as the crucible diameter, several Si ingots with different diameters, and diameter ratios were grown with different  $\Delta T$ . Crucibles with different sizes were used to compare the  $\Delta T$  dependence of the diameter and the diameter ratio. To reduce the melt temperature near the center of the Si melt, it was effective to cool the melt only using the first zone heater. The diameter ratio of ingots was mainly determined by  $\Delta T$  of the first heater and not strongly affected by that of the second heater. Figure 12 shows the diameter ratio as a function of the total

temperature reduction,  $\Delta T$  (Nakajima et al. 2016a). The diameter ratio increases with  $\Delta T$  regardless of the crucible diameter. This tendency is very effective to obtain an ingot with a large diameter because a larger diameter can be obtained only using a larger crucible at a same  $\Delta T$ . The diameter ratio becomes saturated when  $\Delta T$  is large because the fringe of the ingots becomes close to the hotter crucible wall as the diameter ratio increases. The largest diameter ratio of 0.9 was obtained by expanding the low-temperature region in the Si melt. Therefore, if the same size of a crucible (60 cm diameter) used for the CZ method, the NOC method can grow an ingot with 54 cm diameter. Figure 13 shows *n*-type single ingots

**Fig. 12** Diameter ratio of *n*-type ingots as a function of  $\Delta T$ . The diameter ratio increases with  $\Delta T$  regardless of the crucible diameter. A diameter ratio of 0.9 can be obtained by expanding the low-temperature region in the Si melt (From Nakajima et al. (2016a))

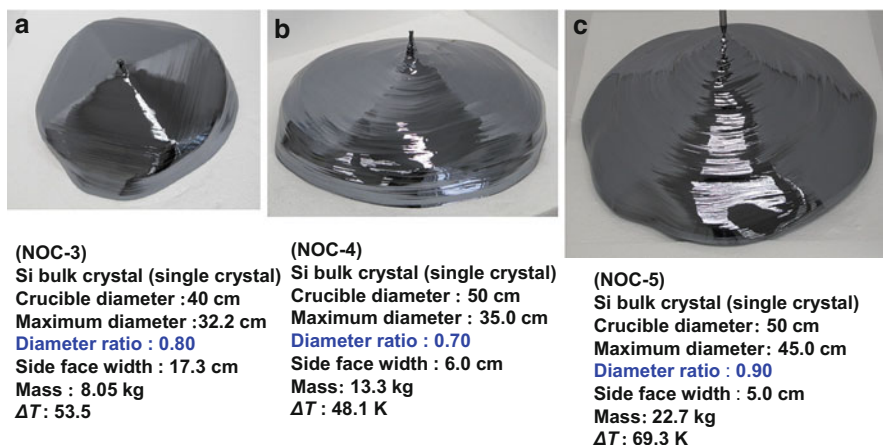
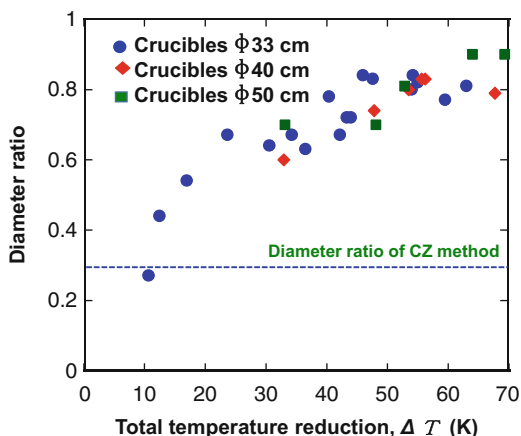


**Fig. 13** *n*-Type bulk crystals (NOC-3, 4 and 5) grown using crucibles of (a) 40 and, (b) and (c) 50 cm diameter. The diameters of the ingots (a), (b) and (c) were 32.2, 35.0 and 45.0 cm, respectively. The diameter ratios were 0.80, 0.70 and 0.90, respectively. Using a Si melt with a depth of 7 cm, the lengths were 9.5, 9.0 and 13.0 cm, respectively (From Nakajima et al. (2016a))



**Si multicrystal with dendrites**  
**Crucible diameter : 50 cm**  
**Maximum diameter : 45.0 cm**  
**Diameter ratio : 0.90**  
**Mass : 19.0 kg**  
 **$\Delta T$ : 64.0 K**

**Fig. 14** Si multicrystalline ingot with some dendrite crystals. The dendrite crystals appeared in front of the growth interface during growth owing to the local temperature fluctuation of larger than 10 K.

(NOC-3, 4 and 5), in which an ingot (a) was grown using a crucible of 40 cm diameter and ingots (b) and (c) were grown using crucibles of 50 cm diameter (Nakajima et al. 2016a). The maximum diameters of the ingots (a), (b), and (c) were 32.2, 35.0, and 45.0 cm, respectively. The maximum diameter of the ingots increases with  $\Delta T$ . The maximum diameter of the ingot grown using a 40- or 50-cm-diameter crucible was larger than that of ingots grown using a 33-cm-diameter crucible even at the same  $\Delta T$ . The diameter ratios of these ingots were 0.80, 0.70, and 0.90, respectively. When the depth of the Si melts was 7 cm, the lengths of the ingots (a), (b), and (c) were 9.5, 9.0, and 13.0 cm, respectively. The maximum values of  $\Delta T$  were 53.5, 48.1, and 69.3 K, respectively. The largest diameter of this ingot (NOC-5) was 45 cm when using a 50-cm-diameter crucible. For the growth of such large ingots, the melt temperature should be kept stable not to generate large local temperature fluctuation in the melt. The local temperature fluctuation should be kept lower than 10 K. If the local fluctuation of larger than 10 K will appear in front of the growing interface, some dendrite crystals will appear from the interface during growth and the ingot will be multicrystalline as shown in Fig. 14 (see ► Chap. 8, “Growth of Multicrystalline Silicon for Solar Cells: Dendritic Cast Method”). From a cross section of the ingot NOC-5, we can get four wafers required for regular-size solar cells. The growth of such large ingots is effective to reduce wafer cost and increase yield of materials. The growth parameters and crystal sizes for these ingots are listed in Table 1 (Nakajima et al. 2017).

---

## Quality of Si Single Ingots Grown Using the Cast Furnace

The etch-pit density (EPD) of dislocations, oxygen concentration, and minority carrier lifetime are important parameters to determine the solar cell performance. To evaluate the EPD in a cross section of each ingot, the surface of the cross section

**Table 1** Growth parameters, crystal sizes and impurity concentrations for grown ingots

	Type	$\Delta T$ (K)	$\Delta T_1$ (K)	$\Delta T_2$ (K)	Crucible diameter (cm)	Crystal mass (g)	Crystal diameter (cm)	Crystal diameter ratio	Crystal length (cm)	C ( $\times 10^{15} \text{ cm}^{-3}$ )	N ( $\times 10^{15} \text{ cm}^{-3}$ )	
	NOC-1	<i>n</i>	54.0	46.0	8.0	33	5,850	26.6	0.80	10.0	14.0	0.8
	NOC-2	<i>n</i>	55.6	45.6	10.0	40	10,850	33.5	0.83	13.0	6.6	0.55
	NOC-3	<i>n</i>	53.5	44.6	8.9	40	8,050	32.2	0.80	8.3	2.4	0.082
	NOC-4	<i>n</i>	48.1	38.1	10.0	50	13,300	35.0	0.70	9.0	—	—
	NOC-5	<i>n</i>	69.3	55.1	14.2	50	22,700	45.0	0.90	13.0	—	—
	NOC-6	<i>p</i>	33.1	33.1	0	50	8,200	35.0	0.70	8.0	—	—

From Nakajima et al. (2017)

From Nakajima et al. (2016a)



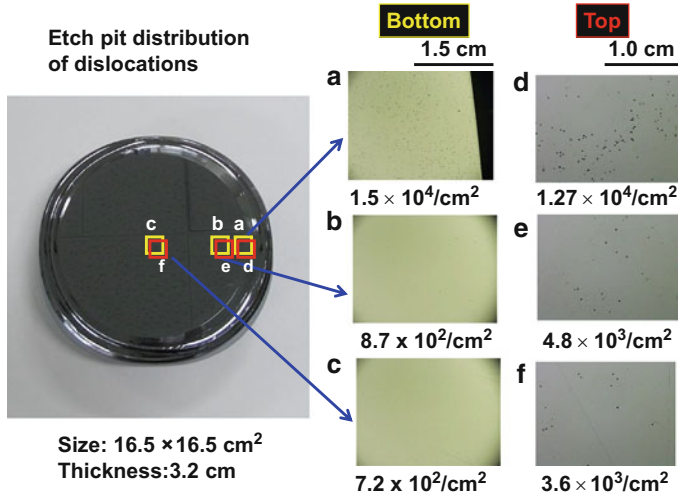
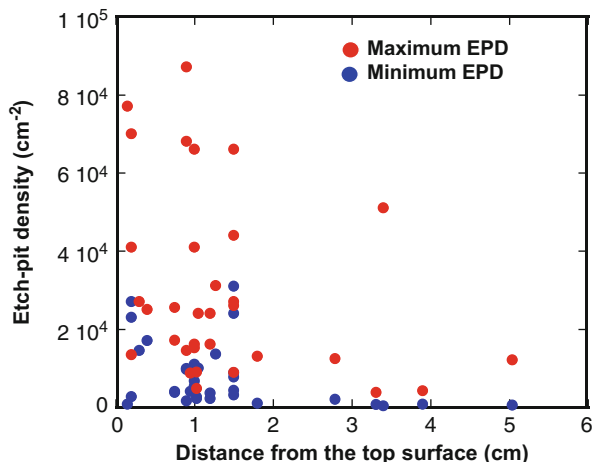


**Fig. 15** (a) Distribution of the EPD of dislocations measured at the periphery of the cross section 2.8 cm below the top surface of an ingot. (b) Distribution of the EPD measured inside the cross section 2.8 cm below the top surface of the ingot. (c) Distribution of the EPD measured at the *center* of the cross section 2.8 cm below the top surface of the ingot. (d) Distribution of the EPD measured at the periphery of the cross section 0.2 cm below the top surface of the ingot. (e) Distribution of the EPD measured inside the cross section 0.2 cm below the top surface of the ingot. (f) Distribution of the EPD measured at the *center* of the cross section 0.2 cm below the top surface of the ingot (From Nakajima et al. (2014a))

was mechanically polished to a mirror finish and then chemically etched with a Secco solution (Secco d’Aragona 1972). The EPD in the cross section of each ingot was determined by counting the number of etch pits in a  $1.0 \times 1.0 \text{ cm}^2$  area by optical microscopy. To determine the effect of the convex bottom on the distribution of the dislocations in an ingot, the distribution of the EPD was measured on cross sections 0.2 and 2.8 cm below the top surface of an ingot as shown in Fig. 15 (Nakajima et al. 2015). The red and yellow squares show illustrated positions where each EPD was measured, but the duplicated squares do not indicate the same position. In Fig. 15, the positions (c) and (f) are near the center of the cross section, (b) and (e) are 4.5 cm from the center, and (a) and (d) are 6.0 cm from the center. The ingot had a size of  $16.5 \times 16.5 \text{ cm}^2$  and a height of 3.2 cm. On the top cross section 0.2 cm below the top surface, the dislocation density was on the order of  $10^3 \text{ cm}^{-2}$  over most of the cross sectional area but much higher at the periphery of the cross section. Even on the top cross section, many dislocations moved from the center to the periphery of the ingot in the initial stage of growth. On the bottom cross section 2.8 cm below the top surface, the dislocation density slightly decreased on the order of  $10^3 \text{ cm}^{-2}$  over most of the cross sectional area but much higher at the periphery. This means that the dislocations in the ingot moved to the periphery from the center of the ingots during growth owing to the convex growing interface. Figure 16 shows the EPD as a function of the distance from the top surface of the ingots (Nakajima



**Fig. 16** EPD as a function of the distance from the top surface of the ingots. The maximum and minimum EPDs were evaluated in a cross section of each ingot. The EPD rapidly decreased as the distance from the top surface of ingots increased. The dislocation density in the center of the ingots was always on the order of  $10^2$ – $10^4$   $\text{cm}^{-2}$  (From Nakajima et al. (2016b))



et al. 2016b). The maximum and minimum EPDs were evaluated in a cross section of each ingot. The maximum and minimum EPDs usually appeared near the periphery and center of ingots, respectively. The EPD near the top surface of the ingots was very high, especially just below the seed crystal. However, the EPD rapidly decreased as the distance from the top surface of ingots increased because dislocations moved to the periphery from the center of the ingots during growth owing to the convex growing interface (Nakajima et al. 2015, 2016b). Finally, the minimum EPD decreased to about  $300/\text{cm}^2$ . So, the dislocation density in the ingots can be reduced to the order between  $10^2$  and  $10^4$   $\text{cm}^{-2}$  without necking technique (Nakajima et al. 2016b). The EPD was much lower than that of ingots grown by the cast method.

To evaluate the oxygen concentration in the ingots, Fourier transform infrared spectrometry (FTIR) analysis was used for longitudinal and horizontal cross sections of the ingots. Oxygen that dissolves in the Si melt from the silica crucible continuously evaporates from the surface of the Si melt. Oxygen in a Si melt has an equilibrium segregation coefficient of  $k_0 \cong 1$ . The oxygen concentration is expected to be lowest near the melt surface and increase toward the bottom of the melt. Figure 17a shows a schematic illustration of the distribution of the oxygen concentration in an ingot grown by the NOC method (Nakajima et al. 2015). The thickness of the Si melt was 5 cm. The ingot was pulled upward at a rate of 0.2 mm/min while cooling the melt by 39.9 K. The diagonal length of the top surface of the ingot was 28.6 cm and the ratio of the diagonal length to the crucible diameter was 0.95. The thickness of the ingot was 9.5 cm. Figure 17b–d shows the distributions of the oxygen concentration in the ingot as a function of the distance from the ingot center immediately below the seed crystal along the surface of the ingot, in the vertical direction to the bottom of the ingot and in the slanting direction to the bottom of the ingot, respectively. The oxygen concentration slightly increased along the surface of the ingot and markedly increased in the vertical and slanting directions to the bottom of the ingot. On the basis of these results, Fig. 17a

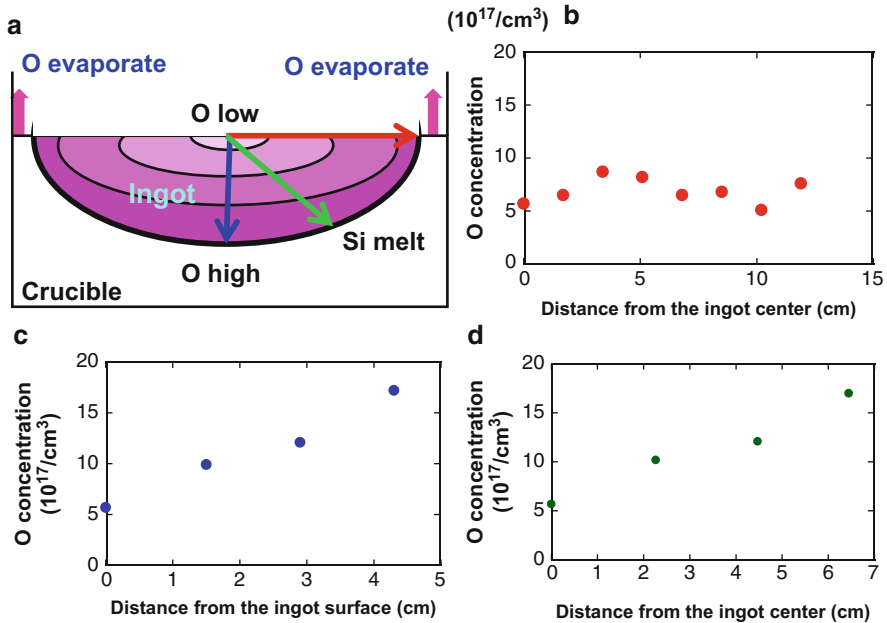


**Fig. 17** (a) Schematic illustration of distribution of the oxygen concentration in an ingot. (b) Oxygen concentration along the surface of the ingot. (c) Oxygen concentration in the vertical direction from the surface to the *bottom* of the ingot. (d) Oxygen concentration in the slanting direction from the surface to the *bottom* of the ingot. The oxygen concentration near the seed was low and increased along the surface of the ingot and in the vertical and slanting directions (From Nakajima et al. (2014a))

was drawn, which schematically shows the concentric distribution of the oxygen concentration on the seed axis. This distribution of the oxygen concentration may be due to the convex growing interface.

Figure 18 shows the oxygen concentration of ingots grown using the present furnace as a function of the diameter ratio (Nakajima et al. 2016a). The oxygen concentration of the ingots was always lower than  $1 \times 10^{18} \text{ cm}^{-3}$  and did not strongly depend on the diameter ratio. The oxygen concentration of the ingots grown using 40- and 50-cm-diameter crucibles has a tendency to be lower than that of the ingots grown using 33-cm-diameter crucibles because the ratio between the reacted crucible innersurface contacted with the Si melt and the amount of the Si melt becomes lower with the diameter of the crucible. This suggests that the convection in the Si melt was very small in our furnace. For a diameter ratio of more than 0.7, the lowest oxygen concentration of  $3.6 \times 10^{17} \text{ cm}^{-3}$  was obtained by gas flow control. This means that the convection in the Si melt or the reaction between the crucible and the Si melt may be small in the present furnace. The convection is markedly suppressed by the low co-rotating speed of the seed and crucible (1 or 0.5 rpm).

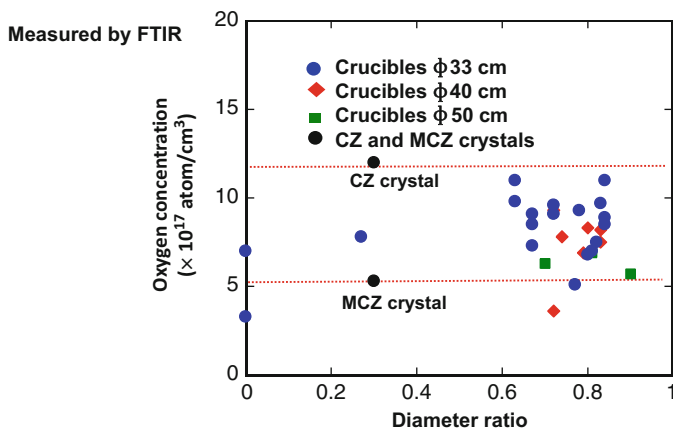


**Fig. 18** Oxygen concentration in ingots grown using 33-, 40- and 50 cm-diameter crucibles furnace as a function of the diameter ratio. It was measured by FTIR. The oxygen concentration of the ingots grown using the new and large furnace did not strongly depend on the diameter ratio. The oxygen concentration of the ingots has a tendency to become lower as the crucible diameter becomes larger (From Nakajima et al. (2016a))

The recombination lifetime was measured at Massachusetts Institute of Technology (MIT) by the transient photoconductance decay (QSSPC: Sinton WCT-120) (Sinton et al. 1996). Using the Sinton method, the effective lifetime of ingots was measured with  $\text{Al}_2\text{O}_3$  passivation deposited with thermal atomic layer deposition (Kivambe et al. 2014) before and after phosphorus diffusion gettering (PDG). Gettering was performed by phosphorus in-diffusion in a  $\text{POCl}_3$  tube furnace using two processes. The first high-throughput process includes loading the sample at  $700^\circ\text{C}$  followed by a 25 min plateau at  $845^\circ\text{C}$  and immediate unloading at  $845^\circ\text{C}$ . The second process includes a controlled cooling step after the  $845^\circ\text{C}$  plateau and a 2 h anneal at  $650^\circ\text{C}$  before unloading (Nakajima et al. 2015). The highest minority carrier lifetime was 3.2 ms which was the first result for the crystal grown inside a crucible (Nakajima et al. 2015; Castellanos et al. 2016). To reduce impurities and oxide particles inside the NOC furnace, the furnace cleaning was performed to mainly reduce Fe contamination by annealing graphite contents inside the furnace chamber in a high vacuum at higher than  $1500^\circ\text{C}$  for a long time. Table 2 shows the minority carrier lifetime of wafers selected from the n-type ingots grown using the present furnace (Nakajima et al. 2017). The furnace cleaning was performed between the NOC-2 and NOC-3 ingots. The minority carrier lifetime of the top parts of the ingots is higher than that of the bottom parts because some oxygen precipitates may remain in the bottom parts (Jensen et al. 2016). The minority carrier lifetime of the ingots grown after furnace cleaning drastically was largely improved even in their bottom parts because Fe contamination was reduced. The millisecond lifetime was obtained after gettering owing to high purity without  $\text{Si}_3\text{N}_4$  coating.

**Table 2** Minority carrier lifetime of wafers selected from the  $n$ -type ingots at  $10^{15} \text{ cm}^{-3}$  injection level

	Wafer number	NOC-1	NOC-2	NOC-3	NOC-4
<b>Top</b>	25	725	742	1344	1580.25
	26	1086	1165	1219	
	101	583	379	562	
	102	486	508	862	
<b>Bottom</b>					

Lifetimes measured in MIT (Prof. T. Bounassisi)

Furnace cleaning was performed between No. 2 and 3 ingots (Fe contamination was reduced)

From Nakajima et al. (2017)

The inductively coupled plasma source-mass spectrometry (ICP-MS) was used to determine trace and ultra-trace metal elements in Si ingots. Regardless of the furnace cleaning, the Fe concentration in the ingots was always lower than  $5.0 \times 10^{12} \text{ cm}^{-3}$  which is the detection limit of the ICP-MS. The Fourier transformed infrared (FT-IR) spectroscopy was used to determine carbon (C) and nitrogen (N) concentrations in Si ingots. The C and N concentrations in the ingots are listed in Table 1. Both concentrations were largely reduced after furnace cleaning.

## Distribution of Conversion Efficiency of $n$ - and $p$ -Type Solar Cells Prepared by the NOC Method After Furnace Cleaning

The minority carrier lifetime of an  $n$ -type wafer is generally higher than that of a  $p$ -type wafer (Nelson 2003).  $n$ -type solar cells were prepared in National Solar Energy Institute (INES) using wafers ( $15.6 \times 15.6 \text{ cm}^2$ ) cut from  $n$ -type ingots (see ► Chap. 9, “Growth of Crystalline Silicon for Solar Cells: Mono-Like Method”). Several  $n$ -type ingots were prepared before and after furnace cleaning. The solar cell performance of wafers cut from these ingots was determined to evaluate the quality of the ingots. The wafer size was 15.6 square cm. Using the same solar cell structure and process to obtain the conversion efficiency of 20.0% for  $n$ -type CZ wafers, the highest conversion efficiency of 19.4% and the average conversion efficiency of 19.0% were obtained for NOC wafers before furnace cleaning. The scattering width was only 1.0%. For wafers cut from the NOC-3 ingot grown after furnace cleaning, the highest conversion efficiency of 19.8% and the average conversion efficiency of 19.3% were obtained using the same solar cell

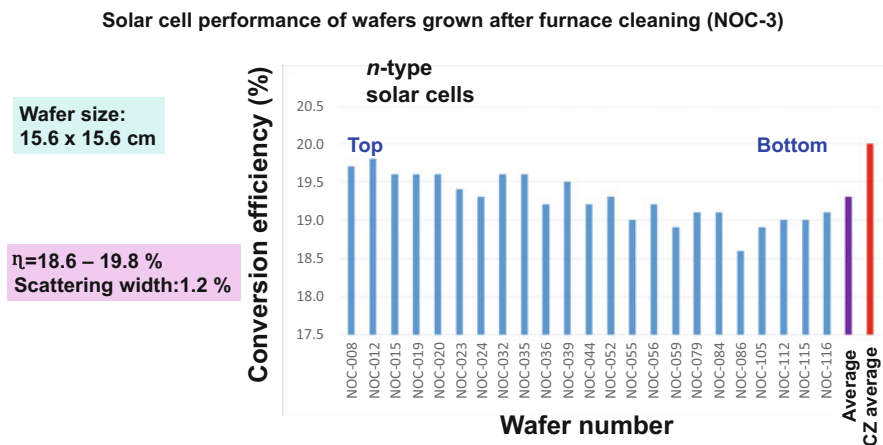


**Fig. 19** Solar cell performance of wafers cut from the *n*-type ingot (NOC-3) after furnace cleaning. Using the same solar cell structure and process to obtain the conversion efficiency of 20.0% for *n*-type CZ wafers, the highest conversion efficiency of 19.8% and the average conversion efficiency of 19.3% were obtained for the NOC wafers. The scattering width of the conversion efficiency was 1.2%. The highest conversion efficiency was almost the same as that of the CZ solar cells

structure and process to obtain the conversion efficiency of 20.0% for *n*-type CZ wafers as shown in Fig. 19 (see ► Chap. 6, “Growth of Crystalline Silicon for Solar Cells: Czochralski Si”). The scattering width of the conversion efficiency was only 1.2%. The top of the ingot had the higher conversion efficiency comparing with the bottom because some oxygen precipitates may remain in the bottom part (Jensen et al. 2016). The highest conversion efficiency was almost the same as the conversion efficiency of the CZ solar cells. The difference between the conversion efficiencies of the NOC and CZ solar cells may be mainly based upon the dislocation density in these ingots. In the NOC ingots, the dislocation density was still on the order between  $10^2$  and  $10^4 \text{ cm}^{-2}$ . On the other hand, the CZ ingots had nondislocations.

As the oxygen concentration in ingots grown by the NOC method was always lower than that of CZ ingots (Nakajima et al. 2016a), *p*-type solar cells are effective for this method because of few B-O complex and oxide precipitates in the ingots (Coletti et al. 2014; Macdonald and Cuevas 2001; Herguth et al. 2006). Figure 20 shows the solar cell structure based on the Al Back Surface Field (Al-BSF) together with the distribution of conversion efficiency of *p*-type solar cells prepared by the NOC method before furnace cleaning (Nakajima et al. 2016b). The solar cells were prepared in the Fukushima Renewable Energy Institute (FREA). The FREA standard processes were used for preparing solar cells using *p*-type NOC wafers (Castellanos et al. 2016). Using the same solar cell structure and process to obtain the conversion efficiency of 19.0% for *p*-type CZ wafers, all solar cells had higher conversion efficiency than 18.2%. The scattering width was only 0.6%. Figure 21 shows a *p*-type single ingot (NOC-6) grown after furnace cleaning (Nakajima et al. 2017).

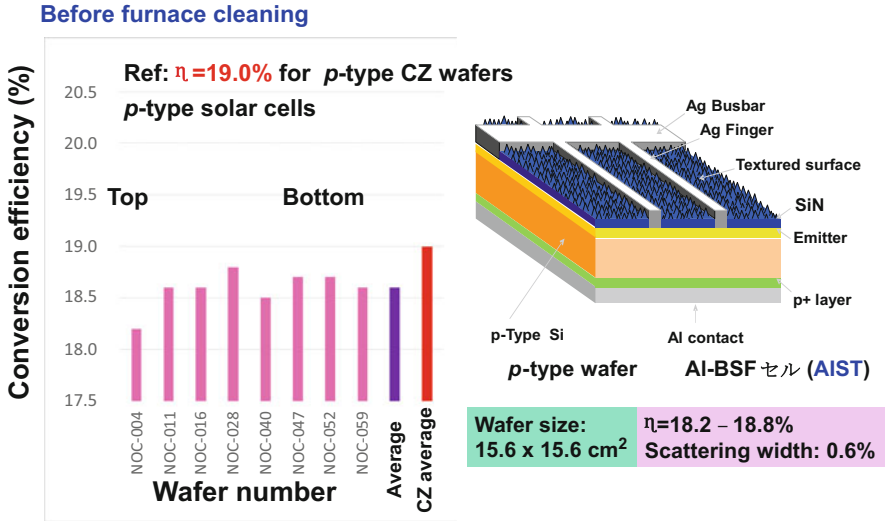


**Fig. 20** Solar cell structure (AI-BSF) together with the distribution of conversion efficiency of *p*-type solar cells prepared by the NOC method before furnace cleaning



***p*-Type single ingot (NOC-6) with a convex growth interface grown after furnace cleaning.**  
**Maximum diameter: 35.0 cm**  
**Diameter ratio: 0.7**  
**Height: 8.0 cm**

**Fig. 21** *p*-Type single ingot grown after furnace cleaning. It had a convex growth interface in the growth direction (From Nakajima et al. (2017))

The ingot had a convex growth interface in the growth direction. It was intentionally made to reduce dislocations using the low pulling and cooling rates at the end of the growth. Solar cells were prepared using wafers (15.6 × 15.6 cm<sup>2</sup>) cut from the ingot (NOC-6). The cell thickness was 175 μm. Figure 22 shows the solar cell performance of the wafers after furnace cleaning (Nakajima et al. 2017). Using the same solar cell structure and process to obtain the conversion efficiency of 19.1% for *p*-type CZ wafers, the highest conversion efficiency of 19.14% and the average conversion efficiency of 19.0% were obtained for the NOC wafers. The conversion

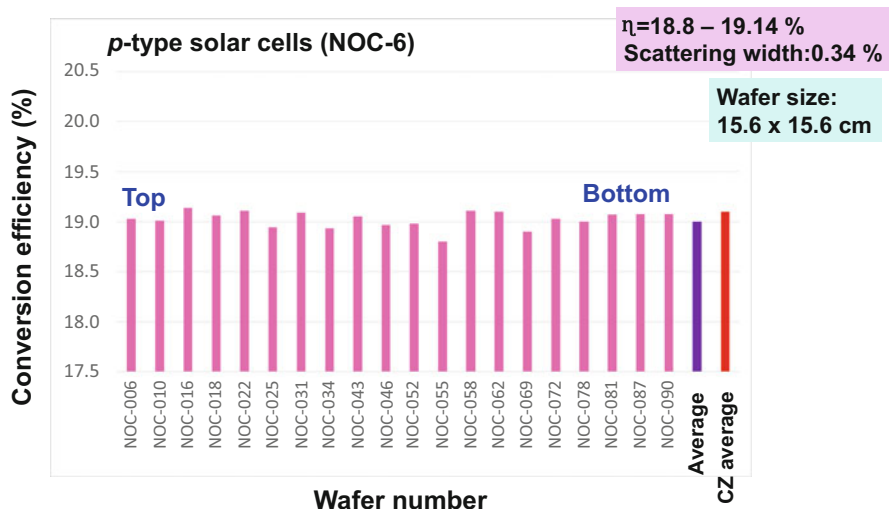


**Fig. 22** Solar cell performance of wafers cut from the *p*-type ingot (NOC-6). The highest conversion efficiency was 19.14% and the average conversion efficiency was 19.0%. Its scattering width was only 0.34%, which was quite narrow because of its high uniformity. The conversion efficiency and yield were almost the same as those of CZ solar cells (From Nakajima et al. (2017))

efficiency was the same as that for the CZ solar cells. The present conversion efficiency was much higher than that of the NOC wafers grown before furnace cleaning (Nakajima et al. 2016b). The scattering width of the conversion efficiency was only 0.34%, which was quite narrow because of its high uniformity. Using the cast furnace, solar cells with the conversion efficiency and yield as high as those of the CZ solar cells can be obtained by the NOC method for the first time. Figure 23 shows the frequency of conversion efficiency of *p*-type solar cells prepared by the high performance (HP) cast method (Lan 2014; Lan et al. 2015) and the present method (Nakajima et al. 2017) (see ► Chap. 7, “Growth of Multicrystalline Silicon for Solar Cells: The High-Performance Casting Method”). Multicrystals were used to prepare the solar cells for the HP method and single crystals were used to prepare the solar cells for the NOC method. The yield of the regular solar cells with the conversion efficiency higher than 18.8% was 100% for the present method when cutting loss was not considered. It was much larger than that for the HP cast method. The conversion efficiency and yield were almost the same as those of CZ solar cells. The quality of the NOC ingots is also almost the same as that of the CZ ingots except for the dislocation density.

## Applications of the NOC Method

On the view point of the comparison between Si wafers grown by the cast and CZ methods in the present market for solar cells, the price of Si multicrystalline wafers is slightly lower than that of single wafers. The Si multicrystalline wafers have a larger

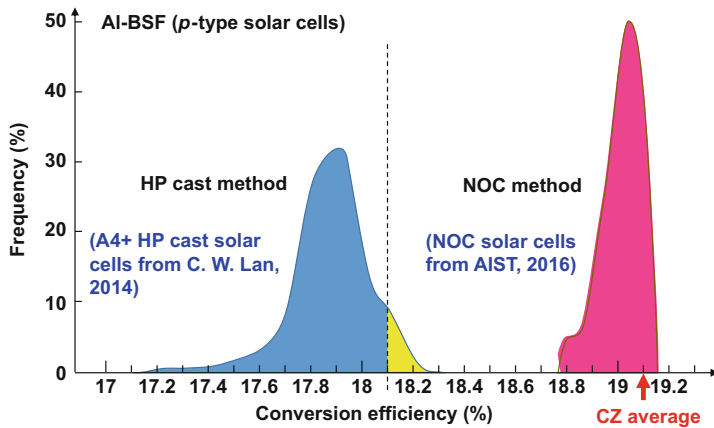


**Fig. 23** Frequency of conversion efficiency of *p*-type solar cells prepared by the HP cast method (Lan 2014; Lan et al. 2015) and the NOC method. Multicrystals were used to prepare the solar cells for the HP method and single crystals were used to prepare the solar cells for the NOC method. For the present method, the distribution was quite sharp and the yield was quite large comparing with that for the HP cast method (From Nakajima et al. (2017))

share than the single wafers because of their high productivity. But they lose 1% efficiency because of their inefficient texture structure. The next target of the cast method should be to develop uniform large Si single ingots using the cast furnace. The next target of the CZ method may be the growth of large ingots from which four wafers can be obtained to improve their low productivity. The present method has a potential to realize these two targets.

As an advanced cast method, the NOC method is effective to grow uniform large Si single ingots with sufficient quality to obtain *p*-type solar cells with high conversion efficiency and high yield using a cast furnace as shown in Figs. 22 and 23. Figure 24 shows each yield of materials for the HP cast and present methods. In this case, an ingot with a 68 cm diameter will be grown for the NOC method. Ten wafers can be obtained from a cross section of the NOC ingot. So, the final yield of the regular solar cells with the conversion efficiency higher than 18.8% will be between 63% and 81% for the present method when that for the HP cast method will be less than 10%. In this estimation, the maximum cutting loss of the NOC ingot was assumed to be 30%, but it will be less than 10% when the cutting-loss crystals will be used again for Si source materials. In this case, the maximum yield will be more than 80% for the NOC method. Figure 25 shows a schematic illustration of a cast ingot grown by the present method (Nakajima et al. 2017). The horizontal growth rate is higher than 1 mm/mi (Nakajima et al. 2014c). So, for practical use, such a flat plate single ingot with large diameter and large volume will be grown using the cast furnace to keep the high productivity. The high buoyancy from the Si melt helps the large ingot to remain in the Si melt. In this growth, the present method has such merits. The dislocation density is on the order between  $10^2$  and  $10^4$   $\text{cm}^{-2}$  in the center of ingots. There was no meaningful



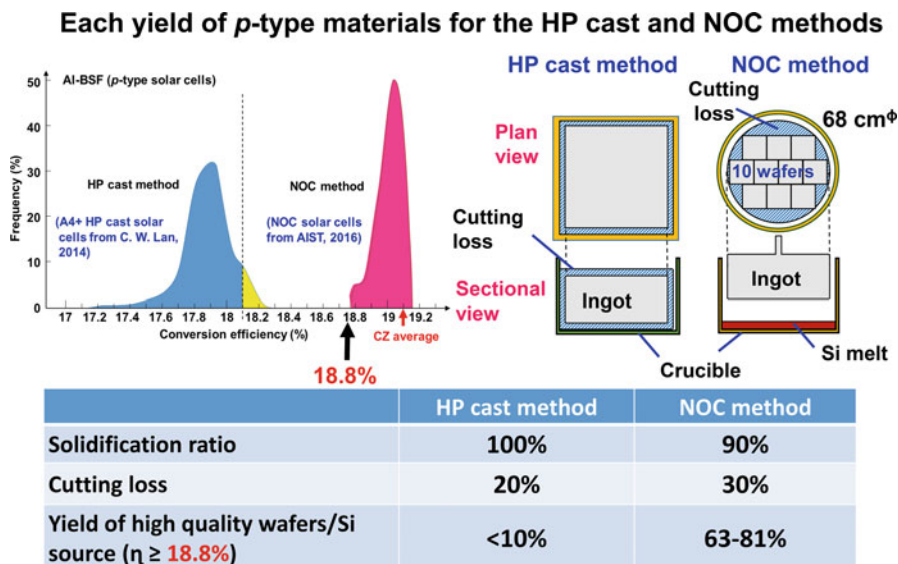


**Fig. 24** Each yield of materials for the HP cast and present methods when an ingot with a 68 cm diameter will be grown

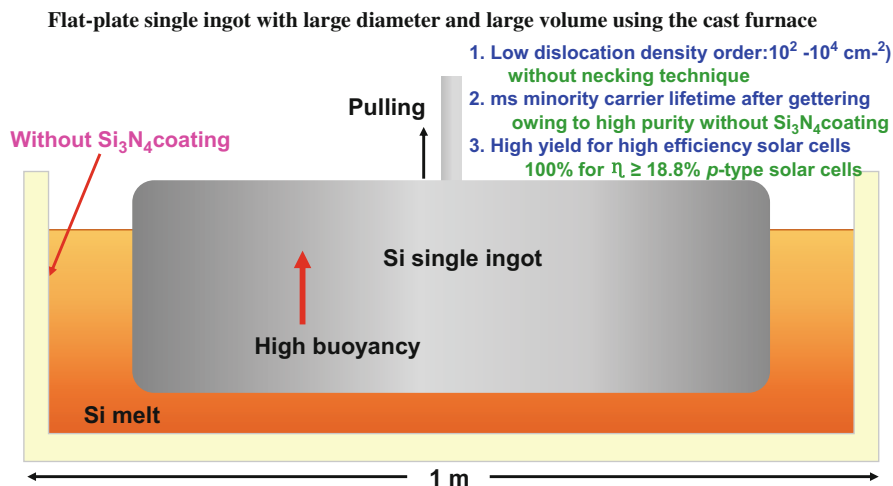


**Fig. 25** Schematic illustration of a cast ingot grown by the NOC method together with its merits. For practical use, such a flat plate single ingot with large diameter and large volume can be grown using the cast furnace (From Nakajima et al. (2017))

difference for the oxygen concentration of the *n*- and *p*-type ingots and it was always lower than  $1 \times 10^{18} \text{ cm}^{-3}$  after the furnace cleaning. The millisecond lifetime is obtained after gettering. The yield of the regular solar cells with high conversion efficiency is much larger. Figure 26 shows a schematic illustration of

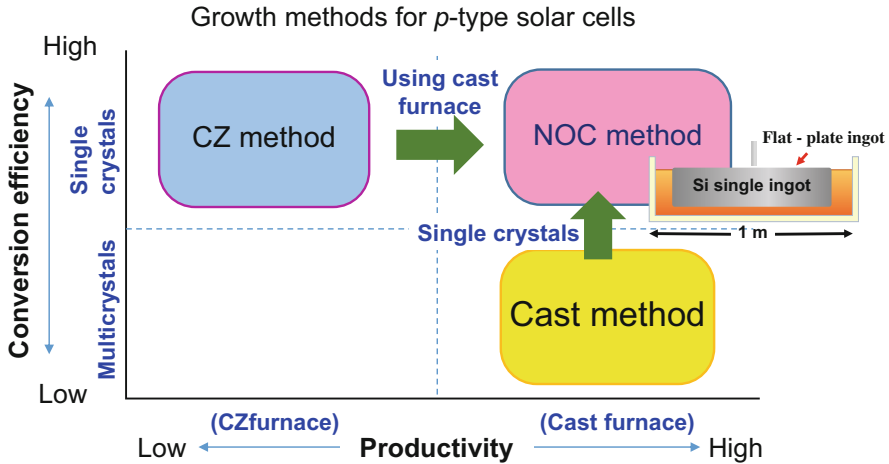


**Fig. 26** Schematic illustration of the growth methods for  $p$ -type solar cells in the mega solar market. When single ingots with large volume will be grown using the cast furnace to keep its high productivity, the present method will be an advanced cast method in this market

the growth methods for  $p$ -type solar cells in the mega solar market. When the large single ingots shown in Fig. 25 will be grown using the cast furnace, the present method will be an advanced cast method to realize uniform large Si single ingots with sufficient quality to obtain solar cells with high conversion efficiency and high yield. To grow such large ingots, it is very important to prevent the local supercooling in the Si melt during growth (Nakajima et al. 2016a).

## Conclusion

The NOC method was proposed to obtain uniform large Si single ingots with sufficient quality to obtain solar cells with the conversion efficiency and yield higher than those of HP cast solar cells. Existence of the low-temperature region was confirmed by rapidly pulling the ingot upward from the Si melt. Using this method, Si single ingots were grown inside Si melts without contact with the crucible wall. The  $\langle 110 \rangle$  growth rate was as high as 1.5 mm/min using the cooling rate of 0.4 K/min. It was higher than that of the cast method. Si single ingots with a perfect square-shape were prepared by the NOC method. The diameter (23 cm<sup>φ</sup>) of an ingot was kept constant during growth using a high cooling rate of 0.4 mm/min. A maximum diameter ratio of 0.9 and a maximum diameter of 45.0 cm were obtained using a 50 cm diameter crucible. Dislocations moved to the periphery from the center of the ingot during growth because of the convex growing interface. Owing to this effect, the dislocation density in the center of the ingots was generally on the order between 10<sup>2</sup> and 10<sup>4</sup> cm<sup>-2</sup> without necking technique. The lowest oxygen concentration of 3.6 × 10<sup>17</sup> cm<sup>-3</sup> was obtained by this method. Minority carrier lifetime at the

injection level of  $1 \times 10^{15}/\text{cm}^3$  was 768  $\mu\text{s}$  before extended P gettering and 3.2 ms after extended P gettering. The highest conversion efficiency of *n*-type wafers was 19.8%, using the same solar cell structure and process to obtain the conversion efficiency of 20.0% for *n*-type CZ wafers. The highest conversion efficiency of *p*-type wafers was 19.14% and the average conversion efficiency was 19.0%, using the same solar cell structure and process to obtain the conversion efficiency of 19.1% for *p*-type CZ wafers. The yield of the *p*-type regular solar cells with the conversion efficiency higher than 18.8% was much larger for the present method than that for the HP cast method. The present method is promising as an advanced cast method for obtaining uniform large Si single ingots with sufficient quality to obtain high-efficiency solar cells with a high yield.

---

## Cross-References

- [Growth of Multicrystalline Silicon for Solar Cells: The High-Performance Casting Method](#)

---

## References

- D.F. Bliss, Evolution and application of the Kyropoulos crystal growth method, in: *50 Years Progress in Crystal Growth: A Reprint Collection*, ed. by R.S. Feigelson (Elsevier, Amsterdam, 2004), pp. 29–33
- W.N. Borle, S. Tata, S.K. Varma, J. Cryst. Growth **8**, 223 (1971)
- S. Castellanos, M. Kivambe, M.A. Jensen, D.M. Powell, K. Nakajima, K. Morishita, R. Murai, T. Buonassisi, Science Direct, Energy Procedia **92**, 779 (2016)
- G. Coletti, P. Manshanden, S. Bernardini, P.C.P. Bronsveld, A. Gutjahr, Z. Hu, G. Li, Sol. Energy Mater. Sol. Cells **130**, 647 (2014)
- J. Czochralski, Z. Phys. Chem. **92**, 219 (1917)
- W. Dash, C. J. Appl. Phys. **30**, 459 (1959)
- S.E. Demina, E.N. Bystrova, M.A. Lukanina, V.M. Mamedov, V.S. Yuferev, E.V. Eskov, M.V. Nikolenko, V.S. Postolov, V.V. Kalaev, Opt. Mater. **30**, 62 (2007)
- K. Fujiwara, K. Maeda, N. Usami, G. Sazaki, Y. Nose, A. Nomura, T. Shishido, K. Nakajima, Acta Mater. **56**, 2663 (2008)
- A. Herguth, G. Schubert, M. Kaes, G. Hahn, in *21st EUPVSEC*, p. 530, 2006
- M.A. Jensen, V. LaSalvia, A.E. Morishige, K. Nakajima, Y. Veschetti, F. Jay, A. Jouini, A. Youssef, P. Stradins, T. Buonassisi, in *Silicon PV*, 2016
- M. Kivambe, D.M. Powell, S. Castellanos, M.A. Jensen, A.E. Morishige, K. Nakajima, K. Morishita, R. Murai, T. Buonassisi, J. Cryst. Growth **407**, 31 (2014)
- E. Kuroda, S. Matsubara, T. Saitoh, Jpn. J. Appl. Phys. **19**, L361 (1980a)
- E. Kuroda, S. Matsubara, T. Saitoh, Jpn. J. Appl. Phys. **19**, L361 (1980b)
- C.W. Lan, in *6th World Conference on Photovoltaic Energy Conversion*, 2014
- C.W. Lan, C. Hsu, K. Nakajima, *Handbook of Crystal Growth, Bulk Crystal Growth: Basic Techniques Vol. II, Part a* (Elsevier, Amsterdam, 2015), pp. 373–411
- D. Macdonald, A. Cuevas, Sol. Energy Mater. Sol. Cells **65**, 509 (2001)
- W. Miller, C. Frank-Rotsch, M. Czupalla, P. Rudolph, Cryst. Res. Technol. **47**, 285 (2012)
- A. Muiznieks, A. Rudevics, K. Lacis, H. Riemann, A. Lüdige, F.W. Schulze, B. Nacke, in *Proceedings of the International Scientific Colloquium, Modelling for Material*, 2006, p. 89

- K. Nakajima, R. Murai, K. Morishita, K. Kutsukake, N. Usami, *J. Cryst. Growth* **344**, 6 (2012a)
- K. Nakajima, K. Morishita, R. Murai, K. Kutsukake, *J. Cryst. Growth* **355**, 38 (2012b)
- K. Nakajima, R. Murai, K. Morishita, K. Kutsukake, *J. Cryst. Growth* **372**, 121 (2013)
- K. Nakajima, R. Murai, K. Morishita, *Jpn. J. Appl. Phys.* **53**, 025501–025501 (2014a)
- K. Nakajima, K. Morishita, R. Murai, N. Usami, *J. Cryst. Growth* **389**, 112 (2014b)
- K. Nakajima, K. Morishita, R. Murai, *J. Cryst. Growth* **405**, 44 (2014c)
- K. Nakajima, R. Murai, S. Ono, K. Morishita, M. Kivambe, D.M. Powell, T. Buonassisi, *Jpn. J. Appl. Phys.* **54**, 015504–015501 (2015)
- K. Nakajima, S. Ono, R. Murai, Y. Kaneko, *J. Electron. Mater.* **45**, 2837 (2016a)
- K. Nakajima, S. Ono, Y. Kaneko, R. Murai, K. Shirasawa, T. Fukuda, H. Takato, in *Proceedings of the 43th IEEE Photovoltaic Specialists Conference*, 2016b, pp. 68–72
- K. Nakajima, S. Ono, Y. Kaneko, R. Mura, K. Shirasawa, T. Fukuda, H. Takato, S. Castellanos, M.A. Jensen, A. Youssef, T. Buonassisi, F. Jay, Y. Veschetti, A. Jouini, *J. Cryst. Growth* **468**, 705 (2017)
- J. Nelson, *Physics of Solar Cells*, Chapter 7 (Imperial College Press, London, 2003)
- G. Ratnieks, A. Muiznieks, A. Mühlbauer, *J. Cryst. Growth* **255**, 227 (2003)
- P.S. Ravishankar, *Sol. Energy Mater.* **12**, 361 (1985)
- P.J. Rudolph, *Jpn. Assoc. Cryst. Growth* **39**, 8 (2012)
- P. Rudolph, M. Czupalla, B. Lux, F. Kirscht, C. Frank-Rotsch, W. Miller, M. Albrecht, *J. Cryst. Growth* **318**, 249 (2011)
- F. Secco d’Aragona, *J. Electrochem. Soc.* **119**, 948 (1972)
- R.A. Sinton, A. Cuevas, M. Stuckings, in *Proceedings of the 25th IEEE Photovoltaic Specialists Conference*, 1996, p. 457
- W. Zulehner, *J. Cryst. Growth* **65**, 189 (1983)

---

## Part III

# Silicon Wafer Preparing



Hans Joachim Möller

## Contents

Introduction .....	270
Cutting and Grinding of Ingots .....	271
Multi-crystalline Silicon .....	272
Monocrystalline Silicon .....	273
Multi-wire Sawing .....	274
Slurry Sawing .....	274
Sawing with Structured Wires .....	282
Fixed Abrasive Sawing .....	283
Basic Sawing Mechanisms .....	287
Slurry-Based Sawing .....	287
Fixed Abrasive Sawing .....	295
Recycling of Kerf Loss and Slurry .....	297
PEG/SiC Slurries .....	298
Water-Based Slurries and Coolants .....	302
Directional Solidification .....	302
Alternative Wafering Technologies .....	303
Cleavage Technologies .....	304
Layer Transfer Technologies .....	305
Conclusion .....	306
Cross-References .....	307
References .....	307

## Abstract

The fabrication of silicon wafers for solar cells and modules is an expensive step in the processing chain. The technological development is therefore primarily driven by the need to reduce cost. The dominant wafering method is multi-wire sawing with a straight steel wire and an abrasive slurry consisting of polyethylene

H. J. Möller (✉)

Fraunhofer Technology Center for Semiconductor Materials, Freiberg, Germany

e-mail: [hans.joachim.moeller@thm.fraunhofer.de](mailto:hans.joachim.moeller@thm.fraunhofer.de)

glycols (PEG) and SiC powders (loose abrasive sawing). Substantial cost reductions are possible with structured steel wires or wires coated with diamond particles (fixed abrasive sawing) and the replacement of PEG by water-based fluids. Apart from the cost, the wafer qualities such as thickness variations, roughness, subsurface saw damage, and fracture stability play an important role and have to be improved as well. These factors depend on many sawing parameters, which makes optimization a difficult task. The chapter describes the requirements on the sawing machines, the wires, the slurries, the wafer quality, and the experimental methods, which have been developed to characterize wafers and the consumables. The fundamental micromechanical sawing processes and models are also described. Their knowledge is helpful to improve the sawing process in a controlled way. Alternative wafering methods and their perspectives are presented briefly.

---

**Keywords**

Silicon wafer · Wafering · Multi-wire sawing · Loose abrasive sawing · Fixed abrasive sawing · Slurry · Diamond wire · Structured wire · Cleavage technology · Silicon recycling · Slurry recycling

---

## Introduction

More than 90% of today's solar cells are fabricated from silicon wafers. Because of the low absorption of silicon, a wafer thickness of about 200–300  $\mu\text{m}$  is required to absorb and convert the main part of the light into electrical power. For a long time, this was also the standard thickness of the wafers. New developments in the solar cell technology allowed a reduction of the wafer thickness to about 180  $\mu\text{m}$  today, and this trend may continue down to about 80  $\mu\text{m}$  or less. The main driving force for this development is the high cost of the silicon material, which has a cost share of about 16% of the final module cost (ITRPV 2016).

The wafer-processing techniques are based on cutting large multi- or monocrystalline silicon crystals by saws (parts ► [“Polycrystalline Silicon Thin Film”](#) and ► [“Crystalline Silicon Growth”](#)). Several processing steps with different types of machines are required to cut the crystals into the final wafer size. Multi-wire sawing is the last step and the main slicing technique for wafers. The advantages are a high yield in production and a good quality for the wafers. This fabrication step needs expensive consumables and has a share of about 12% of the final module cost. Sawing is also accompanied by a substantial loss of high-quality silicon due to the cutting kerf. Reducing the wafer thickness and kerf loss and recycling valuable silicon material are thus important developments, which are currently pursued. Wafers with thicknesses below 100  $\mu\text{m}$  can already be sawn, and the lower limit of the multi-wire technology has certainly not been reached.

A number of kerfless wafering technologies have also been developed in the past by growing the silicon crystals either directly as wafers or in form of ribbons. Some

of these techniques had reached an industrial production level but have been abandoned in the meantime because they were not competitive. Therefore these wafer fabrication methods shall not be presented here.

Other kerfless techniques, which are based on cleavage or layer transfer technologies, are still under development. These methods require monocrystalline material and are often directly integrated into the solar cell process. Since the wafers are usually much thinner, below 50  $\mu\text{m}$ , these techniques may offer an alternative if a future solar cell technology requires wafers with such thicknesses.

The main focus of this chapter is therefore on the standard multi-wire sawing process. This wafering technique depends on many variable parameters, which makes it difficult to optimize the process in view of throughput, material loss, reduction of supply materials, and wafer surface quality. Most of the progress has been made by experience and improved machine technology, but a basic knowledge about the microscopic details of the sawing process is also necessary in order to slice crystals in a controlled way. This is particularly necessary, when the wafer thickness will be reduced further in the future.

The sawing processes damage the ingot and wafer surfaces mechanically. The resulting surface damage has an influence on the mechanical stability of the wafers, the following etching and texturization steps and the contamination with metallic and other impurities. The damaged layers have to be removed for further processing the wafers. This is a material loss, which becomes increasingly detrimental, when the wafer thicknesses are further reduced. Therefore many specialized characterization techniques have been developed to investigate the surface quality of the wafers and the factors which determine the surface damage (► [Chap. 13, “Characterization of Wafers and Supply Materials”](#)).

---

## Cutting and Grinding of Ingots

Both mono- and multi-crystalline silicon are used for solar cells. Due to the different growth techniques, the initial crystals have different shapes. Multi-crystalline crystals are grown in square-shaped crucibles by directional solidification (Fig. 1a). The side lengths increased over the years and have reached sizes up to about  $1 \times 1 \text{ m}^2$ . The height of the ingots remained at about 25–30 cm. Monocrystalline silicon is grown by the Cz technique and yields round crystals (Fig. 2a). For PV applications crystals with diameters of about 20 cm and a length of about 2 m are grown. Since wafers for solar cells have a standard size, the crystals have to be cut into the final shapes. In a first step, the crystals are cut into ingots with an approximate cross section of the final wafer size. Then the side faces and edges of the ingots are ground and polished until the final dimension of the cross section is reached. In a third step, these ingots are sliced into the wafers then. Different types of machines, which have been adapted to the different shapes and sizes of the initial crystals, are required for these steps.



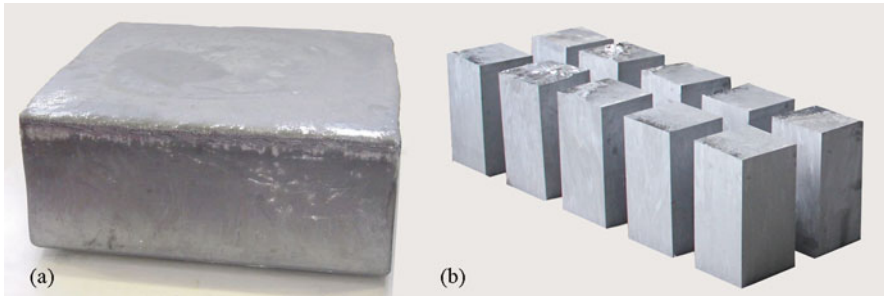


**Fig. 1** Multi-crystalline silicon crystal (a) and ingots after slicing (b)



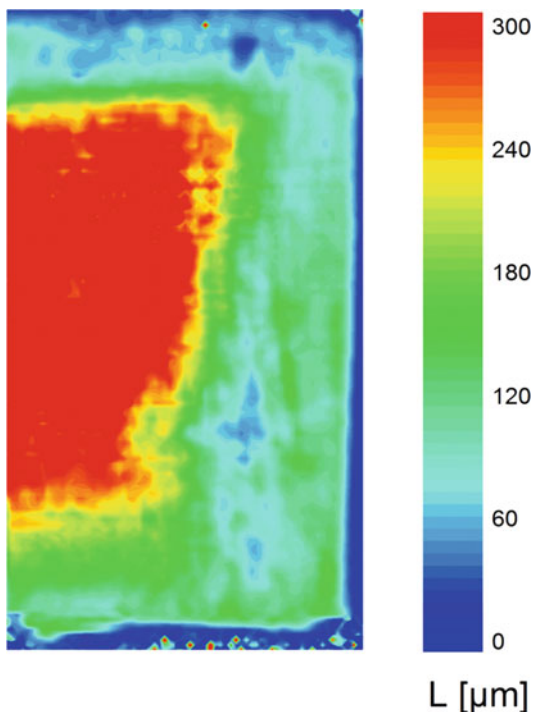
**Fig. 2** Cz silicon crystal (a) and ingot after slicing (b)

## Multi-crystalline Silicon

Due to the permanent contact to the crucible walls during growth, a multi-crystalline crystal is contaminated at the side faces. These parts of the crystal have a much lower lifetime of charge carriers and cannot be used for solar cells (part ► [“Polycrystalline Silicon Thin Film”](#)). The extent of the contamination is measured by lifetime or diffusion lengths methods. A diffusion length topogram at a cross section of a crystal in Fig. 3 shows that a few centimeters of material on each side is deteriorated. These parts of the crystal have to be removed. After cleaning by etching, these parts can be used again as feedstock material. The remaining crystal is sliced into ingots with the diameter of the final wafers (Fig. 1b). The cutting is achieved in one step by diamond-coated multi-wires or multiband saws. Depending on the initial crystal size, one obtains currently mainly  $6 \times 6$  ingots (G6 crystals), but larger crystals up to G8 can still be cut by this technique. The requirements on the precision of the sawing machines and the cutting parameters are much less compared to the multi-wire saws for the following wafering process.

In the next step, the ingots are screened with an infrared transmission camera system to detect (mostly  $\text{SiC}$  or  $\text{Si}_3\text{N}_4$ ) precipitates. Such parts of the ingots are removed before further processing. When the ingots are sliced into wafers, the side faces of the ingots become the edges of the wafers. Since the final wafers are very thin, they are also very fragile. Fracture of the wafers is thus an important issue considering the productivity of the wafering process (► [Chap. 13, “Characterization of Wafers and Supply Materials”](#)). Investigations of the fracture behavior have shown that the wafer edges mostly initiate the fracture because they

**Fig. 3** Diffusion length topogram of a cross section of an ingot showing the bottom, center, and top region as well as one side of the face. Edge parts with diffusion lengths below about 150  $\mu\text{m}$  cannot be used and are removed. The ingot height here is 25 cm



contain larger micro cracks from the previous rough slicing step. Micro-crack lengths can be in the range of 30–50  $\mu\text{m}$ . It is therefore necessary to remove these cracks before the wafering step. Each wafer supplier uses its own method, but generally one applies grinding or polishing techniques to smooth the side faces. Eventually also etching procedures are used. These steps determine the final diameter of the wafers.

### Monocrystalline Silicon

The round shape of the monocrystals requires in the first step the squaring of the crystals (part ► “[Crystalline Silicon Growth](#)”). Since larger parts of the crystal have to be removed, one optimizes the process by cutting a quasi-square shape with rounded edges (Fig. 2b). The fracture stability of the monocrystalline wafers depends on the orientation of the surface and of the side faces. One selects orientations with regard to the wire motion direction, which yield the best stability during sawing. The side faces of the ingots are also treated by grinding and polishing to obtain smooth surfaces with a low micro-crack density. The detection of precipitates in the ingots is not necessary because the material is defect-free due to the growth process. The lengths of the ingots are adjusted to the length of the wire web of the sawing machine to obtain as much wafers as possible in one cut.

## Multi-wire Sawing

Multi-wire saws for cutting silicon wafers are dedicated high-precision machines. Worldwide only few companies have developed saws which can fulfill the current requirements of the photovoltaic industry. The principle of a multi-wire saw is shown in Fig. 4. A single wire is supplied by a spool (not shown here), wound several hundred times around the wire guide rollers and picked up on the other side by another spool (also not shown). Manufacturers have developed different machine types with two, three, or four rollers. Depending on the wire guide arrangement, between one and four ingots can be cut at the same time. The wire guide rollers are coated with a polymer layer into which grooves of a certain shape are cut. These grooves guide the wires and keep them at a defined distance. The groove distance, the wire diameter, and the abrasive particle size determine the final thickness of the wafers. The wires are made from steel and have a thickness between 80 and 120  $\mu\text{m}$  today. New steel wires are usually covered with a thin brass layer from the wire drawing process, which has no function and is quickly removed during sawing.

## Slurry Sawing

Today's dominant sawing technique (Bidiville et al. 2010; Möller 2008) uses saws, where the cutting is achieved by free-floating abrasive particles, which are suspended in a carrier fluid (loose abrasive or slurry sawing). During sawing the suspension or slurry is supplied through nozzles on the wire web and carried by the wires into the sawing channel. The ingots or bricks, which have to be cut into wafers, are pushed through the wire web until the cut is finished. The motion can be either up- or downward into the wire web, depending on the machine type. The sawing velocity (also feed velocity or feed rate) is mainly kept constant except at the beginning and the end of the cut.

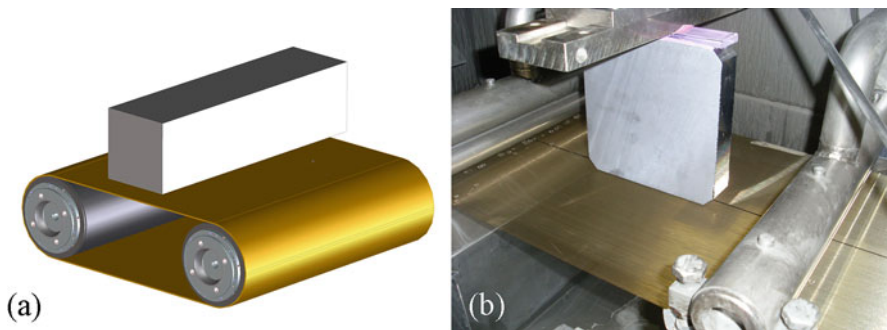


**Fig. 4** Principle of the multi-wire sawing techniques (a) and wire web with short test ingot (b). In production the ingot lengths cover the entire width of the wire web

**Table 1** Typical size specifications of commercial SiC powders. D50 is the mass median diameter, 3% of the SiC particles are smaller than D97 and larger than D3

Grit	D50 [ $\mu\text{m}$ ]	D97 [ $\mu\text{m}$ ]	D3 [ $\mu\text{m}$ ]
F 2000	1.2	0.3	3.5
F 1500	2.0	0.4	5.0
F 1200	3.0	0.5	7.0
F 1000	4.5	0.8	10
F 800	6.5	1.0	14
F 600	9.3	1.0	19
F 500	12.8	1.0	25
F 400	17.3	1.0	32

SiC powder is the most commonly used abrasive today, but diamond or other hard materials can be used as well. The powders are specified regarding their mean size and the width of the size distribution (Table 1). Typically the grain sizes are between 2 and 15  $\mu\text{m}$ , depending on the thickness of the wires which is used.

Most of the commercial slurries are based on polyethylene glycol (PEG)-based fluids. A PEG molecule can have different chain lengths. Commercial products, such as PEG 200, are mixtures of PEG molecules with different lengths. By changing the composition, the viscosity can be varied. Others fluids such as monoethylene glycol (MEG), diethylene glycol (DEG), and dipropylene glycol (DPG) or oils are also used. In fact, oil has been the main fluid in previous years and is still partly used in some Asian countries today. The viscosities are kept in the range 0.05–0.2 Pas, because it gives good transportation capability for the abrasive powder. Other carrier fluids with a much lower viscosity such as water cannot be used directly as will be discussed later ([▶ Chap. 13, “Characterization of Wafers and Supply Materials”](#)).

Both PEG fluid and abrasive particles deteriorate after some cuts. Several factors contribute here: the wear of the SiC particles, the enrichment with silicon debris, and the enrichment of the fluid with water and chemical reactions of some of the components. It is however possible to recycle the fluid and the SiC and mix a new slurry. Since the SiC powder has not the same abrasive sawing capability as before, usually some virgin SiC is added. Because the recycling of the slurry and cleaning of the wafers is cheaper for PEG than for oil, this slurry is mainly used in industry today.

The main purpose of the slurry is to transport the abrasive particles into the sawing channel. Silicon material is continuously removed there through the interaction of the SiC particles with the silicon surface. The abrasive action of the SiC depends on many factors such as wire speed, force between wire and crystal, the solid fraction of SiC in the suspension, the viscosity of the suspension, the size distribution, and the shape of SiC particles. The viscosity of the slurry depends on the temperature and the solid fraction of particles, which changes because of the continuous abrasion of silicon, iron, and brass from the wire. The width of the sawing channel or kerf is mainly determined by the diameter of the wire and the

size distribution of the SiC particles. A kerf loss around 120–140  $\mu\text{m}$  per wafer is typical today.

In the loose abrasive sawing, the wires move in one direction with a speed between 10 and 20 m/s. Therefore a standard cutting process between 300 and 500 km of wire is required. The wires are used only once, the slurry can be used two to four times and is recycled then. The cutting speeds are around 0.3–0.5 mm/min, which yields a total cutting time of about 8–13 h for a standard ingot size.

The ingots, which are sliced into wafers, have currently a size of  $156 \times 156 \text{ mm}^2$ . Modern machines allow to cut several ingots simultaneously and yield between 2000 and 4000 wafers in one run. Currently wafers with a thickness of about 180  $\mu\text{m}$  for multi and 160  $\mu\text{m}$  for mono material are cut. The thickness varies however along the direction of the wire motion and is higher at the wire outlet. This is due to the unidirectional motion of the wire and changes of the sawing action along the wire channel. The change of the wafer thickness should be however less than 25  $\mu\text{m}$  (specified by the total thickness variation parameter – TTV) for high-quality wafers.

The objective of efficient sawing is to slice with a high throughput, a minimum loss of slurry and silicon, and a high quality of the resulting wafers. The control and optimization of the process are very complex, since many parameters can be varied and have an impact on the wafer quality and yield. Important is the control of wire speed, wire tension, cutting speed, and other machine parameters, but also parameters concerning the composition and properties of the abrasive SiC powders and the carrier fluids play a role.

Currently, two improvements of the sawing technology are pursued: the use of structured steel wires and the use of wires, which are coated with diamond particles (fixed abrasive wires). In the first case, the wires have small kinks at distances of millimeters, which results in a better transport of slurry into and through the sawing channel. In the second case, the cutting is achieved by the fixed abrasive diamond particles on the wire. The advantage in both cases is that the cutting speed can be increased. The slightly higher kerf loss can be compensated by a thinner core wire.

Industrial multi-wire saws allow one to record machine parameters during the entire process, such as wire and cutting speed, wire tension, power consumption, slurry flow and temperature, etc. If one wants to learn more about the details of the sawing process, one needs further information. In particular it has been shown that the measurement of the forces on the wires, the resulting wire bow, and the temperature variation along the sawing channel are important. Industrial sawing machines are not equipped with tools to measure these quantities. Force and bow sensors or IR camera systems have therefore been developed and incorporated into dedicated machines to investigate the sawing process more quantitatively. Observations of the particle and slurry transport with high-speed cameras also give valuable insight. Furthermore it is important to analyze the as-cut wafer surfaces, the wire surfaces, and the slurry properties. All these data allow one to develop quantitative models for the sawing process and help to optimize the wide parameter field.

### Force in Ingot Feed Direction

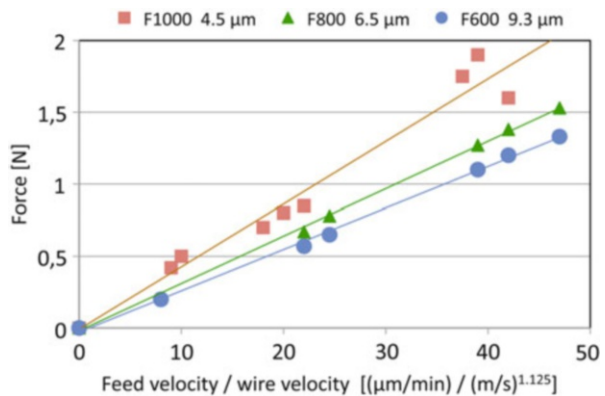
Quantitative force measurements have been carried out on single wires as well as with many wires. In the latter case, one has to consider that the wire properties may change from the first to the last wire due to wire wear (Meißner et al. 2014). Typically one measures the forces perpendicular to the wire, in the direction of ingot motion, and parallel to the wire, in the direction of wire motion. The latter gives the friction force of the sawing process.

Figure 5 shows the average vertical total force on a single wire in a multi-wire experiment as a function of the ratio of feed velocity over the  $n$ th power of the wire velocity. For  $n = 1.125$ , a straight line is obtained. The sawing rate can be summarized by the following equation:

$$v_s = v_{so} v^n F_n \quad (1)$$

where  $v$  is the wire velocity and  $F_n$  the total normal force on the wire in cutting direction. This equation is known as the Preston equation (for  $n = 1$ ) and has been found for material removal processes such as lapping and polishing (Buijs and Korpel van Houten 1993). Some investigations indicate however that the velocity exponent for sawing may be slightly higher in this case, being  $n \approx 1.1 - 1.3$ , but such measurements are often not precise enough to yield an exact value. In some measurements one also observed that the material removal starts above a certain threshold value of about 0.01–0.03 N per wire. This has been explained with a minimum load on the abrasive particle that is required for the material removal mechanism to operate. The prefactor  $v_{so}$ , the Preston coefficient, depends on many factors such as wire tension, slurry viscosity, temperature, SiC concentration, etc. It is therefore difficult to make quantitative predictions about the sawing process when these factors change. A more detailed investigation of the underlying sawing mechanism, as discussed later, will give a better description of this factor.

**Fig. 5** Average force per wire in cutting direction as a function of the ratio of feed velocity over (wire velocity) <sup>$n$</sup>  for different mean grit sizes ( $n = 1.125$ )



## Friction Forces

The friction force in wire direction is depicted in Fig. 6. It increases both with the wire and the feed velocity (Rietzschel et al. 2010). An important feature is that there is friction even without sawing (for zero feed velocity). This indicates that the friction force is less determined by the interaction of the SiC particles with the wire and crystal surfaces but mainly by friction processes inside of the slurry. These can be the interactions between particles, the internal friction in the fluid and the interaction forces between particles and fluid. Therefore it is not surprising that the particle size is also important. In general the friction forces increase for finer grit sizes. It has also been observed that there is a slight dependence on the shape of the size distribution.

Due to the friction, the temperature increases along the sawing channel. Figure 7 shows the temperature variations along the side face of an ingot. These data have been obtained by an infrared thermography camera during a slurry-based cut. The temperature increases from about 20 °C to more than 50 °C along the sawing channel. More precise measurements have shown that the temperatures close to the sawing channel are even higher by about 15 °C (Johnsen et al. 2009). Since the viscosity is exponentially dependent on the temperature, a substantial

**Fig. 6** Friction force measurements parallel to a single wire as a function of the wire velocity for different sawing velocities (PEG 200/SiC 23 vol%)

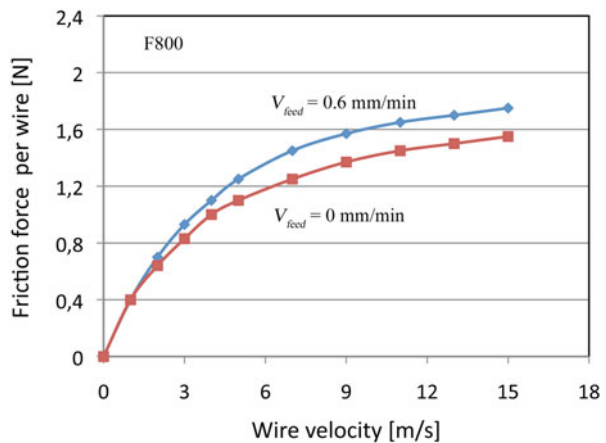
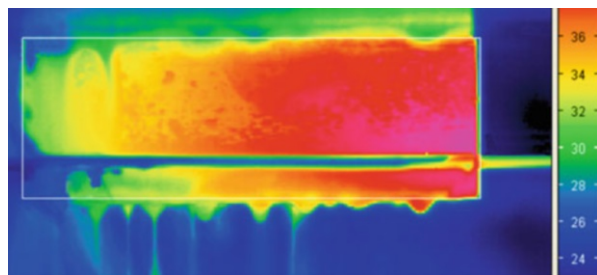


**Fig. 7** Temperature distribution on the cross section of an ingot during sawing (measured by infrared thermography)



change of the viscosity occurs along the sawing channel. All factors, which affect the friction force and temperature, thus also have an impact on the viscosity. Sawing experience shows that small changes of the slurry temperature can have a significant influence on the sawing result. Therefore a good control and stabilization of the slurry temperature within about  $\pm 1\text{ }^\circ\text{C}$  is very important in the sawing process.

**Dependence on Slurry Properties**

Many experimental results show that the slurry properties play an important role in the sawing process. It is however difficult to understand the various dependences because of the complexity of the interactions. The slurry has to transport the abrasive particles into the sawing channel and to remove the silicon and metal debris (from the steel wire) out of the sawing channel (Retsch et al. 2012; Kaminski et al. 2010).

The main slurry property is the viscosity. It depends on the particle load, which is depicted in Fig. 8 in the case of SiC load. The general trend is that with increasing volume fraction  $\phi$  the viscosity  $\eta$  increases. One can also see that a smaller grit size increases the viscosity as well. In general, the dependence can be approximated by the Krieger-Dougherty relationship

$$\eta = \eta_o(1 - \phi/\phi_o)^{-q} \tag{2}$$

if appropriate parameters are selected for  $\eta_o$  and  $q$ .  $\eta_o$  is the viscosity of the carrier fluid (Struble and Sun 1993). The experimental data given here yield a value of  $q \approx 1$ .

During sawing the solid volume fraction in the fluid changes in the sawing channel because of the removed silicon and the wear of the wire. The debris is finer than the average SiC grain size. Therefore one can expect an increase in the viscosity due to the increased volume and the contribution of finer particles. It has also been reported that the shape of the particles has an effect on the slurry viscosity.

**Fig. 8** Relative viscosity as a function of the volume fraction of SiC in a PEG 300 carrier fluid for different grit size distributions. The solid lines are Krieger-Dougherty fits with appropriate parameters

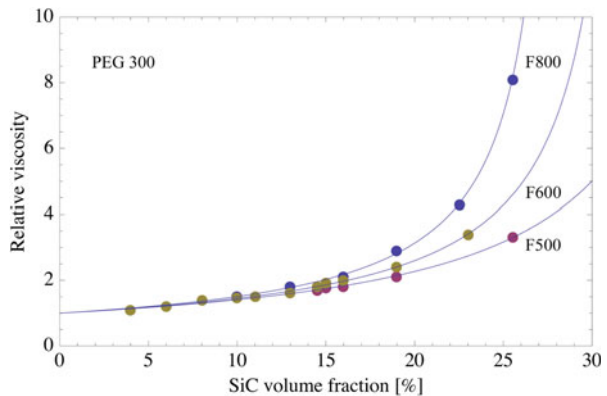
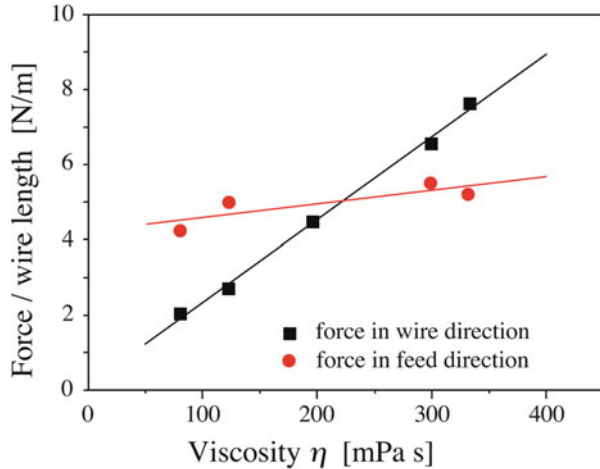




**Fig. 9** Dependence of friction and feed force per wire on the slurry viscosity at the wire inlet. The measured forces are averaged values because of the viscosity changes along the wire channel



Considering all factors the viscosity at the entry and exit of the sawing channel differs and varies along the channel. The dominant effect however is the temperature increase, which decreases the viscosity. The addition of solid material due to debris increases the viscosity but this effect is overcompensated by the temperature induced viscosity decrease.

The influence of the slurry on the sawing performance is a key factor. This can be seen in Fig. 9 which depicts the dependence of the forces on the viscosity. Both the total force on the wire in sawing direction and along the wire (friction force) increase with the viscosity of the slurry. According to the basic Preston equation, this has an impact on the sawing velocity.

It has also been observed that parallel to the viscosity, the pH value increases from around six to seven due to chemical reactions within the slurry. This has an impact on the zeta potential of SiC and silicon powder in the slurry, which is a measure for the surface potential and the charge of particles in a suspension. Highly charged particles are more dispersed in a suspension, which is beneficial for the transport along the sawing channel. The particle dispersion also plays a role in slurry recycling processes.

### Water-Based SiC Slurries

The standard sawing process uses PEG as cutting fluids. A replacement of the PEG by water saves cost but has several drawbacks. The viscous properties of water are too low to efficiently transport the SiC and Si powder particles along the sawing channel. Furthermore silicon interacts with water and produces hydrogen which increases the risk of explosions, particularly in the supply tanks where the slurry remains for a longer time.

Other problems arise from the buildup of waste material in the machine because water evaporates quicker than PEG and the remaining powder material clogs pipes and other parts in the saw. One usually adds a mixture of different chemicals to

reduce these problems but at the expense of higher cost. Water-based slurries therefore could not replace standard PEG/SiC slurry so far but may do so in the future particularly with the use of structured wires.

### Wire Tension

The wire web in modern multi-wire saws is up to 100 cm in width and contains several thousand parallel wire segments depending on the machine type. To build such a wire web, 7–10 km of wire is necessary. The control of the wire tension is essential in the sawing process, both to prevent wire breakage and to guarantee stable sawing conditions. The sawing machines have therefore sophisticated control mechanisms to react very quickly when the tension changes. The wire tension is kept constant before and behind the wire web, mostly between 15 and 25 N at the entry. Changes of the wire tensions between the wire guide rollers in the cutting area cannot be controlled. Recent investigations have shown that the wire tension is actually reduced from the first to the last wire in the web due to two effects (Meißner et al. 2014). During the first 3–5 cm (100–200 loops) in the wire web, the wire is plastically deformed by about 0.2% and loses about 2–3 N in tension force. It could be shown that this is due to the repeated chipping and/or sticking events at SiC precipitates in the silicon crystal, which momentarily hinder the motion of the wire at this position and stretch it beyond the elastic limit. This effect saturates after some time since the wire material hardens due to the plastic deformation. The second reason is the wire wear which reduces the diameter of the wire continuously up to about 10%, depending on the length of ingots, which are cut. Correspondingly the tension decreases gradually to the end. A total reduction of the tension by about 25% has been measured over an ingot length of about 65 cm.

### Wafer Thickness, Wire Diameter, and Particle Size Distribution

The expected reduction of the wafer thickness in the future also requires a reduction of the kerf loss by using thinner wires. It has been demonstrated that one can slice 100  $\mu\text{m}$  thick wafers with 80  $\mu\text{m}$  wires and probably even less (Kaminski et al. 2009). Such investigations also showed that one has to adjust the mean size of the abrasive particle. The results given in Fig. 10 indicate that there is an optimum average grit size for each wire diameter (Meißner et al. 2012).

Finer grain diameters yield however a reduced sawing velocity. In order to maintain a high sawing velocity, one needs higher forces on the wire or higher wire velocities (Eq. 1). There are limitations however because of the fracture strength of the wire and limitations on the maximum speed of a saw. Commercial steel wires have fracture stresses around 4 GPa and can bear forces around 40 N. Calculations of the wire stresses as a function of the total applied forces, which have been obtained from experimental results for different slurries, wire velocities, tensions, diameters, and grit sizes, show that for wires below 80  $\mu\text{m}$  and finer grit sizes, one approaches already the fracture stress (Wagner and Möller 2008).

Because of these limits for commercial wires, one cannot increase the cutting velocity too much. At present it appears that F600 or F800 is already the best choice, so that it is not clear how much the wafer thickness and the kerf can actually be

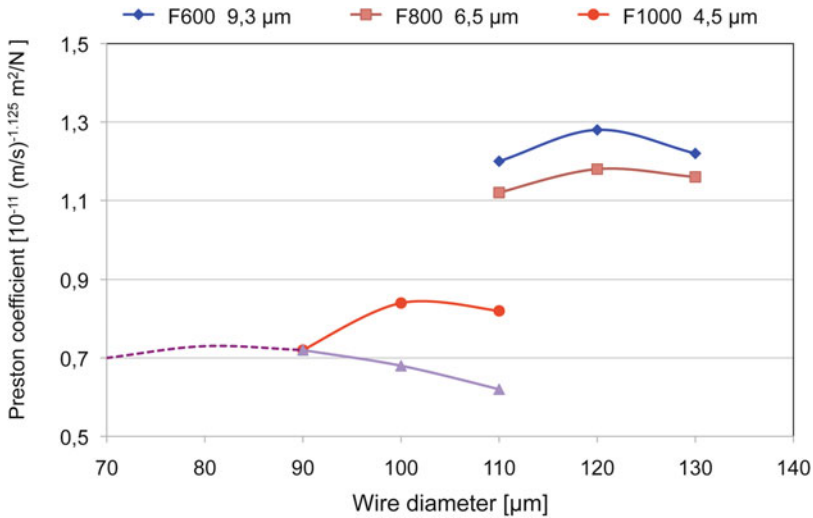


**Fig. 10** Preston coefficient as a function of the wire diameter for different grit sizes (Meißner et al. 2012)

reduced in the future. At present one can saw 120 μm wafers with wires of 80–100 μm under production conditions with a high yield.

## Sawing with Structured Wires

Experimental results as well as the experience from industrial sawing show that the sawing process can become unstable under certain conditions. An occasionally observed problem is the occurrence of deep grooves on the wafer surface. They are called outlet grooves or saw marks (Fig. 11). Such wafers cannot be processed further and therefore reduce the yield.

A typical feature of saw marks is that they are mainly observed at the wafer side, where the wire leaves the sawing channel. They occur randomly and do not affect all wafers in one batch. The quantitative investigations of the problem indicate that they occur when insufficient slurry is transported to the end of the sawing channel. A high sawing velocity  $v_s$ , a low SiC load, and high slurry temperatures enhance the probability for the occurrence of saw marks (Möller et al. 2013; Retsch et al. 2014). In the industrial process, sawing conditions have to be chosen where saw marks can be avoided. This imposes limitations particularly on the sawing speed and thus the productivity.

An improvement of the slurry-based sawing could be achieved by the use of structured wires. These are wires which contain periodic kinks at distances of millimeters (Fig. 12). The wires can be bent in a single plane, in two perpendicular planes, or with a helicoidal arrangement of the kinks. This ensures that the slurry enters the sawing channel more efficiently and results in a more stable sawing

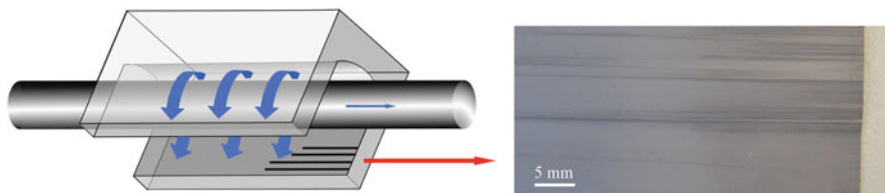


**Fig. 11** Part of an as-sawn multi-crystalline silicon wafer surface showing saw marks ending at the right edge of the wafer (wire outlet side)

**Fig. 12** Structured steel wire with kinks



process, so that no sawing marks or inhomogeneities are visible on the wafer surface. The structured wires produce a slightly higher kerf loss of silicon compared to the straight wire.

Because of the advantages, structured wires have been introduced in mass production a few years ago. An increase of the productivity and a cost reduction by about 40% has been reported because of less wire and slurry consumption. In addition, the total thickness variation (TTV) over the wafer area, which is a quality criterion, is also reduced. A further advantage is that the currently used slurry saws need only slightly modifications to accept structured wire.

Despite these advantages it is generally assumed that sawing with structured wires is only a transient technology because sawing with fixed abrasives has a higher potential for further cost reductions in the future.

## Fixed Abrasive Sawing

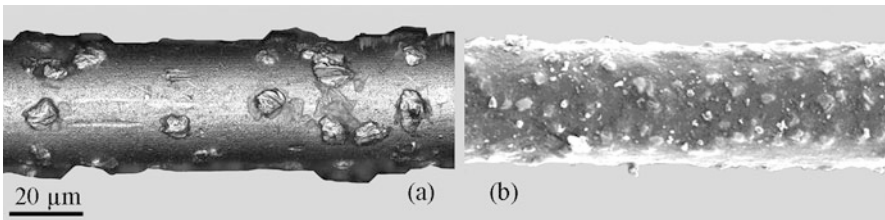
Fixed abrasive sawing uses steel wires, which are coated with diamond particles. This technique has been used for a long time to cut hard materials such as sapphire crystals. It allows much higher cutting speeds and requires less wire and only a cheap cooling fluid such as water. Compared to the established applications of fixed abrasive sawing, the requirements in the PV industry are different. Wafers and wires have to be much thinner to reduce the loss of expensive silicon material. The quality of the wafer surface, such as roughness, thickness variation (TTV), and subsurface damage (SSD), has to be high and at least comparable to conventionally sawn wafers. Furthermore there must be a cost advantage. Since the diamond-coated wires are at present still more than 50 times more expensive (about 50–70 €/km), one has to reduce cost by higher sawing speeds and multiple use of the wires. Developments of wires, sawing machines and process parameters have shown that it can be used to cut silicon wafers (ITRPV 2016), and some companies in Japan and Europe have already converted their production to this sawing technique.

Figure 13 shows the surface of such a wire with fixed diamond particles. There are mainly two techniques to fix the particles on the surface: resin bonding and electroplating bonding. Resin bonding is cheaper to manufacture, but the particles are less strongly bonded. Therefore the wires cannot be loaded as much, which reduces the performance. In the electroplating technique, the particles are embedded in a nickel-coating layer, which gives a stronger bond, but at the expense of the cost. One can expect however that a mass production of such wires will reduce the wire cost substantially.

Most of the industrial multi-wire saws today can also be used with fixed abrasive wires. But the increasing requirements on the wafer quality and productivity can only be met if sawing machines are modified. One of the reasons is the following. Higher cutting speeds increase the forces on the wire, which responds by a larger wire bow  $b_{st}$  according to Eq. (3).

$$b_{st} = F_n \frac{(4l_d + l_o)}{8T} \quad (3)$$

$F_n$  is the total normal force on the wire and  $T$  the wire tension force. The free wire length  $l_d$  and the cutting length  $l_o$  are explained in Fig. 14. Comprehensive investigations of many different sawing conditions have shown that the wire bow is directly proportional to the total thickness variation (TTV) of the wafers (Fig. 15). Higher sawing velocities for the fixed abrasive sawing therefore also lead to a higher TTV because of the force increase. Equation (3) shows, however, that one reduces the bow by decreasing the free wire length. Since  $l_d$  depends on the distance of the wire-guiding rollers in a sawing machine, it can only be changed by a comprehensive structural reconstruction of the frame, which carries the rollers (Fig. 4). In the new generation of wire saws, the distance of the rollers is decreased in anticipation of the transition to fixed abrasive sawing.



**Fig. 13** Wires with fixed diamonds: (a) nickel electroplated and (b) resin bonded

**Fig. 14** Schematic diagram of the wire bow during sawing

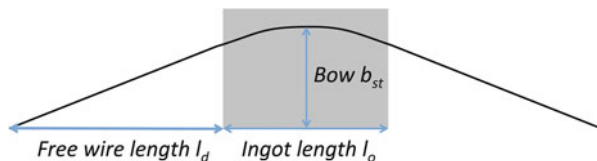
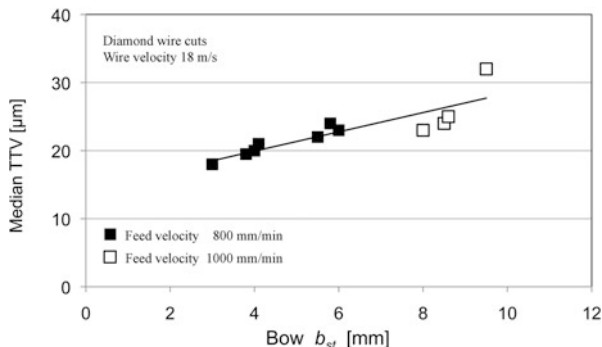


**Fig. 15** Typical dependence of the total thickness variation (TTV) on the wire bow, here for certain sawing parameters (Meißner et al. 2012)



Apart from the necessary machine modifications, there are also several other problems connected with this technology which still have to be solved. In fixed abrasive sawing, the machines are operated in the so-called pilgrim mode, where the wire is running back and forth. Typically the wire is running for several hundred meters in one direction before it is stopped, and the motion direction is reversed. In each cycle a few meters of new wire are added in one direction. Thus, the wire is reused, but each portion of the wire is used less and less in each cycle before it eventually is exhausted and permanently enters the uptake spool. From there it is finally discarded. The wire consumption is thus very much reduced. The forward and reverse lengths must be tuned for each saw, diamond wire type, and wafer specification, in order to optimize the diamond wire lifetime and wafer quality. Since each wafer in a batch is partly cut by used and fresh wire, the surface properties vary over the wafer area. One also has to find conditions for which a relatively uniform and good surface quality can be obtained.

The most important parameter determining the throughput of a wire sawing process is the sawing velocity or the table speed at which the silicon ingot is driven through the wire web. Generally table speeds of more than 1 mm/min can be achieved, which is about twice the table speed of a comparable loose abrasive process. In spite of the higher table speed, the electrical energy consumption is normally only 50% of the corresponding loose abrasive sawing value, because of reduced friction. In addition, many more cuts can be performed between the time-consuming wire spool exchanges in loose abrasive saw processes, due to the pilgrim sawing mode and the higher sawing velocity (Bye et al. 2011).

Wire wear and breakage are also an important problem, because of the high wire cost. Diamond-coated wires are more prone to wire breakage due to the protruding particles on the surface. The wire can get stuck in the sawing channel or during winding up in the spools. Diamond particles can also break out, which reduces the sawing performance. Since improved wires, sawing machines and adapted sawing conditions become available in the future one can certainly still expect a substantial improvement.

A key element in the fixed abrasive sawing process is also the choice of sawing fluid, which is necessary to locally cool the diamonds and silicon ingot and to

remove the silicon kerf (sawdust) from the sawing channel and wire. Whether cooling is actually necessary for the process is not quite clear yet, since the sawing performance does not depend on the temperature. More important is the cleaning effect of the fluid, because silicon debris tends to stick on the wire. This reduces the sawing performance when the diamond particles do not protrude enough out of the coated wire. An advantage of the fixed abrasive sawing technique is that low viscosity water-based sawing fluids with additives aiming at dispersing the sawdust and protecting the wire from corrosion can be used. But the industry also still uses glycol-based sawing fluids mixed with water to control the viscosity.

The experimental results with fixed abrasive wires are at present not as detailed as the slurry-based experiences (Buchwald et al. 2014; Behm et al. 2011). So far one has tried to optimize the process with respect to a low wire wear, a longer lifetime of the wire, process stability, higher sawing speeds, or an improvement of the wafer surface quality. One requires however also an adjustment of the following etching processes for texturization and further solar cell processes.

The experiences so far show that fixed abrasive sawing is able to cut monocrystalline ingots into wafers of standard thickness of 180  $\mu\text{m}$  with a good surface quality and is cost-effective. The competitiveness of the fixed abrasive technique depends on the cost per wafer. In recent years the cost of the fixed abrasive wires could already be reduced. Estimations of the cost per wafer can be made for the different techniques. The main factors are the cost for the wire and the slurry/coolant supply, which depend on the sawing conditions. Table 2 shows estimations for conditions which are feasible today with new machines. It depends on the assumption how much wire is used for one wafer. The goal of 1 m/wafer for diamond wire sawing is currently only possible for monocrystalline silicon and machines of the latest generation. One can see in this case that the cost for sawing with structured and diamond-electroplated wires is comparably low. It is estimated however that the cost reduction potential for diamond-coated wires is higher. Based on such estimations, one expects that the technology will gradually be introduced in mass production over the next 10 years according to the technology roadmap (ITRPV 2016).

**Table 2** Estimated supplies cost per wafer for the different sawing technologies (in 2016). The cost for the water-based coolants includes the estimated cost for additives

	Standard wire	Diamond wire resin bonded	Structured wire	Diamond wire nickel bonded
Wire cost/km	0.5 €	20 €	1 €	50 €
Wire length/wafer	250 m	8 m	40 m	1 m
Wire cost/wafer	0.12 €	0.16 €	0.04 €	0.05 €
PEG/SiC slurry cost	0.15 €			
Water coolant cost		0.02 €		
Water/SiC slurry cost			0.02 €	
Water coolant cost				0.02 €
Total cost/wafer	0.27 €	0.18 €	0.07 €	0.07 €

Experimental results also show that fixed abrasive sawing works less well for multi-crystalline silicon (Buchwald et al. 2013). The wafer surface quality is lower, and wafer breakage is more frequent. One therefore needs reduced sawing conditions for which a cost advantage is not given. Such a difference between the two materials is not observed for slurry-based sawing. The reasons for these differences between mono- and multi-crystalline silicon are not fully understood today. Whether multi-crystalline silicon can be sawn on an industrial scale with this technique is still uncertain but nonetheless also expected.

---

## Basic Sawing Mechanisms

Slurry-based sawing has been optimized for many years now by practical experience and a better understanding of the basic mechanisms. Great progress has been made here over the years (Möller 2004, 2014), particularly for the slurry-based sawing with straight and structured wires. The sawing with diamond-coated wires is still under development, and therefore many of the fundamental problems are less investigated and understood. In the following, the main ideas for both techniques will be described.

### Slurry-Based Sawing

There is a general agreement today that in the slurry-based sawing free-floating abrasive particles in the sawing channel remove material by rolling and indenting into the silicon crystal surface. The same interactions are known from lapping processes, and similar dependencies can be derived here. The coarser particles are in direct contact with the wire and the silicon surface. The wire is pushed against the particles and indents these particles into the silicon surface. The particles below the wire are mainly responsible for the material removal process, and the particles at the side of the sawing channel determine the damage on the wafer surface.

The description of the loose abrasive process is based on the individual process of the interactions of a single particle with the crystal surface and the resulting microfracture processes. Under normal sawing conditions, the space between the wire and the crystal surface is filled with fluid and abrasive particles (slurry). Experimental investigations with a high-speed camera indicate that the wire is in direct contact with the largest particles. They determine the distance between the wire and crystal surface. The smaller particles are floating more freely in between (Fig. 16). SiC particles are faceted and contain sharp edges and tips, which can exert very high local pressures. The microscopic material removal process is explained by the interaction of rolling SiC particles that are randomly indented into the crystal surface until small silicon pieces are chipped away. This “rolling-indenting grain” model forms the physical basis of the slurry-based wire sawing process. The same



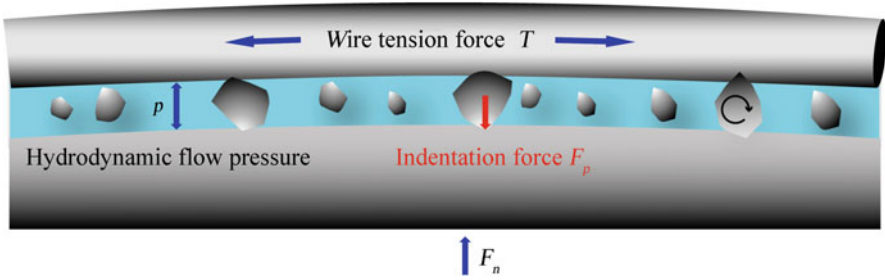


**Fig. 16** Schematic diagram of the sawing channel. It shows the main forces that are assumed in the model (cutting direction upward here)

mechanism also occurs in lapping brittle material surfaces with loose abrasive particles (Buijs and Korpel van Houten 1993).

It is assumed that only the larger particles which are in direct contact participate in the material removal process. During sawing the crystal is pushed against the wires with a constant forward (feed) velocity. With increasing velocity, the total normal force  $F_n$  on the wire increases, and more and more particles are indented. Since the wire is elastic, it will bow under the force like a string. The resulting wire curvature adjusts to achieve an overall constant feed velocity. The forces are maximal directly below the wire in Fig. 16 but decrease toward the side faces. The cutting process at the side and the applied force are important because it determines the final surface quality of the sliced wafers. This will be discussed in more detail in ► [Chap. 13, “Characterization of Wafers and Supply Materials”](#).

Furthermore the fast-moving slurry builds up a hydrodynamic pressure in the fluid, which may exert additional force on the wire. The hydrodynamic pressure also decreases toward the sides of the channel, because it is zero at the free slurry surface, where the slurry can leave the sawing channel. Particles in the channel will be pushed sideways because of a pressure difference and eventually be removed from the sawing channel when they reach the free slurry surface (see Fig. 11). The push effect depends on the particle size, and one can expect a rearrangement of the particle size distribution by the removal of larger particles from the sawing channel below the wire. In fact, several results have been reported, which show that the size distribution varies along the sawing channel.

All processes together determine the local forces on the indenting particles. The individual process of the interaction of a single particle with the surface has been studied by micro-indentation experiments. The main process for material removal during sawing is the formation of lateral cracks and the chipping of material. The median and radial cracks partly remain. This crack system is part of the sawing damage which has to be removed for further processing of the wafers. Combining the rolling-indenting process of free abrasive grains with the fracture mechanics of brittle materials, a quantitative description of the material removal process could be derived. The basic ideas will be explained in the next section. For a detailed review, see Möller (2004, 2006, 2008).

### Basic Modeling of the Slurry-Based Sawing Process

During sawing the feed velocity of the ingot is equal to the material removal rate or velocity  $v_s$ . Under steady-state conditions, it must be constant at any point below the wire. The material removal rate can be calculated from the number of indentation events  $m$  per contact area  $A_{tot}$  and time  $\Delta t$  multiplied by the volume of material  $V_o$  that is removed in a single event

$$v_s = \frac{mV_o}{A_{tot}\Delta t} \quad (4)$$

The material volume  $V_o$  that can be removed in a single event is determined by the microscopic fracture processes under indentation of a single particle. These processes have been investigated in great detail for many materials. The results will be presented in more detail in ► [Chap. 13, “Characterization of Wafers and Supply Materials”](#). For silicon it has been found

$$V_o = \gamma F_p^{2.2} \quad (5)$$

where  $F_p$  is the indenting, vertical force on the particle and  $\gamma$  an experimentally determined geometry factor.

The velocity profile of the laminar flow in the slurry leads to a rotation of the particles. If a rolling grain makes one indentation per cycle, the average time interval for a single indentation event is given by  $\Delta t = 2 d_p/v$ , where  $v$  is the wire velocity and  $d_p$  the particle diameter which is determined by the largest particles in the size distribution.

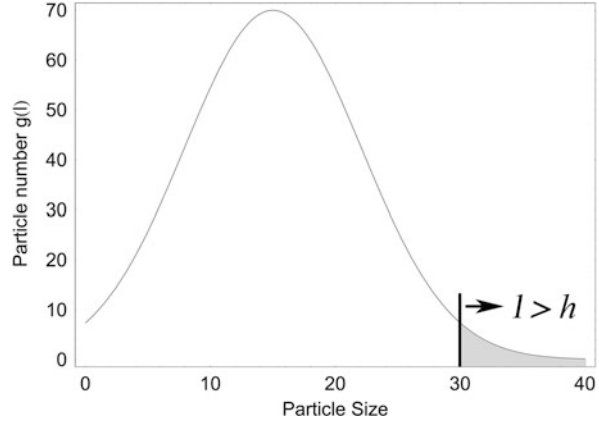
The experimental results show that wire distance, particle size distribution, the temperature, and other parameters vary slightly along the sawing channel. For simplicity one assumes a constant wire bow which exerts a constant force  $F_n$  on the particles. The resulting average force on a single particle  $F_p$  is given by  $F_p = F_n/m$ , where  $m$  is the number of all the particles in contact under wire. One obtains then

$$v_s = \frac{\gamma F_p^{1.2}}{2\pi r_w l_o d_p} v F_n \quad (6)$$

The contact area below the wire has been expressed by  $A_{tot} = \pi r_w l_o$  here with the wire radius  $r_w$  and the cutting length  $l_o$ . The remaining problem that has to be solved is to determine the average force  $F_p$  of the indenting grains in the slurry.

The number  $m$  of particles in contact and the average force  $F_p$  are calculated from the grain size distribution. Commercial virgin SiC particle sizes can be described rather well by a Gaussian distribution. In general, the size distribution will differ from this form, particularly when slurry is transported along the sawing channel and particles are lost or break. It is useful therefore to assume a general size distribution, which shall be expressed by  $g(l) = n_o g_o(l)$ , where  $g_o(l)$  is the normalized distribution and  $n_o$  the total number of all particles in the contact volume below the wire segment (Fig. 17). For a wire segment at a distance  $h$  to the crystal surface all grains with a size  $l > h$  are in direct contact. The contact number  $m$  is calculated from

**Fig. 17** Schematic particle size distribution  $g(l)$  for a typical total number of particles in contact (here  $n_o = 70$ ). Grains with a diameter  $l > h_o$  are in contact both with wire and crystal surface. The total number  $m$  of particles in contact is proportional to the shaded area



$$m = n_o \int_h^{h_{max}} g_o(l) dl \quad (7)$$

where  $h_{max}$  is the maximum distance where just one particle is in contact in the contact area.

If a force  $F_n$  is applied, the distance  $h$  decreases and more grains come into contact with the surface. Neglecting the indentation in the wire, the total force  $F_n$  is equal to the force on all particles, which are actually indented into the crystal surface:

$$F_n = n_o \int_h^{h_{max}} F_{ind}(l-h) g_o(l) dl \quad (8)$$

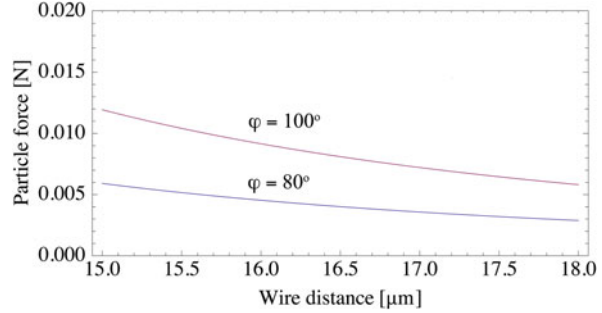
where  $F_{ind}(x)$  is the force law that applies when a single particle is indented by a distance  $x$  into a surface. It depends on the elastic, plastic, and fracture behavior of the material. For sharp Vickers indentations and a brittle material  $F_{ind}$  can be given as a function of the indentation depth  $x = l - h$  by

$$F_{ind}(l-h) = \frac{H}{\alpha} (l-h)^2 \quad (9)$$

$H$  is the hardness of the material and  $\alpha$  a geometry factor. Other force laws have been derived as well, depending on the shape of the indented grains. Combining Eqs. (7, 8 and 9), one can calculate the average force  $F_p = F_n/m$  on a single particle for a given size distribution  $g_o(l)$ . An important result is that for a Gaussian size distribution  $F_p$  remains almost constant for sharp tips ( $\Pi < 90^\circ$ ), when the wire distance decreases (Fig. 18). Only the number  $m$  of indented particles increases. One can therefore simplify Eq. (7) and obtains the following expression:

$$v_s = v_{so} v F_n \quad (10)$$

**Fig. 18** Average normal force on a single particle  $F_p$  as a function of the wire – crystal distance for different tip angles  $\varphi$  of the indenting particle tip



This is the well-known Preston equation, where the sawing rate  $\dot{y}_s$  is proportional to the wire velocity  $\dot{y}$  and the applied force  $F_n$  in the sawing channel. It has been derived here from a microscopic description of the basic particle interaction process with the material. The prefactor  $\nu_{so}$  summarizes the geometry and material parameters. The experimental observations have shown however that this is not sufficient to describe all possible sawing conditions. In particular it does not take into account the observed dependencies on slurry properties such as the viscosity. A possible extension of the model is summarized and given next.

### Elasto-hydrodynamic Behavior of Slurry and Wire

Many experimental results have shown that the slurry plays a role in the sawing process. However, considering the fundamental Preston equation, which has been derived from the micromechanical interaction between wire, particles, and crystal, the slurry properties are not taken into account here. One possibility to do that is to consider the hydrodynamic behavior of the slurry in the sawing channel (Möller 2014). The slurry consists of the fluid and a high volume concentration of particles. In general one has to describe this as a two-phase flow problem, but one can simplify this by assuming a single-phase system, where only the viscosity is changed by the addition of the abrasive powder. The viscosity changes can be described by Eq. (2). Because of the narrow sawing channel one can assume a laminar flow of the slurry. A similar situation occurs in lubrication and polishing processes, where many fundamental aspects for such a fluid system have been derived from experimental and theoretical results (e.g., Larsen-Basse 1993). Some consequences can already be derived from a one-dimensional treatment of the hydrodynamic slurry transport. The starting point to describe the slurry flow directly below the wire is the Reynolds equation

$$\frac{\partial p}{\partial x} = 6 v \eta \frac{h - h_o}{h^2} \quad (11)$$

where  $x$  is the coordinate along the wire,  $h(x)$  the distance between wire and crystal surface,  $v$  the wire velocity,  $\eta$  the slurry viscosity, and  $p(x)$  the hydrodynamic slurry

pressure.  $h_o$  is a constant which has to be derived from boundary conditions, for instance, for a low hydrodynamic pressure. In this case the wire is supported only by the particles which are indented and runs on average at the distance  $h_o$  over the surface. For a given force  $F_n$  corresponding to the wire bow in Eq. (3),  $h_o$  can be calculated then from Eq. (8).

Increasing the hydrodynamic pressure in the slurry, the wire will deform elastically then and increase the distance between wire and surface. This reduces the forces on the individual particles and the number of particles in contact. The so-called hydroelastical behavior of the wire can be taken into account in the following way.

The wire behaves like a pulled string, and the local curvature determines the resulting backward force  $F_n(x)$  normal to the wire, which can vary along the cutting length depending on the local conditions. Describing the shape of the bowed wire by the vertical displacement  $y(x)$ , the force (per length)  $\partial F_n/\partial x$  and the corresponding pressure  $p$  are related to the (negative) curvature, which is the second derivative of  $y$ , by

$$\frac{\partial F_n}{\partial x} = -T y'' \quad p = \frac{1}{\pi r_{eff}} \frac{\partial F_n}{\partial x} = -\frac{T}{\pi r_{eff}} y'' \quad (12)$$

where  $T$  is the tensile force along the wire and  $r_{eff}$  an effective wire radius due to the one-dimensional treatment (Fig. 16). The local width  $h(x)$  of the slurry transport channel can be expressed by  $h(x) = y(x) - y_o(x)$ , where  $y_o(x)$  describes the shape of the crystal surface. One obtains then

$$p = p_o + p_h \quad p_h = -\frac{T}{\pi r_{eff}} \frac{\partial^2 h}{\partial x^2} \quad p_o = \frac{T}{\pi r_{eff}} \frac{\partial^2 y_o}{\partial x^2} \quad (13)$$

where the crystal surface curvature has been expressed by the constant  $p_o$ , which has the dimensions of a pressure. Experimental investigations of the shape of the surface during cutting have shown that it is slightly curved and deviates only very little from a circular shape over the cutting length. If the wire is stabilized by the slurry pressure only, the hydrodynamic pressure in Eq. (11) has to be equal to the pressure from the wire bow in Eq. (13). Since  $p_o$  is assumed constant over the cutting length, the derivative is zero, and one obtains by inserting

$$\frac{\partial^3 h}{\partial x^3} + \frac{6 \pi v \eta r_{eff}}{T} \frac{h - h_o}{h^3} = 0 \quad (14)$$

This equation is the basis for the investigation of the hydrodynamic slurry behavior. It has no analytical solution and has to be solved numerically. With appropriate boundary conditions, one obtains the solution  $h(x)$  and can calculate  $p_h(x)$  and  $p(x)$  from Eq. (13). The solution depends on the parameter  $h_o$ , which is basically determined by the applied force  $F_n$  on the wire (Möller 2014). The numerical results in the next section show that the solution  $h(x)$  deviates only slightly from  $h_o$ , whereas the pressure  $p(x)$  however can vary considerably along the sawing channel.

### Numerical Simulation of the Sawing Process

Although the numerical solutions are very sensitive to boundary conditions, some general conclusions can be derived. Figure 19 shows the calculated pressure along the sawing channel position for two feed velocities  $v_s$  or different applied forces  $F_n$ , respectively. The following boundary conditions have been assumed here: a constant pressure at wire inlet  $p(0) = p_a$ , the outlet  $p(l_o) = 0$ , and the wire distance at the outlet  $h(l_o) = h_o$ . The entry pressure of the slurry arises from the accumulation of fluid at the wire inlet and has been estimated to be about  $p_a < 0.01$  MPa (Bhagavat et al. 2000). In the calculations, it has been taken into account that the viscosity and the size distribution change along the sawing channel, because of the temperature increase, the accumulation of silicon and metal debris in the slurry, and the loss of larger particles, as has been observed experimentally.

Apart from the entry region, the pressure decreases slightly first due to the loss of larger particles and the reduction of the distance between wire and crystal surface. The hydrodynamic pressure is too small here to reduce the forces on the interaction particles, which are exerted by the bowed wire.

A different situation occurs near the exit region of the sawing channel. A typical feature is a strong pressure increase before it drops to zero (for  $v_s = 0.3$  mm/min in Fig. 19). In this case the hydrodynamic pressure exerts higher forces on the wire and thus reduces the force on the particles, which are in direct contact and are responsible for the material removal. The force reduction can become so severe that no material can be removed any more. Even negative pressure values can occur near the wire exit (channel positions  $> 0.9$ ) when the sawing velocity is increased (for  $v_s = 0.35$  mm/min in Fig. 19). This means that the basic assumption of a continuous slurry flow is violated here. It has been suggested that the hydrodynamic pressure situation in this

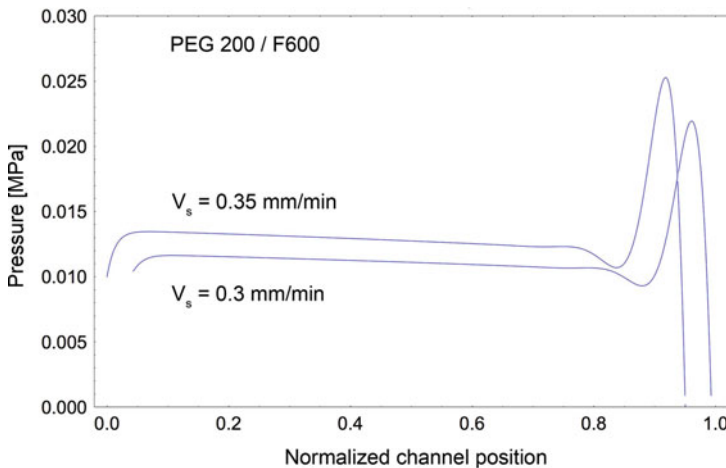


**Fig. 19** Calculated hydrodynamic pressure  $p$  in the slurry film along the wire length for two different feed velocities. Calculation parameters are ingot cutting length  $l_o = 156$  mm, wire speed  $v = 15$  m/s, viscosity  $\eta = 300$  cP, wire tension force  $T = 25$  N, slurry inlet temperature  $T = 22$  °C

part of the channel can lead to an instability of the wire motion (Möller et al. 2013). This will be discussed next.

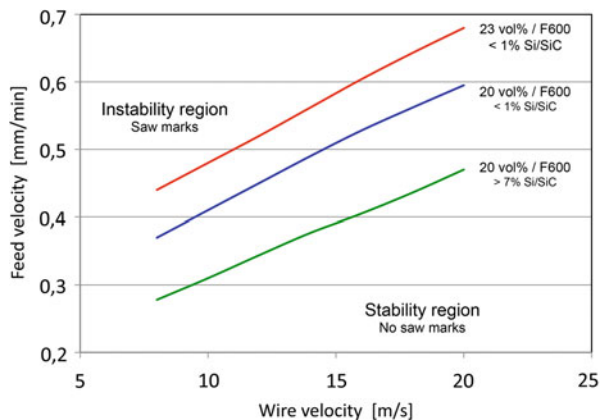
### Slurry Flow Instability and the Origin of Saw Marks

One can use the previous calculations to determine the parameters, which lead to high and negative pressures in the exit regions. Figure 20 shows a diagram with feed velocity versus wire velocity borderlines, which separate the parameter regions where stable and unstable wire motion occurs. Important parameters are the feed and wire velocity, the SiC volume concentration and the fraction of silicon, which accumulates during sawing in the slurry. The results also depend on the grit size of the initial slurry. All factors, which change the slurry viscosity along the sawing channel, can have an effect on the position of the separation lines. The calculation results are in qualitative agreement with experimental observations and can be used to define guidelines for process windows.

The parameter range for the wire and feed velocities, which is used in industrial production, is between 10–18 m/s and 0.3–0.6 mm/min, respectively. Normally one saws with a fixed feed and wire velocity, which determines a point in the diagram. Only values below the corresponding borderline are in the stability region. From the industrial perspective of high productivity and low cost, one will choose a large sawing rate, a small wire velocity, and a small SiC concentration. One can see from the diagram that these are conflicting requirements, which limits suitable sets of parameters.

If one chooses parameters close to the borderline, small changes in the sawing parameters can easily lead to a shift from the stable to the unstable regime. It is therefore necessary to control the specifications of parameters such as the SiC load, the silicon concentration, or the grit size distribution quite tightly.

**Fig. 20** Feed velocity versus wire velocity diagram, showing stability regions of wire motion for different SiC and silicon volume concentrations



## Fixed Abrasive Sawing

Considering the basic sawing mechanisms, the fixed abrasive sawing is very different from the sawing with loose abrasives. Since the abrasive particles are fixed on the wire, they scratch over the crystal surface. The damage pattern on wafers consists of many parallel scratches along the sawing direction. Since the scratches are mostly well separated one can investigate the process at single scratches under defined conditions. Such investigations of the micromechanical processes in this case are still at the beginning, but some results are available and will be presented in ► [Chap. 13, “Characterization of Wafers and Supply Materials”](#). Based on these findings, one can already derive some basic results for the material removal rate by a scratching process.

### Basic Sawing Mechanism

The fundamental process is the removal of material by scratching the particles on the wire over the crystal surface. Because of the size distribution of the diamond particles on the wire, only a certain number is in direct contact and their indentation depth varies. This is shown in Fig. 21 where for a certain distance between wire and crystal surface only the particles marked in red are in contact. Their number also depends on the density of particles on the wire. Because of the different sizes, the forces on the particles also vary. Correspondingly the depths of the scratches and thus the material that is removed vary also.

### Modeling of the Fixed Abrasive Sawing Process

One can start again from the basic Eq. (5) for the case that the feed velocity of the ingot is equal to the material removal rate or sawing velocity  $v_s$ . Under steady-state conditions, it must be constant at any point below the wire. In the scratching mode, the material removal rate can be calculated from the number of scratching particles  $m$  per contact area  $A_{tot}$  and time  $\Delta t$  multiplied by the average volume of material  $V_o$  that is removed by a single particle. The volume  $V_o$  is given by  $V_o = A_{sc} \Delta s$  where

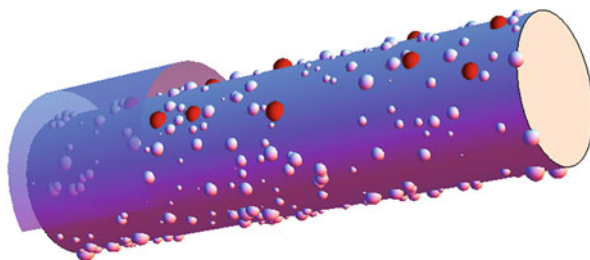


**Fig. 21** Simulation of the number of particles on wire in contact with the crystal surface. The particle heights are normally distributed with a mean height of  $3.5 \mu\text{m}$ . Particles in red are in contact for a given distance of  $5.5 \mu\text{m}$ . (The crystal surface is shown at a greater distance for clarity)



$A_{sc}$  is the average cross section of the scratches and  $\Delta s$  the mean length of the corresponding scratch per time unit  $\Delta t$ . The time unit can be calculated from the wire velocity  $v_s$  by  $\Delta t = \Delta s/v_s$ . Inserting these expressions into Eq. (4) yields

$$v_s = v \frac{mA_{sc}}{A_{tot}} \quad (15)$$

The cross section of a single scratch depends on the force on the particle  $F_p$ , which causes the scratch. The calculation of the sawing rate is thus reduced to determine the average value of the cross section  $A_{sc}$  as a function of the total normal force on the wire  $F_n$ .

Scratch tests with single particles under defined conditions allow one to determine  $A_{sc}$  and many other features of the material removal processes for a single scratch. The dependence on the total force requires also measurements of the height and shape distribution of the particles on the wire, because the number of scratching particles increases when the total force increases and the wire is pushed closer to the crystal surface. Under normal sawing conditions, the size distribution will also change because particles change the shape and break or are pulled out.

First results on single scratch tests are presented in ► [Chap. 13, “Characterization of Wafers and Supply Materials”](#). They show that the cross section of a single scratch  $A_{sc}^{single} = c_p F_p$  increases in good approximation linearly with the applied force  $F_p$ . Since on average  $F_p = F_n/m$  one obtains from Eq. (16)

$$v_s = v_{so} v F_n \quad (16)$$

where  $v_{so} = c_p/A_{tot}$ . This again is a Preston equation for the dependence on wire velocity and applied force if  $c_p$  for a single scratch does not depend on these parameters. It is also independent on the particle density and size.

The micromechanical processes which occur along the scratch are not yet fully understood. At present it is assumed that two modes of material removal occur. Although silicon is a brittle material, it can at low forces be deformed only, probably because of phase transformations into high-pressure phases, which are ductile (Gogotsi et al. 1999). Under these conditions scratching may occur similar to scratching in metals by chip forming. The advantage is that the damage of the surrounding material is rather low. At higher forces the material will break and material will be removed by cracking. This causes a more extended damage at and below the surface. The conditions under which the transition from the ductile to brittle mode in scratching occurs are not clear yet. The knowledge is however important since it affects the surface damage of the sawn wafers, which is an important criterion of the wafer quality. These processes will be discussed in more detail in ► [Chap. 13, “Characterization of Wafers and Supply Materials”](#).

The modeling of the scratching process is still in an early stage. Recently first attempts have been published (Liu et al. 2016). The calculated results are in agreement with Eq. (17) and allow to determine the proportionality constant  $v_{so}$ . The micromechanical description here does not take into account the role of the coolant. If and how to include this in the sawing process is not clear at present.

## Recycling of Kerf Loss and Slurry

In wafer processing the consumption of wire and slurry or coolant is an important cost factor (see Table 2). These consumables degrade in the cutting process and have to be replaced after some time.

In the slurry-based sawing process, the steel wires become thinner by about 8–10% during one cut. They lose so much fracture strength that they have to be discarded afterward as metal scrap. On the contrary, it is already industrial standard in the PV industry to recycle the cutting fluid, mostly polyethylene glycol and the silicon carbide. In the recycling process, both components are recovered separately. New slurry is mixed from both components with an addition of a certain amount of fresh SiC. Typically 80% of the SiC is currently reused.

In the fixed abrasive sawing process, the diamond-coated wires can be used longer. The degradation mainly occurs by wire wear and breakout of the embedded diamonds. Recycling of the diamond wires has been reported in some cases but is not a standard process. It is expected however that recycling will increase over the next years. The cutting fluid consists mainly of water and some organic additives. The development of better additives is still ongoing, and the possibility of its recycling may be taken into account in the future.

Another important cost factor is the loss of silicon. In the previously described mechanical cutting processes, about 40% of that material is lost as cutting waste. The polysilicon consumption in 2015 all over the world was 240,000 tons/year, so it can be estimated about 100,000 tons/year of valuable silicon was wasted in the cutting processes. Although the cost of high-purity silicon powder, which is used for the crystal growth process, has dropped considerably down to 15–20 Euro/kg, the loss still remains significant. Therefore the incentive to recover silicon and to feed it again into the production chain is quite large.

The treatments of PEG/SiC slurries and water or PEG-based coolants without SiC are different. In the first case, one has to separate Si and SiC first, which is difficult to achieve because many physical and chemical properties are rather similar. This separation step will become obsolete with the increasing usage of the fixed abrasive sawing technique and water-based coolants.

Depending on the sawing process, the composition of slurry or coolant differs (Table 3), but in each case the amounts of silicon and metals are similar. One of the

**Table 3** Composition of typical PEG/SiC slurries for loose abrasive sawing and of water-based coolants for fixed abrasive sawing at the end of the sawing process

	Loose abrasive sawing (wt%)	Fixed abrasive sawing (wt%)
Water	< 2	93–96
PEG	45–56	–
SiC	40–45	–
Metal/glass grit	1–2	1–2
Silicon grit	3–8	3–5

major problems in both cases is the contamination of the silicon with metal components from the steel wires and their coating layers, such as iron, nickel, copper, boron, phosphorous etc. But other elements such as aluminum, calcium, or sodium from glass fragments, when the wire cuts into the glass support beam of the ingots at the end of the cut, have also to be removed. In the fixed abrasive process, the coolant will also contain carbon from the diamond coating of the wires. In addition, the kerf loss silicon has a high tendency to oxidize and because of the small particle size can accumulate large amounts of oxygen between 1 and 2 wt% on the particle surface. All these elements are detrimental to the wafer quality and are difficult to remove.

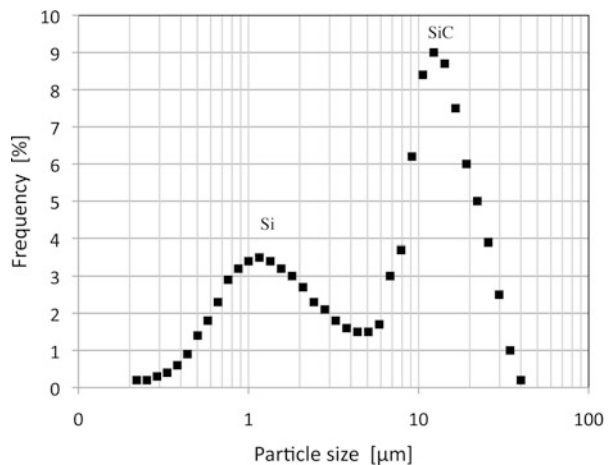
The removal requires extensive purification procedures consisting of many steps to increase the purity to a level where the silicon can be used again. Because of the low price of high-purity silicon feedstock, recycling processes must however be cheap to be competitive. In recent years, many recycling processes have been investigated, which will be described in the next section.

## PEG/SiC Slurries

In the standard sawing process, the PEG/SiC slurry enriches with silicon debris in each cut. The sawing performance decreases by the addition of the silicon micro powder. Up to about 8 wt% can be tolerated before the slurry has to be recycled. Figure 20 shows that one may leave the stability regime for sawing without saw marks when the amount of silicon increases. Depending on the number of ingots in each run, usually several cuts can be made, before the limit is reached.

Figure 22 shows a typical size distribution of the Si and SiC particles in a used PEG slurry. Separation processes for these two components use the different physical and chemical properties of the two components such as the size, the weight, the

**Fig. 22** Particle size distribution of a PEG/SiC slurry after sawing showing the enrichment with silicon micro powder



solubility in different fluids, the electrical surface charge (zeta potential), the different melting points, or the reaction with other elements. In a first step, typically water or acetone is added and the mixture centrifuged to remove the PEG. This washing step is repeated several times. The metals and other elements are removed then by etching in a hydrochloride, hydrofluoride, or nitric acid solutions. In the following steps, Si and SiC are separated. Here a number of different techniques have been developed, which will be described next.

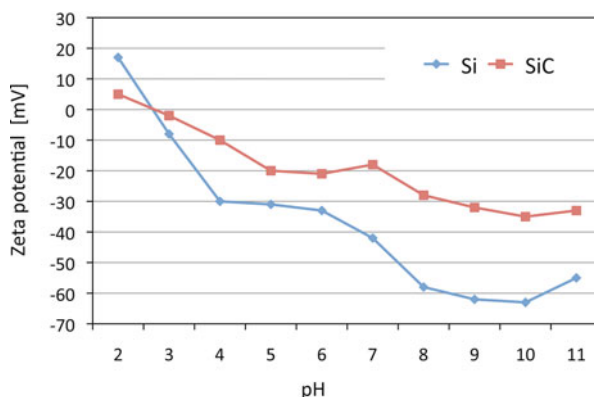
### Separation by Centrifugation and Hydrocyclones

The potential feasibility of recovering silicon powder from kerf loss slurry waste by applying a centrifugation process has been demonstrated by (Lin et al. 2010). The essential step here is the mixing with a heavy liquid with a density between that of Si and SiC. This leads to a separation of the particles in the centrifuge tube with SiC at the outer side.

The authors prepared a heavy liquid by mixing bromoform ( $\text{CHBr}_3$ ) and ethanol in different portions. The separated silicon layer was scooped out and washed with acetone so that the heavy liquid was removed. A solution of 10 wt% HF to remove the boron and calcium was also applied as washing. The variables that can be changed in the centrifugation process are the solid volume fraction, the heavy liquid density, the number of centrifugation steps, and the centrifugation and agitation time. In the best cases, a product with Si purity of 90.8 wt% and a yield of 74.1% was obtained. The disadvantage of the method is however the toxicity of bromoform.

Another possibility is to combine the centrifugation process with a tuning of the surface potential of the particles (Liu et al. 2013). The surface potential can be measured by the zeta potential, which depends on the pH value in the aqueous solutions (Fig. 23). At pH 8–10 the surface charge of both Si and SiC particles is quite large, which means that the electrostatic repulsion is strong and keeps the particles in a dispersing and suspending state. Taking into account that the size of the particles is different, it can be assumed that under the same centrifugation treatment, the larger SiC particles will tend to settle down at the bottom of the centrifugal tube,

**Fig. 23** Measurements of the zeta potential of silicon and silicon carbide particles in an aqueous suspension (Liu et al. 2013)



and the smaller Si particles will be suspended in the upper section of the tube. This has actually been confirmed and used to separate both. Under optimized conditions about 91.8 wt%, rich Si phase could be obtained.

Si and SiC can also be separated by a hydrocyclone process, where only the liquid is rotated. An enrichment of up to 96% of silicon has been reported, showing that this is also an alternative route (Sergiienko et al. 2014).

### High-Temperature Treatment

The high-temperature treatment (HT) method uses the difference in melting points of Si and SiC (Wang et al. 2008). The Si/SiC powders are compacted first and then heated up above the melting point of silicon to about 1470 °C in an argon atmosphere for several hours. As a result Si starts oozing out of the material in the form of clusters. Once the cluster formation is over, the material is cooled down. The Si clusters and the SiC can be separated easily by water cleaning due to the fact that Si clusters are nonadherent to the SiC particles. Beneficial is also that most of the other impurities segregate toward the surface of the Si conglomerates during the cooling-down stage, where they are washed away from this conglomerate skin using hydrofluoric acid. A recovery rate of 45% has been obtained.

### Rapid Thermal Annealing Process

In this process the Si/SiC powder is rapidly annealed for a short time of about 3 min by halogen lamps in an Ar atmosphere (Yang et al. 2015). The maximum temperatures (1420–1500 °C), the heating and cooling rates, and the holding times were varied. Whereas the SiC remains solid under these conditions, the Si particles melt and tend to aggregate depending on the conditions. Spherically shaped agglomerates with an average diameter of about 0.5 mm could be formed. The SiC, impurities, and excess oxide at the Si particle surfaces are removed by an acid etching. The morphologies of the Si agglomerates play an important role in the surface cleaning stage. Under optimized conditions 72% of the silicon could be recycled. The advantage over the previous high-temperature treatment is the shorter process time.

### Alloying Method

The removal of silicon carbide from kerf loss slurry waste by the Al-Si alloying process has been studied by (Wang et al. 2012). After the initial PEG removal and cleaning procedure, the dried Si/SiC powder is mixed with aluminum powder and heated up to 1500 °C for 1 hour. At this temperature both silicon and aluminum melt. Additionally the SiC reacts completely with the aluminum and forms the intermediate phase  $Al_4C_3$  at the top of the solidified ingot. Separating the top layer, an ingot remains which consists of an Al-Si alloy and needles of silicon. The silicon from the Al-Si alloy can be recovered by electrolysis or acid leaching.

### Phase-Transfer Separation Method

In this method the hydrophobicity difference of Si and SiC is used (Hsu et al. 2014; Lin and Tai 2010). The basis is the formation of oil/water interfaces. This can be a

single interface between the two fluids or an emulsion with droplets which creates a much larger interface when many drops are formed.

It has been found that particles, which are slightly hydrophilic with a contact angle of the particles slightly less than  $90^\circ$ , adhere to an oil/water interface and stabilize oil-in-water emulsions. On the other hand, if the particles are slightly hydrophobic, they will stabilize water-in-oil emulsions. However, if the particles are either too hydrophilic or too hydrophobic, they will tend to stay in the water or oil phase, respectively, leading to unstable emulsions. During the Si/SiC separation, the SiC particles (contact angle  $62.9^\circ$ ) prefer to be adsorbed at the interface of oil-in-water emulsions, but Si particles (contact angle  $49.2^\circ$ ) tend to remain in the water phase. As a result, if the top phase is oil, SiC particles are adsorbed on the oil/water interface. This emulsion zone between the bulk oil and water phases plays a key role in keeping sufficient SiC particles there without sedimentation. The separation efficiency is affected by several factors, such as the oil, oil/water volume ratio, pH value of the water phase, solid concentration, and agitation conditions.

In practice the phase transfer process consist of three steps. The Si/SiC powder is dispersed in one of the liquids, e.g., water. Then an oil is added, and the liquids are agitated so that an emulsion forms with many oil droplets in the water. The droplet size is less than  $600\ \mu\text{m}$ . The SiC particles collect at the oil/water interfaces of the droplets, whereas the hydrophilic silicon particles remain in the water. After mixing the system is allowed to settle for about 1–2 hours. The two liquids separate again and form an interface, which collects the stabilized droplets. This enhances the separation of the silicon, which remains in the water. The recovery process depends on several operating variables, such as the pH value of the water, the oil/water volume ratio, and the solid concentration. Lin and Tai (2010) reported an overall recovery rate of 71.1%. The highest Si purity achieved was 99.1 wt%.

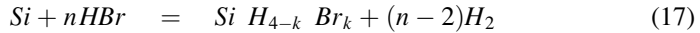
### Sedimentation in an Electrical Field

Since Si and SiC particles in sawing waste have different densities, surface charges, and particle sizes, they can be separated by a combination of gravity and electrical fields (Wu and Chen 2009). The powder is dispersed first in a solution and filled in a sedimentation cell. In addition, a constant electrical field of about 1–2 V/cm is applied on the side of the cell. Charged falling particles are driven to one side of the cell where they can be collected after settling. The sedimentation velocity of the particles depends on their density and size. SiC has a higher density of  $3.16\ \text{g/cm}^3$  compared to silicon ( $2.33\ \text{g/cm}^3$ ) and a larger average size in the sawing waste. The surface charge, which interacts with the electrical field, depends on the zeta potential which is  $-20\ \text{mV}$  for SiC and  $-41\ \text{mV}$  for Si at pH 7. The pH value of the solution can be adjusted by a mixture of phosphoric acid and sodium hydroxide.

After operation for up to 240 h, the silicon particles accumulate at the cell bottom at the positive (anode) side of the electrical field and SiC particles at the negative (cathode) side. The difference in horizontal displacement can be used then to separate both components. Si-rich powders containing up to 92.4 wt% have been reported.

## Hydrobromination

The process consists of the reaction of the Si/SiC powder with HBr gas in a quartz flow reactor. The gas reacts with silicon in the temperature range of 370–450 °C to yield tetra-, tri-, and di-bromosilanes according to the chemical reaction ( $n = 2 - 4$ ):



Bromosilanes are in liquid state around normal temperature, which offers great advantages in their storage and transportation. It could also be shown that the addition of SiC promotes the reaction probably because of a better heat transfer (Tomono et al. 2013). If one replaces SiC by diamond, which occurs in water-based coolants in the diamond wire sawing process, the reaction is even more complete, which may reflect even higher thermal diffusivity. Since SiC and the contaminating metal elements do not react the liquid,  $SiH_{4-n}Br_n$  is very pure. The silicon itself is recovered by annealing the compound.

## Water-Based Slurries and Coolants

Water may replace the cutting fluid in the future, either in combination with SiC in the loose abrasive sawing or as coolant for fixed abrasive sawing. Considering the recycling situation in the first case, one still has the problem to separate Si from SiC. Essentially the same toolbox of separation and purification techniques described in the previous section is available, but one may have to adapt process parameters to the different suspension. In the second case, the situation is different, because one can concentrate on the recovery of silicon alone and eventually of those additives which are more valuable. Here the major problem is to maintain a high purity of the silicon and keep the cost low.

Some of the previous methods have been successfully applied to water-based suspensions. A more dedicated process has been developed recently to recycle silicon by using a thermal plasma process. The basis is an inductively coupled plasma torch, which was generated by the injection of argon or a mixture of argon/hydrogen gas into an electrical arc. The plasma gas jet has a temperature of about 12,000 K and a velocity up to 1000 m/s. The key point is to inject the silicon powder from the kerf into the plasma gas stream, where it melts and vaporizes. Downstream the gas and the silicon rapidly cool down so that the silicon can be collected in a molten silicon bath. One of the problems is to remove oxygen and carbon from the particles, which can be achieved by changing the plasma jet velocity.

## Directional Solidification

The previously described method yields a silicon material, which in most cases is not directly suitable as feedstock for high-quality solar cell material. The quality is

comparable to metallurgical silicon and requires further purification steps. Most detrimental are metal impurities, which reduce the bulk minority carrier lifetime. It is therefore necessary to remove the metals by further processing. The standard technique here is the melting of the material in a silicon nitride-coated quartz crucible followed by directional solidification (part ► “Crystalline Silicon Growth”). Because of the low segregation coefficient of most metals, the solidified silicon can be considerably purified by many orders of magnitude. The impurities are transported to the top of the solidified ingot, which is removed then. One can repeat the process to improve the quality, but the high-energy cost for melting limits the application of number of solidification steps.

A remaining difficulty is that certain doping impurities such as aluminum, boron, or phosphorous, which also occur in the recycled material, are difficult to remove by this process since their segregation coefficients are closer to one. The same is the case for carbon, oxygen, sodium, and calcium. Although the impact on the material properties is different in each case, it is necessary to obtain lower initial concentrations from the previous processing steps.

So far recovery processes of silicon have not reached the industrial scale probably because the cost are still too high, or the material still has not the required purity. The flaws are complex expensive equipment or the use of poisonous media. Since less pure silicon may find other applications in the future, for instance, as an input material for the processing of high-purity  $\text{Si}_3\text{N}_4$ , it is at present unclear whether silicon recycling as an additional feedstock material for the PV industry will actually be developed in the future. Nonetheless the technology roadmap predicts that recycling of silicon and of diamond wires from multi-wire sawing will increase over the next years (ITRPV 2016).

---

## Alternative Wafering Technologies

Many attempts have been carried out to develop alternative “kerfless” technologies, which avoid the inherent drawback of the sawing process that valuable silicon and supply materials are wasted. Although multi-wire sawing is still a developing wafering technology, there are probably limitations when wafers with a thickness below  $100\ \mu\text{m}$  shall be produced in the future. Over the last decades, over 20 variants of kerfless wafering have been proposed, but few have demonstrated a lasting potential to be competitive in cost and quality (Henley 2010).

The most direct route is the production of wafers directly from a silicon melt. The most advanced techniques are the “edge defined film fed growth (EFG)” technique (Wald 1981) and the “string ribbon” method (Ciszek 1981), which have reached the industrial production level. Less successful were the “ribbon growth on substrate (RGS)” method (Lange and Schwirtlich 1990) and the Direct Wafer™ technology (Henley et al. 2008). All liquid-phase approaches have shown great difficulty in achieving good absorber yield and quality for standard wafers much below  $200\ \mu\text{m}$ . At the same time, the wire saw process has undergone impressive evolutionary improvements in the important areas of yield, quality, kerf loss, productivity, and



thickness reduction. As a result, the “kerfless” material efficiency advantage becomes moot if the next-generation wire saw processes yield stronger high-efficiency 120–150  $\mu\text{m}$  wafers. This is why these liquid-phase wafering methods either have been terminated in commercial production or have never started.

Kerfless technologies, which can overcome the quality problem, start from solid monocrystalline silicon. The basic principle is to separate many thin wafers consecutively from a high-quality silicon monocrystal (► [Chap. 6, “Growth of Crystalline Silicon for Solar Cells: Czochralski Si”](#)). Several technologies have emerged following different approaches: induced cleaving (Brailove et al. 2010; Dross 2007), layer transfer (Bergmann et al. 2002; Petermann et al. 2012), and macropore reorganization (Depauw et al. 2009, 2010; Reuter 2008; van Nieuwenhusen et al. 2012). In the following, the approaches will be described in more detail.

## Cleavage Technologies

The most advanced cleavage process uses ion implantation to induce cleaving. First, a high-energy proton beam (or other ions) is directed on the top surface of a Cz silicon ingot. The protons are implanted in a thin layer at a controlled depth under the surface of the silicon. The proton beam has both high current and high energy (2–4 MeV). This supplies a high heat load into the silicon crystal which can reach many tens or even hundreds of kilowatts and has to be removed by cooling the bricks efficiently. The silicon temperature is a critical part of the process because it can deteriorate the material quality. After the implant step, the silicon is induced to fracture, or cleaved, in a highly controlled manner, along the cleave plane defined by the implanted ions. A single wafer of silicon is released, and the process is repeated on the newly exposed surface of the brick. The use of cleaving, rather than sawing, eliminates the waste due to kerf.

A light ion implant avoids damaging the bulk silicon, while the low-energy (threshold) cleave process creates only surfaces with low defect density. Both factors contribute to maintain the high lifetime of the silicon crystal and high mechanical strength. Bulk lifetimes up to 0.5 ms have been reported. Roughness of the cleaved wafers is generally less than 1  $\mu\text{m}$ . The process has also been verified to be capable of repeatedly detaching films from an ingot without surface preparation between successive detachments. The films continue to have repeatable roughness and total thickness variation (TTV < 1–2%) without any interim polishing or other surface modification steps. Such a wafering process (Direct Film Transfer, DFT) has been developed by the US company Silicon Genesis. Although it has not yet reached the industrial production stage, the technique appears to have some potential for an alternative wafering method.

Other cleaving methods use high thermoelastic stresses over the surface. This can be achieved by depositing a thin polymer- or metal layer on the surface of a Cz crystal and applying a strong temperature gradient. If the stress exceeds the required fracture strength, a thin silicon layer can be cleaved from the brick with high yield.

Generally one has to initiate the crack at the side of the crystal, for instance, by laser scribing. After cleavage the deposited layer is removed again.

## Layer Transfer Technologies

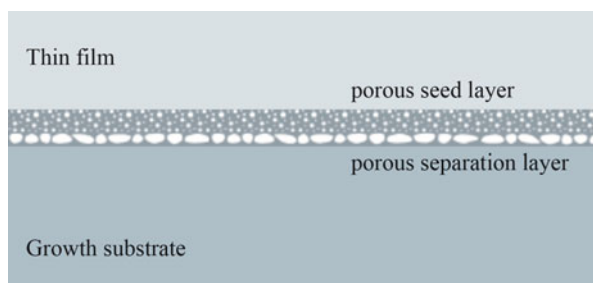
Lift-off techniques have been developed for the microelectronic device technology. They have the potential to yield thin layers between 10 and 60  $\mu\text{m}$ . The basic principle is the following. A high-quality thin silicon film is grown on a sacrificial layer, which can be separated and transferred to a low-cost substrate. Latest developments use double porous silicon layers. On top is a layer of a low porosity for further growth of a high-quality epitaxial film and underneath a high-porosity layer for separation (Fig. 24).

The porous silicon is formed by electrochemical etching of a highly doped monocrystalline silicon crystal. Experimentally different techniques have been explored over the years. Typically vertical trenches are electrochemically etched with an HF-based solution into the surface of highly doped monocrystalline polished substrate. They are transformed into spherical voids by annealing at around 1100  $^{\circ}\text{C}$  in a hydrogen atmosphere. The formation of a perfect detachable film requires a specific aspect ratio and pitch. Today it is possible to form porous silicon layers with a desired void structure. Typically the top layer is 1–3  $\mu\text{m}$  thick with a porosity of 20–30%. This seed layer permits the subsequent growth of a high-quality epitaxial silicon film.

The bottom layer has an initial porosity in the 60–75% range and a thickness of about 0.2–0.3  $\mu\text{m}$ . After annealing several large buried plate-shaped voids form, which allow the further detachment of the epilayer. The separation process is done mechanically by breaking the small supporting pillars in the separation layer. It requires an initiation crack at the edges of the film, for instance, by laser scribing. Depending on the thickness of the epitaxial film, it can either be used as freestanding foil or if thinner has to be transferred to a supporting substrate.

Solar cells have been fabricated in the epitaxial foil with efficiencies up to 15% and have the potential for efficiencies up to 18%. Despite a number of convincing lab-based solar cell showcases, there is no breakthrough of this technology at an industrial level so far.

**Fig. 24** Schematic layer sequence of an epitaxial film grown on a double porous silicon layer

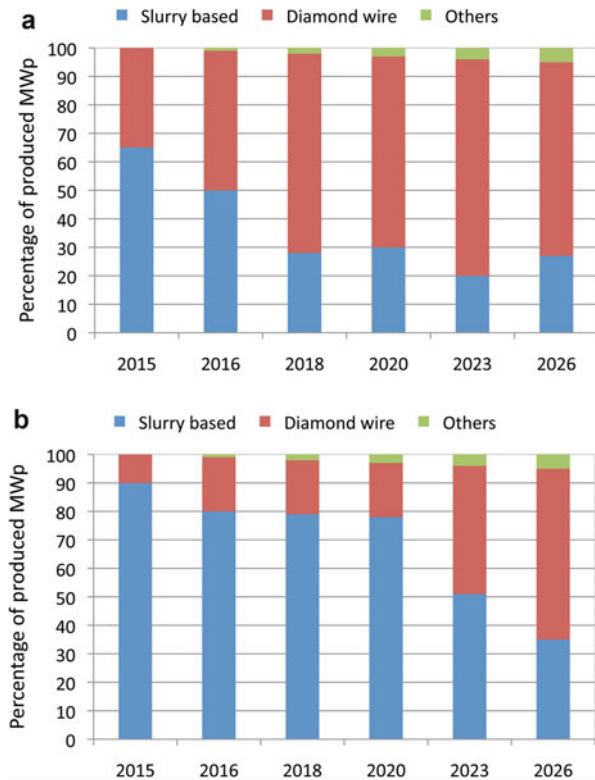


## Conclusion

The standard wafering process is the sawing with a single steel wire and an abrasive slurry made from polyethylene glycol and silicon carbide powder. It is however expected that the industry will change to the fixed abrasive technology with steel wires coated with fine diamond particles (Fig. 25). This reduces the cost of the supply materials by a factor of 4–5 and probably more. Although fixed abrasive sawing is already suitable for monocrystalline material, it still does not fulfill the requirements for multi-crystalline silicon. The sawing with structured wires offers this possibility and cost advantages, but nonetheless one expects that this is a transient technology, which will also be replaced by the fixed abrasive sawing method. To exploit all advantages of the technique, a modified sawing machine is necessary. Therefore the present generation of sawing machines, which is optimized for slurry-based sawing, has to be replaced in the future.

Fixed abrasive sawing requires only water as a coolant. Therefore PEG and SiC recycling processes will be abandoned in the future. On the other hand, one will see more recycling of the silicon, because it can be recovered more easily from a water-based silicon kerf.

**Fig. 25** International technology roadmap of the development of diamond wire sawing for (a) monocrystalline and (b) multi-crystalline silicon (ITRPV 2016)



Optimization of sawing processes is time-consuming because it depends on many parameters. Modeling the sawing process can be helpful here. Simulations require however a multi-scale approach starting from models for the micro-mechanical details in the sawing channel (on the micrometer scale) to the large scale description of the wire motion and coolant transport in the machine (on the meter scale). While a relatively good understanding of the micromechanical details of the slurry-based sawing has been achieved, the fixed abrasive sawing process is still less understood.

Wafers and wire will become thinner in the future and the mechanical stability an important issue. At present such thin wafers cannot be handled in the downstream process of solar cell and module fabrication. Thinner wafers require adapted solar cell designs, because they absorb less light. Such processes have not been implemented into the standard production chain. In addition, the following industrial processing steps, which require mechanical handling of the wafers, are even more prone to breakage because of the lower fracture toughness. Automation of the different process steps can reduce the handling stresses, but material issues have to be solved as well. Fast, inexpensive characterization methods have to be developed to maintain a better quality and production control.

The limit of multi-wire sawing has certainly not been reached. Considering cost, quality, and productivity aspects, alternative, kerfless solutions do not seem to be ready to replace silicon shaping in the short term. If they may take over, when new solar cell technologies demand thinner wafers, cannot be foreseen at present. Therefore one can expect that wafer processing by multi-wire sawing will remain the dominant technology for the next decade.

---

## Cross-References

- ▶ [Characterization of Wafers and Supply Materials](#)
- ▶ [Growth of Crystalline Silicon for Solar Cells: Czochralski Si](#)
- ▶ [Growth of Crystalline Silicon for Solar Cells: Mono-Like Method](#)
- ▶ [Growth of Crystalline Silicon for Solar Cells: Noncontact Crucible Method](#)
- ▶ [Growth of Multicrystalline Silicon for Solar Cells: Dendritic Cast Method](#)
- ▶ [Growth of Multicrystalline Silicon for Solar Cells: The High-Performance Casting Method](#)
- ▶ [Wafer Cleaning, Etching, and Texturization](#)

---

## References

- T. Behm, W. Fütterer, C. Funke, S. Kaminski, H.J. Möller, R. Rietzschel, T. Wagner, *Photovolt. Int.* **11**, 38 (2011)
- R.B. Bergmann, C. Berge, T.J. Rinke, J. Schmidt, J.H. Werner, *Sol. Energ. Mat. Sol. C.* **74**, 213 (2002)
- M. Bhagavat, V. Prasad, I. Kao, *J. Tribol.* **122**, 394 (2000)

- A. Bidiville, K. Wasmer, J. Michler, P.M. Nasch, M. Van der Meer, C. Ballif, *Prog. Photovolt. Res. Appl.* **18**, 563 (2010)
- A. Brailove, S. Kang, A. Fujisaka, F. Henley, In *Proc. 25th EU PVSEC* (WIP, München, 2010), p. 1613
- R. Buchwald, K. Fröhlich, S. Würzner, T. Lehmann, K. Sunder, H.J. Möller, *Energy Procedia* **38**, 901 (2013)
- R. Buchwald, S. Würzner, K. Fröhlich, M.Fuchs, S. Retsch, T. Lehmann, H. J. Möller, In *Proc. 40th IEEE Conf. (IEEE, Denver, 2014)*, p. 654
- M. Buijs, K. Korpel van Houten, *Wear* **162**, 954 (1993)
- J. I. Bye, L. Norheim, B. Holme, Ø. Nielsen, S. Steinsvik, S. A. Jensen, G. Fragiaco, I. Lombardi, In *Proc. 26th EU PVSEC* (WIP, München, 2011), p. 956
- T. F. Ciszek, In *Crystals 5* (Springer, Berlin, 1981), p. 183
- V. Depauw, I. Gordon, G. Beaucarne, J. Poortmans, R. Mertens, J.-P. Celis, *J. Appl. Phys.* **106**, 033516 (2009)
- V. Depauw, Y. Qiu, K. Van Nieuwenhuysen, I. Gordon, J. Poortmans, *J. Prog. Photovolt. Res. Appl.* **18**, 102 (2010)
- F. Dross, *Appl. Phys. A-Mater* **89**, 149 (2007)
- Y. Gogots, C. Baek, F. Kirscht, *Semicond. Sci. Technol.* **14**, 936 (1999)
- F. Henley, In *Proc. 35th IEEE PVSC* (IEEE, Denver, 2010), p. 387
- F. Henley, A. Brailove, A. Lamm, T. Heerwagen, E. Saunar, M. Nese, R. Steeman, B. Hammel, In *Proc. 23rd EU PVSEC* (WIP, München, 2008), p. 2017
- H.P. Hsu, W.P. Huang, C.F. Yang, C.W. Lan, *Sep. Purif. Technol.* **133**, 1 (2014)
- ITRPV, *7th International Technology Roadmap for Photovoltaic* (VDMA, Frankfurt, 2016)
- L. Johnsen, K. Gastinger, L. Bjerkan, R. Rietzschel, H.J. Möller, *Proc. 24th Europ. PVSEC* (WIP, München, 2009), p. 1248
- S. Kaminski, R. Rietzschel, T. Wagner, C. Funke, H.J. Möller, *Proc. 24th Europ. PVSEC* (WIP, München, 2009), p. 1299
- S. Kaminski, T. Wagner, R. Rietzschel, W. Fütterer, C. Funke, H.J. Möller, *Proc. 25th Europ. PVSEC* (WIP, München, 2010), p. 1315
- H. Lange, I. Schwirtlich, *J. Crystal Growth* **104**, 108 (1990)
- J. Larsen-Basse, *Wear* **166**, 93 (1993)
- Y.C. Lin, C.Y. Tai, *Sep. Purif. Technol.* **74**, 170 (2010)
- Y.C. Lin, T.Y. Wang, C.W. Lan, C.Y. Tai, *Powder Technol.* **200**, 216 (2010)
- S. Liu, K. Huang, H. Zhu, *Sep. Purif. Technol.* **118**, 448 (2013)
- T. Liu, P. Ge, W. Bi, Y. Gao, *Mater. Sci. Semi. Proc.* (2016.) in press
- D. Meißner, B. Hurka, R. Rietzschel, H.J. Möller, O. Anspach, *Proc. 27th EU PVSEC* (WIP, München, 2012), p. 1076
- D. Meißner, St. Schönfelder, B. Hurka, J. Zeh, K. Sunder, R. Köpge, Th. Wagner, A. Grün, H. Hagel, H.J. Möller, H. Schwabe, O. Anspach, *Sol. Energy Mater. Sol. Cells* **120**, 346 (2014)
- H.J. Möller, *Adv. Eng. Mater.* **6**, 501 (2004)
- H.J. Möller, *Phys. Stat. Sol. (a)* **657**, 203–204 (2006)
- H. J. Möller, *Crystal sawing technology*, in *Crystal Growth Technology*, ed. by H. J. Scheel, P. Capper (Wiley, VCH Weinheim, 2008), p. 457
- H.J. Möller, *Wafer Processing in Handbook of Crystal Growth*, vol 2, 2nd edn. (Elsevier, 2014.) chapter 18
- H.J. Möller, S. Retsch, R. Rietzschel, *Proc. 28th EU PVSEC* (WIP, München, 2013), p. 927
- J.H. Petermann, D. Zielke, J. Schmidt, *J. Prog. Photovolt. Res. Appl.* **20**, 1 (2012)
- S. Retsch, S. Jentsch, H.J. Möller, *Proc. 27th EU PVSEC* (WIP, München, 2012), p. 947
- S. Retsch, M. Fuchs, H.J. Möller, *Proc. 29th EU PVSEC* (WIP, München, 2014), p. 123
- M. Reuter, *Sol. Energy Mater. Sol. Cells* **704**, 93–96 (2008)
- R. Rietzschel, A. Senf, H.P. Seelmann-Eggebert, S. Kaminski, T. Wagner, C. Funke, H.J. Möller, *Proc. 25th Europ. PVSEC* (WIP, München, 2010), p. 1596
- S.A. Sergiienko, B. Pogorelov, V.B. Daniliuk, *Sep. Purif. Technol.* **133**, 16 (2014)

- L. J. Struble, G.K. Sun, in *Flow and microstructure of dense suspensions*, ed. by L. J. Struble, M. Zukoski and D. Maitland - Symposia Proc. Vol. 289 (Materials Research Society, Pittsburgh, 1993), pp. 173
- K. Tomono, H. Furuya, S. Miyamoto, Y. Okamura, M. Sumimoto, Y. Sakata, R. Komatsu, M. Nakayama, *Sep. Purif. Technol.* **103**, 109 (2013)
- K. Van Nieuwenhuysen, V. Depauw, R. Martini, J. Govaerts, M. Debucquoy, H.S. Radhakrishnan, I. Gordon, T. Bearda, K. Baert, J. Poortmans, *Proc. 27th EU PVSEC* (WIP, München, 2012), p. 2471
- T. Wagner, H.J. Möller, *Proc. 23th EU PVSEC* (WIP, München, 2008), p. 1315
- F.V. Wald, *Crystals 5* (Springer, Berlin, 1981), p. 147
- T.Y. Wang, Y.C. Lin, C.Y. Tai, R. Sivakumar, D.K. Rai, C.W. Lan, *J. Crystal Growth* **310**, 3403 (2008)
- H.Y. Wang, Y. Tan, J.Y. Li, Y.Q. Li, W. Dong, *Sep. Purif. Technol.* **89**, 91 (2012)
- Y.F. Wu, Y.M. Chen, *Sep. Purif. Technol.* **68**, 70 (2009)
- C.F. Yang, H.P. Hsu, C.W. Lan, *Sep. Purif. Technol.* **149**, 38 (2015)



# Wafer Cleaning, Etching, and Texturization 12

André Stapf, Christoph Gondek, Edwin Kroke, and Gerhard Roewer

## Contents

Introduction .....	312
Basics/Fundamentals of Wet-Chemical Silicon Treatment .....	314
Chemical Properties of Silicon Surfaces .....	314
Dissolution of Silicon .....	316
Etching Rate .....	320
Isotropic and Anisotropic Behavior .....	321
Cleaning of Silicon Surfaces .....	324
Types of Contaminations .....	325
Overview of Cleaning Solutions .....	327
The RCA Standard Cleaning Procedures .....	331
Alternative Cleaning Sequences: Ozone, Ohmi-Clean, and IMEC-Clean .....	333
Etching .....	336
Chemical Aspects of Acidic Etching .....	336
Chemical Aspects of Alkaline Etching .....	346
Concluding Remarks/Summary .....	353
Cross-References .....	356
References .....	356

## Abstract

Wafer preparation for silicon PV includes wet chemical cleaning, etching, and texturization steps. Aqueous solutions containing either acids or strong bases result in very different etch rates. Underlying chemistry is used for all three applications. Typical cleaning mixtures such as RCA-SC1 and RCA-SC2, SPM, and dHF are introduced with their respective properties as well as acidic etching systems like hydrofluoric acid/nitric acid (HF/HNO<sub>3</sub>) and alkaline

---

A. Stapf (✉) · C. Gondek · E. Kroke · G. Roewer  
Institute of Inorganic Chemistry, TU Bergakademie Freiberg, Freiberg, Germany  
e-mail: [Andre.Stapf@chemie.tu-freiberg.de](mailto:Andre.Stapf@chemie.tu-freiberg.de); [Christoph.Gondek@chemie.tu-freiberg.de](mailto:Christoph.Gondek@chemie.tu-freiberg.de);  
[Edwin.Kroke@chemie.tu-freiberg.de](mailto:Edwin.Kroke@chemie.tu-freiberg.de); [Gerhard.Roewer@chemie.tu-freiberg.de](mailto:Gerhard.Roewer@chemie.tu-freiberg.de)

mixtures such as potassium hydroxide/isopropanol (KOH/IPA). While the latter is used for texturing monocrystalline wafers due to the anisotropic etching behavior, the former HF-containing systems are generally used for isotropically texturing multicrystalline silicon wafers. Fundamental chemical, physical, thermodynamic, and kinetic aspects of these systems are presented and discussed. In all cases, it has to be pointed out that a complete understanding of the reaction mechanisms causing the observed properties is still missing to a large extent. Therefore, many aspects of silicon cleaning, etching, and texturization have only been optimized empirically. Further studies are necessary to provide a basis for future improvements, which are not only focused on scientific aspects but also on environmental and economic issues.

---

**Keywords**

Wet-chemical treatment · Cleaning · Etching · Texturization · Silicon surface · Silicon dissolution · Saw damage removal · Contaminations · Impurities

---

**Introduction**

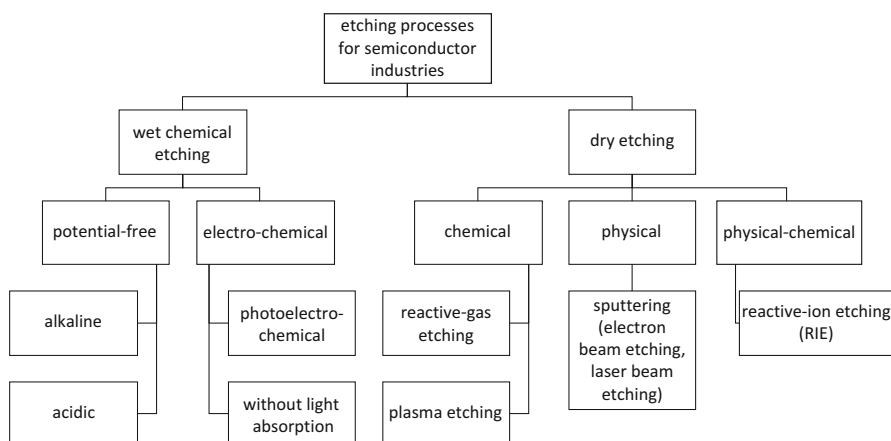
Silicon surfaces must be cleaned, etched, and textured (structured) at different steps during the fabrication processes for various silicon devices in microelectronics (e.g., integrated circuits (IC), micro-electro-mechanical structures (MEMS)) and photovoltaic (PV) industries. Material contamination levels and surface qualities are different in these industrial branches and depend on the performance of devices within the respective branch. In PV, optimized crystalline silicon-based cells and their structures require lower contamination levels in the bulk material and at surfaces as well as improved light trapping to achieve higher efficiency. Process steps concerning cleaning, etching, and texturing of silicon surfaces become more and more crucial and contribute to the present challenges in these fields. Additionally, the strong pressure on prices permanently leads to cost optimization of the cleaning, etching, and texturization concepts. Cleaning and etching are closely related in silicon processing. Generally, contaminations/impurities may be either physisorbed on the surface or, like in most cases, also chemisorbed or even incorporated in the nanometer thick surface layers. Thus, in order to clean silicon surfaces removing all relevant organic, inorganic, and particulate impurities and sometimes also structural defects, it is crucial that silicon surface layers have to be dissolved, i.e., etched. Small etch rates are sufficient for this purpose because only very thin layers in the lower nanometer range have to be removed. The aims of cleaning, etching, and texturing sequences in solar cell processing/treatment of PV silicon are summarized in Table 1.

Several technical opportunities to etch, texture, or also clean silicon surfaces are presented in Fig. 1. The application of different methods depends on respective tasks and the available process chain. All these methods have advantages and disadvantages. Dry etching and cleaning are important in microelectronics, but currently



**Table 1** Aims of cleaning and etching (texturing and polishing) processes in crystalline silicon solar cell processing

Cleaning	Etching
Surfaces as clean as necessary	Defined silicon removal
Removal of:	Removal of surface-near defects (e.g., saw damage)
Molecular organic impurities	Texturization for better light trapping
Atomic/molecular inorganic impurities	PSG/BSG removal <sup>a,b</sup>
Particulate impurities	Polishing <sup>b</sup>

<sup>a</sup>Phosphorous-silicate glass/boron silicate glass<sup>b</sup>Not considered in this chapter**Fig. 1** Etching (and also cleaning and texturing) methods have been developed for the numerous different processing steps in semiconductor and other silicon-based industries. For silicon PV production the lower left two options are relevant and considered in this chapter, namely, wet chemical acidic and alkaline etching (as well as cleaning and texturization)

rarely used in silicon PV industry. A major drawback of dry etching processes is the fact that the formation of nanoparticles and dust is generally more difficult to be avoided, compared to wet chemical processing steps.

In PV, wet-chemical processes are widely used in crystalline silicon solar cell processing. This whole chapter focuses on aqueous wet-chemical cleaning, etching, and texturization sequences and methods. At first, the basics on wet-chemical silicon treatment are given, focusing on the general dissolution process of silicon in aqueous media (section [Basics/Fundamentals of Wet-Chemical Silicon Treatment](#)). Afterward, different typical kinds of contaminations on silicon surfaces and their removal are discussed. Industrially applied cleaning sequences are considered and compared with respect to solar cell manufacturing (section [Cleaning of Silicon Surfaces](#)). Silicon etching is subdivided into acidic and alkaline etching sequences in solar cell processing (section [Etching](#)). Alkaline etching is mostly applied for monocrystalline (100) silicon wafers, whereas acid etching is used for fast texturing or

polishing processes on multicrystalline substrates. Current trends for further optimization are also presented. Defect etching as a further important wet chemical etching application for silicon and other semiconductor surfaces is rarely used in silicon PV processing and therefore not considered in this chapter. Furthermore, nonaqueous solutions, which also may be used for the wet chemical treatment of silicon surfaces, are not taken into account.

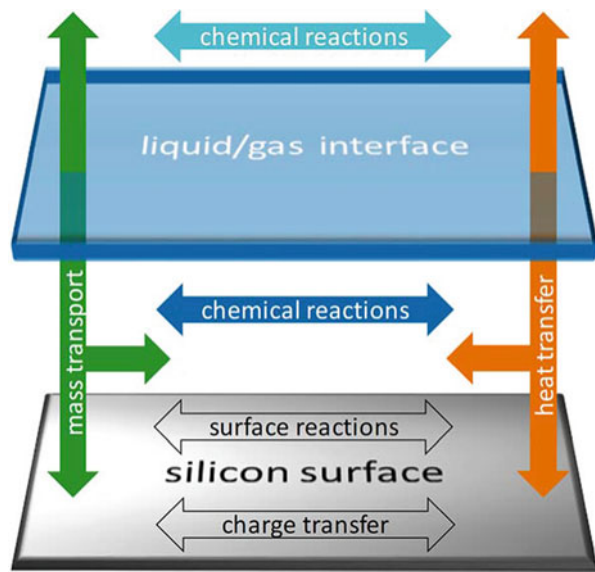
## Basics/Fundamentals of Wet-Chemical Silicon Treatment

The basic processes, including the chemical reaction steps and mechanisms of the wet-chemical treatment of silicon, are very complex and yet not fully understood. Chemical and electrochemical reactions between the silicon surface (surface properties, doping), the type of the particular etching or cleaning mixture, and the gas phase are important as well as the mass and heat transfer processes by convection and diffusion steps. The respective thermodynamic driving force and kinetics of the chemical processes provoked by the solutions during the treatment of the silicon surface are crucial for applications of mixtures for either cleaning or etching of silicon (Fig. 2).

### Chemical Properties of Silicon Surfaces

Considering silicon cleaning and etching processes the chemical properties of the surfaces are of particular importance besides the microscopic and macroscopic

**Fig. 2** Schematic overview of processes during silicon dissolution in electrolyte solutions



roughness and defects. Bare silicon surfaces with lots of dangling bonds are not stable under atmospheric conditions. The dangling bonds are typically saturated under formation of Si-H or Si-O bonds. In addition, also organic and inorganic molecules are adsorbed. Saturation with hydrogen leads to an H-terminated hydrophobic surface, which is common for many as-etched silicon surfaces (Fig. 3 (left)). So-called native oxide layers are formed under oxygen-containing atmosphere or in the presence of oxidizing species. Thickness and completeness of the native oxide depend on the oxidizing conditions. Typical fragments of hydrophilic native oxide layers are shown in Fig. 3 (right).

FT-IR spectroscopy and photoelectron spectroscopy (XPS or PES) are suitable methods to investigate the chemical species or groups at silicon surfaces. Some characteristic vibrational bands of hydrogen-terminated and various oxidized silicon surface groups are shown in Table 2.

Referring to the thermodynamic driving force of the chemical silicon dissolution processes discussed below, a Si-Si bond should be cleaved more readily than a Si-H bond, represented by the bond dissociation energies in Table 3. Nevertheless, in chemical silicon dissolution reactions, the heterolytic bond cleavage yielding ionic

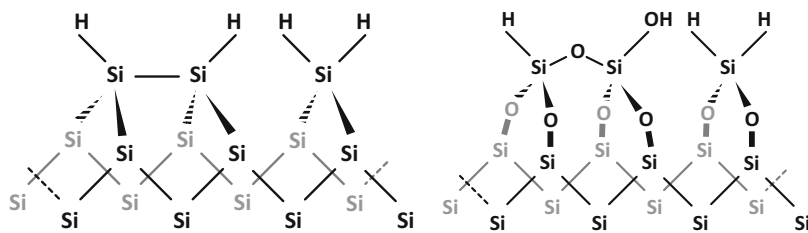


**Fig. 3** Schematic presentation of typical parts of hydrogen-terminated silicon surfaces (*left*, (100) silicon surface with exemplary monohydride and dihydride structure) and a silicon surface, which is partly oxidized (*right*, (100) silicon surface)

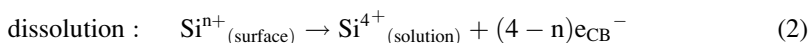
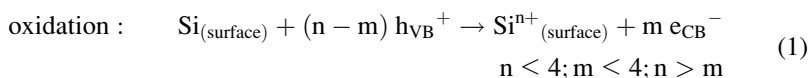
**Table 2** Typical FT-IR sensitive vibrational bands of silicon surface groups (Hull 1999)

Surface species	Vibrational band	Reference
SiH ( $\nu_s(\text{Si-H})$ )	2083 $\text{cm}^{-1}$	Chabal et al. (1993)
SiH ( $\nu_{as}(\text{Si-H})$ )	2071 $\text{cm}^{-1}$	Chabal et al. (1993)
SiH <sub>2</sub> ( $\nu_s(\text{Si-H})$ )	2099 $\text{cm}^{-1}$	Chabal et al. (1993)
H <sub>2</sub> Si...SiH <sub>2</sub> ( $\nu(\text{Si-H})$ )	2108 $\text{cm}^{-1}$	Wang et al. (2005)
SiH <sub>2</sub> ( $\nu_{as}(\text{Si-H})$ )	2114 $\text{cm}^{-1}$	Chabal et al. (1993)
SiH <sub>3</sub> ( $\nu(\text{Si-H})$ )	2134 $\text{cm}^{-1}$	Cerofolini et al. (2008)
SiOSi ( $\nu(\text{Si-O})$ )	1106 $\text{cm}^{-1}$	Schomann and Graff (1989)
H <sub>2</sub> Si(O) <sub>2</sub> ...Si(O)H <sub>2</sub> ( $\nu(\text{Si-H})^2$ )	2141 $\text{cm}^{-1}$	Wang et al. (2005)
H <sub>2</sub> Si(O) <sub>2</sub> ...Si(O)H <sub>2</sub> ( $\nu(\text{Si-H})^3$ )	2185 $\text{cm}^{-1}$	Wang et al. (2005)
HSi-O-Si(O)H ( $\nu(\text{O}_2\text{Si-H})$ )	2165 $\text{cm}^{-1}$	Weldon et al. (1997)
HSi(O <sub>2</sub> )-O-Si(O <sub>2</sub> )H ( $\nu(\text{O}_3\text{Si-H})$ )	2252 $\text{cm}^{-1}$	Wang et al. (2005)
SiOH ( $\nu(\text{SiO-H})$ )	3680 $\text{cm}^{-1}$	Gupta et al. (1991)

species (one reaction product gets both electrons of a bond) is much more important than the homolytic bond dissociation yielding radical species (electrons are distributed equally).

## Dissolution of Silicon

As shown in Fig. 2, wet-chemical treatment and dissolution of silicon materials involve three phases: solid silicon, the etching solution, and gaseous reaction products. Generally, all involved reactions and process steps are influenced by specific thermodynamic and kinetic aspects. In order to etch and dissolve silicon materials, Si-Si bonds have to be cleaved. For this, an average energy of 226 kJ mol<sup>-1</sup> is necessary, giving rise to silicon dissolution under formation of more stable Si-O or Si-F bonds (see section “[Chemical Properties of Silicon Surfaces](#)”). Thermodynamically, a Si-Si bond is cleaved more readily than a Si-H bond (see section “[Chemical Properties of Silicon Surfaces](#),” Table 3). Formally, the dissolution includes the oxidation of silicon surface atoms (Eq. 1) and its complexation (Eq. 2) (Zhang 2001).



$h_{\text{VB}}^+$  = hole in the valence band;  $e_{\text{CB}}^-$  = electron in the conduction band

This means that silicon valence electrons must be removed from surface bonds giving rise to the injection of holes into the valence band. Concerning the specific

**Table 3** Selected experimental bond energies of Si-E bonds from literature, measured data, for bond homolysis reactions (Si-E → Si + E) in the gas phase. Analogous data for heterolytic bond cleavage in condensed phase is not available but may be more relevant for Si dissolution reactions (Luo 2007; Walsh 1981)

Si-E	Bond dissociation energy	Reference
Si-Si (crystalline silicon)	226 kJ mol <sup>-1</sup>	Walsh (1981) <sup>a</sup>
Si-Si (H <sub>5</sub> Si <sub>2</sub> -Si <sub>2</sub> H <sub>5</sub> )	284 kJ mol <sup>-1</sup>	Walsh (1981) <sup>b</sup>
Si-Si (H <sub>3</sub> Si-SiH <sub>3</sub> )	309 kJ mol <sup>-1</sup>	Walsh (1981) <sup>b</sup>
Si-H (H <sub>3</sub> Si-H)	376 kJ mol <sup>-1</sup>	Walsh (1981) <sup>b</sup>
Si-H (Si-H)	293 kJ mol <sup>-1</sup>	Walsh (1981) <sup>b</sup>
Si-H (F <sub>3</sub> Si-H)	418 kJ mol <sup>-1</sup>	Walsh (1981) <sup>b</sup>
Si-F (F <sub>3</sub> Si-F)	669 kJ mol <sup>-1</sup>	Walsh (1981) <sup>b</sup>
Si <sup>+</sup> -O	478 ± 13.4 kJ mol <sup>-1</sup>	Luo (2007)

<sup>a</sup>Calculated from the heat of atomization of elemental Si, derived from the enthalpy of formation ( $\Delta_{\text{HF}}^0$ )

<sup>b</sup>Measured in the gas phase, ±8 kJ mol<sup>-1</sup>

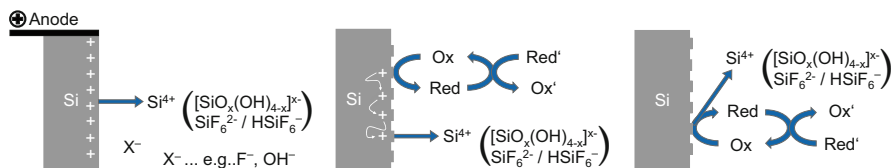


**Fig. 4** Schematic silicon dissolution via anodic etching (*left*), electrochemical electroless etching (*middle*), and chemical etching (*right*): silicon is oxidized by an oxidizing agent ( $\text{Ox} + \text{e}^- \rightleftharpoons \text{Red}$ ) at electroless and chemical etching; furthermore, often complex redox reactions are involved also in solution (symbolized by  $\text{Red}'$  and  $\text{Ox}'$ ). Photo- and metal-assisted dissolution of silicon are further options, but not considered here

oxidation step of silicon, three types of etching processes are classified and schematically shown in Fig. 4: anodic etching, electroless etching, and chemical etching (Kelly et al. 2001). Currently, any anodic etching (electrochemical cell with external circuit) is not relevant for cleaning and etching of silicon in photovoltaics. Electroless dissolution means that the electron transfer occurs at open-circuit potential. Thereby, the rate of oxidation of the semiconductor (hole consumption) is equal to the rate of reduction of the oxidizing agent (hole injection). The electron-hole diffuses in or at the silicon surface. So, the hole is generated at one certain silicon atom but the final oxidation and dissolution steps take place at another silicon atom (Fig. 4, middle). The term “chemical etching” is used to describe a dissolution mechanism which involves only local exchange of electrons between the semiconductor surface bonds and the etching agent in solution. In this case, any free charge carriers do not participate in the reaction (Kelly et al. 2001). Two effective mechanisms are defined referring to the number of electrons removed by the involved oxidizing agent: divalent (oxidizing agent generates only two electron holes ( $h_{\text{VB}}^+$ ) or alternatively one electron-hole plus one captured conduction band electron ( $e_{\text{CB}}^-$ ) per dissolved silicon atom) and tetravalent (all four charge carriers ( $h_{\text{VB}}^+$  and/or  $e_{\text{CB}}^-$ ) for complete oxidation of one silicon atom are injected by the oxidizing agent) (Gerischer et al. 1993; Kolasinski 2009; Lehmann 2002; Turner 1960).

In the aqueous solution, different silicon species are present depending on oxidizing and complexing agents as well as on the pH value. From a thermodynamical point of view, silicon is not noble and should be exothermically converted in water into  $\text{SiO}_2$  and hydrogen (see Eq. 3). The two main reaction steps are the oxidation of silicon and the reduction of protons eventually delivering  $\text{SiO}_2$  and hydrogen (Eqs. 4 and 5). Depending on the pH value  $\text{SiO}_2$  is dissolved leading to mixtures of  $[\text{H}_2\text{SiO}_3]_n$ ,  $[\text{HSiO}_3^-]_n$  and  $[\text{SiO}_3^{2-}]_n$  (Eqs. 6, 7, 8 and 9). In alkaline aqueous media, the chemical dissolution process is exothermic leading to the formation of  $\text{H}_2$  and silicate anions (exact chemical nature depends on pH/degree of protonation). In the literature, these silicate species are usually summarized as “ $\text{SiO}_2$ ”. In acidic media, in principle, a thin layer of  $\text{SiO}_2$  is formed. If fluoride ions are present in such acidic solutions, silicon is dissolved delivering hexafluorosilicate ions (see Fig. 6 and Eq. 10). The thermodynamic behavior of silicon in water without

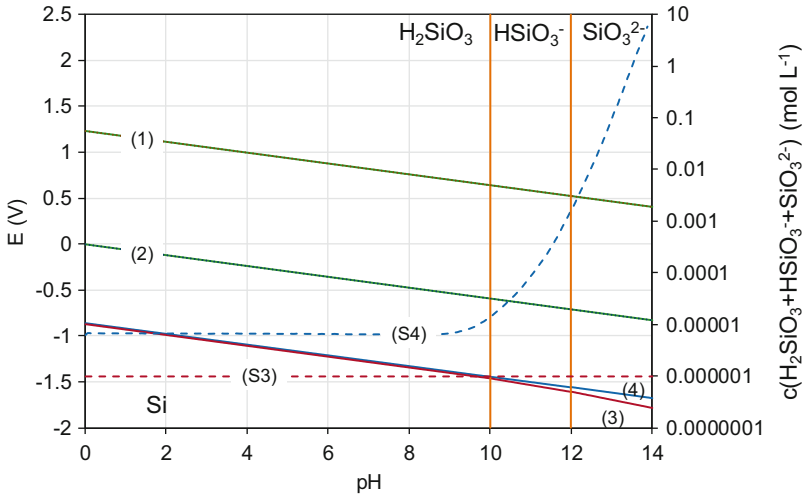
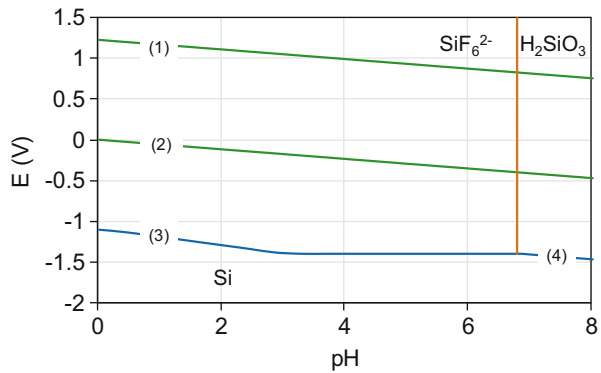


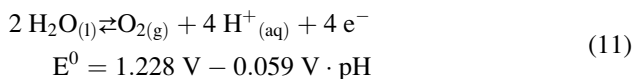
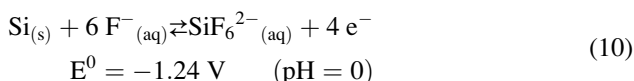
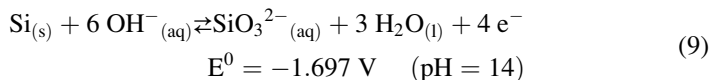
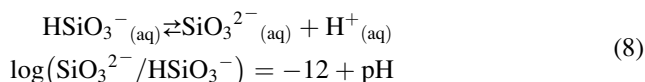
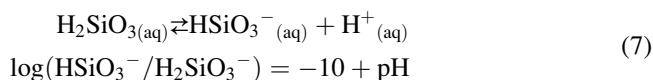
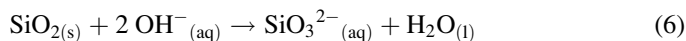
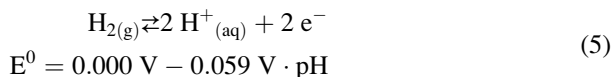
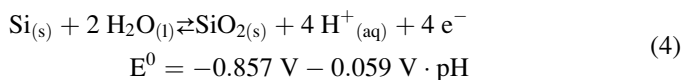
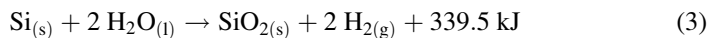
**Fig. 5** Pourbaix equilibrium diagram for the silicon-water system at 25 °C also showing the influence of the pH on the solubility of silica (S, dotted lines): (1) decomposition of water (Eq. 11), (2) formation of hydrogen (Eq. 5), (3) and (4) oxidation of silicon (red lines (3), S3) belong to constant concentration of dissolved silica of  $10^{-6} \text{ mol L}^{-1}$ , blue lines (4), S4) belong to varying concentration of dissolved silica depending on the silicon solubility (considering silica in the form of quartz)), pH = 10 equilibrium of  $\text{H}_2\text{SiO}_3^*$  and  $\text{HSiO}_3^{*-}$  (Eq. 7), pH = 12 equilibrium of  $\text{HSiO}_3^{*-}$  and  $\text{SiO}_3^{2-*}$  (Eq. 8), \*different silica species referring to respective monomer  $\text{H}_2\text{SiO}_3$  or  $\text{H}_4\text{SiO}_4$ )

**Fig. 6** Pourbaix equilibrium diagram for the system silicon-fluoride-water at 25 °C,  $c(\text{Si}) = 0.001 \text{ mol L}^{-1}$ ,  $c(\text{F}^-) = 1.0 \text{ mol L}^{-1}$ , at  $\text{pH} > 6.7$  (depending on  $c(\text{F}^-)$ )  $\text{SiF}_6^{2-}$  hydrolyzes under silica formation. Line (1) see Eq. 11, Line (2) see Eq. 5, Line (3) see Eq. 10, Line (4) see Eq. 9



and with the complexing fluoride ions is schematically summarized in the Pourbaix diagrams in Figs. 5 and 6, respectively.

Consequently, for any wet-etching processes of silicon, the products of the oxidation reaction must be soluble in the respective solution. Thus, in principle one has to distinguish between two different etching systems: acidic solutions with fluoride ions complexing the oxidized silicon atoms and alkaline solutions in which silicon is dissolved by  $\text{OH}^-$ -ions under formation of silicates (Pourbaix 1974).



Besides the thermodynamics, kinetic facts are also important for realizing any silicon dissolution processes. As displayed in Fig. 2 there are mass transport processes (species diffusion from the solution to the surface, surface diffusions of the reactants at the interface electrolyte/silicon, diffusion of the reaction products away from the surface) and chemical surface reactions (heterogeneous, activation barrier). The knowledge of some activation energy values ( $E_A$ ) helps to draw conclusions referring to the rate determining step. If the chemical dissolution process is thermodynamically allowed, it runs kinetically diffusion controlled ( $E_A < 20 \text{ kJ mol}^{-1}$ ), reaction controlled ( $E_A > 40 \text{ kJ mol}^{-1}$ ), or mixed reaction-diffusion controlled ( $20 \text{ kJ mol}^{-1} < E_A < 40 \text{ kJ mol}^{-1}$ ) (Atkins and de Paula 2010; Löwe et al. 1990). The diffusion controlled process types often occur in the case of fast surface reactions (high chemical reactivity). It commonly results in polished surfaces. The rate of diffusion processes can be affected by convection steps, temperature, and additives like surfactants. The process type “reaction control” results from the striking activation barrier of chemical surface reactions, such as passivation effects, steric hindrance, and electrostatic repulsion. Frequently, in the case of reaction controlled dissolution process of silicon, the oxidation/electron hole injection and/or the formation of transition states are considered to act as the rate determining

steps (Kolasinski 2003; Löwe et al. 1990). Emerging surface texturing phenomena in consequence of the applied etching process indicate that a surface reaction is the rate limiting step (Löwe et al. 1990). Different kinetics and surface morphologies are observed depending on the etching system (acidic, basic), concentrations of the etch bath components (also additives), the electronic state of the silicon material (doping, defect density), and the temperature.

## Etching Rate

The etching rate (or etch rate)  $r$  is frequently used to quantify the reactivity of crystalline silicon in etching mixtures. The etch rate  $r$  is defined to be the quotient of the thickness ( $\Delta d$ ) of the etched silicon layer per side and the immersion time ( $t_{\text{etch}}$ ). There are three different methods which can be used to determine the etch rates experimentally:

- The thickness of the removed silicon ( $\Delta d$ ) can be measured directly with microscopic means such as atomic force microscopy (AFM), laser scanning microscopy (LSM), or scanning electron microscopy (SEM), if the surface of a wafer has been masked by an inert coating. To avoid mistakes, fracture surfaces or polished cross-sections should be analyzed in the case of SEM. If relatively thick layers are removed from the surface, a profilometer may also be used.
- Etch rates can also be determined by analyzing the amount of dissolved silicon in the etching solution before and after the etching experiment if the overall size of the etched silicon surface is known.
- The thickness of the removed silicon layer per side  $\Delta d$  can also be calculated from the mass loss obtained by differential weighing of silicon wafers etched on both sides ( $\rho(\text{Si}) = 2.33 \text{ g cm}^{-3}$ ).

$$A = \frac{m_0}{\rho_{\text{Si}} \cdot d_0}$$

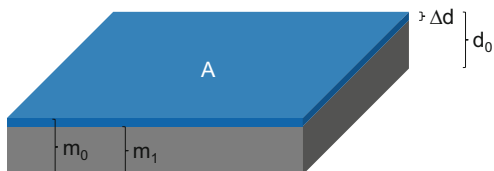
$$\Delta d = d_0 - d_1 = d_0 - \frac{m_1}{\rho_{\text{Si}} \cdot A} = d_0 \left( 1 - \frac{m_1}{m_0} \right)$$

$$r = \frac{\Delta d \cdot 10^7}{2 \cdot 3600 \cdot t_{\text{etch}}} = \left[ \frac{\text{nm}}{\text{s}} \text{ per side} \right]$$

$m$  = mass [g],  $\rho$  = density [ $\text{g cm}^{-3}$ ],  $A$  = area of the wafer [ $\text{cm}^2$ ],  $d$  = thickness of the wafer [cm],  $t_{\text{etch}}$  = etching time [h] (Fig. 7).

The etching rate depends strongly on the composition of the etching solution (oxidizing agent, complexing agent, pH-value, temperature, stirring, and viscosity), on the (electronic) state of the silicon material (doping (n-type, p-type), crystallinity, surface properties, and saw damage), and on further parameters



**Fig. 7** Parameters used for etching rate determination**Table 4** Etch rates of typical isotropic etching solutions on silicon wafers (Hull 1999)

Etchant (Ratio of volumes)	Temperature	Etch rate
1 HF (48%): 4 H <sub>2</sub> O	25 °C	0.00005 μm min <sup>-1</sup>
1 HF (49%): 1 H <sub>2</sub> O <sub>2</sub> (30%): 20 H <sub>2</sub> O	20 °C	0.00012 μm min <sup>-1</sup>
1 HF (49%): 21 HNO <sub>3</sub> (70%)	25 °C	13.8 μm min <sup>-1</sup>
8 HF (49%): 75 HNO <sub>3</sub> (70%): 17 CH <sub>3</sub> COOH	25 °C	5.0 μm min <sup>-1</sup>
5 NH <sub>4</sub> F (40%): 126 HNO <sub>3</sub> (70%): 60 H <sub>2</sub> O	25 °C	0.15 μm min <sup>-1</sup>

**Table 5** Etch rates on various crystal planes in typical alkaline anisotropic etching solutions referring to different crystal planes on silicon wafers (Hull 1999)

Etchant	Temperature	Plane	Etch rate
KOH (34%) (Sato et al. 1999)	70 °C	100	0.6 μm min <sup>-1</sup>
		110	1.3 μm min <sup>-1</sup>
		111	0.009 μm min <sup>-1</sup>
TMAH (22%) (Hull 1999)	90 °C	100	0.9 μm min <sup>-1</sup>
		110	1.8 μm min <sup>-1</sup>
		111	0.018 μm min <sup>-1</sup>
NaOH (1.5%), IPA (3%) (Vazsonyi et al. 1999)	84 °C	100 wafer	0.9 μm min <sup>-1</sup>

such as temperature, bias, gas bubbling, convection, and light exposure (see Table 4). Etching rates are usually specified in units of nm s<sup>-1</sup> or in μm min<sup>-1</sup> (1 nm s<sup>-1</sup> = 0.06 μm min<sup>-1</sup>).

## Isotropic and Anisotropic Behavior

Silicon crystallizes in the diamond crystal lattice. The three most relevant silicon crystal planes referring to their etching rate are (100), (110), and (111). In dependence on the etching mixture composition, the silicon atoms in these three planes react with specific reaction rates with the etching solution, i.e., silicon atoms are dissolved differently rapid on each surface. In case of alkaline solutions, high ratios (100):(110):(111) of the different etching rates are observed, for example, 35:70:1 in TMAH (tetramethylammonium hydroxide, 20%, 80 °C) and 80:160:1 in KOH (35%, 70 °C) (Gosálvez et al. 2010). This reactivity dependence on the different crystal planes gives rise to the so-called anisotropy (Table 5, Fig. 8 right).

On the other hand, in acidic solutions, there is typically no difference concerning the chemical reactivity of different lattice planes. In an HF-HNO<sub>3</sub> solution (10% HF, 56% HNO<sub>3</sub>, 25 °C) the ratio of the etching rates on the above-mentioned crystal planes is 1.10:1.00:1.05 (Schwartz and Robbins 1961). This leads to an isotropy – the etching rates are almost independent of the crystal surface orientation type (Table 4, Fig. 8 left).

In order to explain the resulting different etching rates in case of Si(100), Si(110), and Si(111) surfaces in alkaline solutions, several approaches were made. The simplest approach is based on the specific values of radii and distance of the silicon atoms in the crystal lattice. Depending on the crystal plane type, the voids in-between the terminal silicon atoms have different sizes. This makes a specific attack of the oxidizing agent easier on (100) as well as (110) planes (Fig. 9) (Buchholz 2015).

Another explanation for the anisotropic etching behavior is based on the mobility of silicon surface atoms: The native silicon surface is terminated with hydrogen atoms. The anisotropic dissolution of silicon is initiated by a nucleophilic attack of OH<sup>-</sup> species on these Si-H surface bonds (see also section “[Chemical Aspects of Alkaline Etching](#)”). The transition state of this chemical reaction involves most likely a penta-coordinated silicon atom. Therefore, a change from tetrahedral to a pentavalent configuration would be necessary. The trigonal bipyramidal configuration embodies the most energetically favored pentavalent state. However, only Si-H or Si-OH surface groups are able to change their relative position, the angles of the back bonds are more

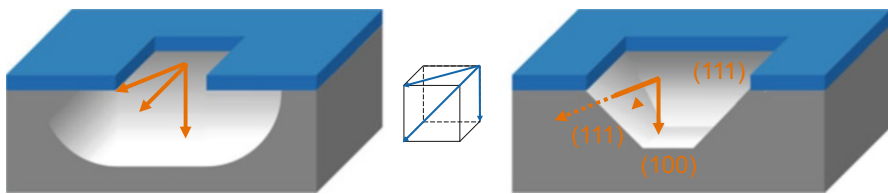


**Fig. 8** Schematic drawing of isotropic (*left*) and anisotropic etching behavior (*right*)

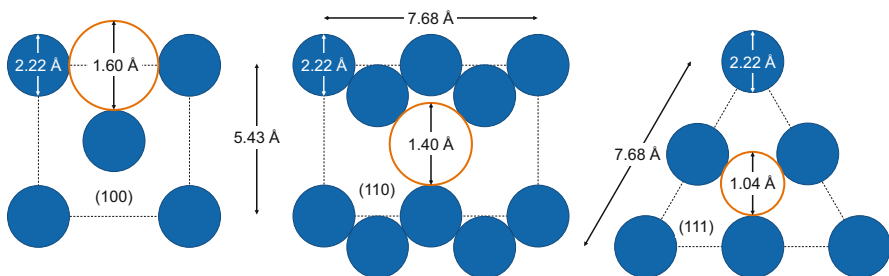


**Fig. 9** Radii of and distances between silicon surface atoms on (100), (110), and (111) surfaces

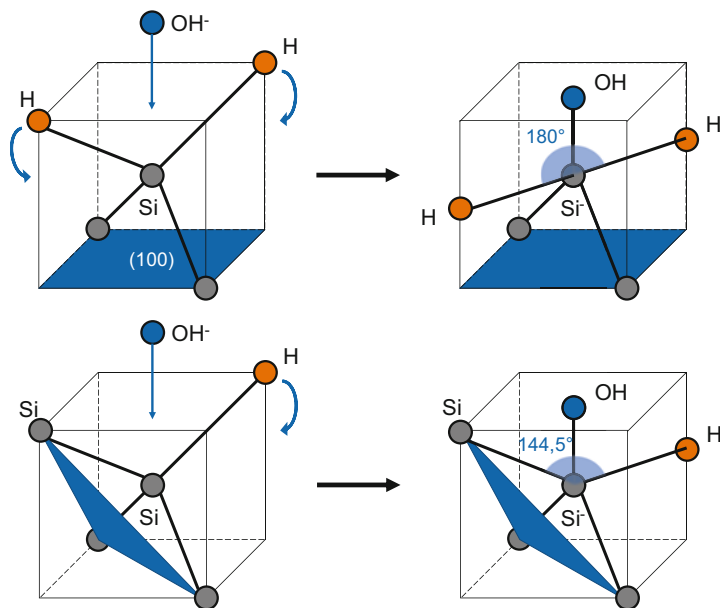


**Fig. 10** Comparison of the formation of pentavalent transition states on silicon (100) and (111) surfaces during anisotropic treatment

or less fixed by the solid lattice (Fig. 10). On Si(111) surfaces with three fixed Si-Si back bonds the creation of a trigonal bipyramidal configuration is blocked. Therefore, a dissolution of silicon atoms in Si(111) surfaces needs a much higher activation energy than the dissolution of Si(100) with only two fixed Si-Si back bonds. This hypothesis is supported by atomistic kinetic Monte Carlo and cellular automaton simulations (Allongue et al. 1993; Glembocki et al. 1985; Gosálvez 2003).

After the Si-OH bond is formed, the attraction of electrons by high electronegativity of the OH-group gives rise to a strong polarization of the Si-Si back bonds resulting in an attack of water to break these bonds. The low dissolution rate on Si(111) surfaces may also be understood as an insufficient polarization of three rear Si-Si bonds by only one Si-OH surface bond. On Si(100) surfaces, two Si-OH bonds are able to polarize two Si-Si back bonds (Baum and Schiffrin 1998; Campbell et al. 1993; Kelly and Philippsen 2005; Lehmann 2002).

In reality, all these influences may sum up to the observed anisotropic etching behavior of crystalline silicon. However, the angles of the resulting pyramids on the silicon surface are in many cases independent of the etching rates but depend on the type of the planes of the crystal lattice of silicon (Fig. 11). The angles in a cubic crystal lattice such as in silicon can be calculated by the Miller indices of two planes ( $h_1k_1l_1$  and  $h_2k_2l_2$ , e.g., 100 and 110) and lead to the values given in Table 6.

**Fig. 11** Angles of resulting pyramids on silicon surfaces after anisotropic chemical treatment

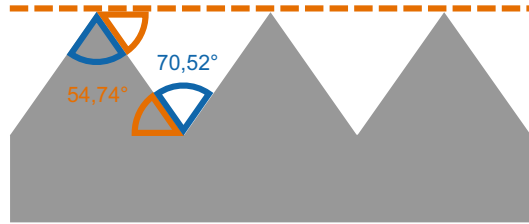


**Table 6** Angles between silicon (100), (110), and (111) planes

Formula	Planes		Angles between planes		
$\cos \alpha = \frac{h_1 h_2 + k_1 k_2 + l_1 l_2}{\sqrt{(h_1^2 + k_1^2 + l_1^2)(h_2^2 + k_2^2 + l_2^2)}}$	(100)	(100)	0	90	
		(110)	45	90	
		(111)	54.74		
	(110)	(110)	0	60	90
		(111)	35.26	90	
	(111)	(111)	0	70.52	

## Cleaning of Silicon Surfaces

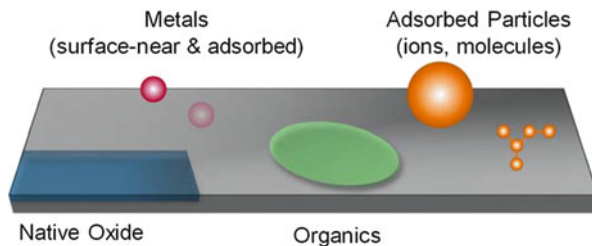
Contaminations on wafer surfaces (originating from different sources: operator, wafer handling, equipment, materials, and processes) exist as physisorbed or chemisorbed ions, uncharged molecules and atoms, thin films, discrete particles, clusters, and (less important) adsorbed gases/vapors (Fig. 12). Some types of contaminations tend to diffuse from/to the surface, into the bulk and at interfaces (e.g., Cu-atoms). These detrimental effects cause a decrease of the minority-carrier lifetime leading to degradation of device performance and yield. Particles or films may cause blocking of etching and/or rinsing and can even lead to short-circuits if they are conducting. All in all, the various effects of contaminants are complex and depend on the nature, location, and quantity of the specific type of impurity.

Thus, techniques to avoid contamination and processes to generate very clean wafer surfaces have become critically important for high-performance applications. Impurities, such as metal ions, metals, and particles are especially detrimental if present on silicon surfaces during high-temperature processing (thermal oxidation, diffusion, etc.), because they may spread and diffuse into the silicon bulk material. Impurities must also be removed from silicon surface before and/or after lower temperature steps.

Wet-chemical process steps, including surface preparation prior to emitter diffusion and prior to passivation or firing steps, are critical parts in crystalline silicon solar cell manufacturing. Therefore, wet-chemical cleaning accounts for an important part of the total consumption of chemicals, and a relatively small improvement in chemical usage has a large overall effect (Heyns et al. 1999).

Thus, the objective of the “cleaning” (also “surface preparation,” “surface conditioning”) is, in fact, to prepare chemically a surface for the subsequent processing steps of a silicon wafer to produce an integrated circuit (IC) or a solar cell. That

**Fig. 12** Examples for impurities on silicon surfaces



means removal of particles and chemical impurities from the silicon surface without damaging or deteriorating the substrate surface.

Both the solar cell manufacturing and semiconductor device processing require several similar surface cleaning and conditioning steps. But, there are also inherent differences between the impurity levels of solar cells and microelectronic devices. In the case of the standard industrial solar cell production with a much higher throughput of wafers in comparison with the number of IC-related wafers, the number of cleaning steps is limited and/or the cost of chemicals should be markedly less than in semiconductor industry production lines.

## Types of Contaminations

Surface contamination and its control, prevention, detection, and measurement are important topics. Referring to the basic line currently used within the front-end of a standard solar cell production sequence (pre-cleaning > texturing > saw-damage-removal > cleaning > pre-diffusion-cleaning > diffusion > rear emitter removal > PSG (phosphor-silicate-glass)/BSG (boron-silicate-glass) removal > post-diffusion cleaning) the relevant cleaning procedures are focused on:

- Past-sawing: particles, slurry residual, surfactant removal, and deglueing after wafering (optionally integrated into wafer separation process)
- Pre-cleaning/surface conditioning: (partially integrated into saw damage etch) organic residuals and metal contaminants (from sawing)
- Pre-diffusion cleaning: porous silicon removal/strip and rinsing (most important metal cleaning step), alkali metal ions and anionic (i.e., physisorbed, e.g.,  $\text{SO}_4^{2-}$ ) contaminants
- Surface cleaning/conditioning after PSG/BSG etching and/or edge isolation: metals from the wafer bulk material have been gettered by/into the PSG/BSG layer
- Organic layer removal or intermediate cleaning (e.g., photoresist removal) in the case of more complex cell structures
- Silicon etching/cleaning if direct plating on the silicon substrate after laser opening was employed

In summary, metals and metal ions, respectively, to a certain extent also organic contamination in some cases, embody the main subjects of cleaning.

### Metal Contamination

Metal contaminants originate primarily from the wafer sawing process and silicon contact with metal containing equipment and solutions. Metal contamination has a dramatic impact on the solar cell performance (► Chap. 17, “Metal Impurities and Gettering in Crystalline Silicon”). Metal ions in low concentration level already can cause a large reduction in bulk minority carrier lifetime for both p- and n-type solar cells. Figure 13 illustrates this relation between metal contamination and minority carrier lifetime for the element iron (Fe). Therefore, minority carrier lifetime – as a key for high-efficiency cells – depends significantly on removal and avoidance of metals. The metal contamination removal is one of the very important criteria for a cleaning step during solar cell manufacturing.

There are different deposition mechanisms when metallic impurities contaminate the silicon wafer surface in aqueous solutions. The variety of metal species present in the solution significantly depends on the pH-value, the redox potential of the solution, and concentrations of available complexing agents:

- Adsorption of metal species on the silicon surface
- Electrochemical deposition (electrochemical reduction of the metal ion by silicon):

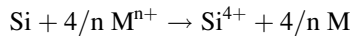
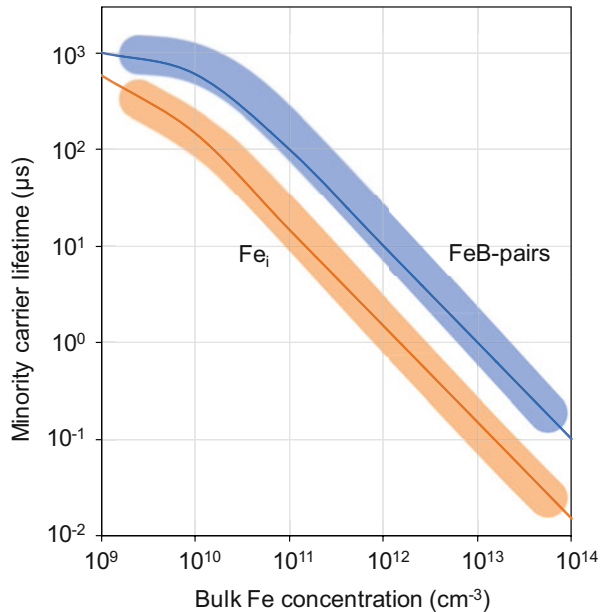
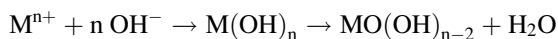


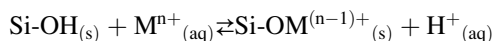
**Fig. 13** The dependence of the minority carrier lifetime on the bulk iron contamination level (limited by iron in the form of interstitial iron  $\text{Fe}_i$  or  $\text{FeB}$ -pairs), adapted from Istratov et al. (2000)



- Precipitation of the metal ion (hydroxide/oxide in particular in alkaline solution (Mori et al. 1995)):



- Film inclusion of the metal ion close to the silicon surface
- Chemisorption of a metal ion hydrate (especially on hydrophilic silicon surfaces and in acidic media, Si-OH groups act as weakly acidic cation exchangers – formation of Si-O-M groups (Loewenstein et al. 1999; Loewenstein and Mertens 1998)):



Referring to the acceptable/tolerable concentration of contaminative transition metal ions, the up-to-date target level has to be below  $10^{10}$  atoms/cm<sup>2</sup>. Ongoing sufficient cleanliness levels varied in the range of  $1 \times 10^{10}$  to  $10 \times 10^{10}$  atoms/cm<sup>2</sup>. Such metal contamination concentration values for the silicon surface correspond to acceptable concentrations of 10–100 ppb in the final cleaning solution. Acidic etching solutions have an intrinsic metal removal power. In contrast, after alkaline texturing removal of metal contaminations is a key issue (Schweckendiek et al. 2012).

### Organic Contamination

Silicon wafers can be contaminated by organic material from surfactants, organic additives, operating equipment, packaging materials (e.g., softeners from plastic foils), and volatile compounds from the air. Organic contamination can hinder surface conditioning, surface texturing, and deposition processes on the surface. In particular, alkaline texturing processes can be detrimentally influenced by traces of organic contaminants. In solar silicon processing, organic contaminants are less critical compared to metallic contaminants. According to the SIA (semiconductor industry association) roadmap, organic matter may be present at a concentration level below 0.1 monolayers or  $1 \times 10^{14}$  carbon atoms/cm<sup>2</sup> – which is a representative target of the cleaning process to choose. However, the portion of organic residues must be reduced significantly if oxides are grown on silicon substrates to gain good oxide quality (Schweckendiek et al. 2012).

### Overview of Cleaning Solutions

Extraction of contaminants via physical desorption (e.g., supported by ultrasonic) and chemical dissolution of impurities lead to soluble species. Chemical dissolution is done via chemical reaction of the cleaning agent mixture with contaminants (oxidation and dissolution) and/or by slight surface etching (e.g., removal of impurities in the native oxide layer (including chemical etching)) (Fig. 14). That means certain

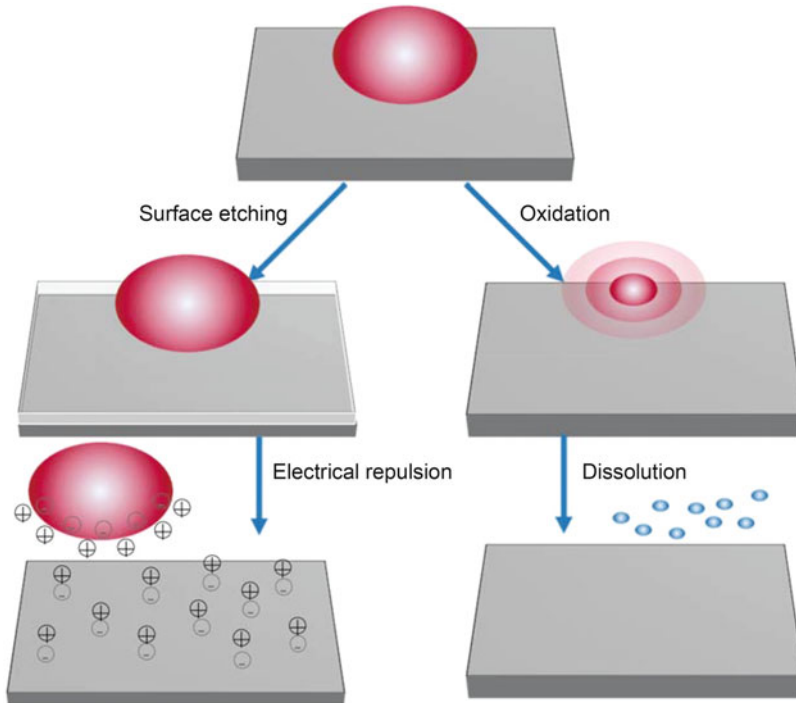


**Fig. 14** Basic chemical cleaning mechanisms: Oxidation and dissolution of the contamination or surface etching

chemical cleaning processes may result in removal of only a few atom layers of the silicon material (“micro-etching”) without changing the silicon surface morphology. Liquid wafer cleaning is based on the application of ultrapure or deionized (DI) water, mineral acids, inorganic bases, weak organic acids and bases (also with surfactant activity, as for example toluenesulfonic acid), metal ions complexing compounds (ligands), silicon oxidizing components (e.g., hydrogen peroxide ( $\text{H}_2\text{O}_2$ ), ozone ( $\text{O}_3$ )) and partially surfactants) (Table 7). Organic solvents are also used (e.g., isopropyl alcohol (IPA)). Different process sequences are established for specific applications which can be realized in a variety of technical equipment (including also rinsing, drying, storing of wafers) for high-volume fabrication/manufacturing.

The relevant processes of wafer cleaning in this equipment are based on immersion processors/wet benches including ultra- as well as mega-sonic support or brush scrubbing support. They can be realized also alternatively by spray processes to reduce the consumption of cleaning and rinsing solutions.

### Removal of Organic Contaminants

Removal of organic contaminants from silicon wafers can be accomplished by using strong oxidizing mixtures. The specific components and their volume ratio, as well as the oxidation process temperature ( $<130\text{ }^\circ\text{C}$ ), depend on the type of the organics



**Table 7** Overview of cleaning solutions and their purpose

Solution	Chemicals	Common names and synonyms	Purpose/ removal of
Ammonia/ hydrogen peroxide/ water	$\text{NH}_{3(\text{aq})}/\text{H}_2\text{O}_2/\text{H}_2\text{O}$	RCA-1, SC-1 (standard-clean-1), APM	Light organics, particles, and metals
Hydrochloric acid/ hydrogen peroxide/ water	$\text{HCl}/\text{H}_2\text{O}_2/\text{H}_2\text{O}$	RCA-2, SC-2 (standard-clean-2), HPM	Metals, oxides, hydroxides
Sulfuric acid/ hydrogen peroxide	$\text{H}_2\text{SO}_4/\text{H}_2\text{O}_2$	Piranha, SPM, Caro's acid	Organics
Choline/ hydrogen peroxide/ water	$[(\text{CH}_3)_3\text{N}(\text{CH}_2)_2\text{OH}]/\text{OH}/\text{H}_2\text{O}_2/\text{H}_2\text{O}$	Choline peroxide	Metals, organics, and particles
Tetramethyl- ammonium hydroxide/ water	$[(\text{CH}_3)_4\text{N}]/\text{OH}/\text{H}_2\text{O}$	TMAH	Light organics, particles, and metals
Persulfuric acid/ sulfuric acid	$\text{H}_2\text{S}_2\text{O}_8/\text{H}_2\text{SO}_4$	PDSA, Caro's acid	Organics
Ammonium persulfate/ sulfuric acid	$(\text{NH}_4)_2\text{S}_2\text{O}_8/\text{H}_2\text{SO}_4$	SA-80	Organics
Ozone/ water	$\text{O}_3/\text{H}_2\text{O}$	Ozonized water	Protective oxide regrowth, organics
Sulfuric acid/ ozone/ water	$\text{H}_2\text{SO}_4/\text{O}_3/\text{H}_2\text{O}$	SOM (sulfuric ozone mix)	Organics
Hydrofluoric acid/ hydrochloric acid/ ozone	$\text{HF}/\text{HCl}/\text{O}_3$		Si-oxide, metals
Hydrofluoric acid/ water	$\text{HF}/\text{H}_2\text{O}$	HF, dHF (diluted HF)	Si-oxide
Hydrofluoric acid/ ammonium fluoride/ water	$\text{HF}/\text{NH}_4\text{F}/\text{H}_2\text{O}$	BOE (buffered oxide etch), BHF (buffered hydrofluoric acid)	Si-oxide
Nitric acid	$\text{HNO}_3$		Organics, metals
Hydrochloric acid/ water	$\text{HCl}/\text{H}_2\text{O}$	HCl, dHCl (diluted HCl)	Metals, metal oxides
Hydrofluoric acid/ nitric acid/ water	$\text{HF}/\text{HNO}_3/\text{H}_2\text{O}$		Slight Si etch, metals
Hydrofluoric acid/ hydrogen peroxide	$\text{HF}/\text{H}_2\text{O}_2$		Slight Si etch, metals
Acetic acid/ water	$\text{H}_3\text{CCOOH}/\text{H}_2\text{O}$		Degreasing

(continued)

**Table 7** (continued)

Solution	Chemicals	Common names and synonyms	Purpose/ removal of
Organic acid (e.g. citric acid)/ water	RCOOH/H <sub>2</sub> O		Deglueing
Hydrofluoric acid/ hydrochloric acid/ water	HF/HCl/H <sub>2</sub> O		Slight Si etch, metals, Si-oxide
Additives/surfactants in acidic or neutral or alkaline media	Acids or bases or buffer solutions with anionic or cationic or nonionic surfactants		Particles, organics, metals

to be destroyed. Typical mixtures are sulfuric acid-peroxide-mixtures (SPM, “Piranha etch” or Caro’s acid, H<sub>2</sub>O<sub>2</sub>/H<sub>2</sub>SO<sub>4</sub> or H<sub>2</sub>SO<sub>5</sub>) and alternative additives instead of H<sub>2</sub>O<sub>2</sub> like sodium and ammonium persulfate (Na<sub>2</sub>S<sub>2</sub>O<sub>8</sub>/(NH<sub>4</sub>)<sub>2</sub>S<sub>2</sub>O<sub>8</sub>) or peroxydisulfuric acid (H<sub>2</sub>S<sub>2</sub>O<sub>8</sub>). Ozone containing cleaning solutions gain importance for organic removal (sulfuric acid-ozone-mixtures (SOM)). After application of H<sub>2</sub>SO<sub>4</sub>-containing cleaning mixtures, an extensive rinsing process is necessary to remove sulfur contamination completely from the surface. Besides H<sub>2</sub>SO<sub>4</sub> sometimes acetic acid is applied. Furthermore, alkaline hydrogen peroxide (H<sub>2</sub>O<sub>2</sub>) solutions are able to remove organic contaminants (see RCA clean SC1).

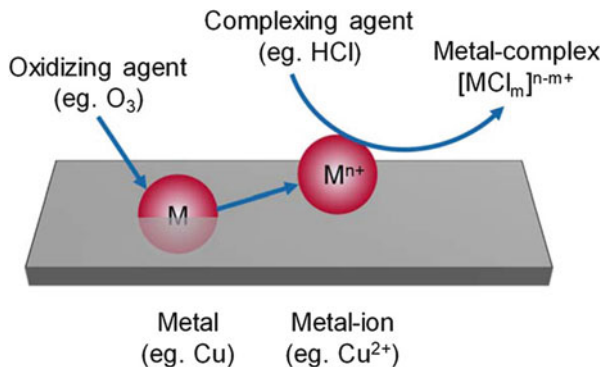
### Removal of Metal Impurities

Metal contaminations are generally removed by diluted hydrochloric acid (HCl) or nitric acid (HNO<sub>3</sub>) solutions, because of their good solubility in these solutions. Some metal contaminations are present in the reduced state (such as Cu) and have to be oxidized. Metals in the silicon oxide layer are removed with hydrofluoric acid (HF) containing solutions (e.g., diluted hydrofluoric acid (dHF)). For some metals, also aqueous ammonia solutions (NH<sub>3(aq)</sub>, see RCA clean SC1) or further complexing ligands (e.g., EDTA (Titriplex II<sup>TM</sup>), Titriplex V<sup>TM</sup>, DEHP, cTRAMP, Deferoxamine) may be used (Fig. 15).

Diluted hydrofluoric acid (dHF) mixtures or aqueous mixtures of HF and ammonium fluoride (NH<sub>4</sub>F, HF/NH<sub>4</sub>F-mixture (“buffered oxide etch (BOE) or buffered hydrofluoric acid (BHF)”) can also be used for solar cell processing steps not considered in this handbook, such as etching of SiN<sub>x</sub>, phosphorous silicate glass (PSG), and borosilicate glass (BSG).

Thin SiO<sub>x</sub> layers on the wafer surface are removed by a brief immersion in dHF solution at room temperature. In consequence of this dHF-treatment, the wetting characteristic is changed from the initially hydrophilic to a hydrophobic surface. This effect has its source in the chemical production of an H-terminated silicon surface (H-Si bonds). If desired, a SiO<sub>x</sub>-film can be regrown by exposure of the H-Si-bonds to solutions containing oxidants like hydrogen peroxide or ozone. Therefore, HF solutions can remove metal ions from the silicon surface.

**Fig. 15** Oxidization and complexation of a metal impurity on a silicon surface



### The RCA Standard Cleaning Procedures

The first systematically developed cleaning process – primarily applied in micro-electronics – for bare or oxidized silicon wafers was based on a two-step oxidizing and complexing treatment with hydrogen peroxide solutions: (i) an alkaline mixture at high pH followed by (ii) an acidic mixture at low pH and rinsing with DI water. The choice of chemicals was based on their specific chemical reactivity, oxidation potentials, reagent purity, reagent volatility, safety, and economy. The process was developed by RCA (Radio Corporation of America) (Kern and Puotinen 1970). The RCA clean is a highly efficient and powerful cleaning process. For solar cell fabrication, there is also high wafer throughput needed. Therefore, cleaning processes for solar cell fabrication are often modified to achieve higher throughputs and lower cost of ownership.

In the first treatment step (standard clean 1 – SC-1), the wafers are exposed to a hot mixture (75–85 °C) of ammonia/hydrogen peroxide/water (APM). This procedure was designed to remove organic surface films by the oxidative breakdown and dissolution to expose the silicon or oxide surface for concurrent or subsequent decontamination reactions. Some group IB (Cu, Ag, Au) and IIB (Zn, Cd) metal ions and ions of several other metals, including Ni<sup>2+</sup> and Co<sup>2+/3+</sup>, are dissolved and removed by the complexing effectiveness of ammonia (NH<sub>3(aq)</sub>, formation of water-soluble ammine complexes). Copper (II), for example, forms the well-known soluble ammine complex [Cu(NH<sub>3</sub>)<sub>4</sub>]<sup>2+</sup>. Both the solvating action of NH<sub>3(aq)</sub> and the powerful oxidizing action of alkaline H<sub>2</sub>O<sub>2</sub> give rise to the resulting cleaning effect (Mori et al. 1995). Furthermore, the SC-1 treatment causes dissolution of the thin native oxide layer on silicon at a low rate as well as the formation of a new silicon oxide which support the removal of particles and chemical impurities on the surface.

The second treatment step (standard clean 2 – SC-2) exposes the rinsed wafer to a hot mixture (75–85 °C) of water-diluted hydrochloric acid/hydrogen peroxide mixture (HPM). This procedure was designed to remove alkali ions and other cations such as Al<sup>3+</sup>, Fe<sup>3+</sup>, and Mg<sup>2+</sup> that form NH<sub>3(aq)</sub>-insoluble hydroxides or

oxides (e.g.,  $\text{AlO}(\text{OH})$ ,  $\text{FeO}(\text{OH})$ ,  $\text{Mg}(\text{OH})_2$ ,  $\text{Zn}(\text{OH})_2$ ) in the SC-1 solution at the wafer surface.

Alkaline conditions like in SC-1 favor the redeposition of metallic contamination on the wafer surface (Martin et al. 1999). The SC-2 treatment does not etch the silicon or silicon oxide and does not force any beneficial surfactant activity for removing particles.

The solution compositions are based on ultra-filtered DI water, electronic grade  $\text{NH}_3(\text{aq})$  (29% (w/w)), electronic-grade HCl (37% (w/w)), and high-purity “unstabilized”  $\text{H}_2\text{O}_2$  (30% (w/w)). The impact of the purity grade of the used chemicals on the cleaning efficiency was studied by Anttila et al. regarding Fe, Cu, Zn contamination (Anttila et al. 1992). The usual volume ratios of  $\text{H}_2\text{O}:\text{H}_2\text{O}_2:\text{NH}_3(\text{aq})$  for the solution used in the SC-1 step are 5:1:1 to 7:2:1. The usual volume ratios of  $\text{H}_2\text{O}:\text{H}_2\text{O}_2:\text{HCl}$  for the SC-2 solution are 6:1:1 to 8:2:1. The thermal instability of  $\text{H}_2\text{O}_2$  especially in SC-1 and to a less extent also in SC-2, respectively, necessitates the use of freshly prepared mixtures. The treatment time is between 10 and 20 min (Kern and Puotinen 1970).

Several improvements to the original RCA cleaning procedure were published by Kern et al. (Kern 1993). Among others, mega sonic systems were recommended for cleaning and rinsing of wafers. Treatment temperature (70–75 °C), as well as treatment time, could be reduced considerably. One optional process step is the wafer treatment with sulfuric acid/hydrogen peroxide mixture (SPM) before SC-1 (APM) followed by stripping the formed oxide/hydroxide film with dHF (50  $\text{H}_2\text{O}$ : 1 HF (48% (w/w)) for several seconds. This dHF stripping to remove the oxide layer can also be applied after SC-1 to prepare the wafer surface for the subsequent SC-2 step. Since the hydrous oxide film from the SPM or SC-1 treatment may trap trace impurities, its removal before the following step (SC-1 or SC-2) should be beneficial (Choi and Ohmi 2001). However, a silicon surface that was exposed to HF is highly reactive and immediately attracts particles and organic contaminants from solutions, DI water, and the ambient air. Already in 1989 Morita et al. reported on the contamination of SC-1/SC-2 cleaned wafers by adsorption of ions such as  $\text{Na}^+$ ,  $\text{K}^+$ ,  $\text{Al}^{3+}$ ,  $\text{Cr}^{3+}$ ,  $\text{Fe}^{3+}$ ,  $\text{Ni}^{2+}$ , and  $\text{Cu}^{2+}$  from solutions, showing that the absence or presence of a  $\text{SiO}_2$  layer on the silicon surface strongly affects adsorption (Morita 1989). Desorption of  $\text{Al}^{3+}$  and  $\text{Fe}^{3+}$  was most effective with HF- $\text{H}_2\text{O}$  and that of  $\text{Cu}^{2+}$  and  $\text{Cr}^{3+}$  with SC-2 (Kern 1990).

There are some further options to modify and to improve the RCA cleaning process in order to reduce the process costs at high level of wafer cleanliness:

- Alternative implementation of centrifugal spray processing and stationary closed system processing (Reinhardt and Kern 2008)
- Reduction of the  $\text{NH}_3(\text{aq})$  concentration in SC-1 by a factor of 2–10 (Reinhardt and Kern 2008)
- Replacement of the volatile  $\text{NH}_3(\text{aq})$  by KOH and dilution (Buchholz 2015)

- Addition of complexing agents and surfactants to SC-1 (APM) to enhance metal removal (Doll et al. 2004; Martin et al. 1999)
- Dilution of SC-1 and SC-2 with DI water (Reinhardt and Kern 2008)
- Replacement of SC-2 with very dilute HCl at room temperature (Reinhardt and Kern 2008)

### **Alternative Cleaning Sequences: Ozone, Ohmi-Clean, and IMEC-Clean**

Currently, several additional solutions for wet-chemical cleaning and surface conditioning are available for use in conjunction with or as a replacement of RCA standard cleaning.

As mentioned already above, HF processing is used to remove potentially metal contamination-rich silicon oxide layers and to create a hydrogen-passivated hydrophobic silicon surface. Instead of such wet processing, the silicon wafers might be exposed to HF-IPA vapor (Reinhardt and Kern 2008). So-called dilute chemistry concepts have been realized in some cases: In order to optimize specific process steps, dilution of cleaning solutions to various concentrations has been established.

Currently, ozonized solutions are also an important part of the cleaning chemistry, because they support a low cost of ownership. The reactions involved in the removal of organics in  $O_3/H_2O$  and oxide formation have been investigated (Reinhardt and Kern 2008). The  $H_2O/O_3$  solution can be combined with  $H_2SO_4$  to the so-called SOM (“sulfuric acid ozone mixture”) mixture for applying also centrifugal spraying. The oxidation-reduction potential of ozone is 2.07 V, whereas for  $H_2O_2$  it is only 1.78 V. Ozone added to dHF mixtures yield organic removal comparable to SPM and metal removal comparable to SC-2 (HPM). Bergman and Lagrange suggest an  $O_3$ -dHF clean that can replace the “four-chem clean” consisting of SPM, dHF, SC-1 (APM), and SC-2 (HPM) (Bergman and Lagrange 2001). Similar results were published by Gottschalk and Schweckendiek (Gottschalk and Schweckendiek 2004). Another part of the cleaning process where the  $O_3$  application is helpful are the re-oxidation processes at the end of the wafer cleaning. There are different ways to apply  $O_3$  in cleaning processes like bubbling  $O_3$  through the mixtures (e.g., micro-bubbles), implementation of a moist  $O_3$  gas phase, or using spray cleaning processes (Claes et al. 2001). Cleaning/conditioning operations with  $O_3$  include reduction of chemical usage, improved cleaning performance, and lowered processing costs (use of  $O_3$  is cheaper than the use of  $H_2O_2$ ). Furthermore, ozonized mixtures do not tend to decompose spontaneously, especially at higher metal concentrations or metal contacts like  $H_2O_2$  does (e.g., catalytic decomposition of  $H_2O_2$  at Fe-contact). Peroxide- and ozone-based chemistries inherently consume more than the 0.1 nm of silicon per clean as defined in the International Technology Roadmap for Semiconductors ITRS 2.0.

In recent years, some new wet-chemical cleaning processes were created. These combine several of the discrete cleaning steps described above. Referring to their

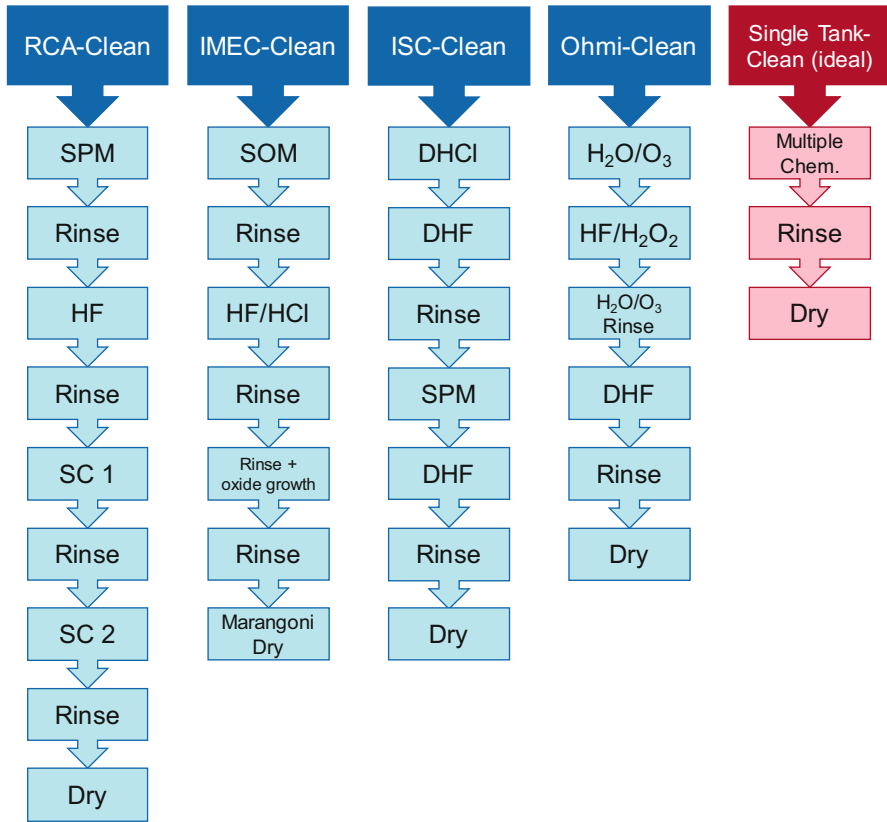


**Fig. 16** Cleaning sequences for silicon wafers used in microelectronic and photovoltaic industries (Buchholz 2015; Kern and Puotinen 1970; Meuris et al. 1999; Ohmi 1996). See Table 7 for abbreviations

potential input in relevant cleaning procedures in current production lines of high-efficiency solar cells, two alternative cleaning systems are especially interesting: Ohmi clean and IMEC clean. An insight in cleaning processes of silicon PV manufacturing gives the cleaning process at ISC Konstanz e.V. There, silicon wafers for PV application were sufficiently cleaned without an alkaline process step (Buchholz 2015). The process chain is inspired by the IMEC clean but varies in process order and process step details, as shown in Fig. 16.

Researchers at IMEC in Leuven (Belgium) have performed outstanding contributions in progress for developing cleaning technologies to removing metal ions and particles as well as to preparing oxide layers (Reinhardt and Kern 2008). The IMEC core concept is based on a two-step cleaning approach (Meuris et al. 1999). The first step consists of a 5 min SOM (sulfuric acid-ozone mixture) treatment at 90 °C followed by a quick dump rinse with hot and cold DI water to remove organic and metal contaminants. The second step consists of a



compatible with almost all standard PV processing sequences and chemicals (Reinhardt and Kern 2008).

Choline (trimethyl-2-hydroxyethyl ammonium hydroxide,  $[(\text{H}_3\text{C})_3\text{-NCH}_2\text{-CH}_2\text{OH}]\text{OH}$ ), as well as tetramethylammonium hydroxide ( $(\text{H}_3\text{C})_4\text{NOH}$ ), can be used beneficially instead of ammonia solution ( $\text{NH}_3(\text{aq})$ ) in SC-1 (Reinhardt and Kern 2008). In order to increase the wettability of the wafer surface, surfactants are frequently added. Surfactants also aid in the removal of fine particles, can prevent micro-roughness generation of silicon during etching, and improve the overall cleaning efficiency (Reinhardt and Kern 2008). Applied surfactants (anionic, cationic, and nonionic) modify the zeta potential and have to be stable in the respective cleaning solution. Their impact in both alkaline and acidic media including SC-1, SC-2, dHF, dHF- $\text{H}_2\text{O}_2$ , or dHF- $\text{O}_3$  enables minimizing of particle deposition. Driven by cost and environmental aspects the trend goes to biodegradable surfactants.

## Etching

Wet-chemical etching steps are an integral part in handling silicon for PV production. As already shown in section [Chemical Properties of Silicon Surfaces](#), there are two general pathways to dissolve/etch silicon in aqueous media: treatment in acidic hydrofluoric acid containing mixtures with oxidizing agents (section [Chemical Aspects of Acidic Etching](#)) or in alkaline mixtures containing strong bases MOH ( $\text{M} = \text{K}, \text{Na}, \text{N}(\text{CH}_3)_4$ ) (section [Chemical Aspects of Alkaline Etching](#)). The main applications of etching silicon wafer material are the removal of saw damage and the texturization to increase the absorption of light in the silicon solar cell (Fig. 18).

## Chemical Aspects of Acidic Etching

Acidic etching of silicon is attractive for PV applications because of the wide adjustable reactivity range as well as to generate different morphologies on silicon surfaces.

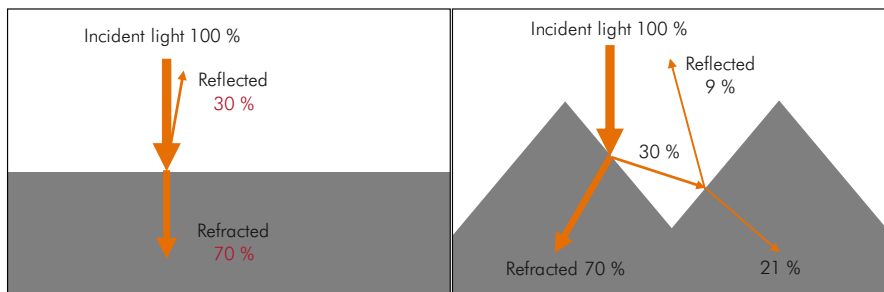
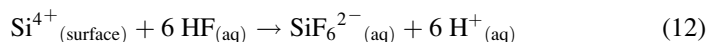
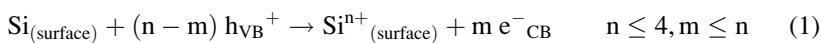


**Fig. 18** Light absorption on a planar (*left*) and a textured surface (*right*)



Generally, acidic etching mixtures give rise to isotropic removal – the etching rates toward the different silicon crystal planes are of a comparable magnitude.

Thermodynamic considerations give evidence that silicon should be easily oxidized and dissolved in aqueous acidic media (section [Chemical Properties of Silicon Surfaces](#), Eq. 1). However, the thin oxide layers are very poorly soluble at pH levels < 12. Acidic etching mixtures need fluoride ions as silicon complexing agent to dissolve the oxidized silicon atoms (Eq. 12, see also Eq. 2) (Kolasinski 2009).



As shown in Table 3 the Si-F bond is very stable, i.e., the driving force of the chemical reaction between an oxidized silicon atom and the fluoride ion is high. But, despite the pronounced fluorophilicity of silicon in aqueous hydrofluoric acid solutions, its rate of dissolution is below  $0.001 \text{ nm s}^{-1}$  depending on the silicon substrate type and the etching time (Willeke and Kellermann 1996). Suitable oxidizing agents added to hydrofluoric acid containing solutions give rise to significantly increased dissolution rates. Electrochemical measurements have shown that adequate oxidizing agents need a redox potential higher than +0.7 V to oxidize silicon surface atoms or to inject electron holes into the silicon valence band (Kolasinski 2010), e.g.,  $\text{HNO}_3$  (Robbins and Schwartz 1959),  $\text{H}_2\text{O}_2$  (Gondek et al. 2014),  $\text{O}_3$  (Gondek et al. 2016),  $\text{IO}_3^-$ ,  $\text{Fe}^{3+}$ ,  $\text{Ce}^{4+}$ ,  $\text{VO}_2^+$ , (Kolasinski 2010), or  $\text{NO}^+$  and  $\text{NO}_2^+$  in highly acidic media (Lippold et al. 2014; Patzig-Klein et al. 2010). As verified by cyclic voltammetry measurements of silicon oxidation in the aqueous hydrofluoric acid solutions electrochemical anodic dissolution of silicon gives rise to the formation of porous silicon in the interval +0.3 V to +0.7 V. Above +0.7 V commonly polishing etching takes place (Lehmann 2002). Electroless etching in such solutions involves electrochemical as well as chemical steps (see also Fig. 4). The respective overall process of silicon dissolution may be dominated by one of the two process types significantly depending on the oxidizing agent used and the etch bath composition. Figure 19 shows the proposed mechanism of dissolution of silicon in HF-containing mixtures.

### Aqueous HF-HNO<sub>3</sub> Mixtures

The most applied acidic silicon etching systems are HF-HNO<sub>3</sub>-based mixtures. A lot of required conditions for realizing controllable reactivities and generated surface morphologies have been identified so far.

The process can be described by a sequence of electrochemical steps including local anodic and cathodic areas on the silicon surface (Turner 1960). The reduction of HNO<sub>3</sub> occurs at cathodic sites generating (electron) holes in the silicon valence band ( $h_{\text{VB}}^+$ , e.g. Eq. 13), which are able to oxidize neighbored silicon surface atoms (anodic sites). These can be dissolved as  $\text{SiF}_6^{2-}$  (Eq. 14), thereby electrons from the conduction band ( $e_{\text{CB}}^-$ ) can be partly consumed by protons generating hydrogen (Eq. 15) (Kooij et al. 1999). In the case of strong oxidizing mixtures containing a

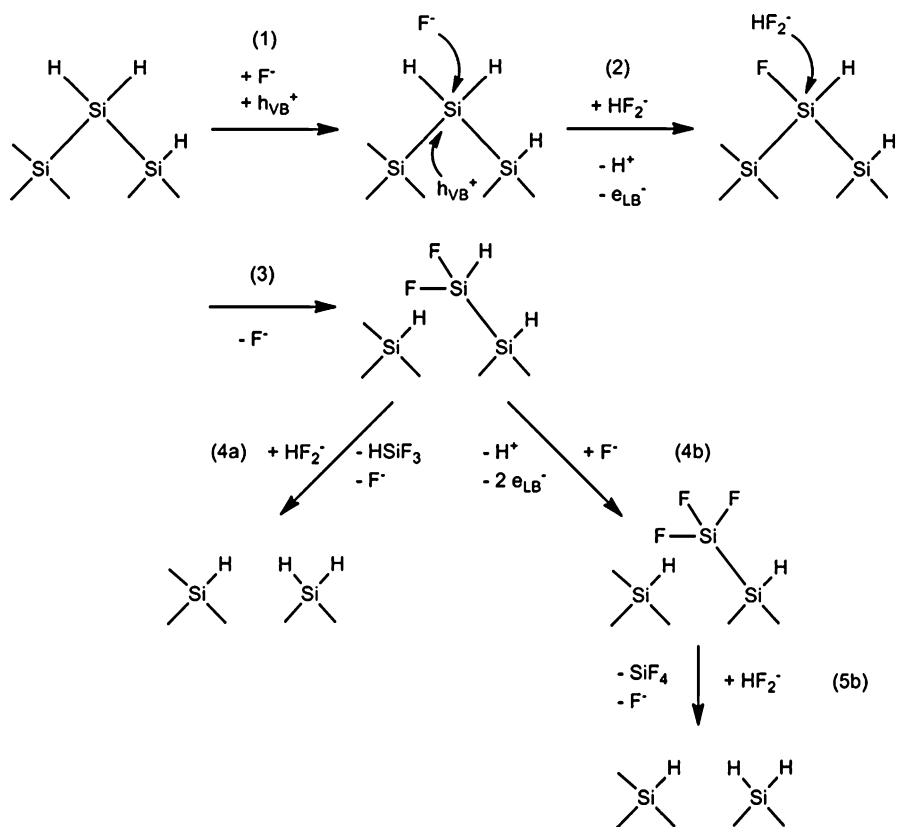
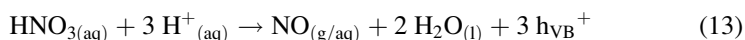


**Fig. 19** Proposed mechanism of electrochemical silicon etching in fluoride-containing solutions as postulated by Kolasinski (2009)

high concentration of  $HNO_3$ , an alternative chemical oxidation of the silicon surface atoms can also occur, giving rise to a quick dissolution of the directly oxidized silicon atoms. Any intermediate silicon oxide layers postulated in the past are not detectable. The resulting silicon surface is terminated by  $Si(H)_x$  bonds (Steinert et al. 2006; Zanoni et al. 1999).



(Kolasinski 2009; Acker et al. 2012)



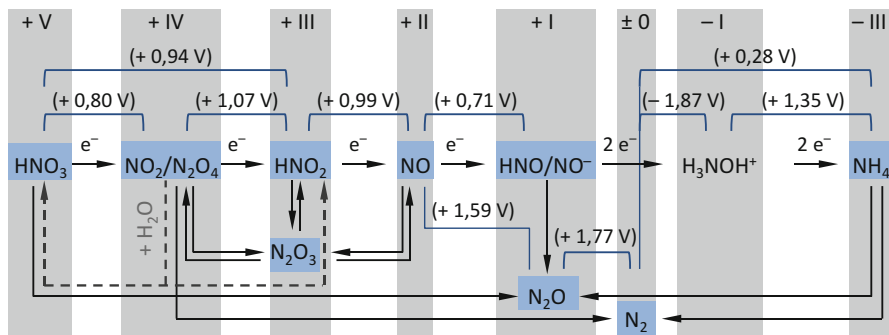


**Fig. 20** Stepwise reduction pathways and redox potentials of N-species in aqueous HF-HNO<sub>3</sub> mixtures during oxidation of silicon; N-species detected in etching solutions are blue framed; NH<sub>4</sub><sup>+</sup> is stable only at low temperatures (<8 °C) in these mixtures

As demonstrated in Fig. 20, besides HNO<sub>3</sub> further N-species like NO<sub>2</sub><sup>-</sup> and NO<sub>x</sub> participate in the stepwise oxidation of silicon. Furthermore, this scheme qualitatively gives insights into the reaction products of subsequent steps of NO<sub>3</sub><sup>-</sup>-reduction observed in practice. Intermediate products formed by the chemical reduction of the nitric acid act as promoters/catalysts, e.g., NO<sub>2</sub><sup>-</sup>. This was proven by the addition of NaNO<sub>2</sub> to aqueous HF-HNO<sub>3</sub> solutions resulting in enhanced chemical reactivity and shortened induction periods (Robbins and Schwartz 1959). Induction periods are characteristic in the case of applying diluted HF-HNO<sub>3</sub> mixtures. This indicates that HNO<sub>3</sub> as well as NO<sub>3</sub><sup>-</sup> are not the dominant oxidizing species in HF-HNO<sub>3</sub> mixtures. Adsorbed NO<sub>2</sub> (Robbins and Schwartz 1960) and different N (III)-species (NO<sub>2</sub><sup>-</sup>, NO<sup>+</sup>, N<sub>2</sub>O<sub>3</sub>, N<sub>4</sub>O<sub>6</sub><sup>2+</sup> (Kelly et al. 1994; Steinert et al. 2006, 2007)) accelerate the silicon oxidation. Recent literature highlights the importance of N(III)-species during the oxidation of silicon.

The occurrence of the respective redox steps depends significantly on the respective concentration ratio in the applied HF-HNO<sub>3</sub>-H<sub>2</sub>O mixtures. In concentrated HF-HNO<sub>3</sub> mixtures containing HNO<sub>3</sub> concentrations below 3.8 mol L<sup>-1</sup> ( $c(\text{HF}) > 16.6 \text{ mol L}^{-1}$ ), the generation of holes ( $h_{\text{VB}}^+$ ) determines the rate of silicon dissolution. In the case of an HNO<sub>3</sub> concentration higher than 3.8 mol L<sup>-1</sup> ( $c(\text{HF}) < 16.6 \text{ mol L}^{-1}$ ), the diffusion of complexing fluoride species (HF<sub>2</sub><sup>-</sup>, HF, F<sup>-</sup>) to the silicon surface is the rate limiting step. Depending on the HNO<sub>3</sub> concentration and the bath temperature, different amounts of reaction products are formed, displayed in Fig. 21 for concentrated HF-HNO<sub>3</sub> mixtures.

As mentioned above molecular hydrogen (H<sub>2</sub>) can also be generated during silicon dissolution, besides above mentioned N-species. The percentage of formed H<sub>2</sub> correlates with the HF:HNO<sub>3</sub> ratio: it increases with higher HF concentration in the mixture (Fig. 21) because of decreasing fractions of alternative oxidizing agents (Acker et al. 2012; Hoffmann et al. 2011).

The different chemical reactivities of HF-HNO<sub>3</sub> mixtures toward silicon depending on their concentration enables the control of resulting silicon surface

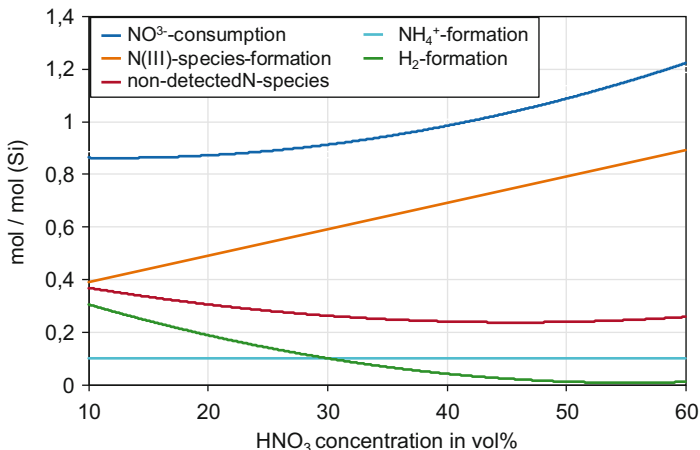
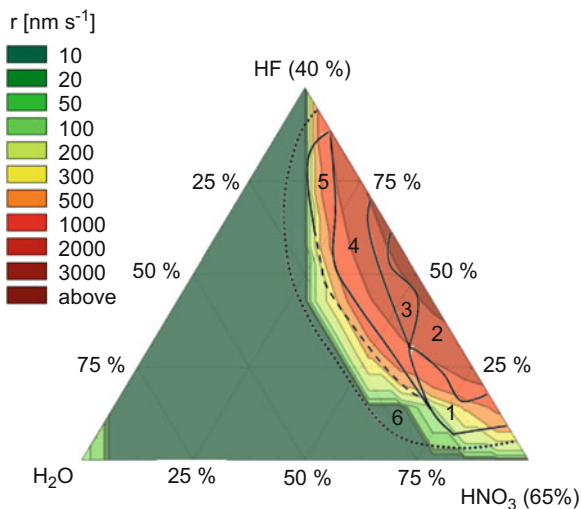


**Fig. 21** Stoichiometric HNO<sub>3</sub> consumption, N(III)-, NH<sub>4</sub><sup>+</sup>-, and H<sub>2</sub>-formation during etching silicon in concentrated aqueous HF-HNO<sub>3</sub> mixtures with different HF:HNO<sub>3</sub> ratios

**Fig. 22** Reactivity studies of HF-HNO<sub>3</sub>-H<sub>2</sub>O solutions and generated silicon surface morphologies, SEM images see Fig. 23



morphologies. First systematic reactivity studies on n-type silicon performed by Robbins and Schwartz indicate reactivity profiles with etching rates up to 27,500 nm s<sup>-1</sup> for concentrated HF-HNO<sub>3</sub> mixtures (65% HF (49%) : 35% HNO<sub>3</sub> (69%), c(HF) = 18.4 mol L<sup>-1</sup>, c(HNO<sub>3</sub>) = 5.4 mol L<sup>-1</sup>). Etching rate measurements on p-type silicon material provide comparable results (Fig. 22) (Röver et al. 2004). Relating to the dissolution of silicon, as shown above, the reactivity pattern is also characterized by two distinctly different areas in the HF/HNO<sub>3</sub>/H<sub>2</sub>O ternary diagram in Fig. 22. In the case of high HNO<sub>3</sub> concentrations, the process rate is limited by the

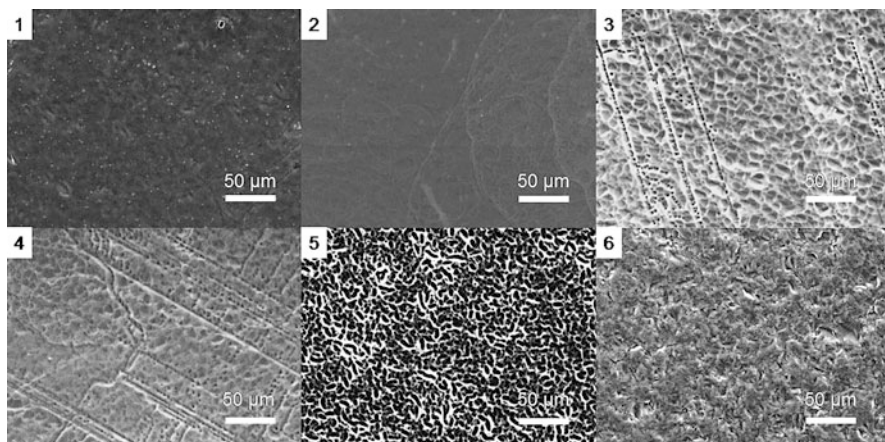


**Fig. 23** SEM images of generated silicon surface morphologies. Numbers refer to the ones in Figs. 22 and 24

HF concentration, but at high HF concentrations, the concentration of  $\text{HNO}_3$  is rate limiting. Diluting the mixtures with water gives rise to a significant reactivity decrease by orders of magnitude (Fig. 22). Isotropic silicon etching was found for all aqueous HF- $\text{HNO}_3$  mixtures, which means there are no prominent differences between the dissolution rates of the silicon atoms in the (100), (110), and (111) surface orientations.

Etching rate measurements as a function of the temperature yielded low apparent activation energies around  $16 \text{ kJ mol}^{-1}$  in the case of  $\text{HNO}_3$ -rich mixtures, but activation energy values above  $42 \text{ kJ mol}^{-1}$  were reported for HF-rich mixtures. In  $\text{HNO}_3$ -rich mixtures, the dissolution process of silicon is limited by some diffusion steps, most likely by diffusion of HF or  $\text{HF}_2^-$  species to the silicon surface. On the other hand, in HF-rich mixtures, the oxidation of silicon surface atoms and the injection of holes, respectively, are rate-determining for the overall process (Schwartz and Robbins 1961).

The distinctly different kinds of rate-controlling steps give rise to a diversity of generated surface morphologies/etch figures in accordance with the reactivity pattern of the mixture (Fig. 22). Diffusion-controlled silicon dissolution in  $\text{HNO}_3$ -rich mixtures leads to surface polishing. The lower redox potential in HF-rich mixtures favors the formation of etching pits enabling texturization of silicon surfaces. Surface defects act as a source for enhanced etching reactions resulting in circular pits (Röver et al. 2004; Schwartz and Robbins 1976). There are various in-between state structures, in diluted mixtures as well as in mixtures with very low portions of  $\text{HNO}_3$ , and a high percentage of HF leading to the formation of porous layers – also called stain etching (Vázsonyi et al. 2001).

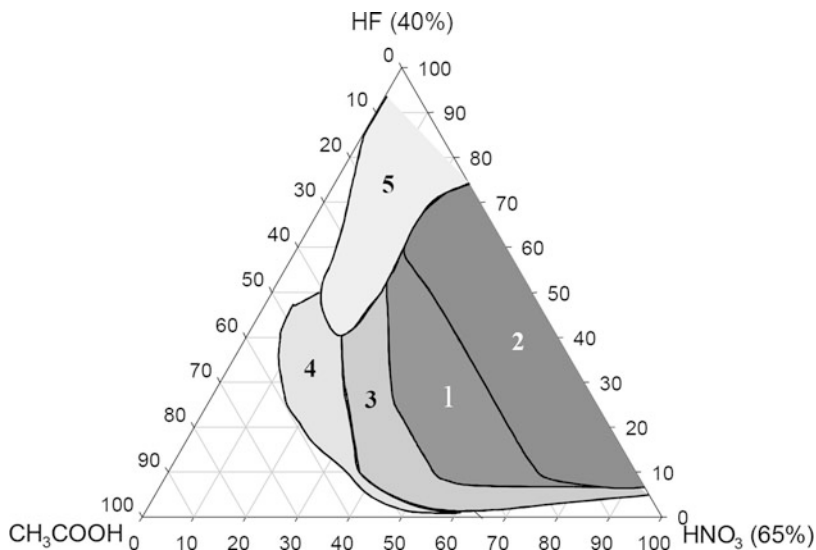


**Fig. 24** Generated surface morphologies of HF-HNO<sub>3</sub>-CH<sub>3</sub>COOH mixtures at 25 °C; see SEM images in Fig. 23

### The Development of Acidic Etching Mixtures

NaNO<sub>2</sub> additives are sometimes used for bath activation at the beginning of the etching procedure (Robbins and Schwartz 1959). In order to control and adjust the reactivity and the resulting surface texture, different percentages of acetic acid (CH<sub>3</sub>COOH) (Robbins and Schwartz 1960), sulfuric acid (H<sub>2</sub>SO<sub>4</sub>) (Lippold et al. 2011), and phosphoric acid (H<sub>3</sub>PO<sub>4</sub>) (Nishimoto et al. 1999) can be added. Dilution of the etching mixture with these acids instead of water results in higher reactivity in comparison with HF-HNO<sub>3</sub>-H<sub>2</sub>O mixtures (Fig. 24).

Such effects are due to the higher redox potentials in these mixtures and thus lead to enhanced silicon oxidation. The impact of sulfuric acid furthermore enables the creation of new surface structures exhibiting lower light reflection (Fig. 25) (Lippold et al. 2014).

Current investigations to replace HNO<sub>3</sub> – because of waste management aspects – lead to aqueous HF-HCl-based and chlorine containing mixtures for silicon etching. These solutions surprisingly exhibit anisotropic silicon dissolution and surface polishing depending on the concentration areas. Using stirred HF-HCl-H<sub>2</sub>O<sub>2</sub> or HF-HCl-Cl<sub>2</sub> mixtures for the treatment of monocrystalline silicon wafers, random inverted pyramidal structures are generated without masking or lithographic processes (Stapf et al. 2016, 2017). Silicon etching rates of up to 0.8 μm min<sup>-1</sup> for monocrystalline, diamond wire-sawn wafers are reached at room temperature. SEM pictures show pyramid edge widths between 2 and 20 μm (Fig. 26). An additional nano-texture is observed on the surface of the inverted pyramids microstructure.

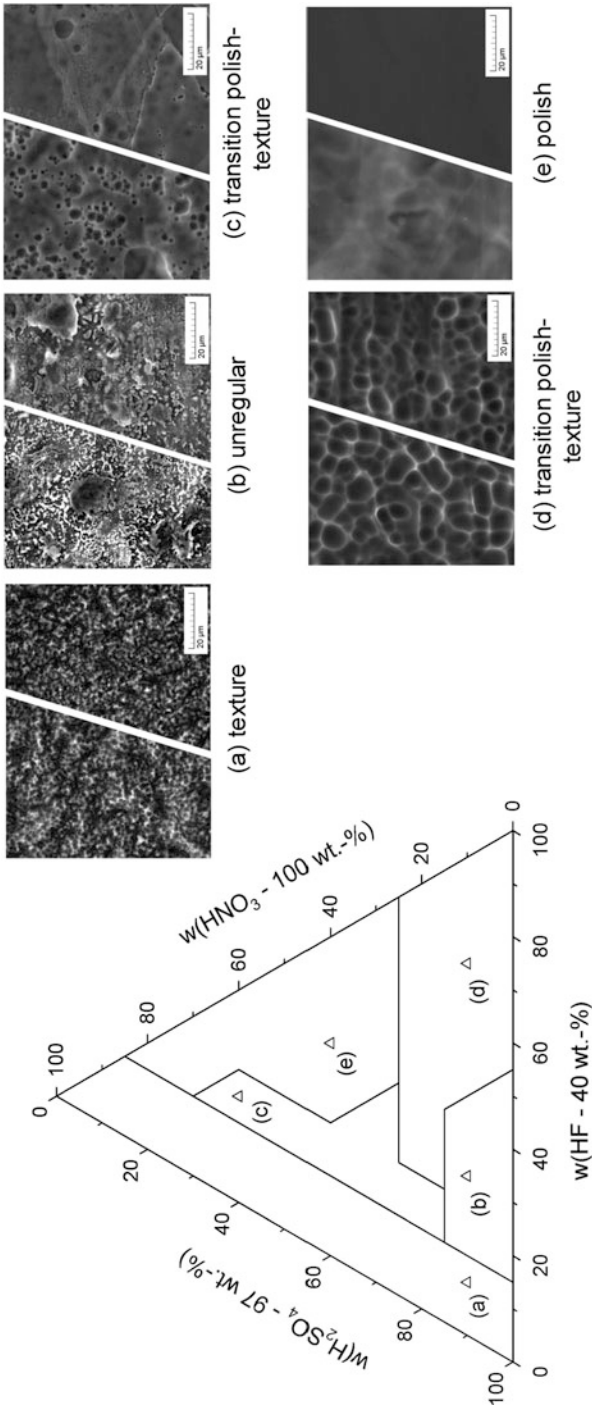


**Fig. 25** Reactivities toward p-type multicrystalline silicon surfaces (*left*, (Lippold et al. 2011)) and generated surface morphologies (*right* (SEM images) (Lippold 2014))



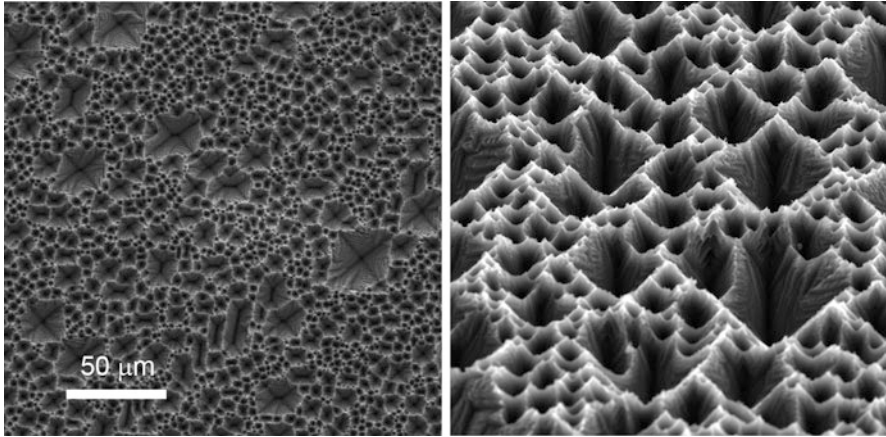
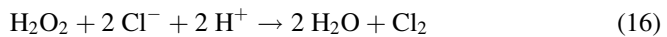


**Fig. 26** SEM pictures of the random inverted structure generated on (100) silicon surface by HF-HCl-Cl<sub>2</sub> treatment

Cl<sub>2</sub> is a strongly oxidizing agent ( $E^0 = 1.36$  V), (Holleman et al. 2007), which is dissolved during bubbling or formed by the oxidation of chloride ions by H<sub>2</sub>O<sub>2</sub> (Eq. 17). Chlorine reforms chloride ions upon oxidation of silicon surface atoms according to Eq. 18. The hydrofluoric acid causes the coordination and dissolution of the oxidized silicon species via Eq. 19. However, not every strong oxidizing agent leads to sufficiently fast silicon etching as shown, e.g., for hydrogen peroxide and ozone based mixtures (Gondek et al. 2014; Gondek et al. 2016).



### Texturization of Multicrystalline Wafers

As shown in section [Etching Rate](#), acidic etching is principally an isotropic process. The etch rate does not depend on the crystal lattice plane orientation. Therefore, HF-HNO<sub>3</sub>-H<sub>2</sub>O-mixtures are normally used for saw damage removal and can also be applied for texturing of multicrystalline silicon wafers. For the acidic texturing process, generally, inline equipment is used. The wafers are moved horizontally on rolls through tanks, with an etching time of around 2 minutes per wafer. The solar cell efficiency depends strongly on the etching depth of the acidic texture. If the etching depth is too low, crystal defects remain and the open-circuit voltage, as well as the short-circuit current, are reduced. If the etching depth is too large, the surface roughness and therefore the surface recombination of the charge carriers ( $e^-/h^+$ )



increases. Depending on the saw type, diamond wire, or SiC-slurry, the saw damage has a different depth, around 5  $\mu\text{m}$  or 10  $\mu\text{m}$ , respectively (► Chap. 11, “Wafer Processing”). Therefore, the etching depth also depends on the wafer material used, as the saw damage should be removed completely.

### Impact of Saw Damage (SiC-Slurry Versus DW)

The different wafer-sawing processes, diamond wire sawing and SiC-slurry sawing, cause an as-cut surface morphology that strongly influences etching processes (Meinel et al. 2014). This saw damage controls the sites where chemical attack preferentially occurs. Furthermore, it controls the morphology of the etched surface and the rate at which this morphology is formed (Fig. 27). The diamond wire-sawn wafers feature a surface with a superficial damage layer. Their etching leads to an easy flattening of the existing rifts and cracks. Only a small surface enlargement and a fast increase of the reflection values with rising thickness loss of the wafers occur. In contradiction, the SiC-slurry-sawn wafers feature a more distinct damage layer on the surface and micro-cracks in the subsurface region. The exposure of such cracks is achieved in short etch times, leading to a remarkable surface enlargement and low reflection values. The existence of such distinct subsurface damage is beneficial to the reflection properties of the etched slurry-sawn wafers. The specific features of the surface damage introduced

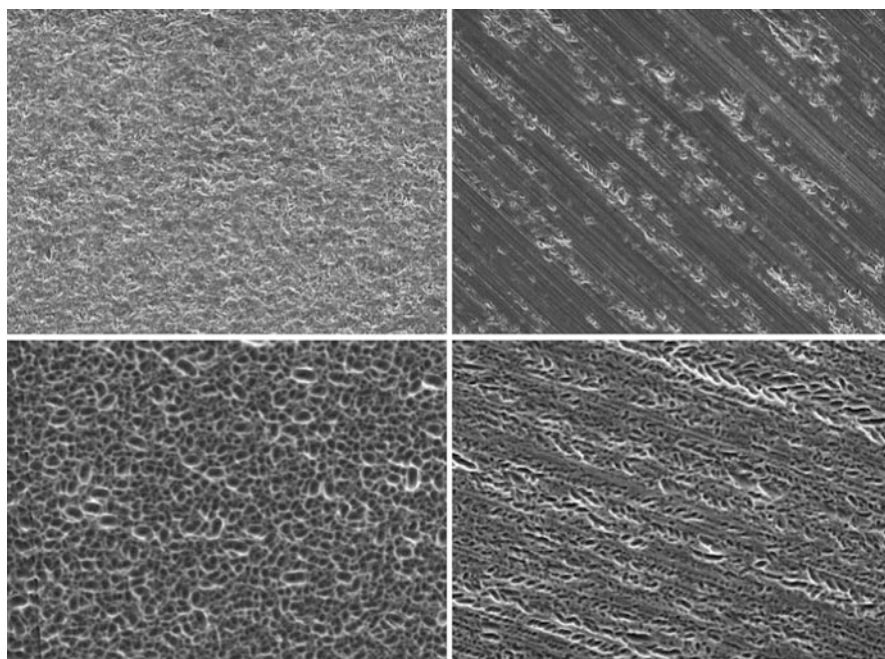


**Fig. 27** SEM images of SiC-slurry (*left*) and diamond wire-sawn (*right*) multicrystalline silicon wafer surfaces before (*top*) and after etching (*bottom*) in HF-HNO<sub>3</sub> etching mixtures

initially by the wafer-sawing process cannot be changed in the etching process. Variations of the acidic mixture do not influence the texturization process of the DW wafers at all. Further adjustments to the DW-sawing process as well as to the texturing mixtures are necessary to create homogeneously texturized DW-sawn wafers of low reflectivity. Additional development of acidic mixtures with new etchants (change of acidic-mixture composition or introducing additives) and different etch conditions (change of the etch regime, temperature, or etch time) are reasonable.

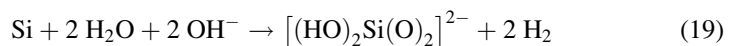
## Chemical Aspects of Alkaline Etching

The fundamental chemical reactions describing alkaline etching and dissolution of silica and silicon have been already presented in section [Dissolution of Silicon](#). The overall process of silicon dissolution in aqueous alkaline mixtures is strongly exothermic with a reaction enthalpy of about 340 kJ/mol. Hydrogen and silica are formed as described by Eq. 3. Silica itself is also dissolved giving rise to various silicate ions depending on the pH (Eqs. 6, 7 and 8). The thermodynamic driving force indicated by the standard redox potential  $E_o$  is significantly higher at pH 14 than in acidic solutions at pH 0 with values of  $-1.697$  V and  $-1.24$  V, respectively (Eqs. 9 and 10).

Generally, only monocrystalline silicon wafers are treated with alkaline etching solutions in order to utilize the observed anisotropic silicon dissolution in the adjusted concentration areas (see also section [“Isotropic and Anisotropic Behavior”](#)). The substrates crystal lattice has to be oriented in (100) direction, because only on such a surface type pyramidal textures – with preferred reflectivity features – can be achieved. All other orientations such as (110) or (111) have no application in industrial solar cell processing. Multicrystalline wafers are also not textured with alkaline mixtures for the same reason.

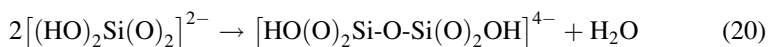
Alkaline etching in PV processing is currently used for saw damage removal and texturing. Depending on the sawing type, the thickness of the silicon layer which should be removed is different. For diamond wire sawing surface damage is about 5 micrometers deep, while for SiC slurry sawing damages like micro-cracks and dislocations are up to 10 micrometers deep (Möller 2004) (► [Chap. 11, “Wafer Processing”](#)). The etching parameters such as concentrations of components in the etching mixture, temperature, and etching time determine the quality of the texture. Experiments and simulations comparing different textures indicated that randomized upright pyramids with an average edge length of 6 micrometers are best for an optimized solar cell performance.

A simplified chemical equation which describes the overall silicon dissolution reaction can be written as follows:



For each mole of dissolved silicon two moles of hydrogen are formed. The oxidation state of the silicon atoms changes from zero to plus four. The oxidizing species are the hydrogen atoms exhibiting a positive partial charge in the H-O-bonds in H<sub>2</sub>O-molecules and OH<sup>-</sup>-ions.

Due to the relatively high pH of the alkaline etching solution, it is correct to state that twofold deprotonated silicic acid [(HO)<sub>2</sub>Si(O)<sub>2</sub>]<sup>2-</sup> is formed. However, depending on the concentration of the silicate ions various reactions between these species can follow. Upon condensation between the monomeric silicate ions [(HO)<sub>4-n</sub>Si(O)<sub>n</sub>]<sup>n-</sup> dimers, trimers, and larger oligomers are generated, which consist of corner-sharing SiO<sub>4</sub>-tetrahedra:

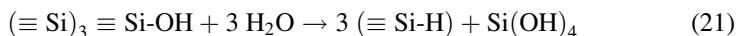


In many publications, all these silicate species are summarized as SiO<sub>3</sub><sup>2-</sup> or even SiO<sub>2</sub> ignoring the OH groups and the specific charge of the anions (see, e.g., Eqs. 3, 4, 5, 6, 7, 8 and 9). Depending on their concentration and other parameters (pH, temperature, stirring, additives) mixtures of larger macromolecular species can be formed and the solubility limit exceeded. This can cause the formation of white silica and/or silicate precipitates, which are deposited on the wafer surface or as particles in the solution.

Equation 20 does not provide significant information about the pathway of the reaction, i.e., the reaction mechanism(s) with the most important reaction steps and the rate determining reaction barrier. Besides, the nature and bonding situation of the involved Si atoms at the surface is not considered by Eq. 20. It is well known that all silicon surfaces – no matter which crystal orientation is present – are terminated with Si-H moieties during and after the etching process. None or only very few Si-OH and/or Si-O-Si groups have been detected on the wafer surfaces.

A chemical surface reaction model which explains this observation is depicted in Fig. 28. Both water molecules as well as OH<sup>-</sup>-ions are involved in oxidizing and attacking of surface silicon atoms.

It has been shown by isotopic studies using deuterated water and hydroxides in anisotropic etching of Si(100) as well as in other kinetic studies that the cleavage of the Si-H bonds represents the rate determining step (Baum and Schiffrin 1998). All other reaction steps including the attack of the Si-Si back bonds and the complete coordination of the surface silicon atoms with four oxygen atoms (or OH groups) are faster. Thus, when the surface Si-H group is replaced by a Si-OH unit a sequence of several fast chemical reaction steps follows leading to the overall result as summarized in Eq. 21. This explains the observed Si-H termination.



Several groups have investigated the concentration and temperature dependence of etch rates for alkaline silicon etching solutions. These studies are on the one hand generally useful for the understanding of reaction mechanisms. On the other hand,

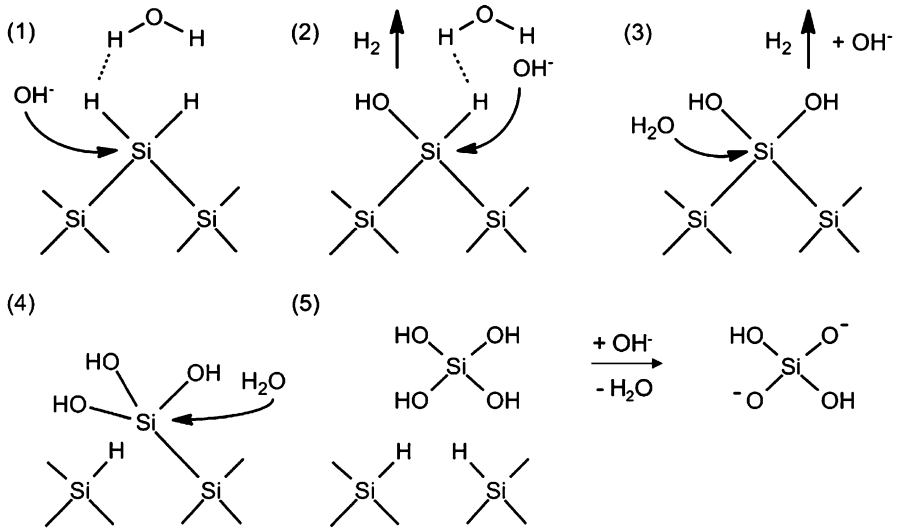


**Fig. 28** Reaction scheme proposed for the chemical dissolution of (100) silicon surfaces in alkaline solutions, adapted from Lehmann (2002)

they are important for the processing times required for alkaline etching steps in the industry. Especially for saw damage etching high etch rates are required and therefore relatively concentrated KOH or NaOH solutions are used. In general, Arrhenius behavior is observed and the following rate law (Eq. 22) and kinetic parameters have been derived (Gosálvez et al. 2010; Seidel et al. 1990):

$$r = k[\text{H}_2\text{O}]^4[\text{OH}^-]^{1/4} = k[\text{H}_2\text{O}]^4[\text{MOH}]^{1/4} = k_0 \left( \frac{E_a}{k_B T} \right) [\text{H}_2\text{O}]^4 [\text{MOH}]^{1/4} \quad (22)$$

(with  $r$  = reaction rate,  $k$  = rate constant,  $M = \text{Na}$  or  $\text{K}$ ,  $k_0$  = rate constant under standard conditions,  $E_a$  = activation energy,  $k_B$  = Boltzmann number =  $8.617 \cdot 10^{-5}$  eV/K,  $T$  = absolute temperature)

Thus, for a given surface orientation and a fixed  $\text{OH}^-$  concentration, experimental data for different temperatures can be plotted linearly with  $\log r$  as a function of  $1/T$  according to Eq. 23:

$$\log r = \log k'_0 - E_a/k_B T \quad (23)$$

This allows the determination of the corresponding apparent activation energy  $E_a$  and an apparent rate constant  $k'_0$  assuming constant concentrations of water and  $\text{OH}^-$  ( $k' = k_0[\text{H}_2\text{O}]^4[\text{MOH}]^{1/4}$ ). From these values or from the linear Arrhenius plot the reaction rate can be calculated. This has been done usually at temperatures in a range from 20 °C to 90 °C. Experimental data correspond quite well with this linear behavior, especially if relatively concentrated solutions are considered.

For the (100) orientation as the most relevant silicon surface for PV processing the following data are found:  $k_0 = 2480 \text{ } \mu\text{m/h}(\text{mol/l})^{-4.25}$ , and  $E_a = 0.595 \text{ eV}$  (57.41 kJ/mol) (Gosálvez et al. 2010). Many further data on tabulated etch rates can be found in the tables (Hull 1999) as already mentioned above (section [Isotropic and Anisotropic Behavior](#)). Activation energies of  $\sim 0.6 \text{ eV}$  (57.6 kJ/mol) indicate a reaction controlled mode for the alkaline etching process (section [Dissolution of Silicon](#)). This corresponds to the formation of texture and the typical anisotropy, although polishing etch regimes, which are most likely induced by diffusion-control, are also encountered (see below).

The concentration dependence of reaction rates in alkaline etching as described by Eq. 22 is remarkable. The equation shows a very strong influence of the concentration of water, as it is represented in this equation to the power of four. Much less influence has the concentration of the  $\text{OH}^-$ -ions, which of course correlates with the pH value of the solution. A detailed model for the reaction mechanism that explains the rate law expressed by Eq. 23, the Si-H terminated silicon surface, and the anisotropy in the case of more diluted solutions is not known (section [Isotropic and Anisotropic Behavior](#) and below). Besides, the etch process may not only be explained as a local molecular mechanism at a certain surface site but by an electrochemical model. The fact that for alkaline etching it is known that high p-doping levels with boron atom concentrations of  $10^{19}\text{--}10^{20} \text{ cm}^{-3}$  result in a so-called etch stop with strongly decreased etch rates supports the electrochemical description since this observation can only be explained by conduction and valence band bending and changes in the surface space-charge region.

Neglecting the change of water content with increasing  $\text{OH}^-$ -ion concentration one would expect a slow but continuous increase of etch rates with increasing pH ( $r \sim [\text{MOH}]^{1/4}$ ). However, in most cases, maximum etch rate occurs between 20 and 40 wt% of MOH in the solution, with significantly lower etch rates below 20 and above 40 wt% (Fig. 29). This is due to an overall decreasing water content, not only caused by the replacement of water molecules by MOH but also by the fact that the dissolved anions and cations are solvated, making the water molecules less available for the attack of the silicon surface.

### Aqueous KOH-IPA Mixtures

Due to their cost, potassium and sodium hydroxide are the most commonly used bases for alkaline etching and texturization of monocrystalline silicon wafers. The solutions are typically modified with different additives, especially surfactants and alcohols in order to improve the etching results. The most frequently used and therefore the most thoroughly investigated additive is isopropyl alcohol (IPA). IPA as well as many other hydroxyl compounds are surface- and tensioactive compounds, causing a decrease of surface tension for both the solid-liquid and the vapor-solid interfaces. Therefore, IPA and related compounds improve the wettability of silicon surfaces. Both, hydrophilic and hydrophobic areas are easily bedewed. In addition, diffusion of reactants and products into as well as away from the interface layer should be enhanced, most likely due to a reduction of the thickness of the Nernst's diffusion layer, which is known to have

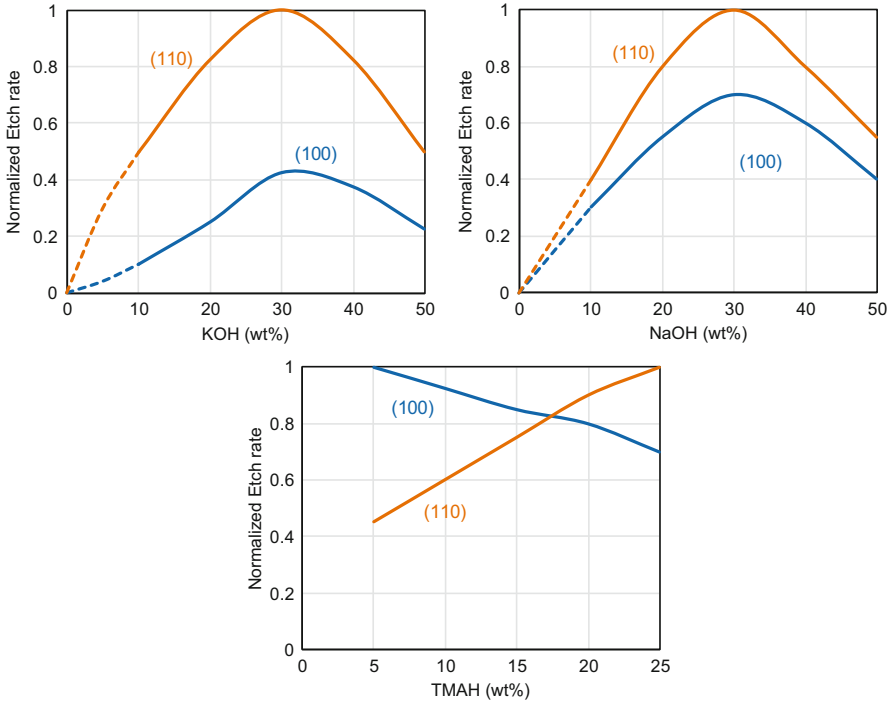


**Fig. 29** Normalized etch rates of (100) and (110) silicon crystal orientation depending on the MOH concentration, adapted from Gosálvez et al. (2010), normalized to highest etch rate observed

a thickness of up to 1  $\mu\text{m}$ . Besides, the morphology of the surfaces is usually improved upon IPA addition. The latter effect has been attributed to a preferred adsorption (and in turn blocking) of OH-terminated surface silicon atoms located at step monomer sites (Gosálvez et al. 2010). Besides, the surface activity of IPA reduced the lifetime and size of the  $\text{H}_2$  bubbles, which also results in improved surface morphologies.

Generally, IPA addition reduces the overall etch rate, especially for high KOH concentrations. For (100) surfaces the roughness, i.e., the tendency to form homogeneously distributed pyramids, is improved (Fig. 30). This effect is especially pronounced at IPA concentrations significantly below 10%, e.g., at 2–4%.

### Alternative Additives

When using KOH-IPA mixtures, IPA has to be redosed frequently in a high amount because it easily evaporates during the process. IPA is highly flammable, toxic to human beings upon longer exposure, and its waste, as well as the exhausted vapor, requires special treatments. Therefore, alternative additives are investigated. The currently most promising additives are polysaccharides such as

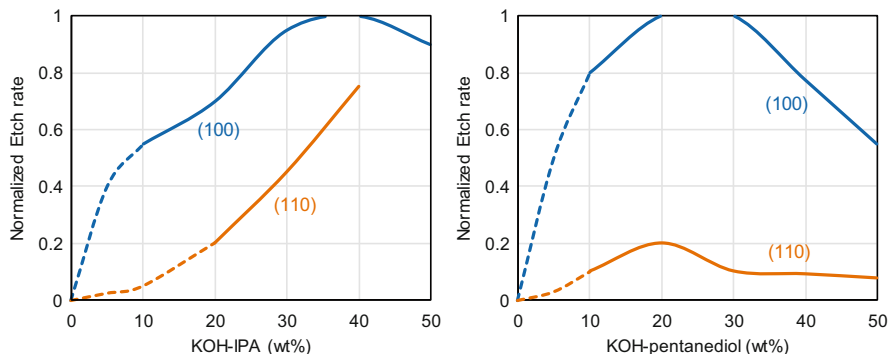


**Fig. 30** Normalized etch rates of (100) and (110) crystal orientation depending on the KOH concentration saturated with various additives, adapted from Gosálvez et al. (2010), normalized to highest etch rate observed

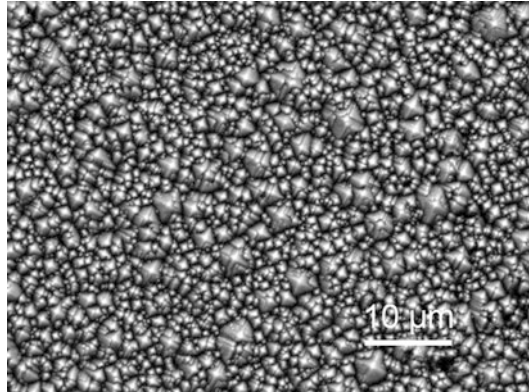
starch, pectin, dextrin (and derivatives thereof), as well as diols, triols, and polyalcohols such as glycols or polyvinyl alcohol (PVA). These additives have a higher boiling point than IPA and therefore do not evaporate at process temperatures of 80 °C. Many of them generate the same texture quality during the etching processes compared to IPA containing mixtures, but sometimes at lower temperatures or during shorter etching times. However, for simple monoalcohols such as propanols, butanols, or pentanols it was found that longer and bulkier organic substituents reduce the etch rates, with the strongest effect reported for tert-butanol (Gosálvez et al. 2010; Zubeł and Kramkowska 2002). Besides, the larger the organic part of the additive, the larger the reduction of surface tension and the lower the solubility in the aqueous alkaline solutions. Further disadvantages of these alternative additives can include higher costs and additional cleaning steps required to remove the low-volatile and strongly adsorbed hydroxyl compounds from the silicon surface.

### Texturization of Monocrystalline Wafers

A solution of NaOH or KOH and IPA in water is generally used for alkaline saw damage removal and texturization on monocrystalline silicon wafers. As shown above and in section [Isotropic and Anisotropic Behavior](#), alkaline etching has different etch rates for different crystal lattice plane orientations of the silicon atoms. This anisotropy results in a pyramidal structure on the wafer surface for monocrystalline silicon wafers with a (100) surface orientation. Applying this texture, the light absorption of the silicon wafer can be highly increased. Using an aqueous etching solution of KOH and IPA, a texturing time of about 20 min at about 70–80 °C is required to remove the saw damage and to generate the texture. Typical concentrations of the solutions are ~2 wt.% KOH and ~4 wt.% IPA. A structure of random pyramids is generated on the silicon wafer surface (Fig. 31).

The edge length of the pyramids has varying dimensions of 1–7 μm. This procedure is performed in batch processes, wherein the wafers are held in carriers

**Fig. 31** Typical structure of a monocrystalline silicon wafer surface texturized by KOH-IPA solutions



that allow chemicals to wet the entire surface. These carriers are moved into tanks filled with the respective chemicals for etching, cleaning, rinsing, and drying. For process control, the loaded carriers are weighed before and after etching to determine the etching depth from the difference in weight.

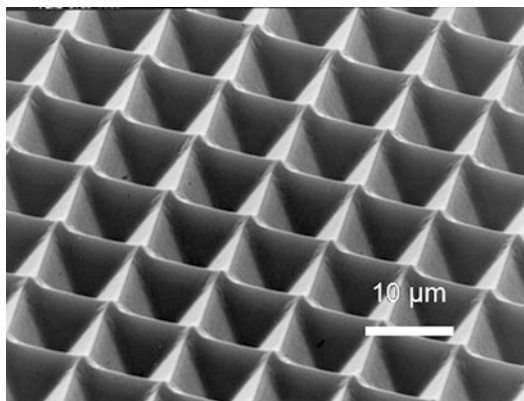
Control over the size and number of pyramids formed during alkaline etching has been gained empirically. It is still not known what source causes the formation of each pyramid tip during the etching process. At least four different “pyramid-initiators” have been considered in the literature:

1. Crystal defects including contaminations (such as heteroatoms)
2. Reactions products (silicate/SiO<sub>2</sub> precipitates)
3. H<sub>2</sub> bubbles (at the silicon surface)
4. Adsorbed additives (IPA, etc.)

None of these potential initiators for pyramids is fully consistent with the experimental observations: Regarding no. 1 it was found that the number of generated pyramids does not show a clear correlation with the defect concentration present in the wafer material. For clean, saw-damage etched, and correspondingly pretreated Cz-wafers, there are more pyramids formed than would be expected from the number of defects. Considering no. 2 it is indeed observed that there are usually more pyramids initiated if the concentration of dissolved silicon in the etching solution is increased. However, pyramids are also formed when fresh solutions are used which do not contain any silicon. Hydrogen bubbles (no. 3) are indeed formed directly on the silicon surface. They stick to the surface until a certain size is reached, but their size is usually much larger than the observed size of the pyramids or the pyramid tips and it is not known if the number of (micro)bubbles correlates with the number of pyramids. The additives which are used, especially IPA and many other hydroxyl compounds, are known to adsorb at the silicon surface changing the surface energy and related surface properties including chemical reaction behavior. However, neither the size nor the concentration of the additive molecules does show a clear and unambiguous correlation with the pyramid formation.



**Fig. 32** Structure of inverted pyramids on a monocrystalline silicon wafer surface texturized by KOH-IPA solutions after photolithographic treatment



Nevertheless, with the random inverted pyramid textures completely covering the silicon surface with pyramids of a typical edge length of  $6\ \mu\text{m}$  are generated very reliably, if the above mentioned KOH/IPA-concentrations are applied. The result is a mean weighted reflectivity  $R_w$  of 11–12.5%, which is significantly lower than the  $R_w$  values which can be obtained by isotropic textures. Only lithographically generated textures (e.g., inverted pyramids) and similar texturing approaches requiring masking and/or laser structuring allow generating significantly lower reflectivity values.

### Inverted Pyramids

To further improve the light absorption of the texture, inverted pyramids can be generated on the silicon wafer surface as shown in Fig. 32 (Goetzberger et al. 1997). An etch mask containing  $\text{SiO}_2$  or  $\text{SiN}_x$  is deposited on the silicon wafer surface via thermal oxidation or PECVD. A photoresist is deposited on this layer through spin coating. The photoresist is dried and lithographically structured in regular distances with an accuracy of  $\sim 1\ \mu\text{m}$ . The exposed areas are dissolved. After the  $\text{SiO}_2$  is etched, the remaining photoresist will be removed. The silicon wafer with the etch mask is now etched in a KOH-IPA mixture. Because of the anisotropy effect the etch mask is not “underetched,” and so inverted pyramids are generated. After the etch process, the remaining etch mask is removed.

As this process is highly time-consuming and expensive it is mainly used in the production of so-called high-efficiency solar cells. A new concept for the maskless generation of inverted pyramids (random inverted pyramids, Fig. 26) is the usage of acidic texturing mixtures containing hydrofluoric acid, hydrochloric acid, and chlorine (see section “The Development of Acidic Etching Mixtures”).

---

## Concluding Remarks/Summary

The preparation of silicon wafers for solar cell manufacturing includes cleaning, etching, and texturization steps (Figs. 33 and 34). Wet chemical cleaning steps are required to obtain good cell performances. This aim is independent of the wafer type

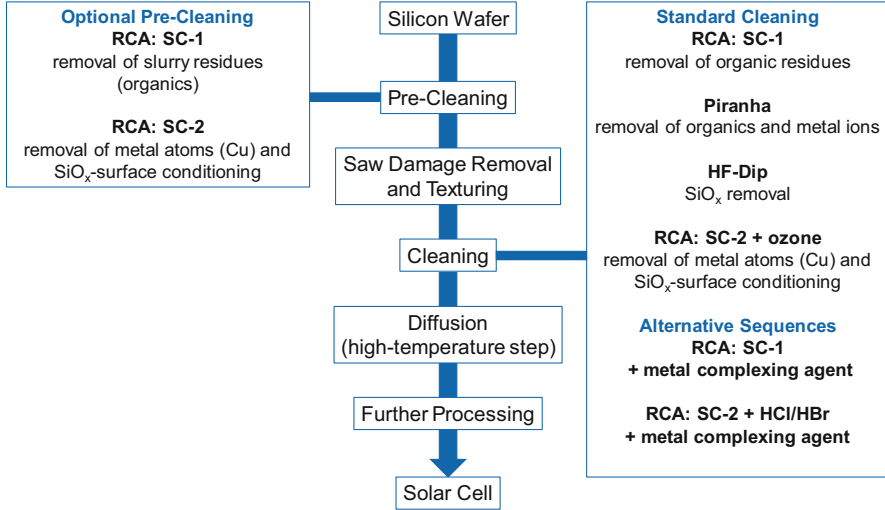


**Fig. 33** Scheme of important cleaning procedures of silicon wafers in solar cell processing

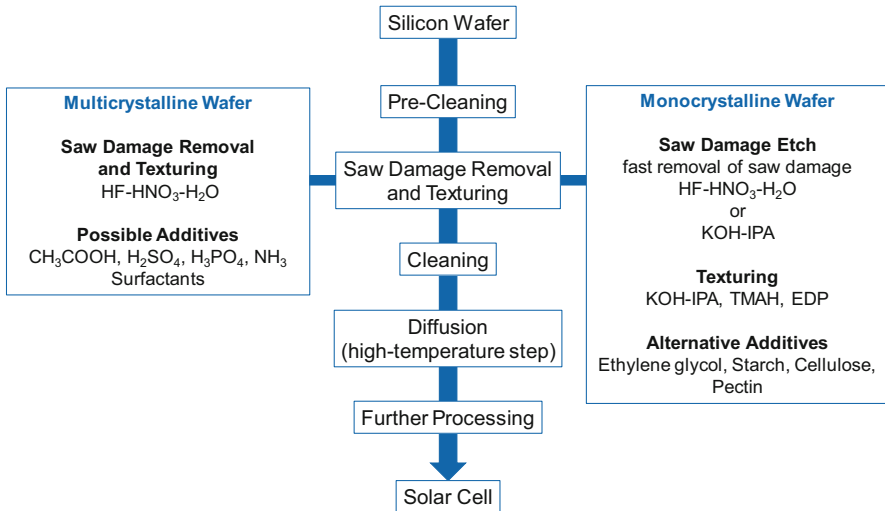


**Fig. 34** Scheme of texturing procedures in solar cell processing

(mono- or multicrystalline, p- or n-doped) and also the type of sawing process (SiC slurry or diamond wire). Standard cleaning solutions developed for microelectronic processing such as so-called RCA, Piranha, or IMEC can be applied for the as-cut wafer before saw damage removal and texturing are performed (Fig. 33). In order to

save cost and processing time and due to the less demanding requirements in PV compared to microelectronics, simplified alternative cleaning sequences may be used. Further cleaning steps are required before high-temperature processing steps such as emitter diffusion. Porous silicon and metal contaminations have to be removed. Silicon oxide layers are generated to protect the silicon from contamination and for surface passivation.

Referring to the specific factors contributing to the costs of the cleaning process (chemical consumption, the number of cleaning steps, tool price, throughput), cell makers have to find out what is “just clean enough” for solar cell manufacturing and how to reach this level.

Useful information to clear this question was published by Wostyn et al. (2012). The authors presented a model that can be used to compare the efficiency of different cleaning mixtures. The input needed in the model is the amount of contamination to be removed and the target cleanliness level after cleaning.

After the pre-cleaning step described in section [Cleaning of Silicon Surfaces](#), there are still small cracks penetrating around 5–10  $\mu\text{m}$  deep into the wafer surface. Such saw damage should be removed from the wafer surface because it reduces the mechanical strength of the wafer and increases charge carrier recombination in the surface region. Alkaline as well as acidic solutions can be employed alternatively for saw damage removal (Fig. 34). Additionally, the etching processes are normally used to generate surface textures in order to reduce the total light reflection of the wafer (Fig. 18). Depending on the used silicon wafer material, different process steps are necessary.

Due to the different crystallite orientations in multicrystalline wafers, isotropic etching has to be used. The standard solutions are based on HF-HNO<sub>3</sub>-mixtures, with optional additives to improve the isotropic texture.

In case of monocrystalline (100) oriented wafers, anisotropic texturing is applied yielding pyramid structures. Established standard systems are alkaline solutions, in particular, aqueous KOH-IPA, which generally is used at around 80 °C. KOH may be replaced by other strong bases, but NaOH is the only competitive base when cost factors are taken into account. More efforts have been taken in order to replace IPA by less volatile and potentially better and cheaper additives.

In general, the aims with regard to wet chemical processing steps for silicon wafer preparation in PV industry are focused on further decrease of contamination and defect levels. Thus, processing might become more and more similar to the micro-electronic industries. This is motivated by the general target to improve the efficiency of the solar cells. On the other hand, costs need to be decreased to stay competitive with other (PV-) technologies.

It is obvious that cleaning, etching, and texturization have an impact on all aspects to be considered for any future development, including cell, module and system efficiency, yield of the production process, fixed costs, variable costs, and the lifetime of the system. Models for taking these factors into account have been described (e.g., Neuhaus and Münzer 2007).

## Cross-References

- ▶ [Metal Impurities and Gettering in Crystalline Silicon](#)
- ▶ [Wafer Processing](#)

---

## References

- J. Acker, A. Rietig, M. Steinert, V. Hoffmann, J. Phys. Chem. C **116**, 20380 (2012)
- P. Allongue, V. Costa Kieling, H. Gerischer, J. Electrochem. Soc. **140**, 1018 (1993)
- O.J. Anttila, M.V. Tilli, M. Schaekers, C.L. Claeys, J. Electrochem. Soc. **139**, 1180 (1992)
- P.W. Atkins, J. de Paula, *Physical Chemistry*, 9th edn. (Oxford University Press, Oxford/New York, 2010)
- T. Baum, D.J. Schiffrin, J. Chem. Soc. Faraday Trans. **94**, 691 (1998)
- E. J. Bergman, S. Lagrange, M. Claes, S. de Gendt, E. Röhr, Solid State Phenom. **76–77**, 85 (2001)
- F. Buchholz, Metal Surface Contamination in c-Si Solar Cell Processing (Dissertation, TU Bergakademie Freiberg, 2015).
- S.A. Campbell, D.J. Schiffrin, P.J. Tufton, J. Electroanal. Chem. **344**, 211 (1993)
- G.F. Cerofolini, A. Giussani, A. Modelli, D. Mascolo, D. Ruggiero, D. Narducci, E. Romano, Appl. Surf. Sci. **254**, 5781 (2008)
- Y.J. Chabal, A.L. Harris, K. Raghavachari, J.C. Tully, Int. J. Mod. Phys. B **07**, 1031 (1993)
- G.-M. Choi, T. Ohmi, J. Electrochem. Soc. **148**, G241–G248 (2001)
- M. Claes, E. Röhr, T. Conard, F. de Smedt, S. de Gendt, W. Storm, T. Bauer, P.W. Mertens, M.M. Heyns, Solid State Phenom. **76–77**, 67 (2001)
- O. Doll, S. Metzger, B.O. Kolbesen, Freiberg. Forschungsh. B **153** (2004)
- M. George, H. Treichel, D. Bohling, A. Goldstein, H. Litvak, S. Ostrowski, I. Mowat, W. Kern, ECS Trans. **41**, 295 (2011)
- H. Gerischer, P. Allongue, V. Costa Kieling, Ber. Bunsen-Ges. **97**, 753 (1993)
- O.J. Glembocki, R.E. Stahlbush, M. Tomkiewicz, J. Electrochem. Soc. **132**, 145 (1985)
- A. Goetzberger, J. Knobloch, B. Voß, *Sonnenenergie: Photovoltaik: Physik und Technologie der Solarzelle* (Teubner, Stuttgart, 1997)
- C. Gondek, M. Lippold, I. Röver, K. Bohmhammel, E. Kroke, J. Phys. Chem. C **118**, 2044 (2014)
- C. Gondek, R. Hanich, F. Honeit, A. Lißner, A. Stapf, E. Kroke, J. Phys. Chem. C **120**, 22349 (2016)
- C. Gottschalk, J. Schweckendiek, Micro **22**, 81 (2004)
- M.A. Gosálvez, Atomistic Modelling of Anisotropic Etching of Crystalline Silicon (Dissertation, Helsinki University of Technology, Espoo, 2003).
- M.A. Gosálvez, I. Zubel, E. Viinikka, in *Handbook of Silicon Based MEMS Materials and Technologies*, ed. by V. Lindroos, M. Tilli, A. Lehto, T. Motooka (William Andrew/Elsevier, Amsterdam, Boston, 2010), pp. 375–407.
- P. Gupta, A.C. Dillon, A.S. Bracker, S.M. George, Surf. Sci. **245**, 360 (1991)
- M.M. Heyns, P.W. Mertens, J. Ruzyllo, M.Y.M. Lee, Solid State Technol. **42**, 37 (1999)
- V. Hoffmann, M. Steinert, J. Acker, J. Anal. At. Spectrom **26**, 1990 (2011)
- A.F. Holleman, E. Wiberg, N. Wiberg, *Lehrbuch der anorganischen Chemie*, 102nd edn. (de Gruyter, Berlin, New York, 2007)
- R. Hull, *Properties of Crystalline Silicon* (Institution of Electrical Engineers, London, 1999)
- A.A. Istratov, H. Hieslmaier, E.R. Weber, Appl. Phys. A **70**, 489 (2000)
- J.J. Kelly, H.G.G. Philippen, Curr. Opin. Solid State Mater. Sci. **9**, 84 (2005)
- M.T. Kelly, J.K.M. Chun, A.B. Bocarsly, Appl. Phys. Lett. **64**, 1693 (1994)
- J.J. Kelly, X.H. Xia, C.M.A. Ashruf, P.J. French, IEEE Sensors J. **1**, 127 (2001)
- W. Kern, J. Electrochem. Soc. **137**, 1887 (1990)
- W. Kern, *Handbook of Semiconductor Wafer Cleaning Technology: Science, Technology, and Applications* (Noyes Publications, Park Ridge, 1993)

- W. Kern, D.A. Puotinen, *RCA Rev.* **187** (1970)
- K.W. Kolasinski, *Phys. Chem. Chem. Phys.* **5**, 1270 (2003)
- K.W. Kolasinski, *Surf. Sci.* **603**, 1904 (2009)
- K.W. Kolasinski, *J. Phys. Chem. C* **114**, 22098 (2010)
- E.S. Kooij, K. Butter, J.J. Kelly, *Electrochem. Solid St.* **2**, 178 (1999)
- V. Lehmann, *The Electrochemistry of Silicon: Instrumentation, Science, Materials and Applications* (Wiley-VCH, Weinheim, 2002)
- M. Lippold, Beiträge zum Verständnis des sauren nasschemischen Ätzens von Silicium – Das System HF-HNO<sub>3</sub>-H<sub>2</sub>SO<sub>4</sub>/H<sub>2</sub>O (Dissertation, TU Bergakademie Freiberg, 2014).
- M. Lippold, S. Patzig-Klein, E. Kroke, *Z. Naturforsch., B: J. Chem. Sci.* **66b**, 155 (2011)
- M. Lippold, F. Buchholz, C. Gondek, F. Honeit, E. Wefringhaus, E. Kroke, *Sol. Energy Mater. Sol. Cells* **127**, 104 (2014)
- L.M. Loewenstein, P.W. Mertens, *J. Electrochem. Soc.* **145**, 2841 (1998)
- L.M. Loewenstein, F. Charpin, P.W. Mertens, *J. Electrochem. Soc.* **146**, 719 (1999)
- H. Löwe, P. Keppel, C. Moritz, D. Zach, *Halbleiterätzverfahren: Kinetik, Verfahrensgrundlagen und Anwendungsgebiete von nasschemischen Ätzverfahren für Si, GaAs, GaP und InP* (Akademie-Verlag, Berlin, 1990)
- Y.-R. Luo, *Comprehensive handbook of chemical bond energies* (CRC Press, Boca Raton, 2007)
- A.R. Martin, M. Baeyens, W. Hub, P.W. Mertens, B.O. Kolbesen, *Microelectron. Eng.* **45**, 197 (1999)
- B. Meinel, T. Koschwitz, C. Blocks, J. Acker, *Mater. Sci. Semicond. Process.* **26**, 93 (2014)
- M. Meuris, S. Arnauts, I. Cornelissen, K. Kenis, M. Lux, S. De Gendt, P.W. Mertens, I. Teerlinck, R. Vos, L.M. Loewenstein, M.M. Heyns, K. Wolke, in *IEEE International Symposium on Semiconductor Manufacturing* (1999), p. 157.
- H.J. Möller, *Adv. Eng. Mater.* **6**, 501 (2004)
- Y. Mori, K. Uemura, K. Shimano, T. Sakon, *J. Electrochem. Soc.* **142**, 3104 (1995)
- E. Morita, T. Yoshimi, Y. Shimanuk, *ECS Extended Abstracts* **89-1**, 22 (1989)
- D.-H. Neuhaus, A. Münzer, *Adv. Optoelectron.* 2007, 15 pages (2007).
- Y. Nishimoto, T. Ishihara, K. Namba, *J. Electrochem. Soc.* **146**, 457 (1999)
- T. Ohmi, *J. Electrochem. Soc.* **143**, 2957 (1996)
- T.M. Pan, T.F. Lei, T.S. Chao, M.C. Liaw, F.H. Ko, C.P. Lu, *J. Electrochem. Soc.* **148**, G315–G320 (2001)
- S. Patzig-Klein, G. Roewer, E. Kroke, *Mater. Sci. Semicond. Process.* **13**, 71 (2010)
- M. Pourbaix, *Atlas of Electrochemical Equilibria in Aqueous Solutions* (National Association of Corrosion Engineers, Houston, 1974)
- K.A. Reinhardt, W. Kern, *Handbook of Silicon Wafer Cleaning Technology*, 2nd edn. (William Andrew, Norwich, 2008)
- H. Robbins, B. Schwartz, *J. Electrochem. Soc.* **106**, 505 (1959)
- H. Robbins, B. Schwartz, *J. Electrochem. Soc.* **107**, 108 (1960)
- I. Röver, G. Roewer, K. Bohmhammel, K. Wambach, *Freiberg. Forschungsh. B* **179** (2004)
- K. Sato, M. Shikida, T. Yamashiro, M. Tsunekawa, S. Ito, *Sens. Actuators, A* **73**, 122 (1999)
- F. Schomann, K. Graff, *J. Electrochem. Soc.* **136**, 2025 (1989)
- B. Schwartz, H. Robbins, *J. Electrochem. Soc.* **108**, 365 (1961)
- B. Schwartz, H. Robbins, *J. Electrochem. Soc.* **123**, 1903 (1976)
- J. Schweckendiek, R. Hoyer, S. Patzig-Klein, F. Delahaye, G. Knoch, H. Nussbaumer, *Solid State Phenom.* **195**, 283 (2012)
- H. Seidel, L. Csepregi, A. Heuberger, H. Baumgärtel, *J. Electrochem. Soc.* **137**, 3612 (1990)
- Y. Shiramizu, K. Watanabe, M. Tanaka, H. Aoki, H. Kitajima, *J. Electrochem. Soc.* **143**, 1632 (1996)
- A. Stapf, F. Honeit, C. Gondek, E. Kroke, Siliziumwafer, Verfahren zum Strukturieren eines Siliziumwafers und Solarzelle, DE 10 2014 001 363 (2016).
- A. Stapf, F. Honeit, C. Gondek, E. Kroke, *Sol. Energy Mater. Sol. Cells* **159**, 112 (2017)
- M. Steinert, J. Acker, M. Krause, S. Oswald, K. Wetzig, *J. Phys. Chem. B* **110**, 11377 (2006)
- M. Steinert, J. Acker, S. Oswald, K. Wetzig, *J. Phys. Chem. C* **111**, 2133 (2007)
- H. Treichel, A. Goldstein, M. George, D. Bohling, J. Rentsch, A. Oltersdorf, M. Zimmer, S. Ostrowski, I. Mowat, L. Wang, W. Kern, *Photovolt Int* **12**, 81 (2011)

- D.R. Turner, *J. Electrochem. Soc.* **107**, 810 (1960)
- E. Vazsonyi, K. de Clercq, R. Einhaus, E. van Kerschaver, K. Said, J. Poortmans, J. Szlufcik, J. Nijs, *Sol. Energy Mater. Sol. Cells* **57**, 179 (1999)
- É. Vázsonyi, E. Szilágyi, P. Petrik, Z. Horváth, T. Lohner, M. Fried, G. Jalsovszky, *Thin Solid Films* **388**, 295 (2001)
- R. Walsh, *Acc. Chem. Res.* **14**, 246 (1981)
- Z.-H. Wang, T. Urisu, H. Watanabe, K. Ooi, G.R. Rao, S. Nanbu, J. Maki, M. Aoyagi, *Surf. Sci.* **575**, 330 (2005)
- M.K. Weldon, B.B. Stefanov, K. Raghavachari, Y.J. Chabal, *Phys. Rev. Lett.* **79**, 2851 (1997)
- G. Willeke, K. Kellermann, *Semicond. Sci. Technol.* **11**, 415 (1996)
- K. Wostyn, W. Baekelant, J. Rip, M. Haslinger, K. Kenis, H. Struyf, M. Claes, P.W. Mertens, S. de Gendt, *Solid State Phenom.* **195**, 293 (2012)
- R. Zannoni, G. Righini, G. Mattogno, L. Schirone, G. Sotgiu, F. Rallo, *JOL* **80**, 159 (1999)
- X.G. Zhang, *Electrochemistry of Silicon and Its Oxide* (Kluwer Academic/Plenum Publishers, New York, 2001)
- I. Zobel, M. Kramkowska, *Sens. Actuators, A* **101**, 255 (2002)



# Characterization of Wafers and Supply Materials

# 13

Hans Joachim Möller

## Contents

Introduction .....	360
Wafer Geometry, Total Thickness Variation, and Warp .....	361
Saw Damage of the Wafer Surface .....	362
Roughness .....	363
Subsurface Damage .....	367
Basic Surface Damage Mechanisms .....	376
Single Indentation Tests: Loose Abrasive Sawing .....	376
Single Scratch Tests: Fixed Abrasive Sawing .....	378
Fracture Behavior .....	382
Wafer Contamination .....	385
Characterization of Wires, Slurries, and Coolants .....	387
Wires .....	387
Slurries and Coolants .....	390
Conclusion .....	394
References .....	395

## Abstract

The technological development of silicon wafer processing for solar cells by multiwire sawing is mainly driven by the need to reduce cost but under the condition to maintain or even improve the wafer quality. This additional requirement becomes even more important because wafer and wire thickness will decrease in the future and the standard loose abrasive sawing technique will be replaced by the fixed abrasive sawing technique.

The essential quality parameters for wafers are total thickness variations (TTV), roughness and grooves, subsurface damage, and fracture strength stability. These factors depend on the properties of wires, consumables, and machine

---

H. J. Möller (✉)

Fraunhofer Technology Center for Semiconductor Materials, Freiberg, Germany

e-mail: [hans.joachim.moeller@thm.fraunhofer.de](mailto:hans.joachim.moeller@thm.fraunhofer.de); [moeller@iphaf.de](mailto:moeller@iphaf.de); [moeller@physik.tu-freiberg.de](mailto:moeller@physik.tu-freiberg.de)

sawing parameters. Their investigation and determination require adequate characterization methods. The chapter describes standard and new methods, which have been developed to characterize wafers, wires, and consumables. Today's optimization processes also require a basic understanding of the interaction processes between wires, sawing fluid, and the silicon material. Special experimental methods, which have been developed to investigate the fundamental micromechanical processes and their ramifications on the wafer quality parameters, are presented.

### Keywords

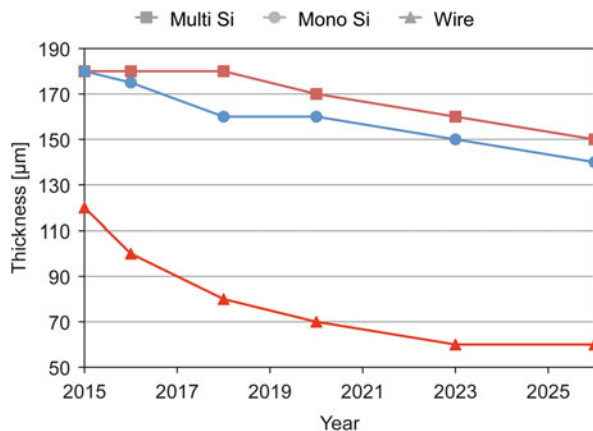
Silicon wafer · Subsurface damage · Roughness · Thickness variation · Fracture strength · Contamination · Particle indentation · Scratching · Slurry · Diamond wire · Structured wire

## Introduction

The wafering of large silicon crystals by multiwire sawing has been specifically developed for the photovoltaic industry because it could fulfill the demands on the wafers for solar cells. The solar cell processes require a certain and uniform thickness, a defect-free and smooth surface, a certain orientation for texturization (for monocrystalline silicon), and a high fracture stability. Above all the wafering process has to be inexpensive, which includes the cost of all consumables and the loss of silicon itself.

The requirements on the wafers become more demanding with the further development of the solar cell technology. Considering the expected decrease in wafer thickness both for mono- and multicrystalline silicon (Fig. 1), one has to handle the decreasing fracture stability of the wafers and to understand the factors, which are responsible here. Correspondingly the wires become also thinner, which makes the control of sawing process more challenging.

**Fig. 1** Annual and predicted development of the thickness of commercial mono- and multicrystalline silicon wafers for solar cells and correspondingly the decrease in wire thicknesses (ITRPV 2016)





Furthermore, wafer properties have to be specified and tested. In mass production wafers are produced at a rate of one wafer per second or less. This requires the development of fast measuring techniques for those properties, which are necessary to guarantee stable sawing conditions. In addition, testing methods have to be developed which allow to determine the specific information about the wafer properties that can affect the following solar cell process.

With the progress of the characterization techniques, one was also able to understand the sawing process better and the impact on the wafer properties. This in return allowed to improve the sawing process and to develop better sawing machines. This development is still ongoing, and at present one cannot predict when and where the limits of the multiwire sawing technology have been reached. Although alternative wafer fabrication techniques are continuously developed, they have not been competitive so far, and many attempts have been abandoned in the past. In the following we shall restrict to the characterization methods, which have been developed for the wire sawn wafers.

---

## Wafer Geometry, Total Thickness Variation, and Warp

The industrial solar cell fabrication requires wafers with a defined and uniform geometry. The standard geometry is the square shape of  $156 \times 156 \text{ mm}^2$  for multicrystalline silicon and the same size but with rounded edges for monocrystalline silicon. The thickness is different for both materials and slightly lower for mono material (Fig. 1). In a multiwire saw, a single wire is used, which is wound several hundred times around two or more spools (guide rollers), forming a parallel arrangement of the wire, the so-called wire web (► Chap. 11, “Wafer Processing”). The thickness of the wafers is determined by the distance of the wires, which are guided in grooves over the wire guide rollers, and the thickness of the wires. The grooves are cut into the polymer coating of the rollers, and their quality (shape, depth, distance, etc.) is important for the process.

In the sawing process, the wafer thickness can only be maintained to a certain degree. One reason is that the grooves deteriorate after some time and have to be renewed then. Wafers cut from an ingot may also have different thicknesses depending on their position along the wire web. For instance, in the slurry sawn process, the wire is worn and thinner at the end. The control of the thickness and wafer surface is thus important for the process stability.

Both the thickness and the surface height profiles on both sides, which are a measure for the thickness uniformity, are measured, for instance, with a laser profiler or by white light interferometry. Standard is a measurement along certain perpendicular lines across the wafer. These values allow to determine the local thickness and if the wafer is bent (warp). The difference between the maximum and minimum height at several (5–15) intersecting points is given as the TTV (total thickness variation) parameter. Good wafers have TTV values below  $25 \mu\text{m}$ . Thickness, TTV, and warp indicate if the sawing process is running stable. For instance, the

deterioration of the PEG/SiC slurry can be seen in the TTV of many wafers and allows to determine the time for replacement and recycling.

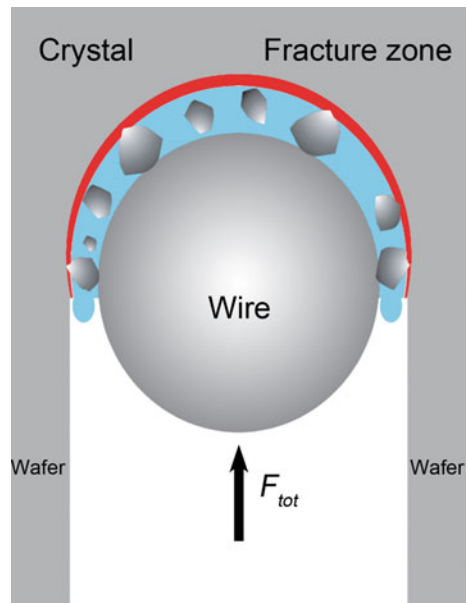
Slurry sawn wafers have a wedge shape and are thicker at the wire outlet side. This is because the material removal process is not uniform along the sawing channel (► Chap. 11, “Wafer Processing”). The wafer thicknesses are more uniform for fixed abrasive sawing because of the back-and-forth motion of the wire.

## Saw Damage of the Wafer Surface

The sawing process damages the wafer surface. There is general agreement today that in the slurry-based sawing, free-floating abrasive particles in the sawing channel remove material by rolling and indenting into the silicon crystal surface. The same interactions are known from lapping processes, and similar dependencies can be derived here. The larger particles are in direct contact with the wire and the silicon surface. The wire is pushed against the particles and indents these particles into the silicon surface. In the fixed abrasive sawing, the damage is produced by scratching the fixed particles on the wire. Considering the cross section of the sawing channel (Fig. 2), one can see that the interaction of the abrasive particles at the side of the channel is responsible for the damage, whereas the particles below the wire are mainly responsible for the material removal process and the sawing velocity.

The damage of the wafer surface is quantified by measuring the surface profile and deriving certain parameters at different length scales. The roughness is usually determined over a defined length of a few millimeters with a resolution of

**Fig. 2** Schematic diagram of the cross section of the sawing channel



micrometers. Grooves vary over larger distances and are characterized by their depth, width, and length on larger scale. The determination methods of these parameters are standardized and specified to some extent.

The wafer can also be damaged below the surface. The subsurface damage (SSD) consists of microcracks below the surface, up to 20  $\mu\text{m}$  in length depending on the sawing conditions. In addition, thin layers of silicon material, which have been transformed into an amorphous or microcrystalline structure, can occur. The investigation of SSD is more difficult, and standard methods have not been established.

Another quality factor is the wafer cleanness, the contamination with impurities and organic residues from the sawing and cleaning process. Although wafers are cleaned after sawing, a certain non-visible contamination remains. They can affect the following etching processes in the solar cell process and become visible then. The measurement of the contamination requires sophisticated methods, and their development is still at the beginning (► [Chap. 12, “Wafer Cleaning, Etching, and Texturization”](#)).

Wafers with visible and deep grooves or scratches cannot be used for the solar cell process. Furthermore if the saw damage is outside the specification range of the wafers, they are also discarded. In mass production more than 95% of all wafers have to be accepted to be cost-effective. A high-quality wafer has a low TTV, a uniform roughness, a low microcrack depth, and a cleanness, which does not disturb the further processing.

## Roughness

The surface profiles of wafers sawn with loose abrasives (slurry) and fixed abrasives (diamond-coated wires) are completely different (Fig. 3). In the first case, a uniform

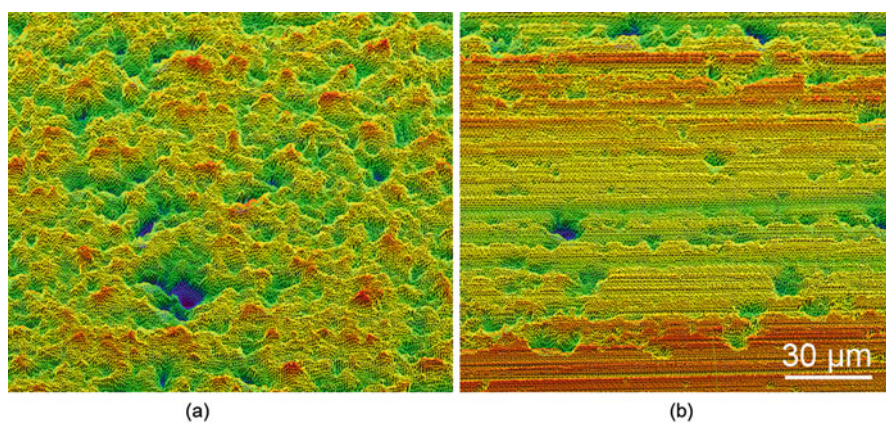


**Fig. 3** Surface height topograms of a slurry sawn wafer (a) and of a fixed abrasive sawn wafer (b) measured by confocal optical microscopy

surface profile, consisting of statistically distributed shallow pits, occurs, whereas in the second case, the surface profile shows mainly parallel scratches. The depths and distances of the scratches depend on the sawing conditions. This indicates already that the underlying material removal process differs in both cases (Bidiville et al. 2010; Wagner et al. 2010).

Today surface height profiles are mainly measured by confocal optical microscopy or by laser optical methods. Both offer a high spatial and height resolution. Different methods are used depending on whether fast or more accurate profiles are needed. Roughness parameters are determined from sampling the height profile over a certain length of a few millimeters. The most common measure is the  $R_a$  value, which is the arithmetic mean of the absolute values of the height difference from the mean value. Also used is the  $R_z$  value, the average distance between the highest peak and lowest valley in each sampling length. This value is greater than  $R_a$ . Since these parameters reduce all of the information in a profile to a single number, great care must be taken in applying and interpreting them. Small changes in how the raw profile data is filtered and how the mean line is calculated and the physics of the measurement system can greatly affect the calculated parameter.

### Loose Abrasive Sawing

Although the slurry sawn wafer surfaces appear rather uniform, measurements show that the wafers are thinner at the side where the wire has entered the sawing channel. They thus have a wedge shape. The thickness difference can be about 20–40  $\mu\text{m}$  depending on the sawing conditions. Correspondingly the cutting or kerf width decreases toward the wire outlet. This indicates that the material removal process varies along the wire motion. These variations also affect the surface roughness and, as shown in the next chapter, also the microcrack length. The general tendency is that the roughness decreases from wire inlet to wire outlet (Fig. 4). The overall level depends however on the sawing parameters. The roughness increases with the wire velocity and decreases with the feed velocity (not shown here), but the dependence is not strong. The main impact comes from the particle size: larger particles cause a rougher surface.

This can also explain the decrease of the roughness along the sawing channel. Analyzing the particle size distribution between wire entry and exit, it could be shown that larger particles are lost along the sawing channel. It appears that the loss of slurry is accompanied by a classification of the particle size (Fig. 11, ► Chap. 11, “Wafer Processing”). This has been explained by the hydrodynamic pressure difference between the position below the wire and at the side, which causes higher forces on the larger particles and drives them faster toward the free slurry surface. In addition larger particles may also break toward the outlet. Since smaller particles cause less roughness, the remaining smaller particles near the wire exit reduce the roughness.

The roughness measurements are also sensitive to individual and deep scratches on a wafer, which can occur when the sawing process is disturbed. Of special importance are scratches, which can occur on those parts of wafers sawn at the

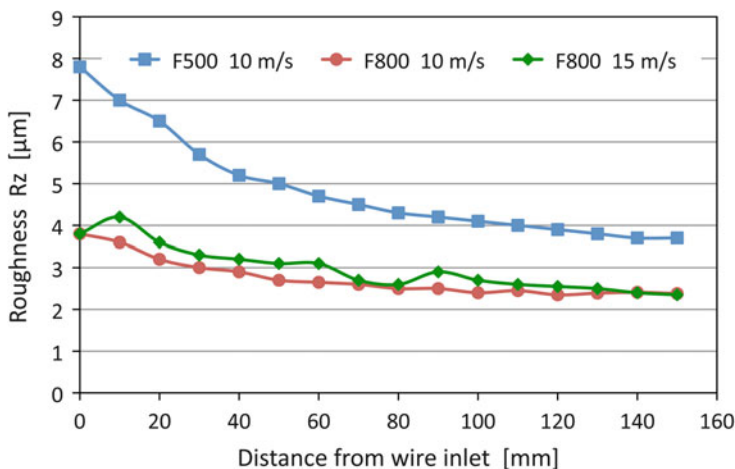


**Fig. 4** Roughness profiles ( $R_z$ ) from the wire inlet to the wire outlet region for wafers sawn with different grit sizes and wire velocities. The feed velocity is 0.4 mm/min and the mean particle size of F800, 6.5  $\mu\text{m}$  and of F500, 13  $\mu\text{m}$

wire exit. These so-called saw marks are visible by the naked eye (Fig. 11, ► Chap. 11, “Wafer Processing”). Such wafers cannot be processed into solar cells. It is assumed that the occurrence of these saw marks is related to an instability of wire motion near the exit region of the sawing channel as described in ► Chap. 11, “Wafer Processing.” It is necessary to select sawing parameters in the stability region (Fig. 21, ► Chap. 11, “Wafer Processing”) to avoid saw marks. If one saws with parameters in the stability region, the roughness correlates with the TTV.

### Structured Wire Sawing

The sawing with structured wires leads to a more uniform distribution of the abrasive along the sawing channel. This is reflected in the roughness, which is very sensitive to the particle size. There is also a decrease of the roughness from the wire entry to exit, but one can find sawing conditions where the variation is very small. This is shown in Fig. 5 where  $R_a$  roughness measurements for wafers sawn with a straight and structured wire are compared. The overall roughness is however higher for the structured wire.

Detailed investigations yield the following picture. A structured wire offers more open spaces between the wire and crystal surface between kink segments and less space where it is in contact with the surface (at the kinks). More slurry and particles are transported in the open spaces and supplied to the contact regions where the material is removed. Depending on the wire structure, the slurry transport can be improved and a more uniform roughness reached along the sawing channel (Anspach et al. 2014). The roughness values are however higher compared to the straight wire probably because of the higher forces in the smaller contact regions at the kinks of the wire.

**Fig. 5** Roughness profiles ( $R_a$ ) from the wire inlet to the wire outlet region for wafers sawn with structured and straight wires. The sawing parameters are the same in each case

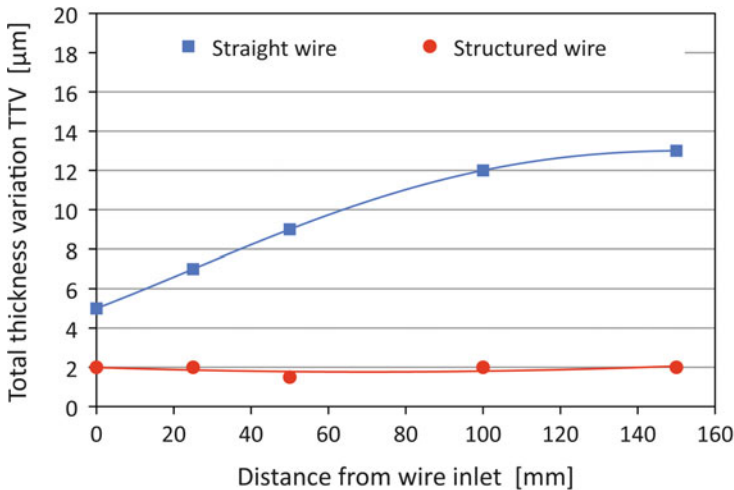
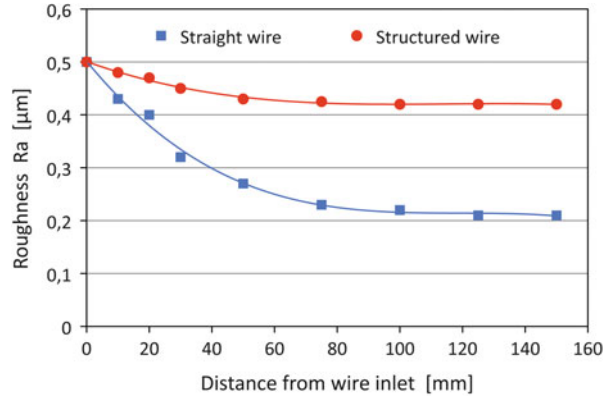


**Fig. 6** Total thickness variation (TTV) from the wire inlet to the wire outlet region for wafers sawn with structured and straight wires. The sawing parameters are the same in each case

The more uniform particle size distribution along the sawing channel is also reflected in the thickness variation (Fig. 6). The TTV values of wafers sawn with structured wires are much lower and show almost no variation along the sawing channel.

### Fixed Abrasive Sawing

The wafers sawn with fixed abrasives show a groove pattern on different length scales. At a mean distance around 1 mm parallel grooves occur, which are visible by the naked eye. They are however shallow with a depth below 10  $\mu\text{m}$ . An example can be seen in Fig. 15. They are due to the oscillating motion of the wire as well as the diamond size Bye et al. (2011). The position of the wires in the grooves of the

guider rollers changes slightly sideways when the motion direction is reversed. This leads to sideways displacement of the wire in the sawing channel. Today oscillation parameters can be chosen which reduce the grooves to an acceptable level for the following solar cell processing.

The roughness values are not affected by these grooves and in good cases are lower than for the slurry sawn wafers. It is determined by the structure of the scratches where material is removed and which is caused by a scratching particle. The roughness is uniform over the entire surface but differs along the scratches in sawing direction and perpendicular to it.

## Subsurface Damage

The saw-damaged region below the surface (subsurface damage: SSD) cannot be used in a solar cell and has to be etched away. The main factor here is the extension of the cracks into the bulk material. If the region reaches deep into the bulk crystal ( $> 5\text{--}10\ \mu\text{m}$  on both sides), the etching is connected with a substantial loss of valuable material. In addition, the damaged layer is responsible for the fracture stability of wafers as will be discussed in the chapter about fracture behavior. With the decreasing wafer thickness, both factors become increasingly important for the wafering process. The investigations require not only adequate characterization methods but also an understanding of the micromechanical processes, which cause the damage.

## Characterization Methods

The most reliable technique to determine the subsurface damage is the direct observation of the microcracks. This can be done on beveled surface segments, which are prepared at a low inclination angle of about  $1^\circ$ . After polishing and a slight structural etch, the traces of the microcracks become visible in an optical microscopy (Fig. 7a, b). The extension of the deepest cracks can be calculated from the inclination angle and the position of the last visible crack. Another method is to prepare cross sections of a wafer and observe the microcracks by scanning electron microscopy (Fig. 7c). In both cases great care has to be taken not to induce new cracks by the preparation method. A smooth preparation method is the ion beam milling of wafer cross sections, which gives very planar surfaces and allows to detect shorter cracks below  $5\ \mu\text{m}$  in length. The examples show typical microcracks for loose and fixed abrasive sawn wafers. These direct observation techniques can be reliable, but they are also tedious and time-consuming and not suitable to analyze larger parts of a wafer or many wafers. Therefore other methods have been developed to shorten the characterization time.

The subsurface damage (SSD) and the roughness originate from the same indentation process during wire sawing as will be described later. Therefore one might expect a correspondence between both parameters. Figure 8 shows the results of roughness and maximum crack depth investigations along the sawing channel and on different positions on the same wafer. Continuous measurements along the wire



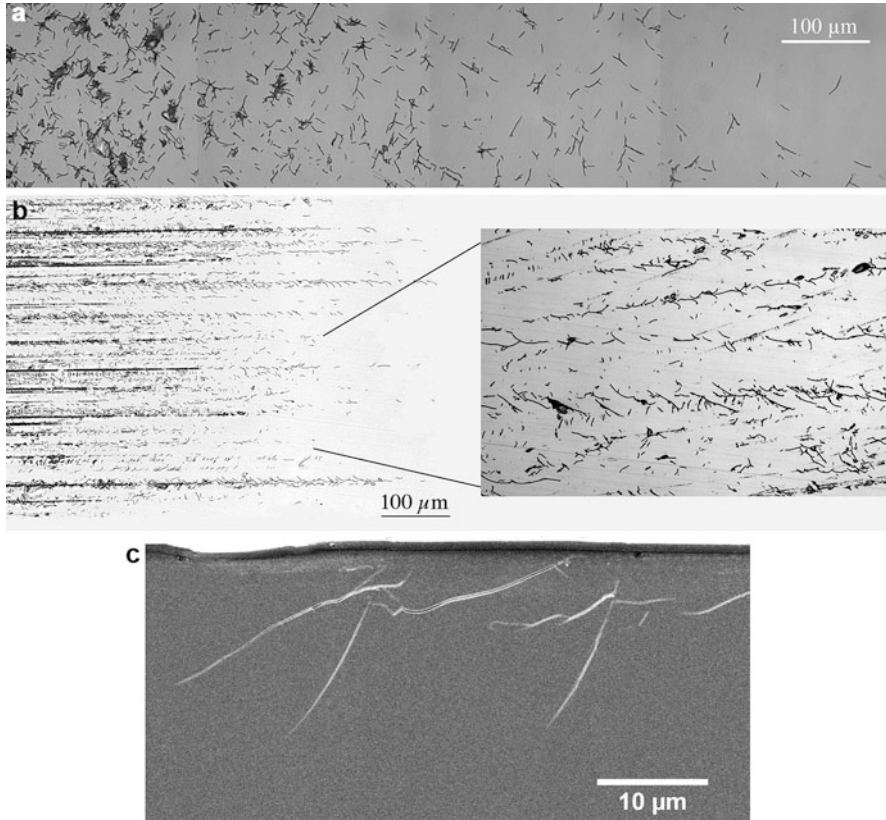


**Fig. 7** (a) Etched traces of microcracks at a beveled, polished surface (slope angle  $1^\circ$ ) of a slurry sawn wafer. (b) Etched traces of microcracks at a beveled (slope angle  $1^\circ$ ), polished surface of a diamond wire sawn wafer. (c) Scanning electron microscopy image of microcracks at a cross section of a fixed abrasive sawn wafer

direction show that the decrease of the roughness is accompanied by a decrease of the maximum crack depth as one would expect. However, measurements at the beginning, in the middle, and at the end of a cut through an ingot show different quantitative relationships (Bidiville et al. 2010; Würzner et al. 2017). This shows that other factors, which change during the cut, are not taken into account here. The investigation of the individual indentation process in the chapter about basic mechanisms will show that the number and density of the indentation events have to be considered as well. Nonetheless, roughness measurements may give a first indication about the corresponding SSD, but additional investigations are still necessary to obtain quantitative values.

A faster, nondestructive method is based on the dispersion of an acoustic surface wave, which is locally excited by a laser pulse (LAWave<sup>®</sup> method). The method utilizes the effect that the dispersion velocity at the surface is changed, when the



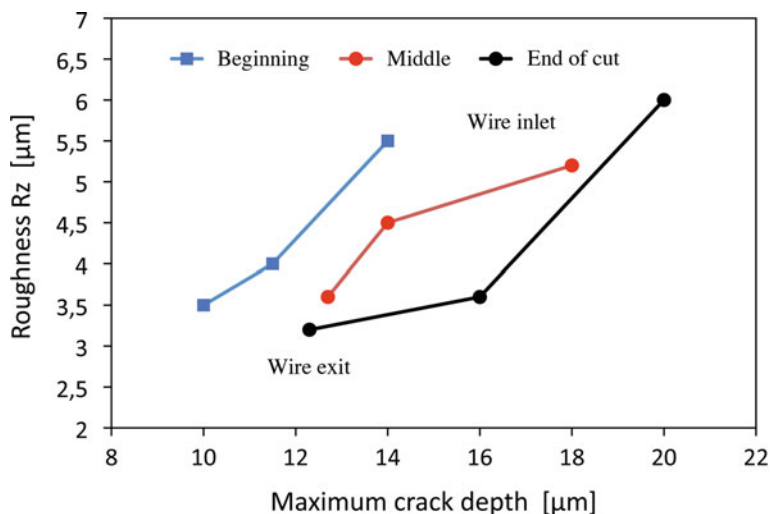


**Fig. 8** Correlation of roughness and maximum subsurface damage depth along the sawing channel and at different positions on a wafer

surface is damaged. The velocity is determined by measuring the run time of the acoustic pulse over a certain distance. This effect can be calibrated with the extension of the SSD depth of a wafer. The method is established and commercially available, however limited to mono crystalline silicon. It only allows to probe the wafer at a limited number of positions.

Another technique is the SIREX (scanning infrared stress explorer) method (Geiler et al. 2006). It is based on the effect of infrared birefringence. A linearly polarized infrared laser beam is scanned over the surface of the wafer, and the intensity and rotation of the polarization direction of the reflected light are measured. Internal elastic stresses can lead to a rotation of the polarization direction and be measured, if there is a difference of the in-plane principal stress components in the wafer plane  $\Delta\sigma = \sigma_1 - \sigma_2$ . Since internal stresses are mostly non-isotropic, one can easily detect stressed regions. The microcracks in the subsurface regions cause elastic stresses there. If the interior of the wafers is stress-free, one can directly detect the stresses in this region (Möller et al. 2016). An example is shown in Fig. 9 for two positions on the same wafer, namely, at the beginning and near the end of the cut. The wafer is sawn with a diamond-coated wire and shows the typical scratch structure. One can also see a different stress level in these parts, which is due to a stronger damage in the lower part of the wafer. Unfortunately a higher stress level does not always correlate with a deeper damage depth. The technique therefore requires additional investigations of the damage depth by direct observation. The method is however very stress sensitive and has a high lateral resolution of a few micrometer.

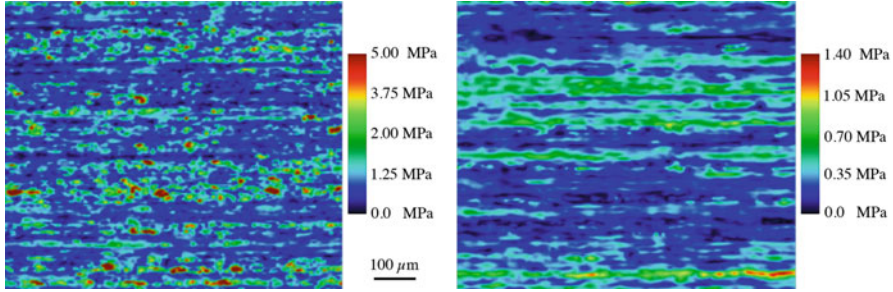


**Fig. 9** Calculated stress difference  $\Delta\sigma$  topograms from SIREX measurements of a part of a diamond sawn wafer: (a) at the beginning and (b) at the end of the cut

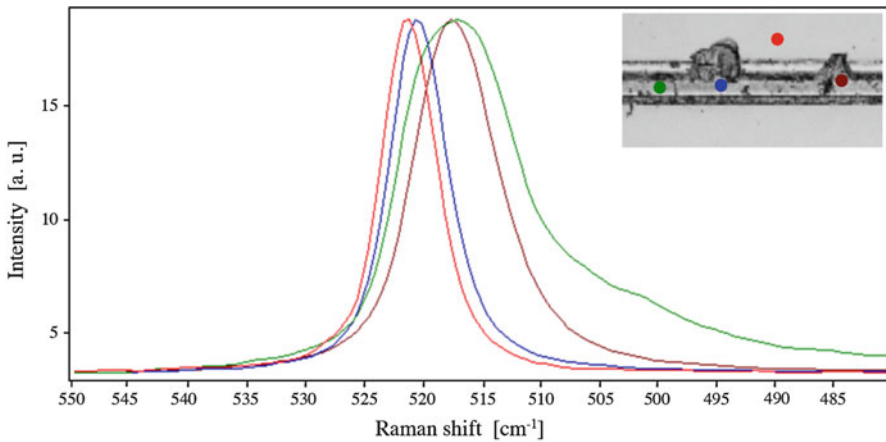


**Fig. 10** Raman spectra at different positions along a single scratch showing peak shift due to local stresses and peak broadening due to amorphization

A method which is also sensitive to microcrack-induced stresses is the Raman spectroscopy. Raman lines in silicon can be obtained by excitation with a laser beam at a wavelength of 532 nm. At this wavelength the laser light penetrates about 800 nm into the crystal. Crystalline silicon gives a Raman line at the wave number  $521\text{ cm}^{-1}$  and amorphous silicon at  $470\text{ cm}^{-1}$  and  $150\text{ cm}^{-1}$ . This allows one to detect also phase transformations of the silicon. Tensile and compressive stresses in the crystalline material shift the peaks to lower or higher wave numbers and can thus be detected (Fig. 10). The peak shifts could be calibrated with stresses: a Raman shift of  $\pm 3.2\text{ cm}^{-1}$  corresponds to  $\pm 1\text{ GPa}$  stress (Gogotsi et al. 1999).

Scanning the excitation beam over the specimen surface and measuring the peak shifts yield stress topograms. An example is shown in Fig. 11 for a wafer which has been sawn by new and used diamond-coated wire. The maximum tensile and compressive stresses are around 1 GPa. These are absolute stress values, whereas the SIREX method detects the difference or anisotropy of the main stress

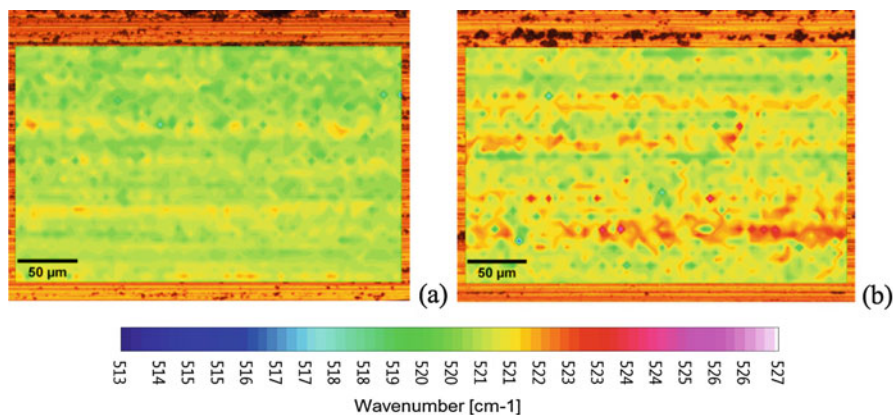


**Fig. 11** Mappings of the wave number shift of the crystalline silicon Raman peak for a wafer sawn with fresh (a) and used wire (b). Both measurements were carried out at the same position of the wafer

components, which is much smaller around 1–5 MPa. Raman measurements at the wafer surface detect the stresses near the surface ( $< 1 \mu\text{m}$ ) that are generated by the microcracks, which extend much deeper into the crystal. Measurements on wafer cross sections allow one to determine the stresses around the microcracks itself.

Raman measurements also revealed that under certain sawing conditions, diamond sawn wafers show amorphous regions on the surface. The distribution of these areas can be depicted in Raman topograms. The fraction of amorphization can be obtained by the integration of the Raman spectra lines at the corresponding wave numbers. A theoretical relation allows one to calculate the thickness of the amorphous layer from the ratio of the amorphous/crystalline peak areas (Yan et al. 2008) and the spatial distribution of the regions.

These topographic techniques are not fast enough for an in-line screening of wafers in production but allow the sampling of wafers produced under different sawing conditions and the investigation of the dependence on sawing parameters. Although these relatively new experimental methods show many details of the sawing process, the full potential of their results has not been explored yet.

### Dependence on Sawing Parameters

The primary industrial interest is to reduce the extension of the damaged layer by using appropriate sawing conditions. Because of the many dependences, it is not easy to find optimum sawing parameters, and usually long series of tests are required. With the development toward thinner wafers and wires (Fig. 1) and the introduction of the structured and diamond wire sawing, previous optimum parameters cannot directly be transferred to the new conditions but have to be determined again. Furthermore the dependence of the SSD on sawing parameters differs for loose and fixed abrasive sawing because of the different micromechanical damage mechanisms. Therefore one also has to consider the two cases separately.

### Loose Abrasive Sawing

The microcracks are generated by indenting the abrasive particles as will be described in the next section. They extend from the wafer surface into the volume, and their length depends on the local indentation force on the particle  $F_p$ . The average force is related to the total normal force  $F_n$  on the wire by  $F_p = F_n / m$  where  $m$  is the number of particles in contact with the wire. It has been shown in ► Chap. 11, “Wafer Processing” that the number  $m$  depends on the total force  $F_n$ , the particle size distribution, their shape, and the hydrodynamic pressure in the slurry, which depends on wire speed and the slurry viscosity. These parameters vary along the sawing channel and usually cannot be measured locally. Correspondingly SSD depth and roughness also vary.

There are not too many quantitative results available because of the high experimental effort to measure SSD depths. Some results have been obtained however, showing the correlation between roughness and SSD (Fig. 8). Similar to the roughness (Fig. 4), the microcrack depth decreases toward the wire outlet, whereas the number of cracks per unit length increases as is shown in Fig. 12. This can be explained by the loss of larger particles and the increasing number of smaller particles, which come into contact toward the end of the sawing channel. The quantitative values of the SSD depths depend mainly on the grit size and much less on sawing rate, wire speed, and SiC concentration. Finer grit sizes reduce the damage depth (Möller 2014), but the reduction of the grit size is limited because this increases the total force on the wire and one reaches the load limit of the wires. This becomes particularly difficult, when thinner wires are used in the future, which have a lower mechanical load capacity. The SSD depths are typically between 5 and 15  $\mu\text{m}$  and can hardly be reduced below these values.

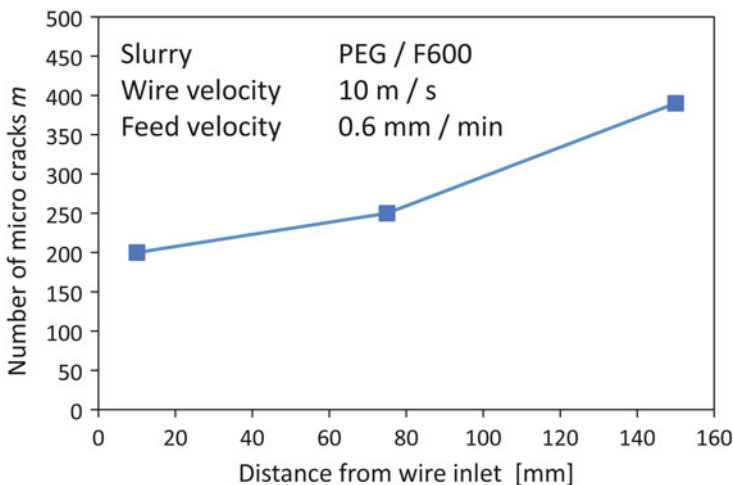


**Fig. 12** Number of microcracks on the wafer surface as a function of the distance from the wire inlet measured along the cutting direction. The numbers depend on the sawing parameters, which are given in the diagram

For structured wires no SSD measurements are available, but considering the roughness measurements, one expects a more uniform damage compared to straight wire sawing (Fig. 5).

### Fixed Abrasive Sawing

Apart from the productivity advantages, the fixed abrasive sawing has also attracted more interest because it appears that less damage can be achieved with this technique. For instance it has been reported by Bye et al. (2011) that comparing loose and fixed abrasive sawing, the roughness of wafers decreases from  $R_a = 0.5 \mu\text{m}$  (loose) to  $0.3 \mu\text{m}$  (fixed) for their industrial process and correspondingly the SSD depth from 6 to  $2.5 \mu\text{m}$  at the wire outlet side of the wafers.

To understand this one has to look at the micromechanical processes. The microcracks are generated by the stresses that the particles generate in the crystal. The stress field of a scratching particle differs from the stress field of an indenting particle (Fig. 13). Due to the horizontal force component in the first case, tensile and compressive stresses occur along the motion direction. Correspondingly the microcrack pattern around a scratching particle differs from that of an indenting particle regarding the distribution and size. The cracks are aligned along the direction of the sawing scratches (Fig. 7b) and show a distinct pattern which is repeated periodically (Fig. 7c). Investigations have also shown that the SSD depth varies over the wafer surface with the highest values near the end of the cut (Würzner 2017). In this particular study, average values between 3 and  $6 \mu\text{m}$  have been measured, which are lower compared to a slurry sawn wafer (for comparison see Fig. 8). Nonetheless there is a great variation in the SSD depth for different sawing parameters, and one has to study the dependences carefully.

Considering the strong dependence of the SSD on the grit size for loose abrasive sawing, one may expect the same for fixed abrasive sawing. Although there are commercial wires with different size distributions for the fixed diamonds, there are at present much less variation and control over size distributions and particle density. In addition the particles on fresh wires are covered by the coating layer, which makes it difficult to determine the actual size, shape, and height distribution. A few results

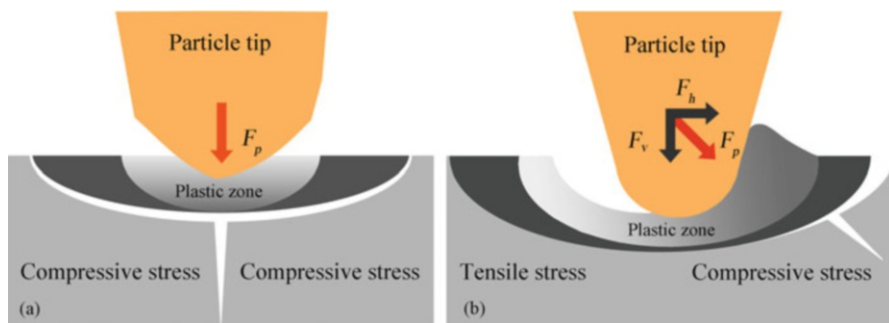
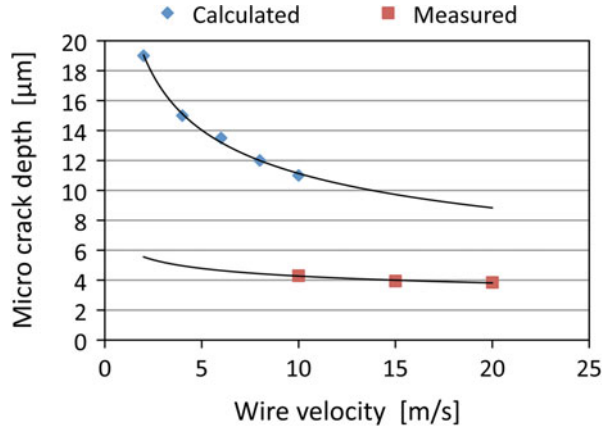


**Fig. 13** Schematic comparison of the stress situation of an indenting (a) and a scratching (b) particle. The forces, plastic zones, and possible microcrack formations are indicated

**Fig. 14** Dependence of the microcrack depth on the wire velocity for single scratches. Single scratch measurement (Würzner et al. 2015) and calculation (Li et al. 2016)



indicate that sharper particles induce lower damage depth, and correspondingly, since the wear of the particles on the wire decreases their sharpness, the damage increases. However, at present an appropriate characterization of particles on diamond wires does not exist; therefore such results still have to be treated cautiously.

More important is that the damage depth decreases with the wire velocity (Fig. 14; Würzner et al. 2015). A recently developed theoretical model for the SSD depth also predicts a decrease with the wire velocity (Li et al. 2016). In the model the stresses and resulting cracks are calculated based on experimental data for the indentation of particles in brittle materials. Although the results for SSD depth are not directly compared with experimental data, some parameters in the model have been determined by experimental measurements on wafers sawn with resin-bonded wires. The calculated damage depths are however higher in this case compared to the experimental data of Würzner et al. (2015). Furthermore the model predicts an increase of the SSD with the sawing (feed) rate.

Since sawing with diamond wires allows higher feed velocities, the SSD should be higher then. On the other hand, one can adjust the wire speed, so that altogether the damage depth can be kept low or even reduced. Due to the back-and-forth sawing mode, the wire speed varies however between zero and the maximum speed. It is therefore necessary to adjust the maximum wire speed and the acceleration phases, to maintain an overall low damage depth. Since the next generation of sawing machines will allow higher sawing speeds, one has more flexibility and can expect that wafers sawn with diamond wires will have less SSD in the future.

A new observation for diamond wire sawn wafers is the occurrence of an amorphous phase at the surface (Würzner et al. 2017). A systematic investigation by Raman spectroscopy topograms has shown that the amorphous/crystalline ratio varies between 0.2 and 1.3. A theoretical relation between the ratio and the corresponding thickness of the amorphous layer allows one to calculate the layer thickness and yields values between 8 and 35 nm (Yan et al. 2008). These amorphous regions are thus very thin. Two factors have been found to increase amorphization, the wire velocity and the wear of the wire. Whether these amorphous

regions have a technological importance, for instance, for the following texturization etching, is not clear yet but is important in view of an understanding of the micromechanical processes.

It has also been found however that the cleaning step after sawing has an influence on the thickness of the amorphous layer on the wafer surface. It was observed that by a standard cleaning procedure, more than 50% of the surface amorphization after sawing is etched away by the chemical process. This may be the reason that the amorphization is not always observed since wafers are normally characterized after the cleaning step.

A striking difference between loose and fixed abrasive sawing has been observed for multicrystalline silicon. Fixed abrasive sawing causes a higher saw damage for multicrystalline than for monocrystalline silicon. These wafers are mechanically less stable and show higher TTV. Such a different behavior does not occur for slurry-based sawing.

The difference between multi- and monocrystalline material is that the crystal orientation varies locally in each grain. Since the crack formation is orientation dependent, it has been assumed that this plays a role here. Figure 15 shows results from microcrack analyses on different grains on the same multicrystalline wafer. One can see that the crack length depends on the local orientation of the grains in the multicrystalline wafer. Even for the same (110) orientation, different crack depths have been observed, which could be explained by the different orientations of the (110) grains with respect to the scratching direction.

It is therefore reasonable to assume that in a multicrystalline wafer, always a number of unfavorable orientations occur which lead to rather deep cracks. These deeper cracks are responsible for the lower fracture toughness of the wafers. Whether these results completely explain the different behavior of these two materials is not quite clear yet, but fixed abrasive sawing is industrially not yet suitable for

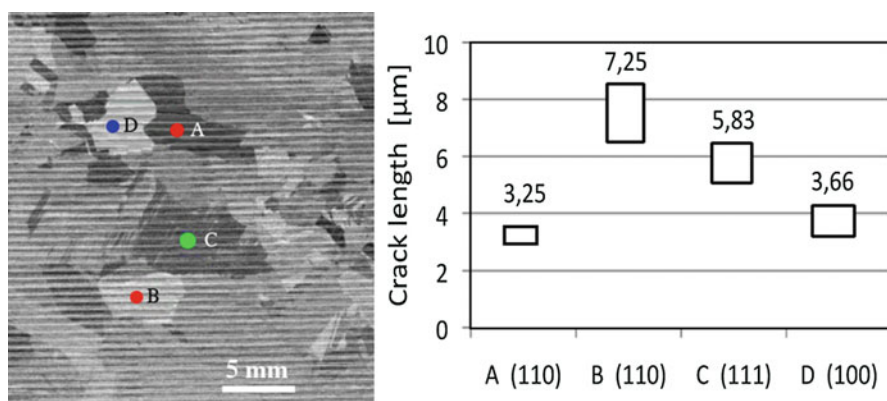


**Fig. 15** Microcrack depth dependence on the grain orientation in a multicrystalline wafer. The grain orientations are normal to the wafer surface. The optical image of the wafer surface also shows the periodic grooves lines, which are typical for fixed abrasive sawn wafers



multicrystalline silicon. There is however the hope that one can solve these problems in the future and can introduce the fixed abrasive sawing technique later for multicrystalline silicon as well.

## Basic Surface Damage Mechanisms

The investigations of the damage pattern on sawn wafers have shown that they consist of many, mostly separated, single events with the abrasive particles. In the case of the sawing with loose abrasives, it is the indentation of a sharp particle into the crystal surface, in the case of fixed abrasive sawing the scratching of a particle over the surface. The basic difference is the direction of the applied force on the particle, which is vertical in the first case and oblique in the scratching mode, because of an additional, horizontal force component (Fig. 13). This induces different micromechanical processes, which can be studied quantitatively with single particles and are described in more detail in the following. For a review see ref. (Möller 2008, 2014). A number of such investigations have been carried out and yield a good picture of these processes. The results help to understand many features of the sawing process as described in ► Chap. 11, “Wafer Processing.” The experiments and the main results of the single event processes are described next.

### Single Indentation Tests: Loose Abrasive Sawing

The individual particle interaction processes have been studied quantitatively by indentation experiments. A geometrically defined sapphire or diamond tip is indented under load into a silicon surface. The resulting damage pattern depends on the shape of the indenter tip. A sharp tip, which is appropriate to investigate the interaction of abrasive particles, is used in a Vickers indenter. It uses a square-shaped tip with an opening angle of  $136^\circ$ . A variation of the Vickers test is the Knoop test, which uses a rhombohedrally shaped tip with an opening angle of  $130^\circ$  for the short edge and  $172,5^\circ$  for the long edge. From the large number of results that have been published for silicon and other brittle materials (Evans and Marshall 1981; Lawn 1993; Li and Bradt 1996), the following sequence of events can be deduced (Fig. 13a).

After indentation and at low loads, a plastic zone forms first, which leads to a permanent pit in the surface (Fig. 16). In the case of the Vickers indenter, the diagonal of the square-shaped pit  $a$  depends on the applied load  $F_p$  and can be described by the following equation:

$$a = \left( \frac{\alpha}{4H \tan[\varphi]^2} F_p \right)^{1/2} \quad (1)$$

where  $H$  is the hardness of the material,  $\varphi$  the opening angle of the indentation tip, and  $\alpha$  a geometry factor. Measurements for monocrystalline silicon at room



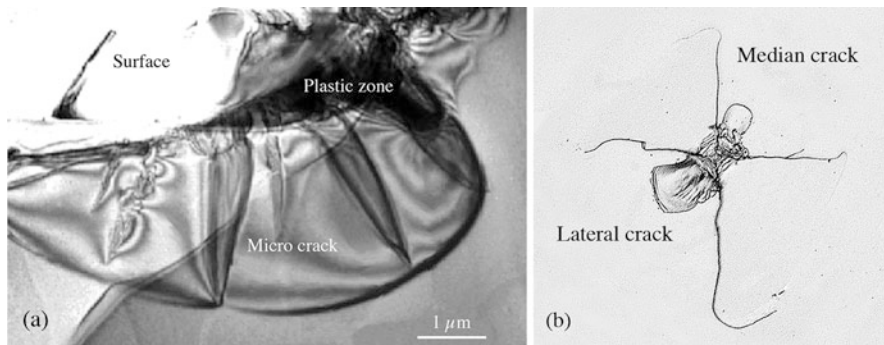


**Fig. 16** Transmission electron microscopy image of the plastic zone and a microcrack at a cross section of an as-sawn wafer (a). Optical micrograph of median and lateral cracks around a Vickers indentation at the wafer surface (b). The extension of the plastic zone corresponds to the extension of the indentation pit

temperature yield  $H = 10.6$  GPa (Hamblin and Stachowiak 1995; Poon and Bushan 1995). This dependence has been found for many brittle materials and also been verified by numerous numerical calculations (Lawn 1993). It is usually used to determine the hardness of a material from the extension of the indentation pit. The plastic zone in the vicinity of the indentation pit is a region where the crystalline silicon is transformed under pressure into high-pressure phases (Gogotsi et al. 1999; Jang et al. 2005; Gassilloud et al. 2005). For instance, under loading at 11.8 GPa, an endothermic transformation to metallic silicon (Si II) occurs. A metallic phase can deform plastically, which leads to a high density of dislocations in this area (Fig. 16a). These regions are very thin ( $< 100$  nm) so that the extension of the plastic zone is not much larger than the indentation pit in Fig. 16b. Raman investigations have also shown that upon unloading, a back transformation of the high-pressure phases takes place into the amorphous silicon phase if the stress release is fast (Domnich and Gogotsi 2002).

It is of more interest, however, when the load is increased further and the material breaks. Different types of crack systems can occur depending on the crystal orientation and the tip geometry. So-called median directly under the load tip and/or radial cracks more at the side extend vertically into the surface. These are halfpenny-shaped cracks with a diameter  $c$  on the surface. The force dependence of the median crack length  $c$  is given by

$$c = \left( \frac{\beta}{K_c} F_p \right)^{2/3} \quad (2)$$

where  $K_c$  is the fracture toughness of the material and  $\beta$  a geometry factor. For the Vickers indenter, the parameter  $\beta$  for monocrystalline silicon is  $\beta = 2$  and for a Knoop indenter  $\beta = 4/\pi$ , while the best fit value for multicrystalline silicon  $\beta = 1/7$  varies considerably in published data. In large-grained polycrystalline silicon,  $K_c = 0.75$  MPa m<sup>1/2</sup> (Chen and Leipold 1980; Anstis et al. 1981).

When the load is removed, the stress difference between the highly strained plastic zone and the stress-free crystalline silicon leads to the formation of lateral cracks. When they reach the surface, a piece of material is removed, in Fig. 16b to the side of the indentation pit. This process is responsible for the material removal in the sawing process. The volume  $V_o$  of the chipped material depends on the extension and depth of the lateral crack. The depth is approximately equal to the depth of the plastic zone (see Fig. 13a).  $V_o$  has been determined experimentally and depends on the applied load according to

$$V_o = \gamma F_p^{2.2} \quad (3)$$

where  $\gamma$  is a geometry factor (Möller and Funke 2003). The volume  $V_o$  for a single indentation event enters into Eq. 5 for the sawing rate in ► Chap. 11, “Wafer Processing.” This is justified if the single event is well separated, which is actually observed.

Since the formation of the median/radial cracks occurs before the chipping, these cracks partially remain in the crystal surface at the side of the sawing channel since they extend deeper into the bulk. They form the subsurface saw damage (SSD) of the as-sawn wafers (Chauhan et al. 1993; Verspui et al. 1995; Cook 1990). When material chips away, the plastic zone is basically removed. Therefore back-transformed, amorphous silicon is not observed on the surface wafers sawn by loose abrasives.

The roughness of the wafers is determined by the depth of the indentation after material is removed. This is basically the depth of the plastic zone, which can be calculated from Eq. 1, if the indentation pits are well separated. If they overlap, the difference between minimum and maximum surface height also depends on the density of the indentation events. This explains that microcrack depth and roughness both depend on the applied force  $F_p$  and are correlated, but the relationship between both quantities also depends on the local number of indenting particles if overlapping occurs. This may explain the observed different roughness vs. SSD dependencies in Fig. 8.

## Single Scratch Tests: Fixed Abrasive Sawing

There is general agreement that in fixed abrasive sawing, material removal occurs by scratching the diamond particles over the crystal surface. Figure 7b showed the typical damage pattern of an as-sawn wafer. It consists of many parallel scratches along the sawing direction. The distance and depth of the scratches depend on the sawing conditions. The microcrack damage below the surface can be determined on the polished, beveled surface parts of the image, but it is difficult to quantitatively investigate the damage structure. It is therefore useful to analyze single scratches, which are produced under controlled conditions.

Simple scratching tests use a sharp needle which is moved with a constant velocity and load over the crystal surface. The scratch velocities are in the range

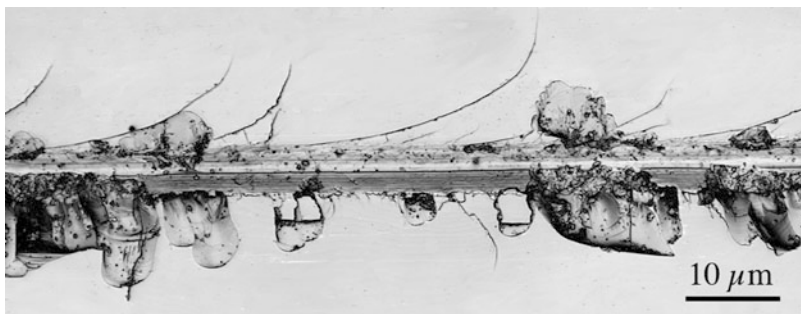


**Fig. 17** Optical image of a single scratch showing a groove in the center, lateral (parallel to the surface), and median cracks (inclined to the surface) to the side

of centimeters per second, which is much lower than the speeds, which occur in diamond wire sawing. High-speed scratching can be achieved by rotating a wheel with a single particle on the outer rim and indenting the particle tip once per rotation into the crystal surface. Using such a method, single scratches were produced on a monocrystalline (100) silicon surface at speeds of meters per second (Würzner et al. 2014a). The forces have been measured vertically (indentation force) and horizontally (friction force) to the surface during scratching. Figure 17 shows a typical scratch after such a test. It consists of a shallow groove in the center, areas where material has been chipped away on the side (lateral cracks) and traces of microcracks, which extend into the bulk. In the groove itself, material is pulverized and the debris spread in the vicinity.

The shape and direction of these microcracks can be observed by the beveled surface technique after polishing and etching (Fig. 18). This allows one to determine the maximum depth of the microcracks. The observed pattern resembles the patterns that are observed on as-sawn wafers. An important feature is the periodicity (Würzner et al. 2014b; Möller 2014) which can also be seen on cross sections parallel to the scratch direction by scanning electron microscopy (Fig. 19b). This pattern is explained by the following sequence of events.

In the first step, the scratching tip is indented into the surface by the back force of the bowed wire. Since the tip is also pulled by the wire in wire motion direction, the resulting force points obliquely into the bulk (see Fig. 13b). The stress, which builds up, has not been calculated so far, but one can assume that it consists of tensile stresses behind the tip and compressive stress components in front of the tip. The stresses depend on the tip shape and the orientation of the crystal. This could be confirmed by the experimental results. The stresses eventually will lead to cracking. Usually one can expect a crack directly in front of the moving direction and several cracks to the sides. Because of the oblique force, some cracks will chip material away mainly in front of the tip. Once the material breaks, the tip can move a certain distance before it is blocked again. Then the process of stress buildup and breakage repeats itself.

The lengths of the cracks depend on the applied forces both in wire direction and in the vertical (indentation) direction. Quantitative measurements yield a crack length

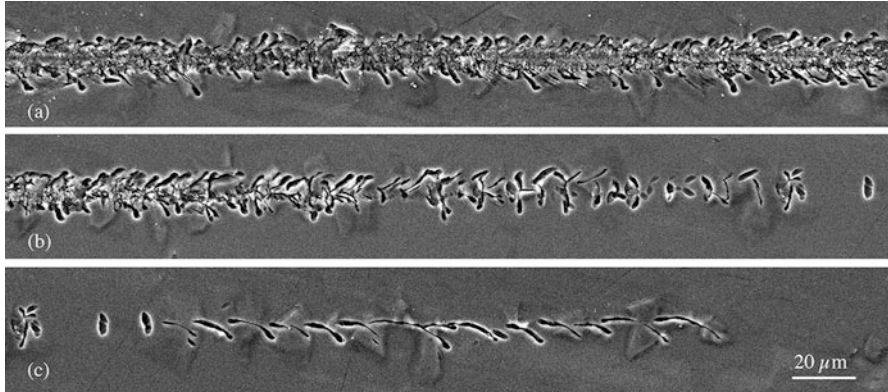


**Fig. 18** Single scratch test showing periodic crack patterns. The upper image shows the damage at the surface. In the images (b and c), the surface is inclined by about  $1^\circ$  from left to right. The right-hand side of image (c) is about  $10\ \mu\text{m}$  below the surface

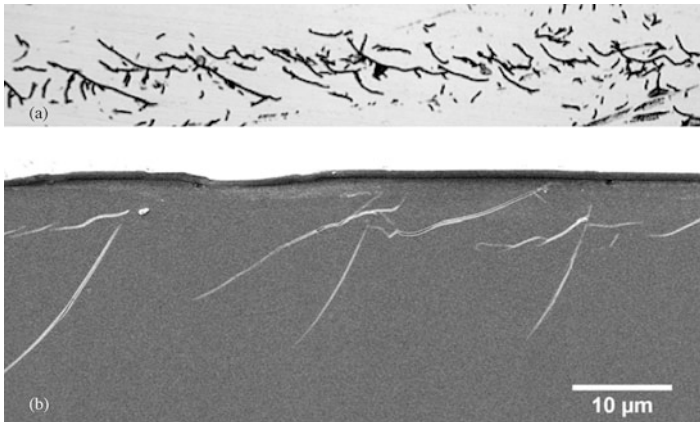


**Fig. 19** Traces of microcracks from a single scratch on a diamond sawn wafer showing periodic crack patterns. The center groove has been removed by etching (a). Scanning electron microscope image of the cross section of a wafer showing the periodic microcrack pattern (b)

dependence on the applied force on the particle tip as given in Fig. 20. One can see that different curves are obtained for different particle shapes. Particles with sharp tips (needles) yield deeper cracks compared to the rounder particles on a diamond-coated wire. A slight dependence on the crystal orientation was also observed. The force on a single abrasive particles  $F_p$  in diamond wire sawing can be estimated from the measured total force on the wire  $F_n$  and the average number of simultaneously scratching particles  $m$ . Estimations show that  $F_p = F_n/m$  is less than 100 mN; therefore microcrack lengths less than  $10\ \mu\text{m}$  can be expected from these curves. This is consistent with the observed microcrack depths on diamond wire sawn wafers.

In the scratching mode, highly strained regions occur in front (compressed region) and behind (tensile region) the indenting tip (Fig. 13b). If the stresses are high enough, the silicon diamond lattice will be transformed into one of the high-pressure phases of silicon, which have already been observed under indentation. When the particle tip moves forward and the stress is released fast, as is expected here, the crystal lattice will transform back into the amorphous phase.

Since chipping occurs mainly in front of the moving tip, any phase changes that occur in this part of the material will be removed. But phase changes behind the moving tip could remain. This may explain why thin amorphous regions have been observed on the surface after fixed abrasive sawing contrary to loose abrasive sawing.

The amount of material which is removed by single scratch consists of the volume of the groove and of chipped regions at the sides. A quantitative investigation of the material removal of a single scratch has yielded the results in Fig. 21 where the average cross section of the scratch  $A_{sc}$  is plotted as function of the indentation force on a single particle  $F_p$  (Würzner et al. 2015). Considering the force range in diamond

**Fig. 20** Experimentally determined crack length dependence on the force applied in indentation direction. Single scratch tests with different particles and tip shapes. For comparison a value is included (marked by “sawing”) which is obtained from a fixed abrasive sawn wafer

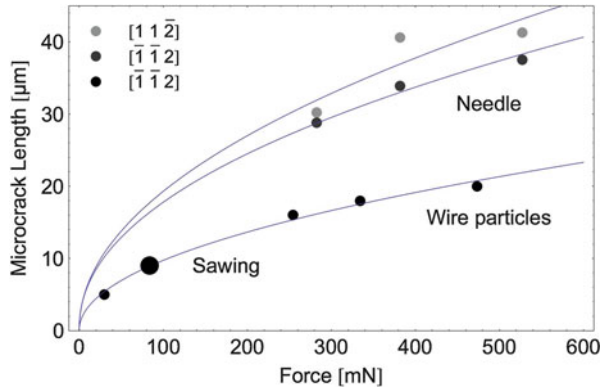
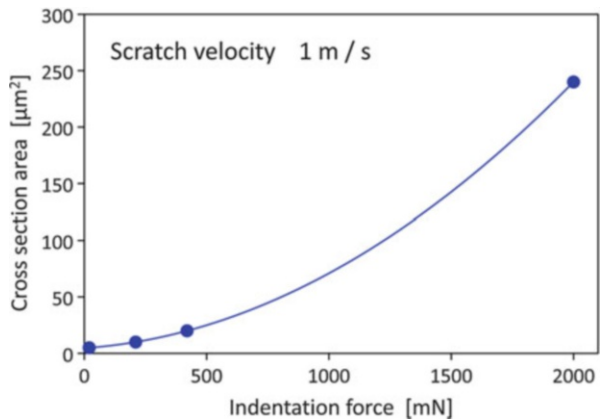


**Fig. 21** Cross-sectional area of the groove of a scratch (including the chipped areas) as a function of the applied indentation force



wire sawing of  $F_p < 100$  mN, the cross section  $A_{sc}$  is approximately linearly dependent on the applied force  $F_p$ . This dependence has been used in Eq. 16 in ► Chap. 11, “Wafer Processing,” which yielded a Preston-like equation for the sawing rate of fixed abrasive sawing.

## Fracture Behavior

In mass production the loss of wafers due to breakage is an important issue, since it limits the productivity. Along the processing chain from wafering to the final module, there are many handling steps which stress the wafer mechanically. The fracture stability is therefore important, particularly, when the thicknesses are reduced further in the future. Several tests have been developed to determine the fracture stability. The standard methods are deformation test where the wafers are bent in a controlled way until it breaks (Funke et al. 2004; Orellana Pérez 2009, 2014). The most common are the four-line bending (Fig. 22a) and the ring-on-ring test. In the ring-on-ring test, the rings can also be replaced by balls to reduce the contact area with the wafer (Fig. 22b). The tests differ in the way how stress is applied across the wafer surface and the edges. In the four-line bending, the center of the wafer is strained along a line across the surface. In addition two opposite edges of the wafers

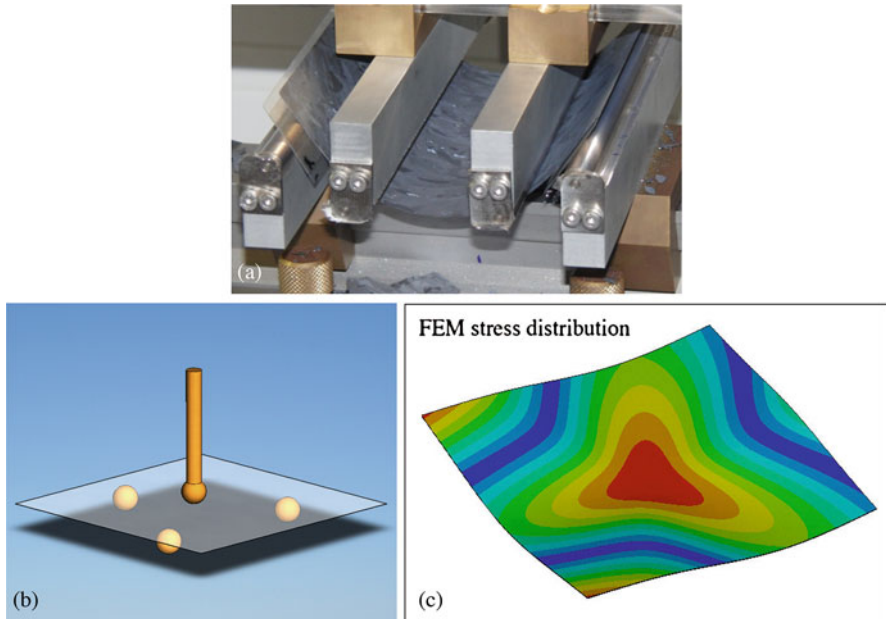


**Fig. 22** Different fracture tests: (a) four-line bending, (b) ball-on-three ball, (c) FEM calculation of the stress distribution in the center of the wafer for the ball-on-three-ball test



are also strained. In the ring-on-ring or ball-on-three-ball test, only the center area is strained, whereas the edges remain unstrained. Therefore the comparison of these two tests allows one to separate the influence of the edges and the wafer surface. Other test geometries have also been applied, such as the twist test. In this case all four edges are strained.

Because of the brittle behavior of silicon, the fracture occurs by the propagation of cracks. They are initiated at defects in the material, in the case of high purity silicon at pre-existing cracks either on the surface or at the edges of the wafers. Depending on their length  $c$ , a certain threshold stress  $\sigma_f$  is required to open them completely and induce breakage. According to the Griffith criterion, they are connected by

$$\sigma_f \sqrt{c} = \sqrt{\frac{2E\gamma_s}{\pi}} \quad (4)$$

where  $E$  is Young's modulus and  $\gamma_s$  the surface energy of the material. The fracture therefore begins at the longest cracks and in the regions of highest stresses.

In all test methods, the applied force and the corresponding deformation or strain are measured until the wafer breaks. To determine the regions of highest stresses, one has to calculate the stress distribution in the wafer from the deformation state and the applied force. A difficulty in these tests is that for thin wafers very large deformations can occur such as in Fig. 22a. This requires in general comprehensive finite element calculations for each deformation mode and wafer geometry, since linear approximations of the stress-strain relationship, which are valid for low deformations only, cannot be applied anymore (Fig. 22c). For a standard wafer size, the results of FEM calculations for wafers still depend on the thickness. Since the thickness varies even in batch of wafers from the same cut, it would be very time-consuming to make a FEM calculation for each wafer. One can derive however a master force-strain curve, which is normalized to a standard thickness and depends on the thickness  $d$  by a simple power law  $d^3$ . This can be applied then to the different thicknesses of each wafer. The determination of the fracture strength of wafers is however still an elaborate method.

Since microcracks are formed during the material removal by the wire sawing process, the mechanical stability of the wafers is mainly determined by these microcracks in the subsurface damage zone and at the edges. The "weakest link," which is the longest crack in the region of highest stresses of the deformed wafer, will cause mechanical failure when the wafer is loaded with stresses exceeding the threshold strength  $\sigma_f$  of that crack. When deforming different wafers in a batch of comparable wafers, the fracture stresses will still vary because of the statistical distribution of the pre-existing crack lengths. Statistical considerations based on a Poisson distribution of crack lengths result in a Weibull distribution of fracture stresses

$$F(\sigma) = 1 - e^{-(\sigma/\sigma_0)^m} \quad (5)$$

Here  $F(\sigma)$  is the failure probability for a stress;  $\sigma$ ,  $\sigma_o$  is the characteristic fracture stress, where 63% of all wafers are broken; and  $m$  is the Weibull parameter which characterizes the width of the fracture stress distribution. A narrow distribution has  $m$  values around 1–3. Usually at least 30 wafers sawn under the same conditions and of comparable properties should be tested for a statistically significant Weibull analysis. The characteristic fracture stress  $\sigma_o$  is taken as the fracture stress value of wafers sawn under the same conditions.

Experimental investigations showed that microcracks at the edges of wafers can cause higher failure than microcracks on the surface, because they are usually longer. In the wafering process, the edges of the wafers are the side wafers of the ingots out of which they are sawn. It is therefore necessary to polish the side faces before the sawing as described in ► Chap. 11, “Wafer Processing.” By such a treatment, one can reduce the usually dominant fracture at the wafer edges to an acceptable level.

Figure 23 shows four-line bending test results for batches of as-sawn wafers and wafers where the damaged surface layers are removed by etching. The data are usually presented as Weibull plots:  $\ln(1/(1-F))$  vs.  $\ln \sigma$ , which gives straight lines. Deviations from the linearity indicate that fracture is not only determined by the pre-existing microcracks but that other factors contribute to the failure, such as inclusions in the material. The removal of the microcracks in the damaged layer and edges increases the fracture strength by a factor of 3–5. As-sawn wafers are therefore rather fragile. Since they run through a number of handling steps (cleaning, measuring, transportation, etc.) before solar cell processing, they can easily break then. A low saw damage is therefore essential to obtain a high yield in production.

In the case of loose abrasive sawing, the fracture stresses  $\sigma_o$  of as-sawn wafers are usually between 140 and 170 MPa. They are lower for SiC powders with larger

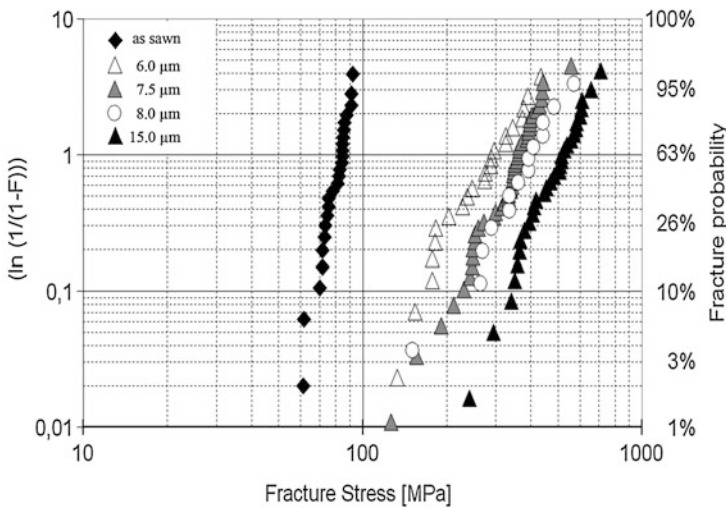


**Fig. 23** Weibull plots (failure probability) for as-sawn and etched wafers. The thicknesses of the removed damage layers are indicated



average grain sizes, which indicate that coarser particles cause longer microcracks and a deeper damage depth.

Fixed abrasive sawing yields usually higher fracture stresses  $\sigma_o$  around 160–200 MPa. There is however an orientation dependence of the fracture stress, since bending the wafers along the groove lines causes lower values than bending perpendicular to it. Therefore in wafer production no large difference in the breakage rate has been observed between loose and fixed abrasive sawn wafers.

If the fracture strength of the wafers is determined by subsurface saw damage only, it does not depend on the wafer thickness if the sawing conditions are the same. However it requires less force to induce the same fracture stress in a thinner wafer. Therefore the handling of thinner wafers is more prone to breakage and has to be done more carefully in a production environment.

---

## Wafer Contamination

Good wafers are cleaned after sawing and then supplied to the cell manufacturer. Before the solar cell process, the surface damage has to be removed by etching. In general, the etching is also used to give the surface a certain texture to reduce the optical reflectivity of the solar cell. The etching process differs for mono- and multicrystalline silicon and depends on the surface profile. It requires, for instance, a different process if the wafers are sawn by fixed abrasive wires instead by loose abrasives. The impact of the difference in surface characteristics also seems to be dependent on the cell process. Some manufacturers seem to be able to utilize fixed abrasive wafers with only minor cell process changes, while others experience challenging problems, for instance, with the texturing process.

The etching rate of fixed abrasive sawn wafers has been reported to be lower than for loose abrasive sawn wafers. It has been suggested that this is due to amorphous silicon on the surface (Bidiville et al. 2009) and a lower roughness (Holt et al. 2010). The texturing of monocrystalline wafers by anisotropic etching is however less dependent on the wafer surface morphology. For multicrystalline wafers the texturing of fixed abrasive sawn wafers becomes challenging, due to the use of an acid-based isotropic etch, which has been designed to develop the texture from the slurry-related pits on loose abrasive sawn wafers. The chemistry behind etching and texturing of silicon wafers is rather complex and will be discussed in great detail in ► [Chap. 12, “Wafer Cleaning, Etching, and Texturization.”](#)

Another wafer quality element, which is relevant for texturing and eventually for minority carrier lifetime in the solar cell, is the wafer cleanliness. An apparently clean wafer can be full of fingerprints or other stains after texturing. This is due to residues from organic compounds on the surface. The detection of organic traces and their chemical composition is a difficult task because of the very low concentrations.

Even more important are metallic impurities. The wear of the wire leads to an enrichment of the slurry or coolant with metal components of the wire. In the case of the straight and structured wire, these are mainly Cu and Zn from the coating of fresh wire; Fe and alloy elements of the core wire such as Cr, Ni, B, or P; etc. For

diamond-coated wire, one has higher concentrations of Ni from the coating layer but much less Fe and other impurities from the core wire. A further source of contamination is from the beam, in which the ingots are glued and in which the wires cut at the end. Different beam materials are used, but glass plates are very common. Al, Na, K, and Ca are typical elements which can be introduced here in relatively high concentrations. Altogether one has about 1–2 wt% of contamination impurities.

How much of these elements is actually deposited on the wafer surface depends on the wafer cleaning procedures and the chemistry in the slurry. It is therefore not sufficient to analyze the impurity content in the slurry or coolant, but one also has to measure the contamination on the wafer surface. Because of the very low concentrations, one needs sophisticated detection methods here such as inductively coupled plasma mass spectroscopy (ICP-MS). For comparison Table 1 gives some results for the main impurities from loose abrasive and fixed abrasive sawn wafers Bye et al. (2011). They show that except for Ni, which can be explained from the wire coating, all other measured elements are lower for sawing with diamond-coated wires. Whether this is generally the case or is just a result of the special cleaning procedures in these cases is not clear yet.

The transition metals are even in low concentrations very detrimental in silicon and deteriorate the minority carrier lifetime. Al, B, and P are doping elements in silicon and could change the doping level. Although the wafers are cleaned and etched after sawing, there are indications from solar cell processes that remnants of these elements are introduced into wafers. It is thus necessary to investigate possible paths from the slurry onto the wafer surface and into the wafers. Most transition metals are only introduced at higher temperatures. In the sawing process, higher temperatures up to eventually 150 °C occur in the sawing channel only locally and for a very short time. A second high-temperature step (below 150 °C) may occur in the cleaning baths. Particularly copper has a high diffusivity and may be introduced into the bulk silicon. One also assumes that even after the wafer cleaning, traces of these elements remain together with very fine silicon saw dust on the rough surface and inside of the microcracks. Even after the damage etches before the solar cell processing, some of these impurities may remain in very deep cracks and diffuse into the bulk silicon during the further processing steps.

Since there is a general lack of characterization methods for quantifying wafer cleanliness, the contamination problem is still in an early stage of investigations. But

**Table 1** ICP-MS results of impurity concentrations on a wafer surface of fixed abrasive sawn (FAS) and loose abrasive sawn (LAS) wafers. For some impurities the detection limit of the method is given as an upper limit for the concentration

Element	FAS ( $\times 10^9 \text{ cm}^{-2}$ )	LAS ( $\times 10^9 \text{ cm}^{-2}$ )
Fe	1000	50.000
Cu	200	30.000
Ni	20	< 8
Zn	< 40	50
Ca	300	600
Na	< 100	200

in the industry, one tries already to prevent the elements to reach the wafer surface by keeping them in the slurry or coolant. This can be done by certain additives, which form compounds with these elements and bind them. In the cleaning process, they may then be removed more easily. At present, only the following solar cell processes show, if cleaning procedures have succeeded or are more efficient.

---

## Characterization of Wires, Slurries, and Coolants

For a long time, the characterization of wires has not attracted much interest, since in the standard slurry sawing process with straight steel wires, they are used only once and discarded then. The main properties of interest are the fracture strength, the wear, and the cost. The wire wear has some importance because the thickness of the wire decreases from the beginning of the cut to the end and correspondingly the strength as well. With the further development of structured and diamond-coated wires, new properties have to be quantified and corresponding characterization methods to be developed.

In slurry-based sawing, the characterization and improvement of the slurry always play an important role, because it can have a strong impact on the sawing performance and is an important cost factor. The technological change from straight to structured and diamond-coated wires requires now the development of new fluid systems. In fixed abrasive sawing, the fluid mainly has the task to cool and remove the silicon kerf. PEG with a higher water content or water with some additives are used here. Because of the cost advantages of water-based fluids, one also tries now the replacement of PEG by water in the case of loose abrasive sawing with structured wires. This requires the selection of additives to improve the SiC transport and other properties.

### Wires

The fracture strength of steel wires depends on the material properties and the homogeneity of the wire diameter. Because of the length of several hundred kilometers on a single spool, it is not easy to investigate the entire length. One method is to measure the diameter optically, while the wire is spooled at a high speed from one spool to another. Such measurements can investigate the uniformity of the wire diameter but do not allow to find local material faults, such as inclusions, which can cause wire rupture. Therefore the risk of a material-related breakage of a wire cannot be avoided completely.

The wire wear is even more important because the thickness of the wire decreases from the beginning of the cut to the end and correspondingly the strength as well. Figure 24 shows the decrease of the diameter of the wire as function of the cutting length in silicon. The cutting length is the distance, over which a wire segment is in contact with the silicon material during cutting. In a typical wire web with about 2000 wires, a segment of the wire has to cut through about 300 m of silicon before it

**Fig. 24** Wear of the wire diameter as a function of the cutting length in silicon

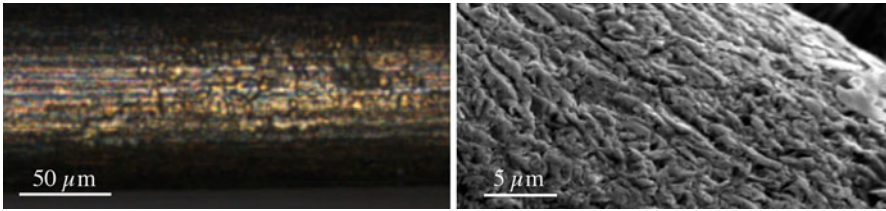
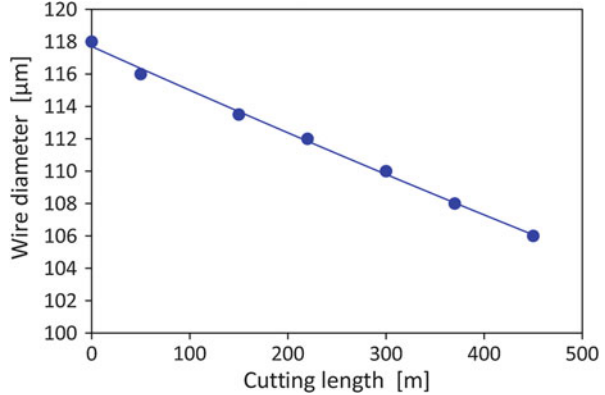


**Fig. 25** Surface structure of a used steel wire: optical image (left), scanning electron microscope image (right)

leaves the ingot. The diameter decreases then by about 8–10  $\mu\text{m}$  but may not be uniform over the cross section. Investigations of the wire surface show a rather uniform surface structure, which can be explained by the grinding action of all SiC particles in the slurry (Fig. 25). This occurs only on the contact side of the wire, but since the wires rotate during winding up and cutting, the wear occurs mostly over the entire wire surface. A wire needs a good wear resistance to this erosion process at the surface. Microhardness measurements on wire cross sections did not show differences between the core and the surface, which indicates that wire manufacturers do not especially modify or harden the surface in the wire drawing process.

In addition to the wear, the wire is also plastically deformed during the cutting. This occurs primarily during the first 100–200 loops in the wire web (Meißner et al. 2014). If a wire segment between the guide rollers is elongated, the wire tension force is reduced. The cutting segments of the wire respond by changing the local bow, which is therefore not uniform for all wire segments in the web. These property changes in one cut have an impact on the wafer thickness and the quality of the wafer surface. The first wafers from an ingot, where the wire enters, have usually better properties compared to the wafers from the end. With the decrease of the wire thickness, the fracture strength and wear become more significant. Recent developments have shown that wires with thicknesses down to 60  $\mu\text{m}$  can be made. Such a wire cannot reduce its diameter much further. The development of a better wear

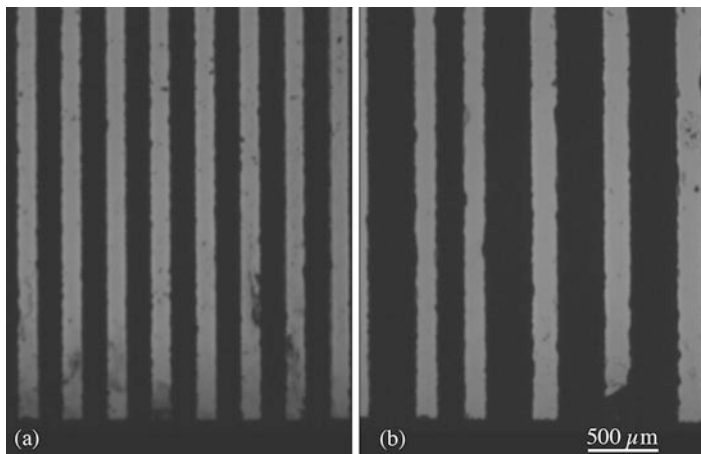


**Fig. 26** Side view of wafers after a cut showing the wafer thickness and the distance or kerf width. The wafers are still fixed to the beam on the top (not shown here). (a) Homogeneous cut for a wire distance of 300  $\mu\text{m}$ , (b) varying thicknesses and distances for a wire distance of 250  $\mu\text{m}$  because of wire pairing

resistance of the wire and the choice of other sawing parameters, e.g., a reduced input wire tension, are required here.

With the decrease of the wire diameters, the distance between the wires, which is determined by the groove distance on the guide rollers, has to be reduced to maintain the same wafer thickness. It turned out, however, that the smaller distance of the wires can have the effect that neighboring wires are attracted to each other before they enter the ingot. This leads to different thicknesses of the wafers. Figure 26 shows an array of wafers and the sawing cuts in between in the normal case for a wire distance of 300  $\mu\text{m}$  and for a distance of 250  $\mu\text{m}$ . In the first case, a uniform wafer thickness and kerf distance occur; in the second case, thickness and distance vary. It is assumed that the reason for this behavior is that neighboring wires become attracted to each other because of capillary forces before they enter the cutting channel. Numerical simulations have confirmed that the slurry film between the wires in the web can exert capillary forces, which are high enough to attract neighboring wires. Important for the effect are the slurry viscosity and the amount of slurry which is available: a high slurry flow and a low viscosity (or temperature) are necessary to avoid the effect. With decreasing wire diameters and wafer thicknesses, this problem will become more severe.

Since the local bow and the distance of the wires in a wire web yield information about the local wire status, measurement methods have been developed to monitor the vertical and horizontal positions of the wires. This gives better control during a cut and allows to detect faults before the wire actually breaks. Such methods are however not established in industrial sawing machines.

The characterization of structured and diamond-coated wires is more difficult. In the first case, one has to develop methods to specify the bends on the wires

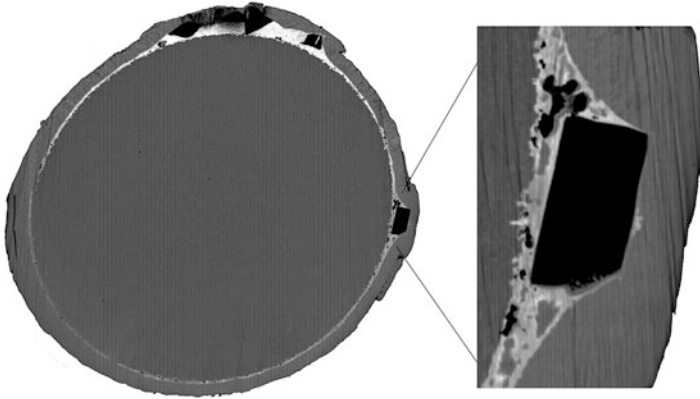


**Fig. 27** Scanning electron microscopy image of the cross section of a nickel-coated steel wire with embedded diamonds. The wire diameter is 120  $\mu\text{m}$

regarding distance and direction. Since sawing with structured wires is industrially not widespread today, there are no systematic investigations available. This is different for diamond-coated wires which have attracted more interest. The important features are the abrasive particle distribution and the size or height on the surface. Depending on the fixing method, the particles are more or less embedded. The cross section of such a wire shows some diamond particles which are partly covered in the coating layer (Fig. 27). In other cases the particles may protrude more out of the layer. The coating on the particles also wears off during the sawing, and the particles stick out higher. This changes the cutting performance. Considering the scratching mechanism, one needs to specify the particle density and the height distribution of fresh and used wires. Optical investigations by confocal or scanning electron microscopy allow to obtain such information on small wire segments, but to screen larger areas or longer segments of a wire requires faster characterization methods in the future.

## Slurries and Coolants

The role of the carrier fluids in the wire cutting is quite complex as has been shown before and not fully understood. It is therefore also difficult to determine which properties are important and have to be characterized well. In slurry-based sawing, PEG is the main carrier fluid for the SiC powders, but oil is also good and has been used in the past. If PEG can be replaced by water mixed with additives is still under investigation. In fixed abrasive sawing, either glycol-based fluids mixed with water or water-based fluids with additives are used. The optimum fluid design remains a challenge for the future. Some aspects will be discussed next.

## SiC Slurries

The main focus is on the viscosity, which is usually measured by conventional viscosimeters. Assuming a laminar flow in the thin sawing channel, the fluid velocity increases linearly from zero (at the crystal side) to the wire velocity (at the wire side). The corresponding shear rates are very high  $>10^5 \text{ s}^{-1}$  and several orders of magnitude higher compared to the shear rates in standard viscosimeters. If one assumes that the slurry is a Newtonian fluid, the viscosity is independent on the shear velocity (here equal to the wire velocity). This is the case for water and PEG, but the fluid contains a high volume fraction of particles (SiC, Si) and may become a non-isotropic Newtonian fluid. It could be shown however experimentally that the shear rates do not deviate much from the values measured at low rates in standard viscosimeters.

The viscosity increases with the concentration of SiC and if the particles become finer (Fig. 8) (► Chap. 11, “Wafer Processing”). Before mixing carrier fluid and SiC powder, the SiC needs to be well characterized regarding size distribution and shape. Several experimental techniques are available to measure the size distribution of powders, for instance, by laser diffraction. Commercial SiC powders are specified mainly by the center part of the size distribution. Typical parameters of today’s SiC powders have been given in Table 1 in ► Chap. 11, “Wafer Processing.” Considering the particle interaction during sawing, only the largest particles in the distribution are indented. Their number is relatively small ( $< 1\%$ ) and difficult to measure; therefore this part of the distribution is not specified separately. It is thus possible that a SiC powder is within the specification but does not work properly because the size distribution of the larger particles differs.

It is even more difficult to characterize the essential particle features such as the shape and number of edges and tips of the SiC particle. This can only be done by direct observation in an optical or scanning electron microscope on a few particles (Fig. 28). Available commercial techniques for the characterization of a larger number of particles only allow to determine the deviation of the particle shape from the spherical shape (circularity). But this may not be sufficient for a complete characterization.

SiC is a polytypic material and can occur in many (up to 250) different crystal structures (Ramsdell 1945). The major ones are the cubic 3C and the hexagonal 4H and 6H structures. Commercial SiC powders mostly have more than 70% of the 6H structure, with different contributions of 4H and 3C. No systematic studies are available regarding which material composition has advantages here. In summary one must admit that some important properties of a SiC powder, such as particle shape and sharpness and large particle fraction and crystal structure, are not adequately specified. Therefore the wafer producer has to test a product regarding the sawing performance before using it in mass production.

A polyethylene glycol is a chain molecule with a certain number of the ethylene glycol base structure. The commercial products are mixtures of molecules of different chain lengths from about 1 to 12. For instance, PEG 200 mainly has chain lengths



**Fig. 28** Scanning electron microscopy image of a SiC particle

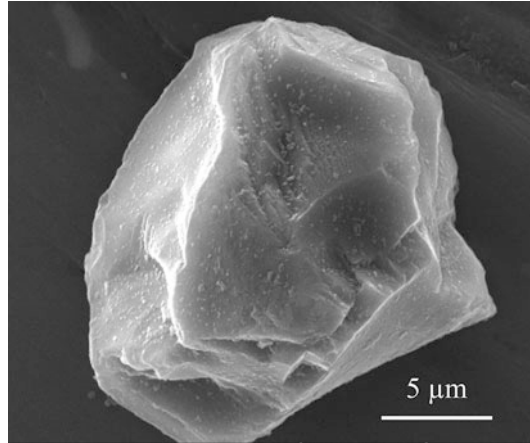


**Table 2** Viscosities of carrier fluids at 20° C

Fluid	Viscosity [Pa s]
PEG 200	0.07
PEG 300	0.09
Oil	0.06–0.2
Water	0.001

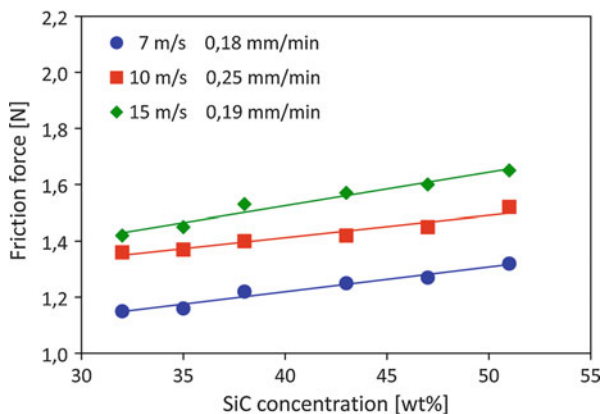
between 3 and 6. Depending on the composition of the mixtures, different viscosities are obtained. Oils are also mixtures of different components, but the composition of commercial products is usually not known exactly. Table 2 lists some of the viscosities of carrier fluids that are used in the sawing process. During cutting with PEG, the composition of the mixture can change and the cutting performance degrade. Since in the slurry recycling process the original composition and viscosity have to be reestablished, one needs to determine the fraction of each component with a certain chain length and renew the original composition.

PEG and SiC powders have to be thoroughly mixed before application. Which concentration is suitable has to be determined experimentally. The sawing rate is almost independent on the SiC concentration between 30 and 55 wt%, but the composition has an impact on the friction force (Fig. 29). Some studies have also shown that new SiC and PEG yield less friction compared to used material. Since most of the industrially used slurry is recycled, the friction forces do not vary that much. It is however clear that higher friction forces increase the energy consumption of the sawing machine, which is thus a cost factor.

Another factor is the temperature dependence of the PEG slurry. With the increase of the temperature along the sawing channel, the viscosity decreases considerably because of its strong temperature dependence. Correspondingly the transportation capability for particles is reduced which can lead to the occurrence of saw marks (► Chap. 11, “Wafer Processing”). One can reduce this effect either by using slurries



**Fig. 29** Measured friction forces as a function of the SiC concentration in a PEG 200/F800 slurry for different sawing conditions



with less temperature dependence or by reducing the friction, which is mainly responsible for the temperature increase.

Other properties of the slurry, such as the water absorption tendency (hygroscopy) and the wetting of the wire, have also been investigated. PEG is hygroscopic and absorbs water over time. That changes the viscosity and wetting behavior. Hygroscopy plays a special role when the air humidity is high, such as in many Asian countries.

Viscosity, friction, temperature dependence, hygroscopy, and wetting behavior depend on the properties of the carrier fluid, the particle size distribution, and the volume fraction. In addition the recycling possibilities and the cost have to be considered. Because of these many parameters, the optimization of the slurry system is a difficult task and requires comprehensive test series. This is mostly done internally in the industry, and the result is usually kept confidential. But many effects and factors, which play a role, are certainly not completely understood.

The sawing with structured wires and PEG slurry improves the particle transport but still requires the adjustment of the various slurry parameters. The replacement of PEG by water is possible, but it is cost-effective only when the additional cost of the necessary additives is lower. Water also has the drawback that it vaporizes quickly already inside of the sawing machine. The remaining SiC particles and Si debris can form a sludge, which can clog filters, tubes, and other critical parts of the sawing machine and requires regular, intensive cleaning. To some extent one can avoid this by modifying the fluid supply system and spraying additional water inside of the machine. It may be however that water-based systems as carrier fluid for SiC powders may be too difficult to handle.

## Coolants

In fixed abrasive sawing, the particle load (mainly Si debris) is much lower here, and it becomes possible to use more water because of cost reasons. The main task of the fluid system is to cool the ingot and wire and to remove the silicon debris, which tends to stick on the wire and reduce the sawing performance. Furthermore the fluid

should keep the submicron silicon particles dispersed considering recycling processes for the silicon saw dust, reduce metallic contamination of the wafers, and suppress the hydrogen formation. The drawback of the higher evaporation rate of water is not so severe compared to the water-based slurries, because the particle load is much lower. One certainly needs additives such as tensides and other chemicals to fulfill these requirements. The alternative is to use a glycol-based sawing fluid mixed with water to control the viscosity. Both fluid designs have pro and cons, and the impact on many properties such as wire lifetime, process stability, or wafer cleanness has not been comprehensively investigated. This development is still at the beginning, and one can expect many modifications in the future.

---

## Conclusion

Apart from the cost of the wafering process, the quality of the wafers is equally important. A uniform thickness, a low total thickness variation (TTV) and roughness, a low subsurface damage, and a high surface cleanness are the requirements here. There are a number of wafer characterization methods available, but only TTV and thickness measurement methods are fast enough to use them inline. The investigation of SSD and wafer cleanness still requires sophisticated methods, which only allow a sampling of wafers to control or develop new sawing processes. Characterization methods for wires and fluid systems are still less developed also because it is not always clear which parameters are really essential. One can expect however that new or improved techniques will be developed here.

The investigation of the individual micromechanical process by indentation and scratching experiments with single particles under controlled condition has been shown to be valuable and gives quantitative results. While a relatively good understanding of the micromechanical details of the slurry-based sawing has been achieved, the fixed abrasive sawing process is still less understood.

Optimization of sawing processes with regard to the wafer quality is time-consuming because it depends on many parameters. Modeling the sawing process can be helpful here. A quantitative description of the sawing process is however a multi-scale problem, because one needs to combine the micromechanical processes of single particles (on the micrometer scale) with the interactions of thousands of particles under the wire and with the fluid (on the meter scale). Although first attempts have been presented here, this remains still a comprehensive task for the future.

The sawing technique will see some major and rapid changes over the next few years from loose abrasive to fixed abrasive sawing and from PEG-based to water-based fluids. Furthermore the wafers and wire will become thinner in the future. The challenges for maintaining or improving the wafer quality are thus high. There is however a good basis of understanding new characterization methods and an improved sawing machine technique available, which will allow to drive the multiwire wafering technique still much further.

## References

- O. Anspach, B. Hurka, K. Sunder, *Solar Energy Materials and Solar Cells* **131**, 58 (2014)
- G.R. Antis, P. Chantikul, B.R. Lawn, D.B. Marshall, *J. Am. Ceram. Soc.* **64–9**, 533 (1981)
- A. Bidiville, K. Wasmer, R. Kraft, C. Ballif, *Proceedings of 24th EU PVSEC* (WIP, München, 2009), p. 1400
- A. Bidiville, K. Wasmer, J. Michler, P.M. Nasch, M. Van der Meer, C. Ballif, *Prog. Photovolt. Res. Appl.* **18**, 563 (2010)
- J.I. Bye, L. Norheim, B. Holme, Ø. Nielsen, S. Steinsvik, S.A. Jensen, G. Fragiaco, I. Lombardi, *Proceedings of 26th EU PVSEC* (WIP, München, 2011), p. 956
- R. Chauhan, Y. Ahn, S. Chandrasekar, T. Farris, *Wear* **166**, 246 (1993)
- C.P. Chen, M. Leipold, *J. Am. Ceram. Soc.* **59**, 342 (1980)
- L.M. Cook, *J. Non-Cryst. Solids* **120**, 152 (1990)
- V. Domnich, Y. Gogotsi, *Rev. Adv. Mater. Sci.* **3**, 1 (2002)
- A.G. Evans, D.B. Marshall, *Fund. of Friction and Wear* (ASM, Metals Park, 1981), p. 441
- C. Funke, E. Kullig, M. Kuna, H.J. Möller, *Adv. Eng. Mater.* **6**, 594 (2004)
- R. Gassilloud, C. Ballif, P. Gasser, G. Buerki, J. Michler, *Phys. Status Solidi (a)* **202**(15), 2858 (2005)
- H.D. Geiler, H. Karge, M. Wagner, St. Eichler, M. Jurisch, U. Kretzer, M. Scheffer-Czygan, *Mater. Sci. Semicond. Process.* **9**, 345 (2006)
- Y. Gogotsi, C. Baek, F. Kirscht, *Semicond. Sci. Technol.* **14**, 936 (1999)
- M. Hamblin, G. Stachowiak, *Wear* **190**, 237 (1995)
- A. Holt, A. Thøgersen, C. Rohr, J.-I. Bye, G. Helgesen, Ø. Nordseth, S.A. Jensen, L. Norheim, Ø. Nielsen, *Proceedings of 25th EU PVSEC* (WIP, München, 2010), p. 1617
- ITRP, International Technology Roadmap for Photovoltaic, SEMI Europe Photovoltaics Group, (2016), <http://itrpv.net>
- J. Jang, M.J. Lance, S. Wen, *Acta Mater.* **53**, 1759 (2005)
- B. Lawn, *Fracture of Brittle Solids* (Cambridge University Press, Cambridge, 1993)
- H. Li, R. Bradt, *J. Mater. Sci.* **31**, 1065 (1996)
- T. Li, P. Ge, W. Bi, Y. Gao, *Mat. Sci. in Semi. Processing* **66**, 53 (2016)
- D. Meißner, St. Schönfelder, B. Hurka, J. Zeh, K. Sunder, R. Köpge, T. Wagner, A. Grün, H. Hagel, H.J. Möller, H. Schwabe, O. Anspach, *Sol. Energy Mater. Sol. Cells* **120**, 346 (2014)
- H. J. Möller, in *Crystal Growth Technology*, ed. by H. J. Scheel and P. Capper (Wiley - VCH Weinheim, 2008) p. 457
- H. J. Möller, *Handbook of Crystal Growth*, vol. 2, 2nd edn.(Elsevier, 2014). Chapter 18
- H. J. Möller, C. Funke, in *Freiberger Forschungshäfte B*, ed. by H.J. Möller, G. Roewer (TU Bergakademie Freiberg, Freiberg, 2003), p. 230
- H.J. Möller, S. Würzner, R. Buchwald, M. Herms, M. Wagner, *Solid State Phenom.* **242**, 466 (2016)
- T. Orellana Pérez, C. Schmid, S. Riepe, H.J. Möller, S. Reber, *Proceedings of 24th European PVSEC* (WIP, München, 2009), p. 1228
- T. Orellana Pérez, E. M. Tejado, C. Funke, S. Riepe, J. Y. Pastor, H. J. Möller, *J. Mat. Science* (2014). <https://doi.org/10.1007/s10853-014-8192-5>
- C. Poon, B. Bushan, *Wear* **190**(76) (1995)
- L.S. Ramsdell, *Am. Mineral.* **32**, 64 (1945)
- M. Verspui, G. de With, P. van der Varst, M. Buijs, *Wear* **188**, 102 (1995)
- T. Wagner, T. Behm, R. Rietzschel, S. Kaminski, C. Funke, H.J. Möller, *Proceedings of 25th EU PVSEC* (WIP, München, 2010), p. 1267
- S. Würzner, R. Buchwald, S. Retsch, H.J. Möller, *Proceedings of 29th EU PVSEC* (WIP, München, 2014a), p. 742
- S. Würzner, R. Buchwald, H.J. Möller, *Phys. Status Solidi C* **12–8**, 1119 (2014b)
- S. Würzner, A. Falke, R. Buchwald, H.J. Möller, *Energy Procedia* **77**, 881 (2015)
- S. Würzner, M. Herms, T. Kaden, H. J. Möller, M. Wagner, *Energies* **10**, 414 (2017)
- J. Yan, T. Asami, T. Kuriyagawa, *Precis. Eng.* **32**, 186 (2008)

---

## Part IV

# Impurity and Defect in Crystalline Silicon



G. Kissinger

## Contents

Introduction .....	400
Basic Features and Measurement of Interstitial Oxygen in Silicon .....	401
Diffusivity and Solubility .....	401
Measurement of Interstitial Oxygen Concentration .....	402
Oxygen Dimers .....	403
Interstitial Oxygen in Solar Silicon Materials .....	404
Thermal Donors .....	405
Nature and Types of Thermal Donors .....	405
Detection and Measurement of Thermal Donors .....	407
The Effect of Thermal Donors on the Lifetime of Charge Carriers .....	408
The Role of Thermal Donors and New Donors in Solar Cell Manufacturing .....	409
Oxygen Precipitation .....	411
Detection of Oxide Precipitates .....	411
Nucleation of Oxide Precipitates .....	413
Nucleation Curves .....	416
Numerical Simulation of Oxygen Precipitation .....	417
Vacancy Concentration in Solar Silicon .....	419
Interaction of Vacancies and Oxygen in Silicon .....	421
Effect of Oxide Precipitates on the Lifetime of Charge Carriers .....	423
Effect of Oxygen Precipitation on the Performance of Solar Cells .....	426
Interaction of Oxygen with Dopants and Other Impurities .....	429
Interaction with Carbon .....	429
Interaction with Nitrogen .....	431
Interaction with Boron .....	431
Interaction with Hydrogen .....	432
Conclusion .....	432
Cross-References .....	433
References .....	433

---

G. Kissinger (✉)

IHP – Leibniz-Institut für innovative Mikroelektronik, Frankfurt (Oder), Germany

e-mail: [gkissinger@ihp-microelectronics.com](mailto:gkissinger@ihp-microelectronics.com)

---

**Abstract**

Oxygen belongs to the most important impurities in many types of solar silicon. Interstitial oxygen is already incorporated in a supersaturated state during crystal growth. Subsequent thermal treatment during solar cell manufacturing leads to its precipitation which degrades the lifetime of minority carriers in solar cell material and also the solar cell efficiency. Oxide precipitate nuclei are formed already during crystal cooling. A special form of oxygen precipitation is the generation of thermal donors which enhance the free carrier concentration and in this way degrade the lifetime of minority carriers. Controlling of oxygen precipitation for optimization of solar cell efficiency involves controlling of all important factors affecting the nucleation and growth of oxygen-related defects. Therefore, this chapter deals with the basic understanding of oxygen precipitation and thermal donor formation, its characterization and measurement, and its impact on solar cell material and solar cell performance. The interaction of intrinsic point defects, light elements, and dopants with oxygen and its impact on precipitation is also discussed.

---

**Keywords**

Czochralski silicon · Multi-crystalline silicon · Interstitial oxygen · Vacancy · Self-interstitial · Oxide precipitate · Thermal donor · Lifetime · Nucleation

---

**Introduction**

Oxygen is one of the most harmful impurities in solar silicon because oxygen-related defects degrade the minority carrier lifetime and also the solar cell efficiency. In many types of solar silicon, it is already incorporated in a supersaturated state during crystal growth. Controlling of oxygen-related defect formation for optimization of solar cell efficiency involves controlling of all important factors affecting the nucleation and growth of these defects during crystal pulling as well as during solar cell fabrication.

Oxygen-related defect formation is a field which is important since decades for microelectronic manufacturing because such devices are also degraded by oxygen-related defects. Therefore, a lot of knowledge exists which can be applied in the field of material optimization for solar cells. However, the strategies of defect engineering in microelectronics and photovoltaics are different because of the different device architecture. This means that the knowledge needs to be adapted for the special needs of solar cell devices and their manufacturing process.

In the first section of this chapter, the basic features of interstitial oxygen in silicon will be explained. Diffusivity and solubility are basic for its role in diffusion-limited solid-state reactions of defect formation. There are varieties of solar cell materials with different content of interstitial oxygen. The characteristics of these materials with respect to interstitial oxygen and the measurement are also described in this section.

One of the two main oxygen-related defect types, the thermal donors, is the subject of the second section. They are known to degrade the lifetime of solar material. Their nature, types, and methods of detection are described as well as their role in solar cell manufacturing.

The second defect type, the oxide precipitates, is described comprehensively in the third section including methods of their detection. Understanding of oxide precipitate nucleation and the role of intrinsic point defects therein are important for efficiently controlling of oxygen precipitation. Special attention is also paid to the effect of oxide precipitates on the lifetime of charge carriers and on the performance of solar cells.

Because oxygen is not the only impurity in solar-grade silicon, it is important to consider also its interaction with other nonmetallic impurities and dopants with respect to defect formation. Most important is the interaction with carbon as a nucleation center for oxygen precipitation. In the last section, the interaction of oxygen with carbon, nitrogen, boron, and hydrogen is elucidated.

---

## Basic Features and Measurement of Interstitial Oxygen in Silicon

### Diffusivity and Solubility

Important basic features are solubility  $C_{O_i}^{eq}$  and diffusivity  $D_{O_i}$  of interstitial oxygen ( $O_i$ ) which are needed to describe the kinetics of oxygen out-diffusion, precipitation, and formation of complexes between dopants and other impurities with oxygen. The most widely accepted equations for the temperature-dependent solubility and diffusivity of interstitial oxygen in silicon were published by Mikkelsen (1986). These are

$$C_{O_i}^{eq}(T) = 9 \times 10^{22} \exp\left(\frac{-1.52\text{eV}}{kT}\right) \text{cm}^{-3} \quad (1)$$

and

$$D_{O_i}(T) = 0.13 \cdot \exp\left(\frac{-2.53\text{eV}}{kT}\right) \text{cm}^2\text{s}^{-1} \quad (2)$$

with  $k$  being Boltzmann's constant. As can be deduced from the high migration energy, interstitial oxygen diffuses slowly compared to metals and intrinsic point defects. Figure 1 shows the solubility as a function of the temperature together with oxygen concentrations typical for Czochralski silicon using the new ASTM standard. The meaning of the standards is explained in the next section. It can be seen that for common temperatures of solar cell processing, the interstitial oxygen is always supersaturated even for low oxygen concentration.

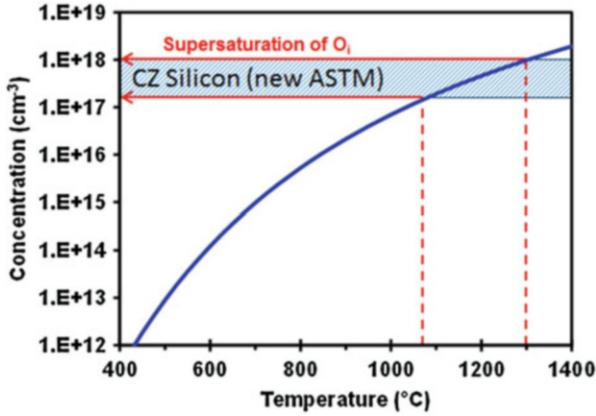
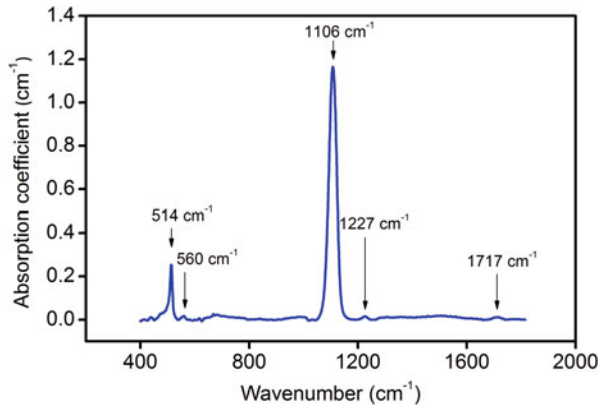


**Fig. 1** Solubility of interstitial oxygen plotted as a function of temperature given in new ASTM standard (Mikkelsen 1986). The hatched area marks the concentration of interstitial oxygen typical for Czochralski silicon, and the dashed lines indicate the onset of supersaturation for decreasing temperature. (Reprinted with permission from Kissinger (2015). Copyright 2015, Springer Nature)

**Fig. 2** Typical absorption spectrum of interstitial oxygen in silicon recorded at room temperature in the wave number range from 400 to 1800  $\text{cm}^{-1}$ . (Reprinted with permission from Kissinger (2015). Copyright 2015, Springer Nature)



## Measurement of Interstitial Oxygen Concentration

Usually, Fourier-transform infrared spectroscopy (FTIR) is used to measure the concentration of interstitial oxygen (see, e.g., Borghesi et al. 1995). In Fig. 2, a typical absorption spectrum of interstitial oxygen in silicon is shown. It was recorded at room temperature in the wave number range from 400 to 1800  $\text{cm}^{-1}$ . As a reference material, usually FZ-Si of the same thickness and resistivity is used. In order to determine the concentration of interstitial oxygen, the absorbance  $A$  at the peak position of the main absorption band at 1106  $\text{cm}^{-1}$  is determined from the incident radiant power  $I_0$  and the transmitted radiant power  $I$  as follows:



**Table 1** Conversion factors for measurement of the concentration of interstitial oxygen by FTIR at room temperature

Conversion factor	Source	Short name
$2.45 \times 10^{17} \text{ cm}^{-2}$	ASTM F 121-83	New ASTM
$2.45 \times 10^{17} \text{ cm}^{-2}$	DIN 50 438/1	DIN
$3.03 \times 10^{17} \text{ cm}^{-2}$	JEIDA	JEIDA
$4.81 \times 10^{17} \text{ cm}^{-2}$	ASTM F 121-79	Old ASTM
$3.14 \times 10^{17} \text{ cm}^{-2}$	ASTM F 1188-88	IOC-88

$$A = \ln\left(\frac{I_0}{I}\right). \quad (3)$$

Knowing the thickness of the sample  $d$ , the absorption coefficient  $\alpha$  with

$$\alpha = \frac{A}{d} = \frac{1}{d} \ln\left(\frac{I_0}{I}\right) \quad (4)$$

is calculated. Then, the  $O_i$  concentration is obtained from the absorption coefficient of the main absorption band at  $1106 \text{ cm}^{-1}$  via multiplication with a conversion factor. However, several conversion factors exist. They can be found in Table 1. Nowadays, the IOC-88 factor is regarded as the most accurate one, but all conversion factors are still in use. Because the factors differ markedly, it is very important to provide the conversion factor in connection with a concentration of interstitial oxygen measured by FTIR. Otherwise the value would be useless.

## Oxygen Dimers

The oxygen dimers  $O_{2i}$  are known to diffuse faster than interstitial oxygen  $O_i$  (Åberg et al. 1998). Their concentration is in the range of a few  $10^{15} \text{ cm}^{-3}$  (Kissinger et al. 2010). With respect to the total oxygen concentration, their part is negligible, but they become important for the oxygen diffusivity at temperatures below  $700 \text{ }^\circ\text{C}$  because then their transport capacity exceeds the transport capacity of interstitial oxygen. This leads to an enhanced effective diffusion of oxygen below  $700 \text{ }^\circ\text{C}$ . Theoretical models of the diffusion path of the dimer are in good agreement with the experiments (Snyder et al. 1988; Ramamoorthy and Pantelides 1998). The higher effective diffusivity results in deeper out-diffusion of oxygen in the temperature range below  $700 \text{ }^\circ\text{C}$  than it would be expected from the interstitial oxygen diffusivity extrapolated from high-temperature diffusivities (Lee et al. 1988; McQuaid et al. 1999; Mikkelsen 1986). It also results in a higher growth rate of oxide precipitates below  $700 \text{ }^\circ\text{C}$  (Takeno et al. 1998).

The concentration of oxygen dimers can be also measured by FTIR at room temperature using the peak amplitudes of the absorption bands at  $1013 \text{ cm}^{-1}$  and

$1062 \text{ cm}^{-1}$ . For this purpose, a conversion factor of  $7.3 \times 10^{16} \text{ cm}^{-2}$  should be used (Quemener et al. 2014).

## Interstitial Oxygen in Solar Silicon Materials

The monocrystalline Czochralski silicon (CZ-Si) is the basic material of electronic devices since decades. It is also one of the most promising materials for solar applications. However for cost reasons, the purity of the feedstock for solar applications is often lower. Oxygen is incorporated in the interstitial form during crystal pulling as the result of the partial dissolution of the walls of the quartz crucible which contains the molten silicon. Typical oxygen concentrations lay in the range of  $10^{17}$ – $10^{18} \text{ cm}^{-3}$  (new ASTM). During pulling oxygen segregates to the solid leading to a decrease of the concentration of interstitial oxygen toward the tail end of the CZ-Si ingots. By controlling of the gas flow, crucible rotation, and temperature, the oxygen concentration of the ingot can be reduced (Arnberg et al. 2012). By magnetically confined Czochralski (MCZ) growth, the oxygen content of the silicon material can be kept very low. Such material was already used successfully for high efficiency solar cells (Zhao et al. 1999).

Float zone silicon (FZ-Si) is a very pure material which is only used for high-end products because it is more expensive. The interstitial oxygen concentration of FZ-Si is usually below the detection limit of  $10^{16} \text{ cm}^{-3}$ . Solar cells with very high efficiencies can be fabricated with FZ-Si (Zhao et al. 1999).

Multi-crystalline silicon (mc-Si) is the main material for solar cell production. The dominant crystallization technique is directional solidification in Bridgman/vertical gradient freeze (VGF) furnaces (Arnberg et al. 2012). The melt is located in nitride-coated quartz crucibles. Older methods of fabrication of the coating resulted in oxidation of the coating which has led to high oxygen contamination of the silicon melt. Nowadays nitride-coated crucibles with low oxygen content of the nitride coating are available; however, nitrogen from the crucible and carbon from the graphite parts can still lead to high nitrogen and carbon concentrations in the melt and thus in the silicon (Arnberg et al. 2012). Usually, an oxygen profile can be found in mc-Si blocks with the oxygen concentration decreasing into the growth direction as the result of evaporation from the melt and segregation (Xi et al. 2007; Miyamura et al. 2015).

Continuous electromagnetic casting is a method which uses an electromagnetic field to melt the continuously fed silicon in a cold crucible. By this method both oxygen and carbon concentrations remain low because there is no contact between silicon and the crucible (Kaneko et al. 2006).

Ribbon technologies are direct wafer crystallization processes like edge-defined-film-fed (EFG) grown silicon or string ribbon (SR) silicon. These materials can be fabricated with a high productivity, but they have a higher density of defects than directional solidified mc-Si. EFG-Si has a high carbon concentration, but the oxygen concentration in both EFG-Si and SR-Si is low (Arnberg et al. 2012).

## Thermal Donors

### Nature and Types of Thermal Donors

The nature of thermal donors and their impact on the resistivity of silicon was debated extensively beginning end of the 1950s (Fuller and Logan 1957). It is well established now that heat treatments in the 350–500 °C temperature range generate shallow double-donor centers, so-called thermal donors (TDs). These are double donors with ionization energies of about 70 and 150 meV (Wruck and Gaworzewski 1979; Benton et al. 1983). They can be easily eliminated by thermal treatments above 500 °C, thus stabilizing the resistivity (Fuller and Logan 1957; Stein et al. 1986; Tokuda et al. 1989).

It is also well accepted now that TDs consist of chains of only oxygen atoms. There is a whole family of TDs named TD1–TD16 which contain a different number of oxygen atoms increasing with their numbering (Wagner und Hage 1989; Götz et al. 1992). They evolve sequentially by attachment of oxygen atoms. The double-donor character of the chains is due to two trifold bonded oxygen atoms involved in the chains (Pesola et al. 2000; Coutinho et al. 2001; Torres et al. 2006). In Fig. 3, the structure of an  $O_6$  chain with (left) and without (right) a thermal double donor is compared. While in the left structure, the oxygen atoms only bridge first neighbor silicon atoms in the second structure, two oxygen atoms also bridge second neighbor silicon atoms.

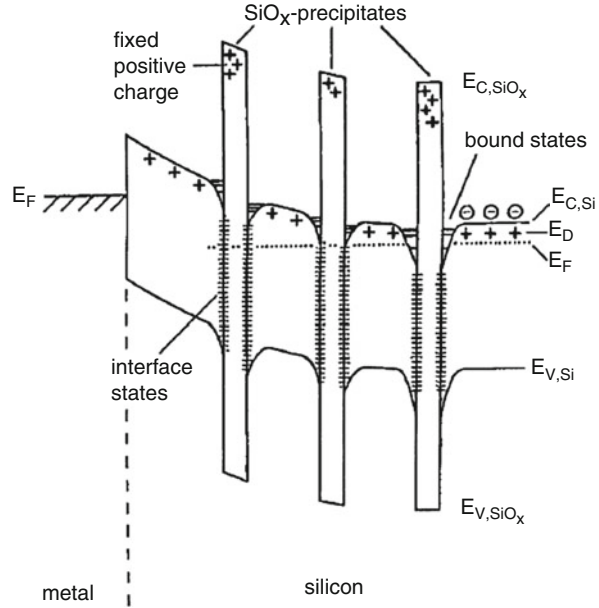
A different type of donor states, so-called new donors (NDs), is observed upon annealing in the temperature range 600–900 °C with a maximum generation rate at 800 °C. Their ionization energy varies between 30 and 120 meV (Schmalz and Gaworzewski 1981). They are more difficult to cure than TDs, and their annihilation requires temperatures above 1000 °C.

Pensl et al. explain the origin of the NDs by a  $\text{SiO}_x$  interface model (Pensl et al. 1989). They demonstrated that a correlation exists between the formation and annihilation kinetics of NDs and oxygen precipitates. In Fig. 4, the model is illustrated. Pensl et al. assume that two types of states contribute to the continuous distribution of energy states. The first type are interface states at the surface of oxygen precipitates in the entire range of measured trap states, and the second type are bound states in the Coulombic wells of fixed positive charges residing in the oxygen precipitate. These are limited to shallow states, e.g., 250 meV below



**Fig. 3** Atomistic picture for the ground-state structure of  $O_6^{\text{1NN}}$  (left) and  $O_6^{\text{2NN}}$  (right) (Torres et al. 2006). Atomistic picture for the ground-state structure of an  $O_6$  chain (left) and a thermal double donor consisting of six oxygen atoms (right). (Reprinted from Torres et al. (2006). Copyright 2006, with permission from Elsevier)

**Fig. 4** Schematic of the Si-SiO<sub>x</sub> (precipitate) band structure illustrating the “SiO<sub>x</sub> Interface Model” for oxygen-related ND defects in silicon according to Pensl et al. (1989). (Reprinted with permission from Pensl et al. (1989). Copyright 1989, Springer Nature)



conduction band edge. Experimental evidence for both types of energy states was provided by hydrogen passivation of NDs. The interface states at the surface of oxide precipitates were completely passivated, but the fixed positive charge in the oxide and thus also the bound states in the Coulombic wells remained unaffected or just slightly affected by the hydrogenation (Pensl et al. 1989).

The donor generation rate depends on the oxygen concentration of the material. Figure 5 shows the donor generation rate for different concentrations of interstitial oxygen in moderately B-doped material with an initial resistivity of 12–19 Ωcm (Cazcarra and Zunino 1980). Here, the two peaks related to TDs and NDs are clearly seen. All TD species possess a temperature- and oxygen-dependent equilibrium concentration which they reach after a certain time of annealing (Wagner and Hage 1989).

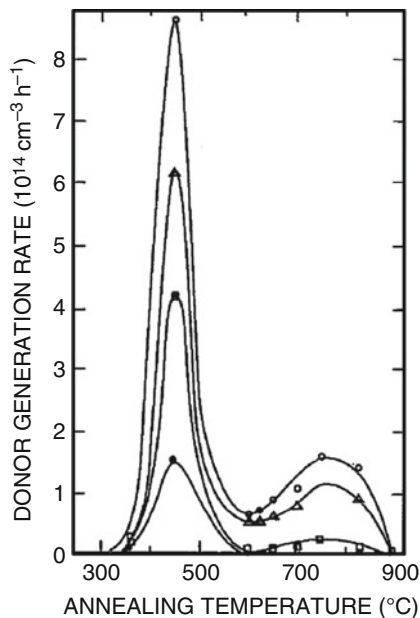
Wijaranakula developed a kinetic model which describes the reduction of interstitial oxygen and the formation kinetics of TDs during a TD anneal by the following analytic solution

$$C_{O_i}(t) = C_{O_i}^0 \cdot \left[ 1 + \frac{2}{3} \cdot D_{O_i} \cdot t \cdot C_{O_i}^0 / 2/3 \right]^{-3/2} \quad (5)$$

$$C_{TD}(t) = k_t \cdot \left\{ C_{O_i}^0 \cdot \left[ 1 + \frac{2}{3} \cdot D_{O_i} \cdot t \cdot C_{O_i}^0 / 2/3 \right]^{-3/2} \right\}^c \cdot t^{1.02} \quad (6)$$

with  $C_{O_i}^0$  being the initial concentration of interstitial oxygen,  $c = 3.44$ , and  $k_t = 4.61 \times 10^{-52}$  (Wijaranakula 1991). It should be noted that the interstitial oxygen concentration is based upon the calibration factor of  $2.45 \times 10^{17} \text{ cm}^{-2}$  here.

**Fig. 5** Donor generation rate as a function of annealing temperature for different initial concentrations of interstitial oxygen:  $1 \times 10^{18} \text{ cm}^{-3}$  (empty circles),  $9.25 \times 10^{17} \text{ cm}^{-3}$  (triangles),  $8 \times 10^{17} \text{ cm}^{-3}$  (squares), and  $6 \times 10^{17} \text{ cm}^{-3}$  (full circles) according to Cazcarra and Zunino (1980). (Reproduced from Cazcarra and Zunino (1980), with the permission of AIP Publishing)



It was also found that high interstitial concentrations increase the formation of TDs (Voronkov et al. 2000, 2008) and high vacancy concentrations delay their formation (Tajima et al. 1994). Furthermore, rodlike defects and NDs are anti-correlated because the precipitation of silicon self-interstitials into rodlike defects, consisting of line-shaped interstitial agglomerates, reduces the ND concentration (Kot et al. 2013). Generation of TDs by thermal pre-treatments was found to increase the generation of NDs (Cadeo et al. 1999; Tokuda et al. 1991).

## Detection and Measurement of Thermal Donors

FTIR spectrometry is most suitable to investigate the different TD species from TD1 to TD16. The location of the infrared absorption bands and the experimental binding energies for TD1–TD11 (neutral and singly ionized states) and TD12–TD16 (neutral state) are known (Wagner and Hage 1989; Götz et al. 1992). The NDs do not seem to have special FTIR lines because they are related to oxygen precipitates.

It was also found that the first three TD species TD0–TD2 are bistable defects with negative  $U$  properties (Markevich et al. 2018). They can exist in two configurations with very different electronic properties. In one configuration the defect is a deep donor and in the other it has two shallow levels.

The total concentration of TDs can be measured by four-point-probe measurements of the resistivity at room temperature. The measurement procedure is standardized (DIN 50431, ASTM F-84-73, ASTM F723-82). The conversion of the resistivity to the total TD concentration is based on the assumption that the TDs are the dominant donors in the samples and that all the TDs are fully ionized at room

temperature. For the determination of the TD concentration from the resistivity measurements, it has to be taken into account that TDs are double-donor centers (Clayborn and Newman 1988). Therefore, the electron concentration equals twice the TD concentration.

TDs can be also detected by DLTS in n-type silicon. A peak can be found around 55 K. This peak shifts with increasing annealing time at 450 °C and increases in height (Tokuda et al. 1989). This means that the energy levels become shallower during the formation of larger clusters.

A new method for TD mapping was proposed by Hu et al. (2012). They extracted a map of the thermal donor concentration with high resolution from free carrier density imaging of n-type silicon wafers before and after TD formation. The interstitial oxygen concentration can also be extracted if the model of Wijanarakula (1991), described in the previous section, is applied in connection with the method. Oxygen striations could be clearly visualized by this mapping technique.

## The Effect of Thermal Donors on the Lifetime of Charge Carriers

Now the question arises if TDs and NDs can act as recombination centers for charge carriers. About the effect of NDs, we will report in the section on oxygen precipitation because these donors are strongly related to oxide precipitates. Several papers reported that the degraded lifetime of silicon materials for solar cells is strongly connected with the increasing density of TDs (see, e.g., Karg et al. 2000; Hu et al. 2012; Tomassini et al. 2016).

Richter et al. investigated the impact of carrier concentration on carrier lifetime for n-type and p-type silicon (Richter et al. 2012). They used their own results and results from other authors but all obtained on FZ-Si, a material with extremely low oxygen concentration as shown in Fig. 6. They found that for dopant concentrations  $>10^{15} \text{ cm}^{-3}$ , the measured values follow a nearly straight line, and the lifetime is mainly determined by radiative and Auger recombination. For dopant concentrations  $<10^{15} \text{ cm}^{-3}$ , the measured lifetime values remain significantly below the Coulomb-enhanced Auger recombination straight line. This cannot be explained by intrinsic recombination processes but is typical for Shockley-Read-Hall recombination, and it can be assumed that the maximum measured effective lifetime of these samples is either dominated by surface or bulk recombination or a combination of both, but not by radiative or Auger recombination (Richter et al. 2012).

Recently, in a special experiment, Miyamura et al. elucidated the effect of thermal donors on the lifetime of CZ-Si crystals (Miyamura et al. 2018). They have grown two similar n-type silicon crystals with different cooling cycles resulting in different concentrations of TDs, one with  $6 \times 10^{13} \text{ cm}^{-3}$  TDs and one without TDs. Bulk lifetimes of both crystals were in the range 15–18  $\mu\text{s}$ . The lifetimes of the donor concentrations of both crystals fit very well to Fig. 6, and they concluded that although thermal donors act as defects that increase the donor concentration, they do not act as recombination centers of carriers. The TD concentrations of Hu et al. which are  $>6 \times 10^{14} \text{ cm}^{-3}$  exhibit a correlation with the inverse lifetime, and for

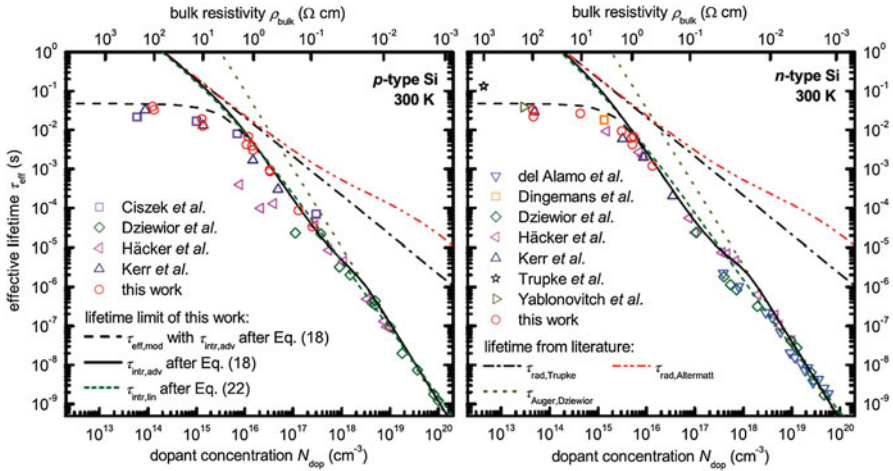


**Fig. 6** Maximum effective lifetime as a function of the dopant concentration measured at 300 K on p-type (left) and n-type (right) silicon, together with literature data. The data are compared to the results of a model for the effective lifetime from Richter et al. (black dashed lines) and other works. (Reprinted with permission from Richter et al. (2012). Copyright 2012 by the American Physical Society)

TD concentrations  $<6 \times 10^{14} cm^{-3}$ , no influence of TD concentration on the lifetime was observed both as it would be expected from the curves in Fig. 6 (Hu et al. 2012). Also Tomassini et al. reported a decreasing lifetime with increasing TD concentration only for TD concentrations  $>5-10 \times 10^{14} cm^{-3}$  (Tomassini et al. 2016).

Markevich et al. investigated in a comprehensive study the impact of the bistable TDs on the lifetime of minority carriers. They found that they can be considered as minority carrier trapping centers in n-type CZ-Si but not as effective recombination center (Markevich et al. 2018).

### The Role of Thermal Donors and New Donors in Solar Cell Manufacturing

Both Häbler et al. and Karg et al. have shown that that TDs can form during the slow ramp down of mc-Si manufacturing (Häbler et al. 2000; Karg et al. 2000). Their concentration depends on the oxygen concentration, and consequently the highest concentration of TDs was found in the bottom region of the ingots where the oxygen concentration is highest. In Fig. 7, transmittance spectra recorded on n-type mc-Si cut from different depths of a block-casted ingot can be seen. The absorption bands of six different types of TDs demonstrate that their concentration decreases with decreasing distance from the ingot bottom. It was also found that the effective lifetime of the charge carries in the silicon material from the bottom region is reduced



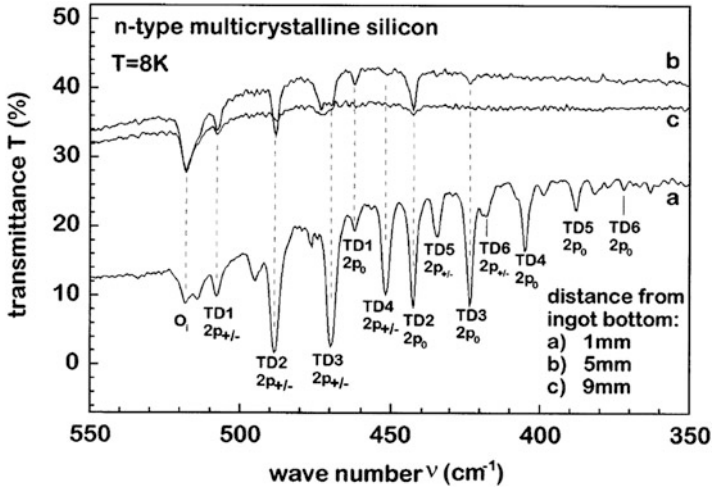


**Fig. 7** Low-temperature ( $T = 8$  K) infrared transmittance spectra taken from different distances (1, 5, and 9 mm) from the ingot bottom of a specially fabricated n-type multi-crystalline ingot. The absorption lines observed are identified as electronic transitions from the ground state into effective mass-like excited states of six different neutral donor species TD1–TD6. Obviously, the TD concentration is decreasing with decreasing distance from the bottom. The absorption line denoted by  $O_i$  is due to a vibrational absorption of oxygen on interstitial lattice sites. (Reproduced from Häbeler et al. (2000). Copyright 2000, with permission from Elsevier)

compared to the material from the middle part. However, surprisingly the solar cells fabricated on material from the bottom region did not reveal significant degradation compared to solar cells on material from the middle part of the ingot. Their average cell efficiency was the same. The reason lies in the solar cell manufacturing process itself where annealing steps  $>600$  °C just for several minutes are sufficient to annihilate the TDs (Häbeler et al. 2000; Karg et al. 2000).

However, it also has to be pointed out that the typical temperatures of solar cell manufacturing being in the range of 600–900 °C would let the NDs become the main efficiency relevant donor defects (Häbeler et al. 2000). Because their dissolution is much more difficult and requires very high temperatures (Cazcarra and Zunino 1980), the reduction of the oxygen concentration of the material would be the best way to increase the solar cell efficiency. Another way to influence ND formation is the ramp optimization as it was demonstrated for ribbon grown on substrate (RGS) silicon which has a very high oxygen concentration ( $\approx 2 \times 10^{18}$   $\text{cm}^{-3}$ ). At usual solar cell processing, a rapid formation of new donors takes place because the oxygen precipitates. An increase of solar cell efficiencies was possible in two ways, via the intentional formation of large oxide precipitates at temperatures above 1000 °C or via rapid cooling scenarios together with RTP (rapid thermal processing) techniques in order to keep the oxygen impurity atoms on interstitial sites of the silicon lattice throughout solar cell fabrication (Häbeler et al. 2000).



## Oxygen Precipitation

### Detection of Oxide Precipitates

The most common method used for detection of oxide precipitates is preferential etching. For (100) oriented wafers, often a (110) cleavage plane perpendicular to the surface is used because then it is possible to study depth profiles of oxide precipitate densities. This is useful because during thermal processing interstitial oxygen can diffuse out and the density of etch pits measured by etching the surface of a wafer is different from the density in the bulk. It can also happen that oxide or nitride layers on the surface decrease or increase, respectively, the density of oxide precipitates below the surface (Kissinger et al. 2017). An overview of suitable preferential etchants can be found elsewhere (Kissinger 2015).

Infrared laser scattering tomography is also a frequently used method to detect oxide precipitates and other grown in defects in silicon (Furukawa and Furuya 1995). It is based on the principle of ultramicroscopy. An infrared laser beam is injected and scanned parallel to the surface of the sample, and the light scattered by the defects is observed by an optical microscope with CCD camera perpendicular to the surface of the sample. In this way defects being much smaller than the resolution of the microscope can be detected. However, if the defect density exceeds a few  $10^{10} \text{ cm}^{-3}$ , the light scattering defects cannot be distinguished anymore. Depth profiles of oxide precipitate density as well as plan views in different depths are possible with IR-LST.

While preferential etching and infrared laser scattering tomography (IR-LST) have a relatively high detection limit with about 20–40 nm, transmission electron microscopy (TEM) can detect very small oxide precipitates. An example is given in Fig. 8, where the size evolution of oxide precipitates during annealing at 1000 °C is demonstrated. The results were obtained with a scanning TEM (STEM). One has to be careful about the detection limit by TEM. TEM allows the observation of defects down to atomic resolution. However, this does not automatically mean that all these tiny defects can be found because at low magnification they remain undetectable. Only step-by-step investigation with a well-focused beam and very high magnification in addition to a sufficiently high density of defects will be crowned with success. Modern TEM methods like STEM are much more suitable for investigation of very small oxide precipitates like the one used to obtain the results in Fig. 8.

In most cases, the density of oxide precipitates observed in silicon with medium oxygen concentration after thermal treatment by STEM is at least one order of magnitude higher than the density observed by preferential etching or IR-LST (Kot et al. 2017).

Both Fourier-transform infrared spectroscopy (FTIR) and photoluminescence (PL) are powerful techniques to study oxygen, its complexes, and precipitates as well as carbon and its complexes in silicon (Binetti et al. 2014). In addition to these, dopants and extended defects can be detected by at least one of these techniques and provide valuable information about their interaction with oxygen and its defects.

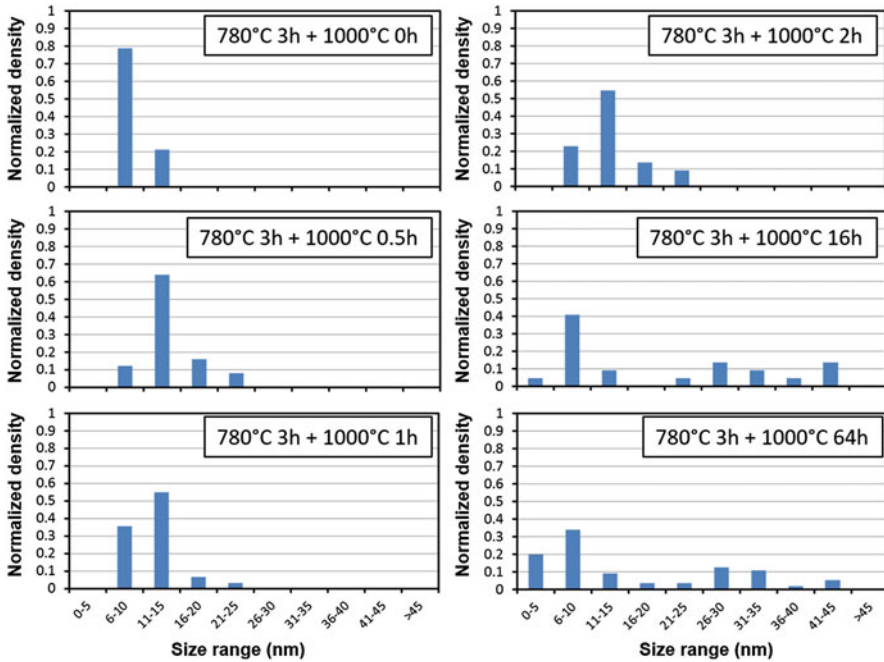


**Fig. 8** Normalized size distributions of oxygen precipitates determined by STEM. (Reprinted with permission from Kot et al. (2017). Copyright 2017, Wiley)

The infrared absorption bands of oxygen precipitates in silicon are located in the spectral range from  $1000$  to  $1300\text{ cm}^{-1}$ . Their exact position strongly depends on their geometry and stoichiometry (Hu 1980; Borghesi et al. 1992). The absorption bands of oxygen precipitates can be theoretically described by assuming a spheroidal geometry and applying effective medium theory (Hu 1980; Borghesi et al. 1992). Usually, two characteristic broad bands at  $1095\text{ cm}^{-1}$  and at  $1225\text{ cm}^{-1}$  can be observed which belong to spherical and plate-like precipitates, respectively (Hallberg and Lindström 1992; Sassella et al. 1999; Borghesi et al. 2000). Dendritic oxygen precipitates possess a broad absorption band at  $1040\text{ cm}^{-1}$  (Kot et al. 2014). Pivac et al. investigated segregation of oxygen to structural defects in EFG silicon by FTIR (Pivac et al. 1996). They observed broad absorption bands in the range from  $980$  to  $1100\text{ cm}^{-1}$ .

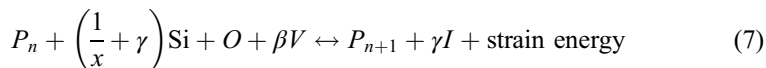
Oxide precipitates can be also investigated by photoluminescence (PL). Tajima et al. assigned the line being at  $0.820\text{ eV}$  from  $77$  to  $150\text{ K}$  and at  $0.768\text{ eV}$  at  $300\text{ K}$ , labeled as  $D_b$  line, to oxide precipitates (Tajima et al. 1991). It is the same energy range were the D-lines D1 and D2 assigned to dislocations are located. Tajima's results were confirmed by several further investigations (Pizzini et al. 2000; Binetti et al. 2002). In PL intensity maps collected at room temperature around small angle

grain boundaries, it was possible to distinguish between emissions related to oxide precipitates and dislocation (Tajima et al. 2012; Kato et al. 2014).

Temperature-dependent PL was also successfully applied during the analysis of defects in striations of n-type solar-grade CZ-Si (Le Donne et al. 2016). In regions with striations, the emission at 0.87 eV was found at 110 K, and in regions without striations, it was absent. It was concluded that the defects responsible for the occurrence of striations are oxide precipitate nuclei.

## Nucleation of Oxide Precipitates

Classical nucleation theory is the simplest way to describe nucleation of oxygen precipitates and to understand the impact of different parameters. Oxygen precipitates in the form of amorphous  $\text{SiO}_x$  ( $x = 1-2$ ) particles. For simplicity, they are assumed to be spherical. Precipitates would be always compressively strained because the density of a certain amount of silicon atoms before being oxidized is nearly double as high as the density after oxidation. However, there are mechanisms to relieve the strain. One possibility is the ejection of silicon self-interstitials  $I$  from the precipitate/matrix interface which diffuse away or aggregate by forming secondary defects like extrinsic stacking faults or punched out dislocation loops. Another possibility for strain relieve is the absorption of silicon lattice vacancies  $V$  by the precipitate. Accordingly, the general equilibrium reaction of oxygen precipitation can be formulated as follows:



where  $P_n$  and  $P_{n+1}$  are precipitates containing  $n$  and  $n + 1$  oxygen atoms, respectively,  $\gamma$  is the number of interstitials ejected, and  $\beta$  is the number of vacancies absorbed both per precipitated oxygen atom. From the equilibrium reaction, it can be concluded that oxygen precipitation is enhanced under vacancy supersaturation and is retarded by interstitial supersaturation. Vacancy supersaturation can be generated, e.g., by rapid thermal annealing (RTA) at temperatures above 1150 °C or below silicon nitride layers, whereas oxidation of silicon leads to the supersaturation of self-interstitials below the oxide layer. It also has to be taken into account that the precipitation of interstitial oxygen itself can cause a supersaturation of interstitials in bulk regions and thus retard precipitation.

The total free energy of formation of a spherical precipitate nucleus  $\Delta G_{\text{hom}}^{\text{sphere}}$  consisting of  $n$  oxygen atoms contains three major contributions. These are the free energy of formation of the precipitated oxide phase  $\Delta G_v$ , the free energy necessary to create the new interface of the sphere with the silicon matrix  $\Delta G_\sigma^{\text{sphere}}$ , and the elastic strain energy  $\Delta G_\epsilon^{\text{sphere}}$  caused by the volume deficiency between the spherical silicon cavity and the volume of the precipitated oxide phase. A temperature dependence of the elastic moduli and of different thermal expansion is neglected. Most classical

considerations of nucleation follow this approach. The total free energy can be obtained then:

$$\begin{aligned}\Delta G_{\text{hom}}^{\text{sphere}} &= -\Delta G_v + \Delta G_{\sigma}^{\text{sphere}} + \Delta G_{\varepsilon}^{\text{sphere}} \quad \text{with} \\ \Delta G_v &= n \cdot k \cdot T \cdot \ln \left[ \frac{C_{O_i}}{C_{O_i}^{\text{eq}}} \cdot \left( \frac{C_V}{C_V^{\text{eq}}} \right)^{\beta} \cdot \left( \frac{C_I}{C_I} \right)^{\gamma} \right], \\ \Delta G_{\sigma}^{\text{sphere}} &= (36\pi)^{\frac{1}{3}} \cdot \left( \frac{\Omega_p \cdot n}{x} \right)^{\frac{2}{3}} \cdot \sigma \cdot \left( \frac{1 + \delta}{1 + \varepsilon} \right)^{-2},\end{aligned}$$

and

$$\Delta G_{\varepsilon}^{\text{sphere}} = \left( \frac{\Omega_p \cdot n}{x} \right) \cdot 6 \cdot \mu \cdot \delta \cdot \varepsilon \cdot (1 + \delta)^{-3} \quad (8)$$

Here  $C^{\text{eq}}$  denotes the equilibrium concentrations and  $C$  the concentrations of vacancies, interstitials, and interstitial oxygen as indicated by  $V$ ,  $I$ , and  $O_i$ , respectively. The strain energy according to Nabarro et al. (Nabarro and Wills 1940) was used here with a correction factor respecting the volume misfit because it originally refers to the volume of the cavity in the matrix. The misfit  $\delta$  and the strain  $\varepsilon$  are

$$\delta = \left\{ \frac{\Omega_{\text{SiO}_x}}{\Omega_{\text{Si}}[1 + (\beta + \gamma)]} \right\}^{\frac{1}{3}} - 1 \quad \text{and} \quad \varepsilon = \frac{\delta}{1 + \left( \frac{4\mu}{3K} \right)} \quad (9)$$

with  $\Omega_{\text{Si}} = 2 \times 10^{-23} \text{ cm}^3$ . Typical values for the molecular volumes of oxygen precipitates  $\Omega_{\text{SiO}_x}$  applied are  $3.448 \times 10^{-23} \text{ cm}^3$  for SiO and  $4.348 \times 10^{-23} \text{ cm}^3$  for unstrained SiO<sub>2</sub> (Vanhellemont 1995). For the calculation of the strain, the shear modulus  $\mu$  of silicon ( $6.41 \times 10^{10} \text{ Pa}$ ) and the bulk modulus  $K$  of the precipitate ( $3.47 \times 10^{10} \text{ Pa}$ ) are needed. Because the interface energy  $\sigma$  cannot be measured, it is often used as a fit parameter when the model is adjusted to experimental data. Typical values of the surface energy reported are in the range of  $10^{-5} \text{ J/cm}^2$  (Zschorsch et al. 2004).

The number of oxygen atoms in a critical nucleus  $n_{\text{crit}}$  can be obtained by setting the first derivative of  $d\Delta G/dn$  to zero. This leads to

$$n_{\text{crit}} = \left( \frac{32\pi \cdot x \cdot \sigma^3}{3 \cdot \Omega_p} \right) \cdot \left( \frac{1 + \delta}{1 + \varepsilon} \right)^{-6} \cdot \left\{ \frac{k \cdot T \cdot x}{\Omega_p} \cdot \ln \left[ \frac{C_{O_i}}{C_{O_i}^{\text{eq}}} \cdot \left( \frac{C_V}{C_V^{\text{eq}}} \right)^{\beta} \cdot \left( \frac{C_I}{C_I} \right)^{\gamma} \right] - 6\mu \cdot \delta \cdot \varepsilon \cdot (1 + \delta)^{-3} \right\}^{-3} \quad (10)$$

Boltzmann's statistics gives the thermodynamic equilibrium concentration of oxide precipitate nuclei of critical size  $N_{\text{crit}}$ :

$$N_{\text{crit}} = N_0 \cdot \exp\left(-\frac{\Delta G_{\text{crit}}}{k \cdot T}\right) \quad (11)$$

with  $\Delta G_{\text{crit}}$  as the total free energy for formation of a critical nucleus and  $N_0$  the density of nucleation sites. Homogeneous nucleation models based on agglomeration of interstitial oxygen assume that  $N_0$  is equal to the initial concentration of interstitial oxygen (Wada and Inoue 1986).

The nucleation rate  $J$  for spherical oxide precipitate nuclei of critical size results from the product of  $N_{\text{crit}}$ , the impingement frequency of an oxygen atom onto a critical nucleus, and the Zeldovich factor  $Z$  as follows:

$$J = N_0 \cdot \exp\left(-\frac{\Delta G_{\text{crit}}}{k \cdot T}\right) \cdot C_{\text{O}_i} \cdot 4\pi \cdot \left(\frac{n_{\text{crit}} \cdot 3 \cdot \Omega_p}{4\pi \cdot x}\right)^{\frac{2}{3}} \cdot \left(\frac{1 + \delta}{1 + \varepsilon}\right)^{-2} \cdot D_{\text{O}_i} \cdot d^{-1} \cdot Z \quad (12)$$

with

$$Z = \sqrt{\frac{\Delta G_{\text{crit}}}{3\pi \cdot k \cdot T \cdot n_{\text{crit}}^2}} \quad (13)$$

according to Becker and Döring (1935). The variable  $n_{\text{crit}}$  is the number of oxygen atoms in a nucleus of critical size, and  $d$  is the atomic distance in silicon (0.235 nm). Because all calculations refer to the strained precipitate radius, a correction factor for the volume of the precipitate has to be taken into account which contains the volume misfit  $\delta$  and the elastic strain  $\varepsilon$  of the precipitated oxide phase.

Many solar silicon materials often contain secondary defects like grain boundaries and dislocations. Even in CZ-Si secondary dislocations or stacking faults can be created as the result of strain relief of the growing oxide precipitates. All these extended defects are nucleation sites for heterogeneous nucleation of oxide precipitates. The energy barrier for heterogeneous nucleation at dislocations is lower than for homogeneous nucleation because of the energy gained by the annihilation of a part of the dislocation. This leads to an additional negative free energy contribution. As an example, the total free energy for heterogeneous nucleation of a spherical precipitate at an edge dislocation loop  $\Delta G_{\text{het}}^{\text{loop}}$  is described here. Because the nucleus is spherical, the part of the surrounding dislocation loop that is annihilated nearly corresponds to the diameter of the sphere. The free energy gained by annihilation of part of an edge dislocation loop of radius  $R$  by a precipitate nucleus of radius  $r$  containing  $n$  oxygen atoms  $\Delta G_{\text{loop}}$  can be obtained using the dislocation energy according to Kroupa (1960). It is assumed that the radius of the dislocation core corresponds to the Burgers vector  $b$ . Then, the free energy for heterogeneous nucleation at an edge dislocation loop would be

$$\Delta G_{\text{het}}^{\text{loop}} = -\Delta G_v + \Delta G_{\sigma}^{\text{sphere}} + \Delta G_{\varepsilon}^{\text{sphere}} - \Delta G_{\text{loop}} \quad \text{with}$$

$$\begin{aligned}\Delta G_{\text{loop}} &= \frac{\mu \cdot b^2}{2\pi \cdot (1 - \nu)} \cdot \ln\left(\frac{8 \cdot R}{b \cdot e}\right) \cdot \left(\frac{1 + \delta}{1 + \varepsilon}\right)^{-1} \cdot \sqrt[3]{\frac{3n \cdot \Omega_p}{4\pi \cdot x}} \\ &= \frac{\mu \cdot b^2}{2\pi \cdot (1 - \nu)} \cdot \ln\left(\frac{8 \cdot R}{b \cdot e}\right) \cdot 2r.\end{aligned}\quad (14)$$

All other free energy contributions remain the same as in Eq. 8. In a similar way, the energy gained if nucleation occurs at a grain boundary, stacking fault, or another type of dislocation can be described.

## Nucleation Curves

Usually, experimental nucleation curves are generated by three-step annealing. The first step is needed to reduce the influence of the thermal history on the results which can be tremendous (Swaroop et al. 1987) because different crystal growth conditions result in different size and density of grown-in oxygen precipitate nuclei. The so-called tabula rasa pre-treatment, rapid heating of the samples to temperatures in the range from 1000 to 1100 °C and keeping them there for 15 min to 1 h, is one possibility to reduce their impact (Falster et al. 1997a). The pre-treatment lets the grown-in oxide precipitate nuclei shrink to nearly equal sizes (Kissinger et al. 1997). A second way would be “overwriting” the thermal history by an RTA pre-treatment at a temperature in the range 1150–1250 °C in quasi inert atmosphere. By this pre-treatment, a vacancy profile is created in the wafer (Falster et al. 1997b). The supersaturated vacancies lead to enhanced nucleation of oxygen precipitates. By this method the impact of the grown-in nuclei is superseded, and the impact of vacancies on the nucleation curves can be also studied.

The second step in the generation of nucleation curves are the so-called nucleation anneals themselves. These are heat treatments for a certain time at different temperatures usually at temperatures up to 1000 °C. At this stage, the precipitate nuclei are too small to be detectable by common methods of investigation. For this reason, during additional growth annealing, the precipitates have grown to a size above the detection limit of the method of investigation. A typical precipitate growth treatment used by many authors is annealing at 1000 °C for 16 h.

The temperature step between nucleation and growth anneals should not be too high and too fast because otherwise many nuclei generated during the nucleation anneal will not survive ramping toward the quite high growth temperature of 1000 °C. Usually, so-called stabilization treatments are inserted after nucleation to circumvent or reduce the problem. Many authors use either 800 °C for 4 h or 780 °C for 3 h (please see, e.g., Kelton et al. 1999; Kissinger et al. 2008a).

Figure 9 shows nucleation curves for oxygen precipitates which were generated with different RTA pre-treatments and 8 h of nucleation time. Higher RTA temperatures lead to higher vacancy supersaturation prior to the nucleation anneal. As expected the bulk microdefect (BMD) density increases with increasing vacancy supersaturation being well in agreement with classical nucleation theory described in

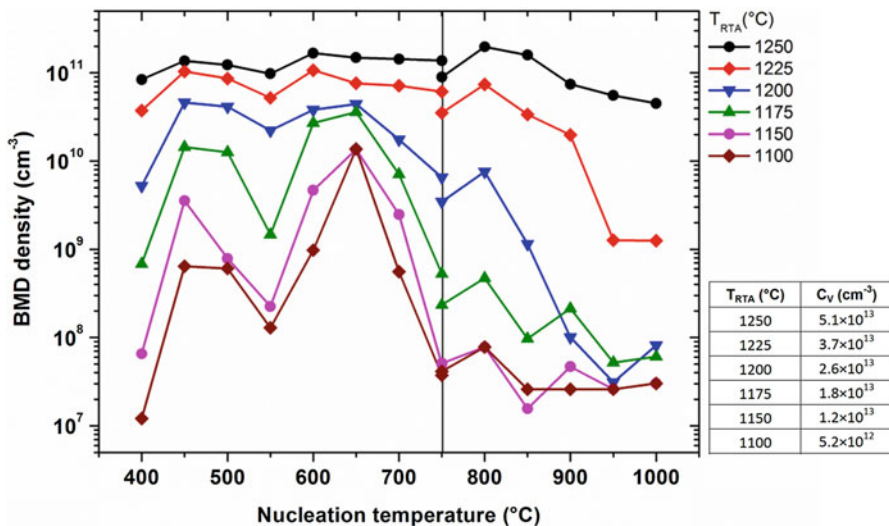


**Fig. 9** Nucleation curves for B-doped (10 Ωcm) CZ silicon wafers ( $C_{O_i} = 6.5 \times 10^{17} \text{ cm}^{-3}$ ) pre-treated by RTA for 30 s in Ar/1000 ppm  $O_2$  atmosphere. Nucleation time was 8 h in  $N_2$  followed by either 780 °C 3 h and 1000 °C 16 h in  $N_2$  for nucleation at 400–750 °C (left part) or only 1000 °C 16 h in  $N_2$  for nucleation at 750–1000 °C (right part). The vacancy concentration obtained from modeling is given in the table. (Reprinted with permission from Kissinger (2015). Copyright 2015, Springer)

the previous section. BMDs are mainly oxide precipitates with or without secondary defects like dislocations or stacking faults. There are three distinct peaks in the nucleation curves, at about 450 °C, 650 °C, and 800 °C. The latter one strongly depends on the vacancy supersaturation.

Nucleation curves generated directly after tabula rasa pre-treatment at 1000 °C for 15 min also exhibit the peaks at 450 °C and 650 °C but not the peak at 800 °C (Kelton et al. 1999). The curves with pre-treatment at 1000 °C for 15 min are in good agreement with the curves after RTA pre-treatment at 1100 °C that practically corresponds to a tabula rasa pre-treatment.

### Numerical Simulation of Oxygen Precipitation

With the help of numerical models, which can describe the evolution of oxide precipitate nucleation, growth, and dissolution during multistep thermal treatments, it is possible to predict the evolution of the size distribution of oxide precipitates during solar cell manufacturing. Such simulations are usually based on rate equations. Möller et al. have applied the following numerical model to describe precipitation of oxygen in mc-Si (Möller et al. 1999). The attachment of oxygen to a precipitate containing  $n$  oxygen atoms is

$$\frac{\partial f(n)}{\partial t} = g(n-1)f(n-1) - (d(n) + g(n))f(n) + d(n+1)f(n+1) \quad (15)$$

with the growth rate  $g(n, t)$ , the dissolution rate  $d(n, t)$  and the size distribution function  $f(n, t)$ . This requires an equation for each number of oxygen atoms in the precipitate which can result in computational problems quickly. Therefore, for larger  $n$  (e.g.,  $n > 20$ ), Fokker-Planck equations of the following type are used:

$$\frac{\partial f(n)}{\partial t} = \frac{\partial I(n)}{\partial t} \text{ with } I(n,t) = -B \frac{\partial f(n,t)}{\partial n} + Af(n,t) \quad (16)$$

$$B(n,t) = \frac{1}{2}[g(n,t) + d(n,t)], \text{ and } A(n,t) = g(n,t) - d(n,t) - \frac{\partial B(n,t)}{\partial n} \quad (17)$$

The growth rate and dissolution rate can be obtained using

$$g(n,t) = 4\pi r^2 \frac{D_{O_i}}{\delta} \exp\left(\frac{-\Delta G}{kT}\right) C_{O_i}^{\text{if}}, d(n,t) = 4\pi r^2 \frac{D_{O_i}}{\delta} \exp\left(\frac{-\Delta G}{kT}\right) C_{O_i}^{\text{if,eq}} \quad (18)$$

$$\begin{aligned} \Delta G &= G(n+1) - G(n) + G_{\text{act}}, \text{ and } G(n) \\ &= -nkT \ln\left(\frac{C_{O_i}}{C_{O_i}^{\text{eq}}}\right) + 4\pi r^2 \sigma \left[1 + \left(\frac{\zeta}{n}\right)^{1/3}\right] \end{aligned} \quad (19)$$

with  $C_{O_i}^{\text{if}}$  and  $C_{O_i}^{\text{if,eq}}$  being the concentration and equilibrium concentration of interstitial oxygen at the precipitate/matrix interface. Further details of the simulation model can be found in Möller et al. (1999).

In Fig. 10, the results of modeling the evolution of oxide precipitates in mc-Si during cooling of the ingot (Fig. 10 left) and subsequent thermal treatment (Fig. 10 right) are shown. Multi-crystalline ingots cool down rather slowly after solidification. Already in the as-grown state, tiny oxide precipitates exist in the material. The slower the cooling rate, the larger the grown-in precipitates become. Part of them is growing during thermal treatments forming larger oxide precipitates. After reaching a certain size, corresponding to the detection limit of the method used, they become detectable. The results obtained with an STEM, the method with one of the highest detection limits, are in agreement with the typical evolution of size distributions obtained from modeling as can be seen in Fig. 8.

The most interesting question is which part of the grown-in size distribution can grow to form large oxide precipitates because these significantly affect the solar cell efficiency as will be demonstrated later. For a given grown-in size distribution, this mainly depends on the heating rate and starting temperature of subsequent thermal processing. Here, rate equation modeling is a well-suited method to predict both the grown-in size distribution and the impact of the thermal cycle of solar cell production on the evolution of oxide precipitates. Generally, it can be said that both high ramp rates and high starting temperatures result in lower densities of oxide precipitates (Kissinger 2015).



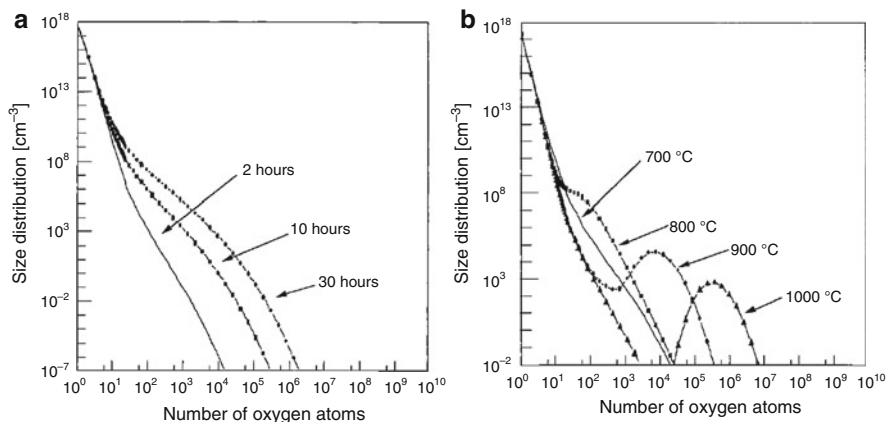
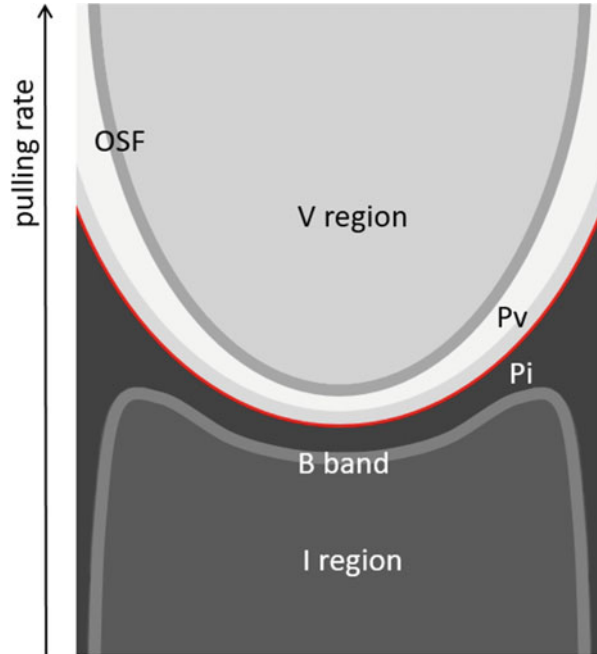


**Fig. 10** The size distribution function  $f(n)$  for a cooling process from 1400 to 400 °C. An exponential time dependence is assumed in (a). In (b) an annealing step follows for the 10 h cooling profile. The initial concentration of interstitial oxygen is  $1 \times 10^{18} \text{ cm}^{-3}$  (IOC-88). (Reproduced from Möller et al. (1999) with permission. Copyright 1999, Wiley)

## Vacancy Concentration in Solar Silicon

Because vacancies  $V$  and self-interstitials  $I$  enhance and retard oxygen precipitation, respectively, it is interesting to know which concentrations of these intrinsic point defects are already incorporated during crystal growth and how they affect the nucleation of oxide precipitates already during ingot fabrication. The dynamics of intrinsic point defects during CZ-Si single crystal growth is very well understood by Voronkov's theory which was later extended by Vanhellemont et al. to describe the impact of stress and doping on the distribution of intrinsic point defects (Voronkov 1982; Vanhellemont et al. 2015). The  $v/G$  criterion derived by Voronkov can predict if a silicon crystal becomes vacancy- or interstitial-rich whereby  $v$  represents the pulling speed and  $G$  is the axial temperature gradient at the solid/melt interface. There is a critical  $v/G = \Gamma_{\text{crit}}$  which means that crystals with  $v/G > \Gamma_{\text{crit}}$  become vacancy-rich, and for  $v/G < \Gamma_{\text{crit}}$ , they become interstitial-rich. The thermal gradient from the center toward the edge of a crystal depends on the design of the hot zone in the crystal puller. Usually, without special efforts,  $G$  is increasing toward the edge of a crystal and  $v/G$  is decreasing. Depending on the pulling speed, different regions with different intrinsic point defect types and concentrations appear in a crystal having different impact on oxygen precipitation. This is demonstrated schematically in Fig. 11 showing a longitudinal section of a crystal grown with decreasing pulling rate. The dark and bright areas represent regions of low and high, respectively, BMD densities as they are obtained after BMD test annealing, e.g., 800 °C for 4 h and 1000 °C for 16 h. At the highest pull rate in the top region of the crystal in Fig. 11, we can find the void region. Here, the concentration of vacancies near the solid/melt interface was highest. They supersaturate during cooling resulting in vacancy agglomeration in the form of octahedral voids at around 1100 °C. The residual

**Fig. 11** Scheme of a typical BMD pattern in a CZ-Si crystal grown with a decreasing pulling rate. The different gray scales correspond to different BMD densities (dark low, light high). The red line marks the boundary between I-rich and V-rich regions



vacancies enhance formation of oxide precipitate nuclei during further cooling when they supersaturate again. With decreasing pull rate, the vacancy concentration decreases, and the critical supersaturation for void formation is not reached anymore during cooling before oxygen precipitation starts. Very large oxide precipitate nuclei of lower density are formed in the narrow region, called OSF region in Fig. 11. These large grown-in defects are prone to develop stacking faults during a wet oxidation at 1100 °C. Therefore, this narrow band is also called OSF ring because on a wafer, it would form a ring. With further decreasing pull rate, a region containing a high density of small oxide precipitate nuclei appears resulting from somewhat lower vacancy supersaturation during cooling. This region is called Pv (perfect vacancy) region because it is a vacancy region without voids. With further decreasing cooling rate, we pass  $\Gamma_{\text{crit}}$  and the I-perfect region appears. Here self-interstitials are the main point defects, but their concentration is low, and they do not agglomerate during cooling. Therefore, this region is called Pi (perfect interstitial) region. Formation of oxide precipitate nuclei is strongly suppressed as can be seen from the very dark color in Fig. 11. With further cooling, the interstitial concentration increases and we meet the B-band. In this band the first small interstitial defects, so-called B-swirls, appear, and oxygen precipitation increases somewhat. At the lowest pull rate, we reach the I-region with large interstitial type dislocation clusters (A-swirls) of low density. As can be seen in Fig. 11, in all interstitial type regions, oxygen precipitation is weak or completely suppressed, and in all vacancy-type regions, it is more or less strong.

**Table 2** Vacancy concentration of different solar-grade Si materials in the as-grown state (Karg et al. 2003, 2004)

Material type	HEM <sup>a</sup>	Multi-crystalline silicon	EFG <sup>b</sup>	String ribbon silicon	Float zone (N-doped)	CZ-Si	Tri-crystalline silicon
Vacancy concentration $10^{12}$ (cm <sup>-3</sup> )	3–10	<0.5	10–20	4–30	30–50	0.5–1	3

<sup>a</sup>HEM (high efficiency multi-crystalline silicon)

<sup>b</sup>EFG (edge-defined-film-fed grown silicon)

Commercial state-of-the-art CZ-Si for photovoltaic applications is usually fast-pulled that means grown under vacancy-rich conditions (Hu et al. 2012). If a P-band with large grown-in nuclei is contained in a Cz-Si wafer, such region was found to result in lower lifetimes even after TD annihilation at 800 °C that is due to the large grown-in precipitate nuclei which are active recombination centers (Hu et al. 2012).

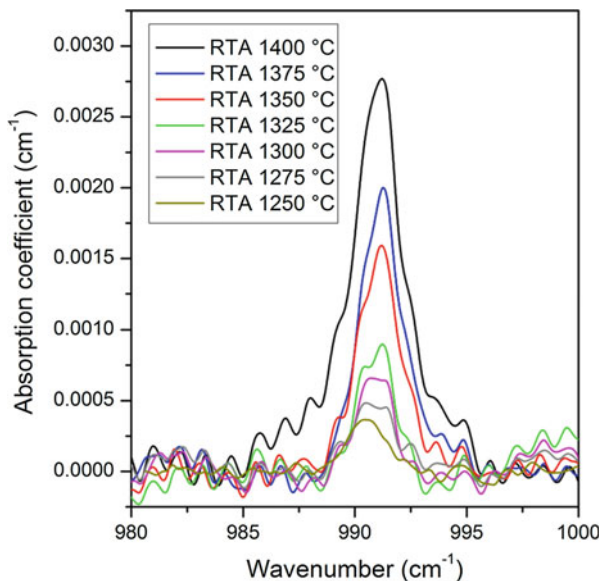
Gaspar et al. found striations of different vacancy concentration in n-type CZ-Si which lead to striations of different concentration of oxide precipitates after thermal treatment of solar cell manufacturing (Gaspar et al. 2016). During cooling of the crystal, the different vacancy concentrations have led to different sizes of the grown-in oxide precipitate nuclei.

Karg et al. measured the vacancy concentrations in different solar silicon materials in the as-grown state using Pt diffusion as shown in Table 2. They found that the grown-in vacancy concentration is not only interacting with oxygen precipitation alone, it also affects the efficiency of H-passivation. In materials with high V concentration and high oxygen concentration, a high density of oxide precipitates can trap hydrogen, thus reducing the H diffusivity (Karg et al. 2004). The lower the density of oxide precipitates, the faster is the H diffusing. In V-rich material with low oxygen, the H-diffusion is even enhanced by vacancies dissociating immobile H<sub>2</sub> molecules (Karg et al. 2004).

## Interaction of Vacancies and Oxygen in Silicon

In oxygen containing silicon, vacancies are mainly bound to oxygen atoms forming VO<sub>n</sub> complexes with *n* being the number of oxygen atoms. The investigation of VO<sub>n</sub> complexes in silicon wafers is very difficult because of their low concentration, which is in the range of 10<sup>13</sup> cm<sup>-3</sup> (Kissinger et al. 2011). Irradiation experiments are the main source of information about VO<sub>n</sub> complexes. By irradiation their concentration is increased to a much higher level compared to the level at which they can be found in processed wafers (Quemener et al. 2015). In earlier papers, the VO<sub>2</sub> species was believed to be the most dominant VO<sub>n</sub> complex that appears in silicon and RTA-treated wafers (Voronkov and Falster 2002; Kissinger et al. 2007). Akhmetov et al. (2009) were the first who published the detection of VO<sub>4</sub> complexes in non-irradiated but RTA-treated silicon wafers. Recently, it was confirmed in a

**Fig. 12** Differential FTIR spectra (6 K) of samples treated by RTA at different temperature. With decreasing RTA temperatures, the maximum absorption coefficient decreases. A sample treated by RTA at 1100 °C was used as the reference. (Reprinted with permission from Kot et al. (2018). Copyright The Electrochemical Society 2018)



more comprehensive investigation of wafers treated by RTA in the temperature range 1250–1400 °C that the only detectable  $\text{VO}_n$  complex is  $\text{VO}_4$  (Kot et al. 2018). Its concentration increases with increasing RTA soak temperature that means with increasing vacancy concentration as shown in Fig. 12.  $\text{VO}_n$  complexes are detectable by FTIR spectroscopy at 6 K. The absorption band at  $985 \text{ cm}^{-1}$  was attributed to  $\text{VO}_4$  (Murin et al. 2005). The  $\text{VO}_n$  complex formation during RTA can be well simulated by a rate equation model using the formation energies of ab initio calculation. Figure 13 demonstrates that the simulated concentration of  $\text{VO}_4$  corresponds well to the measured concentration (Kot et al. 2018). It can be also seen that  $\text{VO}_5$  and  $\text{VO}_6$  should be more abundant than  $\text{VO}_4$ . The problem is that their absorption bands are not well known.

The main effect of  $\text{VO}_n$  formation is the storage of high vacancy concentrations by binding to oxygen. During subsequent annealing, they are released by a backward reaction chain removing gradually the oxygen atoms. Thus they can enhance the growth of oxide precipitates much longer than a pure vacancy profile would do because single vacancies would quickly diffuse out. Binding to oxygen also increases the amount of vacancies stored during RTA compared to vacancy storage without binding to oxygen (Kot et al. 2018).

Silicon oxide phases that can serve as coherent oxygen precipitate nuclei the so-called seed-oxides were investigated by ab initio calculation. Two-dimensional and three-dimensional seed-oxides were proposed, and the features of these artificial phases were also determined by ab initio calculation (Kissinger et al. 2007, 2008b; Kissinger and Dabrowski 2008). In Fig. 14, the seed-oxides are shown that were suitable to model the experimental nucleation curves in Fig. 9. They are planar configurations on  $\{100\}$  consisting of either single or double layers of oxygen

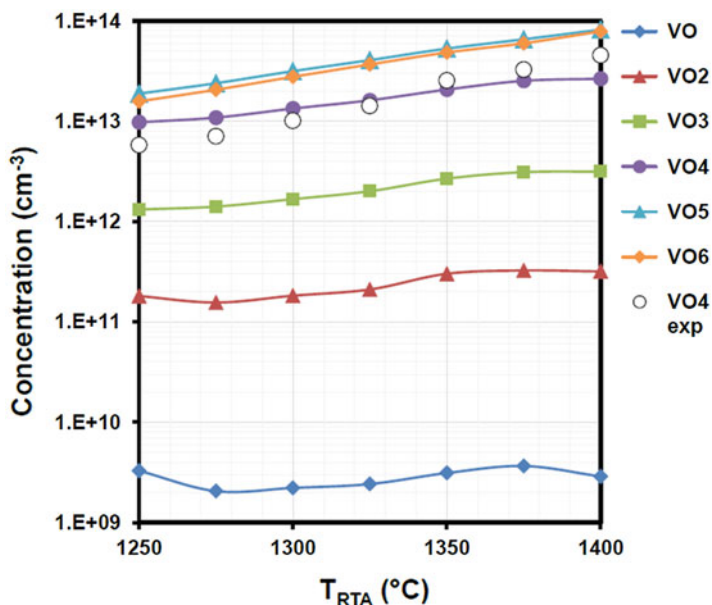


**Fig. 13** Concentration of  $VO_n$  complexes obtained from modeling compared to experimentally obtained  $VO_4$  concentrations. (Reprinted with permission from Kot et al. (2018). Copyright The Electrochemical Society 2018)

dimers or of layers of  $VO_2$ . They could be formed by attachment of  $O_i$ ,  $O_2$ , V, VO, or  $VO_2$  because all these species are diffusive (Quemener et al. 2014). All such seed-oxide platelets possess Burgers vectors  $b$  that result from the difference between the lattice constant in [001] direction with and without the defect. That means the seed-oxide platelets are always strained whereby the maximum strain would be located at the edge surrounding the platelet. While these nuclei continue growing, coherency is lost due to coherency strains resulting from lattice misfit between precipitate and matrix.

### Effect of Oxide Precipitates on the Lifetime of Charge Carriers

Miyagi et al. investigated the impact of grown-in and nucleated oxide precipitates on the lifetime of minority carriers (Miyagi et al. 1982). They found that both the oxide precipitates generated during nucleation anneals and the grown-in oxide precipitates increasing in size during anneals decreased the lifetime when their length exceeded 10 nm. The lifetime of the minority carriers was nearly proportional to the reciprocal length of the plate-like oxide precipitates.

In an extensive experimental study including oxide precipitates and also secondary defects like stacking faults and dislocation loops, Hwang and Schroder found that the oxide precipitates are mainly responsible for the lifetime

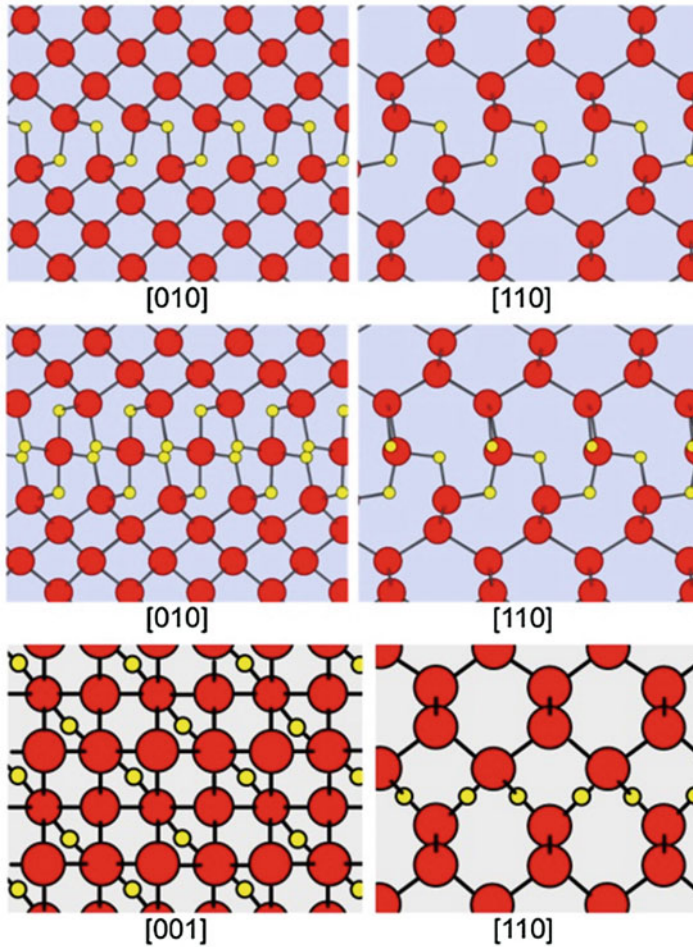


**Fig. 14** Ball-and-stick models of a planar oxygen precipitate consisting of a single plane of oxygen dimers (top) and a planar oxygen precipitate consisting of a double plane of oxygen dimers, (O<sub>i</sub>)<sub>2</sub>-p<sub>2</sub>. The silicon atoms are marked in red and the oxygen atoms are smaller yellow atoms. (Reprinted with permission from Kissinger et al. (2008b). Copyright 2008, Trans Tech Publications Ltd. Ball-and-stick model of a planar oxygen precipitate consisting of a single plane of VO<sub>2</sub> (bottom). Reprinted with permission from Kissinger and Dabrowski (2008). Copyright 2008, The Electrochemical Society)

degradation (Hwang and Schroder 1986). The degradation takes place through interface states, and it is more pronounced in p-type than in n-type silicon. The interface states are similar to the interface states of oxidized silicon in some respect, e.g., localized states due to trivalent silicon dangling bonds, the P<sub>b</sub> centers, were found (Hwang and Schroder 1986). Hwang and Schroder developed a model for recombination at oxide precipitates based on band bending around oxide precipitates due to the positive fixed charges as it is shown in Fig. 15. The positive

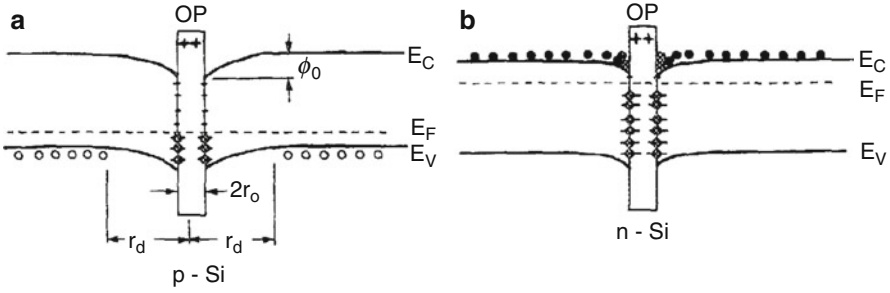


**Fig. 15** Schematic band diagrams with band bending due to positive fixed charges in oxide precipitates which give rise to (a) a depletion region in p-Si and (b) an accumulation layer around oxide precipitates in n-Si. (Reproduced from Hwang and Schroder (1986), with the permission of AIP Publishing)

fixed charges give rise to a depletion region around oxide precipitates in p-type Si, providing a large collection volume for minority electrons. However the accumulation layer in n-type Si acts as reflecting barrier to minority holes. This explains the lifetime difference in n-type and p-type Si. It is assumed that the effective recombination lifetime  $\tau_{\text{eff}}$  is determined by three recombination mechanisms as follows:

$$\frac{1}{\tau_{\text{eff}}} = \frac{1}{\tau_{op}} + \frac{1}{\tau_b} + \frac{1}{\tau_s} \quad (20)$$

where  $\tau_{op}$ ,  $\tau_b$ , and  $\tau_s$  characterize the lifetime contributions of the oxygen precipitates through interface states, the bulk impurities such as point defects, and the surface via surface states, respectively (Hwang and Schroder 1986). The lifetime contribution of the oxygen precipitates can be approximated by

$$\tau_{op} = (4\pi N_{op} S_{\text{eff}} r_d^2)^{-1} \quad (21)$$

with  $N_{op}$  being the density of oxygen precipitates,  $S_{\text{eff}}$  their effective surface recombination velocity, and  $r_d$  the radius of the space charge region. Equation (21) assumes that surface recombination is the rate-limiting step and diffusion of the excess minority carriers is neglected.

Vanhellemont et al. also found that oxygen precipitation-related lattice defects decrease the carrier lifetime in p-type Si acting as traps for minority carriers (Vanhellemont et al. 1995). They also found a close correlation between the D1 and D2 line intensities and the minority carrier lifetime.

While the investigations of lifetime degradation described so far were carried out on microelectronic grade CZ-Si, Murphy et al. published results of extensive studies on lifetime issues using solar-grade CZ-Si (Murphy et al. 2011, 2013, 2014, 2015). They carefully analyzed the contributions from many recombination processes, like band-to-band recombination, Coulomb-



enhanced Auger recombination, and Shockley-Read-Hall recombination at interstitial iron in the bulk, to finally isolate the contribution coming from recombination at oxide precipitates and their secondary defects. They found that even for a high density of very small precipitates, being below the detection limit of their preferential etching method, high lifetimes can be achieved. This result is very similar to the results of Miyagi et al. described above. Murphy et al. call these small precipitates below the detection limit “unstrained precipitates,” and their estimated capture coefficient lies between  $3 \times 10^{-8} \text{ cm}^3 \text{ s}^{-1}$  and  $1.3 \times 10^{-7} \text{ cm}^3 \text{ s}^{-1}$  (Murphy et al. 2011). Correspondingly, the oxide precipitates observed by preferential etching are called “strained precipitates.” At these type of precipitates, much stronger recombination of carriers was observed with a capture coefficient of  $\approx 1 \times 10^{-6} \text{ cm}^3 \text{ s}^{-1}$ . When the oxide precipitates have already developed secondary defects, the capture coefficient increased by a factor of  $\approx 3\text{--}4$  (Murphy et al. 2011). The meaning of a capture coefficient goes back to Shockley-Read-Hall statistics.

In another study, Murphy et al. investigated the impact of iron contamination on the recombination at oxide precipitates (Murphy et al. 2013). The iron atoms segregated to the oxide precipitates during thermal treatments. The Shockley-Read-Hall parameter of the states introduced by intentional iron contamination was the same as for precipitates in CZ-Si without intentional iron contamination (Murphy et al. 2013). This suggests that their electrical activity is also caused by impurity contamination.

Two independent defect states which are related to oxide precipitates were observed by Murphy et al. These are a defect at  $E_v + 0.22 \text{ eV}$  with a capture coefficient for electrons  $\approx 157$  times greater than for holes and a defect at  $E_c - 0.08 \text{ eV}$  with a capture coefficient for holes  $\approx 1200$  times greater than for electrons (Murphy et al. 2014). The concentration of the recombination centers scaled with density of precipitates but not with their size and secondary defects increased the density of recombination centers per precipitate.

Murphy et al. generalized their findings with respect to the surface area of oxide precipitates and its impact on lifetime for both p-type and n-type silicon (Murphy et al. 2015). They found it more likely that the density of recombination centers associated with oxide precipitates depends on their surface area. Comparing n-type and p-type silicon, Murphy et al. concluded that for a given interface area, the lifetime of n-type silicon is never lower than for p-type silicon, with oxide precipitates being substantially more detrimental in the p-type case at lower injection level as used by Hwang and Schroder (Murphy et al. 2015).

## Effect of Oxygen Precipitation on the Performance of Solar Cells

Oxide precipitates do not only influence the lifetime of solar cell material but also the whole solar cell performance (Chen et al. 2011). Chen et al. carried out an



experiment with CZ-Si solar cells fabricated in the same way on material with different concentrations of oxide precipitates. The different BMD densities were generated by two-step annealing. In the first step, a nucleation anneal at 750 °C, the time was varied leading to different concentrations of oxide precipitate nuclei. The second step was just a growth step at 1050 °C for 16 h equally carried out for all wafers. The loss of interstitial oxygen and microscopic images of the preferentially etched surfaces both demonstrating the effect of the wafer pre-treatment can be found in Fig. 16.

On these pre-treated wafers, solar cells were fabricated in a solar cell manufacturing line of a company. As expected and described in detail in the previous section, the lifetime of the minority carriers significantly decreased with an increasing oxide precipitate density. It was also found that the external quantum efficiency (EQE) of the solar cells degrades at long wavelengths in the presence of oxide precipitates. It can be seen in Fig. 17 (left) that, especially for wavelengths from 700 to 1100 nm, the EQE is degraded compared to solar cell fabricated on the reference wafer without pre-treatments. It is known that this long wavelength region reveals information about the quality of bulk material and recombination at the rear side of the cells (Suwito et al. 2010).

Measurement of the leakage currents of the solar cells has shown that the leakage currents increase with increasing oxide precipitate density as demonstrated in Fig. 17 (right). Effects of oxide precipitates on the leakage current are known already very well from microelectronic devices (Shimura 1966; Vanhellemont et al. 1995; Murakami et al. 1998).

Figure 18 provides further cell parameters like the short-circuit current density  $J_{sc}$ , the open-circuit voltage  $V_{oc}$ , the fill factor  $FF$ , and the cell efficiency  $Eff$ . Only the

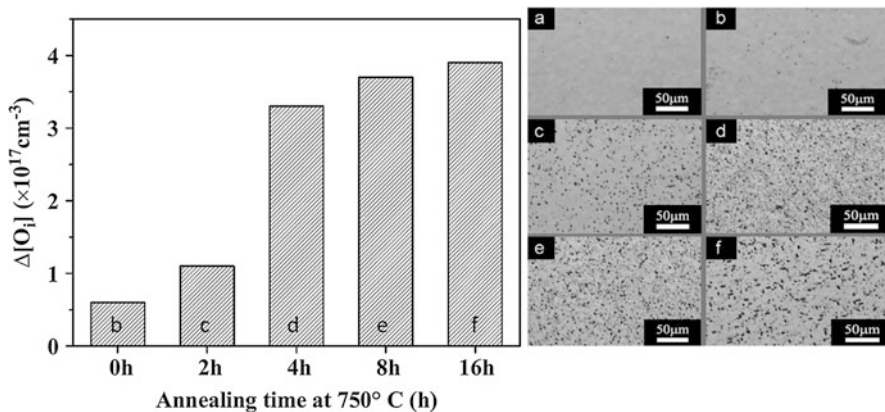


**Fig. 16** Left: Loss of interstitial oxygen concentration  $\Delta[O_i]$  as a function of the annealing time at 750 °C after 750 + 1050 °C 16 h two-step thermal treatments. Right: Optical micrographs of BMDs in silicon after different two-step anneals. (a) The referenced wafer without any thermal treatments, (b) 1050 °C/16 h, (c) 750 °C/2 h + 1050 °C/16 h, (d) 750 °C/4 h + 1050 °C/16 h, (e) 750 °C/8 h + 1050 °C/16 h, (f) 750 °C/16 h + 1050 °C/16 h. (Reprinted from Chen et al. (2011). Copyright 2011 with permission from Elsevier)

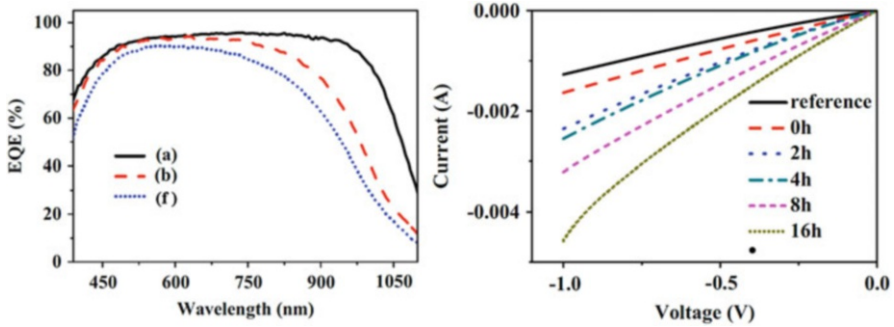
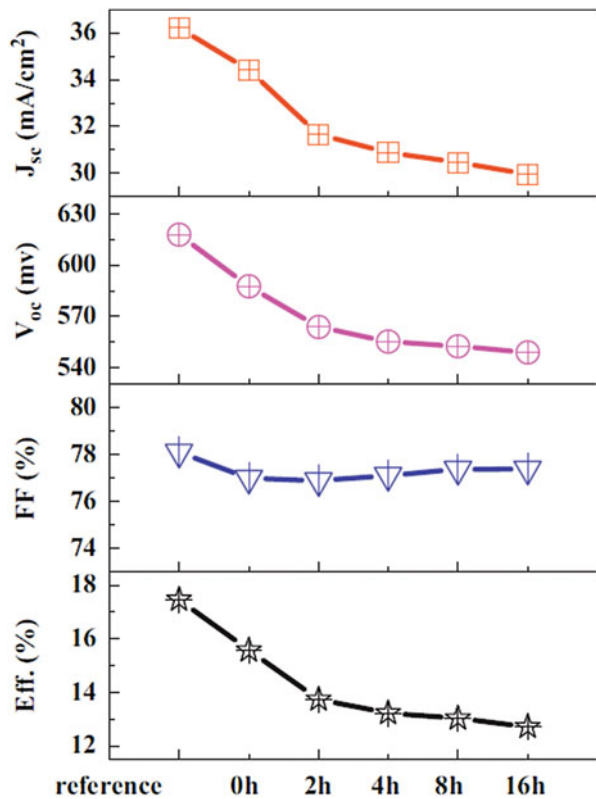


**Fig. 17** Left: Representative external quantum efficiency (EQE) of the solar cells made from (a) the reference sample, (b) the sample subjected to 1050 °C annealing for 16 h without pre-annealing, and (f) the sample subjected to 750 °C pre-annealing for 16 h followed by 1050 °C annealing for 16 h. Right: Inverse current-voltage characteristics of solar cells from the reference sample and the samples are subjected to pre-annealing for different durations at 750 °C followed by 1050 °C annealing for 16 h, which contains different oxygen precipitate concentrations. (Reprinted from Chen et al. (2011). Copyright 2011 with permission from Elsevier)

**Fig. 18** Characteristic parameters of the solar cells from the reference sample and the samples subjected to pre-annealing for different durations at 750 °C followed by 1050 °C annealing for 16 h, which contains different oxygen precipitate concentrations. (Reproduced from Chen et al. (2011). Copyright 2011 with permission from Elsevier)



fill factor remains unaffected by oxide precipitates. All other parameters and especially the solar cell efficiency decrease significantly with increasing density of oxide precipitates (Chen et al. 2011). This indicates that the control of oxygen precipitation is crucial for manufacturing of efficient solar cells.

---

## Interaction of Oxygen with Dopants and Other Impurities

### Interaction with Carbon

Carbon can occupy substitutional  $C_s$  or interstitial  $C_i$  sites in silicon depending on the availability of intrinsic point defects. Interstitial carbon is easily trapped by interstitial oxygen  $O_i$  forming  $C_iO_i$  complexes, known as the C3 centers, which are electrically active with a donor level at  $E_V + 0.36$  eV (Mooney et al. 1977). The carbon-oxygen complex  $C_iO_i$  is stable up to temperatures of about 300 °C before it starts to dissociate (Svensson and Lindström 1986).

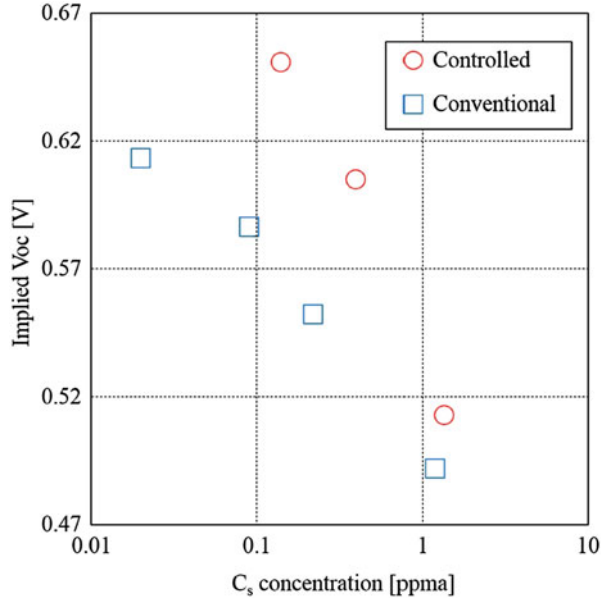
Carbon-oxygen complexes enhance precipitation of oxygen. The enhancement effect of carbon on oxygen precipitation in CZ-Si was investigated by means of infrared absorption spectroscopy at room temperature (Shimura 1986). Carbon enhances oxygen precipitation in two ways. Below a critical temperature in the range 800–850 °C, perturbed  $(C_i-O_i)C(3)$  centers can be observed by IR spectroscopy. These perturbed C(3) centers are estimated to consist of a complex with two to three oxygen atoms per carbon atom, and they are assumed to act as heterogeneous nucleation centers for oxygen precipitation (Shimura 1986). At temperatures higher than the critical temperature, carbon plays a catalytic role in oxygen precipitation. It was shown by Shimura that the formation of  $(C_i-O_i)C(3)$  centers is not affected by high-temperature pre-annealing at 1250 °C.

Yang and Möller investigated the effect of heat treatment on carbon in cast mc-Si (Yang and Möller 2002). Their results are in agreement with Shimura's results. It was found that during annealing at temperatures lower than 850 °C, carbon enhances the nucleation of oxide precipitates. Carbon also enhances the formation of grown-in oxide precipitates during the crystal growth process (Yang and Möller 2002).

Zhang et al. investigated the impact of carbon impurities on as-grown defects and correlated extended defects in n-type CZ-Si (Zhang et al. 2015). They found that the grown-in void concentration was not affected by the concentration of substitutional carbon. Although a high density of vacancies is introduced by carbon during crystallization, obviously, the vacancies were mainly incorporated into the lattice or consumed by the formation of  $VO_n$  complexes or oxide precipitate nuclei (Zhang et al. 2015). After a two-step oxidation (750 °C 4 h + 1050 °C 16 h), a higher density of oxide precipitates and a lower number of stacking faults were observed for higher  $C_s$  because high carbon concentration leads to a higher density of smaller grown-in oxide precipitate nuclei.

Both the results of Tachibana et al. and Kinoshita et al. suggest that although carbon enhances the oxygen precipitation and decreases lifetime and solar cell performance, it is possible to control its detrimental impact by the control of crystal

**Fig. 19** The relationship between the implied  $V_{oc}$  and  $C_s$  concentration after the thermal treatment corresponding to the n-type bifacial solar cell. (Reprinted from Tachibana et al. (2017). Copyright 2017 with permission from the authors)



growth conditions (Tachibana et al. 2017; Kinoshita et al. 2019). Tachibana et al. used CZ-Si wafers from conventionally grown ingots and from ingots with controlled cooling rate with the same concentration of interstitial oxygen and varying  $C_s$  concentration in a fabrication process for n-type bifacial solar cells. As can be seen in Fig. 19, the implied open-circuit voltage  $V_{oc}$  is decreasing with increasing concentration of substitutional carbon; however, for the wafers from the ingots with controlled cooling rate, it is always higher even exceeding the  $V_{oc}$  of cells with lower carbon concentration.

Kinoshita et al. controlled the cooling rate during CZ-Si crystal pulling by an additional heater keeping the crystal at high temperature of 1000–800 °C for 10 h followed by rapid cooling. Compared to conventional pulling, the lifetime degradation and oxygen precipitation were reduced for similar carbon concentration (Kinoshita et al. 2019). So both the appropriate choice of feedstock material with low carbon concentration and control of crystal growth condition are the right ways to increase solar cell efficiency.

Miyamura et al. studied the influence of oxygen and carbon incorporated into seed cast monocrystalline ingots by varying the gas flow conditions and crucible coating material on the efficiency of passivated emitter and rear contact (PERC) solar cells (Miyamura et al. 2015). It can be seen in Fig. 20 that in the crystals the substitutional carbon increases with increasing ingot height, whereas the interstitial oxygen decreases. The solar cell efficiency also increases with increasing ingot height until it reaches efficiencies of 18.8% comparable to monocrystalline CZ-Si with 18.9%. This indicates that it is most important to reduce the oxygen concentration of the material to prevent oxygen precipitation at all. Then carbon is not detrimental anymore.

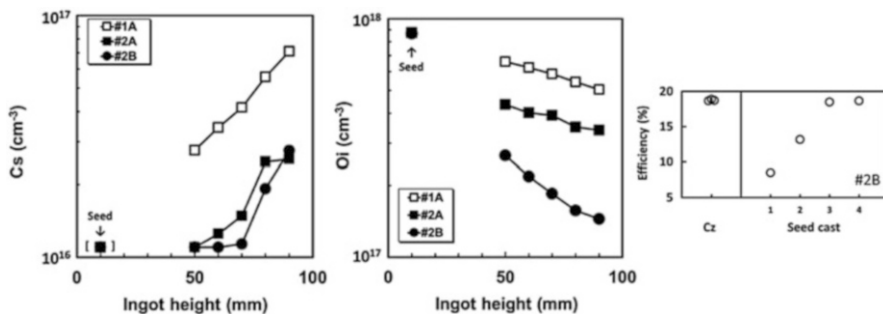


**Fig. 20** Middle and left: Variation of substitutional carbon Cs and interstitial oxygen Oi (JEIDA) concentrations along ingot height in three ingots. Right: Solar cell efficiencies of #2B ingot along ingot height position compared to solar cell efficiencies of CZ-Si. (Reproduced with permission from Miyamura et al. (2015). Copyright 2015 The Japan Society of Applied Physics)

## Interaction with Nitrogen

Nitrogen is well known to enhance oxygen precipitation (Sun et al. 1992; Yu et al. 2002). This is mainly due to a larger size of the grown-in oxide precipitate nuclei which are supposed to be stable up to 1100 °C, whereas most of the nuclei in CZ-Si without nitrogen doping shrink at this temperature (Nakai et al. 2001).

If the concentration of nitrogen is very high like it can happen in mc-Si, nitrogen can precipitate in the form of  $\alpha$ - $\text{Si}_3\text{N}_4$  in addition to oxide precipitates during cooling of the ingot (Ono et al. 2010). If both the concentration of oxygen and nitrogen are also very high,  $\text{Si}_2\text{N}_2\text{O}$  precipitates can appear (Lu et al. 2004).

## Interaction with Boron

It was found that high boron concentrations enhance the diffusivity of oxygen in silicon. This also results in a higher growth rate of oxygen precipitates (Sueoka et al. 2000). Murphy et al. also found an enhanced diffusivity of oxygen in highly B-doped silicon in dislocation locking experiments at 350–550 °C (Murphy et al. 2006). The activation energy was nearly the same as for the effective oxygen diffusivity found in dislocation locking experiments for moderately B-doped wafers, but the pre-factor was increased. Torigoe and Ono clarified this effect (Torigoe and Ono 2017). They found that the boron diffusion during annealing at 850–1000 °C is enhanced with the increase of the oxide precipitate density. Based on a model for boron diffusion mediated by silicon self-interstitials, it was revealed that the enhanced diffusion can be attributed to self-interstitials supersaturated as a result of the emission from oxide precipitates and the absorption by punched-out dislocations (Torigoe and Ono 2017).

Metastable complexes of oxygen and boron are lifetime limiting defects known to degrade solar cell performance in B-doped silicon (Schmidt and Bothe 2004). The correlation of the concentration of the lifetime limiting defects with the

concentrations of oxygen and boron indicated that the defect consists of one boron and two oxygen atoms (Schmidt and Bothe 2004). Fast-diffusing oxygen dimers  $O_2$  are assumed to be captured by immobile substitutional boron  $B_s$  forming  $BO_2$ . Schmidt and Bothe have characterized these complexes very extensively. The formation and annihilation of these metastable  $BO_2$  complexes are both thermally activated processes characterized by two strongly different activation energies of 0.4 eV and 1.3 eV, respectively. Moreover, the defect generation rate increases proportionally with light intensity below  $1 \text{ mW/cm}^2$  and saturates at higher light intensities (Schmidt and Bothe 2004). A lot of further results and theories were published about the origin of this effect. In ► Chap. 6, “Growth of Crystalline Silicon for Solar Cells: Czochralski Si”, this issue is discussed in detail.

## Interaction with Hydrogen

It was found that hydrogen in silicon reduces the migration barrier for oxygen in silicon and in this way enhances the diffusivity of interstitial oxygen (Newman et al. 1991; Stein and Hahn 1994). The oxygen diffusivity can be already enhanced by a hydrogen concentration as low as  $10^8 \text{ cm}^{-3}$ . Newman et al. published a diffusion coefficient for the hydrogen-enhanced diffusion of interstitial oxygen determined in silicon given a post-growth heat treatment at  $900 \text{ }^\circ\text{C}$  for 2 h in hydrogen being:

$$D_{O_i(H \text{ enhanced})}(T) = 7.1 \times 10^{-4} \exp\left(-\frac{2.0\text{eV}}{kT}\right) \text{ cm}^2\text{s}^{-1} \quad (22)$$

The hydrogen-enhanced diffusivity of interstitial oxygen would lead to enhanced growth of oxygen precipitates and to enhancement of thermal donor formation. Hydrogen acts as a catalyzer for forming electrically active ring structures with threefold coordinated oxygen from oxygen chains (Tsetseries et al. 2006). The experimentally determined activation energy for hydrogen-enhanced thermal donor formation amounts to  $1.7 \pm 0.3 \text{ eV}$  (Stein and Hahn 1994). Simoen et al. concluded from DLTS and FTIR measurements that hydrogen actively takes part in donor formation (Simoen et al. 2009). According to their results, the H-related shallow thermal donors are a different species than the usual oxygen thermal donors.

## Conclusion

In this chapter, a comprehensive overview about the formation of oxygen-related defects, methods of their detection, and their impact on solar silicon material and devices is provided. This knowledge can serve as a basis for successful defect engineering in solar-grade crystal manufacturing and solar cell fabrication.

Generally, it can be concluded that the best way to optimize the material for solar cell production is to prevent the incorporation of oxygen during crystal growth. However, at present this is only practicable for high-end products for cost reasons,

where, e.g., FZ-Si could be used. A promising solution is already available for mc-Si where crucible coatings with low oxygen content are available.

Thermal donors which can be formed during crystal manufacturing are less detrimental to solar cell performance because the temperatures used during manufacturing of solar cells are high enough to destroy them. This does not hold for NTDs which are formed at temperatures typical for solar cell manufacturing. The NTDs are connected to oxide precipitates, and controlling oxygen precipitation also serves controlling NTDs.

Oxide precipitates degrade the lifetime of minority carriers and of the whole solar cell performance. There are different ways to suppress oxygen precipitation for a given oxygen content of the material. Already during crystal pulling, grown-in oxide precipitate nuclei are formed. Their size distribution can be controlled by the cooling ramp of the crystal and by the concentration of intrinsic point defects related with the pulling conditions. The larger the grown-in oxide precipitate nuclei, the higher the density which can grow forming large lifetime degrading precipitates.

Another way of influencing the density of oxide precipitates is via ramp rates and processing temperatures in the solar cell manufacturing process. A high ramp rate in the first processing step to high temperature is very efficiently suppressing oxygen precipitation. Longer dwell times in the temperature region of nucleation, however, would enhance oxygen precipitation. One also has to be aware that oxide layers suppress and nitride layers enhance oxygen precipitation especially beneath the layers.

There are also interactions with other impurities incorporated in solar-grade silicon. Carbon impurities are heterogeneous nucleation centers increasing the density of oxide precipitates. Therefore, controlling the carbon concentration is very important. Nitrogen contamination is known to increase size of grown-in nuclei in CZ-Si.

In practice, there are several constraints from process technology, cost, and availability, and it is not possible to apply all the suggestions for efficiently controlling oxygen-related defect formation. However, each step into the right direction is a step to higher solar cell efficiency.

---

## Cross-References

- ▶ [Carbon Impurity in Crystalline Silicon](#)
- ▶ [Growth of Crystalline Silicon for Solar Cells: Czochralski Si](#)
- ▶ [Nitrogen Impurity in Crystalline Silicon](#)

---

## References

- D. Åberg, B.G. Svensson, T. Hallberg, J.L. Lindström, *Phys. Rev. B* **58**, 12944 (1998)
- V. Akhmetov, G. Kissinger, W. von Ammon, *Appl. Phys. Lett.* **94**, 092105 (2009)
- L. Arnberg, M. Di Sabatino, E.J. Øvrelid, *J. Cryst. Growth* **360**, 56 (2012)
- R. Becker, W. Döring, *Ann. Phys.* **24**, 719 (1935)

- J.L. Benton, L.C. Kimerling, M. Stavola, *Phys. B* **116**, 271 (1983)
- S. Binetti, S. Pizzini, E. Leoni, R. Somaschini, A. Castaldini, A. Cavallini, *J. Appl. Phys.* **92**, 2437 (2002)
- S. Binetti, A. Le Donne, A. Sassella, *Sol. Energy Mater. Sol. Cells* **130**, 696 (2014)
- A. Borghesi, A. Piaggi, A. Sassella, A. Stella, B. Pivac, *Phys. Rev. B* **46**, 4123 (1992)
- A. Borghesi, B. Pivac, A. Sassella, A. Stella, *J. Appl. Phys.* **77**, 4169 (1995)
- A. Borghesi, A. Sassella, P. Geranzani, M. Porrini, B. Pivac, *Mater. Sci. Eng. B* **73**, 145 (2000)
- S. Cadeo, S. Pizzini, M. Acciarri, A. Cavallini, *Mat. Sci. Semicond. Proc.* **2**, 57 (1999)
- V. Cazcarra, P. Zunino, *J. Appl. Phys.* **51**, 4206 (1980)
- L. Chen, X. Yu, P. Chen, P. Wang, X. Gu, J. Lu, D. Yang, *Sol. Energy Mater. Sol. Cells* **95**, 3148 (2011)
- M. Claybourn, R.C. Newman, *Appl. Phys. Lett.* **52**, 2139 (1988)
- J. Coutinho, R. Jones, L.I. Murin, V.P. Markevich, J.L. Lindström, S. Öberg, P.R. Briddon, *Phys. Rev. Lett.* **87**, 235501 (2001)
- R. Falster, M. Cornara, D. Gambaro, M. Olmo, M. Pagani, *Solid State Phenom.* **57–58**, 123 (1997a)
- R. Falster, M. Pagani, D. Gambaro, M. Cornara, M. Olmo, G. Ferrero, P. Pichler, M. Jacob, *Solid State Phenom.* **57–58**, 129 (1997b)
- C.S. Fuller, R.A. Logan, *J. Appl. Phys.* **28**, 1427 (1957)
- J. Furukawa, H. Furuya, *Jpn. J. Appl. Phys.* **34**, L156 (1995)
- G. Gaspar, G. Coletti, M. Juel, S. Würzner, R. Søndenå, M. Di Sabatino, L. Arnberg, E.J. Øvrelid, *Sol. Energy Mater. Sol. Cells* **153**, 31 (2016)
- W. Götz, G. Pensl, W. Zulehner, *Phys. Rev. B* **46**, 4312 (1992)
- T. Hallberg, J.L. Lindström, *J. Appl. Phys.* **72**, 5130 (1992)
- C. Häfler, H.-U. Höfs, W. Koch, G. Stollwerck, A. Müller, D. Karg, G. Pensl, *Mat. Sci. Eng.* **B71**, 39 (2000)
- S.M. Hu, *J. Appl. Phys.* **51**, 5945 (1980)
- Y. Hu, H. Schön, E.J. Øvrelid, Ø. Nielsen, L. Arnberg, *AIP Adv.* **2**, 032169 (2012)
- J.M. Hwang, D. Schroder, *J. Appl. Phys.* **59**, 2476 (1986)
- K. Kaneko, K. Nakagawa, T. Onizuka, K. Sasatani, N. Kubo, M. Kida, in *Proc. 16th Workshop on Crystalline Silicon Solar Cells and Modules*, ed. by B. L. Sopori, NREL, (Denver, 2006), p. 2
- D. Karg, G. Pensl, M. Schulz, C. Hässler, W. Koch, *Phys. Stat. Sol. (B)* **222**, 379 (2000)
- D. Karg, G. Pensl, M. Schulz, in *Proc. 3rd World Conf. on Photovoltaic Energy Conversion, WCPEC-3 Organizing Committee*, (Osaka, 2003), p. 1112–1115
- D. Karg, H. Charifi, G. Pensl, M. Schulz, G. Hahn, in *19th Europ. Photovoltaic Solar Energy Conf.: Proc. of the Int. Conf. held in Paris, France, June 7–11 2004*, vol 1, ed. by H. Winfried (WIP, München [u.a.], 2004), pp. 709–712. ISBN 3-936338-14-0
- G. Kato, M. Tajima, F. Okayama, S. Tokumaru, R. Sato, H. Toyota, A. Ogura, *Acta Phys. Pol. A* **125**, 1010 (2014)
- K.F. Kelton, R. Falster, D. Gambaro, M. Olmo, M. Cornara, P.F. Wei, *J. Appl. Phys.* **85**, 8097 (1999)
- K. Kinoshita, T. Kojima, K. Onishi, Y. Ohshita, A. Ogura, *Jpn. J. Appl. Phys.* **58**, SBBF02 (2019)
- G. Kissinger, in *Defects and Impurities in Silicon Materials, Lecture Notes in Physics*, ed. by Y. Yoshida, G. Langouche, vol. 916, (Springer, Japan, 2015), pp. 273–341
- G. Kissinger, J. Dabrowski, *J. Electrochem. Soc.* **155**, H448 (2008)
- G. Kissinger, D. Gräf, U. Lambert, H. Richter, *J. Electrochem. Soc.* **144**, 1447 (1997)
- G. Kissinger, J. Dabrowski, A. Sattler, C. Seuring, T. Müller, H. Richter, W. von Ammon, *J. Electrochem. Soc.* **154**, H454 (2007)
- G. Kissinger, D. Kot, J. Dabrowski, V. Akhmetov, A. Sattler, W. von Ammon, *ECS Trans.* **16**(6), 97 (2008a)
- G. Kissinger, J. Dabrowski, A. Sattler, T. Müller, W. von Ammon, *Solid State Phenom.* **131–133**, 293 (2008b)
- G. Kissinger, J. Dabrowski, V. Akhmetov, A. Sattler, D. Kot, W. von Ammon, *Solid State Phenom.* **156–158**, 211 (2010)
- G. Kissinger, J. Dabrowski, D. Kot, V. Akhmetov, A. Sattler, W. von Ammon, *J. Electrochem. Soc.* **158**, H343 (2011)



- G. Kissinger, D. Kot, J. Dabrowski, T. Grabolla, T. Müller, A. Sattler, *Phys. Status Solidi A* **214**, 1700236 (2017)
- D. Kot, T. Mchedlidze, G. Kissinger, W. von Ammon, *ECS J. Solid State Sci. Technol.* **2**, P9 (2013)
- D. Kot, G. Kissinger, M.A. Schubert, A. Sattler, *ECS J. Solid State Sci. Technol.* **3**(11), P370 (2014)
- D. Kot, G. Kissinger, M.A. Schubert, S. Marschmeyer, G. Schwalb, A. Sattler, *Phys. Stat. Sol. (C)* **14**, 1700161 (2017)
- D. Kot, G. Kissinger, J. Dabrowski, A. Sattler, *ECS J. Solid State Sci. Technol.* **7**, P707 (2018)
- F. Kroupa, *Czechoslov. J. Phys.* **10B**, 284 (1960)
- A. Le Donne, S. Binetti, V. Folegatti, G. Coletti, *Appl. Phys. Lett.* **109**, 033907 (2016)
- S.-T. Lee, P. Fellinger, S. Chen, *J. Appl. Phys.* **63**, 1924 (1988)
- J. Lu, G. Rozgonyi, J. Rand, R. Jonczyk, *J. Cryst. Growth* **269**, 599 (2004)
- V.P. Markevich, M. Vaqueiro-Contreras, S.B. Lastovskii, L.I. Murin, M.P. Halsall, A.R. Peaker, *J. Appl. Phys.* **124**, 225703 (2018)
- S.A. McQuaid, B.K. Johnson, D. Gambaro, R. Falster, M.J. Ashwin, J.H. Tucker, *J. Appl. Phys.* **86**, 1878 (1999)
- J.C. Mikkelsen Jr., *Mater. Res. Soc. Symp. Proc.* **59**, 19 (1986)
- M. Miyagi, K. Wada, J. Osaka, N. Inoue, *Appl. Phys. Lett.* **40**, 719 (1982)
- Y. Miyamura, H. Harada, K. Jiptner, S. Nakano, B. Gao, K. Kakimoto, K. Nakamura, Y. Ohshita, A. Ogura, S. Sugawara, T. Sekiguchi, *Appl. Phys. Express* **8**, 062301 (2015)
- Y. Miyamura, H. Harada, S. Nakano, S. Nishizawa, K. Kakimoto, *J. Cryst. Growth* **489**, 1 (2018)
- H.J. Möller, L. Long, M. Werner, D. Yang, *Phys. Stat. Sol. (A)* **171**, 175 (1999)
- P.M. Mooney, L.J. Cheng, M. Süli, J.D. Gerson, J.W. Corbett, *Phys. Rev. B* **15**, 3836 (1977)
- Y. Murakami, Y. Satoh, H. Furuja, T. Shingyouji, *J. Appl. Phys.* **84**, 3175 (1998)
- L.I. Murin, J.L. Lindström, B.G. Svensson, V.P. Markevich, A.R. Peaker, C.A. Londos, *Solid State Phenom.* **108–109**, 267 (2005)
- J.D. Murphy, P.R. Wilshaw, B.C. Pygall, S. Senkader, *J. Appl. Phys.* **100**, 103531 (2006)
- J.D. Murphy, K. Bothe, M. Olmo, V.V. Voronkov, R.J. Falster, *J. Appl. Phys.* **110**, 053713 (2011)
- J.D. Murphy, K. Bothe, V.V. Voronkov, R.J. Falster, *Appl. Phys. Lett.* **102**, 042105 (2013)
- J.D. Murphy, R.E. McGuire, K. Bothe, V.V. Voronkov, R.J. Falster, *Sol. Energy Mater. Sol. Cells* **120**, 402 (2014)
- J.D. Murphy, M. Al-Amin, K. Bothe, M. Olmo, V.V. Voronkov, R.J. Falster, *J. Appl. Phys.* **118**, 215706 (2015)
- F.R.N. Nabarro, H.H. Wills, *Proc. Roy. Soc. A* **175**, 519 (1940)
- K. Nakai, Y. Inoue, H. Yokota, A. Ikari, J. Takahashi, A. Tachikawa, K. Kitahara, Y. Ohta, W. Ohashi, *J. Appl. Phys.* **89**, 4301 (2001)
- R.C. Newman, J.H. Tucker, A.R. Brown, S.A. McQuaid, *J. Appl. Phys.* **70**, 3061 (1991)
- H. Ono, T. Ishizuka, C. Kato, K. Arafune, Y. Ohshita, A. Ogura, *Jpn. J. Appl. Phys.* **49**, 110202 (2010)
- G. Pensl, M. Schulz, K. Hölzlein, W. Bergholz, J.L. Hutchison, *Appl. Phys. A* **48**, 49 (1989)
- M. Pesola, Y.J. Lee, J. von Boehm, M. Kaukonen, R.M. Nieminen, *Phys. Rev. Lett.* **84**, 5343 (2000)
- B. Pivac, A. Sassella, A. Borghesi, *Mater. Sci. Eng. B* **36**, 53 (1996)
- S. Pizzini, M. Acciarri, E. Leoni, A. Le Donne, *Phys. Stat. Sol. (B)* **222**, 141 (2000)
- V. Quemener, B. Raeissi, F. Herklotz, L.I. Murin, E.V. Monakhov, B.G. Svensson, *Phys. Stat. Sol. B* **251**, 2197 (2014)
- V. Quemener, B. Raeissi, F. Herklotz, L.I. Murin, E.V. Monakhov, B.G. Svensson, *J. Appl. Phys.* **118**, 135703 (2015)
- M. Ramamoorthy, S.T. Pantelides, *Solid State Commun.* **106**, 243 (1998)
- A. Richter, S.W. Glunz, F. Werner, J. Schmidt, *Phys. Rev. B* **86**, 165202 (2012)
- A. Sassella, A. Borghesi, P. Garanzani, G. Borionetti, *Appl. Phys. Lett.* **75**, 1131 (1999)
- K. Schmalz, P. Gaworzewski, *Phys. Stat. Sol. (A)* **64**, 151 (1981)
- J. Schmidt, K. Bothe, *Phys. Rev. B* **69**, 024107 (2004)
- F. Shimura, *Semicond. Semimet.* **42**, 621 (1966)
- F. Shimura, *J. Appl. Phys.* **59**, 3251 (1986)
- E. Simoen, Y.L. Huang, Y. Ma, J. Lauwaert, P. Clauws, J.M. Rafi, A. Ulyashin, C. Claeys, *J. Electrochem. Soc.* **156**, H434 (2009)

- L.C. Snyder, J.W. Corbett, P. Deak, R. Wu, *Mat. Res. Soc. Proc.* **104**, 179 (1988)
- H.J. Stein, S. Hahn, *J. Appl. Phys.* **75**, 3477 (1994)
- H.J. Stein, S.K. Hahn, S.C. Shatas, *J. Appl. Phys.* **59**, 3495 (1986)
- K. Sueoka, M. Akatsuka, M. Yonemura, T. Ono, E. Asayama, H. Katahama, *J. Electrochem. Soc.* **147**, 756 (2000)
- Q. Sun, K.H. Yao, H.C. Gatos, J. Lagowski, *J. Appl. Phys.* **71**, 3760 (1992)
- D. Suwito, U. Jager, J. Benick, S. Janz, M. Hermle, S.W. Glunz, *IEEE Trans. Electron. Devices* **57**, 2032 (2010)
- B.G. Svensson, J.L. Lindström, *Phys. Stat. Sol. (A)* **95**, 537 (1986)
- R. Swaroop, N. Kim, W. Lin, M. Bullis, L. Shive, A. Rice, E. Castel, M. Christ, *Solid State Technol.* **3**, 85–89 (1987)
- T. Tachibana, K. Nakamura, A. Ogura, Y. Ohshita, T. Shimoda, I. Masada, E. Nishijima, *AIP Adv.* **7**, 045111 (2017)
- M. Tajima, H. Takeno, T. Abe, *Mat. Sci. Forum* **83–87**, 1327 (1991)
- M. Tajima, M. Warashina, H. Takeno, T. Abe, *Appl. Phys. Lett.* **65**, 222 (1994)
- M. Tajima, Y. Iwata, F. Okayama, H. Toyota, H. Onodera, T. Sekiguchi, *J. Appl. Phys.* **111**, 113523 (2012)
- H. Takeno, Y. Hayamizu, K. Miki, *J. Appl. Phys.* **84**, 3113 (1998)
- Y. Tokuda, N. Kobayashi, A. Usami, Y. Inoue, M. Imura, *J. Appl. Phys.* **66**, 3651 (1989)
- Y. Tokuda, T. Shimokata, Y. Inoue, A. Usami, M. Imura, *Semicond. Sci. Technol.* **6**, 66 (1991)
- M. Tomassini, J. Veirman, R. Varache, E. Letty, S. Dubois, Y. Yu, Ø. Nielsen, *J. Appl. Phys.* **119**, 084508 (2016)
- K. Torigoe, T. Ono, *J. Appl. Phys.* **121**, 215103 (2017)
- V.J.B. Torres, J. Coutinho, R. Jones, M. Barroso, S. Öberg, P.R. Briddon, *Physica B* **376–377**, 109 (2006)
- L. Tsetseris, S. Wang, S.T. Pantelides, *Appl. Phys. Lett.* **88**, 051916 (2006)
- J. Vanhellefont, *J. Appl. Phys.* **78**, 4297 (1995)
- J. Vanhellefont, E. Simoen, A. Kaniava, M. Libezny, C. Claeys, *J. Appl. Phys.* **77**, 5669 (1995)
- J. Vanhellefont, K. Nakamura, E. Kamiyama, K. Sueoka, in *Defects and Impurities in Silicon Materials, Lecture Notes in Physics*, vol.916, ed. by Y. Yoshida G. Langouche (Springer Tokyo, 2015), pp. 181–240
- V.V. Voronkov, *J. Cryst. Growth* **59**, 625 (1982)
- V.V. Voronkov, R. Falster, *J. Appl. Phys.* **91**, 5802 (2002)
- V.V. Voronkov, G.I. Voronkova, A.V. Batunina, R. Falster, V.N. Golovina, A.S. Guliaeva, N.B. Tiurina, M.G. Milvidski, *J. Electrochem. Soc.* **147**, 3899 (2000)
- V.V. Voronkov, G.I. Voronkova, A.V. Batunina, R. Falster, V.N. Golovina, A.S. Guliaeva, N.B. Tiurina, M.G. Milvidski, *Solid State Phenom.* **131–133**, 387 (2008)
- K. Wada, N. Inoue, *Electrochem. Soc. Proc.* **86–4**, 778 (1986)
- P. Wagner, J. Hage, *Appl. Phys. A* **49**, 123 (1989)
- W. Wijaranakula, *Appl. Phys. Lett.* **59**, 1608 (1991)
- D. Wruck, P. Gaworzewski, *Phys. Stat. Sol. (A)* **56**, 557 (1979)
- Z. Xi, J. Tang, H. Deng, D. Yang, D. Que, *Sol. Energy Mater. Sol. Cells* **91**, 1688 (2007)
- D. Yang, H.J. Möller, *Sol. Energy Mater. Sol. Cells* **72**, 541 (2002)
- X. Yu, D. Yang, X. Ma, J. Yang, L. Li, D. Que, *J. Appl. Phys.* **92**, 188 (2002)
- S. Zhang, M. Juel, E.J. Øvrelid, G. Tranell, *J. Cryst. Growth* **411**, 63 (2015)
- J. Zhao, A. Wang, M.A. Green, *Prog. Photovolt. Res. Appl.* **7**, 471 (1999)
- M. Zschorsch, R. Hölzl, H. Rüfer, H.J. Möller, W. von Ammon, *Solid State Phenom.* **95–96**, 71 (2004)



Bing Gao and Koichi Kakimoto

## Contents

Introduction .....	438
Mechanism of Carbon Incorporation .....	440
Simulation of Carbon Impurity (Reproduced with Permission from J. Electrochem. Soc., 157 H153 (2010). Copyright 2010, The Electrochemical Society) .....	440
Models for Global Heat Transfer .....	441
Models for Argon Gas Flow .....	442
Models for Impurity Transport .....	443
Distribution of Impurities .....	446
Effect of Argon Gas Flow Rate .....	447
Effect of Argon Gas Pressure .....	447
Reduction of Carbon Impurity .....	449
Crucible Cover Design (Reproduced with Permission from J. Cryst. Growth, 312 (9), 1572–1576, Copyright 2010, Elsevier) .....	449
Crucible Cover Material Design (Reproduced with Permission from J. Cryst. Growth, 318 (1), 255–258, Copyright 2011, Elsevier) .....	451
Reaction Control Between Silica Crucible and Graphite Susceptor (Reproduced with Permission from J. Cryst. Growth, 314(1), 239–245, Copyright 2011, Elsevier) .....	456
Conclusions .....	459
References .....	461

## Abstract

Carbon impurity contamination during growth of crystalline silicon has been systematically studied in a representative unidirectional furnace. Mechanism of carbon incorporation into silicon has been illuminated. To better understand the carbon

B. Gao (✉)

The Institute of Technological Sciences, Wuhan University, Wuhan, China  
e-mail: [gaobing@whu.edu.cn](mailto:gaobing@whu.edu.cn)

K. Kakimoto

RIAM, Kyushu University, Fukuoka, Japan  
e-mail: [kakimoto@riam.kyushu-u.ac.jp](mailto:kakimoto@riam.kyushu-u.ac.jp)

contamination process, a global simulation in a unidirectional solidification furnace was implemented. The effects of flow rate and pressure on impurities were examined.

To reduce carbon contamination, an improved unidirectional solidification furnace with a crucible cover was designed. Results show that this improvement enables the production of a high-purity multicrystalline silicon crystal in a unidirectional solidification furnace. In addition, the material of crucible cover has a great influence on carbon contamination. Another possible contamination mechanism due to the reaction between silica crucible and the graphite susceptor has also been given. Results show that the crucible reaction with graphite susceptor has a marked effect on carbon impurity in the crystal.

---

**Keywords**

Carbon contamination · Crystalline silicon · Global simulation · Unidirectional solidification furnace · Argon gas flow rate · Argon gas pressure · Crucible cover · Cover material · Reaction between silica crucible and graphite susceptor

---

**Introduction**

Carbon contamination in crystalline silicon is always a problem in many growth systems, particularly in unidirectional solidification and Czochralski (Cz) processes. Despite these problems, unidirectional solidification and Czochralski processes remain the dominant growth technology for crystalline silicon.

Carbon is one of the major impurities in crystalline silicon. The carbon concentration, existing as substitutional atoms, is electrically inactive, but it can strongly affect the density and electrical activity of dislocations in multicrystalline silicon (Kishino et al. 1979; Pizzini et al. 1988). When the concentration of carbon exceeds its solubility limit in silicon, it will precipitate to form silicon carbide (SiC) particles, which can cause severe ohmic shunts in solar cells and result in nucleation of new grains in silicon ingots (Bauer et al. 2006). Carbon, oxygen, and SiC particles in a solidified silicon ingot can cause significant deterioration of the conversion efficiency of solar cells. If the carbon concentration exceeds  $1 \times 10^{16}$  atoms/cm<sup>3</sup>, it will markedly influence the precipitation of oxygen during thermal annealing of crystals and during device processing of the wafers cut from these crystals (Bornside and Brown 1995; Fukuda et al. 1994; Sun et al. 1990; Ogino 1982; Kolbesen 1983; Goesele and Mikkelsen 1986; Shimura 1989). In addition, carbon impurity may exert considerable indirect effect on impurity gettering, warpage, and slip of wafers during the processing. Control of carbon levels in crystalline silicon is essential for the yield and performance of solar cells and VLSI devices.

The carbon contamination mainly originates from two stages of crystal growth: heating/melting stage and growth stage. Baker (1969) has studied the carbon contamination of Cz crystals grown under various conditions during melting stage. The results show that carbon content increased with the melting time. Raabe et al. (2011) studied the carbon contamination during casting multicrystalline silicon in vertical

Bridgman furnace. The results show that carbon monoxide in furnace chamber first increases promptly at the heating stage and then rapidly decreases at the melting/homogenization stage. The carbon contamination during growth stage (Machida et al. 1998, 2000; Reimann et al. 2007; Higasa et al. 2016; Nagai et al. 2014) has also been experimentally explored. Proposals for reduction carbon contamination, such as SiC coating, mass flow and pressure control of argon gas, and geometry structure improvement, have been put forward.

The process of carbon impurity contamination during the growth of crystalline silicon is complicated. It always accompanies with the transport and chemical reaction of oxygen impurity in system. To find efficient approach for the reduction of carbon contamination, experimental exploration is usually adopted but always a time-consuming and high-cost work, and the acquired data are not easy to analyze due to the nonlinear system.

Developments in computer technology have made it possible to simulate the global environments of crystal growth and find techniques for improving the purity of crystals. Many simulations of impurity transport have been done (Bornside and Brown 1995; Kobayashi 1991; Hirata and Hoshikawa 1992; Kinney and Brown 1993; Kakimoto et al. 1996; Yi et al. 1996; Watanabe et al. 1999; Reimann et al. 2008; Li et al. 2004; Smirnov and Kalaev 2008, 2009); however, most of them were local simulations (Bornside and Brown 1995; Kobayashi 1991; Hirata and Hoshikawa 1992; Kinney and Brown 1993; Kakimoto et al. 1996; Yi et al. 1996; Watanabe et al. 1999; Reimann et al. 2008) that neglected gas transport of impurities. There have been a few studies using global simulations (Li et al. 2004; Smirnov and Kalaev 2008, 2009). However, the oxygen and carbon impurities in the silicon melt were neglected in one of those studies (Li et al. 2004), and the carbon impurity in both gas and silicon melt was neglected in the other studies (Smirnov and Kalaev 2008, 2009). There have been few simulations that took into account not only the oxygen impurity but also the carbon impurity in both cooling gas and silicon melt. We therefore developed a set of analysis system that includes all of processes in crystal growth. This set of analysis system incorporates the silicon melt flow into the global simulation of Bornside and Brown (1995). The original boundary assumption of constant SiO concentration at the melt surface (Bornside and Brown 1995) is replaced by a dynamic update of SiO concentration. Therefore, this set of analysis system enables reasonable prediction of the oxygen and carbon impurity in a crystal. Another assumption of the equilibrium system in the melt (Bornside and Brown 1995), i.e., the carbon flux from the gas into the melt being equal to that from the melt into the crystal, is also replaced by a local nonequilibrium consideration. The carbon flux at the gas/melt interface is calculated locally and thus carbon accumulation in the melt is included. Therefore, the present simulation might be able to correct the difference between the simulation data and experimental data (Bornside and Brown 1995).

Considering the similar mechanism in carbon contamination in both unidirectional solidification furnace and Cz furnace, we will use unidirectional furnace to clarify the following problems using numerical simulations: How to reduce carbon impurities in crystalline silicon?

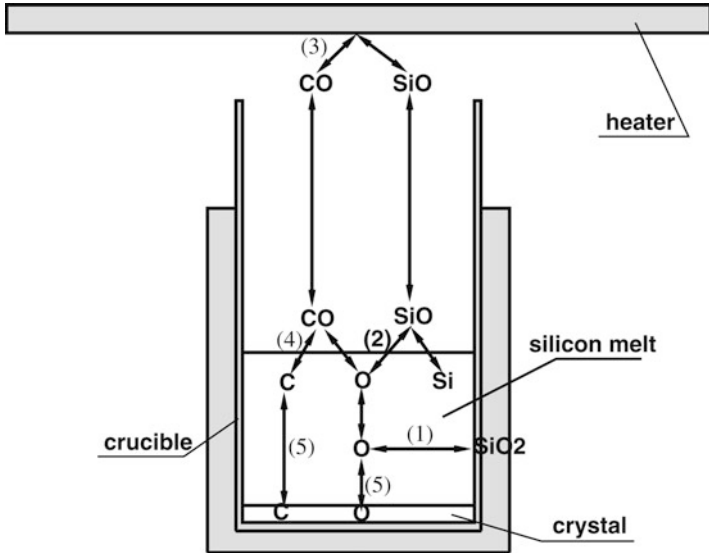


**Fig. 1** Basic processes of carbon incorporation into a crystal

## Mechanism of Carbon Incorporation

Before numerical simulation, the mechanism of carbon impurity incorporation into crystal has to be known. Based on the previous work of Bornside and Brown (1995) in Cz furnace, basic incorporation processes of carbon impurity into a crystal in a unidirectional solidification furnace are shown in Fig. 1. First, the quartz crucible ( $\text{SiO}_2$ ) is dissolved and the oxygen atoms enter into the Si melt. Secondly the dissolved oxygen atoms are transported to the gas/melt interface and evaporate as SiO gas. Then the SiO gas is carried away by the argon gas flow and reacts with all of the graphite components to produce gas-phase CO. After that the resultant CO is transported back to the melt surface by diffusion or convection and dissolves within the melt. Finally, the C and O atoms are segregated into the crystal (Bornside and Brown 1995).

## Simulation of Carbon Impurity (Reproduced with Permission from J. Electrochem. Soc., 157 H153 (2010). Copyright 2010, The Electrochemical Society)

To correctly simulate the impurity transport inside furnace, all of phenomena occurs in the growth furnace should be included. For example, incompressible flow of silicon melt, compressible flow of argon gas, heat transfer inside solid components,

heater radiation inside all enclosures, species transport inside melt and gas flow, and all chemical reactions described in the above.

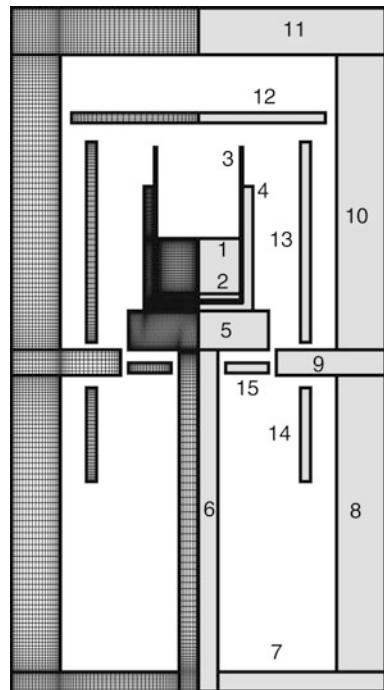
Our simulation implementation involves three steps: first, the temperature distribution of furnace components due to heat transfer and heat radiation is computed without gas flow; second, the flow field and temperature field of the cooling argon gas are computed using the temperature boundary conditions from the first step; and third, carbon and oxygen impurities in the gas and melt are computed using the flow field and temperature field from the second step.

## Models for Global Heat Transfer

For our studies, a unidirectional solidification furnace is assumed to be axisymmetric. All of the components of the furnace are subdivided into a set of block regions, each of which is covered with a structured grid. The configurations of the furnace and its computational grids for gas flow are shown in Fig. 2. In Fig. 2, the crucible 3 is made of quartz and the crucible 4 is made of carbon; the heat shields 7–11, the heaters 12–15, and the pedestal 5 are made of carbon; the pedestal 6 are made of steel. The inner and outer radii of crucible 3 are 53.7 and 56.7 mm, respectively, and its height is 196 mm.

Global modeling of heat transfer in the furnace involves convective heat transfer of the melt in the crucible, conductive heat transfer in all solid components, and

**Fig. 2** Configuration of the unidirectional solidification furnace and subblocks (right) of domain decomposition and structured grids (left) in every subblock for heat transfer simulation



radiation heat transfer in all enclosures of the furnace. The melt flow in the crucible is assumed to be an incompressible laminar flow. The radiative heat exchange in all radiative enclosures is modeled on the basis of the assumption of diffuse-gray surface radiation. The basic time step for the growth system is taken to be 30 s. During this time step, all processes are assumed to reach a steady state. The convective cooling by argon gas is neglected in the computation of thermal fields. For details of the global heat transfer, refer to Liu and Kakimoto (2005).

## Models for Argon Gas Flow

The flow of argon gas through the furnace is considered to be a compressible and axisymmetric flow. The compressible flow solver can accurately simulate the buoyancy-driven flow due to the large density variation in the furnace. Although the flow velocity in this furnace is low, yet the density variation is significant for this buoyancy-driven flow, which is similar as combustion problem. If incompressible flow solver is used, Boussinesq approximation should be included; however, this approximation can introduce errors of the order of 1% if the temperature differences are below 15 degree for air. This error may be more substantial if the temperature differences are higher than 15 degree; it may even be qualitatively wrong if the temperature differences become much higher. In present furnace, the temperature differences are rather large varying from 350 K at the gas inlet to 1722 K at the melt surface. Thus, incompressible solver is not appropriate. On the other hand, absolute pressure of gas flow should be given for calculating the diffusivities of SiO and CO. However, incompressible flow solver cannot provide this absolute value. Therefore, compressible flow solver is a best choice.

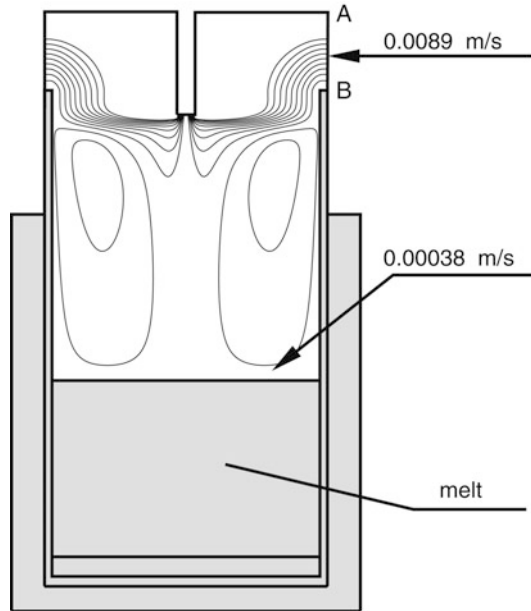
Similar to the simulation of global heat transfer, the flow domain is subdivided into a set of block regions, each of which is covered with a structured grid. The radius of the inlet and width of the outlet for the simulation are 3.5 mm and 4 mm, respectively.

Full Navier-Stokes equations without any assumptions are used. The conservative compressible Navier-Stokes equations for axisymmetric geometry are described in detail in the book (Hoffmann and Chiang 2000). A second-order total variation diminishing (TVD) scheme is used for convection terms and Davis-Yee symmetric TVD is used for the flux limiter vectors (Hoffmann and Chiang 2000). An entropy correction term is also introduced to satisfy the entropy condition. A fourth-order Runge-Kutta scheme is used for time marching and a central difference scheme is used for viscous terms. Local time step (Hoffmann and Chiang 2000) and low Mach number acceleration technique (Jenny and Müller 1999) are adopted for efficiency. The domain-decomposition method is used to solve the whole flow field.

The temperatures at all solid surfaces are set to the values computed from the global heat transfer. The velocities at all solid surfaces are set to zero. For the conditions at inlet and outlet, different methods can be used according to our practical tests. For axisymmetric and subsonic inflow, three characteristic lines enter into the domain and, therefore, three analytical boundary conditions are



**Fig. 3** Stream function of gas flow above the melt at a flow rate of 0.8 liter/min and pressure of 0.1 atm



specified. The remaining one is evaluated on the basis of information from the interior points near the inlet. For subsonic outflow, one characteristic line enters into the computation domain from the outside and, thus, one analytical boundary condition is given and others are evaluated from the interior points near the outlet. For the first simulation, inlet flow rate  $Q$  is set to 0.8 liter/min, inlet static temperature  $T$  is set to 350 K, and inlet tangential velocity  $u$  is set to zero. The outlet static pressure  $p$  is set to 0.1 atm.

The flow field in the whole furnace can refer to the paper (Gao et al. 2010a). The local flow field above the melt is shown in Fig. 3. The recirculation above the melt brings SiO from the gas/melt interface to the top convection flow and takes back CO from the top convection flow to the gas/melt interface.

## Models for Impurity Transport

As stated in section “[Mechanism of Carbon Incorporation](#)”, there are mainly two impurities in argon gas, CO, and SiO. The concentration fields of SiO and CO gas are assumed to be diluted in the argon gas and are computed using the temperature and flow fields. The equations for conservation of moles are written in dimensional form as

$$\frac{\partial c_{\text{SiO}}}{\partial t} + \nabla \cdot (c_{\text{SiO}} \vec{u}_{\text{Ar}}) = \nabla \cdot \left[ c_{\text{Ar}} D_{\text{SiO}} \nabla \left( \frac{c_{\text{SiO}}}{c_{\text{Ar}}} \right) \right], \quad (1)$$

$$\frac{\partial c_{\text{CO}}}{\partial t} + \nabla \cdot (c_{\text{CO}} \vec{u}_{\text{Ar}}) = \nabla \cdot \left[ c_{\text{Ar}} D_{\text{CO}} \nabla \left( \frac{c_{\text{CO}}}{c_{\text{Ar}}} \right) \right], \quad (2)$$

where  $c_{\text{SiO}}$  is the molar concentration of SiO gas,  $c_{\text{CO}}$  is the molar concentration of CO gas, and  $c_{\text{Ar}}$  is the molar concentration of argon gas. The vector  $\vec{u}_{\text{Ar}}$  is the flow vector of argon gas. The diffusivities  $D_{\text{SiO}}$  and  $D_{\text{CO}}$  in Eqs. (1) and (2) depend on temperature and pressure (Bornsidge and Brown 1995; Reid et al. 1987):

$$D_{\text{SiO}} = a_{\text{SiO}} \frac{T^{1.75}}{p}, \quad (3)$$

$$D_{\text{CO}} = a_{\text{CO}} \frac{T^{1.75}}{p}, \quad (4)$$

where  $a_{\text{SiO}} = 0.862611$  and  $a_{\text{CO}} = 1.79548$  if  $D$ ,  $T$ , and  $p$  are measured in  $\text{cm}^2/\text{s}$ , K, and  $\text{dyn}/\text{cm}^2$ , respectively.

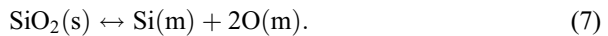
Similarly, the concentrations of oxygen and carbon atoms in the melt are modeled as

$$\frac{\partial c_{\text{C}}}{\partial t} + \nabla \cdot (c_{\text{C}} \vec{u}_{\text{Si}}) = \nabla \cdot \left[ c_{\text{Si}} D_{\text{C}} \nabla \left( \frac{c_{\text{C}}}{c_{\text{Si}}} \right) \right], \quad (5)$$

$$\frac{\partial c_{\text{O}}}{\partial t} + \nabla \cdot (c_{\text{O}} \vec{u}_{\text{Si}}) = \nabla \cdot \left[ c_{\text{Si}} D_{\text{O}} \nabla \left( \frac{c_{\text{O}}}{c_{\text{Si}}} \right) \right], \quad (6)$$

where  $c_{\text{C}}$  is the molar concentration of carbon atoms in the melt,  $c_{\text{O}}$  is the molar concentration of oxygen atoms in the melt, and  $c_{\text{Si}}$  is the molar concentration of silicon atoms. The vector  $\vec{u}_{\text{Si}}$  is the flow vector of silicon melt.  $D_{\text{O}}$  and  $D_{\text{C}}$  are diffusivities of oxygen and carbon in the melt, respectively. Their values are taken to be  $5.0 \times 10^{-8} \text{m}^2/\text{s}$  (Liu et al. 2007).

For every chemical reaction, a detailed illumination is given. The first is the dissolution of the quartz crucible,



In this chapter, the index symbol (s) denotes solid, (m) denotes melt, (g) denotes gas, (l) denotes liquid, and (c) denotes crystal. For a unidirectional solidification furnace, the equilibrium concentration of oxygen atoms  $c_{\text{O}}$  on the wall of the quartz crucible is expressed as (Matsuo et al. 2008).

$$c_{\text{O}} = \frac{b}{1-b} \times 0.5 \times 10^{23} [\text{atom}/\text{cm}^3],$$

$$b = 1.32 \times \exp\left(\frac{-7150}{T} - 6.99\right). \quad (8)$$

The oxygen atoms in the melt are then transported to the melt/gas interface by convection or diffusion. At the interface, they combine with silicon atoms to form SiO gas, that is,

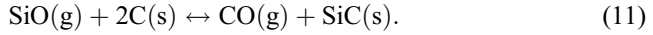


The equilibrium relationship between the concentration of SiO(g) and the concentration of O(m) is given in the paper (Bornside and Brown 1995):

$$c_{\text{SiO}} = \frac{101325}{RT} \frac{c_{\text{O}}}{c_{\text{Si}}} e^{-21000/T+17.8}, \quad (10)$$

where  $R$  is the universal gas constant, which is equal to  $8.314 \text{ J} \cdot \text{K}^{-1} \cdot \text{mol}^{-1}$ .

The third is the transportation of SiO(g) in argon flow. When SiO(g) comes into contact with the hot carbon surfaces during the transportation, it reacts with them,



The free energy change  $\Delta G$  of the reaction in Eq. (11) is expressed as (Bornside and Brown 1995).

$$\begin{aligned} \Delta G &= -81300 + 3.02T \text{ (J/mol)} \text{ for } T < 1640\text{K}, \\ \Delta G &= -22100 - 33.1T \text{ (J/mol)} \text{ for } 1640\text{K} < T < 1687\text{K}, \\ \Delta G &= -72100 - 3.44T \text{ (J/mol)} \text{ for } T > 1687\text{K}. \end{aligned} \quad (12)$$

The equilibrium constant of the reaction in Eq. (11) can be obtained as  $K = e^{-\Delta G/RT}$ . The rate constant for the forward direction  $k^{\text{forward}}$  is assumed to be large enough ( $k^{\text{forward}} = 10^6 \text{ cm/s}$ ) and the rate constant for the reverse direction is computed from the relation  $k^{\text{reverse}} = k^{\text{forward}}/K$  (Bornside and Brown 1995). This extremely large forward rate constant corresponds to small carbon concentration in crystal as pointed out by Bornside and Brown (1995).

After obtaining the rate constants, we can use them to obtain the flux relations at hot carbon surfaces:

$$-\vec{n} \cdot \left[ cD_{\text{SiO}} \nabla \left( \frac{c_{\text{SiO}}}{c} \right) \right] = k^{\text{forward}} c_{\text{SiO}} - k^{\text{reverse}} c_{\text{CO}}, \quad (13a)$$

$$-\vec{n} \cdot \left[ cD_{\text{CO}} \nabla \left( \frac{c_{\text{CO}}}{c} \right) \right] = k^{\text{reverse}} c_{\text{CO}} - k^{\text{forward}} c_{\text{SiO}}, \quad (13b)$$

where the unit vector  $\vec{n}$  points outward from the gas field, and  $k^{\text{forward}}$  and  $k^{\text{reverse}}$  are dimensional forward and reverse rate constants, respectively.

The fourth is the transportation of the product CO back to the gas/melt interface in the argon flow. At the interface, the CO gas dissolves into the melt according to the reaction



The equilibrium relationship between the above reactants and resultants is given as (Bornside and Brown 1995).

$$c_{\text{CO}} = \frac{101325}{RT} \frac{c_{\text{O}}}{c_{\text{Si}}} \frac{c_{\text{C}}}{c_{\text{Si}}} e^{-5210/T+14.5}. \quad (15)$$

The fifth is the segregation of carbon and oxygen from the melt into the crystal. The equilibrium expression is

$$\text{C(m)} \leftrightarrow \text{C(c)}, \quad (16)$$

$$\text{O(m)} \leftrightarrow \text{O(c)}. \quad (17)$$

We use  $\text{C(c)} = k_{\text{Cseg}}\text{C(m)}$  and  $\text{O(c)} = k_{\text{Oseg}}\text{O(m)}$  with  $k_{\text{Cseg}} = 0.07$  (Bornside and Brown 1995) and  $k_{\text{Oseg}} = 0.85$  (Hoshikawa and Huang 2000).

Equations (10) and (15) can be regarded as boundary conditions for the gas/melt interface. Other than those, two extra boundary conditions are required for solving the four unknowns  $c_{\text{SiO}}$ ,  $c_{\text{CO}}$ ,  $c_{\text{O}}$ , and  $c_{\text{C}}$  at that interface. We introduce the conservation of moles for carbon and oxygen. That means the flux of oxygen and carbon at that interface should satisfy the following:

$$\text{Foroxygen } c_{\text{Ar}}D_{\text{SiO}}\nabla\left(\frac{c_{\text{SiO}}}{c_{\text{Ar}}}\right) + c_{\text{Ar}}D_{\text{CO}}\nabla\left(\frac{c_{\text{CO}}}{c_{\text{Ar}}}\right) = c_{\text{Si}}D_{\text{O}}\nabla\left(\frac{c_{\text{O}}}{c_{\text{Si}}}\right), \quad (18)$$

$$\text{Forcarbon } c_{\text{Ar}}D_{\text{CO}}\nabla\left(\frac{c_{\text{CO}}}{c_{\text{Ar}}}\right) = c_{\text{Si}}D_{\text{C}}\nabla\left(\frac{c_{\text{C}}}{c_{\text{Si}}}\right). \quad (19)$$

Except for the above specifications, other boundary conditions in gas and melt are given. For noncarbon walls in gas, zero fluxes of  $\text{SiO(g)}$  and  $\text{CO(g)}$  are applied; for the gas inlet, the concentrations of  $\text{SiO(g)}$  and  $\text{CO(g)}$  are set to zero; for the gas outlet, zero gradients of them are used and for the melt/crucible wall, zero flux of  $\text{C(m)}$  is used.

## Distribution of Impurities

The  $\text{CO(g)}$  in gas and  $\text{C(m)}$  in melt are shown in Figs. 4 and 5. The maximum  $\text{CO}$  concentration in gas is about  $10^{-9}$  mol/cm<sup>3</sup>. The minimum  $\text{CO}$  concentration is about  $10^{-10}$  mol/cm<sup>3</sup>, which lies on the melt surface. The concentration of  $\text{CO}$  is large in the top half of the furnace except inside the crucible and small in the bottom half of the furnace. The basic order of  $\text{C(m)}$  concentration is about  $10^{+18}$  atom/cm<sup>3</sup>, which is the same as the experimental result reported by Ganesh et al. (2008). The concentration of  $\text{C(m)}$  in the melt is large at the top of the melt and small at the bottom of the melt. This distribution is consistent with the process in which  $\text{CO(g)}$  is first absorbed and dissolved in the melt and then carbon is transported to the bottom by convection or diffusion.

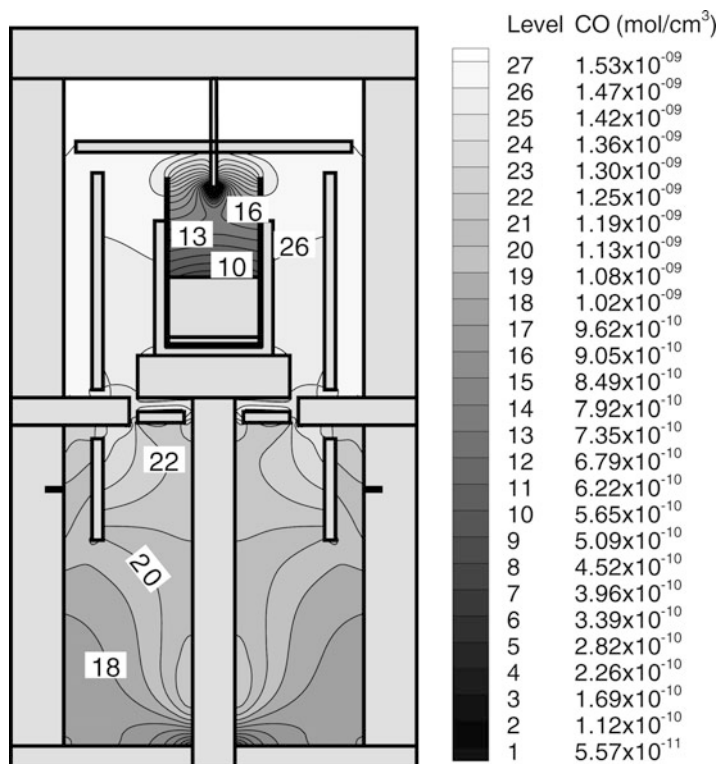


Fig. 4 CO concentration in gas

### Effect of Argon Gas Flow Rate

The effect of flow rate through the furnace on carbon concentrations in the crystal was tested. The inlet static temperature was fixed at 350 K and the outlet static pressure was fixed at 0.1 atm. The simulations were performed with flow rates of 0.8, 1.6, 2.4, 3.2, and 4.0 liter/min. The variations of carbon concentrations with flow rates at a specific point are shown in Fig. 6. A measured carbon concentration in crystal is added to Fig. 6 to affirm whether our calculation is quantitatively close to realistic value. As the flow rate is increased by fivefold from 0.8 liter/min to 4.0 liter/min, the carbon concentration in the crystal decreases by six fold from  $3.28 \times 10^{17}$  atom/cm<sup>3</sup> to  $0.54 \times 10^{17}$  atom/cm<sup>3</sup>. Thus, an increase in flow rate can obviously reduce the carbon impurity in the crystal.

### Effect of Argon Gas Pressure

The effect of furnace pressure on carbon impurities was examined. The mass flux at the inlet was fixed at  $7.68 \times 10^{-5}$  kg/min and the inlet static temperature was fixed at 350 K. The simulations was implemented with outlet pressures of 0.2, 0.3, 0.4,

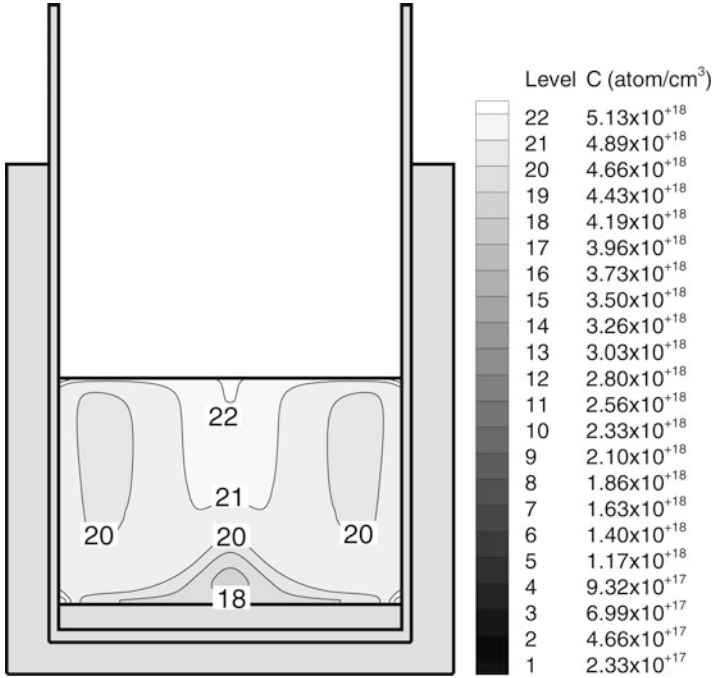
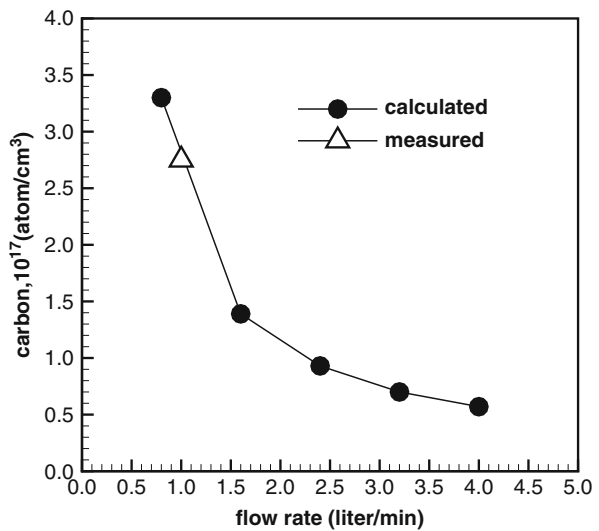


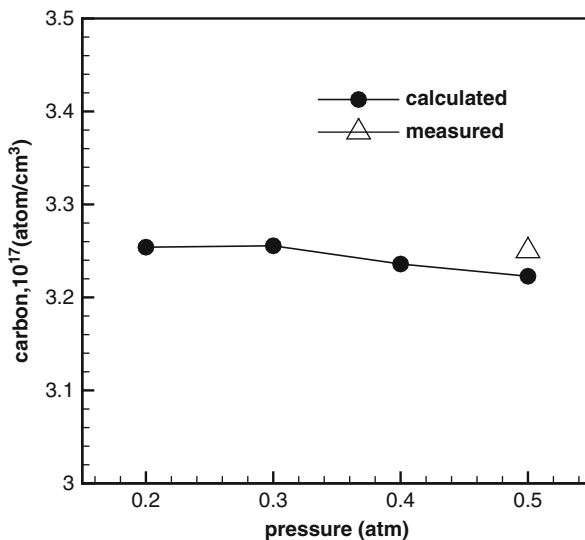
**Fig. 5** Carbon atom concentration in the melt

**Fig. 6** Carbon atom concentration in the crystal with different argon gas flow rate



and 0.5 atm. The variations of carbon concentrations with pressures at a specific point are shown in Fig. 7. When the pressure is increased from 0.2 atm to 0.5 atm, the carbon concentration remains almost constant. Thus, an increase in pressure does not obviously reduce the carbon impurity in the crystal.

**Fig. 7** Carbon atom concentration in the crystal with different argon gas pressure



Carbon concentration in the crystal is mainly determined by the flow conditions at the gap between crucible 3 and heater 12 shown in Fig. 2. An increase in pressure causes a reduction of outgoing velocity at that gap, and it therefore becomes easier for CO(g) to diffuse toward the inside of the crucible. However, the diffusivity of CO is reduced due to the increase in pressure according to Eq. (4). Thus, the effect of resistance reduction is offset by the effect of diffusivity reduction for CO(g). Pressure therefore has no great effect on the carbon concentration in the crystal.

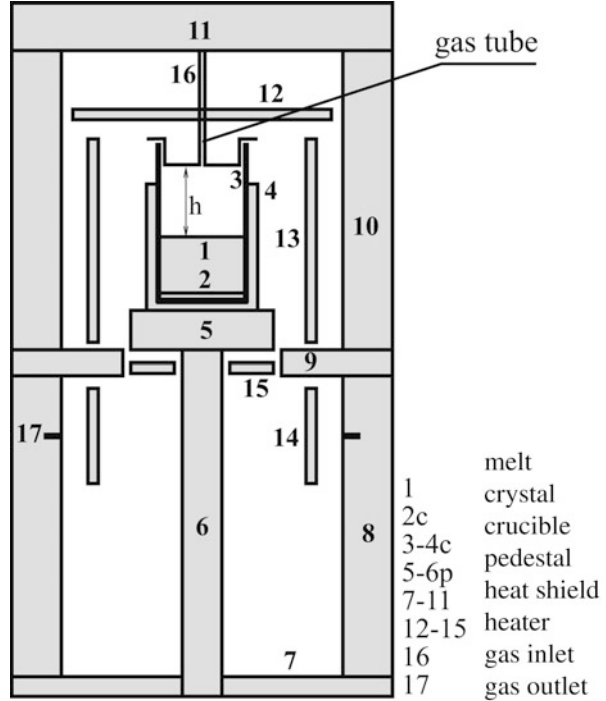
## Reduction of Carbon Impurity

Figure 3 shows that there is a recirculation flow above the melt surface and a main convection flow passing through the top of the crucible. The back-diffusion of CO from the outside of crucible into the melt is hindered by the top convection flow. Therefore, if the top convection flow is strengthened, in addition to elimination of the recirculation flow, CO transportation into the melt might be dramatically reduced. It can be seen from Fig. 3 that CO is transported into the melt mainly by diffusion flux that passes through the area AB. If the diffusion area is markedly reduced, CO flux into the melt can be significantly reduced. An optimized design according to the above analysis is given in the following section.

### Crucible Cover Design (Reproduced with Permission from *J. Cryst. Growth*, 312(9), 1572–1576, Copyright 2010, Elsevier)

To reduce the carbon impurity, the gas tube is extended to form a cover as shown in Fig. 8. The cover material can be made of graphite, tungsten, or molybdenum.

**Fig. 8** Improved design of a unidirectional solidification furnace



The distance  $h$  between the cover and the melt surface is variable. Global simulation of impurity transport was carried out for  $h = 28, 49,$  and  $105$  mm. The third case ( $h = 105$  mm) corresponds to the old furnace that has no cover. All of the calculations show the same inlet and outlet conditions.

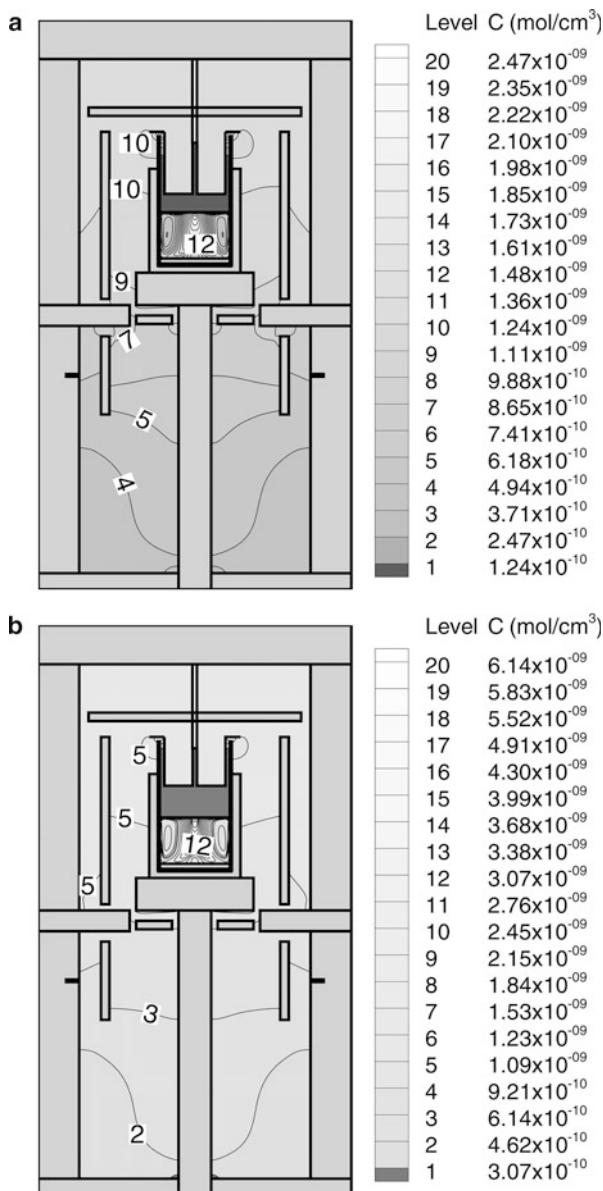
The carbon concentration distributions (CO in gas and C atoms in melt) for the old furnace can be referred to the paper (Gao et al. 2010a). The basic order of CO concentration in gas is  $10^{-9}$  mol/cm<sup>3</sup>. The carbon concentration in the melt is  $10^{18}$  atom/cm<sup>3</sup>, which is close to  $10^{-6}$  mol/cm<sup>3</sup>. Here, we use the relation  $1 \text{ mol} = 0.622 \times 10^{24}$  atoms. Thus, for the old furnace, the carbon concentration in the melt is much larger than that in the gas.

For two new furnace cases of different  $h$  values, the C distributions are shown in Fig. 9a, b. The carbon concentrations in the melt show almost the same order as those in the gas. In the cases of distances of 28 and 49 mm, both the basic orders of carbon concentrations in the melt are  $10^{-9}$  mol/cm<sup>3</sup>. Thus, smaller carbon concentrations are obtained in the melt compared to that in the old case ( $10^{-6}$  mol/cm<sup>3</sup>) (Gao et al. 2010a).

If the segregation relation for carbon atoms is considered, the carbon concentration for a chosen position in the crystal is given in Fig. 10. The basic order of carbon concentration in the crystal for the old furnace was  $10^{17}$  atom/cm<sup>3</sup>. Compared to that, the basic order for the improved furnace is  $10^{13}\sim 10^{14}$  atom/cm<sup>3</sup>, which is of a negligible quantity in crystal growth.



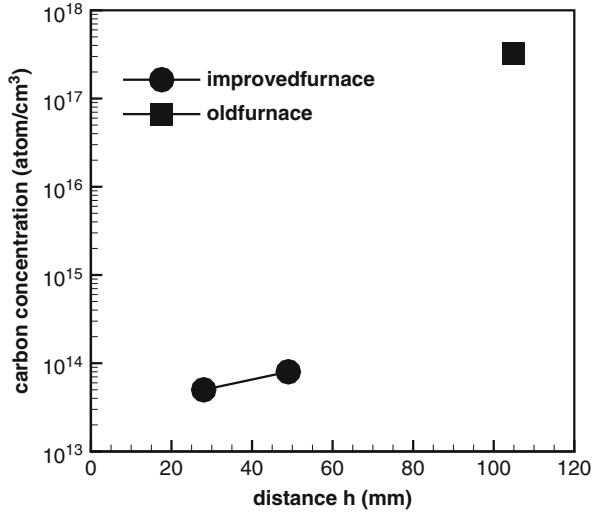
**Fig. 9** (a) Carbon concentration distribution (CO in gas and C in melt) for the improved furnace at  $h = 28$  mm. (b) Carbon concentration distribution (CO in gas and C in melt) for the improved furnace at  $h = 49$  mm



**Crucible Cover Material Design (Reproduced with Permission from J. Cryst. Growth, 318 (1), 255–258, Copyright 2011, Elsevier)**

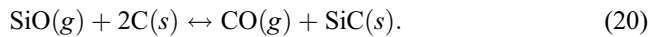
The carbon concentration can be reduced with the gas shield design. The choice of material of the gas shield is important. Some depositions such as SiC particles are possible if the gas SiO reacts with the gas shield. A drop of deposited material can

**Fig. 10** Comparison of carbon concentrations in the crystal for the improved and old furnaces



affect the quality of silicon growth. Therefore, the material of the gas shield should have chemical inertia and a high melting point so that the gas SiO has almost no reaction with it.

For example, when the cover is made from graphite, evaporated SiO gas comes into contact with the hot carbon cover, and it reacts with them:



Then the product CO gas can be transported back to the gas/melt interface in the argon flow. At the interface, the CO gas dissolves into the melt according to the reaction:



Therefore, there are two sources for carbon impurity in a crystal. One is the carbon cover inside the crucible and the other is the graphite components of the furnace outside the crucible.

When the cover is made from tungsten or molybdenum, the evaporated SiO gas does not have a chemical reaction with the cover. Therefore, the only source of carbon in the crystal is the graphite components of furnace outside the crucible.

The CO concentration in a gas and the C atom concentration in melt for the improved furnace with a tungsten cover at  $h = 28$  mm are shown in Figs. 11 and 12, respectively. Figure 11 shows that the basic order of the CO gas concentration is  $10^{-10}$  mol/cm<sup>3</sup> outside the crucible and it is  $10^{-13}$  mol/cm<sup>3</sup> inside the crucible. Figure 12 shows that the carbon concentration in most of the melt is  $10^{14}$  atoms/cm<sup>3</sup>. Therefore, for furnace with tungsten cover, the CO concentration inside the crucible is three orders smaller than that outside the crucible.

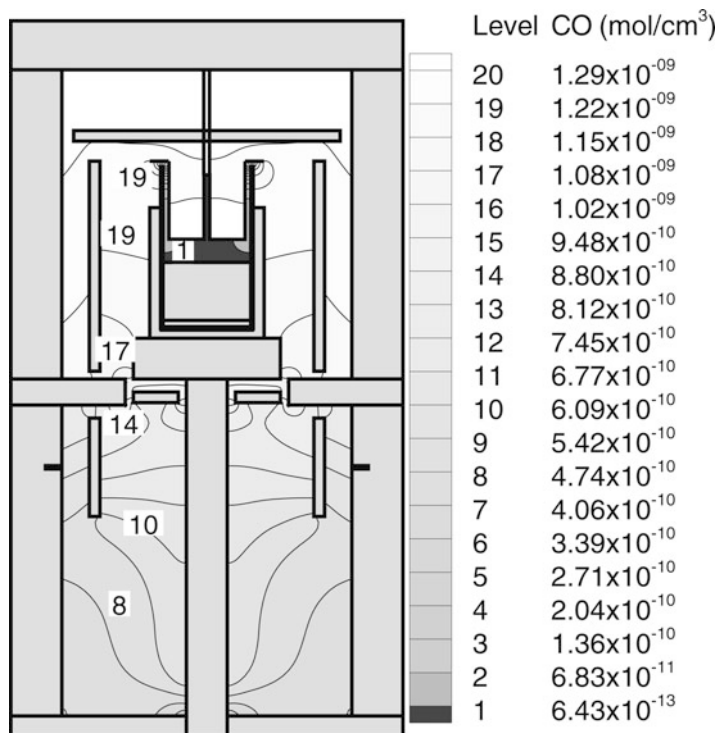


**Fig. 11** CO concentration distribution in gas for the improved furnace with a tungsten cover at  $h = 28$  mm

The CO concentration in gas and the C atom concentration in melt for the improved furnace with a carbon cover at  $h = 28$  mm are shown in Figs. 13 and 14, respectively. From Fig. 13, it can be seen that the basic order of the CO gas concentration is  $10^{-9}$  mol/cm<sup>3</sup> outside the crucible and it is  $10^{-10}$  mol/cm<sup>3</sup> inside the crucible. Figure 14 shows that the carbon concentration in most of the melt is  $10^{17}$  atoms/cm<sup>3</sup>. Therefore, for furnace with carbon cover, the CO concentration inside the crucible is only one order smaller than that outside the crucible.

From Figs. 11, 12, 13, and 14, it can be seen that the reaction of carbon cover obviously increases the CO concentration inside the crucible from  $10^{-13}$  mol/cm<sup>3</sup> to  $10^{-10}$  mol/cm<sup>3</sup> and increases the C impurity in the melt from  $10^{14}$  atoms/cm<sup>3</sup> to  $10^{17}$  atoms/cm<sup>3</sup>.

It has been reported (Gao et al. 2010a) that for the old furnace without the cover, the basic order of the carbon concentration in the melt is  $10^{18}$  atoms/cm<sup>3</sup>. Therefore, the carbon concentration in melt with carbon cover ( $10^{17}$  atoms/cm<sup>3</sup>) is much larger than that with tungsten cover ( $10^{14}$  atoms/cm<sup>3</sup>), but smaller than that without any cover ( $10^{18}$  atoms/cm<sup>3</sup>).

If the segregation relation for carbon atoms is considered, the carbon concentration in crystal along the center axial line of crucible is given in Fig. 15. The basic

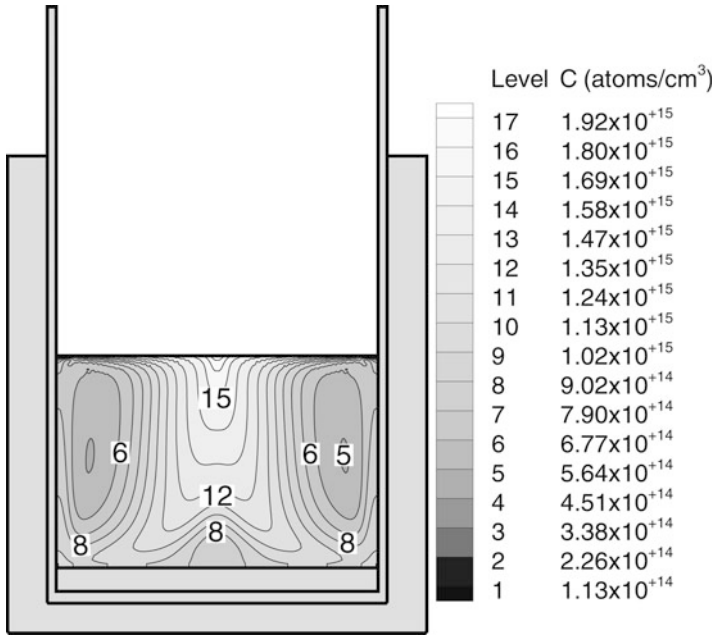


**Fig. 12** C concentration distribution in melt for the improved furnace with a tungsten cover at  $h = 28$  mm

**Fig. 13** CO concentration distribution in gas for the improved furnace with a carbon cover at  $h = 28$  mm

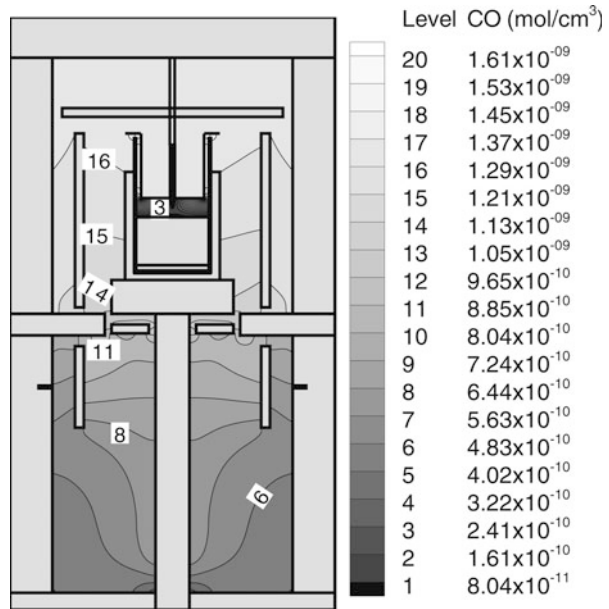


**Fig. 14** C concentration distribution in melt for the improved furnace with a carbon cover at  $h = 28$  mm

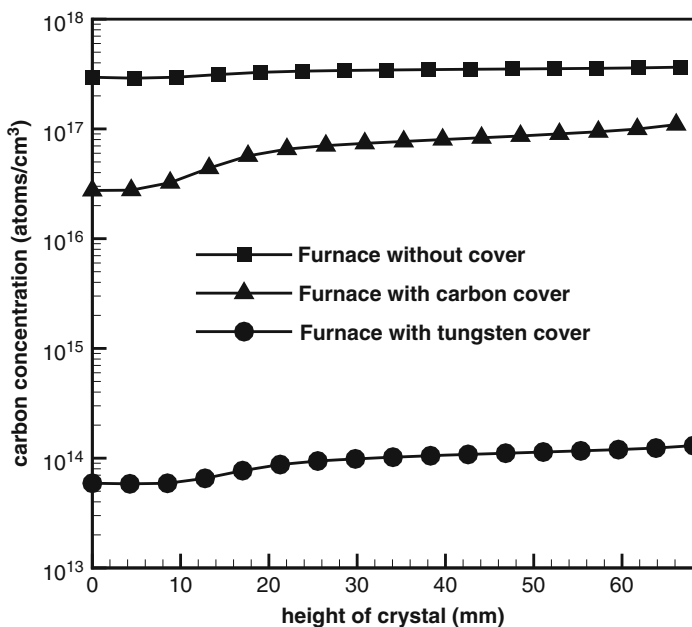
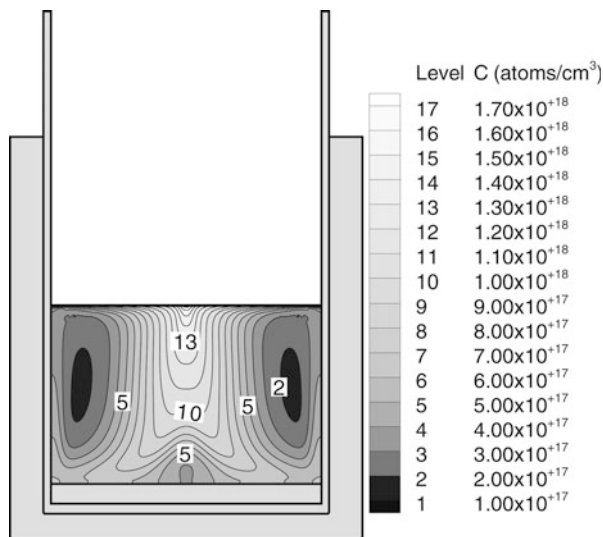


**Fig. 15** Comparison of carbon concentrations in the crystal for the old furnace and improved furnaces with different cover materials

order of carbon concentration in the crystal for the furnace without cover is  $10^{17}$ – $10^{18}$  atoms/cm<sup>3</sup>. The basic order for the improved furnace with a tungsten cover is  $10^{13}$ – $10^{14}$  atoms/cm<sup>3</sup>, which is of a negligible quantity in crystal growth.

However, the carbon impurity for the improved furnace with a carbon cover is  $10^{16}$ – $10^{17}$  atoms/cm<sup>3</sup>, which is much higher than that in the case with a tungsten cover. Therefore, the material of the cover has a large effect on impurity in multi-crystalline silicon. Since a high-purity silicon crystal is required with low cost, we propose a compromise to design the cover. We still use carbon material to design the cover, but we deposit a thin layer of tungsten or tungsten carbide on the surface. This method can save cost and enables a crystal of high purity to be obtained; furthermore, this method can prevent SiC particles falling down to the melt surface.

### Reaction Control Between Silica Crucible and Graphite Susceptor (Reproduced with Permission from *J. Cryst. Growth*, 314(1), 239–245, Copyright 2011, Elsevier)

#### Another Origin of Carbon Impurities

In previous sections, the carbon impurity is mainly caused by the reaction between SiO gas and graphite components of the furnace. However, there is another source of carbon impurity, which might be caused by the direction reaction between graphite susceptor and silica crucible. Figure 16 shows the structure of the silica crucible and the graphite susceptor used in this study. The reactions around the corner, where there are three materials, i.e., the silica crucible, the graphite susceptor, and the gas, can be expressed as

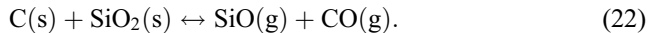
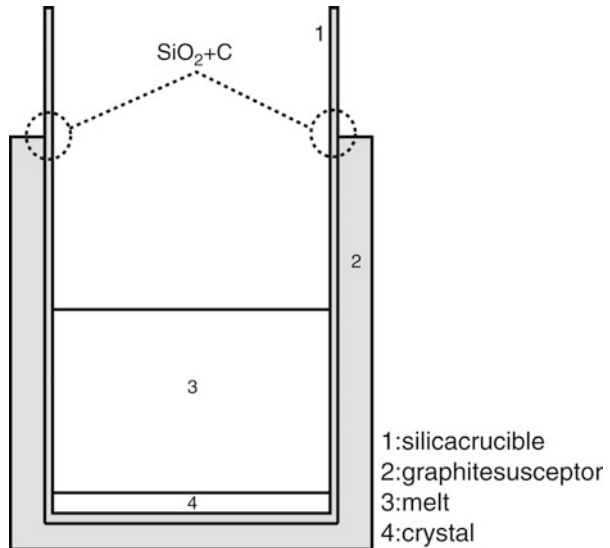
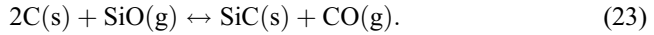


**Fig. 16** Configurations of the silica crucible and the graphite susceptor in a unidirectional solidification furnace



Around the corner, the graphite susceptor can also react with SiO gas evaporated from the melt/gas interface:



The symbol (g) denotes gas and (s) denotes solid; (l) denotes liquid and (m) denotes species in the melt.

The product CO gas in reactions (22) and (23) can be transported back to the gas/melt interface by argon gas and is then dissolved into the melt. Finally, C atoms are incorporated into crystal.

### Chemical Reaction Model Along the Corner

Both of reactions (22) and (23) are considered along the corner. Because of the lack of kinetic data on the heterogeneous reactions, equilibrium reactions are assumed. For effectively modeling the chemical reactions along the corner, a concept of solvent and solute is first introduced. As is well known, the melting point of silica is around 1900 K and that of graphite is about 3800 K (Whittaker 1978). Silica is more active during chemical reaction in a high temperature furnace. Therefore, SiO<sub>2</sub> (silica) can be approximately considered as a solvent and C atoms from the surface of the graphite susceptor can be approximately regarded as a solute inside the SiO<sub>2</sub> solvent.

After introduction of the concept of solvent and solute, analysis of the heterogeneous reactions can be done as follows.

The equilibrium constant for the reaction (22) is taken as

$$K_1 = \frac{a_{\text{SiO}(\text{g})}a_{\text{CO}(\text{g})}}{a_{\text{SiO}_2(\text{l})}a_{\text{C}(\text{m})}} = e^{-\Delta G_{0(1)}/RT}. \quad (24)$$

The activities of species,  $a$ , are expressed as

$$a_{\text{SiO}_2(\text{l})} = 1, \quad a_{\text{C}(\text{m})} = \frac{c_{\text{C}}}{c_{\text{SiO}_2}}, \quad a_{\text{SiO}(\text{g})} = \frac{P_{\text{SiO}(\text{g})}}{101325 \text{ Pa}}, \quad a_{\text{CO}(\text{g})} = \frac{P_{\text{CO}(\text{g})}}{101325 \text{ Pa}}, \quad (25)$$

where  $c_{\text{C}}$  is the concentration of the C solute in the SiO<sub>2</sub> solvent, and  $c_{\text{SiO}_2}$  is the concentration of the SiO<sub>2</sub> solvent, which is set to approximately 43,900 mol/m<sup>3</sup> according to its molar mass (0.06 kg/mol) and density (2648 kg/m<sup>3</sup>) (Greenwood and Earnshaw 1984).

The free energy change for reaction (22) in the temperature range from 1300 K to 1800 K is expressed as (Schmid and Khattack 1979).

$$\Delta G_{0(1)} = 681899 - 339T(\text{J/mol}). \quad (26)$$

Substitution of Eqs. (25) and (26) into Eq. (24) yields one pressure relationship between the SiO and CO gases:

$$P_{\text{SiO(g)}}P_{\text{CO(g)}} = 1.439e^{-82018.162/T+52.775}c_C. \quad (27)$$

Because the reactants of reaction (23) include the gas phase SiO and the solid phase C, the equilibrium constant for reaction (23) can be taken as

$$K_2 = P_{\text{CO(g)}}/P_{\text{SiO(g)}} = e^{-\Delta G_{0(2)}/RT}. \quad (28)$$

The standard free energy change for reaction (23) in the temperature range from 1300 K to 1800 K is expressed as (Schmid and Khattack 1979).

$$\Delta G_{0(2)} = 600691 - 335T(\text{J/mol}). \quad (29)$$

Substitution of Eq. (29) into Eq. (28) yields another pressure relationship between the SiO and CO gases:

$$P_{\text{CO(g)}}/P_{\text{SiO(g)}} = e^{-72250.541/T+40.293}. \quad (30)$$

From Eqs. (27), and (30), the pressures of the SiO and CO gases are expressed as functions of temperature and C solute concentration in the SiO<sub>2</sub> solvent:

$$P_{\text{CO(g)}} = 1.200e^{-77134.352/T+46.534}\sqrt{c_C}, \quad (31)$$

$$P_{\text{SiO(g)}} = 1.200e^{-4883.811/T+6.241}\sqrt{c_C}. \quad (32)$$

### Effect of Crucible Reaction on Carbon Impurity

Four calculations were implemented with C solute concentrations of 0.02, 0.1, 0.2, and 0.4 mol/m<sup>3</sup>. Because of the decoupled calculation between the gas convection and species transport, the entire temperature field and the gas convection for all of the calculations are fixed and only species transports are changed for every case.

For  $c_C = 0.1$  mol/m<sup>3</sup>, the CO concentration in the gas is shown in Fig. 17. The maximum CO concentration in the gas, which is located at the corner, is  $7.07 \times 10^{-9}$  mol/cm<sup>3</sup>. As reported previously (Gao et al. 2010b), if the reaction between the crucible and the susceptor is neglected, the maximum CO concentration in the gas, which is located below the corner, is  $1.53 \times 10^{-9}$  mol/cm<sup>3</sup>. Therefore, the crucible reaction markedly increases the maximum CO concentration in the gas.

To better observe the effect of the crucible reaction on C impurity in the melt, an enlarged figure near the corner is shown in Fig. 18. It can be clearly seen that the maximum CO concentration is exactly located at the corner. There is a large gradient from the corner to the melt surface, which causes a large carbon flux into the melt from the corner. Therefore, the crucible reaction between the silica crucible and the graphite susceptor is an essential source of carbon impurity in the melt and crystal.

If the C solute concentration in the SiO<sub>2</sub> solvent is increased to a larger value, the C impurity concentration in the melt should be increased more. Figure 19 shows the



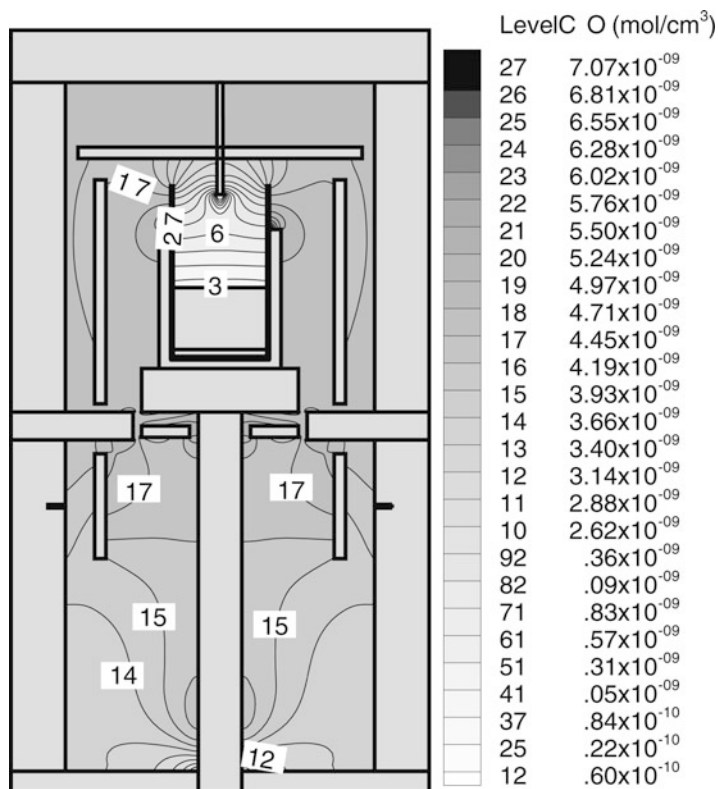


**Fig. 17** CO concentration in the gas for C solute concentration of  $0.1 \text{ mol/m}^3$  in the  $\text{SiO}_2$  solvent

variation of C impurity concentration at the center of the melt surface with increase in C solute concentration in the  $\text{SiO}_2$  solvent. It can be seen that C impurity in the melt is markedly increased with increase in C solute concentration, i.e., increase in C activity on the surface of the graphite susceptor.

## Conclusions

Carbon contamination during the growth of crystalline silicon has been examined by numerical simulation. Due to the similar contamination mechanism in unidirectional solidification and Cz processes, the simulation was performed only in the unidirectional solidification furnace. Both gas transport and melt transport were included. Five chemical reactions were considered. The impurity distributions in the gas and melt were given. Results show that an increase in flow rate can obviously reduce carbon impurity in the crystal, and pressure does not have a great effect on carbon contamination.

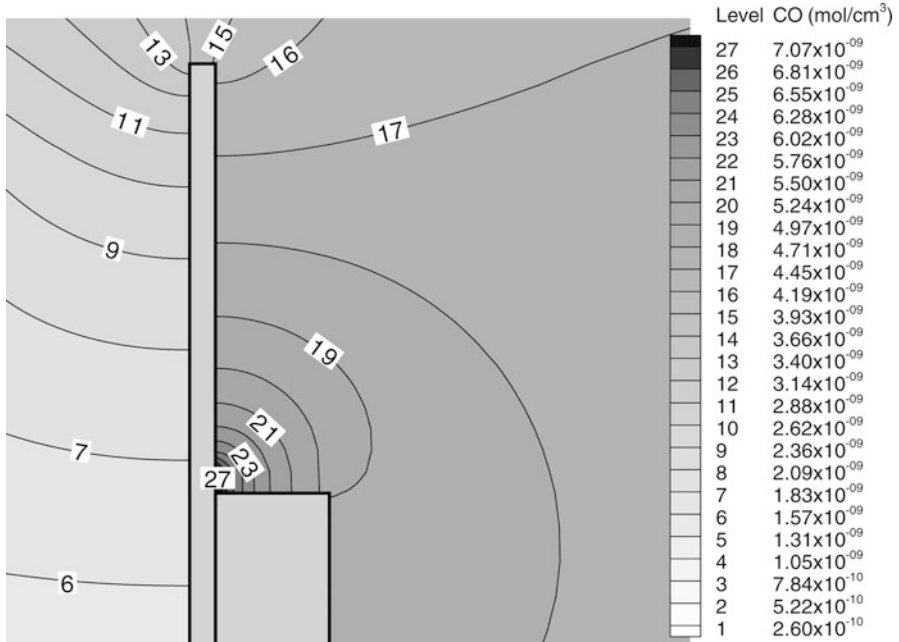


**Fig. 18** Enlarged CO concentration distribution near the corner for C solute concentration of 0.1 mol/m<sup>3</sup> in the SiO<sub>2</sub> solvent

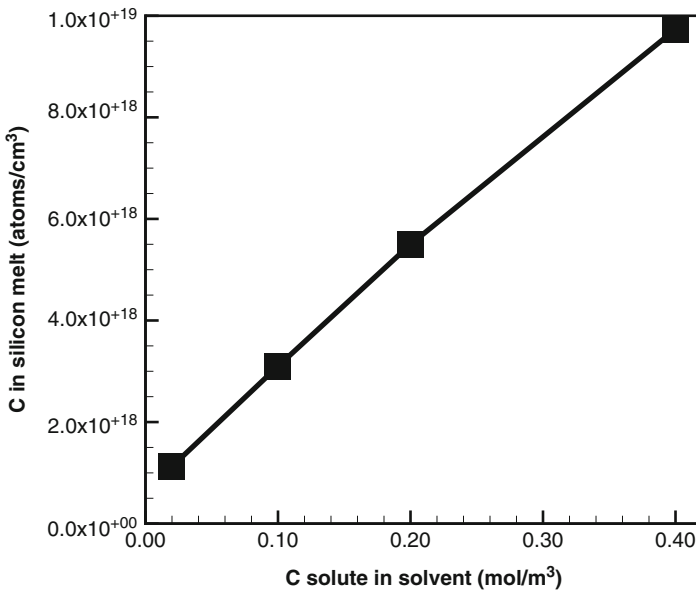


**Fig. 19** Variation of C impurity concentration in the silicon melt with increase in C solute concentration in the SiO<sub>2</sub> solvent

To reduce carbon contamination, an improved unidirectional solidification furnace with a crucible cover was designed. Global simulations of coupled oxygen and carbon transport show that the carbon concentration in the crystal can be reduced from  $10^{17}$  atom/cm<sup>3</sup> to  $10^{14}$  atom/cm<sup>3</sup>. This improvement enables the production of a high-purity multicrystalline silicon crystal in a unidirectional solidification furnace. In addition, the material of crucible cover has a great influence on carbon contamination. The results showed that the carbon impurity can be reduced by ten times if the cover is made from carbon and that the carbon impurity can be reduced by 1000 times if the cover is made from tungsten or tungsten carbide. Therefore, an effective and economical method for designing a cover is to use carbon and deposit a thin layer of tungsten or tungsten carbide on it.

Another possible contamination mechanism due to the reaction between silica crucible and the graphite susceptor has been examined. Results show that the crucible reaction has a marked effect on carbon impurity in the crystal. When carbon activity on the surface of the graphite susceptor increases, carbon impurity increases rapidly. Thus, setting a free space between the silica crucible and the graphite susceptor to prevent reaction between them is an effective method to further reduce carbon contamination in crystalline silicon.

---

## References

- J.A. Baker, *Semiconductor Silicon 1969*, ed. by R.R. Haberecht, E.L. Kern (Electrochemical Society, New York, 1969)
- J. Bauer, O. Breitenstein, J. P. Rakotoniaina, in *Proceedings of 21st EUPVSEC*, Dresden, 2006, p. 1115
- D.E. Borside, R.A. Brown, *J. Electrochem. Soc.* **142**, 2790 (1995)
- T. Fukuda, M. Koizuka, A. Ohsawa, *J. Electrochem. Soc.* **141**, 2216 (1994)
- R.B. Ganesh, H. Matsuo, T. Kawamura, Y. Kangawa, K. Arafune, Y. Ohshita, M. Yamaguchi, K. Kakimoto, *J. Cryst Growth* **310**, 2697 (2008)
- B. Gao, S. Nakano, K. Kakimoto, Global simulation of coupled carbon and oxygen transport in a unidirectional solidification furnace for solar cells. *J. Electrochem. Soc.* **157**(2), H153–H159 (2010a)
- B. Gao, X.J. Chen, S. Nakano, K. Kakimoto, *J. Cryst Growth* **312**, 1572 (2010b)
- U. Goesele, Oxygen, carbon, hydrogen and nitrogen in crystalline silicon, in *Mater. Res. Soc. Symp. Proc.*, ed. by J. C. Mikkelsen Jr., S. P. Peaton, J. W. Corbett, S. J. Pennycook, (MRS, Pittsburgh, 1986), p. 419
- N.N. Greenwood, A. Earnshaw, *Chemistry of the Elements* (Pergamon, Oxford, 1984), pp. 393–399. ISBN 0-08-022057-6
- M. Higasa, Y. Nagai, S. Nakagawa, K. Kashima, *ECS Trans.* **72**(4), 57 (2016)
- H. Hirata, K. Hoshikawa, *J. Cryst Growth* **125**, 181 (1992)
- K.A. Hoffmann, S.T. Chiang, *Computational Fluid Dynamics*, vol II (Engineering Education System, Wichita, 2000), p. 69
- K. Hoshikawa, X. Huang, *Mater. Sci. Eng.* **B72**, 73 (2000)
- P. Jenny, B. Müller, *Comput. Fluids* **28**, 951 (1999)
- K. Kakimoto, K.W. Yi, M. Eguchi, *J. Cryst Growth* **163**, 238 (1996)
- T.A. Kinney, R.A. Brown, *J. Cryst Growth* **132**, 551 (1993)
- S. Kishino, M. Kanamori, N. Yoshihiro, M. Tajima, I. Lizuka, *J. Appl. Phys.* **50**, 8240 (1979)
- N. Kobayashi, *J. Cryst Growth* **108**, 240 (1991)

- B.O. Kolbesen, in *Aggregation Phenomena of Point Defects in Silicon*, ed. by E. Sirtl, J. Goorissen. The Electrochemical Society Proceedings Series, vol 83-4 (Pennington, 1983), pp. 155-175
- Y.R. Li, M.W. Li, N. Imaishi, Y. Akiyama, T. Tsukada, J. Cryst Growth **267**, 466 (2004)
- L.J. Liu, K. Kakimoto, Int. J. Heat Mass Transf **48**, 4481 (2005)
- L.J. Liu, S. Nakano, K. Kakimoto, J. Cryst Growth **299**, 48 (2007)
- N. Machida, Y. Suzuki, K. Abe, N. Ono, M. Kida, Y. Shimizu, J. Cryst Growth **186**, 362 (1998)
- N. Machida, K. Hoshikawa, Y. Shimizu, J. Cryst Growth **210**, 532 (2000)
- H. Matsuo, R.B. Ganesh, S. Nakano, L.J. Liu, Y. Kangawa, K. Arafune, Y. Ohshita, M. Yamaguchi, K. Kakimoto, J. Cryst Growth **310**, 2204 (2008)
- Y. Nagai, S. Nakagawa, K. Kashima, J. Cryst Growth **401**, 737 (2014)
- M. Ogino, Appl. Phys. Lett. **41**, 847 (1982)
- S. Pizzini, A. Sandrinelli, M. Beghi, D. Narducci, F. Allegretti, S. Torchio, G. Fabbri, G.P. Ottaviani, F. Demartin, A. Fusi, J. Electrochem. Soc. **135**, 155 (1988)
- L. Raabe, O. Patzold, I. Kupka, J. Ehrig, S. Wurzner, M. Stelter, J. Cryst Growth **318**, 234 (2011)
- R.C. Reid, J.M. Prausnitz, T.K. Sherwood, *The Properties of Gases and Liquids*, 3rd edn. (McGraw-Hill, Inc, New York, 1987)
- C. Reimann, J. Friedrich, G. Müller, S. Wurzner, H.J. Möller, *22nd European Photovoltaic Solar Energy Conference* (WIP-Munich, Milan, 2007)
- C. Reimann, T. Jung, J. Friedrich, G. Müller, in *Proceedings of the 33rd IEEE Photovoltaic Specialists Conference*, 2008. ISBN 978-1-4244-1641-7
- F. Schmid, C.P. Khattack, J. Electrochem. Soc. **126**, 935 (1979)
- F. Shimura, *Semiconductor Silicon Crystal Technology* (Academic Press, New York, 1989), p. 148
- A.D. Smimov, V.V. Kalaev, J. Cryst Growth **310**, 2970 (2008)
- A.D. Smimov, V.V. Kalaev, J. Cryst Growth **311**, 829 (2009)
- Q. Sun, K.H. Yao, J. Lagowski, H.C. Gatos, J. Appl. Phys. **67**, 4313 (1990)
- M. Watanabe, K.W. Yi, T. Hibiya, K. Kakimoto, Progr. Cryst Growth Charact Mater. **38**, 215 (1999)
- A.G. Whittaker, Science **200**, 763 (1978)
- K.W. Yi, K. Kakimoto, M. Eguchi, H. Noguchi, J. Cryst Growth **165**, 358 (1996)



Shuai Yuan and Deren Yang

## Contents

Introduction .....	464
Basic Properties of Nitrogen in Silicon .....	465
Existence .....	465
Detection and Measurements .....	466
Solubility .....	468
Diffusion .....	469
Nitrogen in Czochralski Silicon .....	470
Doping of N in CZ-Si Growth .....	470
N-O Complexes .....	471
Influence on O-Related Defects .....	474
Effect of N Impurity on Mechanical Properties .....	476
Nitrogen in Cast Multicrystalline Silicon .....	478
Soluble Nitrogen .....	478
Silicon Nitride Precipitates .....	482
Influence on Wafering and the Mechanical Strength of Wafers .....	483
Influence on Electric Properties of Cell Performance .....	485
Growth of Multicrystalline Silicon in Ambient Nitrogen .....	485
Gas Doping of N for Cast Mc-Si .....	485
Improvement in Mechanical Strength .....	487
Impact of N-O Complexes in Mc-Si Grown in Ambient N <sub>2</sub> .....	488
Conclusion .....	490
Cross-References .....	490
References .....	490

---

S. Yuan (✉)

State Key Laboratory of Silicon Materials and school of Materials Science and Engineering,  
Zhejiang University, Zhejiang, Hangzhou, China  
e-mail: [shuaiyuan@zju.edu.cn](mailto:shuaiyuan@zju.edu.cn)

D. Yang

State Key Laboratory of Silicon Materials and school of Materials Science and Engineering,  
Zhejiang University, Hangzhou, China  
e-mail: [mseyang@zju.edu.cn](mailto:mseyang@zju.edu.cn)

---

**Abstract**

This chapter starts with the basic features of nitrogen including the existence of N-related defects, detection and measurements of N content, the solubility, and diffusion of N impurities in silicon materials. From the perspective of photovoltaic application, the nitrogen doping method for Czochralski silicon is then introduced, and the results about the influence of nitrogen impurity on N-O complexes, O-related defects, and mechanical properties are presented. A second focus of this chapter is toward N-related defects in directionally solidified photovoltaic multicrystalline silicon (mc-Si) materials. The existence and distribution of N-related defects, the formation, and influence of silicon nitride precipitates in mc-Si are comprehensively described. Then the results about mc-Si growth in ambient nitrogen are presented as an application to further understand the properties of nitrogen in mc-Si.

---

**Keywords**

Czochralski silicon · Multicrystalline silicon · Nitrogen doping · Silicon nitride precipitates · Ambient nitrogen · Mechanical strength

---

**Introduction**

Crystalline silicon (c-Si) is the most important substrate material for solar cells, which occupies more than 90% of the market share in photovoltaic industry. Czochralski silicon (CZ-Si) and cast multicrystalline silicon (mc-Si) are the main types of c-Si materials. Nitrogen is one of the common light elemental impurities in silicon materials. Related research started decades ago. In the 1970s, nitrogen property in nitrogen-implanted silicon,  $\text{Si}_3\text{N}_4$  films on silicon substrate and even in float-zone silicon was widely studied. And in the 1980s, nitrogen was intentionally doped in CZ-Si wafers used for integrated circuit (IC) industry (Que et al. 1985; Yang et al. 1995). Due to the suppression of crystal-originated particles (COPs) (Yu et al. 2002), the enhancement on the nucleation of oxygen precipitates so as to improve the ability of internal gettering, and the increasement of mechanical strength, N-doped CZ-Si has been world widely applied (Yang et al. 2009; Yu et al. 2013). Moreover, N-doping in CZ-Si can also reduce high purity argon gas consuming expense, which helps to decrease the general cost of silicon crystal growth.

However, for photovoltaic materials as substrates of bulk devices, the modification by introducing oxygen precipitates is unwanted. Then the promising feature of nitrogen doping in CZ-Si crystal is to improve the material mechanical strength and to reduce the cost of protective gas by using cheaper nitrogen instead of high purity argon. So, intentional N-doping in CZ-Si becomes less attractive to photovoltaic manufactures. In the recent two decades, directionally solidified mc-Si has gradually become the leading photovoltaic substrate materials because of its low cost. Despite nitrogen was never intended to be doped into mc-Si, silicon nitride has been the optimal coating material to prevent the sticking between silicon ingots and quartz crucibles. The usage of silicon nitride coating made mc-Si growth in a N-rich environment so that the influence of N-related defects, especially  $\text{Si}_3\text{N}_4$  precipitates, is very important to the crystal quality.

Meanwhile, there are a few researches considering the further control of N impurity in mc-Si by other means.

This chapter firstly summarizes the basic properties of N-related impurity in general silicon materials. Then from the photovoltaic silicon perspective, we briefly introduce the influence of N-doping on the relevant properties in Czochralski silicon. Later, the existence and transformation of N-related impurity and precipitates in mc-Si are described. And finally, the growth of photovoltaic mc-Si using cheaper ambient nitrogen is presented and discussed.

## Basic Properties of Nitrogen in Silicon

### Existence

In crystalline silicon materials, soluble nitrogen atoms exist in the forms of monomer, dimer, or complex in Si lattice, and precipitates are formed when N concentration exceeds the solubility. Various N-containing defects can be formed based on the reaction and combination of N atoms (interstitial and substitutional,  $N_i$ , and  $N_s$ ), defective Si atoms (interstitials and vacancies,  $I$  and  $V$ ), and other impurity atoms like oxygen. The structure of the configurations determines the formation energy, thermal stability, and particular local vibrational modes (LVMS) of the defects. The actual form of N-related defects in a certain sample is strongly influenced by thermal history. And LVMS of the defects result in well-defined shifts in the vibrational frequencies, which help to identify the defects experimentally. The properties such as formation energy and LVMS of the N-containing configurations can be determined using first principle density functional theory; hence, the equilibrium stability can be predicted and the frequencies of the modes can be identified combined with infrared (and Raman) measurements (Jones et al. 1994b; Goss et al. 2003) (see the section “Detection and Measurements”). Table 1 gives the calculated formation energy per N atom of various combinations of  $N_i$ ,  $N_s$ ,  $I$ , and  $V$ , relative to the energy of the  $(N_i-N_i)$  defined as zero. The data shows that all configurations have higher formation energy compared with  $(N_i-N_i)$ , the only exception,  $2(N_i-N_i)$ , possesses a very small binding energy, so it should not be stable and significant. Since  $(N_i-N_i)$  has a large binding energy of 4.30 eV (Sawada and Kawakami 2000), and isolated  $N_i$  has a high mobility (see the section “Diffusion”), therefore, di-interstitial pairs  $(N_i-N_i)$  should be the dominant equilibrium state of nitrogen atoms in silicon lattice under growth temperature ( $>1400$  °C). The vibrational frequencies of many modes

**Table 1** Relative formation energies (eV) per N atom for various N configurations, zero is defined by that of  $(N_i-N_i)$  (Goss et al. 2003)

Structure	$2(N_i-N_i)$	$(N_i-N_i)$	$(N_s-N_s)$	$(N_i-N_s)$	$(N_i)_2I$
$E_f/N$ atom	-0.06	0.00	0.79	0.99	1.25
Structure	$(N_s-N_s)V$	$N_i$	$N_s$	$(N_s-N_s)V_2$	$(N_sV)$
$E_f/N$ atom	1.71	1.83	1.99	2.54	3.71

**Table 2** Calculated and observed frequencies ( $\text{cm}^{-1}$ ) of IR active local modes of  $^{14}\text{N}$  in Si (Goss et al. 2003)

	$(\text{N}_i-\text{N}_j)$	$\text{N}_s$
Calculated	967.8/772.9	637
Observed	962.1/765.6	653

have been investigated (Goss et al. 2003), among which, Table 2 shows the calculated and observed frequencies of the vibration modes of  $(^{14}\text{N}_i-^{14}\text{N}_j)$  and  $^{14}\text{N}_s$ . These two modes are the only detectable modes at room temperature verified in experimental measurements (Goss et al. 2003). Moreover, the fraction of  $\text{N}_s$  in total N atoms is lower than 1%, which indicates that the final state of N dimer at room temperature is  $(\text{N}_i-\text{N}_j)$  and the concentration of  $\text{N}_s$  in normal N-doped Si is usually lower than  $10^{13} \text{ cm}^{-3}$ . Therefore, the influence of ionized  $\text{N}_s$  donors on electrical properties can be ignored.

## Detection and Measurements

To date, secondary ion mass spectroscopy (SIMS) and Fourier transformation infrared spectroscopy (FTIR) are the most widely used methods to determine the N concentration in crystalline silicon. SIMS is usually adopted for total N concentration, independent of its chemical states, the lower detection limit can be extended to  $1 \times 10^{13} \text{ cm}^{-3}$ , but the measurement is relatively complicated and expensive when the N concentration is lower than  $5 \times 10^{14} \text{ cm}^{-3}$ , mainly limited by the background N concentration (Hockett and Sams 2000). IR measurements via the presence of N-related vibration modes can differentiate the forms of N atoms in silicon, as these modes have different absorption frequencies. Figure 1 shows the example of a mid-infrared range FTIR spectrum at room temperature. The quantitative measurement of concentration can be obtained from the absorbance at certain peaks:

$$C = \frac{1}{d} \alpha A = \frac{1}{d} \alpha \ln \left( \frac{I_0}{I} \right),$$

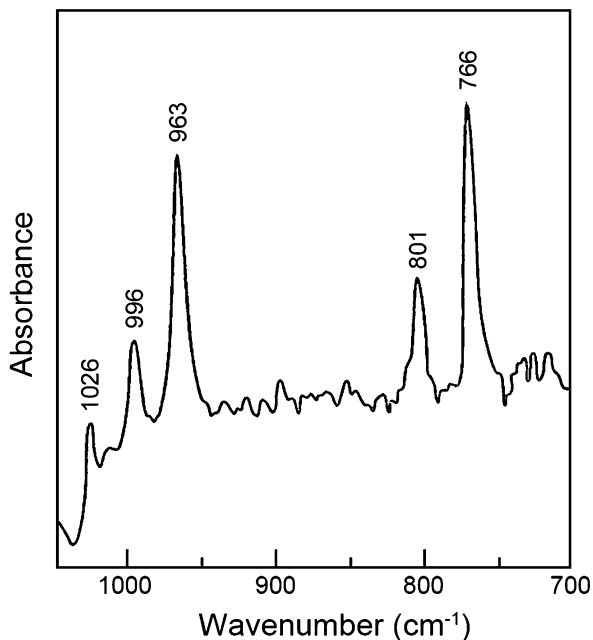
where  $C$  is the impurity concentration,  $d$  is the sample thickness,  $\alpha$  is the absorption coefficient,  $A$  is the absorbance at the peak, and  $I_0$  and  $I$  are the IR signal intensity of the peak and baseline, respectively.

N dimers exhibit main IR vibration absorption peaks at  $963$  and  $766 \text{ cm}^{-1}$ , with the calibrated absorption coefficients of  $1.83 \times 10^{17}$  (Itoh et al. 1985) and  $4.45 \times 10^{17} \text{ cm}^{-2}$  (Wagner et al. 1988), respectively. This method ensures a detection limit of  $\sim 5 \times 10^{14}/d \text{ cm}^{-3}$  ( $\sim 100/d$  ppba, the unit of  $d$  is cm).

As the main form of N in Si under room temperature is N dimer and N-O complex, in oxygen-free float-zone silicon (FZ-Si), the total N concentration measured by SIMS equals to the N concentration measured by FTIR ( $963 \text{ cm}^{-1}$ ), which



**Fig. 1** FTIR absorption peaks of N dimer ( $766, 963 \text{ cm}^{-1}$ ) and N-O ( $801, 996, \text{ and } 1026 \text{ cm}^{-1}$ ) complex at room temperature



proves that the main existing form of N in FZ-Si is N dimers. However, in CZ-Si and mc-Si, the N dimer concentration measured by FTIR is lower than the one measured by SIMS, due to the formation of N-O complexes and the decrease in N dimer concentration. As shown in Fig. 1, N-O complexes also exhibit a series of IR vibration absorption peaks (including  $801, 996, \text{ and } 1026 \text{ cm}^{-1}$ ) (Qi et al. 1991), without well-accepted absorption coefficient. The isotopic effects on these LVMs show that these modes all shift with  $^{15}\text{N}$  (Jones et al. 1994a), showing N atoms to be involved in the complexes. Especially, the absorption intensity of  $801 \text{ cm}^{-1}$  has a linear dependence on the product of  $[\text{N}][\text{O}_i]$ , indicating that these bands arise from the N-O complexes. Therefore, FTIR at room temperature cannot be used to estimate the total N concentration in CZ-Si. While it is controversial to measure total N content in mc-Si because the interstitial oxygen concentration in mc-Si varies with growth details, so that a coarse measurement of total N content using N dimer IR absorption is somehow acceptable.

Low-temperature Fourier transformation infrared spectroscopy (LT-FTIR) helps to extend the detection limit. On one hand, the  $963 \text{ cm}^{-1}$  IR peak of N dimers shifts to  $967 \text{ cm}^{-1}$  and becomes narrower when the sample is cooled down to 77 K, with a calibrated absorption coefficient of  $1.2 \times 10^{17} \text{ cm}^{-2}$  (Zhang et al. 2013), lower than the one under room temperature, which extends the N dimer detection limit to  $\sim 2 \times 10^{14} \text{ cm}^{-3}$  at 77 K. On the other hand, the determination of N concentration in CZ-Si lower than  $10^{14} \text{ cm}^{-3}$  can be performed using LT-FTIR in far-infrared range. The absorption peaks correspond to the ionization levels of the N-O complex

donors in silicon, in the spectral range of 190–350  $\text{cm}^{-1}$ . (see the section “N-O Complex” part) Before the measurement, long-time thermal annealing (mostly at 500–650  $^{\circ}\text{C}$ ) is needed to assure saturated transformation from N dimers into N-O complexes. The detection limit of LT-FTIR method is affected by signal intensity of the spectrometer and sample thickness. Several detection limits have been reported in the range of  $5\text{--}90 \times 10^{12} \text{ cm}^{-3}$  (Nakatsu et al. 2004; Ono and Horikawa 2003; Porrini et al. 2003). Nevertheless, the calibration of IR absorption into absolute concentration is not enough by now.

In addition, there are many other detection techniques for N-related contents in Si, including charged particle activation analysis (CPAA) (Nozaki et al. 1970), deep level transient spectroscopy (DLTS) (Tokumaru et al. 1982), Rutherford backscattering spectrometry (RBS), Auger electron spectroscopy (AES), electron paramagnetic resonance (EPR), luminescence and electrical resistivity (Bucksbaum and Bokor 1984; Hemment et al. 1985). Some of these methods were used to measure implanted substitutional N atoms in the early researches. However, most of them could not reach the sensitivities required to measure a common concentration of N in photovoltaic CZ-Si and mc-Si as low as  $10^{15} \text{ cm}^{-3}$ .

## Solubility

The nitrogen solubility in molten silicon was measured as  $6 \times 10^{18} \text{ cm}^{-3}$  by charged particle activation analysis (CPAA), using a sample at the end of fast cooled FZ-Si ingot (Yatsurugi et al. 1973). When N concentration in molten silicon exceeds the solubility,  $\beta\text{-Si}_3\text{N}_4$  rods/particles will be segregated and float above the molten silicon. This phenomenon can be commonly observed in the growth industrial directionally solidified mc-Si ingots because the soluble N is usually saturated in the molten silicon at the end of growth, however, floating  $\text{Si}_3\text{N}_4$  in CZ growth may cause failure of dislocation-free growth.

The solid solubility of N in Si was initially measured and reported as  $(4.5 \pm 1) \times 10^{15} \text{ cm}^{-3}$  (Yatsurugi et al. 1973), which was determined by the solubility in molten silicon and the small equilibrium segregation coefficient of N in Si ( $k_0 = 7.5 \times 10^{-4}$  (Yatsurugi et al. 1973)). However, a larger solid N concentration at room temperature was measured as  $\sim 1 \times 10^{16} \text{ cm}^{-3}$  (FTIR,  $963 \text{ cm}^{-1}$ ) in directionally solidified mc-Si, where the effective segregation coefficient of N,  $k_{\text{eff}}$ , became larger than  $k_0$  due to the moderate convective transportation in casting method. According to Burton-Prim-Slichter theory,  $k_{\text{eff}}$  is defined by the following formula:

$$k_{\text{eff}} = \frac{k_0}{k_0 + (1 - k_0)\exp(-R\delta_{\text{BPS}}/D_L)}$$

where  $R$  is the growth rate and  $\delta$  the thickness of boundary layer which is determined by diffusivity ( $D_L$ ) of N and convection level. Obviously, compared to CZ growth, casting growth has much weaker convection level so that the boundary layer is

thicker and then the  $k_{\text{eff}}$  become larger. As the N concentration in solidified mc-Si is determined by both the N concentration in molten silicon and segregation effect, which are all strongly affected by convection level, N concentration in molten silicon is also influenced by crucible size and diffusion time, which may cause very complicated local distribution in the whole system. In the cases with weak convection, the N concentration at ingot center is lower than that at the edge, but as the segregated N in the molten silicon increases fast, the N concentration in solid phase can keep increasing along ingot height due to segregation effect. Once the concentration (FTIR,  $963\text{ cm}^{-1}$ ) in solid phase exceeds  $10^{16}\text{ cm}^{-3}$ ,  $\text{Si}_3\text{N}_4$  precipitates will be rapidly generated, along with the decrease in N dimer IR absorption (Reimann et al. 2010) because the N dimers will further segregate on the precipitates. Therefore, the solid solubility of N in Si is usually noted as  $(4\text{--}10) \times 10^{15}\text{ cm}^{-3}$ .

## Diffusion

The diffusivity of N in silicon is controversial during the past decades because of the many forms of N-related defects. Researchers have reported theoretical and experimental results of various diffusion models. Theoretical investigation results indicate that the N monomer has a migration activation energy of 0.4 eV (Schultz and Nelson 2001; Nelson et al. 1998), which means they are highly mobile under high temperature. But the experimental measurements of the N monomer diffusivity in silicon are limited to its relatively low concentration and the detective techniques. Table 3 gives several experimental results, where the diffusion coefficient is expressed by Arrhenius formula:

$$D = D_0 \exp\left(-\frac{E_A}{kT}\right)$$

where  $D$  is the diffusion coefficient ( $\text{cm}^2/\text{s}$ ),  $D_0$  is the pre-exponential factor ( $\text{cm}^2/\text{s}$ ),  $E_A$  is the migration activation energy (eV),  $T$  is the absolute temperature (K), and  $k$  is the Boltzmann constant,  $1.38064 \times 10^{-23}\text{ m}^2\cdot\text{kg}/\text{s}^2\cdot\text{K}$ .

The first measurement of N diffusion coefficient attempted by Clark et al. was based on Hall effect (Clark et al. 1968). After implanting  $^{14}\text{N}^+$  ions to form an  $n$ -type

**Table 3** The pre-exponential factor ( $D_0$ ) and migration activation energy ( $E_A$ ) of various models of N in silicon

	$D_0$ ( $\text{cm}^2/\text{s}$ )	$E_A$ (eV)	Model
Clark et al. (1968), Pavlov et al. (1976)	0.87	3.29	Ion-implanted N
Itoh and Abe (1988)	$2.7 \times 10^3$	2.8	N dimer
Voronkov and Falster (2004)	0.25	1.25	N monomer from the dissociation of N dimer
Murphy et al. (2005)	$6.3 \times 10^{-2}$	1.38	Pinning of N monomer at dislocations

surface layer in the high resistive *p*-type silicon, the evolution of the *p-n* junction depth with the anneal temperature and time reflects the  $^{14}\text{N}^+$  diffusion behavior. Obviously, this experiment is not reliable for the major form of N dimers in N-doped CZ-Si and mc-Si.

The most well-accepted diffusivity of N dimers was based on N dimer model. Theoretical results show that dominant N dimers have a large migration activation energy of 2.5 eV (Sawada et al. 2002; Fujita et al. 2005; Stoddard et al. 2005), which is assumed to be practically immobile at room temperature, indicating the diffusion of N dimers happens before a sample is cooled. Itoh et al. used SIMS (Itoh and Abe 1988) to measure out-diffused N on the profiles of silicon. It was found that the total amount of out-diffused N corresponds with the variation of N dimer IR absorption at the frequency of  $963\text{ cm}^{-1}$ , confirming that the N impurities in silicon diffuse as the form of dimers. The experimental value of activation energy was measured as 2.8 eV, which is close to the calculated values using first principle method, so this model is supported by theoretical investigations.

Moreover, further experiments suggest that the diffusivity of N in silicon is more complicated when the influence of other parameters such as oxygen impurities or dislocations is considered. Hockett (1989) suggested that N dimers may not be the only species responsible for transport, since a small fraction of N diffused rapidly while the majority (N dimers) remained immobile. Later, Mannino et al. found that N diffusion can be enhanced in oxygen-rich CZ-Si (Mannino et al. 2004). Voronkov and Falster proposed a dissociative model to explain the N diffusion in silicon (Voronkov and Falster 2004), where N transport proceeds via dissociation of the practically immobile dimers into mobile monomers by oxygen catalyzing. Meanwhile, Murphy et al. pointed that the barrier of N monomer should be less than 1.5 eV through experiments on the pinning effect of N on dislocations (Alpass et al. 2009; Murphy et al. 2005). These models are not crucial for photovoltaic level CZ-Si and mc-Si materials.

---

## Nitrogen in Czochralski Silicon

### Doping of N in CZ-Si Growth

N-doping in bulk Si is usually achieved by introducing N atoms into molten silicon during crystal growth. Solid and gas N source can be used for constructing N-rich growth environment.

Silicon nitride ( $\text{Si}_3\text{N}_4$ ) powders are the most widely used solid N-doping source. The major parameters of the powders are purity and size. The purity of powders should be better than 1 ppm. The powder size is associated with the dissolution rate. Incompletely dissolved powders will usually float above the molten silicon and generate dislocations and even grain boundaries in a CZ-Si ingot (Yu et al. 2011).  $\text{Si}_3\text{N}_4$  powders can be added to the crucible prior to any heating of polycrystalline silicon (poly-Si) material or during the melting of poly-Si. Another solution is to use

a crucible with  $\text{Si}_3\text{N}_4$  coating on the inner walls. During the melting process, the  $\text{Si}_3\text{N}_4$  coating keeps gradually dissolving into the molten silicon, and the N concentration in the molten silicon is determined by convective transport. This makes it difficult to precisely control the doping amount when a N concentration lower than  $10^{15} \text{ cm}^{-3}$  is needed. So, this technique is usually combined with empirical experience. In addition, boron nitride (BN) powders can also be used as N dopant for *p*-type Si crystal, where the doping amount of B should be well calculated for intended resistivity. BN is more refractory than  $\text{Si}_3\text{N}_4$  at the melting point of Si so that the powder sizes should be further reduced to assure the complete dissolution of BN in the molten silicon, and meanwhile the melting time should be prolonged.

Nitrogen gas was once considered unable to serve as the protective ambient for CZ-Si growth, because  $\text{N}_2$  reacts with polycrystalline silicon (poly-Si) nuggets under high temperature with the regular partial pressure (Kaiser and Thurmond 1959), fierce reaction between solid Si and  $\text{N}_2$  generates macroscopic  $\text{Si}_3\text{N}_4$  particles on the surface of poly-Si and therefore inhibits the growth of defect-free single crystal. The gas doping of N in CZ-Si was first introduced by Que et al. (1985, 1987, 1991, 2000), where  $\text{N}_2$  or  $\text{N}_2/\text{Ar}$  mixture under reduced  $\text{N}_2$  partial pressure was used as the protective gas, and they successfully obtained N-doped Czochralski silicon (NCZ-Si) ingots. For the growth of NCZ-Si, the purity of protective  $\text{N}_2$  atmosphere should be ensured, and the total gas flow rate should be controlled at a relatively high speed to efficiently eliminate SiO vapored above the molten silicon. The doping mechanism is to control the reaction velocity between  $\text{N}_2$  and solid poly-Si feedstock by tuning the partial pressure of  $\text{N}_2$ . During the melting stage,  $\text{N}_2$  reacts with poly-Si, and thin  $\text{Si}_3\text{N}_4$  film (thickness less than 100 nm) is generated on the surface of poly-Si, and these N contents will completely dissolve in the molten silicon. Therefore, the doping amount can be controlled by manipulating the partial pressure and flow rate of  $\text{N}_2$  during the melting stage, instead of during the growth stage. With the decrease of  $\text{N}_2$  partial pressure, the chemical reaction of  $\text{N}_2$  with poly-Si becomes weak, and therefore, the final N concentration in silicon crystals is controllable. The N concentration in the tail of a CZ-Si is usually less than  $5 \times 10^{15} \text{ cm}^{-3}$ , due to the liquid solubility and segregation coefficient of N. When the  $\text{N}_2$  partial pressure is controlled well, the concentration of N in molten Si will not exceed its solubility, and no  $\text{Si}_3\text{N}_4$  will float on the liquid surface, so that the CZ growth will not be disturbed, and a high yield of dislocation-free single crystal can be obtained. Considering the low cost of  $\text{N}_2$  against Ar, and the benefits of NCZ-Si, using  $\text{N}_2$  as the protective atmosphere under reduced pressure has been a cost-effective method for CZ-Si crystal growth.

## N-O Complexes

N-O complexes introduce shallow thermal donors in CZ-Si. The ionization of these donors can be characterized by low-temperature FTIR. A typical LT-FTIR spectrum

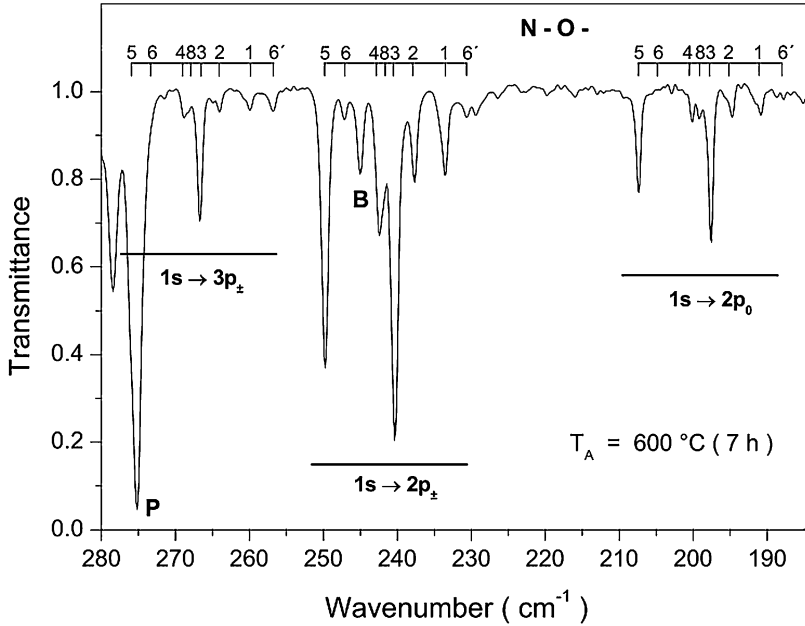


**Fig. 2** LT-FTIR (10 K) transmittance spectrum of N-O shallow donors (Alt and Wagner 2010), the absorption peaks correspond to  $1s \rightarrow 2p_0$ ,  $1s \rightarrow 2p_{\pm}$ , and  $1s \rightarrow 3p_{\pm}$ , noted by Suezawa et al. (1986) and Wagner et al. (2007)

**Table 4** STD absorption peak positions measured at 8 K (Suezawa et al. 1988; Wagner et al. 2007)

Species	$1s \rightarrow 2p_0$ ( $\text{cm}^{-1}$ )	$1s \rightarrow 2p_{\pm}$ ( $\text{cm}^{-1}$ )	$1s \rightarrow 3p_{\pm}$ ( $\text{cm}^{-1}$ )
N-O-1	190.8	233.8	260.1
N-O-2	194.9	237.8	264.2
N-O-3	197.7	240.4	266.8
N-O-4	200.2	242.5	269.0
N-O-5	207.4	249.8	276.4
N-O-6	204.4	247.0	274.2
N-O-6'	187.9	230.6	256.9
N-O-8	199.1	241.5	268.2

of shallow thermal donors (STDs) is shown in Fig. 2 (Alt and Wagner 2010). Three series of bands of the  $1s \rightarrow 2p_0$ ,  $1s \rightarrow 2p_{\pm}$ , and  $1s \rightarrow 3p_{\pm}$  transitions were detected, and eight different species in each band were labeled as N-O- $x$  ( $x = 1, 2, 3, \dots$ ) in Table 4. Several ionization energies of the STDs have been estimated, as shown in Table 5 (Alt and Wagner 2010). There are good agreements between the observed transition energies and the results of the effective mass approximation calculated for the STD states in silicon.

The absorption coefficients of the transitions (N-O-1, N-O-2, N-O-3, N-O-5) increase with the N content in square root dependence (Ewels et al. 1996; Alt

**Table 5** Ionization energies of the shallow donors (Wagner et al. 2007)

Donor Groups	Ionization energy (meV)
1	35.38
2	35.90
3	36.21
4	36.45
5	37.38

et al. 2006). According to the mass action law for the reaction  $n\text{N} + m\text{O} = \text{N}_n\text{O}_m$ , it leads to the integrated absorption values equal to  $[\text{N}]^n[\text{O}]^m$ . The N predominantly exists in the dimer form, so the concentrations of interstitial N atoms  $[\text{N}_i]$  can be expressed as

$$[\text{N}_i] \approx (\rho\text{N}/2)^{1/2} \exp(-E/2kT),$$

where  $\rho$  is the lattice site density. Note that the square root dependence is obtained in the expression. This coincidence shows that the STDs should involve only one N atom. The oxygen concentration dependence of the STDs had been investigated by Wagner et al. (2007; Hara et al. 1989). The chemical compositions of the electrically active N-O complexes in silicon were determined in a specially doped ingot with variable oxygen concentrations and a fixed N concentration by FTIR technique. The result shows that the N-O-5, with its absorption at  $249.8 \text{ cm}^{-1}$  in  $1s \rightarrow 2p_{\pm}$  transition, has a linear dependency, proving N-O-5 to be NO ( $m = 1$ ). The other two species of N-O-4 ( $242.5 \text{ cm}^{-1}$ ) and N-O-6 ( $256.9 \text{ cm}^{-1}$ ) also show the linearity between  $[\text{NO}_m]$  and  $[\text{O}_i]$ ; therefore they have the same NO stoichiometry. N-O-3 with its transitions  $1s \rightarrow 2p_{\pm}$  at  $240.4 \text{ cm}^{-1}$  has a square dependence on  $[\text{O}_i]$ , indicating that it has a  $\text{NO}_2$  composition. The power dependency  $m = 3$  of the complexes N-O-1 ( $233.8 \text{ cm}^{-1}$ ), N-O-2 ( $237.8 \text{ cm}^{-1}$ ), and N-O-8 ( $241.5 \text{ cm}^{-1}$ ) identifies these STDs as  $\text{NO}_3$  defects. The composition of N-O-6 remains unknown.

As N-O complexes are shallow donors in silicon materials, they can influence the resistivity of both  $p$ -type and  $n$ -type wafers. Therefore, the thermal history of the wafers should be noted during the fabrication of solar cells or electronic devices. N-O complexes in CZ-Si gradually degenerate when the sample is annealed with the temperature higher than  $750 \text{ }^{\circ}\text{C}$ . The degeneration velocity increases with annealing temperatures, while the formation of N-O complexes happens in the annealing temperature window of  $450\text{--}750 \text{ }^{\circ}\text{C}$ , when N dimers react with interstitial oxygen and generate N-O complexes. Figure 3 shows the degeneration and regeneration process of N-O complexes in a N-doped CZ-Si sample. The left image shows that the annealing at  $850 \text{ }^{\circ}\text{C}$  for 2 h can completely remove the N-O complex-related peaks at  $801, 996, \text{ and } 1026 \text{ cm}^{-1}$ , and the right image shows that the N dimer peaks at  $766 \text{ and } 963 \text{ cm}^{-1}$  decrease the fastest when annealed at  $550 \text{ }^{\circ}\text{C}$ , and the multiple new peaks are formed during the low-temperature annealing, indicating that the thermal stability of various complexes is different, which means that the degeneration and regeneration of N-O complexes are not absolutely reversible.

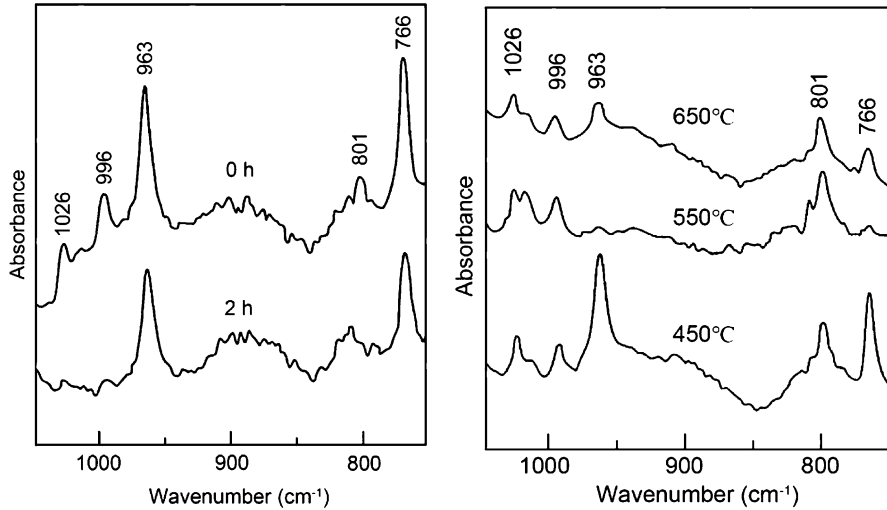


**Fig. 3** The FTIR spectra of N-doped CZ-Si (left) before and after annealing at 850 °C for 2 h, (right) annealed at 450, 550, and 650 °C for 24 h after complete N-O complex degeneration

## Influence on O-Related Defects

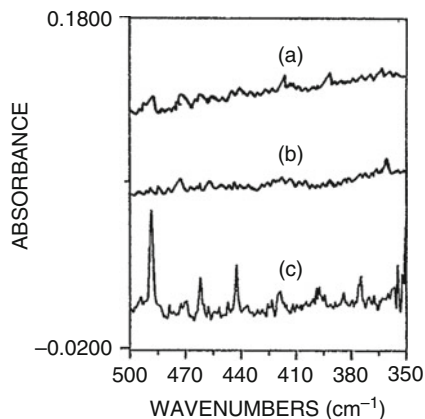
### Thermal Donors

Thermal donors (TDs) are usually accumulated from enriched oxygen impurities during the cooling stage of CZ-Si ingots or in the long-time annealing in the temperature of 350–500 °C. TDs are doubly ionized at room temperature and cause downward shift of resistivity in *n*-type phosphorus (P)-doped silicon, which usually introduces two donor levels of  $E_c-0.05$  eV and  $E_c-0.15$  eV. TDs can be eliminated in the high-temperature courses of normal solar cell processes, i.e., phosphorus diffusion process, so their influence on the performance of wafers and solar cells does not get enough attention. With the developments of high efficiency and low-temperature SHJ solar cell process, this issue starts to become more and more important. Since the maximum temperature of SHJ processes remains below 300 °C, as mentioned above, the as-grown TDs are still retained in the bulk of silicon wafers. TDs have negative influences on the performance of SHJ solar cells. The decrease of minority carrier lifetime is the uppermost factor responsible for the deterioration of efficiency (Li et al. 2018). The results indicate that the solar cell manufacturers should choose the wafer with the concentrations of TDs as low as possible to limit their detrimental effect on the cell efficiency. Furthermore, it is of great importance for silicon crystal growers to manage to reduce the contamination of oxygen during the crystal growth and make the ingot cooling time as short as possible or develop appropriate methods to decrease oxygen concentration and suppress the formation of thermal donors.

Nitrogen has twofold effects on the generation of donors (TDs and STDs) in silicon. As mentioned above, a family of N-O complexes related to both N and O



**Fig. 4** LT-FTIR spectra related to thermal donors in CZ-Si. (a) High [N], (b) low [N], (c) N-undoped (Yang et al. 1995)



impurities forms at temperatures around 650 °C, and as a result, the formation of TDs associated only with oxygen impurity is suppressed. Early research identified new STDs (not as N-O complexes) in NCZ-Si using photothermal ionization spectroscopy (PLIS), along with the suppression of the formation of TDs (Griffin et al. 1989). Then using low-temperature far-infrared spectroscopy (LT-FTIR), as shown in Fig. 4, it was found that N suppresses the formation of TDs in CZ-Si annealed at 450 °C, while N interacts with oxygen atoms to form N-O complexes (Yang et al. 1995). The interaction of N and oxygen atoms is supposed to reduce the TDs.

### Oxygen Precipitates

Supersaturated interstitial oxygen atoms in CZ-Si can aggregate into oxygen precipitates (OPs) and further induce secondary lattice defects during thermal processing. These defects can getter harmful metal contaminants but induce punch-out dislocations causing the decrease of mechanical strength. The controlling of OPs in CZ-Si is very important for improving performance and yield of ICs. The formation of OPs consists of two stages, i.e., nucleation and growing up. It has been reported that N atoms in CZ-Si can introduce heterogeneous nuclei enhancing the generation of OPs (Karoui and Rozgonyi 2004); therefore, NCZ-Si has been well developed and applied in the IC industry since stronger internal getting is demanded when processing temperatures keeps decreasing (Yang and Yu 2004; Yu et al. 2013).

For solar cells as bulk devices, internal getting on the base of OPs and induced extended defects is not suitable. Moreover, OPs within CZ-Si wafers will introduce deep energy levels in band gap and become the recombination centers for minority carriers, so that the lifetime of wafers decreases. The degree of lifetime degradation was more pronounced in *p*-type silicon than in *n*-type silicon because the recombination of OPs takes place through their interface states, where the existence of positive fixed charges around OPs will boost the lifetime degradation in *p*-type silicon. The performance on *p*-type (Ga-doped) CZ-Si Al-BSF solar cells with intentionally formed OPs shows that the degradation increases sharply with the

concentration of OPs, mainly contributed by the long-wave loss related to bulk recombination (Chen et al. 2011). In fact, the influence of N-related impurities on OPs should be noticed in the cases which the CZ-Si wafers containing high oxygen contents go through long-term annealing. However, currently the fabrication temperature of Al-BSF solar cells is lower than 900 °C, and the annealing time is shorter. Thus, the process does not introduce OPs in solar cells if as-grown oxygen contents are not high enough. Moreover, the N concentration in CZ-Si materials used for photovoltaic industry is very low. Therefore, N-doped CZ-Si could be used for the fabrication of solar cells due to the advantages of low-cost protective gas and higher mechanical strength.

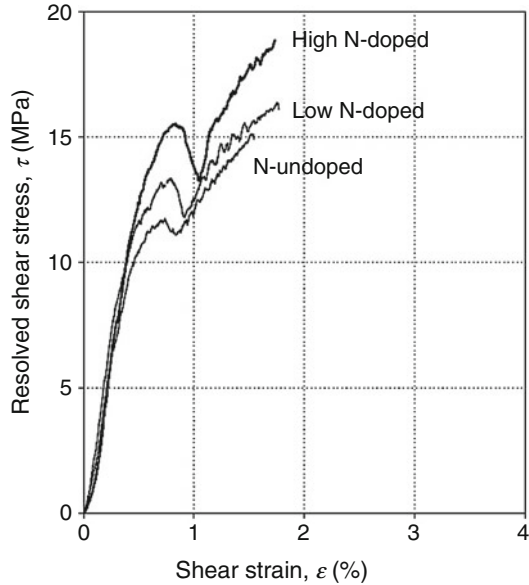
### Effect of N Impurity on Mechanical Properties

The mechanical properties of CZ-Si wafers for solar cells are crucial for ensuring manufacturing yield of wafers and cells, especially when the wafer thickness keeps decreasing in recent years. Silicon, as a brittle material at room temperature, is susceptible to breakage or fracture during cell manufacturing due to any localized stress. Generally, the mechanical properties of silicon are dictated by the generation and extension of microcracks, which is related to the generation and motion of dislocations. For CZ-Si, N as co-dopant also affects the mechanical properties of CZ-Si (Lu et al. 1998; Wang et al. 2001; Yu et al. 2013).

The effect of N-doping on Young's modulus and hardness of silicon has been studied by nano-indentation. N-doping with a concentration of  $2 \times 10^{15} \text{ cm}^{-3}$  can significantly increase the Young's modulus (from 104 to 182 GPa) and hardness (from 6.49 to 8.11 GPa) of float-zone (FZ) silicon (Anderson 2004). The room temperature fracture strength of N-doped wafers was investigated with a double ring bending setup, where FZ silicon wafers with the low N and O concentration ( $< 2 \times 10^{14}$  and  $3\text{--}4 \times 10^{15} \text{ cm}^{-3}$ , respectively) exhibited a significantly higher fracture strength than conventional CZ ( $[\text{O}_i]$ :  $7.2\text{--}8.6 \times 10^{17} \text{ cm}^{-3}$ ) or FZ ( $[\text{O}_i]$ :  $4\text{--}15 \times 10^{15} \text{ cm}^{-3}$ ) wafers, whereas FZ-Si wafers with the high N concentration ( $1.7\text{--}3.6 \times 10^{15} \text{ cm}^{-3}$ ) but without O did not possess the improved fracture strength (Vedde and Gravesen 1996). Besides, for CZ-Si, N-doping can always improve fracture strength. This implies that the improvement in the fracture strength of silicon by N-doping relies on the presence of oxygen. Oxygen precipitates and N-O complexes are suggested to be responsible for the increase in fracture strength for NCZ-Si (Wang et al. 2001; Chen et al. 2008).

Interstitial oxygen can suppress slip and warpage of CZ-Si wafers (Hu and Patrick 1975; Yonenaga et al. 1984). Likewise, interstitial N dimers and N-O complexes have the similar effects. Interestingly, a minor concentration of N ( $< 3 \times 10^{15} \text{ cm}^{-3}$ ) is found to be very effective in reducing slips in low-oxygen content silicon wafers (Wagner et al. 1988). N-doping with a concentration of  $3.6 \times 10^{15} \text{ cm}^{-3}$  can reduce wafer warpage of CZ-Si wafers during annealing

**Fig. 5** Stress-strain curves of dislocation-free Czochralski silicon crystals deformed in the  $\langle 110 \rangle$  direction at  $850^\circ\text{C}$  for different N concentrations. The concentrations of N in the samples are  $3 \times 10^{13}$ – $3 \times 10^{14} \text{ cm}^{-3}$  for low N-doped samples,  $3 \times 10^{14}$ – $3 \times 10^{15} \text{ cm}^{-3}$  for high N-doped samples, and  $< 3 \times 10^{13} \text{ cm}^{-3}$  for the N-undoped samples (Orlov et al. 2002)



(Lu et al. 1998). Moreover, the dislocation glide around an indentation on CZ-Si at high temperatures is found to be significantly suppressed by N-doping (Hu and Patrick 1975; Yonenaga et al. 1984). In CZ-Si with different N concentrations, an increase in the N concentration leads to enhanced upper and lower yield points, as shown in Fig. 5 (Orlov et al. 2002). This implies that N-doping can increase the tolerable processing temperatures at which the plastic deformation of silicon wafers under load can be avoided. The locking of dislocations by N can be directly evidenced by the increased unlocking stress, which refers to the critical stress for dislocation movement. It is proved that the FZ silicon with higher N concentrations has larger unlocking stresses, implying the increase in N concentration results in a stronger locking effect (Murphy et al. 2006). The interaction energy between N and dislocations has also been studied by measuring the unlocking stress as a function of temperatures (Yonenaga 2005). The experimentally estimated energy for dislocation escaping from the locking of N atom is 4.1 eV, slightly higher than that of 3.6 eV between dislocations and oxygen (Yonenaga et al. 2005). This interaction energy cannot be understood in terms of the model in which the dislocations interact with individual impurity atoms. Consequently, it is proposed that impurity atoms segregate at dislocations and pipe diffuse along the dislocation line, forming complexes or clusters which immobilize dislocations strongly (Yonenaga 2005). Molecular dynamics (MD) modeling suggests that the binding energy of N with edge dislocation (1.66 eV/A $^\circ$ ) is slightly lower than that of oxygen (1.8 eV/A $^\circ$ ) (Sumino et al. 1983). In brief, both the experimental and theoretical results agree that N has a strong dislocation locking ability which is comparable with that of oxygen.

## Nitrogen in Cast Multicrystalline Silicon

### Soluble Nitrogen

Cast multicrystalline (mc-Si) materials used in photovoltaic industry, including quasi-single crystal silicon (QSC-Si) which is also called as mono-like silicon (ML-Si), are fabricated using directional solidification method. In this technology, the size of the crucibles is much larger than that of CZ-Si, and the ingots are directly in contact with the crucible wall. However, the contact of molten silicon and quartz crucibles under high temperatures can cause sticking between them, which generates the crack of ingots during cooling because silicon and quartz have different thermal conductivities. Therefore,  $\text{Si}_3\text{N}_4$  coating layer (usually a mixture of  $\alpha\text{-Si}_3\text{N}_4$  and  $\beta\text{-Si}_3\text{N}_4$ ) on the inner surface of quartz crucibles is usually used to prevent the reaction between molten silicon and crucibles. However, N atoms are induced into mc-Si ingots by the  $\text{Si}_3\text{N}_4$  coating (Ghosh et al. 1997). And, the convection of molten silicon in large-scale crucibles during the growth of mc-Si is much weaker compared to the growth of CZ-Si, which weakens the segregation of N during solidification. Consequently, the distribution of N-related impurities in cast mc-Si ingots is more complicated than that in N-doped CZ-Si ingots.

### N Dimers

The distribution of N concentration in a mc-Si ingot is controlled by both the entrance and segregation of N atoms during the whole growth. For normal cast silicon materials, the only but excessive N source is  $\text{Si}_3\text{N}_4$  coatings on the inner wall of crucibles. As the diffusivity and temperature is similar, the distribution of N concentration in molten silicon is strongly influenced by the size of crucible, melting time, and convection. Convection is also the main factor controlling the effective segregation. During melting and solidification,  $\text{Si}_3\text{N}_4$  coating, as the only N dopant, keeps dissolving into the molten silicon; the doping rate is positively correlated with the contacting area between molten silicon and  $\text{Si}_3\text{N}_4$  coating. Since the temperature and time duration respectively are high and long enough, the N concentration in molten silicon should be at high-level, especially almost saturated for the cases using small crucible, which is close to  $6 \times 10^{18} \text{ cm}^{-3}$  as mentioned above.

Small crystals are better for investigating the influence of convection on segregation, where final N concentration in solid phase is usually only controlled by the segregation effect because N is usually well diffused in the molten silicon. Trempa et al. investigated the N distribution in a small ingot with width of 6 cm. Figure 6a shows the axial nitrogen distribution (measured by FTIR) of the central region of ingots. Two ingots (A1 and B1) were grown with enhanced convection using standard  $\text{Si}_3\text{N}_4$  coating, and in one case (B1) additional  $\text{Si}_3\text{N}_4$  powders were added to the feedstock and the homogenization time was extended to 10 h. Another two ingots (C1 and D1) used the crucibles with (D1) or without (C1)  $\text{Si}_3\text{N}_4$  coating. For the process with strong convection (Ingot A1 and B1), nitrogen is axially homogeneously distributed in the range of  $(2\text{--}4) \times 10^{15} \text{ cm}^{-3}$  regardless of the adding of  $\text{Si}_3\text{N}_4$  powders. For moderate convection with  $\text{Si}_3\text{N}_4$

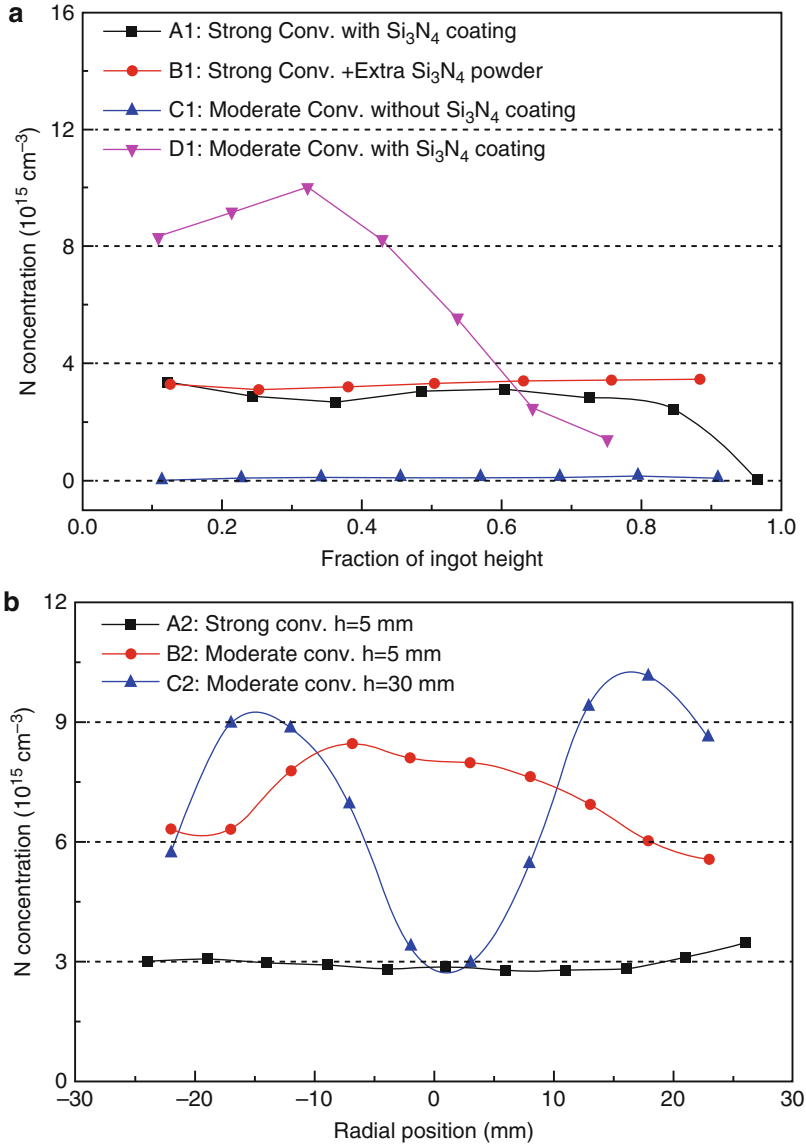


**Fig. 6** (a) The axial N concentration in the center of a mc-Si ingot grown in moderate and increased convection with various N sources, (b) the radial N concentration at the height of 5 mm and 30 mm from the bottom of the ingots grown with moderate and increased convection in  $\text{Si}_3\text{N}_4$ -coated crucible. (The data are extracted from Reimann et al. 2010)

coating, Ingot D1, the axial nitrogen concentration keeps increasing at the beginning and reaches to the limit of  $1 \times 10^{16} \text{ cm}^{-3}$  at 30% solidified fraction and then decreases to below  $2 \times 10^{15} \text{ cm}^{-3}$  at 75% solidified fraction when  $\text{Si}_3\text{N}_4$  and SiC

precipitates were generated so that the soluble N concentration is reduced. As comparison, the sample grown under moderate convection without a  $\text{Si}_3\text{N}_4$  crucible coating (ingot C1) has an extremely low nitrogen content below the detection limit of the FTIR measurement of  $5 \times 10^{14} \text{ cm}^{-3}$ . The radial distribution of N concentration is also strongly dependent on the convection. Figure 6b illustrates the measured radial N distributions at the height of 5 mm (A2, B2) and 30 mm (C2) from the bottom of the ingot. Here two ingots were grown from a pure feedstock in a  $\text{Si}_3\text{N}_4$ -coated crucible with strong (A2) and moderate (B2, C2) convection. With strong convection (A2), N concentration is homogeneously distributed in the range  $(2\text{--}4) \times 10^{15} \text{ cm}^{-3}$ , and it holds also at a height of 30 mm for this sample (not shown in Fig. 6). As comparison, in the sample grown under moderate convection (B2), the radial N concentration increases slightly toward the center ( $8.5 \times 10^{15} \text{ cm}^{-3}$ ) from the edge ( $6 \times 10^{15} \text{ cm}^{-3}$ ). At the height of 30 mm, the nitrogen concentration increases from  $6 \times 10^{15} \text{ cm}^{-3}$  at the edge to the highest values of  $(9\text{--}11) \times 10^{15} \text{ cm}^{-3}$  at about 1/4 and 3/4 positions (C2), and it then rapidly decreased to  $3 \times 10^{15} \text{ cm}^{-3}$  at the center because the soluble N impurities have been segregated and become precipitates. Figure 7 shows the IR-transmission images of vertical cross sections of ingots grown with various growth rates, where the high growth rate corresponds to a thick boundary layer width and weak segregation effect.  $\text{Si}_3\text{N}_4$  precipitates will generate when the soluble N concentration is over the solubility of N.

Once the segregation effect with saturated N in molten silicon is clear, the general situation in larger crystal is easy to discuss. Generally, as the dopant is located at the crucible wall, the distribution of N concentration in molten silicon can be estimated combining diffusion and convection, which means N concentration in the molten silicon usually decreases from the edge toward ingot center, but strong convection and long melting time will reduce the horizontal concentration gradient. During solidification, the distribution of N in solid phase is determined by both the concentration in the molten silicon around the solid-liquid interface and the convection level, of which the latter affects both the effective segregation coefficient and the local enrichment above the growth interface. For the cases with poor convection, the concentration in both solid and local liquid phase might be increased at the same

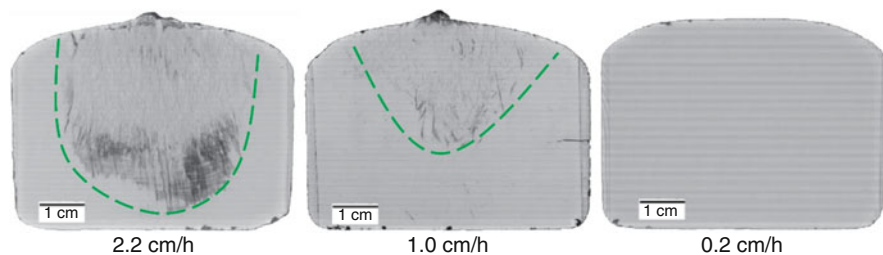


**Fig. 7** IR-transmission images of vertical cuts through the ingot center for ingot grown with the growth rate of 2.2, 1.0, and 0.2 cm/h (Trempa et al. 2010)

time.  $\text{Si}_3\text{N}_4$  precipitates will generate in various forms when the concentration exceeds solubility (see the section “Silicon Nitride Precipitates”). If the convection is strong enough, the N concentration of most parts of the ingot will be stable.

### N-O Complex

The formation of N-O complexes requires adequate N and O concentrations. Currently, the N and  $\text{O}_i$  concentrations in industrial mc-Si ingot are in the range of  $4\text{--}6 \times 10^{15} \text{ cm}^{-3}$  and  $0.5\text{--}5 \times 10^{17} \text{ cm}^{-3}$ , respectively, enough for the formation of N-O complexes. The LT-FTIR absorption peaks of N-O complexes can be easily observed in *n*-type mc-Si (Ghosh et al. 1997). As the N concentration is relatively stable among the whole mc-Si ingot, the formation of N-O complexes is mainly determined by the concentration of interstitial  $\text{O}_i$ , which depends on the coating selection and decreases along the ingot height. Therefore, the generation of N-O complexes in mc-Si changes with the  $\text{O}_i$  concentration. It was reported that in *n*-type mc-Si, the fraction of N-O complexes in total soluble N-related impurities can be up to  $\sim 44\%$  when  $[\text{O}_i] = 3.2 \times 10^{17} \text{ cm}^{-3}$ , but smaller than 10% when  $[\text{O}_i] < 1.0 \times 10^{17} \text{ cm}^{-3}$  (Zhang et al. 2013). As a result, the distribution of N dimers and N-O complexes in mc-Si is complementary, determined by the distribution of interstitial oxygen  $\text{O}_i$ , that is, the fraction of dimers is higher at ingot top, while the complexes higher at bottom, as shown in Fig. 8 (Kusunoki et al. 2011).

The common shallow thermal donor (STD) concentration in *n*-type mc-Si was measured as  $\sim 1 \times 10^{14} \text{ cm}^{-3}$  (Zhang et al. 2013), which is believed to be caused by N-O complexes. To date, the majority of industrial mc-Si ingots are B-doped *p*-type Si, where the B concentration is about  $10^{16} \text{ cm}^{-3}$ , so N-O complex STDs with a concentration of  $\sim 10^{14} \text{ cm}^{-3}$  should not obviously affect the resistivity of *p*-type wafers. Moreover, the majority of N-O complexes can be eliminated during the P diffusion process (under  $800\text{--}900^\circ\text{C}$ ), so that the influence of N-O complexes on the performance of *p*-type mc-Si solar cell is usually ignored.

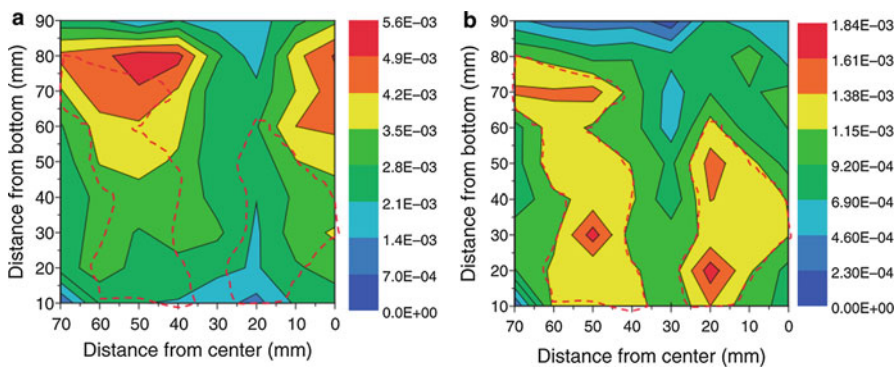


**Fig. 8** Complementary distributions of the absorption peak intensities of (a) NN ( $963 \text{ cm}^{-1}$ ) and (b) NNO ( $996 \text{ cm}^{-1}$ ) over a vertical cross section of mc-Si brick (Kusunoki et al. 2011)



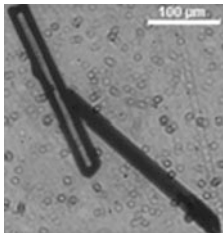
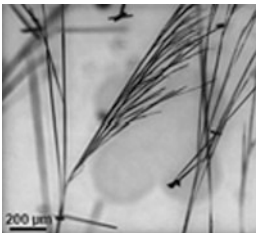
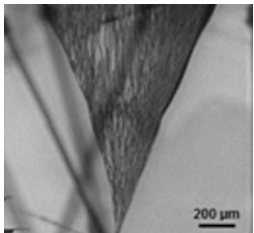
## Silicon Nitride Precipitates

### Formation

The formation of nitrogen-related precipitates strongly depends on the local thermodynamic conditions and impurity transportation during crystallization. As mentioned, the solubility of N in mc-Si is  $\sim 10^{16} \text{ cm}^{-3}$ , and  $\text{Si}_3\text{N}_4$  precipitates are segregated when the local concentration exceeds the solubility. The N concentration in mc-Si at the solid-liquid interface is determined by the effective segregation of N, which is dependent on equilibrium segregation coefficient and convection specifying how heat and mass transfer can take place between liquid and solid interface of silicon. If local N concentration exceeds the liquid solubility,  $\text{Si}_3\text{N}_4$  precipitates will generate at the liquid part of the interface and sink into the solid phase. Then it has a probability to serve as a seed for further growth of  $\text{Si}_3\text{N}_4$  crystal; thus, the convection has an important influence to determine how much N content can be transported nearby, which determines the final size of the precipitates. As a result, the common forms of  $\text{Si}_3\text{N}_4$  precipitates in mc-Si include rods, fibers, and nets, the parameters of which are listed in Table 6 (Richter et al. 2017).

$\text{Si}_3\text{N}_4$  rods have relatively large diameter and small length and are perfectly grown as hexagonal, showing no position preference within the grain structure. It indicates that they are grown in liquid Si where the surrounding influence is much lower than that in solid phase. Poor convection could be the main reason for the

**Table 6** Classification of  $\text{Si}_3\text{N}_4$  precipitates in cast mc-Si crystals (Richter et al. 2017)

	$\text{Si}_3\text{N}_4$ rod	$\text{Si}_3\text{N}_4$ fiber	$\text{Si}_3\text{N}_4$ net
Morphology and phase	 Monocrystalline $\beta\text{-Si}_3\text{N}_4$	 Monocrystalline $\alpha\text{-Si}_3\text{N}_4$	 Multicrystalline $\alpha\text{-Si}_3\text{N}_4$
Size (d: diameter, l: length)	d: <30 $\mu\text{m}$ l: < 2 mm	d: <500 nm l: < 8 mm	d: <500 nm l: < 3 mm
Growth preference	In grain, random	In grain, growth direction	At GB, growth direction
Structure space group lattice constant (nm)	Hexagonal P63 (173) $a = 0.760$ $c = 0.291$	Trigonal P31c (159) $a = 0.775$ $c = 0.562$	Trigonal P31c (159) $a = 0.775$ $c = 0.562$
Impurities, resistance ( $\Omega \text{ cm}$ )	Li, C, O, Mg, Ca > $4.7 \times 10^7$	C, O, Ca ( $5 \pm 4$ ) $\times 10^8$	C, O, Al, Ca ( $1.44 \pm 0.26$ ) $\times 10^{10}$



formation of  $\text{Si}_3\text{N}_4$  rods, when the N concentration in molten silicon is relatively high and the convection is relatively poor; most of the segregated N into the molten silicon cannot be transported away, once the concentration exceeds the solubility, and precipitates will be generated in the liquid phase. Because poor convection usually corresponds to fast growth and  $\text{Si}_3\text{N}_4$  has a higher density ( $3.44 \text{ g/cm}^3$ ) than liquid Si ( $2.55 \text{ g/cm}^3$ ),  $\text{Si}_3\text{N}_4$  rods can sink to the solid-liquid interface and get embedded in the solid phase.

$\text{Si}_3\text{N}_4$  fibers grow in vertical growth direction within grain. Compared to  $\text{Si}_3\text{N}_4$  rods, they have obviously longer length and shorter diameter, which indicates that the fibers grow along with the silicon crystal so that the diameter of the fibers is limited and the length prolonged. Therefore, it can be assumed that  $\text{Si}_3\text{N}_4$  fibers need seeds to start the growth. The equilibrium state of  $\text{Si}_3\text{N}_4$  inclusion is  $\beta$  phase, while  $\text{Si}_3\text{N}_4$  fibers show trigonal  $\alpha$ - $\text{Si}_3\text{N}_4$  crystallographic structure, and they grow in preferred orientation. So far, there is no clear evidence that  $\text{Si}_3\text{N}_4$  fibers start from Si lattice; some results show that the fibers start from a  $\text{Si}_3\text{N}_4$  rod inclusion (Li et al. 2013). Consider that the lattice constant of trigonal  $\alpha$ - $\text{Si}_3\text{N}_4$  ( $a = 0.775 \text{ nm}$  and  $c = 0.562 \text{ nm}$ ), close to the hexagonal  $\beta$ - $\text{Si}_3\text{N}_4$  ( $a = 0.760 \text{ nm}$ ), and Si lattice constant ( $a = 0.543 \text{ nm}$ ), the lattice mismatch between the fiber seed and  $\beta$ - $\text{Si}_3\text{N}_4$  or Si, are both relatively low; therefore, it can be inferred that the seed of  $\text{Si}_3\text{N}_4$  fibers should be generated at some tensile zone or precipitates enlarging the lattice constant.

$\text{Si}_3\text{N}_4$  nets are likewise  $\alpha$  phase precipitates but multicrystal found at grain boundaries (GBs). GBs can offer more nucleation sites for the segregation of  $\alpha$ - $\text{Si}_3\text{N}_4$ , and then a series of fibers can grow within the preferential angle.  $\text{Si}_3\text{N}_4$  fibers and nets are usually found parallel in one ingot, indicating they are same kind of inclusions with different nucleation sites. The extension of  $\text{Si}_3\text{N}_4$  fibers/nets is strongly related to the transportation of N content, which is mainly determined by the convection details, and the butterfly shaped nets shown in Fig. 9 are an example to show the complexity of defect extension.

## Influence on Wafering and the Mechanical Strength of Wafers

The wafering of mc-Si bricks mainly uses SiC slurry wire sawing in the past several decades, and now the wafering technique has been mostly changed to diamond wire sawing (DWS). As SiC particles are usually generated along with  $\text{Si}_3\text{N}_4$  precipitates, the influence of SiC and  $\text{Si}_3\text{N}_4$  precipitates on the mechanical properties should be considered together.

The embedded inclusions such as  $\text{Si}_3\text{N}_4$  precipitates are harder than silicon bulk. Thus, for wire saw wafering process, the un-uniformed hardness of the Si material introduces local tensile stress on the wire and may cause wire rupture during cutting. Table 7 gives the hardness values of Si, SiC,  $\alpha$ - $\text{Si}_3\text{N}_4$ ,  $\beta$ - $\text{Si}_3\text{N}_4$ , and Fe-decorated  $\beta$ - $\text{Si}_3\text{N}_4$  (Richter et al. 2017). It is clear that the SiC and  $\text{Si}_3\text{N}_4$  precipitates are harder than Si, which means they introduce extra local tensile stress on the wire. Despite  $\beta$ - $\text{Si}_3\text{N}_4$  is harder than SiC, it should be mentioned that the main form of  $\text{Si}_3\text{N}_4$  in mc-Si is Fe-decorated  $\beta$ - $\text{Si}_3\text{N}_4$  rods (Buonassisi et al. 2006) and the hardness of

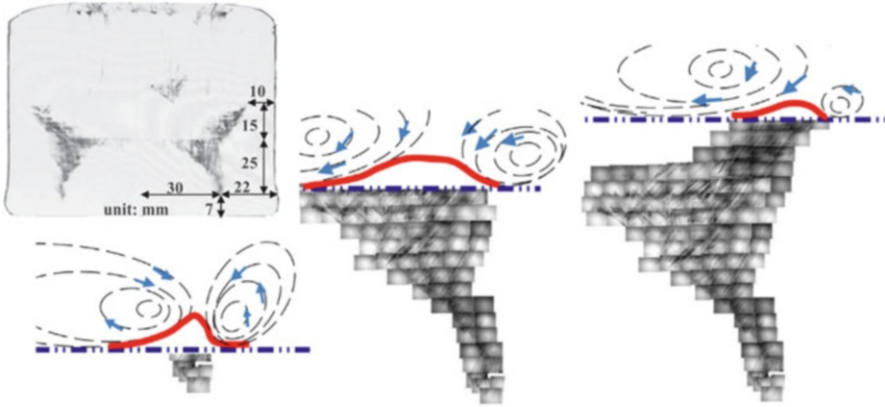


**Fig. 9** IR-transmission image of vertical cross section of the ingot with butterfly-shaped  $\text{Si}_3\text{N}_4$  precipitates and schematic diagram of the convection fluctuation model during the formation (Li et al. 2013)

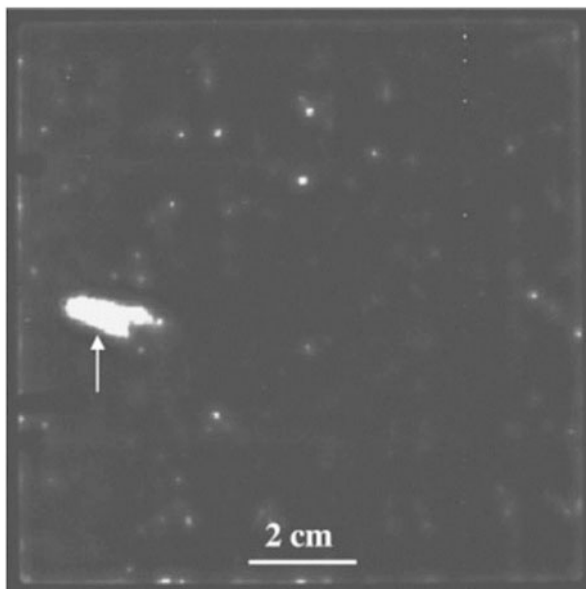
**Table 7** Vickers hardness of Si, SiC,  $\alpha\text{-Si}_3\text{N}_4$ ,  $\beta\text{-Si}_3\text{N}_4$ , and Fe-decorated  $\beta\text{-Si}_3\text{N}_4$

	Vickers hardness (GPa)
Si	$13 \pm 1$ (20 mN load) Vandeperre et al. (2007)
SiC	$23 \pm 2$ Snead et al. (2007)
$\alpha\text{-Si}_3\text{N}_4$	$\sim 38$ (200 g load) Chakraborty and Mukerji (1980)
$\beta\text{-Si}_3\text{N}_4$	$\sim 30$ (200 g load) Chakraborty and Mukerji (1980)
$\beta\text{-Si}_3\text{N}_4$ with 0.1 wt% Fe	$\sim 19$ (200 g load) Chakraborty and Mukerji (1980)

$\beta\text{-Si}_3\text{N}_4$  can be reduced by Fe decoration, lower than the value of SiC but still higher than Si (Chakraborty and Mukerji 1980). Therefore, it is believed that SiC particles and filaments are the major hard inclusions in mc-Si. This supports the fact that the  $\beta\text{-Si}_3\text{N}_4$  rods and very thin  $\alpha\text{-Si}_3\text{N}_4$  are usually easily cut during wafering. However, hard SiC particles are usually highly localized around  $\beta\text{-Si}_3\text{N}_4$  rods. Therefore, the existence of SiC and  $\text{Si}_3\text{N}_4$  precipitates is the main factor of wire rupture (Du et al. 2007, 2008).

Furthermore, embedded SiC and  $\text{Si}_3\text{N}_4$  precipitates in mc-Si wafers also decrease the mechanical strength and increase fracture rate of wafers and devices. The adjacent phases have different thermal expansion coefficients (TEC) (Schoenfelder et al. 2009), and the mismatch of the TECs at the interface of precipitates introduces shear stress. The average tensile shear stresses at  $\beta\text{-SiC/Si}$  and  $\beta\text{-Si}_3\text{N}_4\text{/Si}$  interfaces were reported as  $\sim 24$  and  $\sim 12$  MPa, respectively, measured by infrared birefringence imaging (IBI) (Ganapati et al. 2010). Therefore, when the amount of SiC/ $\text{Si}_3\text{N}_4$  precipitates increases, the heterogeneous degree of local tensile stresses will be increased with enlarged net local shear stress, and the probability of stress concentration is increased, which finally leads to the reduction of wafer fracture strength as the critical stress is more easily reached under same load.

**Fig. 10** Lock-in thermogram of a cell containing a  $\text{Si}_3\text{N}_4$  inclusion (arrow) (Breitenstein et al. 2004)



## Influence on Electric Properties of Cell Performance

The length of  $\text{Si}_3\text{N}_4$  inclusions in mc-Si ingots is usually several millimeters, so they commonly penetrate the wafers (width from 160 to 180  $\mu\text{m}$ ). Despite the resistivity of penetrating  $\text{Si}_3\text{N}_4$  is relatively high (Bauer et al. 2007), these inclusions can still serve as shunts in solar cells under forward bias (Breitenstein et al. 2004), as shown in Fig. 10. Generally, it is considered as shunts that cause degradation in fill factor ( $FF$ ) and open-circuit voltage ( $V_{oc}$ ). However, for the industrial-level mc-Si cells, the series resistance of the devices cannot be ignored, and then the increase in shunts can also reduce the short-circuit current ( $J_{sc}$ ) at the same time. Meanwhile,  $\text{Si}_3\text{N}_4$  inclusions are the nucleation sites for SiC particles. Penetrating SiC filaments at grain boundaries are confirmed low-resistivity shunts, but the size of SiC particles is usually smaller compared to wafer thickness, and  $\sim 80\%$ wt of the inclusions have a diameter between 75 and 385  $\mu\text{m}$  (Søiland et al. 2004).

## Growth of Multicrystalline Silicon in Ambient Nitrogen

### Gas Doping of N for Cast Mc-Si

N-doping through utilizing ambient nitrogen (Yang et al. 2009) has been well applied in CZ-Si growth. NCZ-Si wafers have multiple benefits and features for IC industry, i.e., it provides the flexibility in controlling oxygen precipitates,

suppressing void defects related to vacancies, and improving mechanical strength of wafers. However, for cast mc-Si (including QSC-Si), these features are not as important as for CZ-Si, and certain amounts of N content are incorporated into the crystal due to the reaction of the coated  $\text{Si}_3\text{N}_4$  on the inner walls of crucible with molten silicon (Ghosh et al. 1997), so there are few interests on gas doping of N for mc-Si. To date, mc-Si ingots are mostly grown in ambient argon.

As discussed above, the N concentration in the molten silicon is relatively high, the ideal segregation coefficient of N in silicon is as small as  $7.5 \times 10^{-4}$ , and the most important, the manufacturers usually do not intentionally change the convection level. Thus, the common range of N concentration in a regular mc-Si ingot is  $4\text{--}6 \times 10^{15} \text{ cm}^{-3}$ . And the soluble N concentration in the mc-Si crystal must be controlled lower than  $10^{16} \text{ cm}^{-3}$  in solid phase, or else  $\text{Si}_3\text{N}_4$  precipitates must be generated and then cause dense defects in silicon crystal.

When casting mc-Si ingots in ambient nitrogen, additional N sources are introduced in the system as  $\text{Si}_3\text{N}_4$  film or particles, and they are generated at the solid Si surface by the reaction between polycrystalline Si and  $\text{N}_2$  during the melting stage. Because the convection in casting method is much lower compared with CZ growth, the additional  $\text{Si}_3\text{N}_4$  generated on poly-Si nuggets increases the contact area between  $\text{Si}_3\text{N}_4$  and molten silicon, which increases the localized N concentration in both liquid and solidified silicon. Once the N concentration is oversaturated,  $\text{Si}_3\text{N}_4$  precipitation should be generated in the crystal. Figure 11 shows the minority lifetime mapping images of mc-Si ingots grown in Ar (MC),  $\text{N}_2$  with (NMC1) reduced and (NMC0) regular pressure. The inset of Fig. 11 shows the  $\text{Si}_3\text{N}_4$  precipitates and related cracks in the ingot MNC0 grown in ambient  $\text{N}_2$  with regular pressure of 600 mbar. The mapping of brick shows that the relatively high  $\text{N}_2$  partial pressure can cause many cracks in the crystal. These cracks are filled with  $\text{Si}_3\text{N}_4$  precipitates, and dense dislocations/grain boundaries are generated nearby. SEM photo shows that the precipitates are mostly needle-like, suggesting that they are  $\beta\text{-Si}_3\text{N}_4$ , which means they are not unmelted coating because the coating is usually

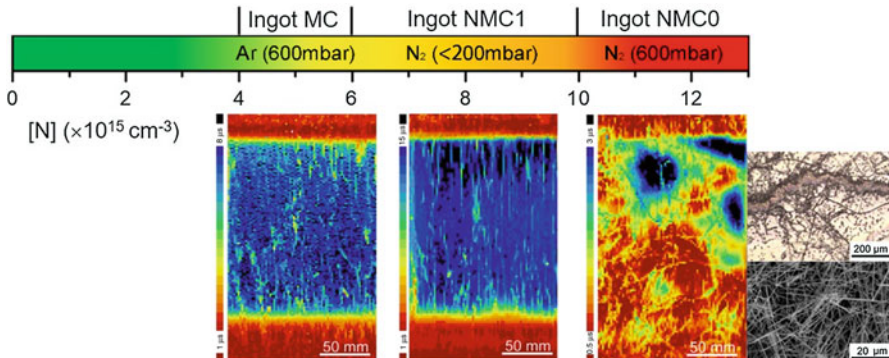


**Fig. 11** The minority carrier lifetime mapping of mc-Si grown in Ar (MC),  $\text{N}_2$  with reduced pressure (NMC1) and normal pressure (NMC0). Inset shows the defect distribution near a crack shown by Secco etching and SEM photo of  $\text{Si}_3\text{N}_4$  precipitates located in the cracks

composed by  $\alpha$ - $\text{Si}_3\text{N}_4$ . Meanwhile,  $\text{Si}_3\text{N}_4$  particles formed before solidification will float upward the surface of the molten silicon and cannot exist in the bulk. The generation of cracks should be related to the high thermal stress after solidification during the hot temperature phase of crystal growth, the fast diffuser N-N pairs could diffuse to the crack surfaces and then form silicon nitride particles. However, the detailed mechanism for the formation of the cracks with silicon nitride aggregation still needs more experiments to reveal.

The N concentration can be controlled through manipulating  $\text{N}_2$  partial pressure. Fine mc-Si ingots can be obtained under ambient nitrogen with reduced pressure. The total N concentration in the top samples was measured to be  $9.4 \times 10^{15} \text{ cm}^{-3}$  by SIMS, which is much higher than the regular range of  $4\text{--}6 \times 10^{15} \text{ cm}^{-3}$ . This indicates that the N concentrations can be effectively improved by the utilization of ambient nitrogen with a reduced pressure. Figure 11 also shows that the minority carrier lifetime of NMC0 is lower than that of NMC1 due to the generation of massive cracks, and the carrier lifetime of NMC1 is even better than MC. This suggests that the increase in N concentrations up to  $9.4 \times 10^{15} \text{ cm}^{-3}$  has no influence on the carrier recombination properties of cast mc-Si materials and, therefore, should do no harm on the performance of solar cells.

## Improvement in Mechanical Strength

It is well known that the introduction of N can enhance the mechanical strength of CZ-Si (Wang et al. 2001); therefore, the extra N-doping in mc-Si can likewise further enhance the fracture strength of wafers. The influence of extra N-doping on fracture strength is investigated using twist breakage test combined with Weibull analysis. Twist test is the most widely used tool to characterize the fracture strength, considering the nonuniform grain structure of mc-Si wafers. Figure 12 shows the scheme of twist test for  $156 \times 156 \text{ mm}^2$  wafers, where wafers were placed on fixed lower dowel

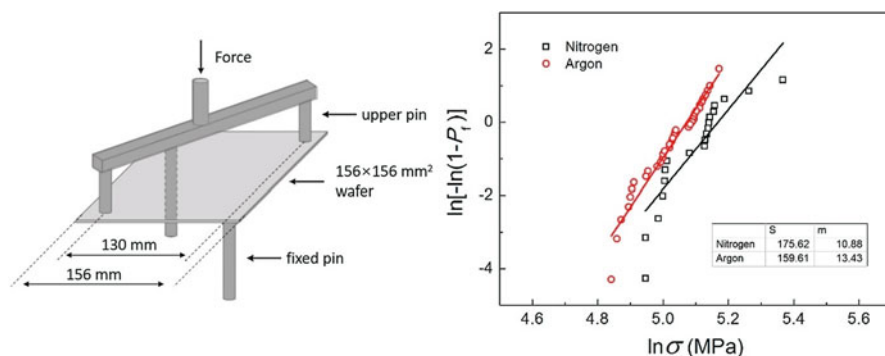


**Fig. 12** Schematic setup of the twist-test configuration and the Weibull plots of the variation of fracture strength with the applied stress for the wafers from the ingots grown in  $\text{N}_2$  and Ar (Yuan et al. 2018)

pins and the upper dowel pins move downward until they reach the wafer surface, and then loads are applied by upper pins moving downward on the unsupported corners of the wafers until the breakage. Nevertheless, the stress distribution of twist test is nonlinear (Schoenfelder et al. 2007), and a characteristic fracture strength value can be defined as  $\sigma = CFb/dl^2$  for evaluation, where  $C$  is a constant ( $C$  was set as 2 in this work),  $F$  is the fracture force,  $d$  the wafer thickness, and  $l$  and  $b$  the geometric parameters for wafer and tester, which are 156 and 130 mm, respectively. The Weibull method describes the failure probability as a function of strength,

$$P_f = 1 - \exp[-(\sigma/\sigma_0)^m],$$

where  $P_f$  is the failure probability at the applied stress  $\sigma$  and  $\sigma_0$  and  $m$  are defined as the characteristic strength and the Weibull modulus, respectively.  $P_f = (n - 1/2)/N$ , dependent on its ranking number,  $n$  ( $N$  is the total number of samples).  $\sigma_0$  equals to the stress when 63% of all samples fail and  $m$  describes the variability of strength data. High  $m$  value means smaller scattering of  $\sigma$ . Therefore, through a linear fit of  $\ln(-\ln(1 - P_f))$  versus  $\ln \sigma$ ,  $\sigma_0$  and  $m$  can be determined from the slope and intercept. Figure 12 also shows the Weibull distribution of the fracture strength of wafers from the ingots grown in  $N_2$  and Ar, the total number of wafers is 36 and 37, and the characteristic strengths are 175.62 and 159.61 MPa, respectively. It is clear that the wafers from the ingot grown in nitrogen are statically harder.

## Impact of N-O Complexes in Mc-Si Grown in Ambient $N_2$

The increase in N concentration in mc-Si grown in ambient  $N_2$  may cause increase in N-O concentration. N-O complexes introduce shallow thermal donors (STD) in silicon and may cause compensation in  $p$ -type mc-Si. As mentioned above, the fraction range of N-O complexes in mc-Si is 10–40% considering O<sub>i</sub> concentration; therefore, when the total N concentration reaches  $\sim 10^{16} \text{ cm}^{-3}$ , the STD concentration can be higher than  $10^{15} \text{ cm}^{-3}$ , when the influence on resistivity cannot be easily ignored.

Figure 13a shows the resistivity distribution of ingots grown in  $N_2$  and Ar along the ingot height. It is interesting that the resistivity of N-doped ingot grown in  $N_2$  increases with ingot height, while that of the referential ingot grown in Ar decreases normally. Since the boron doping is same for both ingots, the difference in resistivity distribution between the two ingots is attributed to the formation of N-O complexes, which serve as shallow donors and compensate boron acceptors (Yang et al. 1996). Note that N-O complexes also exist in normal mc-Si grown in argon, and they are commonly eliminated during phosphorus diffusion process (by annealing under 800–900 °C for ~30 min) so that the substrate material of final Al-BSF solar cell is not compensated. Figure 13b shows the resistivity variation of samples sliced from the top of N-doped and referential ingots, after the annealing under 900 °C and then 650 °C to degenerate and regenerate N-O complexes, respectively. The corresponding interstitial oxygen concentration at the ingot top is measured to be

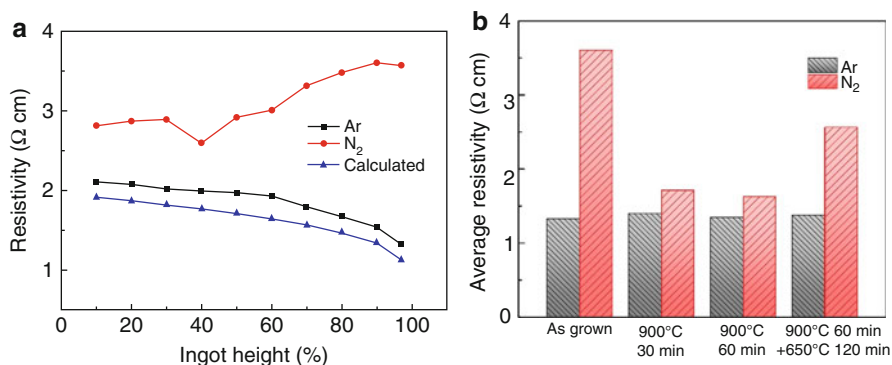


**Fig. 13** (a) The resistivity distribution of B-doped p-type ingots grown in  $\text{N}_2$  and Ar ambient versus various ingot heights. (b) The variation of average resistivity of top samples from the ingots grown in  $\text{N}_2$  and Ar after various thermal annealings (Yuan et al. 2018)

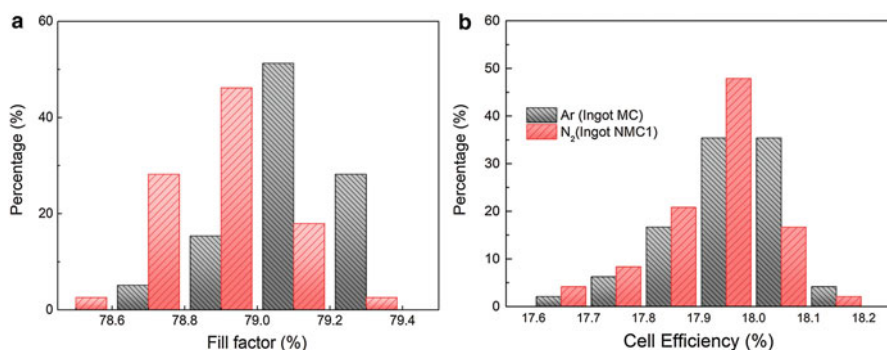


**Fig. 14** (a) Fill factor distribution of solar cells. (b) The resistivity variation after heat treatment of top samples sliced from ingot NMC1 and ingot MC (Yuan et al. 2018)

$\sim 6.8 \times 10^{16} \text{ cm}^{-3}$  by FTIR. The resistivity of the N-doped sample obviously decreases when annealed under 900 °C and increases when latterly annealed under 650 °C. It can be explained by the degeneration and regeneration of N-O complexes in N-doped samples.

Standard Al-BSF solar cells based on wafers from the ingot grown in  $\text{N}_2$  with reduced pressure were fabricated. Since it has been shown that thermal annealing in Al-BSF cell manufacturing cannot totally eliminate N-O complex shallow donors, then the bulk resistivity of NMC1 wafers is higher than the reference after annealing under 900 °C, which causes higher series resistivity and lower fill factor of the solar cells. The distributions of fill factor values are shown in Fig. 14a. As a result, Fig. 14b shows the distribution of solar cell efficiencies for both kinds of the wafers. The average efficiencies are almost the same for the solar cells based on the ingot NMC1 and MC, which are 17.91% and 17.96%, respectively. This indicates that the high concentration of nitrogen has a little influence on solar cell performances. It can



be inferred that a better overall resistivity distribution of the whole ingot can be obtained if N-O complex-related compensation is well controlled. For the consideration of application of N-doped silicon, an additional B doping should be adopted to fit the cell manufacturing process.

---

## Conclusion

This chapter reviews the basic properties of nitrogen in photovoltaic silicon materials. The development of N-doped CZ-Si wafers is crucial for IC industry. As NCZ-Si has not been widely used in photovoltaic fields, related knowledge from the perspective of possible photovoltaic application are introduced. As mc-Si, nitrogen impurity is important subject in casting method due to  $\text{Si}_3\text{N}_4$ -coated crucibles. The concepts of the existence, transportation, and influence of N-related defects are introduced and described to the readers to help understand the relevant phenomena during the solidification process. Finally, cheaper ambient nitrogen for casting multicrystalline silicon ingots has been achieved with comparable crystal quality and solar cell conversion efficiency.

---

## Cross-References

- ▶ [Carbon Impurity in Crystalline Silicon](#)
- ▶ [Grain Boundaries in Multicrystalline Silicon](#)
- ▶ [Growth of Crystalline Silicon for Solar Cells: Czochralski Si](#)
- ▶ [Growth of Crystalline Silicon for Solar Cells: Mono-Like Method](#)
- ▶ [Growth of Multicrystalline Silicon for Solar Cells: Dendritic Cast Method](#)
- ▶ [Growth of Multicrystalline Silicon for Solar Cells: The High-Performance Casting Method](#)

**Acknowledgments** The authors would like to thank the financial support from the National Natural Science Foundation of China (Nos. 51532007, 61721005). It was also partly supported by Key Project of Zhejiang Province (No. 2018C01034).

---

## References

- C. Alpass, J. Murphy, R. Falster, P. Wilshaw, Nitrogen in silicon: diffusion at 500–750 °C and interaction with dislocations. *Mater. Sci. Eng. B* **159**, 95–98 (2009)
- H.C. Alt, H. Wagner, Piezospectroscopy of nitrogen-oxygen shallow donor complexes in silicon. *Phys. Rev. B* **82**(11), 115203 (2010)
- H.C. Alt, Y. Gomeniuk, F. Bittersberger, A. Kempf, D. Zemke, Analysis of electrically active N-O complexes in nitrogen-doped CZ silicon crystals by FTIR spectroscopy. *Mater. Sci. Semicond. Process.* **9**(1–3), 114–116 (2006)
- P.M. Anderson, in *Nanoscale Materials and Modeling – Relations Among Processing, Microstructure and Mechanical Properties: Symposium* held April 13–16, 2004, San Francisco, California, vol 821. Materials Research Society



- J. Bauer, O. Breitenstein, J.P. Rakotoniaina, Electronic activity of SiC precipitates in multicrystalline solar silicon. *Phys. Status Solidi A* **204**(7), 2190–2195 (2007)
- O. Breitenstein, J. Rakotoniaina, M.H. Al Rifai, M. Werner, Shunt types in crystalline silicon solar cells. *Prog. Photovolt. Res. Appl.* **12**(7), 529–538 (2004)
- P.H. Bucksbaum, J. Bokor, Rapid melting and regrowth velocities in silicon heated by ultraviolet picosecond laser pulses. *Phys. Rev. Lett.* **53**(2), 182 (1984)
- T. Buonassisi, A.A. Istratov, M. Pickett, J.-P. Rakotoniaina, O. Breitenstein, M.A. Marcus, S.M. Heald, E.R. Weber, Transition metals in photovoltaic-grade ingot-cast multicrystalline silicon: assessing the role of impurities in silicon nitride crucible lining material. *J. Cryst. Growth* **287**(2), 402–407 (2006)
- D. Chakraborty, J. Mukerji, Characterization of silicon nitride single crystals and polycrystalline reaction sintered silicon nitride by microhardness measurements. *J. Mater. Sci.* **15**(12), 3051–3056 (1980)
- J. Chen, D. Yang, X. Ma, Z. Zeng, D. Tian, L. Li, D. Que, L. Gong, Influence of germanium doping on the mechanical strength of Czochralski silicon wafers. *J. Appl. Phys.* **103**(12), 123521 (2008)
- L. Chen, X. Yu, P. Chen, P. Wang, X. Gu, J. Lu, D. Yang, Effect of oxygen precipitation on the performance of Czochralski silicon solar cells. *Sol. Energy Mater. Sol. Cells* **95**(11), 3148–3151 (2011). <https://doi.org/10.1016/j.solmat.2011.06.044>
- A. Clark, J.D. Macdougall, K.E. Manchester, P. Roughan, F. Anderson, *Nitrogen Donor Level in Silicon*, Bulletin of the American Physical Society, vol 3 (American Institute of Physics Circulation and Fulfillment Division, Woodbury, 1968), p. 376
- G. Du, L. Zhou, P. Rossetto, Y. Wan, Hard inclusions and their detrimental effects on the wire sawing process of multicrystalline silicon. *Sol. Energy Mater. Sol. Cells* **91**(18), 1743–1748 (2007)
- G. Du, N. Chen, P. Rossetto, Wire-sawing defects on multicrystalline silicon wafers grown by a directional solidification method. *Semicond. Sci. Technol.* **23**(5), 055011 (2008)
- C. Ewels, R. Jones, S. Öberg, J. Miro, P. Deak, Shallow thermal donor defects in silicon. *Phys. Rev. Lett.* **77**(5), 865 (1996)
- N. Fujita, R. Jones, J. Goss, P. Briddon, T. Frauenheim, S. Öberg, Diffusion of nitrogen in silicon. *Appl. Phys. Lett.* **87**(2), 021902 (2005)
- V. Ganapati, S. Schoenfelder, S. Castellanos, S. Oener, R. Koepge, A. Sampson, M.A. Marcus, B. Lai, H. Morhenn, G. Hahn, Infrared birefringence imaging of residual stress and bulk defects in multicrystalline silicon. *J. Appl. Phys.* **108**(6), 063528 (2010)
- M. Ghosh, D. Yang, A. Lawrenz, S. Riedel, H. Moller, Investigation of minority carrier lifetime degradation in multicrystalline silicon ingots, in *Proceedings of the 14th European Photovoltaic Solar Energy Conference*, (1997), pp. 724–727
- J. Goss, I. Hahn, R. Jones, P. Briddon, S. Öberg, Vibrational modes and electronic properties of nitrogen defects in silicon. *Phys. Rev. B* **67**(4), 045206 (2003)
- J. Griffin, J. Hartung, J. Weber, H. Navarro, L. Genzel, Photothermal ionisation spectroscopy of oxygen-related shallow defects in crystalline silicon. *Appl. Phys. A*. **48**(1), 41–47 (1989)
- A. Hara, T. Fukuda, T. Miyabo, I. Hirai, Electron spin resonance of oxygen-nitrogen complex in silicon. *Jpn. J. Appl. Phys.* **28**(1R), 142 (1989)
- P. Hemment, R. Peart, M. Yao, K. Stephens, R. Chater, J. Kilner, D. Meekison, G. Booker, R. Arrowsmith, High quality silicon on insulator structures formed by the thermal redistribution of implanted nitrogen. *Appl. Phys. Lett.* **46**(10), 952–954 (1985)
- R. Hockett, Anomalous diffusion of nitrogen in nitrogen-implanted silicon. *Appl. Phys. Lett.* **54**(18), 1793–1795 (1989)
- R. Hockett, D. Sams, The measurement of nitrogen in silicon substrates by SIMS, in *Proceedings-SPIE the International Society for Optical Engineering, 2000*, (International Society for Optical Engineering, 1999), pp. 584–595
- S. Hu, W. Patrick, Effect of oxygen on dislocation movement in silicon. *J. Appl. Phys.* **46**(5), 1869–1874 (1975)
- T. Itoh, T. Abe, Diffusion coefficient of a pair of nitrogen atoms in float-zone silicon. *Appl. Phys. Lett.* **53**(1), 39–41 (1988). <https://doi.org/10.1063/1.100116>
- Y. Itoh, T. Nozaki, T. Masui, T. Abe, Calibration curve for infrared spectrophotometry of nitrogen in silicon. *Appl. Phys. Lett.* **47**(5), 488–489 (1985)

- R. Jones, C. Ewels, J. Goss, J. Miro, P. Deak, S. Oberg, F.B. Rasmussen, Theoretical and isotopic infrared absorption investigations of nitrogen-oxygen defects in silicon. *Semicond. Sci. Technol.* **9**(11), 2145 (1994a)
- R. Jones, S. Öberg, F.B. Rasmussen, B.B. Nielsen, Identification of the dominant nitrogen defect in silicon. *Phys. Rev. Lett.* **72**(12), 1882 (1994b)
- W. Kaiser, C. Thurmond, Nitrogen in silicon. *J. Appl. Phys.* **30**(3), 427–431 (1959)
- A. Karoui, G. Rozgonyi, Oxygen precipitation in nitrogen doped Czochralski silicon wafers. II. Effects of nitrogen and oxygen coupling. *J. Appl. Phys.* **96**(6), 3264–3271 (2004)
- H. Kusunoki, T. Ishizuka, A. Ogura, H. Ono, Complementary distribution of NN and NNO complexes in cast-grown multicrystalline silicon for photovoltaic cells. *Appl. Phys. Express* **4**(11), 115601 (2011)
- J. Li, R.R. Prakash, K. Jiptner, J. Chen, Y. Miyamura, H. Harada, K. Kakimoto, A. Ogura, T. Sekiguchi, Butterfly-shaped distribution of SiN<sub>x</sub> precipitates in multi-crystalline Si for solar cells. *J. Cryst. Growth* **377**, 37–42 (2013)
- J. Li, X. Yu, S. Yuan, L. Yang, Z. Liu, D. Yang, Effects of oxygen related thermal donors on the performance of silicon heterojunction solar cells. *Sol. Energy Mater. Sol. Cells* **179**, 17–21 (2018)
- H. Lu, D. Yang, L. Li, Z. Ye, D. Que, Thermal warpage of Czochralski silicon wafers grown under a nitrogen ambience. *Phys. Status Solidi A* **169**(2), 193–198 (1998)
- G. Mannino, V. Privitera, S. Scalesi, S. Libertino, E. Napolitani, P. Pichler, N.E. Cowern, Effect of oxygen on the diffusion of nitrogen implanted in silicon. *Electrochem. Solid-State Lett.* **7**(8), G161–G163 (2004)
- J. Murphy, A. Giannattasio, S. Senkader, R. Falster, P. Wilshaw, Nitrogen transport in float-zone and Czochralski silicon investigated by dislocation locking experiments. *Phys. Status Solidi A* **202**(5), 926–930 (2005)
- J.D. Murphy, C. Alpäss, A. Giannattasio, S. Senkader, R. Falster, P. Wilshaw, Nitrogen in silicon: transport and mechanical properties. *Nucl. Instrum. Methods Phys. Res., Sect. B* **253**(1), 113–117 (2006)
- M. Nakatsu, A. Hashimoto, A. Natsume, N. Inoue, H. Ono, Measurement of nitrogen concentration in cz-si below 1014/cm<sup>3</sup> by IR absorption spectroscopy, in *High Purity Silicon VIII: Proceedings of the International Symposium*, (The Electrochemical Society, 2004), p. 102
- J. Nelson, P. Schultz, A. Wright, Valence and atomic size dependent exchange barriers in vacancy-mediated dopant diffusion. *Appl. Phys. Lett.* **73**(2), 247–249 (1998)
- T. Nozaki, Y. Yatsurugi, N. Akiyama, Charged particle activation analysis for carbon, nitrogen and oxygen in semiconductor silicon. *J. Radioanal. Nucl. Chem.* **4**(1), 87–98 (1970)
- H. Ono, M. Horikawa, Quantitative detection of small amount of nitrogen in Czochralski-grown silicon crystals. *Jpn. J. Appl. Phys.* **42**(3B), L261 (2003)
- V. Orlov, H. Richter, A. Fischer, J. Reif, T. Müller, R. Wahlich, Mechanical properties of nitrogen-doped CZ silicon crystals. *Mater. Sci. Semicond. Process.* **5**(4–5), 403–407 (2002)
- P. Pavlov, E. Zorin, D. Tetelbaum, A. Khokhlov, Nitrogen as dopant in silicon and germanium. *Phys. Status Solidi A* **35**(1), 11–36 (1976)
- M. Porrini, M. Pretto, R. Scala, Measurement of nitrogen in Czochralski silicon by means of infrared spectroscopy. *Mater. Sci. Eng. B* **102**(1), 228–232 (2003)
- M. Qi, S. Tan, B. Zhu, P. Cai, W. Gu, X. Xu, T. Shi, D. Que, L. Li, The evidence for interaction of the N-N pair with oxygen in Czochralski silicon. *J. Appl. Phys.* **69**(6), 3775–3777 (1991)
- D. Que, X. Chen, *Silicon Materials Science and Technology* (Zhejiang University Press, Hangzhou, China, 2000). (in Chinese)
- D. Que, L. Li, Y. Lin, Nitrogen protective ambience for Czochralski growth of silicon. Chinese Patent CN85100295, 1985
- D. Que, L. Li, X. Chen, Nitrogen gas doping in Czochralski silicon. Chinese Patent CN87105811, 1987
- D. Que, L. Li, X. Chen, Y. Lin, J. Zhang, X. Zhou, J. Yang, Czochralski silicon crystal growth in nitrogen atmosphere under reduced pressure. *Sci. China Ser. A Math. Phys. Astron. Technol. Sci.* **34**(8), 1017–1024 (1991)

- C. Reimann, M. Trempa, J. Friedrich, G. Müller, About the formation and avoidance of C and N related precipitates during directional solidification of multi-crystalline silicon from contaminated feedstock. *J. Cryst. Growth* **312**(9), 1510–1516 (2010)
- S. Richter, J. Bauer, O. Breitenstein, Growth of carbon and nitrogen containing precipitates in crystalline solar silicon and their influence on solar cells. *Phys. Status Solidi RRL* **11**(2), 1600354 (2017)
- H. Sawada, H. Kawakami, First-principles calculation of the interaction between nitrogen atoms and vacancies in silicon. *Phys. Rev. B* **62**(3), 1851 (2000)
- H. Sawada, K. Kawakami, A. Ikari, W. Ohashi, Atomistic model of nitrogen-pair diffusion in silicon. *Phys. Rev. B* **65**(7), 075201 (2002)
- S. Schoenfelder, A. Bohne, J. Bagdahn, Comparison of test methods for strength characterization of thin solar wafer. in *Proceedings of 22nd European Photovoltaic Solar Energy Conference*, Milan, Italy, 2007, vol 7
- S. Schoenfelder, A. Sampson, V. Ganapati, R. Koepge, J. Bagdahn, T. Buonassisi, Quantitative stress measurements of bulk microdefects in multicrystalline silicon. 24th EUPVSEC:977–980 (2009)
- P.A. Schultz, J.S. Nelson, Fast through-bond diffusion of nitrogen in silicon. *Appl. Phys. Lett.* **78** (6), 736–738 (2001)
- L.L. Snead, T. Nozawa, Y. Katoh, T.-S. Byun, S. Kondo, D.A. Petti, Handbook of SiC properties for fuel performance modeling. *J. Nucl. Mater.* **371**(1–3), 329–377 (2007)
- A. Soiland, E. Øvrelid, T. Engh, O. Lohne, J. Tuset, Ø. Gjerstad, SiC and Si<sub>3</sub>N<sub>4</sub> inclusions in multicrystalline silicon ingots. *Mater. Sci. Semicond. Process.* **7**(1), 39–43 (2004)
- N. Stoddard, P. Pichler, G. Duscher, W. Windl, Ab initio identification of the nitrogen diffusion mechanism in silicon. *Phys. Rev. Lett.* **95**(2), 025901 (2005)
- M. Suezawa, K. Sumino, H. Harada, T. Abe, Nitrogen-oxygen complexes as shallow donors in silicon crystals. *Jpn. J. Appl. Phys.* **25**(10A), L859 (1986)
- M. Suezawa, K. Sumino, H. Harada, T. Abe, The nature of nitrogen-oxygen complexes in silicon. *Jpn. J. Appl. Phys. Part 1* **27**(1), 62–67 (1988). <https://doi.org/10.1143/jjap.27.62>
- K. Sumino, I. Yonenaga, M. Imai, T. Abe, Effects of nitrogen on dislocation behavior and mechanical strength in silicon crystals. *J. Appl. Phys.* **54**(9), 5016–5020 (1983)
- Y. Tokumaru, H. Okushi, T. Masui, T. Abe, Deep levels associated with nitrogen in silicon. *Jpn. J. Appl. Phys.* **21**(7A), L443 (1982)
- M. Trempa, C. Reimann, J. Friedrich, G. Müller, The influence of growth rate on the formation and avoidance of C and N related precipitates during directional solidification of multi crystalline silicon. *J. Cryst. Growth* **312**(9), 1517–1524 (2010)
- L. Vandeperre, F. Giuliani, S. Lloyd, W. Clegg, The hardness of silicon and germanium. *Acta Mater.* **55**(18), 6307–6315 (2007)
- J. Vedde, P. Gravesen, The fracture strength of nitrogen doped silicon wafers. *Mater. Sci. Eng. B* **36** (1–3), 246–250 (1996)
- V.V. Voronkov, R.J. Falster, Nitrogen diffusion and interaction with oxygen in Si. in *Solid State Phenomena*, 2004. Trans Tech Publ, pp. 83–92
- P. Wagner, R. Oeder, W. Zulehner, Nitrogen-oxygen complexes in Czochralski-silicon. *Appl. Phys. A* **46**(2), 73–76 (1988)
- H. Wagner, H.C. Alt, W. von Ammon, F. Bittersberger, A. Huber, L. Koester, N-O related shallow donors in silicon: stoichiometry investigations. *Appl. Phys. Lett.* **91**(15), 152102 (2007)
- G. Wang, D. Yang, D. Li, Q. Shui, J. Yang, D. Que, Mechanical strength of nitrogen-doped silicon single crystal investigated by three-point bending method. *Phys. B Condens. Matter* **308**, 450–453 (2001)
- D. Yang, X. Yu, Nitrogen in Silicon. *Defect Diffus. Forum* **230–232**, 199–220 (2004)
- D. Yang, D. Que, K. Sumino, Nitrogen effects on thermal donor and shallow thermal donor in silicon. *J. Appl. Phys.* **77**(2), 943–944 (1995)
- D. Yang, R. Fan, L. Li, D. Que, K. Sumino, Effect of nitrogen–oxygen complex on electrical properties of Czochralski silicon. *Appl. Phys. Lett.* **68**(4), 487–489 (1996)

- D. Yang, X. Yu, D. Que, Nitrogen doping in casting multicrystalline silicon by melting feedstocks in nitrogen ambience. Chinese Patent CN101597790, 2009
- Y. Yatsurugi, N. Akiyama, Y. Endo, T. Nozaki, Concentration, solubility, and equilibrium distribution coefficient of nitrogen and oxygen in semiconductor silicon. *J. Electrochem. Soc.* **120**(7), 975–979 (1973)
- I. Yonenaga, Dislocation–impurity interaction in Si. *Mater. Sci. Eng. B* **124**, 293–296 (2005)
- I. Yonenaga, K. Sumino, K. Hoshi, Mechanical strength of silicon crystals as a function of the oxygen concentration. *J. Appl. Phys.* **56**(8), 2346–2350 (1984)
- I. Yonenaga, T. Taishi, X. Huang, K. Hoshikawa, Dislocation–impurity interaction in Czochralski-grown Si heavily doped with B and Ge. *J. Cryst. Growth* **275**(1–2), e501–e505 (2005)
- X. Yu, D. Yang, X. Ma, J. Yang, L. Li, D. Que, Grown-in defects in nitrogen-doped Czochralski silicon. *J. Appl. Phys.* **92**, 188–194 (2002)
- X. Yu, D. Yang, K. Hoshikawa, Investigation of nitrogen behaviors during Czochralski silicon crystal growth. *J. Cryst. Growth* **318**(1), 178–182 (2011)
- X. Yu, J. Chen, X. Ma, D. Yang, Impurity engineering of Czochralski silicon. *Mater. Sci. Eng. R. Rep.* **74**(1), 1–33 (2013)
- S. Yuan, D. Hu, X. Yu, F. Zhang, H. Luo, L. He, D. Yang, Controllable Nitrogen Doping in Multicrystalline Silicon by Casting Under Low Cost Ambient Nitrogen. *Silicon* 1–6 (2018)
- H. Zhang, M. Stavola, M. Seacrist, Nitrogen-containing point defects in multi-crystalline Si solar-cell materials. *J. Appl. Phys.* **114**(9), 093707 (2013)



# Metal Impurities and Gettering in Crystalline Silicon

# 17

Eugene B. Yakimov

## Contents

Introduction .....	496
Solubility of Transition Metals .....	497
Diffusion of Transition Metals .....	500
Electrical Properties of Transition Metals in Si .....	505
Iron .....	505
Nickel .....	509
Copper .....	510
Chromium .....	511
Cobalt .....	512
Titanium .....	512
Gold .....	513
Silver .....	513
Zinc .....	514
Manganese .....	514
Effect of Metals on Solar Cell Efficiency .....	514
Metal Interaction with Extended Defects .....	520
Metal Impurities Gettering .....	528
Hydrogen Passivation .....	533
Conclusion .....	538
Cross-References .....	539
References .....	539

## Abstract

Solar-grade Si usually contains a considerable amount of metal impurities and extended defects. The detrimental effect of transition metals on solar cell performance is well documented. This necessitates a study of transition metal properties in

E. B. Yakimov (✉)

Institute of Microelectronics Technology, Russian Academy of Science, Chernogolovka, Russia

National University of Science and Technology, MISiS, Moscow, Russia

e-mail: [yakimov@iptm.ru](mailto:yakimov@iptm.ru)

Si and their interaction with point and extended defects. Such studies will form the basis for the development of procedures on suppressing the detrimental effects of transition metals. This chapter briefly describes the solubilities, diffusivities, and electrical properties of metal impurities that are most frequently detected in multicrystalline silicon. The diffusion length values necessary for highly efficient crystalline silicon solar cells, which set a limit on the electrically active metal concentration, are estimated. The effects of dislocations and grain boundaries on the effective diffusion length are evaluated. Finally, the efficiency of gettering and hydrogen passivation procedures used in silicon solar cell technology is considered.

---

**Keywords**

Transition metals · Silicon · Lifetime · Extended defects · Gettering · Hydrogen passivation

---

## Introduction

One of the main requirements for silicon in photovoltaic application is the high excess carrier lifetime  $\tau$  (or diffusion length) because this parameter determines the efficiency of solar cells to a great extent. However, there is also a considerable interest in reducing the cost of solar-grade Si. For this reason, multicrystalline Si wafers produced by casting or Si ribbons are mainly used in Si-based photovoltaics instead of high-quality monocrystalline wafers. These materials usually contain a considerable amount of metal impurities and extended defects, which are widely believed to be the most dangerous lifetime killers in crystalline silicon; for this reason, their concentrations should be minimized.

One of the proposed approaches to reduce material cost is through the use of metallurgical-grade Si for wafer growth, which can reduce chemical purity even further. Thus, the requirements for low metal concentration that are necessary for photovoltaic applications are in conflict with the need to reduce material cost. As shown by Istratov et al. (2006), the concentration of Fe, Cr, Ni, and Cu in multicrystalline Si (mc-Si) solar cells is greater than  $10^{14} \text{ cm}^{-3}$ . Only boron, oxygen, and carbon are detected in higher concentrations. The concentration of other impurities is usually less than  $10^{13} \text{ cm}^{-3}$ . A more recent analysis carried out by Stokkan et al. (2017) in mc-Si ingot showed that only Co, Cr, Fe, Zn, and Ni concentrations exceeded  $10^{12} \text{ cm}^{-3}$ . In mc-Si ingot grown by the Bridgman method from refined metallurgical silicon, notably high concentrations of Ti, Al, and Mn were revealed in addition to the previously mentioned impurities (Peshcherova et al. 2015).

As shown in Heinz et al. (2014) and Orlov et al. (2017), aluminum spikes can be a reason for shunts or prebreakdown site formation in solar elements; however, it can be expected that their effect on the excess carrier recombination rate is not significant. Usually only a small fraction of metal impurities is electrically active because most of them precipitate via a homogeneous nucleation or via a nucleation on the numerous extended defects, such as dislocations and grain boundaries. However, even in this state, they can degrade solar cell performance because some precipitates

– especially those formed on extended defects – demonstrate recombination activity. Moreover, temperature treatment during contact firing procedures can lead to precipitate dissolution and metal impurity redistribution and activation.

Both metal impurities and extended defects usually lead to an increase of the excess carrier recombination rate and thus to a decrease of solar cell efficiency. It is well known that extended defect recombination activity increases due to their decoration with metal impurities. Therefore, one of the ways to suppress the metal impurity effect on solar cell efficiency is to transfer the harmful impurities to any electrically inactive state or remove them from the cell by a gettering procedure. For electronic devices, usually a thin subsurface layer is active; therefore, procedures can be used to remove the harmful impurities from the active regions, transfer them to pre-designed regions where they are unimportant for the device performance, and confine them to these regions. If these regions are located inside the wafer, the corresponding procedures are referred to as *intrinsic gettering*. Such getters may be oxygen precipitates or nanocavities produced by hydrogen or helium implantation.

Solar cells are devices in which whole wafer is active; therefore, the excess carrier recombination rate should be suppressed in the whole wafer. For many metal atoms, their precipitation decreases in total the harmful effect on the lifetime; however, processes that totally remove the detrimental impurities from the wafer are usually more effective. Such processes are classified as *external gettering*. Another way to reduce the electrical activity of metal and extended defects without removing them from the active device region is their passivation by hydrogen. This procedure is also widely used in combination with gettering to improve the efficiency of solar cells. However, its efficiency relative to all metal impurities is not so obvious. Moreover, the stability of many hydrogen-related complexes is not high enough.

This chapter briefly discusses the properties of metal impurities that are usually detected in mc-Si (Fe, Ni, Cu, Cr, Co, Ti, Au, Ag, Zn, and Mn) and can degrade the performance of Si-based solar cells. Their effects on the excess carrier diffusion length are estimated. The interaction of metal impurities with dislocations and grain boundaries is considered. The effects of clean and contaminated with metals extended defects on the effective diffusion length of multicrystalline materials are estimated. The common gettering procedures used in Si-based solar cell technology are discussed. Special attention is paid to metal interactions with hydrogen because hydrogen passivation is now widely used in the production of highly efficient crystalline silicon solar cells (Lee et al. 2018); such passivation can be especially effective when used in combination with gettering procedures.

---

## Solubility of Transition Metals

The “solubility” of foreign atoms usually refers to the amount that can be held by the crystal structure without precipitation of a second phase. Thus, the solubility of any particular impurity in Si is defined as its maximum concentration that can be dissolved in the lattice at a given temperature, when the equilibrium between its solid solution is established with respect to the silicon-richest binary impurity-Si

**Table 1** Parameters describing solubility of some transition metals in intrinsic Si

	$S_0, \text{cm}^{-3}$	$\Delta H, \text{eV}$	$T \text{ range}, ^\circ\text{C}$	$T_{\text{eutectic}}, ^\circ\text{C}$
Fe	$8.4 \times 10^{25}$	2.94	900–1200	1207
Ni	$1.23 \times 10^{24}$	1.68	500–950	966
Cu	$5.5 \times 10^{23}$	1.49	500–800	802
Cr	$5.5 \times 10^{24}$	2.79	900–1300	1335
Co	$1 \times 10^{26}$	2.83	700–1200	1259
Ti	$3.4 \times 10^{24}$	3.05	950–1200	1330
Au	$1 \times 10^{24}$	1.98	800–1100	359
Ag	$5.3 \times 10^{24}$	2.78	1025–1325	845
Zn	$7.1 \times 10^{25}$	2.49	840–1200	420
Mn	$6.1 \times 10^{25}$	2.8	900–1150	1149

phase. At thermal equilibrium, the solid solubility of an impurity in Si is determined by the condition minimizing the Gibbs free energy. In the dilute limit at temperatures lower than the eutectic temperature  $T_{\text{eut}}$ , it can be usually described as follows:

$$S = 5 \times 10^{22} \exp(-\Delta G/kT) = S_0 \exp(-\Delta H/kT), \quad (1)$$

Here,  $\Delta G = \Delta H - T\Delta S$  is the excess Gibbs free energy for impurity introduction in Si;  $\Delta H$  and  $\Delta S$  are the corresponding values of excess enthalpy and entropy, respectively;  $k$  is the Boltzmann constant; and  $T$  is temperature. It can be seen that the solubility decreases drastically when the temperature decreases. As a result, the dissolved impurities become increasingly supersaturated under cooling, which provides the driving force for their precipitation. The parameters used in Eq. 1 for some transition metals are shown in Table 1. The applicable temperature ranges for Eq. 1 are also presented in Table 1. More information about metal solubility and diffusivity can be found in Graff (2000), Pizzini (2012), and Claeys and Simoen (2018).

In most eutectic systems, the point of maximum solid solubility of an element dissolved within a solid matrix occurs at the binary eutectic temperature. However, when the enthalpy of a point defect formation of a dissolved element within a matrix is large, as is the case for many transition metal point defects in silicon, the point of maximum solid solubility can occur at temperatures of several hundred degrees above the eutectic temperature. Precipitates formed at temperatures below the eutectic point can be explained by classical precipitation models, and this temperature range is the most interesting for the problems discussed in this chapter. The chemical states of all measured precipitates are equilibrium single-metal silicides; as a rule, no mixed metal silicide systems are observed in that case, although the formation of such silicides cannot be totally excluded. Precipitate nucleation and growth are facilitated by strain minimization and the presence of extended defects. The eutectic temperatures for the metals discussed are also presented in Table 1.

Generally speaking, every foreign atom may occupy both substitutional and interstitial sites in the lattice. Thus, in a common case, the solubility described by Eq. 1 consists of contributions from interstitial and substitutional species with the



corresponding values of Gibbs free energy. For most impurities, the solubility in the substitution and interstitial states differs by a few orders of magnitudes; therefore, it could be important for describing the microscopic diffusion mechanism but not for the total solubility. However, the equilibrium solubilities on the substitution and interstitial sites can depend sensitively on the solute, the solvent, and the temperature. This can lead to appreciable changes in the interstitial to substitutional concentration relationship with temperature; in some conditions, the solubilities in both positions could be comparable, so both should be taken into account.

In general, foreign atoms in semiconductors may carry electronic charges. Therefore, the position of the Fermi level can also affect their solubility. A concomitant phenomenon is that the ratio between the equilibrium interstitial to substitutional concentrations may change with background doping because of the different electronic structures of the impurities in these states. In particular, for impurities with energy levels inside the bandgap, neutral and the charged species exist; their relative concentrations depend on the position of the energy level relative to the Fermi level. This is a reason why the contributions of neutral and charged species to the solubility depend on the Fermi level position – that is, on the dopant concentration. It is especially important for low temperatures and high dopant concentrations. Sometimes, this can lead to dramatic effects. Thus, it is well established that positively charged interstitial species dominate in extrinsic *p*-type materials, whereas negatively charged substitutional metal impurities prevail in extrinsic *n*-type silicon. For this reason, the solubilities in highly doped *n*- and *p*-types Si can strongly differ. As an example, the predominant species of cobalt in intrinsic Si is interstitial  $Co_i$ , and it is a donor. By contrast, in heavily phosphorous-doped Si, acceptor-like substitutional  $Co_s$  becomes more abundant.

In highly doped Si, metal solubility can strongly increase in comparison with an intrinsic material. Thus, an enhancement of the solubility of Mn, Fe, and Co in phosphorus-doped Si can reach four orders of magnitude, which is mainly determined by a change of the impurity charge state. In addition, metals can form pairs with shallow donor or acceptor impurities, which also can increase the metal impurity solubility in highly doped Si. It is widely believed that the enhanced solubility of transition metals in highly boron-doped Si is mainly due to mobile interstitial species and their pairing with boron, whereas the enhanced solubility in highly phosphorus-doped Si is due to immobile substitutional species and their pairing with phosphorus. This is very important for understanding the mechanisms of gettering by highly doped Si layers.

It should be also stressed that the parameters presented in Table 1 were obtained for the intrinsic Si in thermal equilibrium. Strictly speaking, the term *solubility* is also related to equilibrium conditions only. If the equilibrium is not reached, such as after a rather short annealing and/or at low temperatures, the concentration can exceed the solubility value. Thus, the solubility of Cu and Ni extrapolated to room temperature is negligible. Nevertheless, it is well known that both impurities can be introduced at room temperature during chemical mechanical polishing in measurable concentrations (Zundel et al. 1988; Yarykin and Weber 2016). In addition, as shown in Koveshnikov et al. (1989), gold can be introduced in Si at room temperature by

rf SF<sub>6</sub>-O<sub>2</sub> plasma treatment. Such treatment can introduce also Cu and Ni at a depth of a few micrometers.

Another option to reach impurity concentrations that are higher than the solubility limit is to quench the samples from a high temperature, at which the equilibrium is established. A well-known example of this case is the oxygen in Si. Supersaturation is a state with higher free energy; therefore, impurities tend to form precipitates or diffuse to the surface to decrease energy. However, both procedures need high enough diffusivity. For this reason, it is practically impossible to quench interstitial copper with higher diffusivity, although it is possible for iron with much lower diffusivity at room temperature.

## Diffusion of Transition Metals

It is a well-known fact that 3d transition-metal impurities are among the fastest diffusing species in intrinsic silicon. Usually, the diffusion coefficients as a function of temperature can be expressed as follows:

$$D(T) = D_0 \exp(-\Delta H_m/kT) \quad (2)$$

Here,  $D_0$  is the pre-exponential factor and  $\Delta H_m$  is the migration barrier. Both coefficients depend on the diffusion mechanism.

The parameters for some transition metals frequently found in mc-Si are shown in Table 2. The open structure of the diamond lattice favors interstitial incorporation of foreign atoms. For this reason, interstitial diffusion and interstitial-substitutional exchange diffusion via the dissociative or kick-out mechanisms are rather prominent in Si. Many transition metals, including copper, iron, nickel, chromium, and cobalt, can dissolve in Si on interstitial sites – that is, on tetrahedral, hexagonal, or bond-centered positions between the lattice atoms. Foreign atoms with interstitial site preferences can hop from one interstitial site to another. In other words, they diffuse

**Table 2** Parameters describing the diffusivity of some transition metals in intrinsic Si

	$D_0$ , cm <sup>2</sup> /s	$\Delta H_m$ , eV	$T$ range, °C
$Fe_i$	$1.3 \times 10^{-3}$	0.68	30–1200
$Ni_i$	$1.69 \times 10^{-4}$	0.15	665–885
$Cu_i$	$4.5 \times 10^{-3}$	0.39	–90–930
Cr	$6.8 \times 10^{-4}$	0.79	27–400
	$1 \times 10^{-2}$	0.99	900–1250
Co	$4.2 \times 10^{-3}$	0.53	900–1100
Ti	$1.2 \times 10^{-1}$	2.05	600–1150
Au	$2.58 \times 10^{-2}$	0.965	800–1100
Ag	0.6	1.15	850–1100
Zn	0.64	1.85	870–1210
Mn	$1.63 \times 10^{-3}$	0.71	14–1200

by the direct interstitial mechanism. As a rule, atom concentrations on such interstitial sites are low. Therefore, the diffusion over these sites does not involve direct interaction with intrinsic point defects; however, this does not mean that such interaction is impossible. For this reason, the interstitial diffusion coefficients are usually orders of magnitude larger than those for other mechanisms, and there is no connection of this mechanism with self-diffusion of the semiconductor host. Due to a huge difference in the diffusivities of substitutional and interstitial species, it is very difficult to measure diffusivity for substitutional species when both states are possible; thus, it has been done for a only few metals. For example, the diffusivity over substitutional sites were measured for nickel in the temperature range from 450 °C to 800 °C, where it can be described as  $D_s = 0.1 \exp(-1.92\text{eV}/kT) \text{ cm}^2/\text{s}$ .

Pure substitutional diffusion needs assistance from additional intrinsic point defects, such as vacancies or silicon self-interstitials. If a metal impurity resides predominantly on substitutional sites but its diffusion proceeds via an interstitial position, then such an impurity is frequently denoted as a *hybrid diffuser*; the mechanisms of its diffusion are called *interstitial-substitutional exchange mechanisms*. The high diffusivities of hybrid elements have two major causes: a non-negligible fraction of these foreign atoms resides in interstitial sites of the lattice, and the migration enthalpies controlling jumps of these atoms from interstice to interstice should be small due to the weak coupling to the host lattice. Two main models are usually discussed to describe interstitial-substitutional exchange mechanisms of diffusion: the Frank-Turnbull model or the dissociative mechanism and the kick-out mechanism. The first model assumes that interstitially diffusing impurity atoms occupy preexisting vacancies, which are generated in thermal equilibrium or are frozen as vacancy-related clusters. At high enough temperatures, the missing vacancy can be then replaced by a vacancy diffusing from the sample surface or from any other vacancy source within the bulk of the crystal. For this mechanism, the vacancy diffusion is the limiting factor.

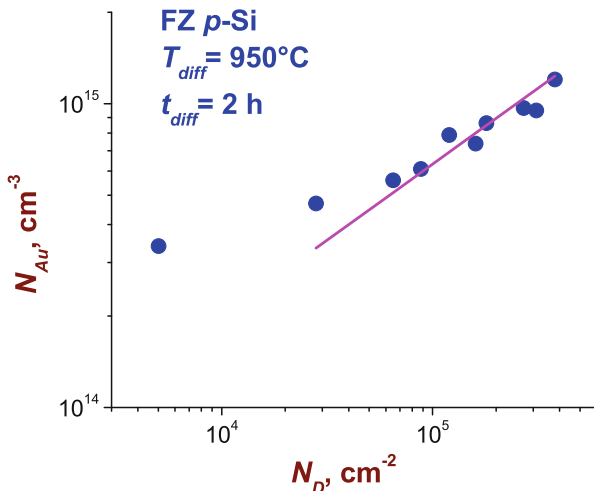
In the kick-out mechanism, impurity atoms diffuse very fast over interstitial sites; then, the substitution species of hybrid diffusers are formed by kicking out silicon atoms from the lattice sites. This mechanism does not allow the diffusion coefficient for the interstitial atoms to be measured directly because the impurity profiles are determined by the effective diffusion in a common case depending on coordinates. In this case, the interstitial atom diffusion coefficient can be only obtained by fitting the impurity profiles. In Si with relatively low defect density, the effective diffusion coefficient can be described as follows:

$$D_{\text{eff}} = (N_s^{\text{eq}} N_I^{\text{eq}} D_I) / N_s^2 \quad (3)$$

Here,  $N_s^{\text{eq}}$  is the equilibrium impurity concentration at substitutional sites;  $N_I^{\text{eq}}$  and  $D_I$  are the self-interstitial equilibrium concentration and diffusivity, respectively; and  $N_s$  is the impurity concentration at substitutional sites.

In defect-free Si, the equilibrium interstitial impurity distribution is established rather fast. Then, these interstitials kick out silicon atoms from the lattice sites and occupy these sites. To reach thermal equilibrium, the silicon self-interstitials formed

**Fig. 1** Dependence of substitutional gold concentration after diffusion at 950 °C on dislocation density



by the kick-out reaction must diffuse to the surface of the sample or any other sink for self-interstitials within the bulk of the sample (e.g., stacking faults or dislocations). The limiting factor in this mechanism is the diffusion of the silicon self-interstitials because the interstitial impurity diffusion is, in general, much faster. This leads to a well-known U-shaped profile with an increase of substitutional atom concentration near the surfaces. Indeed, because the kick-out reaction is reversible, the rate of transition to the lattice site depends on the efficiency of sinks for the self-interstitial. The surface is a rather efficient sink; therefore, the substitutional solubility value is reached at the surface much faster than in the bulk. In dislocated Si, the number of bulk sinks for self-interstitials increases with dislocation density, which leads to an increase in substitutional impurity concentration.

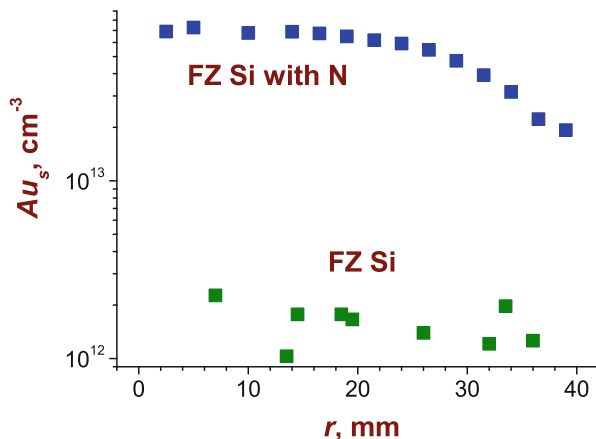
As experimentally shown by Yakimov et al. (1995), in crystals with a moderate dislocation density, the bulk substitutional concentration increases as  $N_D^{0.5}$ , where  $N_D$  is the dislocation density (Fig. 1), which well corresponds with theory predictions. However, the coefficient in this relationship was found to be a few times smaller than theoretically predicted. This was explained by the presence of obstacles on dislocations, preventing their climb, and allows a portion of dislocations to be estimated, which can climb due to absorption of self-interstitials generated by the kick-out reaction.

For highly dislocated Si, when the sink concentration is high enough for the self-interstitial equilibrium concentration to be established very fast everywhere, the effective diffusion coefficient is independent of  $N_s$  and can be expressed as follows:

$$D_{eff} = N_i^{eq} D_i / (N_i^{eq} + N_s^{eq}) \quad (4)$$

Here,  $N_i^{eq}$  and  $D_i$  are the impurity interstitial equilibrium concentration and diffusivity, respectively.

**Fig. 2**  $Au_s$  distribution in floating zone (FZ) Si with and without nitrogen after gold diffusion at 700 °C for 1 h as a function of a distance from the wafer center



Typical examples of metal impurities diffusing in Si via the interstitial-substitutional exchange mechanisms are Au, Pt, and Zn. In crystals with immobile vacancy-type defects, such impurities can be trapped by these defects and occupy the substitutional positions (dissociative diffusion mechanism). This effect can be used for the study of neutral vacancy-type defects; for example, in the case of gold, the concentration of substitutional gold  $Au_s$  can be easily measured by deep-level transient spectroscopy (DLTS). If the  $Au_i$  species is trapped by vacancy-type defects, it cannot move deeper until all traps are fulfilled. Thus, the  $Au_s$  depth profile will have the form of a step, where the height is equal to the vacancy defect concentration and the penetration depth increases with diffusion temperature and duration. This penetration depth  $x_0$  can be expressed as follows:

$$x_0 = \sqrt{D_{Au_i} \frac{Au_{isurf}}{N_t} t} \quad (5)$$

Here,  $D_{Au_i}$  is the  $Au_i$  diffusivity,  $Au_{isurf}$  is its concentration at the surface, and  $N_t$  is the trap concentration.

As an example, the results of nitrogen-vacancy complex investigations are demonstrated in Figs. 2, 3, and 4. First, it is shown that the introduction of nitrogen during the crystal growth can essentially increase the gold concentration introduced during diffusion at 700 °C. In Fig. 2,  $Au_s$  distribution measured by DLTS as a function of the radius from the wafer center is shown for FZ Si undoped and doped with nitrogen. In FZ Si doped with nitrogen, the gold concentration is approximately two orders of magnitude higher than in the undoped one, which is usually explained by the formation of nitrogen-vacancy complexes and interstitial gold trapping in these complexes. As can be seen from Figs. 3 and 4, the gold depth profile has the form of a step. The gold penetration depth increases with diffusion temperature and duration in accordance with Eq. 5. However, the  $Au_s$  concentration is independent of these parameters, which allows the determination of trap concentration. These measurements can be considered as an example of the application of a combination

**Fig. 3** Depth distribution of  $Au_s$  after diffusion at different temperatures

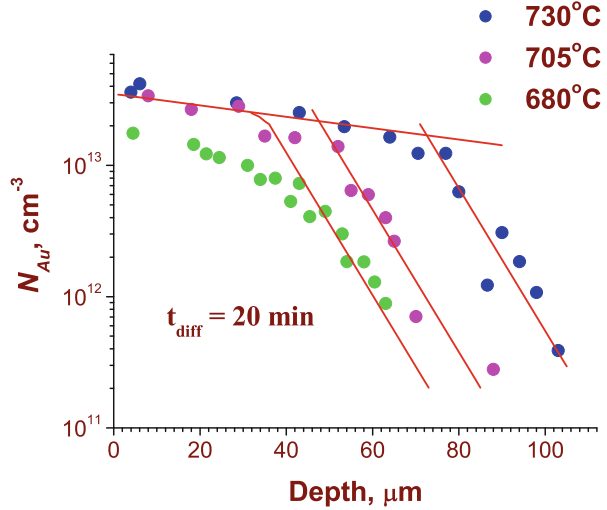
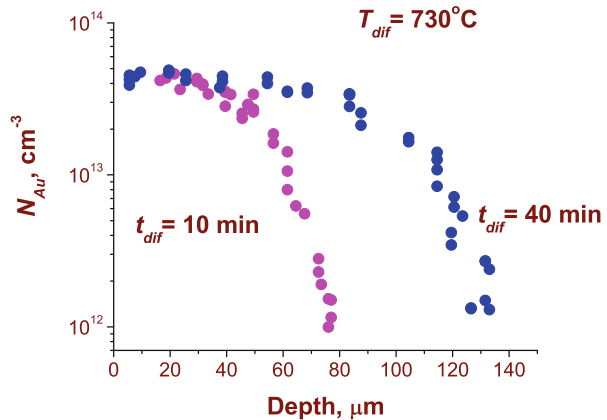


**Fig. 4** Depth distribution of  $Au_s$  after diffusion at 730 °C for 10 and 40 min



of gold diffusion and highly sensitive electrical methods, such as DLTS, to study the distribution of neutral defects.

It should be taken into account that, similar to the case of solubility, the diffusivity of metals can depend on their charge. Thus, at low temperatures, interstitially dissolved atoms may exist in a few charge states characterized potentially by different diffusion coefficients. At higher temperatures, a steady state between different charge states is established very rapidly and the diffusion can be characterized by some effective diffusion coefficient. At low temperatures, it may not be the case and can be a reason for the deviation of diffusion coefficients measured at low temperatures from those extrapolated at high-temperature measurements. Iron in Si, which exists as neutral or positively charged interstitial species, is an example of such behavior. It has different migration barriers for the interstitials in the different

charge states – that is, 0.80–0.84 eV for the neutral and 0.68–0.69 eV for the positively charged species (Heiser and Mesli 1992; Takahashi et al. 1992). A similar dependence may take place for Cu, for which the diffusion coefficients at room temperature calculated using the parameters presented in Table 2 is  $1.27 \times 10^{-9} \text{ cm}^2/\text{s}$ , whereas the experimentally obtained value is  $1 \times 10^{-7} \text{ cm}^2/\text{s}$  (Zundel et al. 1988). However, it is widely believed that all Cu interstitials are positively charged at all temperatures, therefore other reasons for the discrepancy can exist. One of the reasons for increasing the effective diffusion coefficient could be the existence of an internal electric field, which can be screened at high temperatures (Mesli et al. 1994).

Furthermore, the impurity under study may interact with other impurities or with intrinsic point defects forming mobile complexes. The diffusivity of such complexes can increase in comparison with that of the impurity itself. On the contrary, if the impurity is trapped by some defect with rather low binding energy, it cannot immobilize the impurity; however, such trapping can essentially decrease the effective diffusivity. It could be especially important in highly doped Si because many of the transition metals effectively interact with shallow donors and acceptors.

---

## Electrical Properties of Transition Metals in Si

The electrical properties of transition metals have been discussed in many studies. Data concerning the main properties have been collected, for example, in Graff (2000) and Claeys and Simoen (2018). This section briefly discusses the properties of a few metals that are important in photovoltaic technology.

### Iron

Iron is perhaps the best-studied metal impurity in Si because it is the most prominent contaminant in silicon processing and one of the most prominent metallic impurities in solar-grade Si. In addition, as seen in Fig. 12, the iron effect on the diffusion length in Si is rather strong. Substitutional iron is unstable in Si; therefore, it can be presented as interstitial atoms  $\text{Fe}_i$ , complexes with other point defects or precipitates.  $\text{Fe}_i$  is a moderately fast-diffusing metal; therefore, it can be easily quenched at interstitial sites. However, because the interstitial iron concentration after quenching is higher than the solubility limit at room temperature, this state is non-equilibrium; iron tends to turn into a lower energy state, which in p-Si is the formation of Fe pairs with acceptors, such as the formation of an FeB pair. Depending on the boron concentration, it takes from a few hours to a day in low-doped Si. In addition, Fe can form pairs with other impurities, such as with gold.

Interstitial iron has one donor level in the lower half of the silicon bandgap  $E_{\text{Fe}} = E_v + 0.39 \text{ eV}$ ; however, its activation energy determined from an Arrhenius plot is equal to 0.43 eV due to temperature dependence of capture cross-section. FeB pairs have two energy levels: a donor level at  $E_t = E_v + 0.09 \text{ eV}$  and an acceptor level

**Fig. 5** DLTS peaks corresponding to the FeB pair and  $Fe_i$  in  $p$ -Si after dissociation of FeB pairs (blue line) and subsequent storage at room temperature (magenta line)

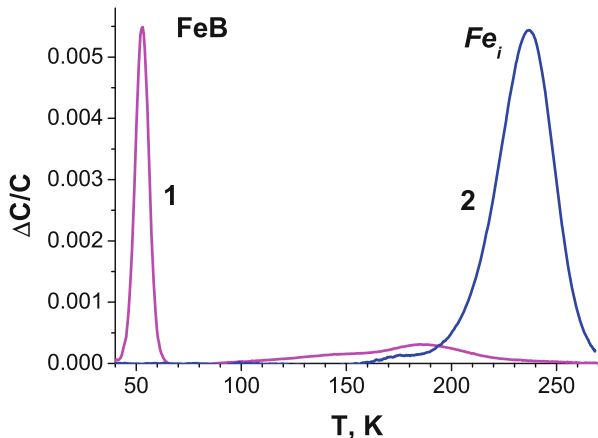
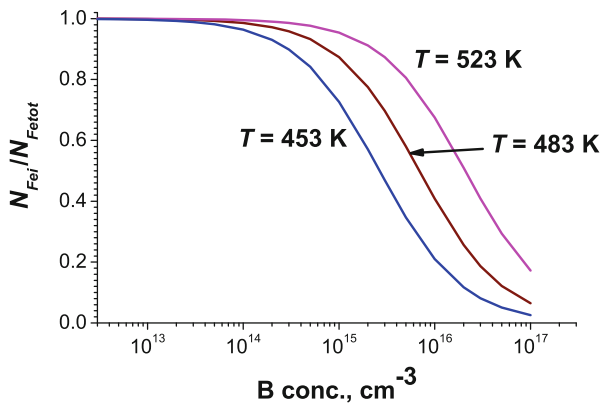


**Fig. 6** A steady portion of released  $Fe_i$  concentration calculated for three annealing temperatures as a function of boron concentration



at  $E_t = E_c - 0.29$  eV. The concentration of both defects can be measured by DLTS (Fig. 5). The binding energy of an FeB pair is rather low ( $\sim 0.6$  eV); therefore, it can be easily destroyed by intensive illumination or thermal treatment at approximately  $200^\circ C$ . The relative amount of  $Fe_i$  that can be obtained after such annealing, calculated for three temperatures, is presented in Fig. 6. After storage at room temperature, FeB pairs form again; their concentration is practically equal to that of  $Fe_i$  (see Fig. 5). This procedure is reversible and can be repeated several times because the iron precipitation rate at such temperatures is rather low. It should be also noted that the amount of  $Fe_i$  released due to annealing, as seen in Fig. 6, decreases with boron concentration and increases with annealing temperature. Therefore, in highly doped Si, this procedure needs a higher temperature that can stimulate iron precipitation, or the dependences presented in Fig. 6 should be used to correct the Fe concentration values.

As mentioned previously, the concentration of iron in  $Fe_i$  and FeB states can be measured by DLTS. However, for the nondestructive estimation of iron



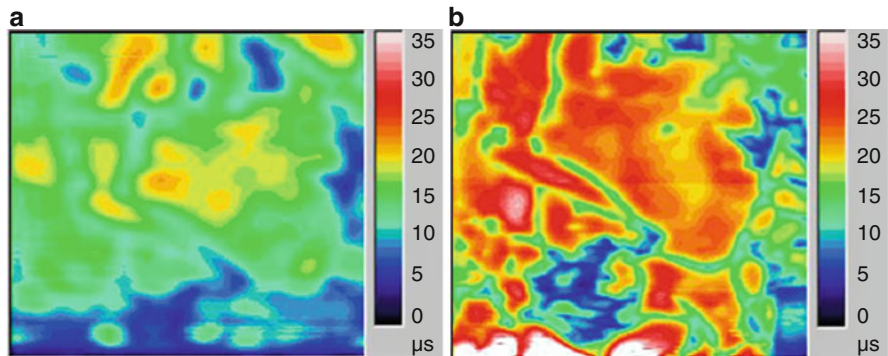


**Fig. 7** Lifetime maps obtained by microwave photoconductivity on mc-Si (a) after annealing at 210 °C for 10 min and quenching and (b) after storage at room temperature. Image size is  $1 \times 1 \text{ cm}^2$

concentration or for iron distribution mapping, a procedure based on the reversible formation and destruction of FeB pairs and measurements of lifetime  $\tau$  or diffusion length  $L = (D\tau)^{0.5}$ , where  $D$  is the excess carrier diffusivity, is widely used. At a low excitation level, the FeB effect on the excess carrier lifetime is smaller than that of  $Fe_i$ . A comparison of  $\tau$  or  $L$  values, measured when FeB pairs are formed and when they are totally destroyed, allows one to determine the concentration of non-precipitated Fe. It can be calculated as follows:

$$[Fe] = K \left( \frac{1}{\tau_{Fei}} - \frac{1}{\tau_{FeB}} \right) \quad (6)$$

For a low excitation level  $\Delta p/p \ll 1$  and a boron concentration of  $10^{15} \text{ cm}^{-3}$ ,  $K = 2 \times 10^6 \text{ cm}^{-3}/\text{s}$ . If lifetime distribution is mapped by microwave photoconductivity or photoluminescence method, the Fe lateral distribution over the wafer can be obtained using this expression. An example of such measurements is presented in Fig. 7. It should be mentioned that the calculated concentration of electrically active Fe in this sample does not exceed  $10^{11} \text{ cm}^{-3}$ .

Lifetime  $\tau$  in Si at room temperature is mainly determined by defect-assisted recombination, described by the Shockley-Read-Hall expression (Shockley and Read 1952; Hall 1952):

$$\tau = \frac{c_n(n_0 + \Delta n + n_1) + c_p(p_0 + \Delta p + p_1)}{(p_0 + \Delta p + n_0)c_n c_p N_t}, \quad (7)$$

Here,  $p_0$  and  $n_0$  are the equilibrium hole and electron concentrations;  $c_n = v_e \sigma_e$  and  $c_p = v_p \sigma_p$  are the electron and hole capture coefficients, index  $e$  or  $p$  pertains to electrons and holes, respectively;  $v_e$  and  $v_p$  are the electron and hole thermal velocities;  $\sigma_e$  and  $\sigma_p$  are the electron and hole capture cross-sections;  $\Delta n$  and  $\Delta p$  are the excess carrier concentrations (usually  $\Delta n = \Delta p$  can be assumed); and  $n_1$  and  $p_1$  are equal to the equilibrium electron and hole concentrations when the Fermi level

coincides with the defect level. If the defect has two or more energy levels inside the bandgap, the expression for lifetime is more complex. For two-level defects, it was derived by Choo (1970). In this case the impurity has three charge states  $N^{s-1}$ ,  $N^s$ , and  $N^{s+1}$ . The condition  $N = N^{s-1} + N^s + N^{s+1}$ , where  $N$  is the total impurity concentration, should be fulfilled and lifetime can be calculated as follows:

$$\begin{aligned} 1/\tau &= \frac{N_{s-1} + N_s}{\tau_1} + \frac{N_{s+1} + N_s}{\tau_2} \\ \frac{1}{\tau_1} &= [p_0 + \Delta p + n_0]c_{n1}c_{p1} / [c_{n1}(n_0 + \Delta n + n_1) + c_{p1}(p_0 + \Delta p + p_1)] \quad (8) \\ \frac{1}{\tau_2} &= [p_0 + \Delta p + n_0]c_{n2}c_{p2} / [c_{n2}(n_0 + \Delta n + n_2) + c_{p2}(p_0 + \Delta p + p_2)], \end{aligned}$$

Here,  $c_{ni}$ ,  $c_{pi}$ ,  $n_i$  and  $p_i$  have the same sense as in Eq. 7 for  $i = 1$  and  $2$  ( $1$  and  $2$  correspond to the first and second energy levels, respectively). For the low excitation conditions values of  $N^{s-1}$ ,  $N^s$  and  $N^{s+1}$  are mainly determined by the Fermi level position and can be easily calculated. If the excitation level is not low enough, they should be calculated using  $\Delta n$  and the electron and hole capture coefficients for both levels.

As follows from Eqs. 7 and 8,  $\tau$  depends on excitation level via  $\Delta p/p_0$ ; therefore, in a common case,  $K$  in Eq. 6 depends on both boron concentration and excitation level. The calculated dependences of lifetime on the excitation level using the capture coefficients and energy levels for  $Fe_i$  and FeB presented in Table 3 are shown in Fig. 8. In mc-Si, the boron concentration is usually about  $10^{16} \text{ cm}^{-3}$  or even higher. At such boron concentrations for a low excitation level,  $K$  rises but only by 4%. With an increase of illumination intensity and/or increase of boron concentration, the  $K$  value increases. It is seen that it can even change a sign, and the  $\Delta p$  value corresponding to the sign inversion point depends on the boron concentration. At an excitation level close to the inversion point, the Fe concentration calculated using Eq. 6 can be strongly underestimated. This is necessary to consider, especially when lifetime mapping is carried out; to obtain the appropriated lateral resolution, it is necessary to increase the local excitation level, which usually does not allow the low excitation conditions to be reached.

During cooling from high temperatures, iron precipitates preferentially via a heterogeneous nucleation mechanism; therefore, lattice defects or other impurity precipitates are needed as nuclei for the precipitation. Usually, the iron precipitates have a form of rod-like inclusions of the  $\alpha$ -FeSi<sub>2</sub> or of  $\beta$ -FeSi<sub>2</sub> phase. With high enough diffusivity, iron can precipitate even at rather low temperatures. As an example, the

**Table 3** The capture coefficients for  $Fe_i$  and FeB obtained from the lifetime dependences on excitation level (Palais et al. 2002)

	Energy level, eV	$c_p, 10^{-7} \text{ cm}^3/\text{s}$	$c_n, 10^{-7} \text{ cm}^3/\text{s}$
$Fe_i$	$E_v + 0.39$	0.15	5.5
FeB	$E_v + 0.09$	4.4	7
FeB	$E_c - 0.29$	25	0.6

**Fig. 8** Calculated lifetime dependence of the excitation level for FeB pairs and  $Fe_i$  for the samples with different dopant concentrations. Fe concentration is  $1 \times 10^{12} \text{ cm}^{-3}$

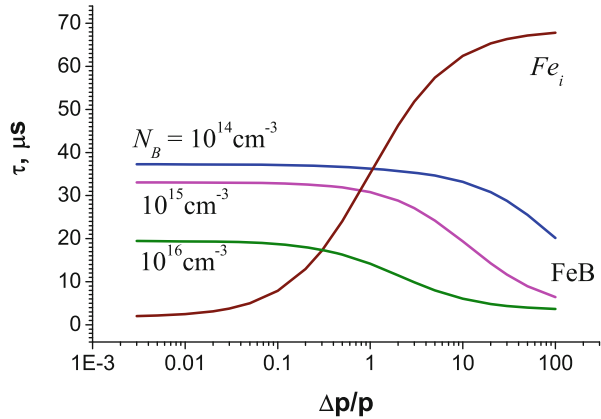
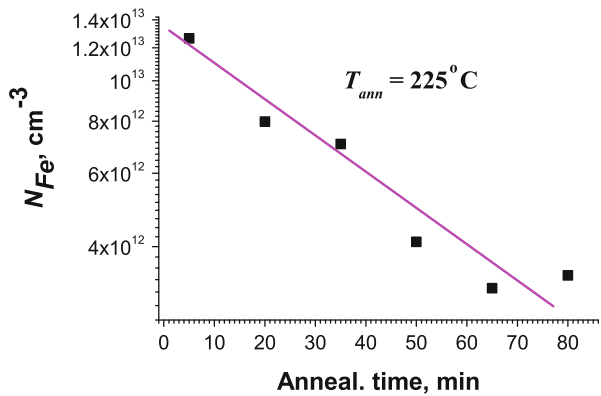


**Fig. 9** Decrease of  $Fe_i$  concentration during annealing by  $225^\circ\text{C}$



dependence of  $Fe_i$  concentration measured by DLTS after annealing at  $225^\circ\text{C}$  as a function of annealing duration is shown in Fig. 9. This dependence shows that iron precipitates even at this temperature and allows the estimation of precipitation rate. Electron paramagnetic resonance (EPR) studies have shown that clustering of Fe starts with the formation of small particles containing two or four Fe atoms, which then dissociate to form larger clusters or precipitates. DLTS investigations showed that Fe precipitates introduced energy levels in the gap, which are usually ascribed to the interface states between the silicide and the silicon matrix. However, the effect of precipitates on the excess carrier lifetime is weaker than that of  $Fe_i$ .

## Nickel

Besides iron, nickel is one of the main impurities in Si-based device production. At elevated temperatures, nickel forms a sequence of silicides, showing increasing silicon content with increasing formation temperatures. The high-temperature Ni

silicide modification  $\text{NiSi}_2$  has cubic lattice symmetry with almost-equal lattice parameters to silicon, which promotes the epitaxial growth of  $\text{NiSi}_2$  precipitates via a homogeneous nucleation. Nickel diffuses mainly via interstitial sites; however, interstitial Ni is neutral and does not affect the electrical properties. Only substitutional nickel or its complexes with other defects can be detected by electrical methods. DLTS measurements reveal three main energy levels in silicon intentionally contaminated with Ni at  $E_c - 0.07$  eV,  $E_c - 0.45$  eV, and  $E_v + 0.16$  eV, which are usually assigned to the double-acceptor, single-acceptor, and single-donor states of substitutional nickel, respectively. However, as argued by Scheffler et al. (2014a), some of them can belong to other Ni-related defects. It should be noted that such energy levels allow substitutional nickel to compensate the shallow dopants in both n- and p-Si. In addition, some other Ni-related defects were observed in Si. For example, as shown by Yarykin and Weber (2016), a center with the energy level at  $E_c - 0.37$  eV can be introduced as a result of nickel interaction with radiation-induced vacancy-oxygen centers.

At room temperature, it can be expected that interstitial nickel is not present in Si wafers in a steady state due to very high diffusivity, which allows its fast outdiffusion to the surfaces, precipitation, or reaction with other defects. As a rule, a portion of electrically active Ni-based defects is rather low; thus, in spite of high substitutional nickel recombination activity, it can be expected that nickel-related defects do not essentially affect the solar cell performance. However, it seems that  $\text{NiSi}_2$  precipitates demonstrate rather high electrical activity, as can be revealed by DLTS and electron beam-induced current (EBIC) methods. As shown by Kittler et al. (1991) in Si with high density of  $\text{NiSi}_2$  precipitates ( $N_{prec}$ ), the effective diffusion length can be described as  $L_{eff} = 0.7 \times N_{prec}^{-1/3}$ . Therefore, as will be shown in next section, in mc-Si for solar cells,  $N_{prec}$  should not exceed  $10^5$ – $10^6$   $\text{cm}^{-3}$ .

## Copper

The third main impurity in Si device production besides iron and nickel is copper. Copper can be found in high concentrations in wafers after processing and on surfaces and can be considered as the most common contaminant of Si. Due to its electronegativity, copper is easily replated on clean wafer surfaces during any wet chemical process such as cleaning, etching, polishing, etc. Similar to nickel, copper exhibits high interstitial solubility and diffusivity, which have the highest values of all transition metals. Thus, although interstitial copper can be revealed by the transient ion drift technique in high enough concentrations up to  $10^{15}$   $\text{cm}^{-3}$  after high-temperature diffusion and subsequent quenching, such a concentration cannot be preserved for a long time. In addition, interstitial copper is always positively charged, implying a shallow donor level in the upper half of the bandgap; therefore it can be expected that, as in the case of other shallow-level defects, its effect on the excess carrier recombination rate is negligible.

If copper is introduced during growth or high-temperature diffusion, it occupies substitutional sites, and this state is rather stable. DLTS measurements reveal three

main energy levels ascribing to the substitutional copper in silicon at  $E_c - 0.17$  eV,  $E_v + 0.430$  eV, and  $E_v + 0.225$  eV, which were usually assigned to the double-acceptor, single-acceptor and single-donor states. In addition, copper can form complexes with other impurities and/or intrinsic point defects. One of them is the well-known copper-related center, which has a donor level at  $E_v + 0.1$  eV and produces intense zero-phonon emission at 1.014 eV. High-resolution photoluminescence studies on isotopically pure Si showed that this defect includes four copper atoms. The first-principles calculations proposed that the complex is composed of a substitutional copper core surrounded by three interstitial Cu interstitial.

Usually, only a fraction of approximately 0.1% of total copper atoms forms electrically active point defects and complexes, giving rise to deep levels in the bandgap. Thus, despite the rather high copper concentration usually presented in mc-Si, it can be expected that the effect of Cu or Cu-related point defects on the recombination lifetime is not so detrimental. The harmful copper effect could arise mainly from the electrically active precipitates and complexes with other crystal imperfections, which can be easily formed due to high interstitial copper diffusivity. The stable copper silicide consists of a metal-rich silicide  $\text{Cu}_3\text{Si}$ , which does not fit the lattice parameter of the silicon. Its lattice parameter is larger than that of Si, which means that compressive stress is built up during precipitation; this can be relaxed by the emission of one interstitial for every two precipitated Cu atoms. This leads to a high barrier for the homogeneous nucleation of Cu precipitates, favoring the heterogeneous nucleation of large precipitate colonies near extended defects. In addition, shear stress near copper precipitates leads to a generation of new dislocations, which in turn can promote the formation of new precipitates. It could be a mechanism of formation of dislocation-precipitate colonies, which are often observed by the transmission electron microscopy in copper-contaminated Si samples. The formation of such colonies could be a reason for a strong copper effect on the extended defect recombination properties. Similar to iron and nickel, Cu precipitates introduced energy levels in the gap demonstrating characteristic features of interface states.

## Chromium

Chromium is an impurity that is frequently detected in mc-Si. It is one of the most abundant and also most detrimental defects in silicon. Chromium is an essential constituent of most of the preferential-etch solutions for revealing crystal defects in samples after processing. Although replating of chromium on Si is not expected because of the rather low electronegativity, an adsorption of chromium on the Si surface sometimes is detected. Chromium has intermediate diffusivity and can occupy both interstitial and substitutional positions in the Si lattice. Chromium can easily form chromium oxides in an atmosphere containing oxygen, which can avoid its diffusion into Si.

After diffusion and fast cooling the sample to room temperature, chromium remains dissolved on interstitial sites, forming metastable electrically active

defects with a donor level at  $E_c - 0.23$  eV. Interstitial chromium forms donor-acceptor pairs with shallow acceptors. In boron-doped silicon with a high dopant concentration, almost all electrical active chromium forms CrB pairs. The CrB pair has a donor level at  $E_v + 0.28$  eV. Under illumination with sufficient energy, these pairs can be dissociated in  $Cr_i$  and B; however, this process is reversible, and after some time all CrB pairs are associated again. As in the case of iron, a dissociation of CrB pairs and lifetime measurements with chromium in the interstitial and CrB pair states can be used for Cr identification in Si. As shown in Fig. 12,  $Cr_i$  and CrB pairs strongly affect the excess carrier lifetime in Si. Chromium precipitation can start during annealing at temperatures as low as 170 °C, but  $CrSi_2$  precipitates exhibit a strongly reduced recombination activity compared to  $Cr_i$ .

## Cobalt

Cobalt is frequently detected in mc-Si, although its concentration is much lower than that of Fe, Ni, or Cu. It is the lightest of the fast-diffusing transition metals and exhibits a medium solubility. Due to high diffusivity, interstitial cobalt is not expected at room temperature. In accordance with one study (Kolkovsky et al. 2014), substitutional Co has an acceptor level at  $E_c - 0.39$  eV. An acceptor level at  $E_v + 0.46$  eV was ascribed to the  $Co_iB_s$  pair. No energy levels were obtained for interstitial Co. Theoretical calculations have confirmed that all centers containing one cobalt atom have only one acceptor level and no donor level. Interstitial Co atoms can react with substitutional ones to form electrically inactive pairs. Similar to Ni, cobalt forms silicides, which exhibit a decreasing metal content with increasing temperatures. The high-temperature modification is  $CoSi_2$ . It was shown that the precipitates have a form of small platelets, which consist of monocrystalline  $CoSi_2$ , epitaxially grown parallel to the silicon {111} planes in a twin configuration.

## Titanium

Titanium concentrations in state-of-the-art mc-Si are too low to essentially affect the electrical properties. However, in mc-Si ingot grown from refined metallurgical silicon, titanium concentrations were found to exceed  $10^{15}$  cm<sup>-3</sup> (Peshcherova et al. 2015). Interstitial titanium is electrically active. Two deep energy levels were ascribed to titanium on the interstitial position: the single-donor state at  $E_c - 0.09$  eV and the double-donor state  $E_v + 0.25$  eV. The energy level at  $E_c - 0.28$  eV was ascribed to the single acceptor state of substitutional titanium. Ti is a rather strong recombination center, especially in *p*-type Si. Its diffusivity is rather low; therefore, its precipitation requires a long annealing duration. Titanium precipitates mainly via a heterogeneous nucleation mechanism. Therefore, some nuclei, such as extended defects, are required for precipitation.

**Table 4** Energy levels of Au pairs with some transition metals

	AuFe	AuNi	AuCu	AuCr	AuMn	AuV
$E_v$ , eV	$E_v + 0.43$ (d)	$E_v + 0.35$	$E_v + 0.32$	$E_v + 0.35$ (d)	$E_v + 0.57$ (d)	$E_v + 0.42$ (d)
	$E_c - 0.35$ (a)	$E_v + 0.48$	$E_v + 0.42$		$E_c - 0.24$ (a)	$E_c - 0.20$ (a)

## Gold

In state-of-the-art mc-Si, gold concentrations are usually much lower than those of iron, copper, and nickel. However, gold is well known to replate on uncoated wafers in every solution containing trace contaminations of gold because of its high electronegativity compared to that of silicon, which could be a source of contamination. It should be also taken into account that, contrary to nickel and copper, practically all gold atoms in Si predominantly occupy the substitutional sites, where they are electrically active and can strongly affect the excess carrier recombination rate. Gold is one of the most investigated metal impurities in silicon. It can very quickly diffuse into Si on interstitial sites, even at rather low temperatures ( $\geq 600$  °C). However, the solubility of interstitial gold is low, usually a few orders of magnitude lower than that for substitutional gold. Therefore, the gold concentration at interstitial positions rather quickly reach the steady value; then, the overall gold concentration increases via occupation of the substitutional sites by kicking out silicon atoms. Thus, it demonstrates the kick-out diffusion mechanism, which was previously discussed in more detail.

Substitutional gold is a stable state because its diffusivity is negligible. Moving it into a mobile interstitial state requires self-interstitials. On the substitutional lattice site, it has two deep energy levels: an acceptor state in the upper half of bandgap at  $E_c - 0.56$  eV and a donor state in the lower half at  $E_v + 0.34$  eV. In addition, gold can form electrically active complexes with different metals such as Cr, Mn, Fe, Ni, Cu, and V. The energy levels ascribed to these pairs are listed in Table 4. These pairs can be of technological importance because they form strong recombination centers, and their effect on excess carrier lifetime can even exceed that of substitutional gold.

## Silver

Silver is not a common contaminant in Si. However, it is widely used as a contact in solar cell production. Moreover, these contacts are usually fired at high enough temperatures exceeding 600 °C; therefore, contamination with silver cannot be totally excluded. Silver can contaminate Si by replating from chemical solutions that contain silver as an impurity. In addition, Ag can penetrate easily through passivating oxide layers on devices under operating conditions, which can result in a degradation of the solar cell parameters. Silver does not form stable silicides at elevated temperatures, but it has a eutectic point at 840 °C. It diffuses rather quickly via interstitial mechanisms; however, contrary to gold, it needs defect assistance to occupy the substitutional sites—that is, it diffuses via the dissociative mechanism.

After implantation, only approximately 30% of the Ag is in the substitutional position; that increases to 80% after a 200–300 °C anneal step. Substitutional silver

has two deep levels: an acceptor at  $E_c - 0.55$  eV and a donor level at  $E_v + 0.37$  eV. If samples were slowly cooled after growth, an energy level at  $E_c - 0.3$  eV would be revealed by the DLTS, which can be ascribed to a pair of substitutional-interstitial silver.

## Zinc

Zinc is frequently found in mc-Si (Peshcherova et al. 2015; Stokkan et al. 2017); therefore, its properties in Si should be also discussed. Zn is one of the impurities it also diffuses in Si via a kick-out mechanism. Therefore, its effective diffusion coefficient is concentration dependent. However, zinc diffusivity is lower than that of gold and platinum at all temperatures. Usually, zinc is not considered to be a detrimental impurity in device fabrication because it easily evaporates from the surface during thermal treatment.

Substitutional zinc has two energy levels in the bandgap: a double acceptor at  $E_c - 0.53$  eV and an acceptor at  $E_v + 0.32$  eV. Due to the acceptor nature of substitutional Zn, it can react with other transition metals, such as Cr and Fe, to form electrically active acceptor-donor pairs.

## Manganese

Manganese, like titanium, has only been found in significant concentrations in mc-Si ingot grown from refined metallurgical silicon. At room temperature, Mn can exist both in interstitial  $Mn_i$  and substitutional  $Mn_s$  sites. It is generally accepted that  $Mn_i$  has four charge states ( $Mn^-$ ,  $Mn^0$ ,  $Mn^+$  and  $Mn^{++}$ ), resulting in three energy levels: an acceptor level at  $E_c - 0.12$  eV, a single-donor level at  $E_c - 0.43$  eV and a double-donor level at  $E_v + 0.27$  eV. Two energy levels are ascribed to substitutional  $Mn_s$ : a donor level at  $E_v + 0.34$  eV and an acceptor level at  $E_c - 0.43$  eV. Like iron and chromium, interstitial manganese forms various pairs with shallow acceptors and other metals, such as Zn, Sn, and Au. For example, an MnB pair is a donor with an energy level at  $E_c - 0.55$  eV. The interstitial Mn can cluster to form an  $Mn_4$  complex with a donor level at  $E_c - 0.28$  eV.

Like most of the other transition metals, manganese forms silicides at elevated temperatures; the high-temperature modification is  $MnSi_2$ . Rather little is known about the precipitation behavior of manganese. In particular, it is not exactly known yet whether the  $Mn_4$  complex is a first step for a homogeneous nucleation.

---

## Effect of Metals on Solar Cell Efficiency

The efficiency of solar cells is determined by the maximum power  $P_{\max} = V_m \times I_m = FF \times V_{oc} \times I_{sc}$ , where  $V_m$  and  $I_m$  are the voltage and current values corresponding to the maximum power, respectively;  $I_{sc}$  and  $V_{oc}$  are the short-



circuit current and open circuit voltage, respectively; and  $FF$  is the filling factor.  $V_{oc}$  can be calculated as follows:

$$V_{oc} = nkT [\ln(I_{ph}/I_0) + 1] \quad (9)$$

Here,  $n$  is the ideality factor,  $I_0$  is the saturation current, and  $I_{ph}$  is the photocurrent.

As follows from Eq. 9, the open-circuit voltage depends logarithmically on the relationship between the photocurrent and the leakage current. Therefore, it can be believed that its dependence on impurity content is not too strong due to rather high illumination intensity under sun exposure. The main effect of metals on the  $V_{oc}$  values can be determined by shunt formation. These shunts can locally reduce the built-in potential barrier of a p–n junction, forming conducting paths. In this case, the leakage current can exceed the theoretical value by many orders of magnitude. This effect is practically impossible to simulate; however, it should be noted that even cells containing shunts and demonstrating large dark reverse currents exceeding  $10 \mu\text{A}/\text{cm}^2$  often have open-circuit voltage values exceeding 500–600 mV. This can be explained by the assumption that illumination decreases potential barriers and thus suppresses the shunt effect.

$FF$  depends on both  $I_{sc}$  and  $V_{oc}$ . However, it can be shown that it is mainly determined by the  $V_{oc}$  value. Indeed, from a condition at maximum power  $d(I_m \times V_m) = 0$ , it follows that

$$\frac{dI_m}{dV_m} = -\frac{I_m}{V_m} \quad (10)$$

Taking into account that

$$I_m = I_0 \left[ \exp\left(\frac{eV_m}{nkT}\right) - 1 \right] - I_{ph} \approx I_0 \left[ \exp\left(\frac{eV_m}{nkT}\right) - 1 \right] - I_{sc} \quad (11)$$

the following can be obtained:

$$\begin{aligned} \frac{dI_m}{dV_m} &= I_0 \frac{e}{nkT} \exp\left(\frac{eV_m}{nkT}\right) = -\frac{I_m}{V_m} \\ V_m &= -\frac{I_m}{I_0 \frac{e}{nkT} \exp\left(\frac{eV_m}{nkT}\right)} \\ &= -\frac{nkT \left[ \exp\left(\frac{eV_m}{nkT}\right) - \exp\left(\frac{eV_{oc}}{nkT}\right) \right]}{e \exp\left(\frac{eV_m}{nkT}\right)} = \frac{nkT}{e} \left\{ \exp\left[\frac{e(V_{oc} - V_m)}{nkT}\right] - 1 \right\} \end{aligned} \quad (12)$$

Thus,

$$V_m = V_{oc} - \frac{nkT}{e} \ln \left( 1 + \frac{eV_m}{nkT} \right) \approx V_{oc} - \frac{nkT}{e} \ln \left( 1 + \frac{eV_{oc}}{nkT} \right) \quad (13)$$

and

$$\begin{aligned} \frac{I_m}{I_{sc}} &= \frac{\left[ \exp \left( \frac{eV_m}{nkT} \right) - 1 \right] - \left[ \exp \left( \frac{eV_{oc}}{nkT} \right) - 1 \right]}{\left[ \exp \left( \frac{eV_{oc}}{nkT} \right) - 1 \right]} = \frac{-\frac{eV_{oc}}{nkT} \exp \left( \frac{eV_{oc}}{nkT} \right)}{\left[ \exp \left( \frac{eV_{oc}}{nkT} \right) - 1 \right] \left( 1 + \frac{eV_{oc}}{nkT} \right)} \\ &\approx \frac{-\frac{eV_{oc}}{nkT}}{\left( 1 + \frac{eV_{oc}}{nkT} \right)} \\ FF &= -\frac{V_m I_m}{V_{oc} I_{sc}} \approx \frac{\frac{e}{nkT} V_{oc} - \ln \left( 1 + \frac{eV_{oc}}{nkT} \right)}{\left( 1 + \frac{eV_{oc}}{nkT} \right)} \end{aligned} \quad (14)$$

Thus, all factors decreasing  $V_{oc}$  lead also to  $FF$  decrease.

For the production of highly efficient solar cells, the effect of defects on the open-circuit voltage and the filling factor should therefore be taken into account. However, the main influence of metal impurities on solar cell performance is caused by their effect on the collection efficiency – that is, on the portion of excess carriers that reach the depletion region of p–n junction and give rise to the photocurrent. The short-circuit current simply equals the collection efficiency multiplied by a number of light-induced excess carriers. In turn, the collection efficiency can be calculated as a convolution of generation function, which is proportional to  $\exp(-\alpha z)$  where  $\alpha$  is the Si absorption coefficient depending on wavelength; and the collection probability  $\psi(z, W, L)$ , which can be obtained as a solution of homogeneous diffusion equation (Donolato 1985). In one-dimensional case,  $\psi(z, W, L)$  can be described as follows:

$$\psi(z, W, L) = \frac{\exp(-z/L) + \frac{LS}{D} - 1}{\frac{LS}{D} + 1} \frac{\exp((z - 2d)/L)}{\exp(-W/L) + \frac{LS}{D} - 1} \frac{1}{\frac{LS}{D} + 1}, \quad (15)$$

Here,  $W$  is the p–n junction depletion region,  $d$  is the cell thickness, and  $S$  is the backside surface recombination velocity. If  $S$  can be neglected, Eq. 15 can be simplified as follows:

$$\psi(z, W, L) = \frac{\exp(-z/L) + \exp((z - 2d)/L)}{\exp(-W/L) + \exp((W - 2d)/L)} \quad (16a)$$

On the contrary, for very high  $S$  that can take place at the backside contact,  $\psi(z, W, L)$  can be described as follows:

$$\psi(z, W, L) = \frac{\exp(-z/L) - \exp((z - 2d)/L)}{\exp(-W/L) - \exp((W - 2d)/L)} \quad (16b)$$

For simplicity, let us assume that a 200- $\mu\text{m}$ -thick cell consists of  $p$ -Si with 1- $\mu\text{m}$ -thick  $n^+$ -Si top layer,  $S = 0$  and only half of the carriers generated in the top  $n^+$ -layer are collected by the p–n junction. The normalized collection efficiency as a function of  $L$  calculated under such assumptions for illumination with different wavelengths is shown in Fig. 10. It can be seen that for a diffusion length larger than 100  $\mu\text{m}$ , the collection efficiency is practically saturated; therefore, the diffusion length in highly efficient solar cells should be larger than 100  $\mu\text{m}$  or the lifetime should be larger than 3  $\mu\text{s}$ . Of course, with a further diffusion length increase, the collection efficiency will also increase; however, as seen in Fig. 10, for  $L > 100 \mu\text{m}$ , this increase is not as essential as at smaller  $L$  values. As can be seen in Fig. 7, in typical mc-Si wafers,  $\tau$  varies in the range from a few to 50  $\mu\text{s}$ , which corresponds to a diffusion length range from 100 to approximately 400  $\mu\text{m}$ . In solar cells, it can be even larger due to recombination center gettering in the technology process. As seen in Fig. 11, in 280- $\mu\text{m}$ -thick solar cells, backside contact strips can be revealed by the light beam induced method (LBIC) as a dark region. Our estimations show that the visible LBIC contrast of these strips can be seen only at diffusion length values exceeding 200–250  $\mu\text{m}$ .

**Fig. 10** The normalized collection efficiency as a function of  $L$  calculated for different wavelength values shown in nm

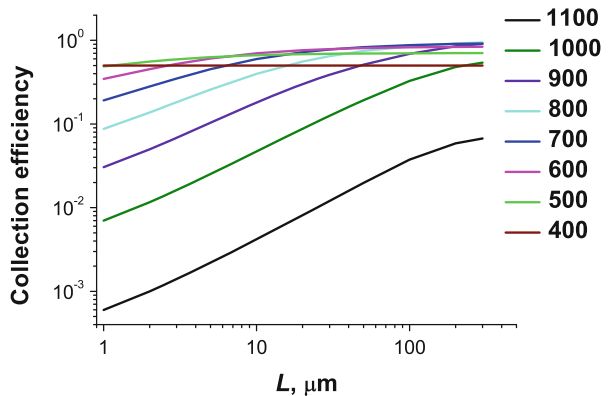
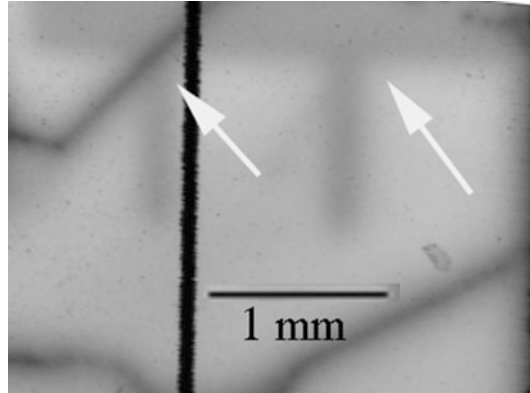


**Fig. 11** LBIC image of a fragment of an mc-Si solar cell obtained with wavelength of 980 nm. Dark backside contact strips are shown by white arrows

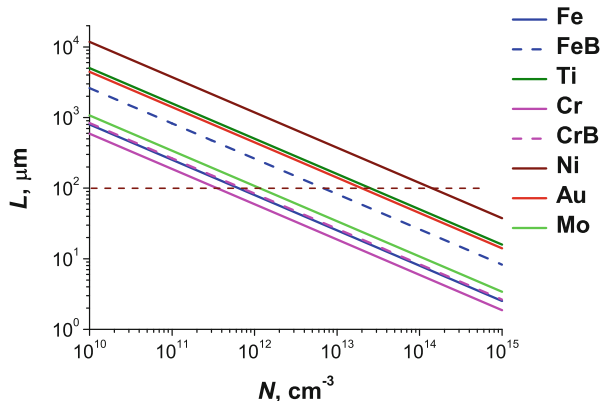


The diffusion length is mainly determined by the lifetime because a dependence of excess carrier diffusivity on impurity content is rather weak. As follows from Eqs. 7 and 8, the lifetime depends on the excitation level, mainly via  $\Delta n$ . Solar cells based on crystalline silicon can deliver a maximum possible current density of  $46 \text{ mA/cm}^2$  under an AM1.5 spectrum. This gives for the excess carrier generation rate  $G$  a value of  $2.9 \times 10^{17} \text{ cm}^{-3}/\text{s}$ . If  $\tau = 3 \text{ }\mu\text{s}$  is assumed  $\Delta n \sim 8.7 \times 10^{11} \text{ cm}^{-3}$ . Even if  $\tau$  increases up to 1 ms, the condition  $\Delta n \ll p_0$  is fulfilled in most cases for mc-Si and the low excitation conditions are realized. However, for solar cells based on monocrystalline Si, this may be not the case due to the higher lifetimes and lower dopant concentration values.

Shallow donors in  $n$ -type semiconductors are positively charged and shallow acceptors in  $p$ -type semiconductors are negatively charged. Therefore, they should repel minority carriers, which strongly decreases the effective capture cross-section. For this reason, defects with shallow levels can affect the carrier concentration and mobility, but their effect on the excess carrier lifetime usually can be neglected. Thus, only the effects of defects with deep energy levels would be considered. To calculate  $\tau$  dependence on the concentration of such defects, the corresponding energy level and capture coefficients should be known. For transition metals, they can be found in the literature (e.g., Graff 2000; Claeys and Simoen 2018). The diffusion length dependences on metal concentrations calculated for some metal impurities in  $p$ -type Si are shown in Fig. 12. Such dependences allow one to estimate the limiting concentrations for any particular impurity to achieve a high performance of solar cells.

It should be stressed that the data presented in Fig. 12 were calculated for the concentrations of electrically active species, which can be much lower than the overall impurity concentration. As seen in Fig. 12, the largest effect on the diffusion length and thus on the solar cell efficiency among the discussed metals is demonstrated by Cr and Fe. To achieve  $L \geq 100 \text{ }\mu\text{m}$ , their concentration in the electrically active state should be lower than  $10^{12} \text{ cm}^{-3}$ ; as mentioned previously, the overall concentration can exceed  $10^{14} \text{ cm}^{-3}$  in state-of-the-art mc-Si. However, for many

**Fig. 12** Dependences of diffusion length in Si on metal concentrations calculated for some metal impurities. A dashed line marks a diffusion length of  $100\ \mu\text{m}$



transition metals, the largest portion of total impurity concentration in mc-Si is precipitated; therefore, usually only a small portion of metal impurities are in an electrically active state, and their overall effect on the diffusion length is smaller than that demonstrated in Fig. 12.

The effect of transition metals on the efficiency of Si-based solar cells has been studied in many works. The simulations of metal effects on the efficiency of state-of-the-art solar cells based on Cz mono-Si had shown that Cr, Co, and Fe can reduce the cell efficiency, even at concentrations as low as  $10^{10}\ \text{cm}^{-3}$  (Schmidt et al. 2013). However, this was the concentration of electrically active species, not the total impurity concentration. A few investigations dealt with measurements of efficiency of solar cells produced from intentionally contaminated wafers (see, e.g., Reis et al. 2009; Coletti et al. 2011). In Reis et al. (2009), mc-Si blocks were intentionally contaminated with iron and copper. Iron concentration was measured of about  $10^{14}\ \text{cm}^{-3}$  in the middle and up to  $10^{17}$ – $10^{18}\ \text{cm}^{-3}$  in the top of blocks. The copper concentration was up to  $10^{15}\ \text{cm}^{-3}$  in the middle and up to  $10^{17}$ – $10^{18}\ \text{cm}^{-3}$  in the top of blocks. In the cells produced on wafers from the middle of blocks,  $V_{oc}$  values practically did not change in comparison with noncontaminated cells for both elements; in the cells produced on wafers from the top of blocks, the values decreased to approximately 5% and 11% for copper and iron contamination, respectively. The efficiency in the middle part basically did not change for copper and decreased from 16% to 15% for iron. On the top wafers, the efficiency decreased to 10–11% for both impurities.

The impact of intentionally introduced iron, chromium, nickel, titanium, and copper on the performance of mc-Si-based solar cells made by a 2008 state-of-the-art industrial process including P-diffusion, Al-back surface field formation, and  $\text{SiN}_x\text{:H}$  firing was studied by Coletti et al. (2011). The added impurity concentration was varied up to  $5 \times 10^{18}$ ,  $5.5 \times 10^{18}$ ,  $5 \times 10^{18}$ ,  $2.7 \times 10^{17}$ , and  $2.1 \times 10^{18}$  for iron, chromium, nickel, titanium, and copper, respectively. It was found that the efficiency of solar cells made on wafers from the middle of the ingot decreased from 16% to 14.5%, 14%, and 13% for the highest concentrations of Fe, Cr, and Ti, respectively. For nickel and copper, the efficiency in the middle of the ingot did not notably change.

However, for all impurities, the efficiency decreased in the bottom and top parts of the ingot. As a result, the limiting concentrations of impurities in the molten silicon charge that resulted in a  $I_{sc}V_{oc}$  product with approximately 2% relative degradation with respect to the uncontaminated ingot up to 90% of the ingot height was estimated. These concentrations were  $2.7 \times 10^{17}$ ,  $2.1 \times 10^{17}$ ,  $3.1 \times 10^{17}$ ,  $3.2 \times 10^{15}$ , and  $1.7 \times 10^{17}$  for iron, chromium, nickel, titanium, and copper, respectively.

Metal precipitates can be the origin of shunts or breakdown sites in mc-Si solar cells, which may have a detrimental effect on the solar cell battery performance. However, this effect strongly depends on the technology process used and on the type and properties of extended defects in the wafer.

---

## Metal Interaction with Extended Defects

State-of-the-art monocrystalline Si does not generally contain extended defects, such as grain boundaries and dislocations, although dislocations can be introduced in some technology processes in highly doped layers. However, this is not the case for mc-Si, which usually contains grain boundaries (GB), dislocations, and precipitates. Therefore, the effect of these defects on the solar cell performance should be taken into account.

The number and type of GBs depend on the growth conditions. GBs are usually classified in terms of special coincident site lattice relationships. The  $\Sigma$ -value reflects the periodicity of atomic arrangements at GBs, and it increases as the boundary coherence is decreased. GBs with small  $\Sigma$  values usually have lower energy; therefore, most boundaries between the neighboring grains are such GBs. In mc-Si ingots grown by casting, the most frequently observed grain boundaries are of the  $\Sigma 3$  type (usually more than 50%), followed by random,  $\Sigma 9$ ,  $\Sigma 27$ , and small-angle (with a misorientation angle of less than  $1^\circ$ ) GBs. In Si ribbons, the portion of  $\Sigma 3$  GBs is even larger (Fig. 13). The dislocation density in some grains can reach  $10^6 \text{ cm}^{-2}$ .

To estimate the effect of extended defects on the diffusion length and in turn on the short circuit current, the defect recombination strength should be known. For GBs, it is equal to the surface recombination velocity  $v_s$ ; for dislocations, it is equal to the line recombination velocity  $\gamma_d$ ; and for precipitates,  $\gamma_p$  can be estimated as a product of surface recombination velocity at the precipitate boundary on its area. The defect recombination strength can be evaluated, for example, from measurements of the defect EBIC contrast  $C_{\max} = 1 - I_{cd}/I_{c0}$ , where  $I_{cd}$  and  $I_{c0}$  are the collected current values, measured with the focused e-beam located at the defect and far from it, respectively. The relationship between the EBIC contrast and the defect recombination strength can be calculated using the expressions presented in many other studies (e.g., Shabel'nikova and Yakimov 2012). The results of such calculations for two values of depletion region width  $W$  are presented in Fig. 14 for a dislocation perpendicular to the surface and in Fig. 15 for GBs. For a dislocation parallel to the surface, the relationship between the EBIC contrast and  $\gamma_d$  can be described as follows (Yakimov 2002):

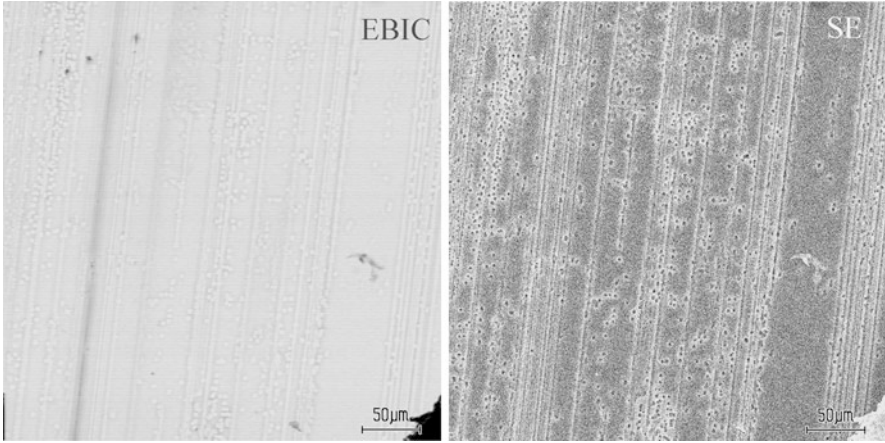
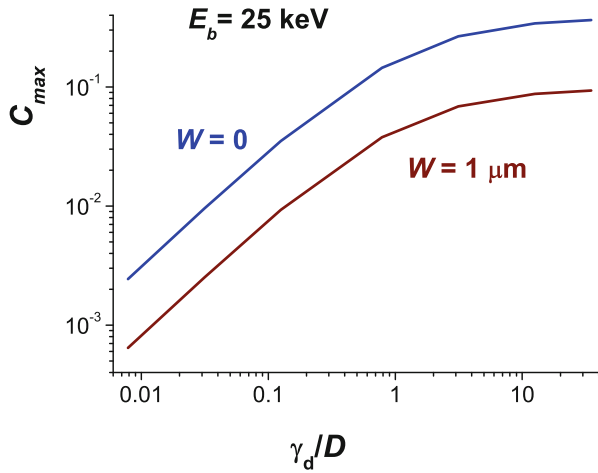


**Fig. 13** EBIC and secondary electron images of an Si ribbon after wet chemical etching. All GBs shown are  $\Sigma 3$  twin boundaries elongated along the  $\langle 112 \rangle$  direction. Only one GB produced a dark EBIC contrast at room temperature

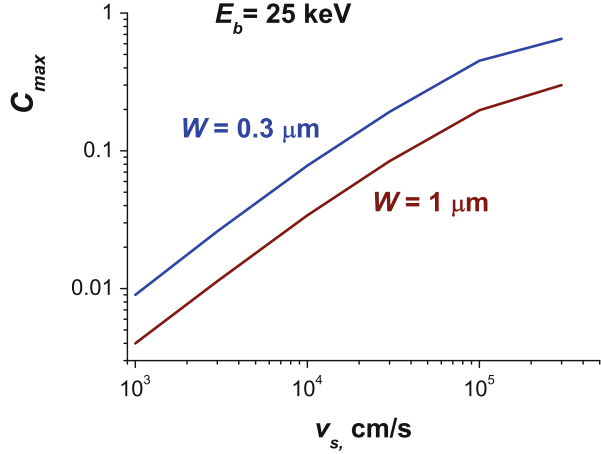
**Fig. 14** Dependences of  $C_{\max}$  on  $\gamma_d D$  for a dislocation perpendicular to the surface in Si simulated for two values of  $W$



$$C_{\max} = \frac{\gamma_d}{1 + \frac{\gamma_d}{2\pi D} \{ \ln[2(z_0 - W)/r_d] + 1/2 \}} \times \frac{\exp[-(z_0 - W)/L] \int_{-\infty}^{\infty} p_0(0, y, z_0) dy}{I_{c0}} \quad (17)$$

Here,  $z_0$  is the dislocation depth,  $r_d$  is the radius of the dislocation defect cylinder, and  $I_{c0}$  and  $p_0(0, y, z_0)$  are the collected current and minority carrier concentration at  $(0, y, z_0)$  in the defect-free region, respectively. For precipitates, the corresponding relationship is as follows:

**Fig. 15** Dependences of  $C_{\max}$  on  $v_s$  for a GB perpendicular to the surface in Si simulated for two values of  $W$



$$C_{\max} = \frac{\gamma_d \exp[-(z_0 - W)/L] \int_{-\infty}^{\infty} p_0(0, y, z_0) dy}{1 + \frac{\gamma_d}{4\pi D} \left\{ \frac{3}{2r_p} - \frac{\exp[-2(z_0 - W)/L]}{2(z_0 - W)} \right\} I_{c0}} \quad (18)$$

Here,  $r_p$  is the precipitate radius (Donolato 1992). In both cases, the contrast depends on the defect depth. However, the depth can be also estimated from the EBIC contrast dependence on beam energy.

Most  $\Sigma$ -type GBs demonstrate rather low recombination strength; only a few of them can be revealed in the EBIC mode. A typical EBIC image of an Si ribbon is presented in Fig. 13, together with the secondary electron image of the same region after selective chemical etching. Many GBs elongated along the growth direction  $\langle 112 \rangle$  can be seen; practically all of them are  $\Sigma$ 3 twin GBs. However, only one of the GBs shown in this fragment demonstrates a dark contrast in the EBIC mode. It can be assumed that this electrically active  $\Sigma$ 3 GBs is an asymmetric  $\Sigma$ 3 GBs (Tachibana et al. 2012) or it is a  $\Sigma$ 3 GB with a zig-zag structure (Chen et al. 2009). The EBIC contrasts at room temperature for  $\Sigma$ 9,  $\Sigma$ 27, and R are larger than that for  $\Sigma$ 3; however, the values usually do not exceed a few percentages in clean mc-Si. Only small angle ( $< 1^\circ$ ) boundary contrast can exceed 5% (Chen et al. 2007). These values can be used for the evaluation of GB effects on excess carrier lifetime in nominally clean mc-Si.

After intentional contamination with Fe, Cu, Ni, or other metals, the GB EBIC contrast strongly increases as a rule in the order of  $\Sigma$ 3,  $\Sigma$ 9,  $\Sigma$ 27, and R. At high contamination levels, the GB contrast can reach 30%; even for the  $\Sigma$ 3 boundary, it can reach 10%. As an example, the EBIC images of mc-Si before and after Cu diffusion at 750 °C for 30 min are presented in Fig. 16. A comparison of images in the EBIC and secondary electron (SE) modes shows that only a few GBs in the initial sample demonstrated dark EBIC contrast. After Cu diffusion,



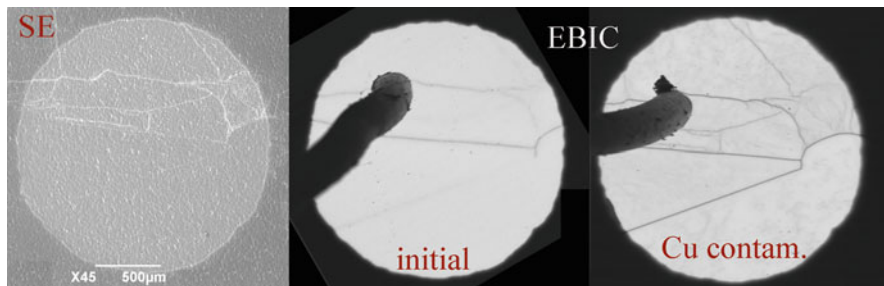


**Fig. 16** EBIC images of mc-Si before and after Cu diffusion. The SE image is shown in the left image

practically all GBs can be revealed in the EBIC mode, and their contrast essentially increases. It should be noted that this increase is not proportional to the initial contrast values. The contrast values after intentional metal contamination can be considered as a limit for GB recombination activity. Estimations of  $\nu_s$  using the dependences presented in Fig. 15 show that it does not exceed  $2\text{--}4 \times 10^3$  cm/s in clean mc-Si. In highly contaminated samples, it can exceed  $10^4$  cm/s; for some boundaries, it can reach a value of  $10^5$  cm/s. These values can be used for an estimation of GB effects on the diffusion length.

For dislocations, the situation is little bit more complex. It is widely accepted that clean dislocations demonstrate very low recombination activity. However, their decoration with transition metals can strongly increase their activity. Many experiments have shown that Fe, Ni, and Au undoubtedly increase the dislocation recombination strength in monocrystalline Si. As an example, the EBIC image of dislocations in plastically deformed Si after iron diffusion at  $1000^\circ\text{C}$  is presented in Fig. 17. The metal contamination effect is not totally understood in the case of Cu because Cu contamination has been reported to increase the dislocation recombination strength in some studies, although no Cu effect or even dislocation passivation was reported in other studies. One possible explanation for such behavior consists of an assumption that the Cu effect nonmonotonically depends on its concentration. In any case, the decoration of dislocations with transition metals can increase the dislocation EBIC contrast in plastically deformed monocrystalline Si up to 25–30% (Feklisova et al. 2012). As follows from Fig. 14,  $\gamma_d$  for such highly decorated dislocations can reach a value of 50–100  $\text{cm}^2/\text{s}$ .

In mc-Si, as seen in Fig. 13, the EBIC does not reveal any contrast related to dislocations despite rather high transition metal content. Moreover, even after intentional contamination with metal impurities, the contrast still remains very low. This is demonstrated in Figs. 18, 19, 20, and 21, where the EBIC images of mc-Si intentionally contaminated with different metals are shown. For all used metals, the GB contrast noticeably increases, whereas dislocations, which can be seen on some images due to the topography contrast of etch pits, do not produce any recombination contrast. For nominally clean mc-Si, the  $\gamma_d$  value was estimated to change in the range from  $10^{-2}$  to  $3$   $\text{cm}^2/\text{s}$  (Adamczyk et al. 2018). Taking into

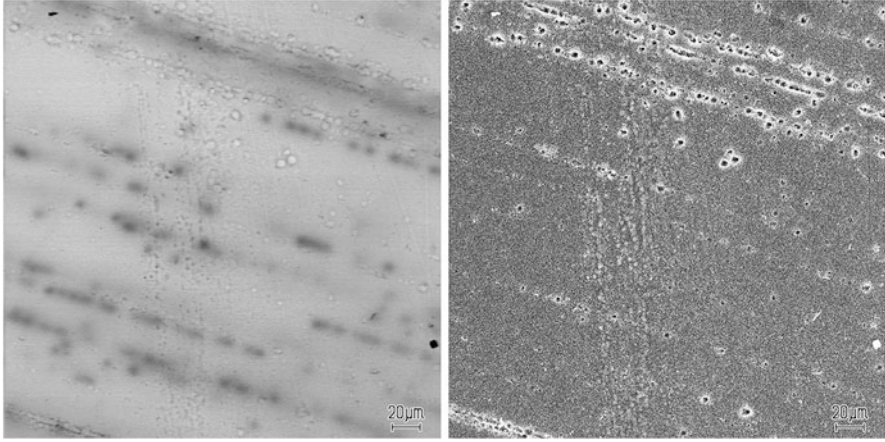


**Fig. 17** EBIC image of dislocations in plastically deformed mono-Si after Fe diffusion at 1000 °C. The corresponding SE image after chemical etching is also shown (right image), in which the dislocation etch pits are well seen

account that the EBIC can reveal dislocations with a contrast  $C_{\max} \geq 1\%$  and that the dislocation EBIC contrast is below the detectivity limit, it can be stated using the dependences from Fig. 14 that the dislocation recombination strength in mc-Si does not exceed  $3 \text{ cm}^2/\text{s}$ , even after contamination with high concentrations of transition metals.

Thus, it seems that the decoration of dislocations with metals in mc-Si is not as efficient as that for dislocations introduced by plastic deformation in monocrystalline Si. Indeed, the dislocation EBIC contrast in mc-Si does not noticeably increase after metal contamination just in the same condition, in which the essential increase of dislocation recombination strength was observed in monocrystalline Si (Feklisova et al. 2012). Thus, dislocations in mc-Si are not serving as efficient getters for metals. The low gettering efficiency of dislocations in mc-Si can be explained by an assumption that they are decorated with some impurities already after growth, but these impurities formed precipitates with rather low recombination activity. As a result, they cannot getter more impurities because of a limited ability to accommodate them, and the overall dislocation recombination activity is low.

As shown by Donolato (1998a), the effective diffusion length in a dislocated crystal with not very small thickness can be expressed as follows:

$$L_{\text{eff}} = L_0 - \frac{2\gamma_d}{\pi D} N_D \int_0^{\infty} \frac{1}{\mu^4} \frac{dk}{1 + \frac{\gamma_d}{\pi D} \left[ \frac{1 - \mu r_D K_1(\mu r_D)}{(\mu r_D)^2} + \frac{I_1(\mu r_D) K_1(\mu a)}{\mu r_D I_1(\mu a)} \right]} \quad (19)$$

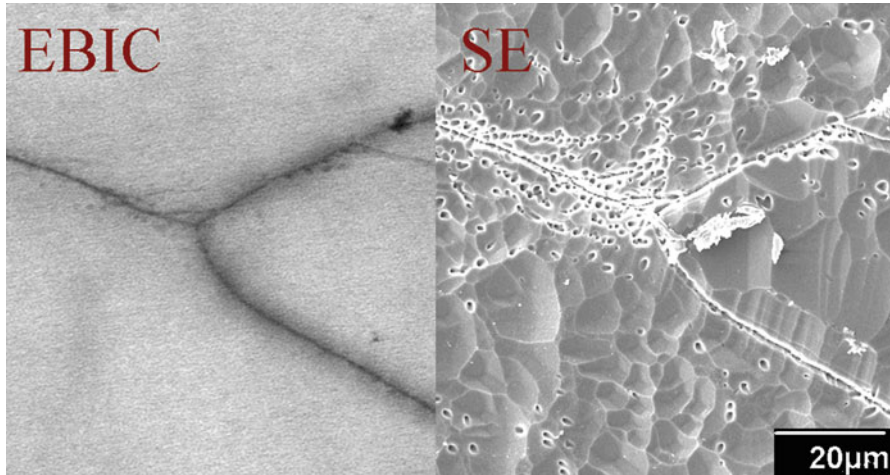
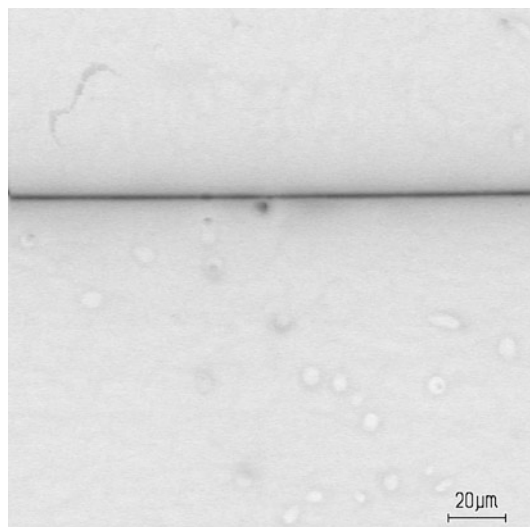


**Fig. 18** EBIC images of Cu contaminated mc-Si. The corresponding SE image after chemical etching is also shown, in which the dislocation etch pits are well seen

**Fig. 19** EBIC image of Ni-contaminated mc-Si. Dislocations are revealed as bright points due to topography contrast



Here,  $L_0$  is the excess carrier diffusion length in the dislocation-free region,  $N_D$  is the dislocation density,  $\mu = (k^2 + 1/L_0^2)^{0.5}$ ,  $r_D$  is the dislocation defect radius, and  $K_1$  and  $I_1$  are the modified Bessel functions of order one. Values of  $L_{eff}$  calculated for a few  $\gamma_d$  values using Eq. 19 with  $L_0 = 100 \mu\text{m}$  and  $r_D = 50 \text{ nm}$  as a function of dislocation density are presented in Fig. 22. It can be seen that at  $\gamma_d$  of the order of  $3 \text{ cm}^2/\text{s}$  dislocations starts to affect the  $L_{eff}$  value at densities exceeding  $10^4 \text{ cm}^{-2}$ ; at

**Fig. 20** EBIC image of Fe-contaminated mc-Si

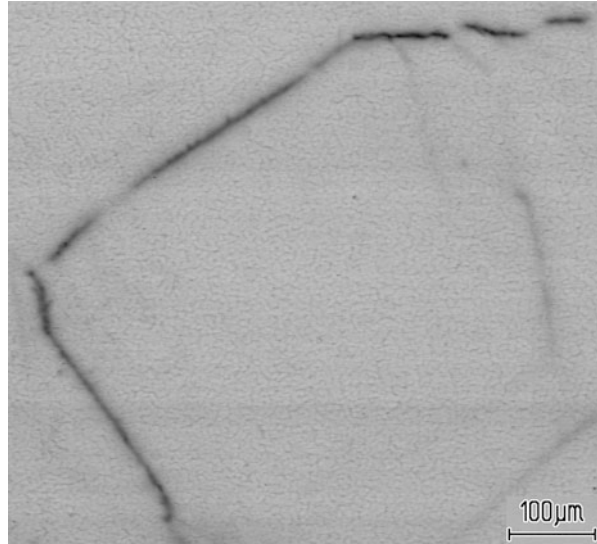
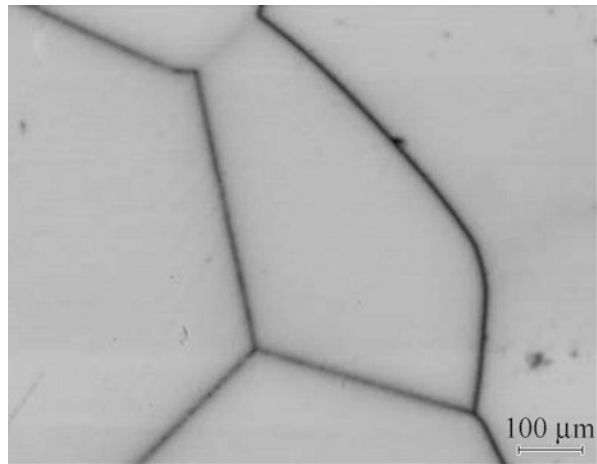


**Fig. 21** EBIC image of Au-contaminated mc-Si



$N_D$  equal to  $10^4$  and  $10^5 \text{ cm}^{-2}$ ,  $L_{eff}$  decreases to 96 and 75  $\mu\text{m}$ , respectively. Thus, in solar cells based on nominally clean mc-Si, only dislocations with a density of  $10^5 \text{ cm}^{-2}$  or higher can affect the cell parameters. If  $\gamma_d$  increases up to  $100 \text{ cm}^2/\text{s}$ , which is the case for metal-contaminated dislocations in plastically deformed monocrystalline Si, even dislocations at a density of  $10^4 \text{ cm}^{-2}$  lead to an approximate 20% decrease in the effective diffusion length.

If the effective diffusion length in polycrystalline materials is determined by the recombination on GBs, their effect can be estimated as follows (Donolato 1998b):

$$1/L_{eff}^2 = 1/L_0^2 + 2v_s/aD \quad (20)$$

**Fig. 22** Dependences of  $L_{eff}$  on dislocation density  $N_D$  calculated using Eq. (19) for a few values of  $\gamma_d$ . The calculations were carried out with  $L_0 = 100 \mu\text{m}$  and  $r_D = 50 \text{ nm}$

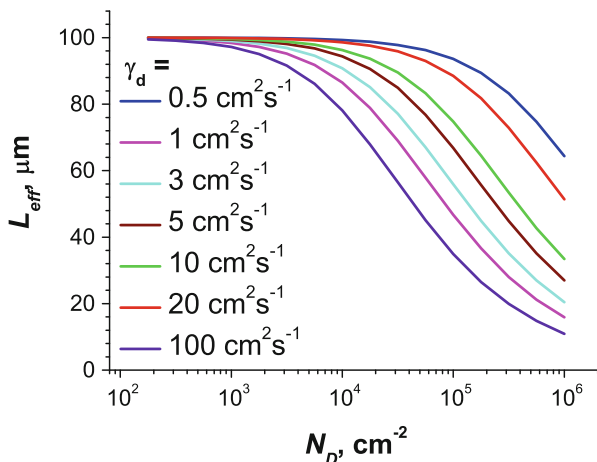
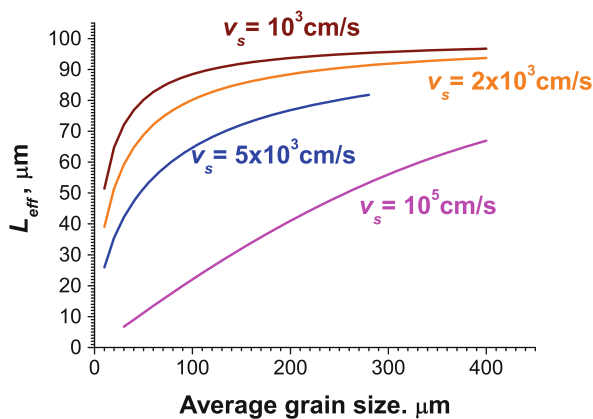


**Fig. 23** Dependences of  $L_{eff}$  on average grain size  $a$  calculated using Eqs. (20) and (21) for a few values of  $v_s$ . The calculations were carried out with  $L_0 = 100 \mu\text{m}$



for  $v_s a/D \ll 4$  and

$$1/L_{eff}^2 = 1/L_0^2 + 2\pi^2/a^2 \quad (21)$$

for  $v_s a/D \gg 4$ , where  $a$  is the average grain size (the average distance between GBs). As shown previously, even in nominally clean mc-Si,  $v_s$  can be estimated as  $2\text{--}4 \times 10^3 \text{ cm/s}$  for small-angle GBs. For most  $\Sigma 3$  boundaries,  $v_s$  is much smaller than  $10^3 \text{ cm/s}$ . For such  $v_s$  values, the condition  $v_s a/D \ll 4$  is fulfilled at an average grain size  $a \ll 400 \mu\text{m}$ —that is, almost always, especially taking into account that the  $v_s$  values will be lower than  $2 \times 10^3 \text{ cm/s}$  for other types of GBs, as follows from the lower EBIC contrast. After metal contamination,  $v_s$  can increase up to  $10^5 \text{ cm/s}$ . Eq. 21 should be used for the estimations. The  $L_{eff}(a)$  dependences calculated using Eqs. 20 and 21 are presented in Fig. 23. The dependence calculated for  $v_s = 10^5 \text{ cm/s}$  can be considered as limit one because it seems that, even in heavily contaminated

samples,  $v_s$  does not exceed this value. For  $\Sigma 3$  boundaries, the most frequently observed in mc-Si,  $v_s$  does not exceed  $10^4$  cm/s even after hard metal contamination. Thus, as seen in Fig. 23, the effect of  $\Sigma 3$  boundaries on the diffusion length can be neglected for  $a \geq 300$   $\mu\text{m}$ . In nominally clean mc-Si, the effect is even smaller. This statement can be confirmed experimentally; for example, in the sample shown in Fig. 13, the effective diffusion length exceeds 50  $\mu\text{m}$  despite a rather high dislocation density (about  $10^6$   $\text{cm}^{-2}$ ) and an average distance between twin boundaries of approximately 10  $\mu\text{m}$ .

For precipitates, the excess carrier lifetime can be estimated as follows:

$$\tau = \left(4\pi N_p r_p^2\right)^{-1} \quad (22)$$

Here,  $N_p$  and  $r_p$  are the precipitate density and radius, respectively. The effective diffusion length can then be estimated as  $L_{\text{eff}} = (D\tau)^{0.5}$ .

---

## Metal Impurities Gettering

Gettering procedures have been used since the early days of silicon microelectronics. The aim of these procedures is to improve device performance by removing harmful metal impurities from the active device region and confine them to pre-designed areas where they are unimportant for the functionality of the respective device. Many different techniques have been developed in Si microelectronics, such as backside damage, backside deposition of polycrystalline Si layers or highly doped glasses, and high-temperature annealing in chlorine-, HCl-, trichloroethane-, or trichloroethylene-containing atmospheres.

In general, any gettering procedure should include the following: (a) dissolution of metal precipitates or other procedures to transform them to mobile species, (b) diffusion of these mobile species to the gettering sites, and (c) trapping of the metals at the gettering sites into stable enough complexes. In microelectronics, it is necessary to decrease the thermal budget – that is, the temperature and/or time of any thermal treatment. However, the temperature and duration of the gettering process must be sufficiently high to dissolve all previously precipitated impurities and the required diffusion time should be high enough to transport impurities from the electrically-active device region to the getter sites, which depends on the distance between these regions. Conversely, the respective solubilities of the impurity metals, which are a function of the diffusion temperature, must exceed their steady-state concentration values required for microelectronics applications. Therefore, the idea of intrinsic gettering is very popular in microelectronics because it allows the getters to be brought closer to the active regions to be cleaned.

The term “defect engineering” was introduced because the defects used as getters should be formed in specially chosen places for internal gettering procedures. The most familiar of these procedures is internal gettering using the well-established procedure of oxygen precipitate formation in Czochralski-grown silicon. Another

example is nanocavity layers formed by hydrogen or helium implantation, the depth of which can be easily controlled by choosing the ion energy. An alternative approach uses getters outside the wafer or those deposited on its surface; the corresponding procedures are called “external gettinger.” The classification of gettinger procedures as internal and external ones is an approach based on the location of getters relative to the bulk of wafer. Another approach that prevails, especially when external gettinger procedures are considered, is based on the physical mechanisms of gettinger. In this approach, gettinger procedures are classified as segregation gettinger, relaxation gettinger, and injection gettinger (Seibt and Kveder 2012).

Relaxation gettinger, which is also called precipitation gettinger, is based on the heterogeneous precipitation of the metal impurities at nuclei formed by extended lattice defects and generated intentionally in selected regions of the wafer or on its surface. By steering the nucleation process in such way that it preferentially occurs in a selected gettinger region while it is suppressed in the device area, a concentration gradient towards the gettinger region is set up and the corresponding metal impurity transport can be established. For example, backside damage produced by different methods, such as mechanical treatment, laser irradiation, and ion implantation, are widely used.

Relaxation gettinger includes techniques that require a supersaturated solid solution of mobile metal impurity species. In the supersaturated solution, metals will precipitate as a rule on preexisting nuclei and the driving force for precipitation can be not only the free energy gain associated with supersaturation of the impurities but also the energy release due to a metal decoration of extended defects. However, this approach may not be appropriate for photovoltaic applications because, even if defects serving as nuclei are introduced at the backside of a wafer, it will lead to an increase of backside surface recombination velocity and, in accordance with Eq. 16a, will decrease the short-circuit current of the cell. Of course, as shown previously, the formation of small metal precipitates in the bulk for some metals can reduce their recombination activity in comparison with completely dissolved atoms. However, it should be taken into account that precipitate formation in the bulk of solar cells can compete with other gettinger processes, impeding the release of mobile species and lowering the effective diffusion coefficient that slows down transport of metal impurities to external gettinger regions.

Injection gettinger is a nonequilibrium gettinger mechanism that is related to the injection of intrinsic point defects. These point defects can be generated as a result of surface reactions such as oxidation, silicide formation, or precipitation in highly doped regions. These intrinsic point defects can stimulate the dissolution of metal precipitates and a release of mobile metal species, which can be further redistributed and precipitate in the regions with a lower intrinsic point defect concentration. Another example of injection gettinger is the redistribution of metal impurities diffusing via the kick-out mechanism stimulated by self-interstitials. As discussed previously, impurities such as Au, Pt, and Zn diffuse in Si as interstitial species but are predominantly dissolved on substitutional sites. To occupy the substitutional site, the metal atom kicks out the Si atom, and this reaction is reversible:



$$M_i \leftrightarrow M_s + I \quad (23)$$

Here,  $I$  is the self-interstitial concentration. If the self-interstitial concentration exceeds the equilibrium concentration, then the interstitial metal concentration increases and they will move to regions with lower self-interstitial concentration, where they can kick out the Si atom and occupy the substitution site. Thus, it can be possible to manage the concentration of, for example, substitutional gold by controlling self-interstitial generation and annihilation (Yakimov and Périchaud 1995). Places with lower self-interstitial concentration can form near extended defects, stimulating self-interstitial annihilation. The concentration of hybrid metals and corresponding recombination rates in such regions increase. Therefore, under the EBIC measurements, it would be not very easy to separate this mechanism of contrast formation from that determined by metal precipitation on the extended defect.

Segregation gettering, which is also called dopant-diffusion gettering, requires contact of the silicon wafer with a material or a region of the silicon wafer itself, which drives the impurities out of the bulk of the silicon wafer. Such materials can be solid or liquid alloys, second-phase inclusions and precipitates, regions of the Si wafer with a different doping level compared to the bulk, or regions containing a high density of traps. Redistribution due to segregation gettering is driven by an enhanced solubility of metal impurities in gettering regions; in these cases, the resulting redistribution of metal impurities does not require the supersaturation of the impurities. In particular, the solubilities of several metal impurities in extrinsic silicon are higher than those in intrinsic Si; therefore, the metal concentrations can be considerably enhanced in the heavily-doped layers. To characterize the gettering efficiency, a segregation coefficient is usually introduced as a ratio of solubilities in the bulk and in the gettering layer.

One example of a segregation gettering mechanism is segregation gettering by highly doped  $n$ -type silicon. This gettering procedure can be considered as a part of phosphorus-diffusion gettering. It is widely accepted that an increase of metal solubility in highly phosphorus-doped Si is mainly determined by the formation of substitutional impurity–phosphorus pairs. In highly phosphorus-doped layers, shear stress appears, and their value is high enough to generate dislocations in densities up to  $10^6$ – $10^7$   $\text{cm}^{-2}$ . These dislocations can also play the role of additional effective sinks for metal atoms. Segregation gettering by highly boron-doped silicon layers can also take place due to the solubility enhancement of the positively charged interstitial metal species and their pairing with the shallow acceptor (boron). However, such mechanisms are usually much less effective than phosphorus gettering.

A rather effective gettering procedure (especially for copper gettering, which also can be considered as segregation gettering) consists of using an Al-rich layer as a sink for metal impurities (so-called aluminum gettering). As follows from the binary Al-Si phase diagram, for temperatures above the eutectic temperature  $T_E = 577$  °C, a liquid Al-Si phase is formed, where the metal solubility is higher as compared to the



solubility in the solid Si; this provides a driving force for gettering metal impurities. In the case of Al gettering, the formation of the getter layer is very fast; therefore, metals with high diffusivity can be efficiently gettered.

The removal of metal impurities by silicon nitride or polysilicon layers is also based on the segregation gettering effect. The former was shown to be effective for iron gettering. In the case of polysilicon film, grain boundaries serve as the getter sites. The driving force for the impurity segregation at the grain boundaries is the difference in the free energy between the perfect silicon and the distorted sites. The type and density of grain boundaries can be controlled by the deposition procedure; for example, a lower deposition temperature results in a smaller grain size and, therefore, in higher getter efficiency. The grain boundary network is rather stable; therefore, such films demonstrate high thermal stability during the getter annealing. Grain boundaries and intragrain defects also play a role as nuclei for impurity precipitation. Therefore, in such a process, relaxation gettering can also take place.

For Si-based photovoltaic devices, the gettering approaches can differ from those developed for electronic-grade Si. First, solar cells are whole-wafer devices in which the active device region is the total volume of the Si substrate; therefore, only processes that remove impurities from the bulk of the wafer are suitable for such devices. This excludes the internal gettering procedures or makes them not very efficient. In addition, solar-grade Si, as a rule, contains a much higher metallic contamination level in multicrystalline feedstock and a large number of extended defects, which are effective getter sinks; this can compete with external getters. It should be also taken into account that cost is an important issue for many solar cells; thus, any additional processing steps should be avoided or their number should be minimized. Therefore, the most optimal strategy for gettering in photovoltaics consists of applying the layers already used in solar cell technology as gettering ones. As an example, silicon nitride films can be considered as a getter; they are frequently used as antireflection coating to increase the absorption of incident sunlight and additionally can be used as a hydrogen source.

Other example is phosphorus diffusion gettering. On the one hand, it is used to form an  $n^+$ -layer of the p-n junction. On the other hand, phosphorus diffusion gettering is known to be a very efficient procedure to remove harmful transition metals. In addition to the segregation gettering briefly discussed above, self-interstitials can be generated in highly phosphorus-doped Si during phosphorus diffusion and/or precipitation. Self-interstitials can stimulate metal precipitate dissolution enhancing their transfer into mobile species. Phosphorus precipitates can also serve as nuclei for metal relaxation gettering in the  $n^+$ -layer. Recent theoretical investigations have shown that vacancies can also play an important role in phosphorus gettering. As calculations have shown, vacancies can form energetically stable  $P_4V$  complexes, and these complexes can be dominant species for phosphorus concentrations larger than  $10^{20} \text{ cm}^{-3}$ . These complexes can trap metal atoms with the formation of metal- $P_4V$  clusters. Furthermore, if non-equilibrium vacancies are generated during phosphorus diffusion, they can directly impact the metal precipitate size and stimulate their dissociation, similar to self-interstitials. The generation of vacancies during in-diffusion of high phosphorus concentrations can also localize

precipitation of oxygen in the highly P-doped regions because vacancies can stimulate oxygen precipitation. These oxygen precipitates can act as additional gettering centers for metal removal from the wafer bulk because these precipitates are well known to be efficient getters, used for many years in intrinsic gettering procedure in microelectronics. Therefore, it could be that an interaction between oxygen, vacancies, and metal impurities is one of the most crucial factors in phosphorus diffusion gettering.

Another procedure frequently used in photovoltaics gettering that works entirely through segregation mechanisms is aluminum gettering. The Al-rich layer deposition on the wafer backside is part of solar-cell manufacturing for the formation of the backside contact and the backside electric field to reflect electrons and thus to reduce the excess carrier recombination. It is also assumed that such layer can inject vacancies stimulating the impurity precipitate dissolution. As shown by Koveshnikov et al. (1989), the injection of intrinsic point defects can essentially enhance the impurity transport, even at rather low temperatures. Thus, it seems that aluminum gettering in combination with phosphorus diffusion gettering allows one to essentially improve the lifetime values of solar cells as compared with mc-Si ingot. It is the main reason for the relatively small effect of intentionally introduced transition metal impurities in the ingot on the cell performance.

A few low-temperature procedures were recently proposed to increase the lifetime value of mc-Si. As shown in Al-Amin and Murphy (2016), annealing of wafers at 400 °C for a few tens of hours can essentially increase lifetime. Another proposal was to use the saw damage at the wafer surfaces (Al-Amin et al. 2017). Most mc-Si wafers are sawn from ingots grown by directional solidification. Saw damage on both faces of the wafer appears as a result of the cutting process. These mechanically damaged regions can be used as effective metal getters. It was demonstrated that a fourfold lifetime increase can be obtained after annealing with saw damage in the temperature range from 500 °C to 700 °C. Usually, chemical etching is used to remove this damage; however, in this approach, it was proposed to etch wafers after gettering annealing. It was also shown that Al<sub>2</sub>O<sub>3</sub> films demonstrated a strong gettering effect, removing about a half of the iron after 30 min of annealing at 425 °C; thus, such layers can also be used for metal gettering (Liu and Macdonald 2018).

Despite much evidences of improved solar cell performance due to gettering processes, the detailed mechanisms that cause the redistribution of impurities from the bulk into the layers near the surface are still under investigation and not totally understood yet. They are determined by complex processes involved in gettering procedures, which commonly consist of several steps, including releasing metals, their diffusion to gettering places, and the formation of stable clusters in these places. The contribution of these steps to gettering mechanisms can differ for different metals. The optimal gettering conditions can also differ for different metals. The optimum gettering sequence should take all of these points, as well as cost, into consideration. This makes the experimental search for optimal gettering procedures rather complex and time consuming. For these reasons, much attention is given to the modeling of gettering processes. It allows one to estimate the stability of different

configurations of impurity clusters, to reveal the dominant gettering sites for any particular metal, to determine the binding energy of metals to getter sites, and to calculate the rates of reactions involved in the gettering procedures, among others. Moreover, simulation methods are continuously being improved, which increases their predictive performance. Modeling has become an essential part of gettering process optimization, and it can be expected that the role of modeling will continue to increase in the future.

---

## Hydrogen Passivation

As shown previously for monocrystalline Si, a few effective ways have been proposed to getter transitional metals. However, in multi-crystalline Si, the gettering techniques can be less effective because the intentionally formed getters compete with extended defects, which also play the role of intrinsic getters. One of the main reasons for the efficiency of phosphorus diffusion gettering in mc-Si may be an injection of intrinsic point defects, which stimulate the dissolution of metal precipitates formed at extended defects. Therefore, some other procedures for reducing the harmful effects of metal impurities should be applied in addition to gettering in a solar cell formation process. Hydrogen passivation is one such procedure that can reduce the detrimental effect of both metal impurities and extended defects on the cell performance.

Hydrogen plays a significant role in Si technology. It has been known for many years that it can passivate the detrimental effects of many point and extended defects in semiconductor materials. Many techniques have been used for hydrogen introduction. In Si, the most popular are hydrogen plasma treatment, wet chemical etching, and postdeposition annealing of a hydrogen-rich  $\text{SiN}_x$  layer. Advanced hydrogen passivation applied on *p*-type, *n*-type, and upgraded metallurgical-grade crystalline silicon solar cells was reviewed by Lee et al. (2018). Hydrogen diffusion from hydrogen-rich  $\text{SiN}_x$  layers can be a very suitable passivation procedure to introduce hydrogen in Si solar cells because such layers are frequently used as an antireflection coating to increase the absorption of incident sunlight. Moreover, as noted previously, these films can be also used for metal gettering. Under a firing step used to improve the metal contact, hydrogen diffuses from the  $\text{SiN}_x$  film into Si and passivates surface and bulk defects. The hydrogen concentration typically introduced by this method is not very high, but it can reach  $10^{15} \text{ cm}^{-3}$ . In this section, the main properties of hydrogen in Si and the results of investigations on the hydrogen interaction with some metals in Si are discussed in more detail.

Isolated interstitial hydrogen is found in Si in two configurations: tetrahedral (T) and relaxed bond-center sites (BC). It has charge states of 0 and + in BC sites and 0 and – in T sites. As shown by DLTS studies, H in Si has the donor level located in the range from  $E_c - 0.16 \text{ eV}$  to  $E_c - 0.175 \text{ eV}$ . The position of the acceptor level is more difficult to obtain because hydrogen atoms need to overcome a barrier to capture electrons to go from the BC to the T site. Nevertheless, it is believed that the most reliable value for the acceptor level is  $E_c - 0.65 \text{ eV}$ . Thus, in *p*-type

and intrinsic Si, the stable charge state is  $H^+$  and hydrogen acts as a donor. In  $n$ -type Si, the stable charge state is  $H^-$  and it acts as an acceptor. Because the hydrogen donor level is above its acceptor level, it is a negative-U defect with an inverted order of levels in the gap. As a negative-U defect, H has an equilibrium occupancy level that lies midway between its donor and acceptor levels, and the hydrogen charge state depends on the position of this level with respect to the Fermi level. If the dopant concentration is very low, the number of positively charged hydrogens should be equal to the number of negatively charged hydrogens.

The activation energy for hydrogen diffusion was experimentally measured in the wide temperature range to be 0.48 eV, and a theory predicts a close value. This value is ascribed to  $H^+$ ; the diffusivities of  $H^0$  and  $H^-$  are difficult to measure. Hydrogen can easily penetrate into Si, even at temperatures lower than room temperature; however, its penetration depth essentially depends on the impurity content and defect density in the crystal because it effectively interacts with shallow donors and acceptors and with other point and extended defects. Therefore, its depth profile is determined by trap-limited diffusion and thus depends on the trap concentration. This is similar to the case of gold diffusion into Si with vacancy-related immobile traps. Therefore, if the hydrogen surface concentration is lower than that of the traps, then its depth profile should have the form of a step, with a depth as described by Eq. 5.

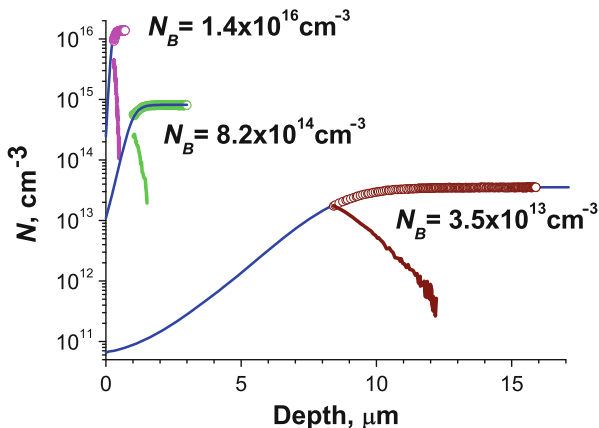
Hydrogen forms neutral complexes with boron and phosphorus, which contain one hydrogen atom. Therefore, a hydrogen depth profile can be monitored by measurements of the depth profiles of electrically active boron or phosphorus in  $p$ - and  $n$ -type Si, respectively, by capacitance-voltage profiling. The overall hydrogen concentration is determined by the total trap concentration. If the shallow dopants are the dominant traps, hydrogen concentration can also be evaluated from such measurements. An example of such measurements is presented in Fig. 24, where the depth profiles of charge carriers measured in  $p$ -Si with different boron concentrations after hydrogen diffusion during wet chemical etching in an acid mixture are shown. The overall hydrogen concentration can be calculated as a difference between the bulk boron concentration and measured carrier concentration; it is also shown with solid colored lines. As seen in Fig. 24, a decay of hydrogen concentration into the bulk can be described by an exponential law. Such dependence is a result of Si etching because the surface layers are removed during diffusion. If the hydrogen surface concentration is higher than that of the traps, then its depth profile can be described as follows:

$$C_H(z) \sim \exp(-z/L_H)$$

$$L_H = \frac{V}{2D_H} + \sqrt{\left(\frac{V}{2D_H}\right)^2 + \frac{1}{\tau D}} \quad (24)$$

Here,  $C_H$  and  $D_H$  are the hydrogen concentration and diffusivity, respectively;  $V$  is the etching velocity;  $\tau = (4\pi D_H r_t N_t)^{-1}$ ; and  $r_t$  and  $N_t$  are the radius of hydrogen capture by the trap and the trap concentration, respectively. In the case of interactions

**Fig. 24** Depth profiles of charge carriers measured in monocrystalline *p*-Si with different boron concentrations  $N_B$  after hydrogen diffusion during wet chemical etching in the acid mixture. Simulated profiles are shown with blue solid lines. Other solid lines show the corresponding hydrogen–boron pair profiles



with boron or phosphorus, the effect of electric fields arising due to dopant passivation on hydrogen transport should be also taken into account (Feklisova et al. 2002). As follows from Eq. 24, the penetration depth should decrease when the trap concentration increases. Indeed, as seen in Fig. 24, the hydrogen penetration depth decreases when the boron concentration increases, but its concentration increases and approaches the boron concentration.

The radius of hydrogen capture by boron is about an order of magnitude larger than that for most other traps. Therefore, if the trap concentration in *p*-type Si is comparable to or lower than that of boron, hydrogen is preferentially captured by boron. However, the P-H and B-H pairs are not stable and are dissociated at approximately 100 °C. Therefore, annealing at higher temperatures can release hydrogen atoms and redistribute them among other traps. If annealing of the hydrogen-rich SiN<sub>x</sub> layer is used for hydrogen introduction, shallow dopants can hardly constrain its penetration due to high annealing temperatures, although trapping can decrease the effective diffusivity. It was shown that the profile of passivated boron also depends on the oxygen or nitrogen concentration, especially if the dopant concentration is low. In this case, some portion of hydrogen also can be captured by oxygen or nitrogen. The carbon concentration in mc-Si can reach a value close to 10<sup>18</sup> cm<sup>-3</sup> – that is, one to two orders of magnitude higher than the boron concentration. Therefore, in mc-Si, carbon can also effectively influence the hydrogen penetration. In the following, the hydrogen interaction with metals considered in this chapter is discussed, with special attention to the possibility of passivation of their electrical activity.

In the common sense, the term “passivation” means that the energy level of a defect disappears as a result of its interaction with hydrogen. The passivation of dangling bonds of extended defects or on the surface is a well-known example of such behavior. However, many transition metals demonstrate more complex behavior; for example, hydrogen-containing complexes formed with such impurities are electrically active, although the initial energy levels disappear. For such metals, only complexes that include a few hydrogen atoms become electrically inactive.

Therefore, a total hydrogen passivation proceeds via successive joining hydrogen atoms up to reaching the neutral state. The centers formed at intermediate states can be electrically active and can still affect the recombination rate.

It is widely believed that the most harmful impurity in Si is iron. In Si-based solar cells, this metal has a predominant detrimental effect on the excess carrier lifetime. However, the question about the possibility of iron passivation still is unanswered. On the one hand, considering that both interstitial hydrogen and iron atoms are generally positively charged in *p*-type Si, it can be expected that the Coulomb repulsion of  $Fe_i$  and H prevents the formation of Fe-H complexes. Indeed, as observed in Feklisova et al. (2000) and Tang et al. (2011), hydrogen promoted dissociation of Fe-B pairs releasing  $Fe_i$ , whereas no detectable passivation of Fe-B or  $Fe_i$  occurred. On the other hand, ab initio calculations predicted that an Fe-H complex should be stable at room temperature and have a deep donor level at approximately  $E_v + 0.40$  eV and a deep acceptor level at approximately  $E_c - 0.3$  eV. An energy level at  $E_v + 0.31$  eV observed in Leonard et al. (2015) was assigned to a Fe-H complex. Nevertheless, no evidence for a complete passivation of  $Fe_i$  and FeB has been found up to date.

Investigations of Ni interactions with hydrogen (Scheffler et al. 2014b) showed that a few centers with different hydrogen content can be formed. NiH introduces into the bandgap of silicon a single-acceptor and a single-donor state at  $E_c - 0.17$  eV and  $E_v + 0.49$  eV, respectively. NiH<sub>2</sub> and NiH<sub>3</sub> were shown to introduce the single-acceptor states at  $E_v + 0.58$  eV and  $E_v + 0.46$  eV, respectively. It was also proposed that the NH<sub>4</sub> complex can be formed, and this complex is electrically inactive. If this is the case, then substitutional Ni can be completely passivated by hydrogen, but it takes four hydrogen atoms.

As shown by Yarykin and Weber (2013), hydrogen interaction with copper leads to the appearance of CuH centers with energy levels  $E_v + 0.104$  eV (donor) and  $E_v + 0.49$  eV (acceptor) and CuH<sub>2</sub> centers with energy levels  $E_v + 0.195$  eV (donor) and  $E_v + 0.46$  eV (acceptor). It was believed that these hydrogen-related centers are formed via a hydrogen reaction with substitutional copper. In these experiments, hydrogen was introduced by wet chemical etching in the mixture of acids. An analysis of defect depth profiles allowed a conclusion that, in the near surface region with the highest hydrogen concentration, the complexes including three (or more) hydrogen atoms, which have no deep levels in the lower half of the gap, are also formed. The theory also predicted that a Cu<sub>3</sub>H<sub>3</sub> complex should not have deep levels. The interaction of a complex consisting of four copper atoms with hydrogen was shown to lead to its destruction—that is, hydrogen stimulates the dissociation of interstitial Cu atoms from this complex (Yarykin and Weber 2014). Thus, it is reasonable to assume that, at a high enough concentration, hydrogen can passivate substitutional copper and its main complexes.

Not as much is known about hydrogen's interactions with Cr. Thus, Sadoh et al. (1994) assigned three donor levels at  $E_c - 0.28$  eV,  $E_c - 0.45$  eV, and  $E_c - 0.54$  eV to interstitial chromium-hydrogen complexes. The complexes were shown to dissociate at temperatures lower than 175 °C. However, the number of hydrogen atoms in the complexes was not obtained. Furthermore, no data were reported about the

possibility of Cr passivation, although the formation of chromium-hydrogen complexes indicates that hydrogen can interact with interstitial chromium. Therefore, by analogy with other transition metals, it can be assumed that its passivation could occur if a large enough number of hydrogen atoms join chromium.

Cobalt's interactions with hydrogen have been studied more intensively than chromium-hydrogen interactions. However, the results obtained were rather controversial. In investigations using Laplace DLTS (Kolkovsky et al. 2014), two electrically active complexes of cobalt with hydrogen  $\text{Co}_5\text{H}$  and  $\text{Co}_5\text{H}_2$  were detected. Both centers have only one corresponding acceptor energy level at  $E_c - 0.35$  eV and  $E_c - 0.29$  eV, respectively. Both centers are stable up to 300 °C. The theoretical calculations allow one to assume that the  $\text{Co}_5\text{H}_3$  complex can be electrically inactive – that is, cobalt passivation with hydrogen is possible.

Hydrogen's interactions with titanium also lead to the formation of new electrically active centers. Single-donor energy levels at  $E_c - 0.08$  eV and  $E_c - 0.34$  eV were ascribed to centers containing one titanium atom. According to theoretical predictions, such centers can have two configurations: with an H atom bonded to a Ti atom at the tetrahedral site ( $\text{Ti}_i\text{H}$ ) and with H tied up to the Si dangling bond with an Si atom moving away from the substitutional site along a trigonal axis ( $\text{Ti}_i\text{H}_{\text{BC}}$ ). The energy level at  $E_c - 0.08$  eV was attributed to the  $\text{Ti}_i\text{H}$ , whereas the level at  $E_c - 0.34$  eV was attributed to  $\text{Ti}_i\text{H}_{\text{BC}}$ . The depth profile measurements allow one to ascribe the energy level at  $E_c - 0.38$  eV to the single-donor state of  $\text{Ti}_i\text{H}_2$ .

Gold was the first impurity for which the formation of a set of hydrogen-related electrically active centers was established. Hydrogen's interactions with gold lead to the appearance of three energy levels: a double acceptor at  $E_c - 0.19$  eV, single acceptor at  $E_c - 0.47$  eV, and single donor at  $E_v + 0.21$  eV for  $\text{AuH}$ . The single-acceptor level at  $E_c - 0.53$  eV was attributed to  $\text{AuH}_2$ . Neutral Au-H complexes were also reported, which means that substitutional gold can be completely passivated at high enough hydrogen concentrations; however, the exact composition of these neutral complexes has not yet been established. The Au-H complexes are rather stable at room temperature. Even at 420 K, it takes a few hours to decrease their concentration.

As in the case of some other transition metals, silver can form complexes with hydrogen. DLTS investigations (Yarykin et al. 1999) showed that two electrically active centers appear as a result:  $\text{AgH}$  and  $\text{AgH}_2$ . Similar to gold,  $\text{AgH}$  has three levels: a double-acceptor level at  $E_c - 0.09$  eV, single-acceptor level at  $E_c - 0.45$  eV, and donor level at  $E_v + 0.28$  eV.  $\text{AgH}_2$  has a single-donor level at  $E_v + 0.38$  eV and possibly a single-acceptor level at  $E_c + 0.5$  eV. The presence of a neutral Ag-H complex is also confirmed. Its composition has not yet been established, but some calculations predict that  $\text{AgH}_3$  should be electrically inactive. Silver-hydrogen complexes are stable up to 400 °C.

The interaction of hydrogen with Zn has been studied only by optical absorption. Nevertheless, such experiments allow one to assume that the Zn-H complexes can be also electrically active.

It has been well established that hydrogen passivation improves the performance of Si solar cells significantly, but which defects' passivation are responsible for such

improvements is yet unknown. Thus, it is widely believed that solar cell performance is mainly deteriorated due to transition metals, particularly iron. However, based on the previous discussion, the possibility of hydrogen passivation of iron and perhaps some other transition metals is not so obvious. The transition metals that are most detrimental for solar cell performance formed new deep-level centers with hydrogen; their complete passivation, if possible, needs high hydrogen concentrations. Moreover, the thermal stability of metal-hydrogen complexes is not very high. Dislocations and grain boundaries were shown to be effectively passivated with hydrogen. However, grain boundary passivation was shown to depend on the boundary type, their faceting, and decorations with metals. As a result, the recombination activity of some grain boundaries strongly decreases after passivation, whereas that of other GBs does not. Nevertheless, even if only a half of the grain boundaries are passivated, it will increase the average distance between the active boundaries and, in accordance with Eqs. 20 and 21, will suppress their effects on the short-circuit current. In addition, hydrogen passivates the surfaces, decreasing the surface recombination velocity, which also can improve the solar cell performance. The stability of hydrogen passivation under subsequent thermal treatments and under sun illumination is also not fully understood. Thus, a deeper microstructural understanding of which defects are most effectively passivated, and which respond poorly to hydrogenation, is needed to guide the optimization of hydrogen passivation in solar cell manufacturing.

---

## Conclusion

Transition metals are the most detrimental defects in Si-based solar cell technology. They play the role of lifetime killer and enhance the recombination activity of extended defects. They both degrade the solar cell performance and decrease the short-circuit current. In addition, decoration with metals and extended defects can increase leakage current and even lead to shunt formation, thus decreasing the open circuit voltage values. However, expensive cleaning procedures should be avoided in solar cell processing because cost is an important issue for photovoltaics. Therefore, relatively inexpensive procedures should be developed to reduce the metal content in the bulk of the wafer or suppress the harmful effects. An important limitation for these procedures is the requirement that they should be compatible with silicon-based solar cell processing. Thus, the optimization of such procedures requires a better understanding of the transition metal and extended defect properties, as well as a deeper understanding of the mechanisms of their diffusion, precipitation, and interactions with extended and point defects. Despite a long history of such investigations, many unanswered questions remain. The efficiency of gettering and hydrogen passivation procedures for any particular metal, as well as its dependence on thermal treatment conditions, should also be studied in more detail. Modeling of the involved mechanisms is expected to be very useful in solving these unanswered questions.



## Cross-References

- ▶ [Defects in Crystalline Silicon: Dislocations](#)
- ▶ [Grain Boundaries in Multicrystalline Silicon](#)
- ▶ [Hydrogenated Microcrystalline Silicon Thin Films](#)
- ▶ [Upgrade Metallurgical Grade Silicon](#)

---

## References

- K. Adamczyk, R. Søndenå, C.C. You, G. Stokkan, J. Lindroos, M. Rinio, M. Di Sabatino, *Phys. Status Solidi A* **215**, 1700493 (2018)
- M. Al-Amin, J.D. Murphy, *J. Appl. Phys.* **119**, 235704 (2016)
- M. Al-Amin, N.E. Grant, J.D. Murphy, *Phys. Status Solidi (RRL)* **11**, 1700268 (2017)
- J. Chen, T. Sekiguchi, D. Yang, *Phys. Status Solidi C* **4**, 2908 (2007)
- B. Chen, J. Chen, T. Sekiguchi, M. Saito, K. Kimoto, *J. Appl. Phys.* **105**, 113502 (2009)
- S.C. Choo, *Phys. Rev. B* **1**, 687 (1970)
- C. Claeys, E. Simoen, *Metal Impurities in Silicon and Germanium-Based Technologies. Origin, Characterization, Control, and Device Impact* (Springer, Basel, 2018)
- G. Coletti, P.C.P. Bronsveld, G. Hahn, W. Warta, D. Macdonald, B. Ceccaroli, K. Wambach, N. Le Quang, J.M. Fernandez, *Adv. Funct. Mater.* **21**, 879 (2011)
- C. Donolato, *Appl. Phys. Lett.* **46**, 270 (1985)
- C. Donolato, *Semicond. Sci. Technol.* **7**, 37 (1992)
- C. Donolato, *J. Appl. Phys.* **84**, 2656 (1998a)
- C. Donolato, *Semicond. Sci. Technol.* **13**, 781 (1998b)
- O.V. Feklisova, A.L. Parakhonsky, E.B. Yakimov, J. Weber, *Mater. Sci. Eng. B* **71**, 268 (2000)
- O.V. Feklisova, E.B. Yakimov, N.A. Yarykin, *Semiconductors* **36**, 282 (2002)
- O.V. Feklisova, X. Yu, D. Yang, E.B. Yakimov, *Phys. Status Solidi C* **9**, 1942 (2012)
- K. Graff, *Metal Impurities in Silicon-Device Fabrication*, 2nd edn. (Springer, Berlin/Heidelberg, 2000)
- R.N. Hall, *Phys. Rev.* **87**, 387 (1952)
- F.D. Heinz, M. Breitwieser, P. Gundel, M. Konig, M. Horteis, W. Warta, M.C. Schubert, *Sol. Energy Mater. Sol. Cells* **131**, 105 (2014)
- T. Heiser, A. Mesli, *Phys. Rev. Lett.* **68**, 978 (1992)
- A.A. Istratov, T. Buonassisi, M.D. Pickett, M. Heuer, E.R. Weber, *Mater. Sci. Eng. B* **134**, 282 (2006)
- M. Kittler, J. Lärz, W. Seifert, M. Seibt, W. Schröter, *Appl. Phys. Lett.* **58**, 911 (1991)
- V.I. Kolkovskiy, L. Scheffler, J. Weber, *Physica B* **439**, 24 (2014)
- S.V. Koveshnikov, E.B. Yakimov, N. Yarykin, V.A. Yunkin, *Phys. Status Solidi A* **111**, 81 (1989)
- S.H. Lee, M.F. Bhopal, D.W. Lee, S.H. Lee, *Mater. Sci. Semicond. Process.* **79**, 66 (2018)
- S. Leonard, V.P. Markevich, A.R. Peaker, B. Hamilton, J.D. Murphy, *Appl. Phys. Lett.* **107**, 032103 (2015)
- A.Y. Liu, D. Macdonald, *Phys. Status Solidi (RRL)* **12**, 1700430 (2018)
- A. Mesli, T. Heiser, E. Mulheim, *Mater. Sci. Eng. B* **25**, 141 (1994)
- V.I. Orlov, E.B. Yakimov, E.P. Magomedbekov, A.B. Danilin, *Adv. Condens. Matter Phys.* **2017**, 1946490 (2017)
- O. Palais, E. Yakimov, S. Martinuzzi, *Mater. Sci. Eng. B* **91–92**, 216 (2002)
- S.M. Peshcherova, E.B. Yakimov, A.I. Nepomnyashchikh, L.A. Pavlova, O.V. Feklisova, *Semiconductors* **49**, 724 (2015)
- S. Pizzini, *Advanced Silicon Materials for Photovoltaic Applications* (Wiley, Chichester, 2012)
- I.E. Reis, S. Riepe, W. Koch, J. Bauer, S. Beljakowa, O. Breitenstein, H. Habenicht, D. Kreßner-Kiel, G. Pensl, J. Schon, W. Seifert, in *Proceedings of the 24th European Photovoltaic Solar Energy Conference and Exhibition*, Hamburg, 2009, p. 2144

- T. Sadoh, M. Watanabe, H. Nakashima, T. Tsurushima, *J. Appl. Phys.* **75**, 3978 (1994)
- L. Scheffler, V. Kolkovsky, J. Weber, *AIP Conf. Ser.* **1583**, 85 (2014a)
- L. Scheffler, V. Kolkovsky, J. Weber, *J. Appl. Phys.* **116**, 173704 (2014b)
- J. Schmidt, B. Lim, D. Walter, K. Bothe, S. Gatz, T. Dullweber, P.P. Altermatt, *IEEE J. Photovoltaics* **3**, 114 (2013)
- M. Seibt, V. Kveder, in *Advanced Silicon Materials for Photovoltaic Applications*, ed. by b. S. Pizzini, (Wiley, Chichester, 2012), p. 127
- Y.L. Shabel'nikova, E.B. Yakimov, *J. Surf. Investig.* **6**, 894 (2012)
- W. Shockley, W.T. Read, *Phys. Rev.* **87**, 835 (1952)
- G. Stokkan, D.S. Marisa, R. Søndena, M. Juel, A. Austruße, K. Adamczyk, H.V. Skarstad, K.E. Ekstrøm, M.S. Wiig, C.C. You, H. Haug, M. M'Hamdi, *Phys. Status Solidi A* **214**, 1700319 (2017)
- T. Tachibana, T. Sameshima, T. Kojima, K. Arafune, K. Kakimoto, Y. Miyamura, H. Harada, T. Sekiguchi, Y. Ohshita, A. Ogura, *J. Appl. Phys.* **111**, 074505 (2012)
- H. Takahashi, M. Suezawa, K. Sumino, *Phys. Rev. B* **46**, 1882 (1992)
- C.K. Tang, L. Vines, B.G. Svensson, E.V. Monakhov, *Appl. Phys. Lett.* **99**, 052106 (2011)
- E.B. Yakimov, *J. Phys. Condens. Matter* **14**, 13069 (2002)
- E. Yakimov, I. Périchaud, *Appl. Phys. Lett.* **67**, 2054 (1995)
- E. Yakimov, G. Mariani, B. Pichaud, *J. Appl. Phys.* **78**, 1495 (1995)
- N. Yarykin, J. Weber, *Phys. Rev. B* **88**, 085205 (2013)
- N. Yarykin, J. Weber, *Appl. Phys. Lett.* **105**, 012109 (2014)
- N. Yarykin, J. Weber, *Appl. Phys. Lett.* **109**, 102101 (2016)
- N. Yarykin, J.-U. Sachse, H. Lemke, J. Weber, *Phys. Rev. B* **59**, 5551 (1999)
- T. Zundel, J. Weber, B. Benson, P.O. Hahn, A. Schnegg, H. Prigge, *Appl. Phys. Lett.* **53**, 1426 (1988)



Ichiro Yonenaga

## Contents

Introduction .....	542
Dislocation Structures .....	543
Crystal Structure .....	543
Dislocation Structures .....	544
Dislocation Motion and Plastic Deformation in High-Purity Si .....	547
Dislocation Velocity .....	548
Plastic Deformation and Yield Strength .....	550
Dislocation Mechanism .....	553
Hirth-Lothe Kink Diffusion Model .....	553
Dislocation Dynamics in Deformation .....	555
Controversy of Shuffle- or Glide-Set Dislocations .....	557
Impurity Effects on Dislocation Activities .....	558
Critical Stress for Dislocation Generation .....	558
Dislocation Immobilization .....	561
Suzuki Effect .....	563
Dislocation Velocity .....	564
Stimulated Dislocation Motion .....	567
Recombination-Enhanced Dislocation Glides .....	567
Hydrogen-Enhanced Dislocation Glides .....	569
Fracture .....	570
Fracture Toughness .....	570
Brittle-to-Ductile Transition .....	571
Electrical and Optical Properties of Dislocations .....	573
Electrical Characters .....	573
Model of Electronic Structures of Dislocations .....	574
Recombination at Dislocations .....	576
Dislocation-Related Deep States .....	576
Dislocation-Related Shallow States .....	577

---

I. Yonenaga (✉)

Tohoku University, Sendai, Japan

e-mail: [yonenaga@imr.tohoku.ac.jp](mailto:yonenaga@imr.tohoku.ac.jp)

Characteristics of Dislocations Specific in Solar Cell Si .....	578
Dislocation Behavior in Multi-crystalline Si .....	579
Effect on Efficiency and Electrical Properties of Si Solar Cells .....	580
Conclusive Remarks for Further Developments .....	581
Cross-References .....	582
References .....	582

---

### Abstract

Current understanding of various properties of dislocations in Si is given comprehensively for photovoltaic applications. Dislocations cause spatial variations in the electrical and optical properties of semiconductor materials and also the degradation of various kinds of semiconductor devices. Thus, establishing knowledge on mechanical properties of dislocations and also interactions between dislocations and impurities is important from both the fundamental and practical viewpoints for development of semiconductor technology. Indeed, the knowledge is widely applied as the basis for dislocation-free crystal growth and device fabrication process in Si.

---

### Keywords

Dislocations · Atomic structure · Dissociation · Stacking fault · Reconstruction · Soliton · Velocity · Yield strength · Plasticity · Twin · Shuffle-glide-controversy · Impurity effect · Immobilization · Locking · Recombination-enhanced dislocation glide · Fracture · Toughness · Brittle-to-ductile transition (BDT) · Electrical-optical properties · Electronic structure · Shallow and deep energy states · Recombination

---

## Introduction

It is well known that dislocations cause spatial variations in the electrical and optical properties of semiconductor materials and also the degradation of various kinds of semiconductor devices, including photovoltaic applications. Thus, a great deal of effort has been conducted that a semiconductor crystal is being kept free from or low density of dislocations during growth and various processes. Dislocations are introduced into a semiconductor crystal under stress or stimulation at elevated temperatures followed by means of their motion and multiplication. Such dislocation processes are governed by the dynamic properties of dislocations. Presence of impurities and point defects affects detrimentally on such dynamic activities of dislocations and the mechanical properties of semiconductor crystals at high temperatures through a variety of interactions. For example, Si crystals containing oxygen (O) impurities, i.e., Czochralski (CZ)-grown Si, are being exclusively used as the materials for integrated devices because of their smaller susceptibility against the generation of dislocations or the occurrence of wafer warpage caused by thermal stress related to device production processing in comparison with oxygen-free Si, i.e., typically float-zone (FZ)-Si. Clarification of behavior of dislocations under stress and/or impurity presence in semiconductor crystals is quite important

practically from the technological viewpoints of the crystal growth and the devices production and, at the same time, important fundamentally.

Interaction between dislocations and impurities in semiconductors has two interesting aspects from the scientific viewpoint. One is the effect of dislocations on the spatial distribution of impurities in a crystal, such as impurity accumulation, defect reaction, and complex formation. The other is the effect of impurities on various kinds of activities of dislocations. Some impurities may accumulate on dislocations when a certain thermal condition is fulfilled. The concentration of such impurities in the region around a dislocation is then different from that in the region far from it, and the electrical and optical properties become inhomogeneous within the crystal. The accumulation of impurities results in immobilizing the dislocation. This leads to mechanically strengthen the crystal through suppression of macroscopic generation of dislocations. Thus, the mechanical properties of the crystals are understood on the basis of a microscopic model with the dynamic properties of individual dislocations with and without effects of impurities.

This chapter gives the current understanding of various properties of dislocations in Si comprehensively in a viewpoint for photovoltaic applications. Section “[Dislocation Structures](#)” briefly reminds atomic structures of dislocations in Si. Section “[Dislocation Motion and Plastic Deformation in High-Purity Si](#)” describes the dislocation velocities and plastic deformation in high-purity Si, followed by the mechanisms governing motion of an individual dislocation and dynamics based on the collective motion of dislocations during plastic deformation in section “[Dislocation Mechanism](#).” In the section, the recent shuffle-glide set controversy, regarding the dislocation structures in Si, is explained. Section “[Impurity Effects on Dislocation Activities](#)” summarizes the dynamic activities of individual dislocations, as generation, immobilization, and velocities under effects of various impurities. Section “[Stimulated Dislocation Motion](#)” shows dislocation motion stimulated by recombination and hydrogen treatment. Section “[Fracture](#)” briefly summarizes fracture behavior of Si. Section “[Electrical and Optical Properties of Dislocations](#)” describes recent understandings on electrical and optical properties of dislocations in Si. Characteristics of dislocations in mc-Si for solar cells are described in section “[Characteristics of Dislocations Specific in Solar Cell Si](#).” There are comprehensive reviews of dislocation-related problems in semiconductors as given by Alexander and Haasen (1968), by Alexander (1986), by Sumino (1994), and by Schröter and Cerva (2002). The reader interested in the dislocations and plasticity of Si governed by dislocation motion may refer to the overview by the present author (Yonenaga 2015).

---

## Dislocation Structures

### Crystal Structure

Si is a purely covalent bonded material and crystallizes in the diamond cubic (DC) structure where atoms are coordinated tetrahedrally. The lattice parameter  $a$  is 0.543 nm at RT. As can be seen in Fig. 1, the structure is two interpenetrating

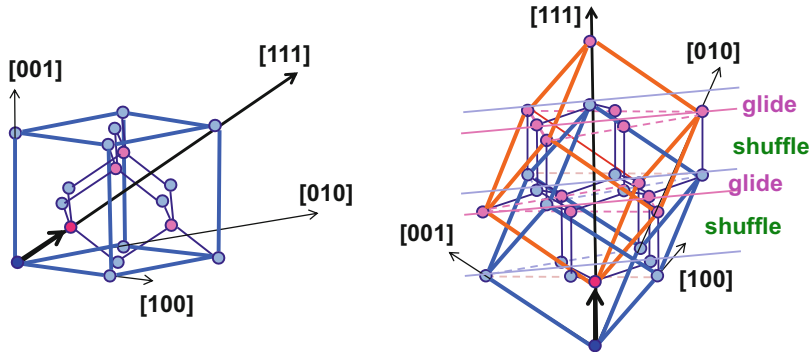


**Fig. 1** Images of the diamond structure. The two interpenetrating unit cells are shown in blue and red, respectively. The right-side image shows the stacking of  $\{111\}$  glide- and shuffle-set planes of Si

face-centered cubic (fcc) lattices with one atom at  $(0, 0, 0)$  and the other at  $(1/4, 1/4, 1/4)$ . Though the  $\{111\}$  atomic plane is the most closely packed one in the structure, there are two kinds of spacing of  $\{111\}$  planes, as illustrated in Fig. 1b, i.e., a widely spaced set, called the shuffle set with a spacing of  $(\sqrt{3})a/4$  between the adjacent planes, and a narrowly spaced one called the glide set with a spacing of  $(\sqrt{3})a/12$  (Hirth and Lothe 1982).

Si is DC structure at the standard pressure (1013 hPa) and up to the melting temperature  $T_M$  of 1687 K. Si transforms to several types of phases under hydrostatic pressure, such as to the metallic phase (Si-I to Si-II) under a pressure of  $\sim 12$  GPa (Kailer et al. 1997). Table 1 shows some basic properties of Si relevant to this chapter (Sze 1981).

## Dislocation Structures

A dislocation glissile in DC structure crystals has the smallest Burgers vector  $\mathbf{b} = a/2 \langle 1\bar{1}0 \rangle$  on the  $\{111\}$  planes. Dislocations are energetically stable when they are parallel to the  $\langle 110 \rangle$  directions on the slip planes in DC structure crystals along the high Peierls potential valley. Hence, the shape of a stable dislocation loop is hexagonal with two opposite screw and four  $60^\circ$  segments, as seen in Fig. 2a.

Such a dislocation can move on the plane situated between widely or closely spaced atomic planes, i.e., shuffle-set or glide-set, respectively. From a geometrical perspective, a dislocation on the glide-set plane is extended into two Shockley partial dislocations bounding a ribbon of intrinsic stacking fault, the width of which is determined by the stacking fault energy. Typically the width is around 6–10 nm as in Fig. 3a (Wessel and Alexander 1977). Thus, the  $60^\circ$  segment consists of a  $90^\circ$  and a  $30^\circ$  Shockley partial of Burgers vector  $a/6 \langle 11\bar{2} \rangle$

**Table 1** Basic properties of Si

Atomic weight: $M$	14
Atomic radius: $r$ nm	0.117
Lattice constant: $a$ nm	0.5431
Density: $\rho$ g/cm <sup>3</sup>	2.33
Atomic number in a unit volume: $N$ cm <sup>-3</sup>	$5 \times 10^{22}$
Bandgap (@0 K/@RT): $E_g$ eV	1.17/1.12
Intrinsic carrier density (@RT): $n_i$ cm <sup>-3</sup>	$1.45 \times 10^{13}$
Elastic constant (@RT):	
$C_{11}$ GPa	166
$C_{44}$ GPa	64.0
$C_{12}$ GPa	79.6
Shear modulus: $G$ GPa	60.5
Strength (@ $T_M$ /@(2/3) $T_M$ ): $\tau$ GPa	1.0/40
Surface energy (111): $\gamma$ erg/cm <sup>2</sup>	1230
Linear thermal expansion (@RT/@ $T_M$ ): $\alpha$ K <sup>-1</sup>	$2.6 \times 10^{-6}/4.4 \times 10^{-6}$
Thermal conductivity (@RT/@ $T_M$ ): $\kappa$ W/m K	157/31
Gibbs standard free energy of dioxide formation (@ $T_M$ ): $\Delta G$ kJ/mol	6.80

bounding a ribbon of stacking fault as in Fig. 2b, while the screw segment consists of two 30° Shockley partials in Fig. 2c. On the other hand, a dislocation in the shuffle-set plane is perfect since there are no stable stacking faults on the shuffle planes. Shockley partial dislocations cannot move in the shuffle-set plane without point defect generation and dragging, leading to a nonconservative energy increase. Figure 2d shows a perfect 60° dislocation in the shuffle-set (Hornstra 1958). From the huge number of published reports on observations of dislocations and structures, it is well understood that dislocations at high temperatures are dissociated, while dislocations are considered to be perfect at low temperatures induced under high stress as seen in Fig. 3b (Rabier et al. 2001, 2010). Here, it notes that the Peierls stress, given by the ratio of the magnitude of Burgers vector to the slip plane spacing, for a glide-set dislocation is higher than that for a shuffle-set one.

Dislocations, glide- or shuffle-set, have geometrical dangling bonds at the core. Based on experimental findings of the electronic state of dislocations and theoretical studies, it is considered that such geometrical dangling bonds are reconstructed to form bonds between two neighboring atoms along the dislocation cores to reduce their energy, which is called reconstruction. A possible reconstruction model consists in the pairing of dangling bonds along the dislocation line. There are two types of reconstructions: one is single periodic (SP reconstruction) and the other is duplet periodic (DP reconstruction) in the 90° partial dislocation. In the 30° partial (Fig. 4), the reconstruction is energetically favor in the order of 1 eV per dimer. In the 90° partial, the SP and DP reconstructions have almost comparable energy and may coexist (Bennetto et al. 1997; Lehto and Öberg 1998; Valladares et al. 1998; Justo

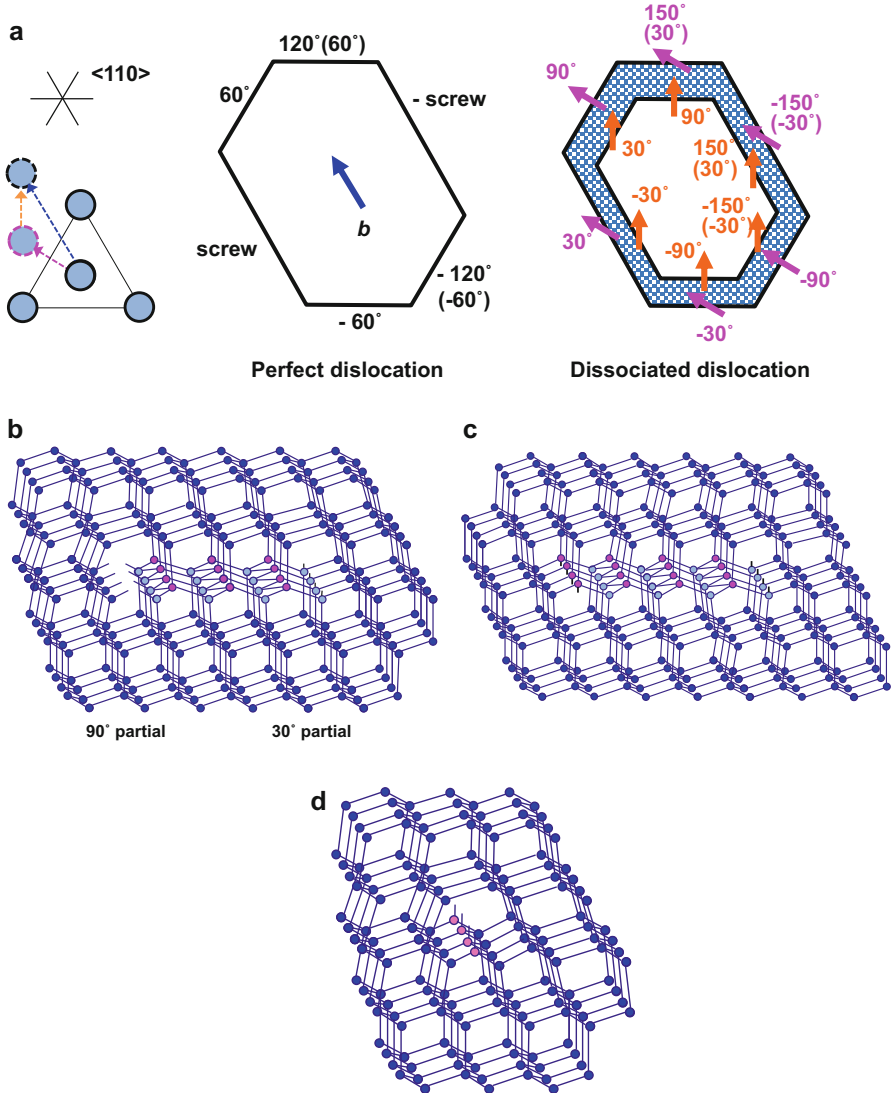


**Fig. 2** (a) Expanding hexagonal loop of perfect and dissociated dislocations in diamond structure. Arrows show perfect and partial displacements of an atom on the (111) plane in the left bottom and correspond to their Burgers vector of each segment of dislocation loops. Atomic configuration of (b) a dissociated  $\langle \text{glide-set} \rangle 60^\circ$  dislocation, (c) a dissociated  $\langle \text{glide-set} \rangle$  screw dislocation, and (d) a perfect  $\langle \text{shuffle-set} \rangle 60^\circ$  dislocation. Stacking fault is between blue and red atomic planes in the glide set. In both sets, red- or sky-colored atoms have a dangling bond

et al. 1999a). Both types of reconstructions leave an unpaired dangling bond along the dislocation line, called an antiphase defect or a soliton, deriving an electrical character into deformed crystals.



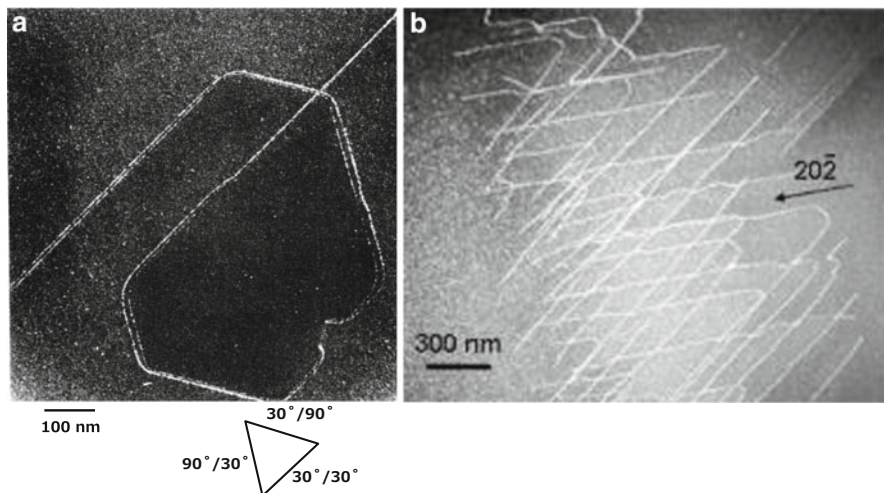


**Fig. 3** (a) A dissociated dislocation loop in Si deformed at 420 °C (by weak-beam observation, from Wessel and Alexander 1977), (b) perfect dislocations in Si deformed at 150 °C (Rabier et al. 2001). (Reused under permissions of Taylor & Francis and Elsevier)

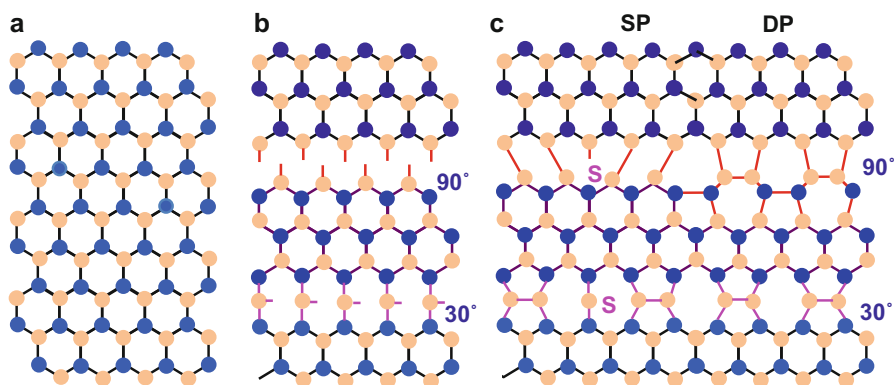


**Fig. 4** (111) plane views of (a) perfect crystal and (b) unreconstructed and (c) reconstructed structure of a 90° and 30° partial dislocations. In (c) unpaired dangling bonds (solitons), single-period (SP) and double-period (DP) reconstructions on partials are illustrated

## Dislocation Motion and Plastic Deformation in High-Purity Si

Plastic deformation of a crystal takes place through the generation, motion, and multiplication of dislocations in the crystal under physical and/or chemical stimulation such as stress and chemical reaction. The processes are governed by the dynamic properties of dislocations. Herein, experimental data on velocities of

dislocations in high-purity or nominally undoped Si crystals are summarized. Some contents are given in the overview by the present author (Yonenaga 2015).

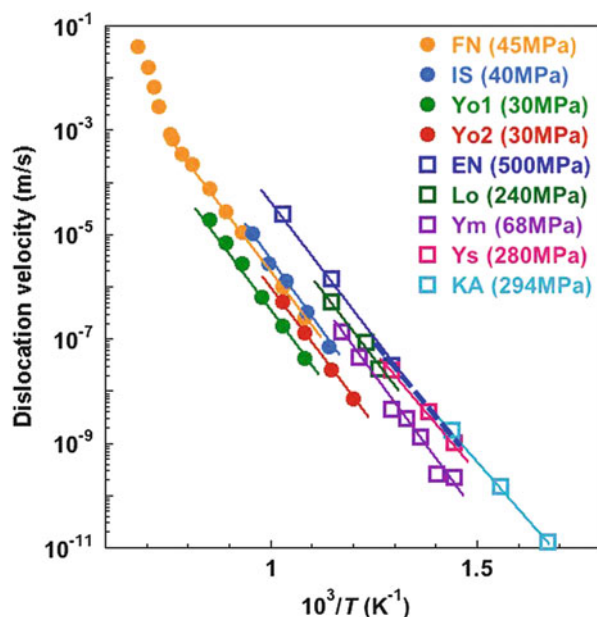
## Dislocation Velocity

A huge number of papers have been published on dislocation velocities in Si crystals. Figure 5 shows the velocities of an isolated  $60^\circ$  dislocation in a temperature range from  $350^\circ\text{C}$  to  $1300^\circ\text{C}$ . The results were obtained by various experimental methods of the ex situ intermittent method as the double and single etch pit techniques, the in situ X-ray topographic and high-voltage transmission electron microscopic (TEM) technique, stressing by the three- and four-point bending or compressive and tensile stressing, static or pulse stress application, and so on. The velocities of dislocations depend strongly on the applied shear stress shown by the numerals in the figure. In a comprehensive view, including the results by microscopic TEM observation, the temperature dependence of dislocation velocities reported by the groups fall into a narrowband with the same slope except for the high-temperature regime. This indicates that the mechanism of dislocation motion is the same in a temperature range with the certain activation energy for dislocation motion. Essentially the same feature was observed for screw dislocations.

The dislocation velocity  $v$  is well expressed by the following empirical equation as a function of applied shear stress  $\tau$  and temperature  $T$ :

$$v = v_0(\tau/\tau_0)^m \exp(-Q/kT), \tau_0 = 1 \text{ MPa}, \quad (1)$$

**Fig. 5** Velocities of  $60^\circ$  dislocations as a function of temperature. FN (Farber and Nikitenko 1982), IS (Imai and Sumino 1983), Yo1 (Yonenaga 1999), Yo2 (Yonenaga unpublished), EN (Erfeev and Nikitenko 1971), Lo (Louchet 1981), Ym (Yamashita et al. 1999), Ys (Yasutake et al. 1987), KA (Küstters and Alexander 1983). Numerals show the stress applied in the studies. Velocity of twins under 280 MPa is superimposed by a blue dotted line (Yasutake et al. 1987)



where  $v_0$ ,  $m$ , and  $Q$  are constants and  $k$  is the Boltzmann constant. Here,  $\tau$  corresponds to the effective stress  $\tau_{\text{eff}}$ , discussed later. Since Si crystals used for these kinds of velocity determination experiments generally have low density of dislocations or no dislocations, the applied stress is almost same as the effective stress. The stress exponent  $m$  and activation energy  $Q$  for dislocation motion of  $60^\circ$  dislocations reported by various groups in Fig. 5 are shown in Table 2 together with the

**Table 2** Magnitudes of  $m$  and  $Q$  for  $60^\circ$  dislocation velocity in Si together with experimental conditions

Groups	$m$	$Q$ (eV)	Stress (MPa)	Temperature ( $^\circ\text{C}$ )	Method
Farber-Nikitenko (1982)	–	4+/-0.1	2–45	1050–1300	*Double etch pit technique
					*4-point pulse bending
Farber-Nikitenko (1982)	–	2.1–2.3	2–45	650–1050	*Double etch pit technique
					*4-point pulse bending
Imai-Sumino (1983)	1	2.20	1–40	603–773	*In situ X-ray topography *Tensile
Yonenaga (1999)	~1	~2.4	3–30	650–950	*Single etch pit technique
					*Surface scratch
					*3-point bending
Yonenaga	~1	~2.3	2–30	560–700	*Single etch pit technique
					*Surface scratch
					*3-point bending
Erofeev-Nikitenko (1971)	1.3–1.43	2.25–2.1	10–500	500–800	*Double etch pit technique
					*4-point bending
Louchet (1981)	(~1.2)	1.9+/-0.1	130–280	520–600	*In situ HVTEM
					*Tensile
Yamashita et al. (1999)	–	2.2	68	420–580	*Double etch pit technique
					*4-point bending
Yasutake et al. (1987)	1.43–1.95	1.96–1.84	80–350	420–500	*Single etch pit technique
					*Surface Knoop impression
					*4-point bending
Küsters-Alexander (1983)	1.87–1.93	1.82	245–326	325–422	*Double etch pit technique
					*Compression
					* $30^\circ/90^\circ$ dislocations

experimental methods and stress and temperature range investigated.  $m$  is 1 or slightly higher than unity, ranging from 1.2 to 1.4 at elevated temperatures, while  $m$  is slightly dependent, increasing to  $\sim 1.9$  with an increase in the applied stress, explicitly at low temperatures.  $Q$  is 2.20–2.40 eV, almost constant under a wide range of applied stress up to 100 MPa, though  $Q$  decreases to around 1.8 eV under a high applied stress, especially at low temperatures. Possibly, the decrease implies an effective reduction of kink formation energy by stress assistance, which is discussed later in terms of the Peierls and kink mechanisms.

In the temperature region from around 1050 °C to the melting temperature, Farber and Nikitenko (1982) reported a strong dependence of dislocation velocity on temperature with  $Q \sim 4$  eV. The cause is understood to be a change of dislocation activation mechanism in relation to the cooperation of self-diffusion (Siethoff 2002).

The shape of moving dislocations was identified to be a regular hexagonal loop or a half-hexagonal loop in in situ and ex situ experiments as seen in Fig. 4a (Wessel and Alexander 1977; Sumino and Harada 1981; Imai and Sumino 1983). Küsters and Alexander (1983) conducted an ex situ experiment where dislocations were generated in advance at a higher temperature and then stressed at 325–422 °C under a stress of 294 MPa. After stressing they observed dislocations in the specimens by TEM and confirmed that dislocations were dissociated as 90° leading and 30° trailing partials (90°/30°) and were well hexagonally shaped. The dissociation width was governed by the applied stresses (Vanderschaeve and Caillard 2007).

In the intermediate-temperature region as 300–500 °C, thin twin bands are observed to develop under a high stress applied (Yasutake et al. 1987). A leading partial dislocation leaves a stacking fault behind it by the motion, if the motion of the paired trailing is slow or in rest. A thin twin develops through such superior motion of leading partial dislocations on successively neighboring atomic planes (Meingast and Alexander 1973). The velocity of a twin, superimposed by the dotted line in Fig. 5, is somewhat higher than that of an isolated dislocation with dependences on applied stress and temperature similar to Eq. (1).

## Plastic Deformation and Yield Strength

Many groups have measured yield strength as a function of temperature for Si by various methods. Figure 6 shows the logarithm of yield strength of Si crystals plotted against the reciprocal temperature from RT to 1300 °C (Yonenaga 2015). Here, the yield strength is defined as the lower yield stress or the first deviation from the linearity (elastic region) of the measured stress-strain curves. It is known that there are two regimes in the temperature dependence of the strength with a knee at 400 °C.

In a temperature regime higher than 600 °C, Si can be deformed by compression or tension under atmospheric pressure. The overall deformation is commonly characterized with a remarkable drop in stress after yielding followed by a gradual increase in stress with strain due to work hardening in the plastic deformation (Yonenaga and Sumino 1978; Yonenaga 1996). The stress-strain behavior depends sensitively on the temperature and the strain rate. The yield strength and the

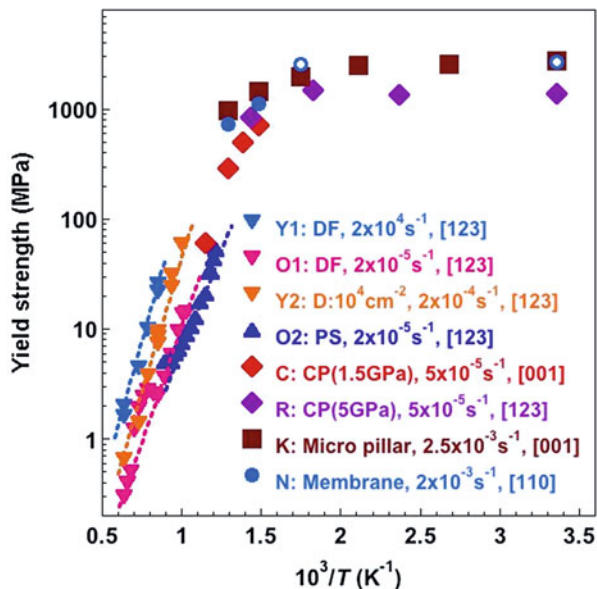


**Fig. 6** Yield strength of Si as a function of temperature. Y1, conventional test of dislocation-free (DF) Si (Yonenaga 1996); O1, conventional test of DF-Si (Omri et al. 1987); Y2, conventional test of Si with grown-in dislocations (Yonenaga and Sumino 1978); O2, conventional test of pre-strained (PS) Si (Omri et al. 1987); C, under a confining pressure of 1.5 GPa (Castaing et al. 1981); R, under a confining pressure of 5 GPa (Rabier et al. 2010); K, compression test of micron-scaled pillars (Korte et al. 2011); N, tension test of membrane Si (Nakao et al. 2008). Sample condition, strain rate for deformation, and axis for stressing are shown in the figure. DF dislocation-free, D dislocated, PS pre-strained, CP under a confining pressure of 1.5 or 5 GPa. Open symbols of N show fracture strength. (Yonenaga 2015; Reused under permission of Elsevier)

subsequent flow stresses decrease with an increase in the temperature, and a decrease in the strain rate brings about the same effect as an increase in the temperature. The yield strength of dislocation-free (DF-) Si such as Y1 is higher than that of Si with grown-in dislocations of  $\sim 10^4 \text{ cm}^{-2}$  as Y2 though there is a limit of the temperature region without fracture before the appearance of ductility. Also, Si pre-strained (PS) in advance at a high temperature (O2) can be deformed at temperatures as low as around  $550 \text{ }^\circ\text{C}$ , slightly lower than that for DF-Si (O1) (Omri et al. 1987). Grown-in dislocations or pre-induced dislocations act as a multiplication source of dislocations for deformation to shift a so-called brittle-to-ductile transition temperature  $T_{\text{BDT}}$  to the lower temperature (see section “[Brittle-to-Ductile Transition](#)”).

In the temperature regime lower than  $600 \text{ }^\circ\text{C}$ , Si can be deformed using specially arranged hydrostatic equipment. As noted for fracture at RT, the size of a specimen for deformation is quite critical. Small, thin plates (membranes), or micron-scaled pillars have been deformed by compression or tension at atmospheric pressure (Nakao et al. 2008; Korte et al. 2011). Nakao et al. (2008) conducted tension tests of micromembrane Si specimens of  $4 \text{ }\mu\text{m}$  in thickness. At temperatures higher than  $300 \text{ }^\circ\text{C}$ , specimens showed the elastic to plastic feature of the stress-strain curves

with development of slip lines before fracture, while at the lower temperatures, the stress-strain relationships were linear until the fracture, showing elastic deformation and then brittle fracture. The yield or fracture strength at temperatures lower than 300 °C were almost constant as ~2.8 GPa. Korte et al. (2011) and Rabier et al. (2013) conducted compression testing of micro-pillars at temperatures up to 500 °C under atmospheric condition. Micro-pillars with diameters of 2 μm were uniaxially deformed along the [001] direction. Stress-strain curves showed little plasticity followed by brittle fracture at RT, concurrent plasticity and cracking at 200 °C, and plastic deformation at 400 °C. Yield stresses at temperatures lower than 300 °C were almost constant as ~2.5 GPa. They observed micro-cracks in specimens deformed at 100 °C and twinning and partial dislocations at 500 °C. Minor et al. (2005) observed dislocation generation in nano-size wedges during in situ indentation in a TEM at RT.

Bulk specimens with a size similar to that for deformation at higher temperatures can be compressively deformed without fracture under a confining (hydrostatic) pressure of 1.5–5 GPa, as explored by the Castaing-Veyssi re-Rabier group (Castaing et al. 1981; Rabier et al. 2010). Strangely, the reported stress-strain curves were not accompanied by yielding or subtle yielding phenomena, depending on the confining pressure. The confining media probably damage specimen surfaces during the deformation (Castaing et al. 1981; Rabier et al. 1983, 2010). In the temperature region higher than 300–400 °C, the temperature dependence of the yield strength is similar to or varies slightly lower than that without pressure. Contrarily, in the low-temperature region below 300–400 °C to RT, the yield strength of Si is almost constant as ~1.5 GPa as seen in Fig. 6 (Si-R), showing a drastic change of temperature dependence.

In the experimental experiences except at extreme temperatures close to the melting temperature, the yield stress  $\tau_y$  of Si in the temperature range higher than the knee around 300–400 °C is described as a function of temperature  $T$  and strain rate  $\dot{\epsilon}$  by the following empirical equation (Yonenaga and Sumino 1978; Yonenaga 2005d):

$$\tau_y = A\dot{\epsilon}^{1/n} \exp(U/kT), \quad (2)$$

where  $A$ ,  $n$ , and  $U$  are constants.  $n$  is reported to be  $\approx 3$  (Yonenaga 1978; Schr ter et al. 1983). Table 3 gives  $U$  experimentally reported for the results shown in Fig. 6.

**Table 3** Magnitudes of  $n$  and  $U$  for yield strength in Si

	$n$	$U$ (eV)	Conditions
Yonenaga (1996)	–	0.80	[123] tension, $2 \times 10^{-4} \text{ s}^{-1}$ Dislocation-free
Omri et al. (1987)	–	0.79	[123] compression, $2 \times 10^{-4} \text{ s}^{-1}$ Dislocation-free
Yonenaga-Sumino (1978)	3.3	0.80	[123] tension, $2 \times 10^{-4} \text{ s}^{-1}$ Grown-in dislocations: $2 \times 10^4 \text{ cm}^{-2}$
Omri et al. (1987)	–	0.72	[123] compression, $2 \times 10^{-5} \text{ s}^{-1}$ Pre-strained

**Fig. 7** Lower yield stress of dislocation-free Si at high temperatures as a function of temperature. Dislocation-free CZ- and FZ-Si. Y1 (Yonenaga 1996), O1 (Omri et al. 1987), S (Siethoff et al. 1999). Yield strength (0.2% toughness) of polycrystalline Si is superimposed (Omri et al. 1985)

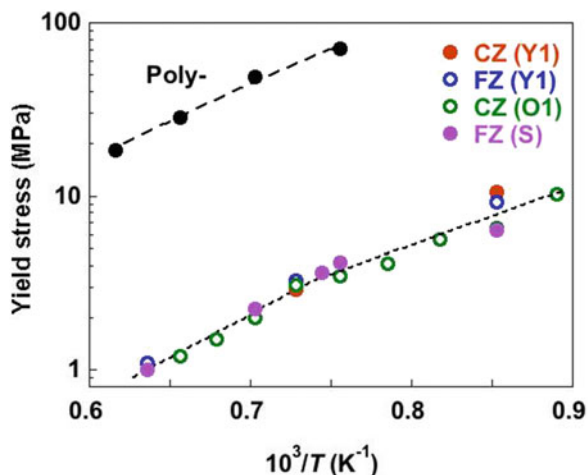


Figure 7 shows the yield strength of dislocation-free Si crystals plotted against a reciprocal temperature at temperatures close to the melting point. The lower yield stress in the temperature region shows the temperature dependence with  $U \approx 1.3$  eV, steeper than that in the lower temperatures. This implies that dislocations move more easily corresponding to the results by Farber and Nikitenko (1982) shown in Fig. 5, probably due to the cooperation of self-diffusion.

## Dislocation Mechanism

### Hirth-Lothe Kink Diffusion Model

It is commonly accepted that the elementary process of dislocation glide in semiconductors consists of the thermally activated nucleation of a kink pair of critical separation on a dislocation line lying along the Peierls valley and the subsequent migration of the nucleated kink along the dislocation line as a second-type Peierls potential. Hirth and Lothe (1982) derived the following equation of a dislocation velocity described by the kink diffusion model:

$$v = (bh^2\nu_D/kT)\tau L \exp[-(F_{kp} + W_m)/kT], \quad (3)$$

where  $b$  is the magnitude of the Burgers vector  $\mathbf{b}$  of a dislocation,  $h$  is the distance between adjacent Peierls valleys [ $h = (\sqrt{3})b/2$ ],  $\nu_D$  is the Debye frequency attempting kink formation and migration,  $L$  is the length of the moving dislocation,  $W_m$  is the activation energy for migration of a kink, and  $F_{kp}$  is the activation energy for formation of a kink pair, determined by the formation energy of a single kink  $F_k$  in a function of stress as



$$F_{kp}(\tau) = 2F_k - \sqrt{(\mu\tau b^3 h^3 / 2\pi)}, \quad (4)$$

$\mu$  is the shear modulus. Though the dislocation velocity increases linearly with the length of the moving dislocation  $L$  in Eq. (3), currently the velocity is considered to become length-independent at around 1–2  $\mu\text{m}$  since the kink migration is considered to be impeded by some localized obstacles on the mean separation  $L^*$  along the dislocation line (Maeda and Takeuchi 1996; Vanderschaeve et al. 2000). The dislocation can overcome the obstacle to go forward when a kink of opposite sign migrates to the location to annihilate the kinks. In such the case,  $L$  in Eq. (3) is replaced by  $L^*$ . Here, it should be noted that Eq. (3) corresponds to the so-called kink-collisionless case. In a kink-collision case where the kink collides and annihilates another kink of the opposite sign generated on the same line, Eq. (3) is given as

$$v = (2b^2 h^2 \nu_D / kT) \tau \exp[-(F_{kp}/2 + W_m) / kT]. \quad (5)$$

However, this case has not been reported experimentally up to now.

Equation (3) has a form similar to the experimentally determined one given by Eq. (1) with respect to the dependence of the dislocation velocity on the stress and the temperature. The activation energy  $Q$  in Eq. (1) is the sum of  $F_{kp}$  and  $W_m$  in Eq. (3).  $F_{kp}$  depends on the stress  $\tau$  and may lead to the observed reduction of  $Q$  under the high stress at low temperatures in Fig. 5 and Table 2. This also explains the observed feature that the stress exponent  $m$  is experimentally observed to be higher than 1, especially under high stress at low temperature as seen in Fig. 5 and Table 2, though dislocation velocity is expected to be proportional to the stress, i.e.,  $m = 1$  in the Hirth-Lothe model. Distinguished determinations of activation energies of  $F_{kp}$  and  $W_m$  are limited in in situ stressing experiments using a TEM, as shown in Table 4 (Louchet et al. 1993; Kolar et al. 1996).

As noted in section “Dislocation Structures,” a dislocation on the glide-set plane (glide-set) is extended into two Shockley partial dislocations bounding a ribbon of intrinsic stacking fault. A partial dislocation operates according to the kink diffusion mechanism, as in the case of a perfect dislocation, where  $b$  in Eq. (3) should be replaced by  $b_p$  of the magnitude of the Burgers vector of a partial

**Table 4** Magnitudes of  $F_k$  and  $W_m$  for dislocations in Si evaluated experimentally and theoretically

Groups	Dislocation type	$F_k$ (eV)	$W_m$ (eV)
<i>Experiments</i>			
Louchet et al. (1993)	Glide set 60°	0.9	1.3
Kolar et al. (1996)	Glide set 90°	0.73	1.24
<i>Calculations</i>			
Cai et al. (2000)	Glide-set screw 30–30°	0.7	1.2
Pizzagalli and Beauchamp (2008)	Glide set 30°	0.8	1.24
Pizzagalli and Beauchamp (2008)	Shuffle-set screw	1.13	0.09



dislocation ( $=b/\sqrt{3}$ ). Activation energies  $F_k$  and  $W_m$  for partial dislocations are shown in Table 4, reported by high-resolution TEM observations (Kolar et al. 1996).

As seen in Table 4, activation energies  $F_k$  and  $W_m$  for glide-set dislocations or partial dislocations are sufficiently fitted to those derived theoretically (Cai et al. 2000; Pizzagalli and Beauchamp 2008). The partial dislocations move in correlation with each other and with the connecting stacking fault. Indeed, Cai et al. (2000) derived pronounced effects of intrinsic coupling of the dissociated partials of a screw dislocation with kinetic Monte Carlo simulations and evaluated dislocation velocities, consistent with experimentally observed velocities. Simulated activation energies of  $F_k$  and  $W_m$  for a shuffle-set screw dislocation are shown in Table 4. It is remarkable that  $W_m$  is very small, though up to now there have been no experimental reports on  $F_k$  and  $W_m$  for shuffle-set dislocations. Here, many groups, especially the Bulatov group and Pizzagalli group, have reported a huge number of theoretical evaluations of  $F_k$  and  $W_m$  of partial dislocations or kinks (Bulatov et al. 2001; Pizzagalli 2016).

## Dislocation Dynamics in Deformation

In the temperature range above the break at around 400 °C, the macroscopic deformation of various semiconductor crystals is rate-controlled by the collective motion of dislocations known as the Alexander-Haasen-Sumino model (Alexander and Haasen 1968; Yonenaga and Sumino 1978; Suezawa et al. 1979; Alexander 1986; Sumino 1994). The flow stress  $\tau_a$  for deformation of a crystal is the stress needed to move dislocations within the crystal at a certain velocity that is determined by the strain rate and the density of dislocations in motion. The stress consists of two components: one is the effective stress  $\tau_{\text{eff}}$  for motion against the Peierls potential and the other is the internal stress  $\tau_i$  which is the component which overcomes the resistance originating from the interaction between dislocations,

$$\tau_a = \tau_{\text{eff}} + \tau_i, \quad (6)$$

$$\tau_i = \mu b \sqrt{N} / \beta, \quad (7)$$

$$\tau_{\text{eff}} = \tau_a - \mu b \sqrt{N} / \beta, \quad (8)$$

where  $N$  is the density of moving dislocations in the crystal and  $\beta$  is an interaction parameter on the order of 3–4. All dislocations are assumed to be mobile in the initial stage of deformation considered here.

In plastic deformation under a constant strain rate, the strain rate  $\dot{\epsilon}$  apparently given by the experimental instrument is the sum of the elastic strain rate  $\dot{\epsilon}_{\text{el}}$  and the plastic strain rate  $\dot{\epsilon}_{\text{pl}}$ . The plastic strain rate  $\dot{\epsilon}_{\text{pl}}$  is given as the product of the velocity  $v$  and density of moving dislocations  $N$ :

$$\dot{\epsilon} = \dot{\epsilon}_{\text{el}} + \dot{\epsilon}_{\text{pl}}, \quad (9)$$

$$\dot{\epsilon}_{\text{pl}} = Nbv. \quad (10)$$

The dislocation velocity in the model is given according to Eq. (1) as

$$v = v_0(\tau_{\text{eff}}/\tau_0)^m \exp(-Q/kT) = v_0[(\tau_a - \mu b\sqrt{N}/\beta)/\tau_0]^m \exp(-Q/kT),$$

$$\tau_0 = 1 \text{ MPa}. \quad (11)$$

Thus, the flow stress  $\tau_a$  is given as follows:

$$\tau_a = \tau_0(\dot{\epsilon}_{\text{pl}}/v_0b)^{1/m}N^{-1/m} \exp(Q/mkT) + \mu b\sqrt{N}/\beta. \quad (12)$$

After starting deformation by applying stress under a given strain rate,  $N$  increases through self-multiplication proportional to  $\tau_{\text{eff}}$  and the crystal passes through two points of stress-strain curve where the stress is constant, and thus  $\dot{\epsilon}_{\text{el}} = 0$ ; these are the upper and lower yield points. After the first point, the stress decreases due to  $\dot{\epsilon}_{\text{el}} < 0$ , and  $\dot{\epsilon}_{\text{pl}}$  ( $=Nbv$ ) becomes a maximum higher than  $\dot{\epsilon}$ . This is the so-called yield drop. Then, an increasing rate of  $N$  induces to the reduction of  $\dot{\epsilon}_{\text{pl}}$  according to Eqs. (1) and (8). When a decrease of  $\dot{\epsilon}_{\text{pl}}$  is initiated after the maximum,  $\dot{\epsilon}_{\text{pl}}$  approaches the given  $\dot{\epsilon}$ . Thus, at the lower yield point, the crystal reaches a certain kind of steady state of plastic deformation under the given condition of strain rate and temperature with minimum stress. The lower yield stress  $\tau_y$  is given by minimizing Eq. (12) with respect to  $N$  at  $\dot{\epsilon}_{\text{pl}} = \dot{\epsilon}$  as follows:

$$\tau_y = C(\dot{\epsilon}/v_0b)^{1/(m+2)} \exp(Q/(m+2)kT), \quad (13)$$

$$C = (m+2) \left[ (\mu b/\beta)^2 (\tau_0/m)^m / 4v_0b \right]^{1/(m+2)}. \quad (14)$$

Here, when a crystal contains a sufficiently high density of dislocations in the initial deformation, there is no appearance of the first (upper) yield point. Dislocation density approaches that at the (lower) yield point, i.e., without a yield drop phenomenon.

Now, it has been verified that the constants  $m$  and  $Q$  in Eq. (1) have the following relations with  $n$  and  $U$  in Eq. (2):

$$m = n - 2, Q = U * n. \quad (15)$$

Indeed, the values shown in Tables 2 and 3 well follow the above relations. A more accurate discussion, including immobilized dislocations during plastic deformation, is given in the paper by Sumino and Yonenaga (1993). Recently, Cochard et al. (2013) have successfully developed a constitutive approach to simulate stress-strain behavior of Si crystals based on the AHS model. On the other hand, a mechanism

determining the yield strength in the low-temperature regime has not yet been clarified.

## Controversy of Shuffle- or Glide-Set Dislocations

As noted in section “[Plastic Deformation and Yield Strength](#),” the temperature dependence of yield strength drastically changes in the two regimes. The involvement of this feature was also considered in the dislocation mechanism rate-controlling the deformation, especially in the low-temperature regime, and brought the so-called shuffle-glide controversy on the core structure of dislocations (Duesbery and Joós [1996](#); Suzuki et al. [1999](#)).

From many observations by weak-beam and high-resolution TEM of deformed samples, it is widely accepted that almost all dislocations induced at high temperatures are dissociated into two Shockley partial dislocations bounding a ribbon of stacking fault (Ray and Cockayne [1971](#); Sato et al. [1980](#); Ohno et al. [2010](#)). That is, glide-set dislocations move easily and control plastic deformation in the high-temperature regime. Indeed, Kolar et al. ([1996](#)) demonstrated paired partial dislocations with double kinks by plan-view high-resolution TEM.

In the low-temperature regime, the Rabier group reported the existence of perfect, straight, zig-zag, or wavy dislocations in Si deformed at RT and 150 °C and at high stress of ~1 GPa under a confining pressure (Rabier et al. [2001](#), [2010](#)). Dislocations lie not only along the usual  $\langle 110 \rangle$  Peierls valleys but also along unusual  $\langle 112 \rangle$  and  $\langle 123 \rangle$  Peierls valleys. The Saka group observed by TEM that perfect dislocations were nucleated by indentation tests and thermal stress at temperatures up to 500 °C, and that the dislocations transformed into a dissociated form of glide-set by subsequent annealing at 400–500 °C (Saka et al. [2006](#); Izumi et al. [2010](#); Okuno and Saka [2013](#)). These results suggest that a shuffle-set dislocation is nucleated and moves in the low-temperature regime at high stress under a confining pressure. However, it should be remembered that Korte et al. ([2011](#)) observed weakly dissociated screw dislocations in a micro-pillar deformed at 100 °C under atmospheric pressure. Also, Küsters and Alexander ([1983](#)) showed widely extended dislocations in a specimen moved at 325–422 °C under a stress of 294 MPa. It notes that the dislocations were introduced in advance by prestressing at higher temperature in their experiment.

Some theoretical approaches with *ab initio* calculation derived that a shuffle-set dislocation is favorable under high stress (Godet et al. [2009](#); Shima et al. [2010](#)). The activation energy for nucleation of a shuffle-set dislocation is lower than that of a glide-set one under a stress above 4 GPa (Shima et al. [2010](#)). This also suggests that a glide-set dislocation is dominant at elevated temperatures since the stress for dislocation generation and motion is much lower than the value. In the intermediate-temperature regime, there may be a transient deformation mode as glide of mobile partial dislocations, leading twins (Yasutake et al. [1987](#); Pirouz et al. [1999](#); Takeuchi [2004](#)). Transformation of dislocations from shuffle-set to glide-set is being modeled by several research groups (Rabier [2013](#); Li and Picu [2013](#); Rodney et al. [2017](#)).

Modeling of dislocation core structures is being conducted intensively by Pizzagalli group (Pizzagalli 2016; Rodney et al. 2017).

---

## Impurity Effects on Dislocation Activities

Establishing knowledge on dislocation-impurity interaction is important from both the fundamental and practical viewpoints for development of semiconductor technology. In CZ-Si, oxygen (O) and nitrogen (N) impurities are well known to have a strong effect on dislocation immobilization due to preferential segregation (Sumino and Yonenaga 1994, 2002; Yonenaga and Sumino 1996; Yonenaga 2005a), and the findings are widely used as basic knowledge in Si crystal growth and device fabrication process. In recent advanced Si technology, wafers prepared from large-diameter crystals heavily doped with electrical impurities are used as substrate for the epitaxial growth of clean materials without grown-in defects.

## Critical Stress for Dislocation Generation

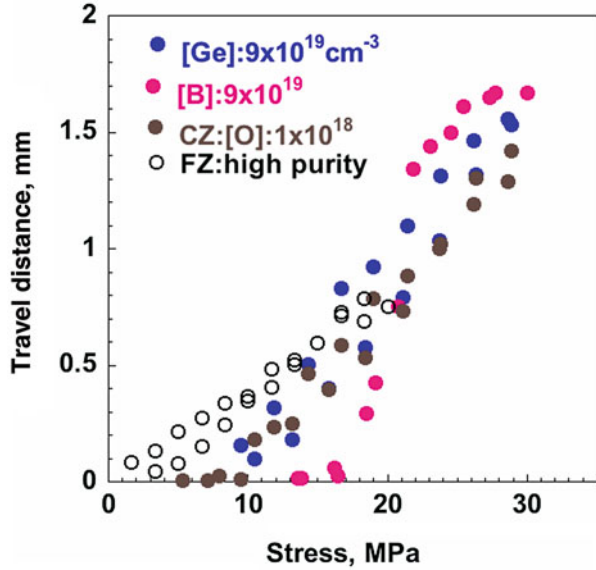
Dislocations are easily generated from the surface flaws in high-purity or nominally non-doped semiconductors even under extremely low stresses at high temperatures. However, in a semiconductor doped with certain kinds of impurities, there is a critical stress below which no dislocation generation takes place even though the flaw accompanies a dislocated micro-region. Making use of intentionally introduced surface flaws such as indentations or scratches, the investigation on how various kinds of impurities affect the generation process of dislocations in different kinds of semiconductors was performed (Yonenaga et al. 2001, 2003; Yonenaga 2005a, b).

Figure 8 shows the distance traveled by the leading  $60^\circ$  dislocation in an array of dislocations that are generated from a scratch plotted against the resolved shear stress for various Si crystals. No appreciable critical stress is measured for dislocation generation in high-purity FZ-Si, whereas a certain critical stress exists for the generation of dislocations in high-purity (O-containing), B-doped, and Ge-doped CZ-Si. The magnitude of the critical stress is  $\sim 7$  MPa in high-purity and Ge-doped CZ-Si. On the other hand, the critical stress is as high as  $\sim 13$  MPa in B-doped CZ Si.

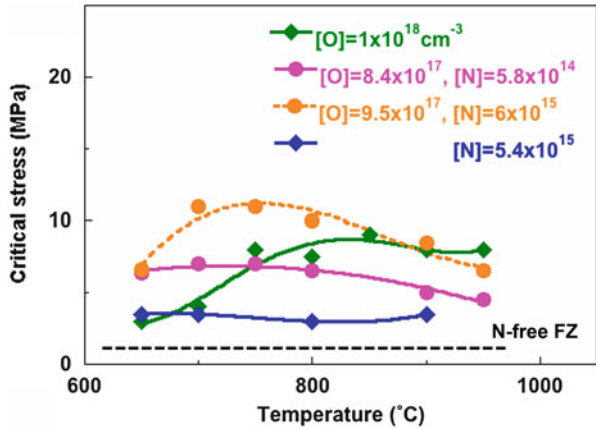
Once the stress exceeds the critical stress for dislocation generation, the travel distance in the high-purity, B-doped, and Ge-doped CZ-Si increases rapidly with stress. In such cases, the travel distance versus stress relationship usually shows a break at some high stress; beyond which the travel distance increases with respect to stress at approximately the same rate as that found for high-purity FZ-Si. At high stress, the travel distance versus stress relationship for high-purity CZ-Si almost overlaps with that of high-purity FZ-Si. The travel distance of dislocations in B-doped and Ge-doped CZ-Si is larger than that in high-purity FZ-Si.

The critical stress for dislocation generation from a surface scratch, termed generation stress  $\tau_c$ , hereafter, depends on the stressing temperature. Figure 9 shows the generation stresses of dislocations in conventional CZ-Si (i.e., O-containing Si) and

**Fig. 8** Travel distance of leading  $60^\circ$  dislocations generated from a scratch during a 10 min stress pulse at  $800^\circ\text{C}$  in various Si crystals plotted against stress. Numerals show the impurity concentration in the crystals

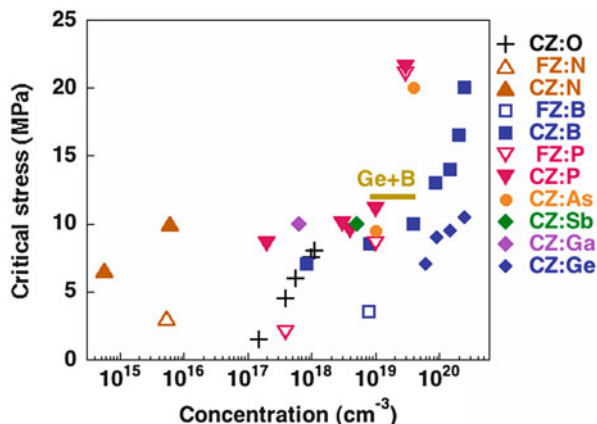


**Fig. 9** Temperature dependence of the critical stress for generation of  $60^\circ$  dislocations in various Si crystals. Numerals show the impurity concentration in the crystals. The dotted black line shows temperature dependence of the critical stress for N-free FZ-Si



nitrogen (N)-doped Si crystals as a function of temperature. In the N-free FZ-Si, dislocations are generated even under a stress lower than 1 MPa at temperatures up to  $900^\circ\text{C}$ . In N-free CZ-Si, the generation stress of dislocations increases with increasing temperature from  $\sim 3$  MPa at low temperatures to  $\sim 8$  MPa in the high-temperature range of  $750\text{--}900^\circ\text{C}$ . In the N-doped CZ-Si, the generation stress is high or becomes high in the temperature range lower than that in N-free CZ-Si and then decreases gradually as the temperature increases. The higher the generation stress, the higher the concentration of involved N impurity in the CZ-Si crystals. At temperatures higher than  $900^\circ\text{C}$ , the generation stress of dislocations is lower in the N-doped CZ-Si

**Fig. 10** Variation in the critical stress for generation of  $60^\circ$  dislocations at  $800^\circ\text{C}$  against the concentration of O, N, B, P, As, Sb, Ga, and Ge impurities in CZ- or FZ-Si crystals. The bar denotes the critical stress in Ge and B co-doped Si at concentrations of  $4 \times 10^{19}$  and  $9 \times 10^{18} \text{ cm}^{-3}$ , respectively. The solid and open marks CZ- and FZ-Si, respectively



crystals than in the N-free CZ-Si. Generation stress is almost constant at about 3 MPa in the N-doped FZ-Si in the whole temperature range investigated. Thus, N impurity has an enhanced effect on the suppression of dislocation generation in cooperation with O impurity in Si at temperatures of  $650\text{--}900^\circ\text{C}$  (Yonenaga 2005a).

Figure 10 shows the dependence of the critical stress for dislocation generation at  $800^\circ\text{C}$  on the concentration of doped impurities in CZ-Si crystals. Data for various concentrations of O impurity are also included in the figure. The critical stress increases with increasing O concentration and becomes 8 MPa at about  $10^{18} \text{ cm}^{-3}$ , the standard level of O concentration in CZ-Si. The critical stress starts to increase remarkably when B, P, and As concentrations exceed  $1 \times 10^{19} \text{ cm}^{-3}$ . This means that B, P, and As impurities at concentrations higher than  $\approx 1 \times 10^{19} \text{ cm}^{-3}$  effectively suppress the generation of dislocations. Thus, the critical stress for dislocation generation observed within crystals doped with concentrations of B, P, and As impurities less than  $1 \times 10^{19} \text{ cm}^{-3}$  can be understood to be mainly due to the effect of O impurity. B and P impurities in FZ-Si have also been found to suppress dislocation generation (Yonenaga 2004). However, the critical stresses for dislocation generation in FZ-Si are lower than those in CZ-Si. The suppression of dislocation generation by Sb impurity is not clear because its solubility limit into Si is lower than those of B, P, and As impurities. In Ge-doped Si, the magnitude of the critical stress for dislocation generation is 8 MPa, i.e., the same as the critical stress for high-purity CZ-Si, and increases slightly to  $\approx 10$  MPa when the Ge concentration exceeds  $10^{20} \text{ cm}^{-3}$ . However, Ge impurity even at a high concentration of  $2.5 \times 10^{20} \text{ cm}^{-3}$  is not effective for suppression of dislocation generation. Indeed, in the dilute SiGe alloys with Ge content of 0.4 at%, strong suppression of dislocation generation has not been observed (Yonenaga 2005c). Contrarily, in (Ge + B) co-doped CZ-Si, the critical stress of dislocation generation is higher than that in Si independently doped with either B or Ge. This shows the effect of (Ge + B) co-doping effect on the suppression of dislocation generation, though such effect is weaker than that observed at  $800^\circ\text{C}$  (Yonenaga et al. 2003). In N-doped CZ-Si, the critical stress for dislocation generation is 9 MPa, somewhat higher than that in high-purity CZ-Si.

## Dislocation Immobilization

Suppression of dislocation generation from a scratch or surface flaw under low stress has been observed for dislocations in Si (Sumino and Harada 1981; Sumino and Imai 1983; Sumino et al. 1983; Sato and Sumino 1985; Sumino and Yonenaga 2002; Jurkschat et al. 2001; Yonenaga and Sumino 1996; Yonenaga et al. 2001, 2003; Yonenaga 2004) doped with certain kinds of impurity. Dislocations are nucleated around a scratch/surface flaw and immobilized due to the impurity segregation along the dislocations even while the crystal is being heated to the test temperature (Sumino and Yonenaga 2002; Yonenaga 2005a). That is, the observed critical stress for dislocation generation from a scratch can be understood as the stress required to initiate dislocation motion from the immobilized state and to penetrate the matrix crystal, which can be detected macroscopically as dislocation generation from the scratch (Fig. 11). This stress is termed release stress  $\tau_R$ .

The characteristic features of dislocation-impurity interaction can be evaluated through the analysis of the stressing temperature dependence of the release stress of aged dislocations. Figure 12 shows the release stress for dislocations in various Si crystals aged at 900 °C for 15 min plotted against the stressing temperature. The release stress decreases linearly with an increase in the stressing temperature,

**Fig. 11** A model of macroscopically observed dislocation generation influenced by impurity segregation

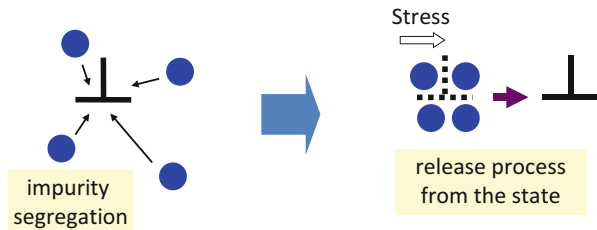


**Fig. 12** Stressing temperature dependence of release stress  $\tau_R$  for dislocations aged at 900 °C for 15 min in various types of CZ-Si

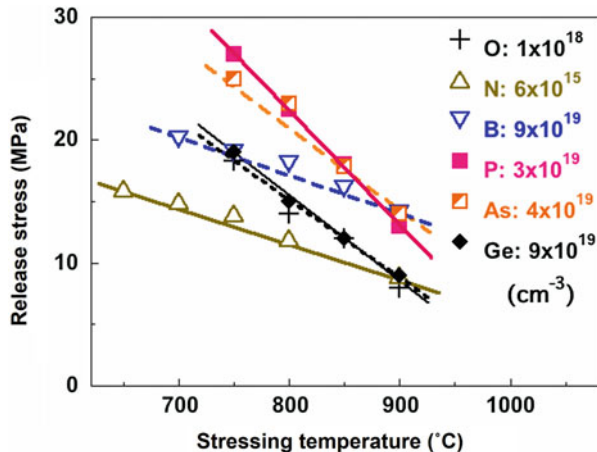


**Table 5** Magnitudes of  $E$  and  $N$  for dislocations in the impurity-doped CZ-Si crystals

Impurity concentration ( $\text{cm}^{-3}$ )		$E$ (eV)	$N$ ( $\text{cm}^{-1}$ )
O	$1 \times 10^{18}$	3.6	$2.4 \times 10^5$
N	$6 \times 10^{15}$	4.1	$1.0 \times 10^5$
P	$3 \times 10^{19}$	3.6	$3.4 \times 10^5$
As	$4 \times 10^{19}$	3.7	$2.8 \times 10^5$
B	$9 \times 10^{19}$	4.5	$1.1 \times 10^5$
Ge	$9 \times 10^{19}$	3.6	$2.6 \times 10^5$

showing that the process is thermally activated. A theory of the thermally activated release of dislocations from locking agents gives the following relation between the release stress  $\tau_R$  and the temperature  $T$ :

$$\tau_R = [E - kT \ln(LN\nu/\Gamma)]Nb^2, \quad (16)$$

where  $E$  is the maximum interaction energy between a dislocation and a locking agent,  $L$  the length of the dislocation,  $N$  the mean density of locking agents along the dislocation line,  $\nu$  the vibration frequency of the dislocation, and  $\Gamma$  the release rate of the locked dislocation (Sumino and Imai 1983; Sato and Sumino 1985; Sumino and Yonenaga 2002; Yonenaga 2004). By using Eq. (16), the density of the pinning agents along the dislocation line  $N$  and the interaction energy  $E$  in the crystals were evaluated as shown in Table 5. The experimentally estimated magnitudes of interaction energy  $E$  are 3–4 eV, too high to be interpreted with a model in which the dislocations interact elastically with individual impurity atoms. The magnitudes of line density  $N$  are  $1\text{--}3 \times 10^5 \text{ cm}^{-1}$ , much smaller than that expected from the concentration of the impurity atoms individually dispersed in the matrix. This result indicates the following image: impurity atoms dispersed within the matrix segregate at dislocations at rest and pipe diffuse along the dislocation line, meeting and coagulating at some discretely separated sites on the dislocation line. As a result, the dislocations are locked/immobilized by such complexes or clusters, which may include a few impurity atoms, intrinsic point defects, or O atoms in CZ-Si. Indeed, agglomerates were detected along a dissociated dislocation in P-doped Si annealed for a prolonged duration as seen in Fig. 13. Radial strain fields about 10 nm in diameter were observed nearby the partial dislocations, and it was known by means of the energy-dispersive X-ray spectroscopy (EDX) that the agglomerates are P-based.

Table 5 means that B and N impurities have larger interaction energy  $E$  and lower density  $N$  than O, Ge, As, and P impurities, which implies that B and N impurities contribute to the prompt formation/development of stronger locking agents with lower density along dislocations. In contrast, P and As impurities are known to form a high density of locking agents, resulting in high release stress. The magnitudes of the release stress and  $E$  and  $N$  in Ge-doped CZ-Si are comparable to those in high-purity CZ-Si. This supports the experimental result in Fig. 10 that Ge impurity even at a high concentration of  $2.5 \times 10^{20} \text{ cm}^{-3}$  does not suppress dislocation generation and confirms that Ge has no effect on dislocation immobilization. In P-doped CZ-Si,



**Fig. 13** A TEM image of a dissociated dislocation in P-doped Si annealed at 900 °C for 10.5 h. Radial strain fields on partial dislocations show P-based agglomerates

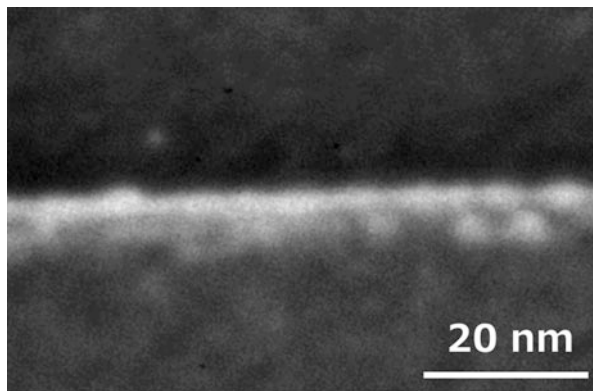


**Table 6** Formation and pinning energies of various impurities on 90° partial dislocation. The location is given by superscripts; (b) a bulk site, (c) a core site, (s) a soliton site, (oc) an off-site. Numerals show energies in a unit of eV (Heggie et al. 1993)

B	P	As	O	N
$B^b \rightarrow B^c+0.4$	$P^b \rightarrow P^c+0.4$	$As^b \rightarrow As^c+0.7$	$O^b \rightarrow O^{oc}+0.3$	$N^b \rightarrow N^c+0.6$
$B^b \rightarrow B^s+2.5$	$P^b \rightarrow P^s+2.3$	$As^b \rightarrow As^s+2.5$	$O_2^b \rightarrow O_2^c+2.5$	$N^b \rightarrow N^s+3.4$
$2B^b \rightarrow B_2^c+2.2$	$2P^b \rightarrow P_2^c+1.7$	$2As^b \rightarrow As_2^c+2.1$	$2O^b \rightarrow O_2^c+4.5$	$2N^b \rightarrow N_2^c+2.6$

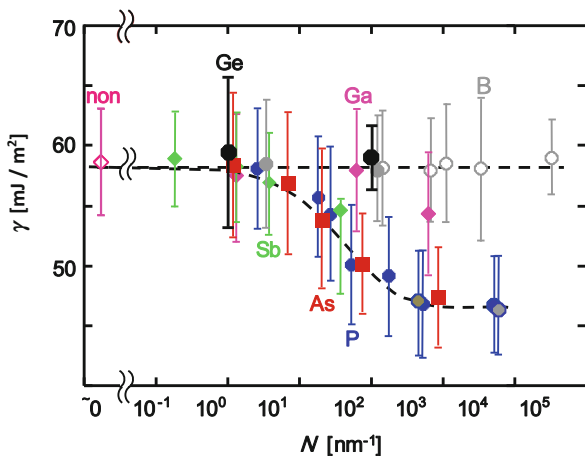
the density  $N$  is higher than that in P-doped FZ-Si, which suggests that a combination of a P atom with an O atom leads to the formation of locking agents with higher density along a dislocation line than in the case of an individual P atom. Similarly, in (Ge + B) co-doped Si, the interaction energy  $E$  is slightly higher, and the density  $N$  is lower than that in high-purity CZ-Si. Strong locking agents are probably constructed in cooperation with Ge and B atoms, resulting in the immobilization of dislocations. These features indicate that a unique reaction of impurities occurs at a dislocation site. It should note that oxygen precipitation might be affected or suppressed in CZ-Si heavily doped with electrically active impurities in comparison to the well-known observations in conventional CZ-Si.

By theoretical approaches with ab initio calculation, Heggie et al. (1993) indicated the preferential occupation of certain impurities on a soliton site of the 90° partial dislocation, originating in elastic and strong chemical interactions, especially for group III and V atoms, as seen in Table 6. Recently, Zirbarth et al. (2015) reported segregation of iron (Fe) atoms at various reconstructed dislocation cores as 30°, 90° SP, and 90° DP (see section “Dislocation Structures”).

## Suzuki Effect

Various impurities segregate on a dislocation (partial dislocations) in Si. Oxygen precipitates develop along a dissociated dislocation line with its climb as observed by TEM (Minowa et al. 1991; Yonenaga and Sumino 1996). In addition, it has been

**Fig. 14** The apparent stacking fault energy  $\gamma$  vs the maximum number of dopant atoms that can agglomerate near by a unit length of dissociated dislocations  $N$ . The closed and open marks mean the data for CZ-Si and FZ-Si, respectively. (Ohno et al. 2012; Reused under permission of Elsevier)

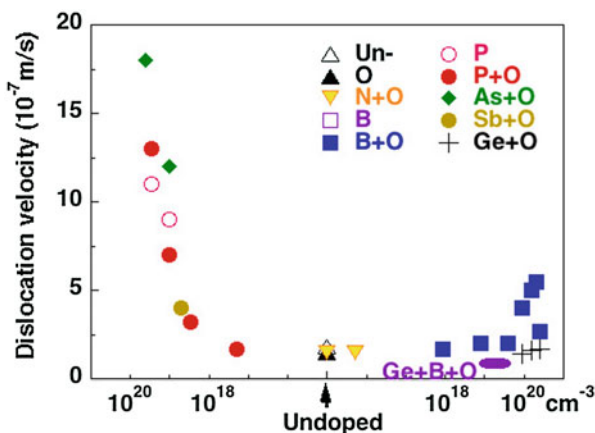


found that the width of a stacking fault ribbon bound by a pair of partial dislocations in Si doped with certain kinds of dopants expanded with the annealing duration, which implies the reduction of the stacking fault energy  $\gamma$  due to the segregation of impurities (Ohno et al. 2009, 2010, 2012). This is known as Suzuki effect (Suzuki 1962) of the interaction of an impurity with a stacking fault. Figure 14 shows the variation of the stacking fault energy  $\gamma$  as a function of the maximum number of impurity atoms agglomerated nearby a unit length of dissociated dislocations via their thermal migration  $N$  (Ohno et al. 2012). Here,  $N$  is defined as  $N = \pi D_a t_{an} c_a$  for an atom;  $D_a$  and  $c_a$  are the diffusion constant and the concentration of an atom, respectively. For example,  $D_a = 2.9 \times 10^{-15}$  cm<sup>2</sup>/s for Ga atoms at elevated temperature 1173 K. As seen in the figure, various Si crystals doped with impurities except B and Ge shows reduction and then saturation of the stacking fault energy  $\gamma$ . Remarkably, the variation of n-type Si, doped with P, As, or Sb, obeys a function of  $N$  irrespective of the n-type dopant species, while B- and Ge-doped Si shows no change of the energy against  $N$ . Ga-doped Si shows an intermediate feature of variation. This implies the small contribution of elastic interaction. Recently, Yamamoto et al. conducted ab initio calculations of the solution energy of heavily impurity-doped Si (Yamamoto et al. 2014). They confirmed that segregations on/around the stacking fault of various impurities are governed by the solution energy differences of the location sites between the perfect lattice and stacking fault. The solution energy variation originates in the electronic structure changes near the bandgaps. According to the stacking fault energy variation with  $N$ , the interaction energy between a stacking fault and the n-type impurities is estimated to be 0.15 eV, comparable to that evaluated theoretically (Justo et al. 1999b).

## Dislocation Velocity

The velocity of dislocations  $v$  in high-purity FZ-Si is described by Eq. (1) in a wide range from the stress as low as 2 MPa. On one hand, it is known that dislocation

**Fig. 15** Velocities of  $60^\circ$  dislocations in impurity-doped CZ-Si crystals under a shear stress of 30 MPa at  $700^\circ\text{C}$ : the dependence on the electrical type and concentration of main impurities. The ellipse denotes the result in Ge and B co-doped CZ-Si at concentrations of  $4 \times 10^{19}$  and  $9 \times 10^{18} \text{ cm}^{-3}$ , respectively



motion in Si doped with light impurities as O or N is suppressed under such low stress due to immobilization by the impurities and is similar with that in high-purity Si under rather high stress (Sumino and Imai 1983; Sumino and Yonenaga 1992; Sumino et al. 1983; Yonenaga 2005a). As shown in Fig. 8, in Si doped with certain kinds of electrically active impurities, dislocation motion is suppressed under stress lower than the critical stress for dislocation generation. Once the stress exceeds the critical stress, dislocation velocity increases rapidly with stress and then shows a break, which depends on the impurity species and concentration. Such a rapid increase in the velocity is related to the dislocation generation/release process from the impurity-immobilized state. Beyond the break, the velocity increases rather slowly with an increase in the stress at a rate comparable to that of dislocations in high-purity FZ-Si. Figure 15 shows how the velocities of  $60^\circ$  dislocations at  $700^\circ\text{C}$  depend on the concentration of impurities in a semiquantitative manner. The velocities of dislocations shown are those under a stress of 30 MPa where the measured velocities are thought to be free from the influence of impurity immobilization. It is seen that the velocity of dislocations in Si doped with donor impurities (P, As, Sb) increases with an increase in the concentration as reported previously (Imai and Sumino 1983; Sumino and Yonenaga 2002; Yonenaga 2004). Additionally, the dislocation velocity in Si doped with acceptor impurity B increases monotonically from that in high-purity Si with an increase in the B concentration (Yonenaga et al. 2001). Ge impurities have almost no effect on dislocation velocity enhancement/reduction. In (Ge+B) co-doped Si the dislocation velocity at  $700^\circ\text{C}$  is somewhat lower than or comparable to that in high-purity Si (Yonenaga et al. 2003).

Figure 16 shows the velocities of  $60^\circ$  dislocations in CZ-Si doped or co-doped with various impurities at various concentrations under a stress of 30 MPa plotted against the reciprocal temperatures. The dislocation velocity in motion was found to be unaffected by the doping of Si crystals with N and Ge impurities in the whole temperature range of  $650\text{--}950^\circ\text{C}$ . In (Ge+B) co-doped CZ-Si, dislocations move with lower velocity than in undoped CZ-Si in the low-temperature range. (Ge+B) co-doping is probably effective at low temperatures. Contrarily, dislocations move far faster in P- and As-doped Si and slightly faster in B-doped than in undoped CZ-Si

**Fig. 16** Velocities of  $60^\circ$  dislocations in impurity-doped CZ-Si and high-purity FZ-Si crystals under a shear stress of 30 MPa against the reciprocal temperature. Numerals show the impurity concentration in a unit of  $\text{cm}^{-3}$ . GeB denotes the results for Ge and B co-doped CZ-Si at concentrations of  $4 \times 10^{19}$  and  $9 \times 10^{18} \text{ cm}^{-3}$ , respectively

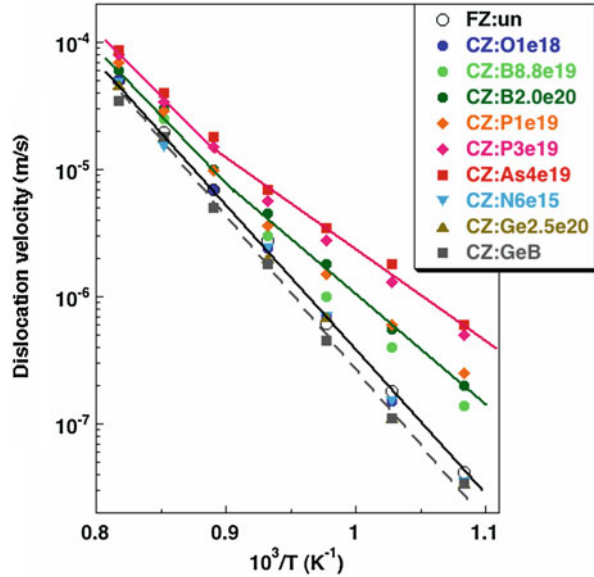


**Table 7** Magnitudes of  $Q$  for dislocations in the impurity-doped CZ-Si crystals

Crystal	Impurity concentration ( $\text{cm}^{-3}$ )	$Q$ (eV)
High-purity FZ		2.35
Undoped CZ	O: $1 \times 10^{18}$	2.35
p-type CZ	B: $2.0 \times 10^{20}$	1.65
n-type CZ	P: $1 \times 10^{19}$	1.53
n-type CZ	As: $4 \times 10^{19}$	1.32
N-doped CZ	N: $6 \times 10^{15}$	2.3

at temperatures lower than about  $800^\circ\text{C}$ . The velocity of dislocations is described as the stress and temperature by Eq. (1). Table 7 shows the activation energy  $Q$  for the crystals. The velocity enhancement and weak temperature dependence in n-type crystals, i.e., reduction of the activation energy  $Q$ , are attributed to the electronic effect through the formation and/or migration of kinks on a dislocation as an elementary process of dislocation motion. An acceptor level is thought to be associated with a kink site in Si as proposed by Hirsch (1979) and Jones (1980). If the enhanced dislocation velocity detected in B-doped Si is related to such a mechanism, then a donor level may seem to be associated with a kink site in Si. Since the reduction amount of  $Q$  in the crystals in comparison with that of high-purity Si depends on the Fermi level of the crystals, it can be supposed that a  $60^\circ$  dislocation has an acceptor level and a donor level in the bandgap at  $\sim 0.5$  and  $\sim 0.25$  eV, respectively, above the valence band edge  $E_v$ . Indeed, the result well corresponds to the theoretical estimation of  $E_v+0.55$  and  $0.34$  eV, respectively, derived by Heggie and Jones (1983). If a kink in the stable configuration

accompanies such an acceptor (donor) level, the equilibrium concentration of kinks on the dislocation may increase in an n-type (p-type) crystal since the free energy of the system decreases if such acceptors (donors) accept electrons from chemically given donors (acceptors). On the other hand, if some acceptor (donor) level is associated with a kink in the saddle point configuration of motion, the migration energy of a kink may be reduced and leads to a higher mobility of the kink. In both cases the velocity of the dislocation is enhanced. For a full understanding of the mechanism direct measurements of the kink velocity are indispensable.

Surprisingly, even at temperatures higher than 800 °C, the dislocation velocity in Si doped with B, P, and As impurities is larger than that of dislocations in undoped CZ-Si. Such enhancement of dislocation velocity observed in heavily impurity-doped Si may not be due to the above mechanism since a break of the temperature dependence of dislocation velocity in B-, P-, and As-doped Si is seen in Fig. 16. The kink configuration of a dislocation is probably concerned with the elementary process of dislocation motion in heavily impurity-doped semiconductors, where the doping level is extremely high, regarded as being in a rather dilute solid solution.

---

## Stimulated Dislocation Motion

### Recombination-Enhanced Dislocation Glides

It is known that rapid degradation of optical devices and light-emitting diodes in compound semiconductors as GaAs takes place through enhanced dislocation glide by carrier injection into a crystal by forward biasing or by laser irradiation during device operation. The phenomenon is called the recombination- (or radiation) enhanced dislocation glide (REDG) (Maeda and Takeuchi 1996). The REDG effect can often lead to softening of the strength in the macroscopic plasticity, called as photoplastic effect.

Figure 17 shows dislocation velocities measured under fixed stresses in the dark and under various kinds of excitation plotted against temperature. The enhancement of dislocation velocity takes place only during excitation at low temperatures but not at high temperatures. The dislocation velocity  $v^*$  under excitation is described as a function of temperature and excitation intensity  $I$  by the following empirical equation:

$$v^* = v_1 \exp(-Q/kT) + v_2(I/I_0) \exp[-(Q - \Delta Q/kT)]. \quad (17)$$

The velocity equation under excitation is represented by the sum of the usual thermal activation term and an enhancement term that is also described with an Arrhenius-type equation with the reduced activation energy and with a pre-exponential factor proportional to the excitation intensity. The latter term dominates at low temperatures, while the former controls the velocity at high temperatures.

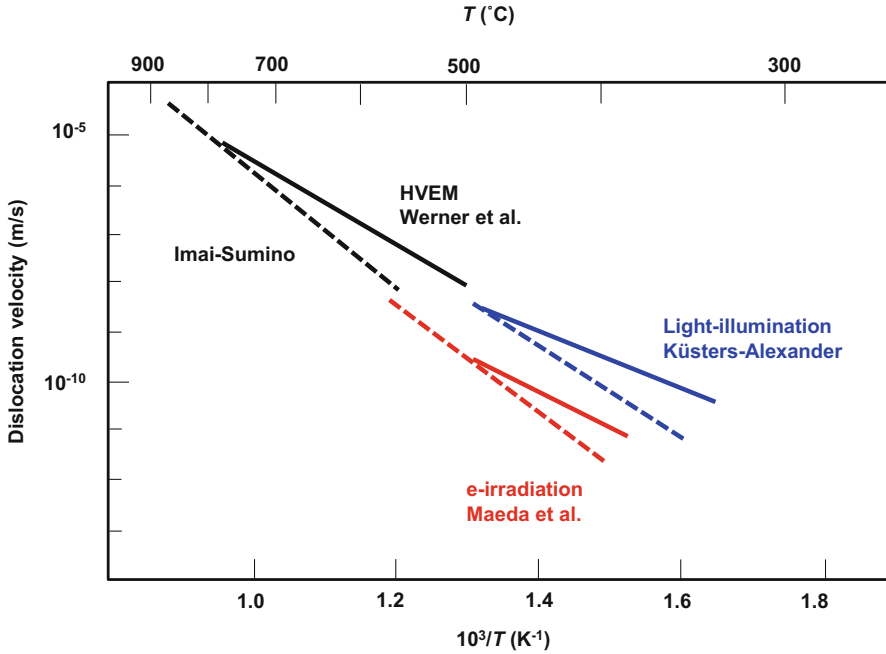


**Fig. 17** The temperature dependencies of dislocation velocity under various stimulations and in the dark in Si. Black solid line, under electron irradiation in in situ measurements with high-voltage electron microscopy (HVEM) (Werner et al. 1995); blue solid line, under light illumination (Küsters and Alexander 1983); red solid line, under electron irradiation in scanning electron microscopy (Maeda et al. 1987). Dotted lines: without stimulation in Si (Imai and Sumino 1983) and respective studies

The REDG effect is well interpreted by the so-called phonon-kick mechanism of defect migration that was originally proposed to explain annealing of point defects enhanced by irradiation (Weeks et al. 1975). It is assumed that the defect concerned has some electronic level within the bandgap of the crystal (see section “[Electrical and Optical Properties of Dislocations](#)”). An injected minority carrier is first captured at the defect, and the non-radiative electron-hole recombination process is completed on subsequently capturing a majority carrier there. The electronic energy released during the capture process of carriers is converted to the lattice vibration of the defect system and then distributed to a specific vibrational mode to lead to defect motion. The defect migration rate  $K_{\text{total}}$  is given by

$$K_{\text{total}} = K_{\text{th}} \exp(-Q_{\text{th}}/kT) + \eta K_{\text{r}} \exp[-(Q_{\text{th}} - \delta Q/kT)], \quad (18)$$

where  $K_{\text{r}}$  is the recombination rate,  $\eta$  is the efficiency factor ( $\eta < 1$ ), and  $\delta Q$  is the energy released during the carrier capture at the defect. The first term shows the rate of the process when there is the thermal activation with activation energy  $Q_{\text{th}}$  and prefactor  $K_{\text{th}}$  and the second term is that related to the recombination process.  $K_{\text{r}}$  is

proportional to the intensity  $I$  of irradiation at a low injection level. Thus, Eq. (17) is essentially same as Eq. (18), meaning that the physics contained in the recombination-enhanced defect motion also hold in REDG. Phonons emitted on recombination process at dislocation sites contribute to the activation process for the dislocation glide through the double-kink formation and/or the kink migration discussed in section “[Hirth-Lothe Kink Diffusion Model.](#)”

## Hydrogen-Enhanced Dislocation Glides

Irradiation of hydrogen plasma affects the dislocation glide in Si (Yamashita et al. 1999). As seen in Fig. 18, the velocity of  $60^\circ$  dislocation is remarkably enhanced by the hydrogen plasma irradiation in the temperature range between 400 and 500 °C but not at higher temperatures. The activation energy  $Q$  was evaluated to be 1.2 eV under the hydrogen plasma, lower than 2.2 eV in the hydrogen-free condition. Pretreatment of hydrogenation was shown to play an essential role for occurrence of the effect. The phenomenon was evidenced to be due to the hydrogen atoms incorporated into the specimens and currently interpreted that hydrogen atoms act as a catalytic agent in the kink migration process or that hydrogen atoms form

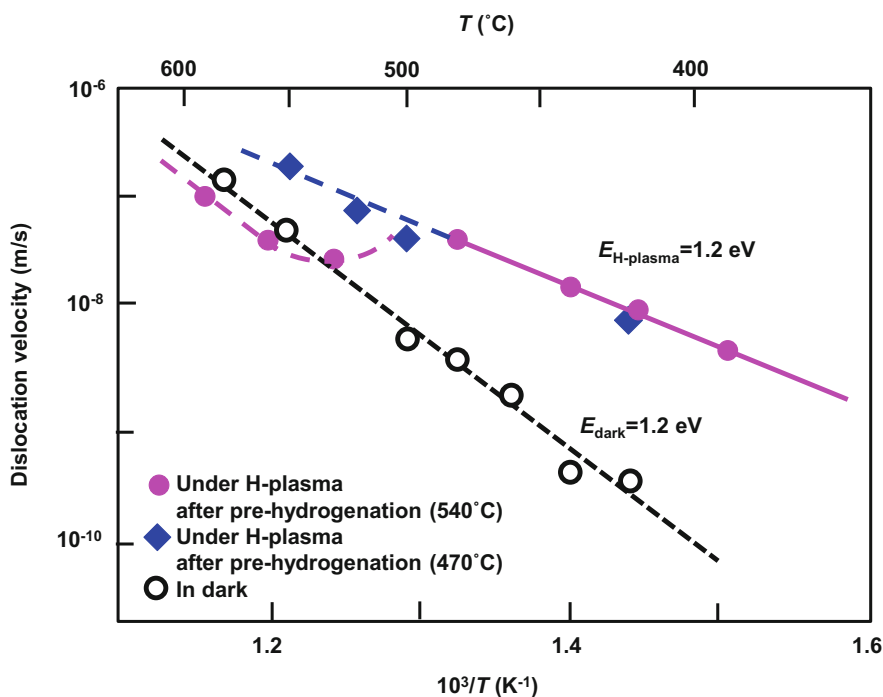


**Fig. 18** The temperature dependencies of dislocation velocity in dark and under hydrogen plasma pretreated at 540 °C and 470 °C. (Drawn under permission of Prof. Yamashita)

complexes with kinks or solitons, lowering their formation energy (see section “Dislocation Dynamics in Deformation”).

## Fracture

### Fracture Toughness

Si is known as a typical brittle solid (see a general review of the concepts and terminology of fracture mechanics of brittle materials by B.R. Lawn (1993)). Fracture of a Si crystal takes place due to cleavage along the certain crystallographic plane, i.e., (111), (110), and (100) in Si. The strength of such a brittle crystal at low temperatures is governed by the presence and/or appearance of cracks or notches that operate as an initiation site of cleavage. Fracture toughness (stress intensity factor)  $K_{IC}$  is the minimum toughness of a material in the presence of a stress concentration such as a crack or notch. At RT,  $K_{IC}$  is 0.62–1.22, 0.68–1.19, and 0.75–1.29 MPa·m<sup>1/2</sup> for {111}, {110}, and {100}, respectively (Yonenaga 1998; Masolin et al. 2013). Fracture toughness  $K_{IC}$ , dependent on the crystallographic plane (hkl) and direction [hkl], is related to the surface energy  $\gamma$  for fracture:

$$\gamma_{(hkl)} = (1/2)K_{IC(hkl)}^2 \{ (1 - \nu^2) / E_{[hkl]} \}, \quad (19)$$

where  $\nu$  is the Poisson ratio and  $E$  is the Young’s modulus.  $\gamma$  is estimated to be 1.24–2.70, 1.81–2.25, and 1.90 J/m<sup>2</sup> for {111}, {110}, and {100}, respectively, in experiments by various groups (Hayashi et al. 1992; Yonenaga 1998; Masolin et al. 2013).  $K_{IC}$  is  $\approx 1$  MPa·m<sup>1/2</sup> for polycrystalline Si (Chasiotis et al. 2006).

Fracture stress  $\sigma_F$  is related to the critical crack length  $c$  and fracture toughness  $K_{IC}$  as represented by the following equation:

$$\sigma_F = K_{IC} / (\pi c)^{1/2}. \quad (20)$$

Fracture strength depends on the surface state of samples. Some groups using a specially designed testing jig free from edge effects have reported that fracture stress of a float-zone grown Si wafer normally prepared by chemical polishing was 3.7 GPa at RT (Stepanov and Shpeizman 1981; Hu 1982; McLaughlin and Willoughby 1987), whereas the fracture strength reached up to 8.8 GPa after the surface removal of 166  $\mu\text{m}$  (Johansson et al. 1989), which is close to the ideal strength 13.7 GPa. If the abovementioned  $\sigma_F = 8.8$  GPa is adopted, according to Eq. (20) the critical crack length  $c$  can be estimated to be 3 nm, which shows the sensitivity of a fracture to extremely shallow surface cracks. Indeed, surface treatments, such as chemical polishing, lapping, implantation, and annealing in various environments, affect the fracture strength of Si (Hu 1982; McLaughlin and Willoughby 1987; Johansson et al. 1989). By lapping with diamond paste or by surface coating with TiN thin film,  $\sigma_F$  decreases to  $\sim 0.5$  GPa, while by annealing in H or O ambient or by ion implantation,  $\sigma_F$  is enhanced to  $\sim 3$  GPa. Details can be seen in Fig. 5 in the article (Yonenaga 1998).



In the recent findings, fracture strength strongly depends on the sample size (thickness) and easily exceeds 1 GPa for wafers, whiskers, and rods with a diameter of about 50  $\mu\text{m}$  or less (Kizuka et al. 2005; Gerberich et al. 2009). As a pioneering work, Johansson et al. (1988) reported elastic bending of micro-cantilever beam specimens of 10–20  $\mu\text{m}$  in thickness in in situ observation of fracture bending using scanning electron microscopy (SEM) and obtained fracture strength of 4–8 GPa. Gerberich et al. (2009) claimed an increase in  $K_{\text{IC}}$  with micron- and nano-sizing of Si crystals at RT. Clarification for these phenomena based on dislocation or plasticity mechanism is expected in the future.

## Brittle-to-Ductile Transition

Si is brittle at low temperatures where fracture takes place with no signs of plastic deformation. With increasing temperature, Si becomes ductile and deforms plastically before the occurrence of fracture, as brittle-to-ductile transition at  $T_{\text{BDT}}$  (St. John 1975; Samuels and Roberts 1989; Hirsch and Roberts 1991; Brede 1993). As seen in Fig. 19 (Yonenaga 2015),  $K_{\text{IC}}$  for bulk Si samples with a notch or an indentation impression shows a sharp increase suddenly at  $T_{\text{BDT}}$  and then a decrease with increasing temperature.  $K_{\text{IC}}$  and  $T_{\text{BDT}}$  depend on the testing method, stressing rate, impurity doping level, and especially the sample size (Hirsch and Roberts 1991).  $T_{\text{BDT}}$  is around 550–800  $^{\circ}\text{C}$  for bulk samples having a bending or cantilever form, strongly dependent on a strain rate. Figure 20 summarizes the strain-rate sensitivity of  $T_{\text{BDT}}$  described in the form of  $\dot{K}_{\text{IC}}$ .  $\dot{K}_{\text{IC}}$  is the increase rate of the fracture toughness  $K_{\text{IC}}$  in a constant strain rate test (St John 1975).  $T_{\text{BDT}}$  is given by the following equation:

**Fig. 19** Fracture toughness  $K_{\text{IC}}$  of the (110) plane of Si as a function of temperature. St. John, tension of tapered double cantilever beam Si (St. John 1975); Samuels, bending of indented Si (Samuels and Roberts 1989); Nakao, tension of notched micrometer-sized membrane Si (Nakao et al. 2008). Open and solid symbols show apparent brittle cleavage and ductile failure. (Yonenaga 2015; Reused under permission of Elsevier)

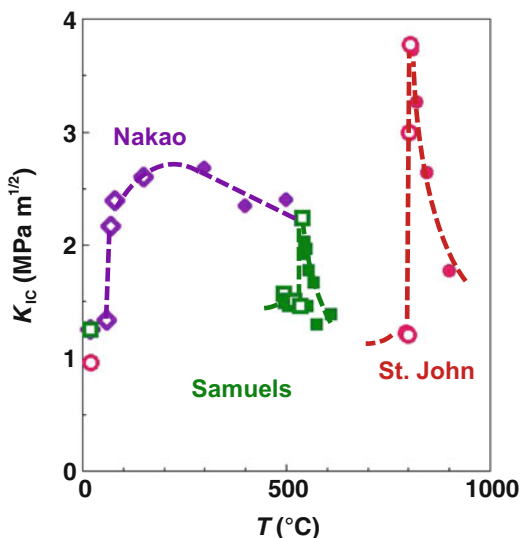
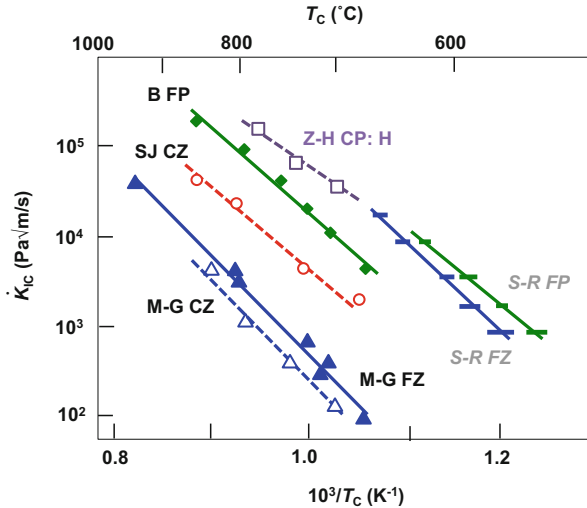


**Fig. 20** Brittle-ductile transition temperatures ( $T_c$ ) at various stress intensity factor rates in Si. SJ CZ (St. John 1975), M-G FZ (Michot 1988), M-G CZ (Michot 1988), S-R FZ (Samuels and Roberts 1989), S-R FP (Samuels and Roberts 1989), Z-H CP: H (Zhang and Haasen 1989), B FP (Brede 1993). CZ, undoped CZ; FZ, undoped FZ; FP, P-doped FZ; CP: H, hydrogenated. Bar-type symbols show data by bending of pre-indented samples while other symbols by tensile of double cantilever beam samples

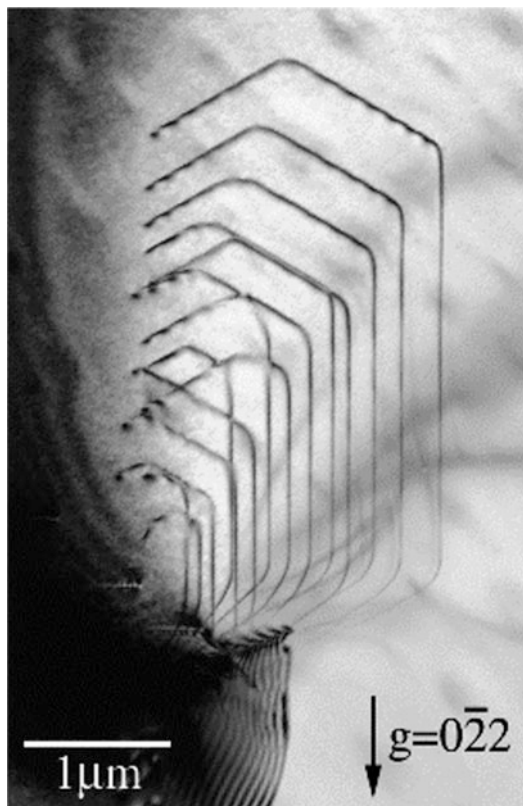


$$\dot{K}_{IC} = A \exp(-Q_{BDT}/kT_c), \quad (21)$$

where  $A$  is a constant and  $Q_{BDT}$  is the activation energy for the brittle-to-ductile transition.  $Q_{BDT}$  are measured to be around 2.2 eV in intrinsic Si and 1.6 eV for n-type Si, comparable to the activation energies of dislocation glide in the crystal types. Donor impurities decrease the  $T_{BDT}$  and increase the  $K_{IC}$ , probably due to the enhancement of dislocation activities. O impurity leads to the increase of  $T_{BDT}$  by  $\sim 40$  K with the slight increase of  $Q_{BDT}$ , probably connected to a dislocation immobilization associated with dissolved O atoms (Michot 1988). Plasma hydrogenation lowers  $T_{BDT}$  by  $\approx 60$  K and  $Q_{BDT}$  by  $\sim 0.8$  eV and connects with a hydrogen-induced increase in dislocation mobility in Si (Zhang and Haasen 1989), as discussed in section “Hydrogen-Enhanced Dislocation Glides” (Yamashita et al. 1999). Thus, it is known that the brittle-to-ductile transition is closely controlled by dislocation activities.

As seen in Fig. 19, micrometer-sized membrane samples with a notch have  $T_{BDT}$  as low as 70 °C, where  $K_{IC}$  increases modestly and then maintains the magnitude or decreases slightly (Nakao et al. 2008). The increase in  $K_{IC}$  around  $T_{BDT}$  is considered to be due to crack shielding or blunting through dislocation emission from the crack tip of a notch or impression (Brede 1993; Michot et al. 1994; Tanaka and Higashida 2004). Dislocations emitted from the crack front relax the stress concentration there, which leads to ductility as seen in Fig. 21 (Tanaka and Higashida 2004). At elevated temperatures the emitted dislocations can move easily and multiply, leading to ductile features with a decrease of the stress or  $K_{IC}$ . In the small samples, dislocations may be emitted under extremely high stress and remain around the crack due to low mobility, which leads to high resistivity against crack expansion in the low-temperature region. Indeed, Nakao et al. (2008) reported the activation of some number of dislocations around a notch. Recently, Huang et al. (2009) pointed out the possibility of energetic preference of amorphization at a crack tip under stress.

**Fig. 21** Dislocation loops emitted from a crack. (Tanaka and Higashida 2004; Reused under permission of Oxford University Press)



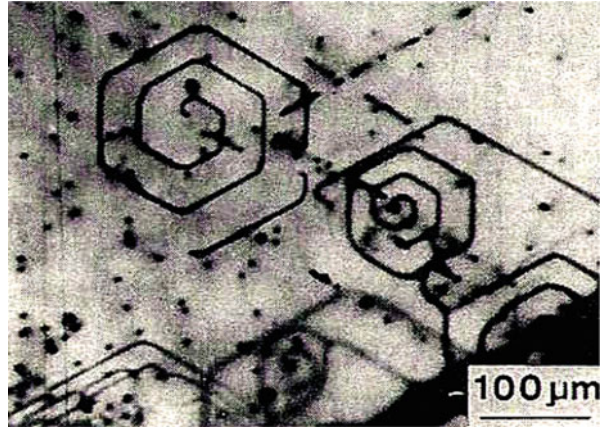
## Electrical and Optical Properties of Dislocations

### Electrical Characters

Dislocations are a linear defect, which can act as a one-dimensional (1D) nanostructure in the current understanding, and their dangling bonds lead to electronic states into the bandgap. Thus, one-dimensional (1D) electronic energy bands can be expected along intrinsic dislocations, such as an essential quantum wire. Such electronic states may cause preferential recombination of electron-hole pairs to change the electrical properties. Indeed, spiral dislocation loops have been observed as a dark line, meaning that dislocations act non-radiatively, in an electron beam-induced current (EBIC) image in Si as seen in Fig. 22 (Kusanagi et al. 1992).

From the beginning decades of semiconductor science and technology, many efforts have been conducted to clarify electrical properties of dislocations in crystals by a variety of research methods. Hall effects observed dislocation levels at  $E_v+0.17$ ,  $+0.27$ , and  $E_c-0.4$  eV in deformed Si (Grazhulis et al. 1977; Eremenko et al. 1977). Electron paramagnetic resonance (EPR) is powerful to identify for determining the

**Fig. 22** EBIC image of hexagonal dislocation loops in Si observed at 100 K. (Kusanagi et al. 1992; Reused under permission of American Institute of Physics)



density and structural symmetry of EPR-active sites along the dislocation lines and, indeed, found several lines characteristic as Si-K1, K2, and so on, relating to dislocation dangling bonds (Grazhulis et al. 1981; Suezawa et al. 1981; Kveder et al. 1982; Weber and Alexander 1983; Alexander et al. 1983). Especially, evaluations of the density of paramagnetic dangling bonds by EPR evidenced the existence of reconstruction along dislocations (see section “Dislocation Structures”).

A major problem in such investigations is the fact that the signals or data may originate in any defects generated by plastic deformation, i.e., not only “intrinsic” dislocations of different types, kinks, and jogs, but also other products as point defects, point-defect clusters, complexes of dislocation and point-defect, clusters of dislocation and impurity, and so forth. Typically trail defects were found (Bondarenko et al. 1986; Khorosheva et al. 2015). Thus, it is very hard to identify and relate particular signals or data to intrinsic dislocation dangling bonds due to ambiguities in interpretations. Here, we briefly summarize electrical and optical properties of dislocation states with intrinsic natures. Comprehensive reviews on such dislocation-related properties in Si can be found elsewhere (Schröter and Cerva 2002).

## Model of Electronic Structures of Dislocations

Based on experiments of plastically deformed Si crystals, two representative models of an electronic state of dislocations in the bandgap were proposed in the early decades: one is a discrete level of acceptor type (Read 1954), and the other is a one-dimensional partially filled band, amphoteric as an acceptor or a donor (Shockley 1953; Schröter and Labusch 1969). In both models, the dislocation electronic state accompanies a long-range screening such as a charge cylinder (so-called Read cylinder) and occupation statistics in the presence of the macroscopic Coulomb band bending formed around the dislocation.

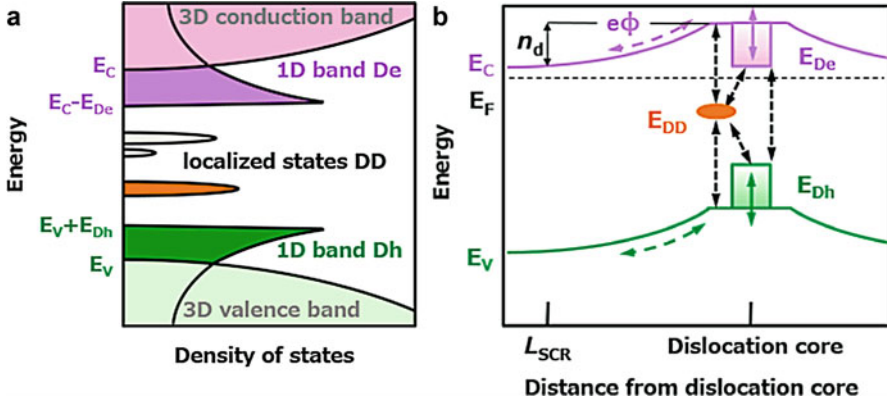


**Fig. 23** (a) Energy diagram for a glide  $60^\circ$  dislocation in Si. 1D bands originate in regular dislocation segments and DD deep localized states in some defects and irregularities on dislocation. (b) Carrier recombination at dislocations. For clean dislocations the recombination is governed by direct recombination of electrons and holes captured by the 1D dislocation bands  $E_{De}$  and  $E_{Dh}$ , and the carriers captured to 1D bands can recombine via the defect-related deep level  $E_{DD}$ . (Drawn under permission of Prof. Kveder)

Currently, the following model is widely accepted: Fig. 23a illustrates the energy diagram for a glide  $60^\circ$  dislocation in Si, showing shallow one-dimensional states and deep localized states (Kveder and Kittler 2008). As previously discussed,  $60^\circ$  and screw dislocations induced by deformation at elevated temperatures higher than around  $600^\circ\text{C}$  are in the glide-set. They are dissociated into  $90^\circ$  and  $30^\circ$  Shockley partial dislocations connected by a stacking fault, and the partial dislocation cores are reconstructed. In these situations, such dislocations were predicted theoretically not to accompany deep electronic states in the bandgap. Alternatively, clean and straight segments of the dislocation produce shallow one-dimensional electronic energy bands (1D bands) caused by the lattice deformation (elastic strain field) and a filled band (quasi-2D band) by the stacking fault (see for review by Schröter and Cerva 2002). The empty band De has energy levels centered around at  $E_C - E_{De}$  below the conduction band bottom, while the occupied band Dh centered at  $E_V + E_{Dh}$  above the valence band top, where  $E_C$  and  $E_V$  denote the edges of the conduction and valence band, respectively. Here, it may note that the tails of De and Dh bands spread into the conduction and valence band, respectively, as seen in Fig. 23a. In the recent studies,  $(E_C - E_{De}) \approx 60$  meV and  $(E_{Dh} - E_V) \approx 70$  meV are reported experimentally (Castaldini et al. 2005).

Besides the 1D bands, deep localized electronic states DD, point-like (zero dimensional, 0D), are produced. The DD states of  $E_{DD}$  originate in some intrinsic core defects and/or irregularities at the dislocation such as reconstruction defects (solitons) and jogs, core defects caused by incorporation of vacancies or impurities, and impurities closely accumulated to dislocations by their elastic strain field. Such impurities bound to dislocations or dislocation cores may show significantly different energy levels from those in the bulk.

## Recombination at Dislocations

The electronic states at a dislocation capture free electron-hole according to occupation statistics. Such captured carriers create a Coulomb band-bending  $e\phi$  around it as seen in Fig. 23b, reducing the capture rate of free electrons to the states approximately by a factor  $\exp(-e\phi/kT)$ . Thus, this potential limits the total equilibrium occupation of electrons to the states and, simultaneously, attracts minority carriers, resulting in acceleration of their capture and recombination at the dislocation. Exact evaluation of  $e\phi$  is rather difficult and approximately given by the following formula (Schröter and Cerva 2002):

$$e\phi = (e^2 N_{\text{tot}} / 2\pi\epsilon\epsilon_0) \left\{ \ln \left[ N_{\text{tot}} (N_{\text{tot}} / \pi n_d)^{1/2} \right] - 0.5 \right\}, \quad (22)$$

where  $N_{\text{tot}}$  is the total dislocation charge per unit length (the concentration of electrons or holes captured to the dislocation energy states),  $\epsilon$  and  $\epsilon_0$  are the dielectric permittivity of Si and in vacuum, respectively, and  $n_d$  is the concentration of shallow donors. Here, Eq. (22) assumes the screening radius  $L_{\text{scr}}$  of the electric field around the dislocation as

$$L_{\text{scr}} = (N_{\text{tot}} / \pi n_d)^{1/2}. \quad (23)$$

Thus,  $N_{\text{tot}}$  is governed by the screening potential  $e\phi$  rather than the total number of DD states per unit length, less than  $(2-5) \times 10^6 \text{ cm}^{-1}$ . Excess minority carriers results in a non-equilibrium occupation of dislocation energy states, and the dislocation electrostatic potential  $e\phi$  is reduced, roughly like  $e\phi \approx kT \ln(n/p)$  for balance.

Recombination processes of charge carriers at dislocations are illustrated in Fig. 23b. For clean dislocations the recombination rate is determined by direct recombination of electrons and holes captured by the 1D bands De and Dh. The carriers captured to 1D bands can recombine via the deep defect state DD (Kveder et al. 2001).

## Dislocation-Related Deep States

Dislocation-related deep energy states are intensively investigated by deep-level transient spectroscopy (DLTS). A lot of knowledge on them has been clarified (see, e.g., Patel and Kimerling 1979; Omling et al. 1985; Ono and Sumino 1985; Schröter et al. 2002), though even now the exact origin of the core defects responsible for all these well-known dislocation-related deep energy levels detected by DLTS is not yet clear completely.

Figure 24 shows a typical DLTS spectrum of n-type FZ-Si deformed at 750 °C to various shear strains. There are several asymmetrically broadened lines as DH<sub>1</sub> ( $E_c - 0.24 \text{ eV}$ ), DH<sub>3</sub> ( $E_c - 0.33 \text{ eV}$ ), and DH<sub>5</sub> ( $E_c - 0.56 \text{ eV}$ ) in the deformed specimen (Ono and Sumino 1985). These lines can be observed for dislocations

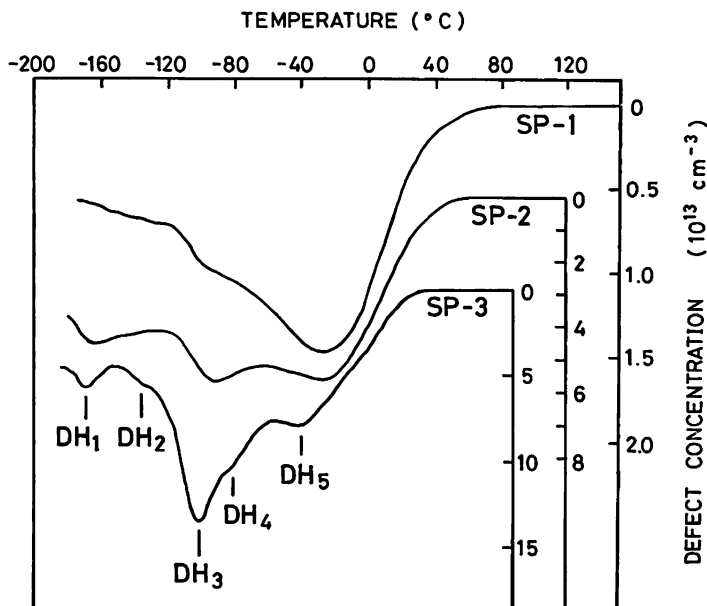


**Fig. 24** Deep-level spectra for plastically deformed Si at 750 °C to shear strains of 2.6 (SP-1), 4.4 (SP-2), and 9.5% (SP-3). (Ono and Sumino 1985; Reused under permission of American Institute of Physics)

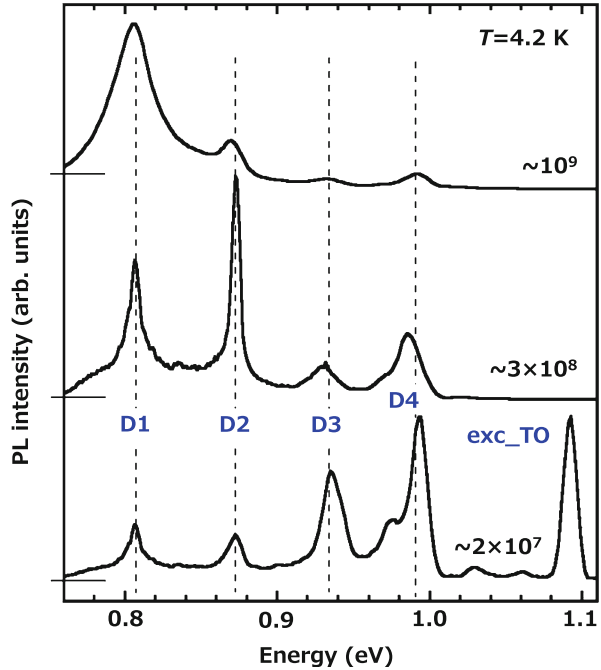
introduced by plastic deformation at temperatures lower than 800 °C. They show the logarithmic dependence of the signal amplitude on capture time and line broadening in the order of 10–50 meV, characteristic for dislocation-related deep defects. Some important features of DLTS lines in plastically deformed Si were analyzed in detail (see for review by Schröter and Cerva 2002). Seibt et al. (2009) recently investigated intensively the interaction of dislocations with metallic impurities with DLTS.

### Dislocation-Related Shallow States

Optical photoluminescence (PL) studies reveal dislocation-related radiative characters as a luminescence consisting of four broadened lines, D1–D4, first proved by Drozdov et al. (1976). Figure 25 shows typical PL spectrum of D1, D2, D3, and D4 at 0.812, 0.875, 0.934, and 1.000 eV, respectively, measured at  $T = 4.2$  K in Si with various densities of dislocations  $N_D$  (Kveder and Kittler 2008). Their intensities strongly depend on  $N_D$ , characteristically with keeping the relative intensity ratio of D1 (D3) to that D2 (D4). D3 and D4 are dominant in samples with low  $N_D$ , while the D1 becomes dominating in samples with high  $N_D$ . Polarization experiments of the D line emission dependent on uniaxial stress were applied to establish that lines of D3 and D4 behave as a pair. Moreover, PL measurements



**Fig. 25** PL spectra of plastically deformed Si with various densities of dislocations. Numerals show dislocation density  $N_D$  in a unit of  $\text{cm}^{-2}$ . (Drawn under permission of Prof. Kveder)



on dislocations in SiGe identified to be D3 as a phonon-assisted replica of D4 (Weber and Alonso 1990; Tanaka et al. 1996). Currently, the line pair D3/D4 is supposed to originate from recombination processes between  $E_{Dc}$  and  $E_{Dh}$  (Fig. 23) at straight segments of dissociated  $60^\circ$  dislocations (Sauer et al. 1986; Schröter and Cerva 2002). On the other hand, the lines of D1 and D2 are still problems, including whether they are pair or not, though there are proposals as impurity atoms, including O precipitates, in the dislocation core (Higgs et al. 1993; Tajima et al. 2012), dislocation jogs (Watson et al. 1998), segments of Lomer dislocations, or vacancy and/or self-interstitial clusters trapped in the dislocation core (Jones et al. 2000). Possibly, the process may relate to recombination between  $E_{Dc}$  and  $E_{Dh}$ , somewhat promoted by the presence of such defects on dislocations (Schröter and Cerva 2002). Elucidation of optical characters of dislocations is important for further development of light-emitting devices (Kveder et al. 2001; Ng et al. 2001).

### Characteristics of Dislocations Specific in Solar Cell Si

Currently, cast multi-crystalline silicon (mc-Si) grown in a crucible dominates the world commercial material markets of solar cells with  $\approx 60\%$  share on balance of conversion efficiency and cost. Inevitably, grain boundaries affect on dislocation



behavior. Here, some characteristics of dislocations in relation with grain boundaries in mc-Si are shown briefly.

## Dislocation Behavior in Multi-crystalline Si

Dislocations in mc-Si crystals are formed during crystal growth. The average dislocation densities vary between  $10^4$  and  $10^6 \text{ cm}^{-2}$  and develop locally bundles of dislocations with densities higher than  $10^8 \text{ cm}^{-2}$ , which can extend over wide range in growth direction (Möller et al. 2005). Kutsukake et al. (2011) reported that dislocations are frequently generated at impingement regions of the growth of crystal grains where Si melt was enclosed by crystalline grains when it solidified. Such dislocations are formed in the crystallized melt to relax strain due to the volume expansion at solidification. Dislocations generate heterogeneously from some specific sites of grain boundary, that is, stress-concentrated positions as step, junctions, and so on, during cooling stage of growth through plastic deformation applied by the thermal stress originating mainly from the crucible shrinkage. Takahashi et al. (2010) observed dislocation generation from an artificially composed grain boundaries and propagation along the growth direction in mc-Si as seen in Fig. 26. They discussed the phenomena according to a finite element model that dislocations move into the grain along a slip system with the highest shear stress.

Dislocation activities in motion intra-grain are similar to those in single-crystalline materials. Indeed, Werner et al. (1994) found no evidence for blocking against dislocation motion in mc-Si by in situ high-voltage TEM studies using a heating-straining stage at elevated temperatures. Typical impurities in the conventional concentration level in mc-Si do not affect dislocation activities remarkably (see section “[Impurity Effects on Dislocation Activities](#)”). Such dislocations multiply as growth proceeds according to the AHS model as shown in section

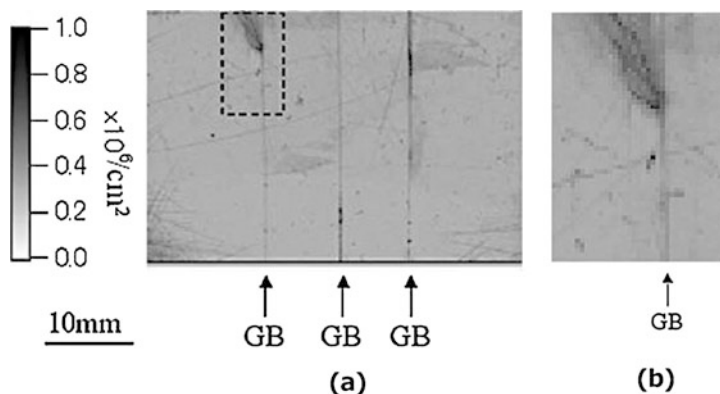


**Fig. 26** Dislocation etch pits developed from an artificial GB and propagated along the growth direction in a cast Si. Enlarged image is shown in (b). (Takahashi et al. 2010; Reused under permission of Elsevier)

“[Dislocation Dynamics in Deformation.](#)” They pile up as dislocation bundles (clusters) of high local density. The piled-up dislocations generally form to lineages or small-angle grain boundaries (sub-boundaries) through their motion, agglomeration, and annihilation to reduce strain energies and then build to cellular structures, as known historically in dislocated Si crystals. Rynningen et al. (2011) and Oriwol et al. (2013) observed such polygonization in mc-Si three-dimensionally by using various methods as X-ray topography, IR microscopy, electron backscattering pattern (EBSP) analysis, etc.

Quantitative information of mechanical properties of polycrystalline Si is rather limited even now. Yield strength of polycrystalline Si is superimposed into Fig. 7 (Omri et al. 1985) in section “[Plastic Deformation and Yield Strength.](#)” In section “[Fracture Toughness,](#)” fracture toughness for polycrystalline Si is known to be  $K_{IC} \approx 1 \text{ MPa}\cdot\text{m}^{1/2}$  (Chasiotis et al. 2006).

## Effect on Efficiency and Electrical Properties of Si Solar Cells

The conversion efficiencies of mc-Si solar cells are generally in the range of 12–15% and up to 18% in sophisticated cases, though the potential of mc-Si is thought to be higher,  $\approx 20\%$ . Dislocations in mc-Si are detrimental for the conversion efficiency. Figure 27 shows the carrier lifetime distribution of a vertical cross section of a mono-like cast Si in comparison with PL image of the same region (Kutsukake et al. 2015). The carrier lifetime is short in the dark regions of a high density of grown-in dislocations and their bundles. It should note that a dislocation itself has shallow electronic levels while that decorated by impurities affects significantly on the carrier recombination due to the deep levels as discussed in section “[Electrical and Optical Properties of Dislocations.](#)” Thus, observed reduction of carrier lifetime attributes to recombination at dislocations accumulated by residual impurities in mc-Si.

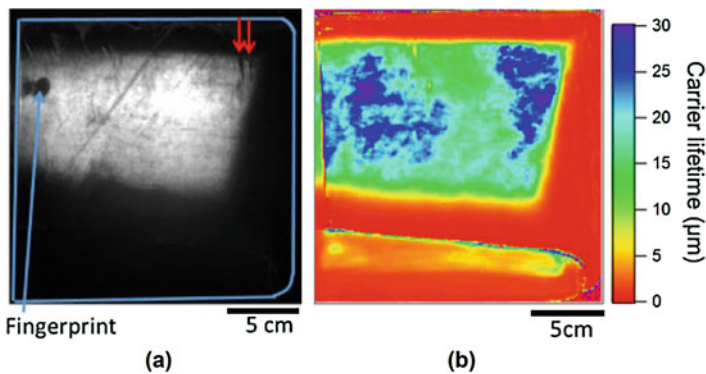
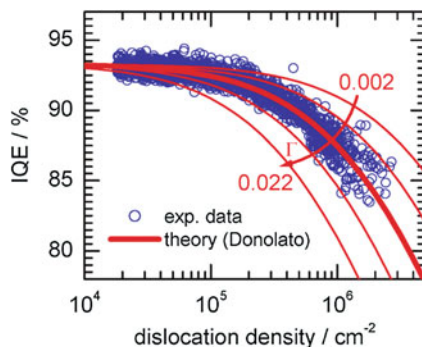


**Fig. 27** (a) PL image and (b) carrier lifetime distribution of a vertical cross section of a mono-like cast Si (Kutsukake et al. 2015; Reused under permission of The Japan Society of Applied Physics)

**Fig. 28** Correlation of the measured IQE values and the dislocation densities in mc-Si. The plotted lines were calculated using the extended Donolato theory for various recombination strengths from 0.002 to 0.022. (Rinio et al. 2011; Reused under permission of Wiley VCH)



In mc-Si recombination is discussed in terms with the relation between the local quantum efficiency (IQE) obtained by light beam-induced current (LBIC) technique and the dislocation density. Figure 28 shows correlation of the measured IQE values and the dislocation densities  $\rho$  in mc-Si. The lines in the figure were calculated using the Donolato theory (1998) with for various recombination strengths (Rinio et al. 2011). IQE decreases with an increase in the grown-in dislocation density and drops drastically beyond  $N \approx 10^5 \text{ cm}^{-2}$ . Therefore, to improve the conversion efficiency, reduction of a density of grown-in dislocations is one of the major subjects through dislocation engineering as stress and temperature control, annealing, hydrogen passivation, gettering, and so forth (Woo et al. 2016).

## Conclusive Remarks for Further Developments

This chapter reviews the current knowledge of the properties of dislocations in Si comprehensively in a perspective viewpoint for the photovoltaic applications. Unfortunately, some topics cannot be introduced here or in details, for example, misfit dislocations (Kittler and Reiche 2009), trailing point defects formed by dislocation motion (Khorosheva et al. 2015), oxygen effects on dislocation properties (Sumino and Yonenaga 1994), metallic impurity clustering on dislocations (Seibt et al. 2009), and preferential oxygen segregation on dislocations under a high magnetic field (Yonenaga and Takahashi 2007). Readers, if necessary, can visit the literatures.

In order to clarify intrinsic properties of dislocations for further developments in Si technology as dislocation engineering (Ng et al. 2001) and impurity engineering (Yu et al. 2013), the most important subject is to investigate dislocations of as clean as possible without influences of point defects and impurities. Misfit dislocations induced by wafer bonding are expected as a key target, though it might be recognized that even such dislocations have many nodes and, possibly jogs, acting as a source or absorber of point defects, due to their invariably induced network. A one-directional array structure of dislocations can be rather powerful for the purpose. In addition, since dislocations are expected as a one-dimensional

conduction quantum wire, such dislocations are useful to study the carrier transportation phenomenon along them as a hopping conduction (the Poole-Frenkel effect) (Trushin et al. 2011).

Generation of a dislocation, including a misfit dislocation, is even now not well clarified in spite of many theoretical predictions, for example, by Pizzagalli's group (Godet et al. 2009). In situ observations in an atomic scale are necessary besides previous postmortem or low spatial resolution studies (Minor et al. 2005; Chen et al. 2018). Elucidation of dynamic behavior of dislocations under an interaction with various grain boundaries is indispensable to realize high-performance photovoltaic devices with multi- and polycrystalline Si. Utilization of artificial grain boundaries may be meaningful for the purpose (Kutsukake et al. 2013).

From a huge number of papers on dislocation researches in Si in the long history, only the limited papers were introduced and/or cited in this chapter. This is responsible solely for the author.

---

## Cross-References

- ▶ [Characterization of Wafers and Supply Materials](#)
- ▶ [Grain Boundaries in Multicrystalline Silicon](#)
- ▶ [Growth of Crystalline Silicon for Solar Cells: Czochralski Si](#)
- ▶ [Growth of Crystalline Silicon for Solar Cells: Mono-Like Method](#)
- ▶ [Oxygen Impurity in Crystalline Silicon](#)

**Acknowledgment** The author expresses his gratitude to his colleagues Profs. Y. Ohno, T. Taishi, K. Kutsukake, Drs. Y. Tokumoto, M. Deura for close and long-standing collaborations on dislocation researches in Si. This chapter is dedicated to the memory of Professor Malcolm I. Heggie.

---

## References

- H. Alexander, Dislocations in covalent crystals, in *Dislocations in Solids*, ed. by F. R. N. Nabarro, vol. 7, (Elsevier, Amsterdam, 1986), pp. 113–234
- H. Alexander, P. Haasen, Dislocations and plastic flow in the diamond structure. *Solid State Phys.* **22**, 27–158 (1968)
- H. Alexander, C. Kisielowski-Kemmerich, E.R. Weber, Investigations of well defined dislocations in silicon. *Physica* **116B**, 583–593 (1983)
- J. Bennetto, R.W. Nunes, D. Vanderbilt, Period-doubled structure for the 90° partial dislocation in silicon. *Phys. Rev. Lett.* **79**, 245–248 (1997)
- I.E. Bondarenko, H. Blumtritt, J. Heydenreich, V.V. Kazmiruk, E.B. Yakimov, Recombination properties of dislocation slip planes. *Phys. Status Solidi A* **95**, 173–177 (1986)
- M. Brede, The brittle-to-ductile transition in silicon. *Acta Metall. Mater.* **41**, 211–228 (1993)
- V.V. Bulatov, J.F. Justo, W. Cai, S. Yip, A.S. Argon, T. Lenosky, M. de Koning, T. Diaz de la Rubia, Parameter-free modelling of dislocation motion: the case of silicon. *Philos. Mag. A* **81**, 1257–1281 (2001)
- W. Cai, V.V. Bulatov, J.F. Justo, A.S. Argon, S. Yip, Intrinsic mobility of a dissociated dislocation in silicon. *Phys. Rev. Lett.* **84**, 3346–3349 (2000)

- J. Castaing, P. Veysseyre, L.P. Kubin, J. Rabier, The plastic deformation of silicon between 300°C and 600°C. *Philos. Mag. A* **44**, 1407–1413 (1981)
- A. Castaldini, D. Cavalcoli, A. Cavallini, S. Pizzini, Experimental evidence of dislocation related shallow states in p-type Si. *Phys. Rev. Lett.* **95**, 076401 (2005)
- I. Chasiotis, S.W. Cho, K. Jonnalagadda, Fracture toughness and subcritical crack growth in polycrystalline silicon. *Trans. ASME* **73**, 714–722 (2006)
- M. Chen, L. Pethö, A. Sologubenko, J. Michler, R. Spolenak, J. Wheeler, Study of mechanical strain induced defects in lithographic silicon at low temperatures via in situ microcompression. in *Abstracts of the 19th international conference on Extended Defects in Semiconductors*, ed. by P. Komninou (Thessaloniki), 24–29 June 2018 (2018)
- J. Cochard, I. Yonenaga, M. M’Hamdi, Z.L. Zhang, A novel constitutive model for semiconductors: The case of silicon. *J. Mech. Phys. Solids* **61**, 2402–2032 (2013)
- C. Donolato, Modeling the effect of dislocations on the minority carrier diffusion length of a semiconductor. *J. Appl. Phys.* **84**, 2656–2664 (1998)
- N.A. Drozdov, A.A. Patrin, V.D. Tkachev, Recombination radiation on dislocations in silicon. *Sov. Phys. JETP Lett.* **23**, 597–599 (1976)
- M.S. Duesbery, B. Joós, Dislocation motion in silicon: The shuffle-glide controversy. *Philos. Mag. Lett.* **74**, 253–258 (1996)
- V.G. Eremenko, V.I. Nikitenko, E.B. Yakimov, The dependence of the electrical properties of silicon on the plastic deformation and annealing temperatures. *Sov. Phys. JEPT* **46**, 598–603 (1977)
- V.N. Erofeev, V.I. Nikitenko, Comparison of theory of dislocation mobility with experimental data for silicon. *Sov. Phys. JETP* **33**, 963–966 (1971)
- B.Ya. Farber, V.I. Nikitenko, Change of dislocation mobility characteristics in silicon single crystals at elevated temperatures. *Phys. Status Solidi A* **73**, K141–K144 (1982)
- W.W. Gerberich, J. Michler, W.M. Mook, R. Ghisleni, F. Östlund, D.D. Stauffer, R. Ballarini, Scale effects for strength, ductility, and toughness in “brittle” materials. *J. Mater. Res.* **24**, 898–906 (2009)
- J. Godet, P. Hirel, S. Brochard, L. Pizzagalli, Evidence of two plastic regimes controlled by dislocation nucleation in silicon nanostructures. *J. Appl. Phys.* **105**, 026104 (2009)
- V.A. Grazhulis, V.V. Kveder, V.Yu. Mukhina, Investigation of the energy spectrum and kinetic phenomena in dislocated Si crystals (I). *Phys. Status Solidi A* **43**, 407–415 (1977)
- V.A. Grazhulis, V.V. Kveder, Yu.A. Ossipyan, Investigation of the dislocation spin system in silicon as model of one-dimensional spin chains. *Phys. Status Solidi B* **103**, 519–528 (1981)
- K. Hayashi, S. Tsujimoto, Y. Okamoto, T. Nishikawa, Fracture toughness of single crystal silicon at high temperatures. *J. Soc. Mater. Sci. Jpn.* **41**, 488–494 (1992) (in Japanese)
- M.I. Heggie, R. Jones, Solitons and the electrical and mobility properties of dislocations in silicon. *Philos. Mag. B* **48**, 365–377 (1983)
- M.I. Heggie, R. Jones, A. Umerski, Ab initio total energy calculations of impurity pinning in silicon. *Phys. Status Solidi A* **138**, 383–387 (1993)
- V. Higgs, E.C. Lightowers, E.A. Fitzgerald, Y.H. Xie, P.J. Silverman, Characterization of compositionally graded Si<sub>1-x</sub>G<sub>ex</sub> alloy layers by photoluminescence spectroscopy and by cathodoluminescence spectroscopy and imaging. *J. Appl. Phys.* **73**, 1952–1956 (1993)
- P.B. Hirsch, A mechanism for the effect of doping on dislocation mobility. *J. Phys. Colloq. (Paris)* **40**, C6-117–C6-121 (1979)
- P.B. Hirsch, S.G. Roberts, The brittle-ductile transition in silicon. *Philos. Mag. A* **64**, 55–80 (1991)
- J.P. Hirth, J. Lothe, *Theory of Dislocations*, 2nd edn. (Wiley, New York, 1982)
- J. Hornstra, Dislocations in the diamond lattice. *J. Phys. Chem. Solids* **5**, 129–141 (1958)
- S.M. Hu, Critical stress in silicon brittle fracture, and effect of ion implantation and other surface treatments. *J. Appl. Phys.* **53**, 3576–3580 (1982)
- S. Huang, S. Zhang, T. Belytschko, S.S. Terdalkar, T. Zhu, Mechanics of nanocrack: Fracture, dislocation emission, and amorphization. *J. Mech. Phys. Solids* **57**, 840–850 (2009)
- M. Imai, K. Sumino, In situ X-ray topographic study of the dislocation mobility in high-purity and impurity-doped silicon crystals. *Philos. Mag. A* **47**, 599–621 (1983)

- S. Izumi, H. Ohta, C. Takahashi, T. Suzuki, H. Saka, Shuffle-set dislocation nucleation in semiconductor silicon device. *Philos. Mag. Lett.* **90**, 707–714 (2010)
- S. Johansson, J.-Å. Schweitz, L. Tenerz, J. Tirén, Fracture testing of silicon microelements in situ in a scanning electron microscope. *J. Appl. Phys.* **63**, 4799–4803 (1988)
- S. Johansson, F. Ericson, J.-Å. Schweitz, Influence of surface coatings on elasticity, residual stresses, and fracture properties of silicon microelements. *J. Appl. Phys.* **65**, 122–128 (1989)
- R. Jones, The structure of kinks on the  $90^\circ$  partial in silicon and a ‘strained-bonded model’ for dislocation motion. *Philos. Mag. B* **42**, 213–219 (1980)
- R. Jones, B.J. Coomer, J.P. Goss, S. Öberg, P.R. Briddon, Intrinsic defects and the D1 to D4 optical bands detected in plastically deformed Si. *Phys. Status Solidi B* **222**, 133–140 (2000)
- K. Jurkschat, S. Senkader, P.R. Wilshaw, D. Gambaro, R.J. Falster, Onset of slip in silicon containing oxide precipitates. *J. Appl. Phys.* **90**, 3219–3225 (2001)
- J.F. Justo, V.V. Bulatov, S. Yip, Dislocation core reconstruction and its effect on dislocation mobility in silicon. *J. Appl. Phys.* **86**, 4249–4257 (1999a)
- J.F. Justo, A. Antonelli, T.M. Schmidt, A. Fazio, Effects of extended defects on the properties of intrinsic and extrinsic point defects in silicon. *Physica B* **273–274**, 473–475 (1999b)
- A. Kailer, Y.G. Gogotsi, K.G. Nickel, Phase transformations of silicon caused by contact loading. *J. Appl. Phys.* **81**, 3057–3063 (1997)
- M.A. Khorosheva, V.V. Kveder, M. Seibt, On the nature of defects produced by motion of dislocations in silicon. *Phys. Status Solidi A* **212**, 1695–1703 (2015)
- M. Kittler, M. Reiche, Dislocations as active components in novel silicon devices. *Adv. Eng. Mater.* **11**, 249–258 (2009)
- T. Kizuka, Y. Takatani, K. Asaka, R. Yoshizaki, Measurements of the atomistic mechanics of single crystalline silicon wires of nanometer width. *Phys. Rev. B* **72**, 035333 (2005)
- H.R. Kolar, J.C.H. Spence, H. Alexander, Observation of moving dislocation kinks and unpinning. *Phys. Rev. Lett.* **77**, 4031–4034 (1996)
- S. Korte, J.S. Barnard, R.J. Stearn, W.J. Clegg, Deformation of silicon – Insights from micro-compression testing at 25–500°C. *Int. J. Plast.* **27**, 1853–1866 (2011)
- S. Kusanagi, T. Sekiguchi, K. Sumino, Difference of the electrical properties of screw and  $60^\circ$  dislocations in silicon as detected with temperature-dependent electron beam induced current technique. *Appl. Phys. Lett.* **61**, 792–794 (1992)
- K.H. Küsters, H. Alexander, Photoplastic effect in silicon. *Physica B* **116**, 594–599 (1983)
- K. Kutsukake, T. Abe, N. Usami, K. Fujiwara, I. Yonenaga, K. Morishita, K. Nakajima, Generation mechanism of dislocations and their clusters in multicrystalline silicon during two-dimensional growth. *J. Appl. Phys.* **110**, 083530 (2011)
- K. Kutsukake, N. Usami, Y. Ohno, Y. Tokumoto, I. Yonenaga, Control of grain boundary propagation in mono-like Si: Utilization of functional grain boundaries. *Appl. Phys. Express* **6**, 025505 (2013)
- K. Kutsukake, M. Deura, Y. Ohno, I. Yonenaga, Characterization of silicon ingots: Mono-like versus high-performance multicrystalline. *Jpn. J. Appl. Phys.* **54**, 08KD10 (2015)
- V. Kveder, M. Kittler, Dislocations in silicon and D-band luminescence for infrared light emitters. *Mater. Sci. Forum* **590**, 29–56 (2008)
- V.V. Kveder, Yu.A. Osipyan, W. Schröter, G. Zoth, On the energy spectrum of dislocations in silicon. *Phys. Status Solidi A* **72**, 701–713 (1982)
- V. Kveder, M. Kittler, W. Schröter, Recombination activity of contaminated dislocations in silicon: A model describing electron-beam-induced current contrast behavior. *Phys. Rev. B* **63**, 115208 (2001)
- B.R. Lawn, *Fracture of Brittle Solids* (Cambridge University Press, Cambridge, UK, 1993)
- N. Lehto, S. Öberg, Effects of dislocation interactions: Application to the period-doubled core of the  $90^\circ$  partial in silicon. *Phys. Rev. Lett.* **80**, 5568–5571 (1998)
- Z. Li, C. Picu, Shuffle-glide dislocation transformation in Si. *J. Appl. Phys.* **113**, 083519 (2013)
- F. Louchet, On the mobility of dislocations in silicon by in situ straining in a high-voltage electron microscope. *Philos. Mag. A* **43**, 1289–1297 (1981)

- F. Louchet, J. Pelissier, D. Caillard, J.P. Peyrade, C. Levade, G. Vanderschaeve, In situ TEM study of dislocation mobility in semiconducting materials. *Microsc. Microanal. Microstruct.* **4**, 199–200 (1993)
- K. Maeda, S. Takeuchi, Enhancement of dislocation mobility in semiconducting crystals by electronic excitation, in *Dislocations in Solids*, ed. by F. R. N. Nabarro, M. S. Duesbery, vol. 10, (Elsevier, Amsterdam, 1996), pp. 443–504
- K. Maeda, K. Kimura, S. Takeuchi, Effects of excitations on dislocation mobility in elemental semiconductors. *Bull. Acad. Sci. USSR Phys. Ser.* **51**, 93–98 (1987)
- A. Masolin, P.-O. Bouchard, R. Martini, M. Bernacki, Thermo-mechanical and fracture properties in single-crystal silicon. *J. Mater. Sci.* **48**, 979–988 (2013)
- J.C. McLaughlin, A.F.W. Willoughby, Fracture of silicon wafers. *J. Cryst. Growth* **85**, 83–90 (1987)
- R. Meingast, H. Alexander, Dissociated dislocations in germanium. *Phys. Status Solidi A* **17**, 229–236 (1973)
- G. Michot, Fundamentals of silicon fracture. *Cryst. Prop. Prep.* **17&18**, 55–98 (1988)
- G. Michot, M. Angela Loyola de Oliveira, A. George, Dislocation loops at crack tips: control and analysis of sources in silicon. *Mater. Sci. Eng. A* **176**, 99–109 (1994)
- A.M. Minor, E.T. Lilleodden, M. Jin, E.A. Stach, D.C. Chrzan, J.W. Morris Jr., Room temperature dislocation plasticity in silicon. *Philos. Mag.* **85**, 323–330 (2005)
- K. Minowa, I. Yonenaga, K. Sumino, Climb of dislocations induced by oxygen precipitation in silicon. *Inst. Phys. Conf. Ser.* **117**, 217–220 (1991)
- H.J. Möller, C. Funke, M. Rinio, S. Scholz, Multicrystalline silicon for solar cells. *Thin Solid Films* **487**, 179–187 (2005)
- S. Nakao, T. Ando, M. Shikida, K. Sato, Effect of temperature on fracture toughness in a single-crystal-silicon film and transition in its fracture mode. *J. Micromech. Microeng.* **18**, 015026 (2008)
- W.L. Ng, M.A. Lourenço, R.M. Gwilliam, S. Ledain, G. Shao, K.P. Homewood, An efficient room-temperature silicon-based light-emitting diode. *Nature* **410**, 192–194 (2001)
- Y. Ohno, T. Shirakawa, T. Taishi, I. Yonenaga, Interaction of phosphorus with dislocations in heavily phosphorus doped silicon. *Appl. Phys. Lett.* **95**, 091915 (2009)
- Y. Ohno, T. Taishi, Y. Tokumoto, I. Yonenaga, Interaction of dopant atoms with stacking faults in silicon crystals. *J. Appl. Phys.* **108**, 073514 (2010)
- Y. Ohno, Y. Tokumoto, H. Taneichi, I. Yonenaga, K. Togase, S.R. Nishitani, Interaction of dopant atoms with stacking faults in silicon. *Physica B* **407**, 3006–3008 (2012)
- T. Okuno, H. Saka, Electron microscopic study of dislocations introduced by deformation in a Si between 77 and 873 K. *J. Mater. Sci.* **48**, 115–124 (2013)
- P. Omling, E.R. Weber, L. Montelius, H. Alexander, J. Michel, Electrical properties of dislocations and point defects in plastically deformed silicon. *Phys. Rev. B* **32**, 6571–6581 (1985)
- M. Omri, J.P. Michel, C. Tete, A. George, Mechanical behavior of polycrystals and single crystals of silicon. in *Proceedings of International Conference on Strength of Metals and Alloys* (1985), pp. 75–80
- M. Omri, C. Tete, J.-P. Michel, A. George, On the yield point of floating-zone silicon single crystals I. Yield stresses and activation parameters. *Philos. Mag. A* **55**, 601–616 (1987)
- H. Ono, K. Sumino, Defect states in p-type silicon crystals induced by plastic deformation. *J. Appl. Phys.* **57**, 287–292 (1985)
- D. Oriwol, E.-R. Carl, A.N. Danilewsky, L. Sylla, W. Seifert, M. Kittler, H.S. Leipner, Small-angle subgrain boundaries emanating from dislocation pile-ups in multicrystalline silicon studied with synchrotron white-beam X-ray topography. *Acta Mater.* **61**, 6903–6910 (2013)
- J.R. Patel, L.C. Kimerling, Dislocation defect states in silicon. *J. Phys. Colloq. (Paris)* **40**, C6-67–C6-70 (1979)
- P. Pirouz, A.V. Samant, M.H. Hong, A. Moulin, L.P. Kubin, On temperature dependence of deformation mechanism and the brittle-ductile transition in semiconductors. *J. Mater. Res.* **14**, 2783–2793 (1999)
- L. Pizzagalli, Atomistic modeling of the dissociation of a screw dislocation in silicon. *J. Mater. Sci.* **51**, 2869–2876 (2016)

- L. Pizzagalli, P. Beauchamp, Dislocation motion in silicon: the shuffle-glide controversy revisited. *Philos. Mag. Lett.* **88**, 421–427 (2008)
- J. Rabier, On the core structure of dislocations and the mechanical properties of silicon. *Philos. Mag.* **93**, 162–173 (2013)
- J. Rabier, P. Veyssière, J.L. Demenet, Plastic deformation of silicon at low temperature and the influence of doping. *J. Phys. Colloq. (Paris)* **44**, C4-243–C4-253 (1983)
- J. Rabier, P. Cordier, J.L. Demenet, H. Garem, Plastic deformation of Si at low temperature under high confining pressure. *Mater. Sci. Eng. A* **309–310**, 74–77 (2001)
- J. Rabier, L. Pizzagalli, J.L. Demenet, Dislocations in silicon at high stress, in *Dislocations in Solids*, ed. by J. P. Hirth, L. Kubin, vol. 16, (Elsevier, Amsterdam, 2010), pp. 47–108
- J. Rabier, A. Montagne, J.M. Wheeler, J.L. Demenet, J. Michler, R. Ghisleni, Silicon micropillars: High stress plasticity. *Phys. Status Solidi C* **10**, 11–15 (2013)
- I.L.F. Ray, D.J.H. Cockayne, The dissociation of dislocations in silicon. *Proc. R. Soc. Lond. A* **325**, 543–554 (1971)
- W.T. Read, Theory of dislocations in germanium. *Philos. Mag.* **45**, 775–796 (1954)
- M. Rinio, A. Yodyunyong, S. Keipert-Colberg, D. Borchert, A. Montesdeoca-Santana, Recombination in ingot cast silicon solar cells. *Phys. Status Solidi A* **208**, 760–768 (2011)
- D. Rodney, L. Ventelon, E. Clouet, L. Pizzagalli, F. Willaime, Ab initio modeling of dislocation core properties in metals and semiconductors. *Acta Mater.* **124**, 633–659 (2017)
- B. Rynningen, G. Stokkan, M. Kivambe, T. Ervik, O. Lohne, Growth of dislocation clusters during directional solidification of multicrystalline silicon ingots. *Acta Mater.* **59**, 7703–7710 (2011)
- H. Saka, K. Yamamoto, S. Arai, K. Kuroda, In-situ TEM observation of transformation of dislocations from shuffle to glide sets in Si under supersaturation of interstitials. *Philos. Mag.* **86**, 4841–4850 (2006)
- J. Samuels, S.G. Roberts, The brittle-ductile transition in silicon. I. Experiments. *Proc. Roy. Soc. Lond. A* **421**, 1–23 (1989)
- M. Sato, K. Sumino, Locking of dislocations by impurity oxygen in silicon crystals, in *Proceedings of 9th Yamada Conference on Dislocations in Solids*, ed. by H. Suzuki, T. Ninomiya, K. Sumino, S. Takeuchi, (University of Tokyo Press, Tokyo, 1985), pp. 391–394
- M. Sato, K. Hiraga, K. Sumino, HVEM structure images of extended 60°- and screw dislocations in silicon. *Jpn. J. Appl. Phys.* **19**, L155–L158 (1980)
- R. Sauer, Ch. Kisielowski-Kemmerich, H. Alexander, Dissociation-width-dependent radiative recombination of electrons and holes at widely split dislocations in silicon. *Phys. Rev. Lett.* **57**, 1472–1475 (1986)
- W. Schröter, R. Labusch, Electrical properties of dislocations in Ge and Si. *Phys. Status Solidi* **36**, 539–550 (1969)
- W. Schröter, H. Cerva, Interaction of point defects with dislocations in silicon and germanium: Electrical and optical effects. *Solid State Phenom.* **85–86**, 67–143 (2002)
- W. Schröter, H.G. Brion, H. Siethoff, Yield point and dislocation mobility in silicon and germanium. *J. Appl. Phys.* **54**, 1816–1820 (1983)
- W. Schröter, V. Kveder, H. Hedemann, Electrical effects of point defect clouds at dislocations in silicon, studied by deep level transient spectroscopy. *Solid State Phenom.* **82–84**, 213–218 (2002)
- M. Seibt, R. Khalil, V. Kveder, W. Schröter, Electronic states at dislocations and metal silicide precipitates in crystalline silicon and their role in solar cell material. *Appl. Phys. A Mater. Sci. Process.* **96**, 235–253 (2009)
- K. Shima, S. Izumi, S. Sakai, Reaction pathway analysis for dislocation nucleation from a sharp corner in silicon: Glide set versus shuffle set. *J. Appl. Phys.* **108**, 063504 (2010)
- W. Shockley, Dislocations and edge states in the diamond crystal structure. *Phys. Rev.* **91**, 228 (1953)
- H. Siethoff, Yield point and dislocation velocity of diamond and zinblende semiconductors in different temperature regimes. *Philos. Mag. A* **82**, 1299–1316 (2002)
- H. Siethoff, H.G. Brion, W. Schröter, A regime of the yield point of silicon at high temperatures. *Appl. Phys. Lett.* **75**, 1234–1236 (1999)



- C. St. John, The brittle-to-ductile transition in pre-cleaved silicon single crystals. *Philos. Mag.* **32**, 1193–1212 (1975)
- W.A. Stepanov, V.V. Shpeizman, A kinetic treatment of the brittle fracture of materials. *Mater. Sci. Eng.* **49**, 195–228 (1981)
- M. Suezawa, K. Sumino, I. Yonenaga, Dislocation dynamics in the plastic deformation of silicon crystals II. Theoretical analysis of experimental results. *Phys. Status Solidi A* **51**, 217–226 (1979)
- M. Suezawa, K. Sumino, M. Iwaizumi, ESR in plastically deformed silicon crystals. *Inst. Phys. Conf. Ser.* **59**, 407–412 (1981)
- K. Sumino, Mechanical behaviour of semiconductors, in *Handbook on Semiconductor*, ed. by S. Mahajan, vol. 3, (North-Holland, Amsterdam, 1994), pp. 73–181
- K. Sumino, H. Harada, In situ X-ray topographic studies of the generation and multiplication processes of dislocations in silicon crystals at elevated temperatures. *Philos. Mag. A* **44**, 1319–1334 (1981)
- K. Sumino, M. Imai, Interaction of dislocations with impurities in silicon crystals studied by in situ X-ray topography. *Philos. Mag. A* **47**, 753–766 (1983)
- K. Sumino, I. Yonenaga, Dislocation dynamics and mechanical behaviour of elemental and compound semiconductors. *Phys. Status Solidi A* **138**, 573–581 (1993)
- K. Sumino, I. Yonenaga, Oxygen effect on mechanical properties, in *Semiconductors and Semimetals*, ed. by F. Shimura, vol. 42, (Academic, San Diego, 1994), pp. 449–511
- K. Sumino, I. Yonenaga, Interactions of impurities with dislocations: Mechanical effects. *Solid State Phenom.* **85–86**, 145–176 (2002)
- K. Sumino, I. Yonenaga, M. Imai, T. Abe, Effects of nitrogen on dislocation behavior and mechanical strength in silicon crystals. *J. Appl. Phys.* **54**, 5016–5020 (1983)
- H. Suzuki, Segregation of solute atoms to stacking faults. *J. Phys. Soc. Jpn.* **17**, 322–325 (1962)
- T. Suzuki, T. Yasutomi, T. Tokuoka, I. Yonenaga, Plasticity of III-V compounds at low temperatures. *Phys. Status Solidi A* **171**, 47–52 (1999)
- S.M. Sze, *Physics of Semiconductor Devices*, 2nd edn. (Wiley, New York, 1981)
- M. Tajima, Y. Iwata, F. Okayama, H. Toyota, H. Onodera, T. Sekiguchi, Deep-level photoluminescence due to dislocations and oxygen precipitates in multicrystalline Si. *J. Appl. Phys.* **111**, 113523 (2012)
- I. Takahashi, N. Usami, K. Kutsukake, G. Stokkan, K. Morishita, K. Nakajima, Generation mechanism of dislocations during directional solidification of multicrystalline silicon using artificially designed seed. *J. Cryst. Growth* **312**, 897–901 (2010)
- S. Takeuchi, Two-step temperature dependence of the yield stress in crystals. *J. Alloys Compd.* **378**, 61–65 (2004)
- M. Tanaka, K. Higashida, HVEM characterization of crack tip dislocations in silicon crystals. *J. Electron Microscopy* **53**, 353–360 (2004)
- K. Tanaka, M. Suezawa, I. Yonenaga, Photoluminescence spectra of deformed Si-Ge alloy. *J. Appl. Phys.* **80**, 6991–6996 (1996)
- M. Trushin, O. Vyvenko, V. Vdovin, M. Kittler, Giant Poole-Frenkel effect for the shallow dislocation-related hole traps in silicon. *J. Phys. Conf. Ser.* **281**, 012009 (2011)
- A. Valladares, J.A. White, A.P. Sutton, First principles simulations of the structure, formation, and migration energies of kinks on the 90° partial dislocation in silicon. *Phys. Rev. Lett.* **81**, 4903–4906 (1998)
- G. Vanderschaeve, D. Caillard, On the mobility of dislocations in semiconductor crystals. *Mater. Sci. Eng. A* **462**, 418–421 (2007)
- G. Vanderschaeve, C. Levade, D. Caillard, Transmission electron microscopy in situ investigation of dislocation mobility in semiconductors. *J. Phys.: Condens. Matter* **12**, 10093–10103 (2000)
- G.P. Watson, J.L. Benton, Y.H. Xie, E.A. Fitzgerald, Influence of misfit dislocation interactions on photoluminescence spectra of SiGe on patterned Si. *J. Appl. Phys.* **83**, 3773–3776 (1998)
- E.R. Weber, H. Alexander, Deep level defects in plastically deformed silicon. *J. Phys. Colloq. (Paris)* **44**, C4-319–C4-328 (1983)
- J. Weber, M.I. Alonso, Detection of dislocation-related photoluminescence bands in Si-Ge alloys grown by liquid phase epitaxy, in *Defect Control in Semiconductors*, ed. by K. Sumino, (North-Holland, Amsterdam, 1990), pp. 1453–1457

- J.D. Weeks, J.C. Tully, L.C. Kimerling, Theory of recombination-enhanced defect reactions in semiconductors. *Phys. Rev. B* **12**, 3286–3292 (1975)
- M. Werner, M. Bartsch, U. Messerschmidt, D. Baiter, TEM observations of dislocation motion in polycrystalline silicon during in situ straining in the high voltage electron microscope. *Phys. Status Solidi A* **146**, 133–143 (1994)
- M. Werner, E.R. Weber, M. Bartsch, U. Messerschmidt, Carrier injection enhanced dislocation glide in silicon. *Phys. Status Solidi A* **150**, 337–341 (1995)
- K. Wessel, H. Alexander, On the mobility of partial dislocations in silicon. *Philos. Mag.* **35**, 1523–1536 (1977)
- S.-B. Woo, M. Bertoni, K.-M. Choi, S.-J. Nam, S. Castellanos, D.M. Powell, T. Buonassisi, H.-J. Choi, An insight into dislocation density reduction in multicrystalline silicon. *Sol. Energy Mater. Sol. Cells* **155**, 88–100 (2016)
- Y. Yamamoto, K. Togase, Y. Ohno, I. Yonenaga, S.R. Nishitani, First principles calculations of solution energies of dopants around stacking faults in Si crystal. *Jpn. J. Appl. Phys.* **53**, 061302 (2014)
- Y. Yamashita, E. Jyobe, Y. Kamiura, K. Maeda, Hydrogen enhanced dislocation glides in silicon. *Phys. Status Solidi A* **171**, 27–34 (1999)
- K. Yasutake, S. Shimizu, M. Umeno, H. Kawabe, Velocity of twinning partial dislocations in silicon. *J. Appl. Phys.* **61**, 940–946 (1987)
- I. Yonenaga, Upper yield stress of Si crystals at high temperature. *J. Electrochem. Soc.* **143**, 176–178 (1996)
- I. Yonenaga, Strength of Si crystals. *Recent Res. Dev. ElectroChem.* **1**, 161–176 (1998)
- I. Yonenaga, Growth and mechanical properties of GeSi bulk crystals. *J. Mater. Sci.: Mater. Electron.* **10**, 329–333 (1999)
- I. Yonenaga, Dislocation-impurity interaction in silicon. *Solid State Phenom.* **95–96**, 423–432 (2004)
- I. Yonenaga, Nitrogen effects on generation and velocity of dislocations in Czochralski-grown silicon. *J. Appl. Phys.* **98**, 023517 (2005a)
- I. Yonenaga, Dislocation-impurity interaction in Si. *Mater. Sci. Eng. B* **124–125**, 293–296 (2005b)
- I. Yonenaga, Growth and fundamental properties of SiGe bulk crystals. *J. Cryst. Growth* **275**, 91–98 (2005c)
- I. Yonenaga, Hardness, yield strength, and dislocation velocity in elemental and compound semiconductors. *Mater. Trans.* **46**, 1979–1985 (2005d)
- I. Yonenaga, An overview of plasticity of Si crystals governed by dislocation motion. *Eng. Fract. Mech.* **147**, 468–479 (2015)
- I. Yonenaga, K. Sumino, Dislocation dynamics in the plastic deformation of silicon crystals I. Experiments. *Phys. Status Solidi A* **50**, 685–693 (1978)
- I. Yonenaga, K. Sumino, Influence of oxygen precipitation along dislocations on the strength of silicon crystals. *J. Appl. Phys.* **80**, 734–738 (1996)
- I. Yonenaga, K. Takahashi, Effect of magnetic field on dislocation-oxygen impurity interaction in silicon. *J. Appl. Phys.* **101**, 053528 (2007)
- I. Yonenaga, T. Taishi, X. Huang, K. Hoshikawa, Dynamic characteristics of dislocations in highly boron-doped silicon. *J. Appl. Phys.* **89**, 5788–5790 (2001)
- I. Yonenaga, T. Taishi, X. Huang, K. Hoshikawa, Dynamic characteristics of dislocations in Ge-doped and (Ge+B) codoped silicon. *J. Appl. Phys.* **93**, 265–269 (2003)
- X.-G. Yu, J. Chen, X.-Y. Ma, D. Yang, Impurity engineering of Czochralski silicon. *Mater. Sci. Eng. R* **74**, 1–33 (2013)
- T.-Y. Zhang, P. Haasen, The influence of ionized hydrogen on the brittle-to-ductile transition in silicon. *Philos. Mag. A* **60**, 15–38 (1989)
- B. Ziebarth, M. Mrovec, C. Elsässer, P. Gumbsch, Interstitial iron impurities at cores of dissociated dislocations in silicon. *Phys. Rev. B* **92**, 195308 (2015)



# Grain Boundaries in Multicrystalline Silicon 19

Matthias Trempa, Georg Müller, Jochen Friedrich, and Christian Reimann

## Contents

Introduction .....	590
Grain Boundaries and Their Influences on Solar Cell Performance .....	592
Classification and Types of Grain Boundaries .....	592
Properties of Grain Boundaries .....	596
Characterization of Grain Boundaries .....	599
Overview .....	599
Optical Grain Detection and Analysis .....	601
Orientation Mapping and Determining Grain Boundary Types .....	605
Characterization of Electronic Material Properties in Relation to Grain Structure and Grain Boundaries .....	607
Formation of Grain Boundaries During Directional Solidification (DS) .....	609
Coarse Grain Structures Without Seed Crystals (Classic mc and Dendritic mc) .....	613
Towards Monocrystals by Using Monocrystalline Seeds (Quasi-Mono QM) .....	618
Fine Grain Structures with Seeding on Si Feedstock (Original HPM) .....	625
Fine Grain Structures Without Seeding on Si Material (HPM 2.0) .....	630
Conclusions for Optimization Strategies with Respect to “Grain Boundary Engineering” .....	633
Cross-References .....	634
References .....	635

---

M. Trempa (✉)

Fraunhofer Institute for Integrated Systems and Device Technology (IISB), Erlangen, Germany  
e-mail: [matthias.trempa@iisb.fraunhofer.de](mailto:matthias.trempa@iisb.fraunhofer.de)

G. Müller

Crystal Consulting, Langensendelbach, Germany  
e-mail: [mueller@crystalconsulting.de](mailto:mueller@crystalconsulting.de)

J. Friedrich · C. Reimann

Fraunhofer Technology Center Semiconductor Materials (THM), Freiberg, Germany

Fraunhofer Institute for Integrated Systems and Device Technology (IISB), Erlangen, Germany  
e-mail: [jochen.friedrich@iisb.fraunhofer.de](mailto:jochen.friedrich@iisb.fraunhofer.de); [christian.reimann@iisb.fraunhofer.de](mailto:christian.reimann@iisb.fraunhofer.de)

---

**Abstract**

Directionally solidified (DS) silicon is typically multicrystalline (mc), i.e., it contains per definition grain boundaries. Even so-called quasi-mono silicon is not free of grain boundaries. The crystallographic arrangement of neighboring grains is used for a definition of the certain types of grain boundaries by the so-called coincidence site lattice parameter  $\Sigma$ . It turns out that the predominant types of grain boundaries are twin ( $\Sigma = 3$ ), small angle ( $\Sigma \sim 1$ ), and large angle (“random”) grain boundaries. For the solar cell application, it is of great relevance that the nontwin boundaries are often accompanied by dislocation defects. These dislocations, especially their clusters, are well known to reduce the minority charge carrier lifetime and hence the efficiency of solar cells. Therefore, the corresponding characterization methods for the types of grain boundaries, their length, spatial distribution, and grain size will be presented in this chapter.

The main part of the chapter presents a detailed treatment of the occurrence of the various types of grain boundaries and the related dislocations structures for different variants of the DS method. The most important DS variants differ from each other mainly by the seeding and nucleation processes which result in different sizes of the grains and also different prevailing grain boundaries. The so-called classic mc, dendritic mc, and quasi-mono Si material have relatively large average grain sizes ranging from mm up to cm. The solar cell performance of this material is mainly limited by the occurrence of dislocation structures which can easily spread in the relatively large grains. This problem seems to be decreased in a recently developed fine grained material (micro-meter up to mm scale). The variety of nucleation concepts to achieve a fine grained structure reaches from seeding with small Si feed or non-Si particles to specially structured profiles of the crucible bottom. The resulting higher performance of solar cells is promising for the future and gave reason to call the material high performance mc Si (HPM).

The whole chapter includes results of recent worldwide research and development activities but provides also its proving under production-like conditions. All results are illustrated by corresponding figures and allocated to important references.

---

**Keywords**

Multicrystalline silicon · Grain boundaries · Directional solidification · Small angle grain boundaries · Large angle grain boundaries · Twin boundaries · Random grain boundaries · Laue scanner method

---

**Introduction**

Most solar cells are produced by using either monocrystalline silicon grown by the Czochralski (CZ) crystal pulling method (► [Chap. 6, “Growth of Crystalline Silicon for Solar Cells: Czochralski Si”](#)) or multicrystalline silicon obtained by directional solidification (DS) of the melt in a crucible (► [Chap. 7, “Growth of Multicrystalline](#)

[Silicon for Solar Cells: The High-Performance Casting Method](#)"). The DS equipment and process technology is less expensive compared to Czochralski. However, solar cells made from DS silicon have about 2% less efficiency compared to CZ-based cells. The main reason for this difference is the fact that DS silicon is not mono- but multicrystalline which means it contains defects like grain boundaries and dislocations, whereas CZ silicon is free of grain boundaries (= definition of monocrystalline) and typically free of dislocations. In combination with a higher amount of metals in DS silicon, the crystallographic defects like grain boundaries get even more detrimental to the solar cell performance.

Grain boundaries are by definition crystal regions where two grains i.e., monocrystalline silicon regions of different crystallographic orientation are neighboring each other. It is obvious that in between the two grains a transition region exists where the atoms are shifted in general from their regular positions in comparison to the lattice of a perfect monocrystal. For example, dislocation defects are typically occurring within the boundary region. It will be shown that the specific difference in orientation between the two grains has an important influence on the degree of lattice disorder within the grain boundary. That means the effect of a grain boundary on the electronic material properties and hence on the solar cell performance can considerably differ depending on the "type of grain boundary."

For example, certain types of grain boundaries can reduce the formation, movement, or multiplication of dislocations which are accompanying the grain boundary defects. Furthermore, certain grain boundaries can interfere with gettering mechanisms during solar cell fabrication processes like the phosphorus or hydrogen gettering.

With respect to the future development of silicon-based solar cells, it is important to consider which potential the DS process has regarding a further improvement of the material quality, i.e., reduction of deleterious crystal defects like grain boundaries and accompanying dislocations. From the point of view of research and development of silicon material preparation, one can state that the work on the CZ crystal growth process started already around 1950. It was mainly driven in the past by the requirements of micro- and power electronic devices. The DS process of silicon was from the beginning only of interest for photovoltaic applications. Intensive research and development activities on DS of silicon started fairly later between 2000 and 2010. Therefore, one can expect that there still exists a considerable potential to improve the DS process further by future research and development activities, especially with respect to an optimization of grain boundary growth.

It is the main goal of this chapter to show how certain conditions and parameters of the DS process like seeding, crucible preparation, or thermal profiles are related to the formation of certain types of grain boundaries (section "[Formation of grain boundaries during directional solidification \(DS\)](#)"). Based on these results, one can draw certain conclusions for "grain boundary engineering," i.e., optimizing the DS process to achieve high solar cell performance material. In the first part, the criteria for classifying the various types of grain boundaries will be introduced and its specific influences on the solar cell performance. In the following an overview of characterization methods for grain boundary types is given with special emphasis on methods which are applicable to the complete solar wafer area of  $156 \times 156 \text{ mm}^2$ .

## Grain Boundaries and Their Influences on Solar Cell Performance

### Classification and Types of Grain Boundaries

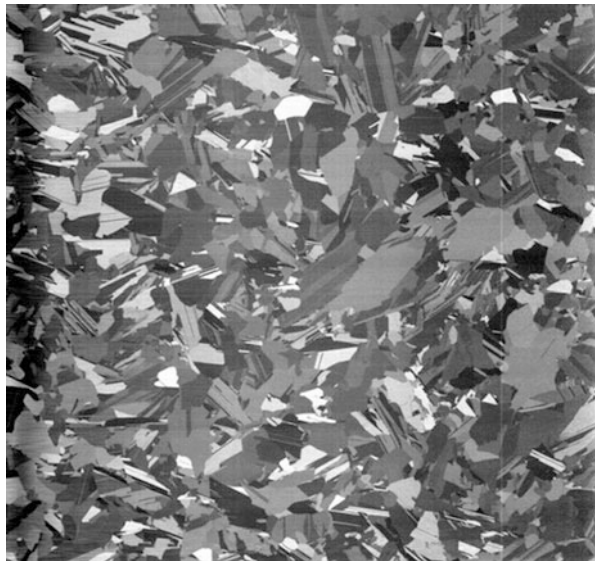
In the previous chapters of this handbook, e.g., ► [Chaps. 17, “Metal Impurities and Gettering in Crystalline Silicon”](#) or ► [18, “Defects in Crystalline Silicon: Dislocations,”](#) it has been shown that various types of crystal defects can occur in photovoltaic Si depending on the production method of the Si crystals or ingots. This chapter treats grain boundaries which are occurring only in multicrystalline Si obtained typically by directional solidification and “kerfless processes” including ribbon growth and direct deposition on alternative substrates.

By definition, “multi”-crystalline (mc) Si consists of a number of monocrystalline grains which are separated from each other by a grain boundary. Typically, the grains in a multicrystalline material like Si have different crystallographic orientations as shown, for example, in [Fig. 1](#) (where the different grain orientations are visible due to the different light reflection).

That means a grain boundary is a transition region between two monocrystalline crystal regions where the regular crystal lattice is distorted.

This misfit on the atomistic scale of a grain boundary is the reason why grain boundaries must be considered generally as a crystal defect which can have deleterious influences on the electronic properties of the solar cell material. However, it is also obvious that the defect generating degree of misfit in a certain grain boundary depends on the orientation of the adjacent crystal lattices of the two neighboring grains. Therefore, one should expect a different degree of deleterious influence on the solar cell performance depending on the orientation between the two grains. In fact the first goal of this chapter will be to explain and demonstrate which type of

**Fig. 1** Typical mc-wafer ( $156 \times 156 \text{ mm}^2$ ) after structural etching (details see later). (© Fraunhofer IISB)



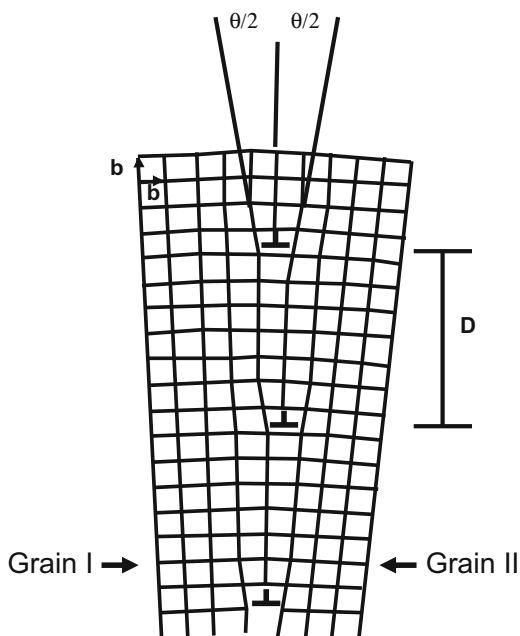
grain boundary in mc-Si is less deleterious and can be tolerated in solar cells and which one is more harmful and should be avoided.

### Description and Types of Grain Boundaries

A grain boundary can be fully described by five independent macroscopic degrees of freedom (DOFs). Three DOFs specify the mutual misorientation of the two grains and two more DOFs are needed to define the orientation of the grain boundary itself between the misorientated grains. Considering the necessity of five DOFs for a complete crystallographic description of a grain boundary, one can expect a huge number of different grain boundaries. However, it turns out that materials like Si prefer only a few types of grain boundaries for energetic reasons. Therefore, it is reasonable to categorize the grain boundaries into groups according to the relationship among individual DOFs.

A very special grain boundary occurring relatively often in mc-Si is the so-called “small angle grain boundary” (SAGB) in contrast to all other grain boundaries which are named as large angle grain boundaries. In SAGBs, the angle of misorientation between the two adjacent grains is small (a few degrees or less). In this case, the lattice mismatch on the atomic scale can be described by an array of edge-type dislocations along the grain boundary. This model is illustrated in Fig. 2 for a cubic primitive lattice. The angle  $\theta$  of the misorientation between the two lattices can be related to the Burgers vector  $b$  and the distance  $D$  between two dislocations.

**Fig. 2** Sketch of a small-angle grain boundary: Two grains (I and II) having a common [001] axis and angular difference in orientation of  $\theta$  are forming a low-angle grain boundary which can be considered to consist of an array of edge dislocations



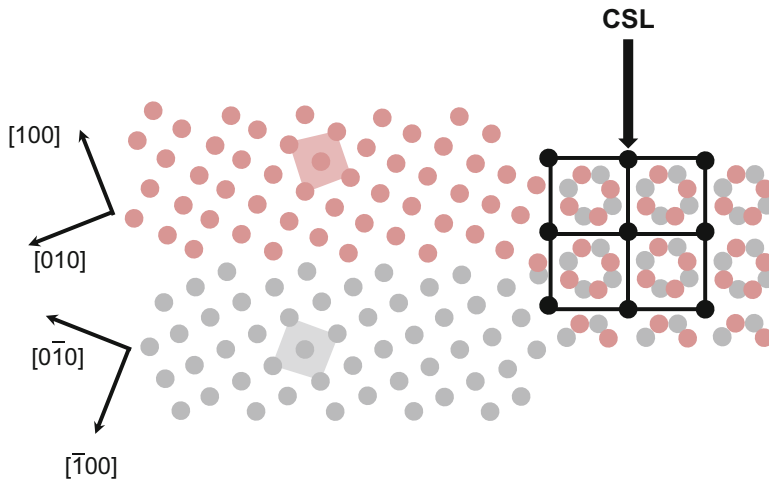


**Fig. 3** Sketch for an evaluation of the coincidence site lattice (CSL). See also text

$$D = \frac{b}{2 \sin\left(\frac{\theta}{2}\right)} \approx \frac{b}{\theta}$$

For very small angles  $\theta$ , the relation can be approximated by  $D = b/\theta$ . This relation allows for an estimation of the tilt angle between the grains if the dislocation density in the grain boundary is known. For increasing grain boundary angle  $\theta$ , the spacing  $D$  between the dislocations decreases and the model above becomes no longer useful. The common concept for these cases is the coincidence site lattice (CSL) model. It is based on the fact that for certain orientations of the two lattices of the two neighboring grains, parts of the lattice sites coincide if one continues the two lattices into the respective grains. This construction is exemplified by Fig. 3.

The CSL model is very popular because it allows describing the grain boundary by only one parameter  $\Sigma$  instead of five.  $\Sigma$  is defined by the ratio between the number of lattice sites within the unit cell of the coincidence lattice and the unit cell of the crystal, i.e.,  $S_i$ . This ratio is equal to the volume of the unit cell of the coincidence lattice divided by the volume of the  $S_i$  unit cell. According to this definition, the values of  $\Sigma$  are always odd numbers.  $\Sigma$  equal to one defines the monocrystal. The small angle grain boundary discussed above would have a  $\Sigma$  value which is close to one. The lowest integer  $\Sigma$  value except one is  $\Sigma = 3$  which describes a so-called first order twin boundary. Twin boundaries are grain boundaries with the highest symmetry and lowest disturbance of the crystal lattice. Figure 4 shows a typical  $\Sigma = 3$  twin configuration of Si where the two Si grains have the same  $\langle 111 \rangle$ -orientation.

Within the twin grain boundary, all Si bonds are saturated, i.e., no open dangling bonds exist. The lattices of the two grains are twisted by  $60^\circ$  to each other within the twin plane only. The formation energy of this grain boundary is very low because it



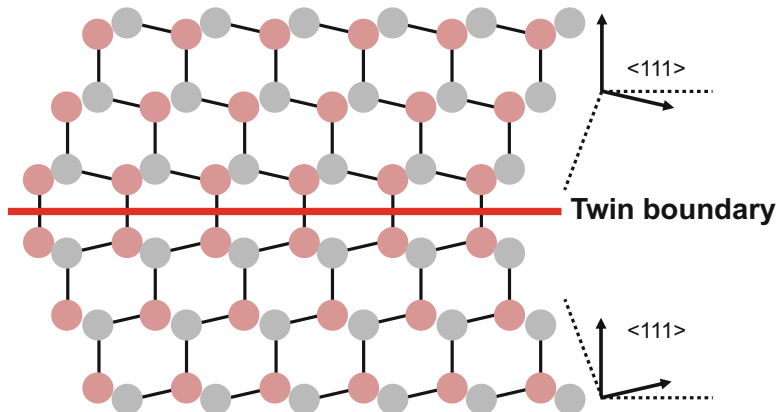


**Fig. 4** Sketch of a  $\langle 111 \rangle \Sigma = 3$  twin boundary

corresponds just to one stacking fault within the sequence of the Si layers. The energy  $E_{SF}$  of the stacking fault formation in Si is relatively low ( $E_{SF} = 26 \text{ mJ/m}^2$ ). Therefore, its formation can occur very often during the growth of mc-Si.

Other types of twin boundaries have values of  $\Sigma = \Sigma 3^n$  whereas their occurrence in mc-Si material decreases in frequency with increasing  $\Sigma$  value from  $\Sigma 3$  to  $\Sigma 9$  to  $\Sigma 27$ . Also other  $\Sigma$  grain boundaries like  $\Sigma 5$  or  $\Sigma 11$  exist but very rarely. In theory, very large  $\Sigma$  values can be calculated; however, a grain boundary with  $\Sigma > 27$  is practically stated as a random large angle grain boundary due to its low symmetry. It has to be noted that one  $\Sigma$  type can be formed by several lattice operations meaning the rotation about a specific crystallographic axis by certain degrees. For instance, there exists beside the already mentioned  $\Sigma 3 \{111\}$  (rotation angle:  $60^\circ$ ) also a  $\Sigma 3 \{112\}$  grain boundary (rotation angle  $180^\circ$ ). Further details, for example, on orientation relations between grains of certain  $\Sigma$  types are discussed in literature (see Vlachavas 1985; Wilhelm 1971).

For a general application of the CSL concept including large angle grain boundaries, one has to consider that in a real crystal, certain deviations of the atoms from the exact CSL relationship may exist. Therefore, it is important to define a criterion for the permissible deviation from exact coincidence. Such a criterion was given by Brandon (1966). Its derivation is based on the assumption that deviations from the exact lattice site coincidence can be attributed to slight orientation deviations caused by arrays of dislocations. Such a dislocation model was already used above for the description of small angle grain boundaries (compare Fig. 2). Brandon's criterion gives a relation for the maximum permissible deviation angle  $\theta$  in dependence of the CSL parameter  $\Sigma$

$$\theta = \theta_0 (\Sigma)^{-1/2}$$

where  $\theta_0$  is constant about  $15^\circ$ . According to this criterion, the transition from a small angle grain boundary ( $\Sigma \sim 1$ ) to a large angle grain boundary is at  $\theta \sim 15^\circ$ .

## Properties of Grain Boundaries

### Energy of Grain Boundaries

Each grain boundary means an extra energy in the crystal lattice compared to the single crystal. This extra energy (grain boundary energy) has the unit  $J/m^2$  and is specific for each type of grain boundary. In Fig. 5, the specific grain boundary energy for Si is plotted versus the tilt angle  $\theta$  against the [110] plane. Certain  $\Sigma$ -values have minima of the grain boundary energy especially the  $\Sigma 3 - \{111\}$  twin boundary – with a tilt angle of about  $70^\circ$  to the [110] direction. These energetic minima correlate with the observation that twin boundaries, especially the type  $\Sigma 3$ , have the highest frequency of occurrence compared to other types of grain boundaries. Obviously, the growing mc crystal follows the thermodynamic principle of minimizing its Gibbs free energy.

It explains also the observation that grain boundaries with lower symmetry split into grain boundaries with higher symmetry, for example,  $R \rightarrow \Sigma 3 + \Sigma 27$  (see Fig. 6 on the left). Another often observed phenomenon is the split of low energy grain boundaries from nonperfect  $\Sigma$  grain boundaries or grain boundaries with higher energy, e.g.,  $R \rightarrow R^* + \Sigma 3$  (see Fig. 6 on the right). In these cases, the gain in grain boundary energy is obviously larger than the extra energy for the extension of the grain boundary length.

### Decoration of Grain Boundaries with Impurity Atoms

The Gibbs free energy of a grain boundary can also be reduced by incorporation of foreign atoms, i.e., impurity atoms. This process is driven by thermodynamics but controlled by kinetics. The diffusive transport of the impurity atoms from the interior

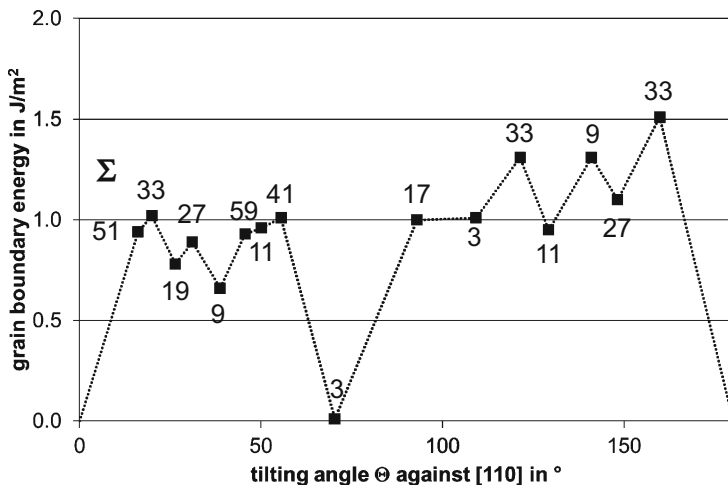


**Fig. 5** Grain boundary energy in Si in dependence on tilting angle  $\theta$  against [110] direction. The corresponding values of  $\Sigma$  are given at the top.  $\theta = 0^\circ$  and  $\theta = 180^\circ$  correspond to  $\Sigma = 1$ . Values after Kohyama et al. (1986)

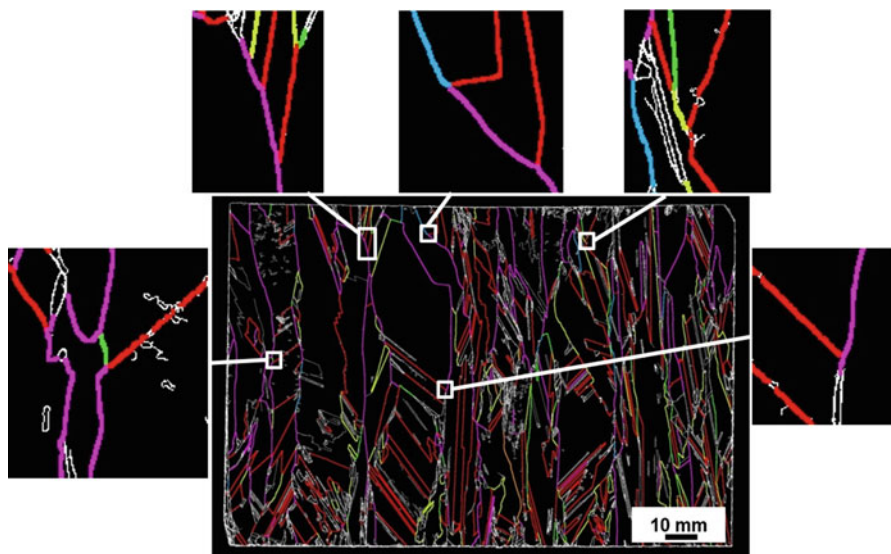


**Fig. 6** Splitting of low symmetry grain boundaries into high symmetry grain boundaries during growth of mc Si, measured on a cut parallel to the growth direction. The colors represent the different grain boundary types;  $\Sigma 3$  (red),  $\Sigma 9$  (yellow),  $\Sigma 27$  (green), and R (purple). (© Fraunhofer IISB)

of a grain into the grain boundary depends on the diffusivity and the temperature – time conditions. It can be expressed in terms of a diffusion length. As a consequence, the region within the diffusion length around a grain boundary is denuded from impurity atoms which are collected within the grain boundary. The latter effect is called “gettering” and can lead to an increased minority charge carrier lifetime  $\tau$  (see, e.g., Martinuzzi et al. 2007). Additionally, the diffusion velocity of impurity atoms is increased along grain boundaries. This can be observed in typical lifetime images of mc Si bricks or wafers (see Fig. 7 on the right) where metal atoms diffuse from the highly contaminated bottom and top into the ingot volume and cause local areas of lower lifetime at grain boundaries and dislocation clusters.

The minority charge carrier lifetime  $\tau$  is one of the main material parameters, which determines the solar cell performance and is often directly correlated to the concentration of the impurity (mainly metal) atoms (► Chap. 17, “Metal Impurities and Gettering in Crystalline Silicon”). A direct clear evidence of the impurity accumulation in grain boundaries of mc-Si was given by Buonassisi et al. (2007) and is shown in Fig. 7.

This result shows additionally that the metal content of grain boundaries increases with increasing CSL number  $\Sigma$ . However, it has to be kept in mind that the accumulation of specific metal atoms in grain boundaries is depending on the specific diffusivity of the metal in Si. This effect was studied for various contaminating metals (Cu, Fe, Ni, Ti) (Buonassisi et al. 2007). They found a clear anticorrelation between the diffusivity and the fraction of impurities inside the grain which do not reach the grain boundary. Additionally it was shown (Bauer et al. 2007) that during the movement of the solid-liquid interface during the crystal growth process, carbon and nitrogen atoms

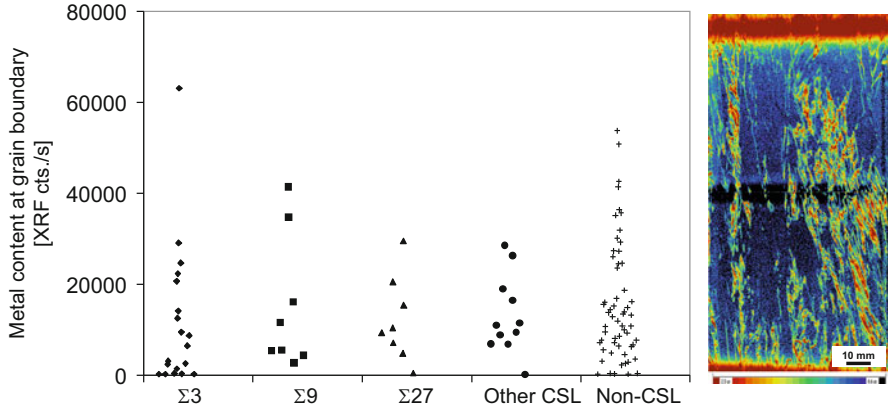


**Fig. 7** Left: Accumulation of metal atoms at grain boundaries detected by X-ray fluorescence analysis for various types of grain boundaries. After Buonassisi et al. (2007). (Right) Lifetime image of a vertical section of an industrial mc Si brick from bottom (below) to top end. (© Fraunhofer IISB)

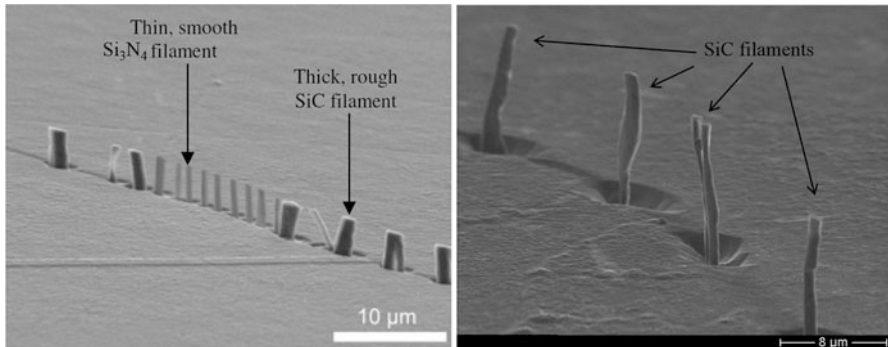


**Fig. 8** SEM images of Si<sub>3</sub>N<sub>4</sub> and SiC filaments along grain boundaries in mc silicon. After Bauer et al. (2007)

can be enriched in grain boundary grooves and lead to the formation of SiC and Si<sub>3</sub>N<sub>4</sub> filaments along the grain boundary (compare Fig. 8).

### Impact of Grain Boundaries on Electronic Properties

The most important impact of grain boundaries on solar cell performance is via its influence on the lifetime  $\tau$  of the minority charge carriers. This effect is related to the classical Shockley-Hall-Read recombination mechanism of dangling bonds which are occurring at certain types of grain boundaries, dislocations, and metallic impurities accumulated within grain boundaries. The influence of grain boundaries on  $\tau$  depends on their type and decoration by metallic impurities. Contaminated grain boundaries are decreasing  $\tau$  mainly because of the metal impurities which form deep recombination levels in the Si band gap. Such contamination-related problems including electric short cuts by decorated grain boundaries can

generally be reduced by the corresponding purity of the Si feedstock (► Chap. 2, “Polysilicon and Its Characterization Methods”) and proper purification measures during the DS process. “Pure,” i.e., noncontaminated grain boundaries are considered to be less or even not harmful for  $\tau$ . This holds at least for low  $\Sigma$  type grain boundaries, compare (Tsurekawa et al. 2007). Other grain boundary types may have also an influence on the mobility of the charge carriers, e.g., by scattering due to the potential barriers.

### Dislocations and Grain Boundaries

Crystal defects in the form of dislocations are of enormous importance for the performance of Si solar cells (► Chap. 18, “Defects in Crystalline Silicon: Dislocations”) Dislocations are mainly generated at grain boundaries during the solidification at the solid-liquid interface and can only be avoided reliably by growing a single crystal. That means the formation of grain boundaries in mc-Si is inherently connected with the formation and existence of dislocations. It was already shown in section “Classification and Types of Grain Boundaries” that small angle grain boundaries can be considered as an array of dislocations (compare Fig. 2). Also any deviations of grain boundaries from the ideal CSL criterion can be attributed to dislocations. Only perfect twin boundaries (means a deviation angle  $\theta = 0$ ) like  $\Sigma 3$ ,  $\Sigma 9$ , and  $\Sigma 27$  are free of dislocations. Therefore, it is not surprising that dislocations in mc-Si can be distributed very inhomogeneously according to the wide variety of different grain boundary types and especially due to the different orientations of glide planes in the neighboring grains in this material. Experimental results show that the density of dislocations and especially the formation of so-called dislocation clusters are strongly depending on the orientation of the grains with respect to the direction of solidification and to the orientation of neighboring grains. This can lead to a distribution where grains with a dislocation density of higher than  $10^6 \text{ cm}^{-2}$  are close to nearly dislocation-free grains.

In summary, one can state that one important prerequisite for producing high quality mc-Si based solar cells consists in a selection of such grain boundaries which do not provoke the formation and multiplication of dislocations within the grown Si ingot. Therefore, the nowadays typically used solidification processes for mc Si will be analyzed in detail with respect to the influence of the thermal boundary conditions and the seeding specifications on the formation of specific grain boundaries and the related dislocations (see section “Formation of Grain Boundaries During Directional Solidification (DS)”). Prior to that, the important methods of characterizing grain boundaries will be introduced.

---

## Characterization of Grain Boundaries

### Overview

Grain boundaries in Si can be characterized by a variety of methods. The selection of the proper method depends on the aim and the expenditure which can be made. A qualitative visualization of grains and grain boundaries is possible by viewing

the light which is reflected from a metallographically treated Si surface. This effect is due to the optical property of a crystalline Si surface that its reflectance is depending on the crystallographic orientation. Such pictures can be evaluated by image processing to provide data like the statistical distribution of the grain size or the total length of the grain boundaries. A quantitative evaluation of the crystallographic orientations of certain grains is possible by electron or X-ray diffraction methods. By combining the crystallographic orientation of various grains with their local position on a wafer, it is possible to display the grain boundaries according to their types, for example, in the CSL notation. This kind of characterization is very helpful for the optimization of solidification processes and will be used extensively in the section “[Formation of grain boundaries during directional solidification \(DS\)](#)”.

So far the methods of characterization mentioned above relate mainly to the geometry and crystallographic orientation relations of grains and grain boundaries. Beyond that a variety of characterization tools is available which can be used to analyze material properties which are relevant for solar cells in relation to certain orientation and size of grains, types of grain boundaries, and their distribution. Among these methods are photoluminescence (PL), electron beam induced current (EBIC), X-ray diffraction, and electron microscopy (SEM, TEM). Table 1 gives an overview of the various characterization methods in relation to the objectives. More details are presented in the following sections.

**Table 1** Characterization of grain boundaries

Objective	Method
Visualization of grains and grain boundaries	Optical microscopy after (chemo-) mechanical treatment & defect selective etching (also small angle grain boundaries and dislocations visible) Optical reflection analysis after metallographic treatment (only large angle grain boundaries visible)
Evaluation of grain size, distribution and total grain boundary length	Image processing of reflection images
Recording and determination of grain orientations on a sample surface (“orientation map”)	Calibrated reflection image Electron back-scatter diffraction (EBSD) X-ray diffraction (Laue method)
Evaluation of types of grain boundaries and their local distribution	EBSD mapping (for small samples!) “Laue Scanner” (for full wafer size)
Evaluation of grain boundaries with a very high local resolution (down to atomic scale)	X-ray topography (XRT) Transmission electron microscopy (TEM)
Local evaluation of electronic properties in correlation with grain structure and grain boundaries	Photoluminescence (PL) Electron beam induced current (EBIC)

## Optical Grain Detection and Analysis

The grain structure of a mc-Si sample or wafer, respectively, is already visible by the naked eye after sawing. This is due to the dependence of the reflectivity of visual light from the crystallographic orientation of a certain grain surface. The precision and information value of the optical grain detection can be improved by using a metallographic treatment (e.g., grinding, lapping) of the surface, an accompanied wafer texturing step and/or image processing. A state of the art in-line grain structure inspection requires fast measuring times and is therefore mostly limited to reflection measurements on as-sawn or textured wafers.

To visualize in detail crystallographic features like small and large angle grain boundaries as well as single dislocations (so-called etch pits), a number of etching solutions is reported in literature with different etching behavior (e.g., nonisotropic or isotropic). A selection of etchants is compiled in Table 2 together with their recipes and the applicability for different electrical resistivity ranges and grain orientations.

**Table 2** Si etchants for grain boundary analysis after Sirtl and Adler (1961), Secco D’Aragona (1972), Wright-Jenkins (1977), Schimmel (1979), Yang (1984), and Sopori (1984)

Etchant	Typical etch rate ( $\mu\text{m}/\text{min}$ )	Resistivity range ( $\Omega\text{cm}$ )	Remarks
<b>Sirtl</b> 1 HF (49%) 1 $\text{CrO}_3$ (5 M)	3.0 on (111)	Not specified	Not as good for (100) orientation
<b>Secco</b> 1 HF (49%) 1 $\text{K}_2\text{Cr}_2\text{O}_7$ (0.15 M)	1.5 on (100)	4–300	
<b>Wright-Jenkins</b> 60 ml HF (49%) 30 ml $\text{HNO}_3$ (69%) 30 ml $\text{CrO}_3$ (5 M) 2 g $\text{Cu}(\text{NO}_3)_2$ 60 ml $\text{CH}_3\text{COOH}$ (100%) 60 ml $\text{H}_2\text{O}$	1.0 on (100)	0.02–20	Not as good for dislocations, especially on (100)
<b>Schimmel</b> 2 HF (49%) 1 $\text{CrO}_3$ (5 M)	~1.8 on (100)	0.6–15 (modified Schimmel etch <0.6)	
<b>Yang</b> 1 HF (49%) 1 $\text{CrO}_3$ (1.5 M)	1.5 on (100) 1.5 on (111)	At least 0.5–20	Better for dislocations than Wright
<b>Sopori</b> 36 HF (49%) 1–2 $\text{HNO}_3$ (70%) 20 $\text{CH}_3\text{COOH}$ (100%)	5–20 on all surfaces	At least 0.1–16	



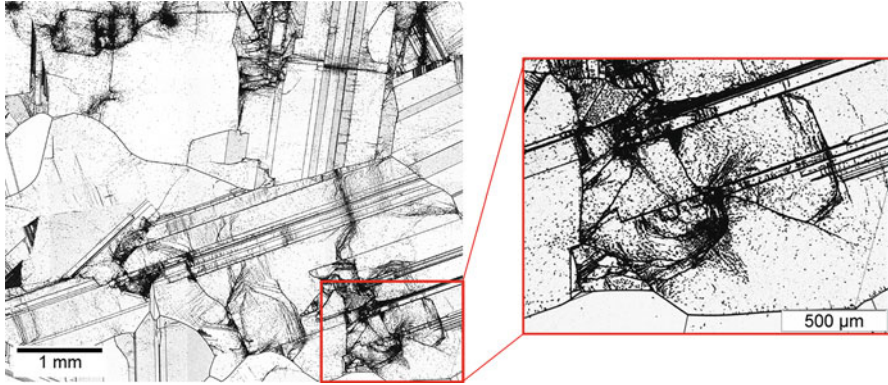


**Fig. 9** Nonsymmetric grain boundaries, twins, and dislocations (e.g., etch pits in the lower right region) visible after mechanical polishing and Secco etching of a mc silicon wafer. (© Fraunhofer IISB)

The number of dislocation-related etch pits per wafer area is called *etch pits density* (EPD, unit  $1/\text{cm}^2$ ) and is an important value for characterizing the material quality with respect to photovoltaic performance (see previous chapter of this handbook).

### **Optical Microscopy for Local Investigation of the Silicon Sample with High Resolution**

After defect selective etching, the EPDs as well as small and large angle grain boundaries can be studied by optical microscopy in the reflection mode (see Fig. 9). This method provides a resolution in  $\mu\text{m}$  range and is of special importance for the study of dislocations and dislocation clusters in correlation with certain types of grain boundaries. This topic will be extensively discussed in the section “[Formation of grain boundaries during directional solidification \(DS\)](#)”.

### **Scanning Electron Microscopy and Transmission Electron Microscopy for Local Investigation of the Silicon Sample with Higher and Ultra High Resolution**

For more detailed investigation of grain boundaries and adjacent dislocations, the Scanning Electron Microscopy (SEM) or the Transmission Electron Microscopy (TEM) can be used. These methods provide extremely high resolutions from sub- $\mu\text{m}$  to sub-nm range. By use of the TEM, even the atomic structure of grain boundaries can be observed as shown in Fig. 10. The disadvantage of these methods is the quite high effort for sample preparation.

### **Image Processing for Evaluation of Grain Sizes and Lengths of Grain Boundaries on Full Wafer Scale**

The information about the grain structure of a mc-Si sample or wafer, respectively, obtained from the reflection patterns can be improved considerably by image



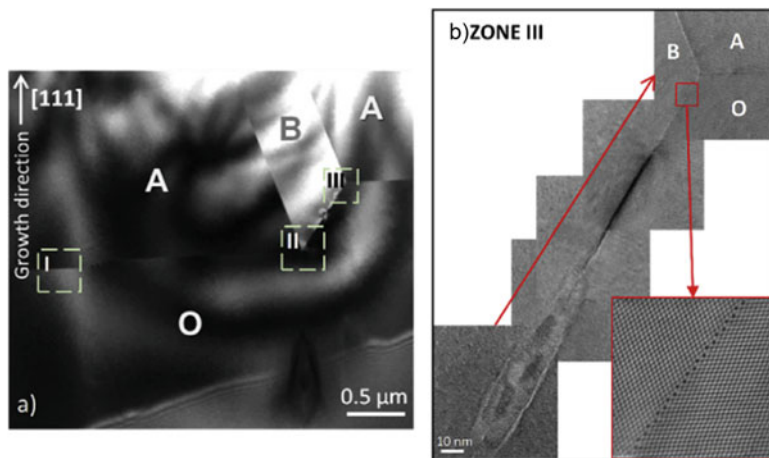


**Fig. 10** (a) TEM image of the cross-section of a twin nucleus. (b) Higher magnifications of zone III of a:  $\Sigma 9 \{221\}$  grain boundary, shown also in ultra high resolution by HR-TEM (lower square). Along the  $\Sigma 9$  interface, the highly distorted regions were followed by coherent (221) interfaces as shown in the HR-TEM magnification. After Oliveira et al. (2016)

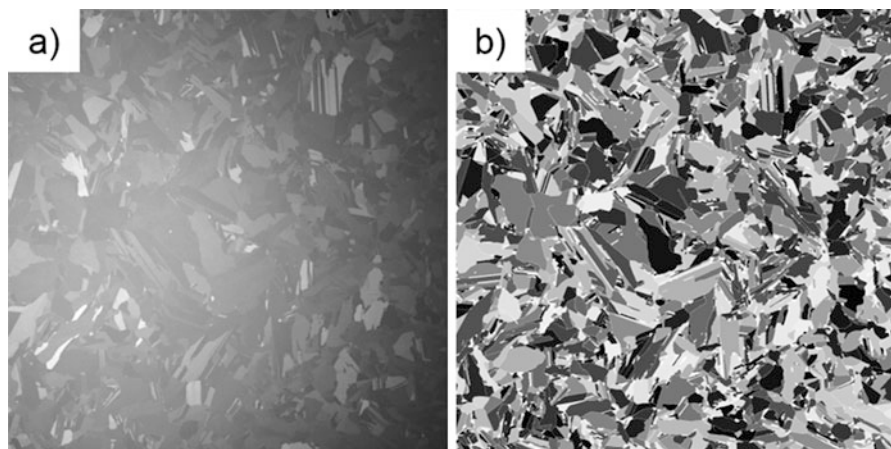


**Fig. 11** Resulting images of a characterized  $156 \times 156 \text{ mm}^2$  mc Si wafer: (a) photograph of the investigated wafer; (b) detected grain structure after image processing. (© Fraunhofer IISB)

processing. In a first step, the reflection image is treated to improve the image contrast between differently oriented grains as illustrated by the example in Fig. 11.

Now a quantitative evaluation of the grain structure is possible by transforming a *gray value* image like the example in Fig. 11b into a *binary* grain image. The examples in Fig. 12 reveal now clearly the grain boundaries. It is important in this kind of image transformation to define the minimum number of pixels which represents one individual grain.

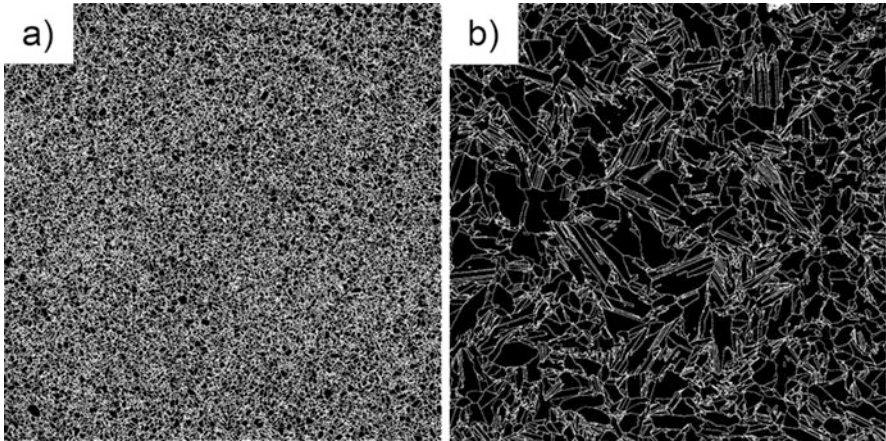


**Fig. 12** Binary grain image of  $156 \times 156 \text{ mm}^2$  wafers for a fine grained structure (a) and a structure with large grains (b). (© Fraunhofer IISB)

Detailed studies in the authors group have shown that a minimum grain size of  $0.05 \text{ mm}^2$  gives reliable results. Based on this evaluation, geometrical data can be obtained like average grain size, distribution of grain size, and length of the grain boundaries on full wafer scale. For example, the quantitative evaluation of the grain structure of Fig. 12 results in an average grain size of  $1.1 \text{ mm}^2$  with a standard deviation of  $1.6 \text{ mm}^2$  for the fine grain structure (a) and  $6 \text{ mm}^2$  with a standard deviation of  $16 \text{ mm}^2$  for the coarse grain structure (b). Obviously, the fine grain structure is more uniform than the coarse one.

Such kind of data may already be useful for the development of solidification processes and industrial fabrication of mc-Si wafers. Tools for an automated grain detection as described above are commercially available (Intego GmbH 2018).

The evaluation of geometrical data of grain structures as described above can be useful but may be not sufficient for an optimization of mc-Si with respect to solar cell performance, especially if one considers the minority charge carrier lifetime. It is known from several studies and extensively discussed in this handbook that the recombination rate of the minority charge carriers is strongly increased by dislocation clusters whose formation is favored by certain grain orientations and certain types of grain boundaries. Therefore, it is necessary to include the crystallographic orientation of the grains into the characterization.

In principle, it is possible to use the dependence of the optical reflectivity from the crystallographic orientation. Sopori et al. (2011) have demonstrated that the non-isotropic KOH-etchant exposes a unique texture shape for each grain orientation which can be calibrated to provide the crystallographic orientations. It was shown that such reflecting maps of a mc-Si sample can be transformed into orientation maps.

More common and effective, however, are diffraction methods like electron beam back scatter diffraction (EBSD) and X-ray diffraction (Laue method) for determining the crystallographic orientation matrix of certain grains and relate them to their exact location within the mc “texture.” (The term “texture” refers to the phenomenon of preferred crystallographic orientation of grains in a mc material).

Furthermore, the unique allocation of grain orientation *and* the correlation to its position is the prerequisite for a determination of the type of grain boundary between two neighboring grains. This topic is subject of the following section.

## Orientation Mapping and Determining Grain Boundary Types

### Electron Beam Back Scatter Diffraction (EBSD)

The principle of EBSD is based on the detection of electrons which are back scattered from a sample surface that is irradiated by a focused electron beam. The backscattered electrons escaping the sample surface may exit at the Bragg condition which is related to the periodic atomic lattice planes. Therefore, the diffraction pattern of these electrons, called “Kikuchi pattern,” contains the information about crystallographic (grain) orientation at the position of the incident electron beam. For more details, the reader is referred to the textbook of Randle (2003).

Experimentally, EBSD is carried out in a scanning electron microscope (SEM) which must be especially equipped for EBSD. This involves the possibility of tilting the sample with respect to the incident electron beam, a detector unit consisting of phosphor screen(s), lens system, and sensitive CCD camera. The analysis of the diffraction pattern is carried out by a special pattern indexing unit. Modern EBSD systems can provide orientation maps and patterns of grain boundary types (according to CSL nomenclature). A typical result of such an EBSD analysis is shown in Fig. 13.

The big advantage of EBSD is its implementation into a SEM system which allows the use of other beneficial characterization units like cathodoluminescence (CL), wave length dispersive X-ray spectroscopy (WPS), and energy dispersive X-ray spectroscopy (EDX). These methods can provide an even deeper insight into the material properties in relation to the grain structure and/or type of grain

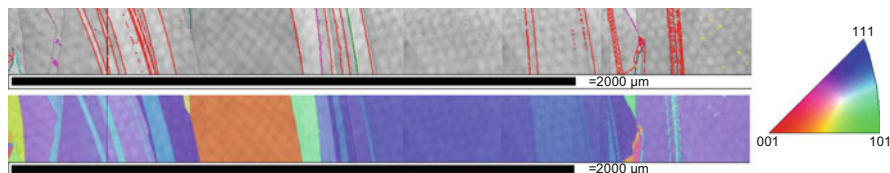


**Fig. 13** Grain orientation map (below) as well as grain boundary types (above) (both color coded) obtained by EBSD measurements on a mc silicon wafer. The color of the grain boundaries relates to  $\Sigma 3$  (red),  $\Sigma 5$  (green), and R (purple). (© Fraunhofer IISB)

boundary. For more details about these methods, the reader is referred to the literature.

EBSD is nowadays the most prevalently used characterization technique for the generation of an “orientation map” of a mc-Si sample, especially in combination with the further SEM-related tools for texture analysis. The main advantage of EBSD is its high spatial resolution ( $\sim 0.5\text{--}10$  nm). The angular resolution is estimated to be  $\sim 0.5\text{--}1^\circ$ . However, sample preparation for EBSD analysis is very time consuming because a polished sample surface with a superior quality is needed since the quality of the Kikuchi pattern is strongly dependent on the surface quality. Further, the mc-Si samples should be etched (leading again to impurities on the surface) to visualize the grain structure for the operator. Moreover, the sample size is limited to the size of the SEM sample holder, due to the large inclination angle needed between the sample surface and the incoming electron beam. As a consequence, the investigation of larger Si samples, especially a standard wafer with an area of  $156 \times 156$  mm is not feasible by EBSD. This disadvantage of EBSD is overcome by a method using X-ray diffraction which is described in the following.

### Laue Scanner Method

The so-called “Laue scanner” system was developed in the authors laboratory (see Lehmann et al. 2014). It uses the well-known X-ray diffraction technique according to the Laue method as it is common for the determination of the crystallographic orientation of single crystals. The determination of the grain orientation map of a mc-Si wafer requires a local correlation of the position of the X-ray spot and the position of the corresponding grain. The diameter of the X-ray spot can be varied between 0.3 mm and 2 mm according to the minimum grain diameter which should be considered. The spot size of the X-ray determines the signal quality, i.e., the measurement time for one Laue pattern. For example, a beam diameter of 0.3 mm results in the measurement time per Laue pattern of 20 s. The Laue pattern of each grain is detected and evaluated automatically. The sample stage (dimension  $380 \times 400 \times 500$  mm<sup>3</sup>, maximum load 40 kg) is motorized to provide a fully automated scanning of the sample surface and allows the measurement of up to four standard size wafers ( $156 \times 156$  mm) per run. The shortest mapping time is achieved if one uses only one Laue measurement for each grain. This can be achieved by using the geometrical data of the grain structure which is evaluated from optical reflection measurements as it was described in the section “[Optical Grain Detection and Analysis](#).” In the case of the Laue scanner, these data are provided by a commercial “grain detector” (Intego GmbH 2018). The position for the X-ray spot for each grain is selected to be the geometrical location which has the largest distance to the surrounding grain boundaries. By combining all these data, it is possible to generate an image of the grain structure of a sample where the crystallographic orientation is allocated to each grain. Based on these data, a complete representation of all grain boundaries of the grain structure can be represented in the CSL notation. A typical result of a mc-Si

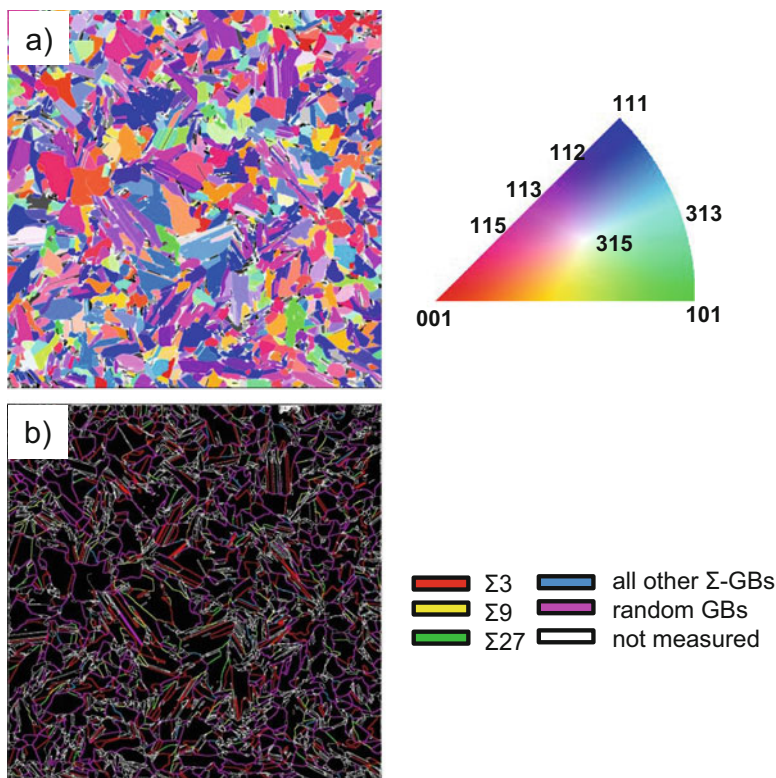


**Fig. 14** Results of characterization of a  $156 \times 156 \text{ mm}^2$  mc Si wafer by the “Laue scanner” (see text). Texture map of grain orientation (a) and types of grain boundaries in the CSL notation (b). (© Fraunhofer IISB)

wafer is shown in Fig. 14. It is the same wafer which was already depicted in Fig. 11 showing the intermediate result of the “grain detector” within the complete “Laue scanner” procedure. The total time for generating the results of Fig. 14 (including Fig. 11) is about 2–5 h depending on the number of grains to be measured per wafer. For further details, see Lehmann et al. (2014).

### Characterization of Electronic Material Properties in Relation to Grain Structure and Grain Boundaries

The characterization methods which were discussed in the previous sections of this chapter refer directly on the grain structure and grain boundaries with respect to their geometric parameters, crystallographic orientation or CSL type, respectively. However, electronic material properties like the spatial distribution of the minority carrier lifetime in relation to the grain structure and grain boundaries are of great interest. This section gives a short compilation of characterization methods which are in use



for analyzing these material properties. For more details, the reader is referred to other chapters in this handbook and the corresponded literature.

### Photoluminescence Imaging

Photoluminescence (PL) is based on the physical effect that excess carriers in Si – generated in PL by “photo”-excitation, typically by Laser illumination – can recombine optically, i.e., by emission of light. Any defect-correlated reduction of the photo-generated excess carriers is reducing the intensity of the PL emission which can be detected directly on the wafer scale. A typical PL characterization tool consists of a couple of exciting laser diodes (emitting in the range of about 800 nm) and a light detection unit collecting the luminescence emission by a CCD camera equipped with filters to reject the laser reflected light.

Due to its very short measurement time (just a few seconds per wafer), PL is a very efficient characterization tool which can even be used for an inline wafer inspection during solar cell production. It has been shown in literature that grain boundaries and related dislocation defects, which are correlating negatively with the open-circuit voltage of a solar cell are clearly visualized in PL images (Demant et al. 2016). PL images can also reveal an increased (or decreased) local contamination of impurities by a reduced average PL intensity. Both effects are illustrated by the examples shown in Fig. 15a, b.

Similar results can be obtained with minority carrier lifetime measurements by, for example, microwave detected photoconductive decay ( $\mu$ -PCD) or microwave detected photoconductivity (MDP). By stimulating the Si sample with a laser charge carriers are generated which recombine in dependence on the locally present electrical active crystal defects especially impurity decorated dislocations and grain boundaries. This recombination signal is detected by the intensity of reflected microwaves which decrease over time. As a result, the minority carrier lifetime

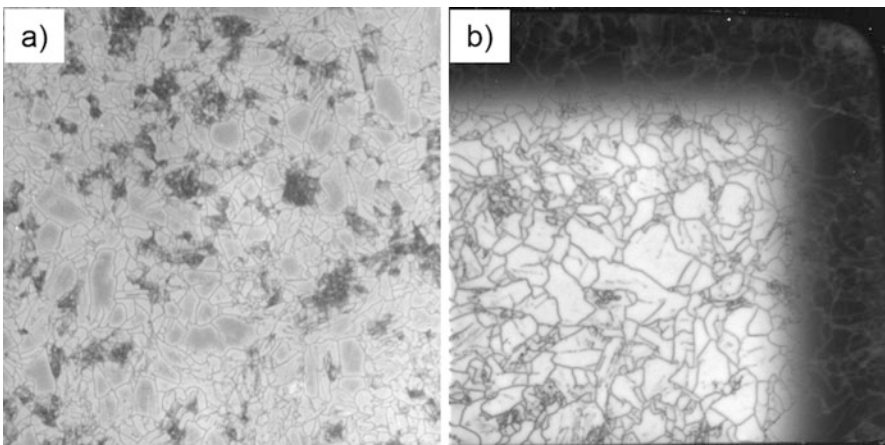


**Fig. 15** PL-images of  $156 \times 156 \text{ mm}^2$  mc-Si wafers taken from the ingot center (a) and the ingot edge (b). (© Fraunhofer IISB)

is the lower the more defected and contaminated the measured sample region is. A typical lifetime-map resulting from these methods is shown in Fig. 7 on the right.

### **Electron Beam Induced Current (EBIC)**

Electron beam induced current (EBIC) is a quite feasible method to investigate the recombination strength of grain boundaries in mc-Si material. The measurement setup is typically integrated in a scanning electron microscope (SEM) which provides a high resolution in the  $\mu\text{m}$  range but it is also limited with respect to the sample area which can be investigated. For the measurement, an electron beam locally induces charge carriers in the semiconducting material which are separated by a p-n- or Schottky-junction. At the ohmic contacts on both surfaces of the sample, a small current (in the range of  $\mu\text{A}$  to nA) can be measured in dependence on the recombination strength of the crystal defects. After mapping the sample gray value images can be produced by software in which a higher contrast corresponds to a higher recombination activity (smaller current). In Fig. 16, an example is shown where the recombination strength of different grain boundary types in mc Si silicon was measured in dependence on the iron contamination level.

---

### **Formation of Grain Boundaries During Directional Solidification (DS)**

Research and development of directional solidification (DS) of Si were driven from the very beginning by the perspective of cost reduction compared to the Czochralski (CZ) growth of Si. Mainly two aspects are behind this idea. Firstly, the upscaling of the DS process is much easier compared to the CZ process. Secondly, DS provides the possibility to avoid the expensive seeding procedure with necking and conical crystal shaping of the CZ process (see, e.g., Friedrich et al. 2015) which offers for DS an up to eight times higher throughput compared to CZ (according to Lan et al. 2017).

Meanwhile several modifications of the DS process were developed. This chapter provides a detailed comparative consideration of the various variants of the DS process and its results with respect to the formation of various types of grain boundaries including dislocation defects.

Previously, it was already shown how grain boundaries can influence the quality of mc-Si. It was also shown that the formation and multiplication of dislocations depend strongly on the occurrence of certain types and structures of grain boundaries. Based on this knowledge, one can formulate the following goals for the formation of a favorable grain structure in a DS process of mc Si:

- (i) As much as possible large grains which means a few grain boundaries, in the ideal case only one single grain, i.e., a monocrystal
- (ii) Preferably grain boundaries which are electrically harmless; this holds especially for twin boundaries, e.g., type  $\Sigma 3$ .

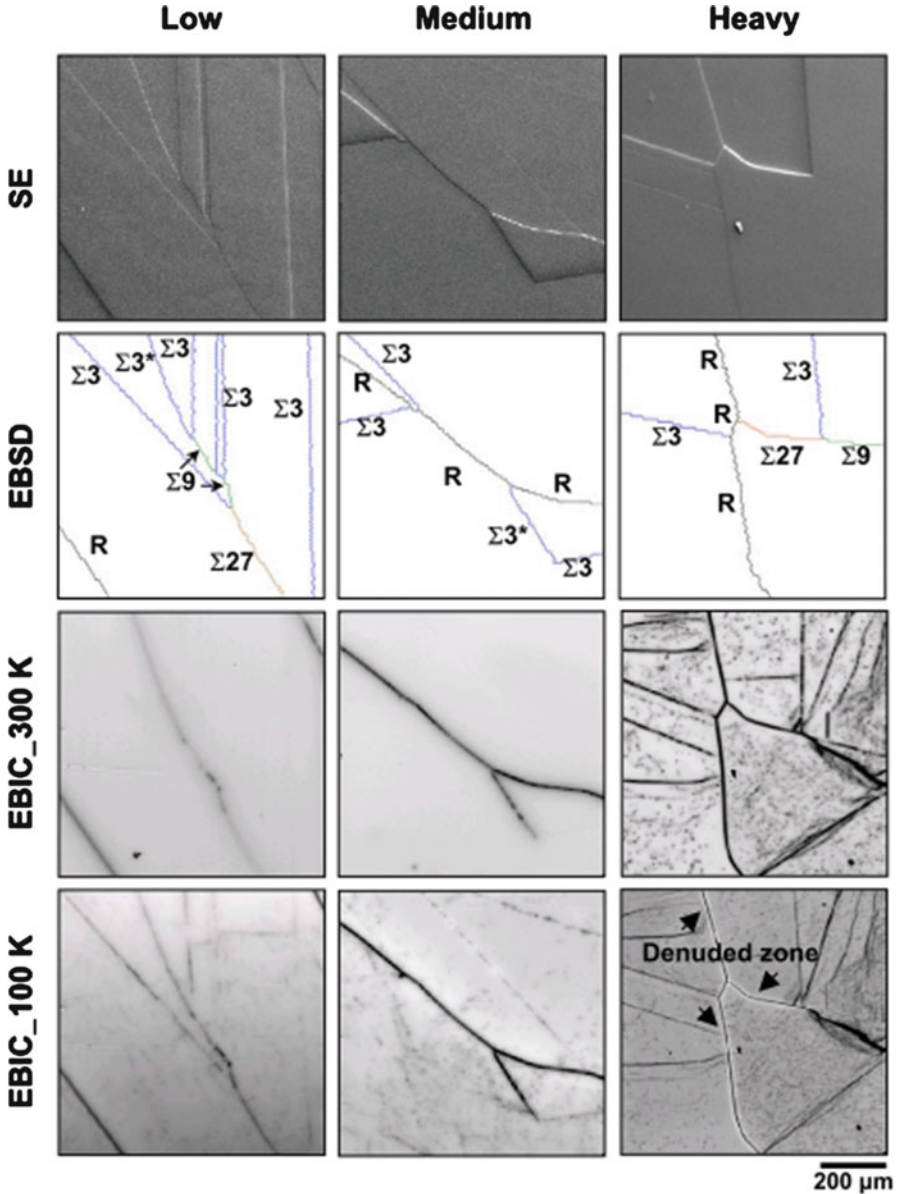


**Fig. 16** Local SE(M), EBSD, and EBIC images of different grain boundaries in mc-Si wafers which are low, medium, and heavy iron contaminated. The SE(M)-images show the GB structure, the EBSD images the GB type, and the EBIC images the electrical activity of the grain boundaries. After Chen et al. (2007)



- (iii) As few as possible dislocations which means preferably grain boundaries which do not provoke the generation of dislocations, i.e., grain boundaries with low stress (congruent grain boundaries). Furthermore, the grain boundaries should impede the movement and multiplication of dislocations; this holds especially for random (R) grain boundaries, whereas twin boundaries (like  $\Sigma 3$ ) are not impeding the movement of dislocations.

The outcome of the objectives i, ii, iii cannot be a unique strategy to achieve high quality of the mc material because the objectives are partly contradictory. In fact, it turns out that different strategies can be successful. In each of these routes, the nucleation at the beginning of the crystallization process plays an important role.

In the beginning of the DS process development, one tried to achieve a material with as much as possible large grains (i). Here, the nucleation respectively the seeding process is initiated as usually in a DS crystal growth process by decreasing the temperature of the totally melted Si feed material with the lowest temperature at the crucible bottom. The seeding crystallization itself is beginning by a heterogeneous nucleation at the surface of the crucible coating (standard is silicon nitride ( $\text{Si}_3\text{N}_4$ )) of the flat crucible bottom. The  $\text{Si}_3\text{N}_4$  coating is necessary to avoid the sticking of Si at the silica crucible and to reduce contamination from the crucible walls. This seeding process which results in a large amount of less harmful twin boundaries (ii) will be called further as “*classic mc*.”

A further coarsening of the grain structure, i.e., increase of the grain size can be achieved by an improved thermal processing during the initial seeding phase with regard to a higher supercooling of the melt. This effect causes the preferential formation of dendrites at the crucible bottom. Therefore, this seeding process will be called further “dendritic” (► Chap. 8, “Growth of Multicrystalline Silicon for Solar Cells: Dendritic Cast Method”). Both the “classic mc” and “dendritic” DS processes will be discussed in detail in section “Coarse Grain Structures Without Seed Crystals (Classic mc and Dendritic mc).”

In order to generate an even more “coarse” grain structure with the final goal of large monocrystalline ingot regions, a seeding variant with Si monocrystal seeds was developed. The principle idea of this technology is to combine the cost benefit of DS growth with the high material quality of monocrystalline Si in order to provide a more cost effective mono Si in comparison to CZ material. For that purpose, monocrystalline Si seed plates, cut from CZ ingots, are placed at the crucible bottom in order to grow a monocrystalline ingot without any grain boundaries and also few dislocations (i + iii). However, this technology exhibited a lot of challenges like the formation of grain boundaries at the ingot periphery or the formation of small angle grain boundaries within and above the joints of the seed plates. This so-called “*quasi-mono*” silicon (QM) was for several years in the worldwide focus of the Si DS research and development (► Chap. 9, “Growth of Crystalline Silicon for Solar Cells: Mono-Like Method”). A more detailed

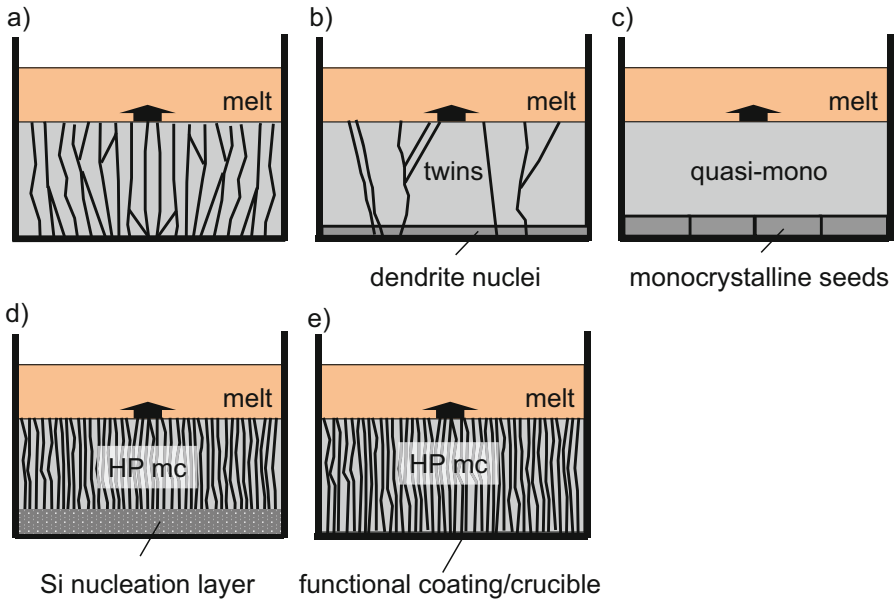
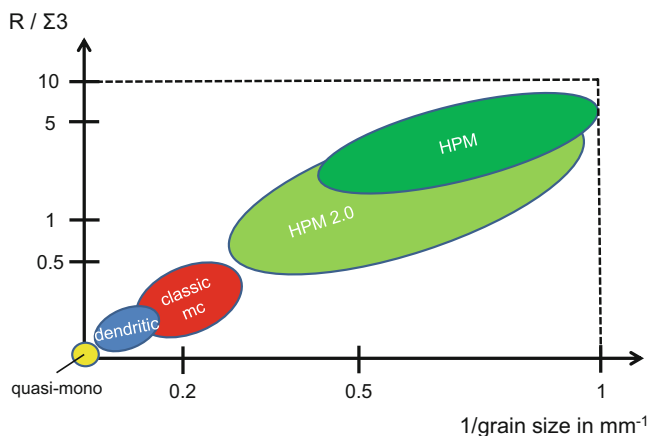


**Fig. 17** Schematic representation of the five important seeding variants which are used to control the formation of the grain structure in the DS of Si: classic mc (a), dendritic mc (b), quasi-mono (c), high performance mc (d), and high performance mc 2.0 (e). For details, see text

description is given in section “[Towards Monocrystals by Using Monocrystalline Seeds \(Quasi-Mono QM\)](#).”

In the course of further research and development of mc-Si growth, it was surprisingly found that a fine grained texture, i.e., small grain sized mc-Si resulted in solar cells with higher efficiencies compared to cells made from classic mc and dendritic mc. This kind of material was henceforward called “*high performance mc Si*” (HPM) (► [Chap. 7, “Growth of Multicrystalline Silicon for Solar Cells: The High-Performance Casting Method”](#)). The fine grained texture of the HPM material contains a high number of random (R) grain boundaries which are impeding the movement of dislocations (iii). These structural conditions can be achieved by various alternative seeding methods. One possibility is to use a fine grained Si feedstock material as a seeding layer. This option needs a careful melting procedure of the feedstock in order to leave a residual layer of not melted Si for seeding (see section “[Fine Grain Structures with Seeding on Si Feedstock \(Original HPM\)](#).”). Such a bit difficult step can be omitted if the coating surface of the crucible bottom can provide nucleation conditions for a fine grained texture. The results of this recent development (named *HPM 2.0*) are presented in section “[Fine Grain Structures without Seeding on Si Material \(HPM 2.0\)](#).”

Figure 17 shows a schematic representation of the five variants of seeding procedures in the DS of Si which will be discussed in the following.



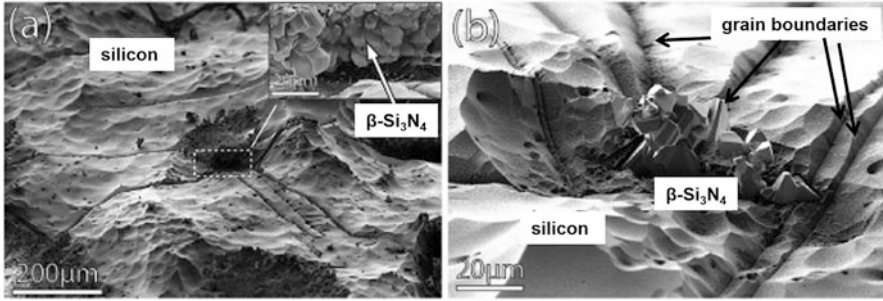
**Fig. 18** Ratio of random to twin grain boundaries  $R/\Sigma 3$  (logarithmic axis) versus the reciprocal grain size for the different silicon materials grown by various variants of the DS method (see text)

Figure 17(a) represents the classic mc Si without any precautions for seeding, (b) illustrates the variant with dendrite formation on top of the crucible  $\text{Si}_3\text{N}_4$  coating layer, (c) shows the quasi-mono method of seeding with monocrystalline seed crystals which comes closest to the single crystal growth of other materials like GaAs by the DS technique, and (d) and (e) display the two variants of the high performance mc material: firstly, the use of a fine grained layer of Si feedstock material which needs a comparable melting process like the quasi-mono approach (d) and secondly, the use of a specially prepared incubation surface of the  $\text{Si}_3\text{N}_4$  coating or the crucible (e).

Figure 18 provides a graphical presentation of the different types of grain structures resulting from the DS variants sketched in Fig. 17. The ratio of the number of random (R) to twin ( $\Sigma 3$ ) grain boundaries is plotted versus the grain size (reciprocal). The five technological approaches *classic mc*, *dendritic*, *quasi-mono*, *HPM*, and *HPM2.0* are represented in the diagram and will be discussed in detail in the following sections.

### Coarse Grain Structures Without Seed Crystals (Classic mc and Dendritic mc)

In the DS processes without seed crystals, it is obvious that the formation of the grain structures, i.e., grain orientation, grain size, type of grain boundaries, as well as the formation of dislocations is decisively influenced by the initial process of self-seeding at the crucible bottom. This so-called heterogeneous nucleation means that the first Si nuclei are forming in contact with the surface of a dissimilar material, in this case the  $\text{Si}_3\text{N}_4$  layer which is coating the inner surface of the  $\text{SiO}_2$  crucible.



**Fig. 19** (a) SEM images of the bottom surface of a mc silicon ingot after Sopori etching which has removed almost the complete residual  $\text{Si}_3\text{N}_4$  coating. (a) Shows regions of physical contact between the particle-layer and the solidified silicon. (b) Faceted beta  $\text{Si}_3\text{N}_4$  particles which are embedded into the silicon. After Ekström et al. (2016)

The conventional or *classic DS process* developed in the late 1980s uses standard silica crucibles with a spray coated layer of  $\text{Si}_3\text{N}_4$ . The main purpose of this  $\text{Si}_3\text{N}_4$  layer is to prevent the sticking of the solidified silicon with the silica crucible wall. Instead of sticking at the silica wall, the solidified Si material sticks more or less at the  $\text{Si}_3\text{N}_4$  coating which separates during cooling from the silica wall depending on its properties. At the end of the cooling process also, the  $\text{Si}_3\text{N}_4$  powder can be easily removed from the Si block. Ekström et al. (2016a) studied the nucleation process of Si directly on the  $\text{Si}_3\text{N}_4$ -coating more in detail (compare Fig. 19). Typically,  $\text{Si}_3\text{N}_4$ -powder containing the crystallographic alpha phase is used for the crucible coating. Due to dissolution of  $\text{Si}_3\text{N}_4$  and transfer of a dedicated amount of nitrogen into the liquid silicon (until the local solubility at elevated temperatures is reached), hexagonal beta  $\text{Si}_3\text{N}_4$ -particles are formed on top of the alpha phase based crucible coating. It is assumed that the initial Si nucleation takes place at the facets of this hexagonal beta  $\text{Si}_3\text{N}_4$ -precipitates. Because the Si nuclei are preferably growing at the hexagonal side, facets of the  $\text{Si}_3\text{N}_4$  most preferably  $\Sigma 3$  grain boundaries were formed.

At this point, the focus will be directed phenomenologically to the formation and development of the grain structure which results from the initial seeding. As soon as the initially isolated nuclei have been grown laterally to a length that they touch each other, the first grain boundaries are generated. Now the crucible bottom respectively the coating is covered by a complete layer of mc Si. During the further growth of this layer, various mechanisms and phenomena can influence the grain growth and hence the formation of grain boundaries:

- Grains with certain crystallographic orientations are growing preferentially (due to the differences in the surface energies depending on the crystallographic orientation) (see the example in Fig. 20)
- Grain boundaries with a low energy are preferentially growing. This holds especially for the twin  $\Sigma 3$  boundary (see Fig. 21).

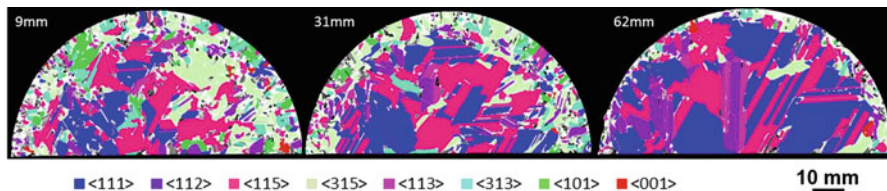


**Fig. 20** Examples of the growth of grains with a preferential orientation ( $\langle 111 \rangle$ ,  $\langle 115 \rangle$ , and  $\langle 112 \rangle$ ): sections perpendicular to the axis of solidification at three different heights (9, 31, and 62 mm) of a G0 ingot. (© Fraunhofer IISB)

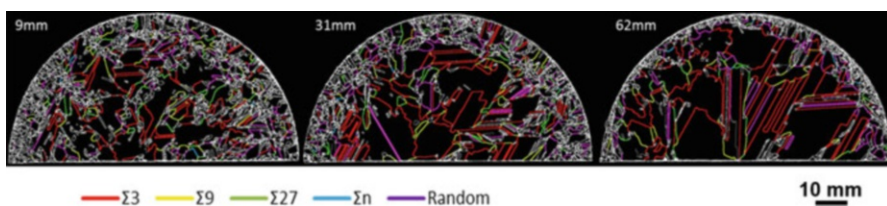


**Fig. 21** Examples of the growth of grains with preferential twin boundaries ( $\Sigma 3$ ): sections perpendicular to the axis of solidification at three different heights (9, 31, and 62 mm) of a G0 ingot. (© Fraunhofer IISB)

- Grain boundaries with a high energy can be converted into grain boundaries with a lower grain boundary energy (compare Fig. 6).
- Dislocations are present a priori along small angle grain boundaries (see below Fig. 28).
- Dislocation lines are spreading across certain grain boundaries, like  $\Sigma 3$  (see, e.g., Fig. 22 left).
- Dislocation lines can be blocked by certain grain boundaries (see, e.g., Fig. 22 right).
- Dislocations can be generated by grain boundaries with a high stress caused by incoherency of the adjacent lattices (see, e.g., Fig. 23).

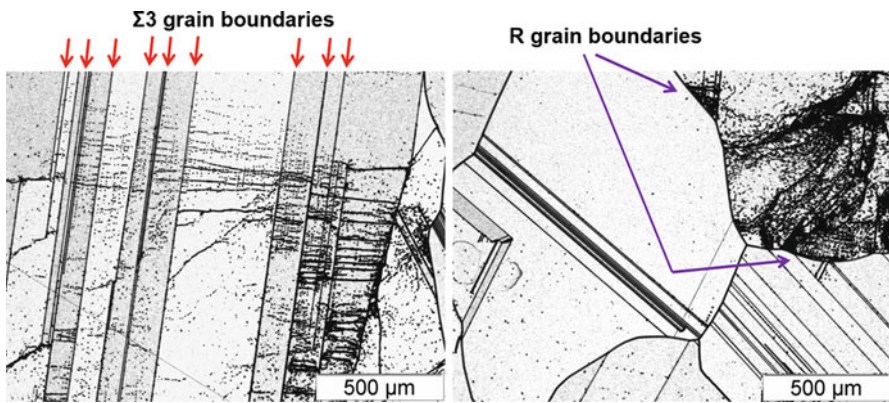
The grain structure resulting from the *classic mc* process is a resulting mixture of all the phenomena specified above. It has typically an average grain size of  $\geq 4 \text{ mm}^2$  and a fraction of R-type boundaries to  $\Sigma 3$  boundaries between 0.5 and 0.25 (compare Fig. 18).

Figure 24 shows an image of such a grain structure. One characteristic feature of this structure is the preferred elongation of the grains along the direction of growth or solidification, respectively. It is also obvious from Fig. 24a that certain grains have a preferred growth and are “overgrowing” other grains.

A generally observed problem of this grain structure is the occurrence of grains with a very high dislocation density ( $\text{EPD} \geq 10^6 \text{ cm}^{-2}$ ), as shown in Fig. 24b. The PL image illustrates the deleterious effect of the dislocations by the strongly reduced PL intensity. There are hints in the literature that the generation of dislocations could

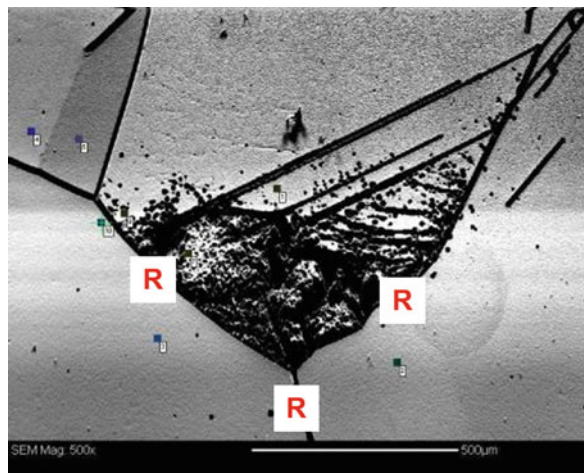
be provoked by the stress generated by the formation of incoherent type R grain boundaries, see, e.g., Fig. 23 or Rynningen et al. (2011).

In summary, the resulting grain structure discloses the advantages as well as the problems of the classic mc material with respect to the performance of solar cells. Relatively large grains are meaning a low number of harmful grain boundaries. The  $\Sigma 3$  grain boundaries with its high percentage do not act as recombination centers for minority charge carriers. However,  $\Sigma 3$  grain boundaries are also not acting as barriers for the transition of dislocations lines (compare Fig. 22 left). Dislocations which are emitted from the regions with a high dislocation density are not hindered by  $\Sigma 3$  grain boundaries. Therefore, the classic mc material with its large areas of high dislocation density has decisive limitations with respect to an application of high performance solar cells.



**Fig. 22** White light microscopy images of dislocation lines which are: (left) spreading across  $\Sigma 3$  twin boundaries and (right) blocked by R-type grain boundaries. (© Fraunhofer IISB)

**Fig. 23** SEM picture of R-type grain boundaries with adjoining region of high dislocation density. The boundary triple junction seems to be the source of the dislocation formation (incoherency). (© Fraunhofer IISB)





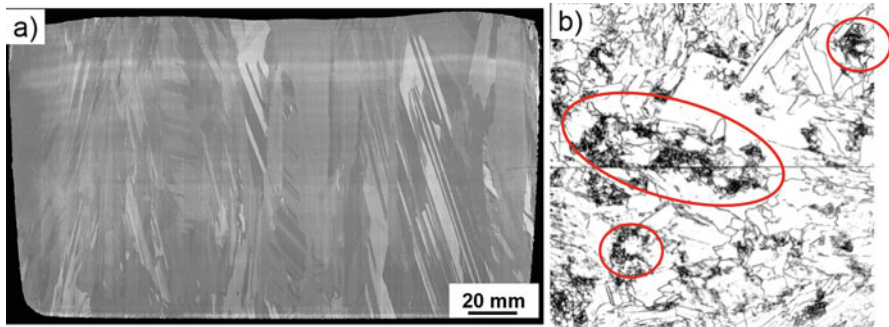


**Fig. 24** (a) Grain structure image of a vertical section parallel to the direction of solidification of a G1 size ingot processed according to the “classic mc” conditions. The typical coarse structure with elongated grains and twins is visible. (b) PL-image of a  $156 \times 156 \text{ mm}^2$  wafer perpendicular to the growth direction at 80 mm height of the same ingot with areas of high dislocation density (inside marked regions). (© Fraunhofer IISB)

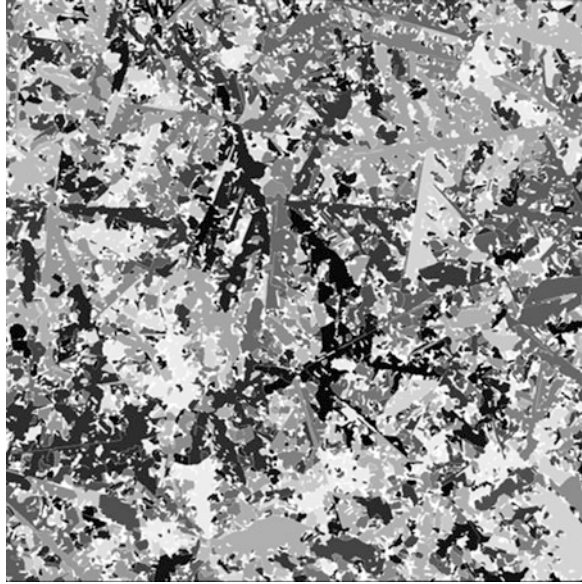
One strategy to overcome the problems of dislocation clusters is to decrease the number of incoherent grain boundaries by a distinct increase of the grain size.

The publication of Fujiwara et al. (2006) was one of the first reports about a successful coarsening of the mc grain structure by an “improvement” of the classic mc process. This improvement consisted mainly in an increase of the supercooling at the beginning of the seeding step followed by an increased rate of solidification. Both measures are causing the formation of dendritic nuclei in the seeding phase and its growth in both directions, lateral on the surface of the  $\text{Si}_3\text{N}_4$  coating and perpendicular to it. A typical example of the resulting grain structure is shown in Fig. 25 where the increased grain size is clearly visible.

The basic cause of the dendrite formation is the relatively high supercooling ( $\geq 10 \text{ K}$ ) of the Si melt at the crucible bottom. This supercooling is possible due to a poor wetting of the  $\text{Si}_3\text{N}_4$  surface by Si. Studies of Fujiwara et al. (2006) and Nakajima et al. (2010) have shown that the dendrites are growing parallel to the crucible bottom with the preferred crystallographic orientations  $\langle 110 \rangle$  and  $\langle 112 \rangle$ . The preferred orientations of the growth interfaces in the direction of solidification are the (112) and (110) planes, respectively. These relatively large elongations of the dendrites are causing the large grain sizes (up to several centimeters) at least for the firstly solidified portions of the ingot. The grain structure is characterized by a very high portion of  $\Sigma 3$  grain boundaries up to 80% (equals to  $R/\Sigma 3 < 0.25$ , see Fig. 18) which result from the uniform dendrite orientation. More details like the selection of competing grain growth in dependence on process conditions (cooling rate, shape of growth interface, rate of solidification) are discussed by Lan et al. (2012).

Solar cells which were fabricated from dendritic mc-Si show cell efficiencies which are increased by nearly 1% in comparison to classic mc Si according to Nakajima et al. (2010). Despite of the positive results of the dendritic mc material, it did not prevail in industrial production. This had several reasons: the conditions for the high super-cooling which is essential for the formation of the initial dendrites

**Fig. 25** Image of a typical dendritic grain structure of a bottom near  $156 \times 156 \text{ mm}^2$  wafer of a G1 ingot which was grown with higher cooling rates in comparison to the classic mc. (© Fraunhofer IISB)



are difficult to be provided reproducibly. The necessary high cooling rates at the beginning of the solidification step pose a certain risk for a breakage of the crucible and its containment. Furthermore, the grain structure of the mc material itself has the disadvantage that its heavily twinned texture does not prevent the spreading and multiplication of dislocations. In consequence, the benefit of the dendritic structure is lost after some centimeters of growth. Finally, according to the author's results, it seems doubtful whether a successful upscaling beyond ingot heights of 300 mm with the growth of large grains with only few dislocations could be possible.

A further improvement of the material quality by increasing the grain size is possible by using monocrystalline Si seeds. This will be the subject of the following section.

## **Towards Monocrystals by Using Monocrystalline Seeds (Quasi-Mono QM)**

The idea of the *quasi-mono* (QM) technology was not new in the end of 2000s when it has come into the field of interest of nearly all Si wafer producers who dealt with the directional solidification technique. The use of a monocrystalline Si plate which is placed at the crucible bottom (see Fig. 17c) in order to grow in the best case a real monocrystal or at least an ingot with only a few grain boundaries ("quasi-mono") was firstly published in the end of the 1970s by Schmid (1975) and Helmreich (1980). However, a serious development of this technology for producing industrial Si monocrystals for PV application has started only in 2007 (Stoddard 2009; Stoddard et al. 2008). The main nominal benefits in comparison to the *classic mc* or *dendritic mc* Si as well as the mono CZ-material are:



- (a) A higher wafer quality due to the absence of crystal defects like grain boundaries and dislocations (i.e., approaching the structure and properties of CZ-Si)
- (b) Better light capturing properties after alkaline texturing due to its uniform  $\langle 100 \rangle$  surface orientation (at the same level as CZ-Si)
- (c) A lower oxygen content compared to CZ-Si
- (d) Less production costs in comparison to the more cost intensive monocrystalline CZ-material

All of these benefits should make the QM material to be competitive, to be better, or even to replace the mono CZ-Si for PV application. However, it turned out pretty soon that the growth of a 100% monocrystalline ingot by this technique is rather complicated. In the following, the main problems or tasks, respectively, during the growth of QM Si material are listed:

- (a) *Seeding control*: Analogue to the HPM technology (see section “[Fine Grain Structures with Seeding on Si Feedstock \(Original HPM\)](#)”), it has to be taken sure that the monocrystalline seed plate is partly melted but not completely melted. This means a more complicated seeding processes in comparison to the *classical mc* approach (Camel et al. 2009).
- (b) *Parasitic nucleation at crucible walls*: In contrast to a CZ crystal, the ingot in a DS process grows in contact with the crucible side walls. Here heterogeneous nucleation can take place in the same way as during the classic mc growth. This results in the growth of a multigrain structure in the regions of the side walls which reduces the monocrystalline ingot volume (Trempa et al. 2012).
- (c) *Dislocation formation within the bulk and/or the surface of the monocrystalline seed plate*: Dislocations can be formed during heating up within the seed plates due to thermal stress and/or mechanical load of the feedstock on top and can propagate into the grown ingot volume (Trempa et al. 2016). See Fig. 26.
- (d) *Formation of small angle grain boundaries (SAGB) and dislocations at the seed joints*: According to the crystallographically non-exact aligning of the seed plates, SAGBs and subsequently dislocations are formed and spread into the ingot volume (Trempa et al. 2014).
- (e) *Iron contamination of the seed crystals – means increased bottom “red zone”*: The original “high purity” seed plates cut from CZ ingots are contaminated with metals, e.g., iron, already during the heating phase which is leading to an enhanced contamination of the bottom region of the QM Si ingot (Trempa et al. 2015a).

Two of these problems (b and d) will be treated in the following in more detail because they are directly correlated to the occurrence of unwanted grain boundaries within the QM material.

Concerning the parasitic grain growth at the crucible walls, it could be found that it is determined by two mechanisms, see, e.g., Trempa et al. (2012). Firstly, the

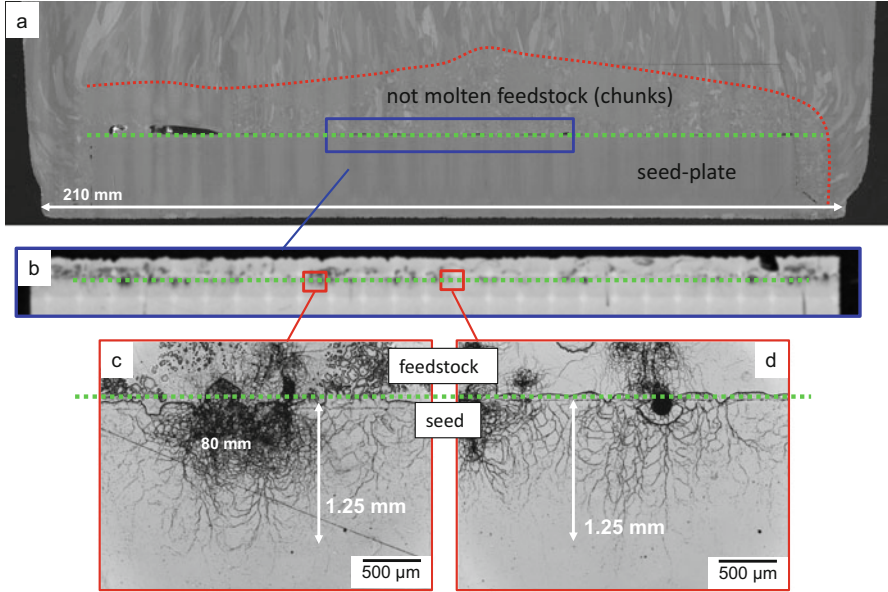


**Fig. 26** Vertical sections parallel to the direction of solidification of an G1 ingot grown by using a monocrystalline seed plate (upper surface is marked by the dotted green line) and Si chunks as feedstock material. **(a)** Grain structure image of the bottom part of the ingot showing the seeding interface (curved dotted red line) which is unintentionally laying within the feedstock material. **(b–d)** White light microscopy images of the interface between the seed plate and the unmelted chunks (dotted green line) revealing the dislocation arrangements **(c, d)** which are caused by the indentation of particle tips. After Trempa et al. (2016)

classical mc-grain nucleation occurs at the  $\text{Si}_3\text{N}_4$  coating at the crucible walls or at the outer bottom regions where no seed crystals are placed. Secondly, a twinning process occurs at the edges of the monocrystalline Si seed plates itself. Both phenomena are illustrated in Fig. 27 which shows a grain orientation mapping of an industrially grown QM Si wafer taken from an edge brick. It can be seen that the twin orientation  $\langle 221 \rangle$  (bright blue) is directly connected to the seed orientation  $\langle 100 \rangle$  (red), whereas the nonuniformly oriented mc grain structure which is induced by the crucible coating is located in the most outer wafer regions.

Two approaches were studied in order to overcome this problem. The most frequently used one is to adjust the shape of the solid-liquid-phase boundary in the edge regions to be of slightly convex shape in order to achieve a preferred growth direction of the mc-grains towards the crucible walls. So the range of the mc-grain growth can be limited to a size of a few millimeters. The avoidance of the formation of twins is rather difficult and cannot be solved by only adjusting the phase boundary shape. Hence, a second approach was proposed by Kutsukake et al. (2013). They found out that the use of so-called “functional grain boundaries,” which are induced by seed crystals with a certain lateral orientation in the periphery regions of the ingot, can avoid the inclining growth of  $\Sigma 3$  twin boundaries. The extra seed near the

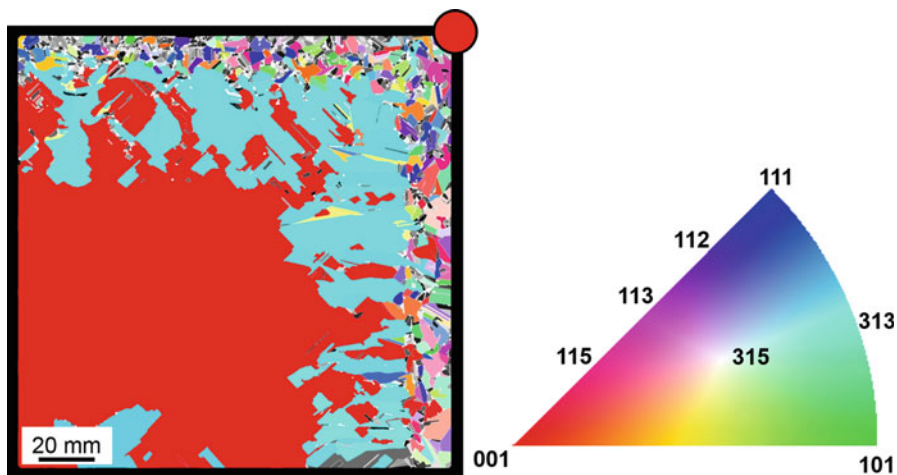


**Fig. 27** Orientation mapping of an industrially grown  $156 \times 156 \text{ mm}^2$  QM Si wafer from an edge brick (left). The red dot marks the edge position of the G5 ingot. The colors represent the grain orientation according to the Euler triangle (right). After Trempa (2014)

crucible wall is blocking the  $\Sigma 3$  twin boundaries by the aid of a  $\Sigma 5$  grain boundary. This technique was successfully demonstrated for ingots with 400 mm edge length corresponding to a G3 scale by Kutsukake et al. (2014).

The other challenge in the growth of high quality QM Si ingots is the formation of dislocations at the seed joints. Due to the fact that no monocrystalline seed plates in dimensions of  $\sim 1 \text{ m}^2$  are available from Cz-growth or other techniques, the industrial producers have to use an arrangement of several seed plates which are placed directly to each other on the crucible bottom like floor tiles, sometimes called “split seeds.” The gaps between the split seeds are growing together within or just above the gaps by forming small angle grain boundaries (SAGB). The cause for the SAGB formation is the very small (unavoidable) mismatch of both Si lattices of the two neighboring seed plates by  $< 1^\circ$ . These SAGBs are forming an array of dislocations along the direction of solidification in the region above the seed joints. The dislocations multiply and widely spread into the ingot volume as it is shown by the microscopic views of an etched lab-scale sample in Fig. 28 as well as by PL images of a G1 ingot in Fig. 29. In consequence, the material quality and finally also the cell efficiency was even worse in these dislocated ingot regions.

A lot of investigations were made by different researchers in order to solve this problem. However, it was found that even very careful positioning of the seed plates or a chemical surface treatment of the side faces does not lead to good results. Finally, it was found that even very small relative misorientations between two adjacent seeds below  $1^\circ$  still result in a tremendous dislocation formation (Trempa et al. 2014; Trempa 2014; Oliveira et al. 2014; Ekstrøm et al. 2015). Only if the mismatch could be kept  $< 0.1^\circ$ , the dislocation formation could be significantly reduced. However, this condition is quite difficult to be reproducibly achieved in

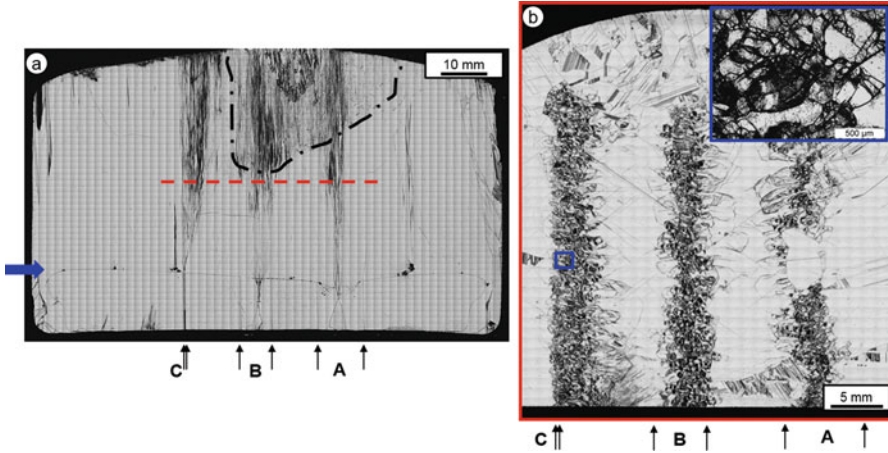


**Fig. 28** Optical micrographs of a Jenkins-etched *vertical* (a) and *horizontal* (b) cut. The axial seed orientation and the gap planes are  $\langle 110 \rangle$  and  $\{100\}$  oriented. The arrows at the bottom of (a) depict the seed edges which define the gap width A (~10 mm), B (~5 mm) and C (<1 mm). The bold blue arrow at the left periphery shows the position of the seeding interface. The red dotted line marks the vertical position of the horizontal cut shown in (b). The arrows at the bottom of the horizontal cut (b) depict the original seed wall positions. After Trempa et al. (2014)

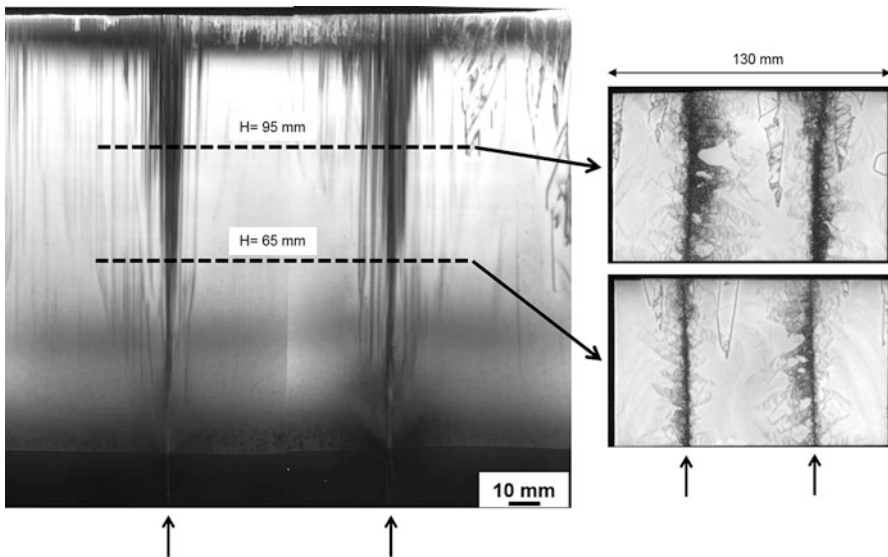


**Fig. 29** PL images of vertical and horizontal sections cut from a G1 quasi-mono Si ingot parallel (left) and vertical (right) to the growth direction. The seeds joints are marked by arrows. (© Fraunhofer IISB)

an industrial production environment. One practical option could be to use rectangular seed plates instead of squared ones to reduce the number of gaps and to be very careful during seed preparation and positioning.

### Grain Boundary Engineering

The problem of the slightly misoriented “ $\Sigma 1$ ” or SAGBs, respectively, with its related dislocation cascades can be overcome by using alternative orientations of the split seeds which are not causing SAGBs but certain types of large angle grain boundaries that do not result in the formation of dislocations. This alternative approach was firstly proposed by Trempa et al. (2015b) in a laboratory scale. It was found that the more nonsymmetric the grain boundary is, the less dislocations are formed. For example, a  $\Sigma 33$  grain boundary or a R grain boundary prohibit the formation of dislocations whereas a nonperfect  $\Sigma 3$  twin grain boundary induces a high amount of dislocations. Figures 30 and 31 illustrate these results.

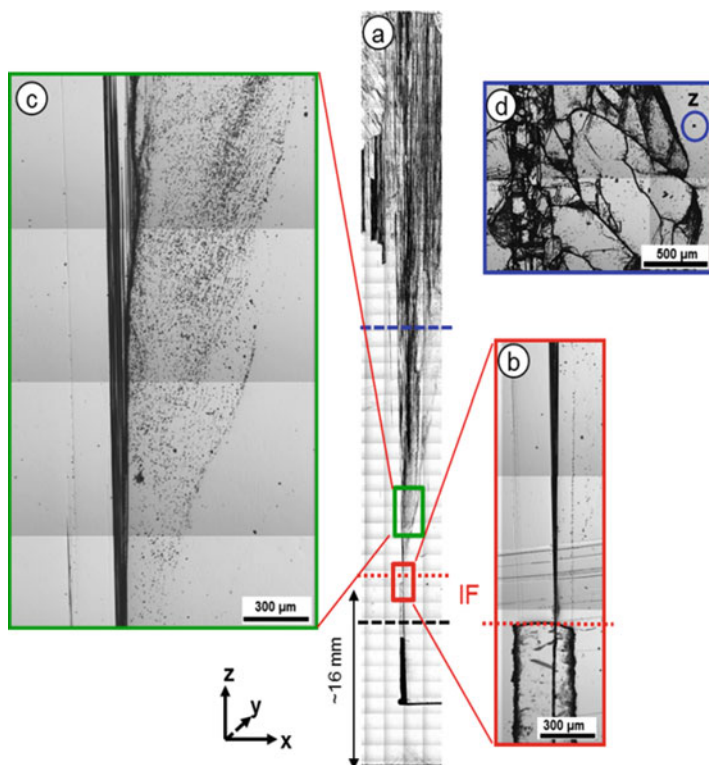
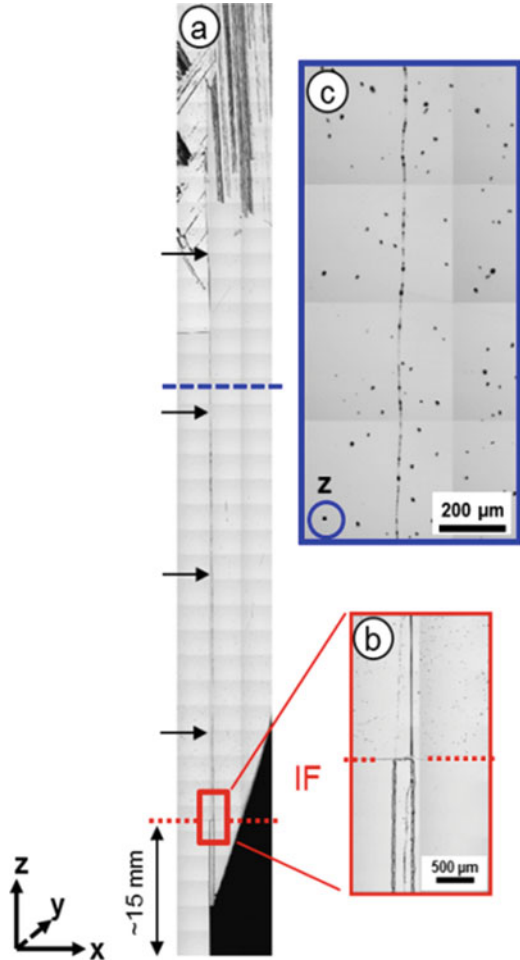


**Fig. 30** (a) Optical micrograph of the grain boundary region of an etched vertical cut ranging from the crystal bottom to the top. The area (rectangle) close to the horizontal seeding interface (IF, red dotted line) is shown in a higher magnification in (b). The grain boundary structure at 50% of the crystal height (dashed blue line) is illustrated in (d) by a section of a horizontal cut. The area within the bigger green rectangle in (a) is shown in (c) in a higher magnification. After Trempa et al. (2015b)

**Fig. 31** (a) Optical micrograph of the  $\Sigma 33$  grain boundary region of an etched vertical cut ranging from the crystal bottom to the top. The area (red rectangle) close to the horizontal seeding interface (IF, red dotted line) is shown in a higher magnification in (b). The grain boundary structure at 50% of the crystal height (dashed blue line) is illustrated in (c) by a section of a horizontal cut. The area within the bigger green rectangle in (a) is shown in (c) in a higher magnification. After Trempa et al. (2015b)



For practical use of this method, it has to be noticed that the various seed plates have to reveal different orientations. Hence, in case of an industrial application, a large amount of seed material is needed which must be cut from CZ crystals in directions which are diagonal to the cylinder (growth) axis. This means considerably increased expenses for an industrial production. Secondly, for securing the beneficial texturing effect of a homogeneously oriented material in growth direction, the orientation of adjacent seed plates should be identical parallel to the growth direction (typically  $\langle 100 \rangle$ ).

Considering these items, Hu et al. (2015) presented the approach to induce large angle grain boundaries by rotating the seed pieces around their vertical axis by keeping the  $\langle 100 \rangle$  growth orientation. It was demonstrated in G5 ingot dimensions (870 mm edge length) that by keeping intentional twist angular deviation of  $10\text{--}45^\circ$  of the adjacent seeds, the formation of dislocation and SAGBs could be almost



completely suppressed. In consequence, the defect-related areas in the whole ingot could be significantly reduced resulting in higher solar cell efficiencies of +0.6% absolute.

An alternative approach also considering the above listed items is the so-called “SMART”-approach (seed manipulation for artificially controlled defect technique) firstly proposed by Takahashi et al. (2015) where two very narrow seed pieces of different orientation are placed between the large regular seed plates which exhibit the original orientation. Instead of one, now three grain boundaries were introduced. The middle one is intentionally configured as a small angle grain boundary generating dislocations in order to reduce the stress in the ingot. The two outer ones are configured as large angle grain boundaries which should prohibit the internal generated dislocations and do not emit such by itself. However, also here several times it is observed that the large angle grain boundaries are growing diagonally and annihilate each other or enlarge the area with the unfavorable second orientation, respectively.

In summary, the material which can be produced by this technology is not really a monocrystalline material but more a “Quasimono”-crystalline (QM) material containing SAGBs and dislocations. Therefore, good QM material can only be an alternative to mono CZ-Si, but cannot replace it. Actually, the worldwide activities in the field of the QM technology are nearly completely shut down. The main reason might be the described dislocation formation above the seed joints which could not be avoided under conditions which are adequate from technical and economical point of view to an industrial production, so far. However, there are still companies working on this technology. Another reason why the work on QM processes was reduced a few years ago is the emergence of a new mc Si material type within the last years which is called “high performance mc-Silicon” (HPM) and reveals similar material properties like the QM-Si (Kutsukake et al. 2015). The HPM material including its production technologies are described in detail in the next two sections.

### **Fine Grain Structures with Seeding on Si Feedstock (Original HPM)**

Since the year 2011 it was reported in the literature that mc Si with an average grain structure of 1–4 mm<sup>2</sup>, which is considerably smaller than classic mc, yields in a notable increase of cell efficiencies up to 1% (Yang et al. 2015; Lehmann et al. 2016). Because of this improvement, the fine-grained PV Si is denoted since that time as “*high performance mc silicon*” (HPM).

The first HPM resulted rather accidentally during the development of the dendritic casting method. It was found by Lan et al. (2012) that certain undercooling rates, which are between that of the classic mc and the dendritic mc, are leading to a fine grained structure at the bottom end of the ingot as well to a reduced dislocation density over the ingot height. However, the process window providing the slight undercooling which is required for the formation of the little grains is rather small. For that reason, this process was not enough reproducible for large-scale production.

Nevertheless, the interest in the HPM material remained high and stimulated further research on the growth of Si ingots with small-sized grains.

A reproducible seeding procedure to achieve this kind of material is firstly reported by Lan et al. (2017). They used a layer of small Si chips or chunks, respectively, at the bottom of the crucible as seeds. This Si seeding layer is in fact a part of the Si feedstock material which makes the process step of the feedstock melting more difficult. The crucible heating must now be controlled – similar to the quasi-mono process (see Fig. 17 and section “[Towards Monocrystals by Using Monocrystalline Seeds \(Quasi-Mono QM\)](#)”) – in order to leave an unmelted layer of the feedstock material.

In comparison to the *classic mc* and the *dendritic mc* described in section “[Coarse Grain Structures Without Seed Crystals \(Classic mc and Dendritic mc\)](#),” it is obvious that the mean grain size with typical values of  $\sim 1\text{--}4\text{ mm}^2$  at the ingot bottom is quite smaller in the HPM material (compare Fig. 12a). In addition, the fraction of R-type grain boundaries is increased up to 70–75% in the HPM material whereas the number of twin grain boundaries is drastically decreased. This results in an even higher ratio of  $R/\Sigma 3 > 3$  as sketched in Fig. 18. Finally, the HPM material exhibits quite lower dislocation content than *classic mc* Si material. All in all these structural properties of the HPM material are responsible for less areas of reduced minority carrier lifetime over the whole ingot volume and consequently also for higher cell efficiencies in comparison to classic mc Si wafers.

As a variety of feedstock materials are available on the market, one has to consider for the seeding layer several aspects. Firstly, the size and geometry of the particles have a strong influence to the penetration behavior of the Si melt into the seeding layer. Secondly, the particles and their microstructure have a direct influence on the grain structure which is growing on top of them. In a study of the authors group (Reimann et al. 2016), the use of various seeding feedstock materials like flat chips, edgy chunks, roundish granules or Si powder varying in size from  $\mu\text{m}$  to cm scale and also in microstructure (mono or multi) was investigated with respect to the resulting grain structure.

In cases where monocrystalline feedstock material (SCS) is used, the obtained mean grain size decreases with decreasing feedstock particle size, because each single feedstock particle acts as one monocrystalline seed, as shown in Fig. 32 on the left. Consequently the number of grains and also the number of grain boundaries increase the smaller the feedstock particles are. Further, the distribution of grain boundary types in such ingots is changed from a high ratio of twin/R (*classic mc*) to a high ratio of R/twin (HPM). In consequence, the relative length of R grain boundaries is quite higher than in the *classic mc* reference material. This is caused by the randomly distributed grain orientations which are predetermined by the feedstock particles. This is in contrast to the preferred grain orientations occurring during *classic mc* or *dendritic mc* growth (see section “[Coarse Grain Structures Without Seed Crystals \(Classic mc and Dendritic mc\)](#)”). Thereby, the smaller the grains and the more new grain boundaries are generated, the higher is the fraction of R grain boundaries. Reimann et al. (2016) have shown that it can increase up to 65% if feedstock particles are used with a size  $< 1\text{ mm}$ .



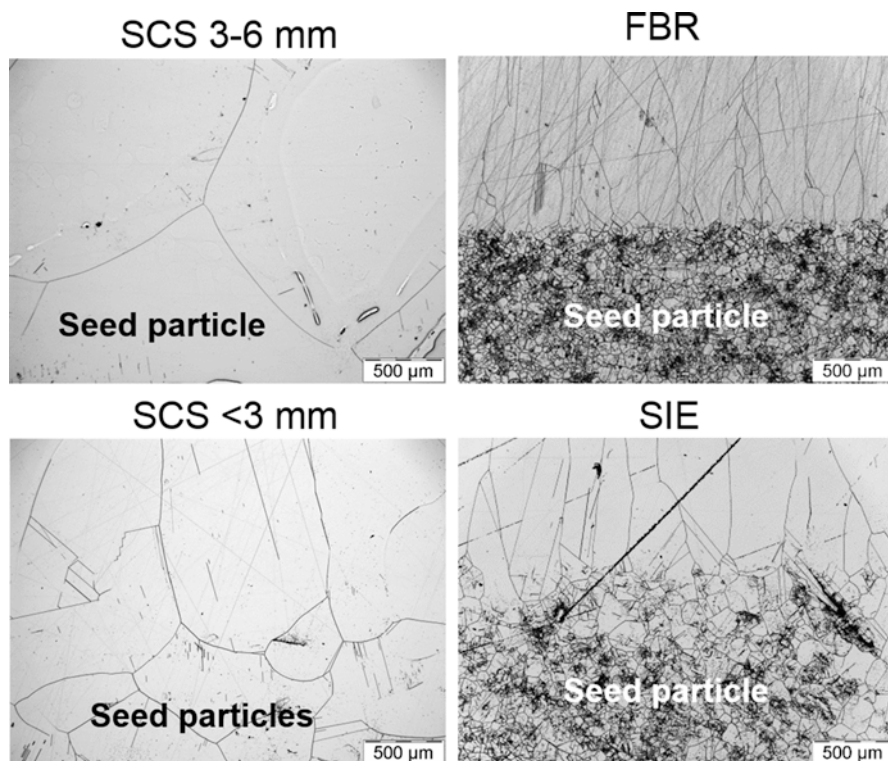


**Fig. 32** Detailed images of vertical sections parallel to the direction of solidification with grain structures near the seeding position for: monocrystalline seed particles (left) and multicrystalline seeds (right). *SCS* single crystalline silicon, *FBR* fluidized Bed Reactor, *SIE* Siemens process. After Reimann et al. (2016)

Due to availability and purity issues, the more widespread approach is to use multicrystalline feedstock particles. The two main variants are Si chunks coming from the Siemens (*SIE*) process and roundish Si granules produced in a fluidized bed reactor (*FBR*). For those materials, the particle size does not influence the grain structure properties in that way as it is the case for the monocrystalline feedstock particles. The resulting  $R$  grain boundary fraction in the material seeded on *SIE* particles with a size between 0.2 and 15 mm as well as seeded on *FBR* granules with a size between 0.5 and 15 mm is on the same (constant) high level of 60–75% which is comparable to the value achieved with the monocrystalline particles with a size  $<1$  mm. This can be related to the multicrystalline microstructure of the *SIE* and *FBR* material. According to their production processes, the feedstock particles exhibit internal grain sizes of 70–270  $\mu\text{m}$  for Siemens and  $\sim 700$   $\mu\text{m}$  for *FBR* material (Ekstrøm et al. 2016b). All of these micrograins which come into contact with the Si melt act as nucleation centers and in consequence the mean size of the grains grown on top of the seed particles is in the same range as the dimensions of their microstructure (compare Fig. 32 on the right). However, the gaps between the

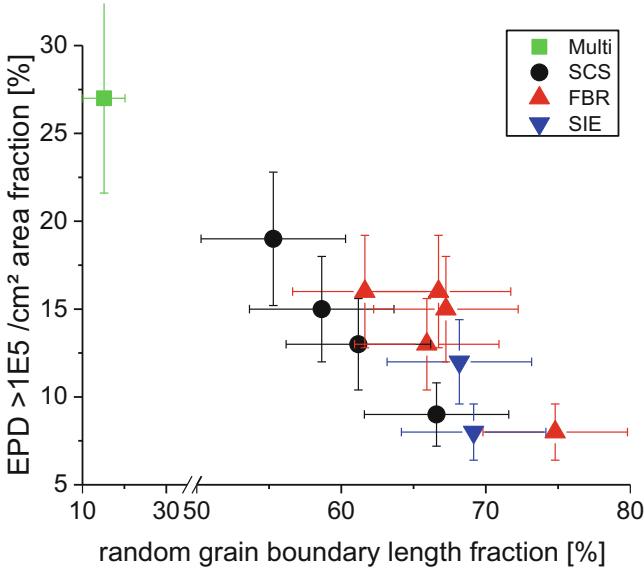


**Fig. 33** Area fraction of wafer regions with etch pit densities  $EPD > 10^5/\text{cm}^2$  versus the fractional amount of random (R) grain boundaries for wafers taken at 25 mm height from laboratory scale HPM Si ingots grown without seeds (multi), monocrystalline seeds (SCS) and multicrystalline seeds (SIE, FBR). After Reimann et al. (2016)

particles which were filled by Si melt are leading to relatively larger grains and therefore the resulting overall grain size is in the range of 1–3  $\text{mm}^2$ .

As mentioned above, the high number of randomly oriented grains leads to a high fraction of R grain boundaries of more than 60% in the HPM material. These R-type grain boundaries are impeding the propagation of dislocations (see above). This property together with the small grain size are the main causes for the lower dislocation content and the significantly reduced wafer area covered by dislocation clusters in comparison to the classic mc Si material.

An experimental proof of this correlation is shown in Fig. 33 for laboratory-scale HPM Si ingots. The fractional amount of areas with dislocation clusters, i.e., an etch pit density ( $EPD > 10^5/\text{cm}^2$ ), is plotted versus the R grain boundary fraction. Obviously, the area fraction of highly dislocated regions can be suppressed below 10% if a high R grain boundary fraction around 70% is present in the HPM material.

Unfortunately, the positive effect of the R grain boundaries in HPM material diminishes more and more with increasing ingot height. It was found that the grain structure properties as well as the fractional amount of highly dislocated wafer area of *classical mc* and *HPM* wafers cut from the top regions of industrial ingots does not differ in such a way as it does in the bottom regions (Lehmann et al. 2016). Further, it was observed for industrial HPM ingots (e.g., by Lan et al. 2017) as well as for lab-scale HPM ingots (e.g., by Trempa et al. 2017) that the fraction of R grain

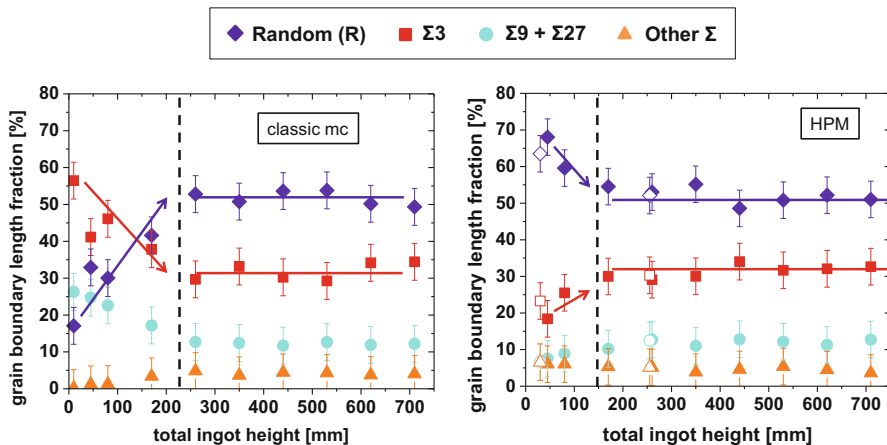


**Fig. 34** Fraction of grain boundary length versus “total ingot height” (see text) for an ingot height of: classic mc G1 size (left) and G1 HPM ingot (right). Additionally, the values for a 300 mm industrial HPM ingot (open symbols) are shown in the right image. After Trempa et al. (2017)

boundaries drastically decreases within the first third of total ingot height. The reasons for this behavior are crystallographic grain boundary reactions which are thermodynamically driven to minimize the grain boundary energy. These processes are causing the annihilation of R grain boundaries, the generation of new twin boundaries and as a consequence a decrease of the R/ $\Sigma 3$  ratio with increasing ingot height (Prakash et al. 2015).

Trempa et al. (2017) simulated a DS process of a very large “total ingot height” of 710 mm by eight successive solidification steps with the same ingot (G1 size). The goal was to study the influence of the above mentioned grain boundary reactions in HPM material in comparison to conventional classic mc Si. The result is shown in Fig. 34 in terms of the fractional amount of the different types of grain boundaries versus the “total ingot height.” Obviously, the grain boundary reactions take place in the firstly solidified 200 mm of the ingot height, irrespectively of the initially different distribution of grain boundary types in HPM and classic mc Si material. Above the height of about 200 mm, both types of materials (including the industrial ingot) reveal the same (constant) fractional amount of the different types of grain boundaries independently from the solidification process. This result holds also for the fraction of the highly dislocated wafer areas which become more and more equal and match each other at an ingot height of about 300–350 mm. This means that for ingot regions above 300 mm, there is no more benefit of the *HPM* material in comparison to the *classical mc* Si.

The main advantage of the “seeding on silicon” HPM growth method is the high reproducibility for the production of industrial ingots. In case that the seeding process is well controlled and suitable feedstock particles are used, the ingot manufacturer can be sure that the result will be a fine grained HPM material. However, there exist also some drawbacks of this method. First, the melting process

of the feedstock needs a more careful control in order to avoid the complete melting of the feedstock (seeding) layer and is more time consuming in comparison to the *classical mc* approach. A Si seed layer with a thickness of about 10–20 mm is necessary because of thermal process fluctuations. But it has to be mentioned that the remaining unmelted Si seed layer leads to an enlarged so-called “bottom red-zone” which results in an ingot part at the bottom region with a very low minority carrier lifetime value and consequently cannot be used for solar cell fabrication. Roughly spoken the length of the bottom red-zone of a HPM ingot is the sum of the red-zone length of a classic mc ingot plus the thickness of the seeding layer.

In summary, the yield losses of a HPM silicon ingot and a more expensive seeding procedure in comparison to a classic mc Si ingot are disadvantageous. To overcome these drawbacks, recent developments deal with seeding approaches without the use of a silicon feedstock layer, which will be the subject of the following section.

### **Fine Grain Structures Without Seeding on Si Material (HPM 2.0)**

The common feature of all the new developed HPM seeding methods is to functionalize the crucible bottom in a way that the silicon feedstock can be completely melted as for the classical mc approach, but in contrast to classic mc a fine grained HPM structure is obtained. In principle, there exist three different approaches for the new processing, called “HPM 2.0,” which can be used separately or in combination:

- (a) Use of “foreign” (i.e., not Si) seed particles which are placed at the crucible bottom embedded or on top of the  $\text{Si}_3\text{N}_4$  coating
- (b) Modification of the surface of the  $\text{Si}_3\text{N}_4$  coating concerning, e.g., morphology, wetting behavior, or roughness
- (c) Modification of the structures of the crucible bottom by using certain contours like knobs or hillocks

For variant (a), it is important that the particles which support the nucleation have a higher melting point than silicon to avoid melting. Also they should exhibit a higher wettability as the surrounding  $\text{Si}_3\text{N}_4$  coating in order to reduce the nucleation energy. But they must not contain harmful impurities like metals or dopants. Two materials which fulfill all the mentioned requirements are  $\text{SiO}_2$  and SiC. Kupka et al. (2017) have tested them by spraying or embedding  $\text{SiO}_2/\text{SiC}$  particles with a size in the range of  $\mu\text{m}$  to mm on the bottom of G1 crucibles. The main conclusions of their results are the following:

- The mean grain size in the first grown part of the ingot decreases with increased surface roughness ( $R_q$ ) of the nucleation layer and remains nearly constant at 1–2 mm<sup>2</sup> for  $R_q > 200 \mu\text{m}$

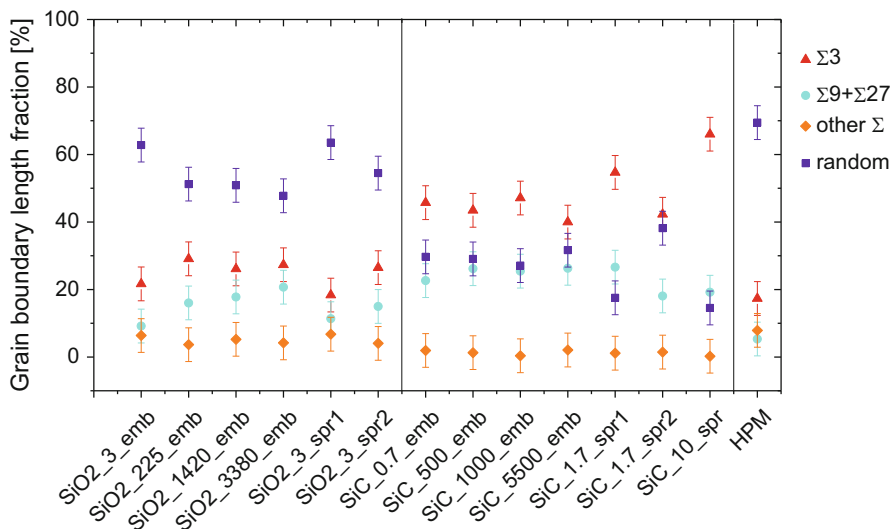


**Fig. 35** Distribution of the grain boundary length fraction in dependence of the different used SiO<sub>2</sub> and SiC nucleation layers. After Kupka et al. (2017)

- Well wetted particles with a resulting mean grain size  $<4 \text{ mm}^2$  must not coercively lead to a high fraction of R grain boundaries over 50% (in the case of the SiC particles)
- Seed particles with low thermal conductivity are needed to achieve HPM properties (in the case of SiO<sub>2</sub> particles)

In summary, SiC particles are not suitable for generating a HPM grain structure with small grains *and* a high fraction of R grain boundaries. Even if relatively small grains grow, comparable to the SiO<sub>2</sub> seeding, the grain structure contains a high number of small dendrites and twins which is attributed to the high thermal conductivity of the SiC particles allowing higher supercoolings. In consequence, the resulting twin fraction is quite high and the R grain boundary fraction is always below 40% for all tested SiC nucleation layers (see Fig. 35 on the right), independently from the particle size (0.7–5000  $\mu\text{m}$ ) and the coating method (embedding or spraying).

In contrast to that, the SiO<sub>2</sub> particles with their low thermal conductivity could be identified as much promising seed material. In Fig. 35 on the left, it is shown that the fraction of R grain boundaries of all SiO<sub>2</sub> nucleation layers is significantly higher than of the SiC particles. In best cases, a R fraction of  $>60\%$  is achievable if small (3  $\mu\text{m}$ ) particles are used.

Also on an industrial scale (G4 ingots), it was demonstrated, e.g., by Laurent et al. (2017) that the addition of small SiO<sub>2</sub> particles at the crucible bottom as functional seeds is a successful method to achieve a HPM grain structure. In Fig. 36, a result

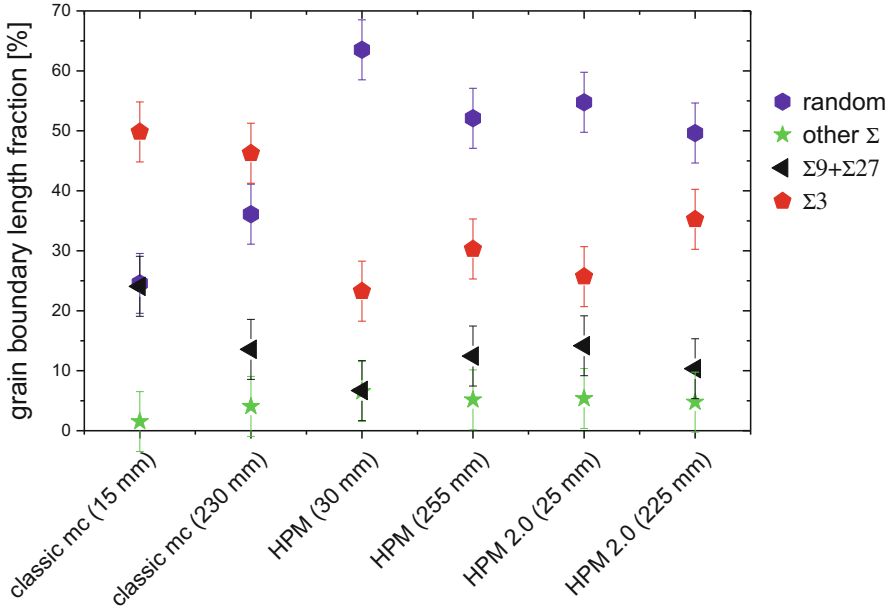


**Fig. 36** Relative length of various types of grain boundaries in industrial scale G4 ingots for different process conditions: Standard (classic) mc-Si (left), reference HPM-mc Si (middle), and vesuvius HPM 2.0-mc Si (right). After Laurent et al. (2017)

with a relatively high fraction of R grain boundaries of 55–50% over ingot height is shown. This value is even better than that of the classical mc reference (25–35%) and only slightly below the conventional HPM values (65–55%) which were achieved by the Si self-seeding method. After making solar cells from these ingots, it could be demonstrated that the cell efficiency of the HPM 2.0 cells is  $\sim 0.5\%$  absolutely higher than for the classic mc cells which matches the reported difference of conventional HPM versus classical mc in section “[Fine Grain Structures with Seeding on Si Feedstock \(Original HPM\)](#).”

The second approach (b) and the third approach (c) are not easy to separate and therefore it will be considered in the following as a “combination.” For instance, Babu et al. (2016) presented a method where they positioned a monolayer of FBR Si feedstock granules at the bottom of a laboratory-scale crucible and coated it with a very thin layer of  $\text{Si}_3\text{N}_4$ . Due to the small thickness of the  $\text{Si}_3\text{N}_4$  coating, the wavy morphology of the monolayer is maintained which is responsible for the nucleation behavior. A full melting process analogue to the classical mc approach was carried out up to  $1470^\circ\text{C}$  for 1 h. However, it is not clear whether the FBR granules remained un-melted or whether they melted and resolidified by keeping their geometry due to the solid cover of  $\text{Si}_3\text{N}_4$ . The final results show that the fraction of R grain boundaries is at 55% close to the ingot bottom which is quite higher than

for the classical mc reference (18%). Also it was shown on etched wafers that the amount of dislocation clusters has significantly decreased.

A similar approach was shown by Zhang et al. (2016) who proposed a mask technique which allows to grow HPM 2.0 Si ingots in industrial G6 scale (840 × 840 mm). In this case a hillock structure of SiO<sub>2</sub> replaces the FBR granules used by Babu et al. (2016). Again the wavy structure was coated with a thin Si<sub>3</sub>N<sub>4</sub> layer to prevent the adhesion of the Si ingot at the crucible/coating composite. In this case, the distribution of the grain boundary types was not investigated. However, the obtained results on solar cells imposingly show that the same cell efficiency distribution could be achieved over the whole G6 ingot with this method as for the conventional HPM approach using the seeding on mc silicon feedstock.

A further similar approach was proposed by Buchovska et al. (2017) who used an industrial G5 crucible containing silica knobs at its bottom to provide a “rough” nucleation layer. It is not mentioned whether these silica knobs were coated with Si<sub>3</sub>N<sub>4</sub> or not. The grain boundary types were not investigated; however, results of PL measurements of a large series of wafers over the complete ingot reveal that the dislocation content is quite comparable to that one grown by a Si feedstock seeding method. Additionally, also cell efficiency data show comparable values for both material types.

In summary, one can state that the results obtained so far by using various approaches to replace the seeding on Si feedstock layer (“original” HPM) are promising. This holds for the achieved grain structures with respect to the dislocation problem and finally for the achieved cell efficiencies. However, it is not clear at that time which one of the different approaches has the potential to provide an increase of the material quality beyond the best HPM results.

Furthermore, it needs to be evaluated which of the different approaches can be implemented into production furnaces and is compatible with the routines of a production process.

Finally, it has to be demonstrated that certain reproducibility can be achieved for large ingot dimensions under production conditions. After that has been achieved, HPM2.0 can become an important DS production process which will then replace HPM and others.

---

## **Conclusions for Optimization Strategies with Respect to “Grain Boundary Engineering”**

Actually, it is an open discussion, which Si material will dominate the PV market in the future. For 2017, the market share was around 20% classic mc, 40% HPM Si, and 40% mono CZ, whereas QM has not shown up in the statistics (ITRPV 2018). It seems to be sure that the high quality mono CZ material will play a significant role also in the future. The HPM Si will completely replace the classic mc in the near

future. However, whether the HPM Si will be also present after the next 5–10 years or if there is a comeback of the QM Si material is still open.

The possible cause is the tendency towards even higher solar cell efficiencies. All the modern solar cell concepts are based on monocrystalline silicon. Therefore, the gap between the efficiencies of mc-Si and mono Si solar cells might increase in the future, such that the cost per efficiency ratio for mono solar cells is superior to the mc-Si one. Therefore, it is forecasted that the share of mono Si wafers will increase in the future. Thus, wafer manufacturers have either to invest heavily in CZ pullers or to solve the existing challenges for QM silicon in order to run the industrial production of QM in the existing DS furnaces.

In fact, the HPM Si and the QM Si material need to be further developed to have a chance to be competitive with the CZ material. But for both growth technologies, the future progress depends on the control of the grain boundaries appearing in these materials.

In the case of the QM growth technology, the main task will be to reproducibly avoid the formation of dislocations and small angle grain boundaries induced by the seed joints. Here the grain boundary engineering with the most promising “SMART”-approach (see section “[Towards Monocrystals by Using Monocrystalline Seeds \(Quasi-Mono QM\)](#)”) might be the best way to solve this problem even on an industrial scale. However, it is not clear whether sufficient good results could be reproducibly achieved by this method.

A perspective of the authors for improving the HPM material quality is to keep the fraction of random grain boundaries as high as possible along the complete ingot height. If this can be achieved the dislocation formation and movement is even more suppressed over longer growth heights and the amount of dislocation clusters should be further reduced. However, because the grain boundary formation and annihilation is also driven by a reduction of the grain boundary energy, it will be difficult to find practical solutions to overcome this physical law.

In general, for all DS growth technologies, the impurity contamination of the ingots will be an important issue in order to increase the Si material quality further. Higher purity of crucibles and Si<sub>3</sub>N<sub>4</sub> coatings as well as cost-effective diffusion barriers between both components would be beneficial and would at the same time reduce the harmfulness of the grain boundaries in the Si due to a reduced impurity decoration.

---

## Cross-References

- ▶ [Defects in Crystalline Silicon: Dislocations](#)
- ▶ [Growth of Crystalline Silicon for Solar Cells: Czochralski Si](#)
- ▶ [Growth of Crystalline Silicon for Solar Cells: Mono-Like Method](#)
- ▶ [Growth of Multicrystalline Silicon for Solar Cells: Dendritic Cast Method](#)
- ▶ [Growth of Multicrystalline Silicon for Solar Cells: The High-Performance Casting Method](#)
- ▶ [Metal Impurities and Gettering in Crystalline Silicon](#)
- ▶ [Polysilicon and Its Characterization Methods](#)



## References

- G.A. Babu, I. Takahashi, S. Matsushima, N. Usami, J. Cryst. Growth **441**, 124 (2016)
- J. Bauer, O. Breitenstein, A. Lotnyk, H. Blumtritt, in *22nd European Photovoltaic Solar Energy Conference*, Milan (2007), p. 994
- D.G. Brandon, Acta Metall. **14**, 1479 (1966)
- I. Buchovska, O. Liaskovskiy, T. Vlasenko, S. Beringov, F.M. Kiessling, Sol. Energy Mater. Sol. Cells **159**, 128 (2017)
- T. Buonassisi, M. Heuer, A.A. Istratov, M.D. Pickett, M.A. Marcus, B. Lai, Z. Cai, S.M. Heald, E.R. Weber, Acta Mater. **55**, 6119 (2007)
- D. Camel, B. Marie, D. Ponthenier, F. Servant, in *3rd International Workshop on Crystalline Silicon Solar Cells*, Trondheim (2009)
- J. Chen, T. Sekiguchi, D. Yang, Phys. Status Solidi C **4**, 2908 (2007)
- M. Demant, S. Rein, J. Haunschild, T. Strauch, H. Höffler, J. Broisch, S. Wasmer, K. Sunder, O. Anspach, T. Brox, Prog. Photovolt. Res. Appl. **24**, 1533 (2016)
- K.E. Ekstrøm, G. Stokkan, R. Søndena, H. Dalaker, T. Lehmann, L. Arnberg, M. Di Sabatino, Phys. Status Solidi A **212**, 2278 (2015)
- K.E. Ekstrøm, E. Undheim, G. Stokkan, L. Arnberg, M. Di Sabatino, Acta Mater. **109**, 267 (2016a)
- K.E. Ekstrøm, G. Stokkan, A. Autruffe, R. Søndena, H. Dalaker, L. Arnberg, M. Di Sabatino, J. Cryst. Growth **441**, 95 (2016b)
- J. Friedrich, W. von Ammon, G. Müller, in *Handbook of Crystal Growth*, 2nd edn., ed. by P. Rudolph (Elsevier, Boston, 2015), p. 45
- K. Fujiwara, W. Pan, N. Usami, K. Sawada, M. Tokairin, Y. Nose, A. Nomura, T. Shishido, K. Nakajima, Acta Mater. **54**, 3191 (2006)
- D. Helmreich, in *Symposium on Electronic and Optical Properties of Polycrystalline or Impure Semiconductors and Novel Silicon Growth Methods*, St. Louis (Pennington, 1980), p. 184
- D. Hu, S. Yuan, L. He, H. Chen, Y. Wan, X. Yu, D. Yang, Sol. Energy Mater. Sol. Cells **140**, 121 (2015)
- Intego GmbH, Gemini-Grain structure analysis (2018), <https://www.intego.de/de/solar1/pruefanlagen-fuer-die-solarfertigung/wafer/gemini-kornstrukturanalyse>. Accessed 18 April 2018
- ITRPV, *International Technology Roadmap for Photovoltaic (ITRPV) 2017* (2018)
- M. Kohyama, R. Yamamoto, M. Doyama, Phys. Status Solidi B **138**, 387 (1986)
- I. Kupka, T. Lehmann, M. Trempa, C. Kranert, C. Reimann, J. Friedrich, J. Cryst. Growth **465**, 18 (2017)
- K. Kutsukake, N. Usami, Y. Ohno, Y. Tokumoto, I. Yonenaga, Appl. Phys. Express **6**, 25505 (2013)
- K. Kutsukake, N. Usami, Y. Ohno, Y. Tokumoto, I. Yonenaga, IEEE J. Photovoltaics **4**, 84 (2014)
- K. Kutsukake, M. Deura, Y. Ohno, I. Yonenaga, Jpn. J. Appl. Phys. **54**, 8 (2015)
- C.W. Lan, W.C. Lan, T.F. Lee, A. Yu, Y.M. Yang, W.C. Hsu, B. Hsu, A. Yang, J. Cryst. Growth **360**, 68 (2012)
- C.W. Lan, A. Lan, C.F. Yang, H.P. Hsu, M. Yang, A. Yu, B. Hsu, W.C. Hsu, A. Yang, J. Cryst. Growth **468**, 17 (2017)
- J. Laurent, G. Rancoule, E. Drode, C. Reimann, M. Trempa, C. Kranert, J. Friedrich, L. Teale, R. Dyer, I. Dorrity, in *33rd European Photovoltaic Energy Specialist Conference*, Amsterdam (2017), p. 305
- T. Lehmann, M. Trempa, E. Meissner, M. Zschorsch, C. Reimann, J. Friedrich, Acta Mater. **69**, 1 (2014)
- T. Lehmann, C. Reimann, E. Meissner, J. Friedrich, Acta Mater. **106**, 98 (2016)
- S. Martinuzzi, I. Périchaud, O. Palais, Sol. Energy Mater. Sol. Cells **91**, 1172 (2007)
- K. Nakajima, K. Kutsukake, K. Fujiwara, N. Usami, S. Ono, Yamasaki, in *25th European Photovoltaic Solar Energy Conference*, Valencia (2010), p. 817
- V. Oliveira, M. Tsoutsouva, T. Lafford, E. Pihan, F. Barou, C. Cayron, D. Camel, in *29th European Photovoltaic Solar Energy Conference*, Amsterdam (2014), p. 793
- V. Oliveira, B. Marie, C. Cayron, M. Marinova, M.G. Tsoutsouva, H.C. Sio, T.A. Lafford, J. Baruchel, G. Audoit, A. Grenier, T.N. Tran Thi, D. Camel, Acta Mater. **121**, 24 (2016)
- R.R. Prakash, K. Jiptner, J. Chen, Y. Miyamura, H. Harada, T. Sekiguchi, Appl. Phys. Express **8**, 35502 (2015)

- V. Randle, *Microtexture Determination and its Applications*, 2nd edn. (Maney for the Institute of Materials Minerals and Mining, London, 2003)
- C. Reimann, M. Trempa, T. Lehmann, K. Rosshirt, J. Stenzenberger, J. Friedrich, K. Hesse, E. Dornberger, *J. Cryst. Growth* **434**, 88 (2016)
- B. Rynningen, G. Stokkan, M. Kivambe, T. Ervik, O. Lohne, *Acta Mater.* **59**, 7703 (2011)
- D.G. Schimmel, *J. Electrochem. Soc.* **126**, 479 (1979)
- F. Schmid, U.S. Patent 3,898,051, 1975
- F. Secco D'Aragona, *Solid State Sci. Technol.* **119**, 948 (1972)
- E. Sirtl, A. Adler, *Z. Metallkd./Mater. Res. Adv. Tech.* **52**, 529 (1961)
- B.L. Sopori, *J. Electrochem. Soc.* **131**, 667 (1984)
- B. Sopori, D. Guhabiswas, P. Rupnowski, S. Shet, S. Devayajanam, H. Moutinho, in *36th IEEE Photovoltaic Specialists Conference*, Seattle (2011), p. 1680
- N. Stoddard, Patent WO 2009/014957 A2, 29 Jan 2009
- N. Stoddard, W. Bei, I. Witting, M. Wagener, P. Yongkook, G. Rozgonyi, R. Clark, *Solid State Phenom.* **131–133**, 1 (2008)
- I. Takahashi, S. Joonwichien, T. Iwata, N. Usami, *Appl. Phys. Express* **8**, 105501 (2015)
- M. Trempa, *Gerichtete Erstarrung von einkristallinen Siliciumkristallen nach dem VGF-Verfahren für die Anwendung in der Photovoltaik* (Fraunhofer-Verlag, Stuttgart, 2014)
- M. Trempa, C. Reimann, J. Friedrich, G. Müller, D. Oriwol, *J. Cryst. Growth* **351**, 131 (2012)
- M. Trempa, C. Reimann, J. Friedrich, G. Müller, A. Krause, L. Sylla, T. Richter, *J. Cryst. Growth* **405**, 131 (2014)
- M. Trempa, C. Reimann, J. Friedrich, G. Müller, L. Sylla, A. Krause, T. Richter, *J. Cryst. Growth* **429**, 56 (2015a)
- M. Trempa, C. Reimann, J. Friedrich, G. Müller, A. Krause, L. Sylla, T. Richter, *Cryst. Res. Technol.* **50**, 124 (2015b)
- M. Trempa, M. Beier, C. Reimann, K. Roßhirth, J. Friedrich, C. Löbel, L. Sylla, T. Richter, *J. Cryst. Growth* **454**, 6 (2016)
- M. Trempa, I. Kupka, C. Kranert, T. Lehmann, C. Reimann, J. Friedrich, *J. Cryst. Growth* **459**, 67 (2017)
- S. Tsurekawa, K. Kido, T. Watanabe, *Mater. Sci. Eng. A* **462**, 61 (2007)
- D.S. Vlachavas, *Acta Crystallogr. A* **41**, 530 (1985)
- F. Wilhelm, *J. Appl. Crystallogr.* **4**, 521 (1971)
- M. Wright-Jenkins, *J. Electrochem. Soc.* **124**, 757 (1977)
- K.H. Yang, *J. Electrochem. Soc.* **131**, 1140 (1984)
- Y.M. Yang, A. Yu, B. Hsu, W.C. Hsu, A. Yang, C.W. Lan, *Prog. Photovolt. Res. Appl.* **23**, 340 (2015)
- H. Zhang, D. You, C. Huang, Y. Wu, Y. Xu, P. Wu, *J. Cryst. Growth* **435**, 91 (2016)

---

**Part V**

**Thin Film Silicon**



# Hydrogenated Amorphous Silicon Thin Film **20**

Ying Zhao, Xiaodan Zhang, and Baojie Yan

## Contents

Introduction .....	640
Fabrication of Hydrogenated Amorphous Silicon and Alloy .....	642
Dc-PECVD .....	643
RF-PECVD .....	646
Vhf PECVD .....	648
Microwave PECVD .....	651
Hot Wire CVD .....	652
Material Properties of Hydrogenated Amorphous Silicon and Alloy .....	655
Structure and Electronic States .....	655
Optical Property .....	658
Electrical Property .....	664
Metastability of a-Si:H: Staebler-Wronski Effect .....	670
Amorphous Silicon Alloy .....	673
A-Si:H Alloy Solar Cells .....	675
Principle of a-Si:H Single-Junction Solar Cell .....	675
A-Si:H Alloy <i>p-i-n</i> Single-Junction Solar Cell .....	677
A-Si:H Alloy <i>n-i-p</i> Single-Junction Solar Cell .....	679
A-SiGe:H Alloy Single-Junction Solar Cell .....	679
A-Si:H Alloy-Based Multijunction Solar Cells .....	682
A-Si:H/a-Si:H Double-Junction Solar Cell .....	684
A-Si:H/a-SiGe:H Double-Junction Solar Cell .....	684
A-Si:H/a-SiGe:H/a-SiGe:H Triple-Junction Solar Cell .....	685
A-Si:H/c-Si Heterojunction Solar Cell (SHJ or HIT) .....	685
Conclusion .....	687
References .....	689

---

Y. Zhao · X. Zhang · B. Yan (✉)  
Institute of Photoelectronic Thin Film Devices and Technology, Nankai University,  
Tianjin, P. R. China  
e-mail: [zhaoygds@nankai.edu.cn](mailto:zhaoygds@nankai.edu.cn); [xdzhang@nankai.edu.cn](mailto:xdzhang@nankai.edu.cn); [baojie.yan@yahoo.com](mailto:baojie.yan@yahoo.com)

---

**Abstract**

From solar cell application point of view, this chapter reviews the aspects of hydrogenated amorphous silicon (a-Si:H) based materials. Spear and LeComer made the first a-Si:H films with glow discharge by decomposing hydrogen containing gases such as SiH<sub>4</sub>, in which hydrogen atoms terminate the Si dangling bonds and reduce the defect density significantly. The reduction of defect density lead to the possibility of doping a-Si:H to form N-type and P-type films and made it possible to make p-n junction, which is the foundation of thin film silicon-based electronic devices such as solar cells and thin film transistors. Since then several methods have been developed to deposit a-Si:H materials and devices. From solar cells point of view, a-Si:H is one of the useful materials with several unique properties: (1) high absorption coefficients in the visible range allowing to use a thin absorber layer, (2) large area uniform deposition for low-cost mass productions, and (3) deposition on various foreign substrates for rigid and flexible solar modules. The main disadvantage of a-Si:H is the lower carriers mobility and lifetime than the crystal copartners, which result in the lower energy conversation efficiency in a-Si:H solar cells than c-Si solar cells. In addition, the so-called Staebler-Wronski effect causes a light-induced degradation in a-Si:H solar cell efficiency. Over the years, a-Si:H science and technology have been very well developed driving by the applications in thin film silicon photovoltaic (PV) solar energy and large area display industries. In the PV applications, a-Si:H solar cell has been one of the most important technologies for the so-called second-generation PV solar energy. However, with the significant cost reduction of poly-Si and c-Si solar panels in the last few years, a-Si:H PV industry has been shrunk to the sideline and can only provide products in the niche market. Fortunately, new application as the surface passivation layer on c-Si to form a-Si:H/c-Si heterojunction solar cells gives a-Si:H a new life in the PV industry.

---

**Keywords**

a-Si:H · Thin film · Glow discharge · PECVD · Dangling bonds · Mobility · Lifetime · Absorption coefficient · Staebler and Wronski effect · Flexible · Large area

---

**Introduction**

Hydrogenated amorphous silicon (a-Si:H) as one of large area electronic materials has been widely used in the modern industry, mainly in photovoltaic (PV) solar energy and large area display such as televisions and computer monitors. The research and development of a-Si:H technology started in the middle of 1970s. Previously, most nonhydrogenated amorphous silicon (a-Si) materials were made mainly by physical vapor depositions (PVD) such as sputtering and thermal evaporation (Moss and Graczyk 1969; Shevchik and Paul 1972; Temkin et al. 1973), where no hydrogen atoms are incorporated into the films. The nonhydrogenated a-Si

have a large density of silicon dangling bond defects, normally in the order of  $10^{18} \text{ cm}^{-3}$  to  $10^{19} \text{ cm}^{-3}$ . When doping atoms incorporated into a-Si, the additional carriers (electrons or holes) go to the defect sites and no contribution to the conduction is made. Therefore, the PVD-made a-Si does not show usefulness in electronic devices.

Spear and LeComber made a remarkable invention in the middle of the 1970s. They used a glow discharge, also called plasma enhanced chemical deposition (PECVD), to decompose silane ( $\text{SiH}_4$ ) and form a-Si:H (Spear and LeComber 1975, 1976) and found that the materials can be doped by P to form N-type materials and by B to form P-type materials. Consequently, a *p-n* junction can be made, which is the fundamental structure of modern electronic devices. The major contribution for the capability of doping is hydrogen (H) atoms. Normally, about 10–20 at.% H is incorporated in a-Si:H, which terminates the Si dangling bonds and reduces the defect density from  $\sim 10^{18} \text{ cm}^{-3}$  to  $\sim 10^{16} \text{ cm}^{-3}$ .

In the RCA lab, Carlson and Wronski invented the first a-Si:H solar cell with an energy conversion efficiency of 2.4% (Carlson and Wronski 1976), which leads to a significant effort to the research and development of thin film a-Si:H solar cells. In 1980, the RCA group increased the a-Si:H solar cell efficiency to 8%. At the same time, the Sanyo group in Japan focused on the research and development of useful a-Si:H solar cells in consumer electronics such as watches and calculators.

In the theoretical study, Anderson proposed the concept of localized electronic states in disordered solids (Anderson 1958). Mott introduced the concept of mobility edge and the localized tail states in disordered semiconductors (Mott 1966, 1967). Following the Anderson and Mott theory, Mott, Cohen, Fritzsche, and Ovshinsky proposed Mott-CFO model for electron structures and transport in amorphous semiconductors (Mott 1967; Cohen et al. 1969), which built the foundation of electronic state structure and carrier transport theory in amorphous semiconductors and had a significant impact on the modern large-area electronic industry.

Also in the RCA lab, Staebler and Wronski observed a light-induced degradation in both the dark and photoconductivities in a-Si:H films after light soaking (Staebler and Wronski 1977), which is called Staebler and Wronski effect or SW effect. The light-induced degradation can be annealed away and the material property returns to its initial state after thermal annealing at a high temperature such as  $> 150^\circ\text{C}$  for over 1 hour. The Staebler and Wronski effect has a significant impact on the device applications. In terms of a-Si:H solar panels, their efficiency decreases with time in the first few hundred hours of installation in the field of light soaking and then saturates. The light-induced efficiency reduction can be as high as 50% in single-junction a-Si:H solar cells and can also be reduced to around 5–10% in multijunction solar cells with optimized material quality and device design.

In the a-Si:H PV technology side, the solar cell efficiency has been constantly improved by optimizing the material quality such as by hydrogen dilution (Guha et al. 1981; Koh et al. 1998), alloying with other elements to adjust the bandgap, and optimization of device structures. In order to cover the solar spectrum properly, hydrogenated amorphous silicon carbon alloy (a-SiC:H) was developed for wide bandgap (Tawada et al. 1982) and hydrogenated amorphous silicon germanium alloy

(a-SiGe:H) for low bandgap (Ovshinsky 1985) materials in multijunction solar cells. Yang et al. optimized a-Si:H/a-SiGe:H/a-SiGe:H triple-junction solar cell structures and achieved initial and stable cell efficiencies of 14.6% and 13.0%, respectively, in 1997 (Yang et al. 1997). With the incorporation of hydrogenated nanocrystalline silicon (nc-Si:H) as the bottom cell, Yan et al. advanced the initial efficiency to 16.3% (Yan et al. 2011). With the continual improvement of a-Si:H solar cell and module efficiency, several large a-Si:H PV module production lines were built around the world, such as the BP Solar and United Solar in the USA; Fuji Electric, Canon, and Kaneka in Japan; Oerlikon/TEL Solar in Swaziland; LG Solar in South Korea. The large area module efficiency has reached 12% by TEL Solar (Cashmore et al. 2016). However, with the dramatic drop of crystalline silicon (both poly-Si and c-Si) PV module price, a-Si:H PV technology lost its competitiveness in the market because of the higher manufacture cost and lower energy conversion efficiency than poly-Si and c-Si modules. Most of the thin film silicon PV companies went out of business in the beginning of this decade. On the other hand, a-Si:H has been used as the passivation layer on c-Si wafer to form silicon heterojunction solar cells (SHJ) or called heterojunction with intrinsic thin layer (HIT) solar cell (Taguchi et al. 1990). Recently, HIT solar cell efficiency has reached 25.6% in 2014 (Masuko et al. 2014) and 26.3% in 2016 ([http://www.kaneka.co.jp/kaneka-e/images/topics/1473811995/1473811995\\_101.pdf](http://www.kaneka.co.jp/kaneka-e/images/topics/1473811995/1473811995_101.pdf)), surpassed the record of 25.0% achieved with traditional homojunction c-Si solar cell (Zhao et al. 1999). The application in HIT solar cells finds the new life for a-Si:H in the PV solar energy industry.

---

## Fabrication of Hydrogenated Amorphous Silicon and Alloy

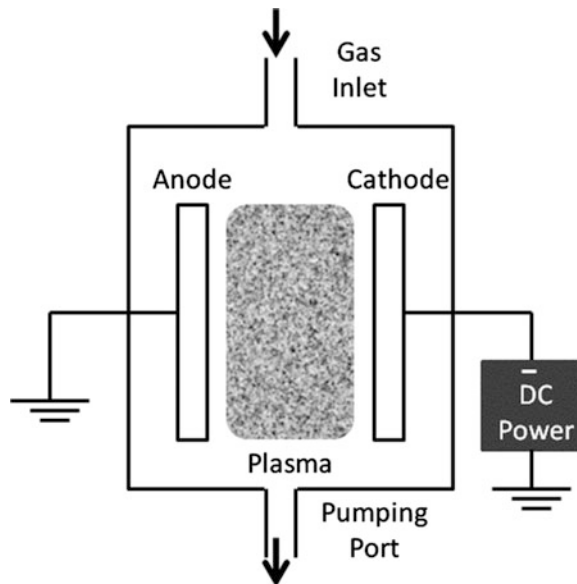
In the last 40 years, many deposition methods have been invented and developed for fabrication of a-Si and a-Si:H films and devices, including PVD and chemical vapor deposition (CVD). Because CVD methods, especially PECVD, have been successfully used in a-Si:H solar cell research and development as well as thin film silicon PV manufacturing, we mainly introduce and discuss various PECVD methods. In principle, all of the CVD methods are with the similar chemical processes. The precursor gases such as SiH<sub>4</sub> and H<sub>2</sub> are introduced into an enclosed deposition chamber at very low pressure and decomposed into various Si-containing radicals such as SiH<sub>3</sub>, SiH<sub>2</sub>, SiH, and Si. The Si-containing species diffuse out from the plasma zone, reach a heated substrate, and then form a film on the substrate surface. Depending on the energy source for decomposing the reactant gases, CVD has been divided into several categories. Commonly used in conventional semiconductor industry is thermal CVD, where the reactant gases are decomposed at a high temperature such as over 1000°C. Because of the high temperature, hydrogen cannot be incorporated into the films, therefore thermal CVD is not used for making a-Si:H films, but for poly-Si and c-Si films. Instead, PECVD and other low-temperature CVD methods are used for a-Si:H deposition, where additional energy sources are used to decompose the reactant gases, including direct current PECVD (DC-PECVD), radio frequency PECVD (RF-PECVD), very high frequency

PECVD (VHF-PECVD), microwave PECVD ( $\mu\text{w}$ -PECVD), photo-induced CVD (photo-CVD), and hot wire CVD (HW-CVD). The main precursors are silane ( $\text{SiH}_4$ ) or disilane ( $\text{Si}_2\text{H}_6$ ) with hydrogen ( $\text{H}_2$ ), helium (He), or argon (Ar) as the dilution gases to improve the material quality. For doped a-Si:H,  $\text{PH}_3$  is used for N-type doping,  $\text{B}_2\text{H}_6$ ,  $\text{B}(\text{CH}_3)_3$ , or  $\text{BF}_3$  are used for P-type doing. Below we present the commonly used methods in a-Si:H material and solar cell depositions.

## Dc-PECVD

PECVD is a process using glow discharge to deposit thin films. Since glow discharge method can be used in other process, such as etching in semiconductor device fabrications, we use “glow discharge” when we discuss the physical properties of plasma and use “PECVD” when we discuss film deposition. From physics point of view, DC glow discharge is the easiest process to be understood. Figure 1 shows a schematic drawing of a DC glow discharge chamber, where two parallel plate electrodes are installed in a vacuum chamber equipped with gas supplying and pumping systems. A DC power supply is connected to one of the electrode and ground the other. The substrate is placed on one electrode, normally on the grounded anode. Under a given low pressure, the electric field breaks the gas molecules to form positive ions and electrons. The charged particles are accelerated by the electric field, collide with other neutral species, and break them down. The positively charged ions and electrons can be lost by the collisions with others and escaping out of the plasma. When the generation rate and the losing rate of the positively

**Fig. 1** Schematic drawing of a DC glow discharge chamber





charged ions and electrons get balanced, a stable plasma state is built, where the average electron density and positive ion density are equal. Because the decomposing of gas molecules by the collisions with high-energy electrons emits light, the process is called glow discharge. By measuring the emission spectrum, one can study the space reactions during plasma deposition. Glow discharge is a complex physical and chemical process. Here we only give a simple conception discussion.

DC glow discharge process has been very well documented in the literature (Chapman 1980), where detailed descriptions of the fundamental theory and applications are given. As shown in Fig. 1, the two parallel electrodes are separated with a small distance ( $d$ ), one connects to the ground (normally the wall of the chamber) as the anode and the other connects to the negative output of the DC power supply, therefore it is called cathode. To sustain stable plasma, the electron generation rate should be high enough to balance the losses of electrons to the anodes and the chamber wall. The electron generation rate depends on the electric field from the applied voltage. Electrons are accelerated by the electric field, collide with neutral molecules to break them, and produce new electrons and ions. In certain conditions, the higher the applied electric field, the higher the disassociation rate and the higher the electron generation rate are achieved. The electron annihilation includes the loss due to the recombination with positive ions, absorption onto the cathode, anode, and other chamber surface. Under a given condition, the applied voltage should be higher than a certain value called the threshold voltage ( $V_{th}$ ) to sustain the plasma. The  $V_{th}$  depends on the structure of the chamber, especially the gap between the cathode and anode ( $d$ ), the process parameters such as pressure ( $p$ ), temperature ( $T$ ), and reactant gases and their flow rates. The most important parameter determining the  $V_{th}$  is the product of the gap distance and pressure ( $pd$ ), which follows the so-called Paschen curve.

Now we discuss a few important parameters of describing the plasma properties. The first important parameter is electron temperature and ion temperature. Because the electron mass is much lighter than the mass of molecules and ions, electrons and ions cannot reach thermal equilibrium. Consequently, electrons and ions have different temperatures in plasma. For an ideal gas, the temperature ( $T$ ) is the measure of average kinetic energy ( $E_k$ ) of gas molecules and they have the following relation:

$$E_k = \frac{1}{2}mv^2 = \frac{3}{2}kT, \quad (1)$$

where  $m$  is the mass of particles,  $v$  the average velocity,  $k$  the Boltzmann constant. This relation applies to ions and electrons in plasma with corresponding ion temperature  $T_i$  and electron temperature  $T_e$ . Both ions and electrons get energy from the applied electric field, thus the ion temperature  $T_i$  is normally slightly higher than the ambient temperature because they lose energy by collision with other particles and the chamber surface. Furthermore, because electrons are much lighter than ions and do not lose much energy by collisions with ions and neutral particles, the electron temperature  $T_e$  is much higher than the ion temperature when they obtain the same energy from the applied field. For example, 1 eV is about 11,600 K for electrons.

In stable plasma, the electron density and positive ion density should be the same and is called the plasma density ( $n$ ), which is one of the important parameters for plasma. A high plasma density is one of the conditions for high rate deposition. Although the equal average positive and negative charge densities lead to an average neutral state in plasma, some variations in the charge distribution in plasma can occur locally. Because the electron speed is much higher than ion speed, the movement of electrons causes an oscillation in charge distribution. The oscillation frequency is named as plasmon frequency ( $\omega_e$ ) and given by

$$\omega_e = \left( \frac{ne^2}{m_e \epsilon_0} \right)^{1/2} = 8.98 \times 10^3 n^{1/2} (\text{Hz}), \quad (2)$$

where  $n$  is the average electron density,  $e$  the electron charge,  $m_e$  the mass of electron,  $\epsilon_0$  is the dielectric constant in vacuum. For a plasma density of  $10^{10} \text{ cm}^{-3}$ , the plasma frequency  $\omega_e$  is around 900 MHz, which is much higher than the RF frequency of 13.56 MHz and VHF frequency of 40–100 MHz used in a-Si:H depositions. Therefore, the concepts developed in DC glow discharge are applicable in RF and VHF glow discharge deposition processes.

The third parameter is the plasma potential  $V_p$ , which is the average electric potential of the plasma body and it normally respects to the floating potential  $V_f$  as the reference. The  $V_f$  is the electric potential of a metal object floating in the plasma. When a metal object is placed in the plasma, electrons diffuse to the surface and make the metal surface negatively charged. Consequently, a lower potential  $V_f$  than the plasma potential is built to repel the additional electrons to come. The difference between the  $V_p$  and  $V_f$  is given by

$$V_p - V_f = \frac{kT_e}{e} \ln \left( \frac{v_e}{v_i} \right) = \frac{kT_e}{2e} \left( \frac{m_i T_e}{m_e T_i} \right), \quad (3)$$

where  $v_e$  and  $v_i$  are the average velocities of electrons and ions,  $m_e$  and  $m_i$  the masses of electrons and ions, respectively. For the plasma used in a-Si:H deposition, the difference between  $V_p$  and  $V_f$  is in the range of a few Volts and a few tens of Volts. Corresponding to floating potential, another parameter called Debye length ( $\lambda_D$ ) describes the space charge thickness around a metal object,

$$\lambda_D = \left( \frac{kT_e \epsilon_0}{ne^2} \right)^{1/2}. \quad (4)$$

Since the plasma is electrically neutral in average, the amount of electrons flowing out from the plasma should be equal to the amount of positive ions flowing out; in addition, the electron diffusion speed is much higher than ion diffusion speed, the plasma potential  $V_p$  should be higher than the potential on the surrounding surface. Normally the substrate is ground and connected to the chamber wall, the cathode is connected to the negative of the power supply. Figure 2 shows a schematic diagram of the electric potential distribution between the two electrodes, where it is divided into three zones: anode sheath, plasma zone, and cathode sheath. Because

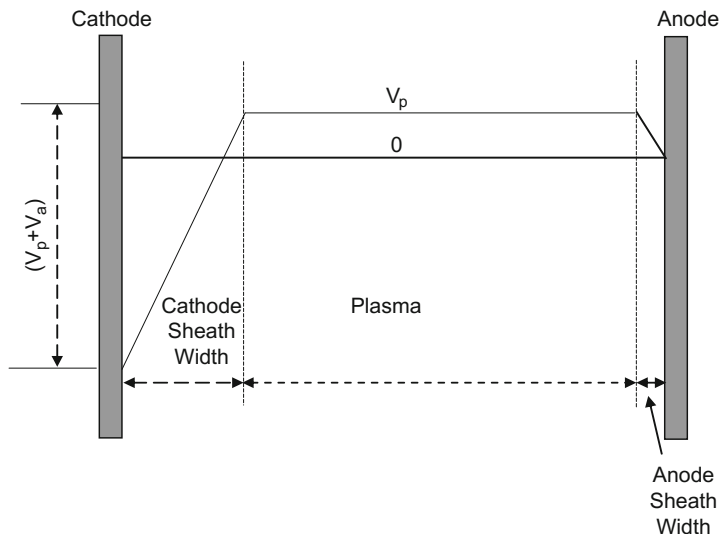


**Fig. 2** A schematic diagram of the electric potential distribution between the two electrodes in a DC glow discharge system

the anode sheath and cathode sheath have no glow, they are also called “dark” space. The voltage across the cathode sheath is the applied voltage plus the plasma potential, while it is just the plasma potential across the anode sheath. The difference between the cathode and anode sheath voltages leads to more positive ion flow to the cathode and more electrons move to the anode, and therefore a constant current flows through the system. In this kind of design, since the substrate is normally attached on the anode, a low ion bombardment on the substrate happens, which is favorable for high-quality a-Si:H deposition.

From large area system design point of view, DC glow discharge is simple and easy for uniform deposition. In the late 1990s, BP Solar built a 20 MW/year a-Si:H PV module production line with DC-PECVD (Carson 2003). Although running well, it was closed for nontechnical reasons.

DC glow discharge also has one major weakness. In order to keep a constant current flow, the substrate needs to have a good conductivity. Nonconductive substrate is hard to be used in DC glow discharge. RF glow discharge overcomes this issue and has been widely used in a-Si:H solar cell research and thin film silicon PV module production.

## RF-PECVD

In RF PECVD system, a RF power supply is used to replace the DC power supply in DC PECVD system. Because the radiation from the RF power could interference communication, it has been agreed by the international community and assigned a special frequency of 13.56 MHz for RF PECVD deposition, where no communication

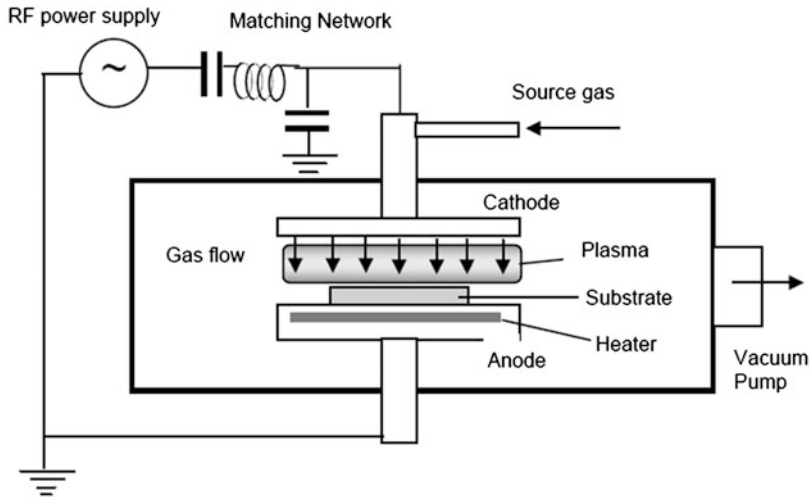


**Fig. 3** Schematic diagram of an RF PECVD system (Kondo 2003)

signal is using this frequency. Figure 3 draws a schematic diagram of an RF PECVD system (Kondo 2003). Similar to DC PECVD system, the output of RF power supply is connected to one of the two parallel plate electrodes, and the other electrode is grounded to the chamber wall, which leads to an effective larger area of the grounded electrode than the RF powered electrode and results in a negative DC self-bias ( $V_{self}$ ) on the RF powered electrode during the plasma process. Therefore, the RF powered electrode is called cathode and the grounded electrode is called anode. The substrate is normally attached onto the anode. As discussed in the previous section, the RF frequency (13.56 MHz) is much lower than plasma frequency ( $\omega_e$ ), the concepts of DC plasma are still applicable in RF glow discharge such as the plasma potential ( $V_p$ ). An average DC potential is built up during RF glow discharge process as shown in Fig. 2 with two dark spaces of anode and cathode sheaths and the plasma zones. Except for the neutral species, electrons and positive ions can also diffuse out from the plasma zone and reach to the cathode and anode as well as other surrounding surface. Within a very short time after the plasma is ignited, a large number of electrons accumulated on the cathode and built a negative  $V_{self}$  on it, repelling the upcoming electrons and accelerating the ions. When the electron current and the ion current reach the same magnitude, no net DC current flows through the system and stable RF plasma is established. Early analyses showed that the magnitude of the  $V_{self}$  is proportional to 4th power of the area ratio of the anode ( $A_a$ ) and the cathode ( $A_c$ ),

$$V_{self} = -\alpha \left( \frac{A_a}{A_c} \right)^4, \quad (5)$$

where  $\alpha$  is a constant. This equation is deduced based on many assumptions, such as there is no collision for ions traveling the dark sheath, the current is limited by the

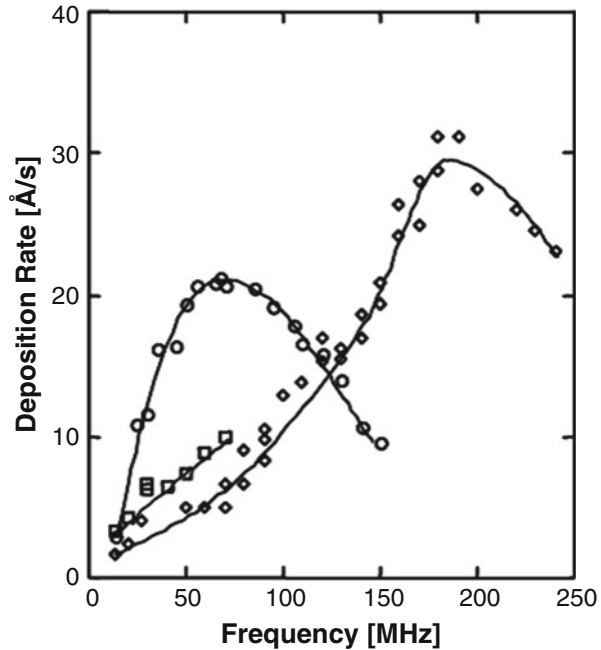
space charge, the capacitance of the dark sheath is proportion to the electrode area and inversely proportion to the dark sheath thickness, and the bias voltage inversely proportion to the capacitance. In reality, the measured self-bias deviates from the theoretical values because the assumptions are not 100% satisfied in a real RF glow discharge. However, it is a very useful number to monitor and control the plasma process such as a-Si:H depositions because any deviation from the designed process condition could cause a self-bias change such as chamber leakage, pressure and temperature change. It has been found that measuring the self-bias is one of the monitor and control methods in a-Si:H solar cell deposition.

RF-PECVD is the most commonly used technique in semiconductor and thin film silicon PV industries. Various large-scale production lines have been built around the world such as Applied Materials made the Sun-Fab production line to make thin silicon deposition on 5.7 m<sup>2</sup> glass substrate. United Solar made 180 MW annual capability using 30 MW large roll-to-roll production lines with six rolls of 2.5-km long stainless steel substrates simultaneously going through a nine-chamber system to deposit a-Si:H/a-SiGe:H/a-SiGe:H triple-junction flexible solar modules.

## Vhf PECVD

In the late 1980s, Shah's group in the University of Neuchatel pioneered to use VHF PECVD to deposit a-Si:H (Curtins et al. 1987a, b; Shah et al. 1992, 2003). In principle, VHF glow discharge is similar to the conventional RF glow discharge because the excitation frequency used in VHF PECVD is normally in the range from 40 MHz to 130 MHz and much lower than the plasma frequency. Nowadays, commonly used VHF frequency is between 40 MHz and 75 MHz. VHF PECVD have several advantages in a-Si:H deposition, especially in hydrogenated microcrystalline silicon ( $\mu\text{-Si:H}$ ), also called hydrogenated nanocrystalline silicon ( $\text{nc-Si:H}$ ), deposition. With the same excitation power density, VHF glow discharge has much higher plasma density than RF plasma, therefore VHF PECVD has been used in high rate a-Si:H deposition. The deposition rate is a very critical parameter for a-Si:H solar module fabrication because it determines the production efficiency and is inversely proportional to the manufacturing cost. Using a conventional RF PECVD, one can also increase the deposition rate by increasing the RF power, but the side effects are to degrade material quality and lower solar cell efficiency. First a high RF power increases the plasma potential, generates high energy ions to bombard the growth surface, increases defect density in the a-Si:H films, and reduces the solar cell efficiency. Second, a high RF power also generates high energy electrons that result in the generation of SiH<sub>2</sub> and SiH in the plasma, which associates to the incorporation of SiH<sub>2</sub> in the deposited a-Si:H films, consequently increases the light-induced metastability of a-Si:H materials, and increases the light-induced efficiency degradation in a-Si:H solar cells. Third, a high RF power often generates high density of large particles (dusts) in the plasma, which are not only incorporated in the a-Si:H films and form microvoids, but also increase the requirements for equipment maintenance, and thus increase the manufacturing cost. By

**Fig. 4** The deposition rate of a-Si:H versus excitation frequency in VHF PECVD deposition (Shah et al. 2003)



compromising the production efficiency and product quality, the deposition rate for a-Si:H solar panels using RF PECVD is usually selected at 0.2–0.3 nm/s.

Under the same excitation power density in PECVD, the deposition rate increases with the excitation frequency as shown in Fig. 4 (Shah et al. 2003), where the two sets of data were from two different groups with different VHF PECVD systems. One can see that for every system there is peak deposition rate. In the low frequency side, the deposition rate increases with the frequency significantly and reaches the maximum at the peak frequency, and then it decreases in the high frequency side. The increase of deposition rate with the excitation frequency in the lower frequency side is caused by the increased plasma density as the increase of excitation frequency; while the decrease of deposition at higher frequency side is caused by the inefficient power coupling to the chamber. It has been found that the VHF signal is much more difficult to be tuned into a plasma chamber. Over the years, the VHF tuning technology has been significantly improved. Therefore, one can reach a wider frequency range to tune VHF power into a deposition system and reach even high deposition rate at >100 MHz. Considering the deposition rate, material quality, large area uniformity, and the complexity of large area machines, the commonly used VHF frequency is in the range between 40 MHz and 75 MHz.

From physics and chemistry point of view, what are the major differences between VHF and RF excitations in PECVD deposition and why does the deposition rate increase with the excitation frequency? A high rate deposition implies that the flux intensity of growing species (neutral radicals and charge ions) reached onto the substrate is high, and correspondingly a high plasma density is built up with a high

excitation frequency. In addition, VHF PECVD not only shows a higher deposition rate, most importantly, but also it produces higher material quality and better device performance than RF PECVD. Experimental results showed that the initial and stable a-Si:H solar cell efficiencies did not depend on the deposition rate in VHF PECVD deposition for a wide range (Yue et al. 2007). As mentioned previously, the ion bombardment is one of the key issues of reducing the material quality and device performance at high rate RF PECVD deposition. Yan et al. studied the ion energy distribution in VHF and RF glow discharge. They found that under the same process condition, in a VHF glow discharge process the energy of ions reaching the substrate is much lower, but ion flux intensity is much higher than in a RF glow discharge (Yan et al. 1999). Figure 5 shows the ion energy distributions measured by a retarding technique, where (a) is the plot for 75 MHz and (b) for 13.56 MHz, with the horizontal axis for the voltage on the collection electrode, and the vertical axis for the derivative of current. The measurements were made with  $H_2$  gas and with 10 W VHF or RF power. From the results, one may make the following observations. Under the lower pressure of 0.1 torr, the VHF glow discharge has a very narrow distribution with a peak at 22 V, a full width at half maximum of 6 V, and a sharp edge at the high voltage side. While under 1.0 torr, the peak position moves to around zero voltage with a much broad peak distribution. Because the reference voltage is  $-40$  V on the grid sheath electrode ( $V_s$ ) the plotted ion energy reached to the negative region, the real ion energy is still positive even the X-axis points are negative. From Fig. 5b, it is noted that with the RF excitation, the peak energy is at 37 V and the width at half maximum is 18 V, both are much higher than the values in the VHF glow discharge under the same conditions. Another important observation was that the ion current density in the VHF glow discharge was about five times higher than in the RF glow discharge, which indicated that the plasma density is higher in the VHF plasma. Because the plasma density is the most important

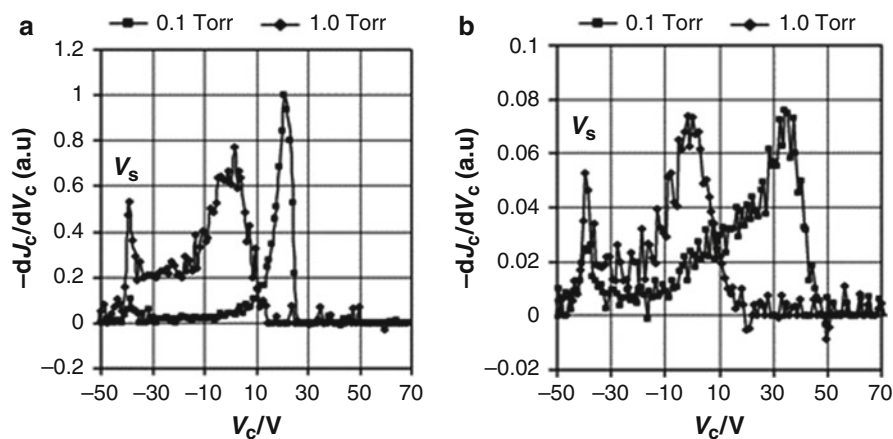


**Fig. 5** Ion energy distribution in (a) VHF (75 MHz) glow discharge and (b) RF (13.56 MHz) glow discharge under the same conditions (Yan et al. 1999)

parameter determining the deposition rate, the higher plasma density in the VHF glow discharge implies that the VHF PECVD gives a higher deposition rate than the RF PECVD under the same conditions, which is consistent with the experiment results. To summarize the results, two conclusions were made: (1) VHF glow discharge has lower ion energies and (2) a higher ion-flux intensity than the RF glow discharge. Such low energy ions with a high flux density ensure a low energy ion bombardment for high-quality a-Si:H films at high deposition rate. In addition, the large amount of low-energy ions on the surface enhance the diffusion length on the growing surface and help the growing species to find low-energy sites to form stable chemical bonds, thus high-quality a-Si:H films are deposited with VHF PECVD at high rates.

The key parameter to determine the ion energy is the potential difference between the plasma potential and the substrate potential, called sheath voltage. In most situations, the substrate is grounded, therefore, the plasma potential determines the energy of ion bombardment on the substrate surface. The plasma potential is proportional to the peak-to-peak voltage on the cathode ( $V_{pp}$ ), thus the  $V_{pp}$  on the cathode affects on the ion bombardment. An early study showed that under the given same condition, the  $V_{pp}$  dropped from 180 V at 13.56 MHz to 50 V at 70 MHz (Shah et al. 1992).

## Microwave PECVD

Microwave PECVD ( $\mu\text{w}$ -PECVD) is a well-developed technology in industrial application for high rate deposition. In crystalline Si solar module manufacturing, it has been used to make a-SiN:H passivation layer, also it is widely used in polycrystalline diamond deposition. In the 1990s, Energy Conversion Device, Inc. (ECD) used  $\mu\text{w}$ -PECVD for high rate deposition of a-Si:H and a-SiGe:H materials and devices (Guha et al. 1994), especially the devices with much thicker layers. In a  $\mu\text{w}$ -PECVD system, the microwave excitation power is introduced into the deposition chamber from a waveguide through an  $\text{Al}_2\text{O}_3$  ceramic window. Under a given pressure, the reactant gases absorb the microwave energy and are dissociated into neutral and charged species, and then form plasma for film deposition. The advantage of  $\mu\text{w}$ -PECVD is the high dissociation rate and therefore high deposition rate. Using  $\mu\text{w}$ -PECVD, Guha et al. (1994) deposited high-quality a-Si:H and a-SiGe:H at 10 nm/s and attained reasonable good solar cells. Because the deposition rate is high, the  $\mu\text{w}$ -PECVD deposited a-Si:H materials are not as good as RF PECVD deposited a-Si:H materials, and it has never been used in real mass solar panel fabrication.

In the recent years, as  $\mu\text{c}$ -Si:H has been widely used as the intrinsic layer of solar cells,  $\mu\text{w}$ -PECVD has been reinvestigated for high rate deposition of  $\mu\text{c}$ -Si:H. In ECD, Jonse et al. used an improved  $\mu\text{w}$ -PECVD with a gas jet structure and successfully made  $\mu\text{c}$ -Si:H solar cells (Jones et al. 2000). Later on Yan et al. of United Solar used a  $\mu\text{w}$ -PECVD system and made  $\mu\text{c}$ -Si:H solar cells at a high rate of 3–4 nm/s (Yan et al. 2003). AIST and other institutes in Japan developed an improved  $\mu\text{w}$ -PECVD system for high rate  $\mu\text{c}$ -Si:H solar cell deposition (Jia et al.



2006a, b; Shirai et al. 1999). Under an optimized condition, they achieved a high rate of 6.5 nm/s for  $\mu\text{-Si:H}$  deposition, and the materials showed a good quality with defect density of  $1\text{--}2 \times 10^{16}/\text{cm}^3$ . ECN Solar Energy in the Netherlands used a linear  $\mu\text{w-PECVD}$  system to deposit  $\mu\text{-Si:H}$  on a moving substrate and achieved very uniform large area depositions (Biebericher et al. 2004; Löffler et al. 2006).

## Hot Wire CVD

Hot wire CVD (HW-CVD) is another widely used method for a-Si:H and  $\mu\text{-Si:H}$  depositions and has been well studied in the literature (Doyle et al. 1988; Holt et al. 2002; Ishibashi 2001; Mahan 2001, 2003; Mahan et al. 2000, Matsumura 2001; Matsumura and Tachibana 1985). It uses hot filaments installed in a vacuum chamber to decompose the reactant gases, where the filaments are normally heated to 1800–2000°C while the substrate keeps at a low temperature between 150°C and 400°C. The hot filament acts as a catalytic for the chemical reaction, therefore this method is also called Cat-CVD; the low substrate temperature allows enough hydrogen incorporated into the films to passivate Si dangling bonds and improves the a-Si:H material quality. Because the reactant gases are disassociated by the high temperature of the hot filament and no electric field exists in the process, HW-CVD has the advantage of no ion bombardment, which is supposed to be important for high-quality a-Si:H materials, especially at high rate.

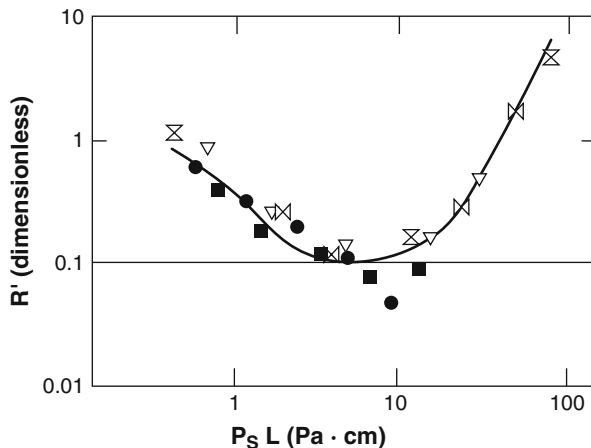
Compared to PECVD deposition where the main contribution for film growth is  $\text{SiH}_3$ , an early study showed that a-Si:H films are mainly deposited from atomic Si radicals in HW-CVD for the two reasons (Doyle et al. 1988). First, most  $\text{SiH}_4$  molecules are decomposed into atomic Si and atomic H when they reach the hot filament. Second, the deposition pressure is normally low such that the atomic Si radicals reach substrate for the film growth. Because the collisions between the decomposed radicals with  $\text{SiH}_4$  and other reactant gas molecules affect the film growth and quality, the process pressure is one of the most important parameters to determine the material quality. Doyle et al. (1988) found that the optimized pressure should be in the range between 4 mTorr and 30 mTorr.

In 1990s, NREL in the USA did a significant study on HW-CVD depositions for high-quality a-Si:H materials and solar cells (Mahan 2001, 2003). They optimized the filament and substrate temperatures and found that when the filament temperature is at 1900°C and the substrate temperature is at 360–390°C, high-quality a-Si:H materials could be made with very low hydrogen content of ~1 at.%, which is much lower than the 10–15 at.% in PECVD deposited a-Si:H. As expected, the lower hydrogen content improved the stability of the materials under prolonged light soaking. In PECVD deposition, if the substrate temperature is too high such as 360–390°C, the hydrogen content is also low, but the defect density would be high because no enough hydrogen terminate Si dangling bonds, while the NREL's study showed that the high substrate temperature HW-CVD deposited a-Si:H materials had a high quality with the photosensitivity above  $10^5$ . In order to improve the material quality further, Mahan studied the HW-CVD deposition mechanisms including the

dissociation of gas molecules on the wire surface, the space reaction of atomic Si and atomic H with molecules and other radicals, and surface reactions of impinging species (Mahan 2001, 2003). Especially, the space reaction is critical for high-quality a-Si:H deposition. As in PECVD deposition, they found that  $\text{SiH}_3$  and  $\text{Si}_2\text{H}_5$  are identified also as the main contributors for good quality a-Si:H deposition, therefore the space reaction of atomic Si and atomic H with other species are important for producing  $\text{SiH}_3$  and  $\text{Si}_2\text{H}_5$ . The parameter for determining the space reaction is the pressure ( $P$ ) and the distance ( $L$ ) from the filament to substrate since the probability of collision for radicals traveling from the filament to the substrates is proportional to the pressure and inversely proportional to the distance. Figure 6 plots the microstructure parameter  $R^*$  versus the product of pressure and distance ( $PL$ ), where the  $R^*$  is defined as the ratio of the integrals of the  $2090\text{ cm}^{-1}$  peak and  $2000\text{ cm}^{-1} + 2090\text{ cm}^{-1}$  peaks in infrared absorption spectra (will be discussed later), corresponding to the Si-H vibration mode and Si-H<sub>2</sub> vibration mode, respectively. The lower the  $R^*$ , the better the material quality and stability of a-Si:H are. From the plot, it is noted that an optimized condition should have the  $PL$  value at around 10 Pa.cm. This optimized  $PL$  value should be used as a guideline for HW-CVD system design. Because the heating from the hot filament to the substrate limits the distance  $L$ , therefore the  $P$  is also limited. Commonly the optimized distance  $L$  is in the range of 5–10 cm and the pressure  $P$  is in the range of 1–2 Pa.

HW-CVD also has three major issues: (1) metal contaminations from the filament, (2) lifetime of the filament, and (3) large area uniformity. It was found that HW-CVD-deposited a-Si:H films contain  $10^{18}$  at./cm<sup>3</sup> of metal impurity. Mahan et al. (2000) compared the films made with a new wire and an old wire and found that the metal content is lower in the a-Si:H made with the old wire than with the new wire. Therefore, they concluded that the evaporation of  $\text{WO}_2$  from the wire surface causes the metal contamination. They used a shutter in front of the substrate. First, prior the deposition, a preconditioning process was made by covering the substrate and heating the filament to a temperature higher than the designed temperature to

**Fig. 6** Infrared microstructure  $R^*$  versus the product of pressure  $P$  and distance  $L$  between the filament and substrate (Mahan 2003)

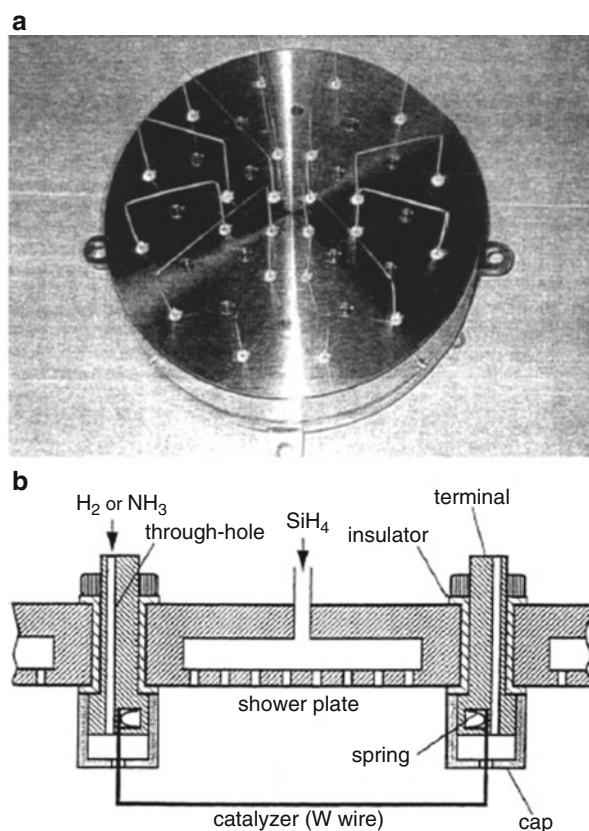


remove the  $\text{WO}_2$  layer on the filament, then opening the shutter for the deposition. SIMS analysis showed that the metal contamination from the filament was lower than the detected limitation of the SIMS system and had no influence on the a-Si:H property (Mahan et al. (2000)).

The second issue of HW-CVD is the breakage of the wire. During the heating process, especially when the wire temperature is not hot enough, metal silicide such as  $\text{W}_5\text{Si}_2$  forms on the surface of the filament and causes the breakage of the wire (Holt et al. 2002). Because the metal silicide easily forms at lower wire temperature than the process wire temperature, it forms mainly on the two terminal ends. A design with additional inert gas or  $\text{H}_2$  inlets at the wire ends reduced the metal silicide formation and increased the wire lifetime significantly.

The third issue of HW-CVD is the large area uniformity. This issue could be resolved by proper filament design and distribution. Figure 7 shows the wire distribution in a large area HW-CVD system (Ishibashi 2001; Matsumura 2001), where multiple short W wires reduce the bending and the springs at the terminals allow an easy replacement for the broken wires. Using this design, large area

**Fig. 7** (a) Wire distribution and (b) gas inlets in a large area HW-CVD system (Ishibashi 2001; Matsumura 2001)



(10 cm × 40 cm) uniform a-Si:H deposition was achieved at a deposition rate of 0.5 nm/s.

In the last 30 years, several institutes have made significant studies on HW-CVD depositions of a-Si:H and  $\mu\text{-Si:H}$  materials and solar cells. Because of no ion bombardment during the film growth, theoretically HW-CVD should have an advantage over PECVD; however, the a-Si:H solar cells made using HW-CVD have not been as good as those made with PECVD. In reality, the solar cell improvement is a systematic optimization process involving many other layers and steps such as the doped layers, the transparent conductive electrodes, and interfaces. HW-CVD just provides one of the methods for high-quality intrinsic layer deposition. Although HW-CVD has a long history in lab researches, it has not been widely used in industrial thin film Si PV module productions mainly because of the low cell efficiency and large area limitation. One interesting result is from the Jülich group. They used HW-CVD method to improve the interface properties in *p-i-n* structured  $\mu\text{-Si:H}$  solar cells and achieved a significant improvement in the cell performance (Mai et al. 2005). In the *p-i-n* structures, the intrinsic  $\mu\text{-Si:H}$  is normally deposited with very high hydrogen dilution and a high RF or VHF power to reduce the a-Si:H incubation layer. The high power deposition with high hydrogen dilution and high power could damage the *p* layer and cause additional defects at the *p/i* interface. A HW-CVD deposition after the *p* layer reduces the defect density at the *p/i* interface and improves the cell efficiency significantly.

---

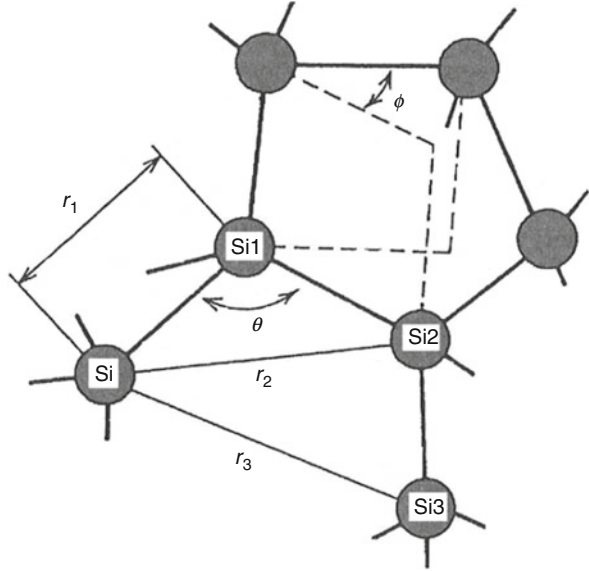
## Material Properties of Hydrogenated Amorphous Silicon and Alloy

Material properties directly affect the solar cell performance. A good material, especially the absorber layer, is the necessary condition, but not the sufficient condition for good solar cell. Therefore, the development and optimization of the material properties are the basic processes of thin film silicon solar cell optimization. Here we discuss the material properties of a-Si:H and its alloys from the solar cell performance perspective.

### Structure and Electronic States

Crystal silicon (c-Si) has a perfect tetrahedral diamond structure with  $sp^3$  covalence bond (short range order, SRD) and the Si atoms are in a perfect periodical crystal structure (long range order, LRD). However, although the most individual Si atoms in a-Si and a-Si:H are also in the tetrahedral diamond structure with  $sp^3$  covalence bond (SRD), they lose the perfect periodicity due to the distortions in the bond length and bond angle, which is called disorder. In addition, because of the imperfection in the structure, some chemical bonds are under strain and some become broken bonds. Figure 8 shows a structure model for a-Si, where five parameters are used to describe the structure disorders (Okamoto et al. 1999), namely, the bond length  $r_1$  to the near

**Fig. 8** Atomic structure model of a-Si, where the five parameters are used to describe the disorders (Okamoto et al. 1999)



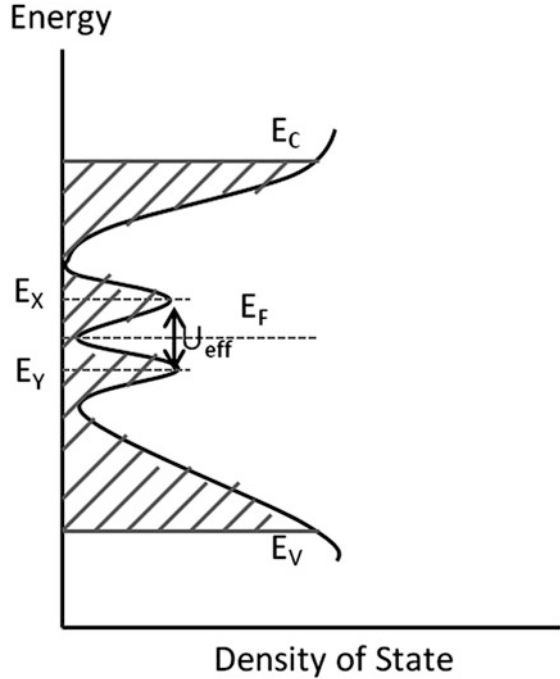
neighbor (Si-Si<sub>1</sub>), the bond angle  $\theta$ , the distance to the next neighbor (Si-Si<sub>2</sub>)  $r_2$ , the distance to the third near neighbor  $r_3$ , and the dihedral angle  $\phi$  formed by the plane determined by the chemical bonds of Si-Si<sub>1</sub> and Si<sub>1</sub>-Si<sub>2</sub>, and the plane determined by the chemical bonds of Si<sub>1</sub>-Si<sub>2</sub> and Si<sub>2</sub>-Si<sub>3</sub>. Actually, the  $\phi$  is described by another two planes in Fig. 8 for clarity. In c-Si, only six-member rings exist, but five-member and seven-member rings also form in a-Si and a-Si:H. The disorders can normally be measured by X-ray diffraction (XRD), where individual bright spots are observed for c-Si, rings for poly-Si, and two fuzzy belts for a-Si:H, indicating the SRD is only extended to the next neighbors.

The structure disorders have a significant impact on the electronic state. Based on the Anderson localization theory and the Mott-COF band structure model (Anderson 1958; Cohen et al. 1969; Mott 1966,1967), the distorted chemical bonds form localized state between the conduction band edge ( $E_C$ ) and valence band edge ( $E_V$ ) and show an exponential distribution towards the inside of the bandgap as shown in Fig. 9, which are called band-tail states and described by the following equations.

$$\begin{aligned} N_C(E) &= N_{C0} \exp\left(\frac{E - E_C}{kT_C}\right) \\ N_V(E) &= N_{V0} \exp\left(\frac{E_V - E}{kT_V}\right), \end{aligned} \quad (6)$$

where  $N_{C0}$  and  $N_{V0}$  are the density of states at the conduction band edge and valence band edge,  $T_C$  and  $T_V$  are the effective characteristic temperature of the conduction and valence band-tail states, respectively. The band-tail states directly affect the carrier transports because they are localized states, where carriers in these states

**Fig. 9** Mott-CFO model for band diagram in amorphous semiconductors



cannot move before being excited back to the extended states. Therefore, the band-tail states are considered as traps for carrier transport. In the middle of the bandgap, some deep level states result mainly from Si dangling bonds, the upper and the lower peaks represent the double-occupied (two electrons in the state) and the single-occupied (one electron in the state) states, respectively, and the difference is the correlation energy  $U_{eff}$  that is assumed to be positive in this figure. It has been a long debate, if the  $U_{eff}$  is positive or negative because two factors contribute to it (Adler 1981). First, when two electrons occupy one state, the Coulomb repulsive force adds an additional energy for the second electron to stay in the same state, which makes the  $U_{eff}$  positive; second, the double occupied electron states could also make a lattice relaxation and reduce the energy needed for the second electrons to occupy the state, and reduce the  $U_{eff}$ . Therefore, the overall effective  $U_{eff}$  could be positive and negative, depending on which factor is dominating. It has been proven that the  $U_{eff}$  is negative in chalcogenide glass. Although no agreement has been made on the long debate about positive or negative  $U_{eff}$  in a-Si and a-Si:H, most of the experimental results support the positive  $U_{eff}$  model. The sign of the  $U_{eff}$  has a significant impact on carrier transport in the materials and material stability as well. For a positive  $U_{eff}$  system, most of the defect states are occupied by one electron and keep the state electrically neutral ( $D^0$ ); while for a negative  $U_{eff}$  system, excess carriers (such as photo-generated electron-hole pairs) make the defect states double-occupied and zero-occupied. The double-occupied states are negatively charged ( $D^-$ ) and zero-occupied states are positively charged ( $D^+$ ). The charged states could be staying

for a much longer time even after the excitation source is turned off, which leads to some metastability phenomena such as persistent photocurrent and light-induced changes in the material property.

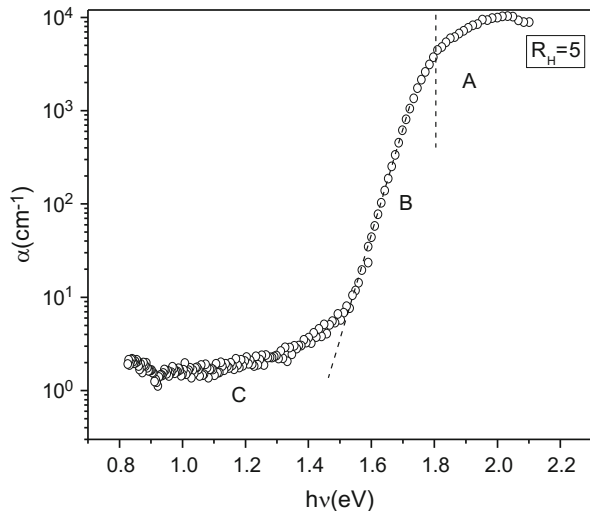
From an application point of view, these band structure parameters are very important for high efficiency solar cells. First, as the bandgap is defined by the difference between the conduction band edge  $E_C$  and valence band edge  $E_V$  ( $E_g = E_C - E_V$ ), the bandgap directly limits the long wavelength cut-off of solar cell spectral response. In a-Si:H, the incorporation of H not only reduces the density of dangling bond states, but also shifts the valence band edge downward and leads to a larger bandgap than in c-Si. The bandgap in a-Si:H is normally in the range between 1.65 eV and 1.85 eV, depending on the hydrogen content. It has been found that the  $E_g$  in a-Si:H has a linear relation with hydrogen content (Matsuda et al. 1981). The band-tail states are from the distorted or strained bonds, especially the stretched bonds. The incorporation of H also relaxes the strained bonds and reduces the band-tail states (Khomyakov et al. 2011). For good a-Si:H, the conduction band-tail width characterized by the  $kT_C$  is around 25 mV and the valence band-tail width  $kT_V$  of 50 mV, the deep defect density is in the order of  $10^{16} \text{ cm}^{-3}$ .

## Optical Property

### Absorption in the Solar Spectrum

As a solar cell material, the optical properties are important for cell efficiency. High absorption coefficients in the solar spectrum imply a high photocurrent density. Figure 10 shows an example of the absorption spectrum of a-Si:H material, where it can be divided into three regions. The region A is the absorption of photons with

**Fig. 10** An absorption coefficient spectrum of a device quality a-Si:H film made with hydrogen dilution ratio  $R_H = 5$  ( $\text{H}_2/\text{SiH}_4$ )



energy larger than the optical bandgap  $E_g$ , and the long wavelength limit of this region corresponds to the optical bandgap  $E_g$  of the material. For good a-Si:H,  $E_g$  is 1.7–1.8 eV, which is slightly smaller than the mobility bandgap. The absorption coefficient at the bandgap energy is in the order  $10^3$ – $10^4$   $\text{cm}^{-1}$ , and it increases by 1 to 2 orders or magnitudes to  $>10^5$   $\text{cm}^{-1}$  at around 550 nm (2.25 eV) of wavelength, which is much larger than the absorption coefficients of c-Si in the solar spectrum. Therefore, a-Si:H has been called quasi-direct bandgap material although the absorption coefficient follows the indirect formulation. In c-Si, the electron transition from the valence band to the conduction band needs not only to satisfy the energy conservation but also momentum conservation with the assistance from phonons. Therefore, c-Si has an indirect bandgap of 1.12 eV, above which the absorption coefficients are in the order of  $10^3$ – $10^4$   $\text{cm}^{-1}$ . When the photo energy is larger than the first direct bandgap of  $\sim 3.0$  eV, the absorption coefficients increase significantly, but the solar spectrum declines at the high energy region. For a-Si:H, the momentum is no longer a good quantum number; and the electron transition is only governed by the energy conservation but not the quasi-momentum conservation, therefore, the absorption coefficients are much higher in a-Si:H than in c-Si in the main solar spectrum. In this range, the absorption coefficient  $\alpha$  and the optical bandgap  $E_g$  follow the Tauc plots (Tauc 1974),

$$(\alpha h\nu)^{1/2} = B(h\nu - E_g), \quad (7)$$

where  $h\nu$  is photon energy,  $B$  is a constant related to the band-tail states. Eq. (7) is the standard indirect bandgap Tauc plot, but it is derived only based on the shape of the band state structure in the conduction band and the valence band, where parabolic conduction and valence band shape was used (Cody 1984). Experimentally, the optical bandgap can be obtained by measuring the optical absorption coefficients with the fitting to the Tauc plot.

Region B corresponds to the band-tail absorptions, where the absorption coefficient is in the range of  $1 < \alpha < 10^3$   $\text{cm}^{-1}$  and decreases exponentially with photo energy,

$$\alpha = \alpha_0 \exp\left(\frac{h\nu}{E_{t0}}\right), \quad (8)$$

where  $\alpha_0$  is a prefactor, and  $E_{t0}$  is a constant describing the decay of the absorption coefficient with photo energy. The exponential decay results from the exponential shape of the band-tail distribution as described by Eq. (6). It was first observed by Urbach in 1953 (Urbach 1953), therefore,  $E_{t0}$  is called Urbach energy or Urbach tail. The transitions in this region include those from the valence band tail to the conduction band and from the valence band to the conduction band tail. Because the valence band-tail distribution is much wider than the conduction band-tail distribution, the measured Urbach tail normally reflects the valence band-tail distribution.

Region C is called sub-bandgap absorption, where the absorption coefficient is in the order of  $1$   $\text{cm}^{-1}$  and  $10$   $\text{cm}^{-1}$  and is less sensitive to the photoenergy in the range



between 0.8 eV and 1.2 eV. The absorption in this region corresponds to the transition from the valence band to the defect band in the middle of the bandgap; the higher the absorption coefficient in this region, the higher the defect density is. Therefore, the sub-bandgap absorption coefficients have been widely used to measure the defect density.

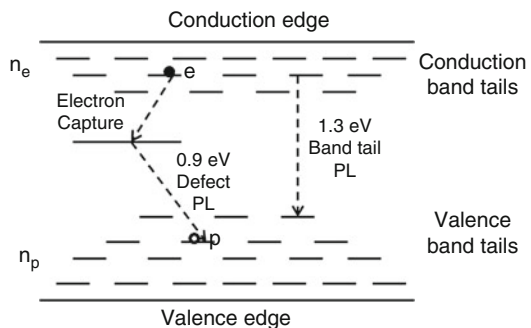
The measurement of optical absorption can be made by the transmission and reflection (T-R) method using an optical spectroscopy in the UV-visible range, where the absorption coefficients are high. However, for the low absorption region (IR), the T-R method is not sensitive enough to measure the absorption coefficients. Advanced methods such as constant photocurrent method (CPM) and photothermal deflection spectroscopy (PDS) have been used to measure the absorption coefficients from the band-tail absorption and sub-bandgap absorption regions. The details of CPM and PDS measurements can be found in Fritzsche et al. (1984) and Jackson and Amer (1981).

### Photoluminescence (PL)

The photoexcited carriers in a a-Si:H film recombine to release the energy. The recombination goes through various radiative and nonradiative channels. The radiative recombination releases energy by emitting photons, which is called photoluminescence (PL) (Han et al. 1996; Han and Wang 2003; Street 1981). By measuring the PL spectra, one can study the defect structure in the materials. The PL experiments for a-Si:H can be using an Ar-ion laser or any light source with photoenergy larger than the bandgap. Because of the thermal quenching, the PL is normally measured at low temperature such as liquid N<sub>2</sub> (77 K). For a good intrinsic a-Si:H film, the PL spectrum has a peak at 1.3–1.4 eV with the half width of 0.3 eV; while for defective or doped a-Si:H, a second peak is also observed at 0.8–0.9 eV with a low intensity of ~1% of the first peak.

The PL process from a-Si:H is a competition of radiative and nonradiative recombination processes. Figure 11 shows the possible recombination channels, where the 1.3–1.4 eV peak corresponds to the radiative recombination of trapped electrons in the conduction band tails and the trapped holes in the valence band tails; while the low energy PL at 0.8–0.9 eV corresponds to two process: electrons are first trapped to the deep defect states and then recombine with trapped holes in the

**Fig. 11** Photocarrier recombination processes in a-Si:H for PL



valence band tails. For a-Si:H with nanostructured c-Si grains embedded, one may observe some blue shift of the band-tail PL. Some researchers believe that it is due to the quantum confinements, but it could be also because of the widening of a-Si:H bandgap resulted from a high hydrogen content. For high defective a-Si:H, two low energy PL peaks were also observed, which could be an evidence of two kinds of defect states (Han et al. 1996).

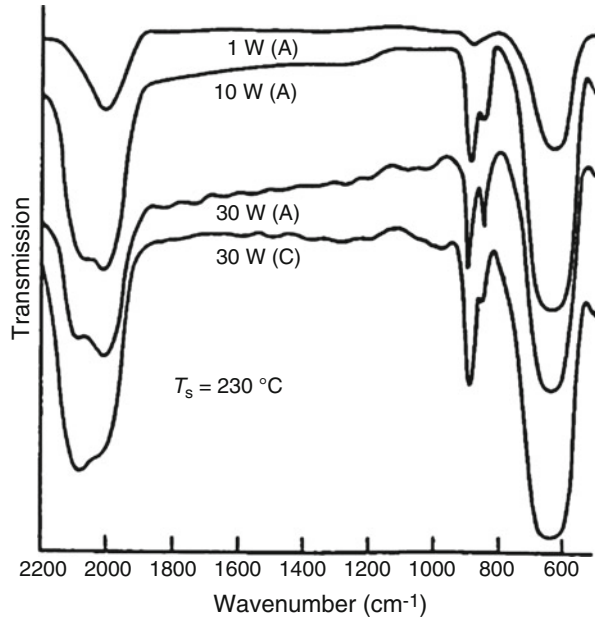
In PL measurement, one may change the excitation frequency and monitor the PL intensity as a function of the excitation energy, which is called PL excitation (PLE) spectra. PLE reflects the absorption in the material. It has been observed that the PLE peak energy is about 0.4–0.5 eV higher than the PL peak energy. This difference is called Stokes shift, caused by the association of phonons during the electron transitions. The half of the Stokes shift (0.2–0.25 eV) corresponds to the lattice relaxation energy during the recombination process, which reflects some degrees of c-Si indirect bandgap characteristics.

### Infrared Absorption

Hydrogen incorporation into a-Si:H reduces the internal stress and passivates Si dangling bonds and therefore plays a significant role in improving the material quality. Most of Si atoms are bonded to four Si atoms in the tetrahedral structure. For some Si atoms, one chemical bond could be terminated by a H atom, and forms a Si-H bond and some others could bond to two or three H atoms and form Si-H<sub>2</sub> and Si-H<sub>3</sub>. It was found that the Si-H configuration most likely appears in dense areas, while Si-H<sub>2</sub> and Si-H<sub>3</sub> in the internal surface of microvoids in a-Si:H materials. Therefore, to measure the H configuration is an effective method to study a-Si:H property and quality. Infrared (IR) absorption is a widely used technique to measure the H configurations, which detects the IR absorption intensities by different Si-H vibration modes. Since the IR absorption measurement is commonly done using a Fourier Transform Infrared Spectroscopy, it is normally called FTIR measurements.

The Si-H vibrations in a-Si:H have two kinds of modes: the relative motion of the Si-H atoms along the bond length called *stretching mode* and the rotation motion of Si-H along different axes called *bending, rocking, and wagging*. The Si-H<sub>2</sub> and Si-H<sub>3</sub> also have the *stretching mode*, and the rotation modes of *bending, rocking, and wagging*; they also have an additional mode called *scissoring* and *twisting* (Zanzucchi 1984). The different vibration modes with different phonon energies are reflected at different wave numbers in IR absorption spectra of a-Si:H (Zanzucchi 1984; Joannopoulos and Lucovsky 1984). The Si-H stretching mode is at 2000 cm<sup>-1</sup>, and rotation mode at 640 cm<sup>-1</sup>; although the *bending/rocking* modes for Si-H<sub>2</sub> and Si-H<sub>3</sub> are also at 640 cm<sup>-1</sup>, their *stretching modes* are at 2090 cm<sup>-1</sup> and 2140 cm<sup>-1</sup>, respectively. In addition the *stretching* modes for clusters and chain structures of (SiH)<sub>n</sub> and (SiH<sub>2</sub>)<sub>n</sub> are also at around 2100 cm<sup>-1</sup>, therefore, those modes are difficult to be separated experimentally. In addition, the SiH<sub>2</sub> and SiH<sub>3</sub> *scissoring/twisting* modes are at 830 cm<sup>-1</sup> and 920 cm<sup>-1</sup>. Figure 12 shows topical IR absorption spectrum of a PECVD deposited a-Si:H, where high-quality materials deposited with low RF power show the stretching modes mainly at 2000 cm<sup>-1</sup>, while the high power samples have an additional large component at 2090 cm<sup>-1</sup>.

**Fig. 12** IR absorption spectra of a-Si:H films made with different RF powers



Because all of the *bending/rocking/waging* modes are at  $640\text{ cm}^{-1}$ , the absorption coefficient at this wave number is proportional to the total bonded hydrogen (not including molecule hydrogen  $\text{H}_2$ ) atoms. Therefore, the total bonded hydrogen content can be obtained by

$$C_H = A_{640} \int \frac{\alpha(\omega)}{\omega} d\omega, \quad (9)$$

where  $\alpha$  is the absorption coefficient,  $\omega$  the wave-number, and  $A_{640}$  is a constant calibrated by nuclear reaction or secondary ion mass spectroscopy (SIMS). The commonly used  $A_{640}$  is  $(2.1 \pm 0.2) \times 10^{19}\text{ cm}^{-2}$  and it needs to be corrected for multiple reflections for thin samples with a factor of  $1/(1.72 - 0.0011\omega d)$  (Langford et al. 1992), where  $d$  is the sample thickness.

The *stretching* band at  $2000\text{--}2100\text{ cm}^{-1}$  mainly contains two peaks at  $2000\text{ cm}^{-1}$  and  $2090\text{ cm}^{-1}$  for the Si-H and Si-H<sub>2</sub> + Si-H<sub>3</sub> stretching modes, respectively. Because high-quality a-Si:H has a high percentage of Si-H and a very little Si-H<sub>2</sub> and Si-H<sub>3</sub>, a parameter called microstructure factor  $R^*$  is defined to measure the quality of a-Si:H,

$$R^* = \frac{I_{2090}}{I_{2000} + I_{2090}}, \quad (10)$$

where  $I_{2090}$  and  $I_{2000}$  are the integrals of the  $2090\text{ cm}^{-1}$  and  $2000\text{ cm}^{-1}$  components, respectively. For high-quality a-Si:H materials,  $R^*$  is  $\sim 0.1$ , while for poor a-Si:H,

such as deposited with a high power or at room temperature,  $R^*$  could be  $>0.8$ . Overall, IR absorption measurement is an important characterization technique and it can give rich information about hydrogen content and hydrogen bonding configurations. IR absorption spectroscopy can also detect the impurities in a-Si:H such as O, N, and O.

## Raman Spectroscopy

Raman scattering is an inelastic scattering of photons with phonons in materials (Lannint 1984, Zhang et al. 2002). For a-Si:H study, visible or near infrared light is used as the excitation source. From Raman spectra, the structural properties of a-Si:H can be obtained. The first order Raman signals from a-Si:H are mainly in the wave number range  $100\text{--}600\text{ cm}^{-1}$ , in the far infrared region. In the study of material structure properties, Raman and IR are complementary to each other.

In c-Si, the conservation of crystal momentum limits the Raman scattering to only a narrow TO mode at  $\sim 520\text{ cm}^{-1}$  with a width at half maximum of  $\sim 3\text{ cm}^{-1}$ . While in a-Si:H, because the disorder relaxes the conservation of momentum, the TO mode broadens and shifts to  $480\text{ cm}^{-1}$  and the other three Raman modes are excited and observed as well, where the LO mode is at  $410\text{ cm}^{-1}$ , LA mode at  $310\text{ cm}^{-1}$ , and TA mode at  $170\text{ cm}^{-1}$ . Figure 13 shows a typical Raman spectrum of a-Si:H with different vibration bands as indicated, where the sample was considered a device quality a-Si:H made at  $200\text{ }^\circ\text{C}$  with a hydrogen dilution ratio for intrinsic layer in a-Si:H solar cells.

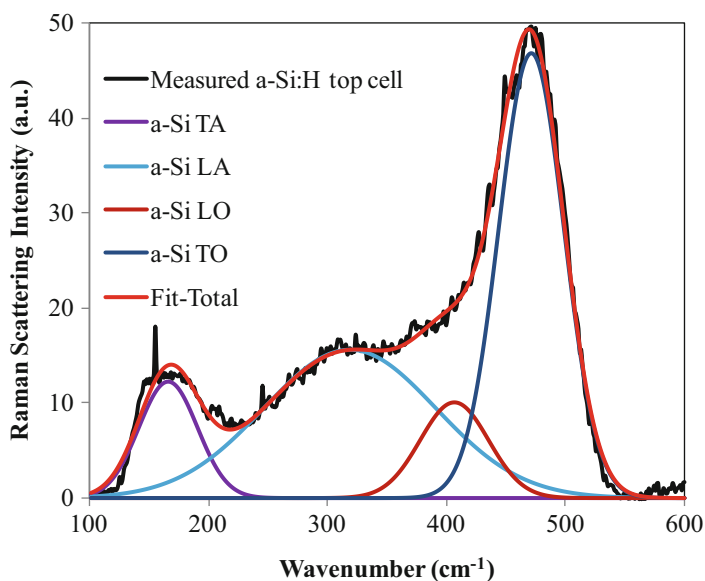


**Fig. 13** A typical Raman spectrum of a device quality a-Si:H film used in high efficiency a-Si:H solar cells. The four fitting curves corresponding to different vibration modes are plotted

As discussed above, the momentum conservation is the main reason for the large difference in the Raman spectra of a-Si:H and c-Si, where in c-Si, only the TO phonons with crystal momentum  $Q$  near zero can participate in Raman scattering. These phonons have an energy of 64 mV and therefore result in the TO Raman scattering at  $520\text{ cm}^{-1}$ . In a-Si:H, the TO mode shifts to the lower energy side at  $480\text{ cm}^{-1}$  and the bandwidth becomes much broader; also the other scattering modes appear. Logically, the bandwidth of the TO mode can be used as a measure of the ordering in a-Si:H, especially the short range order; also the ratio of the TA/TO modes is related to the ordering in the materials. Experimentally, it was observed that both the TO bandwidth  $\Delta\omega$  and the intensity ratio of TA/TO decreases with the increase of deposition temperature, suggesting the short range order improvement with the increase of substrate temperature. From the change of bandwidth  $\Delta\omega$ , the change of bond angle  $\Delta\theta$  from the perfect c-Si can be calculated and it is founded that the bond angle distortion is  $\sim 7^\circ$ , slightly smaller than 10% estimated by other methods. It was also found that the TA mode is a characteristic of inter-medium range order in a-Si:H. With the increase of hydrogen dilution, the intensity of the TA mode decreases, indicating an inter-medium range order increase (Fortner and Lannin 1989). When hydrogen dilution is high enough, nano- and microcrystallites form and nc-Si:H and  $\mu\text{c-Si:H}$  are deposited. The Raman spectra changes dramatically with the appearance of the sharp c-Si peak at  $510\text{--}520\text{ cm}^{-1}$  when the transition happens, therefore Raman spectroscopy is widely used in the study of nc-Si:H and  $\mu\text{c-Si:H}$  materials as discussed in the next chapter.

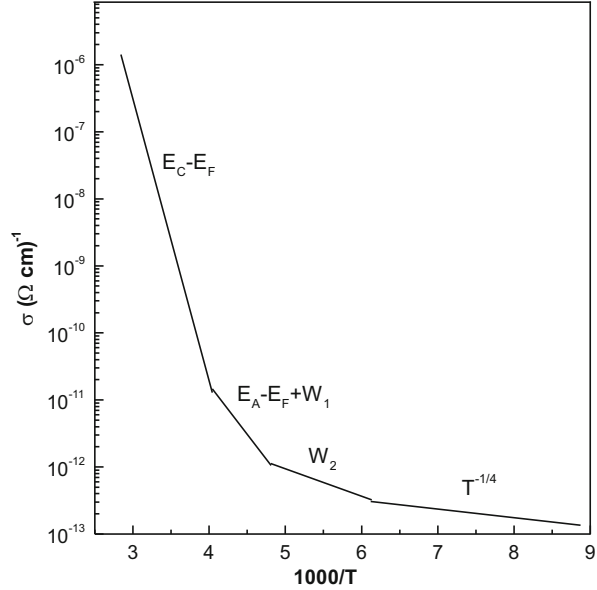
## Electrical Property

As mentioned previously, device quality intrinsic a-Si:H materials made by PECVD contain 10–15 at.% H. They have an optical bandgap of 1.7–1.8 eV, conduction activation energy of 0.8–0.9 eV, and conduction and valence band-tail widths of 25 mV and 50 mV, respectively. They also contain a deep state density of  $10^{15}\text{--}10^{16}\text{ cm}^{-3}$  depending on the deposition condition. At room temperature, the dark conductivity is in the order of  $10^{-10}\text{ (}\Omega\text{cm)}^{-1}$ , AM1.5 photoconductivity of  $10^{-5}\text{ (}\Omega\text{cm)}^{-1}$ , and photosensitivity of  $10^5\text{--}10^6$ . Below we discuss the conductive mechanisms in a-Si:H materials.

### Dark Conductivity in Intrinsic a-Si:H

The transport property is determined by the carrier mobility and carrier concentration. In undoped a-Si:H, the material shows a weak N-type conduction, electron drift mobility of  $\sim 1\text{ cm}^2/\text{Vs}$ , and hole drift mobility of  $\sim 0.01\text{ cm}^2/\text{Vs}$  (Schiff 2004), therefore, the dark conductivity of a-Si:H is dominated by electron transport. Many material characteristics can be studied by the temperature dependence of dark conductivity, which is divided into four regions as shown in Fig. 14 (Mott and Davis 1979). At room temperature and above, the dark conductivity  $\sigma_d$  is mainly

**Fig. 14** Dark conductive  $\sigma_d$  versus temperature  $1000/T$  for a-Si:H (Mott and Davis 1979)



contributed from the free electrons thermally excited to the conduction band and its temperature  $T$  dependence is given by

$$\sigma_d = \sigma_0 \exp\left(-\frac{E_C - E_F}{kT}\right), \tag{11}$$

where  $\sigma_0$  is a pre-factor,  $E_C$  is the conduction band edge,  $E_F$  the Fermi level, and  $k$  the Boltzmann constant. By measuring the temperature dependence of dark conductive, the activation energy of  $E_a = E_C - E_F$  can be calculated from the slope of  $\ln(\sigma_d) - 1/T$  plot. The  $\sigma_0$  is determined by the electron mobility  $\mu_e$  and the effective density of state at the conduction band edge  $N_C$  with  $\sigma_0 = q\mu_e N_C$ . The measured  $E_a$  and  $\sigma_0$  has a relation called Meyer-Neldel rule, which should be used for the correction of the measured  $E_a$ .

The second region is hopping conductivity following

$$\sigma_d = \sigma_1 \exp\left(-\frac{E_A - E_F + W_1}{kT}\right), \tag{12}$$

where  $E_A$  is the characteristic energy of conduction band and  $W_1$  the hopping activation energy in the conduction band tail, which decreases with the decrease of temperature,  $\sigma_1$  is another pre-factor, which is much smaller than  $\sigma_0$ .

The third region is hopping in the states near the Fermi level if the density of state at the Fermi level is not zero. At very low temperature, electrons cannot be excited to high energy levels, the hopping in low energy states near the Fermi level can still provide some conduction, which is described by

$$\sigma_d = \sigma_2 \exp\left(-\frac{W_2}{kT}\right), \quad (13)$$

where  $\sigma_2$  ( $\sigma_2 < \sigma_1$ ) and  $W_2$  are the pre-factor and activation energy, respectively, in this temperature region.

At very low temperature, the transport is through variable range hopping. Electrons have the tendency to go over the nearby sites and search the sites with the similar energy. In this very low temperature, the conductivity follows

$$\sigma_d = \sigma_3 \exp\left(-\frac{B}{T^{1/4}}\right), \quad (14)$$

where  $B$  is a constant with the value of  $B = 1.66(\alpha^3/kN(E_F))^{1/4}$ ,  $\alpha$  is the lattice constant, and  $N(E_F)$  the density of state at the Fermi level.

For solar cell application, one of the most important properties is the transport characteristic in the extended states above the conduction band edge  $E_C$  and below the valence band edge  $E_V$  because solar cells are mainly used at the ambient or high temperatures. In this temperature range, the band-tail states play a role for trapping carriers: (1) excess carriers transport in the extended states, (2) are trapped in the band-tail states, (3) are thermally excited to the extended states for transport, (4) and are trapped again. This process is called *multiple trapping*. The higher the density of the tail states, the more the trapping processes happen. The *multiple trapping* processes reduce the carrier drift mobility  $\mu_D$  significantly by

$$\mu_D = D \frac{n_0}{n_0 + n_T} \mu_0, \quad (15)$$

where  $\mu_0$  is the carrier mobility in the extended states,  $n_0$  and  $n_T$  are the free carrier and trapped densities, respectively. Because of the *multiple trapping* process, the drift mobility in a-Si:H is much lower than in c-Si. The electron drift mobility is normally in the order of  $1 \text{ cm}^2/\text{Vs}$  and hole drift mobility is only in the order of  $10^{-2} \text{ cm}^2/\text{Vs}$  (Schiff 2004). The much smaller hole drift mobility than electron drift mobility partially results from the much wider valence band tails than the conduction band tails. The *multiple trapping* processes also cause dispersion in the transport, especially for hole transport. The drift mobility is normally measured by time-of-flight technique. A carrier sheet generated by a blue laser near one side of a sandwiched a-Si:H *p-i-n* structure moves towards the opposite side under an electric field and produces a transient photocurrent. Ideally, when the carrier sheet reaches the opposite side, the current vanishes. The time for the carriers to travel through the sample (*i*-layer thickness) is called transient time  $t_T$  and inversely proportional to the carrier drift mobility. In reality, the transient photocurrent decreases with time due to the multiple trapping even before  $t_T$ , and decreases much fast after the  $t_T$ . Figure 15 shows electron TOF transient

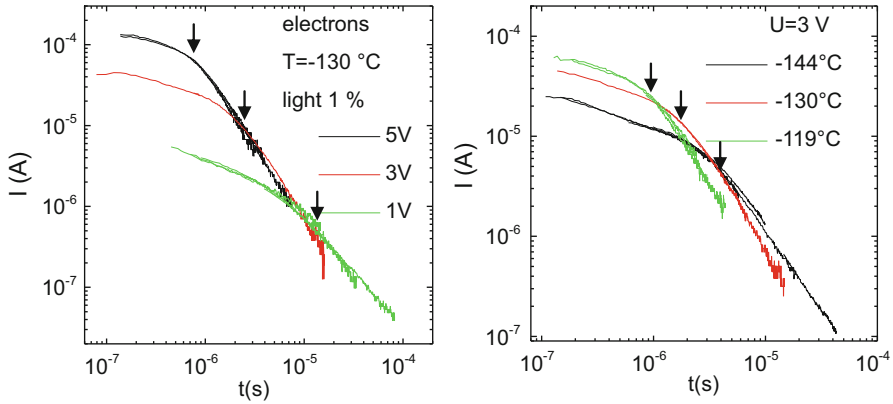
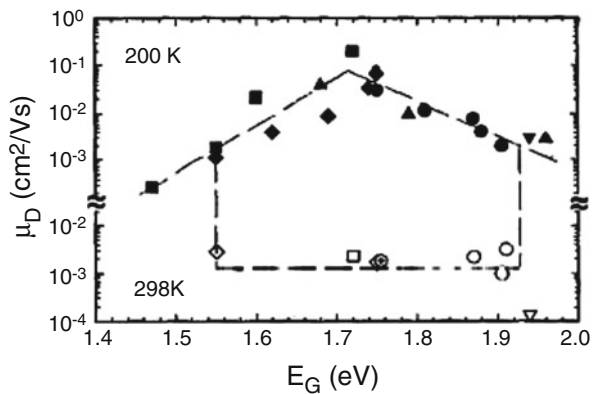


**Fig. 15** TOF transient photocurrent spectra of a 5- $\mu\text{m}$  thick a-Si:H *p-i-n* structure for electron transport. The left plot: three transient photocurrent curves measured at  $-130^\circ\text{C}$  under different bias, and the right plot: three transient photocurrent curves measured at different temperatures under 3 V reverse bias

**Fig. 16** The electron (solid) and hole drift mobility as a function of the bandgap in a-SiC:H, a-Si:H, and a-SiGe:H alloy (Gu et al. 1994)



photocurrent spectra from a 5- $\mu\text{m}$  thick a-Si:H *p-i-n* structure measured (a) at  $-130^\circ\text{C}$  with different reverse bias voltages and (b) measured at different temperatures with 3 V of reverse bias. One can see that the transient time  $t_T$  indicated by the arrows increases with the decrease of applied bias voltage and measurement temperature. Using TOF technique, Gu et al. (1994) systematically studied the carrier drift mobility in various a-Si:H, a-SiC:H, and a-SiGe:H alloy materials. They found that the electron mobility decreases with the incorporation with either C for wide bandgap or Ge for narrow bandgap; but the hole drift mobility does not change at all with the composition changes as shown in Fig. 16, where the drift mobility is plotted as a function of bandgap varied by the



incorporation of C and Ge, for the wide bandgap and narrow bandgap, respectively.

### Photoconductivity in Intrinsic a-Si:H

Under an illumination, the conductivity increases for most semiconductors and is also observed in intrinsic a-Si:H. The increased conductivity by the illumination is called photoconductivity ( $\sigma_{ph}$ ). For a-Si:H, under the standard AM1.5 illumination ( $100 \text{ W/cm}^2$  at  $25^\circ\text{C}$ ), the photoconductivity is  $>10^{-5} (\Omega\text{cm})^{-1}$ , and the photosensitivity is in the order of  $10^5\text{--}10^6$ . The photocarriers are mainly excited by the transition from the extended valance band to the extended conduction band as well as from the valence band tail to the extended conduction band and from the extended valence band to the conduction band tails. The photocarrier density is determined by the generation rate  $G$ , carrier mobility  $\mu$ , and the lifetime  $\tau$  of the carriers, which is directly related to the recombination through the deep level states called recombination centers. Because the hole drift mobility is much smaller than the electron drift mobility, the photoconductivity is dominated by electron transport. Therefore, the photoconductivity is related to the electronic states in the bandgap: the tail states affecting the mobility and the deep states reducing the lifetime. And it can be measured experimentally by the photocurrent through a a-Si:H film on glass substrate with two parallel metal electrodes and calculated by

$$\sigma_{ph} = q\eta\mu\tau F(1 - R)(1 - \exp(-\alpha d)), \quad (16)$$

where  $q$  is the elementary charge,  $\eta$  the quantum yield,  $\mu\tau$  the mobility-lifetime product of electrons,  $F$  the photo flux on the sample surface,  $R$  the reflectance,  $\alpha$  the absorption coefficient, and  $d$  the film thickness. In the high absorption region with  $\alpha d \gg 1$ , Eq. (16) becomes,

$$\sigma_{ph}(H) = e\eta\mu\tau F(H)(1 - R). \quad (17)$$

While in the low absorption region with  $\alpha d \ll 1$ , Eq. (16) becomes,

$$\sigma_{ph} = e\eta\mu\tau F(1 - R)\alpha d. \quad (18)$$

In case  $R$  and  $\eta\mu\tau$  are independent of photon energy  $h\nu$ , the photocurrent is proportional to the absorption coefficient  $\alpha$  with,

$$\alpha(h\nu) \propto \frac{\sigma_{ph}(h\nu)}{F(h\nu)}. \quad (19)$$

Because  $\eta\mu\tau$  depends on the recombination, hence on the split of quasi-Fermi levels, Eq. (19) is valid under the small signal condition, under which the quasi-Fermi level split is very small, or under the same quasi-Fermi level split condition that corresponds to the same photocurrent density. In reality, by measuring the conductivity under the same photocurrent as a function of photon flux, the

absorption coefficients can be measured accurately in the low absorption region. This is the fundamental of CMP measurement (Fritzsche et al. 1984).

### Conductivity of Doped a-Si:H

The advantage of a-Si:H over unhydrogenated a-Si is the hydrogen passivation of Si dangling bonds, which reduces the defect states and makes the material be able to be doped into N-type and P-type by incorporation of V-column and III-column doping elements, respectively. In PECVD deposition, the commonly used N-type doping gas is  $\text{PH}_3$ ; while *p*-type doping gas can be  $\text{B}_2\text{H}_6$ ,  $\text{BF}_3$  or  $\text{B}(\text{CH}_3)_3$  (TMB). The doping ratio such as  $\text{PH}_3/\text{SiH}_4$  and  $\text{B}_2\text{H}_6/\text{SiH}_4$  is in the order of 1% in the application of solar cells, which could make the conductivity changes in a few orders of magnitudes. At the same time, the Fermi level can move to the conduction band tails for N-type doping and valence band tails for P-type doping. Correspondingly, the conductivity  $\sigma_d$  increases to  $\sim 10^{-2} (\Omega\text{cm})^{-1}$  and activation energy  $E_a$  decreases to  $\sim 0.2$  eV for N-type doping and the  $\sigma_d$  increases to  $\sim 10^{-4}$ – $10^{-3} (\Omega\text{cm})^{-1}$  and activation energy  $E_a$  decreases to  $\sim 0.3$ – $0.4$  eV for P-type doping.

Because of the disorder, band tails, and defect states, the doping efficiency is low in a-Si:H. The disorder leads to atoms not necessarily be in the topological limitation, P and B can be in 4-coordination substitution sites and can also be in 3-coordination sites. In addition, the 3-coordination sites have lower energy than the 4-coordination sites, therefore most of dopants are in the 3-coordinated states with their energy levels in the band tails and do not contribute to doping. Only a small portion of the dopants forms shallow donors and shallow acceptors (Stutzmann and Street 1985). The doping also results in additional defect formation because the formation of Si dangling bonds reduces the total energy. Furthermore, most of donor electrons and acceptor holes are trapped in the tail states and defect states, which reduce the doping efficiency. The doping-associated defect generation increases with the increase of doping level. It was found that the doping efficiency follows (Street 1991)

$$\eta_{\text{doping}} = \frac{P_{\text{active}}}{P_{\text{total}}} = C \frac{1}{\sqrt{P_{\text{total}}}}, \quad (20)$$

where  $P_{\text{active}}$  is the active dopant concentration,  $P_{\text{total}}$  the total dopant concentration, and  $C$  a constant. Because doped a-Si:H materials have a much higher defect density than intrinsic a-Si:H, causing a high recombination rate in doped materials, doped a-Si:H can only be used as the contact layers to form the built-in potential but cannot be used as the main absorber layer in solar cells. Therefore, a-Si:H solar cells are normally designed to be *p-i-n* or *n-i-p* structures, where the *p*, *i*, *n* are the *p*-layer, intrinsic-layer, and *n*-layer, respectively. The *i*-layer is the main light absorber layer to harvest the sun light to generate electron-hole pairs, and the built-in electric field formed by the *n* and *p* layer to collect the photo-generated electron-hole pairs. In addition, the doping-associated defect generation and carrier trapping limit the Fermi level shift in the tail states, the Fermi level difference in the *n*-layer, and *p*-layer determines the upper limit of the built-in potential in a-Si:H solar cells. In order to

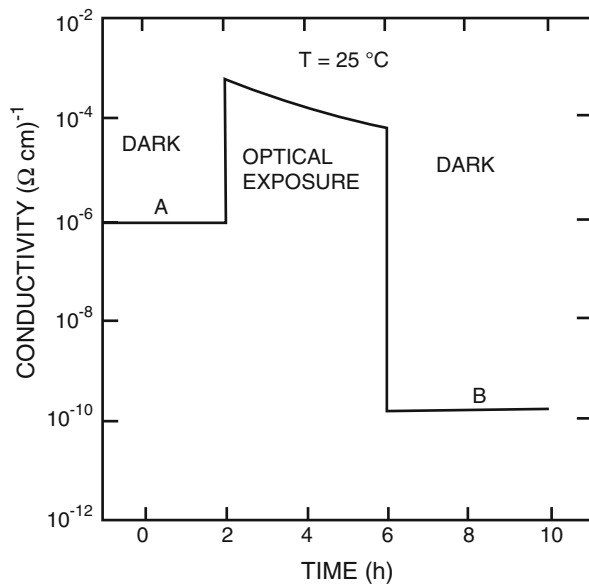
improve the built-in potential, doped  $\mu\text{c-Si:H}$  and  $\text{nc-Si:H}$  have been used for increasing the open circuit voltage ( $V_{\text{oc}}$ ). Furthermore, B doping reduces the bandgap of  $\text{a-Si:H}$ , increases the absorption in the  $p$ -layer, and hence reduces the short circuit current ( $J_{\text{sc}}$ ). To minimize the absorption in the doped layers, wide bandgap doped hydrogenated amorphous and nanocrystalline silicon alloys such as  $\text{a-SiC}_x\text{:H}$ ,  $\text{a-SiO}_x\text{:H}$ ,  $\text{nc-SiC}_x\text{:H}$ , and  $\text{nc-SiO}_x\text{:H}$  have been used, which not only improve the  $V_{\text{oc}}$  by enlarging the built-in potential and but also increase the  $J_{\text{sc}}$  by reducing the absorption in the doped layer.

### Metastability of a-Si:H: Staebler-Wronski Effect

In 1977, Staebler and Wronski observed a light-induced metastable phenomenon in PECVD deposited  $\text{a-Si:H}$  films (Staebler and Wronski 1977): the photoconductivities and dark conductivities decrease with the illumination time and reach to another steady state after a prolonged light soaking. The light-induced degradation of conductivities can be recovered back to their original values after thermal annealing at  $>150^\circ\text{C}$  for 1–3 hours. This effect is called Staebler-Wronski effect, or S-W effect. Figure 17 shows the changes of conductivity as a function of light soaking time.

The Staebler-Wronski effect is an intrinsic bulk effect of  $\text{a-Si:H}$  and alloys, which is not caused by the surface band bending or impurity incorporation. Electron spin resonance (ESR) (Su and Taylor 2003) and other defect measurements showed that light soaking causes the creation of metastable defects, in which the Si dangling bond density could increase from  $\sim 10^{16} \text{ cm}^{-3}$  to  $10^{17} \text{ cm}^{-3}$ . The photo-generated metastable defects have an energy level near the middle of the bandgap and act as

**Fig. 17** Light-induced conductivity changes as a function of light soaking time (Staebler and Wronski 1977)



recombination centers, which reduce a-Si:H solar cell efficiency. Except for the reduction of conductivity, there are other material property changes such as Fermi level shifting towards the middle of the bandgap, the reduction of carrier lifetime, the reduction of diffusion length, the main PL intensity decrease, defect-related PL increase, etc. Several models have been proposed to explore the mechanism of the Staebler-Wronski effect as discussed below.

### **Si-Si Weak-Bond Breaking Model (Stutzmann et al. 1984)**

It is well known that a-Si:H contains a high density of weak Si-Si bonds in the order of  $10^{18}$ – $10^{19}$   $\text{cm}^{-3}$ . Under an illumination, the weak bonds could be broken and form two Si dangling bonds for each broken weak bond, but the two dangling bonds are close to each other and easily recombine to form a Si-Si bond again. Therefore, they are not stable. However, a-Si:H contains  $\sim 10$ – $15\%$  at. H, and many Si-Si weak bonds are close to Si-H bonds; when one Si-Si weak bond is broken by photon energy to form two Si dangling bonds, the nearby H of the Si-H could flip over to form Si-H bond and leave a new Si dangling bond separately from the other originally generated Si dangling bond. Therefore, the weak-bond breaking model includes two steps: the weak-bond breaking and the H movement.

### **Charge Transfer Model (Adler 1981)**

As previously motioned, when a Si dangling bond is occupied by two electrons (double occupation), additional energy is needed, which is called effective correlation energy  $U_{eff}$ . For a-Si:H, most experiments support a positive  $U_{eff}$ , and therefore neutral dangling  $D^0$  bonds are the major defects in a-Si:H. However, Alder (1981) believed that because of the disorder, in a-Si:H the lattices could be relaxed when an additional electron is trapped in the dangling bonds and causes an effective low energy, which could result in a negative  $U_{eff}$ . In this case, the stable Si dangling bonds would be in zero-occupied  $D^+$  and double-occupied  $D^-$  states. Under illumination, photo-generated electrons could be trapped into  $D^+$  and holes into  $D^-$ , and then convert them into  $D^0$ , increase the ESR detected  $D^0$  density, and reduce the dark conductivity and photoconductivity.

### **Hydrogen Collision Model (Branz 1998, 2003)**

In 1998, Branz proposed a new model called hydrogen collision model to explain the Staebler-Wronski effect (Branz 1998, 2003). He proposed that the nonradiative recombination of photo-generated electrons and holes releases the energy to break Si-H bonds, and generates a Si dangling bond and a mobile H atom. When the moving H meets a Si-Si weak bond, it may break the Si-Si weak bond, and form a new Si-H bond and a Si dangling bond. However, when the H moves away the two dangling bonds could recombine to get back into their initial state. In this case, it looks like a mobile H moves in the network. The moving H has two consequences. First, a mobile H meets another Si dangling bond and forms a new Si-H bond, and in this case, no new Si dangling is generated. Second, a mobile H meets another mobile H and forms a metastable state  $(\text{Si-H})_2$ , and leaves a Si dangling bond at the original location. Most of the mobile H atoms end up in the first state with no new defect

generation, but some others end up with second metastable state and produce a new defect. Therefore, the net effect of illumination is the generation of a Si dangling bond and a metastable (Si-H)<sub>2</sub> complex.

The weak-bond breaking model and charge transfer model only consider the local chemical bond changes during an illumination. While the H collision model suggests that the light-induced defect generation not only involves the change of local chemical bonds, but also the long range H transport, therefore the metastability depends on the H content, the degree of disorders, and the microvoids in a-Si:H materials.

### Light-Induced Structure Change in a-Si:H

Light-induced changes in a-Si:H causes not only microscopic structure changes such as defect generation, which results in the electric and optical property change, but also other macroscopic property changes such as the structure. The structure changes are so large that the individual microscopic defect generation cannot explain them; instead the whole amorphous network must be changed during light soaking. The light-induced degradation is definitely related to the energy released during the electron and hole recombination. If one recombination could release about 1.3 eV of energy and transfer this energy into the local amorphous network such as 10 atoms, it could cause a large local temperature rising, result in the deviation from the initial state, and then transfer the energy to far distance. In the case, many physical property changes can only be explained with light-induced structure changes. For example, (1) nuclear magnetic resonance (NMR) measurements found that the dipole relaxation time is related to a large range bonded H atom (Hari et al. 1994); (2) X-ray photoemission spectroscopy (XPS) found that illumination leads to a 0.1 eV red shift in the Si 2P emission peak (Masson et al. 1995); (3) it was found that the 1/f noise spectrum changes from a non-Gaussian distribution to a Gaussian distribution, indicating a massive structure change (Fan and Kakalios 1994); (4) FTIR measurements observed an 1.3% increase of the vibration strength of Si-H stretching mode (2000 cm<sup>-1</sup>), which could result from light-induced Si-H vibration strength increase and the Si-H concentration increase (Zhao et al. 1995); (5) it was also found that light soaking induced a large change in the ratio of isotropic and anisotropic polarization absorption, implying a light-induced bond angle change that is related to a long range disorder (Hata et al. 1997); (6) it was observed that the low frequency dielectric constant showed an eversible light-induced change (Yue et al. 1998); and (7) the volume of a-Si:H material showed an eversible explanation during and after light soaking (Kong et al. 1997). All of these experiments suggest that the light-induced degradation in a-Si:H not only results in metastable Si dangling bond generation, but also causes the amorphous network changes. The defect generation is the consequence of amorphous network change (Shimizu et al. 1998).

## Amorphous Silicon Alloy

The bandgap of a-Si:H is 1.70–1.85 eV, depending on the hydrogen content. Although it covers the large portion of the solar spectrum for wavelength up to ~700 nm, but it still cannot absorb the longer wavelength light. Also for the short wavelength light, the part of photo energy larger than the bandgap is lost by thermal relaxation. In order to achieve a high efficiency, multijunction solar cells with different bandgaps are preferred. By alloying a-Si:H with other elements such as C, Ge, O, and N, the bandgap can be adjusted to desired values. For example, a-SiC<sub>x</sub>:H and a-SiO<sub>x</sub>:H have a larger bandgap, while a-SiGe<sub>x</sub>:H has a lower bandgap than a-Si:H, which are suitable for the absorber layers in multijunction solar cells. However, the wide bandgap a-SiC<sub>x</sub>:H and a-SiO<sub>x</sub>:H alloys normally have a high defect density and hardly can be used as the absorber layers for high efficiency solar cells; they are used as the window *p* layer in a-Si:H solar cells, while a-SiGe:H has been widely used as the intrinsic absorber layer in the middle and bottom cell of multijunction solar cells (Yang et al. 1997).

### A-SiC<sub>x</sub>:H Alloy

In the early 1980s, Tawada et al. made a-SiC<sub>x</sub>:H by PECVD using a SiH<sub>4</sub> and CH<sub>4</sub> mixture and doped with B<sub>2</sub>H<sub>6</sub> to make *p*-type a-SiC<sub>x</sub>:H as the *p*-layer of a-Si:H *p-i-n* solar cells, which improved the V<sub>oc</sub>, J<sub>sc</sub>, and efficiency (Tawada et al. 1982). B incorporation in a-Si:H not only forms dangling sites, but also forms alloy to reduce the *p*-layer bandgap, alloying C into B doped a-Si:H to form *P*-type a-SiC<sub>x</sub>:H compensates the bandgap narrowing by B. The bandgap of a-SiC<sub>x</sub>:H is proportional to C/Si ratio. A good a-SiC<sub>x</sub>:H *p*-layer normally contains ~15% of C and has an optical bandgap of ~2 eV.

Using B<sub>2</sub>H<sub>6</sub> as the doping gas is easy to form B cluster and reduces the transparency of the *p*-layer. Nowadays, the commonly used *p*-type doping gas is B (CH<sub>3</sub>)<sub>3</sub> or BF<sub>3</sub>. In addition, the a-SiC<sub>x</sub>:H *p* layer has a larger bandgap than a-Si:H intrinsic layer, an intrinsic a-SiC<sub>x</sub>:H buffer layer with grading C content is used to smooth the bandgap offset (Komuro et al. 1984).

Internal photo-emission measurements found that the conduction band edge moves up in a-SiC<sub>x</sub>:H, while its valence band edge does not change much, which means that the bandgap offset at a-SiC<sub>x</sub>:H/a-Si:H interface is mainly at the conduction band, which blocks electron back diffusion at the *p*-a-SiC<sub>x</sub>:H/*i*-a-Si:H interface and does not affect the hole transport. Therefore, *p*-a-SiC<sub>x</sub>:H is an ideal *p* layer for a-Si:H solar cells, but it is not suitable for *n* layer, because the conduction bandgap offset blocks the electron transport from the *i*-a-Si:H into *n*-a-SiC<sub>x</sub>:H.

In order to improve a-Si:H solar cell performance, *p*-type nc-SiC<sub>x</sub>:H and μc-SiC<sub>x</sub>:H have been well studied. They have a higher dark conductivity than *p*-type a-SiC<sub>x</sub>:H. By increasing the H dilution, one can change a-SiC<sub>x</sub>:H into μc-SiC<sub>x</sub>:H and increase the conductivity to 10<sup>-3</sup>–10<sup>-2</sup> (Ωcm)<sup>-1</sup> (Demichelis et al. 1992; Hou et al. 2015), which improves V<sub>oc</sub> of a-Si:H solar cells further.

## A-SiGe:H Alloy

a-SiGe:H is a narrow bandgap material used as the absorber layers in the middle and bottom cells of a-Si:H/a-SiGe:H double-junction and a-Si:H/a-SiGe:H/a-SiGe:H triple-junction solar cells, which is made by mixing GeH<sub>4</sub> into SiH<sub>4</sub> and H<sub>2</sub> in the reactant gases of PECVD process.

In the late 1970s, Chevallier et al. (1977) deposited a-SiGe:H alloy using RF PECVD and adjusted the bandgap in the range between 1.7 eV and 1.0 eV. However, for solar cell application, the bandgap is normally in the range of 1.5 eV and 1.65 eV, depending on the design of solar cells. Because the Ge-Ge and Ge-H bonds are much weaker than the Si-Si and Si-H bonds, the defect density increases dramatically with the increase of Ge content in the films, especially for the bandgap <1.5 eV. In addition, the structure nonuniformity in a-SiGe:H also leads to high defect density in a-SiGe:H with high Ge content (Cohen 2003; Paul 1988). The defects in a-SiGe:H is mainly Ge dangling bonds because hydrogen does not passivate Ge dangling bonds effectively (Cohen 2003), and the electron drift mobility is decreased significantly with the increase of Ge content (Bauer et al. 1989; Gu et al. 1994; Schiff 2003).

Because GeH<sub>3</sub> is heavier than SiH<sub>3</sub> radicals and the diffusion coefficient of GeH<sub>3</sub> on the growth surface is much lower than SiH<sub>3</sub>, the optimized deposition temperature for a-SiGe:H should be higher than a-Si:H, especially at high deposition rate. It is normally in the range of 230–300°C (Lundszien et al. 1997). An effective way to improve a-SiGe:H quality is high hydrogen dilution. It was found that the best a-Si:H materials are made under the hydrogen dilution just before the transition from amorphous phase to microcrystalline phase (Guha et al. 2003). However, the transition from a-SiGe:H to μc-SiGe:H requires a higher hydrogen dilution than the a-Si:H to μc-Si:H transition, and therefore an optimized a-SiGe:H also needs a much higher hydrogen dilution than an optimized a-Si:H. With a high hydrogen dilution, the substrate temperature could be lowered for high-quality a-SiGe:H deposition, which is important for *p-i-n* structured a-Si:H/a-SiGe:H multijunction solar cells on TCO-coated glass substrates since the a-Si:H top cell is deposited at a lower temperature first. The side effect of high hydrogen dilution is to reduce the deposition rate. The deposition rate could be increased by increasing the RF power in RF-PECVD deposition, but the high ion bombardment results in a poor quality. Yang et al. (2001) found that using VHF-PECVD can increase the deposition rate of a-SiGe:H without significant material quality degradation.

Another issue of a-SiGe:H deposition with PECVD is the difference of decomposition rates of SiH<sub>4</sub> and GeH<sub>4</sub> (Liao et al. 2005). The decomposition rate of GeH<sub>4</sub> is about 3–5 times higher than SiH<sub>4</sub>, which makes it difficult to control the Ge/Si ratio precisely and uniformly in a-SiGe:H; while Si<sub>2</sub>H<sub>6</sub> and GeH<sub>4</sub> have the similar decomposition rates, and therefore Si<sub>2</sub>H<sub>6</sub> + GeH<sub>4</sub> mixture was used for the champion a-SiGe:H solar cell depositions. However, Si<sub>2</sub>H<sub>6</sub> is much more expensive than SiH<sub>4</sub> and is not cost-effective in mass production for solar panels, where SiH<sub>4</sub> + GeH<sub>4</sub> mixture has been used.

Nowadays, a-SiGe:H has been widely used in multijunction solar cells. For the high efficiency a-Si:H/a-SiGe:H/a-SiGe:H triple-junction solar cells (Yang et al.

2003), the intrinsic a-SiGe:H layer in middle cell was made with Ge content of ~15% and with a bandgap of ~1.65 eV, while the a-SiGe:H in the bottom cell was made with Ge content of ~20–25% and with a bandgap of ~1.55 eV. In addition, other material parameters should be optimized to have an Urbach band-tail energy <60 mV, dark and photoconductivities in the order of  $1 \times 10^{-8} (\Omega\text{cm})^{-1}$  and  $1 \times 10^{-5} (\Omega\text{cm})^{-1}$ , respectively, and activation energy of ~0.7 eV.

---

## A-Si:H Alloy Solar Cells

Because of the material properties of a-Si:H and its alloy as discussed above are very different from c-Si, a-Si:H solar cells should be designed with different device structures by considering the unique material properties, such as high absorption coefficient, low mobility-lifetime product, and light-induced metastability. The advantage of high absorption coefficient allows using a thin absorber layer, but the low mobility-lifetime product and the metastability limits the absorber layer thickness, hence the photocurrent density. In addition, the high defect density in the doped layers results in that the normal *p-n* junction structure used in c-Si solar cell does not work for a-Si:H solar cells; instead *p-i-n* or *n-i-p* structures are used. In addition, for increasing the cell efficiency and reducing the light-induced degradation, multijunction solar cells are used in both research and development as well as PV module production. Below we present various a-Si:H based solar cells and discuss their advantages and issues.

## Principle of a-Si:H Single-Junction Solar Cell

Crystalline solar cells are normally made with *p-n* junctions, where *p* and *n* are N-type and P-type semiconductors, respectively. The carrier diffusion length is longer enough such that photo-generated carriers can diffuse into the junction region and are separated by the narrow built-in electric field. However, the carrier mobility and life in a-Si:H alloys are much lower than in c-Si, consequently the photo-generated carrier diffusion length is too short such that they are recombined before reaching the junction region in a *p-n* junction structure. To resolve this issue, *p-i-n* structures have been used for a-Si:H solar cells, where *p* layer and *n* layer are very thin, which only function to form the built-in potential, *i* represents a relatively thick intrinsic layer, where the sun light is mainly absorbed in this region. As shown in Fig. 18 (Deng and Schiff 2003), in the dark or near dark condition, the three *p*, *i*, and *n* layers have the same Fermi level when they connect with each other to form a solar cell. The difference of the dark Fermi levels in the *p* and *n* layers when they are individual creates a built-in potential  $V_b$  and results in an electric field across the *i* layer. When the cell is illuminated, the photo-generated electron-hole pairs in the *i*-layer are separated by the built-in electric field and move towards the opposite directions: electrons to the *n* layer and holes to the *p* layer. In the open circuit



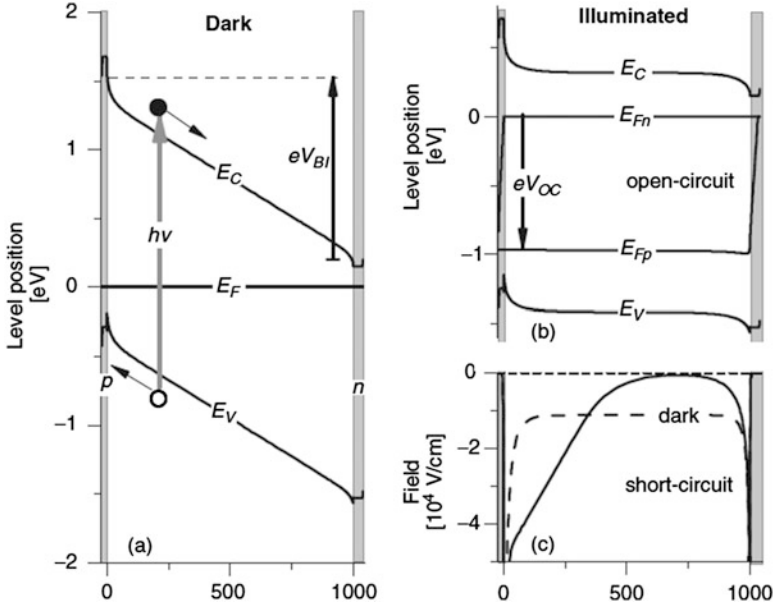


**Fig. 18** Band diagram of a-Si:H solar cell, (a) in the short circuit and near dark condition, (b) under illumination and open circuit condition (Deng and Schiff 2003)

condition, the photo-generated electrons are accumulated in the  $n$  layer and the photo-generated holes in the  $p$  layer, which results in an electric field with the opposite direction with the built-in electric field to reduce the photocarriers accumulation further, and finally it reaches a steady state condition with no net current flow. In this condition, the photo-generated voltage is the open circuit voltage ( $V_{oc}$ ), one of the important parameters determining solar cell efficiency. When the solar cell is in the short circuit condition that the two terminals are connected directly without any load, most of the photo-generated carriers are swiped by the built-in electric field and collected by the  $p$  layer and  $n$  layer to form photocurrent. The photocurrent density obtained in this case is the short current density ( $J_{sc}$ ), another important parameter that determines the solar cell efficiency. When a load is connected to the two terminals of the solar cell, the photocurrent density is normally smaller than the  $J_{sc}$ , and the voltage is smaller than the  $V_{oc}$ . The output power density of the solar cell is the product of the voltage and the current density ( $P=V \times J$ ). The output power depends on the load. Scanning the load (or varying the bias voltage), the output reaches a maximum, which is called the maximum power density ( $P_{max}$ ), and the corresponding voltage and current density are called maximum power voltage ( $V_{max}$ ) and maximum power current density ( $J_{max}$ ). The solar cell efficiency is defined as the ratio of the maximum power density and input light intensity.

$$Eff = \frac{P_{Max}}{P_{Light}} = \frac{V_{max} \times J_{max}}{P_{Light}} = \frac{J_{sc} \times V_{oc} \times FF}{P_{Light}}, \quad (21)$$

where  $FF$  is the fill factor defined by the ratio of

$$FF = \frac{P_{\max}}{J_{sc} \times V_{oc}} = \frac{J_{\max} \times V_{\max}}{J_{sc} \times V_{oc}}. \quad (22)$$

It is clear that the solar cell efficiency is determined by the three factors of  $J_{sc}$ ,  $V_{oc}$ , and  $FF$ . Their values are affected by many material properties and device structures. First, the bandgap of the intrinsic layer determines the  $V_{oc}$  and  $J_{sc}$ . A wide bandgap of the  $i$  layer allows a wide quasi-Fermi level split and hence a high  $V_{oc}$ , but low  $J_{sc}$  because of low absorption for the long wavelength photons, therefore an optimized bandgap for the  $i$  layer is very important for a-Si:H alloy solar cells, especially for multijunction solar cells. In practical a-Si:H alloy solar cells, a-SiC<sub>x</sub>:H and a-SiO<sub>x</sub>:H could be used as the wide bandgap  $i$ -layer for high  $V_{oc}$  top cell and a-SiGe:H as the narrow bandgap  $i$ -layer for high current density in multijunction solar cells. Second, the  $V_{oc}$  is also limited by the built-in potential, and therefore determined by Fermi level difference of the  $p$  and  $n$  layers. Optimized doped layers such as P-type and N-type a-SiC<sub>x</sub>:H, a-SiO<sub>x</sub>:H, nc-SiC<sub>x</sub>:H, and nc-SiO<sub>x</sub>:H are widely used in high efficiency solar cells. Third, the band tails in the  $i$ -layer and the deep level defects also strongly affect the cell efficiency. A wide band-tail state distribution limits the quasi-Fermi level split and therefore limits the  $V_{oc}$ ; it also reduces the carrier drift mobility, hence reduces the  $FF$ . A high defect density leads to a high recombination rate and reduces all three parameters of  $J_{sc}$ ,  $V_{oc}$ , and  $FF$ . Furthermore, the device design such as the thickness of each layer, the interface between the doped layer and the  $i$ -layer also have a significant impact on a-Si:H solar cell performance.

Another important feature of a-Si:H alloy solar cells is the sequence of the layer structure. Because the hole mobility-lifetime product  $(\mu\tau)_h$  is much lower than electron  $(\mu\tau)_e$ , holes have a smaller collection length than electrons. As a consequence, a-Si:H alloy solar cells are normally designed to have the light illumination from the  $p$  side such that the generation of electron-hole pairs is much more in the region near the  $p$ -layer than near the  $n$ -layer, where the majority of holes travel a shorter distance to reach the  $p$ -layer than electrons to the  $n$ -layer. In this way, the solar cell has a high efficiency than the light illumination from the  $n$ -layer. Based on this design principle and the substrate type, a-Si:H alloy solar cells is divided into  $p$ - $i$ - $n$  and  $n$ - $i$ - $p$  structures.

### A-Si:H Alloy $p$ - $i$ - $n$ Single-Junction Solar Cell

As shown in Fig. 19a, a-Si:H alloy  $p$ - $i$ - $n$  single-junction solar cells are deposited on transparent substrates such that the light passes through the substrate to illuminate the solar cell through the  $p$ -layer, thus the substrate is also called “superstrate” in this configuration. The superstrate is normally a glass or transparent polymer with a transparent conductive oxide (TCO) coating, which has two functions of allowing

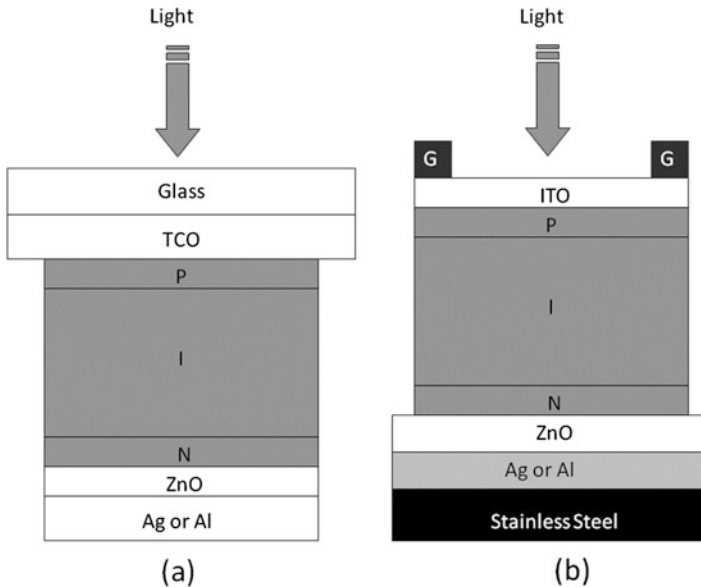


**Fig. 19** a-Si:H single-junction solar cell structure, (a) *p-i-n* structure on TCO/glass substrate and (b) *n-i-p* on ZnO/Ag/SS substrate

light to pass through and providing the electric contact for current collection. Commonly used TCOs are Al doped ZnO (AZO), B doped ZnO (BZO), Ga doped ZnO (GZO), F doped SnO<sub>2</sub>, (FTO), and ITO. The a-Si:H layers are deposited in the sequence of *p*, *i*, *n* on the TCO-coated glass, then another TCO layer is deposited on the *n*-layer following with a metal electrode for photo-electron collection. The *p* layer uses B doped a-SiC:H and a-SiO<sub>x</sub>:H for wide bandgap to reduce the absorption in the *p*-layer, and further uses nc-SiC<sub>x</sub>:H, nc-SiO<sub>x</sub>:H, and nc-Si:H for high conductivity to reduce the electric loss. Because the light first goes through it, the *p*-layer is also called the “window” layer. A wide bandgap *p*-layer not only improves the  $V_{oc}$ , but also the  $J_{sc}$ , hence the efficiency. Because the *P*-type window layer normally has a wider bandgap than the *i* layer, a buffer layer with an intermediate bandgap or a bandgap grading is inserted between the *p* and *i* layers, which reduces the bandgap discontinuity and reduces the interface defect density. A proper buffer layer can effectively improve the  $FF$  and hence the efficiency. The *i*-layer could be undoped a-Si:H, a-SiC<sub>x</sub>:H, a-SiO<sub>x</sub>:H, and a-SiGe:H. The wide bandgap a-SiC<sub>x</sub>:H and a-SiO<sub>x</sub>:H are used as the top cell in multijunction solar cells, while the narrow bandgap a-SiGe:H is used for the middle and bottom cells in multijunction solar cells. However, the undoped a-SiC<sub>x</sub>:H and a-SiO<sub>x</sub>:H have much higher defect density than a-Si:H, they are not commonly used in real multijunction solar panel production except for some research activities. The *n*-layer normally uses nc-Si:H and nc-SiO<sub>x</sub>:H to improve the doping efficiency for high  $V_{oc}$  and to reduce the electric loss for improving  $FF$ . The back TCO has three functions: (1) reducing the plasmonic absorption losses at the Si/metal interface, (2) adding additional texture

for light scattering, and (3) blocking the metal ion diffusion into the a-Si:H layer. Finally, a metal back contact is deposited on the TCO, which provides the electrode for photoelectron collection and reflects the light back to the *i*-layer for improving the  $J_{sc}$ , therefore the back TCO/metal contact is called back reflector. Commonly used back metal contacts are Ag, Al, or Ag/Al bilayers. Ag has a much better reflectivity than Al, but it is more expensive for solar module production.

### A-Si:H Alloy *n-i-p* Single-Junction Solar Cell

Contrast to the *p-i-n* structure, another type of a-Si:H solar cell is *n-i-p* solar cell as shown in Fig. 19b, which is normally deposited on nontransparent substrates such as stainless steel (SS) and polyimide such as Kapton. The solar cell structure consists a back reflector, *n, i, p* a-Si:H layers, a top TCO, and a metal grid. Light illuminates the solar cell on the *p* side through the top TCO and generates a high density of electron-hole pairs near the *p* region to minimize the disadvantage of smaller  $(\mu\tau)_h$  holes than electron's  $(\mu\tau)_e$ . The commonly used back reflectors are Ag/ZnO, Al/ZnO, and Al/Ag/ZnO. On the back reflector, the a-Si:H layers are deposited in the order of *n, i, and p* layers. The top TCO layer is deposited on the *p*-layer to collect photo-generated holes. The top TCO is high conductive ITO, which needs to have two functions: (1) providing the electric contact and (2) adding antireflection effect to reduce the reflection loss. A quarter wavelength ( $\lambda/4n$ ) of the solar spectrum peak at 550 nm is selected for the ITO thickness, which is designed at 70–80 nm. Because the top TCO is very thin, conventional AZO and BZO does not have the high conductivity for collecting the current efficiently. Even with ITO, top metal grids are needed to collect the photocurrent and reduce the series resistance.

Compared with *p-i-n* solar cells, *n-i-p* solar cells have the following characteristics. First, the a-Si:H deposition starts from *n*-layer on the back reflector. Because the normally used Ag/ZnO back reflector is relatively stable in H plasma, a wide range for *n*-layer deposition conditions is allowed, especially for using nc-Si:H and nc-SiO<sub>x</sub>:H *n*-layer, which not only has high conductivity for reducing the resistance loss, but also provides a seeding layer for  $\mu$ c-Si:H growth for  $\mu$ c-Si:H solar cells. Furthermore, the *p*-layer is directly deposited on the *i*-layer, which is much easier to form nc-Si:H, nc-SiO<sub>x</sub>:H, and nc-SiCx:H than on a foreign substrate such as TCO. The shortcomings of *n-i-p* solar cells include that (1) the metal grids on the thin ITO top contact reduce some areas for light illumination; (2) no additional textures are formed by ITO and thus the light trapping solely relies on the back reflector, which requires a high-quality back reflector for an effective light trapping.

### A-SiGe:H Alloy Single-Junction Solar Cell

a-Si:H has a bandgap of  $\sim 1.75$  eV, corresponding to an absorption edge at  $\sim 700$  nm. It does not absorb enough red lights to produce a high photocurrent density. One

**Table 1** Solar cell performance parameters of a-Si:H top cell, a-SiGe:H middle cell, and a-SiGe:H bottom cell used in a-Si:H/a-SiGe:H/a-SiGe:H triple-junction structures (Yang et al. 2003)

Cell type	State	$J_{sc}$ (mA/cm <sup>2</sup> )	$V_{oc}$ (V)	FF	$P_{max}$ (mW/cm <sup>2</sup> )
a-Si:H Top	Initial	9.03	1.024	0.773	7.15
	Stable	8.76	0.990	0.711	6.17
a-SiGe:H Middle	Initial	10.29	0.754	0.679	5.27
	Stable	9.72	0.772	0.600	4.21
a-SiGe:H Bottom	Initial	12.2	0.631	0.671	5.17
	Stable	11.1	0.609	0.622	4.21

might be able to tune the bandgap a little bit by a high substrate temperature and/or low hydrogen dilution, but the change for the bandgap is very limited and it could cause other negative effects such as a high defect density. In order to absorb the red light efficiently, a narrow bandgap absorber layer is needed. Among the choices, a-SiGe:H is the primary candidate, because Ge is next to Si in the periodic table and can form the same crystalline structure as Si when it is alloyed with Si. The bandgap of a-SiGe:H can be varied in a wide range by changing the Ge/Si ratio to satisfy the requirement for multijunction solar cell design. Table 1 lists three component cells in a a-Si:H/a-SiGe:H/a-SiGe:H triple-junction solar cell (Yang et al. 2003). The top cell is with a a-Si:H intrinsic layer, the middle cell with a medium bandgap (~1.65 eV) a-SiGe:H intrinsic layer made of 15–20% of Ge, and the bottom cell with a low bandgap (~1.55 eV) a-SiGe:H intrinsic layer made of 25–30% of Ge. In order to simulate the real situation in the triple-junction structure, the a-Si:H top cell and the a-SiGe:H middle cell were deposited on bare stainless steel (SS) substrates because these two component cells did not receive much of the reflected light in the triple-junction structure. While the a-SiGe:H bottom cell was deposited on a Ag/ZnO back reflector coated SS since this was the same as in the triple-junction structure. In addition, the results show the long wavelength performances similar to the situations in the triple-junction solar cell, where the middle cell was measured with a 530-nm long-pass filter and the bottom cell with a 630-nm long-pass filter. The Ag/ZnO back reflector can significantly increase the photocurrent density. Figure 20 plots a comparison of external quantum efficiencies of an a-SiGe:H solar cell deposited on SS, SS/Al/ZnO, and SS/Ag/ZnO substrates. It clearly shows that the solar cells on the back reflector have a much higher long wavelength response than the cell on the bare SS with total current increase of 20% by the Al/ZnO back reflector and 30% by the Ag/ZnO back reflector. Compared to the a-Si:H top cell, the a-SiGe:H middle and bottom cells have much lower FF caused by the higher defect density in a-SiGe:H than in a-Si:H; and the light-induced degradation is also higher in a-SiGe:H than in a-Si:H solar cells. As mentioned previously, the Ge-H bonds are much weaker than the Si-H bonds and therefore H does not passivate Ge dangling bonds as effective as Si dangling bonds. The defect density increases with Ge content in a-SiGe:H films.

The same as in a-Si:H, the hole mobility-lifetime product  $(\mu\tau)_h$  is much lower than electron mobility-lifetime product  $(\mu\tau)_e$  in a-SiGe:H. The short hole collection length is the major limitation for a-SiGe:H solar cell efficiency. To minimize

**Fig. 20** The quantum efficiency (QE) comparison of an a-SiGe:H single-junction solar cell deposited on bare SS, Al/ZnO, and on Ag/ZnO back reflector coated SS

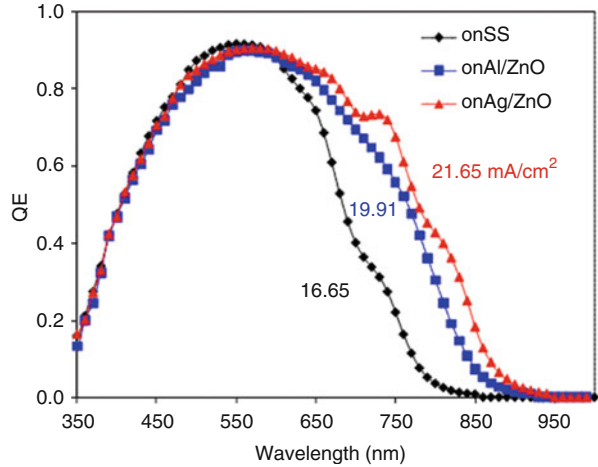
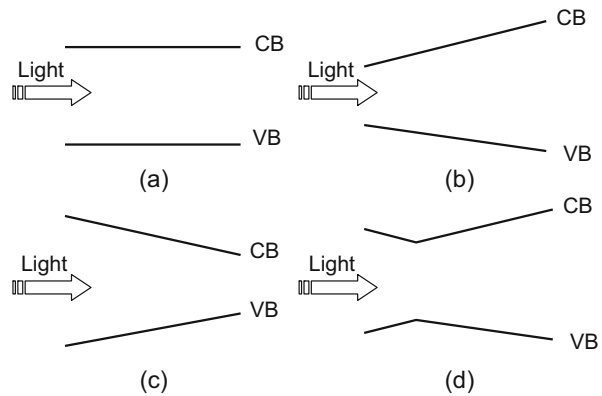


**Fig. 21** Schematics of bandgap profiles investigated in a-SiGe:H solar cells



the influence of unbalanced carrier transport properties on the cell performance, Guha et al. (1989) invented a unique method called “bandgap profiling” to improve a-SiGe:H solar cells. Figure 21 shows four different bandgap profiles: (a) a flat bandgap, (b) a profile of narrower bandgap in the *p* side (illumination side) and wider in the *n* side (the back side), (c) opposite to (b) with wider bandgap in the *p* side (illumination side) and narrower bandgap in the *n* side (the back side), and (d) a profile with a small bandgap decreasing region from the *p*-layer and a large bandgap increase region from the minimum toward *n*-layer (called “V-shape profile”). From carrier transport view, profile (b) is better than (a) because the narrower bandgap near the *p* side results in more photocarrier generation in this region, in which holes travels a short distance to reach the *p*-layer. In addition, the tilted bandgap provides additional force for hole transport and decelerates electrons, balancing the difference between  $(\mu\tau)_h$  and  $(\mu\tau)_e$ . From the absorption point of view profile (c) is better than (b) because high energy photons are absorbed in

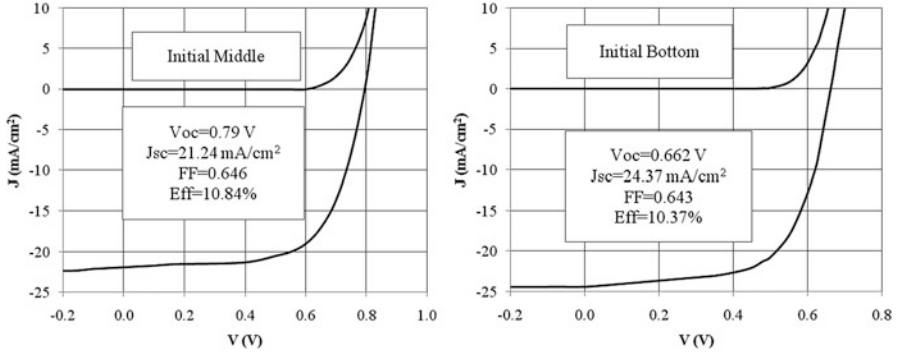


**Fig. 22** J-V characteristics of a-SiGe:H solar cells on SS/Ag/ZnO substrates. The left and right plots are the middle and bottom cells, respectively, used in a-Si:H/a-SiGe:H/a-SiGe:H triple-junction solar cells (Yang et al. 1994)

the shallow region with the wide bandgap and low energy ones are absorbed in the deep region with the narrow bandgap, but the hole transport faces a difficulty to travel longer distance with a decelerating force caused by the bandgap profile. Although (b) is favorable for hole transport, the narrower bandgap near the *p/i* interface causes a large bandgap discontinuity at the *p/i* interface and results in a high density of interface states. To resolve this interface issue, the “V-shape profile” is designed as shown in (d) with a short opposite profile to compromise the hole transport and bandgap continuity at the *p/i* interface. Experimental results showed that the “V-shape profile” is indeed an optimized bandgap profile and yielded high performance a-SiGe:H solar cells. Figure 22 plots the J-V characteristics of the a-SiGe:H middle and bottom solar cells used in high efficiency a-Si:H/a-SiGe:H/a-SiGe:H triple-junction solar cells (Yang et al. 1994). The single-junction a-SiGe:H solar cells have super performance of efficiency over 10%.

## A-Si:H Alloy-Based Multijunction Solar Cells

Because the solar spectrum is very wide from the ultraviolet to infrared, it is obvious that a semiconductor with a given bandgap cannot effectively use all of the solar energy. The photons with energy smaller than the bandgap cannot be absorbed, while the photons with energy higher than the bandgap can only use the part of energy equal to the bandgap and lose the portion of energy larger than the bandgap by thermal relaxation. Multijunction solar cells with different bandgaps in the component cells can resolve this issue with the wide bandgap top cell absorbing the short wavelength photons, the middle cell absorbing the middle wavelength photons, and the bottom cell for the long wavelength ones. For a-Si:H alloys, commonly used multijunction solar cells structures are shown in Fig. 23, including a-Si:H/a-Si:H double-junction, a-Si:H/a-SiGe:H double-junction, and a-Si:H/a-SiGe:H/a-SiGe:H

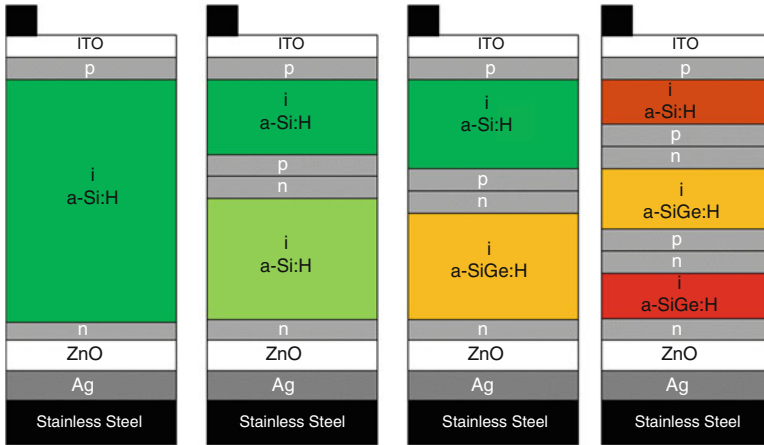


**Fig. 23** a-Si:H alloy multijunction solar cell structures investigated in United Solar (Yang et al. 2003)

triple-junction structures. Compared with a-Si:H single-junction solar cells, multijunction solar cells have not only high efficiency but also improved stability against light soaking.

Basically, a multijunction solar cell is constructed with the component cells stacked on top of each other. We use a-Si:H/a-SiGe:H double-junction as an example to discuss the operation principle of multijunction solar cells. It consists a a-Si:H *n-i-p* top cell on a a-SiGe:H bottom cell. In the ideal condition with no losses at the contact between the top cell and the bottom cell, the voltage of the double-junction cell equals to the sum of the voltages of the top and bottom cells; the photocurrent takes the smaller one; the *FF* is determined by the current mismatching between the top and bottom cells and the *FF* of component cells (Yan et al. 2008). One principle of designing multijunction solar cell is to have the component cell with the highest *FF* and the lowest light-induced degradation as the limiting cell (the smallest current density), which not only leads to a high initial efficiency but also an improved stability. Another important element in multijunction solar cells is the connection between two solar cells, where the *n*-layer of the top cell is directly deposited on the *p*-layer of the bottom cell, which is an invert *n/p* junction respecting to the main *n-i-p* junctions. The photo-electrons from the top cell need to recombine with the photo-holes from the bottom cell to form a continuous current. Because the electrons and holes need to tunnel through a certain distance to meet each other, the *n/p* junction connecting the top and bottom cells is also called recombination tunnel-junction (RTJ). If the carriers cannot tunnel into the opposite side, they accumulate in the *n/p* junction, cause a photo-voltage opposite to the main photo-voltage, and reduce the cell performance. One effective way to optimize the tunnel-junction is to use nc-Si:H *p* and/or *n* layers, where the carrier mobility is much higher than in a-Si:H *n* and *p* layers resulting in a long tunnel length, in this case an Ohmic contact with a low resistance forms.



**Table 2** a-Si:H/a-Si:H double-junction solar cell characteristics (Yang et al. 2003)

Tunnel-junction	$J_{sc}$ (mA/cm <sup>2</sup> )	$V_{oc}$ (V)	FF	Eff (%)	QE(top) (mA/cm <sup>2</sup> )	QE(bottom) (mA/cm <sup>2</sup> )	QE(total) (mA/cm <sup>2</sup> )	$R_s$ ( $\Omega$ cm <sup>2</sup> )
Standard	7.97	1.901	0.752	11.15	7.97	7.80	15.77	15.0
Optimized	8.06	1.919	0.766	11.85	8.06	8.28	16.34	14.3

Note: The short current densities are taken from the integrals of EQE with AM1.5 solar spectrum

## A-Si:H/a-Si:H Double-Junction Solar Cell

a-Si:H/a-Si:H double-junction solar cell is the simplest multijunction solar cell. Although it is constructed with two a-Si:H solar cells with the same or similar bandgap and it does not take the advantage of expanding the absorption spectrum, it usually has a higher FF, hence efficiency and a better stability than a-Si:H single-junction solar cells. a-Si:H/a-Si:H double-junction solar cell had been used for manufactures in the early stage of thin film silicon solar module production. As mentioned previously, the two component cells need to have similar photocurrent densities, the top cell acts as a filter for the bottom cell, therefore, the bottom cell needs to be much thicker than the top cell for matching the current. For example, in a high efficient *n-i-p* structured a-Si:H/a-Si:H double-junction solar cell on SS/Ag/ZnO substrates, the top cell and bottom cell thicknesses are around 100 nm and 300 nm. Table 2 lists the J-V characteristics of two a-Si:H/a-Si:H double-junction solar cells, where the first one is with the conventional tunnel junction and the second one with an improved tunnel junction (Yang et al. 2003). The improved tunnel junction improved all of the three performance parameters, hence improved the efficiency.

## A-Si:H/a-SiGe:H Double-Junction Solar Cell

From the data above, one can see that the limiting factor for a-Si:H/a-Si:H double-junction solar cells is the short circuit current density  $J_{sc}$ , which is limited by the bandgap of the bottom cell. In order to improve the long wavelength response, a-SiGe:H is used to substitute the *i*-layer of the bottom cell. The bandgap of the a-SiGe:H layer is adjustable by varying the Ge content. Because reducing the bandgap not only increases the photo-current density, but also reduces the  $V_{oc}$  and *FF*. Therefore, a systematic optimization is needed to search the optimized a-SiGe:H intrinsic layer. The best a-SiGe:H used in United Solar is with a bandgap around 1.6 eV made with 15–20% Ge content. The a-SiGe:H single-junction solar cell on SS/Ag/ZnO substrate made under this condition shows  $V_{oc}$  in the range of 0.75–0.80 V,  $J_{sc}$  in the range 22–23 mA/cm<sup>2</sup>. Using the a-Si:H/a-SiGe:H double-junction structure, initial and stable efficiencies of 14.4% and 12.4% were achieved, respectively (Yang et al. 1998).

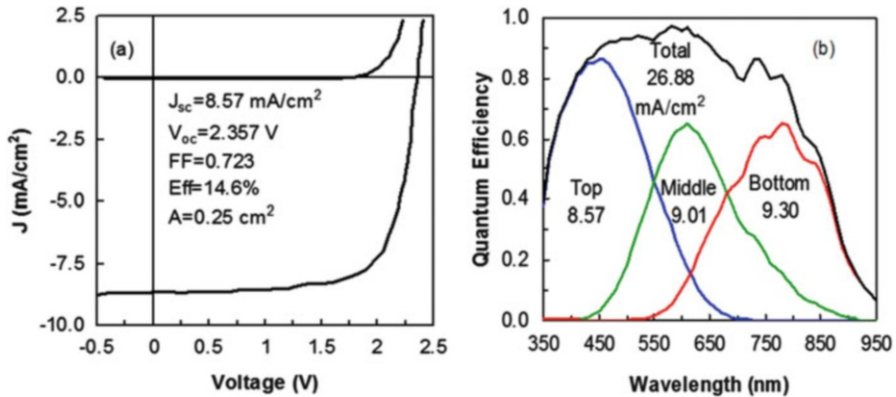


**Fig. 24** J-V characteristics and EQE curves of a a-Si:H/a-SiGe:H/a-SiGe:H triple-junction solar cell with an initial efficiency of 14.6% and stable efficiency of 13.0% (Yang et al. 1997)

### A-Si:H/a-SiGe:H/a-SiGe:H Triple-Junction Solar Cell

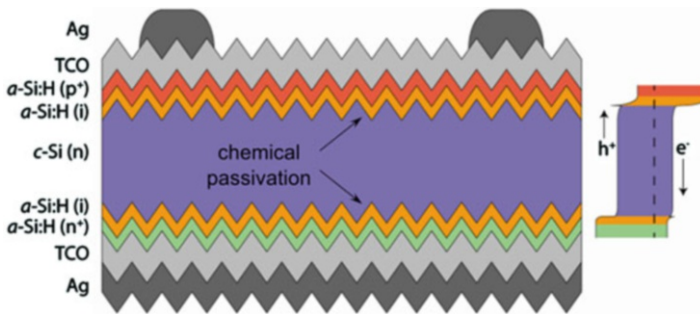
In order to improve the efficiency further, a-Si:H/a-SiGe:H/a-SiGe:H triple-junction solar cell has been studied since 1980s in Energy Conversion Devices, Inc. Similar to the double-junction solar cells, the a-Si:H/a-SiGe:H/a-SiGe:H triple-junction structure is deposited on SS/Ag/ZnO substrate. In 1986, Yang et al. (1986) achieved an initial conversion efficiency of 13%, and later in 1997, they advanced the initial and table efficiencies to 14.6% and 13.0%, respectively (Yang et al. 1997). Figure 24 shows the J-V characteristics and EQE curves of record efficiency solar cell. First, the triple-junction solar cell can use the wide solar spectrum effectively as shown in Fig. 24b, which covers the wide range of 300–950 nm; second, the  $FF$  of the triple-junction solar cell is much higher than single-junction and double-junction solar cells because the current mismatch improves the  $FF$ . The a-Si:H top cell has less defect density than the a-SiGe:H middle and bottom cells, therefore, an optimized cell structure should be designed with a thin top cell such that the top cell is the current-limiting cell to achieve a high  $FF$  in the triple-junction structure. Table 3 lists the solar cell performance parameters of different solar cell structures made in United Solar. Because the a-Si:H/a-SiGe:H/a-SiGe:H triple-junction solar cell structure not only yields the highest efficiency, but also has the best stability, United Solar had used the a-Si:H/a-SiGe:H/a-SiGe:H triple-junction structure for manufacturing flexible solar laminates and had a manufacture capability of 180 MW/year (Izu and Ellison 2003).

### A-Si:H/c-Si Heterojunction Solar Cell (SHJ or HIT)

In recent years, crystalline silicon material price has been dropped significantly and poly-Si and c-Si solar cell technology has been improved remarkably as well, which

**Table 3** The highest cell efficiency achieved by United Solar with different cell structure (Yang et al. 2003)

Cell structure	State	$J_{sc}$ (mA/cm <sup>2</sup> )	$V_{oc}$ (V)	FF	Eff (%)	Deg. (%)
a-Si:H Single-junction	Initial	14.65	0.992	0.730	10.6	12.3
	Stable	14.36	0.965	0.672	9.3	
a-Si:H/a-Si:H Double-junction	Initial	7.90	1.89	0.760	11.4	11.4
	Stable	7.90	1.83	0.700	10.1	
a-Si:H/a-SiGe:H Double-junction	Initial	11.04	1.762	0.738	14.4	13.9
	Stable	10.68	1.713	0.676	12.4	
a-Si:H/a-SiGe:H/a-SiGe:H Triple-junction	Initial	8.57	2.357	0.723	14.6	11.0
	Stable	8.27	2.294	0.684	13.0	

**Fig. 25** Schematic drawing of a HIT solar cell (Wolf et al. 2012)

have led a significant manufacturing cost reduction of crystalline silicon solar modules. On one hand, it has made a great progress towards grid parity for PV technology to provide clean and green energy for the society; but on the other hand, it has made the so-called second-generation thin film solar cell technology to lose their advantages in the market. Most (if not all) thin film silicon PV manufacturing companies went out of business. However, combining a-Si:H and c-Si to make a-Si:H/c-Si heterojunction solar cells (SHJ) has become an advanced high efficiency silicon PV technology. Because it uses a very thin intrinsic (~5 nm) a-Si:H layer to passivate c-Si interface, it is also often called HIT (Heterojunction with Intrinsic Thin layer) solar cell. Except for the a-Si:H passivation layer, HIT solar cell also uses a doped *p*-a-Si:H to form the emitter junction and a doped *n*-a-Si:H to form the back field junction. The cell structure is shown in Fig. 25.

HIT solar cell was initially invented by Sanyo in Japan in the 1990s (now it is Panasonic) (Taguchi et al. 1990). With the expiration of initial Intellectual Property of Sanyo, many companies and institutes have joined the research and development as well as the production of HIT solar cells. The cell and module efficiencies have been steadily improved. The cell efficiency reached 25.6% in 2014 by Panasonic

(Masuko et al. 2014) and 26.3% by Kaneka in 2016 ([http://www.kaneka.co.jp/kaneka-e/images/topics/1473811995/1473811995\\_101.pdf](http://www.kaneka.co.jp/kaneka-e/images/topics/1473811995/1473811995_101.pdf)). With the improvement of cell efficiency and manufacturing technology, HIT solar cell would lead to another big wave in the solar PV industry.

HIT solar cell has several better characteristics than the conventional homo-junction c-Si solar cells. First, it uses N-type c-Si wafer, which has higher minority carrier lifetime than P-type c-Si wafer even with the same impurity level. Second, because of no boron-oxygen complexes in N-type c-Si, HIT solar cell shows much less light-induced degradation than conventional c-Si solar cells with P-type wafer. Third, because of the a-Si:H passivation layer and a-Si:H doped layer, HIT solar cell has much higher  $V_{oc}$  and smaller temperature coefficient than homojunction c-Si solar cell, which leads to a higher energy yield than conventional poly-Si and c-Si PV modules in real applications, especially in hot climates.

The optimization of the a-Si:H passivation and the doped layer in HIT solar cells is different from conventional a-Si:H solar cells because the a-Si:H passivation layer is very thin and pure amorphous phase is needed. A uniform deposition of the very thin a-Si:H layer on a large area is the first challenge for HIT solar cell technology. Second, because the a-Si:H is very thin, the deposition time is very short; the initial ignition of the plasma in a PECVD system affects the passivation property and hence cell performance remarkably. It needs to control and reach steady plasma in a very short time. Third, any epitaxial growth reduces the effectiveness of the a-Si:H passivation. Because the a-Si:H passivation layer is directly deposited on a clean c-Si wafer surface, to make a clean sharp a-Si:H/c-Si interface without any epitaxial layer is another challenge. The optimization of HIT solar cell is another complicated process and different from a-Si:H thin film solar cell optimization, and it is out of the scope of this chapter, therefore, we leave it for other chapters.

---

## Conclusion

The research of a-Si:H material and application has lasted over 40 years and significant progresses have been made by the international community. Because of the complexity of the material structure, a-Si:H material provides one of the best platforms for fundamental studies, such as the microscopic material structures, electronic structure and defect states, the carrier transport, and metastability. Although many phenomena have been understood after the extensive studies, many others still need to be further investigated. The most important contribution is the invention of PECVD deposition by LeComber and Spear to incorporate H in the materials, which significantly reduces the dangling bond defect density and makes the doping possible. The fundamental studies by Anderson and Mott built the foundation of electric structure and carrier transport in the disorder semiconductor materials. A remarkable amount of material characterization works have been done and well documented in the literatures. Great applications of a-Si:H have been found in PV solar energy and large area display, which have been the driving force for the study of a-Si:H science and technology.

The structural properties of a-Si:H and its alloys have been characterized by XRD, Raman, TEM, NMR, and FTIR, which reveal the details in the material structures such as the degree of ordering, inclusion of medium orders, and the transition from amorphous to microcrystalline phases. The commonly agreed assessment on a-Si:H structure is that it is a disorder material without long range periodic order, but with the short range order such that Si atoms are still in the tetrahedral diamond structure with  $sp^3$  covalence bonds. Some high-quality materials include certain amount of highly ordered regions such as inter-medium range orders and isolated crystal grains. a-Si:H materials contain 10–15% of H atoms that terminate a significant amount of Si dangling bonds and form isolated Si-H bonds in high-quality materials and Si-H<sub>2</sub>, Si-H<sub>3</sub>, and (Si-H)<sub>n</sub> chain-like structures in poor materials with microvoids.

The electronic structure and defect characterizations have been measured by transmission/reflection, PDS, CPM, DLTS, ESR, and PL. In high-quality a-Si:H, the bandgap is about 1.70–1.85 eV, depending on the H content. Neutral Si dangling bonds are the major defects with a density in the order of  $10^{16} \text{ cm}^{-3}$ . Weak Si-Si and Si-H bonds form the localized band-tail states, which has an exponential distribution from the conduction band edge and valence band edge towards to the middle of the bandgap with the band-tail characteristic energy of  $\sim 25 \text{ meV}$  and  $\sim 50 \text{ meV}$  for the conduction and valence band tails, respectively. However, what causes the big difference between the conduction band tails and valence band tails is still not very clear, at least for the authors.

The transport properties are measured by dark and photoconductivity, time-of-flight transient photocurrent, and other experiments. For good a-Si:H, the dark conductivity is around  $10^{-10} (\Omega \cdot \text{cm})^{-1}$ , photoconductivity under an AM1.5 illumination is  $\sim 10^{-5} (\Omega \cdot \text{cm})^{-1}$ , and activation energy is  $\sim 0.70\text{--}0.85 \text{ eV}$ . The room temperature electron drift mobility is in the order of  $\sim 1 \text{ cm}^2/\text{Vs}$  and hole mobility of  $\sim 10^{-2} \text{ cm}^2/\text{Vs}$ . The low carrier mobility results partially from the multiple trapping in the tail states. The difference of conduction and valence band-tail widths is one of the origins for the difference of the electron and hole mobility values. The low carrier mobility has a great impact on a-Si:H solar cell design.

One big issue with a-Si:H is the light-induced degradation first observed by Staebler and Wronski, which is an intrinsic property of the materials. Light soaking reduces both dark and photoconductivity, and generates silicon dangling bond defects. The light-induced degradation can be annealed away at an elevated temperature. Reflected in a-Si:H solar cell, the energy conversion efficiency decreases with light soaking time and saturates after a few hundreds of hours. Although several mechanisms have been proposed, including the weak-bond breaking model, the charge transfer model, and the H collision model, no consensus has been made yet.

In the technology side, several new deposition techniques have been invented for improving the material quality and the deposition rate. Although conventional RF PECVD is still the major deposition method in research and development as well as a-Si:H PV and display production, new deposition techniques have been developed to address different issues. For example, VHF PECVD has shown a great advantage in high rate high-quality a-Si:H deposition, especially for  $\mu\text{-Si:H}$  deposition.

Microwave PECVD can deposit a-Si:H at a much higher rate but the high rate a-Si:H material quality needs to be improved further. Hot-wire CVD has no ion bombardment and has advantage for depositing stable a-Si:H with low H content.

In the PV application, a-Si:H solar cells use *p-i-n* and *n-i-p* structure instead of the *p-n* junction used in c-Si solar cells. The new cell structure is designed to overcome the disadvantage of lower carrier mobility-lifetime product in a-Si:H than in c-Si by using the *i*-layer as the absorber layer and thin doped *p* and *n* layers to form a built-in potential to collect the photo-generated carriers. Because of the lower hole mobility than electron mobility, the illumination through the *p* layer is the critical principle for a-Si:H solar cell design. Also because of the low carrier mobility-lifetime product, a-Si:H solar cells have a much thin absorber layer around 200–300 nm; for such thin solar cell, an effective light trapping is needed such as advanced Ag/ZnO back reflector and very textured TCO-coated glass. In order to use the solar spectrum effectively, high and low bandgap alloy materials have been developed, for example, a-SiC:H and a-SiO:H for wide bandgap, and a-SiGe:H for narrow bandgap. Using the variable bandgap alloyed a-Si:H materials, multijunction structures such as a-Si:H/a-SiGe:H double-junction and a-Si:H/a-SiGe:H/a-SiGe:H triple-junction solar cells have been designed for a high efficiency with a low light-induced degradation. The highest initial and stable cell efficiencies have reached to 14.6% and 13.0%, respectively. With such multijunction solar cell structure, large volume flexible thin film solar laminate production line has been built, which produced unique products for various applications such as roof-top installation.

With the significant cost reduction of poly-Si and c-Si solar module in recent years, a-Si:H thin film PV product has lost its advantage of low cost. But the lower efficiency than poly-Si and c-Si solar panels makes a-Si:H PV technology lose its competitiveness and market shares. Thin film silicon PV business has been shrunk significantly and many companies went to bankruptcy. However, a new technology of combining a-Si:H with c-Si to make high efficiency silicon heterojunction (SHJ or HIT) solar cells finds a-Si:H a new application and gives a-Si:H a new life in the PV field.

**Acknowledgments** The authors are grateful for the colleagues in the thin film silicon PV community. They have enjoyed very much the collaborations with several institutions and sharing ideas and results through the international conferences such as the MRS, ICANS, IEEE-PVSEC, and EU-PVSEC. BY acknowledges the hospitality of the Nankai University.

---

## References

- D. Adler, J. Phys. **42**, C4–C3 (1981)
- P.W. Anderson, Phys. Rev. **109**, 1492 (1958)
- G. Bauer, C. Nader, M. Schubert, G. Schumm, Mater. Res. Soc. Symp. Proc. **149**, 485 (1989)
- A.C.W. Biebericher, A.R. Burgers, C. Devilee, W.J. Soppe, Proc. of 19th European Photovoltaic Solar Energy Conference (Paris, 2004), p. 1485
- H.M. Branz, Solid State Commun. **105**, 387 (1998)
- N.M. Branz, Sol. Energy Mater. Sol. Cells **78**, 425 (2003)

- D. Carlson, C. Wronski, Appl. Phys. Lett. **28**, 671 (1976)
- D. Carson, Sol. Energy Mater. Sol. Cells **78**, 327 (2003)
- J.S. Cashmore, M. Apolloni, A. Braga, et al., Sol. Energy Mater. Sol. Cells **144**, 84 (2016)
- B. Chapman, Chapter 4, in *Glow Discharge Process: Sputtering and Plasma Etching*, (Wiley, New York/Chichester/Brisbane/Toronto/Singapore, 1980)
- J. Chevallier, H. Wieder, A. Onton, C. Guarnieri, Solid State Comm. **24**, 867 (1977)
- G.D. Cody, Chapter 2, in *Semiconductors and Semimetals*, Hydrogenated Amorphous Silicon Part B, ed. by J. I. Pankove (Ed), vol. 21, (Academic Press, Orlando/San Diego/San Francisco/New York/London/Toronto/Montreal/Sydney/Tokyo/San Paul, 1984)
- D. Cohen, Sol. Energy Mater. Sol. Cells **78**, 399 (2003)
- M.H. Cohen, H. Fritzsche, S.R. Ovshinsky, Phys. Rev. Lett. **22**, 1065 (1969)
- H. Curtins, N. Wyrsh, A. Shah, Electron. Lett. **23**, 228 (1987a)
- H. Curtins, N. Wyrsh, M. Favre, A.V. Shah, Plasma Chem. Plasma Process. **7**, 267 (1987b)
- F. Demichelis, C.F. Pirri, E. Tresso, J. Appl. Phys. **72**, 1327 (1992)
- X. Deng, E.A. Schiff, Chapter 12, in *Handbook of Photovoltaics Engineering*, ed. by A. Luque, S. Hegedus (Eds), (Wiley, Chichester, 2003)
- J. Doyle, R. Robertson, G.H. Lin, M.Z. He, A. Gallagher, J. Appl. Phys. **64**, 3215 (1988)
- J. Fan, J. Kakalios, Phil. Mag **B69**, 595 (1994)
- J. Fortner, J.S. Lannin, Phys. Rev. B **39**, 5527 (1989)
- H. Fritzsche, J. Kakalios, D. Dernstein, in *Optical Effects in Amorphous Semiconductors*, AIP Conf. Proc, ed. by P. C. Taylor, S. G. Bishop (Eds), vol. 120, (American Institute of Physics, New York, 1984), p. 229
- Q. Gu, Q. Wang, E.A. Schiff, Y.-M. Li, C.T. Malone, J. Appl. Phys. **76**, 2310 (1994)
- S. Guha, K.L. Narasimhan, S.M. Pietruszko, J. Appl. Phys. **52**, 859 (1981)
- S. Guha, J. Yang, A. Pawlikiewicz, T. Glatfelter, R. Ross, S.R. Ovshinsky, Appl. Phys. Lett. **54**, 2330 (1989)
- S. Guha, X. Xu, J. Yang, A. Banerjee, Appl. Phys. Lett. **66**, 595 (1994)
- S. Guha, J. Yang, A. Banerjee, B. Yan, K. Lord, Sol. Energy Mater. Sol. Cells **78**, 329 (2003)
- D. Han, K. Wang, Sol. Energy Mater. Sol. Cells **78**, 181 (2003)
- D. Han, K. Wang, L. Yang, J. Appl. Phys. **80**, 2475 (1996)
- P. Hari, P.C. Taylor, R.A. Street, Mater. Res. Soc. Symp. Proc. **336**, 329 (1994)
- N. Hata, T. Kamei, H. Okamoto, A. Matsuda, Mater. Res. Soc. Symp. Proc. **467**, 61 (1997)
- J.K. Holt, M. Swiatek, D.G. Goodwin, H.A. Atwater, Mater. Res. Soc. Symp. Proc. **715**, 165 (2002)
- G. Hou, J. Fang, Q. Fan, C. Wei, J. Ni, X. Zhang, Y. Zhao, Sol. Energy Mater. Sol. Cells **134**, 395 (2015)
- K. Ishibashi, Thin Solid Films **395**, 55 (2001)
- M. Izu, T. Ellison, Sol. Energy Mater. Sol. Cells **78**, 613 (2003)
- W.B. Jackson, N.M. Amer, AIP Conf. Proc. **73**, 263 (1981)
- H. Jia, J.K. Saha, H. Shirai, Jpn. J. App. Phys. **45**, 666 (2006a)
- H. Jia, H. Shirai, M. Kondo, Mater. Res. Soc. Symp. Proc. **910**, 309 (2006b)
- J.D. Joannopoulos, G. Lucovsky, *The Physics of Hydrogenated Amorphous Silicon I and II*, Topics in Applied Physics, vol 56 (New York/Tokyo, 1984)
- S. Jones, R. Crucet, X. Deng, D.L. Williamson, M. Izu, Mater. Res. Soc. Symp. Proc. **609**, A4.5 (2000)
- P.A. Khomyakov, W. Andreoni, N.D. Afify, A. Curioni, Phys. Rev. Lett. **107**, 255502 (2011)
- J. Koh, Y. Lee, H. Fujiwara, C.R. Wronski, R.W. Collins, Appl. Phys. Lett. **73**, 1526 (1998)
- S. Komuro, Y. Aoyagi, Y. Segawa, S. Namba, A. Masuyama, H. Okamoto, Y. Hamakawa, J. Appl. Phys. **55**, 3866 (1984)
- M. Kondo, Sol. Energy Mater. Sol. Cells **78**, 543 (2003)
- G. Kong, D. Zhang, G. Yue, X. Liao, Phys. Rev. Lett. **79**, 4210 (1997)
- A. Langford, M. Fleet, B. Nelson, W. Lanford, N. Maley, Phys. Rev. B **45**, 13367 (1992)

- J.S. Lannint, Chapter 6, in *Semiconductors and Semimetals*, Hydrogenated Amorphous Silicon Part B, ed. by J. I. Pankove (Ed), vol. 21, (Academic Press, Orlando/San Diego/San Francisco/New York/London/Toronto/Montreal/Sydney/Tokyo/San Paul, 1984)
- X. Liao, W. Du, X. Yang, H. Povolny, X. Xiang, X. Deng, PVSC IEEE-31 Orlando, 3–7 January, 2005, p 1444
- J. Löffler, C. Devilee, M. Geusebroek, W.J. Soppe, H.-J. Muffler, Proc. of 21st European Photovoltaic Solar Energy Conference (Dresden, 2006), p. 1597
- D. Lundszen, J. Folsch, F. Finger, H. Wagner, Proc. of 14th European Photovoltaic Solar Energy Conference (Barcelona, June 1997), p.578
- A.H. Mahan, Thin Solid Films **395**, 12 (2001)
- A.H. Mahan, Sol. Energy Mater. Sol. Cells **78**, 299 (2003)
- A.H. Mahan, A. Mason, B.P. Nelson, A.C. Gallagher, Mater. Res. Symp. Proc. **609**, A6.6 (2000)
- Y. Mai, S. Klein, R. Carius, H. Steibig, X. Geng, F. Finger, Appl. Phys. Lett. **87**, 073503 (2005)
- D.P. Masson, A. Ouhlal, A. Yelon, J. Non-Cryst. Solids **190**, 151 (1995)
- K. Masuko, M. Shigematsu, T. Hashiguchi, D. Fujishima, IEEE J Photovolt. **4**, 1433 (2014). <http://panasonic.net/ecosolutions/solar/hit/>
- A. Matsuda, M. Matsumura, K. Nakagawa, T. Imura, H. Yamamoto, S. Yamazaki, H. Okushi, S. Iizima, and K. Tanaka, in Tetrahedrally Bonded Amorphous Semiconductor, R. A. Street, D. K. Biegelsen, and J. C. Knights (American Inst. Phys., New York 1981), 192
- H. Matsumura, Thin Solid Films **395**, 1 (2001)
- H. Matsumura, H. Tachibana, Appl. Phys. Lett. **47**, 833 (1985)
- S.C. Moss, J.F. Graczyk, Phys. Rev. Lett. **23**, 1167 (1969)
- N.F. Mott, Phil. Mag. **13**, 989 (1966)
- N.F. Mott, Adv. Phys. **16**, 49 (1967)
- N.F. Mott, E.A. Davis, In *Electronic Process in Non-crystalline Materials*, 2nd edn. (Clarendon Press, Oxford, 1979), p. 322
- H. Okamoto, K. Tanaka, E. Maruyama, *Amorphous Silicon* (Wiley, Chichester, 1999)
- S.R. Ovshinsky, *18th IEEE Photovoltaic Specialists Conference* (IEEE, New York, 1985), p. 1365
- W. Paul, in *Amorphous Silicon and Related Materials*, ed. by H. Fritzsche (Ed), (World Scientific Publishing Company, Singapore, 1988), p. 63
- E.A. Schiff, Sol. Energy Mater. Sol. Cells **78**, 567 (2003)
- E.A. Schiff, J. Phys. Condens. Matter **16**, S5265 (2004)
- A. Shah, J. Dutta, N. Wyrsh, K. Prasad, H. Curtins, F. Finger, A. Howling, C. Hollesstein, Mater. Res. Soc. Symp. Proc. **258**, 15 (1992)
- A.V. Shah, J. Meier, E. Vallat-Sauvain, N. Wyrsh, U. Kroll, C. Droz, U. Graf, Sol. Energy Mater. Sol. Cells **78**, 469 (2003)
- N.J. Shevchik, W. Paul, J. Non-Cryst. Solids **381**, 8–10 (1972)
- K. Shimizu, T. Tabuchi, M. Iida, H. Okamoto, J. Non-Cryst. Solids **227**, 267 (1998)
- H. Shirai, Y. Sakuma, H. Ueyama, Thin Solid Films **345**, 7 (1999)
- W.E. Spear, P.G. LeComber, Solid State Commun. **17**, 1193 (1975)
- W.E. Spear, P.G. LeComber, Philos. Mag. **33**, 935 (1976)
- D.L. Staebler, C.R. Wronski, Appl. Phys. Lett. **31**, 292 (1977)
- R.A. Street, Adv. Phys. **30**, 593 (1981)
- R.A. Street, *Hydrogenated Amorphous Silicon* (Cambridge University Press, Cambridge, 1991)
- M. Stutzmann, R.A. Street, Phys. Rev. Lett. **54**, 1836 (1985)
- M. Stutzmann, W.B. Jackson, C.C. Tsai, Appl. Phys. Lett. **45**, 1075 (1984)
- T. Su, P.C. Taylor, Sol. Energy Mater. Sol. Cells **78**, 269 (2003)
- M. Taguchi, M. Tanaka, T. Matsuyama, et al. Proc. Fifth PVSEC (1990), pp. 689–692
- J. Tauc, Chapter 4, in *Amorphous and Liquid Semiconductors*, ed. by J. Tauc (Ed), (Plenum Press, London/New York, 1974)
- Y. Tawada, K. Tauge, M. Kondo, H. Okamoto, Y. Hamakawa, Appl. Phys. Lett. **53**, 5273 (1982)



- R.J. Temkin, W. Paul, G.A.N. Connell, *Adv. Phys.* **22**, 581 (1973)
- F. Urbach, *Phys. Rev.* **92**, 1342 (1953)
- S.D. Wolf, A. Descoedres, Z.C. Holman, et al., *Green* **2**, 7 (2012)
- B. Yan, J. Yang, S. Guha, A. Gallagher, *Mater. Res. Soc. Symp. Proc.* **557**, 115 (1999)
- B. Yan, G. Yue, J. Yang, K. Lord, A. Banerjee, S. Guha, *Proc. of 3rd World Conference on Photovoltaic Energy Conversion*, (Osaka, 11–18 May, 2003), p. 2773
- B. Yan, G. Yue, J. Yang, and S. Guha, *Proc. of 33rd IEEE Photovoltaic Specialists Conference* (IEEE, New York, 2008), paper No. 257
- B. Yan, G. Yue, L. Sivec, J. Yang, S. Guha, C. Jiang, *Appl. Phys. Lett.* **99**, 113512 (2011)
- J. Yang, R. Ross, R. Mohr, J.R. Fournier, *Mater. Res. Soc. Symp. Proc.* **70**, 475 (1986)
- J. Yang, A. Banerjee, T. Glatfelter, K. Hoffman, X. Xu, S. Guha, *Proc. of 1st World Conf. on Photovoltaic Energy Conversion Proc* (IEEE, N. Y., 1994), p. 380
- J. Yang, A. Banerjee, S. Guha, *Appl. Phys. Lett.* **70**, 2975 (1997)
- J. Yang, A. Banerjee, K. Lord, S. Guha, *Proc. of 2nd World Conference and Exhibition on Photovoltaic Solar Energy Conversion* (6–10 July 1998, Vienna), p. 387
- J. Yang, B. Yan, S. Guha, *Mater. Res. Soc. Symp. Proc.* **664**, A11.3 (2001)
- J. Yang, A. Banerjee, S. Guha, *Sol. Energy Mater. Sol. Cells* **78**, 597 (2003)
- G. Yue, G. Kong, D. Zhang, Z. Ma, S. Sheng, X. Liao, *Phys. Rev.* **B57**, 2387 (1998)
- G. Yue, B. Yan, J. Yang, S. Guha, *Mater. Res. Soc. Symp. Proc.* **989**, 359 (2007)
- P.Z. Zanzucchi, Chapter 4, in *Semiconductors and Semimetals*, Hydrogenated Amorphous Silicon Part B, ed. by J. I. Pankove (Ed), vol. 21, (Academic Press, Orlando/San Diego/San Francisco/New York/London/Toronto, Montreal/Sydney/Tokyo/San Paul, 1984)
- S. Zhang, Y. Xu, Z. Hu, Y. Wang, X. Zeng, H. Diao, W. Wang, G. Kong, X. Liao, *Proc. PVSC IEEE-29 New Orleans*, 21–24 May, 2002, p. 1182
- Y. Zhao, D. Zhang, G. Kong, G. Pan, X. Liao, *Phys. Rev. Lett.* **74**, 558 (1995)
- J. Zhao, A. Wang, M.A. Green, *Prog. Photovolt. Res. Appl.* **7**, 471 (1999)



# Hydrogenated Microcrystalline Silicon Thin Films 21

Ying Zhao, Xiaodan Zhang, Lisha Bai, and Baojie Yan

## Contents

Introduction .....	694
Basic Material Properties of $\mu\text{c-Si:H}$ .....	695
Structure Properties of $\mu\text{c-Si:H}$ .....	695
Electronic Properties of $\mu\text{c-Si:H}$ .....	701
Optical Properties of $\mu\text{c-Si:H}$ .....	704
Application of $\mu\text{c-Si:H}$ in Solar Cells and Issues for Efficiency Improvement .....	708
Crystalline Evolution and Hydrogen Dilution Profile .....	709
Impurity Issue and Controlling .....	714
Light-Induced Metastability in $\mu\text{c-Si:H}$ Solar Cells .....	719
Light Trapping in $\mu\text{c-Si:H}$ Solar Cells .....	725
Microcrystalline Silicon Germanium Alloy $\mu\text{c-SiGe:H}$ .....	736
High Rate Deposition of $\mu\text{c-Si:H}$ .....	737
$\mu\text{c-Si:H}$ Thin Film Silicon Solar Cell Design and Optimization .....	740
Doped Layer .....	740
Interface Layers .....	744
High Efficiency $\mu\text{c-Si:H}$ Single-Junction Solar Cell .....	746
A-Si:H and $\mu\text{c-Si:H}$ Based Multijunction Solar Cell and Modules .....	747
Summary .....	751
References .....	753

## Abstract

We review  $\mu\text{c-Si:H}$  material's properties, deposition techniques, and applications in solar cells. The focus is on the issues that limit  $\mu\text{c-Si:H}$  solar cell performance. Because of unintentional impurity incorporation,  $\mu\text{c-Si:H}$  shows an N-type conductivity, especially in the early days,  $\mu\text{c-Si:H}$  was used only as the doped layers. Meier et al. used VHF-PECVD technique with reduced

---

Y. Zhao · X. Zhang · L. Bai · B. Yan (✉)  
Institute of Photoelectronic Thin Film Devices and Technology, Nankai University,  
Tianjin, P. R. China  
e-mail: [zhaoygds@nankai.edu.cn](mailto:zhaoygds@nankai.edu.cn); [xdzhang@nankai.edu.cn](mailto:xdzhang@nankai.edu.cn); [baojie.yan@yahoo.com](mailto:baojie.yan@yahoo.com)

impurity levels and made first  $\mu\text{c-Si:H}$  solar cell in 1994. Since then the research and development of  $\mu\text{c-Si:H}$  solar cells have attracted a great attention, and a significant progress has been made for using  $\mu\text{c-Si:H}$  as the bottom cell in multijunction structures. Compared to a-Si:H,  $\mu\text{c-Si:H}$  structure is much complicated with nanometer sized grains, grain boundaries, amorphous tissues, and microvoids. The complexity in the structure leads to complicated material properties, such as electronic structure, optical absorption, carrier transport, and stability. The material's property affects the solar cell performance significantly. The material structure changes with the film thickness under a constant deposition condition, which influences the solar cell performance. For solar cell applications, it has been found that the best  $\mu\text{c-Si:H}$  material should be compact with a low defect density and a crystalline volume fraction around 50% in the whole absorber layer. In order to obtain a high photocurrent density, an effective light trapping is achieved using textured substrates. However, a high textured substrate causes a degradation of material quality. A thick  $\mu\text{c-Si:H}$  up to 5  $\mu\text{m}$  requires a high rate deposition. Here, we will discuss the techniques for resolving the  $\mu\text{c-Si:H}$  issues and the approaches for achieving the high quality materials and high efficiency  $\mu\text{c-Si:H}$  solar cells.

---

**Keywords**

$\mu\text{c-Si:H}$  · nc-SiOx:H · Thin film · PECVD · Impurity · Light trapping · p-i-n · n-i-p · Solar cell · Multi-junction

---

**Introduction**

Hydrogenated microcrystalline silicon ( $\mu\text{c-Si:H}$ ) was invented in 1968. It was first made with a remote hydrogen plasma transport method (Vepteck and Marecek 1968). Later on, it was found that in plasma enhanced chemical vapor deposition (PECVD) process, when high hydrogen dilution and high RF power were used, the deposited films showed crystal-like structures in their electron scattering pattern and with high conductivity (Usui and Kikuchi 1979). The materials contain crystal grains with the sizes in the range of a few nm and a few tens nm embedded in hydrogenated amorphous silicon (a-Si:H) tissues; therefore, the materials are also called hydrogenated nanocrystalline silicon (nc-Si:H) in the literature. Although some researchers believe that the grains in nc-Si:H are smaller than in  $\mu\text{c-Si:H}$ , no clear distinguish between nc-Si:H and  $\mu\text{c-Si:H}$  has been made and they are mixed in the literature. Therefore, we used  $\mu\text{c-Si:H}$  only in this chapter for consistency. The deposition of  $\mu\text{c-Si:H}$  with PECVD uses the same gases as used for a-Si:H deposition with only some differences in the process parameters such as hydrogen dilution, excitation power, pressure, and temperature. Therefore, the  $\mu\text{c-Si:H}$  fabrication techniques are compatible with a-Si:H, which is important for solar panel production.

The early stage  $\mu\text{c-Si:H}$  materials have very high conductivity with N-type carrier transport, which has been identified as the contribution of unintentional doping by oxygen and/or nitrogen. Therefore,  $\mu\text{c-Si:H}$  was mainly used as the N-type and

P-type doped layer in a-Si:H solar cells (Guha et al. 1986; Yang et al. 1997). An important breakthrough of using  $\mu\text{-Si:H}$  as the absorber layer in solar cells was made by Meier et al. at the University of Neuchatel by using Very High Frequency (VHF) PECVD (Meier et al. 1994a, b). Later on they used a gas purifier to reduce the impurity level and improved  $\mu\text{-Si:H}$  material quality and solar cell performance (Meier et al. 1996). Since then, the study of  $\mu\text{-Si:H}$  material property and the research and development of high efficiency  $\mu\text{-Si:H}$  solar cells have got a great attention worldwide, and a significant amount of results has been published in the literature. For reviews, readers may be referred Finger (2010), Guha et al. (2013), Kondo (2003), and Shah et al. (2003). With the great efforts from the thin film silicon photovoltaic (PV) community, the efficiencies of multijunction thin film silicon solar cells and modules with  $\mu\text{-Si:H}$  as the bottom cell absorber layer have been improved steadily with the highest initial cell efficiency of 16.3% (Yan et al. 2011), stable cell efficiency 13.4% (Kim et al. 2013), and stable module efficiency of 12.3% (Cashmore et al. 2016).

From the material structure point view,  $\mu\text{-Si:H}$  is a mixture of crystallites embedded in amorphous tissues. The material structures are much more complicated than a-Si:H and crystal silicon (c-Si). Although a significant amount of studies has been made in the last a few decades, many problems are still unresolved. Here we will not discuss the complicated physics problems with the materials. Instead, we will focus on a few major issues affecting  $\mu\text{-Si:H}$  solar cell performance and the solutions of the problems. The first phenomenon is the so-called crystalline evolution, in which the crystalline volume fraction increases with the film thickness; second the impurity issue and the ambient degradation of  $\mu\text{-Si:H}$  solar cells and light-induced degradations; third the optical property and the light trapping in  $\mu\text{-Si:H}$  solar cells; and fourth, the microcrystalline silicon germanium alloy ( $\mu\text{-SiGe}_x\text{:H}$ ) for extension of absorption to longer wavelength and microcrystalline silicon oxide ( $\mu\text{-SiO}_x\text{:H}$ ) for doped layers. We also address the issues in solar cell design and optimization such as the doped layer and interface layers and finally the high rate deposition of  $\mu\text{-Si:H}$  for solar panel production. Before the discussion of those issues, a brief review the basic properties of  $\mu\text{-Si:H}$  materials is given.

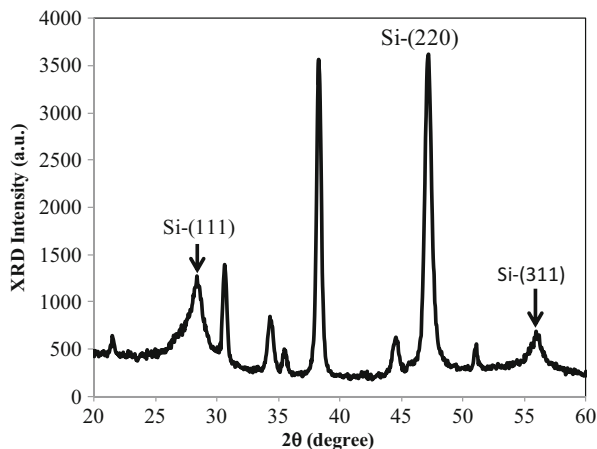
---

## Basic Material Properties of $\mu\text{-Si:H}$

### Structure Properties of $\mu\text{-Si:H}$

Since  $\mu\text{-Si:H}$  is a mixture of crystalline grains and amorphous silicon tissues, the material structures can be characterized by various methods, including X-ray scattering (XRD) spectroscopy, Raman spectroscopy, transmission electron microscopy (TEM), scanning electron microscopy (SEM), atomic force microscopy (AFM), and real time spectroscopic ellipsometry (RTSE). Below, we will discuss some basic observations with these characterizations methods.

**Fig. 1** An XRD pattern of  $\mu\text{-Si:H}$  solar cell deposited on Ag/ZnO back reflector coated SS substrates, where the three crystalline Si peaks are marked and the others unmarked are from the substrate



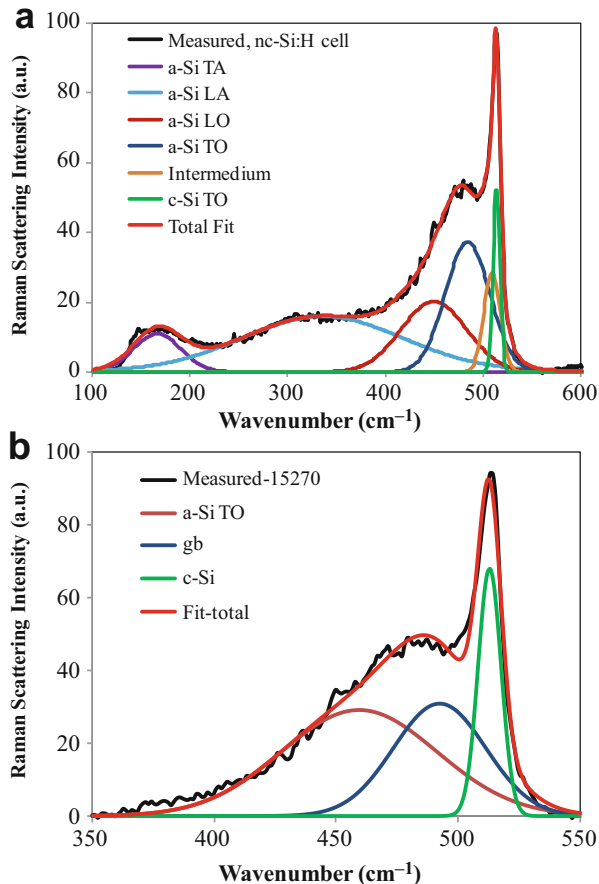
XRD is one of the commonly used characterization methods for  $\mu\text{-Si:H}$  materials (Ray et al. 2002; Sobajima et al. 2007). Figure 1 shows a typical XRD pattern of a  $\mu\text{-Si:H}$  solar cell made with VHF-PECVD on ZnO/Ag-coated stainless steel (SS) substrate, where the preferential crystalline orientation is the (220) at  $2\theta = 47.311^\circ$  and two other peaks at  $28.451^\circ$  and  $56.131^\circ$  corresponding to the (111) and (311) crystalline orientations, respectively. In addition, a few unmarked peaks are from the ZnO/Ag/SS substrate. The crystallite size  $d$  and the internal stress  $\eta$  could be estimated by the Debye-Scherrer equation (Debye and Scherrer 1916),

$$\Delta\theta \cos \theta = \frac{k\lambda}{d} + \eta \sin \theta, \quad (1)$$

where  $\lambda$  is the wavelength of the X-ray,  $\theta$  the scattering angle,  $\Delta\theta$  the full width at the half maximum (*FWHM*), and  $k$  a constant in the range of 0.8 and 1.39. The commonly used X-ray is the  $K_\alpha$  radiation line of Cu with the wavelength of 0.15418 nm. One could plot  $\Delta\theta \cos(\theta)$  versus  $\sin(\theta)$  and obtain the internal stress from the slope and the crystallite size from the intersection. In most case, the internal stress is ignored with  $\eta = 0$ , and the crystalline size is estimated by the Scherrer equation. One should keep in mind that the Debye-Scherrer equation is assumed spherical grain structures. However, in real  $\mu\text{-Si:H}$  materials, the crystallites are elongated perpendicularly to the growth surface, and therefore, the estimated grain size is normally smaller than the real average value. As observed in Fig. 1, the *FWHM* of the (220) peak is narrower than the other two peaks, which indicates that the grains with (220) preferential orientation are larger than the (111) and (311) orientated grains. For most of high quality  $\mu\text{-Si:H}$  materials, the estimated grain sizes from the (220) peak are in the range of 20–30 nm.

Raman spectroscopy is another most commonly used method to analyze  $\mu\text{-Si:H}$  materials (Ledinsky et al. 2006; Vallat-Sauvain et al. 2006a). Because  $\mu\text{-Si:H}$

**Fig. 2** Raman spectra of a  $\mu\text{-Si:H}$  solar cell deposited on a ZnO/Ag back reflector coated SS, where (a) is the as measured spectrum with four a-Si:H modes, one c-Si TO mode, and one intermedium component, (b) the measured spectrum with baseline correction and the three component fittings



contains crystallites and a-Si:H tissues, roughly speaking its Raman spectrum is a combination of the spectra of a-Si:H and c-Si. The a-Si:H component has four vibration modes of TA, LA, TO, and LO vibrations as shown in Fig. 2a with the deconvolution for the measured spectrum with multiple components. Since the c-Si Raman spectrum has only the TO mode because of the conservation of momentum, the most information of the crystalline structure is in the TO mode, where it is a combination of the amorphous silicon TO mode and the crystalline silicon TO mode with some differences, where the crystalline TO peak broadens and shifts to the low energy side at around  $510 - 520 \text{ cm}^{-1}$ , the amorphous TO peak narrows and shifts to the high energy side at around  $480 - 490 \text{ cm}^{-1}$ . In addition, an intermedium peak at around  $500 - 505 \text{ cm}^{-1}$  is observed and normally assigned to the vibration at grain boundaries and the crystallites with the size smaller than 3 nm. From the red shift and the bandwidth of the c-Si peak (Iqbal and Veprek 1982), the grain size could be estimated, but the accuracy is affected by the internal stress and can only be applied to small grains. Therefore, accurate estimations of grain sizes and distributions

cannot be obtained by Raman spectra, but can be obtained from cross-sectional TEM images.

The deconvolution of Raman spectra with all of the possible vibration modes is complicated and with a high level of arbitrariness because of the multiple fitting parameters in each component. The commonly used method for the Raman spectral analysis is taking a baseline correction to remove the contributions from the other modes except the TO mode. An example is given in Fig. 2b, where a linear baseline correction is taken in the range of  $350\text{ cm}^{-1}$  to  $550\text{ cm}^{-1}$ . The baseline corrected spectrum is fitted with three Gaussian curves assigned to the a-Si:H TO mode, the grain boundary TO mode, and c-Si TO mode. Using the three component fitting, the most important structure information of crystalline volume fraction,  $f_c$ , is estimated by

$$f_c = \frac{I_c + I_i}{I_c + I_i + mI_a}, \quad (2)$$

where  $I_c$ ,  $I_b$ , and  $I_a$  are the integrals of TO modes of c-Si, grain boundary, and a-Si:H, respectively, and  $m$  is a correction factor for the Raman cross-sections of amorphous and crystalline phases and its value relates to the size of crystallites  $d_c$ ,

$$m = 0.1 + \exp\left(-\frac{d_c}{250}\right). \quad (3)$$

However, the real  $m$  value is very controversial, and it also depends on the probe light wavelength. Some early published values are in the range from 0.1 to 0.9 (Brodsky et al. 1977; Bustarret et al. 1988; Tsu et al. 1982), but Vallat-Sauvain et al. (2006a) determined that  $m = 1.68$  for the measurements with 633 nm red laser and 1.78 for 514 nm green laser. Because of the uncertain of the  $m$  value, the absolute crystalline volume fraction may not be able to be determined by Raman measurements, but a relative comparison between samples provides very useful information. In this sense, a simple treatment using  $m = 1$  is widely used.

Measured Raman spectra could be also different when using different excitation lasers because of the different absorption coefficients for different wavelengths: a short wavelength probes the top layer of the sample due to a high absorption coefficient, and a long wavelength gives the bulk information due to a nearly uniform absorption. Also the measurements with the illumination on the top surface and on the rear surface of  $\mu\text{c-Si:H}$  deposited on a glass substrate can obtain different results because of the crystalline evolution as will be discussed later. Another important factor in real measurement is to keep the light intensity low enough to avoid light-induced crystallization, which easily happens when micro-Raman is performed with a focused laser beam.

Cross-sectional TEM is a direct observation method to measure the structures of  $\mu\text{c-Si:H}$  films. Depending on the selection of the resolution, one can study the overall structure and fine structures. Figure 3 presents two TEM images with different resolutions. The left one (Bailat et al. 2002) is taken with a low resolution to examine the structure cross the entire film thickness, where several features are observed with

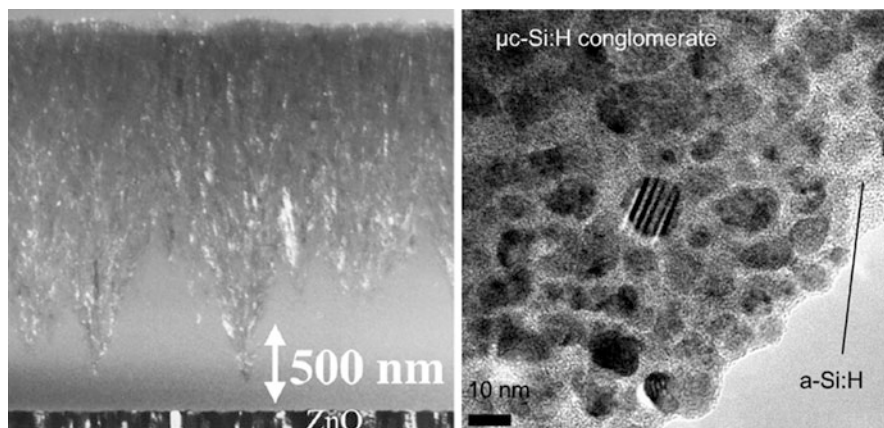


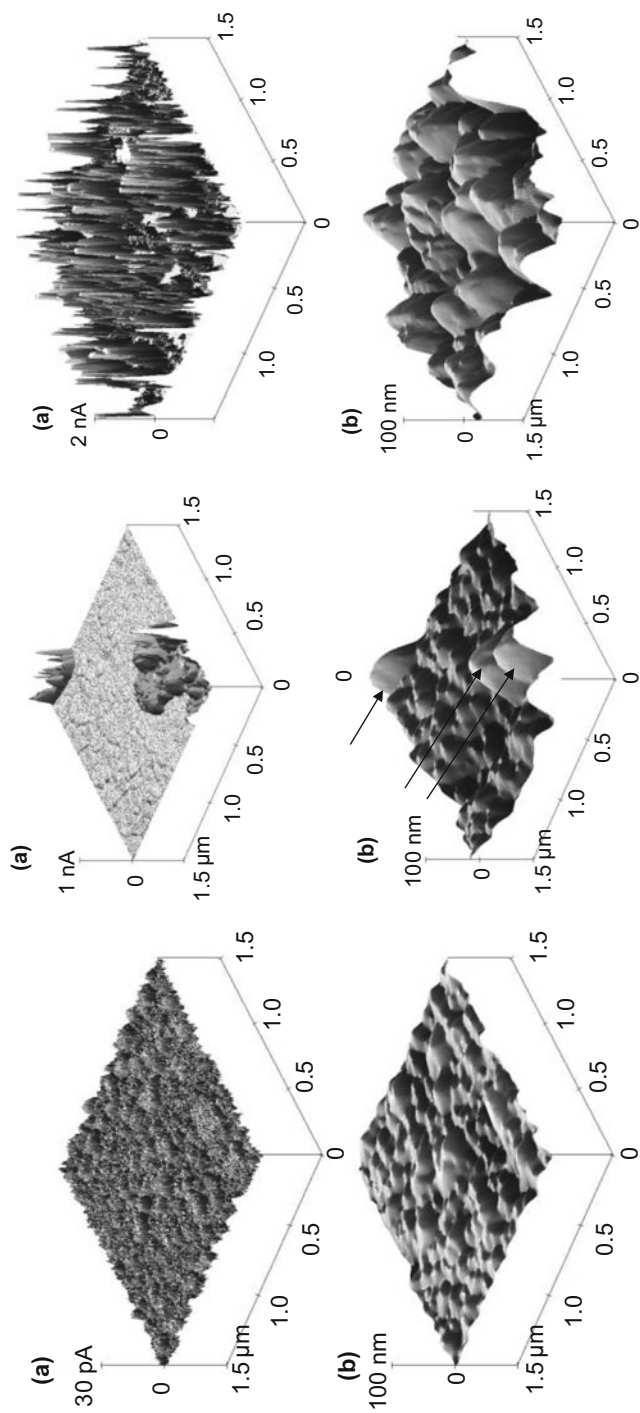
**Fig. 3** The left image is a low resolution cross-sectional TEM of a  $\mu\text{c-Si:H}$  film on glass (Bailat et al. 2002), and the right one is a high resolution TEM image showing the nanometer sized c-Si grain embedded a-Si:H matrix (Vallat-Sauvain et al. 2006b)

an a-Si:H incubation layer in the bottom smooth area, the formation of crystalline seeds as seen by the spike-like structures, and the growth of the crystalline volume fraction as approaching the top part of the sample. This phenomenon is called “crystalline evolution” and will be discussed in detail later part of this chapter. The right image (Vallat-Sauvain et al. 2006b) is a high-resolution TEM showing nanometer sized nc-Si grain embedded in an a-Si:H tissue. By carefully examining high resolution TEM images, one could obtain the crystallite density, grain size distribution, and compactness of the materials.

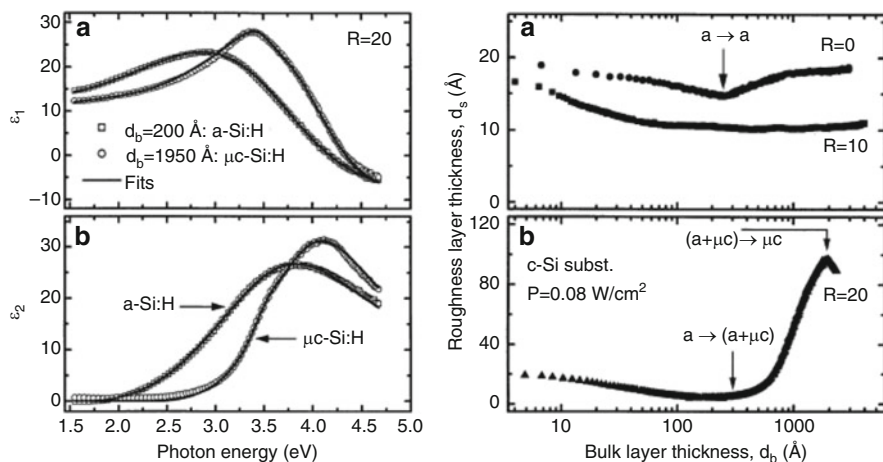
AFM is another very useful microscopic analysis tool for  $\mu\text{c-Si:H}$  characterization, especially combining the surface morphology mode with conductive mode (Rezek et al. 2002; Yan et al. 2007). Because a-Si:H is normally smoother than  $\mu\text{c-Si:H}$ . The formation of large grains, especially the clusters formed with nanometer sized grains, generates higher surface textures than pure a-Si:H. In addition,  $\mu\text{c-Si:H}$  has much higher conductivity than a-Si:H; a surface current distribution measured with c-AMF reveals a lot of useful information for microcrystalline formation.

Figure 4 shows a comparison of (a) the c-AFM images and (b) the regular AFM morphology images taken in the same corresponding areas on the surface of an a-Si:H (left one), a mixed-phase Si:H (middle one), and a  $\mu\text{c-Si:H}$  (right) samples (Yan et al. 2007). It is observed that the a-Si:H surface is relatively flat with a much lower surface current as shown by the left images. The most interesting observation is from the mixed-phase sample, where the two areas as pointed by the arrows have high mountain-like humps on the morphology image, correspondingly the current is much higher in these areas than the rest of the areas (note the current axis unit is 1 nA). For the  $\mu\text{c-Si:H}$  film with a high crystallinity, many mountain-like humps aggregate together and form very rough surface, correspondingly, the c-AFM image shows very high current spikes all over the surface (note the current axis unit is 2 nA). These results give a clear picture of the transition from a-Si:H and  $\mu\text{c-Si:H}$ .





**Fig. 4** Regular surface morphology AFM images (bottom) and corresponding c-AFM images (top) in the same areas for an a-Si:H (left), a mixed-phase (middle), and a  $\mu$ c-Si:H (right) samples (Yan et al. 2007)



**Fig. 5** Left panel: (a) Real  $\epsilon_1$  and (b) imaginary  $\epsilon_2$  parts of the dielectric functions at 200 °C for the R = 20 Si:H film at the bulk thickness of 20 nm and 195 nm, right panel: surface roughness layer versus the bulk layer thickness for three samples with different hydrogen dilution R (Collins et al. 2003)

Real-time spectroscopic ellipsometry (RTSE) is also widely used for a-Si:H and  $\mu$ c-Si:H characterization, especially the transition from a-Si:H to  $\mu$ c-Si:H. By analyzing measured real and imaginary parts of the dielectric functions of a thin film versus photo-energy, the bulk thickness and surface roughness can be obtained. Reviews of RTSE and details of the analyses can be found in Ref. Collins et al. (2003) and Dahal et al. (2014).

Figure 5 shows an example of measurement and analysis results, where the left plots are the measured real and image parts of the dielectric function spectra for the deposition with hydrogen dilution ratio R = 20 ( $H_2/SiH_4$ ) at 200 °C at two thickness of 20 nm and 195 nm, and the right plot gives the analysis results of the surface roughness as a function of bulk layer thickness for three deposition processes with hydrogen dilution ratios R of 0, 10, and 20. By systematic measurements and analyzing different deposition processes, the transition model from a-Si:H to  $\mu$ c-Si:H has been built (Collins et al. 2003), which gives a very useful guideline for  $\mu$ c-Si:H material and device optimizations.

## Electronic Properties of $\mu$ c-Si:H

Dark- and photo-conductivities are critical parameters for solar cell applications. The absorber layer needs to have a low dark conductivity, a high photo-conductivity, and hence a high photosensitivity. Because of the inclusion of crystalline phase, the dark-conductivity of  $\mu$ c-Si:H is higher than of a-Si:H and it increases with the increase of crystalline volume fraction. Figure 6 gives examples of dark- and photo-conductivities as a function of silane concentration ( $SiH_4/(SiH_4 + H_2)$ ) in the deposition process (Vettea et al. 2002). It shows that both the dark- and photo-

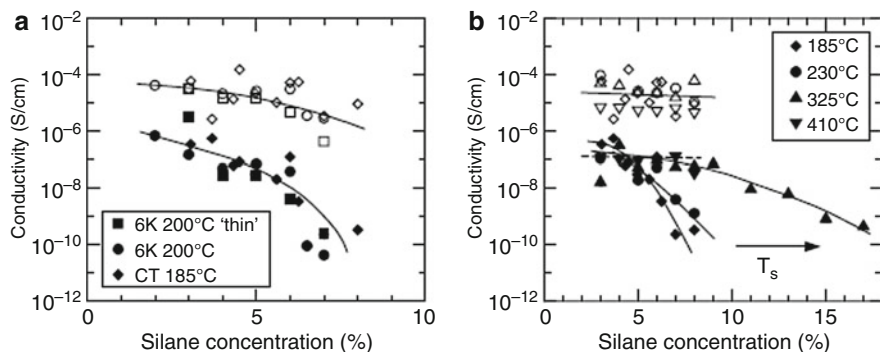


**Fig. 6** Dark-conductivity (filled symbols) and photo-conductivity (open symbols) of films prepared at various silane concentrations. (a) Results for similar substrate temperatures of 200 °C and 185 °C in two different deposition systems, also including a series with a reduced thickness of 50–100 nm ("thin"). (b) Substrate temperature dependent results. Measurement error is within marker size (Vettea et al. 2002)

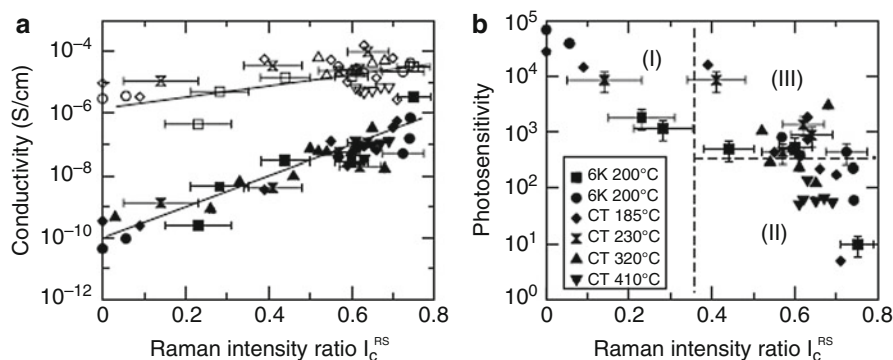
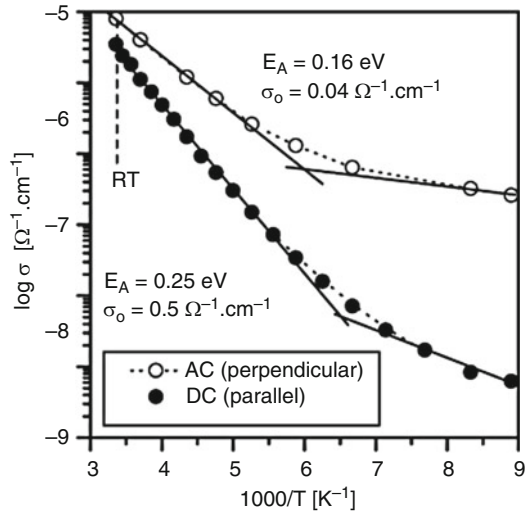


**Fig. 7** (a) Dark-conductivity (filled symbols) and photo-conductivity (open symbols) as a function of integrated Raman intensity ratio  $I_C^{RS}$ , (b) photosensitivity as a function of  $I_C^{RS}$ . Same symbols are used in both figures. For better readability, only exemplary error bars are included (Vettea et al. 2002)

conductivity increase with the decrease of silane concentration. As will be discussed later, high hydrogen dilution (low silane concentration) promotes the formation of microcrystalline phase. Therefore, conductivity is related to the material structure. Figure 7 (a) plots the dark- and photo-conductivities and (b) the photosensitivity as a function of crystalline volume fraction from the Raman measurement (Vettea et al. 2002). It shows that both the dark- and photo-conductivities increase with the increase of crystallinity, but the photosensitivity decreases with the increase of crystallinity. The dark-conductivity increases from  $10^{-11} (\Omega\text{cm})^{-1}$  of a-Si:H to  $10^{-6} (\Omega\text{cm})^{-1}$  of high crystallinity  $\mu\text{c-Si:H}$  by 5 orders of magnitude, while the increase of photo-conductivity is much slower than the dark-conductivity by only

**Fig. 8** Arrhenius plot of parallel conductivity (DC) (parallel to the substrate) and perpendicular conductivity (AC) (perpendicular to the substrate) measured on the  $\mu\text{-Si:H}$  sample with 2.2 mm thickness (Kocka et al. 2003)



one order of magnitude, which results in the decline of photosensitivity with the increase of crystallinity.

The conductivity of  $\mu\text{-Si:H}$  materials is anisotropy, which means that it is different between the directions of parallel and perpendicular to the film surface with a much higher conductivity in the perpendicular than the parallel directions. This is caused by the unique material structure with crystalline columnar structures perpendicular to the substrate. Even with a smaller crystalline volume fraction than the percolation threshold, the crystalline columnar structure can form perpendicular transport paths for current flow. Figure 8 shows a comparison of perpendicular conductivity (AC) and parallel conductivity (DC) as a function of inverse temperature, indicating a much higher conductivity and lower activation energy in the perpendicular direction than in the parallel direction (Kocka et al. 2001, 2003). With a simple mind thinking, if  $\mu\text{-Si:H}$  has columnar structured nanocrystalline clusters perpendicular to the substrate, the crystalline phase is easy to form transport path for current flow, while the carrier transport in the parallel direction needs go over the amorphous tissues and the grain boundaries.

The anisotropy conductivity of  $\mu\text{-Si:H}$  has a significant impact on solar cell design and fabrication where the carrier transport is in the perpendicular direction, while the commonly used conductivity measurement with two parallel electrodes deposited on the sample surface does not give the real transport properties in solar cells. In addition, the parallel conductivity might be dominated by the high conductive layer on the top surface, while the perpendicular conductivity might be influenced by the low conductive a-Si:H incubation layer. Therefore, the optimization of  $\mu\text{-Si:H}$  materials for solar cell application needs to carefully consider the perpendicular transport. The anisotropy conductivity of  $\mu\text{-Si:H}$  has some advantages, especially in the doped layers. The high perpendicular conductivity with a low crystallinity allows enough conductances for the current flow, but the low parallel

conductivity prevents the lateral collection to improve the open circuit voltage ( $V_{oc}$ ) and fill factor (FF).

For solar cell application, the most important transport parameter is the hole mobility-lifetime product, which limits the collection length of carriers and hence the maximum cell thickness allowing to have enough short circuit current density ( $J_{sc}$ ) without significant loss in FF. Time-of-flight (TOF) measurements found that the hole drift mobility in a-Si:H is normally in the order of  $0.01 \text{ cm}^2/\text{Vs}$  (Gu et al. 1994), while it increases by two orders of magnitude to the level of  $1 \text{ cm}^2/\text{Vs}$  (Dylla et al. 2005). The high hole mobility allows to use much thicker absorber layer in  $\mu\text{c-Si:H}$  solar cells ( $3\text{--}5 \text{ }\mu\text{m}$ ) than in a-Si:H solar cells ( $0.2\text{--}0.3 \text{ }\mu\text{m}$ ).

### Optical Properties of $\mu\text{c-Si:H}$

The advantage for using  $\mu\text{c-Si:H}$  as the intrinsic layer in solar cell is absorbing the long wavelength light for high  $J_{sc}$ ; therefore, a high absorption coefficient ( $\alpha$ ) at the long wavelength is an important signature of  $\mu\text{c-Si:H}$ . Figure 9 shows an example of the comparison of measured absorption coefficients of  $\mu\text{c-Si:H}$ , intrinsic a-Si:H, and c-Si, from which a few observations are made (Shah et al. 2003). First, comparing to a-Si:H,  $\mu\text{c-Si:H}$  has a significant high absorption coefficient in the energy below the a-Si:H bandgap, proving the advantage of  $\mu\text{c-Si:H}$  for the long wavelength absorption in solar cell application. Second, the absorption coefficient spectrum of  $\mu\text{c-Si:H}$  has a similar shape as of c-Si but with much higher values. It has been confirmed that the measured high absorption is caused by the scattering of the rough surface and the internal scattering by the grain boundaries in the films. The scattering effects can be removed and the measured absorption coefficients are reduced. Figure 10 shows a

**Fig. 9** Effective absorption coefficient spectra of as measured  $\mu\text{c-Si:H}$ , c-Si, and intrinsic a-Si:H materials (Shah et al. 2003).

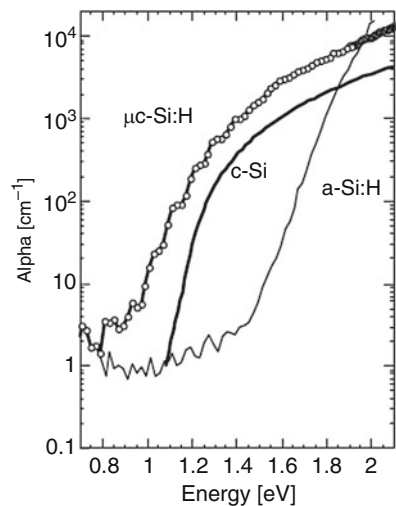
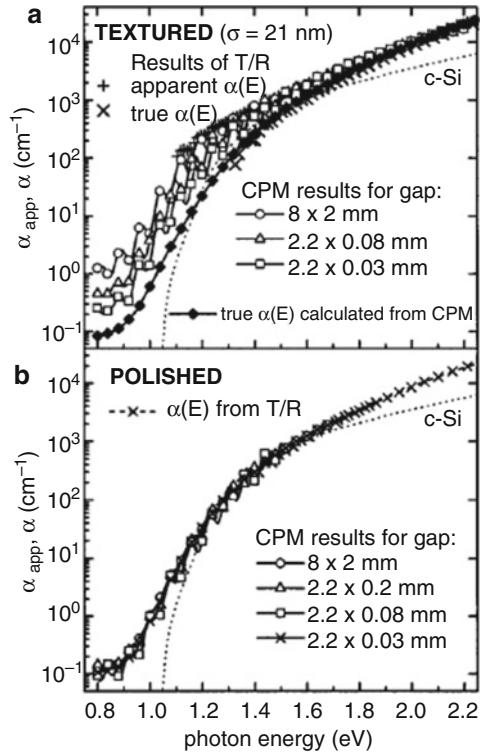
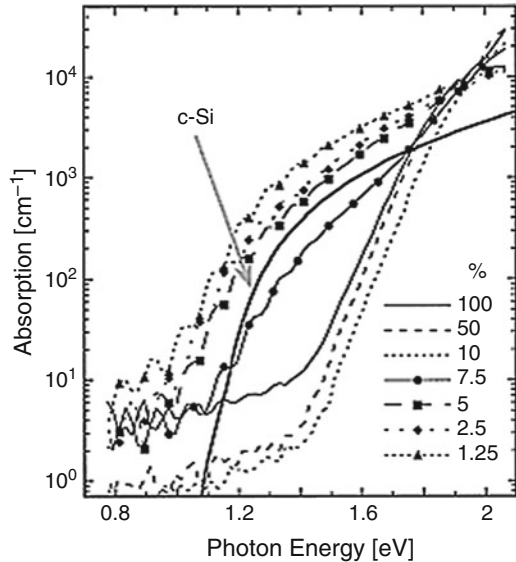


**Fig. 10** Apparent optical absorption coefficients of a  $\mu\text{-Si:H}$  sample measured by CPM with different interelectrode spacing (gap) and calculated from T/R measurements: (a) in the as-grown state (textured sample) and (b) after a chemomechanical polishing. The evaluated spectral dependence of the true absorption coefficient  $\alpha(E)$  is shown as the main result by full diamonds;  $\alpha(E)$  of crystalline silicon is shown for comparison. The value of the RMS surface roughness of  $\sigma = 21$  nm of the as-grown sample was evaluated from the T/R data (Poruba et al. 2000)



careful study of removing the scattering effect to obtain the true absorption coefficient spectra in  $\mu\text{-Si:H}$ . The measurements were made with the regular transmission (T) and reflection (R) spectra and constant photocurrent method (CPM) (Poruba et al. 2000), where (a) plots the apparent results with different electrode gaps that affects the scattering effect and the true absorption coefficients by modeling the results to remove the scattering effect, and (b) is the results from a polished sample with different gaps showing the same results without the influence from the scattering. Comparing the results in Fig. 10 (a), one can see that the scattering indeed affects the apparent absorption significantly, especially the long wavelength region, where the low absorption coefficients require a long path for the light to be absorbed. Although the scattering effect leads to a great challenge to obtain the true absorption coefficients, from solar technology point of view, the enhanced absorption by scattering is an important feature for solar cell application because it allows using a much thinner absorber layer than c-Si solar cells. Third, the true absorption coefficients of  $\mu\text{-Si:H}$  in the energy higher than the bandgap of a-Si:H are much higher than in c-Si, which is due to the contribution of the a-Si:H phase; it is also higher than in c-Si in the energy lower than the c-Si bandgap, which results from the absorption in the tail states in  $\mu\text{-Si:H}$ . The absorption coefficient of  $\mu\text{-Si:H}$  does not go down to zero in the energy below the bandgap of c-Si:H at 1.12 eV. This does not

**Fig. 11** Optical absorption of the a-Si:H and  $\mu$ c-Si:H films prepared at different silane concentrations as indicated in the figure. For comparison, the absorption of monocrystalline silicon is added (Kroll et al. 1998).



mean  $\mu$ c-Si:H has a narrower bandgap than c-Si, instead indicates a band-tail absorption as the case of a-Si:H.

Logically thinking, the absorption spectrum of  $\mu$ c-Si:H should depend on the crystalline volume fraction with the higher the crystalline volume fraction, the higher the long wavelength absorption is. This trend has been observed experimentally as shown in Fig. 10 (Kroll et al. 1998), where the absorption coefficient spectra of  $\mu$ c-Si:H films made with different silane concentrations for achieving different crystalline volume fractions. It demonstrates that the absorption coefficient at photon energy below the a-Si:H bandgap of  $\sim 1.8$  eV increases significantly but decreases slightly at above  $\sim 1.8$  eV. The increases of the low energy absorption coefficients with the reduction of silane concentration are due to the increases of the absorption in the crystalline phase and the increased scattering effect; the slight reductions of absorption in the high energy region result from the reduced a-Si:H component (Fig. 11).

There was a confusion concept about the bandgap of  $\mu$ c-Si:H. Because it has normally observed that the  $V_{oc}$  of  $\mu$ c-Si:H solar cells increases with the decrease of crystallinity (Droz et al. 2004). Logically one would expect the bandgap of  $\mu$ c-Si:H increases with the decrease of the crystallinity. But it might not be true. First, the definition of bandgap is the energy between the conduction band edge  $E_c$  and the valence band edge  $E_v$ . It should be no energy states between  $E_c$  and  $E_v$  in the ideal case. Since  $\mu$ c-Si:H is a mixture of amorphous tissues and c-Si grains, the definition of the bandgap is sometime confusion and ill-defined. First, the areas of c-Si phase should have the same bandgap as c-Si bulk materials without considering the quantum confinement, while the areas of amorphous phase should have the similar optical properties as a-Si:H. For the  $\mu$ c-Si:H materials used in solar cells, the crystalline phase must form a transport path and the carrier transport mainly takes place in the c-Si phase; therefore, the transport or mobility bandgap of the  $\mu$ c-Si:H



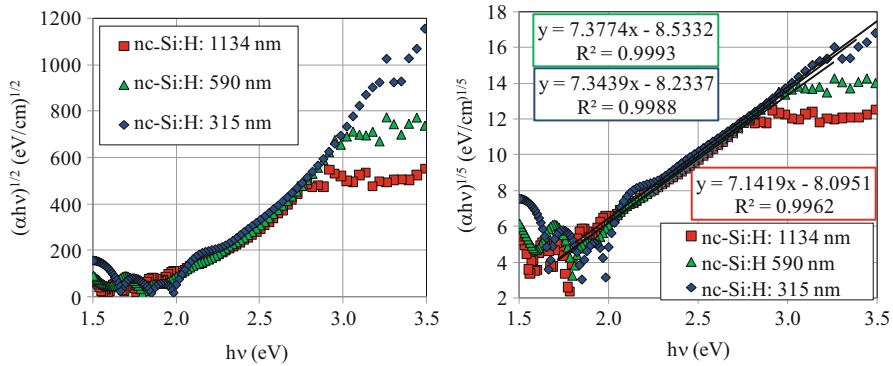


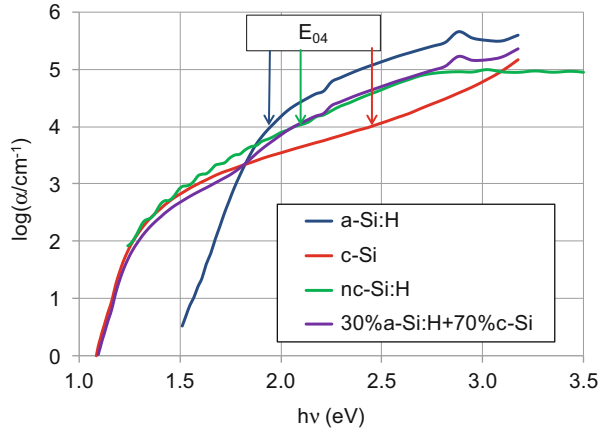
**Fig. 12** (left): the Tauc plot of  $(h\nu\alpha)^{1/2}$  versus  $h\nu$ , and (left):  $(h\nu\alpha)^{1/5}$  versus  $h\nu$  of three  $\mu c$ -Si:H films with different thicknesses made under the same condition

should be the same as c-Si of 1.12 eV. By analyzing the dark current-voltage characteristics of  $\mu c$ -Si:H solar cells, Yan et al. (2013) proved that the mobility bandgap of  $\mu c$ -Si:H is indeed the same as c-Si. Therefore, when considering the carrier transport in  $\mu c$ -Si:H, one should only consider the bandgap of c-Si phase with the same value of 1.12 eV. The optical bandgap does not have a unified definition for the mixed-phase materials. For a-Si:H, the optical bandgap is normally defined by the linear Tauc plot of  $(h\nu\alpha)^{1/2}$  versus  $h\nu$ ; Yan et al. (2013) also showed that the Tauc plot of  $(h\nu\alpha)^{1/2}$  versus  $h\nu$  does not have a good linear relation as given in Fig. 12; instead the  $(h\nu\alpha)^{1/5}$  versus  $h\nu$  yields a linear relation and gives an intersection at around 1.2–1.3 eV. However, it is difficult to find out an acceptable physics to explain such relation. Therefore, the optical bandgap is difficult to be obtained by the Tauc plot. The curvature in the Tauc plot can be explained with effective medium theory by the composition of the absorption coefficient spectra of a-Si:H and c-Si with a given crystalline volume fraction as shown in Fig. 13 (Yan et al. 2013). It is obvious that combining the two absorption spectra with different bandgaps does not obtain a straight line in the Tauc plot. It is also often to use the energy at which the absorption coefficient is  $10^4 \text{ cm}^{-1}$  as the definition of optical bandgap ( $E_{04}$ ), but the  $E_{04}$  is sometimes misleading as shown in Fig. 13, where the  $E_{04}$  of c-Si is larger than the  $E_{04}$  of  $\mu c$ -Si:H and the  $E_{04}$  of  $\mu c$ -Si:H is larger than the  $E_{04}$  of a-Si:H. Therefore, the  $E_{04}$  in  $\mu c$ -Si:H may not give the information of the optical bandgap.

To summarize the optical properties of  $\mu c$ -Si:H, we may conclude that the absorption coefficients of  $\mu c$ -Si:H can be composited by combining the spectra of c-Si and a-Si:H with a given crystalline fraction. Therefore, the absorption coefficient in the high energy region decreases and in the low energy region increases with the increase of crystalline volume fraction. The mobility bandgap in  $\mu c$ -Si:H is the same as in c-Si when carrier transport takes place in the crystalline phase, but the optical bandgap does not have a clear definition yet. The measured absorption coefficients of  $\mu c$ -Si:H could be much larger than the real ones because of the



**Fig. 13** Absorption coefficient spectra of  $\mu\text{c-Si:H}$ , c-Si, a-Si:H, and a combination of 30% of a-Si:H and 70% of c-Si (Yan et al. 2013)



scattering by the rough surface or the internal grain boundaries, which is an important feature for  $\mu\text{c-Si:H}$  allowing to use much thinner absorber layer in solar cells.

## Application of $\mu\text{c-Si:H}$ in Solar Cells and Issues for Efficiency Improvement

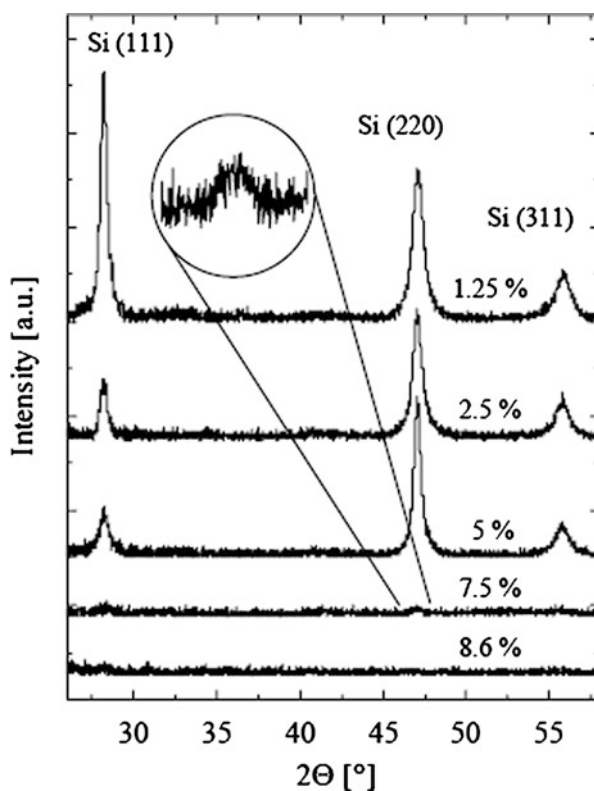
The fabrication of high quality  $\mu\text{c-Si:H}$  materials and efficient solar cells has been facing numerous challenges. First the material structure is not uniform along the growth direction when a constant deposition condition is used; the materials show an initial a-Si:H incubation layer and the crystallinity increases with the film thickness, which is called “crystalline evolution” and has a significant impact on solar cell optimization. Second,  $\mu\text{c-Si:H}$  films made with no intentional doping normally contain a high concentration of impurity that results in  $10^{17} \text{ cm}^{-3}$  donors, which leads to the Fermi level close to the conduction band edge and therefore with a low activation energy, a high dark conductivity, and a low photo-response. This high conductive  $\mu\text{c-Si:H}$  cannot be used as the absorber layer in solar cells. The third challenge is to make compactly structured  $\mu\text{c-Si:H}$  materials to avoid the postdeposition impurity diffusion. It has been often found that a high density of microvoids and microcracks in  $\mu\text{c-Si:H}$  materials made under unoptimized conditions, especially at high deposition rates. The microvoids and microcracks are mainly at the grain boundaries in the samples with a high crystalline volume fraction, where the grain boundaries between large grains are difficult to be passivated. The fourth challenge is the required thickness of  $\mu\text{c-Si:H}$  intrinsic layer in solar cells. For an a-Si:H solar cell, the intrinsic layer is normally in the range of 200–300 nm, but it requires approximately ten times more thicker in a  $\mu\text{c-Si:H}$  solar cell. Although the long wavelength absorption in  $\mu\text{c-Si:H}$  is higher than in a-Si:H, it is still an indirect bandgap in the crystalline phase and the absorption coefficient is not high enough to absorb sufficient long wavelength light with a thin  $\mu\text{c-Si:H}$  layer. Normally the intrinsic  $\mu\text{c-Si:H}$  layer needs to be 2–3  $\mu\text{m}$  thick and even up to 5  $\mu\text{m}$ . Although it is

significantly thinner than a wafer used in c-Si solar cell, it is much thicker than the intrinsic layer in a-Si:H solar cells. Consequently, the deposition rate of  $\mu\text{c-Si:H}$  should be approximately 10 times higher than the deposition rate of a-Si:H for reaching the same production rate of thin film solar modules as using a-Si:H and a-SiGe intrinsic layers. For this consideration, the target deposition rate should be 2–3 nm/s for  $\mu\text{c-Si:H}$  in thin film silicon solar panel production. Below we will address these issues and approaches to resolve these issues for high efficiency  $\mu\text{c-Si:H}$  solar cells.

### Crystalline Evolution and Hydrogen Dilution Profile

As mentioned above, the key technique for depositing  $\mu\text{c-Si:H}$  is the high hydrogen dilution. Using a PECVD system, one can make a-Si:H and  $\mu\text{c-Si:H}$  with different deposition conditions such as high hydrogen dilution, high excitation power, and high pressure. The most effective parameter controlling the amorphous/microcrystalline transition is the hydrogen dilution ratio defined as  $R = \text{H}_2/\text{SiH}_4$  or the silane concentration defined as  $\text{SC} = \text{SiH}_4/(\text{H}_2 + \text{SiH}_4)$ . Figure 14 shows an example of XRD patterns of Si:H films deposited with different SC (Kroll et al. 1998). It notes

**Fig. 14** XRD spectra of Si:H films made with different silane concentrations (Kroll et al. 1998)



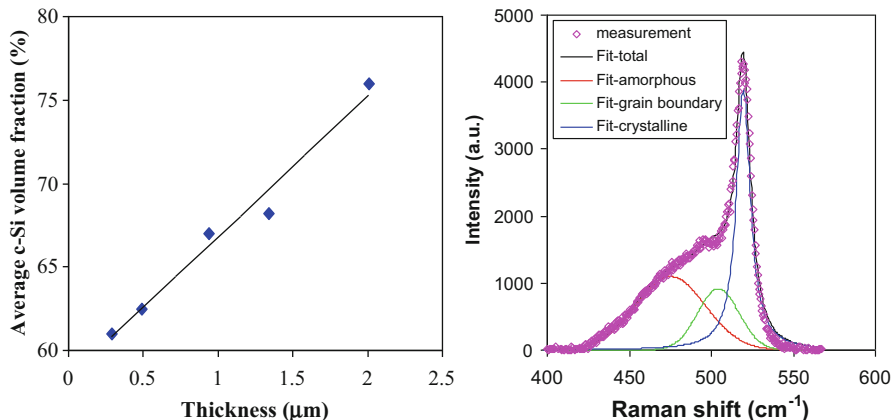


**Fig. 15** (right): A Raman spectrum of  $\mu\text{c-Si:H}$  film with three component fittings after a linear baseline correction; (left) crystalline volume fraction as a function of film thickness (Yan et al. 2004a)

that the film made with 8.6% of silane shows no any indication of c-Si peaks, 7.5% with an indication of c-Si formation with the (220) preferential orientation peak as observed in the enhanced scale, and the c-Si peaks increase with the decrease of silane concentration. The films made with 5% and 2.5% show a strong (220) preferential orientation, while the (111) peak becomes stronger than the others in the sample with 1.25% silane concentration. This result clearly proves that the hydrogen dilution is an effective parameter to control the crystallinity in  $\mu\text{c-Si:H}$  materials.

Another interesting phenomenon in  $\mu\text{c-Si:H}$  deposition is the so-called crystalline evolution as shown in Fig. 15a, where the crystalline volume fraction increases with the film thickness increase when the deposition is made under a constant condition. The crystalline volume fraction is measured by the Raman spectra as shown in Fig. 15b with three component fittings (Yan et al. 2004a) as discussed previously with  $m = 1$ . The Raman measurements were made with Ar ion laser with the wavelength of 514 nm, which only probes the top layer of the samples.

Collins et al. have done a systematic study about the transition from a-Si:H to  $\mu\text{c-Si:H}$  and the crystalline evolution with the comparison of cross-sectional TEM and RTSE (Collins et al. 2003; Dahal et al. 2014). Figure 16 shows an example of cross-sectional TEM, where one could observe (1) a clear cone structured crystalline phase formed with a cone angle  $\theta$  and (2) a crystallite seed density  $N_d$  after an a-Si:H incubation layer deposition (Collins et al. 2003). The cone growth with the film thickness agrees well with the increase of crystallinity with film thickness.

On the same sample, RTES was measured and analyzed to obtain the crystallinity with the result shown in Fig. 17 (Collins et al. 2003), in which the crystallinity increases starting from around 30 nm of the a-Si:H incubation layer. Based on this analysis, a cone growth structure model is built as shown in Fig. 18 (Collins et al. 2003). It includes three zones: (I) the a-Si:H incubation layer, (II) the cone growth zone, and (III) the zone after the cone coalescence. In zone I, the crystalline volume

**Fig. 16** A cross-sectional TEM image of a  $\mu\text{c-Si:H}$  film made with hydrogen dilution  $R = 20$ . A clear-cone structured crystalline phase formed with a cone angle  $\theta$  and crystallite seed density  $N_d$  (Collins et al. 2003)

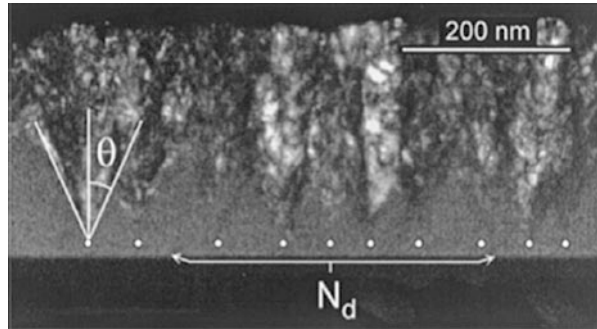
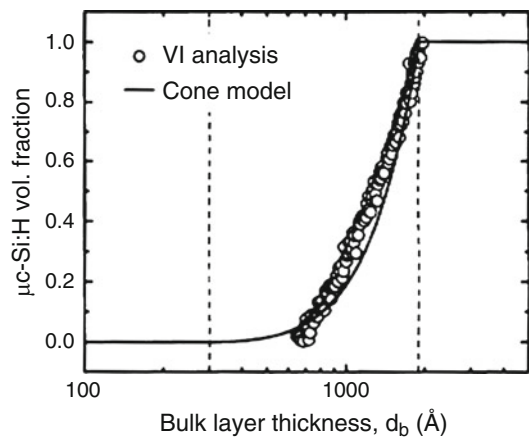


**Fig. 17** Crystalline volume fraction estimated from the RTSE analysis as a function of film thickness. The crystalline formation starts from around 30 nm (Collins et al. 2003)



fraction is undetectable and the surface roughness slightly decreases due to the coalescence of the amorphous islands; in zone II, the crystalline volume fraction and the surface roughness both increase with the film thickness due to the growth of the cones; and finally in zone III, the crystalline volume fraction reaches 100% and the surface roughness starts to decrease due to the coalescence of the crystalline cones. It needs to point out that the estimated crystalline volume fractions by RTSE are normally larger than the estimations from Raman spectra.

Based on this RTSE analysis, a phase diagram was built up as shown in Fig. 19 (Collins et al. 2003), where the horizontal axis is hydrogen dilution  $R$ , and vertical axis the bulk film thickness. Three transitions between four zones are identified as the amorphous unstable surface zone to amorphous stable surface zone transition ( $a \rightarrow a$ ), amorphous stable surface zone to mixed-phase zone transition ( $a \rightarrow a + \mu\text{c}$ ), and mixed-phase zone to microcrystalline phase zone ( $a + \mu\text{c} \rightarrow \mu\text{c}$ ). Details of the analyses and the meaning of each zone and transition are referred to Ref. Collins et al. (2003). This phase diagram is a very useful tool for guiding the design and optimization of thin film solar cells. It has been found that the best a-Si:H solar cells are made at a high hydrogen dilution close to the transition from amorphous to

**Fig. 18** (a) Surface roughness layer thickness ( $d_s$ ) versus bulk layer thickness ( $d_b$ ) for the  $R = 20$  Si:H film; (b) schematic of the cone growth model used to estimate the crystallite nuclei density and cone angle based on the surface roughness evolution (Collins et al. 2003)

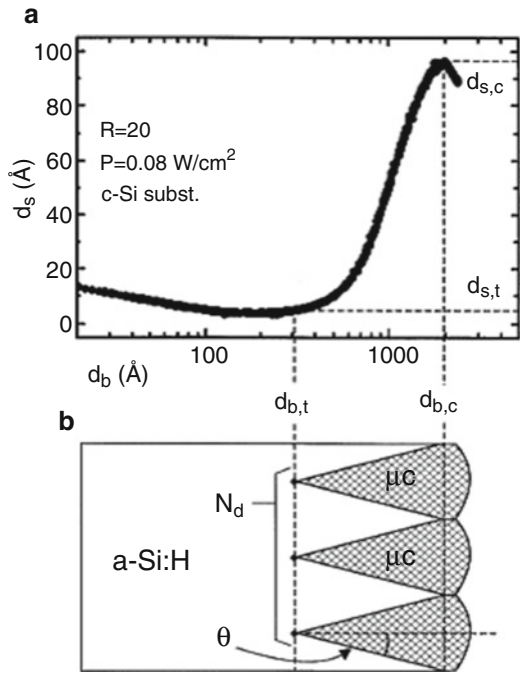
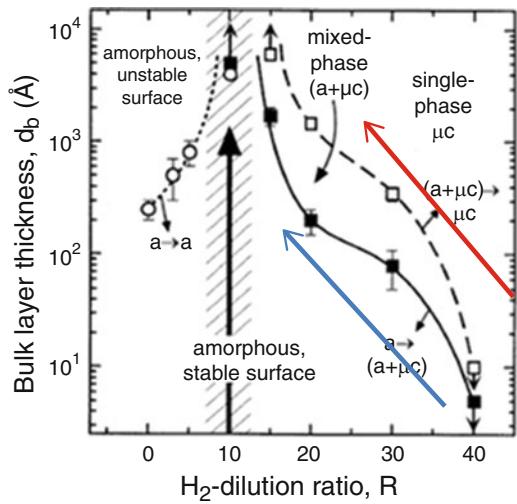


**Fig. 19** A phase diagram of Si:H film deposition under a condition given in Collins et al. (2003)



microcrystalline phases and keep it out of the mixed-phase zone; therefore, to make high efficiency a-Si:H solar cells, one should design a process along the blue arrow; similarly, for high efficient μc-Si:H solar cells, they are made with a condition close to the transition from microcrystalline to amorphous phases but still in the

microcrystalline phase; therefore, one should design a process along the red arrow in the figure for high efficiency  $\mu\text{-Si:H}$  solar cells.

The crystalline evolution has several negative impacts on the solar cell performance. First, the a-Si:H incubation layer has a high resistivity than  $\mu\text{-Si:H}$ , in which photocarriers have to pass through with a low mobility that results in additional series resistance and reduces the FF. Second the mixed phase region normally has a high defect density that affects the cell performance remarkably, and finally the top layer with very high crystallinity easily forms a high density of microvoids and cracks, which results in the postdeposition impurity diffusion. Therefore, for high efficiency solar cells, one has to avoid the crystalline evolution.

To resolve the crystalline evolution issue, a hydrogen dilution profile technique was proposed by Yan et al. (2004a, b) and was proven to be an effective method to improve the performance of  $\mu\text{-Si:H}$  solar cells. The basic concept of hydrogen dilution profile is consistent with the red arrow as in Fig. 19. A very high hydrogen dilution ratio at the starting of the deposition removes the a-Si:H incubation layer and follows with a continual decrease of hydrogen dilution with deposition time to maintain the same crystallinity as the film growth. Figure 20 shows a cross-sectional TEM image of a  $\mu\text{-Si:H}$  film deposited with a hydrogen dilution profile, where the bottom thin layer is an a-Si:H n-layer. The result shows no a-Si:H incubation layer and a uniform crystalline structure. It demonstrates the effectiveness of the hydrogen dilution profile on the controlling of crystalline evolution. This technique is also effective on the solar cell efficiency improvement. Table 1 lists the current density versus voltage (J-V) characteristics of the  $\mu\text{-Si:H}$  solar cells made with various hydrogen dilution profiles (Yan et al. 2004a, b). Three baseline cells show a  $J_{\text{sc}}$  around 22–23 mA/cm<sup>2</sup>. But the two cells with 20% longer intrinsic layer

**Fig. 20** A cross-sectional TEM image of a  $\mu\text{-Si:H}$  film deposited with a hydrogen dilution profile, showing an uniform crystalline structure

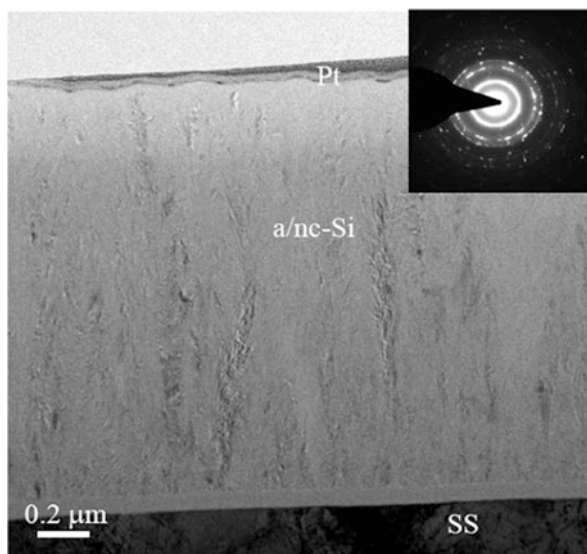


**Table 1** Performance parameters of  $\mu\text{-Si:H}$  solar cells made with various hydrogen dilutions

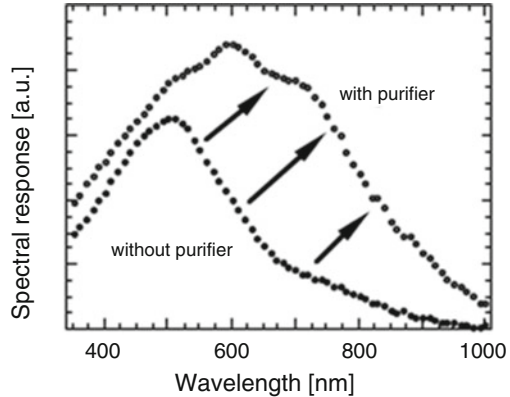
Sample #	$J_{sc}$ (mA/cm <sup>2</sup> )	$V_{oc}$ (V)	FF			Eff (%)	Comments
			AM1.5	Blue	Red		
14,554	22.58	0.495	0.603	0.652	0.615	6.74	Flat baseline
14,568	22.15	0.488	0.599	0.648	0.599	6.48	
14,596	22.05	0.482	0.622	0.656	0.605	6.61	
14,559	21.48	0.482	0.632	0.678	0.637	6.54	20% thicker than baseline
14,562	21.57	0.484	0.652	0.692	0.651	6.81	
14,578	23.22	0.482	0.594	0.646	0.631	6.63	Profiling 1
14,580	22.58	0.484	0.644	0.688	0.662	7.04	Profiling 2
14,612	24.41	0.485	0.616	0.659	0.647	7.29	Profiling 3
14,619	24.63	0.492	0.645	0.683	0.641	7.81	Profiling 4
14,642	23.42	0.502	0.681	0.706	0.700	8.01	Profiling 5
<b>14,660</b>	<b>25.15</b>	<b>0.502</b>	<b>0.663</b>	<b>0.679</b>	<b>0.693</b>	<b>8.37</b>	<b>Profiling 6</b>

deposition time show a lower  $J_{sc}$ , mainly due to the reduction in the long wavelength response. The six hydrogen dilution profiles from 1 to 6 are designed with the increase of the grading slope of the hydrogen dilution ratio but with the same average hydrogen dilution, which means that profile-6 has highest hydrogen dilution ratio at the beginning of the deposition but the lowest at the end of the deposition. It clearly demonstrates that the hydrogen dilution profiling has improved the cell performance significantly, especially the long wavelength response. The cells with the constant hydrogen dilution have an average initial active-area efficiency of 6.6%. By using the hydrogen dilution profiling, an efficiency of 8.37% was obtained. The hydrogen dilution profile technique has been widely used in the community for improving  $\mu\text{-Si:H}$  solar cell performance. Because the  $\mu\text{-Si:H}$  deposition is a multivariable system and the material structure and quality depend on all of the parameters, the crystalline evolution could be also controlled by other parameters such as the excitation power and temperature. Han et al. (2010) using a RF power profile method achieved the same effect as hydrogen dilution profile. We need to point out that the initial grow of the film is very important such that one has to eliminate the a-Si:H incubation layer. Several methods have been proposed for making incubation free  $\mu\text{-Si:H}$  layers such as a very high hydrogen diluted seed layer (Vetterl et al. 2003), a prehydrogen plasma treatment (Zhang et al. 2011), and using reactive etching gases such as F or Cl containing gases (Kasouit et al. 2002; Chung et al. 2011).

## Impurity Issue and Controlling

As pointed previously, most of  $\mu\text{-Si:H}$  films made in the early stage showed a high conductivity with N-type carrier transport, and it was found that the high conductivity is caused by O impurity because O becomes weak donors in  $\mu\text{-Si:H}$ . The tolerance for O in a-Si:H is in the order of  $1\text{--}2 \times 10^{19} \text{ cm}^{-3}$ , but it is only  $5 \times 10^{18} \text{ cm}^{-3}$  in  $\mu\text{-Si:H}$  (Merdzhanova et al. 2012; Woerdenweber et al. 2012). The incorporation of O in

**Fig. 21** EQE comparison of  $\mu\text{-Si:H}$  solar cells made with and without a gas purifier in the deposition system (Torres et al. 1996)



$\mu\text{-Si:H}$  comes from the residual impurities in the deposition system, gases, and postdeposition diffusion from the ambient. In order to reduce the unintentional doping, using a clean system with high purity gases, especially  $\text{H}_2$ , is critical for the deposition of high quality  $\mu\text{-Si:H}$  films. In addition, optimized deposition conditions are essential for highly compacted material structure to avoid postdeposition impurity diffusion.

Figure 21 shows a comparison of two  $\mu\text{-Si:H}$  silicon solar cells with different impurity levels achieved with and without a gas purifier. It clearly demonstrates that the gas purifier significantly improved the cell performance. Secondary ion mass spectroscopy (SIMS) analysis showed that the gas purifier can reduce the O level from above  $10^{19} \text{ cm}^{-3}$  down to  $5 \times 10^{18} \text{ cm}^{-3}$  (Meier et al. 1996).

The impurities in  $\mu\text{-Si:H}$  are not only incorporated in during the deposition, but also diffuse into the materials after the deposition and air exposure if the materials are not compact enough. Small angle X-ray scattering (SAXS) measurements showed that unoptimized  $\mu\text{-Si:H}$  materials could have a few percent of microvoids in volume (Williamson 2003), which allow impurities diffuse into the materials and degrade the solar cell performance. Figure 22 (upper) shows the dark-conductivity of an individual  $\mu\text{-Si:H}$  layer as a function of time keeping the sample in the ambient without light soaking, which clearly shows an increase of the dark-conductivity and associates with the reduction of activation energy from 0.52 eV to 0.17 eV; while as shown in lower panel of Fig. 22, the  $\mu\text{-Si:H}$   $p\text{-i-n}$  solar efficiency did not change at all during the air exposure, which was explained with the blocking the impurity diffusion by the back ZnO/metal contact in the solar cell (Meier et al. 1998).

The  $n\text{-i-p}$   $\mu\text{-Si:H}$  solar cells are not as lucky as the  $p\text{-i-n}$  solar cells because the  $n\text{-i-p}$  solar cells are normally deposited on nontransparent substrates and the top contact on the  $p$ -layer is an Indium-Tin-Oxide (ITO) layer with a thickness of  $\sim 75 \text{ nm}$  for the antireflection effect, which is not effective to block the impurity diffusion. Figure 23 shows the J-V characteristics and external quantum efficiency (EQE) curves of an early unoptimized  $\mu\text{-Si:H}$   $n\text{-i-p}$  solar cell in the as-deposited state and after 30 days keeping in the ambient (Yan et al. 2002). One can clearly see that the solar cell performance was degraded just keeping the cell in the ambient. A controlled experiment showed that the



**Fig. 22** Comparison of an intrinsic  $\mu\text{c-Si:H}$  film and the corresponding  $p-i-n$  solar cell as the function of air exposure after deposition. The film was characterized by the dark conductivity measurement and the cell by J-V measurements under AM 1.5. The dashed lines are drawn to guide the eye (Meier et al. 1998)

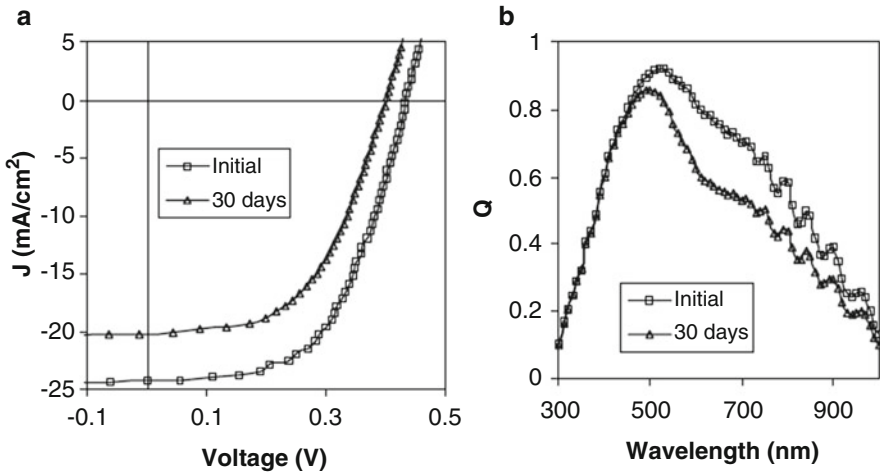
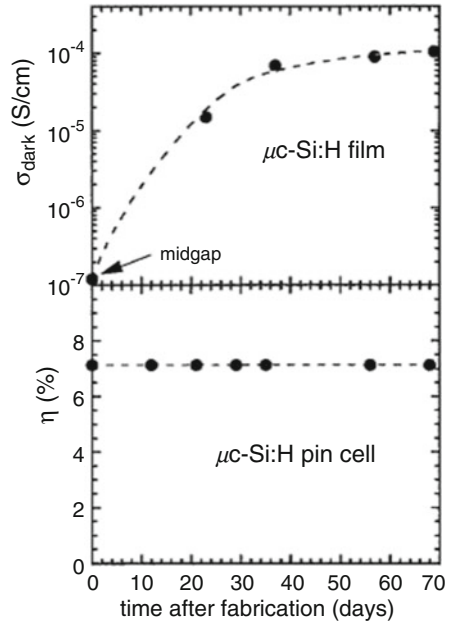


**Fig. 23** J-V characteristics and quantum efficiency (Q) of a  $\mu\text{c-Si:H}$  solar cell in the initial state and after 30 days exposure in the ambient without light soaking (Yan et al. 2002)

ambient degradation results mainly from the moisture in the air because keeping the cells in  $\text{N}_2$  and dry cold air prevented the ambient degradation, but the cell in hot and humid air accelerated the degradation (Yan et al. 2002). The ambient degradation mainly happened in the early stage of  $\mu\text{c-Si:H}$  solar cell study. After the

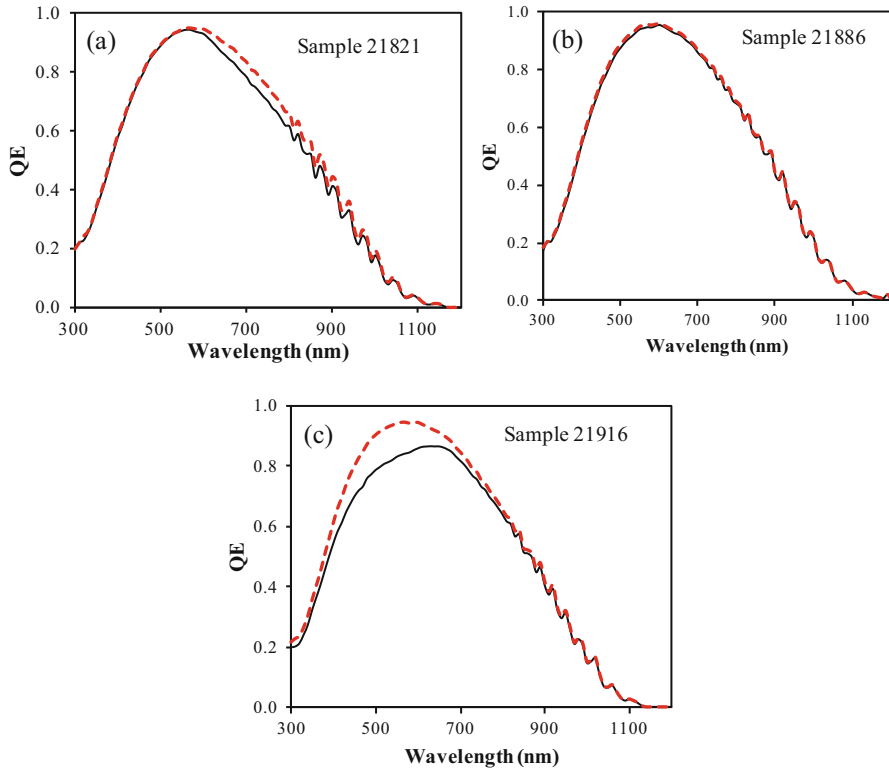


**Fig. 24** Quantum efficiency (QE) measured under -5 V bias (red dash lines) and the short circuit condition (thin solid black lines) for three samples with different QE losses, where (a) Sample 21,821 has a long wavelength QE loss; (b) Sample 21,886 has a minimal QE loss; and (c) Sample 21,916 has a short wavelength QE loss (Yue et al. 2012b)

optimization of the deposition process, high quality  $\mu\text{-Si:H}$  materials and  $n\text{-i-p}$  solar cells with compact structures and low density of microvoids do not suffer the ambient degradation problem. The optimization of the deposition process will be addressed later.

For the high quality  $\mu\text{-Si:H}$  materials and high efficiency  $\mu\text{-Si:H}$  solar cells, the impurity is still an issue. Yue et al. (2012a, b) have carefully studied the effect of impurity on high efficiency  $\mu\text{-Si:H}$  solar cells. Because of the high sensitivity of  $\mu\text{-Si:H}$  to impurity, most high efficiency solar cells are deposited in multichamber systems to reduce the cross-contaminations. Even in multichamber systems, the cross-contaminations cannot be absolutely avoided. Especially for B contamination, the level of  $10^{16} \text{ cm}^{-3}$  of B can cause a noticeable effect on  $\mu\text{-Si:H}$  solar cell performance. An example is given in Fig. 24, where the quantum efficiencies (QE) of three  $\mu\text{-Si:H}$  solar cells with the same background B contamination at  $2 \times 10^{16} \text{ cm}^{-3}$ , but with different O concentrations obtained by different deposition chamber conditionings as shown in Fig. 25. The QE measurements were made under

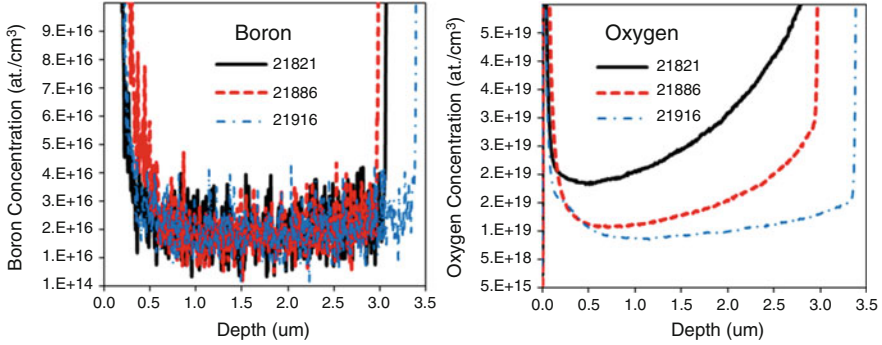


**Fig. 25** Boron and oxygen profiles measured with SIMS in three  $\mu\text{c-Si:H}$  solar cells made with different chamber conditionings (Yue et al. 2012b)

zero bias (short circuit) and  $-5$  V bias conditions. The photocurrent difference obtained from the two curves is called QE loss, which reflects the recombination loss. Because a reverse bias enhances the electric field in the intrinsic layer and reduces the recombination rate, the larger the difference between the reverse biased QE and the zero biased QE, the more the recombination loss is. In addition, the recombination occurring in different regions in the intrinsic layer reflects in the different wavelength ranges in the QE spectrum. A short wavelength light is mainly absorbed in the shallow region near the  $p/i$  interface; thus, the short wavelength QE loss reflects the recombination occurs mainly in the region near the  $p/i$  interface, while a long wavelength light is absorbed uniformly in the entire intrinsic layer, but the holes generated in the region near the  $i/n$  interface travel a longer distance than those generated in the  $p/i$  region; thus, the long wavelength loss detects the recombination in the region near the  $i/n$  interface. If the solar cell has more effective P-type contamination than effective N-type contamination, the electric field in the  $p/i$  region is weakened and in the  $i/n$  region is enhanced. As a result, a noticeable short wavelength loss is observed, while for the same reason a long wavelength QE loss measures an N-type contamination. Comparing the results in Figs. 24 and 25, one can see the correlation between the QE losses and the impurity distributions. Sample 21,821 has a high O content, especially in the  $i/n$  region, and has a noticeable long wavelength QE loss; sample 21,886 has the medium O content, the QE loss is almost undetectable, which means that the P-type and N-type contaminations are compensated each other, while sample 21,916 has the lowest O content, which shows a large short wavelength QE loss because the O contamination is not enough to compensate the B contamination. Table 2 lists the performance parameters of these three solar cells. Although sample 21,916 has the lowest O contamination, it has the lowest performance because of the loss of photo-current in the short wavelength; the middle O contaminated cell has the best efficiency of 10.5% with less than 1% of QE loss; but when the high O content is more than enough to compensate the B contamination as in 21,821, it causes the long wavelength QE loss. From these results, one can see how sensitive the  $\mu\text{c-Si:H}$  solar cells to impurities.

**Table 2** The performance parameters of  $\mu\text{-Si:H}$  solar cells with different impurity contaminations (Yue et al. 2012b)

Sample	Source	$V_{oc}$ (V)	FF	QE(mA/cm <sup>2</sup> )		QE loss (%)	Eff. (%)
				0 V	-5 V		
21,821 (N-type)	Filter 610	0.525	0.720	15.15	16.15	6.19	5.73
	AM1.5	0.541	0.720	26.54	27.65	4.01	10.34
21,886 (comp)	Filter 610	0.529	0.709	16.93	17.07	0.82	6.35
	AM1.5	0.543	0.691	28.15	28.43	0.98	10.56
21,916 (P-type)	Filter 610	0.516	0.649	15.79	16.34	3.37	5.29
	AM1.5	0.532	0.630	26.02	27.90	6.74	8.72

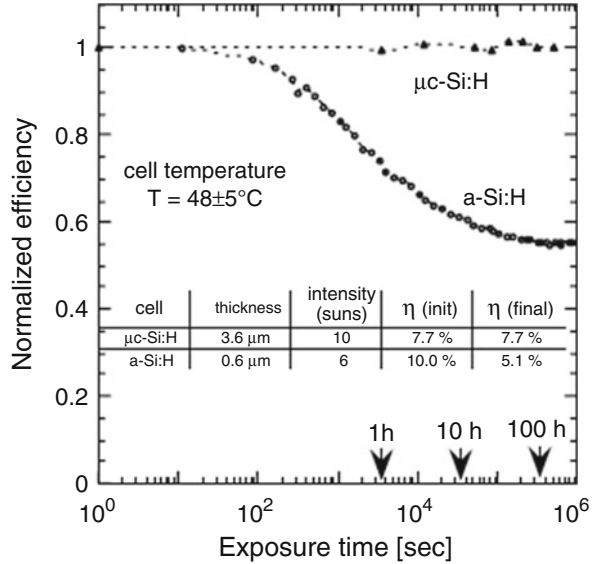
The above results demonstrate that the  $\mu\text{-Si:H}$  solar cells are very sensitive to impurities. For the P-type contamination by B, a very low level at  $10^{16} \text{ cm}^{-3}$  could cause a noticeable change in the cell performance as indicated by the short wavelength loss. The reason for such a low tolerance is that B is a strong donor in  $\mu\text{-Si:H}$ . In the early study, Meier et al. (1996) first used B to compensate the unintentional O doing to improve  $\mu\text{-Si:H}$  solar cell performance and achieved reasonable good results at the time and named the technique as microdoping. However, the high sensitivity of B doing leads to a narrow window for a proper compensation that also depends on the back ground N-type contamination; therefore, the microdoping technique might be only used as a method to study the fundamental contaminations and prove some concepts, but hardly be used in real high efficiency solar panel production. Similar to B, the sensitivity of  $\mu\text{-Si:H}$  to P is also very high. However, the back ground contaminations from O and N cover the residual P effect in most cases, and less attention has been made on P contamination. From the real solar cell fabrication point of view, multichamber systems with a very low degassing rate and using high pure gases are preferred. In addition, special cares must be taken in the process to avoid any cross contaminations from the doing gases.

### Light-Induced Metastability in $\mu\text{-Si:H}$ Solar Cells

One of the advantages of  $\mu\text{-Si:H}$  solar cells over a-Si:H counterparts is low or no light-induced degradation. Early studies showed that  $\mu\text{-Si:H}$  solar cells did not show any light-induced degradation as proven by Fig. 26 (Meier et al. 1998), where the  $\mu\text{-Si:H}$  solar cell efficiency did not change after 1000 hours of light soaking, while the a-Si:H solar cell degraded by almost 50%. However, some  $\mu\text{-Si:H}$  solar cells also show some degrees of light-induced degradations, especially those with a high percentage of amorphous phase.

Yan et al. (2004c) did a systematic study on the light-induced degradations in  $\mu\text{-Si:H}$  solar cells and compared a-Si:H and a-SiGe:H solar cells by using different light sources to determine where the light-induced degradation occurs. The design of the experiment is based on the hypothesis below. High efficiency  $\mu\text{-Si:H}$  solar cells are usually deposited near the transition from the microcrystalline to the amorphous

**Fig. 26** Comparative behavior of a  $\mu\text{-Si:H}$  solar cell and an a-Si:H solar cell under intensive light illumination, from a sodium lamp. Efficiencies were measured before/after light soaking under standard conditions (Meier et al. 1998)



phase (Vetterl et al. 2000; Roschek et al. 2000), which means that a finite amount of the amorphous phase still exists in the  $\mu\text{-Si:H}$  materials used in high efficiency solar cells. One therefore suspects that some light-induced degradations may present in the  $\mu\text{-Si:H}$  solar cells due to the amorphous component. Indeed, Klein et al. (2003) found that  $\mu\text{-Si:H}$  solar cells made with hydrogen dilution close to the microcrystalline/amorphous transition showed light-induced degradations and that the degree of degradations depended on the dilution ratio and hence on the crystalline volume fraction. In general,  $\mu\text{-Si:H}$  can be considered as a two-phase material with crystalline grains surrounded by amorphous tissues. The photons with energy higher than the bandgap of a-Si:H are mainly absorbed in the amorphous phase while the lower energy ones in the grains. Inside the grains, the material properties are similar to crystalline silicon, and no light-induced defect generation is expected. Therefore, one may speculate that no light-induced defects are generated in grains when exposed to red light with photon energies lower than the optical band gap of a-Si:H. If this hypothesis is true, then one expects very little or no light-induced degradation in the  $\mu\text{-Si:H}$  bottom cell of an a-Si:H/ $\mu\text{-Si:H}$  double-junction or of an a-Si:H/a-SiGe:H/ $\mu\text{-Si:H}$  triple-junction structure because the high energy photons are absorbed in the a-Si:H top and a-SiGe:H middle cells and do not reach the  $\mu\text{-Si:H}$  bottom cell.

To prove or disprove the above hypothesis, a light soaking experiment was made on  $\mu\text{-Si:H}$  and a-SiGe:H solar cells under different light spectra. Figure 27 shows a comparison of the normalized maximum power,  $P_{\text{max}}$ , as a function of light soaking time for a  $\mu\text{-Si:H}$  solar cell and an a-SiGe:H solar cell, where the red and blue lights were obtained using a 665 nm long-pass filter and a 650 nm short-pass filter, respectively. The long-pass filter allows photons with energies lower than 1.86 eV

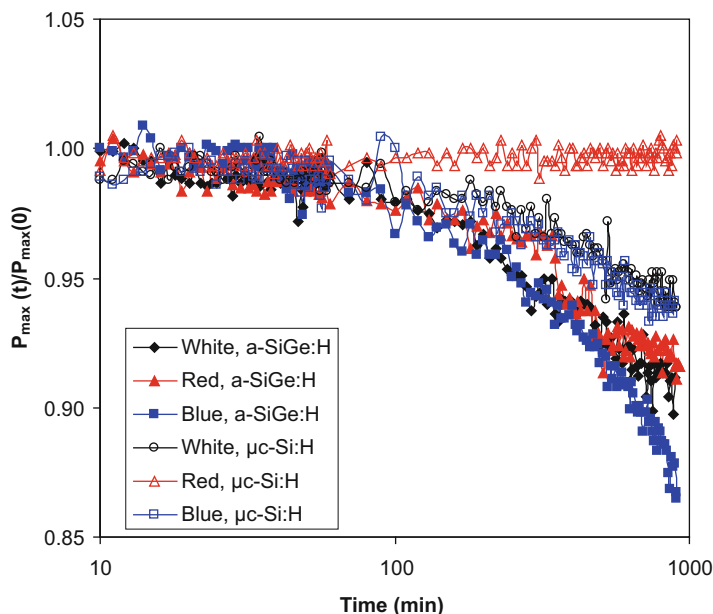


**Fig. 27** Light soaking kinetics of the normalized efficiency of a  $\mu\text{c-Si:H}$  single-junction solar cell and an  $\text{a-SiGe:H}$  single-junction solar cell with different spectral regions

**Table 3** Summary of light soaking results for  $\mu\text{c-Si:H}$  single-junction solar cells. IN represents the initial state, LS the light soaked state, and DEG the percentage of degradation

Light	State	$J_{sc}$ (mA/cm <sup>2</sup> )	$V_{oc}$ (V)	FF	Eff. (%)
White	IN	22.20	0.474	0.621	6.53
	LS	22.00	0.467	0.598	6.14
	DEG.	0.9%	1.48%	3.70%	5.97%
Red	IN	22.19	0.472	0.620	6.49
	LS	22.11	0.473	0.619	6.47
	DEG	0.36%	0%	0%	0.31%
Blue	IN	21.98	0.476	0.621	6.50
	LS	21.78	0.469	0.591	6.04
	DEG	0.91%	1.47%	4.83%	7.08%

to pass through to illuminate the sample. For the  $\mu\text{c-Si:H}$  cell, the light intensities for the two spectra were adjusted to generate  $J_{sc} \sim 44 \text{ mA/cm}^2$ , which is approximately twice of the  $J_{sc}$  under AM1.5 illumination. For the  $\text{a-SiGe:H}$  cell, the light intensities were adjusted to generate  $J_{sc} \sim 46 \text{ mA/cm}^2$  with the same consideration. Tables 3 and 4 summarize the J-V characteristics of the two series of cells in their initial and light soaked states. We need to point out that the light-soaked state is not a saturated state since only 15 hours of light soaking were made. Figure 27 clearly shows that there is no light-induced degradation for the  $\mu\text{c-Si:H}$  cell under the red light, but

**Table 4** Summary of light soaking results for a-SiGe:H single junction solar cells

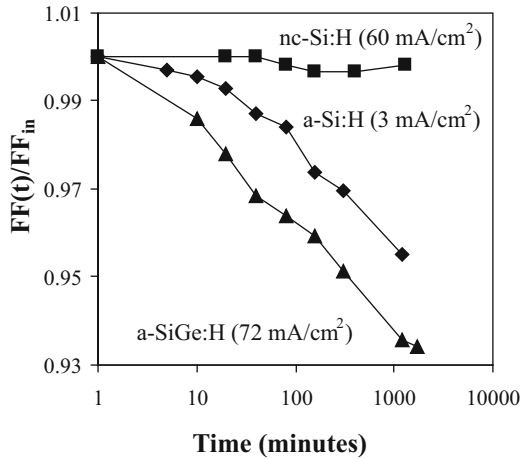
Light	State	$J_{sc}$ (mA/cm <sup>2</sup> )	$V_{oc}$ (V)	FF	Eff (%)
White	IN	23.10	0.628	0.601	8.72
	LS	22.88	0.601	0.567	7.80
	DEG	0.95%	4.30%	5.66%	10.55%
Red	IN	23.91	0.614	0.587	8.62
	LS	23.48	0.601	0.563	7.94
	DEG	1.80%	2.12%	4.09%	7.89%
Blue	IN	23.50	0.621	0.572	8.35
	LS	22.91	0.591	0.539	7.30
	DEG	2.51%	4.83%	5.77%	12.57%

some degradations under the white light (see Table 3) and more degradation under the blue light. As explained above, the absence of light-induced degradation under the red light illumination is due to the lack of absorption in the amorphous phase and no light-induced defect generation in the crystalline phase. In contrast to the red light illumination, the white and blue light illuminations showed noticeable degradation in the cell performance. The difference in the degradation between the white- and blue-light soaked  $\mu\text{-Si:H}$  cells could be explained in two ways. First, the blue light has a large portion of photons absorbed in the amorphous phase, which produces defects. Second, the blue light is absorbed near the  $i/p$  interface more than in the bulk. Pawlikiewicz and Guha (1988) showed that the  $i/p$  junction is the dominant junction and any change in this junction causes noticeable changes on the cell performance. For the a-SiGe:H cell, we consider the material to be homogenous having one optical band gap of about 1.5 eV. The differences among the light soaking results with the three lights with different spectra are mainly due to the second mechanism discussed above. Overall, the light-induced degradation in  $\mu\text{-Si:H}$  is much less than that in the a-SiGe:H cell even under white and blue light.

As pointed out earlier, the spectrum dependence of light-induced degradation in  $\mu\text{-Si:H}$  solar cells has a significant impact on the real solar module application. Thin film silicon solar modules are normally made with a-Si:H/ $\mu\text{-Si:H}$  double-junction, a-Si:H/a-SiGe:H/ $\mu\text{-Si:H}$  triple-junction, and a-Si:H/ $\mu\text{-Si:H}$ / $\mu\text{-Si:H}$  triple-junction cell structures. The  $\mu\text{-Si:H}$  middle and bottom cells do not see the blue light and therefore do not suffer any light-induced degradation, and overall multijunction solar cell stability is significantly improved. Yue et al. demonstrated that high efficiency a-Si:H/ $\mu\text{-Si:H}$ / $\mu\text{-Si:H}$  solar cells degraded only 3–5% after prolonged light soaking and a stable cell efficiency of 13.6% was achieved with this cell structure (Yue et al. 2006b).

In a-Si:H solar cells, the metastability was also observed under a forward bias (Street 1991). The physics is similar to the Staebler-Wronski effect under light soaking. Under a forward bias, electrons and holes are injected from the  $n$  side and  $p$  side into the  $i$ -layer, respectively, and recombine there. The electron-hole recombination releases energy, generates metastable defects in the  $i$ -layer, and hence degrades the cell performance. A question is whether or not a forward bias carrier

**Fig. 28** The kinetic changes or normalized FF under 1 V forward bias for the a-Si:H, a-SiGe:H, and  $\mu$ c-Si:H solar cells (Yue et al. 2007)



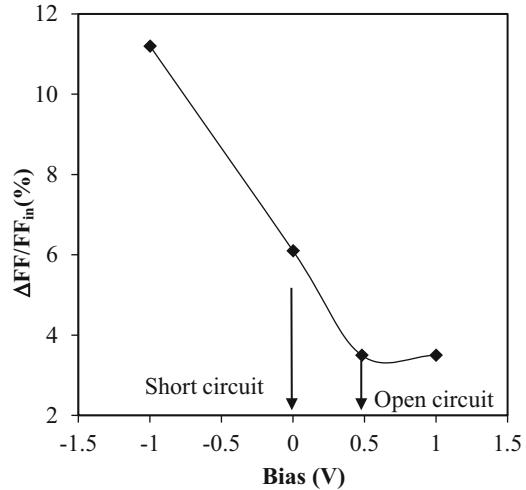
injection results in any degradation in  $\mu$ c-Si:H solar cell. Because the carrier transport mainly takes place in the crystalline phase and the recombination would take place there as well. As shown by the red light soaking experiment, the recombination in the grains does not produce any degradation in  $\mu$ c-Si:H solar cell; therefore, one would expect that a forward bias on  $\mu$ c-Si:H should not result in any degradation in the cell performance.

Figure 28 shows a comparison of forward injection current-induced FF changes as a function of forward bias time (Yue et al. 2007). Three solar cells of a-Si:H, a-SiGe:H, and  $\mu$ c-Si:H were under forward bias of 1 V, which leads to the initial forward current densities of 3 mA/cm<sup>2</sup> for the a-Si:H cell, 72 mA/cm<sup>2</sup> for the a-SiGe:H cell, and 60 mA/cm<sup>2</sup> for the  $\mu$ c-Si:H cell. The FF of the a-SiGe:H degrades significantly; the a-Si:H cell also shows some degrees of degradation even though the forward current density is only 3 mA/cm<sup>2</sup>, while the  $\mu$ c-Si:H cell does not degrade within the experimental errors. This experiment proved that the recombination in the crystalline phase indeed does not produce metastable defects to degrade the  $\mu$ c-Si:H solar cell performance.

Another interesting phenomenon of light-induced metastability in  $\mu$ c-Si:H is the electric bias effect (Yue et al. 2005, 2006b, 2007). For a-Si:H solar cells, it has been found that a reverse bias on an a-Si:H solar cell reduces the magnitude of the light-induced degradation because the reverse bias enhances the electric field in the intrinsic layer and reduces the probability of recombination, which is the driving force of the Staebler-Wronski effect (Yang et al. 1992; Yang et al. 2002). However, an electric bias on  $\mu$ c-Si:H solar cells has an opposite effect on the light-induced degradation. A negative bias enhances the light-induced degradation, but a forward bias reduces the light-induced degradation as shown in Fig. 29 (Yue et al. 2005, 2007), where the light-induced degradation of FF under an AM1.5 illumination is plotted as a function of applied bias. In this experiment, eight  $\mu$ c-Si:H cells on the same substrate were light-soaked



**Fig. 29** Light-induced degradation in FF versus the electrical bias during light soaking, where  $\Delta FF$  denotes the variations in FF. The light soaking was carried out at 50 °C under one sun white light for 309 h



simultaneously under 100 mW/cm<sup>2</sup> white light at 50 °C with various bias conditions of -1 V, short circuit (0 V), open circuit (+0.48 V), and +1 V. To check the reproducibility of the degradation rate, two cells at each bias condition were included. The short circuit corresponds to the 0 V bias, and the open circuit is considered to be a forward bias of  $V_{oc}$ , which is around 0.48 V. It is clearly seen that the light-induced degradation in FF was increased by the increase of the magnitude of the reverse bias. Under the -1 V bias condition, the FF degrades on the average by 10.9%, while the FF degrades only by 7.6% under the short circuit condition. Under the open circuit and +1 V bias conditions, however, the degradation in the FF is the same, around 3.8%. This unusual phenomenon has been repeatedly observed and confirmed as the universal characteristics of  $\mu c$ -Si:H solar cells. To explain the observation, Yue et al. proposed a “back-to-back” diode module. For details, please refer Yue et al. (2005, 2006a, 2007).

To summarize the metastability of  $\mu c$ -Si:H solar cells, we make the following conclusions. First, the light-induced degradation in  $\mu c$ -Si:H solar cells is generally lower than in a-Si:H solar cells and some  $\mu c$ -Si:H solar cells even show no light-induced degradation. Second, the light-induced degradation depends on the crystallinity in the intrinsic layer; the high the crystallinity, the lower the light-induced degradation is. Third, the light-induced degradation is only caused by the photons with the energy higher than the bandgap of a-Si:H phase, and no light-induced degradation results from red light illumination, which indicates that the light-induced degradation occurs only in the amorphous phase and grain boundaries. Fourth, a double-carrier injection by a forward electric bias does not cause any degradation in  $\mu c$ -Si:H solar cells, which is different from a-Si:H solar cells. Finally, during light soaking, a reversers electric bias enhances the light-induced degradation and a forward bias reduces the light-induced degradation, which is also opposite with a-Si:H solar cells. Among these characteristics, the most important feature is no light-induced degradation with red light because  $\mu c$ -Si:H solar cells are normally

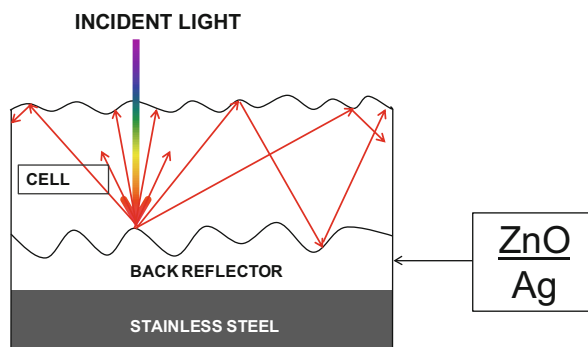
used as the middle and bottom cells in multijunction solar cells, where the high energy photons are absorbed by the a-Si:H top cell.

## Light Trapping in $\mu\text{c-Si:H}$ Solar Cells

Although  $\mu\text{c-Si:H}$  has a much broader absorption spectrum than a-Si:H, which covers up to 1100 nm, the absorption coefficients are still low in the long wavelength region because of the indirect band gap absorption. Therefore, the required  $\mu\text{c-Si:H}$  thickness for effectively absorbing the sun light is much thicker than a-Si:H. However, even the carrier mobility in  $\mu\text{c-Si:H}$  is higher than in a-Si:H, the absorber layer in  $\mu\text{c-Si:H}$  solar cells still cannot increase too much without significantly suffering the loss in FF and  $V_{oc}$ . Considering all of the performance parameters, the optimized  $\mu\text{c-Si:H}$  intrinsic layer thickness has been determined to be in the range of 3–5  $\mu\text{m}$ . However, with the consideration of production efficiency and current mismatching, the  $\mu\text{c-Si:H}$  intrinsic layer could be limited to 1–2  $\mu\text{m}$  for double-junction cells and 3–5  $\mu\text{m}$  for triple-junction solar cells, which is still not thick enough to absorb the sun light to give enough current. Therefore, effective light trapping techniques are needed. Based on the solar cell structures, the light trapping methods for *p-i-n* and *n-i-p* structured  $\mu\text{c-Si:H}$  solar cells are different.

The light trapping in *n-i-p* structured solar cells is mainly from the scattering at the back interface between the silicon layer and the back reflector (BR). The top TCO is  $\sim 75\text{-nm}$  thick highly conductive ITO, which cannot provide enough textures for light trapping. The thin ITO functions as an antireflection (AR) coating to reduce the reflection loss. The BRs are made with Ag/ZnO or Al/ZnO double-layer structures as shown in Fig. 30. Figure 31 shows a comparison of EQE curves of three  $\mu\text{c-Si:H}$  solar cells deposited with the same recipe but on different substrates, where a significant enhancement of the long wavelength response is achieved by the light trapping. The  $\mu\text{c-Si:H}$  solar cell on the bare stainless steel has a total photocurrent density of  $15.56\text{ mA/cm}^2$ ; the ones on the Al/ZnO and Ag/ZnO BRs have the values of  $20.48\text{ mA/cm}^2$  and  $24.48\text{ mA/cm}^2$  and the gains of 31.6% and 57.3%,

**Fig. 30** Schematic of light trapping in an *n-i-p* structured  $\mu\text{c-Si:H}$  solar cell by a ZnO/Ag back reflector



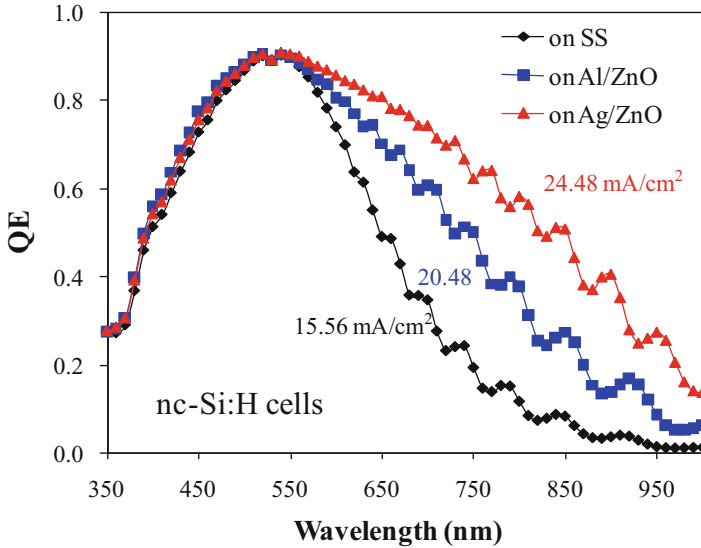


**Fig. 31** EQE curves of three  $\mu\text{c-Si:H}$  solar cells deposited with the same recipe but on different substrates

respectively. It demonstrates that the Al/ZnO and Ag/ZnO are very effective for light trapping in  $\mu\text{c-Si:H}$  solar cells.

The design and optimization of BR should take the following considerations. The textured metal layer (Ag or Al) reflects and scatters the light that reaches the BR; the ZnO layer reduces the plasmonic losses at the Ag/Si interface by shifting the plasmonic resonance frequency to the short wavelength region where the light is absorbed in the first path. The ZnO layer also adds additional textures for light scattering. Therefore, the effectiveness of light trapping is determined by three factors of (1) the reflectivity, (2) the scattering, and (3) the reduction of surface absorption. For high efficiency  $\mu\text{c-Si:H}$  solar cells, Ag is normally used in the BR for its high reflectivity as shown in Fig. 30, but Al is used in some products for low cost. The scattering could occur at the texture surface of Ag and the texture surface of ZnO. The scattering at the Ag surface is much more effective than at ZnO surface, which means that a small scale texture on the Ag surface could provide a high level of scattering, while the texture of Ag surface could cause the plasmonic absorption. Thus, in order to reduce the plasmonic absorption, a flat Ag surface and a highly textured ZnO layer are preferred theoretically, and it has been also confirmed in a-SiGe:H solar cells. However, a high textured ZnO could cause the degradation of  $\mu\text{c-Si:H}$  quality as discussed later. Therefore, the design and optimization of Ag/ZnO BR need to compromise the textures of ZnO and Ag. Experimentally, it was found that a textured Ag with a thin ZnO (100 nm) is a good choice of the ZnO/Ag BR for  $\mu\text{c-Si:H}$  solar cells (Yan et al. 2012; Sivec et al. 2012). The texture on the Ag surface is much more effective than on ZnO to scatter light and therefore some moderate

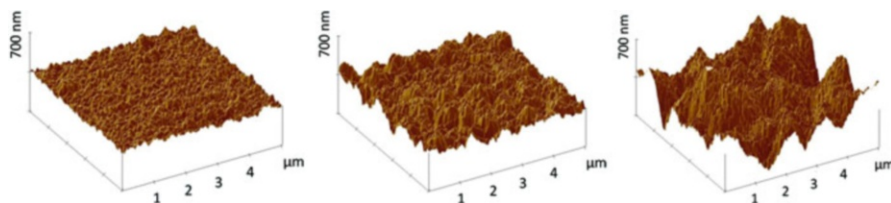


**Fig. 32** AFM images of three Ag/ZnO BRs with different Ag textures, (left) low texture with RMS = 17 nm, (middle) medium texture with RMS = 40 nm, and (right) high texture with RMS = 118 nm

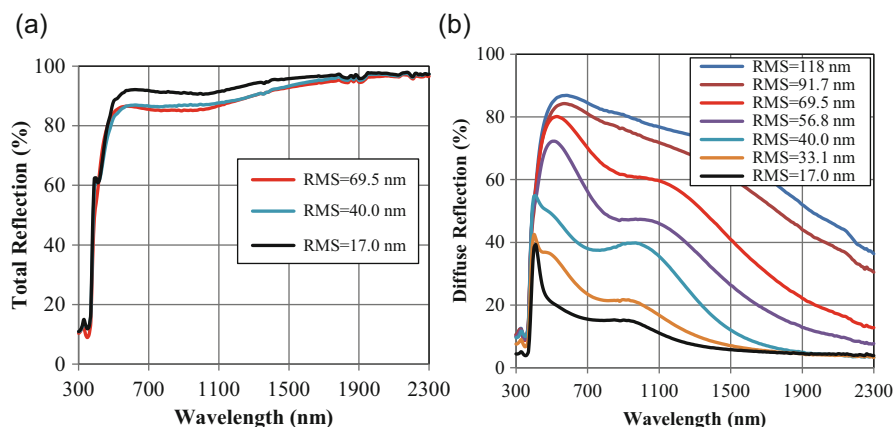
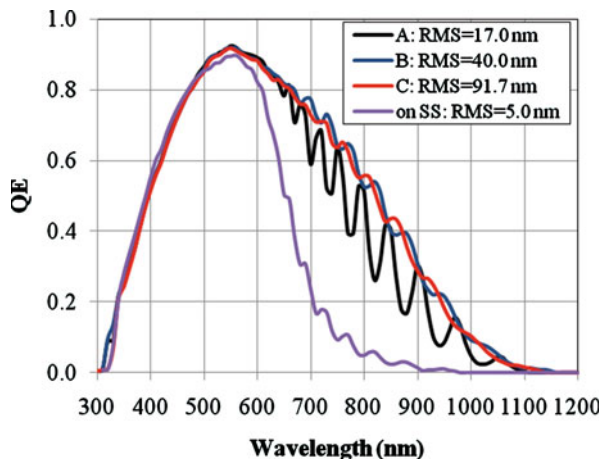


**Fig. 33** The (a) total and (b) diffuse reflection spectra of Ag/ZnO back reflectors with various textures as measured by the RMS from AFM images

textures are good enough to provide the scattering for good light trapping. On the other hand, the thin ZnO layer shifts the plasmonic resonance frequency to the short wavelength region, where the light is absorbed before reaching the back contact. Figure 32 shows the surface morphologies of three ZnO/Ag BRs, where the textures are mainly from the Ag layer and the ZnO layers are the same for all of the samples with a thickness of 100 nm. Figure 33 plots the total and diffuse reflection spectra of the BRs. It shows that the total reflectance spectrum decreases slightly with the increases of Ag texture, which could result from the absorption at the Ag/ZnO interface and the light trapping in the ZnO layer because the optical constant of ZnO is larger than in air. However, the diffuse reflectance spectra are very different with different Ag texture. A significant increase in the diffuse reflectance is observed by the increase of Ag texture, implying a potential enhancement for light trapping.

The same  $\mu\text{-Si:H}$  solar cells with 1  $\mu\text{m}$  thick  $\mu\text{-Si:H}$  intrinsic layer were deposited on this type of ZnO/Ag BR coated stainless steel substrates with different textures from the Ag layers. The EQE curves of four selected  $\mu\text{-Si:H}$  solar cells are plotted in Fig. 34 and the cell performance parameters are listed in Table 5. It notes

**Fig. 34** EQE spectra of  $\mu\text{-Si:H}$  solar cells made with the same recipes but on different Ag/ZnO BRs. The  $\mu\text{-Si:H}$  intrinsic layer is  $1\ \mu\text{m}$



that the solar cells on the Ag/ZnO BR have a significant higher response in the long wavelength region than on the bare SS and demonstrates again the effectiveness of the light trapping. The solar cell on the BR with  $\text{RMS} = 17\ \text{nm}$  shows a significant interference fringes, indicating a large amount of direct reflection, while with the increase of the texture, the interference fringes are reduced, associating the enhancement of scattering. The solar cell on the SS has only  $15.12\ \text{mA/cm}^2$  of  $J_{\text{sc}}$ , while the one on the Ag/ZnO BR with  $\text{RMS} = 40\ \text{nm}$  has  $25.03\ \text{mA/cm}^2$ , and a gain of 66% is observed. It is also found that increasing the texture further does not increase the spectral response further even the diffusive reflection is enhanced. Instead, the photocurrent density decreases slightly. Furthermore, the FF also decreases and the EQE loss ( $\Delta\text{QE}$ ) increases with the increase of the substrate texture, a phenomenon is often observed in  $\mu\text{-Si:H}$  solar cells, and it relates to the structural defect formation caused by the high textured substrates. The details will be discussed later. By making a thicker  $\mu\text{-Si:H}$  solar cell ( $3.1\ \mu\text{m}$ ) on the optimized Ag/ZnO BR, a high photocurrent density of  $30.5\ \text{mA/cm}^2$  was obtained with the J-V curve and EQE spectrum plotted in Fig. 35.

From the above results, we conclude that the optimized Ag/ZnO BRs are very effective to increase the spectral response of  $\mu\text{-Si:H}$  solar cells. A current gain over 60% compared to  $\mu\text{-Si:H}$  solar cells on bare flat SS substrates can be obtained. The best Ag/ZnO BRs with a textured Ag layer and thin ZnO (100 nm) is made with a proper texture of RMS around 40 nm. For the RMS beyond this value, no additional gain in the photo-response is observed. Furthermore, the FF of the solar cells decreases with the increase of the surface roughness. With the optimized Ag/ZnO, a short circuit current density more than  $30\ \text{mA/cm}^2$  has been obtained with the cell thickness of  $3\ \mu\text{m}$ .

The *p-i-n* structures are normally deposited on transparent conductive oxide (TCO) coated glass substrates. Because the light actually illuminates the solar cells on the substrate side and passes through the glass/TCO to reach the semiconductor layers, the substrate is also called “superstrate.” The light trapping in the *p-i-n*

**Table 5** The J-V characteristics of  $\mu\text{-Si:H}$  solar cells made with the same recipes but on different Ag/ZnO BRs. The  $\mu\text{-Si:H}$  intrinsic layer is 1  $\mu\text{m}$ 

RMS (nm)	light	$V_{oc}$ (V)	FF	$FF_b$	$FF_r$	QE(0 V) (mA/cm <sup>2</sup> )	QE(-3 V) (mA/cm <sup>2</sup> )	$P_{max}$ (mW/cm <sup>2</sup> )	$\Delta QE$ (%)
A 17.0	Color			0.722	0.720				
	>610 nm	0.515	0.738			11.61	11.69	4.41	0.7
	AM1.5	0.530	0.723			22.43	22.55	8.59	0.5
B 40.0	Color			0.716	0.72				
	>610 nm	0.522	0.726			13.86	14.16	5.25	2.1
	AM1.5	0.541	0.711			24.62	25.03	9.47	1.6
C 91.7	Color			0.703	0.704				
	>610 nm	0.519	0.717			13.59	14.06	5.06	3.3
	AM1.5	0.537	0.702			24.30	24.98	9.16	2.7

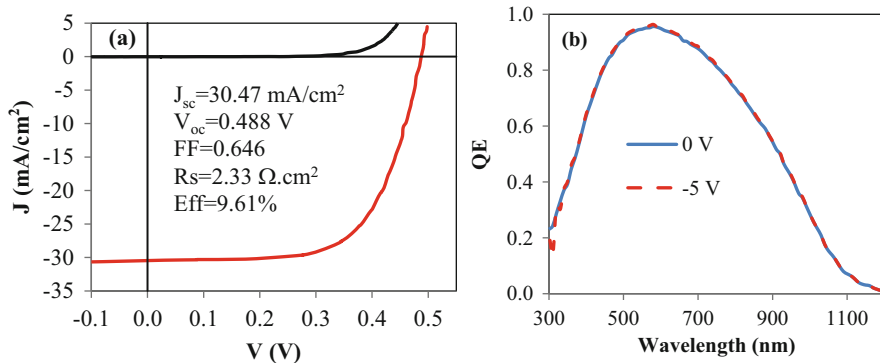


**Fig. 35** J-V characteristics and EQE spectrum a  $\mu\text{c-Si:H}$  solar cell with total photocurrent density  $> 30 \text{ mA/cm}^2$

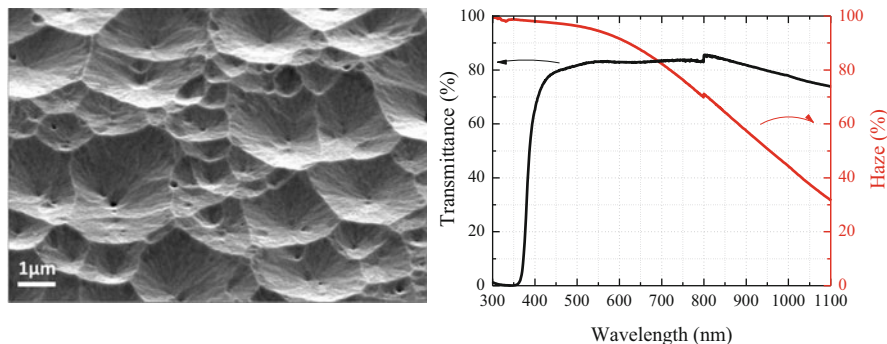
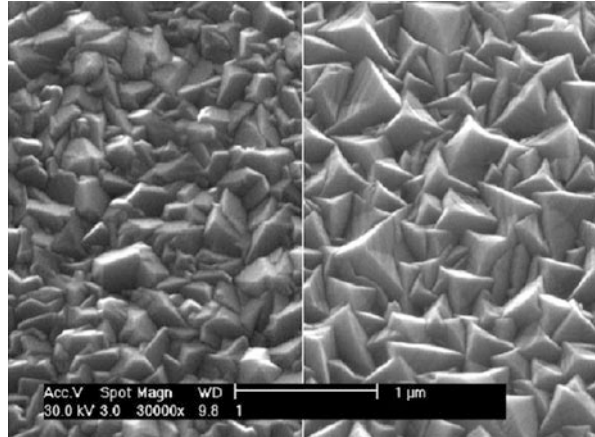


**Fig. 36** Tilt-view scanning electron microscope (SEM) images and experimentally measured total transmittance and haze spectra of a magnetron-sputtered and texture-etched AZO

structured solar cells are normally achieved by using a textured TCO layer. Tin Oxide ( $\text{SnO}_2$ ) TCO layer is widely used in a-Si:H alloy based solar cells, but it is not suitable for  $\mu\text{c-Si:H}$  solar cell deposition because  $\text{SnO}_2$  reacts with the high density atomic hydrogen during the  $\mu\text{c-Si:H}$  deposition. Alternatively, ZnO is used as the TCO for  $\mu\text{c-Si:H}$  solar cells. Although undoped ZnO already has an N-type transport, the conductivity is not high enough to meet the low series resistance requirement; Al, B, or Ga is added as the doping elements during the ZnO deposition to increase the conductivity. The Al doped ZnO is called AZO, which usually deposited using magnetron sputtering of an  $\text{Al}_2\text{O}_3$  doped ZnO ceramic target. The effectiveness of light trapping strongly depends on the texture of the TCO. Normally, the as-deposited AZO is relatively flat and does not have the required textures for effective light trapping; a chemical etching method using diluted HCl is used to increase the texture of AZO (Müller et al. 2001; Müller et al. 2003; Hüpkens et al. 2012). Figure 36 shows the surface morphologies of a AZO sample after chemical

**Fig. 37** Comparison of (left) SnO<sub>2</sub> and (right) LP-CVB BZO surface morphology SEM images (Meier et al. 2002)



etching and its transmittance as well as the haze spectra. One can see that the surface texture with “crater-like” structures and the haze is very high in the wide spectrum range.

The surface of sputtered AZO can also be changed by optimizing the deposition process, such as the substrate temperature, film thickness, excitation power, and pressure. Huang et al. (2012) found that adding H<sub>2</sub> during the sputtering process can increase the surface texture. The AZO substrate made with this method shows an effective enhancement for photocurrent in μc-Si:H solar cells. Most importantly, this method can eliminate the chemical etching process and reduce the thin film solar panel manufacturing cost.

The B doped ZnO is called BZO, which is normally made using a low pressure chemical vapor deposition (LP-CVD) process. The textures of the LP-CVD deposited BZO form during the deposition and can be modified by the process parameters, especially the substrate temperature and process pressure (Meier et al. 2002; Nicolay et al. 2011). Figure 37 shows the surface morphology comparison of an LP-CVD prepared BZO sample with the industrially used SnO<sub>2</sub> TCO samples; both samples show very similar surface structures. The LP-CVD deposited BZO has “crystal-like” surface structures instead of the “crater-like” structures on the chemically etched AZO substrates. The LP-CVD deposited BZO is also an effective light trapping substrate for μc-Si:H solar cells and has been incorporated in TEL Solar’s thin film silicon solar module manufacturing lines (Cashmore et al. 2016).

As previously mentioned, a highly textured substrate could cause the degradation of μc-Si:H material quality and solar cell performance. If only considering the optical properties for light trapping, a highly textured substrate would be preferred for μc-Si:H solar cells; however, in reality it is much complicated in μc-Si:H solar cell fabrications. The main issue is that the surface texture directly impacts the growth of μc-Si:H materials. It has been found that the crystallites have the tendency to form columnar structures perpendicular to the local growth surface. The shape of the textured surface, such as the average slope and the angle at the bottom of valleys,



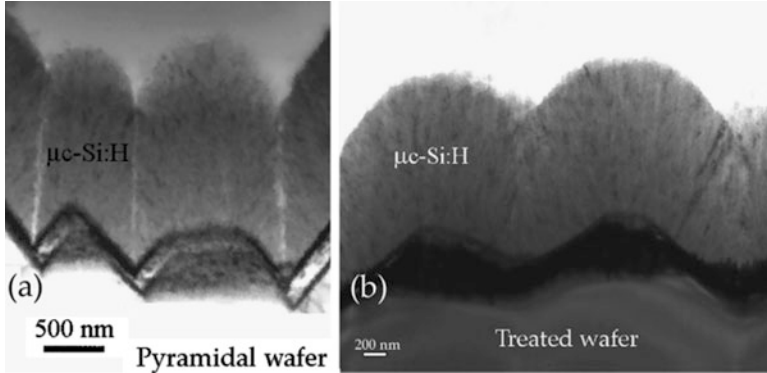


**Fig. 38** TEM micrograph cross-section of a single-junction *p-i-n* solar cell deposited on a pyramidal wafer substrate. On the left, the “V-shaped” valleys of the substrate lead to “cracks” crossing the whole *p-i-n* device. On the right, the “U-shaped” substrate valleys result in a “crack” only in the last half of the  $\mu\text{c-Si:H}$  layer (Python et al. 2009)

affects the  $\mu\text{c-Si:H}$  solar cell performance significantly (Nasuno et al. 2001). If the substrate has a high texture, the columnar structures on the local surface could meet each other and lead to microvoids and microcracks as shown in Fig. 38 (Python et al. 2009), where the left image reveals the cross-section of a  $\mu\text{c-Si:H}$  solar cell deposited on a c-Si wafer having a pyramidal structured surfaces with sharp angles at the bottom of valleys called “V” shape, while the right one is on the substrate with chemically smoothed the surface to remove the sharp peaks and valleys and make the surface having the textures of “U” shape. It is clear that the  $\mu\text{c-Si:H}$  deposited on the “V” shaped substrate has microcracks all the way going through the entire thickness of the sample, while not much microcracks can be observed in the  $\mu\text{c-Si:H}$  solar cell on the “U” shaped substrate. The texture-induced microcracks not only reduce  $\mu\text{c-Si:H}$  solar cell efficiency, but also cause ambient degradation from the postdeposition impurity diffusion. Based on the results above, Bailat et al. proposed using a plasma treatment to smooth the textures on ZnO substrates and demonstrated a noticeable improvement in  $\mu\text{c-Si:H}$  solar cell performance (Bailat et al. 2006).

The group in AIST, Japan, invented an electric flat and optical textured back reflector as shown in Fig. 39 (Sai et al. 2011, 2012), which is made of two materials with different dielectric constants and forms a flat surface. The flat surface of the back reflector ensures microcrack-free deposition of  $\mu\text{c-Si:H}$  layers and the array made with two dielectrics scatters the light for light trapping. In reality, they used N-type a-Si:H and ZnO to form such back reflector (Fig. 40) and made a significant improvement in  $\mu\text{c-Si:H}$  solar cell performance as listed in Table 6 (Sai et al. 2011). Comparing the baseline cell on the flat substrate, the  $\mu\text{c-Si:H}$  solar cell deposited on the textured back reflector has a significant gain in the current due to the effective light trapping, but some losses in the  $V_{\text{oc}}$  and FF caused by the degradation of  $\mu\text{c-Si:H}$  material quality by the texture. Such detrimental effect becomes more serious in the cells on the normal grating substrate because of the highly structural texture. However, the solar cell on the flattened grating substrate shows the same  $V_{\text{oc}}$  and FF as the cell on the flat substrate, indicating the same high quality

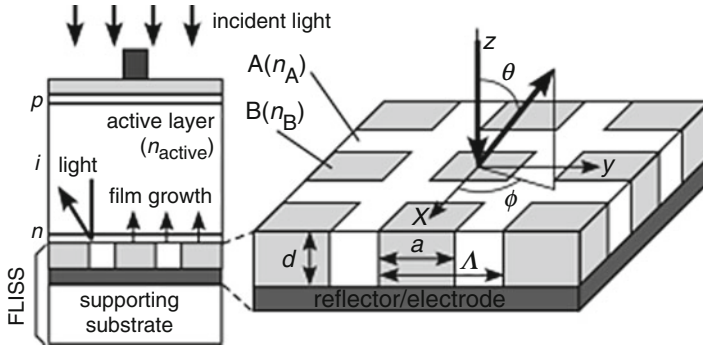


**Fig. 39** Schematics of (left) a  $\mu\text{-Si:H}$  solar cell on (right) an electric flat and optical textured back reflector (Sai et al. 2011)

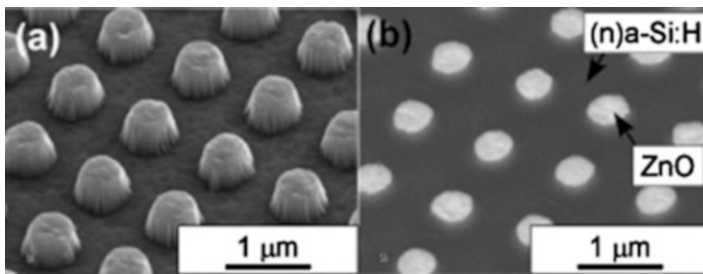


**Fig. 40** SEM images of (a) the conventional a-Si:H and ZnO grating and (b) the flattened a-Si:H and ZnO grating (Sai et al. 2011)

**Table 6** J-V characteristics of  $\mu\text{-Si:H}$  solar cells deposited on different textured substrates (Sai et al. 2011)

Substrate	$V_{oc}$ (V)	$J_{sc}$ (mA/cm <sup>2</sup> )	FF	Eff (%)
Flat	0.538	17.8	0.764	7.3
Texture	0.526	20.8	0.729	8.0
Grating	0.445	18.81	0.655	5.5
Polished grating	0.539	19.3	0.757	7.9

$\mu\text{-Si:H}$  as the one on the flat substrate. However, although the  $J_{sc}$  is higher than the cell on the conventional grating substrate, it is not as high as the one on the randomly textured reference substrates. Two issues might cause the less effectiveness of light trapping of the grating substrate: first the grating substrate might be effective in some wavelength region, but the sun light has a broad spectrum; second the N-type a-Si:H in the flattened back reflector absorbs some of the light reaching there. In this specific structure, the grating substrate does not have high response in the middle wavelength region, which was attributed to the absorption in the N-type a-Si:H layer in the back reflector. Such losses could be minimized when the  $\mu\text{-Si:H}$  solar cells used as the

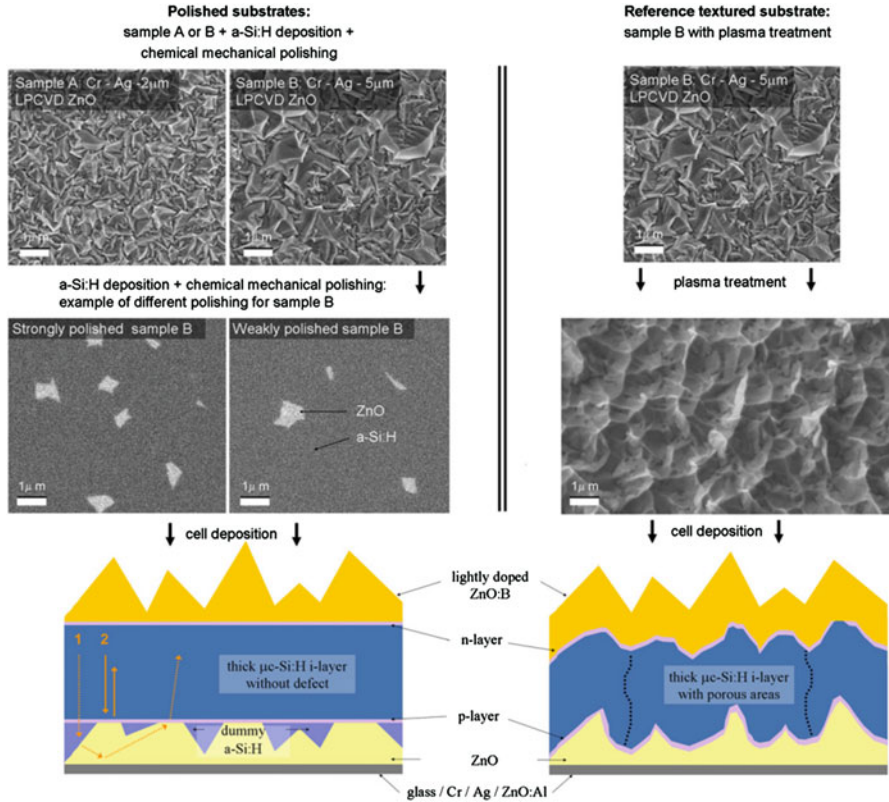


**Fig. 41** SEM images of (left) polished substrates and (right) reference textured substrate during fabrication. Schematic drawings of cells grown on both types of substrates appear below. The colored arrows in the lower left panel illustrate loss in light trapping due to the flat ZnO/Si zones. The dashed lines in the lower right panel illustrate porous areas due to defective  $\mu\text{c-Si:H}$  growth (Söderströmn et al. 2012a)

bottom cell in multijunction solar cells. In addition, the antireflection effect of the ITO layer on the flat solar cell is not as effective as on textured solar cells.

Using the same principle, the Neuchal group made electric flat and optical texture back reflector by depositing an a-Si:H on randomly textured Ag/ZnO back reflector and then polishing the a-Si:H layer to use the remaining a-Si:H in the valleys to obtain a flat surface for high quality  $\mu\text{c-Si:H}$  deposition as shown in Fig. 41 (Söderströmn et al. 2012a, b). The left panel shows the SEM images of the surface morphologies before and after the polishing as well as the schematic of the  $\mu\text{c-Si:H}$  solar cell on such substrates; the right panel gives the same sequence of the plasma treatment process for smoothing the ZnO texture as the reference. In the polished substrates, the textures of the ZnO layer provide the effective light trapping and the flattened a-Si:H layer provides the flat surface for maintaining the  $\mu\text{c-Si:H}$  quality. In addition, the high peaks of the ZnO reached out of the filling

**Table 7** Results of two co-deposited cells with a p-( $\mu\text{-Si:H}$ ) doped layer optimized for polished substrates and for a cell with a p-doped  $\mu\text{-SiO}_x\text{:H}$  layer optimized for textured substrates (Söderströmn et al. 2012a)

Type of substrate/p-doped layer	FF	$V_{oc}$ (V)	$J_{sc}$ ( $\text{mA}/\text{cm}^2$ )	Eff (%)
Textured/p- $\mu\text{-Si:H}$	0.58	0.494	28.0	8.0
Polished A/p- $\mu\text{-Si:H}$	0.67	0.520	27.3	9.5
Textured/p- $\mu\text{-SiO}_x\text{:H}$	0.62	0.491	28.3	8.6

a-Si:H layer and flattened as well, which provide the electric contact for the current flow such that an undoped a-Si:H layer can be used as the filling materials without additional serious resistance. Table 7 summarizes the solar cell performances on different back reflectors. Comparing the first two rows of  $\mu\text{-Si:H}$  solar cells, it is noted that the polished substrate results in a significant improvement in the FF and  $V_{oc}$ , which leads to an efficiency increase from 8.0% to 9.6%. The slightly low  $J_{sc}$  is caused by the additional absorption by the filling a-Si:H materials that result in a dip in the EQE at around 700 nm (Söderströmn et al. 2012a). It has also found that the detrimental effect of the substrate texture could be mitigated by using well-designed cell architectures. The use of a p-(SiO<sub>x</sub>:H) doped layer helps the cell to be less sensitive to locally porous material, which leads to an increase of the reference cell FF, as expected and demonstrated in the third row of Table 7. Nevertheless, the cell on the polished substrate with a p-( $\mu\text{-Si:H}$ ) doped layer outperforms the reference cell in  $V_{oc}$  and FF. This result demonstrates that textures of the substrate indeed have a detrimental effect on  $\mu\text{-Si:H}$  solar cell deposition and using an electric flat and optical textured substrate is an effective method to resolve this issue. Söderströmn et al. used the polished substrate to make a-Si:H/ $\mu\text{-Si:H}$ / $\mu\text{-Si:H}$  triple-junction solar cells and achieved initial and stable solar cell efficiencies of 13.7% and 12.5% (Söderströmn et al. 2012b).

As discussed above, light trapping is an important technique for improving  $\mu\text{-Si:H}$  solar cell performance. Beside the conventional light trapping schemes using randomly textured Ag/ZnO back reflectors for *n-i-p* structures and randomly textured AZO or BZO coated glass substrates for *p-i-n* structures, new advanced light trapping methods using plasmonic metal nanostructures (Pillai et al. 2007; Spinelli et al. 2012; Tan et al. 2013) and periodic photonic structures (Battaglia et al. 2012; Chen et al. 2015; Sai et al. 2009) have been extensively studied in recent years. Although some improvements have been achieved in the photocurrent gain, it is still not conclusive whether the modern light trapping approaches are better than the classic light trapping with randomly textured substrates and all of the record efficiencies for thin film silicon solar cells are achieved using the traditional randomly textured substrates. Because the advanced light trapping techniques are mainly dealing with the optical properties instead of the influence on  $\mu\text{-Si:H}$  properties, it is not in the scope of this chapter. Readers are referred to the articles Battaglia et al. (2012), Chen et al. (2015), Pillai et al. (2007), Sai et al. (2009), Spinelli et al. (2012), and Tan et al. (2013).

## Microcrystalline Silicon Germanium Alloy $\mu\text{c-SiGe:H}$

Similar to a-Si:H alloys, several microcrystalline silicon alloys have been studied for various applications. Used as the absorber layer to extend the infrared absorption, hydrogenated microcrystalline silicon germanium ( $\mu\text{c-SiGe:H}$ ) is proposed by the ASIT group (Ganguly et al. 1996) and has been studied by the community (Carius et al. 1998; Matsui et al. 2006, 2007, 2009; Ni et al. 2014). Alloying Ge into  $\mu\text{c-Si:H}$  can reduce the bandgap further, which could expand the absorption edge beyond 1100 nm that is usually limited by the bandgap of the crystalline phase in  $\mu\text{c-Si:H}$  absorber layer. Figure 42 shows some EQE curves of  $\mu\text{c-SiGe:H}$  solar cells with various Ge contents, and Table 8 lists the cell performance parameters, where the  $\mu\text{c-SiGe:H}$  intrinsic layer is  $\sim 1 \mu\text{m}$ . It is noted that the long wavelength response is increased remarkable by the incorporation of Ge. The  $J_{sc}$  for the cell without Ge is  $18.5 \text{ mA/cm}^2$ , while the one with 20% Ge content goes up to  $24.1 \text{ mA/cm}^2$  with a gain of 30% in the photocurrent density. However, a further increase in Ge content leads to a considerable degradation in all solar cell parameters. For Ge content of  $x = 40.2\%$ , the decrease in  $V_{oc}$  is much greater than the band gap narrowing, indicating that the solar cell performance is dominated by the carrier recombination due to the increased dangling bond defects in the  $\mu\text{c-SiGe:H}$  *i*-layer. It is also noted that in the high Ge content solar cells, the short wavelength length response is reduced significantly by the increase of Ge related defects, which act as weak P-type doping and weaken the electric field in the region near the *p/i* interfaces. A proper O doping can

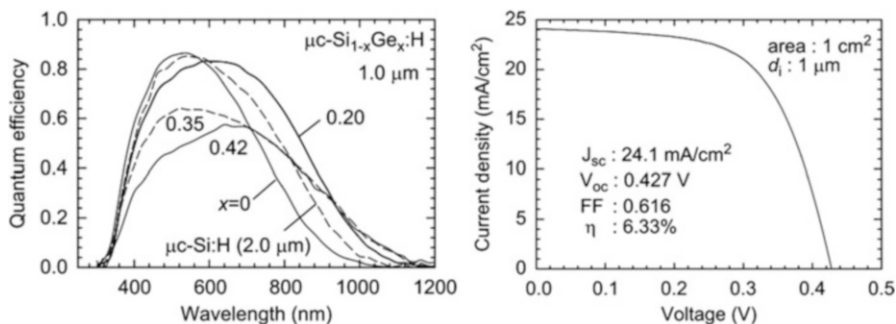


**Fig. 42** (left) EQE curves of  $\mu\text{c-Si}_{1-x}\text{Ge}_x\text{:H}$  solar cells with various Ge contents, (right) J-V curve of a  $\mu\text{c-Si}_{1-x}\text{Ge}_x\text{:H}$  solar cell with 20% of Ge content (Matsui et al. 2009)

**Table 8** Illuminated J-V parameters of the  $\mu\text{c-Si}_{1-x}\text{Ge}_x\text{:H}$  *p-i-n* solar cells with different Ge contents in the *i*-layer (Matsui et al. 2009)

G content x	Thickness ( $\mu\text{m}$ )	$V_{oc}$ (mV)	$J_{sc}$ ( $\text{mA/cm}^2$ )	FF	Eff (%)
0.00	1.0	560	18.5	0.730	7.75
0.20	1.0	412	23.6	0.663	6.12
0.35	1.0	214	20.6	0.380	1.67
0.42	0.9	195	18.8	0.354	1.29

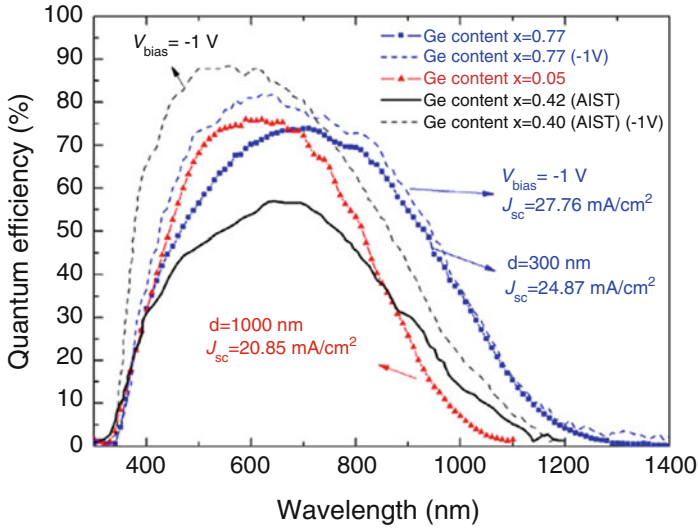


**Fig. 43** Quantum efficiency spectra of  $\mu\text{c-Si}_{1-x}\text{Ge}_x\text{:H}$  *p-i-n* solar cells with different Ge contents (squares:  $x = 0.77$ , dashed blue line:  $x = 0.77$  measured under reverse bias voltage of  $-1$  V, triangles:  $x = 0.05$ ). The  $\mu\text{c-Si}_{1-x}\text{Ge}_x\text{:H}$  solar cells with champion response in the long-wavelength regions are shown for comparison (solid black line:  $x = 0.42$  from AIST, see; dashed black line:  $x = 0.40$  measured under reverse bias voltage of  $-1$  V (Ni et al. 2014))

compensate such P-type defect and improve the cell performance. Ni et al. (2014) used a proper ion bombardment technique to improve the  $\mu\text{c-SiGe:H}$  quality with a high Ge content up to 77% and made reasonable good solar cells with the EQE extended to 1300 nm as shown in Fig. 43. The short wavelength EQE losses can be recovered by a reverse bias voltage to enhance the electric field for carrier collection as shown in Fig. 43, confirming the losses is indeed from recombination.

As a narrow bandgap material,  $\mu\text{c-SiGe:H}$  can extend the long wavelength response of solar cells. However, the overall material quality still needs to be further improved. Currently, the losses in FF and  $V_{oc}$  with the incorporation of Ge are more than the gain in the current for the efficiency contributions; therefore, a higher efficiency with  $\mu\text{c-SiGe:H}$  as bottom cell than with  $\mu\text{c-Si:H}$  bottom cell has not been achieved in double- and triple-junction solar cells. There might be a hope to use  $\mu\text{c-SiGe:H}$  in quadruple-junction solar cells to obtain a high efficiency.

## High Rate Deposition of $\mu\text{c-Si:H}$

Because  $\mu\text{c-Si:H}$  solar cells needs the absorber layer around 3–5  $\mu\text{m}$ , a high rate deposition of  $\mu\text{c-Si:H}$  is a critical technology for a-Si:H and  $\mu\text{c-Si:H}$  based multi-junction solar cell application. As previously discussed, high hydrogen dilution is the key parameter for  $\mu\text{c-Si:H}$  deposition, but high hydrogen dilution normally reduces the deposition rate; one could increase the deposition rate by increasing



the RF power, but a high RF power causes high energy bombardments and reduces the material quality. Therefore, using the conventional RF PECVD is difficult to achieve high rate deposition for  $\mu\text{-Si:H}$  materials. Over the years, many techniques have been explored for  $\mu\text{-Si:H}$  depositions including RF PECVD, VHF PECVD, microwave PECVD, hot-wire CVD, and Photo-CVD. The most successful and widely used method for high rate  $\mu\text{-Si:H}$  is VHF PECVD in the high power, high pressure depleting regime. Therefore, we present some details of this method below.

The Neuchatel group was the pioneer using VHF PECVD for thin film silicon deposition (Meier et al. 1994a, b, 1996; Shah et al. 2003). As shown in the previous chapter, under the same excitation power, the deposition rate increases with the excitation frequency, which is attributed the high dissociation rate with high frequency and therefore a high plasma density. The high dissociation rate results in a high atomic hydrogen flux intensity to the growth surface and promotes the formation of  $\mu\text{-Si:H}$ . Therefore, VHF PECVD is the mostly used method for high rate  $\mu\text{-Si:H}$  solar cells. Because of the shortened wavelength of VHF electromagnetic wave with the increase of frequency, the large area uniformity is a challenge in large area VHF PECVD system design. A compromised frequency for large area PECVD deposition and good  $\mu\text{-Si:H}$  quality is in the range of 40 MHz to 80 MHz, and 60 MHz or 65 MHz is often selected. With VHF PECVD, high-quality  $\mu\text{-Si:H}$  materials can be made at the deposition rate in the range of 2–3 nm/s, which can reach the same production efficiency as a-Si:H and a-SiGe:H multijunction solar panel production.

The group at AIST, Japan, invented high pressure depleting (HDP) mode in RF PECVD for high rate  $\mu\text{-Si:H}$  deposition (Fukawa et al. 2001; Gou et al. 1998; Kondo 2003). The logic is that a high RF power is needed for achieving a high rate deposition, but the high RF power generates high energy ions that bombard the growth surface and results in a high defect density in the deposited materials; to reduce the high energy ion bombardments, one could increase the process pressures to increase the collision of ions during the transport to the growth surface and reduce the ion energy. A high RF power also increases the dissociation rate and produces additional hydrogen atoms by breaking  $\text{SiH}_4$  molecules, especially at the depleting conditions where all of the active gases are dissociated for film deposition. In this case, the required hydrogen dilution for microcrystalline formation is reduced because of the extra atomic hydrogen from  $\text{SiH}_4$  molecules. Based on the Paschen curve, one needs to reduce the gap between the cathode and the anode for getting stable plasma when the pressure is increased. Therefore, the electrode gap is normally narrower when the HDP mode is used. For example, a gap of 4–6 cm could be used when the deposition pressure is at 1–2 torr, and it should be reduced to around or below  $\sim 1.0$  cm when the pressure is increased to  $>5$  torr.

Another method to reduce the ion energy in the high RF power deposition is to insert a mesh electrode in front of the substrate (Kondo 2003; Matsui and Kondo 2013); by biasing or grounding the mesh electrode, the ion energy can be controlled and the deposited material quality can be improved. However, the mesh electrode blocks some species from reaching the growth surface and therefore it reduces the deposition rates in some degrees. Figure 44 shows deposition rates as a function of RF power in an RF PECVD system with and without the mesh electrode. It is noted

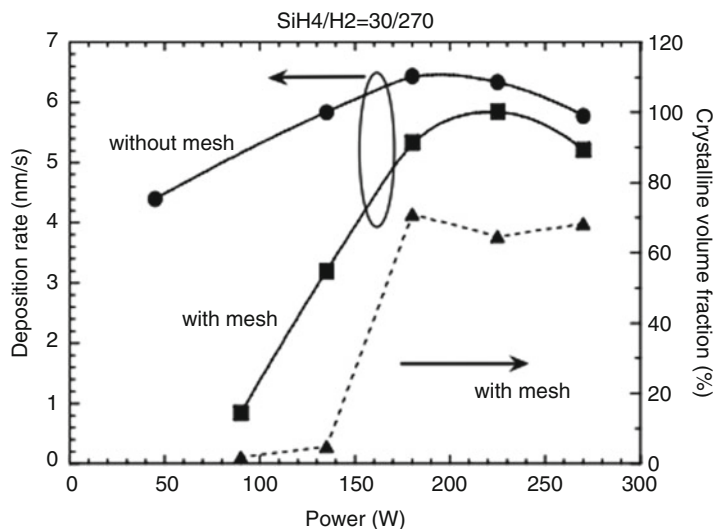


**Fig. 44** The deposition rate and the crystalline volume fraction as a function of the power under high-pressure depletion conditions using VHF plasma with and without the mesh. The film structure is shown only the case with the mesh because the film structure without using the mesh is always amorphous (Kondo 2003)

that in the un-depleting regime, the deposition rate increases with the RF power due to the increase of dissociation rate and the plasma density, and then it saturates and starts to decrease with the RF power, indicating a depleting of the active gases where the increased atomic hydrogen etches the growth surface and reduces the deposition rates. Figure 44 also plots the crystallinity as a function of RF power, showing the sharp increase of crystallinity when the depleting mode is reached. Figure 45 shows the defect density measured by electron spin resonance (ESR) versus the deposition rate in three cases of the conventional, HPD, and meshed RF PECVD depositions. In the conventional RF PECVD, the defect density increases sharply with the deposition rate, the slope of defect increase with RF power becomes shallower in the HPD case, and much lower defect density is obtained with the meshed configuration, indicating the advantages of the HPD and meshed PECVD depositions.

It has also been found that an optimized design of the cathode and gas distribution/pumping systems can also improve the  $\mu\text{-Si:H}$  material quality and solar cell efficiency. A multihole cathode also designed by the ASIT group is shown in Fig. 46. Using this system (Niikura et al. 2004, 2006), the defect density was further reduced to  $\sim 5 \times 10^{15} \text{ cm}^{-3}$  for  $\mu\text{-Si:H}$  deposited at 8 nm/s as shown in Fig. 47 (Niikura et al. 2004). Panasonic has also designed a similar system named Localized Plasma Confinement (LPC-CVD) (Terakawa 2013) and improved their large area a-Si:H/ $\mu\text{-Si:H}$  module efficiency significantly at a high deposition rate. A group at Osaka University used an atmosphere pressure 150 MHz VHF-PECVD to increase the deposition rate of  $\mu\text{-Si:H}$  to 80 nm/s and demonstrated the good material quality, but the techniques have some difficulty for large area deposition (Kakiuchi et al. 2009).



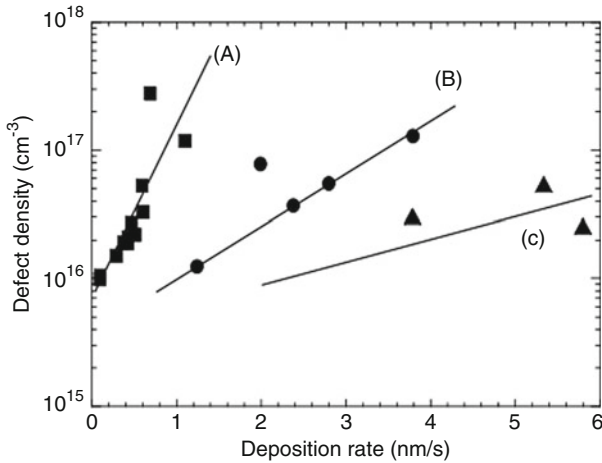


**Fig. 45** Defect density measured by ESR as a function of deposition rate using three different methods; (a) conventional method, (b) high pressure depletion method, and (c) triode method (Kondo 2003)

Strobel et al. (2015) increased the VHF frequency to 140 MHz, which could increase the deposition further, but also facing large area uniformity issue.

High rate deposition  $\mu\text{c-Si:H}$  is still a bottle neck for a-Si:H/ $\mu\text{c-Si:H}$  based solar cell module production with large area systems. By compromising the deposition rate, uniformity, material quality, and the complexity of large system design, a commonly used production technique is VHF PECVD under the HPD regime with a narrow gap space between the cathode and the substrate. The excitation frequency is in the range between 40 MHz and 80 MHz with a deposition rate in the order of 1–2 nm/s. For example, TEL Solar's production machine uses 40 MHz VHF PECVD.

## $\mu\text{c-Si:H}$ Thin Film Silicon Solar Cell Design and Optimization

A good material quality is the necessary condition, but not the sufficient condition for achieving high efficiency solar cells. The optimizations in device design and fabrication are all important procedures for achieving high efficiency solar cells. For  $\mu\text{c-Si:H}$  solar cells, several topics as directly related to the material properties and their influence on cell performance have been addressed above, such as the hydrogen dilution profile, improving the compactness of  $\mu\text{c-Si:H}$  materials, and light trapping. Below, we discuss two other important aspects: the doped layer and the interface.

### Doped Layer

In the early time, B-doped and P-doped a-Si:H layer are used as the *p* and *n* layers, respectively, in *p-i-n* and *n-i-p* structured thin film solar cells. The B-doped a-Si:H

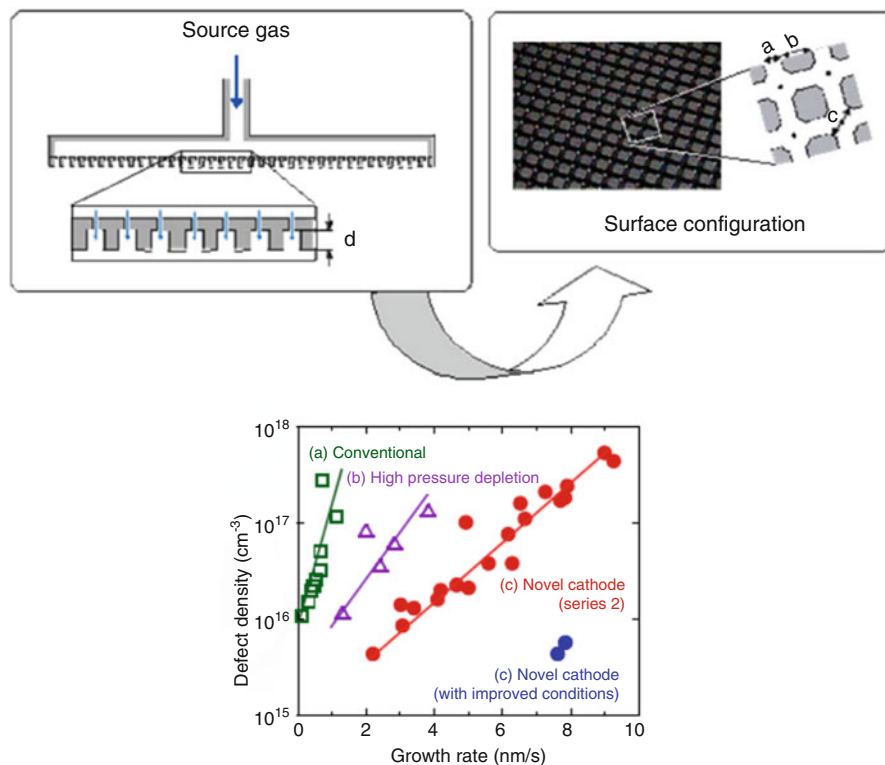
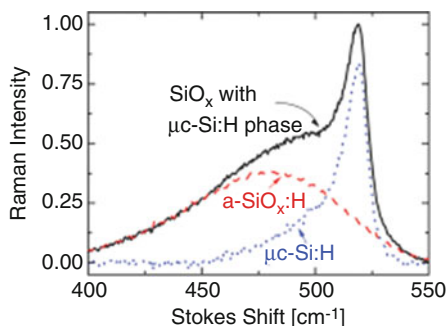


**Fig. 46** (upper) A multihole cathode designed by the ASIT group, and (lower) the defect density versus the deposition rate with various methods (Niikura et al. 2004, 2006)

**Fig. 47** The spectra of the  $\mu\text{c-SiO}_x\text{:H}$  layer is deconvoluted in an  $\text{a-SiO}_x\text{:H}$  peak (dashed line) and a  $\mu\text{c-Si:H}$  peak (dotted line) to calculate the crystalline volume fraction (Lambertz et al. 2011)



was deposited with  $\text{B}_2\text{H}_6$  as the doping gas and  $\text{PH}_3$  as the N-type doping gas. Because  $\text{B}_2\text{H}_6$  is not stable and could be thermally dissociated in the cylinder, the process parameter could shift with time. In addition the bandgap of B-doped  $\text{a-Si:H}$  narrows with the increase of B content, and it reduces the short wavelength response of solar cells. Alternatively, B-doped  $\text{a-SiC}_x\text{:H}$  has been widely used as the  $p$  layer in  $\text{a-Si:H}$  and  $\mu\text{c-Si:H}$  solar cells with Trimethylboron (TMB) as the doping gas

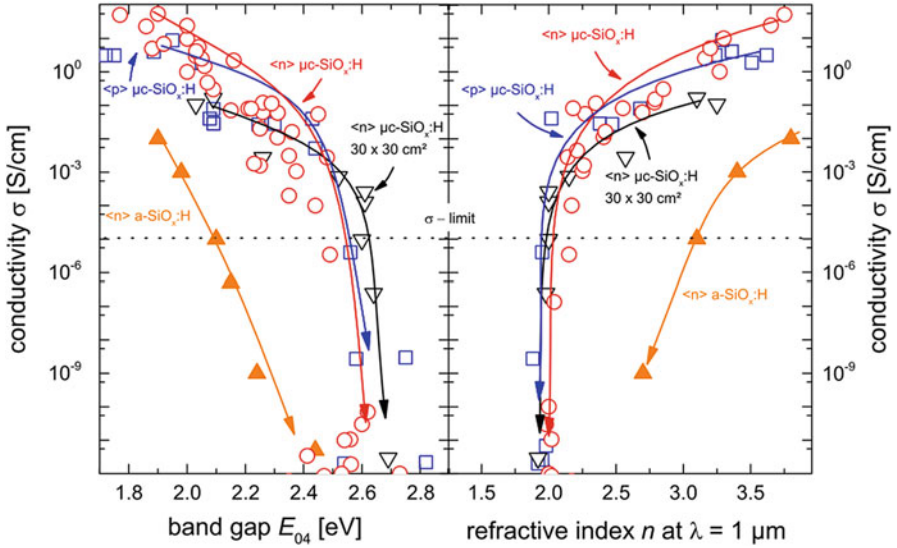


**Fig. 48** The electrical conductivity values for  $\mu\text{c-SiO}_x\text{:H}$  n-type (circles, triangles) and p-type (squares) films as a function of the band gap energy  $E_{04}$  (left) and as a function of the refractive index  $n$  (right), respectively (Lambertz et al. 2013)

(Tawada et al. 1982; Komuro et al. 1984). The group at United Solar invented B-doped  $\mu\text{c-Si:H:F}$  using  $\text{BF}_3$  as the doping gas and improved the  $V_{oc}$  significantly in a-Si:H, a-SiGe:H and  $\mu\text{c-Si:H}$  solar cells (Guha et al. 1986). Nowadays, for high efficiency  $\mu\text{c-Si:H}$  solar cells, the doped layers (both  $p$ -layer and  $n$ -layer) use microcrystalline silicon oxide  $\mu\text{c-SiO}_x\text{:H}$  (Buehlmann et al. 2007; Bugnon et al. 2012; Hou et al. 2015; Janthong et al. 2012; Lambertz et al. 2011, 2012, 2013; Smirnov et al. 2012), which is also called  $\text{nc-SiO}_x\text{:H}$ . Therefore, we will mainly discuss  $\mu\text{c-SiO}_x\text{:H}$  below.

$\mu\text{c-SiO}_x\text{:H}$  materials are a mixture of nanometer sized Si grains (nc-Si) embedded in an a-SiO<sub>x</sub>:H matrix. Figure 47 shows a Raman spectrum of  $\mu\text{c-SiO}_x\text{:H}$  material with the deconvolution with c-Si TO mode and the a-SiO<sub>x</sub>:H component (Lambertz et al. 2011). Such a two-phase structure results in the following unique properties. First, the crystalline phase is mainly nanometer sized silicon, where the doping efficiency could be high and form high conductive paths for current flow, especially in the vertical direction to the sample surface. The high doping efficiency and high conductivity establish the fundamental of the doped layers for solar cell application. The material can be doped in both N-type and P-type as shown in Fig. 48. Second, the a-SiO<sub>x</sub>:H tissue has a wide optical bandgap as measured by  $E_{04}$ , where the absorption coefficient equals  $10^4 \text{ cm}^{-1}$ , and low absorption coefficients for the window layer application; it greatly improves the short wavelength response on solar cells as shown in Fig. 49, which shows the performance a  $\mu\text{c-Si:H}$  solar cell with the  $\mu\text{c-SiO}_x\text{:H}$   $p$ -layer. One can see that the EQE at the short wavelength is very high, benefited from the low absorption in the  $\mu\text{c-SiO}_x\text{:H}$   $p$ -layer and the additional

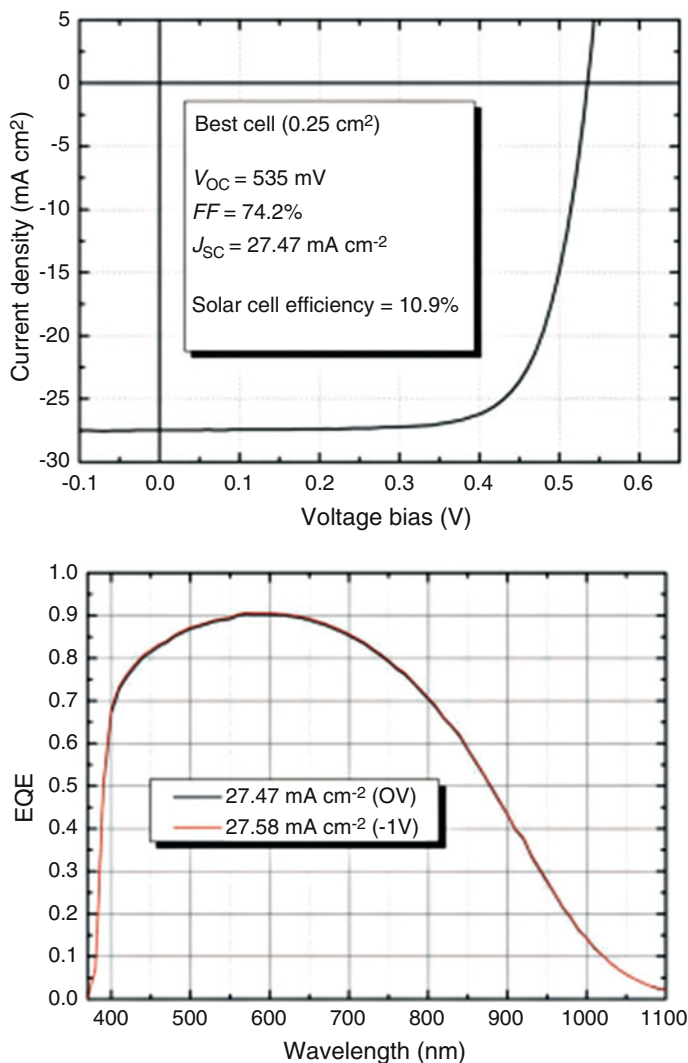


**Fig. 49** J-V characteristics and EQE curves under 0 V and  $-1$  V of the best-performing single-junction  $p$ - $i$ - $n$   $\mu\text{c-Si:H}$  solar cell ( $0.25\text{ cm}^2$ ) with an intrinsic layer thickness of  $2\text{ }\mu\text{m}$  deposited at  $3\text{ }\text{\AA}/\text{s}$  with optimized  $\text{SiO}_x\text{:H}$  doped layers and interfaces along with an anti-reflective coating at the air/glass interface (Bugnon et al. 2012)

antireflection coating effect. Using a  $\mu\text{c-SiO}_x\text{:H}$   $n$ -layer also improves  $\mu\text{c-Si:H}$  solar cell performance, by reducing the long wavelength loss absorbed in the  $n$ -layer, enhancing the light trapping and preventing microshunting caused by the textured substrates.

The refractive index  $n$  of  $\mu\text{c-SiO}_x\text{:H}$  changes with the O content and can be tuned between 3.5 and 2.0 as shown in Fig. 48, which can act as the dielectric layer for light

trapping and light management such as an intermedium reflection layer in multi-junction solar cells by reflecting some portion of light back to the a-Si:H top cell to achieve the designed current mismatching between the subcells (Janthong et al. 2012; Jung et al. 2014; Lambertz et al. 2013; Yamamoto et al. 2005). Because of the functions as doped layer and intermedium reflection layer, Yan et al. (2011) used it as the dual-function layer of n layer and intermedium reflection layer in a-Si:H/a-SiGe:H/ $\mu$ c-Si:H triple-junction solar cells and achieved a record efficiency of 16.3%.

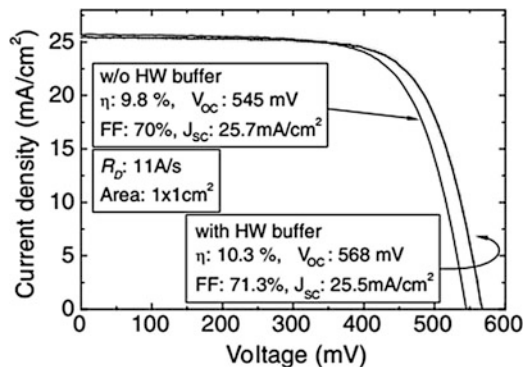
## Interface Layers

Except for the intrinsic and doped layers, the interfaces between the intrinsic and doped layers also affect the cell performance significantly. Mai et al. incorporated an intrinsic  $\mu$ c-Si:H buffer layer at  $p/i$  interface prepared by hot-wire CVD process into PECVD fabricated  $\mu$ c-Si:H solar cells and improved the  $V_{oc}$  by weakening the ion bombardment damage at the  $p/i$  interface (Mai et al. 2006). The J-V characteristic curves the cells with and without the hot-wire CVD buffer layer are shown in the Fig. 50, which demonstrates the effectiveness of the hot-wire deposited buffer layer in the improvement of  $V_{oc}$  and results in an record efficiency of 10.3% at the time.

An intrinsic a-Si:H buffer layer can also improves  $\mu$ c-Si:H solar cell performance by reducing the microshunt path, blocking the diffusion of doping atom into the intrinsic layer (Yue et al. 2008; Bai et al. 2015a). Since  $\mu$ c-SiO<sub>x</sub>:H  $p$  layer has been widely used as the window layer in  $\mu$ c-Si:H solar cells, it is logical to use an a-SiO<sub>x</sub>:H or  $\mu$ c-SiO<sub>x</sub>:H as the  $p/i$  buffer layer. Figure 51 depicts the illuminated J-V characteristics and EQE curves of two  $\mu$ c-Si:H single-junction solar cells with and without the intrinsic  $\mu$ c-SiO<sub>x</sub>:H buffer, which show an noticeable improvement in the cell performance (Bai et al. 2015a).

It was also found that the use of intrinsic silicon oxide as a buffer layer at the  $p/i$  interface of  $\mu$ c-Si:H solar cells provided significant advantages (Bugnon et al. 2014) in  $\mu$ c-Si:H solar cells: an improvement in carrier collection in the blue region of the spectrum is systematically observed, as shown in Fig. 52, which might result from

**Fig. 50** J-V characteristics of  $\mu$ c-Si:H single-junction solar cells with and without a hot wire CVD deposited  $p/i$  buffer, where the bulk  $i$ -layer was deposited by PECVD at 1.1 nm/s (Mai et al. 2006)



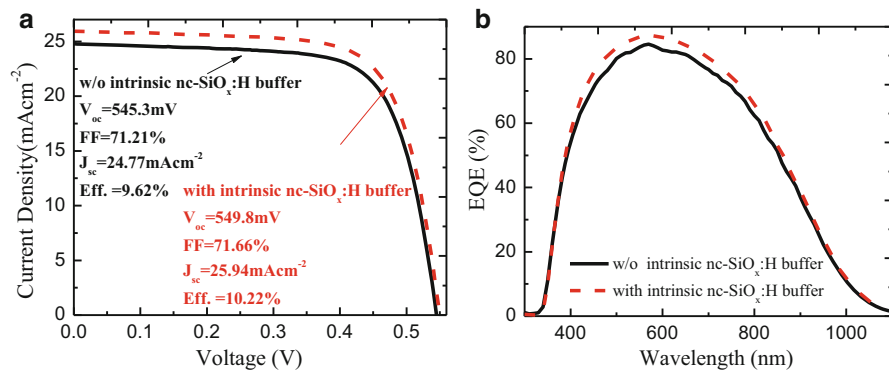


**Fig. 51** (a) Illuminated J-V characteristics and (b) EQE curves of  $\mu\text{c-Si:H}$  single-junction solar cells with and without intrinsic  $\mu\text{c-SiO}_x\text{:H}$  buffers (Bai et al. 2015a)

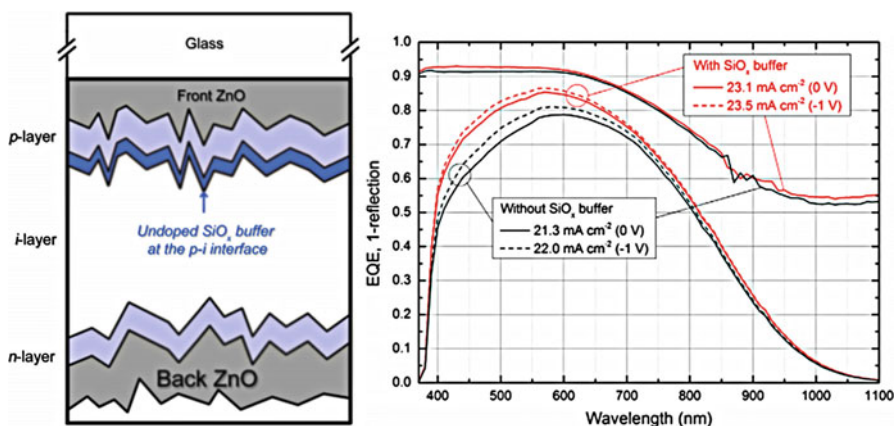


**Fig. 52** Sample scheme of a  $p-i-n$  cell with a  $\text{SiO}_x\text{:H}$  buffer at the  $p/i$  interface, and the EQE of the  $p-i-n$   $\mu\text{c-Si:H}$  solar cells, with (red) and without (black) the  $\text{SiO}_x$  buffer layer at the  $p/i$  interface (Bugnon et al. 2014)

the reduction of B contamination from the  $p$ -layer and the change of crystalline structure in the  $i$ -layer near the  $p/i$  interface.

An intrinsic or N-type a-Si:H buffer layer inserted between the  $\mu\text{c-Si:H}$  intrinsic and nc-SiO<sub>x</sub>:H  $n$  layers can also improve the cell performance by reducing the bandgap mismatching, blocking the diffusion of doping atoms into the intrinsic layer, and removing the micro-shunt paths (Bai et al. 2015b; Söderström et al. 2008). An example is shown in Fig. 53 (Bai et al. 2015b), where a series of  $\mu\text{c-Si:H}$  single-junction solar cells were made with the same condition except with different  $n$ -type a-Si:H buffer thicknesses (0, 4, 6, 8, and 10 nm). It evidently shows that as the buffer layer thickness gradually increased from 0 nm to 10 nm, the  $V_{oc}$  of the samples maintained nearly the same value (about 0.545 V). However,

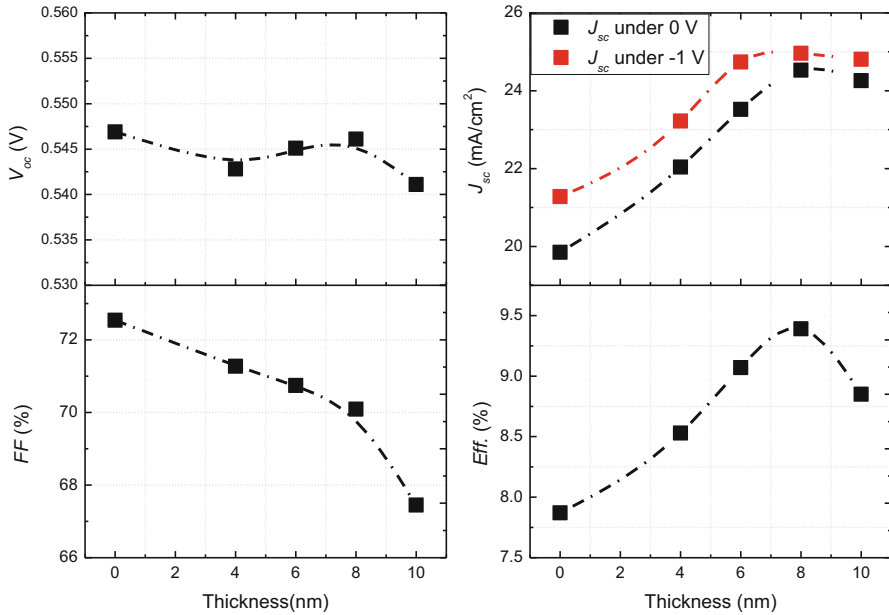


**Fig. 53** Device parameters of single-junction of  $\mu\text{c-Si:H}$  solar cells with different thicknesses of the n-a-Si buffer layers (Bai et al. 2015b)

the FF continuously decreased from 72.54% to 67.45%, which might be due to the additional series resistance, while the  $J_{sc}$  values obtained from the EQE at 0 V and  $-1$  V gradually increased with the buffer thickness until it reached the maximum at the 8 nm thickness, after which it slightly decreased. The increase in  $J_{sc}$  values mainly originates from the increases of the long-wavelength response. The variation trend of efficiency (Eff) with the buffer layer thickness values is similar to that of  $J_{sc}$ , an experimental observation proving that the  $J_{sc}$  variation has the strongest influence on the overall power output in this study. A maximized efficiency of 9.39% was achieved when an  $n$ -type a-Si:H buffer layer with a thickness of 8 nm is inserted between the  $\mu\text{c-Si:H}$  intrinsic and  $n$ -type nc-SiO<sub>x</sub>:H layers.

## High Efficiency $\mu\text{c-Si:H}$ Single-Junction Solar Cell

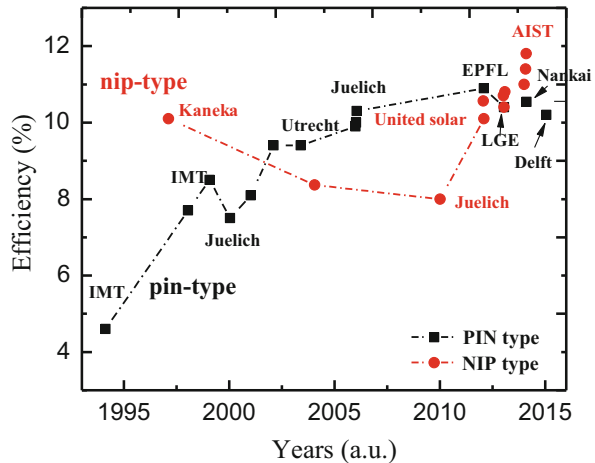
From the results above, one may realize that the design and optimization of  $\mu\text{c-Si:H}$  solar cell efficiency is a complicated scientific and engineering process. A better understanding of the deposition process and its correlation with the material properties helps to design a cell fabrication process to deposit high quality materials; an optimized device design with the best materials and well-controlled interface is also critical for solar cell performance. In addition, the transparent electrodes and back reflectors have to be optimized as well. Over the years, the community has made a

**Table 9** The detail parameters of the highest efficiency single junction  $\mu\text{-Si:H}$  solar cells

Year	Type	Institute	$V_{oc}$ (V)	FF (%)	$J_{sc}$ ( $\text{mA}\cdot\text{cm}^{-2}$ )	Eff. (%)
2006.03	p-i-n	Utrecht	0.52	74.0	25.9	10
2006.05	p-i-n	Juelich	0.568	71.3	25.5	10.3
2012.09	p-i-n	EPFL	0.535	74.2	27.47	10.9
2013.05	p-i-n	LGE	0.54	73.0	26.1	10.4
2015.06	p-i-n	Delft	0.552	72.6	25.6	10.2
2014.12	p-i-n	Nankai	0.552	71.76	26.6	10.54
2012.06	n-i-p	Uni-solar	0.543	69.1	28.15	10.56
2014.10	n-i-p	AIST	0.548	73.1	29.4	11.77

Note: Utrecht: (Gordijn et al. 2006); Juelich: (Mai et al. 2006); EPFL: (Bugnon et al. 2012); LGE: (Jung et al. 2014); Delft: (Tan et al. 2015); Nankai: (Zhang 2016); Uni-Solar: (Yue et al. 2012b); AIST: (Sai et al. 2015)

**Fig. 54** The highest efficiency of  $p-i-n$  type and  $n-i-p$  type  $\mu\text{-Si:H}$  single-junction solar cells achieved by different research institutions



significant progress in  $\mu\text{-Si:H}$  cell efficiency improvement. Table 9 lists some selected high efficiencies achieved by different institutes, and Fig. 54 shows the progress made by the community. The best single-junction  $\mu\text{-Si:H}$  solar cell efficiency is 11.8% achieved by the AIST group with certified performance characteristics shown in Fig. 55 (Sai et al. 2015).

### A-Si:H and $\mu\text{-Si:H}$ Based Multijunction Solar Cell and Modules

As discussed above, the advantage of  $\mu\text{-Si:H}$  over a-Si:H and a-SiGe:H as the absorber layer in solar cells is the extended absorption spectrum to the long wavelength for high photocurrent. Using  $\mu\text{-Si:H}$  as the middle and bottom cells in multijunction solar cells can absorb the sun light in a wide range and achieve high solar cell efficiency. Over the years, several multijunction solar cell structures have



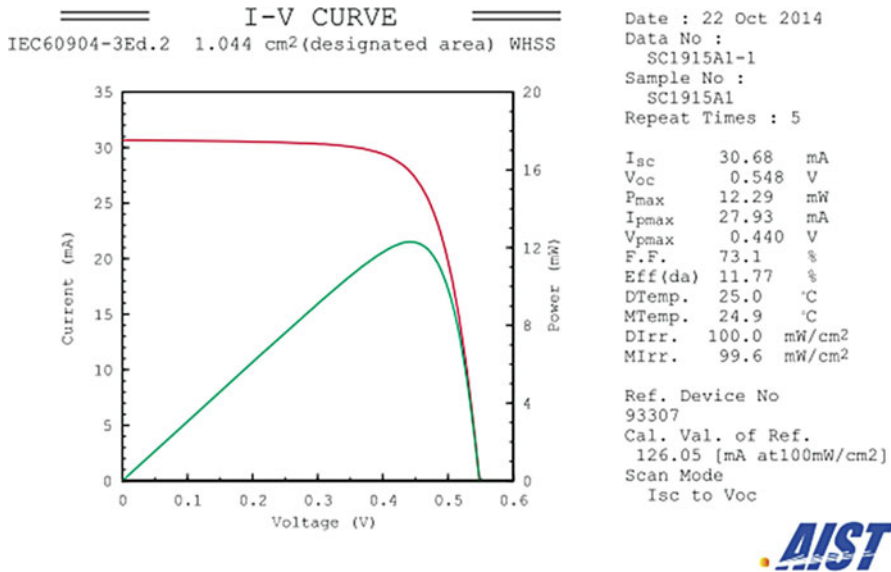


**Fig. 55** J-V curves of the highest efficiency  $\mu\text{-Si:H}$  cell independently confirmed by the CSM-RCPVT-AIST ( $V_{oc} = 0.548$  V,  $J_{sc} = 29.4$  mA / cm<sup>2</sup>, FF = 0.731, Eff = 11.77%) (Sai et al. 2015)

been extensively studied. For example, Fig. 56 shows the commonly used  $n-i-p$  multijunction solar cells.

The design and fabrication of multijunction solar cells are much more complicated than single-junction solar cells. First, additional attentions must be paid to the current matching because the  $J_{sc}$  of a multijunction solar cell takes the smallest photocurrent density among the individual component cells. A proper design, the component cell thicknesses, and selection of the bandgap of the absorber layers in each component cell should be optimized to give the desired current matching for the best stable efficiency. Second, the connections between individual component cells need to be optimized to minimize the losses at the connection because the top cell  $n$ -layer and the bottom cell  $p$ -layer form an opposite  $p-n$  junction with the main  $p-i-n$  junctions, where the current flows through a tunneling and recombination process; therefore, the junction there is called the tunnel-junction. A good tunnel-junction should have a minimum voltage loss for high  $V_{oc}$  and a low resistance for good FF. Because these topics are more engineering, and the concept is similar to other multi-junction solar cells, we will not discuss the details here. But as expected the multijunction solar cells provide higher efficiency than single-junction solar cells. As mentioned previously, the highest initial efficiency for thin film silicon solar cells is 16.3% achieved using an a-Si:H/a-SiGe:H/ $\mu\text{-Si:H}$  triple-junction structure with the J-V characteristics and EQE curves in Fig. 57 (Yan et al. 2011). Using an a-Si:H/ $\mu\text{-Si:H}$ / $\mu\text{-Si:H}$  triple-junction structure, LG Solar have demonstrated an NREL confirmed 13.44% stable efficiency with the results shown in Fig. 58 (Kim et al. 2013). The progress

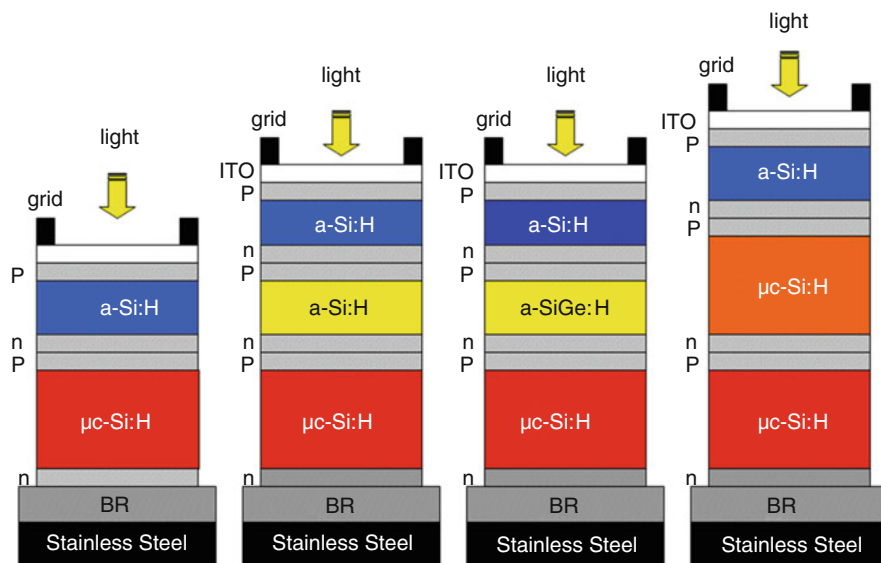


**Fig. 56** Schematics of *n-i-p* multijunction solar cells with  $\mu\text{c-Si:H}$  in the bottom cell

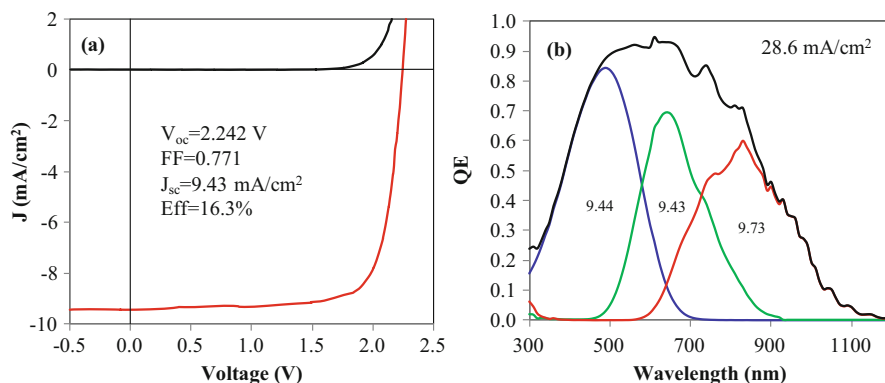


**Fig. 57** (a) J-V characteristics and (b) EQE spectra of an a-Si:H/a-SiGe:H/ $\mu\text{c-Si:H}$  triple-junction solar cell with an initial efficiency of 16.3% (Yan et al. 2011)

of a-Si:H, a-SiGe:H and  $\mu\text{c-Si:H}$  multijunction solar cell efficiency made by the community is shown in Fig. 59. Although over 16% initial cell efficiencies have been achieved with both the *n-i-p* and *p-i-n* structures, the progress has been slowed down in recent years; especially the thin film silicon photovoltaic industry has been significantly shrunk. However, a remaining question for the thin film community is whether the thin film silicon solar cell efficiency has reached the

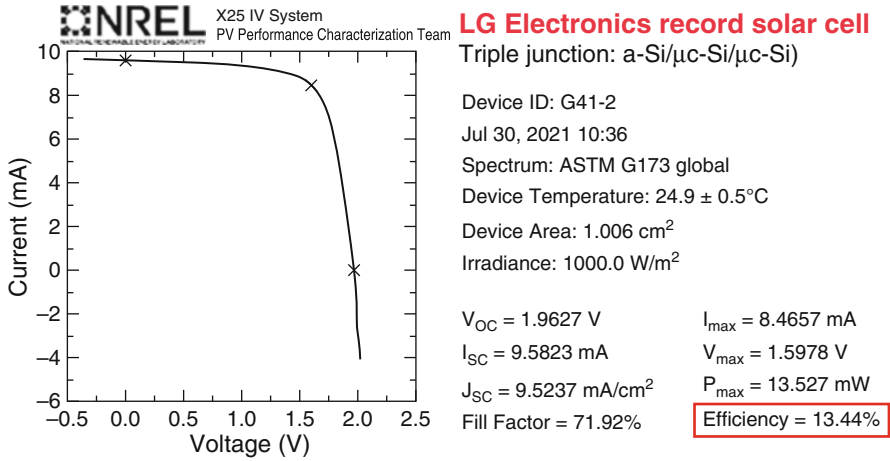
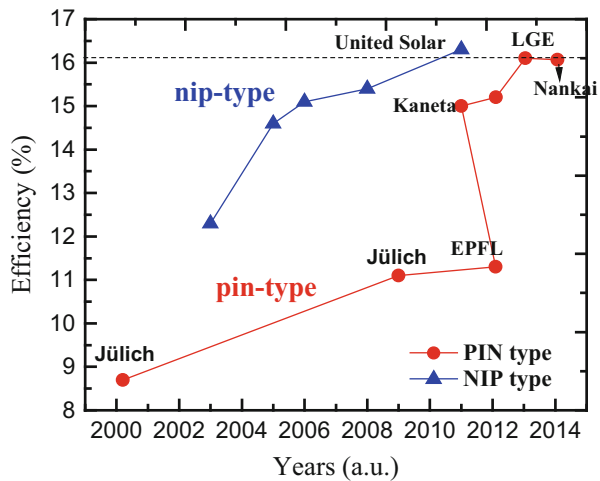


**Fig. 58** The established performance of the a-Si:H/ $\mu$ c-Si:H/ $\mu$ c-Si:H triple-junction solar cell after 1000 h light soaking. This new record was confirmed by NREL (Kim et al. 2013)

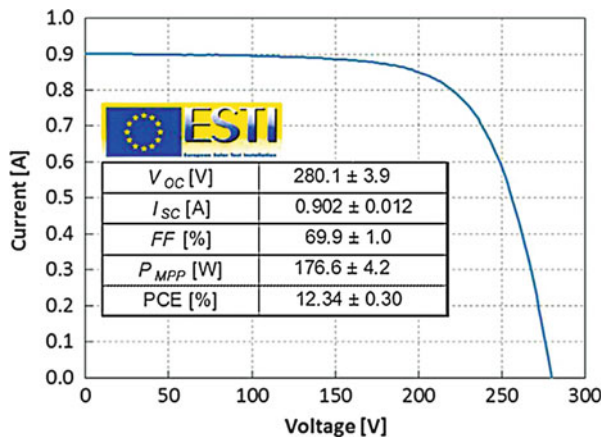
**Fig. 59** The highest efficiency of a-Si:H/a-SiGe:H/ $\mu$ c-Si:H triple-junction solar cells achieved in different research institutions



upper limit. Simulation studies have shown that with quadruple structures, around 20% cell efficiencies could be attained (Isabella et al. 2014).

a-Si:H and  $\mu$ c-Si:H multijunction solar cells have been also incorporated into production lines with increased module efficiency over a-Si:H and a-SiGe:H multijunction product. Large area module efficiency has been steady improved. A stable large area ( $1.43 \text{ m}^2$ ) efficiency of 12.34% has been achieved by TEL Solar and confirmed by ESTI as shown in Fig. 60 (Cashmore et al. 2016).

**Fig. 60** Stabilized I-V curve and parameters of the record module (1.43 m<sup>2</sup>) made by TEL Solar and certified by ESTI (Cashmore et al. 2016)



## Summary

$\mu\text{-Si:H}$  is a unique material with nanometer sized crystallites embedded in amorphous silicon tissues. The complex in the material structure provides a great platform for material studies with rich physics and chemistry in the material deposition, characterization, and device applications. Here we reviewed the material properties with the main focuses to address the major issues affecting the  $\mu\text{-Si:H}$  solar cell performance and the approaches to resolve these problems.

The key process parameter controlling the transition from a-Si:H to  $\mu\text{-Si:H}$  is the hydrogen dilution. The  $\mu\text{-Si:H}$  deposition needs a much higher hydrogen dilution than a-Si:H deposition. One of the interesting phenomena is the crystalline evolution: the  $\mu\text{-Si:H}$  deposition starts with an a-Si:H incubation layer, follows with crystallite seed formation, grows cone-structured crystallite aggregations, and increases the crystalline volume fraction with film thickness. Such crystalline evolution with the film thickness has a negative impact on solar cell performance. To resolve this issue, a hydrogen dilution profile technique was invented with a very high hydrogen dilution to remove the a-Si:H incubation layer and growth  $\mu\text{-Si:H}$  from the beginning, following a continually decreasing the hydrogen dilution to maintain a desired crystallinity distribution along the film thickness. The hydrogen dilution profiling technique is proven to be an effective method for high efficiency  $\mu\text{-Si:H}$  solar cell deposition. The similar result can also be obtained by changing other parameters such as the excitation power in PECVD deposition with a high power at the initial deposition to promote the crystalline formation and gradually reducing the power during the deposition to maintain the same crystallinity.

$\mu\text{-Si:H}$  is more sensitive to impurity than a-Si:H especially to O. The tolerance for O in a-Si:H is in the level of  $1\text{--}2 \times 10^{19} \text{ cm}^{-3}$ , but it is below  $5 \times 10^{18} \text{ cm}^{-3}$  in  $\mu\text{-Si:H}$ .

In addition, it is more sensitive to the normal doping elements of B and P. Therefore, a clean multichamber deposition system with pure gases is essential for high quality  $\mu\text{-Si:H}$  materials and high efficiency solar cells. The O impurity can be compensated by adding a small amount of B called “microdoping.” However, the window of “microdoping” is narrow and difficult to control. The impurities are not only incorporated during the deposition process, but also diffuse into the material after deposition and exposure to air for un-optimized  $\mu\text{-Si:H}$  materials and solar cells, which cause the conductivity increase and solar cell efficiency decrease. To resolve the postdeposition impurity diffusion problem, one needs to optimize the process to deposit compact  $\mu\text{-Si:H}$  materials to block the channel of impurity diffusion.

Light trapping is an effective method to improve the photocurrent density of  $\mu\text{-Si:H}$  solar cells, hence efficiency. The *n-i-p* structured solar cells use a back reflector to achieve the light trapping, while the *p-i-n* cells use textured TCO such as AZO and BZO. Using an optimized Ag/ZnO back reflector, the current gain can be as high as 60%. However, the textures of the substrates could cause a negative effect on the  $\mu\text{-Si:H}$  structure and quality. To resolve this issue, electric flat and optical textured back reflectors are invented. There is no conclusion whether a periodically structured back reflector is better than the randomly textured back reflector. Although some theories may provide a positive supporting, most high efficiency  $\mu\text{-Si:H}$  based solar cells are made on randomly textured substrates.

The high rate deposition is a bottleneck for reducing the a-Si:H and  $\mu\text{-Si:H}$  based thin film solar module production cost. The commonly used method for high rate deposition nowadays is VHF PECVD at the high power, high pressure depleting regime. The deposition rate could be in the range of 2–3 nm/s for good cell performance. Other techniques such as atmospheric VHF PECVD can make  $\mu\text{-Si:H}$  at much high rate, but the scale-up to large area machine faces problems.

After the over 20 years of fundamental research and technology development,  $\mu\text{-Si:H}$  single-junction solar cell efficiency has been over 11%, multijunction cell over 16%, and stable module efficiency over 12%. With the dramatic reduction of c-Si solar module price in recent years, thin film silicon PV product has lost the advantages in the market, especially in large scale utility level PV power station. However, the unique properties of the thin film silicon PV product such as the flexibility and light weight may keep the product in some niche market such as consumer electronic chargers, unmanned space vehicles and BIPV applications.

Looking forward for improving the thin film silicon cell and module efficiency, new materials and cells structures such as poly-Si thin film solar cells and modules will be discussed in the next chapter.

**Acknowledgments** The authors are grateful for the colleagues in the thin film silicon PV community. They have enjoyed very much for the collaborations with several institutions and sharing ideas and results through the international conferences such as the MRS, ICANS, IEEE-PVSEC, and EU-PVSEC. BY acknowledges the hospitality of the Nankai University.

## References

- L. Bai, B. Liu, J. Zhao, et al., *J. Appl. Phys.* **117**, 175309 (2015a)
- L. Bai, B. Liu, Q. Huang, et al., *Sol. Energy Mater. Sol. Cells* **140**, 202 (2015b)
- J. Bailat, E. Vallat-Sauvain, L. Feitknecht, C. Droz, A. Shah, *J. Non-Cryst. Solids* **1219**, 299–302 (2002)
- J. Bailat, D. Dominé, R. Schlüchter, J. Steinhäuser, S. Fay, F. Freitas, C. Bücher, L. Feitknecht, X. Niquille, T. Tschamer, A. Shah, C. Ballif, *Proc. 4th World Conf. on Photovoltaic Energy Conversion (Hawaii, 2006)*, p. 1533
- C. Battaglia, C.-M. Hsu, K. Söderström, J. Escarre, F.-J. Haug, M. Charriere, M. Boccard, M. Despeisse, D.T.L. Alexander, M. Cantoni, Y. Cui, C. Ballif, *ACS Nano* **6**, 2790 (2012)
- M.H. Brodsky, M. Cardona, J.J. Cuomo, *Phys. Rev. B* **16**, 3556 (1977)
- P. Buehlmann, J. Bailat, D. Domine, A. Billet, F. Meillaud, A. Feltrin, et al., *Appl. Phys. Lett.* **91**, 143505 (2007)
- G. Bugnon, G. Parascandolo, T. Söderström, P. Cuony, M. Despeisse, S. Hänni, J. Holovský, F. Meillaud, C. Ballif, *Adv. Funct. Mater.* **22**, 3665 (2012)
- G. Bugnon, G. Parascandolo, S. Hänni, et al., *Sol. Energy Mater. Sol. Cells* **120**, 143 (2014)
- E. Bustarret, M.A. Hachicha, M. Brunel, *Appl. Phys. Lett.* **52**, 1675 (1988)
- R. Carius, J. Folsch, D. Lundszen, L. Houben, F. Finger, *Mater. Res. Soc. Symp. Proc.* **507**, 813 (1998)
- J.S. Cashmore, M. Apolloni, A. Braga, O. Caglar, V. Cervetto, Y. Fenner, S. Goldbach-Aschemann, C. Goury, J.E. Hötzel, T. Iwahashi, J. Kalas, M. Kitamura, M. Klindworth, M. Kupich, G.-F. Leu, J. Lin, M.-H. Lindic, P.A. Losio, T. Mates, D. Matsunaga, B. Mereu, X.-V. Nguyen, I. Psimoulis, S. Ristau, T. Roschek, A. Salabas, E.L. Salabas, I. Sinicco, *Sol. Energy Mater. Sol. Cells* **144**, 84 (2016)
- P. Chen, G. Hou, Q. Fan, J. Ni, J. Zhang, Q. Huang, X. Zhang, Y. Zhao, *Sol. Energy Mater. Sol. Cells* **143**, 435 (2015)
- Y.-B. Chung, D.-K. Lee, J.-S. Lim, N.-M. Hwang, *Sol. Energy Mater. Sol. Cells* **95**, 211 (2011)
- R.W. Collins, A.S. Ferlauto, G.M. Ferreira, C. Chen, J. Koh, R.J. Koval, Y. Lee, J.M. Pearce, C.R. Wronski, *Sol. Energy Mater. Sol. Cells* **78**, 143 (2003)
- L.R. Dahal, J. Li, J.A. Stoke, Z. Huang, A. Shan, A.S. Ferlauto, C.R. Wronski, R.W. Collins, N.J. Podraza, *Sol. Energy Mater. Sol. Cells* **129**, 32 (2014)
- P. Debye, *Physik. Z.* **17**, 277 (1916)
- C. Droz, E. Vallat-Sauvain, J. Bailat, L. Feitknecht, J. Meier, A. Shah, *Sol. Energy Mater. Sol. Cells* **81**, 61 (2004)
- T. Dylla, F. Finger, E.A. Schiff, *Appl. Phys. Lett.* **87**, 032103 (2005)
- F. Finger, in *Thin-Film Silicon Solar Cells*, ed. by A. Shah (Ed), (EPFL Press, Lausanne, 2010) Chapter 3
- M. Fukawa, S. Suzuki, L. Guo, M. Kondo, A. Matsuda, *Sol. Energy Mater. Sol. Cells* **66**, 217 (2001)
- G. Ganguly, T. Ikeda, T. Nishimiya, K. Saitoh, M. Kondo, A. Matsuda, *Appl. Phys. Lett.* **69**, 4224 (1996)
- A. Gordijn, J.K. Rath, R.E.I. Schropp, *Prog. in Photovoltaics: Res. and Appl* **14**, 305 (2006)
- Q. Gu, Q. Wang, E.A. Schiff, Y.-M. Liand, C.T. Malone, *J. Appl. Phys.* **76**, 2310 (1994)
- L. Guo, M. Kondo, M. Fukawa, K. Saitoh, A. Matsuda, *Jpn. J. Appl. Phys.* **37**, L1116 (1998)
- S. Guha, J. Yang, P. Nath, M. Hack, *Appl. Phys. Lett.* **49**, 218 (1986)
- S. Guha, J. Yang, B. Yan, *Sol. Energy Mater. Sol. Cells* **119**, 1 (2013)
- X. Han, G. Hou, X. Zhang, C. Wei, G. Li, J. Zhang, X. Chen, D. Zhang, J. Sun, Y. Zhao, X. Geng, *Sol. Energy Mater. Sol. Cells* **94**, 254 (2010)
- Q. Huang, Y. Liu, S. Yang, Y. Zhao, X. Zhang, *Solar Ener. Mater. & Sol. Cells* **103**, 134 (2012)
- G. Hou, J. Fang, Q. Fan, C. Wei, J. Ni, X. Zhang, Y. Zhao, *Sol. Energy Mater. Sol. Cells* **134**, 395 (2015)
- J. Hüpkens, H. Zhu, J.I. Owen, G. Jost, E. Bunte, *Thin Solid Films* **520**, 1913 (2012)

- O. Isabella, A.H.M. Smets, M. Zeman, *Sol. Energy Mater. Sol. Cells* **129**, 82 (2014)
- Z. Iqbal, S. Veprek, *J. Phys. C* **15**, 377 (1982)
- B. Janthong, A. Hongsingthong, T. Krajangsang, L. Zhang, P. Sichanugrist, M. Konagai, *J. Non-Cryst. Solids* **358**, 2478 (2012)
- S.J. Jung, B.J. Kim, M. Shin, *Sol. Energy Mater. Sol. Cells* **121**, 1 (2014)
- H. Kakiuchi, H. Ohmi, K. Ouchi, K. Tabuchi, K. Yasutake, *J. Appl. Phys.* **106**, 013521 (2009)
- S. Kasouit, S. Kumar, R. Vanderhaghen, P. Roca i Cabarrocas, I. French, *J. Non-Cryst. Solids* **113**, 299–302 (2002)
- S. Kim, J.-W. Chung, H. Lee, J. Park, Y. Heo, H.-M. Lee, *Sol. Energy Mater. Sol. Cells* **119**, 26 (2013)
- S. Klein, F. Finger, R. Carius, T. Dylla, B. Rech, M. Grimm, L. Houben, M. Stutzmann, *Thin Solid Films* **430**, 202 (2003)
- J. Kocka, A. Fejfar, P. Fojtik, K. Luterova, I. Pelant, B. Rezek, H. Stuchlikova, J. Stuchlik, V. Svrcek, *Sol. Energy Mater. Sol. Cells* **66**, 61 (2001)
- J. Kocka, A. Fejfar, H. Stuchlikova, J. Stuchlik, P. Fojtik, T. Mates, B. Rezek, K. Luterova, V. Svrcek, I. Pelant, *Sol. Energy Mater. Sol. Cells* **78**, 493 (2003)
- S. Komuro, Y. Aoyagi, Y. Segawa, S. Namba, A. Masuyama, H. Okamoto, Y. Hamakawa, *J. Appl. Phys.* **55**, 3866 (1984)
- M. Kondo, *Sol. Energy Mater. Sol. Cells* **78**, 543 (2003)
- U. Kroll, J. Meier, P. Torres, J. Pohl, A. Shah, *J. Non-Cryst. Solids* **68**, 227–230 (1998)
- A. Lambertz, T. Grundler, F. Finger, *J. Appl. Phys.* **109**, 113109 (2011)
- A. Lambertz, F. Finger, B. Holländer, J.K. Rath, R.E.I. Schropp, *J. Non-Cryst. Solids* **358**, 1962 (2012)
- A. Lambertz, V. Smirnov, T. Merdzhanova, K. Ding, S. Haas, G. Jost, R.E.I. Schropp, F. Finger, U. Rau, *Sol. Energy Mater. Sol. Cells* **119**, 134 (2013)
- M. Ledinsky, L. Fekete, J. Stuchlik, T. Mates, A. Fejfar, J. Kocka, *J. Non-Cryst. Solids* **352**, 1209 (2006)
- Y. Mai, S. Klein, R. Carius, et al., *J. Non-Cryst. Solids* **352**, 1859 (2006)
- T. Matsui, M. Kondo, K. Ogata, T. Ozawa, M. Isomura, *Appl. Phys. Lett.* **89**, 142115 (2006)
- T. Matsui, C.W. Chang, M. Kondo, K. Ogata, M. Isomura, *Appl. Phys. Lett.* **91**, 10211 (2007)
- T. Matsui, C.W. Chang, T. Takada, M. Isomura, H. Fujiwara, M. Kondo, *Sol. Energy Mater. Sol. Cells* **93**, 1100 (2009)
- T. Matsui, M. Kondo, *Sol. Energy Mater. Sol. Cells* **119**, 156 (2013)
- J. Meier, R. Fluckiger, H. Keppner, A. Shah, *Appl. Phys. Lett.* **65**, 860 (1994a)
- J. Meier, S. Dubail, R. Fluckiger, D. Fischer, H. Keppner, A. Shah, *Proc. of 1st World Conference on Photovoltaic Energy Conversion (1994b)*, p. 409
- J. Meier, P. Torres, R. Platz, S. Dubail, U. Kroll, J.A. Anna Selvan, N. Pellaton Vaucher, C. Hof, D. Fischer, H. Keppner, A. Shah, K.D. Ufert, P. Giannoulès, J. Koehler, *Mater. Res. Soc. Symp. Proc.* **420**, 3 (1996)
- J. Meier, S. Dubail, J. Cuperus, U. Kroll, R. Platz, P. Torres, J.A.A. Selvan, P. Pernet, N. Beck, N.P. Vaucher, C. Hof, D. Fischer, H. Keppner, A. Shah, *J. Non-Cryst. Solids* **1250**, 227–230 (1998)
- J. Meier, S. Dubail, S. Golay, U. Kroll, S. Fay, E. Vallat-Sauvain, L. Feitknecht, J. Dubail, A. Shah, *Sol. Ener. Mater. & Sol. Cells* **74**, 457 (2002)
- T. Merdzhanova, J. Woerdenweber, W. Beyer, T. Kilper, U. Zastrow, M. Meier, H. Stiebig, A. Gordijn, *J. Non-Cryst. Solids* **358**, 2171 (2012)
- J. Müller, O. Kluth, S. Wieder, H. Siekmann, G. Schöpe, W. Reetz, O. Vetterl, D. Lundszen, A. Lambertz, F. Finger, B. Rech, H. Wagner, *Sol. Ener. Mater. & Sol. Cells* **66**, 275 (2001)
- J. Müller, G. Schöpe, O. Kluth, B. Recha, V. Sittingerb, B. Szyszkab, R. Geyserc, P. Lechnerc, H. Schadec, M. Rusked, G. Dittmare, H.-P. Bochemf, *Thin Solid Films* **442**, 158 (2003)
- Y. Nasuno, M. Kondo, A. Matsuda, *Jpn. J. Appl. Phys.* **40**, 303 (2001)
- J. Ni, Q. Liu, J. Zhang, J. Ma, H. Wang, X. Zhang, Y. Zhao, *Sol. Energy Mater. Sol. Cells* **126**, 6 (2014)

- S. Nicolay, M. Despeisse, F.-J. Haug, C. Ballif, *Solar Ener. Mater. & Sol. Cells* **95**, 1031 (2011)
- C. Niikura, M. Kondo, A. Matsuda, *J. Non-Cryst. Solids* **42**, 338–340 (2004)
- C. Niikura, M. Kondo, A. Matsuda, *Sol. Energy Mater. Sol. Cells* **90**, 3223 (2006)
- A. Pawlikiewicz, S. Guha, *Mater. Res. Soc. Symp. Proc.* **118**, 599 (1988)
- S. Pillai, K.R. Catchpole, T. Trupke, M.A. Green, *J. Appl. Phys.* **101**, 093105 (2007)
- A. Poruba, A. Fejfar, Z. Remes, J. Springer, M. Vanecek, J. Kocka, *J. Appl. Phys.* **88**, 148 (2000)
- M. Python, O. Madani, D. Domine, F. Meillaud, E. Vallat-Sauvain, C. Ballif, *Sol. Energy Mater. Sol. Cells* **93**, 1714 (2009)
- S. Ray, S. Mukhopadhyay, T. Jana, R. Carius, *J. Non-Cryst. Solids* **761**, 299–302 (2002)
- B. Rezek, J. Stuchlik, A. Fejfar, J. Kočka, *J. Appl. Phys.* **92**, 587 (2002)
- Y. Sobajima, S. Nakano, T. Toyama, H. Okamoto, S. Omae, T. Minemoto, H. Takakura, Y. Hamakawa, *J. Appl. Phys.* **101**, 103537 (2007)
- T. Roschek, T. Repmann, J. Müller, B. Rech, H. Wagner, *Proc. of 28th IEEE Photovoltaic Specialists Conference (IEEE, Anchorage, 2000)*, p. 150
- H. Sai, H. Fujiwara, M. Kondo, *Sol. Energy Mater. Sol. Cells* **93**, 1087 (2009)
- H. Sai, Y. Kanamori, M. Kondo, *Appl. Phys. Lett.* **98**, 113502 (2011)
- H. Sai, K. Saito, M. Kondo, *IEEE J. Photovoltaics* **3**, 5 (2012)
- H. Sai, K. Maejima, T. Matsui, T. Koida, M. Kondo, S. Nakao, *Jap. J. Appl. Phys* **54**(8S1), 08KB05 (2015)
- A.V. Shah, J. Meier, E. Vallat-Sauvain, N. Wyrsh, U. Kroll, C. Droz, U. Graf, *Sol. Energy Mater. Sol. Cells* **78**, 469 (2003)
- L. Sivec, B. Yan, G. Yue, J. Owens-Mawson, J. Yang, S. Guha, *IEEE J. Photovoltaics* **2**, 27 (2012)
- V. Smirnov, A. Lambertz, B. Grootoonk, R. Carius, F. Finger, *J. Non-Cryst. Solids* **358**, 1954 (2012)
- T. Söderström, F.-J. Haug, V. Terrazoni-Daudrix, X. Niquille, M. Python, C. Ballif, *J. Appl. Phys.* **104**, 104505 (2008)
- K. Söderström, G. Bugnon, F.-J. Haug, S. Nicolay, C. Ballif, *Solar Ener. Mater. & Sol. Cells* **101**, 193 (2012a)
- K. Söderström, G. Bugnon, R. Biron, C. Pahud, F. Meillaud, F.-J. Haug, C. Ballif, *J. Appl. Phys.* **112**, 114503 (2012b)
- P. Spinelli, V. E. Ferry, J. van de Groep, M. van Lare, M. A. Verschuuren, R. E. I. Schropp, .H. A. Atwater, and A. Polman, *J. Opt.* **14**, 024002 (2012)
- R.A. Street, *Appl. Phys. Lett.* **59**, 1084 (1991)
- C. Strobel, B. Leszczynska, U. Merkel, J. Kuske, D.D. Fischer, M. Albert, J. Holovský, S. Michard, J.W. Bartha, *Sol. Energy Mater. Sol. Cells* **143**, 347 (2015)
- H. Tan, L. Sivec, B. Yan, R. Santbergen, M. Zeman, A.H.M. Smets, *App. Phys. Lett.* **102**, 153902 (2013)
- H. Tan, E. Moulin, F.T. Si, et al., *Progr. in Photovoltaics: Res. and Appl.* **23**, 949 (2015)
- Y. Tawada, K. Tsuge, M. Kondo, H. Okamoto, Y. Hamakawa, *J. Appl. Phys.* **53**, 5273 (1982)
- A. Terakawa, *Sol. Energy Mater. Sol. Cells* **119**, 204 (2013)
- P. Torres, J. Meier, R. Fluckiger, U. Kroll, J.A.A. Selvan, H. Keppner, A. Shah, S.D. Littlewood, I.E. Kelly, P. Giannoules, *Appl. Phys. Lett.* **69**, 1373 (1996)
- R. Tsu, J. Gonzalez-Hernandez, S.S. Chao, S.C. Lee, K. Tanaka, *Appl. Phys. Lett.* **40**, 534 (1982)
- S. Usui, K. Kikuchi, *J. Non-Cryst. Solids* **34**, 1 (1979)
- E. Vallat-Sauvain, C. Droz, F. Meillaud, J. Bailat, A. Shah, C. Ballif, *J. Non-Crystal. Solids* **352**, 1200 (2006a)
- E. Vallat-Sauvain, A. Shah, J. Bailat, *Advances in microcrystalline silicon solar cell technologies* (Wiley, Chichester, 2006b), pp. 133–171
- O. Vetterl, F. Finger, R. Carius, P. Hapke, L. Houben, O. Kluth, A. Lambertz, A. Mück, B. Rech, H. Wagner, *Sol. Energy Mater. Sol. Cells* **62**, 97 (2000)
- O. Vetterl, M. Hulsbeck, J. Wolff, R. Carius, F. Finger, *Thin Solid Films* **427**, 46 (2003)
- S. Veprek, V. Marecek, *Solid State Electron.* **11**, 683 (1968)
- O. Vettea, A. Groß, T. Jana, S. Ray, A. Lambertz, R. Carius, F. Finger, *J. Non-Cryst. Solids* **772**, 299–302 (2002)



- D.L. Williamson, *Sol. Energy Mater. Sol. Cells* **78**, 41 (2003)
- J. Woerdenweber, T. Merdzhanova, T. Zimmermann, A.J. Flikweert, H. Stiebig, W. Beyer, A. Gordijn, *J. Non-Cryst. Solids* **358**, 2183 (2012)
- K. Yamamoto, A. Nakajima, M. Yoshimi, et al., *Prog. in Photovoltaics: Res. and Appl.* **13**, 489 (2005)
- B. Yan, K. Lord, J. Yang, S. Guha, J. Smeets, J.-M. Jacquet, *Mater. Res. Soc. Symp. Proc.* **715**, 629 (2002)
- B. Yan, G. Yue, J. Yang, S. Guha, D.L. Williamson, D. Han, C.-S. Jiang, *Mater. Res. Soc. Symp. Proc.* **808**, 575 (2004a)
- B. Yan, G. Yue, J. Yang, S. Guha, D.L. Williamson, D. Han, C.-S. Jiang, *Appl. Phys. Lett.* **85**, 1955 (2004b)
- B. Yan, G. Yue, J.M. Owens, J. Yang, S. Guha, *Appl. Phys. Lett.* **85**, 1925 (2004c)
- B. Yan, C.-S. Jiang, C.W. Teplin, H.R. Moutinho, M.M. Al-Jassim, J. Yang, S. Guha, *J. Appl. Phys.* **101**, 033712 (2007)
- B. Yan, G. Yue, L. Sivec, J. Yang, S. Guha, C.-S. Jiang, *Appl. Phys. Lett.* **99**, 113512 (2011)
- B. Yan, G. Yue, L. Sivec, J. Owens-Mawson, J. Yang, S. Guha, *Sol. Ener. Mater. & Sol. Cells* **104**, 13 (2012)
- B. Yan, G. Yue, J. Yang, S. Guha, *Sol. Energy Mater. Sol. Cells* **111**, 90 (2013)
- L. Yang, L. Chen, J.Y. Hou, Y.M. Li, *Mater. Res. Soc. Symp. Proc.* **258**, 365 (1992)
- J. Yang, A. Banerjee, S. Guha, *Appl. Phys. Lett.* **70**, 2975 (1997)
- J. Yang, K. Lord, B. Yan, A. Banerjee, S. Guha, *Proc. of 29th IEEE Photovoltaic Specialists Conference (IEEE, New Orleans, 2002)*, p. 1094
- G. Yue, B. Yan, J. Yang, S. Guha, *Appl. Phys. Lett.* **86**, 092103 (2005)
- G. Yue, B. Yan, G. Ganguly, J. Yang, S. Guha, *Mater. Res. Soc. Symp. Proc.* **910**, 29 (2006a)
- G. Yue, B. Yan, G. Ganguly, J. Yang, S. Guha, C. Teplin, *Appl. Phys. Lett.* **88**, 263507 (2006b)
- G. Yue, B. Yan, G. Ganguly, J. Yang, S. Guha, *J. Mater. Res.* **22**, 1128 (2007)
- G. Yue, B. Yan, C.W. Teplin, J. Yang, S. Guha, *J. Non-Crystal Solids* **354**, 2440 (2008)
- G. Yue, B. Yan, L. Sivec, T. Su, Y. Zhou, J. Yang, S. Guha, *Mater. Res. Soc. Symp. Proc.* **1426**, 33 (2012a)
- G. Yue, B. Yan, L. Sivec, Y. Zhou, J. Yang, S. Guha, *Sol. Energy Mater. Sol. Cells* **104**, 109 (2012b)
- X. Zhang, G. Wang, X. Zheng, C. Wei, X. Geng, S. Xiong, Y. Zhao, *Sol. Energy Mater. Sol. Cells* **95**, 2448 (2011)
- X. Zhang, *In OSA Light Energy Nanostructures and Advanced Materials for Photovoltaics (PV)*, Leipzig (2016)



Fengzhen Liu and Yurong Zhou

## Contents

Introduction .....	758
Growth Technology of Poly-Si Thin Film .....	760
Solid Phase Crystallization (SPC) .....	761
Liquid Phase Crystallization (LPC) .....	764
Vapor Phase Deposition (VPD) .....	766
Seed Layer and Transfer Technology for Poly-Si Thin Film Solar Cells .....	773
Seed Layer Techniques .....	773
Lift-Off and Transfer of Poly-Si Thin Films .....	774
Light Trapping Technology for Poly-Si Thin Film Solar Cells .....	775
Quality Characterization of Poly-Si Thin Films .....	780
Poly-Si Thin Film Solar Cells .....	784
Conclusions .....	786
Cross-References .....	787
References .....	787

## Abstract

By eliminating the costly steps of Si wafer, polycrystalline silicon (poly-Si) thin film solar cells become the very promising candidates for cost-effective photovoltaics in the future. In order to maintain the high efficiency character of crystalline silicon (c-Si) wafer-based solar cells, competitive material qualities and appropriate device structures are required for poly-Si thin film solar cells on

F. Liu (✉)

College of Materials Science and Opto-Electronic Technology, University of Chinese Academy of Sciences, Beijing, China

e-mail: [liufz@ucas.ac.cn](mailto:liufz@ucas.ac.cn)

Y. Zhou

University of Chinese Academy of Sciences, Beijing, China

e-mail: [zhouyurong@ucas.ac.cn](mailto:zhouyurong@ucas.ac.cn)

inexpensive substrates. Low cost fabrication processes are also demanded from the point of view of industrial production.

In the past few decades, a wide variety of poly-Si thin film solar cell approaches have been investigated to improve device performance and to identify suitable technology to boost poly-Si thin film solar cells towards competitive photovoltaic devices. The efficiencies of poly-Si thin film solar cells increase gradually. However, they are still much lower than that of c-Si solar cells or other compound semiconductor thin film solar cells. More efforts are needed in the future.

This chapter reviews the technological and scientific developments in the field of poly-Si thin films and solar cells. After an introduction, basic knowledge involved in the fabrication of poly-Si thin films is presented in the first part. In the second part, seed layer and transfer techniques for poly-Si thin film solar cells are described. In the third part, suitable light trapping technology is discussed. In the fourth part, material characterization techniques and properties of poly-Si thin films are shown. In the final part, the developing status of poly-Si thin film solar cells is summarized.

---

**Keywords**

Poly-Si thin film solar cell · Solid phase crystallization · Aluminum induced crystallization · Liquid phase crystallization · Epitaxial growth · Seed layer · Lift-off and transfer · Light trapping structure

---

## Introduction

The worldwide PV market is dominated by wafer-based silicon solar cells using either single crystalline or poly-crystalline silicon. However, fabrication of Si feedstock materials and crystalline growth of silicon ingots are both costly and energy intensive steps (► Chaps. 3, “Siemens Process,” ► 4, “Fluidized Bed Process with Silane,” ► 5, “Upgrade Metallurgical Grade Silicon,” ► 8, “Growth of Multicrystalline Silicon for Solar Cells: Dendritic Cast Method,” ► 7, “Growth of Multicrystalline Silicon for Solar Cells: The High-Performance Casting Method,” ► 9, “Growth of Crystalline Silicon for Solar Cells: Mono-Like Method,” ► 10, “Growth of Crystalline Silicon for Solar Cells: Noncontact Crucible Method,” and ► 6, “Growth of Crystalline Silicon for Solar Cells: Czochralski Si”). In addition, the wafer sawing process suffers from high material losses (► Chap. 11, “Wafer Processing”). Therefore, material costs have been shown to contribute over one third of total module costs in the conventional PV solar cells.

Methods for purification of silicon materials have been improved. Many poly-Si production plants have been constructed and ramped up. Therefore, the feedstock shortage regime for the PV industry, appeared 10 years ago, may not happen again. However, considering the total consumption of materials and long term development, reducing the amount of Si material used in the solar cells is an inevitable direction.

With the development of the slicing technology, typical thickness of Si wafer has been reduced to 140–180  $\mu\text{m}$  (► Chap. 11, “Wafer Processing”). However, still far more Si is used than is actually required for light absorption in the solar cells. The excess Si leads to excess recombination of photo generated carriers and restricts open circuit voltage ( $V_{oc}$ ) of the solar cells. In addition, it is hard to avoid kerf loss in the commercial slicing process, e.g., multiwire fixed abrasives slicing technology (► Chap. 11, “Wafer Processing”). Wire cost and wire breakage together with the postsawing surface treatment are all challenges.

Some approaches have been suggested as ways to reduce the consumption of Si materials in the module. SLiM-Cut lift off based on reorganization of porous silicon and kerf less approach based on implant-cleaving are both attractive techniques. However, since the silicon ingot comes from energy consumption process, the production cost still needs to be demonstrated. Furthermore, a technical challenge exists in handling the thin Si wafer ( $\sim 50 \mu\text{m}$ ) all the way through solar cells fabrication and modules formation. So, what is needed is a completely different approach to manufacture the Si and to reduce the cost.

Solar cells based on amorphous silicon (a-Si) are the well-known approaches to reduce the materials consumption and the overall cost (► Chaps. 20, “Hydrogenated Amorphous Silicon Thin Film,” and ► 21, “Hydrogenated Microcrystalline Silicon Thin Films”). However, a-Si solar cells have not yet been able to perform in terms of efficiency as well as c-Si wafer solar cells. Therefore, to obtain crystallized Si thin films on low-cost substrates through bottom-up approaches could be a good compromise. In this case, an unavoidable issue is the inadequate light absorption related to the inherent indirect band gap of c-Si. This problem can be well solved from the perspective of Photonics. When an absorber surface is ideally rough, optical path length in the absorber can be enhanced by a factor of  $4n^2$  compared with a flat surface, where  $n$  is the refractive index of the absorber film. The  $4n^2$  enhancement is well known as the Lambertian limit or the Yablonovitch limit. For Si with  $n$  of 3.5, the wafer thickness can be reduced from the current 100–300  $\mu\text{m}$  to a few micrometers in the case that this limit can be followed through optimization of the light trapping structure, as Wang et al. (2012) illuminates. And many researchers have been making efforts to overcome the Lambertian limit. Texturing c-Si surfaces at the light wavelength scale and using plasmonic nanostructures are both possible approaches. Based on optimized light trapping structures, a short circuit current density ( $J_{sc}$ ) as high as 38  $\text{mA}/\text{cm}^2$  was predicted by Hsu et al. (2016) on a 10- $\mu\text{m}$ -thick crystalline silicon absorber.

Excellent results have already been obtained on ultrathin silicon substrates with the thickness of 10–40  $\mu\text{m}$  (Kapur et al. 2013; Branham et al. 2015; Han et al. 2014). Conversion efficiencies above 20% have been achieved for a 40- $\mu\text{m}$ -thick back contact mono-crystalline silicon solar cell by Kapur et al. (2013). Based on silicon-on-insulator (SOI) wafer, conversion efficiencies  $>15\%$  have been realized by Branham et al. (2015) on nano-textured 10  $\mu\text{m}$  mono-crystalline silicon absorber. These remarkable research works demonstrate the feasibility of using much less silicon than the conventional silicon wafer in the solar cells. However, mono-crystalline silicon wafer or silicon-on-insulator technology was used, which is irrelevant to low-cost PV.

In the long term, poly-Si thin film technology, as a bottom-up approach, could be a prospective low-cost and highly efficient solar cell approach. The hot Si melt process of Si wafer can be avoided and the cost can be much reduced. The handling problem can also be well solved through the application of inexpensive substrates.

In the past few decades, some cost-effective poly-Si thin film fabrication methods have been investigated including thermal solid phase crystallization (SPC), liquid phase crystallization (LPC) by laser or electron beam, and high or low temperature epitaxial growth from vapor phase, etc. For SPC and LPC technologies, poly-Si thin films can be formed on low-cost foreign substrates directly. For epitaxial growth of c-Si thin film, a large-grained seed layer is needed to promote the crystallization. If epitaxial growth happens on a c-Si wafer, transferring of the epitaxial layer is required. According to these techniques, many research works have been carrying out. A common goal of these approaches is to achieve competitive electronic properties as c-Si wafer.

In this chapter, a review of recent technological and scientific developments in the field of poly-Si thin films and solar cells is presented. In the first part of this chapter, basic knowledge about the poly-Si thin film fabrication techniques is described. This is the main part of this chapter. The techniques what we are concerned about here are those that can obtain poly-Si thin film directly by gas phase deposition or by the combination of gas phase deposition and subsequent crystallization processing. So, liquid epitaxial growth from melt is excluded. In the second part of this chapter, seed layer formation and transfer technique involved in the poly-Si thin film solar cells fabrication are discussed. In the third part of this chapter, research studies on light trapping structures related to the poly-Si thin film solar cells are presented. In the fourth part, characterization methods of poly-Si thin films are described. Since most characterization and analysis methods of poly-Si thin films are similar to those of poly-Si wafer, this part will be very brief. The main properties of the poly-Si thin films according to different fabrication methods are summarized here. In the final part, the status of the poly-Si thin film solar cells based on different approaches is summarized.

---

## **Growth Technology of Poly-Si Thin Film**

In the past four to five decades, many techniques have been invented and developed to fabricate poly-Si thin films and devices from gas phase. According to the crystallization process, the preparation methods of poly-Si thin films can usually be classified into three types: solid phase crystallization, liquid phase crystallization, and vapor phase epitaxial growth. In the stage of 1970s and 1980s of last century, solid phase crystallization and high temperature vapor phase epitaxy were dominant techniques. After that, liquid phase crystallization and vapor phase epitaxy at low temperature have been developed gradually.

## Solid Phase Crystallization (SPC)

Solid phase crystallization means crystallization of amorphous phase happens in the solid phase. The crystallization can be caused directly by heating or can be promoted by means of a medium. In the literature, solid phase crystallization usually refers only to an annealing based SPC or thermal SPC. Solid phase crystallization induced by medium (usually metal) is named as metal-induced crystallization (MIC).

### Thermal SPC

Thermal SPC (or SPC based on annealing) is a simple technique to obtain crystallized Si thin film. The crystallization is based on the thermal annealing of an a-Si thin film. For example, the a-Si thin film or layer stack (with different doping types) with certain thickness is first deposited by plasma enhanced chemical vapor deposition (PECVD) at low substrate temperature. Then, the a-Si film or layer stack goes through thermal treatment at a moderate temperature (around 600 °C) in a N<sub>2</sub> atmosphere. Inexpensive substrates like glass can be used under such temperature. However, the crystallization process often lasts for several or above 10 h. The as-crystallized Si thin film by SPC is usually in a poly-Si status with randomly oriented grains. If textured substrates are used, light trapping structure can be formed on the Si thin film layer directly. Based on the amorphous Si stack deposition, p-n homo-junction structure can be obtained after the SPC. The thermal SPC process is schematically described in Fig. 1.

During the annealing process, possible diffusion of impurities into the crystallized silicon bulk needs to be prohibited by using high quality substrates or block barrier layers. Due to the high cost of pure substrates with high quality, diffusion barriers (e.g., SiN<sub>x</sub>) are commonly preferred as a solution. The SiN<sub>x</sub> film can also act as an antireflection coating for the SPC poly-Si solar cell in a superstrate configuration. Difference in the thermal expansion coefficients between the silicon bulk and the substrate needs to be considered to avoid cracking and flaking during the thermal treatment. After SPC, a rapid thermal anneal (RTA) process in N<sub>2</sub> atmosphere is often carried out to remove crystallographic defects from the SPC poly-Si thin films and to activate the dopants. A SiO<sub>x</sub> capping layer is usually deposited onto the a-Si thin films



**Fig. 1** The schematic of thermal SPC process. (Reprinted with permission from Kumar et al. 2015)

before the SPC process. The  $\text{SiO}_x$  layer can act as a barrier for impurities from the ambient during the SPC and the subsequent RTA process (Kumar et al. 2015).

Annealing time, crystallization temperature and substrate situation together determine the nucleation and growth process and the final grain size. The grain size of the SPC poly-Si thin films could vary from 2  $\mu\text{m}$  to 15  $\mu\text{m}$ . Stress and intra-grain mis-orientations exist in the SPC poly-Si thin films. The SPC poly-Si usually contains many deep level intra-grain defects and grain-boundary defects. The intra-grain defects and dislocations in the films limit the electrical properties of SPC poly-Si thin films. Postcrystallization treatment and hydrogen passivation technique are needed to meet the requirement of the photovoltaic applications.

Although the structure and electronic property of SPC poly-Si thin films mainly depend on the postdeposition treatments, deposition parameters of a-Si also have effects on the poly-Si thin films. Kumar et al. (2015) found that for the hydrogenated amorphous silicon (a-Si:H) films deposited by PECVD (► [Chap. 20, “Hydrogenated Amorphous Silicon Thin Film”](#)), both deposition temperature and gas flow ratio have influence on the stress and intra-grain mis-orientation in the SPC poly-Si thin films. They demonstrated that an increase in the substrate temperature of the a-Si:H thin films deposited by PECVD leads to a significant improvement in the property of the SPC poly-Si thin films.

Solid phase crystallization had been matured to industrial production. CSG Solar was the only company that had produced poly-Si thin film solar cells on glass on industrial scale. Relying on the technology of thermal SPC poly-Si thin films on glass substrate, a module efficiency of 10.4% was demonstrated on a textured borosilicate glass with an area of  $10 \times 10 \text{ cm}^2$  by CSG in year 2007 (Keevers et al. 2007). The technological drawbacks of SPC could lie in the long annealing time of usually more than 10 h and the moderate quality of the poly-Si thin films with random oriented grains and high density defects.

### **Metal-Induced Crystallization (MIC)**

Metal-induced crystallization is also a kind of solid phase crystallization technique. Presence of the metal films lowers the crystallization temperature of the a-Si thin films. The metals that lower the crystallization temperature the most are Pt, Ni, Pd, Ag, Cu, Al, and Au (Knaepen et al. 2008). According to the reaction between metal and Si, two models for MIC process were proposed, as described by Knaepen et al. (2008). One is eutectic reacting, the other is compound formation. For eutectic reacting metals (e.g., Al, Au, Ag), Si atoms diffuse into the metal film during heating and find some preferred nucleation sites at the metal grain boundaries. With the supply of Si atoms, the Si crystal nuclei grow up, contact, and finally form a continuous poly-Si thin film. In this case, the MIC process is limited by the solubility and diffusion of Si atoms in the metal film. For compound-forming metals (e.g., Ni, Cu, Pt, Pd), crystallization occurs after the formation of a silicide phase. The main diffusion element, could be either metal or Si, diffuses through the silicide layer and promote the crystallization. In a dissociative model, the silicide forms at the silicide/a-Si

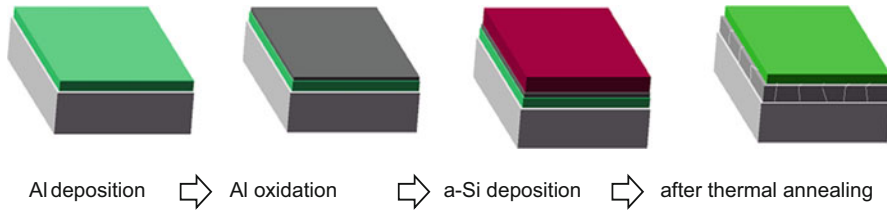


**Fig. 2** The schematic of AIC process

edge and dissociates at the silicide/poly-Si edge. The main diffusing element is the metal. In a nondissociative model, Si is the main diffusing element and the silicide serves as a transport layer for Si atoms.

The most commonly used metal for MIC poly-Si thin films is aluminum. Crystalline silicon grains with the size larger than 20  $\mu\text{m}$  can be achieved using aluminum-induced crystallization (AIC). AIC poly-Si thin films have gained considerable attention in photovoltaics. The schematic of AIC process is depicted in Fig. 2. An aluminum layer with certain thickness (dozens to several hundred nanometers) is first deposited onto the substrate (e.g., glass) before the a-Si thin film deposition. Then, the Al/a-Si double layers, usually separated by a thin native oxide layer, are thermally treated at a moderate temperature for certain time (usually 1–4 h). With the Al element moving up to the top of the double layer, crystallization of the silicon happens simultaneously. The temperature and duration of the thermal annealing process and the thicknesses of aluminum and a-Si layers are all played important roles in the poly-Si quality. The typical annealing temperature is 400–500  $^{\circ}\text{C}$  and the grain sizes are ranging from 10  $\mu\text{m}$  to 30  $\mu\text{m}$ .

Due to the advantages of large grain size and simple process, AIC of a-Si is usually considered to be an economical seed layer technique in poly-Si thin film solar cells. Large-grained poly-Si absorber layers on inexpensive substrates have been achieved by combining AIC poly-Si seed layer with high temperature epitaxial growth of Si thin film. In the early stage, grain size enlargement of AIC poly-Si was thought to be the most important parameter to improve material quality and therefore solar cell performance. Later, electrically active defects were considered as the main reason to limit the structural characteristics and electrical properties of poly-Si layers based on AIC and epitaxial growth. The AIC seed layer has a crucial impact on the formation of a high density of intra-grain defect. So, increasing the intra-grain quality is essentially important to improve the material quality and hence device performance. Plasma hydrogenation treating is helpful to passivate the defects and increase the effective diffusion length of carriers in the poly-Si layer. For example, by using high-temperature remote plasma hydrogenation, an efficiency of 8.54% was achieved by Qiu et al. (2014) on a poly-Si thin film solar cell with a 2- $\mu\text{m}$  thick absorption layer (AIC seed layer + thermal epitaxial growth at 1130  $^{\circ}\text{C}$ ) and a heterojunction a-Si emitter. Further efforts are needed to understand the role of hydrogen and to improve the film quality.



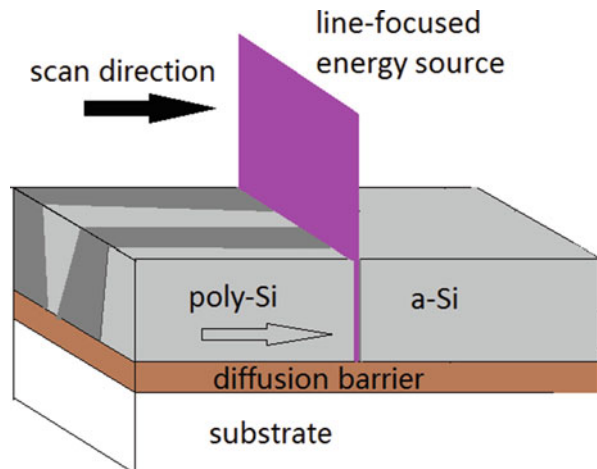
## Liquid Phase Crystallization (LPC)

In the early 1990s, liquid phase epitaxy technology was investigated to obtain epitaxial growth of c-Si thin film from Si/metal (Cu, In, or Ga) melt. Epitaxial c-Si films with thickness of 5–50  $\mu\text{m}$  can be achieved on Si substrate. Such liquid phase epitaxy is based on melt but not on gas phase deposition. So, it will not be reviewed here.

As early as 1979, Schwarzschild (1979) reported on *Physics Today* a successful growth of oriented crystalline Si by the MIT Lincoln laboratory group. The oriented crystalline Si was realized from a-Si using laser LPC with the aid of a man-made structure with long range order. This research work opened a broad new range of possibilities for the production of microelectronic devices and solar cells. The above LPC is such a technique that energy sources are line-focused into the amorphous or nano-crystalline silicon layer (with the thickness of 5–40  $\mu\text{m}$ ) and heat up the silicon above the melting point of 1414  $^{\circ}\text{C}$ . The energy sources could be laser, electron-beam, or halogen-lamps. According to the literatures, laser is the most commonly used energy source. During the scan, the molten silicon layer re-crystallizes along the scanning direction into large-grained poly-Si. And the crystallization time of LPC is usually several seconds. Therefore, the production time and thermal budget can be greatly reduced compared with SPC and AIC.

The LPC process is schematically depicted in Fig. 3. Before the Si thin film deposition, a dielectric interlayer is usually deposited on the glass substrate first. During the crystallization process, the dielectric layer acts as diffusion barrier against impurities from the glass and may prevent dewetting of the silicon. Some dielectric materials can also passivate the interface between the LPC poly-Si absorber and the substrate because of chemical as well as field-effect passivation effects. Moreover, the interlayer can function as antireflection coating when illuminating the solar cell in superstrate configuration. So far, aluminum oxide ( $\text{Al}_2\text{O}_3$ ), silicon oxide ( $\text{SiO}_2$ ),

**Fig. 3** The schematic of LPC process



silicon nitride ( $\text{SiN}_x$ ), silicon oxynitride ( $\text{SiO}_x\text{N}_y$ ), silicon carbide ( $\text{SiC}_x$ ), or their stacks were ever used as interlayer in LPC poly-Si solar cells. Recently, the significant improvements in conversion efficiencies of LPC poly-Si solar cells made by Preissler et al. (2017a) are to a great extent due to the carefully optimized dielectric layers. They successfully developed PECVD-grown  $\text{SiO}_x/\text{SiN}_x/\text{SiO}_x$  stack to achieve crystallization without prior annealing. Nitrogen-rich  $\text{SiN}_x$  layer in the stack was proved to be beneficial to achieve adhesion and avoid delamination during the crystallization.

A major advantage of LPC is the fact that the deposition conditions of a-Si are decoupled from the electronic quality of the poly-Si layer. The quality of LPC-Si is mainly determined by the crystallization process. So, the deposition technique and growth rate of a-Si are not critical. Simple deposition technique and high deposition rate are feasible. Either physical vapor deposition (PVD) or chemical vapor deposition (CVD) can be used to deposit a-Si film. If the a-Si thin film is deposited by PECVD, moderate temperature annealing ( $450\text{ }^\circ\text{C} - 650\text{ }^\circ\text{C}$ ) needs to be carried out before the LPC process to effuse the hydrogen (► Chap. 20, “Hydrogenated Amorphous Silicon Thin Film”).

The a-Si thin film can be crystallized in ambient atmosphere or in vacuum by sweeping a line-shaped energy source across the surface. A moderate substrate temperature ( $\sim 600\text{ }^\circ\text{C}$ ) is usually set to preheat the silicon thin film. Both scanning velocity and intensity of the energy source exhibit influence on the microstructure (grain size, grain orientation, and type of grain boundaries) of the crystallized Si. The scanning speed shows greater impact on film quality. A scanning speed of  $2\text{--}3\text{ mm/s}$  is usually used during the motion of the line-shaped energy sources. However, during the cooling down from silicon melting temperature to preheating temperature, cracking may occur. High temperature gradients within the sample cause large thermal stresses. And then cracking may happen in the crystallized silicon. Slowing down the scanning speed is beneficial to reduce the thermal stresses within the sample.

Doping of the LPC-Si layer can be well controlled by predeposition doped a-Si thin layer ( $\sim 80\text{ nm}$ ) on the main Si layer. During the crystallization, dopant atoms from the doping layer distribute homogeneously throughout the poly-Si absorber. Doping concentration in the order of  $10^{16}\text{ cm}^{-3} \sim 10^{17}\text{ cm}^{-3}$  can be obtained. Both n-type and p-type poly-Si absorbers can be achieved. A  $\text{SiO}_x$  capping layer is often deposited on top of the Si film to enhance the absorption of the laser power and enlarge grain size of the film. After LPC, stresses from the glass can be relieved by a subsequent RTA process.

Like SPC poly-Si or AIC seeded poly-Si, plasma hydrogenation treating is commonly performed to passivate the defects in the LPC poly-Si absorbers. Both the process temperature and duration of hydrogen plasma and the interlayer material sequence play important roles in the effectiveness of passivation. Hydrogen atoms in the interlayer and from the plasma may diffuse into the LPC poly-Si absorber and passivate silicon dangling bonds. Significant improvement in the solar cell performance (mainly for n-type LPC poly-Si bulk) can be achieved by using hydrogen plasma treatment (Preissler et al. 2017).

Since the grains are grown from silicon melt, they can grow up to centimeters in length and millimeters in width for LPC poly-Si. With appropriate laser power density to completely melt the entire film, large linear grains grown parallel to the laser scan direction can be achieved. A wafer-like electronic quality might be maintained. For example, Hall mobility up to  $530 \pm 80 \text{ cm}^2/\text{V}\cdot\text{s}$  can be successfully achieved (Sonntag et al. 2017). Compared with SPC poly-Si, grain size and electrical quality of LPC poly-Si are significantly increased. The crystallization time of LPC poly-Si is shortened from at least 10 h for SPC poly-Si down to only several seconds. The thermal budget is greatly reduced. Due to the feature of large grain and cost effective process, LPC has been considered to be the highest potential approaches for poly-Si thin film solar cells in industrial production (Becker et al. 2013). Additionally, on account of the feature of large grain size, the LPC poly-Si can also serve as a seed layer for further epitaxial thickening.

In recent years, LPC poly-Si solar cells on low cost substrates (e.g., glass) have been paid more and more attention. The solar cell performance is improved continuously. Based on an interdigitated back-contact (IBC) system featuring an a-Si:H/c-Si heterojunction (SHJ), a power conversion efficiency of 13.2% was recently demonstrated by Paul Sonntag et al. (2017) on 13  $\mu\text{m}$  LPC absorbers on glass.

## Vapor Phase Deposition (VPD)

Silicon vapor phase epitaxial growth has been studied since the early 1950s. Initially, high temperature processes ( $>1000 \text{ }^\circ\text{C}$ ) were preferred to guarantee epitaxial layers with sufficient quality. Later, moderate and low temperature epitaxial growth gradually gained more and more attention. Recently, poly-Si thin film can also be obtained by physical vapor deposition. Different vapor phase deposition methods for poly-Si solar cells will be described in turn.

### High Temperature Vapor Phase Epitaxy

Atmospheric pressure chemical vapor deposition (APCVD) and low pressure chemical vapor deposition (LPCVD) are the conventional high temperature homo-epitaxy techniques in semiconductor industry. Before epitaxial growth, the silicon surface can be well cleaned by volatilizing contaminants under elevated temperatures. Then, reactant gases ( $\text{SiH}_4$ ,  $\text{SiCl}_4$ ,  $\text{SiHCl}_3$ , or  $\text{SiH}_2\text{Cl}_2$ ) are thermal decomposed and/or reduced under high temperature ( $>1000 \text{ }^\circ\text{C}$ ). Thermal activation helps incoming radicals to settle in crystalline sites. Therefore, crystal growth with high quality can be achieved. Typical growth rate of  $3\sim 10 \mu\text{m}/\text{min}$  can be realized. The doping concentration profile and the accurate layer thickness can be well defined.

High temperature vapor phase epitaxy has already been successfully implemented in bipolar transistor and other advanced integrated circuits processes. And producing high quality poly-Si thin films or even silicon wafers by high throughput vapor phase epitaxial growth has long been pursued to reduce the manufacturing cost of c-Si photovoltaics. However, the high substrate temperature character makes it incompatible with low cost substrates. As a result, the epitaxy

substrates are usually limited to silicon sheets, metallurgical silicon, and porous silicon (usually combined with a layer transfer technology) in poly-Si thin film photovoltaic application. Furthermore, unintentional doping and impurity diffusion may occur at high temperatures, which are harmful to the quality of the epitaxial layer and the device properties gained by earlier processing steps. Therefore, a high quality epitaxy substrate and a carefully selected and optimized fabrication process sequence are both critical important.

Porous Si is the most commonly used substrate for high temperature vapor phase epitaxy of poly-Si thin film. Conversion efficiency above 19% can be achieved on the free-standing high temperature epitaxial Si layers with the thickness less than 50  $\mu\text{m}$  by using the porous silicon layer transfer process (Petermann et al. 2012). However, handling and processing of the free-standing silicon with thickness below 50  $\mu\text{m}$  are very challenging as they are highly flexible and fragile. And the stresses and microcracks arising during the interconnection of the ultra thin silicon solar cells may lead to reduced reliability and operational lifetime of solar modules. To make the process flow to module-level processing, the ultra thin silicon solar cells are usually bonded onto low cost mechanical carriers. Of course, bonding technology will also face new challenges. Light absorption losses, conductive conditions, contamination risks, and industrial applicability related to the bonding agent need to be considered. To minimize the negative impact of bonding on the solar cell performance, the bonding glue type, the bonding process, and the whole solar cell fabrication process sequence need to be carefully optimized according to the specific solar cell structure. Conversion efficiencies of 15~17% have been obtained for solar cells on epitaxial Si foils bonded on different substrates, such as low-cost Si, glass, steel.

Very recently, based on the integrated interconnect-module ( $i^2$ -module) concept, IMEC (Radhakrishnan et al. 2017) reported the results on high temperature vapor phase epitaxy poly-Si solar cells bonded to glass. Epitaxial layers with a thickness of  $\sim 50 \mu\text{m}$  and lifetime of  $\sim 30 \mu\text{s}$  (injection level of  $10^{15} \text{cm}^{-3}$ ) were grown on parent substrates with a sacrificial porous silicon seed layer at 1130  $^\circ\text{C}$  in a CVD reactor. The epitaxial layers were lifted off from the parent substrate using the porous silicon as the detachment layer and layer-transferred and bonded onto module glass using ethylene vinyl acetate (EVA) sheets for further processing. A heterojunction interdigitated back-contact (HJ-IBC) technology based on a-Si:H and IBC solar cell process was adopted to fabricate the devices. According to their process sequence implemented in their work, the thin Si foil is mechanically supported throughout the solar cell processing and interconnection stages, thus enabling high mechanical yield during the device processing. A best solar cell efficiency of 16.1% was obtained.

### **Moderate or Low Temperature Vapor Phase Epitaxy**

The vapor phase epitaxy approaches discussed above involve high temperature processes in excess of 1000  $^\circ\text{C}$ . This temperature limits the type of substrates. Moderate or low temperature epitaxial growth of thin film crystalline silicon has always been a pursuing goal in microelectronics and also in large area electronics. It has the well-known advantages. For example, thermal problems such as inter-diffusion

between doped layers and auto-doping effects can be overcome. And the structure and fabrication process of the devices could therefore be very flexible.

Silicon homo-epitaxy under low temperature has been demonstrated by many deposition techniques including molecular beam epitaxy (MBE) (Eaglesham 1995), ion-assisted deposition (IAD) (Nerding et al. 2003), electron-cyclotron resonance chemical vapor deposition (ECR-CVD) (Rau et al. 2004), hot-wire chemical vapor deposition (HWCVD) (Mason et al. 2003), and PECVD (Moreno and Cabarrocas 2010). Considering the degree of the difficulty to scale to large-area deposition for PV application, only HWCVD and PECVD techniques will be reviewed here.

### Hot Wire Chemical Vapor Deposition (HWCVD)

HWCVD, or catalytic chemical vapor deposition, is a conventional technique for Si thin films deposition. Compared with PECVD, HWCVD could be considered as a relatively new deposition technology that has shown technological and scientific developments over the past 20 years. During the HWCVD process, precursor gases (e.g., silane and hydrogen) are catalytically dissociated into atomic H and Si at surface of resistively heated filament (e.g., Ta or W wires) with very high efficiency. Plenty of atomic H in the gas phase makes HWCVD a suitable technique for hydrogenated microcrystalline silicon ( $\mu\text{-Si:H}$ ) thin film deposition (► [Chap. 21, "Hydrogenated Microcrystalline Silicon Thin Films"](#)). And in low-temperature silicon epitaxy, HWCVD also appears promising for the advantage of being simple and high deposition rate.

Lowering process temperature has the well-known advantages. So, in the late 1990s and early 2000s, epitaxial growth of Si thin film in a relatively low temperature region ( $<600\text{ }^\circ\text{C}$ ) was first concerned for HWCVD technique (Mason et al. 2003; Watahiki et al. 2000). Researchers had carried out a lot of works to study the influence of the filament material, substrate temperature, and growth rate on the properties of epitaxial Si thin film. It was found that either based on tungsten or tantalum filament, Si epitaxy growth was possible for substrate temperatures ranging from  $200\text{ }^\circ\text{C}$  to  $500\text{ }^\circ\text{C}$ . At a relatively low substrate temperature, all of the films can be epitaxial in the initial growth stage. But microcrystalline Si with different orientations and even amorphous phase appear above a critical thickness. As an example, TEM images of films grown at about  $250\text{ }^\circ\text{C}$  on c-Si substrate by HWCVD are shown in [Fig. 4](#).

Adequate diffusion capacity of the radicals on the growing surface is a key point for successful epitaxial growth. The diffusion mobility of adsorbed radicals can be influenced by substrate temperature, deposition rate and surface condition. Low substrate temperature limits the surface mobility of adsorbed radicals. High deposition rate may interrupt the diffusion of adatoms. Surface transition from dihydride to monohydride termination at higher substrate temperature will reduce the surface diffusion capacity of adatoms. Gas chemistry (radical species, radical-radical reactions, depleted or nondepleted regime) also plays a big role during the epitaxial growth of Si thin film. The overall result is that the critical thickness is no more than 500 nm for epitaxy below  $600\text{ }^\circ\text{C}$  by using HWCVD.

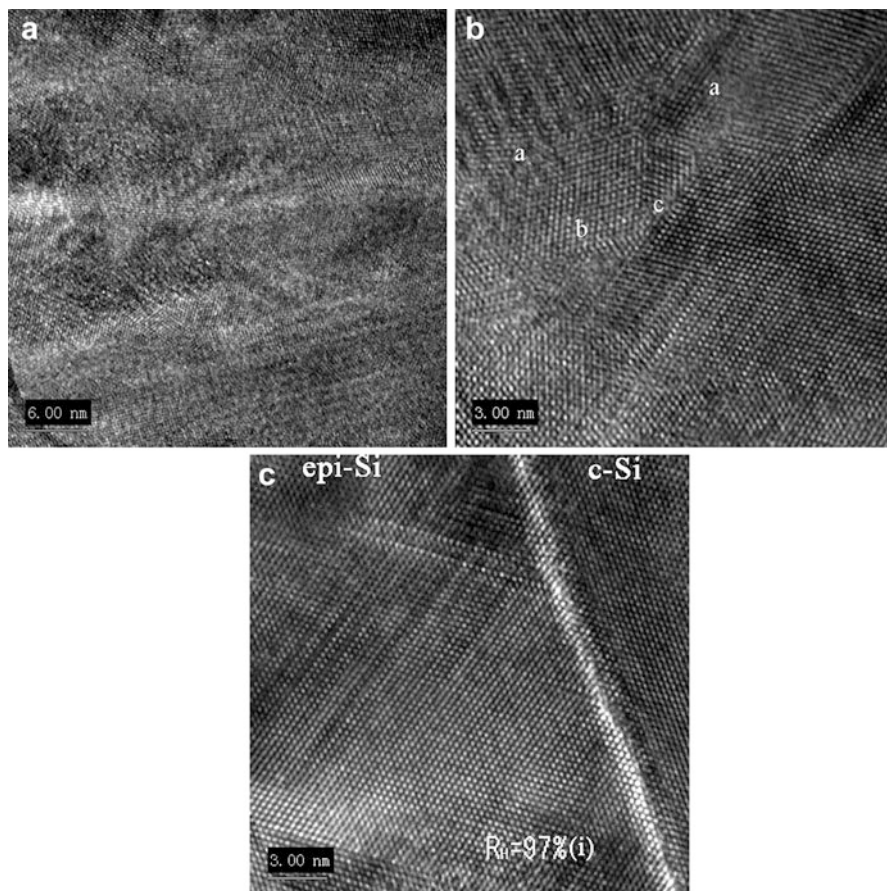


**Fig. 4** Cross-section transmission electron microscopy images at different positions of the Si thin film growth on c-Si wafer by HWCVD at 250 °C. (a) About 150 nm from the substrate surface, (b) about 50 nm from the substrate surface, (c) near the epitaxial Si/c-Si interface. (Reprinted with permission from Gaucher et al. 2016)

Aiming at increasing in both the growth rate and achievable thickness of epitaxy Si by HWCVD, substrate temperature was further increased into above the dehydrogenation temperature of the silicon surface. At the substrate temperature of 610° C, phase-pure epitaxial growth of more than 10  $\mu\text{m}$  was achieved by Wang et al. (2006) at a growth rate of 110 nm/min on (100) silicon wafers using HWCVD. In contrast, mixed-phase breakdown was seen at lower temperatures of 520–580 °C. The growth regime suggests that rapid dehydrogenation of the growing surface is critical for silicon epitaxy by HWCVD.

To obtain high-quality silicon layer at high rates while maximizing  $\text{SiH}_4$  utilization, substrate temperatures between 620 °C and 800 °C, still compatible with substrates such as display glass and metal foil, were further considered for epitaxial



growth of Si by HWCVD. At this temperature range, the sticking coefficients of the growth radicals approach unity and thermal CVD of  $\text{SiH}_4$  at the growth surface also contributes to the growth rate. Epitaxial growth can continue to several tens of micrometers on HF-dipped hydrogen-terminated (100) silicon wafers. Device-quality epitaxial silicon thin films at growth rates up to  $1.8 \mu\text{m}/\text{min}$  were grown by Bobela et al. (2011) using HWCVD from silane at substrate temperatures below  $750^\circ\text{C}$ . Epitaxial layers with a wide range of controllable dopant densities for both n-type and p-type can be easily obtained by using HWCVD. Devices with  $2\text{-}\mu\text{m}$ -thick epitaxial Si absorber grown on heavily doped “dead” Si wafers have shown  $V_{\text{oc}} \sim 630 \text{ mV}$  and efficiencies up to  $\sim 8\%$  without light trapping features (Young et al. 2012).

Epitaxial Si thin films can also be prepared on seeded glass by using HWCVD. The seed layers could be AIC of a-Si:H or crystalline Si layer transferred on display glass. Corning EAGLE XG glass is usually chosen as the substrate, since it has an annealing temperature of  $722^\circ\text{C}$  and a softening point of  $971^\circ\text{C}$ . The crystallographic quality and morphology of the seed layer greatly influence the epitaxial Si and device quality. High intra-grain dislocation densities can be revealed for epitaxial Si on AIC seed layer by electron beam-induced conductivity (EBIC) measurements. The solar cells on seeded glass show a decrease of  $70 \text{ mV}$  on  $V_{\text{oc}}$  compared with the devices grown on  $\text{n}^+$  Si wafers with similar  $2\text{-}\mu\text{m}$  absorber (Young et al. 2012).

We can see that to realize epitaxial growth of Si with considerable thickness and high quality for device application, the substrate temperature goes higher and higher for HWCVD. Otherwise, an epitaxial growth breakdown into poly-crystalline Si or even amorphous phase can be observed at low temperature. The energy required for the migration of adatoms merely comes from the substrate temperature in the HWCVD process. If additional energy is provided, epitaxial growth can be sustained at a lower temperature range.

### Plasma Enhanced Chemical Vapor Deposition (PECVD)

Capacitively coupled radio frequency-plasma enhanced chemical vapor deposition (RF-PECVD) is a standard technique for the production of a-Si:H and  $\mu\text{c-Si:H}$  thin films (► Chaps. 20, “Hydrogenated Amorphous Silicon Thin Film,” and ► 21, “Hydrogenated Microcrystalline Silicon Thin Films”). RF-PECVD has also been extended to the epitaxial growth of crystalline silicon thin films at low temperature. Actually, in the case of a-Si/c-Si heterojunction solar cells, unexpected epitaxial growth happens and usually leads to poor surface passivation. This is what we have been trying to avoid during the heterojunction solar cells fabrication. However, from different point of view, we can make use of this epitaxial growth to produce crystalline silicon thin films. In the recent years, researchers (from LPICM at Ecole Polytechnique in France) have done lots of works on epitaxial growth of crystalline silicon films on (100) oriented crystalline silicon substrates by RF-PECVD at a temperature below  $200^\circ\text{C}$  (Morenoa and Cabarrocas 2010; Cabarrocas et al. 2012; Cariou et al. 2016). Crystalline silicon thin films with the thicknesses of  $1\text{--}8 \mu\text{m}$  can be obtained on heavily boron-doped (100)-oriented Si wafers.

The plasma-assisted epitaxial growth at low temperature is explained in the context of plasma synthesis of silicon nano-crystals. The enhanced gas phase reactions with atomic hydrogen will lead to the formation of silicon nano-crystals in the plasma. And the silicon nano-crystals are believed to be the most plausible building blocks for the deposition of  $\mu\text{-Si:H}$  on glass and epitaxial layer on c-Si substrate. This is different from the traditional  $\mu\text{-Si:H}$  deposition model based on  $\text{SiH}_3$  radicals. According to the traditional opinion, increasing hydrogen dilution shifts the growth from a-Si:H to  $\mu\text{-Si:H}$  on glass substrate. However, opposite picture was observed for epitaxial growth of Si thin film on (100)-oriented Si substrate. At a fixed hydrogen flow rate of 500 sccm, the Si thin film changes from  $\mu\text{-Si}$  to epitaxial layer as the silane flow rate increases from 8 sccm up to 35 sccm, which proves the difference between the nano-crystal and silicon radicals growth processes (Cabarrocas et al. 2012).

The plasma surface treatments prior to deposition and the nature of the substrate surface play a critical role on the epitaxial growth process. Removing the native oxide layer by sufficient HF solution treatment prior to loading the substrates into the reactor is critical. Otherwise, the epitaxial growth will be prevented by the thin oxide layer. The Si thin film growth on Corning glass and on HF dipped (100) and (111)-oriented crystalline Si substrates under the same deposition conditions by RF-PECVD were ever compared by Cabarrocas et al. (2012). Spectroscopic ellipsometry measurement shows that the pseudo-dielectric function  $\epsilon_i$  of film deposited on (100) c-Si is similar to that of c-Si; however, the films deposited on Corning glass and (111)-oriented crystalline Si are more close to a-Si. The difference between the Si thin films on (100) and (111)-oriented c-Si substrates is attributed to the different atomic arrangements on the surfaces. Each silicon atom in the growing plane has to form two bonds or one bond with the atoms in the previous (100) or (111) planes, respectively. Silicon atom is more inclined to be geometrically constrained at a crystalline lattice position for the (100) plane condition than that of a (111) plane.

Spectroscopic ellipsometry and TEM measurements show that epitaxial layers with high quality can be achieved by RF-PECVD at low temperature, as shown in Fig. 5 (Cariou et al. 2016). This opens new perspectives to the possibility of growing poly-Si thin films in the same equipment as that used for a-Si:H or  $\mu\text{-Si:H}$  thin films.

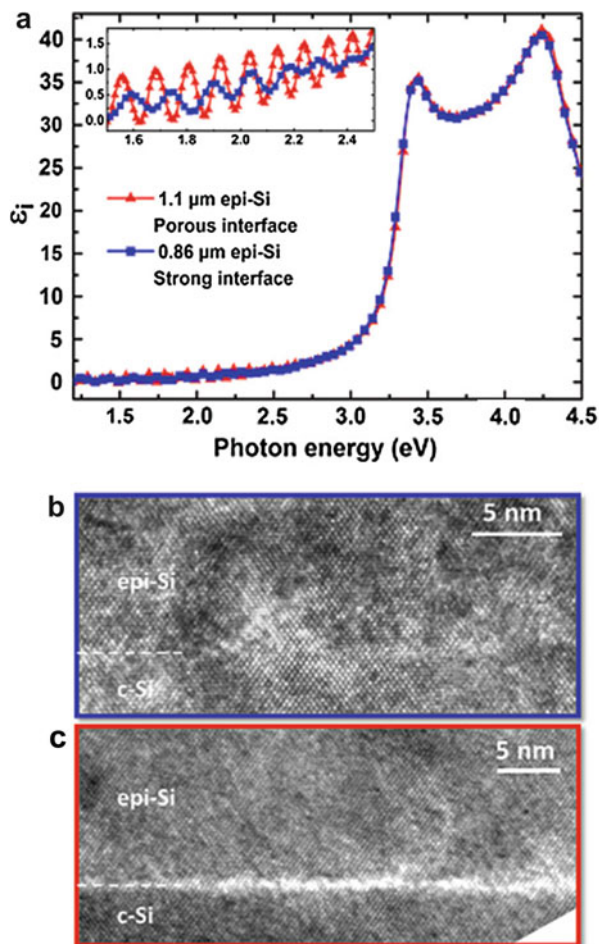
A conversion efficiency of 7.3% was obtained by Cariou et al. (2016) for a poly-Si thin film solar cell with a 5.5  $\mu\text{m}$  PECVD epitaxial Si absorber and a hetero-junction structure of Al/epitaxial Si/i a-Si:H/p a-Si:H/ITO/Ni-Au.

### Physical Vapor Deposition

Electron-beam evaporation (EBE) technique is one of the rather simple physical vapor deposition techniques. It has been developed in Helmholtz-Zentrum Berlin für Materialien und Energie as a high throughput and low-cost alternative to conventional CVD for poly-Si thin film solar cells (Becker et al. 2013). In the main chamber of the electron-beam evaporation system, the electron beam is generated from an electron gun (a tungsten hot cathode at a voltage of 10 kV). The electron beam is



**Fig. 5** Pseudo-dielectric function  $\epsilon_2$  measured on epi-PECVD Si layers with the two types of interface measured by spectroscopic ellipsometry (a). Cross-section transmission electron microscopy bright-field images of the sharp (b) and the high-porosity (c) epitaxial Si/c-Si interface. (By Cariou et al. 2016)



then directed by the magnetic field towards the silicon target and induces the melting and evaporation of silicon. As the substrate temperatures are below 350–400 °C, amorphous silicon films are formed on the substrate. At higher substrate temperatures, poly-Si films are grown directly. No additional crystallization step is required. Accurate control of boron doping between  $1 \times 10^{16} \text{ cm}^{-3}$  and  $1 \times 10^{20} \text{ cm}^{-3}$  can be achieved by co-evaporation of high-purity elemental boron during silicon evaporation.

As we know, the electron-beam evaporated silicon impinges the substrate with a certain flux direction. As a result, conformal coating of Si thin film on textured substrates is not easy. And improving the short circuit current density by means of a conventional light trapping structure becomes a tough task. However, Becker et al.

(2013) took advantage of the “drawback” of the specific growth characteristic of EBE. By combining nanoimprint lithography and high-rate EBE deposition of amorphous Si, they obtained periodic crystalline silicon nanoarrays.

---

## Seed Layer and Transfer Technology for Poly-Si Thin Film Solar Cells

### Seed Layer Techniques

It is difficult to obtain high quality poly-Si thin films with large grains directly from vapor phase deposition on foreign substrates such as glass or metal foil. A thin silicon seed layer with excellent crystallographic properties will settle the problem by transfer the structural information of the crystallized seed layer to the epitaxial film. Detaching and transferring of ultrathin monocrystalline silicon or porous silicon layer from silicon wafer to a foreign substrate is one of the seed layer formation approaches. Based on anodic bonding and implant-induced separation, Corning Inc. developed a proprietary technology to create monocrystalline Si seed layers by transferring 300 nm-thin (001)-oriented monocrystalline Si layers onto glass-ceramic substrates (Dawson-Elli et al. 2007). Besides the layer-transfer Si, many other crystallization techniques, including SPC, AIC, and LPC, are all under developing as candidate seed layers for Si epitaxy.

Since the seed layer serves as a crystalline template for epitaxial growth of Si, the microstructure of the seed layer will be get copied into the epitaxial layer. Therefore, many requirements need to be met for a qualified seed layer. First, the grain size provided by the seed layer approach need be much larger than the thickness of the target poly-Si epitaxial layer. Second, the surface orientations of the seed layer should be conducive to the epitaxial growth. Finally, the densities of intra-grain defects or high-recombination grain boundaries are demanded to be as low as possible.

Compared with SPC, poly-Si thin films with larger grains can be achieved by LPC or AIC. As the seed layer techniques, both LPC and AIC have gained considerable attention in the poly-Si thin film solar cells fabrication. Based on the AIC and LPC seed layers, different gas phase deposition techniques (e.g., thermal CVD and HWCVD) can be used to realize the further epitaxial growth. Poly-Si thin film solar cells based on AIC and LPC seed layers have been developed. Better material quality of epitaxial Si and higher efficiency of poly-Si thin film solar cells have been demonstrated on LPC-Si seed layer than on AIC-Si seed layer. The main reason is much larger grain size of LPC-Si than that of AIC-Si.

The thin monocrystalline Si layers on glass-ceramic substrates created at Corning Inc. have been proved to be a good seed layer approach. The typical defect density of the epitaxial Si layers (by thermal CVD) on the Corning monocrystalline Si seed layers was found to be 4 orders lower than that on AIC seed layers (Gordon et al. 2011).  $V_{oc}$  values up to 610 mV were achieved by

Gordon et al. (2011) for poly-Si solar cells with a very simple and nonoptimized structure, which illustrate the good material quality of the thin monocrystalline Si layers on glass-ceramic substrates.

## Lift-Off and Transfer of Poly-Si Thin Films

Lift-off of silicon seed layers or epitaxial layers and transferring them to a secondary low cost substrate are critical steps to build the final devices. Different approaches have been explored including Smart-Cut™ process based on hydrogen implantation (Briel et al. 1997), substrate or ingot spalling by means of a tensile layer (Bedell et al. 2012), electrochemical etching of a wafer by forming porous silicon (Radhakrishnan et al. 2014), etc. In the case of transferring a seed layer to a secondary substrate before epitaxial thickening of the poly-Si thin films, the original c-Si wafers can be peeled into many layers. The consumption rate of the silicon wafers is related to the lift-off technology and the thickness of the seed layer. If lift-off and transfer are carried out after the epitaxial growth of the poly-Si thin films, the c-Si parent wafer substrates can be reused for many times to repeat the epitaxial procedure.

The reported lift-off and transfer techniques are multifarious. A transferring technique reported recently (Moreno and Cabarrocas 2010; Cariou et al. 2016; Moreno et al. 2013) will be presented here as an example. Without ion implantation, high-temperature annealing, or electrochemical etching, an ultrathin fragile porous epitaxial-layer/wafer interface can be created by plasma treatment before epitaxial growth. This plasma treating process enables easy detachment of the PECVD epitaxial Si layer.

The procedure, starting from the plasma treatment of a c-Si parent wafer and finishing with successful transferring the epitaxial layer to a glass substrate, was illustrated by Cariou et al. (2016), as shown in Fig. 6. A (100)-oriented c-Si wafer was used as the parent substrate. Before the epitaxial growth, a critical important in situ SiF<sub>4</sub> plasma cleaning process was carried out. Native oxide layer on the c-Si wafer can be etched off. And, a hydrogen-rich fragile interface between the epitaxial layer and the c-Si wafer can be formed simultaneously. Then, silicon epitaxial growth was carried out on the parent wafer in a standard RF-PECVD reactor. After the epitaxial growth, the whole sample was anodic bonded onto a glass substrate at 200 °C. By a short thermal annealing (2–3 min, 350 °C) treatment, the epitaxial layer can be detached from the c-Si parent wafer successfully.

The porosity of the interface is critical for the detachment. It can be tuned by adjusting the plasma process to control the accumulation of H at the interface. A threshold of 13–14% porosity was demonstrated. As the interface porosity or hydrogen concentration is above the threshold, a crack front that propagates parallel to the interface will appear and result in the detachment of the epitaxial layer under moderate annealing temperature. Taking advantage of the fragility of the H-rich interface, epitaxial Si layer with size of ~10 cm<sup>2</sup> can be easily cleaved and transferred onto glass substrates.

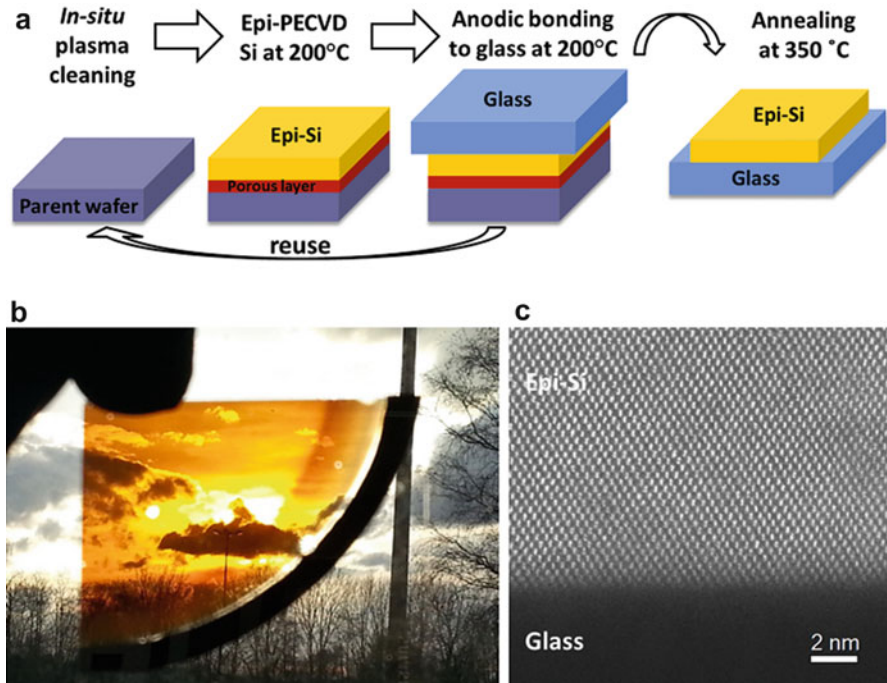


**Fig. 6** Steps involved in low temperature PECVD epitaxial silicon lift-off leading to an epitaxial Si layer on glass. **(a)** Schematic of the process flow for the growth and transfer of PECVD epitaxial Si layers onto glass substrate. **(b)** Sunlight through a 1.5  $\mu\text{m}$  epitaxial Si bonded to glass. **(c)** Scanning transmission electron microscopy high-angle annular dark-field image of the epitaxial Si/glass bonded interface (Cariou et al. 2016)

Heterojunction solar cells with the structure of Al/epitaxial Si/i a-Si:H/p a-Si:H/ITO/Ni-Au were fabricated and transferred to glass substrates by Cariou et al. (2016). Epitaxial Si by low temperature PECVD acts as the absorber. The Al layer was deposited onto the epitaxial Si layer before the anodic bonding process and served as the back contact. The intrinsic and p doped amorphous layers, ITO and Ni/Au contact were deposited after anodic bonding and layer transfer. An efficiency of 7.3% was obtained by Cariou et al. (2016) for a poly-Si thin film solar cell with a 5.5  $\mu\text{m}$  epitaxial Si absorber.

## Light Trapping Technology for Poly-Si Thin Film Solar Cells

Cost and electrical collection considerations will likely limit the thickness of the poly-Si thin film absorber to only several or dozens microns. The inherent indirect band gap of crystalline silicon results in low absorption coefficient and then inadequate light absorption. Antireflective coating and back reflector layer do have effects on the light absorption. But comparatively speaking, developing excellent light

trapping structures is more important to permit sufficient optical absorption and electron-hole pair generation in the device.

However, typical light trapping structure used in conventional c-Si solar cells (► Chap. 12, “Wafer Cleaning, Etching, and Texturization”) seems no longer appropriate for poly-Si thin films. Pyramids with the average size of several microns bring high Si consumption. Therefore, light-trapping structures in submicron or nanometer scales have been studied to meet the requirement of the poly-Si thin films.

So far, many random or periodic nano-scale light-trapping models have been proposed to control the propagation of light and then overcome the “Lambertian limit” or “Yablonovitch limit” of light trapping, as reported by Wang et al. (2012) and Mellor et al. (2013). Although most light trapping approaches based on nanostructures are now aimed at c-Si solar cells, they are also suitable for poly-Si thin films.

One approach to form random nanostructure (e.g., Si nanowires) is based on a well-known “bottom-up” vapor–liquid–solid (VLS) technique using metal as catalysts. However, the application of VLS could be limited by the metal catalyst contamination related deep levels which bring serious carriers recombination.

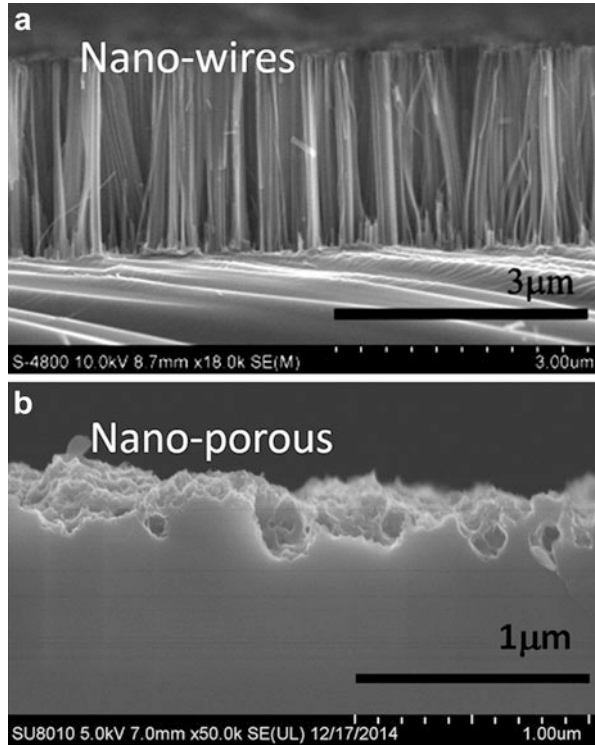
Random silicon nano-wires, nano-holes, or nano-porous can be fabricated by metal assisted chemical etching (MACE, also called metal catalyzed electroless etching, MCEE) of silicon in aqueous hydrofluoric acid (HF) solution (Liu et al. 2014). Due to its simplicity and scalability, MACE is now a widely employed fabrication approach of silicon nanostructures. Average surface reflectivity (300–1000 nm) of Si wafer based on MACE technique can be reduced to as low as 1~2%, as Liu et al. (2014) and Oh et al. (2012) reported, which is so-called “black silicon.” Typical SEM images of silicon nano-wires and nano-porous based on MACE are shown in Fig. 7. At present stage, most research works related to MACE nanostructures mainly focus on solar cells based on silicon wafer. For ultra thin Si or poly-Si thin films, MACE nanostructures are also available. For example, the MACE silicon nano-wires, as an efficient light trapping structure, have been successfully applied in the ultrathin crystalline silicon with the thickness of 20  $\mu\text{m}$  by He et al. (2015).

Nano-photonics with wavelength-scale periodic nanostructures opens up the possibility to reach or surpass the Lambertian limit. In the past several years, significant effort has been made to enhance the light absorption by nano-scale light trapping using various periodic nanostructures.

Periodic nanostructures can also be fabricated from bottom up VLS process. When periodic metal particles are used, periodic nano-wires array can be grown on the c-Si surface from Si precursors and metal catalysts. However, the metal catalyst contamination is still an insurmountable weakness in PV devices application.

Another approach is based on nanostructures fabricated by a top down etching process through a mask. By combining a pattern mask with an etching technique, nano-patterns will be transferred onto the silicon surface. Various techniques have been developed to form the pattern mask including laser interference lithography (LIL), nanoimprint lithography (NIL) from polymer resist, colloidal lithography

**Fig. 7** SEM images of typical silicon nano-wires and nano-porous by MACE



from colloidal nanoparticles, etc. The etching techniques are either dry plasma etching (Inductively Coupled Plasma etch, ICP, or Reactive Ion Etching, RIE) or wet chemical etching (NaOH, KOH, or TMAH).

Various combinations of pattern masks and etching techniques lead to a large variety of periodic nanostructures such as nanocones, nanowires, nanodomes, nanoholes, nanopyramids, invert nanopyramids, and so on. Many nanopatterning techniques have been successfully applied to ultra thin crystalline silicon thin films as Gaucher et al. (2016) and Chen et al. (2016) reported. By using UV nanoimprint lithography combined with KOH etching, Gaucher et al. (2016) obtained inverted pyramids structuration on epitaxial layers grown by PECVD at low temperature and fabricated patterned poly-Si solar cells on glass. The SEM images of the inverted pyramids structuration are shown in Fig. 8. A short-circuit current density of  $25.3 \text{ mA/cm}^2$  was demonstrated for an equivalent thickness of absorber of  $2.75 \text{ }\mu\text{m}$ . Nanopatterns obtained via wet-etching cannot only lead to better photo-current generation but also keep good passivation quality. In contrast, nanoholes obtained by dry-etching with steep and deep profiles represent a challenge for surface passivation (Chen et al. 2016).

By combining polymer sphere pattern with alkali etching, periodic pyramids, inverted pyramids, and their combination can be obtained on c-Si as shown in Fig. 9.



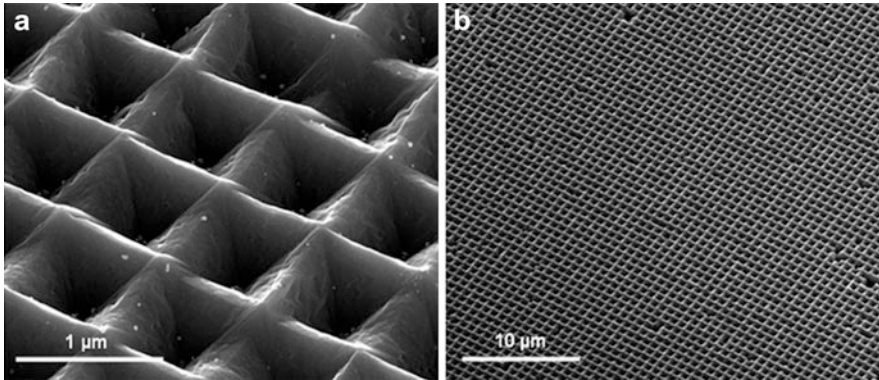


**Fig. 8** SEM images of the inverted pyramids structuration resulting from nanoimprint lithography and KOH etching. (Reprinted with permission from Gaucher et al. 2016)

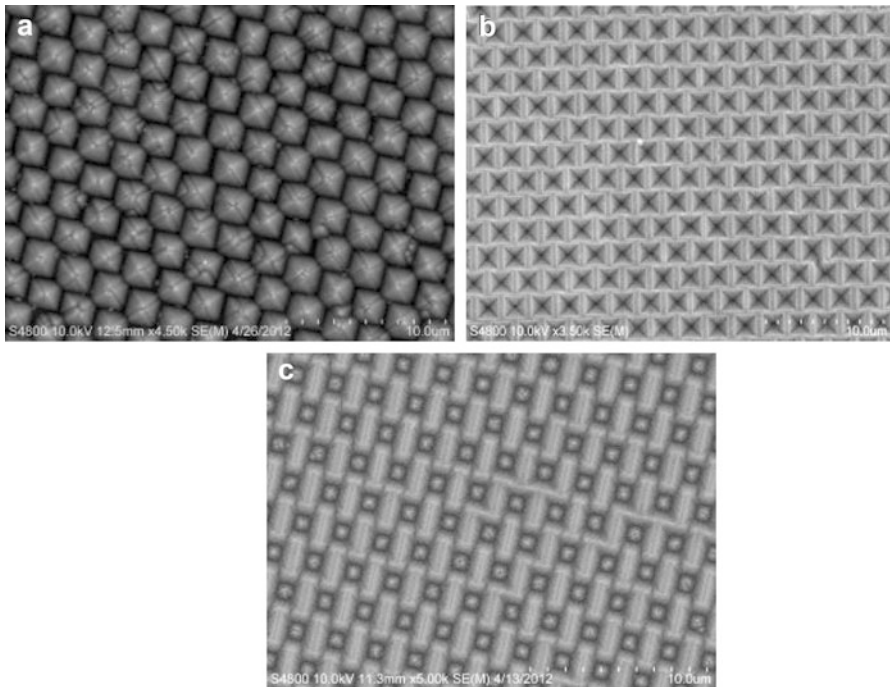
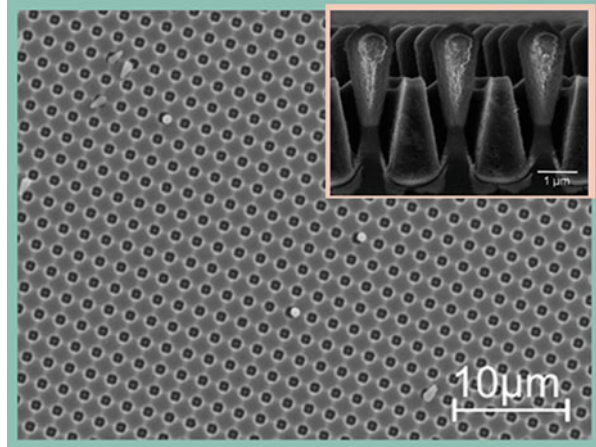


**Fig. 9** SEM images of periodic pyramids (a), periodic inverted pyramids (b), and their combination (c) fabricated by using polymer sphere pattern combined with alkali etching

This provides more options for periodic light trapping structures on poly-Si thin film solar cells.

As a convenient and powerful approach, computer modeling has been widely used to identify the most beneficial nanopattern structure for solar energy harvesting.

**Fig. 10** SEM image of a periodically structured poly-Si film grown on nanoimprinted-textured glass by EBE. The inset is the cross-sectional SEM image of periodic arrays of Si crystals on nanoimprinted-textured glass. (By Sontheimer et al. 2011 and Becker et al. 2012)



Rigorous coupled-wave analysis (RCWA) and Finite-Difference Time-Domain (FDTD) are the most popular modeling methods. Computer modeling indicates that nanoholes array textured Si surface shows superior light trapping capability than the nanopillars textured one. The computer modeling can also provide us a practical guideline to reach the highest short circuit current ( $J_{sc}$ ) for a specific solar cell architecture. The super-Gaussian holes and the inverted nano-pyramids were modeled and compared by RCWA or FDTD at different thicknesses of c-Si absorption layer. The inverted nano-pyramids with optimal pitch and fill factor present higher  $J_{sc}$  than super-Gaussian holes. A highest  $J_{sc}$  up to 35 mA/cm<sup>2</sup> was predicted for an 8- $\mu$ m thin silicon film (Depauw et al. (2014)). The  $J_{sc}$  value predicted from the simulation is consistent with the experimental results obtained by Branham et al. (2015). Based on microelectronic techniques, Branham et al. (2015) achieved peak efficiency of 15.7% and peak  $J_{sc}$  of 34.5 mA/cm<sup>2</sup> for 10- $\mu$ m-thick crystalline silicon solar cells using periodic inverted nano-pyramids as the light-trapping structure. This confirms the feasibility of obtaining high efficiency poly-Si thin film solar cells by suitable light trapping based on nanostructures.

Light trapping nanostructures can also be formed on glass substrates, especially for solar cells in a superstrate configuration, such as SiO<sub>2</sub> bead coated, abrasion etch textured, aluminum induced textured, and nanoimprinted glass substrates. Combined nanoimprinted glass substrates with e-beam evaporated silicon, highly absorbing periodic poly-Si nano- or microarchitectures can be formed directly, as shown in Fig. 10 (Sontheimer et al. 2011 and Becker et al. 2012). Backside texturing of the silicon film, plasmon enhanced light trapping by metal nanoparticles has also been studied.

Although nanostructures can achieve efficient light management by reducing reflectivity significantly over a broad range of wavelength and incident angle, it is still a challenging job to obtain high efficiency on solar cell devices with nanostructures. The damage and defects induced by etching process (especially dry-etching) bring serious surface recombination. And the increased surface area



makes the surface passivating a very difficult task. As a result, a striking drop of  $V_{oc}$  is usually observed. So, simple and effective surface passivation technique is critical important and highly desired.

For the condition that textures formed on glass substrates, in addition to high surface recombination velocities, the textured interfaces cause deterioration of silicon material quality when going on SPC or LPC process. To solve this problem, a novel texture method named the smooth antireflective three-dimensional (SMART) texture was put forward by Eisenhauer et al. (2017) for poly-Si thin film solar cells on glass. The SMART texture is produced by combining nanoimprint lithography of hexagonal  $\text{SiO}_x$  nanopillar arrays with spin-coating of titanium oxide layers. The voids between the  $\text{SiO}_x$  nanopillars are preferentially filled by the spin-coating of  $\text{TiO}_x$ . A smooth surface morphology without edges and steep flanks can be formed on glass substrate. The SMART texture has the characteristics of optically rough and morphologically flat. LPC poly-Si films grown on SMART textured glass substrate show equivalent electronic quality compared with planar references.  $V_{oc}$  values above 630 mV were achieved. Additional light management measures at the air/glass interface and silicon rear side can be combined with the SMART texture to increase the light absorption over a wide spectral range.

And one more point, the fabrication cost of the light trapping structures and the compatibility with the PV industry need to be taken into consideration. All fabrication processing steps of the light trapping structures should be able to be up-scalable to large areas. Producing of low-cost poly-Si thin film solar cells with advanced nanostructure can be expected based on reasonable integrating in the fabrication process.

---

## Quality Characterization of Poly-Si Thin Films

All of the techniques to obtain poly-Si thin films are aiming at a material quality as close as possible to c-Si wafers. Therefore, characterization techniques and analysis methods of the structural and opto-electronic properties of poly-Si thin films are similar to those of c-Si or poly-Si wafers (► Chaps. 2, “Polysilicon and Its Characterization Methods,” and ► 13, “Characterization of Wafers and Supply Materials”). Transmission electron microscope (TEM) measurement is commonly used to characterize the microstructure and the interface quality of the poly-Si thin films. Raman scattering, X-ray diffraction (XRD), and electron backscattered diffraction (EBSD) measurements can give us information about the crystallization of poly-Si thin films. Light absorption, optical-conductivity, and mobility measurements can provide us the optical or electrical properties of poly-Si thin films. Electron beam-induced conductivity (EBIC) measurement can be used to investigate the diffusion length of minority carriers and dislocation density in the poly-Si thin films. Electron spin resonance can yield the density of dangling bond defects. Spectroscopic ellipsometry is often used to determine the quality of epitaxial thin films. The measured structural and opto-electronic properties are usually compared with those of ideal c-Si to

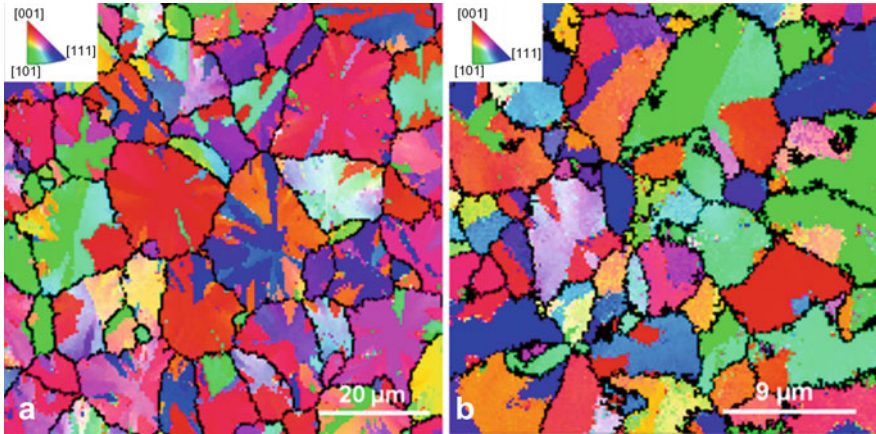


**Fig. 11** EBSD grain size and orientation map of the n-type poly-Si thin films prepared from the SPC of a-Si:H films deposited at (a) 380 °C and (b) 410 °C, respectively, for a  $\text{PH}_3$  (2% in  $\text{H}_2$ )/ $\text{SiH}_4$  gas flow ratio of 0.25. (Reprinted with permission from Kumar et al. 2015)

determine the quality of poly-Si thin films. EBSD, EBIC, Raman scattering, and spectroscopic ellipsometry will be briefly introduced here.

EBSD is widely used in the study of poly-Si thin films. EBSD can provide detailed information on grain size, crystallographic orientation of grains, and density and type of grain-boundaries. Qualitative and quantitative information on the intra-grain mis-orientation (plastic deformation) in poly-Si thin films subjected to strain gradients can also be obtained from the EBSD measurement. Most EBSD systems can generate graphical displays of the distribution of individual phases, of mis-orientation between individual grains and pole figures for displaying statistical distributions of orientations of individual grains. EBSD images, including pattern quality mappings, orientation distribution maps, and grain average mis-orientation (GAM) maps, are usually shown in literatures to illustrate the crystallization quality of poly-Si thin films after different processing. As an example, Fig. 11 shows the EBSD grain size and orientation maps of poly-Si thin films prepared from the SPC of a-Si:H films by Kumar et al. (2015).

EBSD can be combined with EBIC by obtaining the scanning electron images for both measurements from the same location. This combination of analyses can reveal the correlation between the electrical properties of the poly-Si grains and their crystallographic characterization. Figure 12 shows an EBSD GAM map, an EBIC image, and a superposition of the GAM and EBIC images of a SPC poly-Si thin film (Ke et al. 2014). Electrically active intra-grain defects seem appearing near the grain boundaries of grains larger than 3  $\mu\text{m}$ . These electrically active defects may be attributed to the increasing density of geometrically necessary dislocations (GNDs).

Raman scattering is an inelastic scattering of photons with phonons in materials. A small fraction of the scattered photons have a frequency different from, and usually lower than, that of the incident photons. The difference in energy

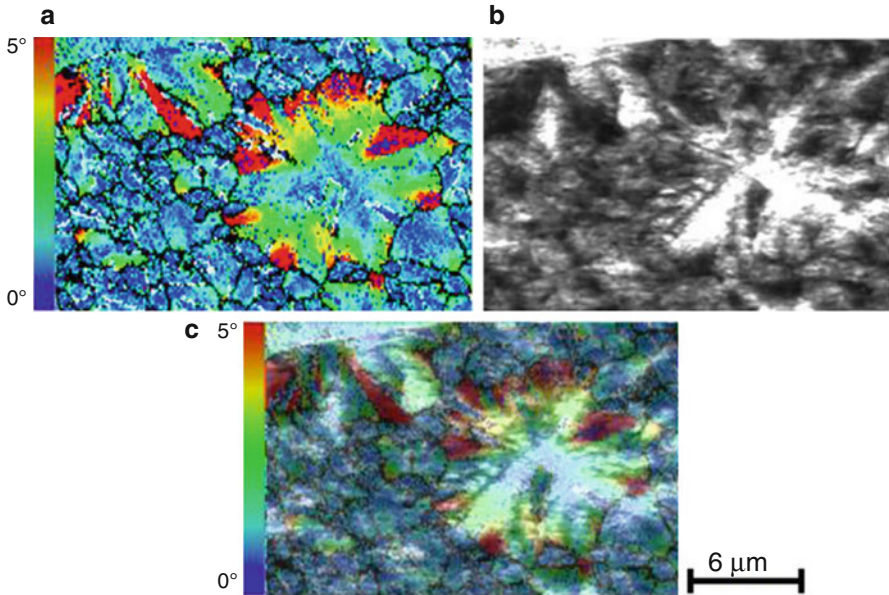


**Fig. 12** (a) GAM map of a SPC poly-Si region with large grains. The black lines were added to indicate grain boundaries. (b) EBIC image of the same region (white = large signal). (c) Superposition of images (a) and (b). (By Ke et al. 2014)

(or frequency) between the incident photons and the scattered photons corresponds to the energy required to excite an atom or a molecule to a higher vibrational mode. For c-Si, the Raman scattering is limited to a narrow transverse optical phonon (TO) mode at  $\sim 520 \text{ cm}^{-1}$  with a full width at half maximum (FWHM) of  $\sim 3.2 \text{ cm}^{-1}$  by the conservation of crystal momentum. The increase of defects and disorder in poly-Si thin films leads to the broadening of the TO peak. So, the FWHM of the TO mode at  $520 \text{ cm}^{-1}$  is an excellent indicator of the crystal quality of poly-Si thin films. To characterize the structural order of poly-Si thin films, FWHM of the TO mode is often measured and compared with that of c-Si. The FWHM value of poly-Si thin films obtained by using LPC technique ( $\sim 3.5 \text{ cm}^{-1}$ ) is much closer to the ideal FWHM of c-Si than those obtained from AIC ( $\sim 3.8 \text{ cm}^{-1}$ ) or SPC ( $\sim 4.8 \text{ cm}^{-1}$ ) (Becker et al. 2013). Therefore, LPC is more suitable for seed layer fabrication.

Compared with a standard Raman spectrometer, a Raman microspectrometer (Micro-Raman) is more powerful to determine the local structural in different zone of poly-Si thin films. Micro-Raman consists of a specially designed Raman spectrometer integrated with an optical microscope. Evolutionary process of AIC seed layer is often investigated by using Micro-Raman. The frequency of Raman modes is affected by the stress or mechanical strain in the films. So, Micro-Raman is widely used to study stress in the films. There is usually a shift in the peak position toward lower wave numbers for poly-Si thin films compared with c-Si wafer, which indicates the increase of tensile stress in the poly-Si thin films. For SPC poly-Si

thin films, the stress can be reduced by increasing the deposition temperature of the a-Si:H films as Kumar et al. (2015) reported.

Spectroscopic ellipsometry is a powerful technique which has already been widely used during the optimization of epitaxial thin films. For better characterization of the film growth, real-time spectroscopic ellipsometry is commonly adopted. At this condition, the PECVD or HWCVD reactor should be equipped with windows that allow optical access for real-time measurement. The optical reflection data can be analyzed to track the progress and breakdown of epitaxy growth as carried out by Teplin et al. (2005). By fitting the measured optical reflection data (pseudo-dielectric functions  $\epsilon_i$  or  $\text{Im}[\epsilon]$ ) with optical model, information according to the epitaxial silicon thin film can be determined. Usually, epitaxial silicon thin films can be described by a three layer model, as reported by Morenoa and Cabarocas (2010) and Teplin et al. (2005), which divided the epitaxial layer into a very thin ( $\sim 1$  nm) interface layer, a bulk layer, and a roughness top layer. Film thickness, surface roughness, interface condition, crystallinity, and voids content of the bulk layer and optical properties of the epitaxial silicon film can be obtained by using the powerful spectroscopic ellipsometry.

The typical  $\text{Im}[\epsilon]$  spectra of epitaxial films prepared by using PECVD (Cariou et al. 2016) are shown in Fig. 5a. In the high energy part ( $>3$  eV), the two  $\text{Im}[\epsilon]$  curves are similar and have the same shape as that of the bare c-Si wafer, suggesting same structural composition and quality as the c-Si wafer. Modeling of the spectra indeed shows 100% c-Si of the bulk layer. The amplitude of the oscillations at low energy (below 2.5 eV) differs for these two spectra, which was attributed to the difference in the interface by Cariou et al. (2016). The sharp interface leads to interferences with low amplitude, while a high-porosity interface shows higher amplitude of the oscillations in the low-energy range.

Grain size, FWHM of Raman peak, diffusion length of carriers, and dislocation density of poly-Si thin films prepared by different methods are summarized in Table 1. The LPC poly-Si shows the largest grain size which indicates the most suitable approach as an epitaxial seed layer. To ensure efficient carrier collection in a solar cell, a satisfactory diffusion length larger than three times of the absorber thickness is usually required. So, thicker poly-Si absorber demands higher material

**Table 1** Summarization of grain size, FWHM of Raman peak, diffusion length, and dislocation density of poly-Si thin films prepared by different methods

Methods	Grain size	FWHM of Raman TO mode ( $\text{cm}^{-1}$ )	Diffusion length ( $\mu\text{m}$ )	Dislocation or defect density ( $\text{cm}^{-2}$ )
SPC	1 ~ 15 $\mu\text{m}$	$\sim 4.8$	0.5 $\mu\text{m}$ ~ 10 $\mu\text{m}$	$(1-2) \times 10^{10}$
AIC	5 ~ 30 $\mu\text{m}$	$\sim 3.8$	–	–
LPC	mm ~ cm	$\sim 3.5$	2~20 $\mu\text{m}$	$10^6 \sim 5 \times 10^8$
HWCVD on c-Si	Epitaxial	$\sim 3.9$	1.5~14 $\mu\text{m}$	$10^4 \sim 10^8$

Kumar et al. (2015), Becker et al. (2013), Watahiki et al. (2000), Ke et al. (2014), Kühnapfel et al. (2015, 2016), Alberi et al. (2010), Huang et al. (2015), and Delachat et al. (2013)

quality. For a poly-Si layer with the thickness of 4–5  $\mu\text{m}$ , at present stage, LPC poly-Si and epitaxial Si on c-Si seem to be able to meet the above requirement.

---

## Poly-Si Thin Film Solar Cells

According to the diverse growth techniques of the poly-Si thin films, fabrication processes of poly-Si thin film solar cells are quite different from each other. However, the main structure of the solar cells is still p-n junction just like conventional c-Si solar cells. And both p-type- and n-type-based devices have been demonstrated.

In the early stage, conventional homo-junction designs are mainly adopted for poly-Si thin film solar cells. In recent years, a-Si:H/poly-Si hetero-junction devices, with doped a-Si:H as the emitter and intrinsic a-Si:H as the passivation layer, enable much higher open circuit voltages than diffused homo-junctions. Junction type, main fabrication process, champion efficiency, and absorber thickness of poly-Si thin film solar cells prepared by diverse methods are summarized in Table 2.

For the thermal SPC and the LPC poly-Si thin film solar cells, devices are fabricated directly on glass or metal substrates. Both substrate and superstrate configurations have been implemented. For epitaxial approaches, seed layer fabrication and/or growth layer transfer techniques are usually involved. Two types of solar cells fabrication processes related to epitaxial growth of poly-Si thin films are schematically illustrated in Fig. 13. For process A, epitaxial growth is carried out on c-Si wafer substrate. Lift-off and transferring of the epitaxial layer are included in the fabrication process of the solar cells. For process B, a seed layer is first created on glass substrate, followed by epitaxial thickening of the crystalline silicon seed layer. The seed layer could be large-grained AIC, LPC, or SPC poly-Si thin films grown on glass substrate. It could also be layer-transferred c-Si thin films oxide-bonded to Corning EAGLE XG glass substrate (SiOG).

Based on the combination of high temperature vapor phase epitaxy and bonding technology, efficiencies around 16% can be achieved for poly-Si thin film solar cells on low cost substrates. Very recently, Radhakrishnan et al. (2017) processed kerfless epitaxial foils (47  $\mu\text{m}$ , CVD 1130  $^{\circ}\text{C}$ ), which are lifted-off and layer transferred onto glass, into HJ-IBC devices. The fabrication process sequence of the solar cells is carefully optimized and is compatible with EVA-bonded Si. Most solar cell processing steps are carried out after bonding process, which enabling high mechanical yield. Based on the HJ-IBC solar cell technology, a best solar cell efficiency of 16.1% was achieved. Improvements to the solar cell performance of future epitaxial silicon foil devices on low cost substrate are expected by increasing the bulk lifetime, optimizing the contact stack, using alternative bonding agents, and implementing advanced light trapping structures.

A LPC device with much less thickness (13  $\mu\text{m}$ ) than that of the high temperature epitaxial silicon foil (47  $\mu\text{m}$ ) shows pretty good result as reported recently by Sonntag et al. (2017). After sequentially depositing the triple dielectric stack ( $\text{SiO}_x/\text{SiN}_x/\text{SiO}_x$ , PECVD), precursor Si absorber (electron-beam evaporation),

**Table 2** Junction type, main processes, maximum efficiency, and absorber thickness of poly-Si thin film solar cells prepared by different approaches

Fabrication method	Junction type	Main processes	Texture	Absorber thickness	$\eta$ (%)	Source
SPC	Homo	Borosilicate glass; PECVD; SPC 600 °C; RTA; H-passivation	Textured borosilicate glass	1–2 $\mu\text{m}$	10.4	Keevers et al. (2007)
AIC seed layer	Hetero	Alumina substrate; AIC seed layer, 500 °C, 4 h; thermal CVD 1130 °C; plasma texturing; remote plasma hydrogenation	Plasma texturing	2 $\mu\text{m}$	8.54	Yu Qiu et al. (2014)
LPC	Hetero	Glass substrate; SiO <sub>x</sub> /SiN <sub>x</sub> /SiO <sub>x</sub> stack layer; electron-beam evaporation; line-shaped 808 nm laser; H plasma treatment	KOH texturing	13 $\mu\text{m}$	13.2	Sonntag et al. (2017)
High T epitaxy	Hetero	Porous Si seed layer; CVD 1130 °C; epitaxial foil detachment; bonded to glass; HJ-IBC; most cell processing after bonding	TMAH texturing	47 $\mu\text{m}$	16.1	Radhakrishnan et al. (2017)
PECVD epitaxy	Hetero	PECVD 175 °C on c-Si; Epi-layer transfer; on glass	No	5.5 $\mu\text{m}$	7.3	Cariou et al. (2016)
HWCVD epitaxy	Hetero	“Dead” n <sup>+</sup> wafer substrate; HWCVD 750 °C; H passivation	No	2 $\mu\text{m}$	7.9	Young et al. (2012)

phosphorous doped a-Si:H (PECVD), and capping layer (SiO<sub>x</sub>) on alumino-silicate glass substrates, the LPC process was carried out in vacuum using a line-shaped 808 nm wavelength CW laser. Rapid thermal annealing process, hydrogen plasma treatment, and a common KOH texturing process were carried out subsequently. Finally, an interdigitated back-contact (IBC) a-Si:H/c-Si heterojunction (SHJ) solar cell structure was adopted. LPC-Si solar cells with above 630 mV open circuit voltage and a conversion efficiency of up to 13.2% were obtained on poly-Si absorber with thickness of roughly 13  $\mu\text{m}$  by Sonntag et al. (2017). LPC poly-Si technology shows the potential to surpass 15% conversion efficiency in the near



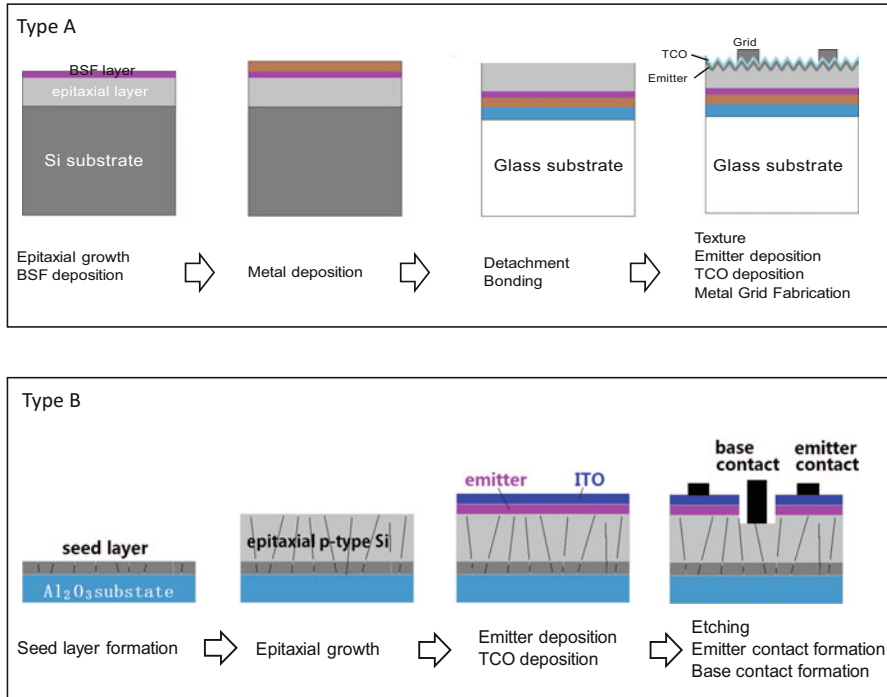


**Fig. 13** Two typical poly-Si thin film solar cells fabrication processes. Lift-off and transferring of the epitaxial layer are included in type A process. Seed layer fabrication is involved in type B process

future by better control of the crystallization process and by improving the solar cell structure.

Up to now, SPC-Si solar cell is still the only poly-Si thin film solar cell technology that had ever been carried out to industrial production. The moderate material quality and relative complex processes involved in most poly-Si thin film approaches are drawbacks limiting the device efficiency and large scale fabrication of poly-Si thin film solar cells.

## Conclusions

In the past years, diverse techniques have been developed for the fabrication of poly-Si thin film solar cells as described in this chapter. A lot of efforts have been made to improve the quality of poly-Si thin films, to rationalize the device structure, to optimize the fabrication techniques, and thus to increase the solar cells efficiency. The gradual increasing of the efficiency of poly-Si thin film solar cells is demonstrated.

Up to the present, the efficiency for poly-Si thin film solar cells on low cost substrates reached above 16% by lifting off and bonding high temperature epitaxial

silicon foils to the low cost substrates. The solar cell processing and interconnection can be carried out at the module level by carefully optimization of the solar cell fabrication procedure, which makes the large-scale production possible.

It also seems, from the current research results, the LPC approach for poly-Si thin film solar cells has the high potential to achieve solar cell efficiencies above 15% and to expand the fast fabrication processes to an industrial production scale. More efforts are needed to further improve the material qualities and device interfaces, to develop a cost-effective fabrication process, and finally to achieve highly efficient poly-Si thin film modules.

Besides the conventional p-n homo- or hetero-junction solar cells, some new type solar cell structures based on c-Si including organic-inorganic hybrid solar cells (He et al. 2015) and solar cells with dopant-free asymmetric heterocontacts (Bullock et al. 2016) are being investigated extensively. The low temperature and simple fabrication processes make them suitable for poly-Si thin film solar cells with ultrathin absorption layer.

On the longer term, poly-Si thin film solar cells on large area inexpensive substrates, with the advantages of less silicon consumption, high efficiency, and flexible device structure, have the potential to take a place in the global PV market.

---

## Cross-References

- ▶ [Characterization of Wafers and Supply Materials](#)
- ▶ [Fluidized Bed Process with Silane](#)
- ▶ [Growth of Crystalline Silicon for Solar Cells: Czochralski Si](#)
- ▶ [Growth of Crystalline Silicon for Solar Cells: Mono-Like Method](#)
- ▶ [Growth of Crystalline Silicon for Solar Cells: Noncontact Crucible Method](#)
- ▶ [Growth of Multicrystalline Silicon for Solar Cells: Dendritic Cast Method](#)
- ▶ [Growth of Multicrystalline Silicon for Solar Cells: The High-Performance Casting Method](#)
- ▶ [Hydrogenated Amorphous Silicon Thin Film](#)
- ▶ [Hydrogenated Microcrystalline Silicon Thin Films](#)
- ▶ [Polysilicon and Its Characterization Methods](#)
- ▶ [Siemens Process](#)
- ▶ [Upgrade Metallurgical Grade Silicon](#)
- ▶ [Wafer Cleaning, Etching, and Texturization](#)
- ▶ [Wafer Processing](#)

---

## References

- K. Alberi, I. Martin, M. Shub, C. Teplin, M. Romero, R. Reedy, E. Iwaniczko, A. Duda, P. Stradins, H. Branz, D. Young, Material quality requirements for efficient epitaxial film silicon solar cells. *Appl. Phys. Lett.* **96**, 073502 (2010)
- C. Becker, V. Preidel, T. Sontheimer, C. Klimm, E. Rudigier-Voigt, M. Bockmeyer, B. Rech, Direct growth of periodic silicon nanostructures on imprinted glass for photovoltaic and photonic applications. *Phys. Status Solidi C* **9**, 2079 (2012)



- C. Becker, D. Amkreutz, T. Sontheimer, V. Preidel, D. Lockau, J. Haschke, L. Jogschies, C. Klimm, J. Merkel, P. Plocica, S. Steffens, B. Rech, Polycrystalline silicon thin-film solar cells: Status and perspectives. *Sol. Energy Mater. Sol. Cells* **119**, 112 (2013)
- S. Bedell, D. Shahrjerdi, B. Hekmatshoar, K. Fogel, P.A. Lauro, N. Sosa, D. Sadana, Kerf-less removal of Si, Ge, and III–V layers by controlled spalling to enable low-cost PV technologies. *EPJ Photovolt.* **2**, 141 (2012)
- D. Bobela, C. Teplin, D. Young, H. Branz, P. Stradins, Epitaxial crystal silicon absorber layers and solar cells grown at 1.8 microns per minute, in *The 37th IEEE Photovoltaic Specialists Conference (PVSC37) Seattle*, 19 (2011)
- M.S. Branham, W.C. Hsu, S. Yerci, J. Loomis, S.V. Boriskina, B.R. Hoard, S.E. Han, G. Chen, 15.7% efficient 10- $\mu\text{m}$ -thick crystalline silicon solar cells using periodic nanostructures. *Adv. Mater.* **27**, 2182 (2015)
- M. Bruel, B. Aspar, A.-J. Auberton-Hervéa, New silicon on insulator material technology based on hydrogen implantation and wafer bonding. *Jpn. J. Appl. Phys.* **36**, 1636 (1997)
- J. Bullock, M. Hettick, J. Geissbühler, A. Ong, T. Allen, C. Sutter-Fella, T. Chen, H. Ota, E. Schaler, S. Wolf, C. Ballif, A. Cuevas, A. Javey, Efficient silicon solar cells with dopant-free asymmetric heterocontacts. *Nat Energy* **1**, 15031 (2016)
- P. Cabarocas, R. Cariou, M. Labrune, Low temperature plasma deposition of silicon thin films: from amorphous to crystalline. *J. Non-Cryst. Solids* **358**(17), 2000 (2012)
- R. Cariou, W. Chen, I. Bolanos, J. Maurice, M. Foldyna, V. Depauw, G. Patriarche, A. Gaucher, A. Cattoni, I. Massiot, S. Collin, E. Cadel, P. Pareige, P. Cabarocas, Ultrathin PECVD epitaxial Si solar cells on glass via low-temperature transfer process. *Prog. Photovolt. Res. Appl.* **24**(8), 1075 (2016)
- W. Chen, R. Cariou, M. Foldyna, V. Depauw, C. Trompoukis, E. Drouard, L. Lalouat, A. Harouri, J. Liu, A. Fave, R. Orobtschouk, F. Mandorlo, C. Seassal, I. Massiot, A. Dmitriev, K. Lee, P. Cabarocas, Nanophotonics-based low-temperature PECVD epitaxial crystalline silicon solar cells. *J. Phys. D: Appl. Phys.* **49**, 125603 (2016)
- D. Dawson-Elli, C. Williams, J. Couillard, J. Cites, R. Manley, G. Fenger, K. Hirschman, Demonstration of high performance TFTs on silicon-on-glass (SiOG) substrate. *ECS Trans.* **8**(1), 223 (2007)
- F. Delachat, F. Antoni, P. Prathap, A. Slaoui, C. Cayron, C. Ducros, Thin film pc-Si by aluminium induced crystallization on metallic substrate. *EPJ Photovolt.* **4**, 45102 (2013)
- V. Depauw, I. Abdo, R. Boukchicha, R. Cariou, W. Chen, I. Cosme Bolanos, O. Deparis et al., Nanophotonics for ultra-thin crystalline silicon photovoltaics: when photons meet electrons, in *29th European Photovoltaic Solar Energy Conference and Exhibition 3B0.5.5* (2014)
- D.J. Eaglesham, *J. Appl. Phys.* **77**, 3597 (1995)
- D. Eisenhauer, G. Köppel, K. Jäger, D. Chen, O. Shargaieva, P. Sonntag, D. Amkreutz, B. Rech, C. Becker, Smooth anti-reflective three-dimensional textures for liquid phase crystallized silicon thin-film solar cells on glass. *Sci. Rep.* **7**, 2658 (2017). <https://doi.org/10.1038/s41598-017-02874-y>
- A. Gaucher, A. Cattoni, C. Dupuis, W. Chen, R. Cariou, M. Foldyna, L. Lalouat, E. Drouard, C. Seassal, P. Cabarocas, S. Collin, Ultrathin epitaxial silicon solar cells with inverted nano-pyramid arrays for efficient light trapping. *Nano Lett.* **16**(9), 5358 (2016)
- I. Gordon, F. Dross, V. Depauw, A. Masolin, Y. Qiu, J. Vaes, D. Van Gestel, J. Poortmans, Three novel ways of making thin-film crystalline-silicon layers on glass for solar cell applications. *Sol. Energy Mater. Sol. Cells* **95**, S2–S7 (2011)
- J. Han, L. Wang, A. Lochtefeld, A. Gerger, H. Li, M. Carroll, Y. Yao, A. Lennon, R. Opila, A. Barnett, Fabrication of large area ultra-thin silicon solar cells, in *29th European Photovoltaic Solar Energy Conference and Exhibition* (2014), p. 1502
- J. He, P. Gao, M. Liao, Y. Xi, Z. Ying, S. Zhou, J. Ye, C. Yi, Realization of 13.6% efficiency on 20 $\mu\text{m}$  thick Si/organic hybrid heterojunction solar cells via advanced nanotexturing and surface recombination suppression. *ACS Nano* **9**, 6522 (2015)
- W. Hsu, J. Tong, M. Branham, Y. Huang, S. Yerci, S.V. Boriskina, G. Chen, Mismatched front and back gratings for optimum light trapping in ultra-thin crystalline silicon solar cells. *Opt. Commun.* **377**, 52 (2016)

- J. Huang, S. Varlamov, J. Dore, J.S. Yun, M.A. Green, Micro-structural defects in polycrystalline silicon thin-film solar cells on glass by solid-phase crystallisation and laser-induced liquid-phase crystallisation. *Sol. Energy Mater. Sol. Cells* **132**, 282 (2015)
- P. Kapur, M. Moslehi, A. Deshpande, V. Rana, J. Kramer, S. Seutter, H. Deshazer, S. Coutant, A. Calcaterra, S. Kommera, Y.-S. Su, D. Grupp, S. Tamilmani, D. Dutton, T. Stalcup, T. Du, M. Wingert, A manufacturable, non-plated, non-Ag metallization based 20.44% efficient, 243cm<sup>2</sup> area, back contacted solar cell on 40 um thick mono-crystalline silicon, in *28th European Photovoltaic Solar Energy Conference and Exhibition* (2013), p. 2228
- C. Ke, F. Law, P. Widenborg, A. Aberle, I. Peters, Electrical activity of geometrically necessary dislocations in polycrystalline silicon thinfilms prepared by solid phase crystallization. *Phys. Status Solidi* **A211**, 2488 (2014)
- M. Keevers, T. Young, U. Schubert, M. Green, 10% efficient CSG minimoduls, in *22nd European Photovoltaic Solar Energy Conference* (2007), p. 1783
- W. Knaepen, C. Detavernier, R.L. Meirhaeghe, J.J. Sweet, C. Lavoie, In-situ X-ray Diffraction study of metal induced crystallization of amorphous silicon. *Thin Solid Films* **516**, 4946 (2008)
- S. Kühnapfel, J. Huang, A. Teal, H. Kampwerth, D. Amkreutz, S. Gall, S. Varlamov, Lifetime analysis of laser crystallized silicon films on glass. *J. Appl. Phys.* **118**, 055304 (2015)
- S. Kühnapfel, S. Gall, P. Sonntag, N. Schäfer, D. Abou-Ras, Direct correlation of microstructure and device performance of liquid phase crystallized Si thin film solar cells on glass. *Phys. Status Solidi RRL* **10**, 657 (2016)
- A. Kumar, P.I. Widenborg, G.K. Dalapati, C. Ke, G.S. Subramanian, A. Aberle, Controlling stress in large-grained solid phase crystallized n-type poly-Si thin films to improve crystal quality. *Cryst. Growth Des.* **15**, 1067 (2015)
- L. Liu, K. Peng, Y. Hu, X. Wu, S. Lee, Fabrication of silicon nanowire arrays by macroscopic galvanic cell-driven metal catalyzed electroless etching in aerated HF solution. *Adv. Mater.* **26**, 1410 (2014)
- M.S. Mason, C.M. Chen, H.A. Atwater, Hot-wire chemical vapor deposition for epitaxial silicon growth on large-grained polycrystalline silicon templates. *Thin Solid Films* **430**, 54 (2003)
- A. Mellor, H. Hauser, C. Wellens, J. Benick, et al., Nanoimprinted diffraction gratings for crystalline silicon solar cells: implementation, characterization and simulation. *Opt. Express* **21**, A295 (2013)
- M. Moreno, G. Patriarche, P. Roca i Cabarrocas, Fine tuning of the interface in high-quality epitaxial silicon films deposited by plasma-enhanced chemical vapor deposition at 200 °C. *J. Mater. Res.* **28**, 1626 (2013)
- M. Moreno, P. Cabarrocas, Ultra-thin crystalline silicon films produced by plasma assisted epitaxial growth on silicon wafers and their transfer to foreign substrates. *EPJ Photovolt.* **1**, 10301 (2010)
- M. Nerdling, L. Oberbeck, T.A. Wagner, R.B. Bergmann, H.P. Strunk, Single to polycrystalline transition in silicon growth by ion-assisted deposition at low temperatures. *J. Appl. Phys.* **93**, 2570 (2003)
- J. Oh, H.C. Yuan, H.M. Branz, An 18.2%-efficient black-silicon solar cell achieved through control of carrier recombination in nanostructures. *Nat. Nanotechnol.* **7**(11), 743 (2012)
- J.H. Petermann, D. Zielke, J. Schmidt, F. Haase, E.G. Rojas, R. Brendel, 19%-efficient and 43 mm-thick crystalline Si solar cell from layer transfer using porous silicon. *Prog. Photovolt. Res. Appl.* **20**, 1 (2012)
- N. Preissler, D. Amkreutz, P. Sonntag, M. Trahms, R. Schlattmann, B. Rech, Interface engineering for liquid-phase crystallized-silicon solar cells on glass. *Sol. RRL* **1**, 1700015 (2017a)
- N. Preissler, J. Töfflinger, O. Gabriel, P. Sonntag, D. Amkreutz, B. Stannowski, B. Rech, R. Schlattmann, Passivation at the interface between liquid-phase crystallized silicon and silicon oxynitride in thinfilm solar cells. *Prog. Photovolt. Res. Appl.* **25**, 515 (2017b)
- Y. Qiu, O. Kunz, A. Fejfar, M. Ledinský, B. Chan, I. Gordon, D. Gestel, S. Venkatachalm, R. Egan, On the effects of hydrogenation of thin film polycrystalline silicon: a key factor to improve heterojunction solar cells. *Sol. Energy Mater. Sol. Cells* **122**, 31 (2014)

- H. Radhakrishnan, R. Martini, V. Depauw, K. Van Nieuwenhuysen, M. Debucquoy, J. Govaerts, I. Gordon, R. Mertens, J. Poortmans, Improving the quality of epitaxial foils produced using a porous silicon-based layer transfer process for high-efficiency thin-film crystalline silicon solar cells. *EPJ Photovolt* **4**, 70 (2014)
- H. S. Radhakrishnan, M. Xu, T. Bearda, M. Filipič, K. Van Nieuwenhuysen, V. Depauw, I. Gordon, M. Debucquoy, J. Szlufcik, J. Poortman, Heterojunction IBC solar cells on thin ( $< 50 \mu\text{m}$ ) epitaxial Si foils produced from Kerfless layer transfer process, in *33rd European Photovoltaic Solar Energy Conference and Exhibition* (2017), p. 740
- B. Rau, I. Sieber, B. Selle, S. Brehme, U. Knipper, S. Gall, et al., Homo-epitaxial Si absorber layers grown by low-temperature ECRCVD. *Thin Solid Films* **644**, 451 (2004)
- T. Sontheimer, E. Rudigier-Voigt, M. Bockmeyer, C. Klimm, P. Schubert-Bischoff, C. Becker, B. Rech, Large-area fabrication of equidistant free-standing Si crystals on nanoimprinted glass. *Phys. Status Solidi RRL* **5**, 376 (2011)
- M. Schwarzschild, Crystalline thin film grows on amorphous base. *Phys. Today* **32**(8), 21 (1979)
- P. Sonntag, N. Preissler, M. Bokalič, M. Trahms, J. Haschke, R. Schlatmann, M. Topič, B. Rech, D. Amkreutz, Silicon solar cells on glass with power conversion efficiency above 13% at thickness below 15 micrometer. *Sci. Rep.* **7**, 873 (2017)
- C. Teplin, D.H. Levi, E. Iwaniczko, K.M. Jones, J.D. Perkins, H.M. Branz, Monitoring and modeling silicon homoepitaxy breakdown with real-time spectroscopic ellipsometry. *J. Appl. Phys.* **97**, 103536 (2005)
- Q. Wang, C.W. Teplin, P. Stradins, B. To, K.M. Jones, H.M. Branz, Recent advances in hot-wire CVD R&D at NREL: from 18% silicon heterojunction cells to silicon epitaxy at glass-compatible temperatures. *J. Appl. Phys.* **100**, 93520 (2006)
- K. Wang, Z. Yu, V. Liu, Y. Cui, S. Fan, Absorption enhancement in ultrathin crystalline silicon solar cells with antireflection and light-trapping nanocone gratings. *Nano Lett.* **12**, 1616 (2012)
- T. Watahiki, A. Yamada, M. Konagai, New approach to low-temperature Si epitaxy by using hot wire cell method. *J. Cryst. Growth* **209**, 335 (2000)
- D. Young, S. Grover, C. Teplin, P. Stradins, V. LaSalvia, T. Chuang, J. Greg, C. Howard, M. Branz, Characterization of epitaxial film silicon solar cells grown on seeded display glass, in *The 2012 I.E. Photovoltaic Specialists Conference* 3 (2012)

---

**Part VI**

**Nano-structure Silicon Materials and Solar Cells**



Deyuan Wei, Shuyan Xu, and Igor Levchenko

## Contents

Introduction .....	794
Properties of Nanocrystalline Silicon .....	798
Properties of Intrinsic Materials .....	798
Properties of the Doped Materials .....	807
Fabrication of Nanocrystalline Silicon Films .....	808
Mainstream Deposition Methods .....	808
Alternative Deposition Methods .....	813
Solar Cell Technology .....	816
Device Formation and Operation .....	817
Design of a Typical Single-Junction Solar Cell .....	818
Multijunction Solar Cell .....	822
Light-Induced Degradation .....	824
Advanced Technologies for Efficiency Improvement .....	825
Improved Absorber Material on Textured Substrate .....	825

---

D. Wei (✉)

Plasma Sources and Application Center, NIE, Nanyang Technological University, Singapore, Republic of Singapore

Micromachines Lab 1, School of Mechanical and Aerospace Engineering, Nanyang Technological University, Singapore, Republic of Singapore

e-mail: [dywei@ntu.edu.sg](mailto:dywei@ntu.edu.sg)

S. Xu

Plasma Sources and Application Center, NIE, Nanyang Technological University, Singapore, Republic of Singapore

e-mail: [shuyan.xu@nie.edu.sg](mailto:shuyan.xu@nie.edu.sg)

I. Levchenko

Plasma Sources and Application Center, NIE, Nanyang Technological University, Singapore, Republic of Singapore

School of Chemistry, Physics and Mechanical Engineering, Queensland University of Technology, Brisbane, QLD, Australia

e-mail: [levchenko.igor@nie.edu.sg](mailto:levchenko.igor@nie.edu.sg)

Interface Treatment .....	827
Optical Design for Light Management .....	829
Present Status of Solar Cell Efficiency .....	837
Conclusion and Prospects .....	838
References .....	839

## Abstract

Thin-film solar cell technology based on nanocrystalline silicon has made a significant progress since the production of the first hydrogenated nanocrystalline silicon (nc-Si:H) solar cell in 1994. Up to date, the highest conversion efficiency of single-junction nc-Si:H thin-film solar cells has reached 11.8%, and further progress is expected. In this chapter, we aim to outline the progress, trends, and major approaches to enhance the nanocrystalline silicon solar cell technology and achieve considerably higher efficiency numbers. Comprising of two parts, this chapter in its first part describes the fundamentals of nanocrystalline silicon properties, typical fabrication methods, and technologies for solar cells as well as recent progress in nc-Si:H fabrications and properties. The second part states the recent advanced technologies for efficiency improvement and provides an overview of the significant achievements, current status, and future prospects of the thin-film solar cells based on nc-Si:H. In particular, the highest reported open-circuit voltage of 608 mV has been demonstrated in a 650-nm-thick single-junction nc-Si:H solar cell by applying amorphous silicon passivation layers at the n/i interface. Besides, the multijunction solar cell technique has significantly contributed to the improvement of the conversion efficiency. In particular, the best triple-junction tandem solar cells reach an initial active-area efficiency of about 16% in the a-Si:H/a-SiGe:H/nc-Si:H structure. Such an impressive success in light management paves the way to the application of nanocrystalline silicon for many vital fields such as novel texture structures, window layers, intermediate reflectors for the improvements of photocurrent density, and conversion efficiency.

## Keywords

Nanocrystalline silicon · Microcrystalline silicon · Solar cells · Thin-film solar cells · Fabrication · Light management

## Introduction

Energy crisis and environment deterioration caused by burning of fossil fuels and other pollutants have been ranked among humanity's top issues. Clean and renewable energy, including solar, wind, and hydroenergy techniques, becomes the important energy alternative all over the world. Photovoltaic technology, which converts solar light directly to electrical power, is one of the most promising candidates. Starting from A. E. Becquerel's epochal discovery of the photovoltaic effect in 1839,

a continuous progress in the photovoltaic energy technique resulted in the announcement in 1954 by Chapin et al. of the first “usable” solar cell based on silicon. Up to date, various solar cell technologies have been developed, and they are traditionally divided into three generations.

The first-generation solar cells refer to the crystalline silicon (c-Si) wafer-based technique utilizing mono- and multicrystalline silicon. These solar cells are the most established type of light-harvesting devices produced in the present-day photovoltaic industry. However, the c-Si solar cells feature significant drawbacks restricting their wide applications. Specifically, high energy consumptions required for the formations of highly pure c-Si wafers and the complex fabrication process of solar cells imply high costs of the devices and, hence, high costs of the cell-produced electric energy, as compared to the traditional fossil fuel routes. Therefore, the second- and third-generation solar cells based on thin film technologies have become the primary focus of the present-day solar energy research efforts.

The second-generation solar cells are usually based on hydrogenated amorphous silicon (a-Si:H), hydrogenated nanocrystalline silicon (nc-Si:H), copper indium gallium selenide (CIGS), and cadmium telluride (CdTe). These devices are produced by applying thin-film inorganic coatings onto inexpensive large-area substrates such as glass, stainless steel, or polymers. The core light-absorbing layers in these cells are usually very thin (several micrometer) films, so that these devices show the distinct advantages such as small amounts of material required, low energy consumptions and carbon emissions in fabrication, and the resulting low production costs. Moreover, some other important advantages also arise including the possibility of deposition over large-area substrates and simple techniques of mass production. In addition, these thin film devices are very suitable for BIPV (building integrated photovoltaics) strategy, flexible and portable instruments, etc. Silicon-free materials such as CIGS and CdTe result in relatively high energy conversion efficiency exceeding 20% (Polman et al. 2016), but the need in use of toxic elements and/or the lack of their availability limits their global applications.

The third-generation solar cells are innovative photovoltaic devices fabricated by modern techniques; typical examples are hybrid organic-inorganic perovskite solar cells, dye-sensitized solar cells, organic solar cells, quantum dot solar cells (see ► Chaps. 24, “Nanocrystalline Silicon-Based Multilayers and Solar Cells,” and ► 26, “Colloidal Silicon Quantum Dots and Solar Cells”), etc. Although perovskite solar cells have been hot spots with the highest efficiency above 20%, they often involve toxic materials and still suffer the stability issues when exposed to heat, continuous illumination, moisture atmospheres, etc. The other third-generation solar cells usually have low conversion efficiencies and/or poor stabilities (Polman et al. 2016).

Silicon has ever been a base of one of the most promising photovoltaic technologies. In fact, the amorphous silicon photovoltaic technology has been used in the last decades. The best initial efficiency reaching 16.3% (Yan et al. 2011) has been achieved for the triple-junction architecture involving amorphous silicon, nanocrystalline silicon, and silicon alloys (mainly with germanium, Ge). In spite of the lower

efficiencies compared with CIGS and CdTe, silicon-based materials have their own advantages, namely:

1. Nearly infinite stock of silicon material, as compared with relatively rare elements used in CIGS and CdTe cells; silicon could be an ideal material for the mass photovoltaic applications.
2. Silicon material is nontoxic and eco-friendly.
3. Silicon thin film processes have been mature due to the long-standing development of the semiconductor manufacturing and liquid crystal display industries.

Besides, according to the Shockley-Queisser (S-Q) detailed-balance model, the upper limit of conversion efficiency for a single-junction silicon solar cell approaches ~30% (Polman et al. 2016). Therefore, there is still a large room and potential for further improvement of silicon thin-film solar cells, and the hydrogenated amorphous and nanocrystalline silicon structures and composites could be materials of the next-stage cheap, efficient, mass-used solar cell energetics.

Amorphous silicon (a-Si) firstly appeared as a light-absorbing material in silicon-based second-generation thin-film solar cells (see ► Chap. 20, “Hydrogenated Amorphous Silicon Thin Film”). a-Si is composed of silicon atoms which are spatially arranged on a lattice that presents only short range order. The conventional amorphous silicon material deposited by a glow discharge usually contains some percentages of hydrogen atoms bonded to the amorphous silicon structure. This form of amorphous silicon is generally known as hydrogenated amorphous silicon (a-Si:H). Some bonds are broken in this structure, thus resulting in the formation of so-called dangling bonds. Nevertheless, hydrogen can passivate a large part of these dangling bonds, significantly improving the film quality.

The hydrogenated amorphous silicon has a bandgap of ~1.7 eV and exhibits high light absorption coefficients for the photons with energies above 1.7 eV. However, the insufficient response in red and infrared light blocks the further efficiency improvement of a-Si:H solar cell. In addition, the hydrogenated amorphous silicon cell suffers the light-induced degradation of efficiency which is so-called Staebler-Wronski effect (SWE). The stabilized efficiency, which is defined as the efficiency measured after 1000 h exposure at 1 sun intensity at 50 °C, is 70–90% of the initial efficiency for the high-quality a-Si:H solar cell. Multijunction solar cell consisting of stacked a-Si:H top cell and hydrogenated amorphous silicon-germanium a-SiGe:H bottom cell with narrow bandgap is also widely studied to ensure absorption of the whole solar spectrum and thus boost cell efficiency. However, its production cost is still considerably high because germanium is exceedingly expensive and less abundant.

Hydrogenated nanocrystalline silicon (nc-Si:H), sometimes also known as hydrogenated microcrystalline silicon ( $\mu$ c-SiH:H), is defined as a complex material composed of nanoscale crystalline grains (typically >5 nm) and amorphous tissues, plus grain boundaries. The difference between nanocrystalline and polycrystalline silicon (poly-Si) (see ► Chap. 22, “Polycrystalline Silicon Thin Film”) is that the amorphous phase only exists in nc-Si rather than poly-Si. In addition, nanocrystalline



silicon also differs from the silicon nanocrystal material that consists of small nanocrystals (typically <5 nm) demonstrating quantum effects (see ► Chaps. 24, “Nanocrystalline Silicon-Based Multilayers and Solar Cells” and ► 26, “Colloidal Silicon Quantum Dots and Solar Cells”).

Although nc-Si:H has a complex microstructure, its optical properties feature a marked crystalline characteristic, namely, an optical gap at 1.12 eV (like in the case of c-Si). As distinct from a-Si:H material which absorbs light up to 800 nm, the nc-Si:H structure absorbs light in a wider-range spectrum, extending up to 1100 nm. Thus, the nc-Si:H material has a stronger long wavelength response than a-Si:H material. The other merit of nc-Si:H-based solar cells is stability under long-time sunlight irradiation. Some nc-Si:H solar cells are also subject to light-induced degradations, but these degradations are much weaker and slower than most of a-Si:H solar cells. Furthermore, material costs of nc-Si:H films are far lower than those of c-Si wafers because the required thickness of the absorber in nc-Si:H solar cell is two orders of magnitude smaller (typically 1 ~ 3  $\mu\text{m}$ ) than that of silicon wafer. In addition, material costs of nc-Si:H films are also greatly lower than those of a-SiGe:H films with costly Ge component. Therefore, the nc-Si:H material is considered as a low-cost alternative for the a-SiGe:H material in a silicon-based multijunction thin film cell.

The pioneering work for the first nc-Si:H solar cells was first reported in 1991 by G. Lucovsky et al. A complete nc-Si:H cell with an efficiency of 4.6% opened up a new area of photovoltaic development in 1994 (Meier et al. 1994). However, cell efficiency was limited by a low open-circuit voltage ( $V_{oc}$ ) and fill factor ( $FF$ ) in that early stage. In general, open-circuit voltage representing the presence of built-in electric field is considered as a significant prerequisite for solar cells. In the 1990s, the absorbers with a high (typically >70%) crystalline volume fraction were mostly investigated, since researches wished to improve cell efficiency by obtaining the high carrier mobility in large crystals. However, short-circuit current density ( $J_{sc}$ ) was not improved, and the  $V_{oc}$  was still limited to 500 mV (Meier et al. 1994).

Further progresses were achieved in later years. Vetterl et al. reported that the nc-Si:H solar cell with a low crystalline volume fraction of 60% shows an improved  $V_{oc}$  of 520 mV. The efficiency of 7.5% for a 2- $\mu\text{m}$ -thick nc-Si:H single-junction solar cell and 12% for an a-Si:H/nc-Si:H stacked solar cell was achieved (Vetterl et al. 2000). The intrinsic layer of the best solar cell consists of the medium rather than largest grains. It was supposed that grain boundaries are well passivated by the increase in the fraction of amorphous phase, reducing bulk recombination and improving  $V_{oc}$ . Thus, the concept of “transition region” with a typical crystalline volume fraction between 30% and 70% was adopted, and the best solar cells are often obtained in this region.

The controlling interface passivation efforts contribute to the technological development toward higher  $V_{oc}$ . Y. Mai reported a 10.3% solar cell with  $V_{oc}$  of 570 mV by applying a hot-wire chemical vapor deposition (HWCVD)-deposited buffer layer between p/i interface (Mai et al. 2005). Later, van den Donker obtained a nc-Si:H solar cell with an efficiency of 9.8% and a  $V_{oc}$  of 603 mV by combining

HWCVD-deposited buffer layer and SiH<sub>4</sub> flow profiling technique in 2007 (Van Den Donker et al. 2007).

In recent years, light management strategies have been widely implemented to enhance light absorption for the  $J_{sc}$  improvement. First of all, one common strategy is to achieve light trapping by applying the nanometer- or micrometer-scale periodic or random texture on the surface of front/back electrode or even directly to the glass substrate by means of wet etching, lithography (plus dry etching), nanoimprint lithography, or photonic crystal. Secondly, the wide-bandgap materials such as silicon oxide (SiO<sub>x</sub>) and silicon carbide (SiC<sub>x</sub>) have been used as novel window layers to reduce the parasitic absorption losses of high-energy photons in a window layer. Then, another hot spot is to insert intermediate reflector (such as SiO<sub>x</sub>, ZnO, etc.) between the top and bottom cells of tandem solar cell to reflect the short wavelength light back to the top cell and enhance the overall light absorption inside it.

However, the present efficiencies of nc-Si:H solar cells are still far lower than the theoretical efficiency limit (over 30%) according to the Shockley-Queisser (S-Q) detailed-balance model (Polman et al. 2016). The major challenge of commercialization is how to achieve the high conversion efficiency with a high deposition rate and low process cost.

---

## Properties of Nanocrystalline Silicon

In this section, material properties of the intrinsic and doped thin films in nc-Si:H solar cells are introduced and discussed. The intrinsic materials are used to act as the light absorber, so that the structure with low defect density and impurity contamination is required to reduce the carrier recombination. The doped materials are used to form the n- and p-type layer on both sides of the intrinsic layer to form the junction, build up an internal electric field, and form a good contact with the electrodes. Therefore, material properties of individual function layers are the bases of solar cell performance. The device-grade materials are required for solar cell application. The criteria for device-grade material depend on which part of the device the material is used for and its function in a solar cell.

### Properties of Intrinsic Materials

The intrinsic nc-Si:H material acting as the core light-absorbing layer largely determines the general performance of solar cell. Therefore, the structural, optical, and electrical properties of the intrinsic nc-Si:H materials have been extensively investigated.

#### Structural Properties

**Microtopography.** A typical nc-Si:H is a complex material composed of crystalline and amorphous silicon phases plus grain boundaries. The crystallinity of Si:H film

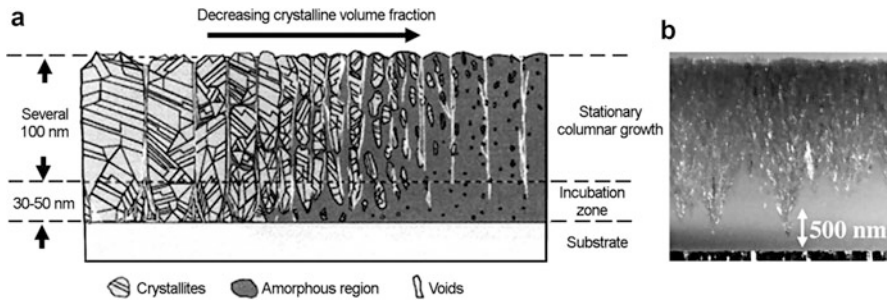


**Fig. 1** (a) Schematic diagram of microstructures of nc-Si:H thin film. From *left to right*, the phase of nc-Si:H film evolves from highly crystalline to prevailing amorphous phase. (b) TEM micrograph of a typical nc-Si:H layer deposited on the flat sputtered ZnO:Al film. (Reproduced from Vetterl et al. (2000) and Bailat et al. (2002). Copyright (2000 and 2002), with permissions from Elsevier)

can be varied in a large scale and is determined by deposition conditions. Figure 1a shows that with the decrease in the degree of crystallinity of thin film, the phase evolution occurs from the highly crystalline phase on the left-hand side to the prevailing amorphous phase on the right-hand side. As mentioned above, the nc-Si:H materials which are most suitable for solar cell applications are the materials in the phase transition region in the middle of Fig. 1a. As seen, typical pencil-like conglomerates which are formed by nanocrystals, voids, and amorphous phase are represented by light gray polygon areas, white holes, and continuous dark gray area, respectively. Figure 1b shows a cross-sectional TEM micrograph of a typical nc-Si:H film deposited on flat sputtered ZnO:Al film (Bailat et al. 2002). The inhomogeneous structure throughout its thickness is clearly observed, and the widely reported amorphous incubation layer appears at the bottom of the silicon thin film. It is worth noting that this inhomogeneous structure has been significantly improved in recent years. As shown in Fig. 11b, the nc-Si:H films with the relatively homogeneous structures have been fabricated by inserting a seed layer (diminishing the bottom incubation layer), controlling the crystallinity uniformity by hydrogen dilution profiling technique, etc.

**Crystalline volume fraction and phase transition.** According to the fraction of crystalline phase, the nc-Si:H materials can be grouped into three categories:

- (i) The highly crystalline silicon with large crystal columns throughout the film
- (ii) Near the transition region from crystalline to amorphous phase where crystal columns are smaller and a large fraction of amorphous phase and grain boundaries are present between the columns
- (iii) Dominant amorphous matrix with embedded small crystallites

It is widely reported that the nc-Si:H solar cells with the highest efficiencies consist of light-absorbing materials prepared close to the transition region. Vetterl et al. (2000) reported that one important requirement for the device-grade nc-Si:H

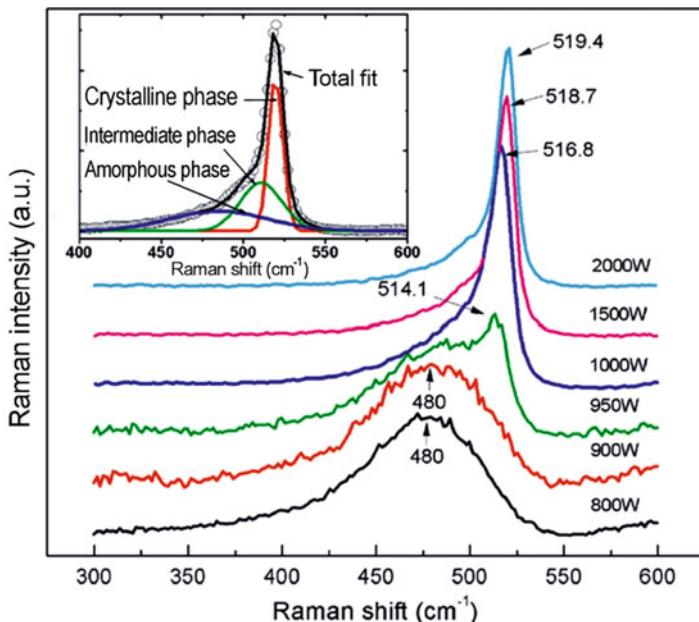


**Fig. 2** Series of Raman spectra of Si:H films deposited by ICP-CVD on glass substrate at different discharge powers. The inset is the single Raman spectrum deconvoluted into two Gaussian functions and one Lorenzian-Gaussian mixed function near 480, 510, and 520  $\text{cm}^{-1}$ . (Reprinted with permission from Wei et al. (2013). Copyright (2013) © IOP Publishing Ltd)

material is the intermediate crystallinity (30 ~ 70%) of the absorber. The possible reason for these results is that the large volume of amorphous tissues passivates the defects at surfaces of crystalline phase, reducing the overall defect density and the resultant carrier recombination rate.

The crystallinity of nc-Si:H film is widely characterized by Raman spectroscopy. The characteristic peak corresponding to the transverse optical (TO) mode of c-Si is at 520  $\text{cm}^{-1}$ , whereas amorphous band appears at around 480  $\text{cm}^{-1}$  in Raman spectrum. For the qualitative analysis, the spectrum can be deconvoluted into two Gaussian functions and one Lorenzian-Gaussian mixed function near 480, 510, and 520  $\text{cm}^{-1}$ , as shown in the inset Fig. 2. The intermediate phase evidenced by the function at 510  $\text{cm}^{-1}$  is attributed to a defective part of the crystalline phase, which originates from crystallites with diameters less than 10 nm, as well as a silicon wurzite phase resulting from twins or bond dilation at grain boundaries (Rath 2003).

The degree of crystallinity is estimated by crystalline volume fraction ( $X_c$ ) defined as follows:

$$X_c = (I_g + I_{gb}) / (I_g + I_{gb} + I_a), \quad (1)$$

where  $I_a$ ,  $I_{gb}$ , and  $I_g$  are the integrated intensity of peak near 480, 510, and 520  $\text{cm}^{-1}$ , respectively.

The abovementioned follows that a wide process window for transition region is required to fabricate the high-efficiency nc-Si:H solar cell. Figure 2 illustrates the Raman spectra of Si:H films deposited by inductively coupled plasma CVD (ICP-CVD) on glass substrates at different discharge powers (Wei et al. 2013). As discharge power increases, the feature TO mode shifts from  $480\text{ cm}^{-1}$  to almost  $520\text{ cm}^{-1}$ , indicating the phase transition from a-Si:H to nc-Si:H. The similar phase transition is commonly achieved by varying silane concentration, RF power density, substrate temperature, process pressure, etc., in plasma-enhanced CVD (PECVD) or other deposition techniques (Rath 2003).

In addition, the crystallographic orientation of the crystalline grain is also believed to greatly affect the nc-Si:H material properties and cell performance. It is widely reported that a preferred (220) oriented growth is very important for solar cells with the best efficiencies, since silicon films with (220) facets feature electrically inactive (220)-tilt boundary and compact columnar structure (Rath 2003). However, Schicho et al. (2012) reported that the tandem solar cell with the efficiency above 12% exhibits no preferential orientation in the absorber. It was also stated that the preferential orientation of the intrinsic material is not an essential prerequisite to achieve device-grade material for good solar cell performance. Therefore, the effect of the preferential orientation on material quality and device performance is still a controversial issue.

**Incubation layer.** The deposition of nc-Si:H thin film results in an inhomogeneous growth throughout the film thickness. The initially deposited layer is usually amorphous phase resting on a foreign substrate, and the so-called incubation phase is deposited first on the bare substrate before the localized phase transformation, namely, nucleation, takes place. Once nucleation starts, crystalline phase begins growing around it. A cross-sectional micrograph in Fig. 1b shows a typical incubation layer at the bottom of the thin film. Several models for the nucleation process have been proposed, but the exact physical mechanism of nucleation is still unclear. To avoid formation of unwanted incubation layer, a two-step deposition process is usually utilized. At the first step, a thin highly crystalline seed layer is deposited with high hydrogen dilution. For example, the first step could be depositing a seed layer at  $\text{SiH}_4/\text{H}_2 = 0.33/99$  sccm by PECVD, while the second step is the film growth at  $\text{SiH}_4/\text{H}_2 = 1.2/99$  sccm on the top of the seed layer (Rath 2003). The two-step process can also be replaced by a single process with hydrogen profiling, in which the hydrogen dilution is continuously varied from high to low values to control crystallinity of the film.

**Bond configuration and film compactness.** The Fourier transform infrared (FTIR) spectroscopy is widely applied to analyze the Si-H and Si-O bonding configurations and compactness of nc-Si:H films. Typically, the FTIR spectrum of Si:H film consists of four main absorption regions: the band at  $630\text{ cm}^{-1}$  related to  $\text{SiH}_x$  ( $x = 1, 2, 3$ ) wagging or rocking modes, a doublet near  $850$  and  $890\text{ cm}^{-1}$  related to  $\text{SiH}_2$  and  $(\text{SiH}_2)_n$  bending modes, the peak at  $2000\text{--}2150\text{ cm}^{-1}$  related to  $\text{SiH}_x$  stretching modes, and the band at  $950\text{--}1150\text{ cm}^{-1}$  related to the SiO stretching mode (Klein et al. 2005). The critical absorption band is the Si-H stretching mode in the range of  $2000\text{--}2150\text{ cm}^{-1}$ , which indicates the hydrogen configurations of Si:H

materials. An absorption band centered at  $2000\text{ cm}^{-1}$  corresponding to hydrogen in mono-hydride bonds (Si-H) can be typically observed in device-quality nc-Si:H, whereas hydrogen bonded in either multihydrides ( $\text{SiH}_2$  or  $\text{SiH}_3$ ) or internal voids contributes at around  $2100\text{ cm}^{-1}$  (Klein et al. 2005). Therefore, low signals around  $2100\text{ cm}^{-1}$  are expected from compact grown material. The *microstructure factor* ( $R^*$ ) defined as a ratio of the SiH stretching mode intensity at  $2100\text{ cm}^{-1}$  to the total intensity of the SiH stretching modes is often used to evaluate the compactness of the Si:H materials. For nc-Si:H, a dominant absorption band at around  $2000\text{ cm}^{-1}$  and the resultant low  $R^*$  values are desirable.

The Si-O absorption band between  $800$  and  $1200\text{ cm}^{-1}$  can also be applied to study the compactness of the nc-Si:H films. In general case, Si-O doublet absorption bands are interpreted as an indication of less dense material, since oxygen incorporation would occur in a less dense Si:H film. These bands consist of the Si-O-Si asymmetric stretching doublet between  $960$  and  $1150\text{ cm}^{-1}$  and another peak near  $880\text{ cm}^{-1}$ , attributed to the  $\text{O}_3\text{-Si-H}$  configuration (Klein et al. 2005).

**Hydrogen content.** FTIR and secondary ion mass spectrometry (SIMS) are widely used to measure hydrogen content in the nc-Si:H film. The bonded hydrogen content ( $C_H$ ) can be evaluated by the absorption band at  $630\text{ cm}^{-1}$  in FTIR spectrum as follows:

$$N_H = AI_{630}, \quad (2)$$

where  $A = 2.1 \times 10^{19}\text{ cm}^{-3}$  and  $I_{630}$  are the integrated absorption of the corresponding band (Schropp and Zeman 1998). The peak around  $630\text{ cm}^{-1}$  includes the rocking modes of bonded hydrogen in every possible configuration, so the total amount of the bonded hydrogen atoms is accessed. Hydrogen content ( $C_H$ ) of nc-Si:H film can be obtained through the following equation:

$$C_H = N_H / (N_H + N_{Si}), \quad (3)$$

where a value of  $5 \times 10^{22}\text{ cm}^{-3}$  for the silicon density ( $N_{Si}$ ) is being commonly accepted (Schropp and Zeman 1998). SIMS measurement can also be used to confirm hydrogen contents in Si:H films. In general, all kinds of H can be measured in the form of sputtered ions in SIMS measurement.

Hydrogen plays an important role in improving the quality of the Si:H films by passivating dangling bonds and decreasing defect density. As a rule, hydrogen content is typically 10% or less in the PECVD-deposited nc-Si:H films. However, the nc-Si:H films with a low (<3%) hydrogen content can also exhibit high photo-conductivities of  $\sim 10^{-4}\text{ S/cm}$  and photosensitivities of up to 130 (Kosku and Miyazaki 2006). Therefore, the optimum value of the hydrogen content is still a matter of controversy for device-quality nc-Si:H materials. However, extraordinarily high hydrogen contents may lead to light-induced degradation of solar cell, which will be discussed in section “[Light-Induced Degradation](#).”

**Impurity contamination.** One prerequisite for the high-efficiency Si:H solar cells is the low contamination level of external impurities in the light absorber. Oxygen

and nitrogen impurities create donor states in nc-Si:H and thus result in the increase in spin density and dark conductivity, plus the decrease in photo-response (Kilper et al. 2009). SIMS and FTIR are often used to characterize impurity concentrations in nc-Si:H films. In general, oxygen concentration should be limited to  $\sim 10^{18} \text{ cm}^{-3}$  in the device-quality nc-Si:H films (Rath 2003). Thus, a gas purifier is often installed near gas inlet to reduce the oxygen contaminations from the gas supply lines.

Oxygen impurities can aggregate at grain boundaries or in amorphous domains, since the structural disorder allows oxygen atoms to readily fit into the structures, decreasing the total system energy (Kamei and Wada 2004). The defects formed by carbon are less electrically active, but they cannot be negligible because of their ramifications on oxygen precipitations. Both oxygen and carbon can precipitate at grain boundaries and dislocations and thus change their electrical behaviors.

**Defects.** Lattice defects originate from surfaces of nanocrystals and grain boundaries, as well as amorphous phase. Defect density cannot be neglected, although hydrogen incorporation can passivate a considerable amount of the dangling bonds. Defects participate in bulk and interface recombinations of carriers, strongly affecting material quality and photovoltaic properties. In addition, some defects such as cracks and voids would lead to electrical shunts (Python et al. 2009).

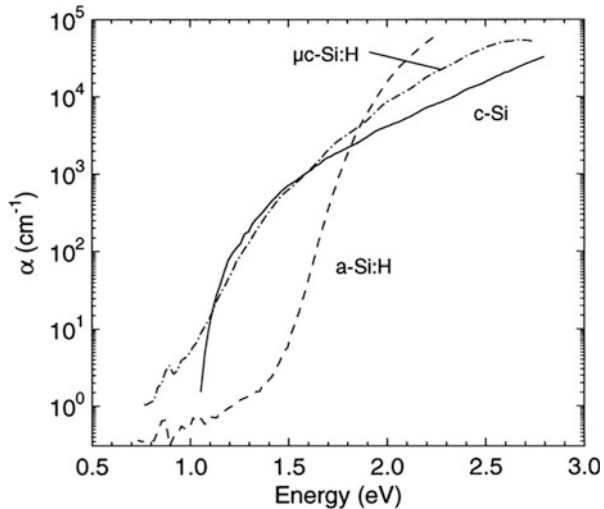
According to their origins, defects can be divided into intrinsic defects and impurity-related defects. The intrinsic defects usually originate from the dangling bonds. It has been found that one type of mid-gap defects attributed to the dangling bonds at column boundaries exhibits  $g = 2.0052$  in electron spin resonance (ESR) results, where  $g$  is a dimensionless quantity which characterizes the magnetic moment and gyromagnetic ratio of the defect. This  $g$  value is slightly lower than the dangling bond line of amorphous silicon, but they have the same width. However, the silicon dangling bond centers with  $g = 2.0055$ , which is the same as that in amorphous silicon, were also identified in poly- and nc-Si:H materials in many other reports, and these dangling bond centers are randomly oriented in nc-Si:H materials (Rath 2003). Apart from the intrinsic defects, it was reported that the impurity-related dangling bond centers also exist in nc-Si:H materials. A center at  $g = 2.0043$  is related to dangling bonds in oxygen-rich regions, while the other detected center at  $g = 2.0026$  is considered to be oxygen-related and originates from oxygen contamination in the deposition chamber (Rath 2003).

Not all the defects ( $g = 2.0052$ ) attributed to dangling bonds at the column boundaries may be active as recombination centers if they are remote from the main current paths. It was found that the nc-Si:H film is already suitable for use in solar cells if its ESR defect density does not exceed  $\sim 10^{17} \text{ cm}^{-3}$ . Therefore, the ESR defect density ( $< 10^{17} \text{ cm}^{-3}$ ) has been a criterion for device-grade nc-Si:H material for solar cell applications.

Besides ESR, subbandgap absorption spectra measured by the photothermal deflection spectroscopy (PDS), the constant photocurrent method (CPM), and the following Fourier transform photocurrent spectroscopy (FTPS) are used for defect characterization (Rath 2003; Meillaud et al. 2009). For example, FTPS can be used to evaluate the quality of intrinsic material on a complete nc-Si:H solar cell. The absorption coefficients of intrinsic material for energies ranging 0.6–1.6 eV can be



**Fig. 3** Typical absorption coefficients of single crystalline silicon (c-Si), hydrogenated amorphous silicon (a-Si:H), and hydrogenated nanocrystalline silicon (nc-Si:H) materials, as measured by PDS. (Reprinted from Vetterl et al. (2000). Copyright (2000), with permission from Elsevier)



measured by using FTPS technology. The absorption at 0.8 eV is usually considered as the defect-related absorption, so it is widely used to estimate the density of recombination centers within the bandgap.

### Optical Properties

**Absorption coefficient.** Typical absorption coefficients of a-Si:H, nc-Si:H, and c-Si material measured by PDS are shown in Fig. 3 (Vetterl et al. 2000). The absorption coefficients of nc-Si:H film are much lower than those of the a-Si:H material in the high-energy range ( $>1.7$  eV), while the result is opposite in the low-energy range (1.1–1.7 eV), in which the absorption coefficients of nc-Si:H are similar to those of c-Si material. Therefore, the stronger response to red and near-infrared light in nc-Si:H is complementary to the light response of a-Si:H. Thus, both of them can be applied together to absorb the different parts of sunlight in a more effective way in a-Si:H/nc-Si:H tandem solar cells.

Absorption coefficients are often estimated by measuring optical transmittance spectrum of the absorber using ultraviolet-visible-near-infrared (UV-Vis-NIR) spectrophotometer. Absorption coefficients can be calculated according to the equation  $T = \exp(-\alpha d)$  where  $T$  is the transmittance,  $d$  is the thickness of the films, and  $\alpha$  is the absorption coefficient in the measured transmittance spectrum. However, many UV-Vis-NIR spectrophotometers cannot ensure accurate measurement of the transmission of near-infrared light with absorption coefficients below  $10^4 \text{ cm}^{-1}$ . Thus, the measured absorption coefficients of the light (photo energy  $<2$  eV) are usually higher than the real values, thus resulting in the false estimation of absorption coefficients and optical bandgaps. The accurate measurement for the lower absorption region should be performed by PDS, FTPS, or CPM. In general, the absorption coefficients of both a-Si:H and nc-Si:H films monotonously increase with the increase in photon energy. Some typical absorption coefficients at certain



wavelengths (or photon energies) are selected to estimate the light-absorbing ability of the photovoltaic materials.

**Optical bandgap.** The optical bandgap is critical for solar cell performance because it determines the wavelength range of the absorbed light in the absorber. One common definition of an optical bandgap is Tauc's optical bandgap ( $E_g$ ) which is estimated from transmittance data by considering Tauc's plot according to the equation (Tauc et al. 1966):

$$\sqrt{\alpha E} = A(E - E_g) \quad (4)$$

where  $A$  is the joint optical density of states,  $E$  is the photon energy, and  $E_g$  is Tauc's optical bandgap. While featuring a considerable amount of the amorphous phases, the nc-Si:H material at the transition region still demonstrates the low optical bandgap which is nearly the same as that of c-Si ( $\sim 1.1$  eV).

The other definition of the optical bandgap is  $E_{04}$  or  $E_{05}$ , and the iso-absorption value of  $E_{04}$  or  $E_{05}$  is the photo energy at which the absorption coefficient has a value of  $10^4$  or  $10^5$   $\text{cm}^{-1}$ , respectively. Tauc's optical bandgap is often unreasonable (more than 1.1 eV) when it is calculated by using the false transmittance data measured by some UV-Vis-NIR spectrophotometers with low measuring accuracy in the near-infrared range. In fact, the bandgap of nc-Si:H cannot be widened unless crystal size is controlled within 5 nm to trigger quantum confinement effect of carriers inside. The bandgap can be reliably measured by PDS, CPM, or FTPS (Rath 2003; Meillaud et al. 2009).

## Electrical Properties

Electrical properties of the intrinsic absorber are critical for the photo carrier transport, significantly affecting the cell performance.

**Dark conductivity.** Dark conductivity ( $\sigma_d$ ) is the material conductivity measured without light illumination. Specifically, the conductivity mentioned here is the lateral conductivity measured parallel to substrate surface. The lateral conductivity is a conventional parameter used to estimate the electrical and photovoltaic properties of the nc-Si:H films. In the measurement, two evaporated aluminum bars with an interval of 0.5 or 1 mm are deposited to form the coplanar electrodes on the top surface of the Si:H film. After annealing to form ohmic contact, dark current  $I$  is measured by picoammeter by applying voltage  $V$  between the two metallic electrodes. The  $\sigma_d$  value is then calculated through the following equation:

$$\sigma_d(T) = IW/(AV) = IW/(ALd(V - IR_0)), \quad (5)$$

where  $W$  is the gap between the electrodes,  $L$  is their length,  $R_0$  is the reference resistance to protect the picoammeter, and  $d$  is film thickness that is typically about 1  $\mu\text{m}$  for the nc-Si:H samples. For the device-grade material, the dark conductivity should be smaller than  $1.5 \times 10^{-7}$  S/cm (Rath 2003; Schropp and Zeman 1998).

**Photoconductivity:** Photoconductivity is often measured by the steady-state photoconductivity (SSPC) technique that involves the same electrode configuration

as for the dark conductivity measurements. Photoconductivity ( $\sigma_p$ ) corresponds to the measured conductivity under the standard illumination conditions with one sun intensity ( $100 \text{ mW/cm}^2$ ). For the device-grade material, photoconductivity should be larger than  $1.5 \times 10^{-5} \text{ S/cm}$  or  $2 \times 10^{-5} \text{ S/cm}$  for a film with the thickness of  $\sim 1 \mu\text{m}$  (Rath 2003; Schropp and Zeman 1998).

**Photo-response.** The  $\sigma_p$  value is dramatically influenced by the position of the Fermi level. Although  $\sigma_p$  can be sometimes very high, the corresponding  $\sigma_d$  may also be high since the Fermi level shifts due to impurities. Thus,  $\sigma_p$  value must be examined jointly with  $\sigma_d$ , so that only samples exhibiting high  $\sigma_p$  values and low  $\sigma_d$  are suitable for use in solar devices. The quality of photovoltaic material can be quantified by photo-response ( $S$ ), which is simply defined as the ratio of  $\sigma_p$  to  $\sigma_d$ . For the device-grade material, photo-response should be larger than 100 (Schropp and Zeman 1998; Rath 2003).

**Activation energy.** The large photo-response indicates the good photovoltaic properties of the nc-Si:H material, but it is independent of the position of the Fermi level. Activation energy of the dark conductivity is equal to the energy difference between the conduction band edge and the Fermi level for electrons, or the valence band edge for holes. The activation energy ( $E_a$ ) can be obtained by measuring  $\sigma_d$  as a function of temperature  $T_s$ , as they are linked by the equation:

$$\sigma_d(T_s) = \sigma_0 \exp(-E_a/kT_s), \quad (6)$$

where  $k$  is the Boltzmann constant and  $\sigma_0$  is dark conductivity pre-factor. For an intrinsic material, the Fermi level should be at the middle of its bandgap. However, Fermi level is slightly above the middle position of the bandgap and exhibits weak n-type semiconductor properties with the  $E_a$  at around 0.4 eV, due to the unintentional oxygen incorporation which leads to n-type doping (Schropp and Zeman 1998). This behavior can be eliminated by avoiding oxygen contamination or slightly doping boron to compensate the n-type. For the device-grade intrinsic material, activation energy should be in the range between 0.53 eV and 0.57 eV (Schropp and Zeman 1998). Assuming that the bandgap of the material is known, the value of the activation energy can be used as the indication of doping level or the absence of the unwanted impurities. However, if more impurities incorporate and compensate each other, the high activation energy would provide a misinterpreted indication of the high-quality intrinsic material.

**Mobility-lifetime product.** The SSPC experiments allow the evaluation of mobility-lifetime product  $\mu\tau$ , which mainly characterizes the transport properties of the majority carriers. For the device-grade intrinsic material, the mobility-lifetime product should be at least  $10^{-7} \text{ cm}^2/\text{V}$  for the monochromatic red light at 600 nm (Schropp and Zeman 1998).

In summary, the criteria for the device-grade intrinsic nc-Si:H thin film for solar cell applications are listed in Table 1.

**Table 1** Criteria for the device-grade intrinsic nc-Si:H thin film for solar cell applications

Key parameter of material property	Requirement
Crystalline volume fraction (Raman)	30–70%
Density of states (ESR)	$<1 \times 10^{17} \text{ cm}^{-3}$
Optical bandgap	$\sim 1.1 \text{ eV}$
Dark conductivity	$<1.5 \times 10^{-7} \text{ S/cm}$
Photoconductivity	$>1.5 \times 10^{-5} \text{ S/cm}$
Photo-response	$>100$
Activation energy	0.53–0.57 eV
Mobility-lifetime product	$>10^{-7} \text{ cm}^2/\text{V}$

## Properties of the Doped Materials

Doped nc-Si:H thin films are used as n- and p-type layers in solar cell to build up an internal electric field for carrier drift and form a good contact with transparent and conductive oxide (TCO) or metal electrodes. The firstly deposited thin doping layer acts as a seed layer for the subsequent thicker intrinsic layer; this means that the doped layer should feature high crystalline volume fraction. Besides, the p-layer should also act as a window layer of a solar cell. In addition, the heavily doped layer may also be used to form tunneling junction in multijunction solar cells. Hence, the doped layer should have high doping efficiency, high crystalline volume fraction, and low parasitic absorption losses.

The nc-Si:H layer can be doped to become n-type layer by mixing phosphine ( $\text{PH}_3$ ) with silane or p-type doped by adding diborane ( $\text{B}_2\text{H}_6$ ), boron trifluoride ( $\text{BF}_3$ ), or trimethyl-boron [TMB,  $\text{B}(\text{CH}_3)_3$ ] into silane during the deposition. Due to the presence of crystalline phases, it is easier to dope nc-Si:H and activate the dopants in it, than in a-Si:H. Thus, the Fermi level can be pushed closer to conduction or valence band edge in the nc-Si:H material than in a-Si:H. The activation energy of the a-Si:H structure is usually above 200 meV, while activation energy of the nc-Si:H can be 50 meV or less. Therefore, the higher conductivity can be achieved in the nc-Si:H films with the same thickness. The dark conductivity can approach 20 S/cm in a 70-nm-thick n-type doped nc-Si:H film, while this parameter can reach 1.5 S/cm if the p-type doping is implemented in a 300-nm-thick nc-Si:H film (Schropp and Zeman 1998).

However, a thinner (around 20 nm or less) p-type and n-type (tens of nanometer) doped layers are usually required in the nc-Si:H solar cells. The conductivity of the thinner doped layer would be several orders lower than that of the thicker one. Thin nc-Si:H film also faces the problems of incubation in the initially deposited layer on a foreign substrate. Therefore, the key factor is to deposit the seed layer with a higher crystallinity, and even the top doped layer still needs the high crystallinity to achieve high conductivity. Compared with n-type doped layer, it is harder to promote the crystallinity of p-doped layer because boron hampers the nucleation and growth of crystals. Several approaches have been proposed to promote the nucleation of crystalline phase. These layers are usually prepared under the condition of higher

hydrogen dilution ( $H_2/SiH_4 > 100$ ), higher substrate temperatures, or higher discharge power density. The other advanced methods such as the use of fluorine-containing gases, layer-by-layer deposition, or very high frequency (VHF)-PECVD can further promote the doping efficiency and the resultant conductivity. It is stressed that high-density plasma techniques such as ICP-CVD, microwave CVD, and ECR-CVD have been successfully used to fabricate the conductive doped layers for solar cell applications.

There are no standard criteria for the device-grade doped materials, but some requirements can still be referred. For example, the 20 nm p-type doped nc-Si:H layer with good cell performance usually has the conductivity of  $>10^{-2}$  S/cm and activation energy of around 60 meV, while the high-quality 70 nm n-type doped nc-Si:H layer often exhibits the conductivity of  $>20$  S/cm and activation energy of around 100 meV (Schropp and Zeman 1998). Aside from nc-Si:H, silicon alloys such as doped  $SiO_x$  and  $SiC_x$  have also been developed as the doped layer and window layer instead of nc-Si:H layer. These materials will be discussed in detail in section “[Window Layer](#).”

---

## Fabrication of Nanocrystalline Silicon Films

Methods of the nc-Si:H thin film fabrication are similar to the mainstream deposition methods of a-Si:H thin films, which have already proved to be mature enough in semiconductor and display industries. The nc-Si:H thin films can be deposited by various chemical vapor deposition (CVD) and physical vapor deposition (PVD) methods. It is worth noting that there are two basic requirements for the nc-Si:H depositions. Firstly, a high deposition rate is needed for depositing the intrinsic layer of the nc-Si:H film. Owing to the less absorption coefficients compared with the a-Si, the intrinsic light-absorbing layer of nc-Si:H solar cell is thicker (1–3  $\mu\text{m}$ ) than that of the a-Si (<500 nm). Therefore, faster deposition is preferred for low-cost commercialization. The high-density plasma technologies are also proposed and used for this purpose. Secondly, a low growth temperature (<600 °C) is an important criterion since hydrogen severely effuses at 600 °C or higher, while low-temperature processes with the abundant hydrogen can provide the passivation of grain boundaries and thus greatly improve the material quality.

## Mainstream Deposition Methods

The chemical vapor deposition (CVD) is the most widely used method for the nc-Si:H deposition. All three mainstream deposition ways such as PECVD, VHF-PECVD, and HWCVD are essentially the CVD methods. Up to now, a large portion of the nc-Si:H thin-film solar cells with the highest efficiencies are fabricated by these three methods.

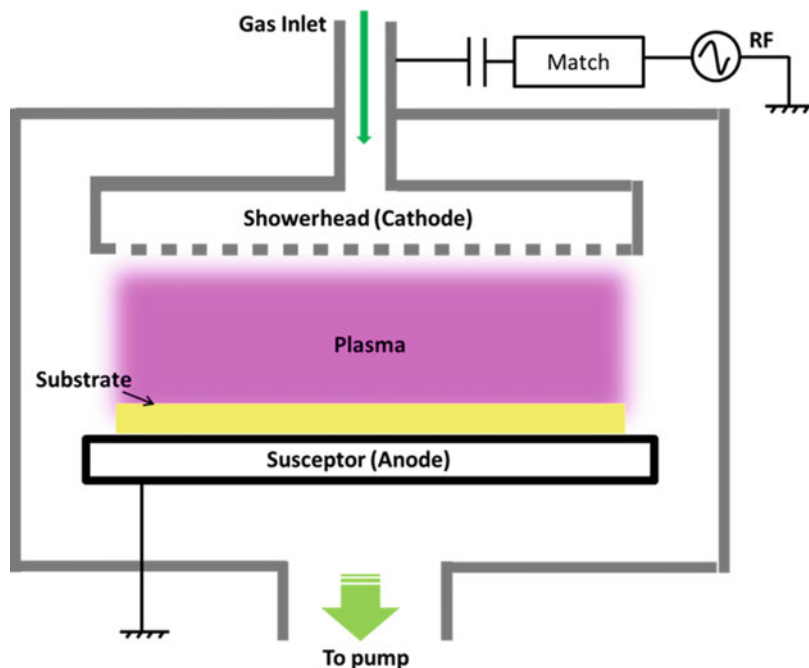


**Fig. 4** Schematic diagram of the radio-frequency PECVD deposition system

### PECVD

In 1965, Sterling and Swann firstly used the glow discharge technique, also known as PECVD, to deposit thin silicon films with the incorporated hydrogen. The nc-Si:H films are now commonly deposited by PECVD. In this method, a glow discharge is excited by applying a radio-frequency (RF) signal at the standard 13.56 MHz frequency between the parallel plate configuration, and thin film is deposited from plasma to a solid state onto substrate by chemical reactions in plasma sustained in the reactive gases. Figure 4 shows a typical schematic diagram of the RF-PECVD deposition system.

Due to the electromagnetic interaction of the charged particles with each other and the external fields, both electrons and ions are accelerated in the electric field. Due to higher energies and smaller masses, it is easier for electrons to diffuse toward the electrodes and chamber wall than ions, leaving the plasma bulk positively charged. When there is a separation of a large number of electrons from positive ions in the plasma reactor, the neutrality is violated, and the electric field arises between the positive- and negative-charge layers, like in a parallel plate capacitor. All the surfaces contacting the plasma carry a negative charge, and the localized electric field between surfaces and plasma bulk creates a thin sheath. All species reach the sheath by diffusion, and the charged species are then driven by electric field in the sheath. The energy of ion approaching growth surface is determined by sheath

potential. The ions bombard the growth surface and thus affect the growth and the resultant material properties of the nc-Si:H thin film.

Silicon-based radicals are considered as the main precursors for the nc-Si:H growth. It is widely reported that SiH<sub>3</sub> is the main precursor for the device-quality films, while reactive radicals (SiH, SiH<sub>2</sub>, etc.) and higher silane radicals (Si<sub>2</sub>H<sub>5</sub>, Si<sub>3</sub>H<sub>8</sub>, etc.) are considered as hindrances to the high-quality nc-Si:H deposition. The atomic hydrogen flux reaching the growing surface plays an important role in the crystal nucleation. In addition, ion bombardment also affects the film deposition. High-energy ions deteriorate nucleation process and increase the defect density, whereas high ion flux enhances the surface diffusion of impinging species and yields good crystallinity (Rath 2003).

The nc-Si:H deposition process includes complex gas reactions and surface reactions which are controlled by the deposition parameters such as RF power density, gas composition, gas pressure, substrate temperature, electrode geometry, etc. The deposition conditions should be controlled within certain ranges that are desirable for high-quality nc-Si:H growth. The nc-Si:H films are commonly deposited under the condition of high hydrogen dilution and low gas pressure. The nc-Si:H can be formed by diluting silane in hydrogen at a ratio of H<sub>2</sub>/SiH<sub>4</sub> = 20 or more combined with high RF power density. High hydrogen flux approaching growth surface improves the surface mobilities of precursors and yields the nucleations of crystals. The gas pressure range is usually maintained between 0.5 Torr and 2 Torr. RF power density is often set in the range of 10–100 mW/cm<sup>2</sup>, while higher power density is desirable for higher deposition rate. However, the rapid reactions at too high power can create the silicon polyhydride powders that contaminate the growing Si film.

Substrate temperature is usually set between 150 °C and 350 °C. Lower temperature generally hinders precursor diffusion and film-forming reactions on growing surface and thus deteriorates the film quality (Rath 2003), while less hydrogen is incorporated at higher substrate temperature and may lead to the poorer passivation effect of hydrogen on nc-Si:H thin film. The electrode spacing in PECVD is usually set between 1 and 5 cm for the nc-Si:H deposition; larger spacing makes it easier to maintain the plasma, while small spacing is more desirable for the uniform deposition.

A drawback of the conventional PECVD is the relatively low deposition rate of the nc-Si:H film, usually not exceeding 0.5 nm/s. Another deposition method called HPD (high-pressure depletion) was proposed by the ETL group (Guo et al. 1998) to enhance the growth rate of the nc-Si:H film. In HPD, a high gas pressure is set to achieve the high radical generation rate (high growth rate) and ensure low plasma potential (low ion energy), which can reduce the high-energy ion bombardment to the growth surfaces. However, this technique features low atomic hydrogen density hindering the crystallization due to the annihilation reaction  $H + SiH_4 \rightarrow SiH_3 + H_2$ . This disadvantage can be compensated by the deposition in a depletion regime, which can be achieved using a high RF power. Using HPD method, a high deposition rate of 0.93 nm/s (Guo et al. 1998) was obtained with low defect density and high crystallinity, and this deposition rate was then further promoted up to at least

1.5 nm/s (Rath 2003). However, the considerable amount of dusts are easily formed in HDP regime so that microvoids appear in the nc-Si:H film, degrading the material quality and device performance.

### VHF-PECVD

VHF-PECVD has the same configuration and work principle with 13.56 MHz RF PECVD. The higher excitation frequency (20–110 MHz) in VHF-PECVD is generally applied, while the best nc-Si:H is often obtained around 50–110 MHz.

The shift to higher excitation frequencies modifies the shape of the electron energy distribution function (EEDF) in plasma. As the frequency increases, the electron density increases while electron temperature decreases, which means that the average electron energy drops. The ion density in the plasma is determined by the electron density, whereas the kinetic energies of the ions are determined by the electron temperature. As a result, sheath potential is reduced, and thus the maximum ion energy at the substrate is dropped with the increasing frequency. This leads to the bombardments of lower-energetic ions at the growing surface at the higher frequencies. On the other hand, the higher electron density with the increasing frequency results in the higher ion flux approaching the growth surface.

Compared to standard PECVD, one key to the success of VHF-PECVD is that higher excitation frequency enables researchers to deposit the nc-Si:H films at higher rates while retaining the good material qualities. In addition, VHF allows the use of higher power densities in the powder-free deposition conditions. Up to now, a larger portion of nc-Si:H solar cells with the highest efficiencies have been fabricated by VHF-PECVD. VHF technique combined with HPD method could further promote the deposition rate. AIST group (Matsui et al. 2003) reported cell efficiencies of 8.2% at 2.1 nm/s (7 Torr) and 7.9% at 3 nm/s (8 Torr) at 70–100 MHz, although problems of inhomogeneity appeared when cells were fabricated in large-scale areas.

The high rate obtained by VHF plasma has two explanations: (1) The high excitation frequency increases the electron density and decreases the electron temperature. Thus, a higher density of low-temperature electrons collides with silane molecules and generates the higher density of precursors, enhancing the deposition rate. (2) The high deposit rate can also be attributed to the high ion flux. Higher frequency increases the ion flux reaching the growth surface and shifts the EEDF toward lower energy (Heintze and Zedlitz 1996). High ion flux with low energy is thought to enhance surface diffusion of the impinging species, promote the crystallization (Rath 2003), and enhance the deposition rate. Meanwhile, the high quality of nc-Si:H by VHF-PECVD is usually attributed to low-energy ion bombardments on the growth surface. Suppression of high-energy ions on the growth surface is thought to be the effective way to improve the crystallinity and hinder the defect formations in nc-Si:H thin film.

However, there are still two principal challenges to applying VHF deposition on a large-scale manufacturing. (1) Nonuniform deposition on a large-area substrate. RF standing wave effect is formed on the electrode when the electrode size is comparable to the half-wavelength of RF wave. (2) Power coupling. It is difficult to couple VHF power from the generator to the large-area electrodes. To date, these two

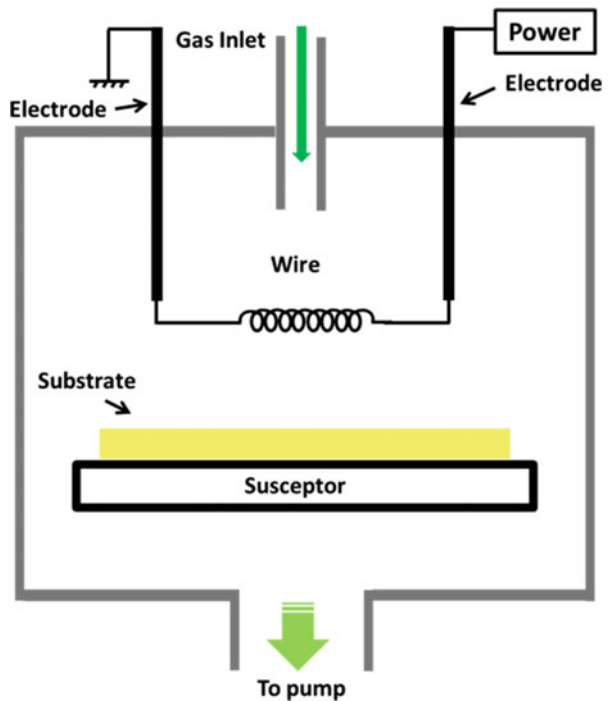
challenges are still open issues. But it is hopeful to solve these issues by using reasonable design of deposition system and selected process in the future.

### HWCVD

The hot-wire chemical vapor deposition (HWCVD), also known as the catalytic chemical vapor deposition (CAT-CVD), is also used for the nc-Si:H film deposition. In HWCVD, silicon thin films are deposited upon catalytic decomposition of the reactant gases (silane/hydrogen mixture) at the surface of a resistively heated filament at the low substrate temperatures.

A setup for the HWCVD system is similar to that of PECVD except that one of RF electrode plates is replaced with a heated filament; Fig. 5 shows the schematic diagram of the cross section of a typical HWCVD setup. The wire that is made of tungsten or tantalum is usually used as the heated filament. The cross section diameter of a typical filament wire is between 0.25 and 0.5 mm (Schropp and Zeman 1998). The filament is resistively heated up to 1500–2000 °C by an AC or a DC current. The substrate is placed a few centimeters away from the filament. In the HWCVD process, reactant gases are supplied to the chamber and then catalytically excited or decomposed into species by the heated filament. The silicon radicals then diffuse inside the chamber and deposit onto a substrate heated to an elevated temperature between 150 °C and 450 °C (Rath 2003).

**Fig. 5** Schematic diagram of the cross-sectional view of a typical HWCVD setup





In the HWCVD process, primary gas reactions are the catalytic dissociations of the gas molecules ( $\text{SiH}_4$  and  $\text{H}_2$ ) on the hot filament surfaces to Si and H radicals, which are immediately released if the filament temperature is high enough and diffuse throughout the gas phase. Before approaching the growth surface, they may react with other molecules or radicals to form the secondary gas reactions if the mean free path between collisions is shorter than the filament-substrate distance.

The main secondary gas reactions are the insertion and hydrogen abstraction reactions between Si and H radicals with  $\text{SiH}_4$  molecules:



These secondary reactions are exothermic without energy barrier. The reaction rates have the same order as the collision rates of Si radicals with  $\text{SiH}_4$  molecules. One product of the reaction in Eq. 8 is the less reactive silane radical  $\text{SH}_3$  which cannot react with  $\text{SiH}_4$  or  $\text{H}_2$  molecules in the gas phase. As the major precursors, the stable  $\text{SH}_3$  radicals are very important for the growth of nc-Si:H thin film and the resultant material quality. Finally, the nc-Si:H films are nucleated and grown by surface reactions. The nc-Si:H solar cells prepared by the HWCVD method have demonstrated the high efficiencies which are comparable to those of high-efficiency solar cells prepared by the conventional PECVD.

The most remarkable feature of the HWCVD process is the lack of ions. The electrons emitted from the filament usually have too low energies to ionize the gas molecules and radicals. In any case, the ion bombardment in the HWCVD technique, if any, is much lower than in the other deposition methods. The absence of strong ion bombardments is widely considered as a large advantage of the HWCVD. The roughly ion-free deposition condition is believed to reduce the damage at the device interfaces induced by high-energy ion bombardments, resulting in the higher  $V_{oc}$  ( $>600$  mV) (Van Den Donker et al. 2007). However, it is also thought that the absence of ion bombardments limits the further improvement of the HWCVD-fabricated solar cells. Few ion bombardments would result in the low density of nc-Si:H material, while a flux of ions with moderate energies could be beneficial for the densification of the growing nc-Si:H film (Rath 2003).

The HWCVD technique still needs to overcome several main challenges such as large-area nonuniformity, filament lifetime and aging, filament contaminations, and the possible filament radiation-induced degradation of film quality.

## Alternative Deposition Methods

To date, fast deposition of the high-efficiency nc-Si:H solar cells is still a challenge for the present mainstream deposition techniques. Some emerging alternative high-density plasma techniques such as electron cyclotron resonance (ECR), microwave plasma, and inductively coupled plasma have been introduced for the fast depositions of nc-Si:H films.

## Microwave CVD

In the microwave CVD (MWCVD) process, microwaves are coupled into the reactor via a dielectric window such as quartz to transfer their energies to the electrons, which then transfer energies to gas molecules through collisions, so that gas molecules are decomposed to generate active species and the nc-Si:H films are finally deposited. MWCVD can generate the high-density plasma ( $10^{11} \sim 10^{12} \text{ cm}^{-3}$ ) at the low electron temperature of  $<10 \text{ eV}$  (Rath 2003).

Compared with conventional PECVD, MWCVD with the higher plasma density can be used to fabricate the nc-Si:H films at the lower hydrogen dilutions. Jones et al. (2000) applied a gas jet deposition technique to deposit the nc-Si:H films. This method uses high-speed gas source and microwaves to ignite plasma and decompose gases close to the gas jet nozzle, resulting in high silane decomposition rates and a large amount of atomic hydrogen. Atomic hydrogen etches the weak Si-Si bonds (amorphous mode) and forms strong and rigid Si-Si bonds (crystalline mode) at growth surface, yielding the nucleation and crystallization of nc-Si:H film. The 7.0% ( $V_{oc} = 0.543 \text{ V}$ ,  $FF = 0.610$ ,  $J_{sc} = 21.2 \text{ mA/cm}^2$ ) single-junction nc-Si:H solar cell at 1.6 nm/s and a 9.8% a-Si:H/nc-Si:H tandem solar cell at 1.5 nm/s were fabricated by the microwave deposition technique.

## ECR-CVD

The full name of the ECR-CVD technique is the electron-cyclotron resonance (ECR) chemical vapor deposition. The difference between microwave CVD and ECR-CVD is that the plasma in the latter case is in a resonance condition. In a typical configuration of ECR-CVD, the microwaves are coupled by a waveguide through a dielectric window into a cylindrical vacuum chamber which is surrounded by electromagnets. A magnetic confinement is ensured by the axial magnetic field. The energies of microwaves are absorbed in the resonant region, in which the electron cyclotron frequency matches the frequency of microwave.

The electron cyclotron frequency is defined as  $\omega_e = Be/m_e$  where  $B$  is the magnetic field intensity,  $e$  is the elementary charge, and  $m_e$  is the electron mass. The heated electrons in the resonant zone dissociate the silane molecules to generate active species that diffuse onto the substrate surface to form the nc-Si:H film. The ECR-CVD method also has the advantages of the high plasma density ( $10^{12} \text{ cm}^{-3}$ ), low ion energy, little plasma bombardment effect, and low hydrogen consumption for nc-Si:H growth, as well as the high growth rate (2.5 nm/s) for nc-Si:H film with device quality (Hsu et al. 2014).

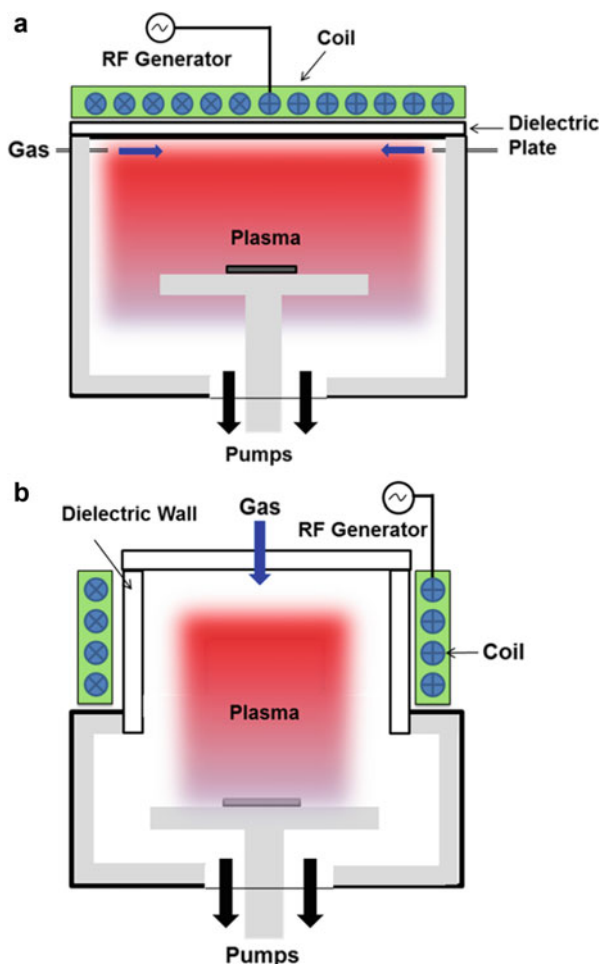
C. H. Hsu fabricated the nc-Si:H single-junction solar cells and a-Si:H/nc-Si:H tandem solar cells by ECR-CVD. Single-junction nc-Si:H solar cell has shown the efficiency of 6.21%, while 13.3% initial conversion efficiency and a 12.7% stabilized efficiency were achieved for a micromorph tandem solar cell (Hsu et al. 2014); merely 4.7% light-induced degradation was obtained, indicating the highly stabilized micromorph tandem solar cell.

### ICP-CVD

Inductively coupled plasma (ICP), namely, transformer coupled plasma (TCP), is another type of a plasma source in which the energy is supplied by electric current generated by electromagnetic induction. In the ICP-CVD, reactive gases are decomposed into species by a glow discharge created by induction-introduced electromagnetic field, and thus the gas-state species are deposited onto substrate to form solid-state films by chemical reactions.

There are three types of the ICP induction coil geometries: planar, cylindrical, and half-toroidal. The ICP coil is separated from the vacuum vessel by a dielectric window or placed inside the vacuum chamber. Figure 6 shows the schematic diagrams of ICP-CVD with external configurations of planar (a) and cylindrical (b) induction coils. As mentioned above, the high atomic hydrogen flux is

**Fig. 6** Schematic diagrams of planar (a) and cylindrical (b) ICP-CVD systems



considered to be beneficial for the nc-Si:H film growth, whereas the low-energy ion bombardments also promote the nc-Si:H film growth without introducing the additional defects (Rath 2003). Fortunately, ICP technique can provide an ideal combination of these two effects, i.e., the enhancement of atomic hydrogen flux and suppression of high-energy ion bombardment, due to its advantages of the high electron density ( $\sim 10^{11}$ – $10^{12}$  cm<sup>-3</sup>), the low electron temperature, and the low plasma sheath potential (Xu et al. 2001).

The ICP sources have a long history from the first report published by Hittorf in 1884. Kosku and Miyazaki (2006) reported that the ICP-deposited nc-Si:H films exhibit the high photoconductivity of  $10^{-5}$ – $10^{-4}$  S/cm but the low photo-response of  $\sim 3$ – $10$ . Wei et al. (2013) achieved phase transition from a-Si:H to nc-Si:H by low-frequency (460 kHz) ICP-CVD at growth rate of  $\sim 0.5$  nm/s. High photoconductivity ( $5 \times 10^{-5}$  S/cm) and high photo-response of 340 were obtained. However, an activation energy of 0.41 eV is still lower than the common values (0.53–0.57 eV), as shown in Table 1, of device-grade nc-Si:H materials (Schropp and Zeman 1998).

According to the modern growth theories (Rath 2003), the nc-Si:H material properties are deteriorated by high-energy ion bombardments due to the high energy tail of EEDF which is present in the H-mode. Thus, several methods such as halogenated silane gas sources (Moon et al. 2001) and remote deposition (Wei 2014) were implemented to optimize the nc-Si:H material properties by varying plasma characteristics. Moon et al. (2001) added SiH<sub>2</sub>Cl<sub>2</sub> into SiH<sub>4</sub> plasma to promote the growth of crystalline phases. The additional Cl species have the strong etching effects on the growth surface by breaking weak Si-Si bonds, as atomic hydrogen does for nc-Si:H growth under the H-rich plasma conditions. Wei (2014) introduced the remote deposition method to ICP-CVD system in which the coil-to-substrate distance was increased by 4.6 times to separate plasma discharge zone from the film deposition zone. The wider parameter windows for device-quality nc-Si:H films with low dark conductivity of  $\sim 10^{-8}$ – $10^{-7}$  S/cm and high photoconductivity of  $> 10^{-5}$  S/cm were obtained with the side effect of the decreased deposition rate.

The ICP-CVD systems have many advantages for high-rate deposition of the nc-Si:H films, but very few works have been successfully performed to fabricate the high-efficiency solar cells. An efficiency of 3.14% ( $V_{oc} = 230$  mV,  $J_{sc} = 19.7$  mA/cm<sup>2</sup>,  $FF = 0.54$ ) measured at the light intensity of 79 mW/cm<sup>2</sup> was achieved for a single-junction n-i-p solar cell by adding SiH<sub>2</sub>Cl<sub>2</sub> into SiH<sub>4</sub> plasma, with a growth rate of 0.42 nm/s (Moon et al. 2001). Wei fabricated a 4.14% single-junction nc-Si:H solar cell without light-trapping structure, by introducing remote deposition method in 2013 (Wei 2014).

---

## Solar Cell Technology

The family of the silicon thin-film solar cells includes single- and multijunction solar devices. The single-junction nc-Si:H solar cell has the similar structure to that of single-junction a-Si:H solar cell.

## Device Formation and Operation

### Device Structure

A schematic diagram of a typical single-junction nc-Si:H solar cell is shown in Fig. 7a. The single-junction nc-Si:H solar cell usually consists of the core layer of silicon photodiode with the p-i-n junction as well as the TCO and/or metal electrodes in the two terminals and is often fabricated on glass or other foreign substrates. The fundamental photodiode inside the nc-Si:H solar cell has three layers deposited in either p-i-n or the n-i-p sequence. The three layers are specifically a very thin ( $\leq 20$  nm) p-type layer, a much thick ( $\sim 1\text{--}3$   $\mu\text{m}$ ) intrinsic layer (i-layer), and a thin n-type layer ( $\leq 100$  nm).

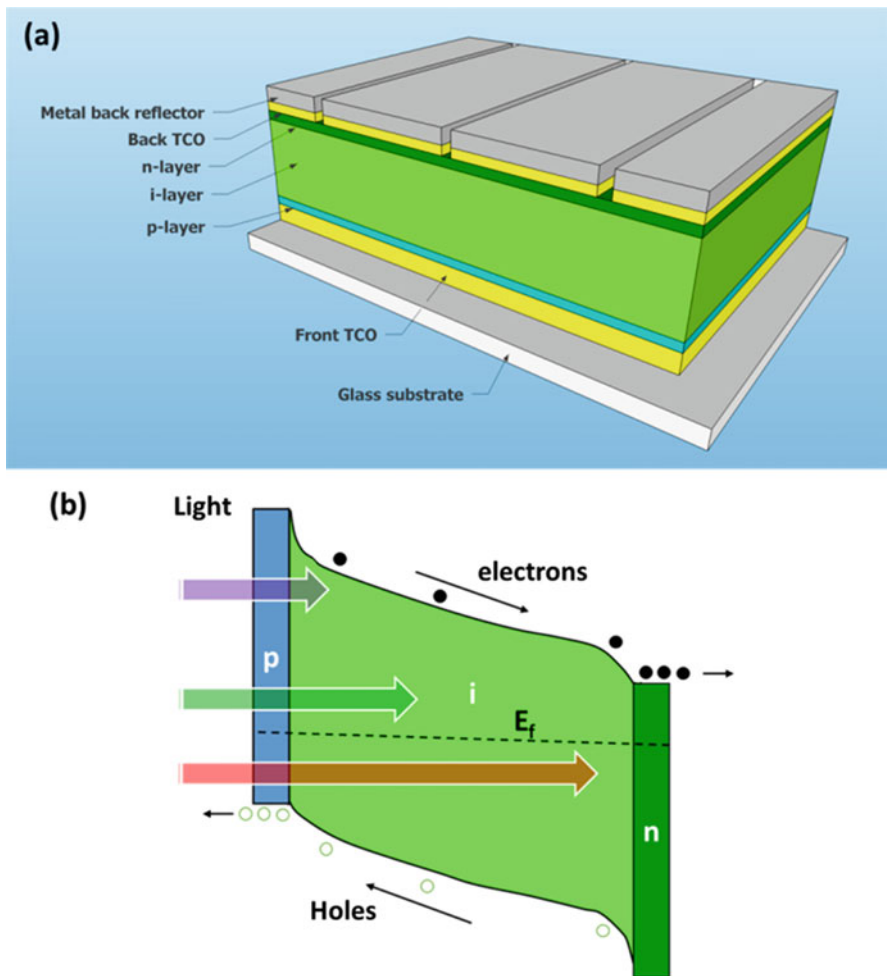


**Fig. 7** Schematic diagrams of geometric structure (a) and energy band (b) of single-junction nc-Si:H thin-film solar cell

## Principles of Cell Operation

As the core of nc-Si:H solar cell, the p-i-n junction has the similar electrical properties to those of a conventional p-n junction. In the doped nc-Si:H layers, the minority photocarriers (holes in n-type layer, electrons in p-type layer) cannot move very far due to the high carrier recombination rates enhanced by heavy doping. Therefore, a p-n junction can only collect photocarriers in the ultra-thin layer of doped nc-Si:H material. Instead, the p-i-n junction is usually used for nc-Si:H thin-film solar cell in which the high-quality intrinsic layer with a low defect density is usually selected as the light absorber. As illustrated by energy band diagram in Fig. 7b, some excess electrons in the p-i-n junction are donated from n-type layer, while parts of excess holes also diffuse from p-type layer. As a result, these doped layers are positively and negatively charged, respectively, leading to a built-in electric field (typically  $>10^4$  V/cm) within the photodiode with p-i-n junction. When sunlight enters the photodiode, most of the photons can pass through the thin p-type layer, which is designed as window layer with much low absorption and high transparency, and are then absorbed by the thick intrinsic layer. One photon absorbed can generate one pair of photocarrier (one electron and one hole) in the i-layer. Generally, the high-energy photons in the UV and blue light are quickly absorbed in a thin layer due to the high absorption coefficients. The lower-energy photons need longer optical paths to be absorbed due to lower absorption coefficients.

Next, the photon-generated electron-hole pairs are then separated by the built-in electric field. The electrons in the conduction band and holes in the valence band are then swept away by the built-in electric field to n-type and p-type layers, respectively. Here, the main mechanism of carrier transport in nc-Si:H solar cell is the carrier drift in the built-in electric field, rather than carrier diffusion like in the case of c-Si. This is attributed to the much shorter lifetime and diffusion length of minority carriers in nc-Si:H materials due to the presence of considerable carrier recombination centers at band tail states and mid-gap states. Finally, electrons and holes arrive at the contacts and are then collected by external wires, thus forming external current and generating the electricity.

## Design of a Typical Single-Junction Solar Cell

The total thickness of a typical nc-Si:H thin-film solar cell is usually less than 10  $\mu\text{m}$ . Therefore, all the functional layers of solar cell should be supported on a much thicker substrate for mechanical stability. As illustrated in Fig. 8, the two configurations of the nc-Si:H solar cell have been designed for opaque and transparent substrates. The light in the superstrate-type configuration penetrates through the transparent substrate before it enters solar cells. Therefore, the deposition sequence of solar cell layers is different for these two designs to make sure that photons always enter through p-type layer first.

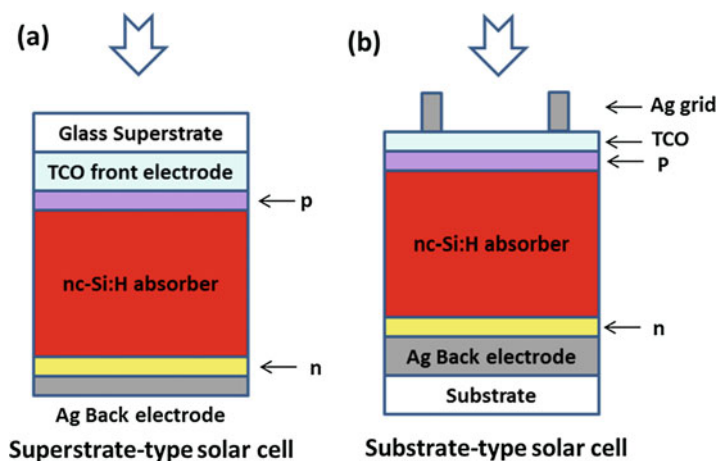


**Fig. 8** Schematic diagrams of cross-sectional structures of nc-Si:H thin-film solar cells in superstrate- (a) and substrate-type (b) configurations, respectively

### Solar Cell of Superstrate-Type Design

The solar cell with superstrate-type design is deposited on a carrier which is usually glass or a transparent plastic. Usually, this insulating substrate needs a transparent conductive oxide (TCO) film as the front electrode. The sublayers of nc-Si:H p-i-n photodiode are then deposited onto the TCO film, starting with a p-type window layer. Finally, a metal film such as Ag or Al is deposited onto n-layer of p-i-n photodiode as the back electrode and back reflector.

**Front electrode.** In superstrate-type design, the front electrode of a nc-Si:H solar cell is usually a TCO film with a thickness between 0.5 and 5  $\mu\text{m}$ . The common TCO materials include indium tin oxide (ITO), fluorine-doped tin oxide ( $\text{SnO}_2\text{:F}$ ), aluminum-doped zinc oxide ( $\text{ZnO:Al}$ ), etc. When applied to solar cells, the TCO front electrode needs to meet several requirements, namely, (1) low sheet resistance ( $<10 \Omega/\square$ ) or resistivity ( $\leq 10^{-4} \Omega\text{-cm}$ ) to reduce the resistance losses, (2) high optical transmittance (at least  $>80\%$  in the range of 350–1100 nm), (3) low ohmic contact resistance with p-type window layer, and (4) chemical resistance to plasma during the plasma-aided CVD deposition.

Typical properties of the device-grade TCO front electrode are listed in Table 2. In practice,  $\text{SnO}_2\text{:F}$  and  $\text{ZnO:Al}$  are widely used for the front electrode of the nc-Si:H cells made in superstrate-type design.

TCO front electrodes are commonly fabricated by sputtering, CVD, evaporation, etc. Sputtering is widely used to deposit TCO films by using ceramic or metal targets at a substrate temperature below 300  $^\circ\text{C}$ . In addition,  $\text{SnO}_2\text{:F}$  and  $\text{ZnO:Al}$  can also be fabricated by CVD methods such as atmospheric pressure CVD (APCVD) and low pressure CVD (LPCVD). The polycrystalline film is usually formed to yield high conductivity due to the high doping efficiency and high transmittance due to the wide bandgap. TCO front electrode is usually textured to form rough surface for the improved light trapping and the resultant enhanced light absorption.

**Table 2** Typical properties of the device-grade TCO front electrode

Property parameter	Device-grade requirement	TCO properties		
		ITO	SnO <sub>2</sub> :F	ZnO:Al
Transmittance (%)	>80	95	90	90
Sheet resistance ( $\Omega/\square$ )	<10	3–5	6–15	6–15
Buck resistivity ( $\Omega\cdot\text{cm}$ )	$\leq 10^{-4}$	$\leq 10^{-5}$	$\leq 10^{-4}$	$\leq 10^{-4}$
Contact resistance	Low ohmic	Low ohmic	Low ohmic	Low ohmic
Stability under plasma	Good resistance	Low	Good	Excellent

**The p-i-n junction structure.** In the superstrate-type design, the conventional p-i-n junction consists of p-type nc-Si:H layer, intrinsic nc-Si:H layer, and n-type nc-Si:H layer. The p-type nc-Si:H layer needs to meet certain requirements:

1. The good function of a p-type junction layer. It is easier for the nc-Si:H to be heavily doped due to the presence of crystalline phase. The low activation energy of the acceptor makes it easy to shift the Fermi level and build up the internal electric field.
2. Contact layer. The high conductivity ( $10\text{--}10^2$  S/cm) of the p-layer itself does not lead to the large series resistance. In addition, since the work function of the p-layer is larger than that of n<sup>+</sup>-type TCO, the p-layer/n<sup>+</sup>-type TCO contact would lead to the depletion of carrier in the p-layer. The resulting Schottky barrier would block the transport of holes into the front electrode and reduce the built-in field and the resulting  $V_{oc}$  and  $FF$  of solar cell. Therefore, heavy doping is utilized to form the tunneling junction at p-layer/n<sup>+</sup>-type TCO interface to overcome this issue.
3. Seed layer. Since TCO front electrode is usually textured in the real device, the p-layer which is the first 10–20 nm layer on this textured substrate has the great impact on the following growth of intrinsic layer. As the seed layer, p-type nc-Si:H with high crystallinity needs to be deposited uniformly in the textured substrate.
4. Window layer. This layer is required to exhibit the small thickness and low absorption coefficients to reduce the parasitic absorption losses. The thickness of ~20 nm is determined by the trade-off between conductivity and transparency of p-layer. The concept of wide-bandgap window layer such as SiO<sub>x</sub> and SiC<sub>x</sub> is proposed later to decrease the parasitic absorption loss.

The n-layer that is placed close to back contact is conventionally made of n-type nc-Si:H material. The presence of crystalline phases in n-type nc-Si:H leads to the high doping concentration and small activation energy. This makes n-type nc-Si:H a good candidate for n-layer of p-i-n junction, building up the internal electric field and reducing the series resistance loss.

**Back electrode.** In a superstrate-type solar cell, the conventional back electrode is made of silver or aluminum film with the thickness of 0.5 ~ 3  $\mu\text{m}$ . The metal electrode acts as not only back electrode of p-i-n diode with low contact resistance



but also as a highly reflective mirror-like back reflector to increase the overall optical path and the resulting absorption of the long-wavelength light.

To further increase the reflection, the present back electrode commonly consists of thin TCO/metal stacks by adding thin ITO or doped ZnO layer between the n-layer and metal layer. TCO layer is often designed to be the ~80-nm-thick reflection-enhancing coating layer. Combined with the textured n-layer surface replicated from front electrode, the large grade of refractive index between TCO and silicon makes a large portion of light reflected at this interface, thus enhancing the overall reflection at back electrode. This excellent back reflector can yield the  $J_{sc}$  of nc-Si:H solar cells. In addition, TCO layer also acts as barrier layer to avoid cross-diffusion between the metal layer and n-layer. Due to the presence of neighboring back metal layer, this thin TCO film is not required to be as highly conductive as the thick front TCO electrode.

### Solar Cell of Substrate-Type Design

In this design, light enters the device first and finally reaches the carrier, namely, substrate. The back electrode is firstly deposited on the substrate, and then the p-i-n junction (starting with n-type layer) is fabricated, followed by the topmost TCO and/or metal grid front electrode, as shown in Fig. 8b. The deposition sequence of individual layers is opposite to those of the superstrate-type design. Since there is no requirement for the transparency of substrate, this design can be applied to various rigid or flexible substrates. Stainless steel (SS) and polymer foils are the widely used substrates.

**Back electrode.** In the substrate-type design, back electrode of nc-Si:H solar cell consists of stacked Ag/thin TCO bilayer to enhance the reflection. Silver thin film with the thickness of  $0.5 \sim 3 \mu\text{m}$  is deposited firstly on the substrate as back electrode and back reflector. The surface of silver film is textured for light trapping, which is similar to the case of thick TCO front electrode in superstrate-type design. ZnO:Al thin film with the thickness of  $70 \sim 100 \text{ nm}$  is often deposited between metal back contact and n-layer of p-i-n junction. This thin oxide layer has the same function as the case of thin TCO layer used in back electrode in superstrate-type design. First of all, ZnO:Al thin film acts as the reflection-enhancing coating layer to enhance the reflection combined with metal back electrode. Secondly, this layer is also a barrier layer to prevent the interdiffusion of silver and n-type silicon layer. In addition, ZnO:Al thin film has the excellent resistance to plasma so that the growth surface is chemically stable during the following n-layer deposition.

Silver films are usually fabricated by thermal evaporation, electron beam evaporation, or sputtering techniques, while doped ZnO thin films are often deposited by sputtering or LPCVD. The absence of silicon layers allows the high-temperature deposition process of back electrode.

**The n-i-p junction.** The function of n-i-p junction in substrate-type configuration is also to build up the internal electric field, which is the same as that of p-i-n junction in superstrate design. Compared with the latter, the reversed deposition sequence of n-i-p junction means that the firstly deposited n-layer acting as the seed layer has an

important impact on properties of the following silicon layers. The n-i-p structure makes the critical p-layer window layer deposited last. Thus, it is easier to fabricate a high-quality p-type layer on an intrinsic nc-Si:H layer in the substrate-type design than a foreign TCO film in superstrate-type configuration.

**Front electrode:** The front electrode is composed of TCO thin film and a silver grid in substrate-type design. This is different from the back electrode in superstrate-type design in which the single thick TCO film is applied;  $\sim 70$  nm front TCO layer is deposited finally so that the deposition temperature cannot exceed the deposition temperature of the existing layers. This limits the process window of TCO layer within the range of low-temperature depositions. As this last process step, the concern of good resistance to plasma in CVD process is not needed so that ITO thin film with better conductivity can also be a good candidate for this thin TCO layer. Nevertheless, the  $\sim 80$  nm front TCO electrode cannot be as highly conductive as the thick TCO electrode in a superstrate-type solar cell. The sheet resistance of  $70 \sim 80$  nm ITO film can be around  $50 \Omega/\square$  or more. Thus, the micrometer-thick silver grid is applied to assist the thin TCO front layer to effectively collect the photo-generated carriers and reduce the series resistance of cell. Meanwhile, a tunnel contact should be formed between the degenerated  $n^+$ -type TCO and p-type nc-Si:H layer to reduce the contact resistance. In addition, the thin TCO layer also acts as an antireflection layer for light harvesting, and its thickness is usually around 80 nm to minimize light reflection. Finally, the thin TCO layer is the barrier of interdiffusion of p-type nc-Si:H layer and Ag grids.

As one candidate of thin TCO film, ITO film is usually fabricated by evaporation or sputtering, while doped ZnO film is usually deposited by sputtering or MOCVD techniques. Silver grid is often deposited by evaporation or sputtering with a shallow mask.

## Multijunction Solar Cell

Due to the nature of bandgap, the single-junction solar cell made of one material has the strong photo-response when light energy  $E$  is large than  $E_g$ , while its photo-response can be negligible when light energy  $E$  is smaller than  $E_g$ . The common multijunction solar cell is created by stacking several p-i-n (or n-i-p) single-junction solar cells on top of each other. In 1994, University of Neuchatel first proposed the concept of “micromorph” tandem cell in which an a-Si:H top cell is stacked by a nc-Si:H bottom cell (Meier et al. 1994). The schematic diagrams of cross-sectional structures of typical micromorph tandem solar cell and triple-junction solar cell are illustrated in Fig. 9. For a solar cell with triple or more junctions, a-SiGe:H cells with different Ge contents would be added as middle or bottom component cells. All component cells are connected electrically in series by p-n tunnel junctions to form the ohmic contacts in the most common series-connected stacked multijunction solar cell.

The main advantage of multijunction solar cell is its “spectrum-splitting” design. Ideally, the absorption coefficient of the light significantly increases with the

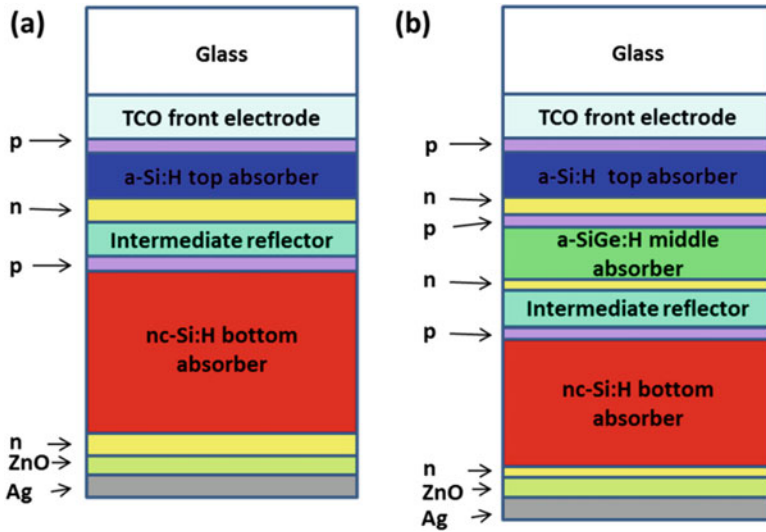


**Fig. 9** Schematic diagrams of cross-sectional structures of typical micromorph tandem solar cell (a) and triple-junction solar cell (b)

increasing photon energy. However, when photon with energy  $E > E_g$  enters nc-Si:H material, it would lose a part of its energy by interacting with phonons due to the indirect bandgap nature, and then the relaxed photon with energy approaching  $E_g$  can be converted into an electron-hole pair. Therefore, a single-junction solar cell has the highest quantum efficiency for the light whose photo energy is near to the bandgap due to the lowest absorption losses induced by lattice relaxation. Thus, the bandgap of component cell in a multijunction solar cell is usually designed to decrease from the top to bottom for the higher energy conversion efficiency. The a-Si:H top cell with a wider bandgap ( $\sim 1.7$  eV) mainly captures the UV and visible light and acts like a “low pass” optical filter for other light, while the remaining red and infrared light are more effectively absorbed by the middle and/or bottom a-SiGe:H and nc-Si:H ( $\sim 1.1$  eV) cells. Furthermore, the multijunction solar cell can have the higher collection efficiency of carriers than single-junction cell because of the higher electric fields in the thinner absorbers of component cells in multijunction. The higher electric field in the middle of absorber enhances the drifts of carriers, reducing the drift time and path of carriers and promoting the carrier collection efficiency. In addition, compared with single-junction a-Si:H solar cell, the light-induced degradation is improved in multijunction solar cell because the thickness of a-Si:H cell, whose efficiency is most negatively affected by the light illumination, is cut by nearly half in the multijunction solar cell.

To fabricate a high-efficiency multijunction solar cell, several key requirements should be met: (1) the high-quality light absorber in each component cell, (2) the proper current matching of component cells, (3) the low series resistance losses by using low-resistance tunnel junctions, (4) excellent

light confinements by antireflection layer, intermediate reflector, back reflector, etc., which will be discussed in section “[Optical Design for Light Management](#).”

**Current matching:** In the most common multijunction solar cell, component cells are connected in series to form a two-terminal device so that current densities in all component cells are equal. Thus, the total current density of multijunction is limited by the component cell with the minimum current density during the operation. Therefore, current densities of all component cells are required to be nearly the same as each other, which is, namely, current matching, at the maximum power point of every component cells. The  $J_{sc}$  of single component cell can be considered as a rough guide for current matching. The optimization of current matching requires a combined modeling and empirical approach in consideration of the cell-to-cell bandgap difference, internal light diffusion, the different effects of back reflector on component cells, properties of tunneling recombination junction, the different light-induced degradations, etc. (Schropp and Zeman 1998).

**Tunnel junction:** A p-n junction is unintentionally created at the interface between two adjacent p-i-n component cells. Once a classic p-n junction is formed, the overall built-in potential in multijunction would be counteracted by this p-n junction with reversed built-in potential. Therefore, an ohmic-like contact is needed to minimize the loss of built-in potential. Tunnel junction is composed of two oppositely and heavily doped a-Si:H and/or nc-Si:H junction layers, and thus the density of defects such as dangling bonds increases with the increasing doping concentration. As a result, carriers trapped on one side of p-n junction interface can move to the traps on the other side by quantum tunneling effect. It is sufficiently effective for this kind of electrical transport to form an ohmic-like contact with small contact resistance. In addition, space charges would be accumulated at interface of adjacent cells once the recombination rate of carriers cannot keep pace with the approaching carriers. This accumulation gives an adverse effect on electric field in the adjacent cell and leads to the loss of built-in potential. The tunnel junction gives an efficient channel of carrier recombination. Therefore, this tunnel junction is also nominated as tunnel-recombination junction (TRJ).

## Light-Induced Degradation

The firstly reported nc-Si:H solar cell shows the full stability under light soaking, but its intrinsic layer has a high crystallinity. However, from the following studies, it is found that nc-Si:H solar cells with i-layers of medium crystalline volume fraction (40–60%) undergo the mild form of degradation when exposed to blue or white light (Meillaud et al. 2009), as shown in Fig. 10. The amorphous phase, which is more sensitive to blue light, is considered to be attributed to the degradation. In addition, it is found that the efficiency degradation is closely related to the increasing defect-related absorption at 0.8 eV, which can be measured by FTPS method. As shown in Fig. 10, after the light soaking, the

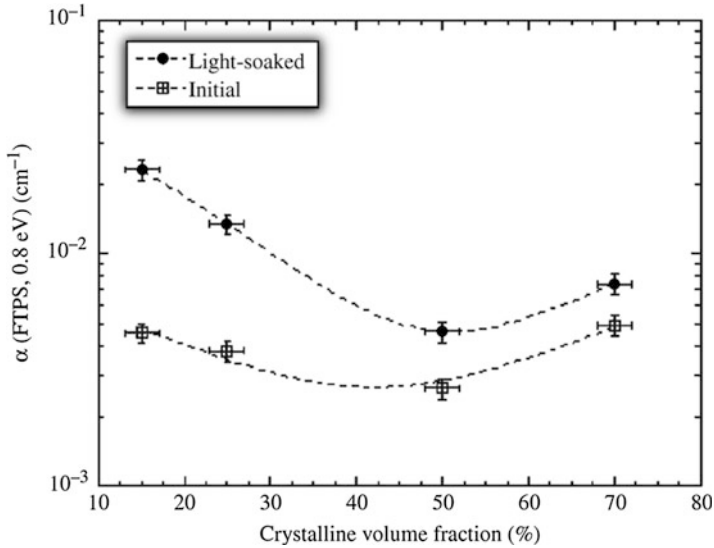


**Fig. 10** Defect-related absorptions (0.8 eV) in initial and light-soaked states (1000 h under standard condition) of single-junction n-i-p nc-Si:H solar cells with the varying crystalline volume fractions of the intrinsic layers. (Reprinted from Meillaud et al. (2009). Copyright (2009), with permission from Taylor & Francis)

increase in defect-related absorption at 0.8 eV in the solar cell with the higher fraction of amorphous phase is much larger than that in the solar cell with the higher crystallinity.

Chowdhury et al. (2009) observed that amorphous component is not the only determining factor for light-induced degradation. Small grains (less than 3 nm in diameter) and/or intermediate phases are also considered to provide a better stability in i-layer near the p/i interface. However, exact identifications of microscopic natures of light-induced defects in nc-Si:H remain unclear, and further investigations are required in the future. Few significant light-induced degradations have been observed in the nc-Si:H bottom cells of multijunction solar cells because the top a-Si:H cells usually act as the filters for the blue light. The main concern for light-induced degradation in multijunction solar cell is mainly focused on its top a-Si:H cell.

---

## Advanced Technologies for Efficiency Improvement

### Improved Absorber Material on Textured Substrate

Material properties of intrinsic absorber have been discussed in section “[Properties of Nanocrystalline Silicon](#).” However, nc-Si:H with high material quality (such as proper crystallinity, low defect-related absorption, appreciable photovoltaic

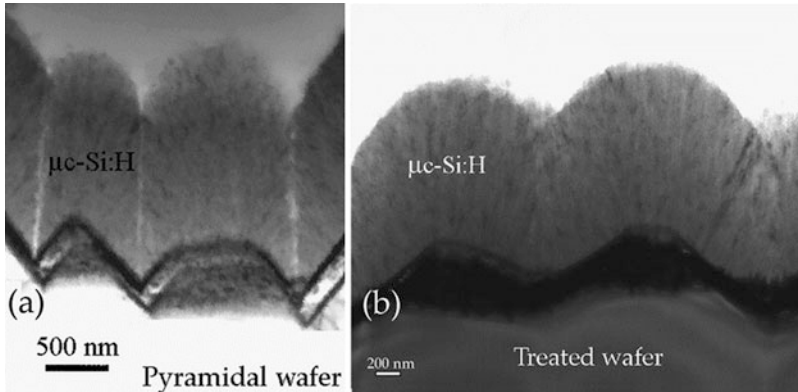


**Fig. 11** Cross-sectional TEM micrographs of single-junction p-i-n solar cells fabricated on pyramidal substrates. The *white lines* represent “cracks.” Cracks resulted from V-shaped valleys of substrate in (a) cross the whole p-i-n device while only a “crack” is present in the last half of nc-Si:H layer deposited on a substrate with U-shaped valleys in (b). (Reprinted from Python et al. (2009). Copyright (2009), with permission from Elsevier)

properties) is not sufficient to ensure the high efficiency of solar cell. The additional microstructure defects such as cracks would be generated at the highly rough TCO surface. For example, cracks are often formed during the growth of i-layer at the rough surface of V-shaped textured ZnO:Al front electrode with large, steep pyramids. Cracks including defective and porous zones may typically appear at the bottom of the valley of texture structure, as shown in Fig. 11a. Cracks represented by white lines may propagate through the entire junction. A high-density recombination centers occur around crack regions with the reduced structural order. SIMS result reveals that the oxygen concentration increases in the crack regions, leading to the reduced charge collection efficiency, lower fill factor, and lower open-circuit voltage (Kilper et al. 2009). However, the high-quality intrinsic layers prepared on flat or smooth substrates do not exhibit cracks and/or voids. As the roughness of substrate increases, the crack density in intrinsic layer is increased. By means of plasma surface treatment, the V-shaped texture on the doped ZnO surface can be transformed into the smoother U-shaped features by suppressing the small pyramid roughness, as shown in Fig. 11b. With this surface treatment, crack density can be significantly reduced. Thus, both cell efficiency and  $FF$  can be improved when solar cell is fabricated on the smooth doped ZnO front electrode. Tamang et al. (2016) investigated the interplay of light trapping and crack formation for nc-Si:H solar cells on periodically textured honeycomb substrates. It is found that the height-to-period ratio of the surface texture should be smaller or equal to 0.25 to avoid the formation of cracks while maintaining the good light trapping effect. This means that the smooth and large-scale texture structure with “shallow” units yields the crack-free growth of intrinsic absorber.

## Interface Treatment

A high  $V_{oc}$  is of great importance to achieve the high conversion efficiency. The  $V_{oc}$  is typically subjected to doped layers, the mobility gap of intrinsic layer, bulk properties of intrinsic layer, and the recombinations at p/i interface region.

### The p/i Interface Treatment

The treatments of junction interface, especially p/i interface alone, have been widely studied for  $V_{oc}$  improvement. A regular nanoscale a-Si:H or nc-Si:H film is inserted between p- and i-layers as the buffer to improve the p/i interface property. By inserting a HWCVD-deposited buffer layer between the p- and i-layers, nc-Si:H solar cell with a high  $V_{oc}$  of ~570 mV and an initial efficiency of 10.3% was fabricated by VHF-PECVD in 2005 (Mai et al. 2005). A 9.8% nc-Si:H solar cell with a higher  $V_{oc}$  of 603 mV was fabricated through the combination of the HWCVD-deposited buffer layer at the p/i interface and PECVD-deposited absorber using controlled  $\text{SiH}_4$  flow profiling technique in 2007 (Van Den Donker et al. 2007). The controlled bulk and interface properties yield the effective charge carrier collection from *i* layer with a crystalline volume fraction of 30%. Compared with  $V_{oc}$  in PECVD-deposited cells, the higher  $V_{oc}$  in HWCVD-deposited nc-Si:H solar cells are attributed to the improved p/i interface quality, which is verified by the greatly enhanced blue light response in such solar cells, likely due to the ion-free depositions on p-layers in HWCVD processes.

Interface can also be improved by introducing a  $\text{SiO}_x$  or  $\text{SiC}_x\text{:H}$  buffer layer between the doped layer and the absorber. Higher electrical performance was achieved through the use of mixed-phase  $\text{SiO}_x$  doped layer in nc-Si:H solar cell. An intrinsic  $\text{SiO}_x$  buffer layer inserted at the p/i interface seems to promote the nucleation of the intrinsic absorber and depress boron cross-contaminations. The improved transparency in short-wavelength range was demonstrated. A p-i-n single-junction nc-Si:H solar cell shows the efficiency of 10.9% (Meillaud et al. 2009). Although high  $V_{oc}$  is often attributed to the improved p/i interface quality, the exact reason for this improvement has not been clearly illustrated yet.

### The n/i Interface Treatment

The n/i layer interface is not usually thought to be a key to cell performance because the local generation rate at n/i interface is much smaller than that at p/i interface. The n-layer is usually made of nc-Si:H thin film to contact the back electrode. In a n-i-p nc-Si:H solar cell, an a-Si:H buffer layer and a seed layer are often inserted at the n/i interface. The a-Si:H buffer layer is added to reduce phosphorous incorporation into the intrinsic layer. In recent years, phosphorus-doped mixed-phase  $\text{SiO}_x$  (n- $\text{SiO}_x$ ) thin films have been introduced to act as the advanced n-layers, intermediate reflectors, or back reflectors in micromorph solar cells. As the doping layer and back reflector, n- $\text{SiO}_x$  thin film has been shown to promote the cell efficiency (Hanni et al. 2015).



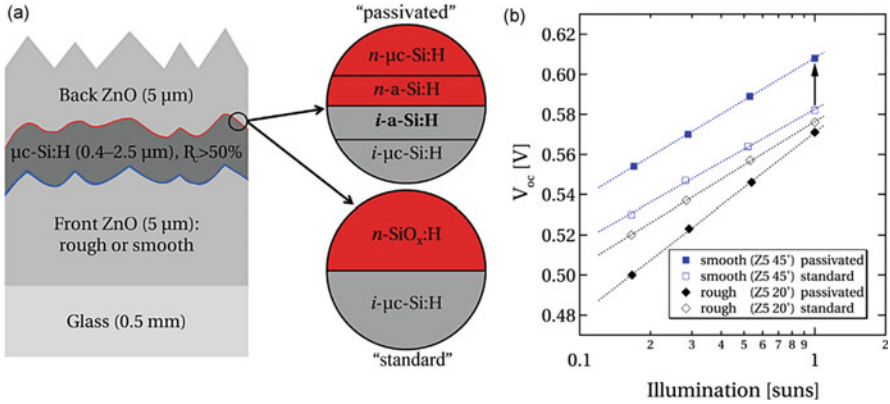


**Fig. 12** (a) Cross-sectional schematic diagram of nc-Si:H solar cell with two designs with different n/i interfaces: a passivated design with a-Si:H layers (“passivated”) and a standard n-SiO<sub>x</sub> layer (“standard”). (b) The  $V_{oc}$  of single-junction nc-Si:H solar cells on smooth and rough superstrates versus illumination level. The diode ideality factors were calculated from the slopes of the fits, represented by the dotted lines. (Reproduced from Hanni et al. (2015). Copyright (2015), with permission from John Wiley and Sons)

Hanni et al. (2015) introduced a passivated n/i hetero-interface design consisting of a stacked 20-nm-thick intrinsic a-Si:H buffer layer and an a-Si:H n-doped layer as good contact with the back electrode, as shown in Fig. 12a. The other standard design including a single n-type SiO<sub>x</sub> layer acts as the reference structure. Figure 12b shows the  $V_{oc}$  values of two designs of cells deposited on smooth and rough superstrates as functions of variable illumination. The diode ideality factor ( $n$ ) could be extracted by fitting the  $V_{oc}$  illumination data with the one-diode model (Merten et al. 1998). It is found that the diode ideality factor which corresponds to slope of fit is independent of the n/i interface design for cells on smooth superstrates, while the  $V_{oc}$  of cell in passivated design drops more than that of cell in standard design at lower illumination, which is attributed to the more efficient shunt quenching effect of the standard design with a n-SiO<sub>x</sub> layer. This result indicated that the high-quality absorber layers with no or few zones of porous and defective materials (“cracks”) were obtained in all these cells. This can also be verified by the high efficiencies (7.5–9.2%) of all cells. For such cells, the influence of the bulk recombination due to defect density in intrinsic absorber is decreased, and thus the recombination at junction interfaces has the major impact on  $V_{oc}$ . By applying a-Si:H passivation layer at n/i interface, the 650-nm-thick single-junction nc-Si:H cell with medium crystallinity i-layer demonstrates the highest reported  $V_{oc}$  of 608 mV and an efficiency of 9.45%. Aside from the high quality of bulk material, good passivation at n/i interface is the key factor to achieve the high  $V_{oc}$ . This approach is similar to passivation effect of amorphous/crystalline silicon heterojunction solar cell, where passivation of crystalline surface significantly increases the  $V_{oc}$  when compared to traditional diffused-junction c-Si solar cells.



## Optical Design for Light Management

Light management is an important strategy for efficiency improvement. The light losses in nc-Si:H solar cells mainly include the following three aspects: (1) the insufficient front-side in-coupling of light due to the reflections at layer interfaces, induced by the difference in refractive indexes in both sides, (2) the parasitic absorption loss in p-type window layer, and (3) the absorption loss of red and near-infrared light due to the low absorption coefficients and insufficient optical paths. The aim of light management is to reduce these losses.

### Antireflection Structure at Air/Cell Interface

As the incident sunlight enters the top planar surface of solar cell, part of the light would be reflected back by the mirror-like interface and escape to the outside of device. This so-called Fresnel reflection is typically reduced by coating an anti-reflective layer at the air/cell interface. Antireflection coating techniques are widely applied to effectively reduce surface reflection in various optical and optoelectronic devices. Fresnel reflection strongly depends on the contrast of refractive indexes ( $n_1$  and  $n_2$ ) of two neighboring media. A planar and transparent dielectric buffer layer with intermediate refractive index can be coated to reduce the reflection at air/cell interface. The reflected light from the back and front surfaces of the transparent film undergoes the destructive interference with each other if the thickness of coating film is equal to one-quarter of the wavelength. Fresnel reflection can be minimized by destructive interference if the refractive index ( $n_{arc}$ ) of a buffer layer approaches  $(n_1 \cdot n_2)^{0.5}$ , and the thickness of the antireflection layer is designed to be one-quarter of the wavelength ( $\lambda/(4 n_{arc})$ ), where  $\lambda$  is the light wavelength.

In substrate-type solar cell, the top p-type nc-Si:H layer has the high refractive index ( $\sim 4.0$ ) so that a wide range of materials can be chosen as antireflection layer if their refractive index is between 1.0 and 4.0. Thin TCO front electrode such as ZnO:Al, ITO, etc., also acts as the antireflection coating layer in the conventional substrate-type solar cell. In addition, the common dielectric materials ( $\text{SiO}_2$ ,  $n = 1.4$ ;  $\text{Al}_2\text{O}_3$ ,  $n = 1.8$ ;  $\text{Si}_3\text{N}_4$ ,  $n = 2.0$ ;  $\text{TiO}_2$ ,  $n = 2.3$ ) can also be coated as the antireflection layers at air/cell interfaces. In superstrate-type solar cell, since the glass superstrate has relatively low refractive index ( $1.4 \sim 1.6$ ), it is difficult to find a perfect natural antireflection coating material with the optimal refractive index ( $1.1 \sim 1.3$ ) (Schuster 2017). Silicon oxide is the common material of antireflection layer in conventional superstrate-type solar cells.

However, since the designed thickness of antireflection coating is determined by a specific wavelength (e.g., 600 nm) in visible light range, the resulting low reflection is achieved in the range around this specific wavelength. Single layer antireflection coating cannot achieve the effective antireflection in the full range of solar spectrum. In an ideal case, if the refractive index can vary continuously in the transition region from air to cell, anti reflection can be achieved in a broad band. In fact, the inhomogeneous refractive index profile can be approximated by the multilayer coating, so that the refractive index varies step by step. For example, a  $\text{ZnS}/\text{MgF}_2/\text{SiO}_2$  multilayer can decrease the reflection at air/silicon interface down to 2% in the

broad wavelength range (440–960 nm) (Schuster 2017). However, the multilayer coating often has a higher fabrication cost, and thus single antireflection layer is still widely used for antireflection of solar cells.

### Texture of Front Electrode for Superstrate-Type Solar Cell

There are two challenges related to the front side of nc-Si:H solar cell: (1) in-coupling sunlight with the minimum reflection and (2) the enhancement of the red and NIR light trapping. In a superstrate-type solar cell, the texture commonly formed at front TCO/p-layer interface is the conventional solution for these two challenges. In the texture, the propagation direction of light would be changed due to light scattering at interfaces of neighboring medium layers with different refractive indexes, as seen in Fig. 13a.

The mechanism of light scattering can be roughly categorized into reflection/refraction and diffraction according to the feature size of texture. If the feature sizes in texture structure are much larger than the wavelengths, the part of incident light will generally be reflected at texture surface, bounce onto the textured surface multiple times, and be trapped within the texture rather than out to the air, as shown in Fig. 13a. Meanwhile, the part of light is refracted at interface so that the

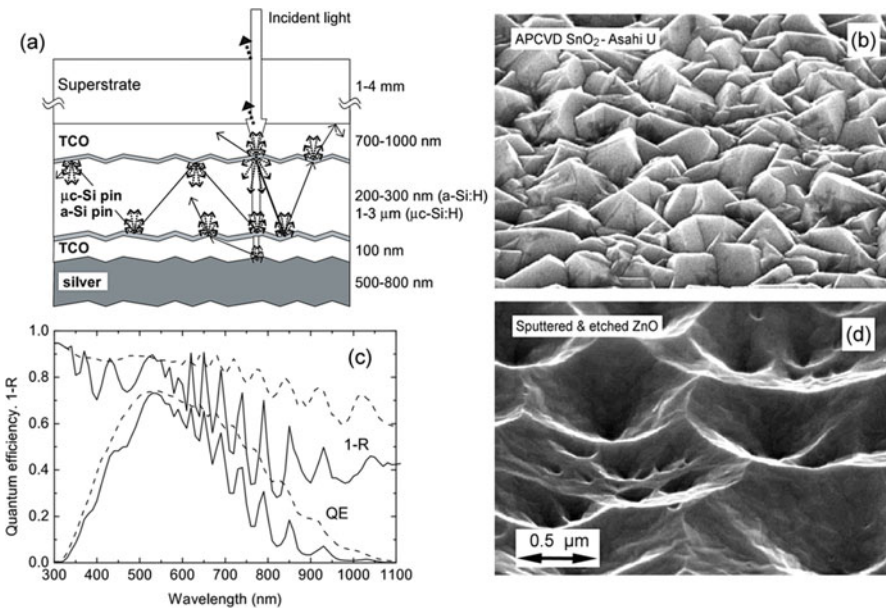


**Fig. 13** (a) Schematic diagram of the cross section of a superstrate-type silicon thin-film solar cell with textured interface. The concept of light trapping is illustrated by the *black arrows* which represent the incident and scattered light. Various optical paths of light reflecting and scatterings are sketched. (b) SEM image of typical top surface of CVD-grown  $\text{SnO}_2\text{:F}$  (Asahi Glass Co., type U). (c) Quantum efficiency ( $QE$ ) and  $(1-R)$  curves of nc-Si:H p-i-n solar cells on thin texture-etched (*dashed lines*) and smooth doped ZnO (*solid lines*).  $R$  is total cell reflectance. (d) SEM image of typical top surface of sputtered and texture-etched ZnO. (Reproduced from Müller et al. (2004). Copyright (2004), with permission from Elsevier)

light changes its direction and then enters the p-layer and the following absorbing layer. If the feature sizes are comparable or smaller than the wavelengths, the concepts of reflection and refraction in the geometric optics are not applicable. The light is scattered by the diffraction effect at media interface. This effect can also be understood by the breakdown of a texture into multilayers, and the aspect ratio of texture corresponds to transition region from TCO layer to nc-Si:H cell. Thus, the texture can be approximately in analogy to multilayer, antireflection coating and considered as a medium with a stepwise increasing index from TCO to silicon (Schuster 2017).

As a result, compared with planar structure, more light at texture interface is coupled into the absorbing layer, and the optical path is also increased by changing the light propagation direction via texture. The more effective light in-coupling and longer optical path would translate into the higher absorption, especially the absorption of NIR light. Thus, the texture structure can finally increase the  $J_{sc}$  of solar cell even though it meanwhile reduces the open-circuit voltage. Fortunately, the yield of short-circuit current density enhancement is larger than the loss of open-circuit voltage. Therefore, the light trapping by texture is an effective way for efficiency improvement of solar cell by reducing reflection loss at interface and absorption loss of NIR light in the intrinsic layer.

The effect of light scattering can be estimated by the haze ratio which is defined as the ratio of diffuse transmittance to total transmittance. The higher haze ratio indicates that more light is scattered. The high haze in a broad wavelength range is therefore a requirement for absorption enhancement of a thin absorbing slab. However, haze alone is not the sufficient characterization of light-trapping structure. Path length enhancement, which is defined as the ratio of path length to absorber thickness, is a better parameter. The larger scattering angle  $\theta$  and the longer path through the absorber would lead to the high path length enhancement. In theory, the maximum limit of path length enhancement in an ideal Lambertian scatterer is  $4n^2$ , where  $n$  is the refractive index of TCO film (Yablanovitch and Cody 1982). Many methods to form random or periodic textures have been developed for effective light trapping.

**Random textured TCO:** The bottom-up approaches for random texture of thick TCO layer are widely used for light trapping in nc-Si:H solar cells. The random textures with microscale feature sizes are conventionally fabricated by post-deposition etching process. For example, the texture on sputtering-deposited ZnO:Al films, which are often initially flat with little roughness, can be formed by wet etching in the diluted HCl solution, leading to the decrease in reflection and enhancement of quantum efficiency, as seen in Fig. 13c, d. It is worth noting that too rough TCO layers with steep slopes would lead to the decrease in  $V_{oc}$  and  $FF$  in nc-Si:H solar cells. Therefore, the topography is also required to be smooth enough to avoid the formation of defects (such as cracks, voids, etc.), which can lead to electrical transport issues such as shunting, etc.

The textured structure can also be natively formed during some CVD deposition processes. For example, SnO<sub>2</sub>:F film which is deposited by APCVD can natively form a textured structure on surface (Gordon et al. 1989). Generally, as-grown

CVD-SnO<sub>2</sub>:F films have the typical V-shaped surface roughness, and the V-shaped large and steep pyramids are also typically formed in the as-grown LPCVD-deposited ZnO films. Nevertheless, the roughness shape of the latter texture can be modified by plasma treatment from V-shape to U-shape. Figure 13b, d shows SEM images of the typical V-shaped surface roughness of CVD-grown SnO<sub>2</sub>:F (Asahi Glass Co., type U) and the U-shaped surface roughness of sputtered and texture-etched ZnO.

**Random textured superstrate:** The random texture can also be formed by texturing the glass superstrate instead of texturing TCO front electrode. Hongsingthong et al. (2013) reported that reactive ion etching (RIE) treatment with carbon tetrafluoride (CF<sub>4</sub>) is used to modify surface morphology of soda-lime glass superstrate and form texture with very high haze ratio. The surface morphology of doped ZnO film grown on the glass strongly depends on the morphology of the etched glass. As shown in Fig. 14b, the conventional as-grown pyramid-like texture in doped ZnO film can be changed into cauliflower-like double texture by crater-like glass texture shown in Fig. 14a, resulting in the increases in root mean square of feature size and haze ratio of surface roughness. The haze ratio of over 92% at the wavelength of 800 nm can be achieved in the double-textured ZnO films. As shown in Fig. 14c, the enhancement in the quantum efficiency in the long-wavelength region and  $J_{sc}$  of 24.70 mA/cm<sup>2</sup> have been achieved when introducing this double textured ZnO film as front electrode in nc-Si:H solar cell.

**Periodic textured superstrate:** Recently, periodic light-trapping textures have been introduced in nc-Si:H solar cells in both substrate- and superstrate-type configurations. A commercial transparent superstrate embossed with micrometer-scale 2-D grating, which is fabricated by nanoimprint lithography, is coated with a thin conductive layer of hydrogenated indium oxide and then applied as front electrodes with periodic 2-D texture for micromorph tandem solar cells (Moulin et al. 2014). Combining this periodic 2-D texture with as-grown LPCVD-deposited random texture at surface of doped ZnO, the transparent front electrode with double texture was obtained for the enhanced light trapping. This double texture makes the efficiency of solar cell with 1.6- $\mu$ m-thick ZnO:B front electrode to be as high as that of the solar cell with 2.3- $\mu$ m-thick doped ZnO front electrode with random single-texture.

### Texture of Back Electrode for Substrate-Type Solar Cell

In substrate-type configuration, the textures of n-i-p solar cells for light trapping are different from those of p-i-n solar cells in superstrate-type configuration. The substrate is usually coated with reflective metal such as silver or aluminum film, which acts as back electrode and reflector. The back reflector mainly reflects the red and NIR light since the blue and green light are already absorbed within the first few hundreds of nanometers in silicon layer. The natural texture structures can be formed at surfaces of these metal films for light trapping when these metal films are deposited at high temperatures between 300 °C and 400 °C (Schropp and Zeman 1998). However, the back reflector of a textured metal film would cause plasmonic

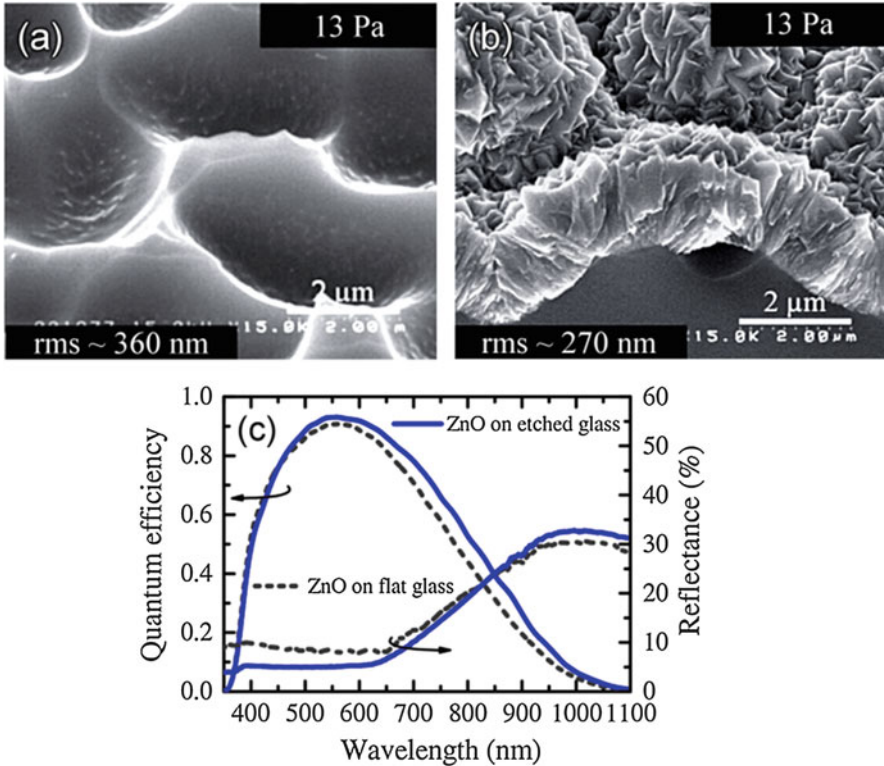


**Fig. 14** SEM top-view micrograph of textured soda-lime glass superstrate (a) and cross-sectional SEM micrograph of doped ZnO film deposited on the textured soda-lime glass (b) at the etching pressure of 13 Pa. (c) is quantum efficiencies and reflectance of two typical nc-Si:H solar cells using doped ZnO films deposited on the etched glass (rms ~270 nm) and the flat glass (rms ~63 nm), respectively, as the front TCO electrodes. *rms* root mean square. (Reproduced from Hongsingthong et al. (2013). Copyright (2013), with permission from Elsevier)

absorption losses (Sai et al. 2012). These kinds of optical losses can be minimized when a metal layer is separated from a silicon layer by a transparent oxide layer. Stacked TCO/textured metal structure has become a standard structure of back reflector for light trapping.

In recent years, periodically textured substrates have been applied for light trapping. Periodically textured substrates with hexagonal dimple arrays (hereafter, “honeycomb texture”) were developed and applied to nc-Si:H cells as the back reflector (Sai et al. 2015). A  $J_{sc}$  of 26 mA/cm<sup>2</sup> was achieved in a 1- $\mu$ m-thick nc-Si:H cell by optimizing the period and aspect ratio of honeycomb texture (Sai et al. 2012).

Sai et al. (2015) reported the high-efficiency nc-Si:H solar cells on honeycomb textured substrates fabricated by VHF-PECVD. The honeycomb structure was fabricated by a top-down approach in which honeycomb structure was formed by



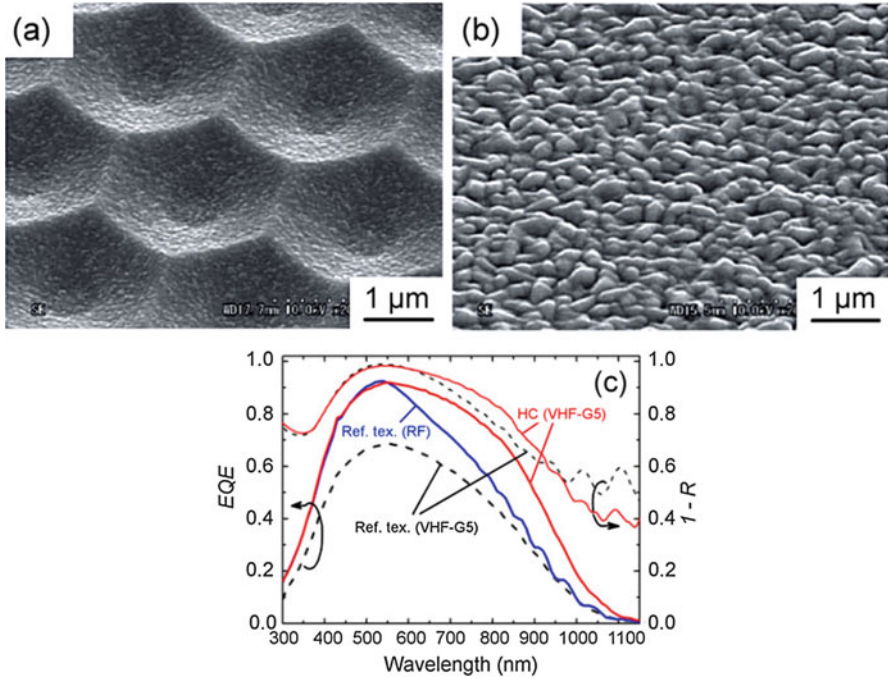


**Fig. 15** (a, b) Represent SEM images of a honeycomb textured and a reference textured substrates, respectively. (c) Represents EQE and absorption (1-R) spectra of nc-Si:H cells deposited on the honeycomb and reference substrates (commercial textured  $\text{SnO}_2$ :F-coated glass) using the lab-scale RF-PECVD (RF) and Gen-5-sized VHF-PECVD (VHF-G5) systems. Gen-5-sized means a large substrate area scale of  $1.1 \times 1.4$  m. All the cells have the thickness of  $\sim 2$   $\mu\text{m}$ . (Reproduced with permission from Sai et al. (2015). Copyright (2015) The Japan Society of Applied Physics)

the wet etching of a grown silicon oxide film via a mask with the honeycomb patterns obtained by photolithography method. The honeycomb texture has the larger feature size ( $\sim 4$ – $5$   $\mu\text{m}$ ) than texture in commercial  $\text{SnO}_2$ :F-coated glass, as shown in Fig. 15a, b. The honeycomb textures improve the infrared response (see Fig. 15c) as well as the nc-Si:H film growth. Rounded concaves in the honeycomb structure with an appropriate period promote the efficiency of substrate-type nc-Si:H solar cell up to 11.8% at a deposition rate of 1 nm/s.

### Window Layer

Aside from light confinements mentioned above, the other aspect to enhance the light management is to reduce parasitic absorption losses in window layer. In nc-Si:H solar cell, the conventional window layer is made of p-type nc-Si:H material, whose advantages are the high doping efficiency and low activation energy. Thus, the high conductivity of  $10$ – $10^2$  S/cm can be achieved to increase built-in potential and reduce series resistance of solar cell. However, this material

has a narrow bandgap ( $\sim 1.1$  eV), leading to the considerable parasitic absorption losses in short wavelength range and the resultant photocurrent losses.

The wide-bandgap materials are the promising alternatives for new window layers instead of p-type nc-Si:H. They need to meet certain requirements as follows: (1) The bandgap of more than 2 eV is desirable to effectively reduce parasitic absorption losses. (2) As a junction layer, the conductivity needs to be larger than  $10^{-6}$  S/cm to reduce series resistance and increase fill factor of solar cell. (3) For a p-i-n solar cell, it is better for the window layer to act as the seed layer of intrinsic absorber as well. Thus, the additional step of specific seed layer deposition can be avoidable.

p-type nanocrystalline (or, i.e., microcrystalline) silicon alloys such as  $\text{SiO}_x$  or  $\text{SiC}_x$  are recently used for window layers. These materials consist of silicon crystals and amorphous silicon alloy networks. The crystals with the high doping efficiencies facilitate the overall conductivity of the window layer, while amorphous silicon alloys contribute to the wide bandgap of the window layer. Therefore, these two-phase mixed materials partially decouple the optimizations of the optical and electrical properties by adjusting deposition conditions that deliver the appropriate mixture of the two phases.

The hydrogenated p-type nanocrystalline silicon oxide (p-nc- $\text{SiO}_x$ :H) is recently reported as a wide-bandgap window layer which exhibits the bandgap of 2.33 eV and the conductivity of 0.2 S/cm (Chen et al. 2016). As the oxygen content increases, the response in short wavelength range is enhanced, leading to the increase in  $J_{sc}$  from  $19.73$  mA/cm<sup>2</sup> to  $21.62$  mA/cm<sup>2</sup>. Meanwhile, a barrier in the conduction band that is formed at p/i interface suppresses the electron diffusion, reducing the recombination rate and increasing the  $V_{oc}$  from 490 mV to 510 mV. In addition, p-type nc- $\text{SiO}_x$ :H also induces the shunt quenching of cracks in the absorber, leading to high shunt resistance and the resultant increase in fill factor (Hanni et al. 2015). H. Tan reported the PECVD-deposited p-nc- $\text{SiO}_x$  films which have the perpendicular filament-like Si nanocrystalline phases, leading to the adequate transverse conduction in spite of low planar conduction. The p-nc- $\text{SiO}_x$  window layer results in higher  $V_{oc}$  and the stronger blue light response and yields the 14.4% a-Si:H/nc-Si:H tandem solar cell (Tan et al. 2015).

The hydrogenated p-type nanocrystalline silicon carbide (p-nc- $\text{SiC}_x$ :H) is also a good alternative for window layer. Boron-doped p-nc- $\text{SiC}_x$ :H thin film (<30 nm) exhibits the high conductivity of  $1.7 \times 10^{-3}$  S/cm and bandgap of 2.21 eV ( $E_{04}$ ) (Ma et al. 2013). The high conductivity is associated with the percolation channels in crystalline phases. Al-doped p-nc- $\text{SiC}_x$ :H thin films deposited by HWCVD using trimethylaluminum (TMAI) as dopant exhibit the structures with cubic (3C) SiC polytypes, the wide optical bandgaps ( $E_{04}$ ) of 2.0  $\sim$  2.8 eV, and high dark conductivities between  $\sim 10^{-5}$  S/cm and 0.1 S/cm (Chen et al. 2014).

### Intermediate Reflector

In the multijunction solar cell, the amorphous absorbers made of a-Si:H or a-SiGe:H material should be thin to minimize the light-induced degradation effects, which may decrease the overall device current density by the reduced current densities of

amorphous component cells. To overcome this issue, a so-called intermediate reflector (IRL) is added between component cells. For micromorph tandem solar cell, an IRL would reflect the short wavelength light back to a-Si:H top cell and enhance the overall light absorption inside it. For a triple-junction (a-Si:H/a-SiGe:H/nc-Si:H) cell, an IRL is usually added between the middle and bottom cells to compensate for the current of middle cell. IRL can increase the reflection of the incident light at interface and make the reflected light return the top and middle cells. Therefore, the IRL allows the reduced thicknesses of amorphous absorbers in the top and middle cells. This effect is favorable for carrier transport, leading to the reduction of light-induced degradation in amorphous cells. Good IRL requires low refractive index ( $n$ ) and high transmittance. If the refractive index of IRL is much lower than those of amorphous cells, IRL can effectively reflect the short-wavelength light to amorphous cells. Meanwhile, if IRL has the wide bandgap with low optical absorption, it can also enable more long-wavelength light to enter bottom cell. In addition, as contact layers of component cells, IRLs are also required to have the appreciate conductivities. If their conductivities are lower than a certain level, IRLs cannot give a good function in solar cells because their poor contacts would result in high series resistances and low  $FF$ s. Vertical conductivity of IRL is usually required to be higher than  $10^{-5}$  S/cm in multijunction solar cell (Buehlmann et al. 2007).

It is crucial for an intermediate reflector to have a lower refractive index than that of silicon layer ( $\sim 4.0$ ) to enhance the internal reflection. The conductive metal oxides (such as doped ZnO) and Si alloy (e.g., SiO<sub>x</sub>:H) are promising candidates for IRL. Doped ZnO is suitable for IRL material in a cell because it usually has a refractive index of around 1.8  $\sim$  2.0 and a conductivity of  $\sim 10^2$  S/cm. It was reported that highly conductive ZnO IRLs with  $n$  of  $\sim 2.0$  significantly increase efficiencies of a-Si:H/nc-Si:H tandem solar cells in superstrate-type design (Myong et al. 2007). To date, multijunction solar cells with highly conductive metal oxides often exhibit higher efficiencies than those of cells with Si alloy IRLs. However, their high lateral conductivities lead to unintended shunts during the processes of monolithic series integration of segments. An additional laser scribe or a coating process is needed to avoid the lateral shunt creations, resulting in high production cost.

The other alternative of IRL material is hydrogenated n-type amorphous silicon-oxide (n-a-SiO<sub>x</sub>:H) or hydrogenated n-type nanocrystalline (or microcrystalline) silicon oxide (n-nc-SiO<sub>x</sub>:H). SiO<sub>x</sub>:H IRLs can significantly reduce lateral shunting because of the lower lateral conductivities than ZnO IRLs. In addition, no additional step for the monolithic integration of a-Si:H/nc-Si:H tandem PV module is needed because SiO<sub>x</sub>:H IRLs could be removed together with adjacent Si layers in the step of the laser scribing. Hence, SiO<sub>x</sub>:H IRLs are the promising options for the cost-effective mass production. A “micromorph” tandem cell (a-Si:H/nc-Si:H) with a low refractive ( $n = 1.75$ ) n-nc-SiO<sub>x</sub>:H IRL exhibits a certified stabilized efficiency of 12.63% (Boccard et al. 2014).



## Present Status of Solar Cell Efficiency

The extensive research efforts in recent years have led to new record efficiencies for both single-junction and multijunction solar cells. Table 3 lists the present status of the highest conversion efficiencies of nc-Si:H-based thin-film solar cells around the world. It should be addressed that the active area efficiency is often calculated by subtracting the area shaded by the grid from the total cell area.

As one can see from Table 3, the highest cell efficiency of single-junction nc-Si:H thin-film solar cell to date is 11.8% made with a deposition rate of 1 nm/s at AIST (Sai et al. 2015) in Japan in 2015. The completed solar cell consists of the following layers from the bottom to the top: textured substrate/Ag/ZnO:Ga/(n) nc-SiO<sub>x</sub>:H/(i) nc-Si:H/buffer/(p) nc-SiO<sub>x</sub>:H/TCO/Ag grid. The periodic honeycomb textures with rounded concaves on substrate and MOCVD-deposited ZnO:B instead of sputtered-ITO were introduced into the VHF-PECVD-fabricated nc-Si:H cells for efficiency improvement.

Table 3 also includes the best a-Si:H/nc-Si:H micromorph tandem solar cells. So far, the highest initial efficiency of 14.4% was achieved for a cell (active area: 1.1 cm<sup>2</sup>) made at Delft University of Technology in 2015 (Tan et al. 2015). p-nc-SiO<sub>x</sub>:H window layer leads to the higher  $V_{oc}$  and the better blue spectral response. The highest stabilized efficiency now stands at 12.63% for a micromorph

**Table 3** Present status of conversion efficiencies of nc-Si:H-based thin-film solar cells

Cell structure	Configuration	Initial efficiency (%)	Stabilized efficiency (%)	Organization
Single junction	nc-Si:H	11.80	–	AIST (Chen et al. 2014)
Double junction	a-Si:H/nc-Si:H	14.40	–	Delft University of Technology (Tan et al. 2015)
Double junction	a-Si:H/nc-Si:H	13.20	12.63	EPFL (Boccard et al. 2014)
Triple junction	a-Si:H/a-SiGe:H/nc-Si:H	16.3 <sup>a</sup>	–	United Solar Ovonic (Yan et al. 2011)
Triple junction	a-Si:H/nc-Si:H/nc-Si:H	14.50	14.04	AIST (Sai et al. 2016)
Triple junction	a-SiO <sub>x</sub> :H/a-Si:H/nc-Si:H	12.58	–	Delft University of Technology (Kim et al. 2015)
Quadruple-junction	a-Si:H/a-Si:H/nc-Si:H/nc-Si:H	14 <sup>b</sup>	12.40	Helmholtz-Zentrum Berlin (Kimer et al. 2015)

<sup>a</sup>Active-area efficiency

<sup>b</sup>Aperture-area efficiency

tandem solar cell developed by inserting a silicon oxide ( $\text{SiO}_x$ ) film with low refractive index as intermediate reflector in EPFL (Boccard et al. 2014).

Multijunction solar cells with more than two component cells have also been attracted to further enhance cell efficiency and reduce light-induced degradation. The best triple-junction solar cell now reaches an initial active-area efficiency of 16.3% in a a-Si:H/a-SiGe:H/nc-Si:H structure fabricated by United Solar Ovonix in 2011 (Yan et al. 2011). The standard n-type junction layer between the middle and bottom cells was replaced by nc- $\text{SiO}_x$ :H layer as both doped layer and intermediate reflector. AIST (Sai et al. 2016) achieved the highest stabilized efficiency of 14.04% in an a-Si:H/nc-Si:H/nc-Si:H triple-junction solar cell with the minimum light-induced degradation of 4% in 2016. They developed the a-Si:H top cell that is greatly stable against light soaking and investigated quantitatively the effect of current mismatch of component cells to find the best balance. Quadruple-junction solar cell and module with a-Si:H/a-Si:H/nc-Si:H/nc-Si:H configuration were developed by Helmholtz-Zentrum Berlin (Kirner et al. 2015) in 2015. The  $1 \times 1$  cm solar cell demonstrates the initial and stabilized efficiencies of 14.0% and 12.4%, respectively, while a mini-module with an aperture area of  $61.44 \text{ cm}^2$  shows the efficiency of 13.4% before and 12.0% after more than 1000 h of light soaking, respectively. The highlight of this quadruple-junction solar cell is the optimization of the doping concentration of nc- $\text{SiO}_x$ :H intermediate reflector.

---

## Conclusion and Prospects

In the last decade, huge research efforts and advanced technologies have helped improve the performance of nc-Si:H thin-film solar cells. However, the present highest efficiency is still much lower than the theoretical efficiency limit (over 30%) for nc-Si:H solar cells based on Shockley-Queisser (S-Q) detailed-balance model, leaving much room for further improvement. In addition, since most of the market is now occupied by competitive low-priced c-Si modules, thin-film silicon modules are indeed under pressure to further enhance the efficiency.

For nc-Si:H solar cells, defects in the bulk absorber and at interfaces still sink minority carriers, leading to the voltage loss, while strong current losses resulted from the insufficient absorption of red and NIR light. Therefore, the general strategy to further improve solar cell efficiency includes two aspects. On one hand, although light management technologies have been widely implemented in recent years, the novel designs of cell structure will still be required to further increase the photocurrent density by enhancing the light trapping and reducing parasitic absorptions of non-absorbing layers. On the other hand, further profound understanding and controlling of carrier recombination mechanisms in the device will also be required. Therefore, further research studies on advanced material engineering are still needed for carrier management including identifications of recombination centers such as bulk and interface defects, their energies, densities, passivation methods, their effects on electrical transport, etc.

Aside from the routine approaches mentioned above, several novel methods for efficiency improvement are suggested as follows:

1. Some novel and dedicated device structures are needed for further enhancement of light management in consideration of carrier management. (1) The emerging finely modulated textures such as multi-scale (micro- and nano-) double-texture in front or back electrode, double-side textures at both front and back electrode, etc., should be further studied by combining conventional micrometer-scale texture and subwavelength texture. Furthermore, the enhanced light trapping can also reduce the required thickness of the absorber, thereby reducing bulk recombination and light-induced degradation. (2) Distinguished from the present bottom-up random textures or simple periodic texture methods, novel top-down approaches, which are based on the further understanding and simulation of light reflection and/or diffraction theories, can be tried to develop finely designed periodic textures by lithography or other techniques for better light trapping effect. (3) The emerging physical flat structure with optical texture effect can be further investigated. For example, the localized nonuniform distribution of refractive index can be intentionally achieved by adding the planarization process of top a-Si:H cell by etch-back or chemical mechanical planarization (CMP) method or inserting the 2-D photonic crystal in the cell. In addition, the contact-free “remote” texture can be applied by texturing glass substrate at air/glass interface or inserting a transparent layer (such as plastic) with fine texture between the glass and air, so that TCO front electrode is not needed to be textured and silicon layer can be grown in a flat substrate. This will further improve the quality of the bulk absorber which is degraded by the textured substrate, reducing the recombination rate and the resulting  $V_{oc}$  loss.
2. Multijunction solar cell technique is considered as another key approach to further improve cell efficiency. (1) For triple-junction solar cell, the higher efficiency can also be expected by new design of component cell bandgap. Simulation result shows the highest theoretical conversion efficiency of 21.4% is expected to be obtained when the bandgaps of the top, middle, and bottom cells are 2 eV, 1.45 eV, and 1.1 eV, respectively (Konagai 2011). Novel silicon alloys (e.g.,  $\text{SiO}_x\text{:H}$ ,  $\sim 2$  eV) can be introduced to replace the a-Si:H (1.7 eV) in the typical triple-junction solar cell with a structure of a-Si:H/a-SiGe:H/nc-Si:H. In fact,  $\text{SiO}_x\text{:H}$  alloys have emerged as the absorber material in the top cell of a-SiO<sub>x</sub>:H/a-Si:H/nc-Si:H triple-junction solar cell (Kim et al. 2015). To date, few works for  $\text{SiO}_x\text{:H}$ /a-SiGe:H/nc-Si:H structure have been done, and this structure is expected to further increase the efficiency by improving the  $V_{oc}$  and other aspects. (2) More efforts on the emerging quadruple-junction solar cells should be taken to further improve the efficiency. The maximum initial efficiency of 19.8% has been theoretically simulated and projected for quadruple-junction solar cells (Isabella et al. 2014).

---

## References

- J. Bailat, E. Vallat-Sauvain, L. Feitknecht, C. Droz, A. Shah, J. Non-Cryst. Solids **299–302**, 1219 (2002)
- M. Boccard, M. Despeisse, J. Escarre, X. Niquille, G. Bugnon, S. Hanni, M. Bonnet-Eymard, F. Meillaud, C. Ballif, IEEE J. Photovoltaics **4**, 1368 (2014)

- P. Buehlmann, J. Bailat, D. Domine, A. Billet, F. Meillaud, A. Feltrin, C. Ballif, *Appl. Phys. Lett.* **91**, 143505 (2007)
- P. Chen, P. Chen, M. Hsiao, C. Hsu, C. Tsai, *Int. J. Photoenergy* **2016**, 8172518 (2016)
- T. Chen, F. Köhler, A. Heidt, R. Carius, F. Finger, *Jpn. J. Appl. Phys.* **53**, 05FM04 (2014)
- A. Chowdhury, S. Mukhopadhyay, S. Ray, *Sol. Energy Mater. Sol. Cells* **93**, 597 (2009)
- R. Gordon, J. Proscia, F.B. Ellis, A.E. Delahoy, *Solar Energy Mater.* **18**, 263 (1989)
- L. Guo, M. Kondo, M. Fukawa, K. Saitoh, A. Matsuda, *Jpn. J. Appl. Phys.* **37**, L1116 (1998)
- S. Hanni, M. Boccard, G. Bugnon, M. Despeisse, J.W. Schuttauf, F.J. Haug, F. Meillaud, C. Ballif, *Phys. Status Solidi Appl. Mater. Sci.* **212**, 840 (2015)
- M. Heintze, R. Zedlitz, *J. Non-Cryst. Solids* **198–200**, 1038 (1996)
- A. Hongsingthong, T. Krajangsang, A. Limmanee, K. Sriprapha, J. Sritharathikhun, M. Konagai, *Thin Solid Films* **537**, 291 (2013)
- C.H. Hsu, Y.S. Lin, Y.S. Cho, S.Y. Lien, P. Han, D.S. Wu, *IEEE J. Quantum Electron.* **50**, 515 (2014)
- O. Isabella, A.H.M. Smets, M. Zeman, *Sol. Energy Mater. Sol. Cells* **129**, 82 (2014)
- S.J. Jones, R. Crucet, M. Izu, in *28th IEEE Photovoltaic Specialists Conference*, Anchorage, Alaska, 2000, pp. 134–137
- T. Kamei, T. Wada, *J. Appl. Phys.* **96**, 2087 (2004)
- T. Kilper, W. Beyer, G. Bräuer, T. Bronger, R. Carius, M.N. van den Donker, D. Hrunski, A. Lambertz, T. Merdzhanova, A. Mück, B. Rech, W. Retz, R. Schmitz, U. Zastrow, A. Gordijn, *J. Appl. Phys.* **105**, 074509 (2009)
- D.Y. Kim, E. Guijt, F.T. Si, R. Santbergen, J. Holovský, O. Isabella, R.A.C.M.M. van Swaaij, M. Zeman, *Sol. Energy Mater. Sol. Cells* **141**, 148 (2015)
- S. Kirner, S. Neubert, C. Schultz, O. Gabriel, B. Stannowski, B. Rech, R. Schlatmann, *Jpn. J. Appl. Phys.* **54**, 08KB03 (2015)
- S. Klein, F. Finger, R. Carius, M. Stutzmann, *J. Appl. Phys.* **98**, 024905 (2005)
- M. Konagai, *Jpn. J. Appl. Phys.* **50**, 30001 (2011)
- N. Kosku, S. Miyazaki, *Thin Solid Films* **511–512**, 265 (2006)
- J. Ma, J. Ni, J. Zhang, Z. Huang, G. Hou, X. Chen, X. Zhang, X. Geng, Y. Zhao, *Sol. Energy Mater. Sol. Cells* **114**, 9 (2013)
- Y. Mai, S. Klein, R. Carius, H. Stiebig, X. Geng, F. Finger, *Appl. Phys. Lett.* **87**, 073503 (2005)
- T. Matsui, M. Kondo, A. Matsuda, in *3rd World Conference on Photovoltaic Energy Conversion*, Osaka, 2003, pp. 1548–1551
- J. Meier, S. Dubail, R. Flückiger, D. Fischer, H. Keppner, A. Shah, in *Proceedings of the 1st IEEE World Conference on Photovoltaic Energy Conversion*, Hawaii, 1994, pp. 409–412
- F. Meillaud, A. Feltrin, D. Dominé, P. Buehlmann, M. Python, G. Bugnon, A. Billet, G. Parascandolo, J. Bailat, S. Fay, N. Wyrsh, C. Ballif, A. Shah, *Philos. Mag.* **89**, 2599 (2009)
- J. Merten, J.M. Asensi, C. Voz, A. Shah, R. Platz, J. Andreu, *IEEE Trans. Electron Devices* **45**, 423 (1998)
- B.Y. Moon, J.H. Youn, S.H. Won, J. Jang, *Sol. Energy Mater. Sol. Cells* **69**, 139 (2001)
- E. Moulin, M. Steltenpool, M. Boccard, G. Bugnon, M. Stuckelberger, E. Feuser, B. Niesen, R. Van Erven, J. Sch, F. Haug, C. Ballif, *IEEE J. Photovoltaics* **4**, 1177 (2014)
- J. Müller, B. Recha, J. Springer, M. Vanecek, *Sol. Energy* **77**, 917 (2004)
- S.Y. Myong, K. Sriprapha, S. Miyajima, A. Yamad, M. Konagai, *Appl. Phys. Lett.* **90**, 263509 (2007)
- A. Polman, M. Knight, E.C. Garnett, B. Ehrler, W.C. Sinke, *Science* **352**, aad4424 (2016)
- M. Python, O. Madani, D. Dominé, F. Meillaud, E. Vallat-Sauvain, C. Ballif, *Sol. Energy Mater. Sol. Cells* **93**, 1714 (2009)
- J.K. Rath, *Sol. Energy Mater. Sol. Cells* **76**, 431 (2003)
- H. Sai, K. Saito, M. Kondo, *Appl. Phys. Lett.* **101**, 1 (2012)
- H. Sai, K. Maejima, T. Matsui, T. Koida, M. Kondo, S. Nakao, Y. Takeuchi, H. Katayama, I. Yoshida, *Jpn. J. Appl. Phys.* **54**, 08KB05 (2015)

- H. Sai, T. Matsui, K. Matsubara, *Appl. Phys. Lett.* **109**, 1 (2016)
- S. Schicho, F. Köhler, R. Carius, A. Gordijn, *Sol. Energy Mater. Sol. Cells* **98**, 391 (2012)
- R.E.I. Schropp, M. Zeman, *Amorphous and Microcrystalline Solar Cells: Modeling, Materials, and Device Technology*, 1st edn. (Springer, New York, 1998)
- C.S. Schuster, *Diffraction Optics for Thin-Film Silicon Solar Cells*, 1st edn. (Springer, Cham, 2017)
- A. Tamang, H. Sai, V. Jovanov, S.I.H. Bali, K. Matsubara, D. Knipp, *Sol. Energy Mater. Sol. Cells* **151**, 81 (2016)
- H. Tan, P. Babal, M. Zeman, A.H.M. Smets, *Sol. Energy Mater. Sol. Cells* **132**, 597 (2015)
- J. Tauc, R. Grigorovici, A. Vancu, *Phys. Status Solidi* **15**, 627 (1966)
- M.N. Van Den Donker, S. Klein, B. Rech, F. Finger, W.M.M. Kessels, M.C.M. Van De Sanden, *Appl. Phys. Lett.* **90**, 183504 (2007)
- O. Vetterl, F. Finger, R. Carius, P. Hapke, L. Houben, O. Kluth, A. Lambertz, A. Mück, B. Rech, H. Wagner, *Sol. Energy Mater. Sol. Cells* **62**, 97 (2000)
- D.Y. Wei, Ph.D. thesis, Nanyang Technological University, 2014
- D.Y. Wei, S.Q. Xiao, S.Y. Huang, C.S. Chan, H.P. Zhou, L.X. Xu, Y.N. Guo, J.W. Chai, S.J. Wang, S. Xu, *J. Phys. D. Appl. Phys.* **46**, 215501 (2013)
- S. Xu, K.N. Ostrikov, Y. Li, E.L. Tsakadze, I.R. Jones, *Phys. Plasmas* **8**, 2549 (2001)
- E. Yablanovitch, G.G. Cody, *IEEE Trans. Elec. Dev.* **ED-29**, 300 (1982)
- B. Yan, G. Yue, L. Sivec, J. Yang, S. Guha, C.S. Jiang, *Appl. Phys. Lett.* **99**, 113512 (2011)



# Nanocrystalline Silicon-Based Multilayers and Solar Cells

# 24

Yunqing Cao and Jun Xu

## Contents

Introduction .....	844
Fabrication of Size-Controllable Nanocrystalline Si-Based Multilayers .....	847
The General Idea to Get Size-Controllable nc-Si Dots in Multilayered Structures .....	848
Fabrication of nc-Si/SiO <sub>2</sub> Multilayers .....	849
Fabrication of nc-Si/SiC Multilayers .....	851
Size-Dependent Photovoltaic Properties of Hetero-junction Solar Cells Containing nc-Si/SiC Multilayers .....	855
Photovoltaic Properties of Hetero-junction Solar Cells Containing nc-Si/SiC Multilayers .....	856
Size-Dependent Optical and Photovoltaic Properties of nc-Si/SiC Multilayers .....	859
Broadband Spectral Response for Hetero-junction Solar Cell Containing Graded-Sized nc-Si/SiC Multilayers .....	861
Study of Fabrication and Photovoltaic Properties of All-nc-Si-Based Solar Cells .....	863
Light Harvesting and Enhanced Performance of nc-Si-Based Hetero-junction Solar Cells Fabricated on Nanopatterned Substrates .....	864
Preparation of Nanopatterned Si Structures for nc-Si-Based Solar Cells .....	864
Enhanced Performance of nc-Si-Based Hetero-junction Solar Cells Fabricated on Si Nanowire Substrates .....	867

Y. Cao (✉)

National Laboratory of Solid State Microstructures and School of Electronic Science and Engineering, The Collaborative Innovation Center of Advanced Microstructures, Nanjing University, Nanjing, China

College of Physics Science and Technology, Yangzhou University, Yangzhou, China  
e-mail: [yqcao@yzu.edu.cn](mailto:yqcao@yzu.edu.cn)

J. Xu

National Laboratory of Solid State Microstructures and School of Electronic Science and Engineering, The Collaborative Innovation Center of Advanced Microstructures, Nanjing University, Nanjing, China  
e-mail: [junxu@nju.edu.cn](mailto:junxu@nju.edu.cn)

High Efficiency Solar Cell Containing Graded-Sized nc-Si/Si NWs Hetero-junction	
Structure .....	872
Conclusion .....	873
Cross-References .....	876
References .....	876

### Abstract

Nanocrystalline Silicon (nc-Si) is a promising material to develop the next generation of solar cells since it can efficiently absorb the incident solar light in a wide spectral range via the size modulation. The idea of all Si-based tandem type solar cells containing the sub-cells with various bandgaps motivates the extensive studies on the synthesis, physical properties, as well as the device applications of nc-Si material. Currently, the fabrication of size-controllable nc-Si is one of the challenging issues and the utilization of nc-Si in actual photovoltaic device is still at the stage of exploration. In this chapter, we describe the preparation of size-controllable nc-Si dots in multilayer by using thermally annealing or laser crystallization technique to crystallize amorphous Si/SiO<sub>2</sub> or amorphous Si/SiC stacked structures. It is shown that the dot size can be well confined with the initial amorphous Si layer thickness and the size-dependent properties are observed. The chapter focuses on the utilization of prepared nc-Si-based multilayers in prototype hetero-junction solar cells. The photovoltaic properties with different dot size, surrounding insulator materials, as well as the novel grade-sized structures are present. Furthermore, the efforts to improve the device performance by combining light trapping structures with nc-Si-based multilayers are introduced.

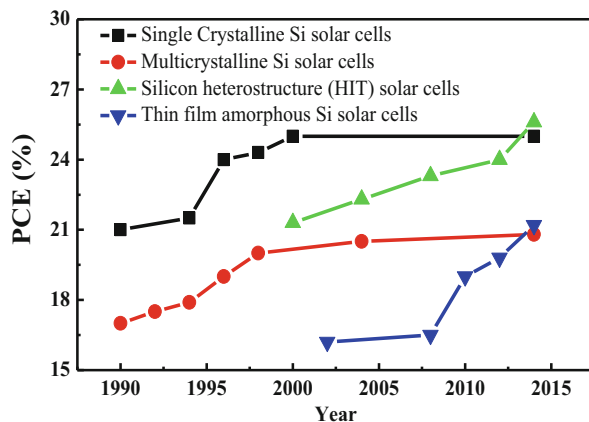
### Keywords

Size-controllable nanocrystalline silicon (nc-Si) · Si/SiC multilayers · Solar cell · Size-dependent photovoltaic properties · Graded-sized nc-Si · All-nc-Si-based solar cell · Light trapping effect · Si nanowires (Si NWs)

## Introduction

Silicon (Si) is the dominant material in today's photovoltaic (PV) industry because of its abundance, nontoxicity, and contaminant-free and mature fabrication process though it is not the most suitable PV material if one considers its relatively narrow bandgap (1.1 eV). The so-called first generation solar cells, which include single crystalline silicon (c-Si) and multicrystalline silicon (mc-Si) solar cells, exhibit the quite high power conversion efficiency (PCE) and stability, and the recorded PCE is as high as 25%. In order to reduce the cost of PV devices, mainly due to the Si wafers, it was proposed to develop the thin film technology (or the "second generation" technology) and amorphous Si (a-Si) thin film solar cell is one of the candidates. Regardless of the semiconductor involved, thin film technology offers

**Fig. 1** The PCE of Si-based solar cells varying with time reported by NREL (Copyright by the authors)



prospects for a large reduction in material costs by eliminating the costs of the Si wafer. Figure 1 shows the PCE of Si-based solar cells varying with time reported by the National Renewable Energy Laboratory (NREL). It is found that on the efficiency front, with time, the PCE of the second generation a-Si solar cells increased steadily close to that of first generation solar cells. However, the serious stability problem impedes the wide use of thin film a-Si solar cells.

However, as shown in Fig. 2 (Conibeer et al. 2006), for a single p-n junction crystalline silicon solar cell, the maximum theoretical power conversion efficiency is only 29.8%, because of the incomplete utilization of high energy photons and the transmission of photons with less energy than the Si bandgap, which is called the Shockley-Queisser limit (S-Q limit) (Shockley and Queisser 1961). Consequently, the concept of “third generation” technology was proposed which aims to exceed the S-Q limit together with reducing the cost of Si-based solar cells. The third generation technology includes several approaches such as increasing the number of bandgaps (tandem solar cells), capturing carriers before thermalization (hot carrier solar cells), and multiple carrier pair generation per high energy photon (up-conversion solar cells) or single carrier pair generation with multiple low energy photons (down-conversion solar cells).

One of the promising methods is to form all Si-based tandem solar cell (or multijunction solar cell) by using a stack of Si-based solar cells, in which each cell has a bandgap that is optimized for the absorption of a certain spectral region. Figure 3 shows the schematic diagrams of two-junction and three-junction tandem solar cell structures. The efficiency limits for tandem solar cells can be theoretically computed considering: (a) a perfect balance between top and bottom cell current densities and (b) the idealized case, where the bottom cell absorbs all the light transmitted by the top cell. The theoretical efficiency of two-junction tandem solar cell with a conventional bulk Si p-n junction bottom cell increases to 42.5% when one additional solar cell with bandgap of 1.7 eV is used, and to 47.5% with two further solar cells with bandgap of 1.5 eV and 2.0 eV placed on top of the bulk Si cell (Meillaud et al. 2006). Since the bandgap of nc-Si dots with three-dimension



**Fig. 2** Loss processes in a standard solar cell:  
 (1) nonabsorption of below bandgap photons;  
 (2) lattice thermalization loss;  
 (3) and (4) junction and contact voltage losses;  
 (5) recombination loss  
 (Conibeer et al. 2006)  
 (Copyright 2006 Elsevier)

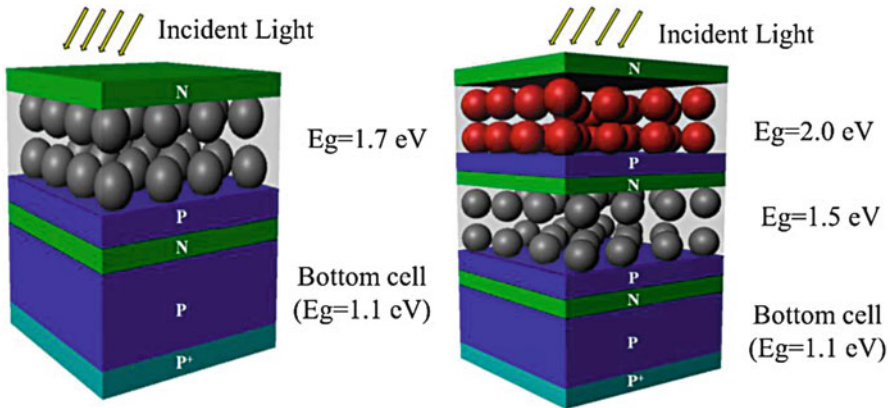
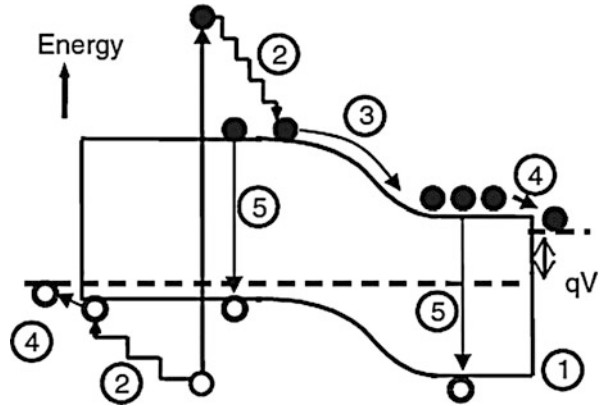


**Fig. 3** The schematic diagrams of two-junction and three-junction tandem solar cell structures  
 (Copyright by the authors)

confinement can be expanded compared to that of the bulk counterpart and the gap is tunable with changing the dot size based on the quantum size effect, it provides an effective way to adjust the energy band structures to get better spectral matching. Therefore, it looks like that one can prepare the nc-Si dots with various sizes to get the suitable bandgaps as expected by the theoretical model, and how to get the size-controllable nc-Si material becomes the key issue for its application in the PV devices.

So far, many approaches have been proposed to obtain nc-Si materials, including: (1) gas phase annealing Si nanoparticles synthesized by pulsed laser ablation (Hirasawa et al. 2006); (2) fabrication of nc-Si directly on ultrathin thermally grown SiO<sub>2</sub> layers by controlling the early stages of low pressure chemical vapor deposition (LPCVD) by using SiH<sub>4</sub> (Miyazaki et al. 2008); (3) implantation of Si<sup>+</sup> ions into SiO<sub>2</sub> films with subsequently high temperature annealing or by directly annealing the substoichiometric SiO<sub>x</sub> ( $x < 2$ ) films (Kanemitsu et al. 1996); (4) Ar<sup>+</sup>

laser or KrF excimer pulsed laser irradiation of ultrathin amorphous Si films (Xu et al. 2005). For example, Pavesi et al. prepared nc-Si by negative ion implantation into ultra-pure quartz substrates or into thermally grown silicon dioxide layers on Si substrates, followed by high-temperature thermal annealing (1100 °C for 1 h). The size of obtained nc-Si was about 3 nm (Pavesi et al. 2000). Park et al. fabricated a-Si nanoparticles in plasma enhanced chemical vapor deposition (PECVD) system by using nitrogen-diluted SiH<sub>4</sub> and pure N<sub>2</sub>. The size of a-Si nanoparticles could be controlled by the additional N<sub>2</sub> flow rate (Park et al. 2001). Besides, they fabricated nc-Si with high density of  $1.1 \times 10^{18} \text{ cm}^{-3}$  by using gas mixture of SiH<sub>4</sub> and NH<sub>3</sub> (Kim et al. 2006). Pai reported that by depositing Si-rich SiO<sub>x</sub> nanorod in nanoporous anodic aluminum oxide (AAO) membrane using PECVD, the spatially confined synthesis of nc-Si could be obtained after low-temperature annealing (Pai and Lin 2011).

However, precisely controlling the dot size of nc-Si is still a challenging topic nowadays. In order to control the dot size, the multilayered structures containing nc-Si dots were proposed and studied. For example, Cho et al. fabricated multiple alternate layers of amorphous silicon-rich oxide (SiO<sub>x</sub>,  $x < 2$ ) and stoichiometric SiO<sub>2</sub> by RF-magnetron sputtering. The nc-Si precipitated from the SiO<sub>x</sub> layers during subsequent high-temperature post-annealing (1100 °C for 1.5 h) in a nitrogen atmosphere to form nc-Si/SiO<sub>2</sub> multilayers (Cho et al. 2008).

This chapter mainly brings out an overview of the fabrication and photovoltaic properties of hetero-junction solar cell devices based on nc-Si multilayers, especially nc-Si/SiC system. Preparation and structural characterization of nc-Si/SiO<sub>2</sub> multilayers and nc-Si/SiC multilayers are introduced in section “[Fabrication of Size-Controllable Nanocrystalline Si-based Multilayers.](#)” Afterwards, section “[Size-Dependent Photovoltaic Properties of Hetero-junction Solar Cells Containing nc-Si/SiC Multilayers](#)” summarizes the optical and photovoltaic properties of size-controllable nc-Si-based solar cells and graded-sized nc-Si-based solar cells. In order to further enhance the PCE of the solar cells, section “[Light Harvesting and Enhanced Performance of nc-Si-based Hetero-junction Solar Cells Fabricated on Nanopatterned Substrates](#)” reports the current findings on light management process by using nanopatterned Si substrates. Finally, section “[Conclusion](#)” summarizes the whole chapter and gives the future perspectives. Moreover, other types of crystalline Si or nanostructure Si-based solar cells are discussed in ► [Chap. 22, “Polycrystalline Silicon Thin Film,”](#) and ► [Chap. 26, “Colloidal Silicon Quantum Dots and Solar Cells.”](#)

---

## **Fabrication of Size-Controllable Nanocrystalline Si-Based Multilayers**

As mentioned before, nc-Si-based materials have shown potential application prospect in third generation photovoltaic technology because they can efficiently match a broad solar spectrum via band engineering, due to the quantum size effect. By restricting the dimensions of silicon to less than Bohr radius of bulk crystalline

silicon (almost 5 nm), quantum confinement causes its effective bandgap to increase. If these dots are close together, carriers can tunnel between them to produce nc-Si superlattices. In such superlattices, nc-Si can be fabricated by using magnetron sputtering (Cho et al. 2008), e-beam evaporation (Martínez et al. 2011), plasma-enhanced chemical vapor deposition (PECVD) (Chen et al. 1992), and LPCVD (Kurokawa et al. 2006). In order to get size-controllable nc-Si superlattices to form minibands for carrier transfer, nc-Si dots are usually embedded in dielectric layers, such as  $\text{SiO}_2$ ,  $\text{Si}_3\text{N}_4$ , and SiC layers.

## The General Idea to Get Size-Controllable nc-Si Dots in Multilayered Structures

Chen's group first proposed the constrained crystallization principle in order to get high density size-controllable nc-Si/SiN multilayers by laser-induced crystallization technique (Chen et al. 1992). Similarly, as shown in Fig. 4, nc-Si/ $\text{SiO}_2$ , nc-Si/ $\text{Si}_3\text{N}_4$ , and nc-Si/SiC multilayers can be fabricated by excimer laser crystallization or thermal annealing of a-Si/ $\text{SiO}_2$ , a-Si/ $\text{Si}_3\text{N}_4$ , and a-Si/SiC stacked structures with ultrathin a-Si sublayers. During the annealing process, a-Si crystallization would be constrained by the interfaces between a-Si and the dielectric layers, to form nc-Si with uniform size. It was found that the size of formed nc-Si dots in the multilayers can be well controlled. Consequently, it provides an effective way to obtain size-controllable nc-Si-based multilayers by changing the a-Si sublayer thickness.

The molecular dynamics simulations based on the Tersoff potential was performed to investigate the crystallization mechanism of ultrathin a-Si film under laser irradiation with various conditions (Chen et al. 2012). It is interesting to find that the initial nucleation has occurred randomly in the whole a-Si film. The proper laser fluence leads to high crystallization ratio and high density nc-Si, and the nucleation rate is about  $3.59 \times 10^{-8}$  at 1800 K and increases to  $3.30 \times 10^{-7}$  at 2000 K. It is suggested that the low cooling rate of a-Si layer can enlarge the nc-Si to

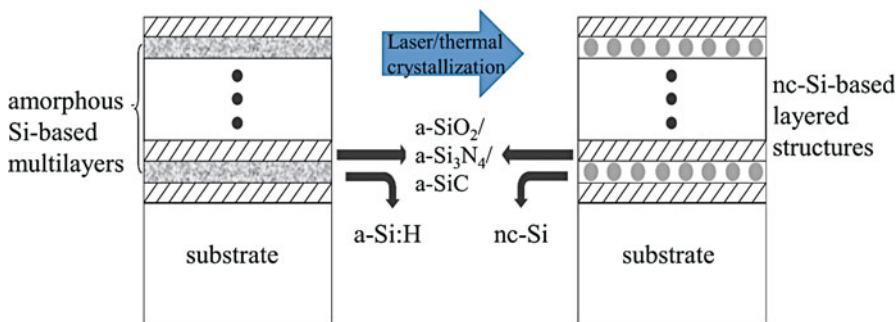


**Fig. 4** The schematic diagrams of the constrained crystallization principle (Copyright by the authors)

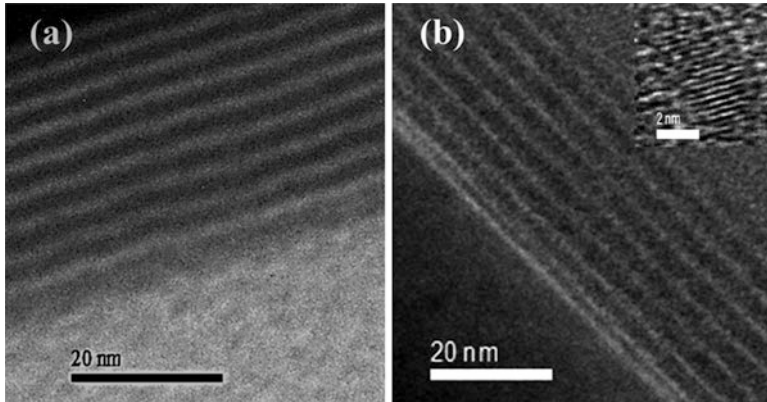
the size of 2–6 nm and enhance the crystallization ratio. The constraint effect of thickness of a-Si films on the crystallization of a-Si has been proved by molecular dynamics simulations. The theoretical simulation indicates that the constraint crystallization technique is appropriated to get the uniformly distributed monolayer nc-Si dots with the size less than 10 nm.

So far, it has been widely applied to fabricated size-controllable nc-Si by using the a-Si-based multilayers. For example, Zacharias et al. produced a-Si/SiO<sub>2</sub> multilayers by RF-magnetron sputtering and plasma oxidation. Nanosized Si crystals were formed after thermal annealing. In contrast to conventional one-step annealing crystallization technique, they used two-steps annealing process to get nc-Si, which included rapid thermal annealing (600–1000 °C for 40–60 s) and long-time thermal annealing (1050 °C for 15 min). It indicates that during the rapid thermal annealing process, a-Si will crystallize rapidly and the crystallization density will be high. After long time quasi-static thermal annealing, nc-Si with controllable size and good disparity can be obtained because of the growth and self-purification process (Zacharias et al. 1999). Later, Heitmann's group reported a relatively new approach for tight control of nc-Si dot size by using the phase separation of ultra SiO<sub>x</sub> layers with SiO<sub>x</sub>/SiO<sub>2</sub> multilayers, where  $1 \leq x \leq 2$  (Zacharias et al. 2002). The phase separation was a well-defined process in the formation of a-Si clusters in SiO<sub>2</sub> matrix at lower annealing temperature. Quantum confinement effect of nc-Si was investigated and room-temperature PL was observed. Moreover, the size of nc-Si could be controlled by the thickness and the x rate of SiO<sub>x</sub> layer (Li et al. 2002).

In a word, using different thin film techniques including magnetron sputtering, e-beam evaporation, and pulsed laser deposition (PLD), a-Si-base sandwich or multilayered structures with clear and abrupt interfaces can be successfully fabricated, such as a-Si/SiO<sub>2</sub>, a-Si/SiN<sub>x</sub>, and a-Si/SiC multilayers. After post-laser or thermal annealing process, size-controllable nc-Si will be obtained in initial ultrathin a-Si sublayers, which can be attributed to the constrained crystallization principle.

## Fabrication of nc-Si/SiO<sub>2</sub> Multilayers

The nc-Si/SiO<sub>2</sub> multilayers can be obtained by thermally annealing a-Si/SiO<sub>2</sub> stacked structure prepared in a conventional PECVD system with a RF of 13.56 MHz as shown in Fig. 5. During the deposition process, the RF power was kept at 50 W and the substrate temperature was fixed at 250 °C. The a-Si:H sublayers were deposited using a pure silane gas with a flow rate of 5 sccm for 15 s. Subsequently, in situ plasma oxidation was performed to form ultrathin SiO<sub>2</sub> sublayers using oxygen with flow rate of 20 sccm for 90 s. The thickness of a-Si:H sublayer and SiO<sub>2</sub> sublayer was designed to be 2.5 nm and 2 nm, respectively. These processes were alternatively changed and a SiO<sub>2</sub> lapping layer was deposited on the top surface of the film. After deposition, the as-deposited samples were first dehydrogenated at 450 °C and then annealed at 1000 °C both in N<sub>2</sub> ambient for 1 h (Zhang et al. 2014a).



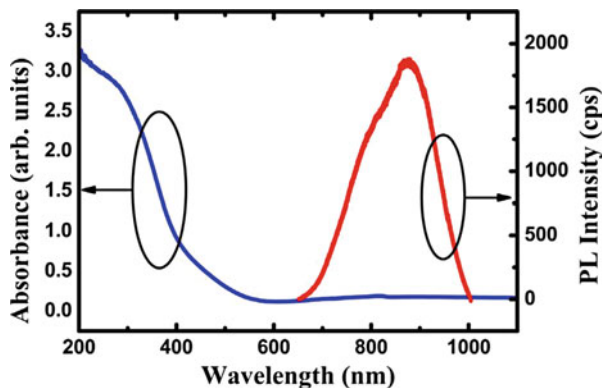
**Fig. 5** The cross-sectional TEM micrographs of (a) as-deposited a-Si/SiO<sub>2</sub> multilayers and (b) nc-Si/SiO<sub>2</sub> multilayers annealed at 1000 °C (Zhang et al. 2014b) (Copyright 2014 Elsevier)

Figure 5a and b shows the cross-sectional transmission electron microscopy (TEM) images of as-deposited and 1000 °C annealed Si/SiO<sub>2</sub> multilayers. The stacked layers are clearly identified in TEM images, and the periodic structures can be kept even after thermal annealing at high temperature as shown in Fig. 5b. The thickness of nc-Si and SiO<sub>2</sub> sublayer well agrees with the predesigned value. The formation of nc-Si dots are further verified by high resolution TEM image as given in the inset of Fig. 5b. It is shown that the formed nc-Si dot has a size of 2.5 nm in vertical (growth) direction with slightly larger lateral size.

Figure 6 is the optical absorbance spectrum of nc-Si/SiO<sub>2</sub> multilayers in the wavelength range of 200–1100 nm. It is shown that the absorbance is quite weak at the long wavelength region and the absorbance becomes strong when the wavelength is shorter than 600 nm. From absorbance spectrum, one can calculate the absorption coefficient and the optical bandgap can be deduced according to the Tauc's plot, which is 2.1 eV (Tauc et al. 1966). The large bandgap of nc-Si compared with that of bulk Si is expected due to the quantum confinement effect. An intense photoluminescence (PL) is observed at room temperature for nc-Si/SiO<sub>2</sub> multilayers under a 325 nm laser excitation. The PL spectrum is also given in Fig. 6, which shows a broad luminescence band centered at 870 nm (~1.4 eV). It is noticeable that there is a large stoke shift between the absorption edge and emission band as shown in Fig. 6, which suggests that the emission is mainly via the gap states instead of the band-to-band recombination of photo-excited electron-hole pairs within nc-Si (Zhang et al. 2014b). In addition, by controlling the dot size, the light absorption and optical bandgap of nc-Si/SiO<sub>2</sub> multilayers can be obviously shifted due to quantum confinement effect. In contrast, the light emission wavelength was almost unchanged. Qin attributed this visible light emission to the nc-Si/SiO<sub>2</sub> interfacial states (Qin et al. 1998).

The initial effort to get nc-Si-based solar cells was made by designing nc-Si/c-Si hetero-junction solar cells containing nc-Si/SiO<sub>2</sub> multilayers. Cho et al. fabricated

**Fig. 6** Absorbance and photoluminescence spectra of nc-Si/SiO<sub>2</sub> multilayers (Zhang et al. 2014b) (Copyright 2014 Elsevier)



a phosphorus-doped nc-Si/SiO<sub>2</sub> superlattice as an active layer on a p-type crystalline silicon substrate as a hetero-junction solar cell. Phosphorus-doped nc-Si/SiO<sub>2</sub> superlattices were fabricated by alternate deposition of a SiO<sub>2</sub> layer and a SiO<sub>x</sub> layer, using Si, SiO<sub>2</sub>, and P<sub>2</sub>O<sub>5</sub> as the targets in RF magnetron sputtering system. The dot size of nc-Si could be tunable as 3, 4, 5, and 8 nm with changing the x rate (Cho et al. 2008). It was demonstrated that the optical bandgap of the nc-Si/SiO<sub>2</sub> superlattice depended on the dot size. Temperature-dependent dark *I-V* measurements suggest that the carrier transport in the devices was controlled by recombination in the space-charge region. It was found that the IQE was very high in the short wavelength region for 3 nm nc-Si, while there was poorer response in the high energy region for the 8 nm nc-Si device. The spectral response wavelength was red shift from 500 nm to about 700 nm with increasing the size of nc-Si, which can be attributed to the quantum confinement effect (Park et al. 2009).

Furthermore, the prototype p-i-n solar cell device containing intrinsic nc-Si/SiO<sub>2</sub> multilayers was fabricated, which exhibit the photovoltaic properties with the PCE of 3.1%, preliminarily (Xu et al. 2014). This low PCE result is mainly due to the large band offset between Si and SiO<sub>2</sub>, which may deteriorate low carrier tunneling probability and deteriorate the performance of devices. Compared with SiO<sub>2</sub>, amorphous silicon carbide (a-SiC) has a lower bandgap, which is helpful for enhancing the carrier transport efficiency to improve the device performance. Hence, it is interesting to study the structural and physical properties of nc-Si embedded in amorphous SiC matrix.

## Fabrication of nc-Si/SiC Multilayers

Recently, nc-Si embedded in amorphous SiC host matrix (nc-Si/SiC) films have attracted much attention since they can be applied for many kinds of optoelectronic devices, such as the next generation of solar cells (Cheng et al. 2010) and light emitting devices (Chang et al. 2010). It was reported that the band offset both in conduction band and valence band for nc-Si/SiC superlattice is much lower



compared with other conventionally used dielectric materials (such as SiO<sub>2</sub> and Si<sub>3</sub>N<sub>4</sub>) (Jiang and Green 2006). Moreover, the band offset difference between the conduction band and valence band is quite small which is also helpful for the electrons and holes transport and in turn to improve the device performance.

In the previous work, Li prepared hydrogenated amorphous SiC (a-SiC:H) films and studied the influences of the gas ratio ( $R = [\text{CH}_4]/[\text{SiH}_4]$ ) on the structural and optical properties. It was found that optical bandgap was linearly proportional to carbon content in the films, and it could be controlled in a range of 1.8–2.4 eV by changing the gas ratio. The photosensitivity can be as high as  $10^4$  for as-deposited sample with optical bandgap of 1.96 eV (Li et al. 2012).

After thermal annealing process, a-SiC<sub>x</sub> was partly crystallized and the nc-Si/SiC superlattice was formed. By adjusting  $x$  and post-annealing temperature, the size of nc-Si can be controlled from 1.4 nm to 4.2 nm accordingly. Size-dependent EL was observed, and the EL intensity was higher for the sample containing small-sized nc-Si, which can be attributed to the quantum confinement effect. It was found that although the EL peak energy was as a function of the nc-Si size, the experimental results do not well match the effective mass approximation (EMA) model. This is because the infinite confined barrier potential is not a case in a real dielectric matrix, such as SiO<sub>2</sub>, Si<sub>3</sub>N<sub>4</sub>, and SiC. Then finite barrier potential will gain a decreased confinement energy, particularly for nc-Si embedded in SiC matrix. Rui adopted the theoretical model of quantum confinement effect based on the modified EMA with spherical nanocrystal dot and a finite barrier at the nc-Si/SiC interface to develop a modified EMA model (Rui et al. 2011). Considering the Coulomb effect and the correlation energy terms, the optical bandgap ( $E_g^{opt}$ ) can be expressed as:

$$E_g^{opt} = 1.12 \text{ (eV)} + \Delta E_{e,h,\text{reduced}} - \frac{0.4512}{R} - 0.003394 \text{ (eV)} \quad (1)$$

in which, 1.12 is the bandgap of crystalline silicon,  $R$  is the average diameter of nc-Si, 0.4512 is the Coulomb coefficient, 0.003394 is the correlation energy terms, and  $\Delta E_{e,h,\text{reduced}}$  is the decreased confinement energy related with the barrier height in conduction and valence band. Figure 7 shows the EL peak energy of nc-Si as a function of dot size. The experimental data are shown by filled circles. The solid line and dot line represents the theoretical results based on EMA model with infinite and finite barrier potential, respectively. It is shown that the energy gap in finite barrier potential model is smaller than that in an infinite barrier potential model. From the experimental data, one can deduce and well fit the barrier height in conduction and valence band, which is 0.4 and 0.8 eV in our case, respectively. Therefore, the energy band diagram is shown in the inset of Fig. 7.

In order to get high density size-controllable nc-Si/SiC superlattice for photovoltaic application, a-Si:H/SiC multilayers were first prepared in conventional PECVD system. The thickness of a-Si:H was designed to be 4 nm and the thickness of amorphous SiC layer was 2 nm. Due to the constrained crystallization principle, nc-Si with controllable size were achieved by annealing the as-deposited samples

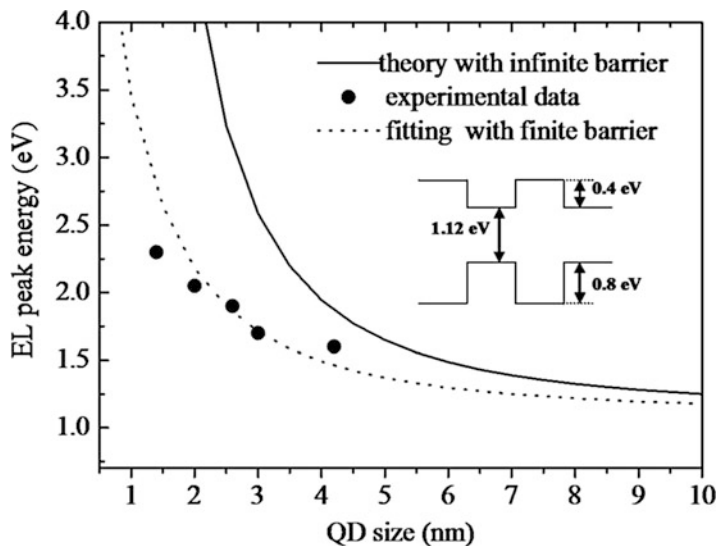
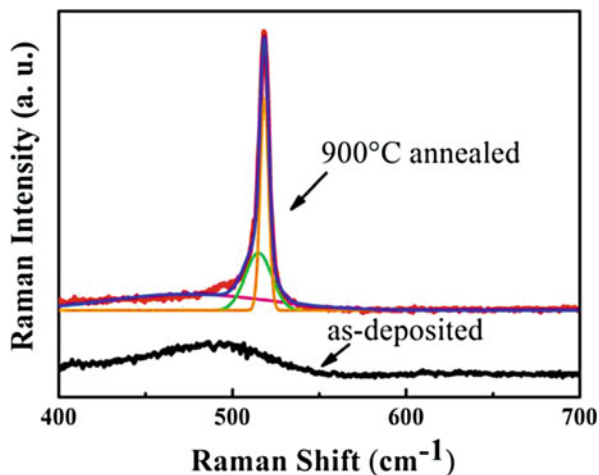


**Fig. 7** The EL peak energy of nc-Si as a function of dot size. Inset is the energy band diagram of nc-Si:SiC superlattice (Rui et al. 2011) (Reproduced from Journal of Applied Physics 110, 064322 (2011), with the permission of AIP Publishing.)

**Fig. 8** Raman spectra of as-deposited Si/SiC multilayers and 900 °C annealed nc-Si/SiC multilayers (Cao et al. 2014) (Copyright by the authors)



at 900 °C for 1 h. Figure 8 shows the Raman spectra of as-deposited and 900 °C annealed multilayered samples. It is noted that only one broad band centered at  $480\text{ cm}^{-1}$  exists in the as-deposited sample, which is attributed to the transverse optical (TO) mode of amorphous Si-Si bonds. However, an intense peak at  $517\text{ cm}^{-1}$  associated with crystallized Si TO mode appears for 900 °C annealed sample, which indicates that the amorphous Si layers have been crystallized to form nanocrystallized Si. In order to estimate the crystallinity ratio and size of nc-Si, the



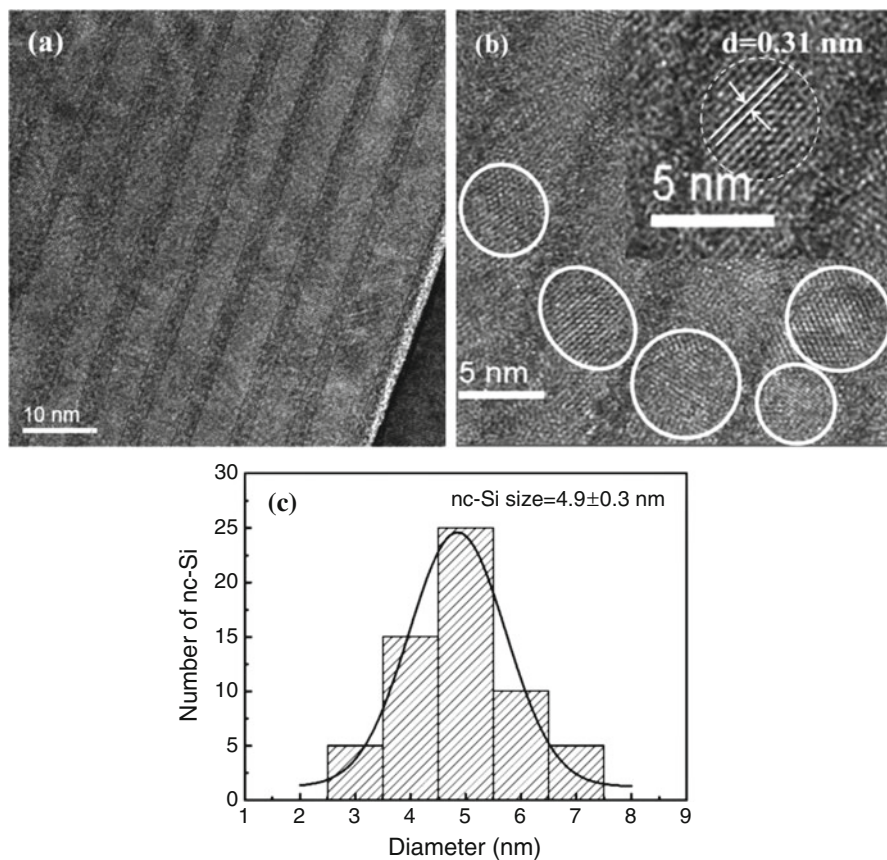


**Fig. 9** (a) Cross-sectional TEM image of nc-Si/SiC multilayers; (b) High-resolution TEM image; (c) Size distribution of nc-Si (Copyright by the authors)

Raman spectrum was fitted via the Gaussian deconvolution by three components, which is located at  $480\text{ cm}^{-1}$ ,  $510\text{ cm}^{-1}$ , and  $520\text{ cm}^{-1}$ . The crystallinity ratio ( $X_c$ ) is figured out as 49.5% by integrated Gaussian peaks of  $520\text{ cm}^{-1}$  and  $480\text{ cm}^{-1}$ . The average size of nc-Si is about 4.8 nm, according to the phonon confinement model, which indicates the formation of nc-Si.

The structural change of the nc-Si/SiC multilayers after annealing was characterized by the cross-sectional TEM measurements. Figure 9a shows the cross-sectional TEM image of nc-Si/SiC multilayers after  $900\text{ }^\circ\text{C}$  annealing. The layered structures and smooth interfaces can be clearly identified. The formation of nc-Si in a-Si layers can be identified in the high-resolution TEM image. As indicated in the inset of Fig. 9b, the crystalline interplanar spacing is 0.31 nm of formed Si QDs, which suggests the Si (111) crystalline faces. Figure 9c shows the nc-Si size distribution obtained from TEM image. It is found that the size of formed nc-Si is  $4.9 \pm 0.3$  nm.

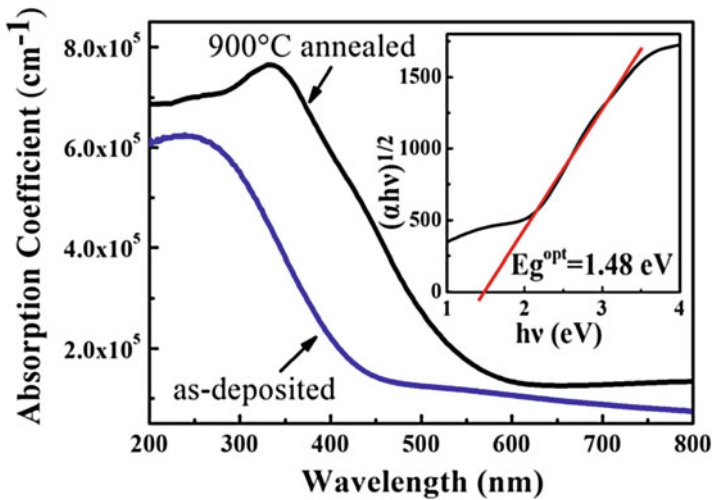


**Fig. 10** Optical absorption coefficient spectra of as-deposited Si/SiC multilayers and 900 °C annealed nc-Si/SiC multilayers. The inset is the  $(\alpha h\nu)^{1/2} \sim h\nu$  relationship of 900 °C annealed sample (Cao et al. 2014) (Copyright by the authors)

The optical properties of Si/SiC multilayers before and after annealing are studied by measuring the optical transmission spectra and reflection spectra in the spectral range of 200–800 nm. The optical absorption coefficient  $\alpha$  is calculated and given in Fig. 10. It is found that the optical absorption of as-deposited a-Si/SiC multilayers is quite high which is above  $10^5 \text{ cm}^{-1}$  when the wavelength is less than 400 nm. However, the absorption coefficient of 900 °C annealed nc-Si/SiC multilayers is much higher in the whole visible light region (300–800 nm), which indicates that the nc-Si/SiC multilayers can strongly absorb the visible light photons, especially in short-wavelength range. Based on the Tauc's model, the optical band gap of nc-Si/SiC multilayers can be deduced from the linear fitting of  $(\alpha h\nu)^{1/2} \sim h\nu$  relationship, as shown in the inset of Fig. 10. The deduced optical bandgap of our nc-Si/SiC multilayers after 900 °C annealing is 1.48 eV, which is blue shifted compared to that of crystallized Si, which can be attributed to the quantum size effect (Cao et al. 2014). According to formula (1), the estimated bandgap of nc-Si with dot size of 4–5 nm is 1.4–1.5 eV, which well agrees with the experimental result.

### Size-Dependent Photovoltaic Properties of Hetero-junction Solar Cells Containing nc-Si/SiC Multilayers

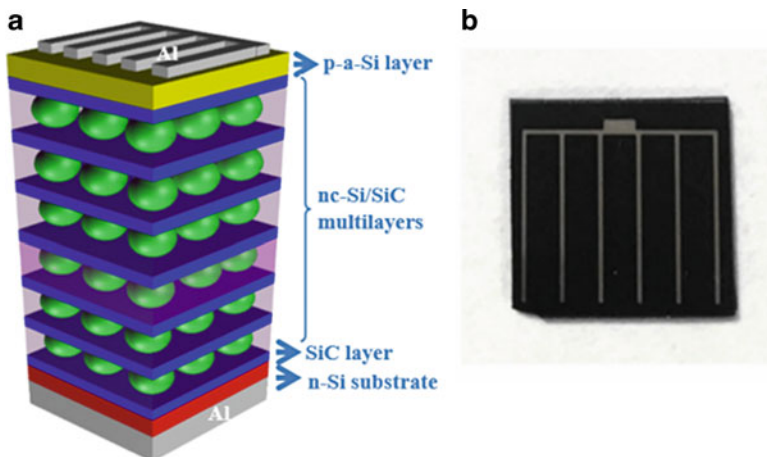
Based on the structural and optical properties of prepared Si/SiC multilayers, the p-i-n device structures containing phosphorus-doped a-Si:H and nc-Si/SiC (or a-Si/SiC) multilayers on p-Si substrates were fabricated.

## Photovoltaic Properties of Hetero-junction Solar Cells Containing nc-Si/SiC Multilayers

The prototype solar cell devices were fabricated by evaporating the Al strip-shaped electrode on the p-i-n structures, and the schematic diagram of the device structures is shown in Fig. 11a. Figure 11b is the photo of solar cell device and the cell area is about  $0.8 \text{ cm}^2$ .

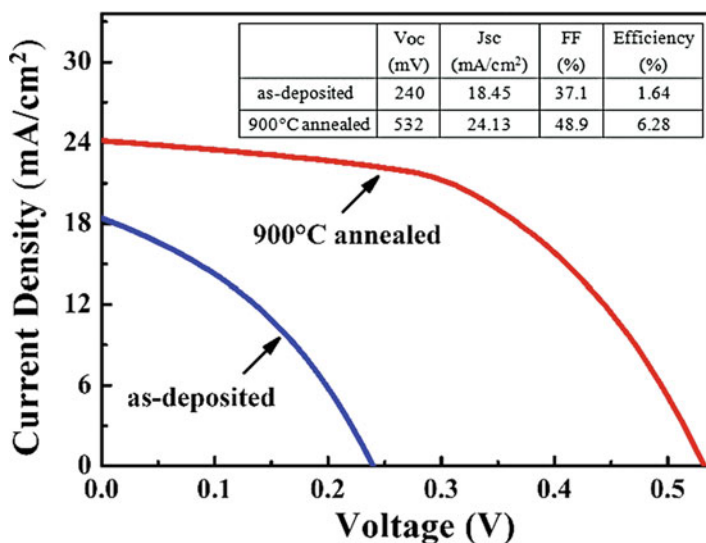
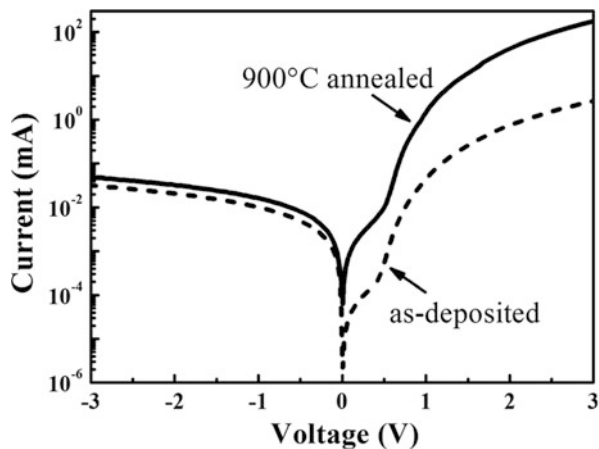
Figure 12 shows the current-voltage ( $I$ - $V$ ) relationships of p-i-n structures with and without annealing. The rectification characteristics are clearly observed for both samples which indicate that the p-i-n structures are well formed by the present approach. Compared with that of as-deposited sample, the reverse current of annealed sample is in the same order ( $\sim 10^{-2}$  mA at  $-3$  V) while the forward current is increased by almost two orders of magnitude (from  $10^0$  mA to  $10^2$  mA at  $+3$  V), which indicates that the rectification ratio of  $900^\circ\text{C}$  annealed p-i-n structure reaches to  $2 \times 10^3$  at the applied voltage  $V = \pm 3$  V. The increase in the forward current of annealed p-i-n sample can be attributed to the increase of the conductivity in crystallized Si layers.

Figure 13 is the AM 1.5 ( $100 \text{ mW/cm}^2$ ) illuminated  $I$ - $V$  curves of solar cells based on as-deposited and  $900^\circ\text{C}$  annealed p-i-n structures. It is shown that the open circuit voltage ( $V_{oc}$ ), short circuit current density ( $J_{sc}$ ), and fill factor (FF) for device based on as-deposited p-i-n structure is 240 mV,  $18.45 \text{ mA/cm}^2$ , and 37.1%, respectively. The PCE is about 1.64%. However, the device performance of p-i-n structure containing nc-Si/SiC multilayers after annealing is significantly enhanced. The  $V_{oc}$  is increased to 532 mV and the  $J_{sc}$  is increased to  $24.13 \text{ mA/cm}^2$  with the FF of 48.9% and the PCE reaches to 6.28%. The increased  $V_{oc}$  of the



**Fig. 11** (a) The schematic diagram of the hetero-junction solar cells containing nc-Si/SiC multilayers; (b) the photo of solar cell device (Copyright by the authors)

**Fig. 12** Current-voltage ( $I$ - $V$ ) relationships of p-i-n structures with and without annealing (Cao et al. 2014) (Copyright by the authors)



**Fig. 13** One-sun-illuminated  $I$ - $V$  curves of p-i-n structures with and without annealing (Cao et al. 2014) (Copyright by the authors)

annealed cell compared to that of as-deposited one can be attributed to the increased film quality as well as the improved p-i-n structure after annealing. For as-deposited sample containing a-Si: H/SiC multilayers, high density of defect states, such as dangling bonds and interface states between amorphous Si and SiC layers, may lead to the pinning of the Fermi levels which results in the low  $V_{oc}$ . After high temperature annealing, the film quality can be significantly improved, which is helpful for increasing  $V_{oc}$  by reducing the defect states.

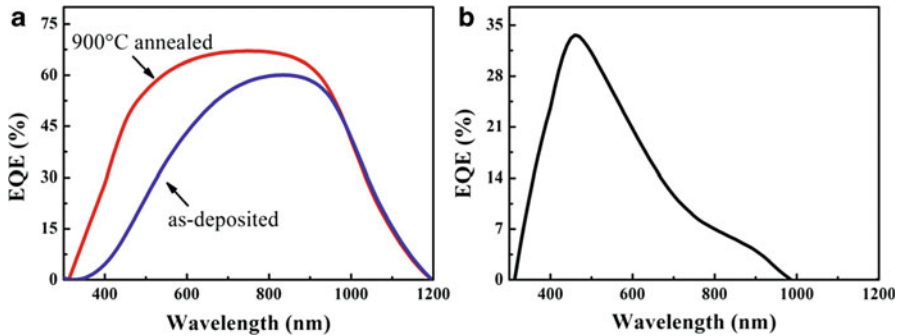


**Fig. 14** (a) The EQE results of p-i-n structures with and without annealing; (b) The EQE results of p-i-n solar cell containing nc-Si/SiC multilayers by subtracting the EQE of cell containing as-deposited one (Cao et al. 2014) (Copyright by the authors)

Moreover, post-annealing can also improve the p-i-n structure. As shown in Fig. 12, the obvious rectification behavior can be observed in the annealed p-i-n structure. The shunt resistance of cell device is increased from  $56 \Omega$  to  $108 \Omega$  after annealing, which also indicates the improved p-i-n structure after annealing, due to the improved interface quality and the enhanced doping effect in n-a-Si layer by thermally activating dopants. The improvement in the cell performance for annealed sample can be attributed to the formation of nc-Si after  $900^\circ\text{C}$  annealing, which enhances the photon-generated carrier separation and carrier transportation properties due to the improved electronic property of p-i-n structure.

In order to further understand the role of nc-Si in the present cell device, we measured the external quantum efficiency (EQE) of p-i-n device sample and compared with that of as-deposited one. Figure 14a is the EQE of p-i-n device structures containing as-deposited and  $900^\circ\text{C}$  annealed Si/SiC multilayers in the spectral range of 300–1200 nm. It is found that in the long wavelength region, the EQE results for two cells are almost the same. However, the EQE is significantly improved in the whole visible light region (300–900 nm), which can be attributed to the contribution of the formed nc-Si in annealed sample. In our cell devices, part of the carriers was generated from Si substrates with the incident photons with long wavelength. They contributed to the  $J_{sc}$  both in as-deposited and annealed cells. In order to further investigate the contribution of nc-Si, the EQE result of p-i-n solar cell containing nc-Si/SiC multilayers by subtracting the EQE of cell containing as-deposited one was investigated. As shown in Fig. 14b, the improved EQE is located in the spectral range of 300–1000 nm with the peak at 500 nm. As mentioned before, the optical bandgap of the nc-Si/SiC multilayers in our case is about 1.5 eV ( $\sim 820$  nm), the incident photons with high energy can be effectively absorbed by nc-Si to generate the electron-hole pairs which are separated by the built-in field in p-i-n structure. The electrons and holes can be

effectively collected in annealed sample due to its improved carrier transportation properties as shown in Fig. 12.

### Size-Dependent Optical and Photovoltaic Properties of nc-Si/SiC Multilayers

Size-controllable nc-Si/SiC multilayers were formed by thermal annealing the a-Si/SiC multilayers. During the deposition process, the thickness of a-Si:H was designed to be varied from 2 nm to 8 nm, and thickness of amorphous SiC layer was kept at 2 nm. Figure 15a–c shows the high-resolution TEM images of different sized nc-Si/SiC multilayers, which exhibit the formation of nc-Si. The crystallization of nc-Si was well constrained by the interfaces between a-Si and SiC layers and the size of nc-Si is controlled about 2.5 nm, 5.0 nm, and 9.0 nm, respectively. The absorption properties of nc-Si/SiC multilayers with various sizes were studied by measuring the optical transmission spectra and reflection spectra in the spectral range of 200–800 nm. The optical

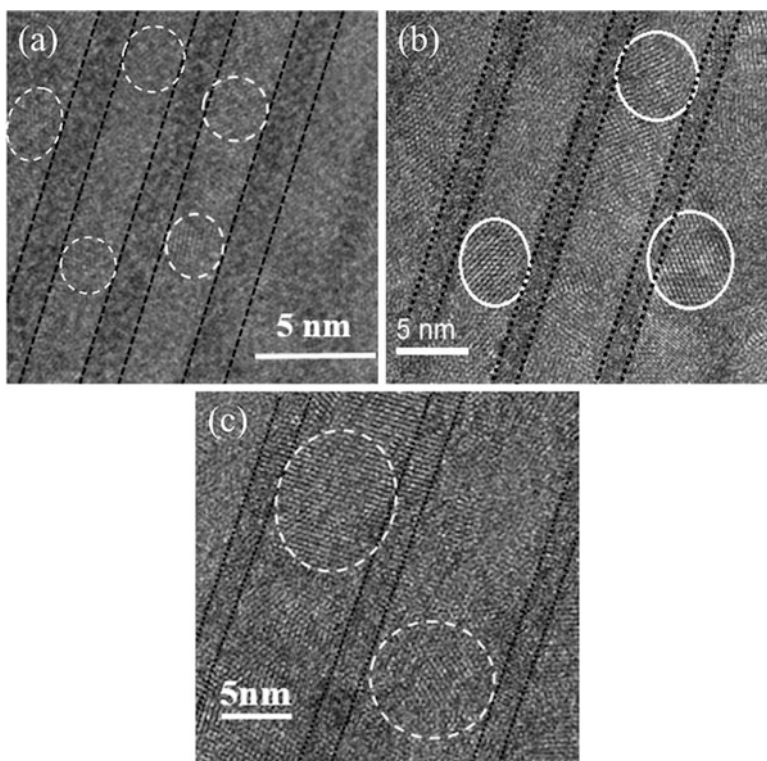
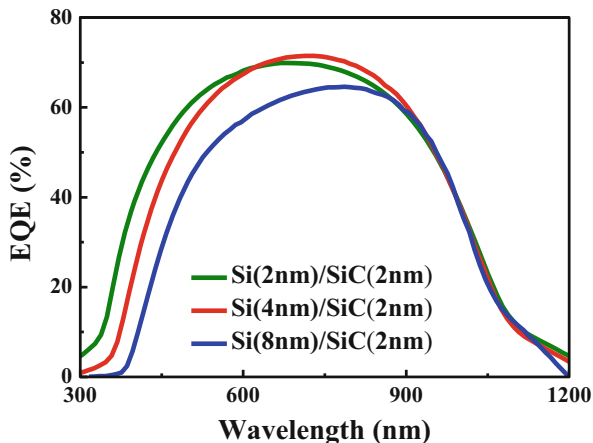


**Fig. 15** The cross-sectional TEM images of (a) nc-Si (2 nm)/SiC (2 nm) multilayers; (b) nc-Si (4 nm)/SiC (2 nm) multilayers; (c) nc-Si (8 nm)/SiC (2 nm) multilayers



**Fig. 16** The EQE spectra of hetero-junction solar cells containing controllable sized-nc-Si/SiC multilayers



absorption coefficient  $\alpha$  is calculated. Based on the Tauc's plot, the optical bandgap of nc-Si/SiC multilayers can be deduced from the linear fitting of  $(\alpha h\nu)^{1/2} \sim h\nu$  relationship. The deduced optical bandgap of nc-Si/SiC multilayers is 2.0, 1.5, and 1.2 eV, respectively, which well agrees with the deduced result of the modified EMA model, as mentioned before.

Hetero-junction solar cells containing controllable sized-nc-Si/SiC multilayers were fabricated and the EQE spectra were collected by the spectral response measurement system in the wavelength range of 300–1200 nm. Figure 16 is the EQE of hetero-junction solar cells. It is clearly shown that the EQE for nc-Si/SiC multilayers is gradually shifted to the short wavelength side with reducing the dot size from 8 nm to 2 nm. As discussed before, the improved EQE is located in the spectral range of 400–800 nm with the peak at 500 nm, which can be attributed to the formation of nc-Si. So the size-dependent EQE results can be explained in terms of the enlarged optical bandgap on account of the quantum size effect. In our case, the PCE of hetero-junction solar cells is 6.19%, 6.28%, and 5.38%, as the size of nc-Si from 2, 4, 8 nm.

Optical and photoluminescence properties of controllable sized-nc-Si/SiC multilayers were studied by Yamada and his coworkers. Kurokawa successfully prepared nc-Si/SiC multilayers by the thermal annealing of stoichiometric hydrogenated amorphous silicon carbide (a-SiC:H)/silicon-rich hydrogenated amorphous silicon carbide (a-Si<sub>1-x</sub>C<sub>x</sub>) multilayers (Kurokawa et al. 2006). By using hydrogen plasma treatment (HPT), enhanced photoluminescence of nc-Si was observed. In contrast with nc-Si/SiO<sub>2</sub> multilayers, nc-Si embedded in SiC matrix showed size-dependent photoluminescence. The luminescence peaks shifted to shorter wavelength with decreasing the diameter of nc-Si (Kurokawa et al. 2007). Furthermore, in order to suppress the crystallization of a-SiC phase during the high temperature annealing process, O-containing nc-Si superlattices were prepared and the dark conductivity was reduced, suggesting that the leakage in barrier layers was suppressed and the carrier transport through nc-Si became predominant (Kurokawa et al. 2010).

## Broadband Spectral Response for Hetero-junction Solar Cell Containing Graded-Sized nc-Si/SiC Multilayers

As before, hetero-junction solar cells containing controllable sized-nc-Si/SiC multilayers were fabricated, and size-dependent optical and photovoltaic properties were demonstrated. However, up to now, the used multilayers containing nc-Si with fixed size in one cell device and in turn the corresponding bandgap and spectral response is limited in a certain wavelength range. To further expand the spectral response range and improve the cell performance, Cao proposed a novel device structure by using graded-sized nc-Si instead of the fixed-sized one in the same multilayered structure to form hetero-junction solar cells to realize the wide and efficient spectral response and improve the device performance (Cao et al. 2015). In order to get graded-sized nc-Si/SiC stacked structures, the graded thickness a-Si:H/SiC multilayers were fabricated with a-Si sublayers thickness of 8 nm, 4 nm, and 2 nm from the bottom to the top. Figure 17a is the cross-sectional TEM image of as-deposited graded sized a-Si (8, 4, 2 nm)/a-SiC (2 nm) multilayers. The layered structures and smooth interfaces of Si/SiC can be clearly identified. The thickness of a-SiC sublayers is 1.95 nm and the thickness of a-Si sublayers is 8.4 nm, 4.3 nm, and 2.1 nm, respectively. Figure 17b is the cross-sectional TEM image of the sample annealing at 900 °C, which exhibits the formed nc-Si after annealing. The layered structures are well kept and the interfaces are still smooth. The formation of nc-Si with different size in a-Si layers can be identified.

Figure 18a is the EQE of p-i-n device structures containing graded-sized nc-Si/SiC multilayers together with the periodic ones. It is interesting to find that the EQE of solar cell containing graded-sized nc-Si/SiC multilayers is obviously enhanced in a wide spectral range (400–1200 nm), compared with that of the conventional

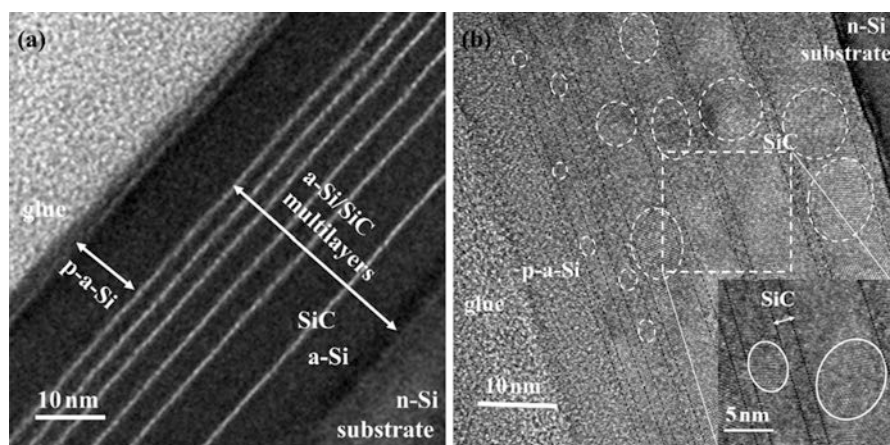
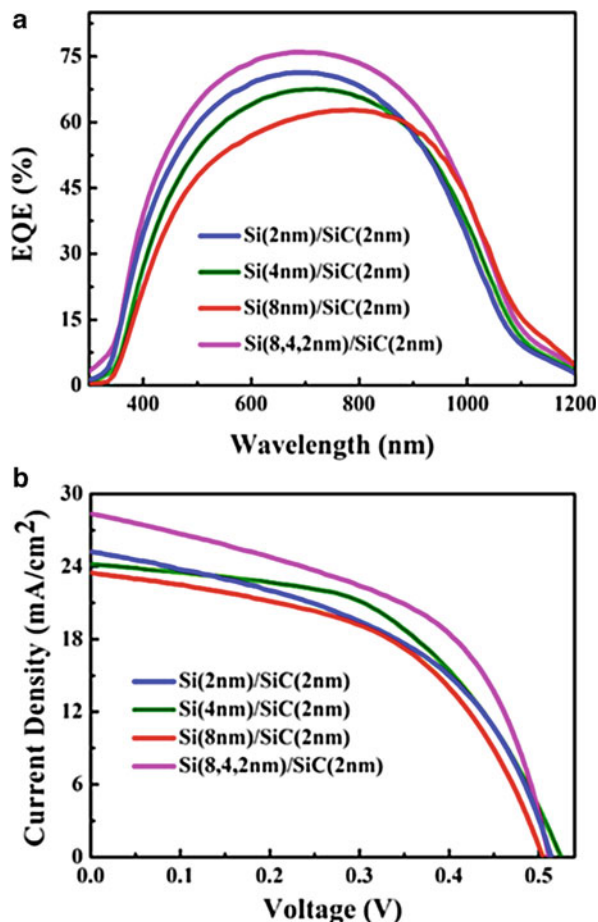


**Fig. 17** Cross-sectional TEM image of (a) as-deposited graded-sized Si/SiC multilayers; (b) 900 °C annealed graded-sized nc-Si/SiC multilayers (Cao et al. 2015) (Copyright 2015 Royal Society of Chemistry)



**Fig. 18** (a) EQE spectra of solar cells containing graded-sized nc-Si/SiC and nc-Si/SiC periodic multilayers; (b) The measured illuminated  $J-V$  characteristics of solar cells containing graded-sized nc-Si/SiC and nc-Si/SiC periodic multilayers (Cao et al. 2015) (Copyright 2015 Royal Society of Chemistry)



periodic nc-Si/SiC multilayers-based solar cells. At the wavelength of 500 nm, the EQE is increased from 47.6% to 64.4%. It is because that the graded-sized nc-Si-based cell has the graded optical bandgap from the top to bottom, the incident solar photons with short wavelength (high energy) can be first absorbed by the smaller-sized nc-Si, and the photons wavelength (low energy) will penetrate the top layers and efficiently be absorbed by the following layers with gradually enlarged nc-Si and Si substrate, which effectively reduce the heat loss and enhance the optical absorption as revealed by our results. It is worth noting that even at the wavelength of 300 nm, the EQE is also increased from 1.3% to 3.5%, compared with that of the conventional periodic nc-Si/SiC multilayers-based cell. As a consequence, the calculated short circuit current density is improved due to the more incident photons can be utilized to photo-electric conversion. Figure 18b shows the AM 1.5G (100 mW/cm<sup>2</sup>) illuminated current density-voltage ( $J-V$ ) characteristics of p-a-Si/(nc-Si/SiC) multilayers/n-Si hetero-junction solar cells. It is found that the cell

**Table 1** The summarized photovoltaic parameters of cell devices (Cao et al. 2015) (Copyright 2015 Royal Society of Chemistry)

	$V_{oc}$ (mV)	$J_{sc}$ (mA/cm <sup>2</sup> )	FF (%)	PCE (%)
Si(2nm)/SiC(2nm)	513	25.23	47.8	6.19
Si(4nm)/SiC(2nm)	502	24.18	52.1	6.32
Si(8nm)/SiC(2nm)	504	23.43	51.2	6.05
Si(8,4,2nm)/SiC(2nm)	510	28.36	51.5	7.15

containing graded-sized nc-Si/SiC multilayers has higher short current than the periodic ones, as expected by the EQE spectra, while almost the same open circuit voltage and fill factor. As given in Table 1, the cell containing graded-sized nc-Si (8, 4, 2 nm)/SiC(2 nm) multilayers has a  $V_{oc}$  of 510 mV, a  $J_{sc}$  of 28.36 mA/cm<sup>2</sup>, a fill factor of 51.5%, and a PCE of 7.45%.

### Study of Fabrication and Photovoltaic Properties of All-nc-Si-Based Solar Cells

Usually, nc-Si-based hetero-junction solar cells are all fabricated on c-Si substrates to get the observable efficiency. As a result, most of the light in this type of solar cell devices is absorbed in the Si substrates, which has been revealed in the EQE results. The role of nc-Si in the solar cells is still not clear enough. Wurfl et al. made the initial effort to fabricate p-i-n structures containing nc-Si by sputtering SiO<sub>2</sub>/SRO multilayers onto quartz substrates with in-situ boron (B) and phosphorous (P) doping and then 1100 °C annealing. Al electrodes were evaporated on the top of B-doped layer and the bottom of P-doped layer to obtain the all-nc-Si-based solar cell device with area of 2.2 mm<sup>2</sup>. The device showed a rectifying behavior with the  $V_{oc}$  of 492 mV under a simulated AM 1.5 illumination. A circuit model was then proposed to explain the observed  $I$ - $V$  characteristics (Wurfl et al. 2012). Löper's group present a novel device structure containing nc-Si/SiC superlattice but without any c-Si for the electrically active parts, in order to clearly investigate the properties of nc-Si-based device alone. In this device structure, the c-Si substrate was locally removed by chemical etching for full flexibility regarding the electron and hole selective contacts. This enabled large-area rear side access to the nc-Si layer and represents a nanocrystalline membrane fully accessible from both sides (Löper et al. 2012). The  $V_{oc}$  was 282 mV and the  $J_{sc}$  was 0.339 mA/cm<sup>2</sup>. Due to this low value, only 6.8% of the optically generated current was collected under short circuit conditions. It shows that besides the optimization of the effective band gap of the material, special emphasis on the electronic quality is to be given in future material development (Löper et al. 2013). Yamada et al. fabricated the solar cell structure of n<sup>++</sup>-type poly silicon/nondoped (O-containing nc-Si/SiC multilayers)/p-type a-Si/Al electrode on a quartz substrate and successfully observed the photovoltaic properties (Yamada et al. 2010). Then they added a niobium-doped titanium dioxide (TiO<sub>2</sub>:Nb) barrier layer to reduce the phosphorous diffusion and get the improved photo-generated carrier

collection in the nc-Si layer. As a result, The  $J_{sc}$  of the solar cell with the diffusion barrier layer was significantly improved to  $1.6 \text{ mA/cm}^2$  without any degradation of open circuit voltage and fill factor (Yamada et al. 2013).

---

## Light Harvesting and Enhanced Performance of nc-Si-Based Hetero-junction Solar Cells Fabricated on Nanopatterned Substrates

As discussed above, a p-i-n device structure was proposed, in which ultrathin nc-Si/SiC multilayers were used as intrinsic layer embedded in n-a-Si and p-type crystalline Si substrate. It was found that the improvement in EQE result for annealed cell device can be attributed to the formation of nc-Si which enhanced the absorption of incident photons, especially in the short wavelength range and the carrier transport process. Size-dependent optical and photovoltaic properties were demonstrated. Moreover, a novel device structure containing graded-sized nc-Si/SiC multilayers was proposed to get enhanced broadband spectral response and energy conversion efficiency. However, the ultrathin nc-Si layers with the total thickness around several ten to hundred nanometers will result in a poor optical absorption. On the other hand, high density of surface and interface states introduced by increasing film thickness (or periodicity of multilayers) will also deteriorate the cell performance. Therefore, it is necessary to seek an appropriate way to reduce the reflection and enhance the optical absorption of ultrathin nc-Si-based multilayers in a wide spectral range.

## Preparation of Nanopatterned Si Structures for nc-Si-Based Solar Cells

Light management is currently an interesting topic in optoelectronic devices which is helpful for improving the device performance of thin film solar cells. Up to now, many kinds of Si nanostructures, such as Si nanopillars, Si nanoholes, and Si nanocones, were fabricated to realize the broadband antireflection and light-harvesting properties. For example, Zhu fabricated Si nanocone structures and found that the absorption can be obviously enhanced to 94% (Zhu et al. 2010). Jin and Liu fabricated the mixed Si nanostructures with nanopores and nanopillars by means of deep ion-reactive etching (DRIE) process. In the visible wavelength range (300–800 nm), the diffusion reflection can be as low as 2.2% (Jin and Liu 2012). Nanosphere lithography technique was also developed to prepare periodically nanopatterned Si structures containing the 2D nanocone-like arrays by using a monolayer of polystyrene (PS) nanosphere array as a mask (Lu et al. 2015).

The preparation procedures can be described as follows: First of all, a monolayer of PS nanospheres was coated on the c-Si wafer by self-assembly technique. The diameters of the nanospheres were selected as 220 nm and 300 nm to form different periodicities. With the monolayer of nanospheres as a mask, the Si wafer was etched

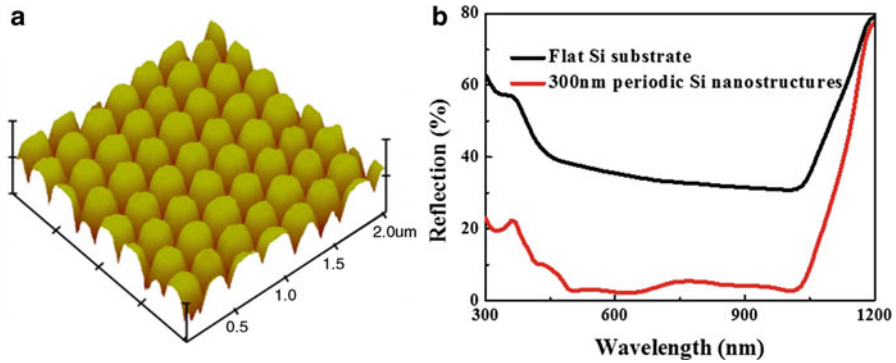


**Fig. 19** (a) AFM 3D image of formed 300 nm periodic Si nanostructures; (b) the reflection spectra of the flat Si substrate and the 300 nm periodic Si nanostructures (Lu et al. 2015) (Copyright 2015 Elsevier)

in the conventional reactive ion etching (RIE) system. The flow rate of  $\text{CF}_4$  gas was 30 sccm and the RF power was kept at 50 W during the etching process. After removing the remaining PS nanospheres in the tetrahydrofuran (THF) solution, the periodically nanopatterned Si structures were obtained. Figure 19a shows the AFM 3D image of formed 300 nm periodic Si nanostructures. The ordered and hexagonal-close-packed Si nanocone-shaped structures can be clearly identified in the scanning area ( $2 \mu\text{m} \times 2 \mu\text{m}$ ), and the periodicity of the formed Si nanostructures is consistent with the size of nanospheres. Figure 19b is the reflection spectra of 300 nm periodic Si nanostructures together with the flat Si substrate. By forming the periodic Si nanostructures, the good antireflection characteristics can be observed. According to the Fresnel theory, the reflection at the interface of two media is dominated by the difference between the refractive index. When it comes to the reflection of a textured surface, the effective refractive index is used as below:

$$\sum_{i=1}^k f_i \frac{(n_i^2 - n^2)}{(n_i^2 + 2n^2)} = 0 \quad (2)$$

where  $n$ ,  $f_i$ , and  $n_i$  is the effective refractive index, the filling factor, and the refractive index of the materials. The nanocone-shaped nanostructures can be considered as the mixed material of Si and air, and the gradually changing occupied area of Si from the top to the bottom of the cones is leading to a gradually changing refractive index. The reduced reflection in the broad wavelength range can be attributed to the formation of the gradually changing refractive index layer between air and Si. Moreover, since the size of the formed Si nanostructures in our case is about several hundred nanometers, which is comparable to the wavelength of the incident light, a strong light scattering occurs according to the wave optics. Consequently, the normal incident light changes its direction and the optical path in the absorption layer increases obviously.

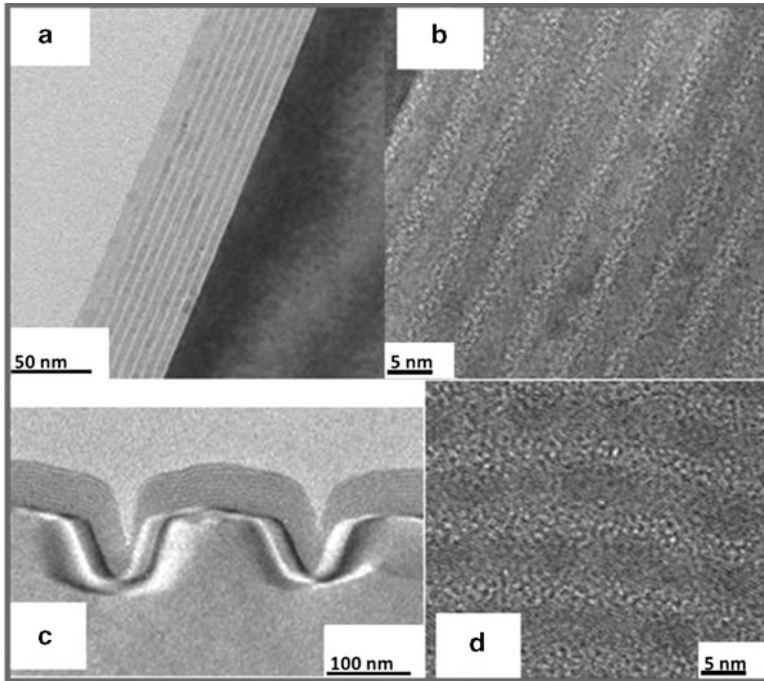


**Fig. 20** (a) The cross-sectional TEM image of nc-Si/SiO<sub>2</sub> multilayers on flat Si substrate; (b) high-resolution TEM image of nc-Si/SiO<sub>2</sub> multilayers; (c) cross-sectional TEM image of nc-Si/SiO<sub>2</sub> multilayers deposited on nanopatterned substrate; (d) high-resolution TEM image of nc-Si in nanopatterned sample (Xu et al. 2014) (Copyright 2014 John Wiley & Sons, Inc.)

Subsequently, nc-Si/SiO<sub>2</sub> multilayers were deposited on both the flat and the nanopatterned Si substrates by using the methods mentioned before, to obtain hetero-junction solar cells (Xu et al. 2014). Figure 20a is the cross-sectional TEM image of nc-Si/SiO<sub>2</sub> multilayers on flat Si substrate, the well-defined periodic structures can be identified, and the thickness is about 4 nm and 2.3 nm for nc-Si and SiO<sub>2</sub> sublayers, respectively. From the high-resolution TEM image as shown in Fig. 20b, the crystallized nc-Si can be clearly seen, and the size is about 4 nm, which is in agreement with the thickness of amorphous Si sub-layer. Figure 20c shows the cross-sectional TEM image of nc-Si/SiO<sub>2</sub> multilayers deposited on nanopatterned substrate. It is shown that the stacked structures are still kept on the nanopatterned substrates. The formation of nc-Si can be clearly identified in the high-resolution TEM as given in Fig. 20d.

Figure 21 shows the EQE results of both solar cell devices. The significant enhancement of EQE can clearly be demonstrated. It is found that the EQE is quite low for a flat device in the measurement spectral range. However, the EQE of a nanopatterned device obviously increases in the whole spectral range (300–1200 nm), which is consistent with the good antireflection result. The inset in Fig. 21 shows the current  $J$ - $V$  characteristics measured under AM1.5 solar

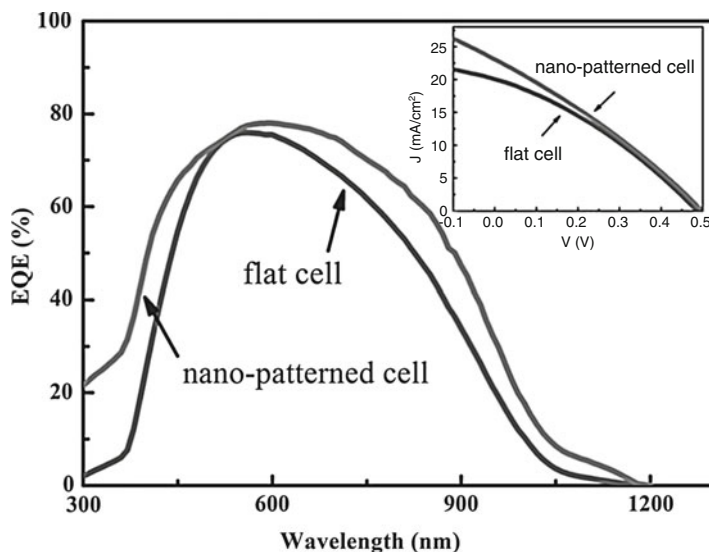


**Fig. 21** The EQE results of solar cells containing nc-Si/SiO<sub>2</sub> multilayers on flat and nanopatterned Si substrate. Inset is the illuminated  $J$ - $V$  curves (Xu et al. 2014) (Copyright 2014 John Wiley & Sons, Inc.)

spectrum. It is found that the  $V_{oc}$  is almost the same for both cells, which is 487 mV (flat cell) and 500 mV (nanopatterned cell), respectively. Meanwhile, the  $J_{sc}$  is improved for nanopatterned cell, which is in good agreement with the EQE results. It is found that the PCE is improved from 3.1% to 3.8% by forming nanopatterned structures.

### Enhanced Performance of nc-Si-Based Hetero-junction Solar Cells Fabricated on Si Nanowire Substrates

It has been demonstrated that the nanopatterned light-trapping structures can significantly harvest the incident light which may improve the nc-Si-based cell device performance. However, the low aspect-ratio of nanopatterned Si structures limits the further improvement of light harvesting. Moreover, the cell area is also limited by using the nanosphere lithography technique. Recently, metal-assisted chemical etching method is used to achieve vertically aligned Si nanowire (Si NW) arrays, which is on a large area simple and low-cost process. Consequently, Si NWs-based radial p-n junction solar cells, such as crystalline Si NWs cells (Li et al. 2011), a-Si/Si NWs shell/core cells (Wang et al. 2013), and organic polymers/Si NWs hybrid cells (Syu et al. 2012), have been widely studied. In the design of such Si NWs-based solar cells, incident light-trapping within the vertically aligned Si NW arrays leads to higher absorption per unit thickness than flat Si-based solar cells, which is more suitable for nc-Si-based cell because the absorption layer is usually very thin.

Another important advantage is that vertically aligned Si NW arrays will enlarge the radial junction areas, due to the high aspect ratio, which is helpful for enhancing the carrier separation and collection efficiency to improve the device performance.

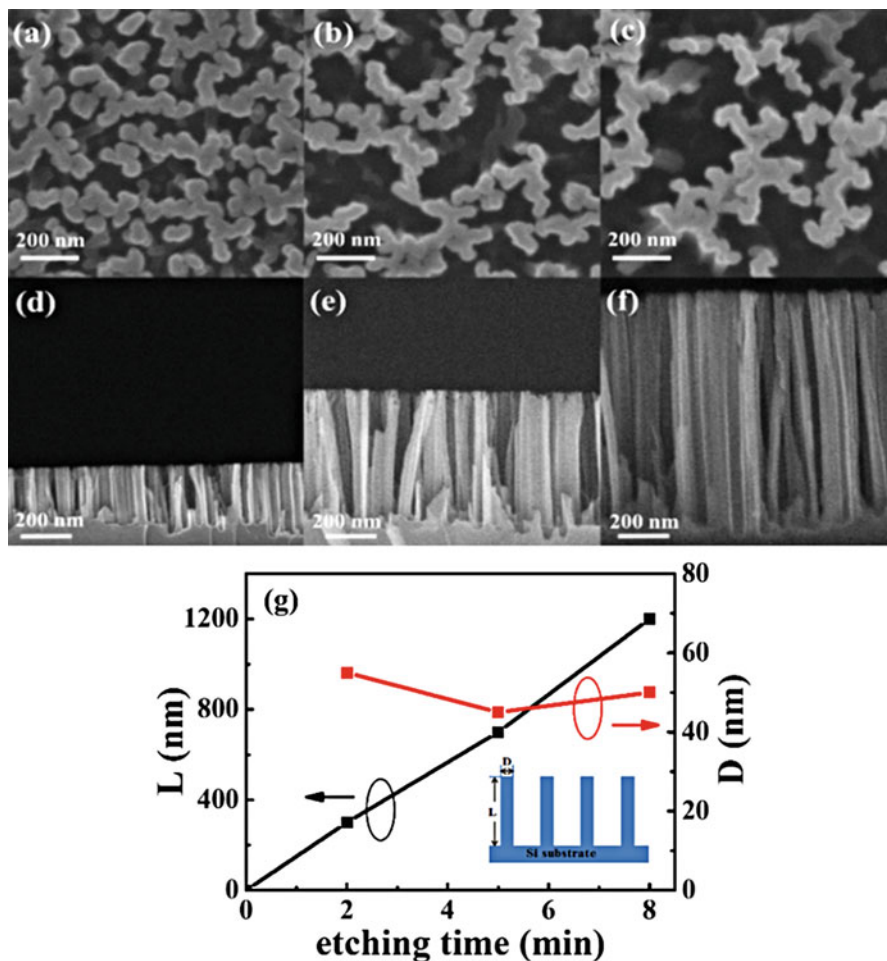
The c-Si wafers were well cleaned and then immersed into the solution composed of hydrofluoric acid and silver nitrate mixtures for an anisotropic wet-chemical etching process at the room temperature. The etching time were 2, 5, and 8 min to get the Si NWs structures' various aspect ratios. After the etching processes, the tree-like silver pattern wrapping the silicon samples was detached using a HNO<sub>3</sub> solution. Finally, Si NW arrays were aligned vertically to the wafers. The present etching technique can be applied to large-area solar cells, even to 4-in. wafer. Subsequently, nc-Si/SiC multilayers were deposited on both flat Si wafers and wafers with vertically aligned Si NW arrays to form hetero-junction solar cells. Figure 22a–c shows the top-view SEM images of Si NWs. Oriented Si NW forests could be clearly seen. The cross-sectional images of the Si wafers with vertically aligned Si NW arrays are shown in Fig. 22d–f. It is observed that the length of Si NWs etched for 2, 5, and 8 min is about 300 nm, 700 nm, and 1.2 μm, respectively. Figure 22g shows the length (L) and the diameter (D) of an individual nanowire for all the nanostructures with different etching time. It is found that the length of Si NWs gradually increased with the etching time while the diameter is almost the same, which is about 50 nm (Cao et al. 2016).

Figure 23a is the reflection spectra for flat Si wafers and wafers with vertically aligned Si NW arrays. The reflectance of the flat Si substrate is quite high in the whole measurement range (300–1200 nm). The Si NW wafers show the significant antireflection characteristics compared to the flat one. As shown in Fig. 23a, the reflectance is gradually reduced with increasing the etching time in the measurement spectral range. As for 8 min etching sample, the reflectance is less than 5% in the wavelength range from 300 nm to 1000 nm. The antireflection and light trapping effect of Si NWs structures can helpful for light harvesting in nc-Si-based solar cell structures deposited on Si NW structures. The optical transmission (T) spectra and reflection (R) spectra were measured for nc-Si/SiC multilayers deposited on flat Si wafer and wafers with vertically aligned Si NW arrays to get hetero-junction structures. The optical absorption A can be deduced by  $A = 1 - R - T$ , and the mean absorption weighted by AM 1.5G solar spectrum in the wavelength range from 300 nm to 1200 nm can be estimated according to equation:

$$A_w = \frac{\int_{\lambda_1}^{\lambda_2} F(\lambda) \cdot A(\lambda) d\lambda}{\int_{\lambda_1}^{\lambda_2} F(\lambda) d\lambda} \quad (3)$$

where  $F(\lambda)$  and  $A(\lambda)$  is the flux of incident light and absorption at the wavelength of  $\lambda$ . The different light harvest behaviors of the nc-Si-based solar cell structures can be identified with changing the etching time, as shown in Fig. 23b. The weighted mean absorption ( $A_w$ ) for flat cell is about 60.9%, which increases to 79.5% by forming the present vertically aligned Si NW arrays. By increasing the etching time to 8 min, the  $A_w$  can be further increased to 88.9%, which is enhanced by 46% compared with



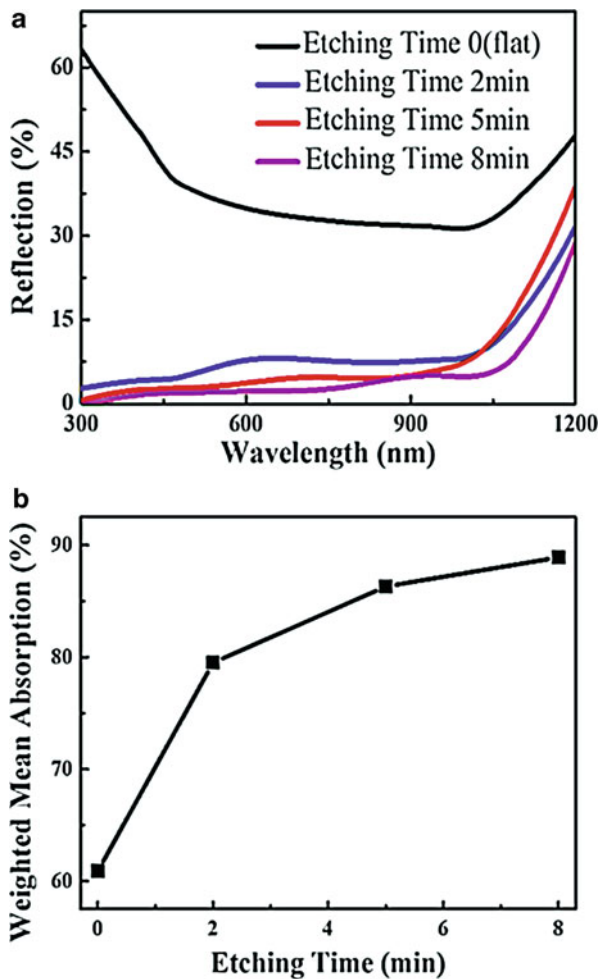


**Fig. 22** (a–c) The top-view SEM images of Si NWs etched for 2, 5, and 8 min; (d–f) The cross-sectional SEM images of vertically aligned Si NW arrays etched for 2, 5, and 8 min; (g) The length ( $L$ ) and the diameter ( $D$ ) of an individual nanowire for all the nanostructures with different etching time (Cao et al. 2016) (Copyright 2016 John Wiley & Sons, Inc.)

the flat cell. It can clearly be seen that these light-trapping properties of Si NW arrays can lead to the significantly enhanced optical absorption in a wide spectral range (300–1200 nm). It has been demonstrated that the strong scattering effect to the incident light can strongly prolong the optical path length when the light wavelength is compatible with the Si NW array periodicity and lead to the significant light-trapping effect. Hu analyzed the effects of wire diameter, length, and filling ratio on the absorbance of NW arrays and found that NW arrays with moderate filling ratio have much lower reflectance compared to thin films, especially in the high-frequency regime (Hu and Chen 2007). Yu carried out a comprehensive modeling



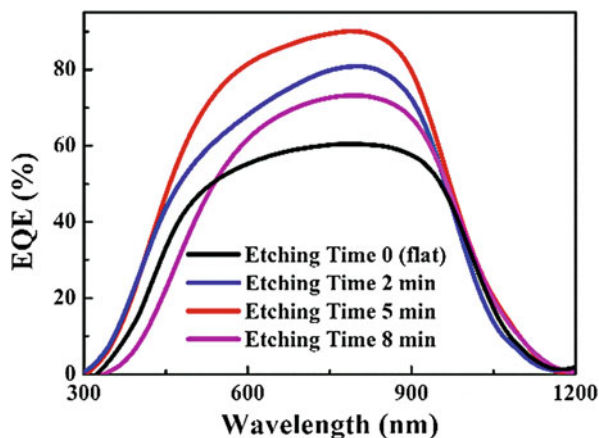
**Fig. 23** (a) The reflection spectra for flat Si wafers and wafers with vertically aligned Si NW arrays; (b) The  $A_w$  of nc-Si/Si NWs solar cell structures deposited on both the flat and nanopatterned wafers (Cao et al. 2016) (Copyright 2016 John Wiley & Sons, Inc.)



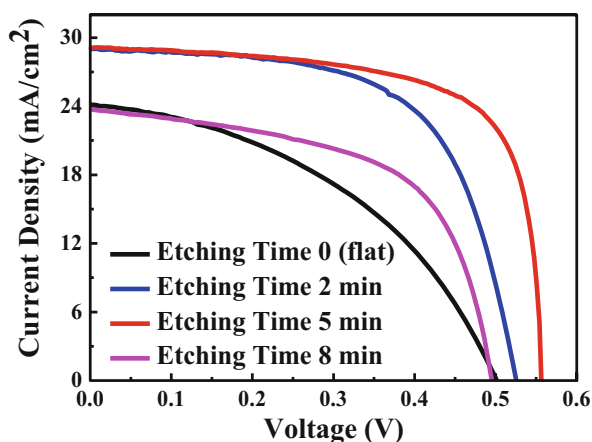
of the light in-coupling, propagation and absorption profile within radial junction thin film cells and found that the resonance mode absorption and antenna-like light in-coupling behavior in the radial junction cell cavity can lead to a unique absorption distribution in the absorber and wavelength-dependent light trapping effect (Yu et al. 2014).

Figure 24 is the EQE spectra of cell device samples and compared with that of flat one. It is observed that the EQE of flat cell is lower than 60% in the whole spectral range of 300–1200 nm. The EQE of nc-Si/Si NWs cell is strongly enhanced over a wide spectral range of 500–1000 nm, due to the light trapping effect. Nevertheless, the EQE strongly depends on the length of Si NWs, which is determined by the etching time. When the etching time increases to 8 min, the EQE decreases obviously almost in the whole spectral range, which can be attributed to the decrease in

**Fig. 24** EQE results of nc-Si/Si NWs solar cell structures with different etching time (Cao et al. 2016) (Copyright 2016 John Wiley & Sons, Inc.)



**Fig. 25** AM 1.5G illuminated  $J$ - $V$  relationships of nc-Si/Si NWs solar cell structures with different etching time (Copyright by the authors)



**Table 2** The summarized photovoltaic parameters of cell devices. Copyright by the authors

Etching time (min)	$V_{oc}$ (mV)	$J_{sc}$ (mA/cm <sup>2</sup> )	FF (%)	Efficiency (%)
0 (flat)	500	24.02	43.2	5.19
2	525	28.89	62.9	9.54
5	556	29.13	70.1	11.35
8	495	23.71	58.4	6.85

carrier collection efficiency caused by the enhancement of carrier recombination during the transport to electrodes, due to the increased transportation distance (Cao et al. 2016).

Figure 25 shows the AM 1.5G illuminated  $J$ - $V$  characteristics of nc-Si/Si NWs hetero-junction solar cells. The photovoltaic parameters of  $J_{sc}$ ,  $V_{oc}$ ,  $FF$ , and PCE, calculated from the  $J$ - $V$  results, are summarized in Table 2. The cell performance is

improved for the nc-Si/Si NWs hetero-junction solar cells, compared to the flat cell. nc-Si/Si NW cell with the etching time up to 5 min attained a  $J_{sc}$  of 29.1 mA/cm<sup>2</sup>, a  $V_{oc}$  of 556 mV, a  $FF$  of 70.1%, and a PCE of 11.3%. Among these enhanced photovoltaic parameters, the increased  $J_{sc}$  is mainly due to the enhanced light absorption. Another significant increase in the  $FF$  may be owing to two reasons. The first one is the reduction of series resistance ( $R_s$ ). It is known that contact resistance is inversely proportional to the area for carriers passing through. Si NW arrays will reduce  $R_s$  of solar cells, due to their high aspect ratio. For a single-diode model, the relation of the current density and the voltage is given in Eq. 4

$$J = J_0 \left( \exp \left( \frac{q(V - R_s J)}{nk_B T} \right) - 1 \right) + \frac{V - R_s J}{R_{sh}} - J_p \quad (4)$$

where  $J_0$  is the saturation current density,  $J_p$  the photocurrent,  $R_s$  the series resistance,  $R_{sh}$  the shunt resistance,  $n$  the ideality factor,  $q$  the electron charge,  $k_B$  the Boltzmann constant, and  $T$  the temperature. The  $R_s$  value extracted by a fit to the illuminated  $J$ - $V$  curve is 1.6  $\Omega$  of nc-Si/Si NWs cell with the etching time of 5 min, which is 10  $\Omega$  in the flat cell. The other reason of increasing  $FF$  is the radial p-n junction configuration can alleviate the negative impact of Si NWs' surface defects. Moreover, it is expected that a-SiC layers will passivate Si NWs and suppress the defect recombination. As a result, nc-Si/Si NWs cell with the etching time of 5 min has a highest  $FF$  of 70.1%. The  $R_{sh}$  value is enhanced from 110  $\Omega$  to 290  $\Omega$ , which also indicates the improved p-i-n structure of the nc-Si/Si NWs cell. Consequently, the  $V_{oc}$  is increased to 556 mV. Because of those improvements, the PCE of nc-Si/Si NWs cell is obviously enhanced.

## High Efficiency Solar Cell Containing Graded-Sized nc-Si/Si NWs Hetero-junction Structure

Since the multilayers containing graded-sized nc-Si can help to obtain enhanced broadband spectral response and energy conversion efficiency, it is interesting to prepare radial junction cell containing graded-sized nc-Si/SiC multilayers with Si NWs substrates in order to further improve the photovoltaic properties of the nc-Si-based solar cells. The schematic diagrams of hetero-junction solar cells containing nc-Si/SiC multilayers on flat Si substrates and Si NWs substrates are shown in Fig. 26 (Cao et al. 2015).

Figure 27a is the EQE spectra of grade-sized nc-Si/SiC multilayers-based cell deposited on flat Si substrate and Si NWs structures, respectively. It is shown that the EQE is further enhanced in a wide spectral range by using Si NWs structures owing to the light trapping effect discussed before. Figure 27b is the illuminated  $J$ - $V$  curve of grade-sized nc-Si/Si NWs cell and flat cell. The grade-sized nc-Si/Si NWs cell has a  $V_{oc}$  of 549 mV, a  $J_{sc}$  of 31.73 mA/cm<sup>2</sup>, a fill factor of 73.5%, and a PCE of 12.80%. The performance of device with Si NWs is generally better than that of the flat one. Our results demonstrate that the graded-sized nc-Si/Si NWs cell devices prepared by

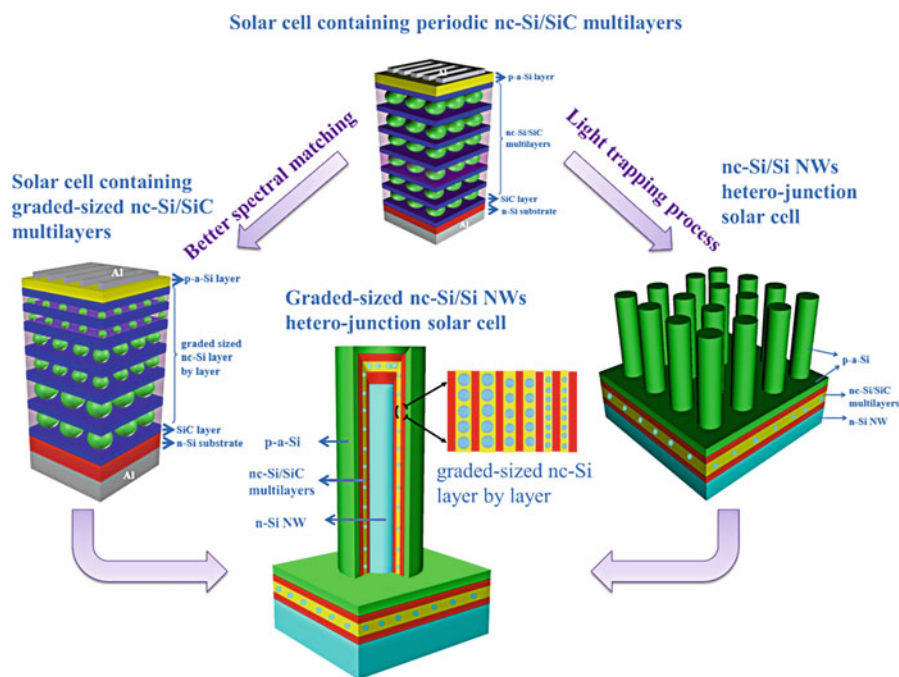


**Fig. 26** The schematic diagram of hetero-junction solar cells containing nc-Si/SiC multilayers on flat Si substrates and Si NWs substrates (Cao et al. 2015) (Copyright 2015 Royal Society of Chemistry)

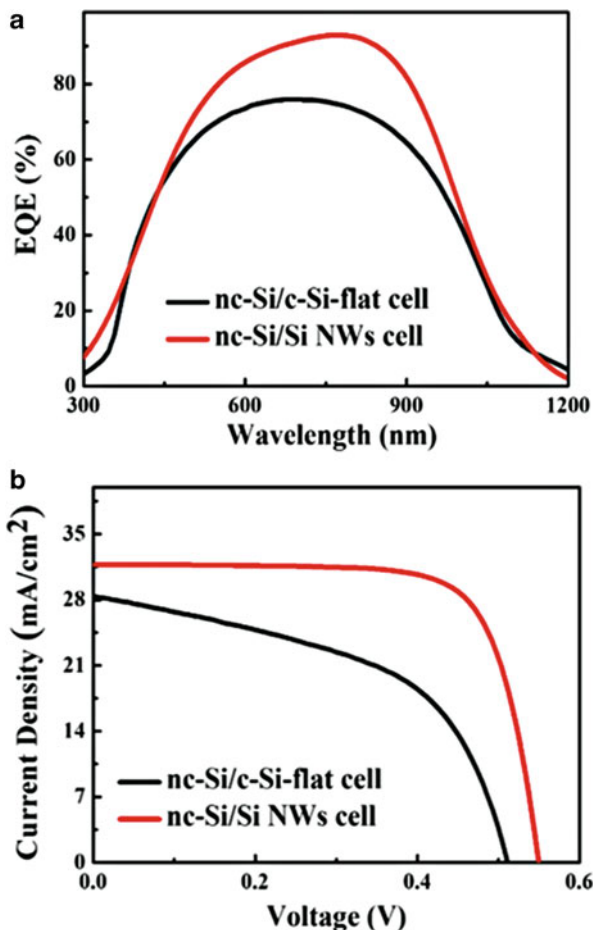
the present approach offer a simple and low-cost process to achieve broadband and high spectral response and in turn to improve the cell performances, especially the  $J_{sc}$  and PCE. It is worth noting that parameters of the present cells have not been optimized. Further device optimization such as substrate resistivity, front metallization, and back-surface field will improve the photovoltaic properties.

## Conclusion

It is expected that the broadband spectral absorption can be realized by forming the all Si-based tandem solar cells, whose power conversion efficiency can exceed the Shockley-Queisser limit. As a low-dimensional quantum material, the energy band structures of nc-Si can be well changed by controlling the dot size because of the quantum confinement effect, which provides an effective approach to modulate the bandgap of nc-Si to match the broad solar spectrum efficiently. As a consequence, the study on nc-Si-based advanced high efficiency photovoltaic devices has attracted much attention in the recent years.

The main topic of this chapter is to study the fabrication and device performance of nc-Si-based hetero-junction solar cells. First of all, a-Si-based multilayers with

**Fig. 27** (a) The EQE results of graded-sized nc-Si/c-Si and graded-sized nc-Si/Si NWs hetero-junction solar cells; (b) The illuminated  $J-V$  curves of graded-sized nc-Si/c-Si and graded-sized nc-Si/Si NWs cells (Cao et al. 2015) (Copyright 2015 Royal Society of Chemistry)



various amorphous silicon thicknesses were deposited in PECVD system, and the nc-Si-based multilayers (nc-Si/SiO<sub>2</sub> multilayers and nc-Si/SiC multilayers) were obtained after high temperature thermal annealing. The microstructures and optical properties were characterized. The prototype p-i-n structure solar cell devices containing size controllable nc-Si were fabricated and the photovoltaic properties were investigated. In order to further enhance the PCE of the solar cells, the nanosphere lithography technique and metal-assisted chemical etching technique were used to prepare the Si sub-wavelength nanostructures with good antireflection characteristic. Light harvesting and enhanced performance of nc-Si-based solar cells were achieved. Furthermore, a novel hetero-junction cell structure containing graded-sized nc-Si-based multilayers was proposed, which extended the spectral response range and improved the device performance. By combining the graded-sized nc-Si-based multilayers with light-trapping structure, the corresponding PCE of hetero-junction solar cell can be as high as 12.8%. It is worth noting that

parameters of the present cells have not been optimized. Further device optimization such as substrate resistivity, front metallization, and back-surface field will improve the photovoltaic properties.

However, there is still a long way to achieve all Si-based tandem-type solar cells experimentally. More experimental researches in this area are required. For example, the high mobility of charge carriers and high conductivity are important and challenging for the nc-Si-based solar cells based. To meet the requirements, the spacing between the nc-Si should be small enough so that the wave functions of the carriers can overlap with each other and the minibands can be formed for the transportation and collection of the carriers. At the same time, effective built-in electric field is indispensable to the carrier separation in the nc-Si-based sub-cells. In the experiments, the boron (B) and phosphorus (P) doping is the usual and effective method to obtain the p-n junction. However, doping of the nc-Si is still a challenging topic and several fundamental problems need to be solved. First, whether the dopants can be incorporated into the nc-Si is still not clear. The “self-purification effect” of nc-Si plays a critical role when the scale is only several nanometers, which means the nanocrystals tend to repel the impurities to the surface so that the formation energy can remain the lowest. So the doping efficiency of the nanocrystals is much lower than that of the bulk Si, and most of the dopants exist at the surface. Second, the location of the dopants inside the nanocrystals is still not fully understood. Recently, many theoretical and experimental reports are published, but unfortunately, the conclusions are often different or even opposite. The different locations of dopants are often influenced by the surface condition of nanocrystals (defects or Si dangling bonds) or the fabricating methods, and the problems need further studies. Third, the dopants can also change the crystalline structures of the nc-Si. For example, the doped P atoms can passivate the Si dangling bonds at the surface of nanocrystals and they can cause some damage to the Si structure and introduce extra defects when annealing temperature is over 1000 °C.

On the other hand, in this chapter, most of the nc-Si-based hetero-junction solar cells are all fabricated on c-Si substrates. The role of nc-Si in the solar cells is still not clear. Besides, in order to meet the low-cost demand to the development of third generation solar cells, it is an interesting question to study the photovoltaic properties of all-nc-Si-based solar cells, which were fabricated on glass substrates. So far, as mentioned in this chapter, in order to get all-nc-Si-based solar cells, complex processes including high temperature annealing, self-aligned evaporating method, and chemical or reactive ion etching were used. As discussed in this chapter, the laser-induced crystallization technique can be used to crystallize a-Si layer to form nc-Si, which could avoid damaging the glass substrates during the high-temperature annealing process.

It is worth noting that in order to further improve the photovoltaic properties of nc-Si-based solar cells, device optimization such as substrate resistivity, front metallization, and back-surface field will be taken into account. Moreover, surface passivation will help for reducing the density of defect states and improving the cell performance, especially for the device fabricated on high aspect ratio light trapping substrates.

## Cross-References

- ▶ [Colloidal Silicon Quantum Dots and Solar Cells](#)
- ▶ [Polycrystalline Silicon Thin Film](#)

---

## References

- Y.Q. Cao, P. Lu, X.W. Zhang, Enhanced photovoltaic property by forming p-i-n structures containing Si quantum dots/SiC multilayers. *Nanoscale Res. Lett.* **9**, 634 (2014)
- Y.Q. Cao, J. Xu, Z.Y. Ge, Enhanced broadband spectral response and energy conversion efficiency for hetero-junction solar cells with graded-sized Si quantum dots/SiC multilayers. *J. Mater. Chem. C* **3**, 12061 (2015)
- Y.Q. Cao, Z.Y. Ge, X.F. Jiang, Light harvesting and enhanced performance of Si quantum dot/Si nanowire heterojunction solar cells. *Part. Part. Syst. Charact.* **33**, 38 (2016)
- G.R. Chang, F. Ma, D.Y. Ma, Growth and characterization of ceria thin films and Ce-doped  $\gamma$ -Al<sub>2</sub>O<sub>3</sub> nanowires using sol-gel techniques. *Nanotechnology* **21**, 465606 (2010)
- K.J. Chen, X.F. Huang, J. Xu, Visible photoluminescence in crystallized amorphous Si:H/SiNx:H multiquantum - well structures. *Appl. Phys. Lett.* **61**, 2069 (1992)
- G.R. Chen, J. Xu, W. Xu, Dynamical process of KrF pulsed excimer laser crystallization of ultrathin amorphous silicon films to form Si nano-dots. *J. Appl. Phys.* **111**, 094320 (2012)
- Q.J. Cheng, E. Tam, S.Y. Xu, Si quantum dots embedded in an amorphous SiC matrix: nanophase control by non-equilibrium plasma hydrogenation. *Nanoscale* **2**, 594 (2010)
- E.C. Cho, S. Park, X.J. Hao, Silicon quantum dot/crystalline silicon solar cells. *Nanotechnology* **19**, 245201 (2008)
- G. Conibeer, M. Green, R. Corkish, Silicon nanostructures for third generation photovoltaic solar cells. *Thin Solid Films* **511**, 654 (2006)
- M. Hirasawa, T. Orii, T. Seto, Size-dependent crystallization of Si nanoparticles. *Appl. Phys. Lett.* **88**, 093119 (2006)
- L. Hu, G. Chen, Analysis of optical absorption in silicon nanowire arrays for photovoltaic applications. *Nano Lett.* **7**, 3249 (2007)
- C.W. Jiang, M.A. Green, Silicon quantum dot superlattices: Modeling of energy bands, densities of states, and mobilities for silicon tandem solar cell applications. *J. Appl. Phys.* **99**, 114902 (2006)
- H. Jin, G.L. Liu, Fabrication and optical characterization of light trapping silicon nanopore and nanoscrew devices. *Nanotechnology* **23**, 125202 (2012)
- Y. Kanemitsu, N. Shimizu, T. Komoda, Photoluminescent spectrum and dynamics of Si<sup>+</sup>-ion-implanted and thermally annealed SiO<sub>2</sub> glasses. *Phys. Rev. B* **54**, 14329 (1996)
- T.W. Kim, C.H. Cho, B.H. Kim, Quantum confinement effect in crystalline silicon quantum dots in silicon nitride grown using SiH<sub>4</sub> and NH<sub>3</sub>. *Appl. Phys. Lett.* **88**, 123102 (2006)
- Y. Kurokawa, S. Miyajima, A. Yamada, Preparation of nanocrystalline silicon in amorphous silicon carbide matrix. *Jpn. J. Appl. Phys.* **45**, L1064 (2006)
- Y. Kurokawa, S. Tomita, S. Miyajima, Photoluminescence from silicon quantum dots in Si quantum dots/amorphous SiC superlattice. *Jpn. J. Appl. Phys.* **46**, L833 (2007)
- Y. Kurokawa, S. Yamada, S. Miyajima, Effects of oxygen addition on electrical properties of silicon quantum dots/amorphous silicon carbide superlattice. *Curr. Appl. Phys.* **10**, S435 (2010)
- L.X. Li, J. Heitmann, M. Schmidt, Si rings, Si clusters, and Si nanocrystals-different states of ultrathin SiOx layers. *Appl. Phys. Lett.* **81**, 4248 (2002)
- H.F. Li, R. Jia, C. Chen, Influence of nanowires length on performance of crystalline silicon solar cell. *Appl. Phys. Lett.* **98**, 151116 (2011)

- S.X. Li, Y.J. Rui, Y.Q. Cao, Annealing effect on optical and electronic properties of silicon rich amorphous silicon-carbide films. *Front. Optoelectron.* **5**(1), 107 (2012)
- P. Löper, D. Stüwe, M. Künle, A Membrane Device for Substrate - Free Photovoltaic Characterization of Quantum Dot Based p - i - n Solar Cells. *Adv. Mater.* **24**, 3124 (2012)
- P. Löper, M. Canino, D. Qazzazie, Silicon nanocrystals embedded in silicon carbide: investigation of charge carrier transport and recombination. *Appl. Phys. Lett.* **102**, 033507 (2013)
- P. Lu, J. Xu, Y.Q. Cao, Preparation of nano-patterned Si structures for hetero-junction solar cells. *Appl. Surf. Sci.* **334**, 123 (2015)
- A. Martínez, S. Hernández, P. Pellegrino, Comparative study of the nonlinear optical properties of Si nanocrystals fabricated by e - beam evaporation, PECVD or LPCVD. *Phys. Status Solidi C* **8**, 969 (2011)
- F. Meillaud, A. Shah, C. Droz, Efficiency limits for single-junction and tandem solar cells. *Sol. Energy Mater. Sol. Cells* **90**, 2952 (2006)
- S. Miyazaki, K. Makihara, M. Ikeda, Control of electronic charged states of Si-based quantum dots for floating gate application. *Thin Solid Films* **517**, 41 (2008)
- Y.H. Pai, G.R. Lin, Spatially confined synthesis of SiOx nano-rod with size-controlled Si quantum dots in nano-porous anodic aluminum oxide membrane. *Opt. Express* **19**, 896 (2011)
- N.M. Park, C.J. Choi, T.Y. Seong, Quantum confinement in amorphous silicon quantum dots embedded in silicon nitride. *Phys. Rev. Lett.* **86**, 1355 (2001)
- S. Park, E.C. Cho, D.Y. Song, n-Type silicon quantum dots and p-type crystalline silicon heteroface solar cells. *Sol. Energy Mater. Sol. Cells* **93**, 684 (2009)
- L. Pavesi, L. Dal Negro, C. Mazzoleni, Optical gain in silicon nanocrystals. *Nature* **408**, 440 (2000)
- I. Perez-Wurfl, L. Ma, D. Lin, Silicon nanocrystals in an oxide matrix for thin film solar cells with 492 mV open circuit voltage. *Sol. Energy Mater. Sol. Cells* **100**, 65 (2012)
- G.G. Qin, S.Y. Ma, Z.C. Ma, Electroluminescence from amorphous SiSiO<sub>2</sub> superlattices. *Solid State Commun.* **106**, 329 (1998)
- Y.J. Rui, S.X. Li, J. Xu, Size-dependent electroluminescence from Si quantum dots embedded in amorphous SiC matrix. *J. Appl. Phys.* **110**, 064322 (2011)
- W. Shockley, H.J. Queisser, Detailed Balance Limit of Efficiency of p - n Junction Solar Cells. *J. Appl. Phys.* **32**, 510 (1961)
- H.J. Syu, S.C. Shiu, C.F. Lin, Silicon nanowire/organic hybrid solar cell with efficiency of 8.40%. *Sol. Energy Mater. Sol. Cells* **98**, 267 (2012)
- J. Tauc, R. Grigorovici, A. Vancu, Optical properties and electronic structure of amorphous germanium. *Phys. Status Solidi* **15**, 627 (1966)
- H.P. Wang, T.Y. Lin, C.W. Hsu, Realizing High-Efficiency Omnidirectional n-Type Si Solar Cells via the Hierarchical Architecture Concept with Radial Junctions. *ACS Nano* **7**, 9325 (2013)
- J. Xu, X. Li, Z. Cen, Formation of a dense nanocrystalline Si array on an insulating layer by laser irradiation of ultrathin amorphous Si films. *Scr. Mater.* **53**, 811 (2005)
- J. Xu, S.H. Sun, Y.Q. Cao, Light Trapping and Down - Shifting Effect of Periodically Nano-patterned Si - Quantum - Dot - Based Structures for Enhanced Photovoltaic Properties. Part. Part. Syst. Charact. **31**, 459 (2014)
- S. Yamada, Y. Kurokawa, S. Miyajima, High open-circuit voltage oxygen-containing silicon quantum dots superlattice solar cells. *Proceedings 35th IEEE Photovoltaic Specialists Conference*, (2010), 000766
- S. Yamada, Y. Kurokawa, S. Miyajima, Improvement of electrical properties of silicon quantum dot superlattice solar cells with diffusion barrier layers. *Jpn. J. Appl. Phys.* **52**, 04CR02 (2013)
- L.W. Yu, S. Misra, J.Z. Wang, Understanding light harvesting in radial junction amorphous silicon thin film solar cells. *Sci. Rep.* **4**, 4357 (2014)
- M. Zacharias, J. Blasing, P. Veit, Thermal crystallization of amorphous Si/SiO<sub>2</sub> superlattices. *Appl. Phys. Lett.* **74**, 2614 (1999)



- M. Zacharias, J. Heitmann, R. Scholz, Size-controlled highly luminescent silicon nanocrystals: A Si/SiO<sub>2</sub> superlattice approach. *Appl. Phys. Lett.* **80**, 661 (2002)
- P. Zhang, X.W. Zhang, J. Xu, Tunable nonlinear optical properties in nanocrystalline Si/SiO<sub>2</sub> multilayers under femtosecond excitation. *Nanoscale Res. Lett.* **9**, 28 (2014a)
- P. Zhang, X.W. Zhang, P. Lu, Interface state-related linear and nonlinear optical properties of nanocrystalline Si/SiO<sub>2</sub> multilayers. *Appl. Surf. Sci.* **292**, 262 (2014b)
- J. Zhu, C.M. Hsu, Z. Yu, Nanodome solar cells with efficient light management and self-cleaning. *Nano Lett.* **10**, 1979 (2010)



# Polymorphous Nano-Si and Radial Junction Solar Cells 25

Linwei Yu and Pere Roca i Cabarrocas

## Contents

Introduction .....	880
Polymorphous Silicon Thin Film for Solar Cells .....	882
Silicon Nanowire for Solar Cells .....	888
Top-Down Etching Approach and Radial p-n Junction Solar Cells .....	889
Self-Assembly Approach and Radial p-i-n Junction Solar Cells .....	892
Conclusion .....	928
Cross-References .....	928
References .....	929

## Abstract

Nanostructured silicon (Si) materials are exciting new building blocks for Si-based photovoltaics to achieve a stronger light trapping, absorption, and antireflection with the least material consumption. Constructed upon Si nanowires (NWs), a novel 3D radial junction solar cell architecture decouples the optical absorption thickness from the electric distance that photocarriers need to travel to be collected. This allows a radical reduction of the absorber layer thickness that will benefit a fast photo-carriers separation and extraction. In addition, the light incoupling and absorption distribution among the antenna-

---

L. Yu (✉)

School of Electronics Science and Engineering/National Laboratory of Solid State Microstructures, Nanjing University, Nanjing, China

Laboratoire de Physique des Interfaces et Couches Minces (LPICM), CNRS, Ecole Polytechnique, Palaiseau, France

e-mail: [yulinwei@nju.edu.cn](mailto:yulinwei@nju.edu.cn); [linwei.yu@polytechnique.edu](mailto:linwei.yu@polytechnique.edu)

P. Roca i Cabarrocas (✉)

Laboratoire de Physique des Interfaces et Couches Minces (LPICM), CNRS, Ecole Polytechnique, Palaiseau, France

e-mail: [pere.roca@polytechnique.edu](mailto:pere.roca@polytechnique.edu)

like radial junction units can be largely enhanced by the resonant modes in the nanostructured photonic cavities, which necessitates a set of new theoretical models and high-precision simulation capabilities to address and predict the photovoltaic performance of the radial junction units, as a key basis for seeking optimal structural design. Recent progress in radial junction solar cells has accomplished a device performance comparable or even superior to their planar counterparts, with still plenty of room for further improvement. This chapter starts with a presentation of hydrogenated polymorphous silicon, a nanostructured material with enhanced optoelectronic properties with respect to hydrogenated amorphous silicon, and then continues with a review on the major fabrication strategies, growth theories, and key technologies involved in developing a new generation of high performance and low cost Si solar cells, with a particular focus on the radial junction thin film solar cells fabricated upon SiNWs grown via a plasma-assisted low temperature vapor-liquid-solid procedure. Critical issues, such as the geometry, density, and doping control in Si nanowires and the radial junction deposition and optimization, will be addressed in a systematical but concise way.

---

**Keywords**

Nanostructured silicon · Radial junction solar cells · Silicon nanowires · Photovoltaics

---

**Introduction**

Silicon nanowires (SiNWs) are quasi-one-dimensional (1D) crystalline nanostructures that feature a high aspect-ratio geometry with a diameter in the range from several to hundreds nanometers. Vertical SiNWs usually demonstrate a very efficient light trapping and antireflection effect and thus can achieve a light absorption much stronger than that in the same thin film material of equal volume. As illustrated in Fig. 1, three different mechanisms could be responsible for the outstanding light harvesting performance. (i) First, in a geometrical scattering model as depicted Fig. 1a, light trapping is achieved by scattering of incident light among the NWs forest and thus being closely related to the density and arrangement of the SiNWs structure (Street et al. 2008, 2009); (ii) second, the quasi-1D NWs could by themselves play a role of antenna, as illustrated in Fig. 1b, where the NWs with a given diameter can capture a specific range of incident light at resonant wavelengths, as recently witnessed in individual SiNWs (Brönstrup et al. 2010; Cao et al. 2010). Furthermore, the air/SiNW/submultilayer interface, especially for the NWs with a tapering diameter or in a shape of nanocones as represented in Fig. 1c, is known to form a gradient index change interface that contributes to the omni-direction and broad spectrum light trapping or in-coupling (Huang et al. 2007a; Zhu et al. 2008). While all these mechanisms are beneficial for maximizing the light absorption for photovoltaics, the optimal strategy with respect for a specific light trapping mechanism can be different. Compared to the common solar cells in planar configurations,

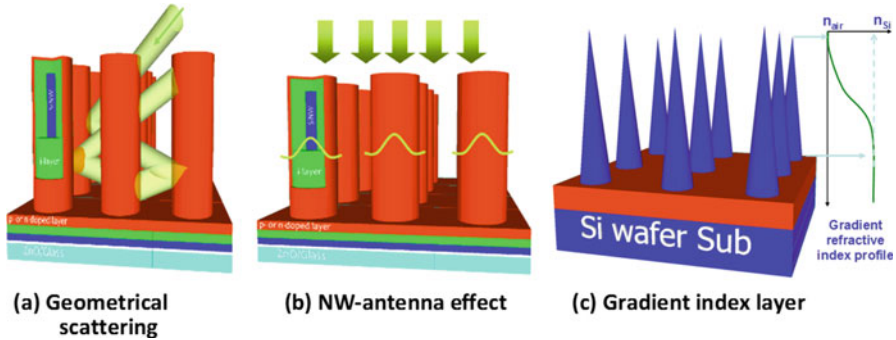


**Fig. 1** Illustrations for the different light trapping mechanisms that could contribute to an enhanced anti-reflection and light trapping effects realized among SiNW arrays (Copyright by the authors)

as addressed with great details in ► [Chaps. 2, “Polysilicon and Its Characterization Methods,”](#) ► [20, “Hydrogenated Amorphous Silicon Thin Film,”](#) and so on, there are many new geometric factors, dimensions of control and even unprecedented opportunities to discover in the structural design of Si NW arrays for optimal light harvesting for solar cells, as will be addressed in following sections.

Thanks to a strong light trapping effect among the 3D SiNW framework, the absorptive material consumption can be greatly reduced. This can help to achieve a very economic use of the high quality light absorbing materials, which is one of major concerns in the field of photovoltaics as explained in ► [Chaps. 7, “Growth of Multicrystalline Silicon for Solar Cells: The High-Performance Casting Method,”](#) and ► [22, “Polycrystalline Silicon Thin Film.”](#) On the other hand, in conventional planar photo diode structures, the photocarrier collection distance in the junction is more or less the same as the optical absorber layer thickness. This means that if the absorber layer thickness is designed to be very thick, in pursuit of a maximal light absorption, the photocarriers generated in the absorber layer have to travel, on average, a very long distance to be collected by the electrodes at the p-n junction boundaries, leading to an inefficient carrier collection, increased recombination, and as a consequence a decreased open circuit voltage  $V_{oc}$ . This becomes particularly unacceptable in p-i-n thin film solar cells, where a high electric built-in field in the intrinsic i-layer (inversely proportional to the i-layer thickness) is necessary and crucial to achieve a rapid photocarrier separation in the amorphous intrinsic absorber. Fortunately, this dilemma, in seeking simultaneously an electrically short photocarrier collection distance and an optically long absorption distance/path in the same junction, can be resolved in a nanostructured radial p-i-n or p-n junction configuration built upon the Si NWs or nano pillars (NPs), where the concepts of the electric junction layer thickness and the optical absorption distance can be completely decoupled. The strong light trapping effect realized among the 3D Si NWs or NPs can well compensate the reduced junction layer thickness, and thus leaving plenty of room for the structural optimization of the diode junction for efficient photo-carrier collection in both p-n and p-i-n solar cell configurations.

## Polymorphous Silicon Thin Film for Solar Cells

In the previous chapter, standard hydrogenated silicon thin films (amorphous and microcrystalline) produced by plasma enhanced chemical vapor deposition (PECVD) have been presented and their growth processes discussed, see the three chapters in ► “Thin Film Silicon” part a PECVD is a versatile technique which allows producing a wide range of materials for large area electronics. In the field of a-Si:H and  $\mu\text{c-Si:H}$  deposition, the standard model is based on the use of  $\text{SiH}_3$  radicals which are supposed to be the main film precursor as they are often found to be the most abundant species in the plasma. As a matter of fact, the growth of  $\mu\text{c-Si:H}$  by the sole combination of  $\text{SiH}_x$  radicals and atomic hydrogen has been discussed in (Roca i Cabarrocas 2011). However, industrial applications require high deposition rate, which is synonymous of forming clusters, aggregates and even powder in the reactor. Thus, tuning the process conditions for high deposition rates leads to a rich and complex plasma chemistry, which also opens the way to faster deposition rates and the obtaining of nanostructured materials (Roca i Cabarrocas et al. 2007). Besides radicals and clusters, ions also play an important role on the growth of thin films by giving energy to the growth surface. Indeed ion bombardment has been shown to have beneficial or detrimental effects depending on ion energy, with a threshold of 20–50 eV for defect creation, depending on the growth rate. Figure 2 illustrates the rich chemistry involved in PECVD deposition of silicon thin films from silane hydrogen mixtures. While the importance of ions and radicals has been widely discussed, much less is known on the role of electrons, photons, and clusters.

Figure 3 shows an example of the wide range of silicon structures and thin films that can be produced when one process parameter, in this case the total pressure, is increased while keeping the other process conditions constant (3% silane in hydrogen, 22 W and 250 °C). At relatively low pressure (less than 1 Torr in this case), gas phase reactions are avoided and the main film precursors are silicon radicals and atomic hydrogen. These species react on the substrate to form a  $\mu\text{c-Si:H}$  thin film as shown in the TEM cross section in the inset. As pressure is increased, gas phase reactions take place and lead to the formation of silicon clusters and nanocrystals. These nanoparticles will contribute to deposition provided they are not negatively charged. Indeed, only neutral or positively charged species can overcome the sheath potential and contribute to deposition. More interestingly, in the case of positively charged clusters, they will be accelerated by the plasma potential (of the order of 50–100 Volts) and thus will reach the surface with energies of the order of 1 eV/atom, which have been shown to be sufficient to melt the clusters at the moment of the impact (Chaâbane et al. 2006). Further increase in pressure will lead to the increase of the cluster density up to some critical concentration ( $10^{10}$ – $10^{11}$   $\text{cm}^{-3}$ ) above which agglomeration will take place. These agglomerates can grow to larger sizes and lead to formation of powder or eventually escape before getting negatively charged and contribute to the growth. These changes in the composition of the plasma species will reflect in the electrical parameters of the discharge as electrons will tend to get trapped by the clusters and powders leading to a decrease in the plasma density, an

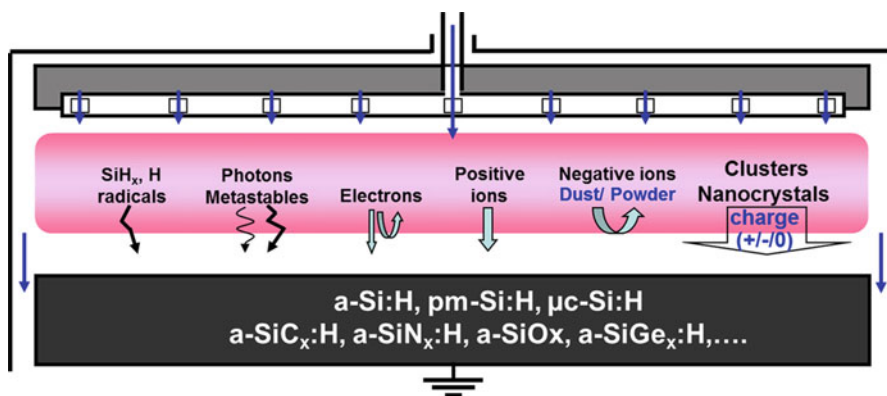


**Fig. 2** Schematic representation of a capacitively coupled PECVD reactor. A broad variety of thin films can be deposited depending on the gases feed into the reactor. Moreover, by varying the process conditions (pressure, RF power, substrate temperature, gas mixture, and interelectrode distance) film precursors can change from radicals, to ions and even clusters and nanocrystals (Copyright by the authors)

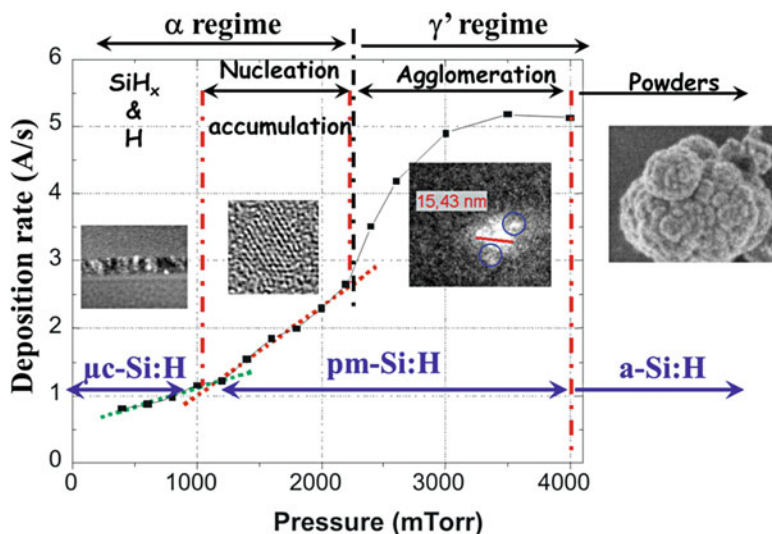


**Fig. 3** Deposition rate as a function of pressure for a 3% silane in hydrogen mixture at 250 °C under an RF power of 22 W. As pressure increases the plasma changes from a regime where only silicon radicals and atomic hydrogen contribute to deposition to a regime where silicon nanocrystals contribute to growth, still in the  $\alpha$  regime. Then the deposition rate increases sharply, which corresponds to the regime where nanocrystals form larger agglomerates ( $\sim 10$  nm). With further increase in pressure, the agglomerates become too large and are confined in the plasma, which results in the formation of powders and a decrease in the deposition rate (Copyright by the authors)

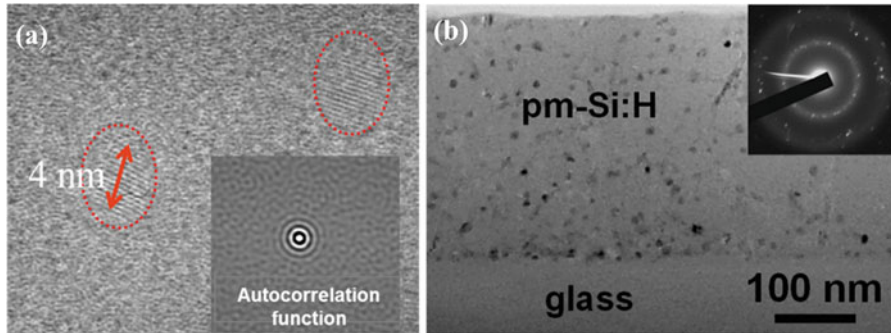


**Fig. 4** (a) High resolution TEM planar view of a 10 nm thin pm-Si:H thin film where large silicon nanocrystals can be clearly seen. The autocorrelation function of the disordered matrix shows that it has a medium range order. (b) Shows a cross section of a 300 nm thick film deposited on Corning glass where a rather uniform distribution of silicon nanocrystals is demonstrated (Kim et al. 2017) (Copyright 2017 Nature Publishing Group)

increase in the electron temperature (to sustain ionization), and overall a transition from a capacitive regime of the discharge ( $\alpha$  regime) towards a more inductive regime (also referred to as  $\gamma'$ ).

Dusty or complex plasmas have attracted increasing interest in recent years and are the basis of a new discipline. Here the focus is on the films obtained under conditions where silicon clusters and nanocrystals contribute to the growth leading to a nanostructured material that is named hydrogenated polymorphous silicon (Longeaud et al. 1999). The main characteristic of this nanostructured material is the use of plasma born silicon nanocrystals as building blocks for the film growth. Of course only positively charged and neutral ones can contribute to the growth, and it has been shown that their contribution may be as high as 75% of the film (Hamers et al. 2000) with a strong effect of the impact energy, a parameter which can be used to control their landing and switch from fully crystallized to fully amorphous thin films. Figure 4 shows a planar and cross section view of pm-Si:H thin films. The planar view was obtained by depositing a 10 nm thin pm-Si:H film on NaCl and transferring it later on a Cu grid for high resolution TEM characterization. In this case, one can see larger nanocrystals (3–4 nm in diameter) while the rest of the matrix seems amorphous. However, the analysis of the disordered matrix shows that it has a medium range order, as revealed by the autocorrelation function shown in the inset. It is possible that such medium range order results from the particular growth conditions where small nanocrystals partly of completely melt upon impact on the substrate. However, the obtained thin film keeps some memory of its growth process, completely different from standard a-Si:H deposition from radicals, in which case medium range order is absent. Figure 4b shows a cross section of a pm-Si:H film deposited on a glass substrate. Again, one can see that silicon nanocrystals are embedded in the amorphous matrix (as revealed by the electron diffraction pattern). This is very different from the case of microcrystalline silicon films deposited at low pressure (see

Fig. 3), in which case the crystalline fraction tends to increase as the film thickness increases, usually leading to a cone shaped growth. Thus, while in some respect pm-Si:H can be considered as the incubation phase of nanocrystalline silicon (also known as protocrystalline silicon), the fact that the growth process relies on silicon nanocrystals produced in the gas phase allows us to obtain films where the fraction of nanocrystals is independent of the film thickness.

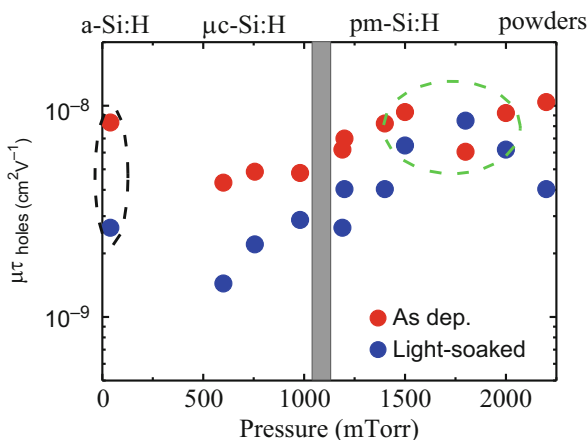
Compared to nano- and microcrystalline silicon thin films, the crystalline fraction in pm-Si:H is rather low ( $< 10\%$ ). Thus, the transport properties of the material are most likely controlled by the amorphous phase with medium range order. However, the presence of nanocrystals in the amorphous matrix may lead to quantum confinement effects and indeed pm-Si:H films show luminescence in the red. Moreover, electroluminescent PIN diodes have been demonstrated in the case of pm-SiC:H layers where the disordered matrix is made of a wide gap ( $\sim 2$  eV) a-SiC:H alloy (Wang et al. 2012). However, one could suspect that the use of pm-Si:H films as the absorber layer in PIN solar cells may lead to poor transport properties as photo generated carriers could be trapped in the silicon nanocrystals and recombine there, thus deteriorating the transport properties and the solar cell efficiency. Interestingly, extensive transport measurements have shown that the electronic properties of pm-Si:H are far better than these of standard a-Si:H films. In particular, the defect density at the Fermi level determined using both capacitance measurements on Schottky barriers and space-charge-limited current measurements on  $n^+/i/n^+$  structures have demonstrated defect densities as low as  $7 \times 10^{14} \text{ cm}^{-3} \text{ eV}^{-1}$  (Kleider et al. 1999). Moreover, time of flight measurements have revealed that the drift mobility of holes in pm-Si:H films is the highest among a-Si:H type materials (Schiff 2006).

Of course, having excellent transport properties in the as-deposited and annealed states is necessary for high efficiency solar cells; however, the stability of the properties against prolonged light soaking is even more important. Indeed, a-Si:H thin films are known to suffer from light-induced degradation, which results in a decrease of cell efficiency. Figure 5 shows the mobility lifetime product deduced from steady-state photo grating measurements on a series of silicon thin films in the as-deposited and light-soaked states. The same parameter for standard a-Si:H films is shown on the left hand side (low pressure). One can see that as pressure is increased and thus process conditions move towards polymorphous silicon deposition (see Fig. 3), there is an improvement in the  $\mu\tau$  product of holes and most importantly, this value is stable in the pm-Si:H deposition régime.

The excellent transport properties in the as-deposited and light-soaked states have motivated a strong research effort to implement this material as the absorber layer in PIN solar cells. The solar cells are usually deposited on a glass substrate coated with a textured tin-oxide layer doped with fluorine ( $\text{SnO}_2:\text{F}$ ) or on textured Al doped ZnO ( $\text{ZnO}:\text{Al}$ ). The roughness of the  $\text{SnO}_2:\text{F}$  (in the micron range) is standard in silicon thin film solar cells and allows to enhanced light absorption in the active layer of the devices. These substrates are loaded on the PECVD reactor for the successive deposition of a P-type a-SiC:H layer, then the intrinsic (I) pm-Si:H absorber, and finally a N-type a-Si:H layer. The structure is completed by the back contact which is



**Fig. 5** Mobility lifetime product for holes in the as-deposited and light-soaked states for a series of silicon thin films deposited as a function of the total pressure. The values for standard a-Si:H films deposited at low pressure are also shown as a reference (Longeaud et al. 1999) (Copyright 1999 Materials Research Society)



usually made of Al or Ag. The optimization of the deposition conditions and cell structure has allowed to reach initial conversion efficiencies in the range of 9–10%. Moreover, the same layer stack on  $10 \times 10 \text{ cm}^2$  substrates has been used to process thin film modules as shown in Fig. 6, where the I(V) characteristics of two mini-modules having the same doped layers and different intrinsic absorber layers are compared. One can see that the use of pm-Si:H results in an improved conversion efficiency despite the increase of deposition rate by a factor of 6 compared to the standard a-Si:H module deposited at 1.5 A/s.

While the properties of pm-Si:H films are outstanding, the efficiency of the solar cells is limited to 10% and they suffer from light induced degradation. Further studies to optimize the solar cells involve both experimental studies and electro-optical modeling using ASDMP program (Abolmasov et al. 2016). These studies have shown the importance of using a substrate (NIP) rather than the standard superstrate (PIN) layout. Indeed, in the case of PIN solar cells on glass/SnO<sub>2</sub>:F, the p-type a-SiC:H layer is exposed to the bombardment by ions and charged silicon nanocrystals which induce defects in the p-layer and P/I interface. Detailed modeling of the solar cell J(V) characteristics and spectral response have revealed a strong interface defect density in this case, which is not present when the deposition is performed in the NIP order. Moreover, experimental studies of the kinetics of light-induced defects on the PIN and NIP solar cells and their stability have shown a much stronger resistance of the substrate type (NIP) pm-Si:H solar cells to light soaking. This is illustrated in Fig. 7 where the efficiency is plotted as a function of the light-soaking time for standard a-Si:H and pm-Si:H PIN solar cells (superstrate) compared to the efficiency of a pm-Si:H NIP (substrate) solar cell. One can see that indeed the NIP pm-Si:H cell has a higher efficiency and stability compared to a-Si:H one. Moreover, the same pm-Si:H absorber layer in the substrate configuration leads to as stronger degradation than the a-Si:H cell, and its efficiency does not recover with an annealing after light soaking. This is interpreted as an irreversible damage induced by the strong ion bombardment by charged nanocrystals on the P-type a-SiC:H layer.

**Fig. 6** I(V) characteristics of a pm-Si:H module compared to a standard a-Si:H deposited at 1.5 A/s. The pm-Si:H deposition conditions allow to increase both the deposition rate and module output power (Copyright 1999 Materials Research Society)

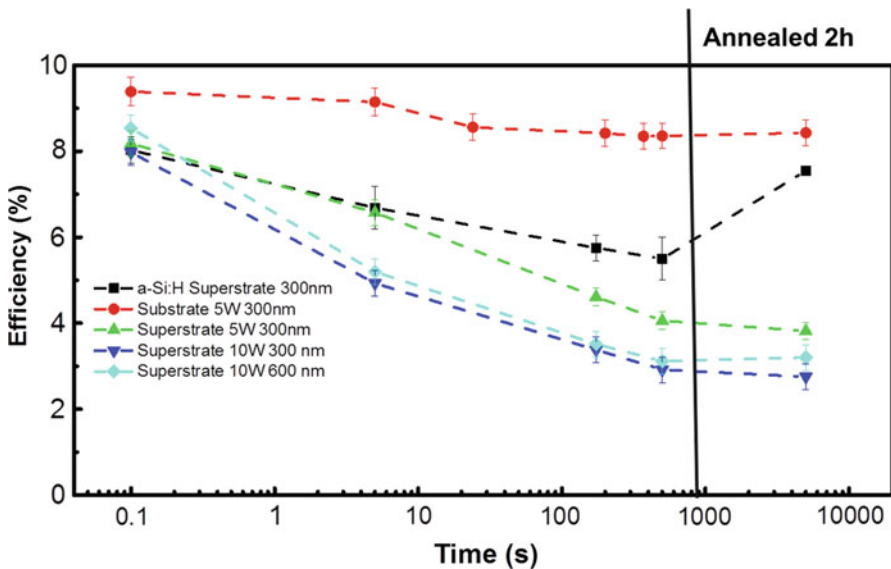
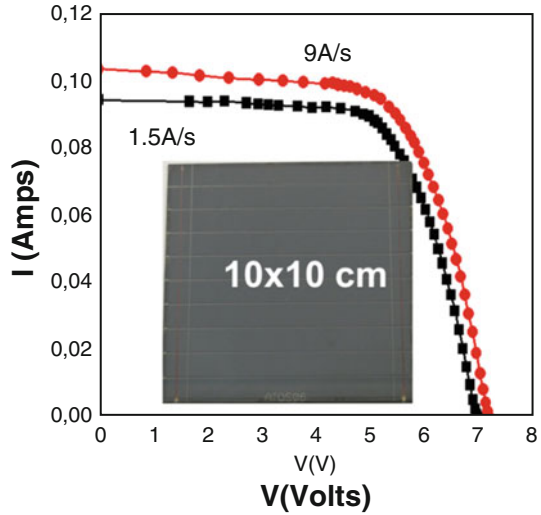


**Fig. 7** Stability of the PIN versus NIP thin film solar cells (Abolmasov et al. 2016) (Copyright by the authors under the Creative Commons)

This leads to further optimization of the solar cells by incorporating  $\mu\text{-SiO}_x$  materials for the P and N layers. Indeed, besides their higher conductivity, these materials also benefit from a lower refractive index which help to increase coupling of the light into the absorber layer. As a matter of fact, modeling, combined with experimental studies, has shown that it should be possible to reach stabilized

**Table 1** Solar cell output of pm-Si:H solar cells, deposited NIP (superstrate structure), but with the light entering on the P-side. In the first line of the table, the pm-Si:H layer is deposited at 175 °C and in the rest of the table at 210 °C. The subsequent lines show the effect of different window layers and back contacts in the initial and light-stabilized states. The ZnO/P-c-SiO<sub>x</sub> surface band bending is taken = 0.2 eV. The last two rows show the effect of using MgF<sub>2</sub> antireflection coating on ZnO. Thickness of the pm-Si:H layer is 250 nm except for the last case where it is 150 nm

Cell type	Status	J <sub>sc</sub> (mA cm <sup>-2</sup> )	V <sub>oc</sub> (volts)	FF	Efficiency (%)
ZnO/P-μc-Si/P-a-SiC/I-pm-Si:H (175 °C)/N-a-Si:H/ZnO/Ag/glass	Initial	13.31	0.985	0.792	10.39
	Stabilized	13.22	0.980	0.744	9.63
MgF <sub>2</sub> / ZnO/P-μc-SiO <sub>x</sub> / I-pm-Si:H/ N-μc-SiO <sub>x</sub> / ZnO/Ag/glass	Initial	16.64	1.125	0.759	14.20
	Stabilized	16.49	1.059	0.686	11.98
MgF <sub>2</sub> / ZnO/P-μc-SiO <sub>x</sub> / I-pm-Si:H/ N-μc-SiO <sub>x</sub> / ZnO/Ag/glass	Initial	15.98	1.129	0.764	13.78
	Stabilized	15.92	1.080	0.714	12.27

efficiencies up to 12% by using these pm-Si:H materials. This is illustrated in Table 1 where the current experimental status for NIP solar cells (corresponding to Fig. 7) in their as-deposited and light-soaked states are shown.

These results show that nanostructured materials such as pm-Si:H have the potential for 12% stabilized efficiency thin film solar cells. However, today's PV market is dominated by c-Si and polycrystalline silicon solar cells. To compete in this aggressive market, higher efficiencies are therefore necessary. Modeling has shown that triple and quadruple thin film solar cells based on a-Si:H technology have the potential for 20% efficiency (Isabella et al. 2014) even on flexible substrates. However, using the standard approach may not be sufficient because of the limited transport properties of silicon thin films and alloys. Thus, an approach where a high light absorption and easier collection of photo-generated carries can be achieved may be an asset in this competitive field. Radial junction solar cells discussed below could be the winning approach.

## Silicon Nanowire for Solar Cells

In order to fabricate Si NWs or NPs, there are many different approaches that include molecular beam epitaxy (Kanungo et al. 2008), vapor–liquid–solid (VLS) growth (Wagner and Ellis 1964) in chemical vapor deposition (CVD) or plasma-enhanced CVD (PECVD) systems and various lithography or template etching techniques (Chen and Ahmed 1993) combined with reactive ion etching (RIE) (Garnett and Yang 2010), wet chemical etching (Huang et al. 2007b; Choi et al. 2008), etc. A nice review on the SiNW fabrication techniques is already available in the literature (Schmidt et al. 2010). In general, these fabrication techniques can be classified into two major strategies: (i) the top-down etching approach that carves into crystalline bulk Si (c-Si) wafer with the aid of lithography or nanotemplates, or (ii) the bottom-up self-assembly approach that grows NWs out of molten catalyst droplets with gaseous precursors as feedstock.

## Top-Down Etching Approach and Radial p-n Junction Solar Cells

### Silicon Nanowires Etching Formation

In a top-down fabrication procedure, Si NWs are formed by etching into mono or poly crystalline Si substrates and thus inherit a high lattice quality and precise doping control from the standard c-Si wafer technology. Etching can be accomplished via RIE (Garnett and Yang 2010) or wet chemical solution process (Huang et al. 2007b; Choi et al. 2008), where the diameter, density, and spatial arrangement of the NWs are precisely controlled by photo or electron beam lithography patterns, or taking mono-layer nanospheres or nano-imprint lithography as template. In contrast to the expensive and low-throughput lithography techniques, the nanosphere assembly of polystyrene (PS) or silica (SiO<sub>2</sub>) can be easily spin-coated or dip-coated over Si wafer to serve a periodic etching mask. For example, a uniform silica nanosphere mono-layer has been successfully assembled over an entire 4 inch. wafer, via a Langmuir–Blodgett (LB) method (Hsu et al. 2008), and *translated* by subsequent RIE etching to regular Si nano pillars or cones. Large area (10 cm<sup>2</sup>) periodic NW arrays have been fabricated by deep reactive ion etching (DRIE) using SF<sub>6</sub> (Garnett and Yang 2010), as seen in the titled-view SEM image in Fig. 8b, through the mask provided by a uniform dip coating of silica bead in a procedure as depicted in Fig. 8a.

In addition, a metal assisted chemical etching (MACE) technique has been developed to etch into c-Si wafer, with the aid of silver (Ag) nanoparticles in an aqueous HF solution containing oxidizing agents (for instance H<sub>2</sub>O<sub>2</sub>) (Huang et al. 2007b; Choi et al. 2008; Rey et al. 2015). The Ag particles catalyze a rapid oxidation of Si at the Ag/Si contact interface and dig into the underlying Si wafer when the newly formed oxide layer is continuously removed by HF solution. In this way, very high aspect-ratio (>30:1) vertical Si NW arrays can be easily prepared upon the c-Si substrate, with a tunable diameter ranging from tens to hundreds of nanometers. Remarkably, the density or the arrangement of the MACE Si NWs can be further controlled by using self-assembly nanosphere monolayer as template (Huang et al. 2007b; Rey et al. 2015). At the end of the top-down MACE etching, the remnant Ag nanoparticles have to be completely removed by HNO<sub>3</sub> solutions to avoid metal contamination and extra recombination centers.

The light harvesting performance of periodic Si nanowire or pillar structures can be well simulated and optimized via proper structural design. Foldyna et al. theoretically calculated the short circuit current density ( $J_{sc}$ ) for c-Si NW arrays as a function of the NW length, type of packing and pitch (Foldyna et al. 2013). The amount of light absorbed in the SiNW arrays is calculated using 3D rigorous coupled-wave analysis and then the absorptance is transformed into  $J_{sc}$  using standard AM 1.5G solar spectrum under the assumption of a 100% internal quantum efficiency, i.e., every absorbed photon leads to carrier generation and successful collection. Two types of SiNW organization, namely, a square periodic grid and a densely packed hexagonal periodic grid, were considered (see Fig. 9a). The variation of  $J_{sc}$  as a function of diameter and pitch is shown in Fig. 9b for 3 μm long SiNW arrays. Interestingly,  $J_{sc}$  for the optimal combination of NW diameter and pitch is independent of the array organization, as shown in Fig. 9c where the maximum value

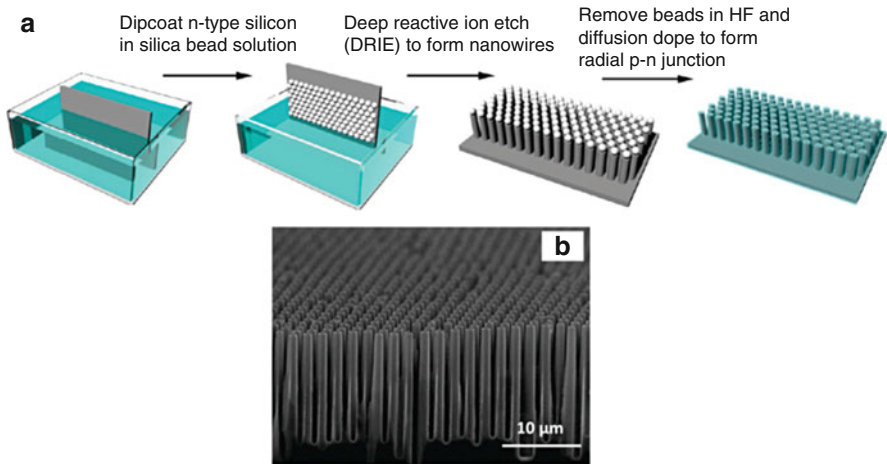


**Fig. 8** (a) Schematic illustration of a silica nanosphere assembly via dip-coating and subsequent deep reactive ion etching, (b) tilted cross-sectional scanning electron microscope (SEM) image of the vertical SiNW array (Figure adapted with permission from (Garnett and Yang 2010). Copyright 2010 American Chemical Society)

of  $J_{sc}$  is plotted as a function of NW length for both square and hexagonal organizations. Moreover, it has been shown that the performance of NW arrays can be further improved by a combination of NWs with two different diameters in a compact periodic arrangement. As an example, Fig. 9d shows  $J_{sc}$  as a function of two NW diameters with distinct maxima placed off the diagonal representing the single diameter NW array. The results support the experimental observation that random NW arrays, with a wide distribution of diameters, lead to a lower total reflectance than uniform arrays.

### Radial p-n Junction Solar Cells

Upon the Si NWs or NPs, radial p-n junctions can be formed by either conventional thermal diffusion of dopant atoms (Garnett et al. 2009) or by depositing wide bandgap intrinsic and doped a-Si:H thin films to accomplish a radial heterojunction HIT solar cell structure (Gharghi et al. 2012). Radial p-n junction SiNW solar cells, fabricated upon periodic SiNWs defined by parallel electron beam lithography, with a diameter, height and pitch of 340 nm, 3.5  $\mu\text{m}$  and 800 nm, respectively, demonstrated a power conversion efficiency of 10.8% with a relatively low  $V_{oc}$  of 0.59 V (Lu and Lal 2010). With the introduction of a better interface passivation in a radial heterojunction configuration, where  $\sim 12$  nm thick hydrogenated amorphous silicon (a-Si:H) thin film is coated upon crystalline silicon microwires, the radial HIT microwire solar cells deliver a photocurrent of  $\sim 30$  mA/cm<sup>2</sup> and a voltage close to 600 mV that leads to an efficiency in excess of 12% (Gharghi et al. 2012). It is important to note that the 3D nanostructuring approach also enables an economic use of the high quality c-Si absorber materials, where the required wafer thickness can be

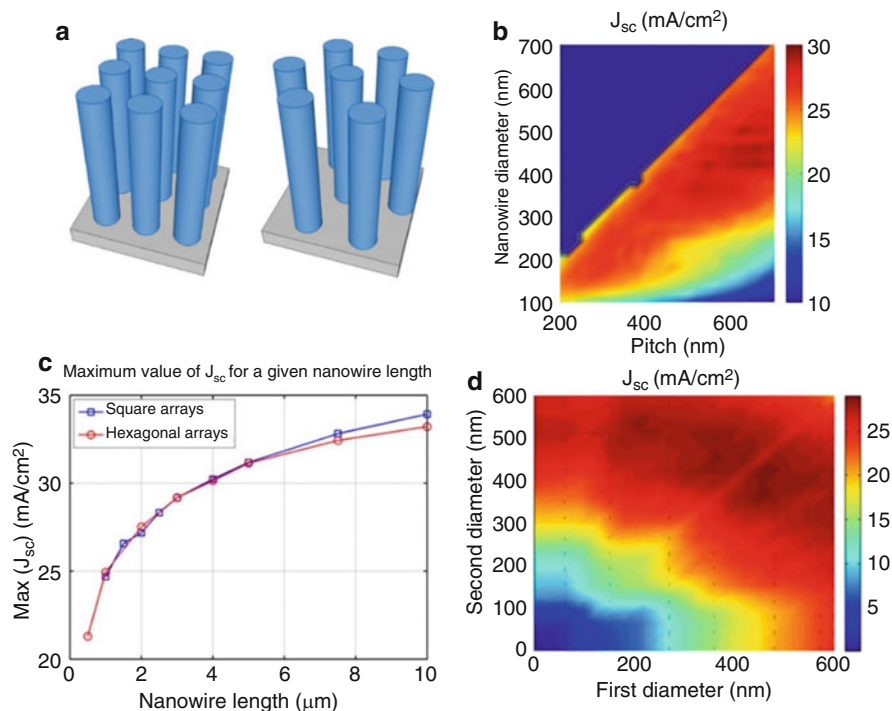


**Fig. 9** (a) Square periodic grid and densely packed hexagonal periodic grid for c-SiNW arrays on silver mirror. (b) Short circuit current density as a function of diameter and pitch for 3  $\mu\text{m}$  long SiNWs, arranged in square array. (c) Maximum value of  $J_{sc}$  as a function of NW length. The maximum is calculated for diameters and pitches below 700 nm. The device performance is found to be independent of the organization. (d)  $J_{sc}$  as a function of two SiNW diameters with length and pitch of 3  $\mu\text{m}$  and 600 nm, respectively (Figure adapted with permission from (Foldyna et al. 2013). Copyright 2012 Elsevier)

reduced from typically 180  $\mu\text{m}$  (see ► Chaps. 6, “Growth of Crystalline Silicon for Solar Cells: Czochralski Si,” ► 9, “Growth of Crystalline Silicon for Solar Cells: Mono-Like Method,” and ► 10, “Growth of Crystalline Silicon for Solar Cells: Noncontact Crucible Method”) to less than 40  $\mu\text{m}$  for achieving the same light harvesting performance.

However, despite an obvious gain in light harvesting and antireflection effect, the power conversion efficiencies of the radial p-n junction solar cells, fabricated over top-down etched Si NWs, are in general far below what has been achieved in conventional planar cells (now >26% in laboratory). The reasons behind can be manifold, for example, the damage by energetic ions during RIE etching, the inhomogeneous doping and junction profile formed over a deep NW framework, and the extra electric contact loss among the rough 3D surface, etc. Particularly, a major challenge arises from the fact that as a consequence of the top-down etching to form Si NWs, the front interface area is also largely increased, which inevitably leads

to a much higher surface recombination speed, an enhanced photocarrier recombination, and thus a degraded voltage output. Therefore, seeking an efficient surface and interface passivation technique has been crucial in order to unleash the full potential of the Si NWs-based solar cells.

Interestingly, it has been proven, both theoretically and experimentally, that making a periodic NP array is not always necessary or advantageous in view of maximal light absorption (Battaglia et al. 2012). Contrary to common belief, introducing somewhat spatial randomness among the Si NW array can even help to boost the overall light harvesting over a broader wavelength spectrum. This also implies that the high processing cost, associated to precise location control and template preparation, can be largely relieved in radial junction solar cell fabrication. While a sufficient light harvesting can be easily guaranteed among the top-down etched Si NWs, more research attention is now directed to achieve a high quality junction formation and address the key electrical aspects, so as to minimize photo-carrier recombination and boost the overall light conversion performance.

### Self-Assembly Approach and Radial p-i-n Junction Solar Cells

In complement to the mainstream bulk Si wafer solar cells, hydrogenated amorphous Si (a-Si:H) thin film deposition also enables a promising low-cost and flexible solar cell technology, which can be manufactured in an automated and continuous production process and deposited at low temperature on bendable substrates for large scale deployment. According to the classification in Fig. 10a, the a-Si:H thin film solar cells belong to the 2nd generation (Gen) Si photovoltaics, which boast a low fabrication cost but also suffer from a lower power conversion efficiency (PCE) in comparison to the 1st Gen bulk Si solar cells. This is because the a-Si:H thin film, though passivated by hydrogen, is still disordered and defective with a bulk defect density of  $\sim 10^{16} \text{ cm}^{-3}$ . As a consequence, the photo-carrier lifetime and diffusion length are very short, compared to those in high quality bulk c-Si. So, in order to facilitate carrier separation and minimize photocarrier recombination, the absorber intrinsic i-layer has to be sandwiched in a p-i-n junction structure, where the sweeping built-in field can help to separate the photo-generated electrons and holes rapidly. However, a dilemma exists that the i-layer is supposed to be optically thick for sufficient light absorption while being electrically thin to allow a fast extraction of photocarriers from the defective a-Si:H absorber layer. In a planar thin film solar cell, these are opposite requirements as both of them are defined by the i-layer thickness. Thus, a trade-off has to be sought and usually the planar i-layer thickness is controlled to be around 260 nm to 300 nm, leaving little room for further structural optimization of the planar a-Si:H thin film solar cells.

A new approach to break this fundamental limitation has become possible with the introduction of Si NWs as 3D framework, as illustrated in Fig. 10b, where the 3rd generation Si thin film solar cells can now be deposited radially over the doped Si NW cores, which are grown via a vapor-liquid-solid (VLS) mechanism (Wagner and Ellis 1964) in a low temperature thin film process. This preserves the low cost



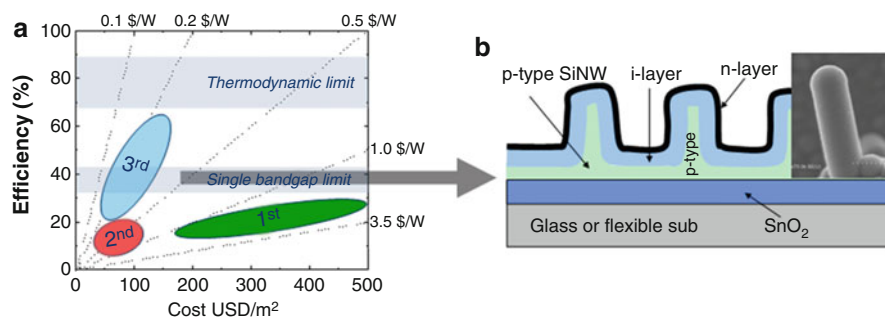


**Fig. 10** (a) The efficiency-cost plots and performance regimes for the three generation (Gen) of different Si solar cell technologies, which are the 1st Gen of bulk Si, the 2nd Gen of a-Si:H thin film, and the 3rd Gen of nanostructured Si solar cells; (b) structural illustration of radial junction thin film solar cells built on self-assembly Si NWs, representing a promising approach towards the 3rd Gen high performance and low-cost solar cells (Copyright 2017 by the authors)

advantage of the 2nd Gen solar cells, while holding a promise to boost the PCE performance of Si thin film cells further to match or even surpass that of the 1st Gen c-Si cells. In this radial p-i-n junction configuration, the equivalent optical path for the incident light is strongly enhanced by a factor of ten to thousands, depending on the specific wavelength, thanks to the strongly enhanced light trapping and absorption realized among the SiNW array, while the electric travel distance for the photo-carriers can be greatly reduced by adopting a thinner absorber i-layer to allow for effective carrier separation and collection. More theoretical and experimental details, as well the latest progress, will be addressed in the rest of this Chapter, where the key fabrication techniques and design principles of the radial junction Si thin film solar cells will be reviewed. This will involve the key fundamental and technical aspects in the VLS growth of Si NW, and the design principles, fabrication techniques, characterizations and performances, as well as theoretical simulation and modeling of the radial p-i-n junction solar cells.

### VLS Growth of Silicon Nanowires in a CVD System

Targeting at a high performance but low cost photovoltaic applications, the Si NWs matrix should be manufactured via a low-cost, scalable, and reliable technology that provides efficient and versatile control over the geometry, density, doping, and surface passivation of the NWs. In view of industrial production, the fabrication procedure is also supposed to be compatible with the established thin film or wafer solar cell technologies. To this end, self-assembly growth of SiNWs via a vapor-liquid-solid (VLS) mechanism provides a good choice. During a typical VLS growth process in a chemical vapor deposition (CVD) system, as schematically illustrated in Fig. 11, metal catalyst droplets (for example the widely used Au, as well as Ni, and Al et al.) are heated to a temperature above the eutectic point (for Au-Si alloy system, it is 363 °C). Then, gas precursors such silane ( $\text{SiH}_4$ ) are fed, decomposed at the catalyst droplet surface and absorbed into the Au droplet (Schmidt et al. 2010). With



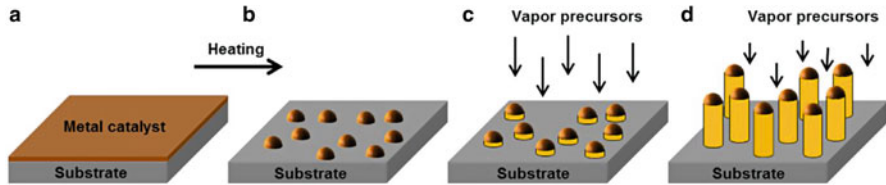


**Fig. 11** Schematic illustration of the VLS process. (a) A metal catalyst layer is deposited on the substrate. (b) Upon heating, dewetting of the metal layer forms small droplets. (c) Introduction of vapor precursors leads to incorporation of the precursor inside the droplet and its precipitation at the catalyst–substrate interface. (d) Growth of SiNW via a VLS process

the increase of dissolved Si concentration, the solid Au droplets become molten and supersaturated, leading to nucleation of c-Si seeds at the catalyst droplets/substrate interface as illustrated in Fig. 11c. Then, continuous Si atoms precipitation and deposition at the c-Si seed/catalyst interface will kick off a unidirectional NW growth, with NW diameters being proportional to the sizes of the leading catalyst droplets.

Obviously, during such a VLS growth, the metal droplets serve as soft templates to define both the initial position and the diameters of the as-grown Si NWs. Importantly, an effective n-type or p-type doping control of the SiNWs can be accomplished by introducing corresponding dopant gases such as  $\text{PH}_3$  or  $\text{B}_2\text{H}_6$ , respectively (Gudiksen et al. 2002). Meanwhile, the VLS growth mechanism has been successfully applied to grow various nanowire structures in radically different material systems (Si, Ge, III-V compound, metal oxide, and alloys), with a wide range of choices in the suitable metal catalysts and precursor gas species (Schmidt et al. 2010). Thus, given an effective control over the size and the distribution of the metal catalyst droplets, the VLS growth strategy provides a straightforward and efficient approach to grow and optimize the Si NW structures, providing for the specific needs in the subsequent deposition and fabrication of radial junction solar cells.

However, the use of Au as a catalyst poses a serious threat to solar cell applications as the Au atoms dissolved into the SiNWs during VLS growth will introduce a middle bandgap level in c-Si, as indicated in Fig. 12a (Schmidt et al. 2010), which is known to be a very efficient recombination center for photo-carriers. According to the Shockley–Read–Hall recombination statistics (Shockley and Read 1952), the closer the energy level is to the middle of the band gap, the higher is the recombination rate and the lower is the carrier lifetime. Meanwhile, the persisting catalyst metals residing at the tips or left on the sidewall of the VLS-grown SiNWs are also serious contamination to the p-n or p-i-n junction interfaces and thus have to be removed and cleaned by post-growth chemical etching. On the other hand, forming a liquid catalyst droplet is a criterion for the VLS growth. Usually, the eutectic temperature of the metal-Si alloy is much lower than that of pure catalyst metals. For instance, the eutectic temperature of Au-Si alloy is only 363 °C, compared to the melting temperature of 1064 °C for Au and

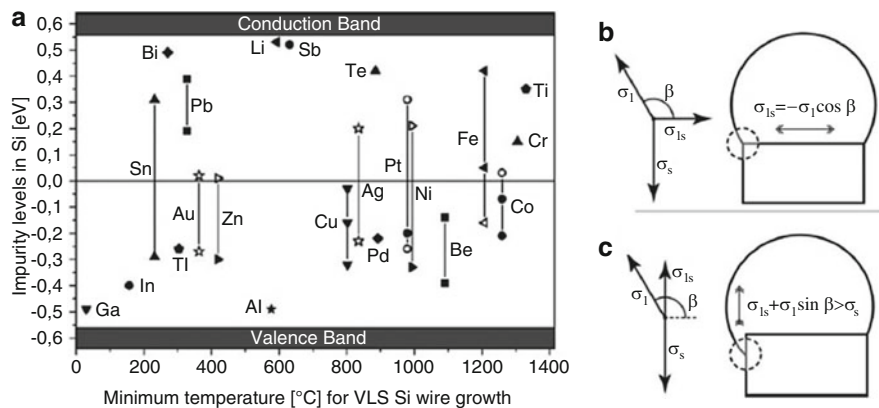


**Fig. 12** (a) Energy levels for different impurities in Si with respect to the middle of the band gap as a function of the minimum temperature required for VLS growth. The lines connect the defect energies available for the same impurity (Figure adapted with permission from (Schmidt et al. 2010). Copyright 2009 Wiley-VCH Verlag GmbH & Co. KGaA, Weinheim). (b) For the catalyst droplet to be in mechanical equilibrium during growth, the horizontal components of the interface tensions must cancel out. (c) Nonequilibrium position where a net vertical force is required to re-establish the equilibrium and carry out stable growth (Figure adapted with permission from (Schmidt et al. 2010). Copyright 2010 American Chemical Society)

1414 °C for Si, as seen in the phase diagram of Au-Si in Fig. 13a. Searching for a low melting point catalyst is particularly important to achieve a low temperature VLS-growth of SiNWs. To this end, alternative catalyst metals, ideally with a lower eutectic/melting point than the Au-Si alloy, have to be sought in order to establish a reliable, low-cost, and clean SiNW framework for constructing high performance radial junction photovoltaics.

## Plasma Assisted VLS Growth

### Low Melting Point Metal as Catalyst

In order to develop a low temperature growth of Si NWs, a group of low-melting-point (LMP) metals, including tin (Sn), indium (In), bismuth (Bi), and gallium (Ga), are recently explored as alternative catalyst metals to the commonly used Au to carry out a VLS growth of Si NWs (Alet et al. 2008; Yu et al. 2008, 2009, 2010a, b, 2011; Zardo et al. 2009, 2010, Misra et al. 2013a, b). As shown in Fig. 12a, the melting temperatures of this group of metals are well below 300 °C, and all of them feature a metal-Si phase diagram similar to that of the alloy Sn-Si system (see Fig. 13b), where the eutectic temperature lies extremely close to the pure metal end. This enables, first of all, a low temperature VLS growth that is fully compatible with conventional Si thin film solar cell deposition process (typically <350 °C). More importantly, as witnessed in Fig. 12a, in contrast to the detrimental mid-bandgap recombination centers caused by Au atoms in c-Si, the dissolution of LMP metal atoms into c-Si is far less harmful for the photocarriers, as they introduce only impurity levels far away

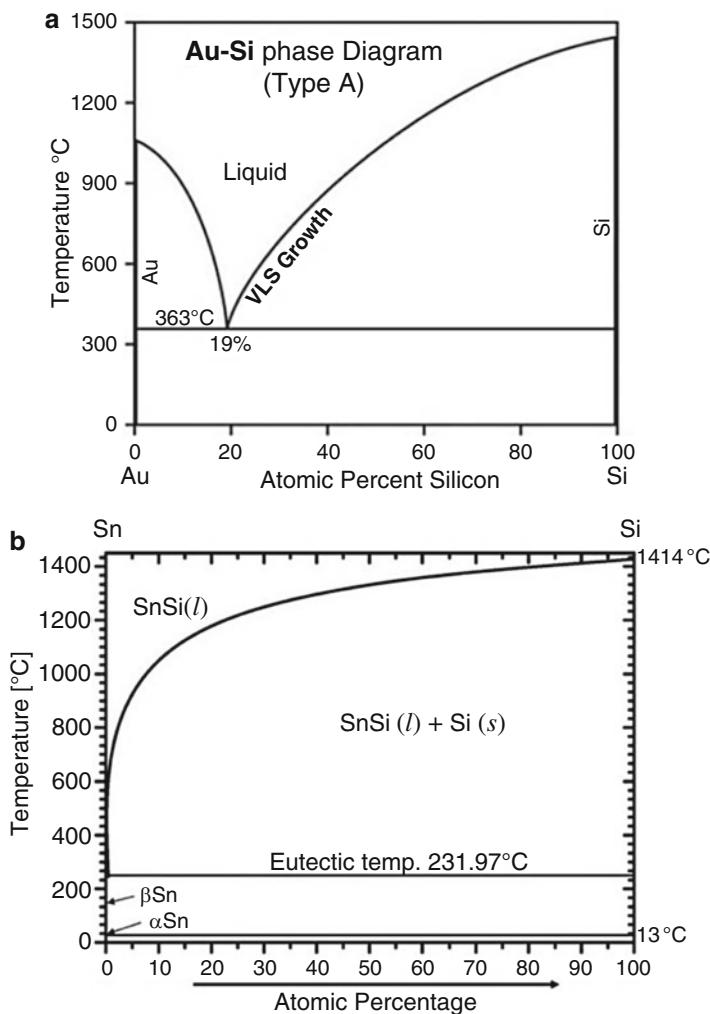


**Fig. 13** Schematic phase diagram of (a) Au–Si and (b) Sn–Si systems (Figures adapted with permission from (Schmidt et al. 2010), Copyright 2009 Wiley-VCH Verlag GmbH & Co. KGaA, Weinheim)

from the mid-bandgap. For example, the incorporation of Sn (Group-IV element in the same Column of the Periodic Table as silicon) leads to only neutral impurity levels in c-Si.

On the other hand, this catalyst atom incorporation can also be useful for constructing SiNW-based radial junction solar cells. It has been known that the dissolution of Group III element (In or Ga) atoms can result in effective p-type doping in the as-grown SiNWs, while the incorporation of Group V elements (Bi) will lead to opposite n-type doping. This catalyst doping effect can be

considered as an extra bonus for the VLS-growth fabrication, as it enables not only a significant procedure simplification (for doping) but also exempts from the use of extremely toxic and hazardous dopant gases of diborane or phosphine. It is also important to note that in strong contrast to the case of the widely used boron and phosphorus dopant atoms, which cause shallow doping levels in c-Si that can be completely ionized at room temperature to give off holes and electrons, In atoms lead to a deeper donor level located 160 meV above the valence band top, which can't be completely ionized at room temperature. As a consequence, despite of a high concentration of incorporated In, the actual p-type doping effect is quite limited and is equivalent to the boron doping effect at orders of magnitude lower concentration. In comparison, the impurity doping level caused by Bi atoms is much closer to the conduction band bottom edge (70 meV), which allows it achieve an effective and sufficient n-type doping in Bi-catalyzed SiNWs to fabricate radial p-i-n junction solar cells upon the SiNWs as shown in Ref. (Yu et al. 2012a).

However, the LMP metals were not considered, from the very beginning, as ideal or even viable candidates to mediate a stable VLS growth of Si NWs. This is because, as summarized in Table 2, the low-melting-point metals all feature a low surface tension  $<0.5$  N/m compared to those of the c-Si sidewall facets, typically in a range of 1.0–1.5 N/m for major facets (Schmidt et al. 2009). As illustrated in Fig. 12b, c, a criterion for a stable VLS growth arises that the triple phase line (TPL) where the three phases (vacuum, liquid, and solid) meet has to be stable at the periphery of the growing SiNW top. Particularly, in the vertical direction, when new atomic layers are continuously deposited and formed at the SiNW top interface, the projected surface tension of the liquid metal droplet has to be larger than the surface tension on the sidewall of the SiNW, that is,  $\sigma_l \sin \beta + \sigma_{ls} > \sigma_s$ , in order to pull up the TPL line to the top corner of the SiNW tip and stabilize the liquid droplet residing always at the tip. Otherwise, the catalyst liquid will tend to spread on and wet the SiNW sidewall. For the commonly used metals (Au, Al, and Cu), this criterion can be easily met thanks to a relatively large surface tension of the catalysts compared to that of c-Si. However, this is not guaranteed for the LMP metals like Sn, In, and Bi, which all feature a much lower surface tension  $<0.7$  N/m. It is because of this criterion, first proposed by Nebol'sin in 2003 (Nebol'sin and Shchetinin 2003) and later re-formulated by Schmit in 2009 (Schmidt et al. 2009, 2010), that the LMP catalysts (Sn, In and Bi) are in general excluded from the list of suitable catalysts to mediate a stable VLS growth of SiNWs. Indeed, there are only few reports on the LMP metal catalyzed VLS growth of SiNWs in typical CVD environment.

However, successful VLS growths of SiNW by using Sn or In as catalyst metals have been reported by Yu et al. in 2008 within a plasma enhanced chemical vapor deposition (PECVD) system (Alet et al. 2008; Yu et al. 2008, 2009) and then by Ga (Zardo et al. 2009), Bi (Yu et al. 2012a) or an alloy of Bi-Sn in 2015 (Yu et al. 2015). These exceptions have been explained in a surface wetting layer model, where an ultra-thin LMP metal liquid layer is identified spreading on the sidewall of SiNWs during the VLS growth, which helps to modify and reduce the effective surface tension on the SiNW sidewalls and thus stabilize the catalyst droplets at the tip of the SiNWs (Misra et al. 2013a, b). A good news for solar cell applications is that as a

**Table 2** Surface tension of metals in liquid forms (Misra et al. 2014)

Metal	$\sigma_1$ (Nm <sup>-1</sup> )	Metal	$\sigma_1$ (Nm <sup>-1</sup> )
Ga	0.69–0.718	Cu	1.23–1.37
In	0.5–0.566	Ag	0.9–0.925
Sn	0.545–0.575	Pd	1.24–1.482
Bi	0.355–0.371	Pt	1.22–1.860
Au	0.91–1.22	Ni	1.3–1.838
Zn	0.767–0.815	Fe	1.83–1.859
Al	0.82–1.070		

member of LMP metals, Sn can be completely removed by H<sub>2</sub> plasma (van Herpen et al. 2010) from the SiNWs after growing them to required length. This allows a monolithic integration of clean SiNWs into the well-established low-temperature thin film technology for fabricating high performance radial junction solar cells in conventional PECVD systems. More details of the LMP metal mediated VLS growth and the solar cell fabrication will be presented in later sections.

### Plasma-Assisted VLS growth of Silicon NWs

During a typical VLS growth of SiNWs in a thermal activated CVD system, it is the catalyst metal drop, for instance, the most widely used Au, which catalyzes the dissociation of gas precursors (SiH<sub>4</sub>). Unfortunately, this simple CVD strategy does not apply to the LMP metals, as there is no proof of such catalytic dissociation mechanism that will take place on the surface of LMP metals. In addition, the LMP metals can be easily oxidized in air or exposure to remnant oxygen or water vapor in low vacuum system. The formation of a thin oxide layer covering the droplet will prevent the absorption of gas precursors by the droplets and make it impossible to growth SiNWs via a VLS mechanism. This is however not an issue if the LMP metals are exposed to plasma enhanced gas feeding in a PECVD system, where the precursor gases are dissociated into active radicals of SiH<sub>x</sub> by a high frequency electric field modulation, usually at 13.56 MHz or higher. Therefore, no catalytic effect is required for the metal droplets. More importantly, the thin oxide layer covering on the LMP droplets can be easily reduced by the H-rich plasma environment back into metal, which thus re-open the surface of LMP droplets to absorb silicon radicals and precipitate SiNWs via a VLS mechanism. As a consequence of a radical precursor feeding, the growth rate of SiNWs is also significantly enhanced in the PECVD system and the VLS growth can take place now at a much lower growth temperature, even down to 230 °C (Yu et al. 2009). Meanwhile, as the PECVD method is a nonequilibrium process, the growth kinetics of NWs can be quite different from the conventional VLS situation. For example, a concurrent a-Si:H deposition on the SiNW sidewall usually happens and results in a tapering geometry of the SiNWs, where composite SiNWs with a crystalline core and amorphous/or polycrystalline shell structure are usually observed, especially at low temperature growth (Yu et al. 2010a, b). A more comprehensive theoretical description and discussion, as well as the key supporting experimental observations, on the unique

aspects of LMP metal catalyzed VLS growth are available in the References (Yu et al. 2010a, b, 2011; Misra et al. 2013a, b).

### Density Control of Catalyst Droplets

In order to optimize light trapping in SiNW solar cell arrays, it is very important to control the density and the size distribution of the metal droplets, as they will be translated during the VLS growth into the density and diameter of the SiNWs. As mentioned above, there have been several ways to arrange the metal droplets on the substrate, e.g., by optical lithography, nano-imprint lithography, nanosphere lithography, or the use of a porous alumina mask. The simplest, as well the most economic, method is to form metal droplets via self-assembly process. In this process, a thin film of metal is evaporated on the substrate and annealed either above the eutectic temperature (when the substrate is a Si wafer) or above the melting point of the metal (for any substrate other than Si). If an Au covered Si substrate is heated above 363 °C (eutectic temperature of Au–Si, see Fig. 13), liquid Au–Si alloy droplets will form with a density and size distribution determined by the annealing temperature, the surface chemistry, and the annealing atmosphere. The advantage of “self-assembly” is that all process steps, starting from organizing metal droplets to the SiNW growth, can be carried out without removing the samples from the vacuum system.

For low surface tension metals such as Sn, In, Ga, or Bi, the metal layer can be obtained either by evaporating a thin metallic film or by reducing a metal oxide substrate, such as tin oxide (SnO<sub>2</sub>) (Yu et al. 2008, 2009) or indium tin oxide (ITO) (Alet et al. 2008) via a simple H<sub>2</sub> plasma treatment in a PECVD system. Yu et al. applied a H<sub>2</sub> plasma to superficially reduce 100 nm SnO<sub>2</sub> deposited on a Corning glass substrate at a nominal temperature of 300 °C and investigated the effect of the plasma treatment time (Yu et al. 2008, 2009). With the increase of the temperature and the duration of the H<sub>2</sub> plasma treatment, the molten Sn droplets are formed on the substrate surface and promoted to coalesce with neighboring ones over a longer distance (being proportional to the diffusion distance of the metal atoms). As a result, larger and sparse droplets can be obtained by enhancing the surface diffusion at a higher temperature. The effect of annealing temperature on the In catalyst droplet density and size distribution were studied quite systematically in Ref. (Yu et al. 2012b), where In droplets were formed by reducing a thin layer of sputtered ITO on ZnO:Al coated Cg. The temperature of the substrate was varied between 160 °C and 260 °C, and a gradual decrease in the droplet diameter with decreasing substrate temperature was observed (the corresponding SEM images are shown in Fig. 14a). The diameter distribution and the size dispersion are shown in Fig. 14b–d. Obviously, with the increase in temperature, the distribution becomes wider, and the size dispersion increases. Therefore, the substrate temperature and H<sub>2</sub> plasma treatment conditions are very efficient control parameters to engineer the density and size dispersion of the catalyst droplets, as well as the as-grown SiNWs, which have to be properly controlled in pursuit of an optimal light trapping and high quality radial junction formation.

On the other hand, the initial thickness of the evaporated or sputtered metal layer is another effective parameter to control the density and size of the droplets.

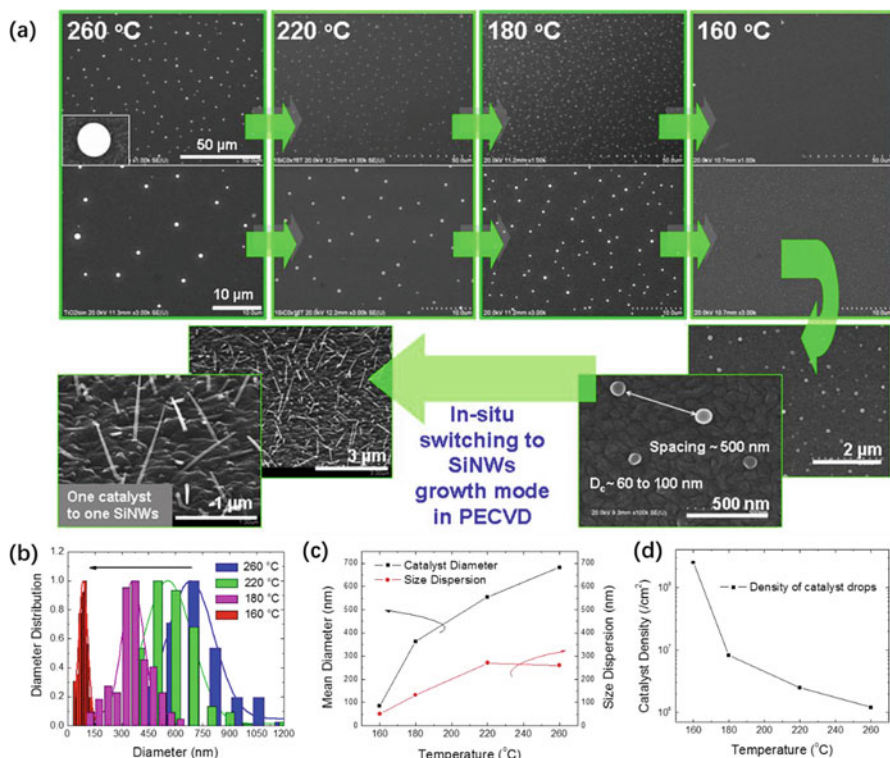


**Fig. 14** (a) SEM images of the indium catalyst drops formed on top of ZnO:Al-coated glass at various substrate temperatures by hydrogen plasma treatment, as well as the SEM images of the as-grown SiNWs. (b–d) Present the extracted distributions, in terms of diameter, density, and size dispersion of the indium catalyst drops obtained as a function of the substrate temperature (Yu et al. 2012b) (Copyright 2012 IOP Publishing Ltd)

Moreover, several factors, e.g., roughness and chemical homogeneity of the substrate, the surface energy of the substrate, as well as the choice of the metal, can affect particle formation.

### VLS Growth of SiNWs

In contrast with the abundant literature on VLS growth of NWs, usually by Au or other noble metals, very few researches have been carried out to investigate the plasma-assisted SiNW growth, particularly with LMP metals as catalyst. TEM studies on PECVD grown SiNWs reveal a variety of morphologies consisting of a crystalline core and a shell which can be either crystalline, amorphous, or nanocrystalline (Alet et al. 2008; Yu et al. 2008, 2009, 2010a, b, 2011). Normally, NWs are randomly tilted when they are grown on top of an amorphous substrate. For low surface tension LMP metals, it has been observed that NWs do not exhibit clear preferential growth direction, even when grown on single crystalline substrates. Figure 15a shows the



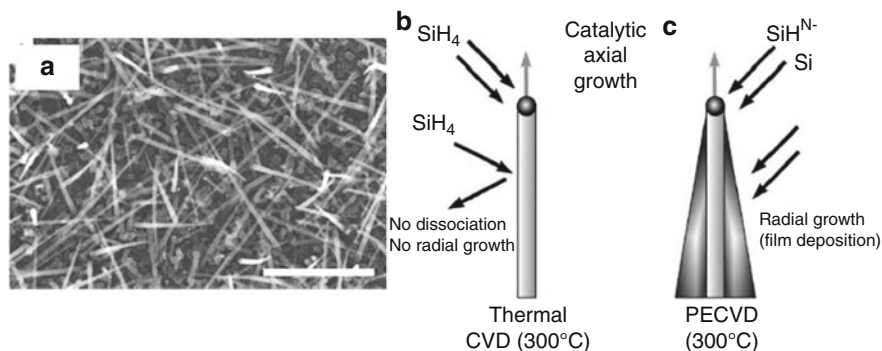


**Fig. 15** (a) Randomly tilted SiNWs grown on a Si  $\langle 100 \rangle$  substrate using In in a PECVD reactor (scale bar is 1  $\mu\text{m}$ ) (Adapted with permission from (Yu et al. 2014b). Copyright 2010 Springer-Verlag). Schematic illustration of (b) low-temperature thermal CVD and (c) PECVD. For thermal CVD only catalytic axial growth occurs, while in PECVD the dissociation of SiH<sub>4</sub> molecules by electron impact leads to both radial expansion and axial growth (Figure adapted with permission from (Ball et al. 2013). Copyright 2007 American Institute of Physics)

plasma-assisted VLS-grown randomly tilted SiNWs on a Si  $\langle 100 \rangle$  – oriented c-Si substrate (Zardo et al. 2010). This is in strong contrast to the best known Au-catalyzed epitaxial growth of SiNWs on c-Si substrates which have undergone the same treatment as in the case of Sn catalyst. A possible reason is that Au is known to catalyze the reduction of SiO<sub>2</sub> layer upon annealing at elevated temperature, which is critical to establish a coherent interface between the c-Si substrate with the SiNW standing upon. Unfortunately, this mechanism does not exist for the LMP metals and the oxide layer between the metal droplet and the c-Si substrate is hard to remove during typical VLS growth condition. Nevertheless, epitaxial growth of in-plane SiNWs, which is an interesting reference system with the same catalyst (In) but using a-Si:H thin film as precursor, has been successfully observed on c-Si substrate (Yu et al. 2014b). This means that epitaxial growth of In catalyzed SiNWs with VLS is still feasible given a proper control of the interface oxide.

For VLS growth in a CVD reactor at temperatures low enough to prevent thermal dissociation of SiH<sub>4</sub> ( $< 650\text{ }^\circ\text{C}$ ), single-crystal Au-catalyzed SiNWs with uniform diameters can be obtained. As the dissociation of SiH<sub>4</sub> molecules occurs only at the surface of the Au catalyst, the process only promotes axial growth. This is illustrated schematically in Fig. 15b (Ball et al. 2013). However, an uncatalyzed radial growth leading to a conical shape can occur at temperatures high enough for the thermal decomposition of gas precursors. For plasma-assisted VLS, the plasma dissociates the source gas. In that case, the reactive species can promote both axial and radial growth, leading to a tapered structure, as shown schematically in Fig. 15c. Yu et al. observed plasma-enhanced sidewall deposition for Sn-catalyzed SiNWs grown at low temperature using pure SiH<sub>4</sub> precursor, where the size of the crystalline core is determined by the size of the metal droplet (Yu et al. 2008, 2009). The SiNWs were observed to become straighter at higher temperatures.



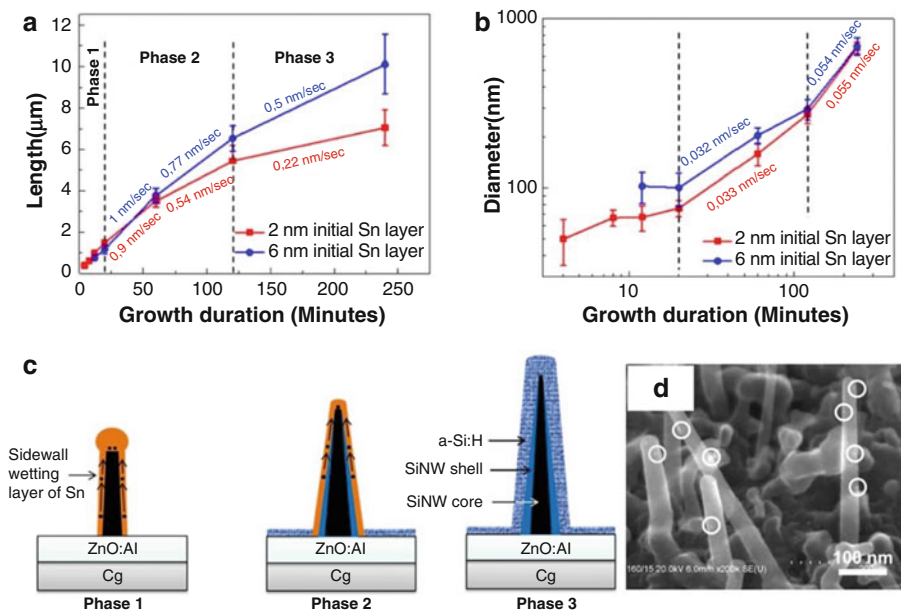


**Fig. 16** (a, b) SiNW length and diameter as functions of growth duration for two values of the Sn thickness. (c) Schematic illustration of the Sn-assisted SiNW growth process, which can be divided into three phases. In the first phase, Sn droplets and the sidewall wetting layer coexist, while in the second phase mainly the ultrathin wetting layer promotes the growth, both in axial and radial directions. In the third phase, the wetting layer is exhausted and growth continues via a-Si:H deposition from silicon radicals. (d) Sn droplets on the sidewalls, resulting from the breakdown of the wetting layer after plasma extinction (observed in phases 1 and 2) (Figure adapted with permission from (Misra et al. 2013a, b). Copyright 2013 American Chemical Society)

More interestingly, recent studies have shown that Sn-assisted SiNW growth can continue without any visible metal droplet on top. To trace the growth evolution, a series of samples with growth durations ranging from 4 min to 4 h have been prepared. The average length and average diameter measured at the base of the NWs are estimated from SEM images and plotted against growth duration in Fig. 16a, b, respectively. Up to 20 min, the growth follows a normal VLS behavior with Sn droplets resting on top of the SiNWs and the average length increasing linearly with the growth duration. During this initial phase, the radial growth is negligible, as can be observed in Fig. 16b. When the growth duration was extended to 60 min, SiNWs became sharply tapered and continued to grow longer with average length proportional to the growth duration, even though SEM images did not reveal any Sn droplet on top of the NWs. On the other hand, a radial expansion was observed for this growth duration (phase 2), as shown in Fig. 16b. At 240 min of deposition time, the axial growth rate was found to saturate, while the radial growth rate increased and became comparable to the a-Si:H growth rate on planar substrates. These observations can be explained by the presence of an ultrathin Sn wetting layer

on the SiNW sidewall (Yu et al. 2010a, b; Misra et al. 2013a, b). The wetting layer helps to stabilize low surface tension metal catalyst droplets on top of the NWs and also enhances the axial growth rate as Si adatoms landing on sidewalls may diffuse along the wetting layer to the top. This effectively suppresses the radial expansion in the first phase (up to 20 min), where the lengths of NWs remain smaller than the diffusion length of adatoms, and the sidewall wetting layer and Sn droplet on top of the NWs coexist. A schematic illustration of the growth model is given in Fig. 16c. In the next phase (up to 120 min of growth duration), the ultrathin Sn wetting layer mediates the absorption of  $\text{SiH}_x$  radicals and the axial growth continues, despite the disappearance of the catalyst droplet from the top of the NWs. On the other hand, when the SiNWs become longer than the diffusion length of adatoms, Si atoms nucleate on the sidewall surface and therefore enhance the radial growth rate. This leads to a core-shell SiNW structure with a crystalline core and a polycrystalline shell. Further support to the hypothesis of a wetting layer during plasma-assisted VLS growth is given by the SEM image in Fig. 16d, where tiny Sn droplets are observed on the SiNW sidewalls. This is attributed to the breakdown of the wetting layer during the cooling process in the absence of a plasma. In the final phase (after 120 min of growth), when the liquid wetting layer is completely exhausted due to continuous etching, the axial growth begins to saturate and the plasma exposure leads to a-Si:H deposition, which turns needle-like SiNWs into more uniform cylinders.

### Optical Properties of Si NWs

Minimizing reflection and transmission losses is a critical issue for any kind of solar cell. Reflection losses can be reduced by depositing an antireflective coating (ARC), normally a thin film of an index-matched dielectric material, on the front surface of the cells. A bare Si substrate reflects over 30% of the incident light at normal incidence, but this can be brought down to <3% using an ARC. The refractive index and the thickness of the layer can be chosen in such a way that light reflecting from the air-ARC interface and the ARC-substrate interface interfere destructively. This eliminates reflection for normal incidence of a single wavelength, while multilayers of dielectric can be used to broaden the range of wavelengths with some added complexity in the deposition process. NWs with proper diameters and densities significantly reduce reflectance over a broad range of solar spectrum. Tapered NWs or nanocones, with tips much smaller than their base, provide an effective medium with a gradual change in refractive index and can outperform both NWs and thin films over a wide range of angles (Huang et al. 2007a; Zhu et al. 2008), but at the cost of sharp features which are more difficult to passivate. On the other hand, transmission losses can be minimized by using light trapping schemes which geometrically increase the optical path inside the absorber and allow to reduce the amount of material. For wafer-based c-Si solar cells, surface texturing is usually achieved by KOH wet etching of <100> c-Si wafers (for more details see ► Chap. 12, “Wafer Cleaning, Etching, and Texturization”), while for thin-film Si solar cells the conventional way is to texture the front TCO (see ► Chap. 20, “Hydrogenated Amorphous Silicon Thin Film”). Texturing of TCOs can be achieved

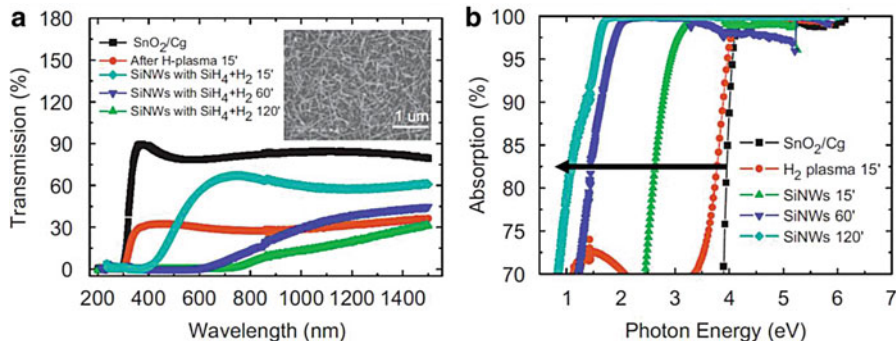


**Fig. 17** (a) and (b) show the optical transmission and absorption spectra of random SiNWs grown on SnO<sub>2</sub> coated Corning glass substrate via plasma enhanced VLS mechanism, with hydrogen diluted silane gas as precursor, for different growth duration from 15' to 120'. The data of reference samples of bare and hydrogen plasma treated SnO<sub>2</sub> coated Corning glass substrates are also presented for comparison (Figure adapted with permission from (Yu et al. 2010a, b). Copyright 2010 American Chemical Society)

either by controlling the deposition process (low-pressure CVD) or by treating a sputtered ZnO:Al layer in a hydrochloric acid solution. In such cases, light propagates at some angle, rather than perpendicular to the substrate, resulting in an increased optical path. Yablonovitch and Cody showed that for a perfect Lambertian reflector, the optical path can be increased by a factor of  $4n^2$ , where  $n$  is the refractive index of the material (Yablonovitch and Cody 1982).

Excellent light trapping and harvesting performance can be easily achieved for randomly tilted PECVD grown SiNWs. For example, Fig. 17a, b shows the transmission and absorption spectra of a matrix of VLS-grown SiNWs catalyzed by tin on SnO<sub>2</sub> coated Corning (Cg) glass, with different deposition durations of 15, 60, and 120 min, which are characterized by using a Perkin–Elmer Lambda 950 spectrophotometer with an integrating sphere. The inset of Fig. 17a presents a typical SEM image of the as-grown SiNWs after 15 min deposition. For comparison, reference samples of SnO<sub>2</sub>/Cg substrate before and after H<sub>2</sub> plasma treatment are also presented. The H<sub>2</sub> plasma treatment is necessary to reduce superficially (not completely) the SnO<sub>2</sub> to release and form Sn droplets as catalyst for subsequent VLS growth of SiNWs. It is clear that with the increase of deposition time of the SiNWs, the falling edge of the transmission curve shifts significantly to longer wavelength (to lower photon energy). In parallel, the absorption edge of the SiNW matrix approaches the c-Si bandgap limit of 1.1 eV with the increase of the length of SiNWs as a consequence of longer deposition time. This observation indicates that the increased light trapping and absorption effects observed here are related to the growth of SiNWs on top of the SnO<sub>2</sub> layer. Actually, the SiNW samples with the longest deposition duration look totally black, indicating a very strong and efficient enhanced light trapping and absorption effect.

It is also noteworthy that while SiNWs can provide strong light trapping, this does not guarantee an efficient collection of the photo-generated carriers. In this respect, the electronic properties of the wires and the passivation of surface defects are crucial. The benefit of plasma-assisted VLS is that a-Si:H can provide an excellent passivation to the c-Si surface or SiNW cores as demonstrated in the case of heterojunction solar cells and the radial junction solar cells addressed in our following sections.

### Doping Effect and Dopant Distribution in VLS-Grown Si NWs

While “top-down” SiNWs have the same doping as the original wafer, the doping type and level for “bottom-up” ones depend on doping precursors added to the silane plasma. During a VLS growth, dopant gases such as  $\text{PH}_3$  or  $\text{B}_2\text{H}_6$  can be introduced along with the precursor gases to achieve n-type or p-type doping in the as-grown SiNWs, respectively (Gudiksen et al. 2002). However, measuring the doping effect or concentration in SiNWs is not straightforward because the common Hall effect or secondary ion mass spectrometry measurement techniques cannot be easily implemented on such nanostructures. For that purpose, atom probe tomography (APT) is better suited as it allows one to quantitatively reconstruct a particular volume of the NWs and to measure the dopant distribution. A nonuniform distribution of dopant atoms with a higher surface dopant concentration has been observed for in situ doped NWs by using APT analysis. Figure 18a shows the cross-section of radial and axial boron (B) concentration in the core of an Au-catalyzed SiNW fabricated using CVD (Chen et al. 2012). Within the analyzed volume of  $30 \times 30 \times 116 \text{ nm}^3$ , the B atoms are inhomogeneously distributed. The radial concentration profile of B in SiNW is shown in Fig. 18b. It can be deduced that the B concentration is  $8.1 \times 10^{18} \text{ cm}^{-3}$  in the center of the SiNW and gradually increases towards the edge to  $7.1 \times 10^{19} \text{ cm}^{-3}$ . Meanwhile, the incorporation of Sn or In catalyst atoms into the VLS-grown SiNWs was also investigated by APT technology (Chen et al. 2014). Interestingly, the concentration of In atoms, which are also a p-type dopant in c-Si, is found to be around  $3 \times 10^{18}/\text{cm}^3$ , but could increase further at higher growth rate.

Although theoretical predictions are very promising, the journey of NW-based radial junction solar cells is quite challenging. Most of the early radial junction prototypes were limited by a series of problems such as catalyst contamination, nonconformal coating, and poor electrical quality, leading to low energy conversion efficiencies. Often, the reported values of the open circuit voltage were below 300 mV. Top-down approaches based on the etching of the c-Si wafer pushed the open circuit voltage beyond 500 mV and drove the energy conversion efficiency above 10%. On the other hand, using Cu and combining it with the proper catalyst cleaning method, Atwater’s group demonstrated 7.9% power conversion efficiency for NWs produced via the VLS method (Putnam et al. 2010). The following sections will proceed to describe the formation and characterization of radial junction solar cells highlighting the specific steps, which require extra care during the fabrication.

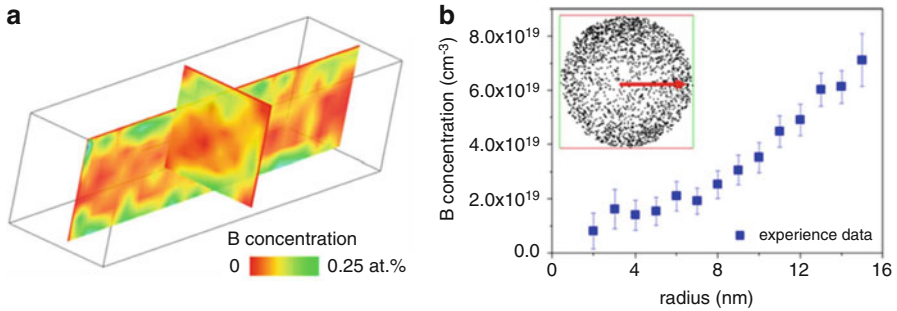


**Fig. 18** (a) Cross-section of radial and axial B concentration in SiNWs. The analyzed volume is  $30 \times 30 \times 116 \text{ nm}^3$ . (b) Radial concentration profile of B in a SiNW. The inset is the cross-section view of individual B atom distribution in SiNW. The red arrow represents the path along which the B concentration is measured (Figure replotted with permission from (Chen et al. 2012). Copyright 2012 American Institute of Physics)

## Radial p-i-n Junction Thin Film Solar Cells

### Radial Junction Deposition Over SiNWs

Once the NWs are fabricated, a junction must be formed for a successful collection of photo-generated carriers after the absorption of incident photons in the active layer. For silicon thin-film solar cells (a-Si:H and  $\mu\text{-Si:H}$ ), an intrinsic layer must be introduced between p-type and n-type doped layers, because the doped layers are highly defective and do not contribute to the collected photocurrent. Thus, for optimized performance of a radial PIN junction, the intrinsic layer thickness should be limited by the diffusion length of the minority carriers in the material under consideration, i.e., 100–200 nm and  $\sim 1 \mu\text{m}$  for a-Si:H and  $\mu\text{-Si:H}$ , respectively. In general,  $J_{\text{sc}}$  increases with the NW length as the absorption is enhanced, and eventually it saturates when the NW becomes much longer than the optical thickness of the material. In contrast,  $V_{\text{oc}}$  usually decreases with increasing NW length as the dark current is also proportional to the surface recombination. Unlike  $J_{\text{sc}}$ ,  $V_{\text{oc}}$  changes significantly with the defect density in the depletion region. The fabrication, characterization, and device performance of radial p-i-n junction solar cells will be discussed in following sections.

### Individual Radial Junction Solar Cells

The study of single NW solar cells is very challenging as well as extremely important to understand the absorption, transport, doping, and surface properties of the cells. Individual NW solar cells have been measured in some cases by lithographically contacting VLS-grown single SiNWs. Tian et al. were the first to experimentally realize the concept of coaxial PIN SiNW radial junction solar cells (Tian et al. 2007). The p-type SiNWs were grown via an Au-catalyzed VLS process and subsequently coated with an i-type and an n-type polycrystalline shell. After that, they contacted the n-type shell and p-type core and measured efficiencies up to

3.4% under AM 1.5G illumination with a remarkable  $J_{sc}$  of  $23.9 \text{ mA cm}^{-2}$  (upper bound). There is also report on single vertical core-shell PIN junction GaAs NW solar cell which can accomplish one order of magnitude higher absorption beyond the Lambert-Beer law (Krogstrup et al. 2013). The results are a very inspiring consequence of the antenna concept, but it must be kept in mind that the collective absorption of an array of radial junctions in an actual device can be significantly different from the single one.

Alternatively, electron and optical beam-induced current (EBIC and OBIC) techniques, as well as conductive atomic force microscopy (AFM) can be used to locally assess the properties of individual radial junctions (Fejfar et al. 2013; Yu et al. 2013). These characterization techniques are really important, as there are millions of individual units in a solar cell and a weak diode can shunt photocurrents generated by a large number of neighboring junctions. In EBIC or OBIC measurements, an electrical or optical beam is swept across the sample and the output current of the device is recorded. The resolution is limited by the beam spot sizes, which are 2 nm and 2  $\mu\text{m}$  for EBIC and OBIC, respectively. The current responses from individual radial junction solar cells are probed and compared with their planar counterparts.

Remarkably, the high spatial resolution provided by EBIC microscopy allows tracing the current generated in different segments of a single RJ cell. The measured EBIC signal is proportional to the electron-hole generation rate in the intrinsic absorber layer caused by the impinging electron beam. Indeed, in the case of slightly tilted SiNW cells seen in Fig. 19a, b, the EBIC current signal is found to vary along the NW axis. The highest EBIC signal has been recorded at the tip of RJ cells, and then the EBIC current decreases towards their roots. This finding implies that a good core conductivity and thus an efficient p-type doping have been achieved in the ultrathin SiNW cores, despite the small diameter of the sharply tapered tips. And it is indeed possible to use ultra-thin SiNWs (only  $\sim 20 \text{ nm}$  in diameter) as inner cores to construct radial p-i-n junction. As the size of the EBIC probing electron beam is around 2 nm. Within the PIN junctions, the probability of inelastic collisions is proportional to the effective thickness of the intrinsic layer. As a consequence, given the same absorber medium, the magnitude of detected EBIC signal provides a reasonable measure of the effective volume of the active intrinsic absorber within a local PIN junction under electron beam probing. More experimental results and discussions are available in Ref. (Yu et al. 2013).

Surprisingly, the radial junctions are quite robust against geometrical disorder and even crossing, as shown in Fig. 19d, e. As a matter of fact, mutual shadowing and even crossing are basically inevitable among a randomly oriented matrix of VLS-grown SiNWs. Figure 19d shows, for example, the SEM image captured among a dense matrix of random SiNW/RJ cells, where crossing and even merging between neighboring RJ-Cell units are clearly witnessed. Regardless of these geometrical “imperfections” as marked by the arrows, EBIC mapping in Fig. 19e on these regions indicates no significant current degradation. Actually, the joining parts of SiNW units generate a comparable or even higher current with respect to neighboring isolated radial junctions. These observations show a larger-than-expected tolerance of our radial junction solar cells to the geometrical disorder of



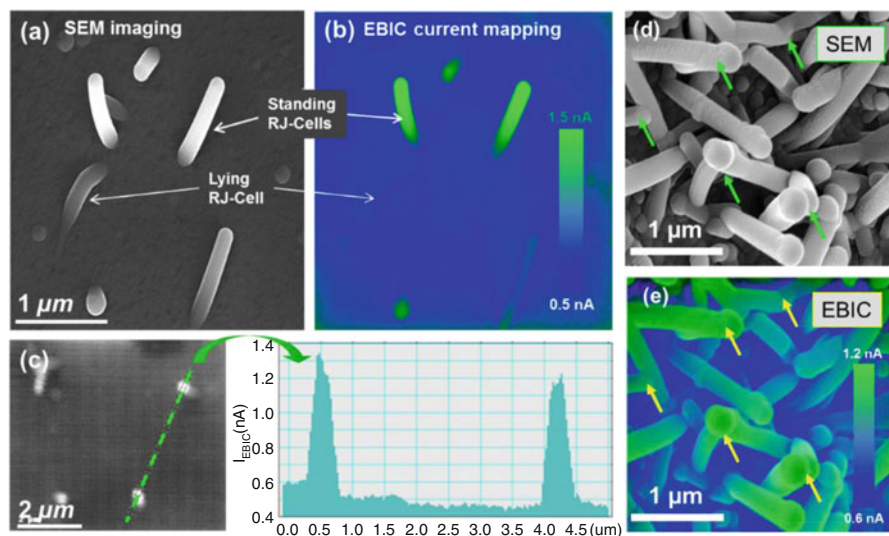


**Fig. 19** (a) and (b) show the secondary electron SEM imaging and the corresponding EBIC current signal mapping of the same regions of sparse SiNWs RJ-cells, respectively. A line-profile analysis of the EBIC signal intensity, crossing two standing RJ-cells, is presented in (c). (d) and (e) present the secondary electron SEM and EBIC current mapping of the radial junctions realized on top of a dense matrix of SiNWs, with the arrows pointing at the strong EBIC current generation points despite apparently crossings of radial junctions (Figure adapted with permission from (Yu et al. 2013). Copyright 2013 IOP Publishing Ltd)

the random SiNW matrix and provide a strong experimental proof that it is possible to fabricate efficient radial junctions over random SiNW arrays.

In addition, conductive AFM characterization provides another convenient and straightforward means to probe the local (opto) electronic properties of the radial junction units grown upon the SiNWs (Fejfar et al. 2013), where the local conductivity mapping can be determined with peak force tunneling AFM. Note that conductivity maps of the SiNWs are influenced by scattered light from the laser, which cannot be switched off during the measurement. With some additional advancement, this instrument can also be used to scan the variation of the local J–V characteristics of the cells.

### From Single NW Cells to Millions/cm<sup>2</sup> in Parallel

Although there are numerous approaches to grow SiNWs and hence radial junctions over them, this section will focus on building radial junction thin film solar cells over plasma-assisted VLS-grown SiNW framework. Over the last 6 years, the performance of radial junction thin film solar cells, in terms of power conversion efficiency, has made steady progress from below <1% to 9.2% (Yu et al. 2010a, b, 2012a, b; O'Donnell et al. 2012; Cho et al. 2013; Misra et al. 2013a, b, 2015; Qian et al. 2015). At the beginning, a TCO (either ITO or SnO<sub>2</sub>) covered glass was used substrate, which is then exposed to H<sub>2</sub> plasma treatment to superficially reduce the

top layer and produce metal droplets for plasma-assisted VLS growth of SiNWs (Yu et al. 2010a, b). The very first radial junction solar cells were fabricated in a standard *superstrate* configuration with a multilayer thin film structure of glass/TCO/intrinsic c-Si NW/intrinsic a-Si:H/n-type a-Si:H/Al back contact. To characterize the solar cell performance, light was shined through the glass substrate and then the TCO layer. For these cells, conversion efficiencies were poor mainly due to the insufficient p-type doping of the SiNW cores solely by the incorporation of catalyst atom of In, without other dopant gases during the VLS growth. Then, the solar cell performance was largely improved thanks to two contributions: (1) first, the doping in SiNWs was greatly enhanced by adding trimethylboron (TMB) during their VLS growth, and (2) second, the light was changed to shed from the top through a transparent TCO layer, in order to expose the 3D radial junction interface directly to the incident light for a maximal light trapping effect. These modifications brought in exciting progresses that boosted the efficiency of the radial junction solar cells to 4.9% for Sn-catalyzed SiNWs (O'Donnell et al. 2012). Further on, optimizing the doping control in the SiNW cores and the thin film layers helped to achieve an even higher  $V_{oc}$  of 0.80 V and  $J_{sc}$  of  $12.4 \text{ mA cm}^{-2}$ , which is close to the value obtained for planar cells deposited on Asahi U-type textured  $\text{SnO}_2$  substrates.

A schematic structure and the corresponding SEM image of the solar cells are shown in Fig. 20a, b, respectively. The p-type SiNWs are grown on glass substrates covered with  $1 \mu\text{m}$  thick ZnO:Al (which serves as the back contact), and a thin layer of evaporated Sn. After that, NWs were covered with 'conformal' layers of intrinsic and n-type a-Si:H by exposing the samples to silane and silane plus phosphine plasmas, respectively. Finally, ITO was sputtered through a shadow mask to form the transparent top contact and connect millions of radial junctions in parallel. The inset in Fig. 20d shows a picture of an actual device with silver dots on the ITO pad to place the probe for electrical measurements. The current density–voltage (J-V) characteristics of SiNW solar cells are presented in Fig. 20c with different partial pressures of TMB (diluted in 98%  $\text{H}_2$ ). It can be observed that the open circuit voltage increases with the TMB partial pressure and saturates above 42 mTorr. It has been found that the length of NWs and the thickness of the n-type a-Si:H significantly affect the device performance. Increasing the length of NWs from 1 to  $3 \mu\text{m}$  leads to 50% more current generation and correspondingly the energy conversion efficiency increases from 3.4% to 6%. Reducing the deposition time of the n-type a-Si:H improves the spectral response in the blue part, but thinner n layers also lead to reduced FF.

Then, the impact of the SiNW density on  $J_{sc}$ , as well as the overall performance, was investigated and optimized. By controlling the density of In and Sn droplets and hence the density of NWs, a trade-off has to be sought in order to have simultaneously a sufficiently high density of radial junctions leading to a sufficient light trapping, and enough space between them to allow for a uniform deposition of subsequent thin film layers. As discussed in previous sections, the density of the catalyst droplets can be varied by controlling the plasma parameters and the initial metal film deposition conditions. Optimizing the density of SiNWs has resulted in a high power conversion efficiency of 8.14% for radial junctions built over a Sn-catalyzed SiNW matrix (Misra et al. 2013a, b). It must be noted that a relatively



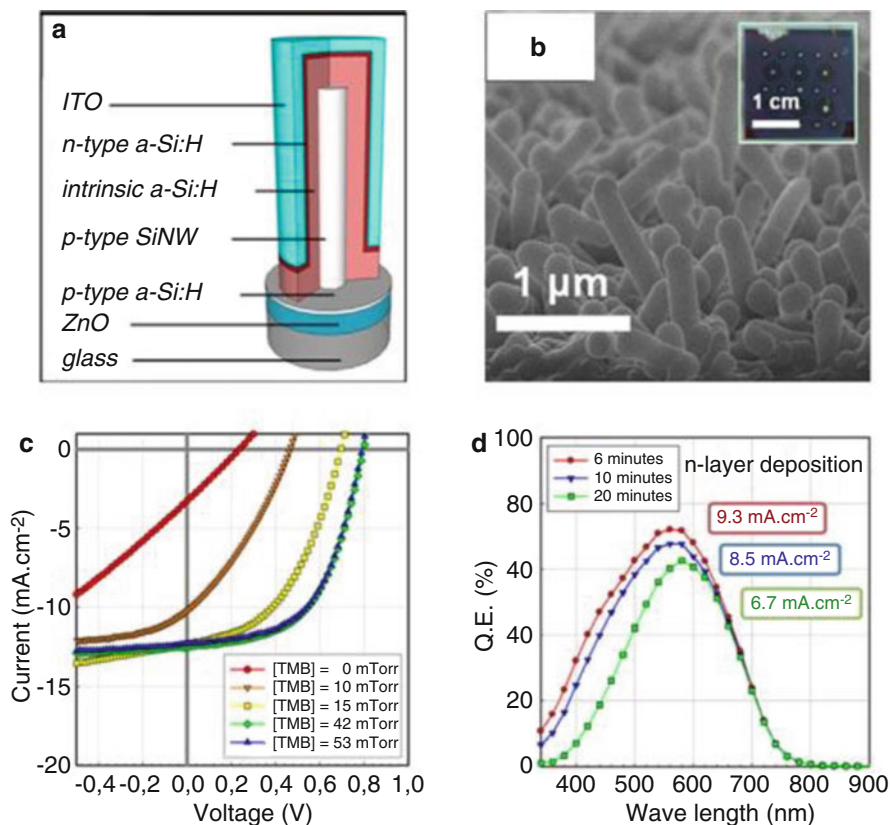


**Fig. 20** (a) Schematic diagram of a SiNW radial junction unit cell. (b) SEM micrograph of radial junction solar cells after sputtering the ITO top contact. The inset shows a picture of the completed device. (c) J–V characteristics of radial junction PIN solar cells with different TMB (diluted in 98% H<sub>2</sub>) partial pressures, used to grow p-type SiNWs. Note that the  $V_{oc}$  increases with the partial pressure of the doping gas and saturates beyond 42 mTorr. (d) Spectral response of SiNW solar cells grown with different thicknesses of n-type a-Si:H (Figure adapted with permission from [149]. Copyright 2011 Elsevier)

high short circuit current density of  $16.1 \text{ mA cm}^{-2}$  has been achieved with only 100 nm a-Si:H intrinsic layer, which is much thinner than the usual thickness of planar a-Si:H cells ( $\sim 250 \text{ nm}$ ) deposited on textured substrates. Using very thin absorber layers has two major advantages, apart from reducing the material consumption: firstly, for the same doping level, it provides a stronger built-in field for better collection of carriers and secondly, the thinner i-layer improves the stability of the device under light soaking, also related to the stronger field within the intrinsic layer of the solar cell. The second advantage is demonstrated in Fig. 21, showing the J–V curves before and after 120 h of light soaking. These measurements confirm the excellent stability of the cells, with a mere 6% light-induced degradation compared with 15–20% observed in planar cells.

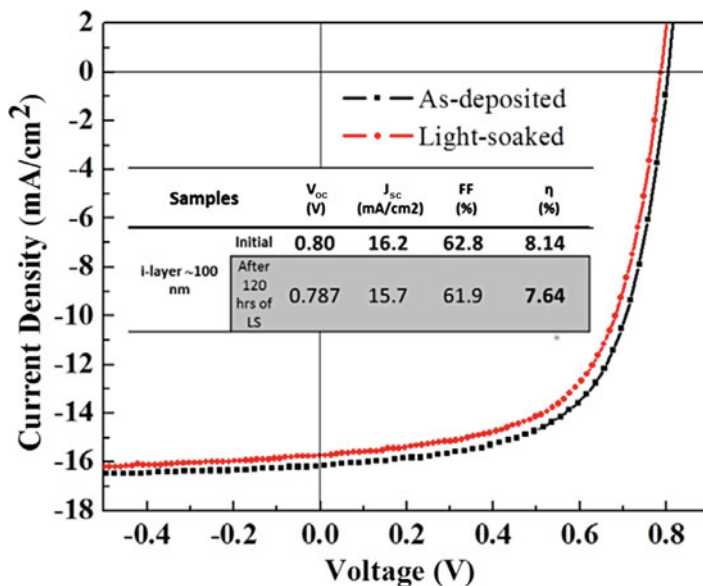


**Fig. 21** J–V characteristics measured in the as-deposited state and after 120 h of light soaking. The use of only a 100 nm intrinsic layer remarkably improves the stability under light soaking (Figure adapted with permission from (Misra et al. 2013a, b). Copyright 2013 Elsevier)

Nevertheless, the PIN configuration with the light impinging from the n-type a-Si:H is not ideal from the electrical point of view. Indeed, in this case, most of the high-energy photons are absorbed and produce the highest generation rate of electron–hole pairs near the i-aSi:H/n-aSi:H interface. Having a shorter diffusion length compared with electrons, most of the holes may recombine before being collected. Moreover, the electric field at the interface depends on the Fermi level difference between the two layers. As intrinsic a-Si:H is slightly n-type, this results in a stronger field at the p–i interface than at the n–i interface. Thus, n-type c-SiNW/i-aSi:H/p-type a-Si:H should be more efficient than its reverse configuration. Xie et al. fabricated NIP radial junction solar cells on flexible stainless steel substrates and demonstrated an efficiency of 3.57% (Xie et al. 2013). In a similar way to our process, they reduced a thin layer of ITO by atomic hydrogen treatment and then used a  $\text{SiH}_4 + \text{PH}_3$  gas mixture to grow n-type SiNWs. Adachi et al. used an original structure to demonstrate a 6% conversion efficiency for NIP configuration with a remarkable  $V_{oc}$  of 0.83 V (Adachi et al. 2013). First, they grew Sn-catalyzed SiNWs on Al-coated glass substrates by PECVD and then covered them by a thin layer of ZnO:Al. The purpose of the ZnO:Al barrier layer is to isolate the nanocluster catalyst from the active NIP structure and prevent counter doping by Al from the back contact.

As discussed earlier, the catalyst incorporation is inevitable inside NWs and the catalyst metals can generate an effective and useful doping in the SiNWs for solar cell fabrication. In a novel approach, Yu et al. used Bi to mediate VLS growth and

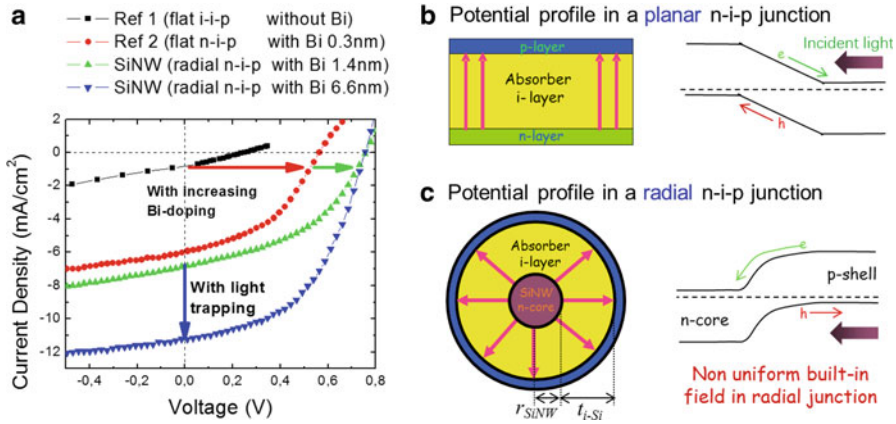


**Fig. 22** (a) 3D cross-section illustration of a core-shell SiNW device structure. The intrinsic region can be either amorphous or microcrystalline. (b) EQE spectra of a microcrystalline SiNW core-shell structure and planar cells. The core-shell solar cell with the longest NWs demonstrates the highest quantum efficiency at all wavelengths (Yu et al. 2012a) (Copyright 2012 American Chemical Society)

utilized the n-type doping provided by metal incorporation for building radial NIP solar cells (Yu et al. 2012a). This work provides the first evidence that catalyst doping in the SiNW cores, caused by incorporating Bi catalyst atoms as n-type dopant, can be utilized to fabricate radial junction solar cells. As seen in Fig. 22a, the incorporation of Bi atoms can lead to significant n-type doping effect in both crystalline SiNWs and amorphous a-Si:H samples. With the aid of Bi-catalyzed SiNWs, a strong light trapping effect helped to boost the short circuit current to  $J_{sc} = 11.23 \text{ mA/cm}^2$ , while the open circuit voltage also ramped up to  $V_{oc} = 0.76 \text{ V}$ , without the use of extremely toxic phosphine gas. This is an advantage for radial junction solar cells as it will lead to significant procedure simplification and cost reduction for scalable photovoltaic applications.

In addition, there is also a unique aspect for radial junction configuration, which is very different from their planar counterpart, as depicted schematically in Fig. 22b and c. In contrast to the uniform built-in field in a planar junction, the built-in field in a radial junction is established by a pair of asymmetrical electrodes with different facing areas, as seen for instance in Fig. 22c, and thus becomes nonuniform over the *i*-layer. Specifically, when coating on top of a SiNW with radius of  $r_{SiNW}$ , the built-in field in a radial *i*-layer is described as a function of the distance *t*, measured from the *n-i* interface, as

$$E_{\text{radial}}(t) = \frac{V_{oc}}{(r+t)Ln(1+t/r)} = E_{\text{planar}}(t) \cdot \frac{1}{(1+r/t)Ln(1+t/r)} \quad (1)$$

As a consequence,  $E_{\text{radial}}(t)$  in the radial junction will decreases gradually from the maximum field intensity of  $E_{\text{radial-}n-i}^{\text{max}} = E_{\text{planar}}$  at the inner *n-i* interface, to the

minimum intensity of  $E_{\text{radial}_{p-i}}$  at the outer  $p-i$  interface. Particularly, at the outer  $p-i$  interface, the ratio of the radial junction building field over that in a planar counterpart, with the same intrinsic layer thickness, can be written as

$$E_{\text{radial}_{p-i}}/E_{\text{planar}} = \frac{1}{(1 + 1/f)Ln(1 + f)}, \text{ where } f = t_{i-Si}/r_{SiNW}. \quad (2)$$

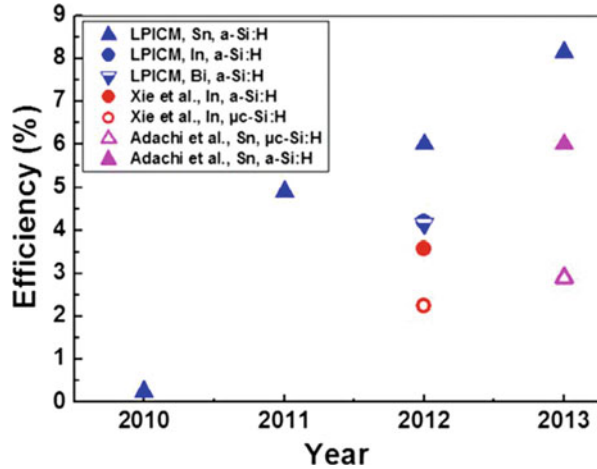
This implies that the sweeping electric field at the outer  $p-i$  interface in a radial junction solar cell will be somehow reduced with a thick intrinsic absorber layer compared to the diameter of SiNW core. As a consequence, increasing the  $i$ -layer thickness is not always beneficial. An optimal geometry design of the multilayer radial junction structure has to take into account this unique feature of nonuniform built-in electric field in radial junction solar cells.

Until now, only a few groups have explored  $\mu\text{-Si:H}$  as a potential candidate for radial junction thin-film solar cells. Compared with  $\text{a-Si:H}$ ,  $\mu\text{-Si:H}$  offers better stability under light soaking and a broad wavelength absorption owing to its low band gap energy. However, the overall performance of the cells with longer SiNWs is worse, despite their higher  $J_{\text{sc}}$ , mainly due to lower  $V_{\text{oc}}$  and FF. Note that the spectral response extends up to 1000 nm, which makes  $\mu\text{-Si:H}$  a promising candidate for the bottom cell in tandem  $\text{a-Si:H}/\mu\text{-Si:H}$  radial junction solar cells. Recently, in order to minimize the absorption loss in the highly doped window  $\text{a-Si:H}$  layers, a wide bandgap material, e.g., hydrogenated microcrystalline silicon oxide ( $\mu\text{-SiO}_x\text{:H}$ ) is used, which is a phase mixture of  $\mu\text{-Si:H}$  and hydrogenated amorphous silicon oxide ( $\text{a-SiO}_x\text{:H}$ ). The  $\mu\text{-Si:H}$  phase is mainly affected by  $n$ -type doping and provides the channel for the electrical conductivity, while the  $\text{a-SiO}_x\text{:H}$  phase is responsible for the transparency of the film. In  $\mu\text{-SiO}_x\text{:H}$  deposition, there is a tradeoff between the transparency and the conductivity of the film, which can be controlled by varying the  $\text{CO}_2/\text{SiH}_4$  ratio. Replacing  $n$ -type  $\text{a-Si:H}$  by  $n$ -type  $\mu\text{-SiO}_x\text{:H}$  significantly enhances the blue response and consequently improves the integrated  $J_{\text{sc}}$ , obtained from EQE, from 14.2 to 15.2  $\text{mA}/\text{cm}^2$ . Along with a  $V_{\text{oc}}$  of 0.82 V and FF of 73.7%, it leads to an overall efficiency of  $\sim 9.2\%$  for 0.126  $\text{cm}^2$  area (Misra et al. 2015). The year by year evolution of radial junction thin-film solar cell performances, built over plasma-assisted VLS-grown SiNWs (up to 2013), is plotted in Fig. 23. Different catalysts, used for the NW growth, are also indicated. The performances of solar cells increase every year with a clear trend towards values closing up to the records by  $\text{a-Si:H}$  or  $\mu\text{-Si:H}$  thin-film cells deposited on textured TCO substrates.

### Resonant Absorption in Radial Junction Units

Though several recent works have addressed the light absorption by an array of Si nanowire/rods, the light in-coupling and absorption profile in a more sophisticated and complex multilayer  $p-i-n$  thin film solar cell structure, as well their implications for device performance, remain largely unexplored. Within a coaxial radial junction (RJ) thin film solar cell, a sequence of layers of materials with distinctive optical properties are deposited around individual SiNW cores. In such a 1D cavity-like

**Fig. 23** Year by year evolution of plasma-assisted VLS-grown SiNW-based radial junction thin-film solar cells. Different colors are used to differentiate the laboratories working on this topic. Triangles, circles, and inverted triangle represent the various low melting temperature metals (Sn, In, and Bi) used to mediate the growth. Solid symbol means the intrinsic layer is a-Si:H, while the hollow symbol represents  $\mu$ -Si:H (Misra et al. 2014)



composite, photonic and resonant mode-matching effects in the RJ units via optical antenna coupling or leaky-mode-resonance can play an important role in determining light absorption and scattering. How this resonant absorption or scattering will affect the light harvesting behavior in a coaxial p-i-n junction thin film solar cell remains an interesting aspect to address. The goal is thus to establish a comprehensive optical model for a coaxially deployed multilayer radial junction thin film solar cell, in order to develop critical clues and a new strategy for optimizing such devices.

In order to model the resonant absorption in the individual NW solar cell, we consider a coaxial radial junction unit as illustrated in Fig. 24a. Figure 24b presents a SEM view of a single radial junction cell. To carry out an accurate simulation, the optical dispersion n-k curves of each material have been extracted from the modeling of spectroscopic ellipsometry measurements on co-deposited planar thin films (Yu et al. 2014a). Assume that the SiNW core is represented by a cylinder of radius  $R_w = 20$  nm and with lengths ( $L_w$ ) from 0.6  $\mu$ m to 2.4  $\mu$ m. The intrinsic a-Si:H layer thickness ( $T_i$ ) has been varied from 20 nm to 140 nm, while the thickness of the n-type a-Si:H layer and ITO layers are fixed to have typical values of  $T_n = 10$  nm and  $T_{ito} = 50$  nm, respectively. In this simulation, a single radial cell is placed at the center of a square simulation box (1.5 x 1.5  $\mu$ m) on top of a glass substrate. Polarized light propagating along the y-axis originates from the top plane. Dissipative scattering conditions are applied to the entirety of the wall and bottom boundaries. The finite element solver module in COMSOL MULTIPHYSICS was used to carry out the structural modeling and optical simulation.

In the upper panel in Fig. 25a, the  $E_y$ -field distribution in a single radial junction solar cell unit is shown, under different incident wavelengths of  $\lambda = 350$  nm, 550 nm, and 750 nm, with a SiNW length of  $L_w = 1.7$   $\mu$ m and an i-layer thickness of  $T_i = 100$  nm. At  $\lambda = 350$  nm (high energy photons), the incident light is screened by the outer ITO and n-type emitter layers, with only a small fraction reaching the

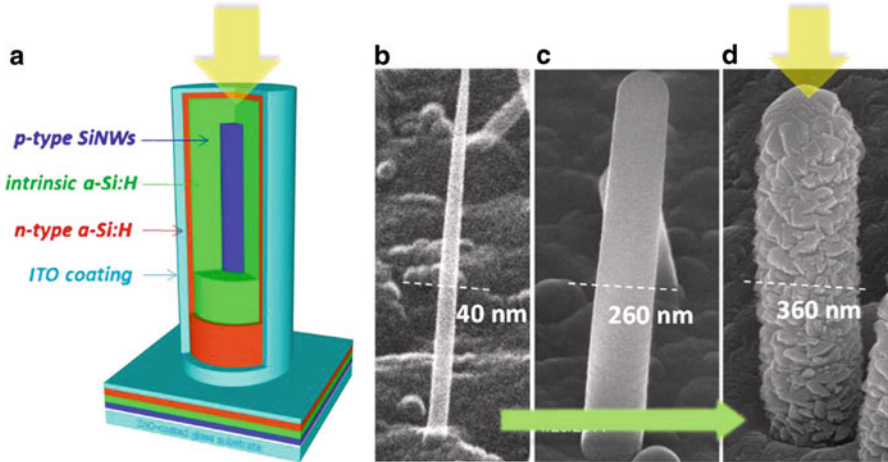


**Fig. 24** (a) Schematic illustrating the coaxial multilayer structure of a radial junction solar cell unit; (b), (c), and (d) show, respectively, the SEM images of a single SiNW, a p-i-n RJ cell, and an ITO coated RJ cell (Yu et al. 2014a) (Copyright 2014 Nature Publishing Group)

buried absorber i-layer. At longer wavelengths ( $\lambda = 550 \text{ nm}$  to  $750 \text{ nm}$ ), the incident light propagates deeper into the radial junction and can be better coupled into the cavity-like radial junction cell, which starts to behave particularly like a waveguide or antenna at  $\lambda = 750 \text{ nm}$ .

Based on these field distribution results, the local power dissipation – that is the local absorption occurring within the radial junction multilayer – is calculated according to

$$P_{abs}(\lambda) = c \cdot I_{\text{light}} \cdot \alpha(\lambda) = c \cdot I_{\text{light}} \cdot 4\pi k(\lambda) / \lambda \quad (3)$$

where  $I_{\text{light}}$  is the local electromagnetic energy intensity,  $c$  is the speed of light in vacuum, and  $\alpha(\lambda)$  and  $k(\lambda)$  are the absorption coefficient and the imaginary part of the complex refractive index  $\tilde{n}(\lambda) = n(\lambda) + ik(\lambda)$ . The corresponding power absorption mappings in the radial junction cell structure are calculated and presented in Fig. 25b. The absorption of high energy photons ( $\lambda = 350 \text{ nm}$ ) mostly takes place within the outer ITO and n-type emitter layers, with little absorption occurring in the PV active inner intrinsic a-Si:H layer. At  $\lambda = 550 \text{ nm}$ , the inner i-layer becomes the dominant zone for light harvesting, while the absorption in the c-SiNW core remains still very weak, in spite of a strong field within the core region as seen in the corresponding  $E_y$  field distribution in Fig. 25a. This is because at  $\lambda = 550 \text{ nm}$ , the absorption coefficient of a-Si:H is almost two orders of magnitude higher than that of c-Si (typically  $\alpha_{\text{a-Si}}/\alpha_{\text{c-Si}} \sim 10^2$ ). At even longer wavelengths of  $\lambda = 750 \text{ nm}$ , the incident photon energy approaches the optical bandgap of the a-Si:H absorber and gets strongly confined within the radial junction cell. However, the effective



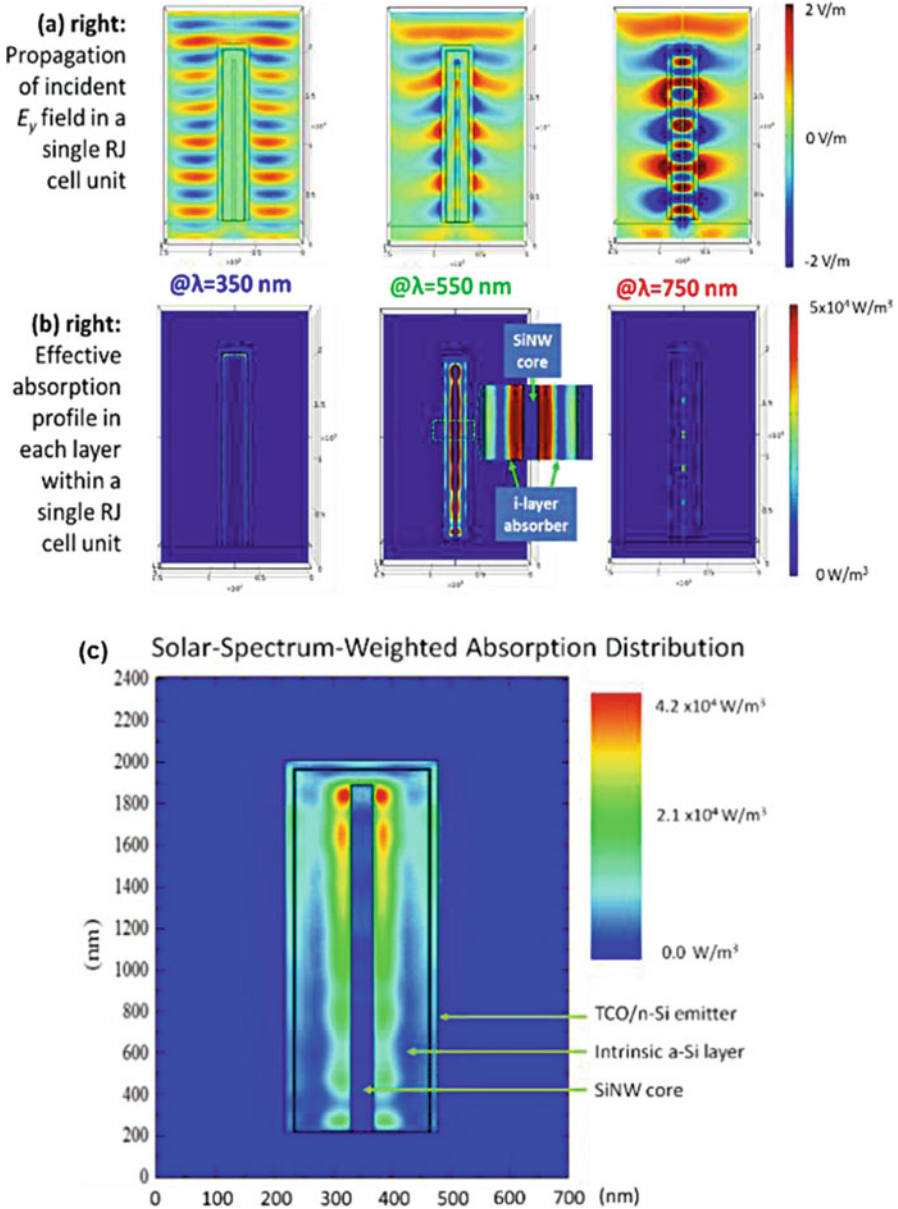


**Fig. 25** (a) Upper panels show the simulated electrical field distribution ( $E_y$ ) through a single radial junction cell at different photon wavelengths, while the lower panels (b) present their corresponding absorption profile within each material layer in the multilayer radial junction structure. (c) Solar-spectrum-weighted absorption distribution within the radial junction solar cell unit, over a spectrum through  $\lambda = 300$  nm to 800 nm (Yu et al. 2014a) (Copyright 2014 Nature Publishing Group)

absorption realized within the intrinsic a-Si:H layer drops dramatically, while most incident photons get absorbed in the crystalline SiNW core, which is considered as a dead zone because of its high doping level.

Close examination of the absorption mapping at  $\lambda = 550$  nm shown in Fig. 25c reveals more intriguing features of the absorption profile within a single radial junction cell. For example, the highest absorption regions in the i-layer are actually located very close to the inner i-layer/SiNW interface, as witnessed in the enlarged inset in Fig. 25b for  $\lambda = 550$  nm, instead of at the outer emitter/i-layer interface, as one would expect in a planar p-i-n thin film solar cell. Furthermore, to give a quantitative estimation of PV performance, a solar-spectrum-weighted absorption profile  $P_{av}$  is calculated within a radial junction solar cell unit, as shown in Fig. 25c, defined as

$$P_{av} \equiv \int P_{abs}(\lambda) \cdot W_{AM1.5}(\lambda) \cdot d\lambda, \quad (4)$$

where  $W_{AM1.5}(\lambda)$  is the weighting factor derived from the standard AM1.5 solar mass spectrum with  $\int W_{AM1.5}(\lambda)d\lambda = 1$  when integrating over  $\lambda = 300$  nm to 800 nm (the most relevant spectrum range for a-Si:H absorption). It is clear that the absorption intensity profile shows its highest absorption zones in the vicinity of the inner i-layer/SiNW core interface, instead of the outer emitter/i-layer interface. This is strikingly different to the situation in planar p-i-n junction a-Si:H cells, where the highest absorption zones are always located at the outer emitter/i-layer interface, and therefore a p-type emitter layer is always preferable to shorten the collection distance of photo-generated holes. This finding reveals however that a higher concentration of photo-carriers is generated in close proximity to the inner interface, and thus a p-type SiNW core is favorable for the radial p-i-n junction solar cells.

To understand the optical losses and effective absorption within the radial junction cell, the absorption broken down by different material layers is extracted and plotted in Fig. 26a, for a typical radial junction a-Si:H solar cell unit with  $L_w = 1.7$   $\mu\text{m}$ ,  $T_i = 100$  nm, and  $W_{sub} = 1.5$   $\mu\text{m}$ . It is clear that a majority of the short wavelength absorption losses are mainly caused by the outer ITO and doped a-Si:H layers, emphasizing the need to adopt a wider band-gap emitter layer of doped a-SiC or  $\mu\text{c-SiO}_x$ . To the long wavelengths, the absorption in the i-layer drops rapidly when approaching the bandgap of a-Si:H. Figure 26b shows the absorption occurring in the i-layer as a percentage of the total absorption in the radial junction cell, for different i-layer thickness ( $T_i$ ) ranging from 20 nm to 140 nm. It is interesting to see that a thicker i-layer can boost the light absorption for longer wavelengths  $\lambda > 450$  nm, but this tends to saturate for  $T_i > 100$  nm.

Furthermore, the calculated absorption curves for different intrinsic layer thickness of  $T_i$  ranging from 20 nm to 140 nm are shown in Fig. 27a. To have a better view of the evolution of the absorption peaks with decreasing i-layer thickness, all these absorption curves are normalized to their maxima and shown in Fig. 27b. 2D mode analysis on the cross section of a coaxial radial junction cell with an i-layer thickness of  $T_i = 140$  nm reveals that the highest contribution comes from a pair of



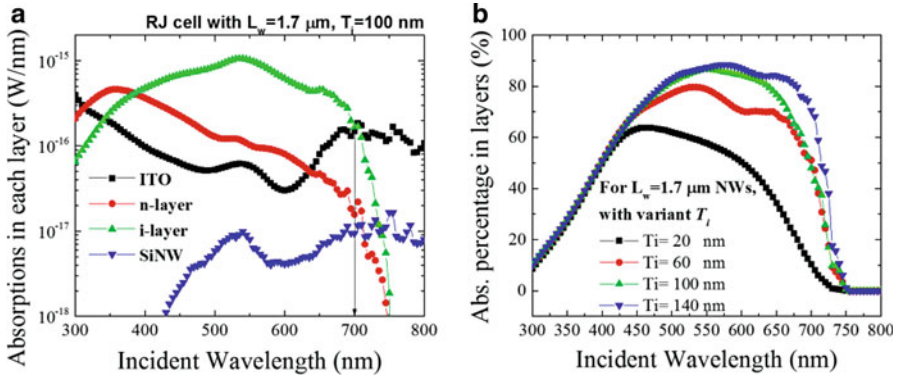


**Fig. 26** (a) Absorbed power broken down by different material layers as a function of incident photon wavelength for a radial junction cell with SiNW length of  $L_w = 1.7 \mu\text{m}$  and i-layer thickness of  $T_i = 100 \text{ nm}$ . (b) Percentage of effective absorption in the i-layer relative to total absorption in the radial junction multilayer structure (Yu et al. 2014a) (Copyright 2014 Nature Publishing Group)

propagation modes with mutually orthogonal field distribution patterns, one of which is shown in Fig. 27c. As it has been shown that, for this cavity mode, the field distribution is concentrated in the annular i-layer, resulting in a maximal useful absorption in the radial junction cell. This resonant-mode-selection feature or criterion is indeed a unique aspect in the coaxial radial p-i-n cell, as compared to the situation in a simple radial p-n junction solar cell.

Comparing the normalized  $P_{\text{eff}}$  curves with different i-layer thickness of 80 nm (red), 100 nm (green), and 120 nm (blue) to the normalized experimental EQE spectrum (black), as seen in Fig. 28a, measured on a real radial junction cell array shown in the top-view SEM image of Fig. 28b, a nice agreement has been achieved between the simulated and experimental EQE curves in the short-wavelength range, from  $\lambda = 300 \text{ nm}$  to 550 nm. At longer wavelengths, a higher EQE response was measured for the actual “forest” of radial junction solar cells, compared to the simulated response for a single radial junction solar cell. The enhancement ratio of the normalized experimental EQE over the absorption response of a single radial junction cell is plotted as a function of incident wavelength in Fig. 28d, which implies that the contribution of light trapping arising from multiple scattering events among individual radial junction units is indeed highly wavelength-dependent. This also provides an insightful and powerful tool to resolve the wavelength-dependent contributions arising from individual radial junction units and/or from strong light trapping due to the presence of the radial junction cell array.

### The Impact of Tilting on Radial Junction Performance

Another fundamentally interesting as well practically important concern for building such a 3D radial p-i-n junction solar cells lies that mutual or self-shadowing becomes a quite common situation that would cause nonuniform photo-current generation among/or along the standing radial junction units, see the situation in the SEM image

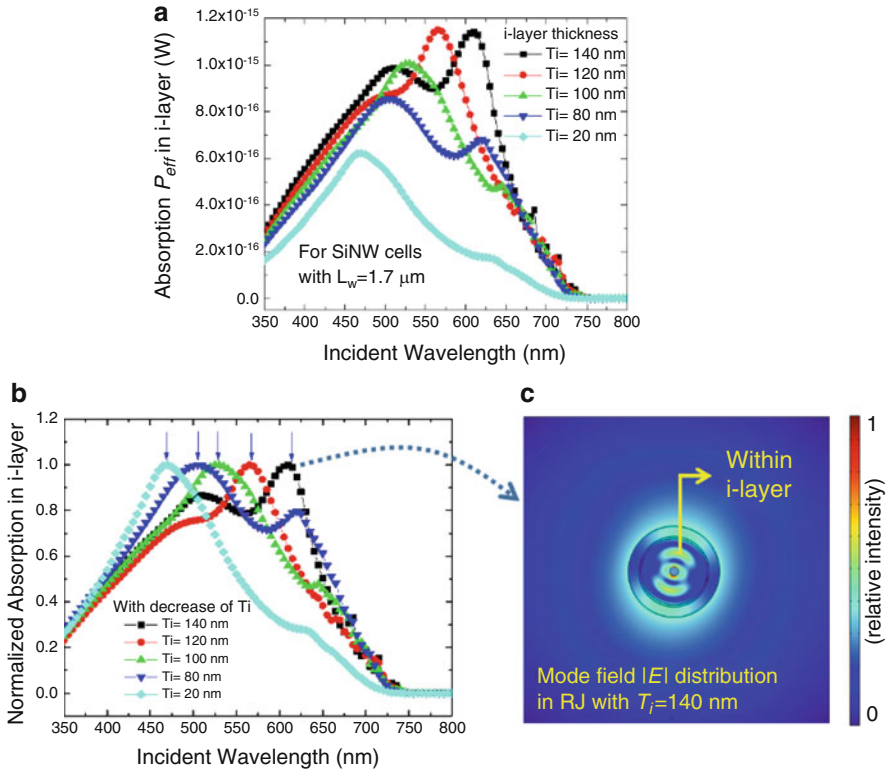


**Fig. 27** (a) Absorption spectra in active i-layer while varying i-layer thickness ( $T_i$ ) from 20 nm to 140 nm, (b) full spectrum integrated absorption in i-layer as a function of  $T_i$ . (c) field distribution of mode in the radial junction cross section with  $T_i = 140$  nm (Yu et al. 2014a) (Copyright 2014 Nature Publishing Group)

of a random matrix of radial junction solar cells in Fig. 29a. This issue is absent or far less important in conventional planar solar cells, but has to be taken into account seriously in choosing a best trade off in the SiNW length design, particularly when one comes to construct radial junction solar cells over a random matrix of VLS-grown SiNWs on low cost glass substrates instead of periodic array of up-right standing Si nano-pillars. As seen in Fig. 29b, in spite of the distinctive geometric arrangement, the simulation based on a periodic array of up-right standing radial junction units has reproduced very well the overall trend of the EQE response measured experimentally. Comparing the simulated EQE responses of the radial junction thin film solar cells to that of a planar reference (with the same absorber i-layer thickness), the contribution of an enhanced light trapping and absorption effect realized within a 3D architecture is indeed quite prominent, particularly to the long wavelength end. So, is it true that a tilting geometry among the radial junction matrix has little influence on the light harvesting

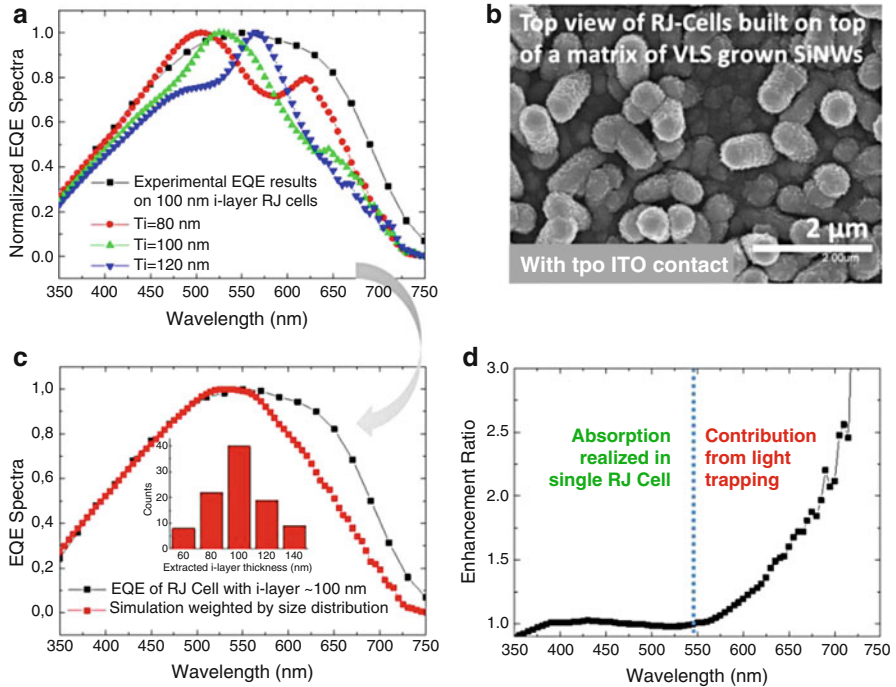


**Fig. 28** (a) Normalized experimental EQE spectrum (black square-line) measured for radial junction cells on VLS-grown SiNWs (example SEM image in (b)), compared to the normalized calculated absorption curves for  $T_i = 80$  nm, 100 nm and 120 nm. (c) Normalized experimental EQE and averaged simulated absorption curves weighted according to their appearance statistics. (d) Spectrum of the absorption enhancement ratio observed for an array of radial junction cells (with strong light trapping effect) over that of a single radial junction cell, as extracted from (c) (Yu et al. 2014a) (Copyright 2014 Nature Publishing Group)

performance? How and to what extent this could be valid emerges as an intriguing question to explore.

To shed light upon this aspect, it will be critical to gain a comprehensive understanding on how the incident light field will incouple and propagate among a tilted array of radial junction units. This has been taken into account in a radial junction model configuration demonstrated in Fig. 29c. It is important to note that in a tilted geometry, the polarization symmetry (valid for an up-right standing geometry) is broken. The absorption of high energy photons happens only superficially at the outer shells (ITO and  $n +$  window layers), while longer wavelengths have deeper penetration depth into the radial junction units. The strongest absorption has been achieved at wavelengths from 550 nm to 600 nm, where the overlapping of the incident light field and the absorption strength (which decreases monotonically with longer wavelengths) reach a best trade-off. Interestingly, regardless of the different incident wavelengths, the simulated light field distributions, presented in Fig. 30, reveal an oblique propagation of the light field along the tilted sideway among radial

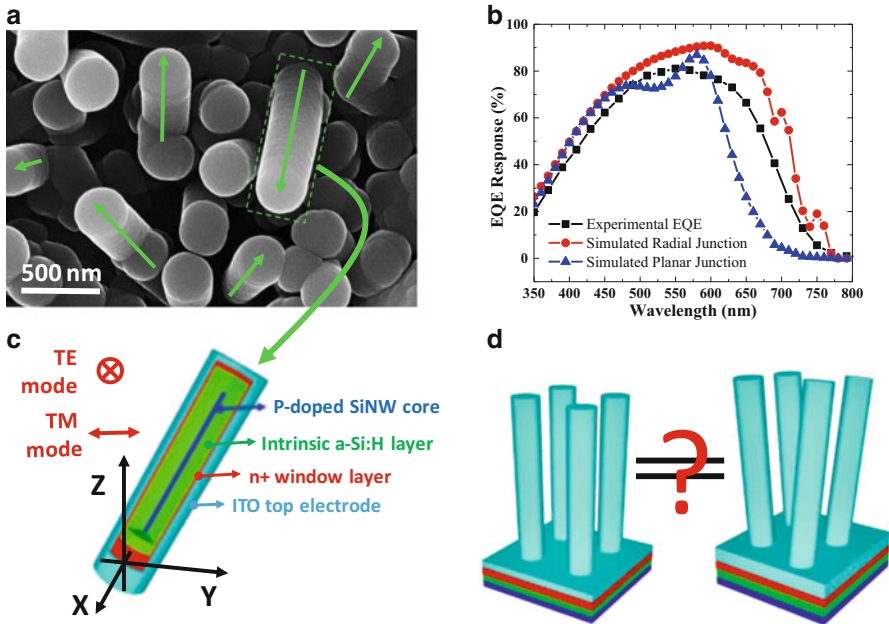


**Fig. 29** (a) SEM image of radial p-i-n junction a-Si:H thin film solar cells constructed over randomly oriented VLS-grown SiNWs, with a schematic illustration of the multilayer structure with an ITO top contact presented in (c); (b) a comparison of the experimental EQE response (black) of the radial junction cells, as seen in (a), to the simulated EQE response of a periodic up-right standing radial junction arrays (red) and that of a planar reference with the same i-layer thickness (blue); (c) shows the definition of the incident polarization situation as a TE mode or a TM mode with the E field component being aligned with the x-axis or the y-axis, respectively; (d) displays the different geometric configurations of an upright standing radial junction matrix and that of an aperiodic random one (Lu et al. 2015) (Copyright 2015 Optical Society of America)

junction units. With the increase of the wavelength of incident photons, the propagation of light field into the “shadowed” area becomes easier for both polarization situations.

Looking at the absorption profiles in Fig. 31, it is easy to find that the absorption intensity along a tilted radial junction unit is not uniform. Interestingly, the face-down back-halves (experience self-shadowing) seem to realize a higher absorption than that in the face-up front-halves. This is particularly true among the top segments of the radial junction cell units, while in the bottom segments the discrepancy becomes less prominent. Strikingly, in the lower segment of the radial junction unit, starting more or less from the middle, the back-half even out-performs its front-half counterpart. Taking a 50–50 weighting average, it is clear that the absorptions realized in the front or the back halves of the radial junction units (among a matrix arrangement) are basically the same. In other words, the self-shadowing effect has only negligible influence for a tilting radial junction matrix, while a nonuniform absorption profile does exist along the length of radial junction unit.

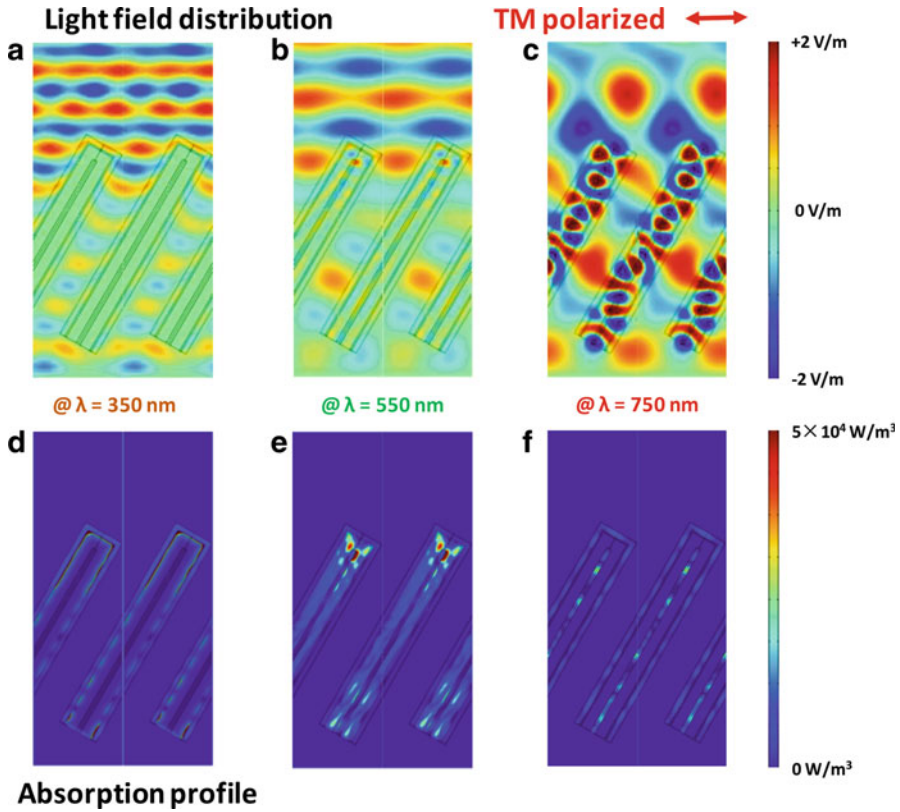


**Fig. 30** The incident light field distributions and their corresponding absorption profiles realized within a tilted (30 Degree) array of radial junction units at different incident wavelengths under TM mode polarized incidence are presented in (a–c) and (d–f), respectively (Lu et al. 2015) (Copyright 2015 Optical Society of America)

This also indicates an important aspect to be taken into account in the design of the radial junction solar cells, where a photo-current generation gradient could impose a limit for achieving a high Fill Factor and voltage output.

In Fig. 31c, d, the EQE responses of a tilted radial junction matrix with different density (or spatial separation) are calculated, under different angle of  $\theta = 0, 15^\circ, 30^\circ$ , and the EQE curves are obtained with 50–50 weighting for TE and TM incidences. Interestingly, for a dense radial junction matrix, with a radial junction unit separation of  $W = 800 \text{ nm} = 0.4 L_{RJ}$  (corresponding to an areal density of  $\sim 2 \times 10^8/\text{cm}^2$ ), it has been found that the tilting angle has basically negligible influence on the overall absorption performance, as witnessed in Fig. 31c. However, the tilting effect manifests itself in a sparser matrix (with  $W = 1600 \text{ nm} = 0.8 L_{RJ}$ ), as seen in Fig. 31d, where a tilting angle from  $15^\circ$  to  $30^\circ$  seems to have a broader absorption compared to that of up-right standing situation. Meanwhile, resonant absorption peaks emerge at wavelengths of 550 nm, 650 nm, and 725 nm for the up-right standing radial junction

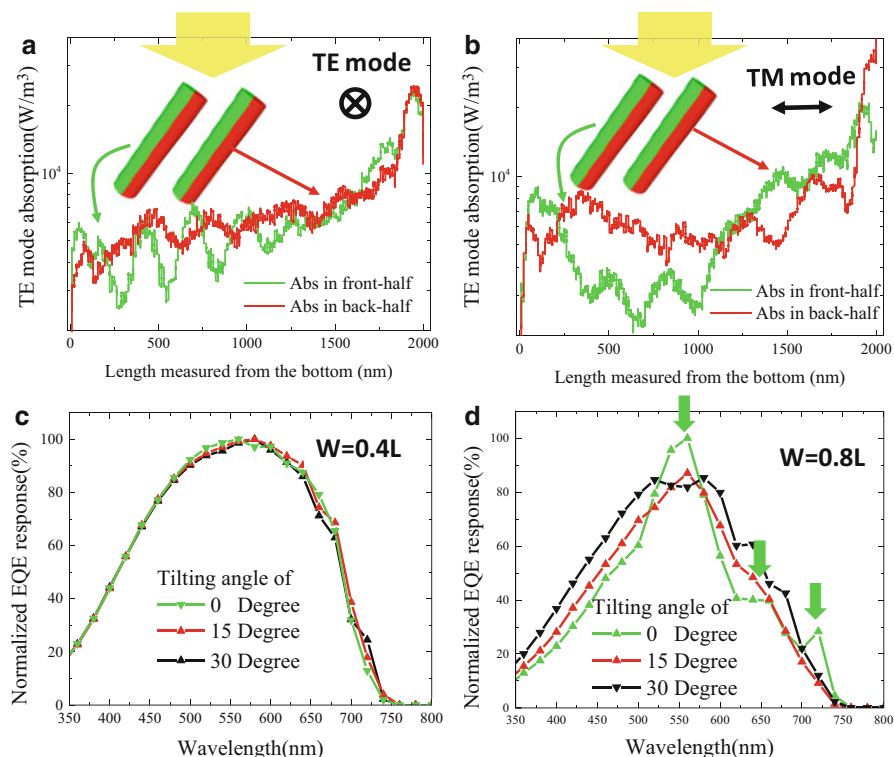


**Fig. 31** (a) and (b) present the distribution of absorption intensity realized within the face-up front-half and the face-down back-half of the tilted radial junction cells, along the length measured from the bottom, under TE mode incidence, respectively; (c) and (d) show the normalized EQE responses (with 50–50% TE and TM mode weighted) with a tilting angle = 0°, 15°, 30°, with an intercell spacing of  $W = 0.4 L$  and  $W = 0.8 L$ , respectively, where  $L$  stands for the length of the radial junction cell (Copyright 2015 Optical Society of America)

units, as marked by three arrows in Fig. 31d, while these signals quickly disappear or displace under tilting angles. Therefore, as long as the radial junction matrix is dense enough, probably within the range of effective absorption cross-section of individual radial junction units, a tilting angle by itself is not a critical parameter. This finding paves the way for adopting a properly controlled random matrix of VLS-grown SiNWs as the framework in pursuit of high performance radial junction thin film solar cells.

### Towards High Performance Radial Tandem Junction Solar Cells

Silicon thin film solar cells are low cost, light weight, and environment-friendly technology, with no fundamental limitation in material supply to reach a Tera-Watt scale deployment. However, in competition with other thin film technologies based on CIGS or CdTe material compounds, a higher conversion efficiency is definitely needed to revive the Si-based thin film technology to make it more competitive for



photovoltaics. In order to broaden the spectral response and achieve a higher voltage output, a stacking of tandem a-Si:H PIN junction (with a bandgap of  $E_g \sim 1.7$  eV) over another nanocrystalline Si (nc-Si:H, with a bandgap of  $E_g \sim 1.1$  eV) has been adopted in planar Si thin film solar cells, which has achieved an efficiency of 12.3% with a  $J_{sc} = 12.9$  mA/cm<sup>2</sup>. However, this advanced tandem radial junction (TRJ) concept has not yet been explored, either theoretically or experimentally, apparently due to a lacking of a fundamental understanding and the assessment tool for seeking an optimal 3D tandem design.

In order to address a more sophisticated TRJ configuration, a theoretical description of radial single junction array solar cells will be established, emphasizing the benefit of adopting a wide band gap  $\mu\text{-SiO}_x\text{:H}$  window layer and identifying the potential improvement at long wavelengths ( $>550$  nm). Then, based on a solid experimental basis, the potential of a tandem radial junction cell, as illustrated in Fig. 32c, will be addressed by examining the contributions of resonance mode absorption and the potential of maximal power extraction under a constraint of balanced photo-current generation in the outer and inner PIN junctions. As seen in the current-density voltage curves of two single radial junction (SRJ) solar cells, measured under standard AM1.5G illumination (Newport's Solar Simulator) at 25 °C and shown in Fig. 32a, a rather high open circuit voltage approaching  $V_{oc} = 0.9$  V (the red curve in Fig. 32a) has been achieved in the single radial junction cells, thanks to the adoption of a wide bandgap  $\mu\text{-SiO}_x\text{:H}$  window layer. This is indeed a remarkable value achieved over a 3D nanostructure complex even compared with the state-of-the-art planar junction counterpart. The best external quantum efficiency (EQE) recorded among the SRJ cells is presented in Fig. 32b (corresponding to the black J-V curve in 32a), which according to a solar-spectrum-weighted integral gives a high short-circuit current density of  $J_{sc} = 15.2$  mA/cm<sup>2</sup>. So far, the highest power conversion potential achieved here is 9.2%, with a  $V_{oc}$ , Fill-Factor (FF) of 0.82 V and 73.7%, respectively, for a cell area of 0.126 cm<sup>2</sup>.

As shown in Fig. 32b, the EQE responses of the experimental SRJ cells can be well reproduced at short wavelengths below  $\lambda < 550$  nm. Comparing the simulations to the experimental results within this range, an n-type  $\mu\text{-SiO}_x\text{:H}$  window layer thickness of 15 nm provides a better fit to the experimental data (the black curve) than a thinner layer of 10 nm (that is actually the targeted  $\mu\text{-SiO}_x\text{:H}$  layer thickness in our experiment control). Though the experimental EQE response demonstrates an enhanced absorption into the long wavelengths, there is still plenty of room (at least 2 mA/cm<sup>2</sup>) for improvement compared to periodic array of radial junction units. It is remarkable that the absorption performance is not very sensitive to the randomness of the fabricated SiNW matrix, a desired feature for a robust radial junction fabrication.

On the other hand, the modeling also helps to reveal the unique light-incoupling behavior into the cavity-like SRJ cell units and identify the critical parameters that have large impacts on the radial junction cell performance. For example, the incident light field ( $E_y$  component) distributions and corresponding absorption ( $|I_{abs}|$ ) profiles realized within a single radial junction are presented in the upper-row of Fig. 33a in three face-to-face pairs corresponding to different incident wavelengths at 350 nm,

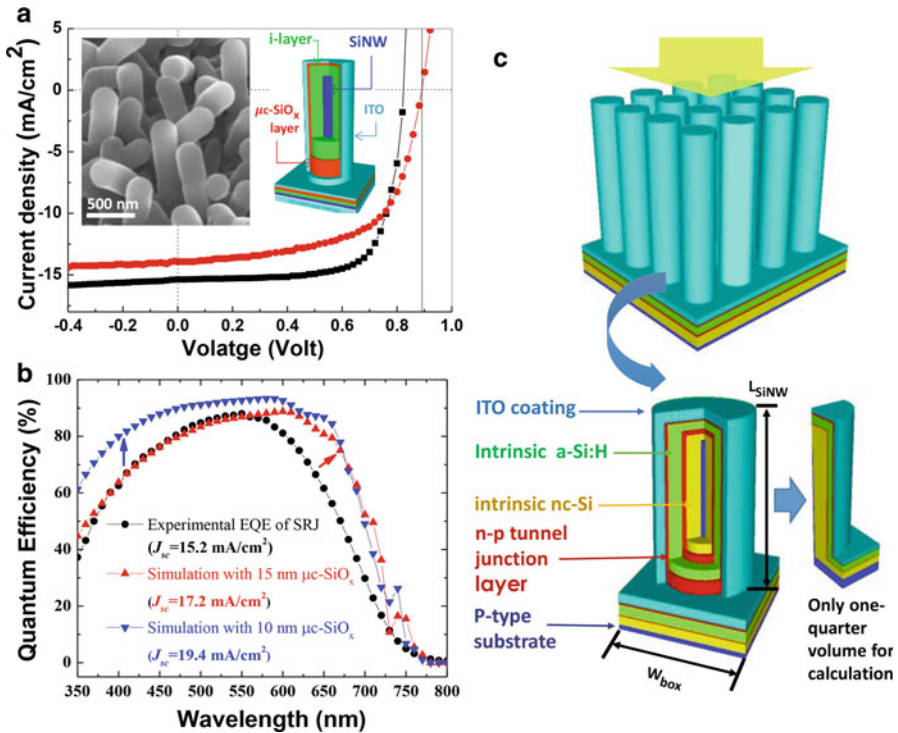


**Fig. 32** (a) J-V curves of the single radial junction solar cells fabricated over a VLS-grown SiNWs matrix, with corresponding SEM image and structural illustration displayed in the top-left inset; (b) experimental and calculated EQE curves of the single radial junction units with two n-type μc-SiO<sub>x</sub> : H window layer thicknesses; (c) shows a schematic of the NW arrangement used in the modeling of a periodic matrix of single radial junction or tandem radial junction solar cells. Taking into account the periodicity and reflection symmetries, the overall calculation can be reduced into a quarter volume of the simulation box (Copyright 2015 AIP Publishing LLC)

600 nm, and 800 nm (from left to right), respectively. It is interesting to see that the penetration of the incident light field into both the radial junction structure is highly wavelength dependent: For the short wavelengths at ~350 nm, the absorption is rather superficial as the incident light field has been largely screened by the outer ITO/n-type emitter shell. To longer wavelengths at  $\lambda = 600 \text{ nm}$ , the incident light field propagates much deeper into the a-Si:H absorber in radial junction, benefiting from a strong resonant-mode-enhanced incoupling into such a quasi-1D radial junction antenna. At  $\lambda = 800 \text{ nm}$ , it is clear that the a-Si:H layer in SRJ unit can hardly harness the lower energy photons because of the wide bandgap of the a-Si:H absorber.

In pursuit of higher performance, a tandem PIN junction configuration represents a promising approach to achieve a wider EQE spectrum response and a higher Voc output. Figure 32c shows the schematic diagrams of a tandem radial junction solar cell under consideration, where the outer a-Si:H or the inner nc-Si:H absorber layers



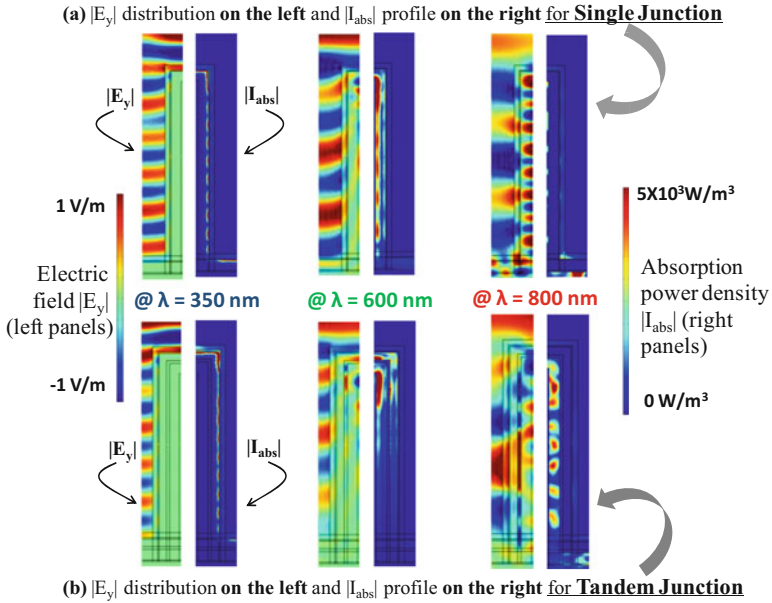


**Fig. 33** (a) and (b) showcase the light field  $E_y$  distributions and corresponding absorption ( $|I_{abs}|$ ) profiles realized within a single radial junction (SRJ) or tandem radial junction (TRJ) solar cell unit, respectively, under different incident wavelengths of 350 nm, 600 nm, and 800 nm (from left to right), where in each face-to-face pair, the electric field component  $|E_y|$  (or the absorption power density  $|I_{abs}|$ ) is displayed in the left (or the right) panel (Copyright 2015 AIP Publishing LLC)

have an optical bandgap of  $E_g^a = 1.7$  eV and  $E_g^{nc} = 1.1$  eV, respectively. The thicknesses of the n+/p+ tunneling junction, the outer  $\mu\text{-SiO}_x\text{:H}$ , and the ITO outer layers are fixed to be 30 nm, 15 nm, and 70 nm, respectively. The light field incoupling into a matrix of TRJ structure, under different wavelengths, is presented in the lower panels displayed in Fig. 33b. Compared to the SRJ situation, both the outer a-Si:H and the inner nc-Si:H layers in a TRJ configuration participate in the light absorption with an absorption profile mostly concentrating in the top segment. Remarkably, when the outer a-Si:H matrix allows an easy penetration of the incident light field (at longer wavelengths  $\lambda = 800$  nm) to reach the inner PIN layer, the absorption in the nc-Si:H absorber is maximized with a quite uniform distribution along the length of the tandem radial junction unit. This has enabled a broader spectrum response in the TRJ thin film solar cell, extending further into the near-infrared wavelengths. In Fig. 34b, the absorption percentages of each material layers in a TRJ thin film solar cells are presented. Their thickness has been optimized to maximize the photo-current output, while keeping a balanced photo-current generation within the inner and the outer p-i-n junctions. This is a critical aspect that has to be taken into account a priori in tandem solar cell design.

The EQE responses realized within tandem planar and radial junction solar cells are presented in Fig. 34c–d, respectively, with corresponding short-circuit current

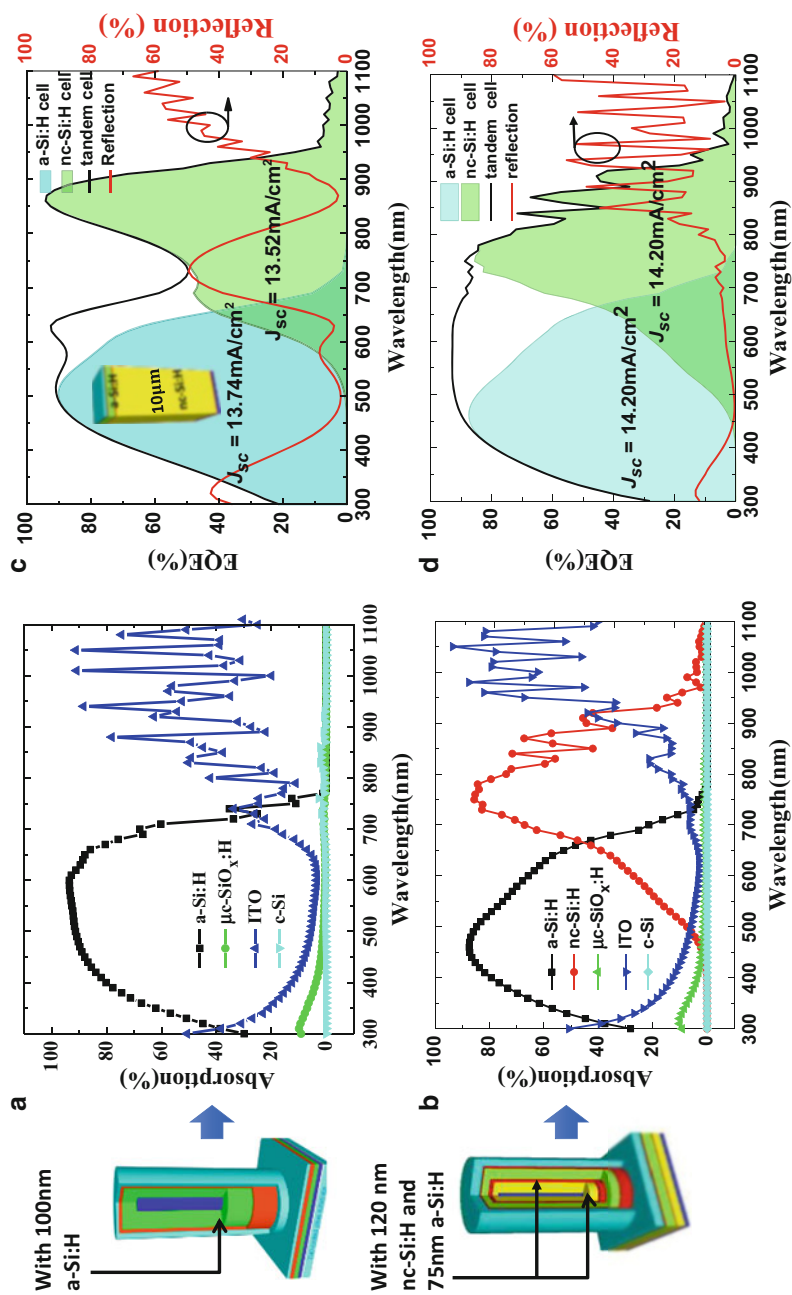


**Fig. 34** (a) and (b) provide the absorption percentages in different material layers in a single or a tandem radial junction solar cell, respectively; (c) and (d) show the EQE responses achieved in a planar or a tandem solar cell, respectively, while the *red curves* indicate their corresponding reflection spectra, the structural illustration of a planar tandem solar cell is displayed in the inset of (c) (Copyright 2015 AIP Publishing LLC)

densities  $J_{sc}$  also calculated. After parametric optimizations for a maximal balanced photo-current generation, it has been found that the TRJ has the potential to deliver a balanced photo-current density of  $J_{sc}^{RTJ} = 14.2 \text{ mA/cm}^2$ , as seen in Fig. 34d, with a radially coated a-Si:H layer and nc-Si:H layer thicknesses of 75 nm and 120 nm, respectively, upon SiNW cores of 2  $\mu\text{m}$  long. This compares favorably with that achieved by a planar tandem solar cell, where  $J_{sc}^{\text{planar}} = 13.7 \text{ mA/cm}^2$  necessitates a very thick nc-Si:H layer of 10  $\mu\text{m}$  in the bottom junction. Indeed, as explained in ► [Chap. 22, “Polycrystalline Silicon Thin Film,”](#) the deposition of high quality nc-Si:H bottom layer of such thickness is the most time-consuming and costly step in Si thin film tandem solar cells fabrication. An aggressive reduction of the expensive bottom nc-Si:H absorber from 1–3  $\mu\text{m}$  in planar tandem cells to only 120 nm in radial tandem solar cells implies thus a huge cost reduction and time-saving, which are critical considerations for industry-viable thin film photovoltaics.

---

## Conclusion

In summary, the introduction of nanostructured Si building blocks into photovoltaics has inspired and enabled a wide range of exciting new opportunities and design principles to address the major challenges in developing a new generation of high performance low cost solar cell applications. The nanostructured nature of pm-Si:H has allowed to improve the electronic properties of the material, and it should allow for 12% stabilized single junction solar cells. However, this material still suffers from light induced degradation. This can be solved by using radial junction solar cells. Indeed, radial junction thin film solar cells, based on a plasma-assisted low temperature VLS growth of Si nanowires, hold a strong promise to establish a new generation of high efficiency thin film solar cells, thanks to a series of breakthroughs over the last decade in nanostructure manufacturing, self-assembly growth control, and innovative material engineering. Targeting at a scalable and competitive photovoltaic application, the development and implementation of new understandings and technologies, which may involve advanced nanophotonic design, efficient surface passivation and multibandgap radial junction, are crucial. Given the large unexplored potential of the nanostructured radial junction Si solar cells, it is widely believed that there is still plenty of room for the radial junction approach to boost the performance further and become eventually one of a revolutionary mainstream photovoltaic technologies.

---

## Cross-References

- [Growth of Crystalline Silicon for Solar Cells: Mono-Like Method](#)
- [Growth of Multicrystalline Silicon for Solar Cells: The High-Performance Casting Method](#)

- ▶ [Hydrogenated Amorphous Silicon Thin Film](#)
- ▶ [Hydrogenated Microcrystalline Silicon Thin Films](#)
- ▶ [Polycrystalline Silicon Thin Film](#)
- ▶ [Polysilicon and Its Characterization Methods](#)
- ▶ [Wafer Cleaning, Etching, and Texturization](#)

---

## References

- S. Abolmasov, P. Roca i Cabarrocas, P. Chatterjee, *EPJ Photovoltaics* **7**, 70302 (2016)
- M. Adachi, M. Anantram, K. Karim, *Sci. Rep.* **3**, 1546 (2013)
- P.-J. Alet, L. Yu, G. Patriarche, S. Palacin, P.R.i. Cabarrocas, *J. Mater. Chem.* **18**, 5187–5189 (2008)
- J. Ball, L. Bowen, B.G. Mendis, H.S. Reehal, *CrystEngComm* **15**, 3808–3815 (2013)
- C. Battaglia, C.-M. Hsu, K. Söderström, J. Escarré, F.-J. Haug, M. Charrière, M. Boccard, M. Despeisse, D.T.L. Alexander, M. Cantoni, Y. Cui, C. Ballif, *ACS Nano* **6**, 2790–2797 (2012)
- G. Brönstrup, N. Jahr, C. Leiterer, A. Csáki, W. Fritzsche, S. Christiansen, *ACS Nano* **4**, 7113–7122 (2010)
- L. Cao, P. Fan, A.P. Vasudev, J.S. White, Z. Yu, W. Cai, J.A. Schuller, S. Fan, M.L. Brongersma, *Nano Lett.* **10**, 439–445 (2010)
- N. Chaâbane, V. Suendo, H. Vach, P. Roca i Cabarrocas, *Appl. Phys. Lett.* **88**, 203111 (2006)
- W. Chen, H. Ahmed, *Appl. Phys. Lett.* **63**, 1116–1118 (1993)
- W. Chen, V.G. Dubrovskii, X. Liu, T. Xu, R. Lardé, J.P. Nys, B. Grandidier, D. Stiévenard, G. Patriarche, P. Pareige, *J. Appl. Phys.* **111**, 094909 (2012)
- W. Chen, L. Yu, S. Misra, Z. Fan, P. Pareige, G. Patriarche, S. Bouchoule, P. Roca i Cabarrocas, *Nat. Commun.* **5**, 4134 (2014)
- J. Cho, B. O'Donnell, L. Yu, K.-H. Kim, I. Ngo, P. Roca i Cabarrocas, *Prog. Photovolt. Res. Appl.* **21**, 77 (2013)
- W.K. Choi, T.H. Liew, M.K. Dawood, H.I. Smith, C.V. Thompson, M.H. Hong, *Nano Lett.* **8**, 3799–3802 (2008)
- A. Fejfar, M. Hývl, M. Ledinský, A. Vetushka, J. Stuchlík, J. Kočka, S. Misra, B. O'Donnell, M. Foldyna, L. Yu, P. Roca i Cabarrocas, *Sol. Energy Mater. Sol. Cells* **119**, 228–234 (2013)
- M. Foldyna, L. Yu, P. Roca i Cabarrocas, *Sol. Energy Mater. Sol. Cells* **117**, 645–651 (2013)
- E. Garnett, P. Yang, *Nano Lett.* **10**, 1082–1087 (2010)
- E.C. Garnett, Y.C. Tseng, D.R. Khanal, J. Wu, J. Bokor, P. Yang, *Nat. Nanotechnol.* **4**, 311–314 (2009)
- M. Gharghi, E. Fathi, B. Kante, S. Sivonthaman, X. Zhang, *Nano Lett.* **12**, 6278–6282 (2012)
- M.S. Gudiksen, L.J. Lauhon, J. Wang, D.C. Smith, C.M. Lieber, *Nature* **415**, 617–620 (2002)
- E. Hamers, A. Fontcuberta i Morral, C. Niikura, R. Brenot, P. Roca i Cabarrocas, *J. Appl. Phys.* **88**, 3674–3688 (2000)
- C.-M. Hsu, S.T. Connor, M.X. Tang, Y. Cui, *Appl. Phys. Lett.* **93**, 133109 (2008)
- Y.-F. Huang, S. Chattopadhyay, Y.-J. Jen, C.-Y. Peng, T.-A. Liu, Y.-K. Hsu, C.-L. Pan, H.-C. Lo, C.-H. Hsu, Y.-H. Chang, C.-S. Lee, K.-H. Chen, L.-C. Chen, *Nat Nanotechnol* **2**, 770–774 (2007a)
- Z. Huang, H. Fang, J. Zhu, *Adv. Mater.* **19**, 744–748 (2007b)
- O. Isabella, A.H.M. Smets, M. Zeman, *Sol. Energy Mater. Sol. Cells* **129**, 82–89 (2014)
- P.D. Kanungo, N. Zakharov, J. Bauer, O. Breitenstein, P. Werner, U. Goesele, *Appl. Phys. Lett.* **92**, 263107 (2008)
- K.-H. Kim, E.V. Johnson, A.G. Kazanskii, M.V. Khenkin, P. Roca i Cabarrocas, *Sci. Rep.* **7**, 40553 (2017)
- J. Kleider, C. Longeaud, M. Gauthier, M. Meaudre, R. Meaudre, R. Butté, S. Vignoli, P. Roca i Cabarrocas, *Appl. Phys. Lett.* **75**, 3351–3353 (1999)

- P. Krogstrup, H.I. Jorgensen, M. Heiss, O. Demichel, J.V. Holm, M. Aagesen, J. Nygard, A. Fontcuberta i Morral, *Nat Photonics* **7**, 306–310 (2013)
- C. Longeaud, J. Kleider, M. Gauthier, R. Brtiggemann, Y. Poissant, P. Roca i Cabarrocas, *MRS Online Proc. Libr. Arch.* **557**, 1 (1999)
- Y. Lu, A. Lal, *Nano Lett.* **10**, 4651–4656 (2010)
- J. Lu, S. Qian, Z. Yu, S. Misra, L. Yu, J. Xu, Y. Shi, P. Roca i Cabarrocas, K. Chen, *Opt. Express* **23**, A1288–A1296 (2015)
- S. Misra, L. Yu, W. Chen, P. Roca i Cabarrocas, *J. Phys. Chem. C* **117**, 17786–17790 (2013a)
- S. Misra, L. Yu, M. Foldyna, P. Roca i Cabarrocas, *Sol. Energy Mater. Sol. Cells* **118**, 90–95 (2013b)
- S. Misra, L. Yu, W. Chen, M. Foldyna, P. Roca i Cabarrocas, *J. Phys. D. Appl. Phys.* **47**, 393001 (2014)
- S. Misra, L. Yu, M. Foldyna, P. Roca i Cabarrocas, *IEEE Journal of Photovoltaics* **5**, 40–45 (2015)
- V.A. Nebol'sin, A.A. Shchetinin, *Inorg. Mater.* **39**, 899–903 (2003)
- B. O'Donnell, L. Yu, M. Foldyna, P. Roca i Cabarrocas, *J. Non-Cryst. Solids* **358**, 2299–2302 (2012)
- M.C. Putnam, S.W. Boettcher, M.D. Kelzenberg, D.B. Turner-Evans, J.M. Spurgeon, E.L. Warren, R.M. Briggs, N.S. Lewis, H.A. Atwater, *Energy Environ. Sci.* **3**, 1037–1041 (2010)
- S. Qian, S. Misra, J. Lu, Z. Yu, L. Yu, J. Xu, J. Wang, L. Xu, Y. Shi, K. Chen, P. Roca i Cabarrocas, *Appl. Phys. Lett.* **107**, 043902 (2015)
- B.M. Rey, R. Elnathan, D. Ran, K. Geisel, M. Zanini, M.A. Fernandezrodriguez, V.V. Naik, A. Frutiger, W. Richtering, T. Ellenbogen, *Nano Lett.* **16**, 157 (2015)
- P. Roca i Cabarrocas, *Physics and Technology of Amorphous-Crystalline Heterostructure Silicon Solar Cells, Engineering Materials* (Springer, Berlin, 2011), p. 131
- P. Roca i Cabarrocas, T. Nguyen-Tran, Y. Djeridane, A. Abramov, E. Johnson, G. Patriarche, *J. Phys. D. Appl. Phys.* **40**, 2258 (2007)
- E.A. Schiff, *J. Non-Cryst. Solids* **352**, 1087–1092 (2006)
- V. Schmidt, J.V. Wittemann, S. Senz, U. Gosele, *Adv. Mater.* **21**, 2681–2702 (2009)
- V. Schmidt, J.V. Wittemann, U. Gösele, *Chem. Rev.* **110**, 361–388 (2010)
- W. Shockley, W.T. Read, *Phys. Rev.* **87**, 835–842 (1952)
- R.A. Street, P. Qi, R. Lujan, W.S. Wong, *Appl. Phys. Lett.* **93**, 163109–163103 (2008)
- R.A. Street, W.S. Wong, C. Paulson, *Nano Lett.* **9**, 3494–3497 (2009)
- B. Tian, X. Zheng, T.J. Kempa, Y. Fang, N. Yu, G. Yu, J. Huang, C.M. Lieber, *Nature* **449**, 885–889 (2007)
- M.M.J.W. van Herpen, D.J.W. Klunder, W.A. Soer, R. Moors, V. Banine, *Chem. Phys. Lett.* **484**, 197–199 (2010)
- R.S. Wagner, W.C. Ellis, *Appl. Phys. Lett.* **4**, 89 (1964)
- J. Wang, L. Yu, S. Abolmasov, K.H. Kim, P. Roca i Cabarrocas, *J. Appl. Phys.* **111**, 053108 (2012)
- X. Xie, X. Zeng, P. Yang, H. Li, J. Li, X. Zhang, Q. Wang, *Phys. Status Solidi* **210**, 341–344 (2013)
- E. Yablonovitch, G.D. Cody, *IEEE Trans. Electron Devices* **29**, 300–305 (1982)
- L. Yu, P.-J. Alet, G. Picardi, I. Maurin, P. Roca i Cabarrocas, *Nanotechnology* **19**, 485605 (2008)
- L. Yu, B. O'Donnell, P.-J. Alet, S. Conesa-Boj, F. Peiro, J. Arbiol, P. Roca i Cabarrocas, *Nanotechnology* **20**, 225604 (2009)
- L. Yu, B. O'Donnell, P.-J. Alet, P. Roca i Cabarrocas, *Sol. Energy Mater. Sol. Cells* **94**, 1855–1859 (2010a)
- L. Yu, B. O'Donnell, J.-L. Maurice, P. Roca i Cabarrocas, *Appl. Phys. Lett.* **97**, 023107–023103 (2010b)
- L. Yu, F. Fortuna, B. O'Donnell, G. Patriarche, P. Roca i Cabarrocas, *Appl. Phys. Lett.* **98**, 123113 (2011)
- L. Yu, F. Fortuna, B. O'Donnell, T. Jeon, M. Foldyna, G. Picardi, P. Roca i Cabarrocas, *Nano Lett.* **12**, 4153–4158 (2012a)
- L. Yu, B. O'Donnell, M. Foldyna, P. Roca i Cabarrocas, *Nanotechnology* **23**, 194011 (2012b)

- L. Yu, L. Rigutti, M. Tchernycheva, S. Misra, M. Foldyna, G. Picardi, P. Roca i Cabarrocas, *Nanotechnology* **24**, 275401 (2013)
- L. Yu, S. Misra, J. Wang, S. Qian, M. Foldyna, J. Xu, Y. Shi, E. Johnson, P. Roca i Cabarrocas, *Sci. Rep.* **4**, 4357 (2014a)
- L. Yu, M. Xu, J. Xu, Z. Xue, Z. Fan, G. Picardi, F. Fortuna, J. Wang, J. Xu, Y. Shi, K. Chen, P.R.i. Cabarrocas, *Nano Lett.* **14**, 6469–6474 (2014b)
- Z. Yu, J. Lu, S. Qian, S. Misra, L. Yu, J. Xu, L. Xu, J. Wang, Y. Shi, K. Chen, P. Roca i Cabarrocas, *Appl. Phys. Lett.* **107**, 163105 (2015)
- I. Zardo, L. Yu, S. Conesa-Boj, S. Estrade, P.J. Alet, J. Rossler, M. Frimmer, P. Roca i Cabarrocas, F. Peiro, J. Arbiol, J.R. Morante, A. Fontcuberta i Morral, *Nanotechnology* **20**, 155602 (2009)
- I. Zardo, S. Conesa-Boj, S. Estradé, L. Yu, F. Peiro, P. Roca i Cabarrocas, J.R. Morante, J. Arbiol, A. Fontcuberta i Morral, *Appl. Phys. A Mater. Sci. Process.* **100**, 287–296 (2010)
- J. Zhu, Z. Yu, G.F. Burkhard, C.-M. Hsu, S.T. Connor, Y. Xu, Q. Wang, M. McGehee, S. Fan, Y. Cui, *Nano Lett.* **9**, 279–282 (2008)



# Colloidal Silicon Quantum Dots and Solar Cells

# 26

Shuangyi Zhao and Xiaodong Pi

## Contents

Introduction .....	934
Preparation .....	934
Electronic and Optical Properties .....	936
Electronic Properties .....	936
Optical Properties .....	937
Photovoltaic Applications .....	937
Si-Wafer-Based Solar Cells .....	937
Si QDs and Organic Solar Cells .....	939
Summary .....	954
References .....	956

## Abstract

Colloidal silicon quantum dots (Si QDs) that are usually no more than 10 nm large crystalline Si nanoparticles dispersed in solvent have been attracting great attention largely due to their remarkable electronic and optical properties and flexible incorporation into device structures. In this work we begin with the introduction to the preparation of colloidal Si QDs. The electronic and optical properties of both undoped and doped Si QDs are then discussed. The use of colloidal Si QDs in Si-wafer-based solar cells and all kinds of hybrid solar cells is reviewed in detail. We briefly present the outlook of the development of colloidal Si QDs for solar cells in the end.

## Keywords

Colloidal · Silicon quantum dots · Solar cells

S. Zhao · X. Pi (✉)

State Key Laboratory of Silicon Materials and School of Materials Science and Engineering,  
Zhejiang University, Zhejiang, Hangzhou, China

e-mail: [shyzhao@zju.edu.cn](mailto:shyzhao@zju.edu.cn); [xdpi@zju.edu.cn](mailto:xdpi@zju.edu.cn)

## Introduction

Colloidal silicon quantum dots (Si QDs) have attracted considerable interest for a wide range of applications including photovoltaics (Kortshagen et al. 2016; Reiss et al. 2016; Mangolini and Vac 2013; Dohnalová et al. 2014; McVey and Tilley 2014; Ni et al. 2015). Si QDs may exhibit novel electronic and optical properties that traditional Si materials do not possess (Fujii et al. 1998; Mangolini and Kortshagen 2007; Pi et al. 2007, 2008; Anthony and Kortshagen 2009; Gresback et al. 2013; Yu et al. 2016). The QD size, surface state, and doping all play important roles in the tuning of the electronic and optical properties of Si QDs (Gresback et al. 2013; Kortshagen 2009; Lopez and Mangolini 2014; Hua et al. 2005; Jurbergs et al. 2006; Sangghaleh et al. 2015; Kelly et al. 2011; Dasog et al. 2013), for example, the bandgap of Si QDs may be facilely tuned by the QD size given the quantum confinement effect (van Buuren et al. 1998; Bostedt et al. 2004). Ligands attached to the surface of Si QDs not only render the dispersibility of Si QDs in solvents (Wheeler et al. 2015; Yang et al. 2014; Botas et al. 2014; Buriak 2013; Anoop Gupta and Wiggers 2009; Nelles et al. 2007) but also change the color of the light emission from Si QDs (Mangolini 2014; Hua et al. 2005; Jurbergs et al. 2006; Sangghaleh et al. 2015; Kelly et al. 2010, 2011; Dasog et al. 2013; Purkait et al. 2014; Boukherroub et al. 2011). Heavy doping can extend the optical absorption of Si QDs from the conventional ultraviolet and visible regions to the mid-infrared region (Zhou et al. 2015, 2016; Ni et al. 2016).

A series of methods have been developed to produce colloidal Si QDs (Park et al. 2001; Zacharias et al. 2002; Belomoinet al. 2002; Fujii et al. 2004; Khelifi et al. 2013; Pettigrew et al. 2003; Hryciw et al. 2005; Sychugov et al. 2012; Wolkin et al. 1999; Sandu et al. 2007; Švrček et al. 2002; Nayfeh et al. 2004; Bley and Kauzlarich 1996; Warner et al. 2005; Sugimoto et al. 2012; Kelly et al. 2010). Up to now, freestanding Si QDs have been the most conveniently synthesized by gas-phase approaches such as thermal heating (Ostraat et al. 2001), laser ablation (Li et al. 2003), and plasma (Mangolini et al. 2005; Knipping et al. 2004; Sankaran et al. 2005). Among these gas-phase approaches, the nonthermal plasma synthesis of Si QDs has a series of advantages such as excellent size control, high production yield, and good flexibility in tuning surface chemistry (Pi et al. 2014). Therefore, we will focus on the preparation of colloidal Si QDs by the nonthermal plasma synthesis and subsequent surface modification. After a brief introduction to the electronic and optical properties of Si QDs, we will discuss the use of colloidal Si QDs in solar cell structures in detail.

---

## Preparation

Silane ( $\text{SiH}_4$ ) is the routine precursor for the synthesis of Si QDs in nonthermal plasma. The decomposition of silane in nonthermal plasma leads to the formation of Si radicals, which nucleate and then grow to form Si QDs. Since electrons are the most mobile species in nonthermal plasma, Si QDs are usually negatively charged.



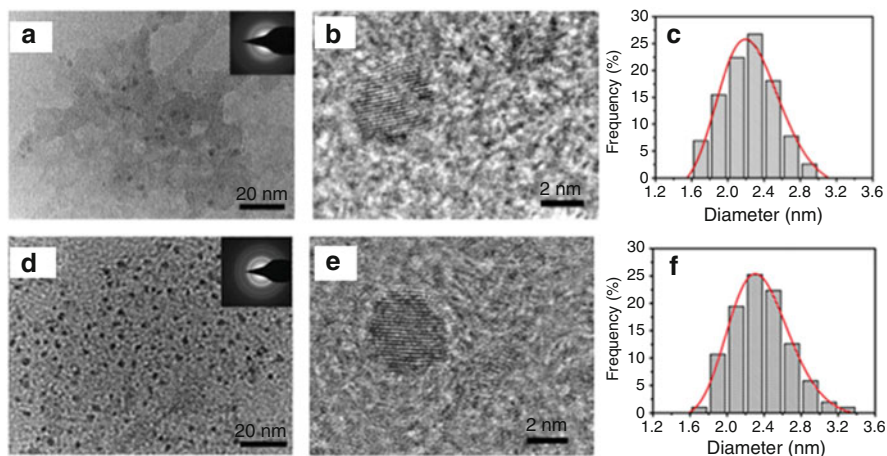


**Fig. 1** TEM results of undoped and 17% B-doped Si QDs with the mean size of 2.4 nm. (a) Low-resolution TEM image of undoped Si QDs. The inset shows the selected area electron diffraction (SAED) (b) High-resolution TEM image of undoped Si QDs. (c) Size distribution of undoped Si QDs with a log-normal fit. (d) Low-resolution TEM image of 17% B-doped Si QDs. The inset shows the selected area electron diffraction (SAED) (e) High-resolution TEM image of 17% B-doped Si QDs. (f) Size distribution of 17% B-doped Si QDs with a log-normal fit (Reprinted with permission from Ni et al. 2016, Copyright 2016 John Wiley and Sons)

This unipolar charging helps avoid or reduce QD agglomeration, giving rise to relatively narrow QD size distribution. Negatively charged Si QDs may be effectively repelled by strong electric field in the space charge sheath region of nonthermal plasma. Therefore, the diffusion loss of Si QDs to the reactor wall of nonthermal plasma is minimized. The production yield of Si QDs can be rather high. The contamination of Si QDs produced in silane-based nonthermal plasma is negligible. There may be only hydrogen at the QD surface to passivate Si dangling bonds. This greatly facilitates the surface modification of Si QDs.

B- or P-doped Si QDs may be synthesized by incorporating diborane ( $B_2H_6$ ) or phosphine ( $PH_3$ ) into silane-based nonthermal plasma. The size and crystallinity of Si QDs can be hardly affected by the doping. The doping level of Si QDs may be tuned in a wide range. Figure 1 shows the typical results of transmission electron microscopy (TEM) image of undoped and B-doped Si QDs. Low-resolution TEM images demonstrate that sphere-like Si quantum dots are synthesized whether they are undoped or doped (Ni et al. 2016). Both undoped and doped Si QDs are highly crystalline. Their size distributions are relatively narrow.

It has been recently discovered that B doping or B/P codoping enables the good dispersion of Si QDs in polar solvents such as ethanol and benzonitrile. This is largely due to the negative potential produced by ionized B atoms at the surface/subsurface of doped Si QDs (Zhou et al. 2016). In contrast, undoped Si QDs cannot be well dispersed in common solvents. This limits the processing of undoped Si QDs. Hydrosilylation has been adopted to replace H atoms at the surface of undoped

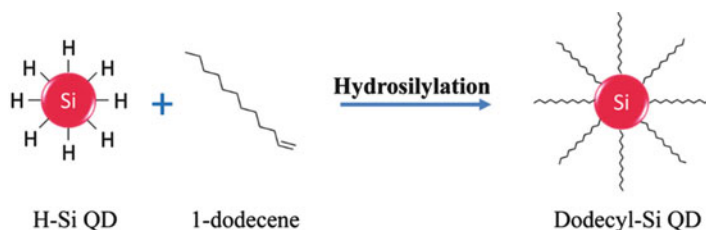


**Fig. 2** Schematic of the hydrosilylation of hydrogen-passivated Si QDs by using 1-dodecene (Reprinted with permission from Pi et al. 2014, Copyright 2014 John Wiley and Sons)

Si QDs with organic ligands, facilitating the dispersion of undoped Si QDs in solvents (Pi et al. 2014). Figure 2 schematically shows the process of the 1-dodecene hydrosilylation of an undoped Si QD. When Si QDs are well dispersed in solvents, colloidal Si QDs are obtained.

## Electronic and Optical Properties

### Electronic Properties

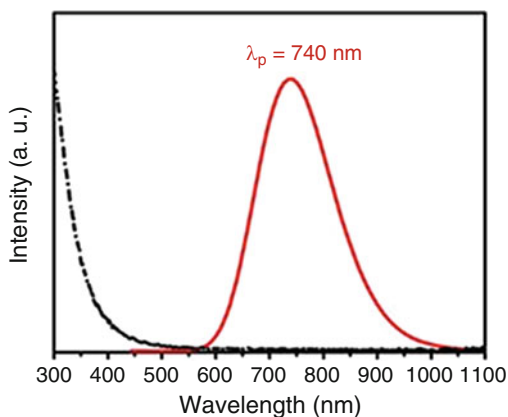
Since the Bohr radius of an exciton in Si is  $\sim 5$  nm, the size regions of  $< 5$  and 5–10 nm approximately correspond to the strong quantum confinement and weak quantum confinement for Si QDs, respectively. The quantum confinement results in the enlargement of the bandgap ( $E_g$ ) of Si QDs. It has been shown that the quantum-confinement effect of Si QDs renders the following relationship between  $E_g$  and  $d$  (QD size):

$$E_g = E_0 + Ad^{-2} + Bd^{-1}$$

where  $E_0$  is the bandgap of bulk Si (1.12 eV),  $A$  is  $2.56 \text{ eV nm}^{-2}$ , and  $B$  is  $0.83 \text{ eV nm}^{-1}$  (Liu et al. 2015). Clearly, the bandgap of Si QDs increases with the decrease of the QD size.

The surface of Si QDs may also impact the electronic properties. For example, a dangling bond at the surface of a Si QD introduces a defect energy level in the bandgap of the Si QD. Hence, the light emission of Si QDs is usually quenched by the dangling bonds at the QD surface (Lu et al. 2016). Ligands at the surface of Si QDs are mainly employed to make Si QDs soluble in solvents. However, certain ligands can modify the electronic structures of Si QDs. Veinot et al. have recently demonstrated that ligands containing amine, phosphine, and acetal functional groups cause the bandgap of Si QD to change (Dasog et al. 2014). Doping is an added means to tune the electronic properties of Si QDs (Ma et al. 2011; Pi et al. 2011; Hori et al. 2016). Dopants such as B and P introduce energy levels in the bandgap of Si QDs. The bandgap of Si QDs may change after doping.

**Fig. 3** Optical absorption and photoluminescence (PL) spectra of Si QDs (Reprinted with permission from Yu et al. 2016, Copyright 2016 John Wiley and Sons)



## Optical Properties

In most cases, Si QDs effectively absorb light in the short-wavelength (e.g., <500 nm) region and emit light in the long-wavelength (600–1,000 nm) region (Liu et al. 2015; Hessel et al. 2012), as exemplarily shown in Figure 3. Since the bandgap of Si QDs increases with the decrease of the QD size (van Buuren et al. 1998; Bostedt et al. 2004), both the absorption onset and light emission move to the shorter-wavelength region as the QD size decreases (Gresback et al. 2013; Pi et al. 2012).

It is interesting that dopants may introduce radiative energy levels in the bandgap of Si QDs (Ni et al. 2016). Xu et al. (Lu et al. 2016) observed light emission at the wavelength of ~1,300 nm from P-doped ultra-small (~2 nm) Si QDs. It was believed that this subband light emission resulted from the P-introduced energy level in the bandgap of Si QDs. Heavy doping may lead to band-tail states for Si QDs. The band-tail states actually help extend the absorption of Si QDs to the near-infrared region (Zhou et al. 2016; Ni et al. 2016). Localized surface plasmon resonance (LSPR) can make both B- and P-doped Si QDs efficiently absorb mid-infrared light (Zhou et al. 2015; Ni et al. 2016). Figure 4 representatively shows the mid-infrared absorption of Si QDs doped with B at the nominal concentrations from 7% to 31% (Ni et al. 2016). When the doping levels of B and P are similar, the LSPR energy of B-doped Si QDs is higher than that of P-doped Si QDs (Zhou et al. 2016), because in Si QDs B is more efficiently activated to produce free carriers than P.

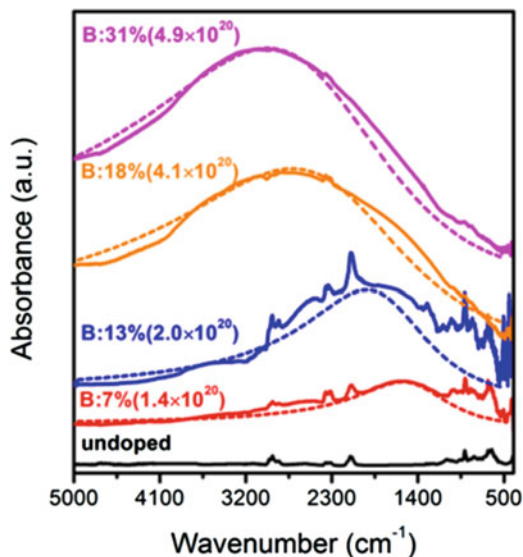
---

## Photovoltaic Applications

### Si-Wafer-Based Solar Cells

Si-wafer-based solar cells dominate in the photovoltaic industry. It is highly desired to improve the efficiency of Si-wafer-based solar cells without considerably increasing the manufacturing cost. It is well known that the response of Si-wafer-based solar

**Fig. 4** Fourier transform infrared (FTIR) spectra of undoped and heavily B-doped Si NCs. The dash lines show the fitting of LSPR-induced absorption for each heavily B-doped Si NCs by using the Drude model. The free carrier concentrations obtained from the fitting are indicated in parentheses (Reprinted with permission from Zhou et al. 2016, Copyright 2016 American Chemical Society)



cells to short-wavelength light is usually poorer than that to long-wavelength light (Wurfl et al. 2009; Sun et al. 2009; Gao et al. 2013). Since Si QDs can efficiently absorb short-wavelength light and then emit long-wavelength light (i.e., the so-called down-shifting effect), Si QDs may be readily used to improve the performance of Si-wafer-based solar cells in the short-wavelength region (Sontheimer et al. 2014; Bronger et al. 2014).

Švrček et al. (2004) tried taking advantage of the down-shifting effect of Si QDs in 2004. They prepared Si QDs by pulverizing the electrochemical etched porous silicon. The obtained Si QDs were incorporated into liquid spin-on-glass (SOG), which was spin-coated onto the surface of a Si-wafer-based solar cell. Their Si QDs could absorb UV-blue light (<500 nm) and emit light at the wavelength around 680 nm. The current-voltage characteristics ( $I$ - $V$ ) of solar cells with or without Si QDs are shown in Figure 5. It was found that the short-circuit current ( $J_{SC}$ ) slightly increased by  $\sim 2.5$  mA/cm<sup>2</sup>. The power conversion efficiency (PCE) increased by  $\sim 0.4\%$ . No improvement of the open-circuit voltage ( $V_{OC}$ ) was observed. Given the fact that the down-shifting efficiency of Si QDs dislocated from porous was not high enough ( $< \sim 10\%$ ) (Cullis et al. 1997) to compensate the difference in the solar cell quantum efficiency between short-wavelength light and long-wavelength light, the down-shifting effect of Si QDs should have caused decrease in solar cell efficiency. The improvement of the solar cell performance might be due to the simple anti-reflection effect of the SOG containing Si QDs.

In 2012 Pi et al. (2012) used hydrosilylated Si QDs that had much higher down-shifting efficiency ( $\sim 53\%$ ) to enhance the performance of Si-wafer-based solar cells. Ink-jet printing was employed to deposit Si QDs at the solar cell surface because hydrosilylated Si QDs could be easily dispersed in organic solvent to form Si-QD ink. Figure 6 shows the schematic of the ink-jet printing of Si-QD ink at the surface

**Fig. 5** Current-voltage characteristics of a Si-wafer-based solar cell. *Open circles:* spin-on-glass (SOG) containing Si QDs. *Solid line:* SOG only (Reprinted with permission from (Pi et al. 2013, Copyright 2003 Elsevier)

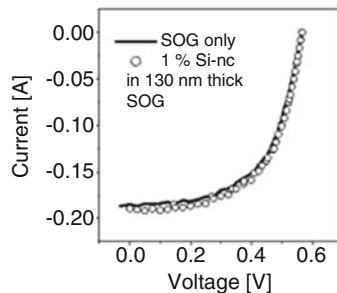
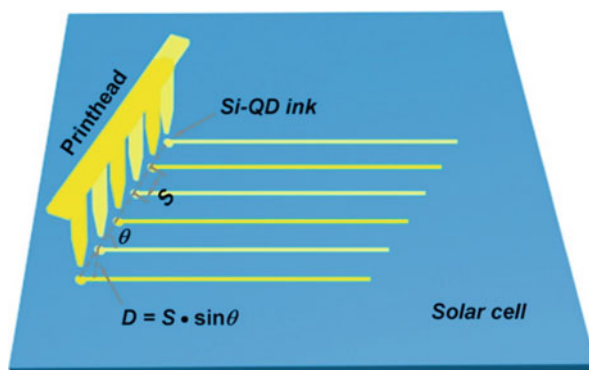


**Fig. 6** Schematic of the ink-jet printing of Si QD ink at the surface of multicrystalline Si solar cells. Drop spaces ranging from 20 to 80  $\mu\text{m}$  have been selected to obtain Si QD films with varying thickness and porosity after the evaporation of the solvent of Si QD ink (Reprinted with permission from Pi et al. 2012, Copyright 2012 American Chemical Society)



of a multicrystalline Si solar cell. The thickness of the Si-QD film was tuned by adjusting the drop space ( $D$ ). With the increase of  $D$  from 20 to 80  $\mu\text{m}$ , the thickness of the Si QD film decreased from  $\sim 74$  to 16 nm. The enhancement of solar cell efficiency reached the maximum (up to 2%, i.e., from 17.2% to up to 17.5%) when  $D$  was 20  $\mu\text{m}$ . The improvement of  $I_{SC}$  mainly led to the enhancement of the solar cell efficiency. The external quantum efficiency (EQE) curves are shown in Figure 7. It was noteworthy that the antireflection of Si QD films could not account for all the increase of EQE in the 300–400 nm region. The down-shifting effect of hydrosilylated Si QDs indeed improved the solar cell response in the short-wavelength region. It was concluded that the down-shifting effect of Si QDs together with the antireflection of Si QD films contributed to the enhancement of multicrystalline Si solar cells.

## Si QDs and Organic Solar Cells

Organic materials including polymers and small molecules (Scharber et al. 2006; Li et al. 2005; Zuo et al. 2015; Lee et al. 2015; Guo et al. 2013) have been intensively investigated for thin-film solar cells. One of the methods to further improve the performance is the incorporation of semiconductor QDs to form hybrid solar cells. This is largely due to the desirable energy alignment with polymer and absorption in

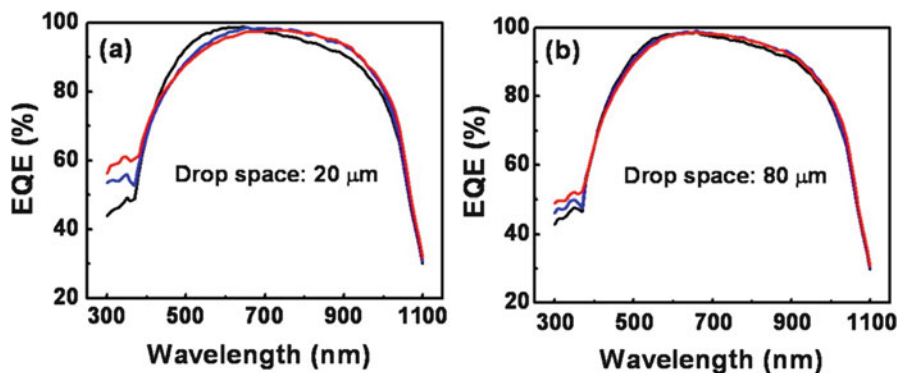


**Fig. 7** EQE of solar cells before (*black lines*) and after (*red lines*) the ink-jet printing of Si QD ink with the drop space of (a) 20 and (b) 80  $\mu\text{m}$ . Calculated EQE curves (*blue lines*) that are obtained by only considering the antireflection of Si QD films are also included (Reprinted with permission from Pi et al. 2012, Copyright 2012 American Chemical Society)

the short wavelength (Wendy et al. 2002; Liu et al. 2009, 2013; Ren et al. 2011; Xue et al. 2011; Liao et al. 2012). Up to now, various promising organic/inorganic hybrid solar cells have been reported, in which cadmium selenide (CdSe) (Greenham et al. 1996), zinc oxide (ZnO) (Beek et al. 2006), titanium dioxide ( $\text{TiO}_2$ ) (Kwong et al. 2004), lead sulfide (PbS) (Günes et al. 2007), lead selenide (PbSe) (Arici et al. 2003), and copper indium disulfide ( $\text{CuInS}_2$ ) (Cui et al. 2006) QDs were used. It should be noted that among all kinds of QDs Si QDs hold an advantageous position because of the nontoxicity and abundance of Si. Therefore, Si QDs are worth incorporating into the organic/inorganic hybrid solar cell structures.

### Si QDs/P3HT Solar Cells

Liu et al. (2009) demonstrated hybrid solar cells based on Si QDs and poly(3-hexylthiophene) (P3HT) in 2009. They fabricated the Si QDs/P3HT solar cells by spin-coating the blends of Si QDs and P3HT onto indium tin oxide (ITO)-coated glass substrates. Firstly, roughly 50 nm of poly(3,4-ethylenedioxy-thiophene)/poly(styrenesulfonate) (PEDOT:PSS) was spun onto the pure ITO glass substrates. The PEDOT:PSS film was then annealed on the hot plate to remove excess water at 130  $^{\circ}\text{C}$ . The Si QDs/P3HT solution was then sonicated and spun on top of the PEDOT:PSS layer in a glovebox to form a film, which was approximately 100 nm thick. Finally, 2 mm wide aluminum (Al) electrodes (100 nm thick) were evaporated on top of the Si QDs/P3HT film. Figure 8a shows the band alignment of Si QDs and P3HT. It is clear that a type II structure can be formed by using Si QDs and P3HT. Therefore, the exciton dissociation at the interface of the type II structure is energetically favorable. The schematic in Figure 8b illustrates the device structure, in which the ITO and Al are the anode and cathode, respectively.

To understand the role of Si QDs in these hybrid solar cells, Liu et al. used Si QDs with the sizes of 3–5, 5–9, and 10–20 nm and different Si QDs/P3HT weight ratios. Figure 9a shows that  $V_{\text{OC}}$  was inversely related to the QD size, regardless of the Si

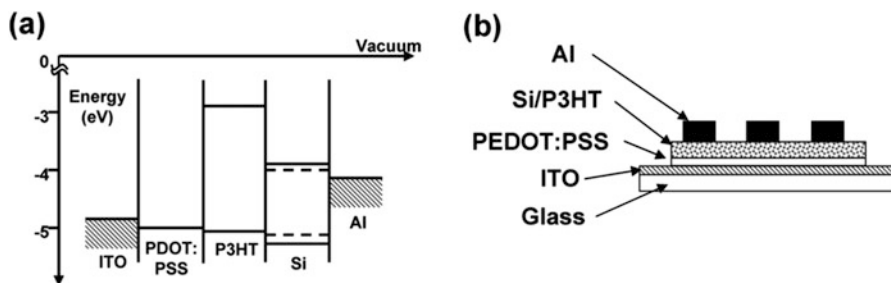


**Fig. 8** (a) Energy band diagram of a Si QDs/P3HT solar cell. The *dotted lines* represent the valence and conduction bands of bulk Si, while the *solid lines* are representative of 4 nm Si QDs. (b) Schematic of a Si QDs/P3HT hybrid solar cell. In the Si QDs/P3HT hybrid device, P3HT can absorb the incident light to generate the photo-generated carriers. The Si QDs act as the electron acceptors, transferring the photo-generated electrons to the cathode (Reprinted with permission from Liu et al. 2009, Copyright 2009 American Chemical Society)

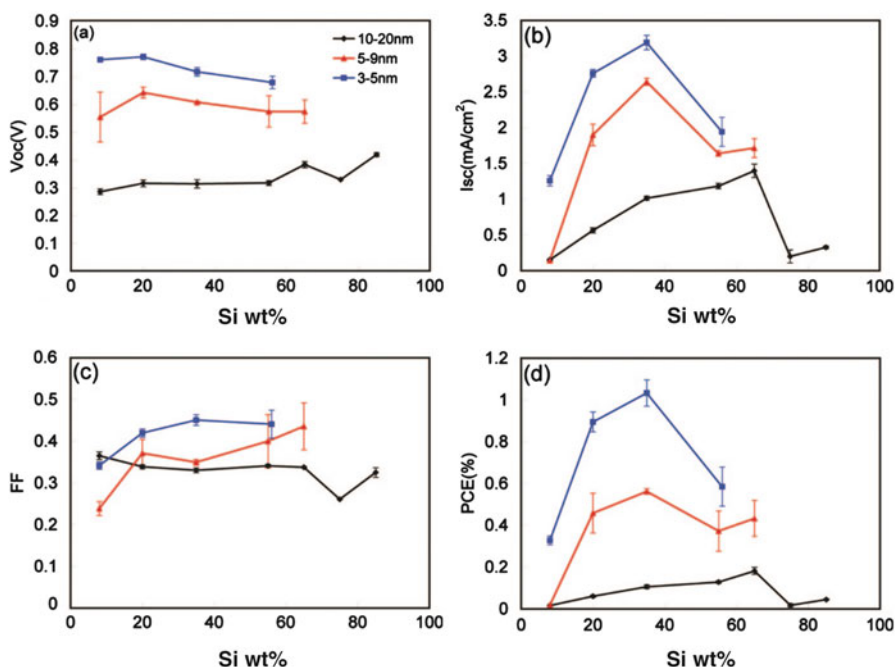


**Fig. 9** Silicon QDs/P3HT solar cell performance characteristics for devices with different Si QDs/P3HT ratios and QD sizes. 3–5, 5–9, and 10–20 nm Si QDs are represented with *blue squares*, *red triangles*, and *black diamonds*, respectively (Reprinted with permission from Liu et al. 2009, Copyright 2009 American Chemical Society)

QDs/P3HT weight ratio. The increase of the Si bandgap resulted in a smaller conduction band offset between Si QDs and P3HT (Figure 8a) and therefore less voltage loss during exciton dissociation. This result clearly indicated the importance



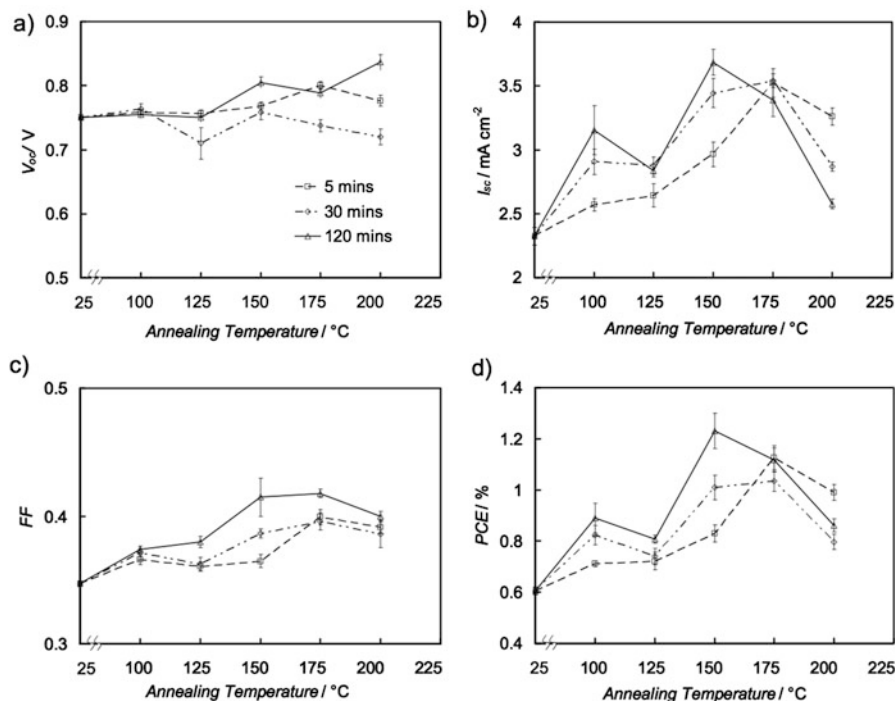


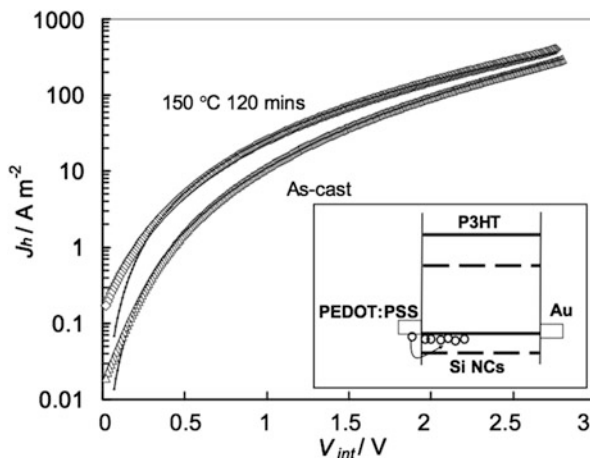
**Fig. 10** Hybrid solar cell performance of 50 wt% Si QD/P3HT devices with different annealing temperatures (100, 125, 150, 175, 200 °C) and periods (5, 30, and 120 min). 5, 30, and 120 min annealing periods are represented with *squares*, *diamonds*, and *triangles*, respectively (Reprinted with permission from Liu et al. 2010, Copyright 2010 John Wiley and Sons)

of the size of Si QDs for the device performance.  $I_{SC}$  also increased when the size of Si QDs decreased. For smaller Si QDs, the transfer of an electron to the Al electrode in a device needed fewer hopping events. Hence, the electron transport was enhanced in devices with smaller Si QDs. However, for all the QD sizes, the values of  $I_{SC}$  were the maximum when the Si QDs/P3HT weight ratio was between 30% and 70%. This should be due to the balance between electron and hole transport. For a rather high Si QD/P3HT weight ratio, Si QD agglomeration seriously deteriorated film uniformity, giving rise to a larger film resistance. Hence,  $I_{SC}$  decreased when the Si QD/P3HT weight ratio was rather high. The measured fill factor ( $FF$ ) was nearly independent of the Si QD size and Si QDs/P3HT weight ratio (Figure 9c). The change of the power conversion efficiency (PCE) actually followed the trend of the change in  $I_{SC}$  (Figure 9d).

Apart from the size of Si QDs and Si QDs/P3HT weight ratio, the temperature and time of the post-annealing of the Si QDs/P3HT film were found to affect the performance of Si QDs/P3HT hybrid solar cells (Liu et al. 2010). Si QDs/P3HT films with the Si QD/P3HT weight ratio of 50 wt% were annealed from 100 to 200 °C for different annealing time (5, 30, and 120 min). Figure 10a shows that  $V_{OC}$



**Fig. 11** I–V characteristic of a hole-transport-only device of 50 wt% Si QD/P3HT (active layer thickness around 150 nm) before and after 150 °C annealing for 120 min. The as-cast and annealed data are represented with triangles and diamonds, respectively. The inset shows the device configuration (Reprinted with permission from Liu et al. 2010, Copyright 2010 John Wiley and Sons)



was nearly independent of annealing temperature and time.  $I_{SC}$ , however, was apparently dependent on annealing temperature and time. The maximum  $I_{SC}$  was obtained at the annealing temperature of 150 °C and the annealing time of 120 min.  $FF$  increased with the increase of the annealing temperature up to 175 °C.  $FF$  only slightly increased as the annealing time increased (Figure 10c). As shown in Figure 10d, the maximum PCE (1.47%) was obtained as the Si QDs/P3HT film was annealed at 150 °C for 120 min.

The enhanced performance of the post-annealed devices was attributed to the improved hole transport. Hole mobility in the P3HT phase was enhanced by almost one order of magnitude after annealing because of the increase in the P3HT polymer conjugation length (Figure 11). The improved hole transport might reduce the electron/hole recombination, enhancing  $I_{SC}$  and  $FF$ .

Liu et al. also studied the effect of cathodes on the performance of the hybrid Si QDs/P3HT solar cells. Metals (Ca, Mg, Al, Ag, and Au) with different work functions were evaporated on the active layer. When the cathodes with work functions smaller than that of Al (−4.3 eV) were used,  $V_{OC}$  was determined by the energy difference between the highest occupied molecular orbit (HOMO) of P3HT and the conductive band (CB) of Si QDs. When the cathodes with work functions larger than that of Al were used,  $V_{OC}$  and  $I_{SC}$  rapidly decreased with increasing metal work function. These results were helpful to the further improvement of the Si QD/P3HT hybrid solar cells.

The surface control of Si QDs was found to be critical to the performance of Si QDs/P3HT hybrid solar cells. In 2014 Ding et al. (2014a) compared Si QDs with varying surfaces for organic/inorganic hybrid solar cells, as shown in Figure 12.

Si QDs with Cl, O, and H at the QD surface were denoted by Cl:Si QDs, O:Si QDs, and H:Si QDs, respectively. Please note that there was O at the QD surface even for Cl:Si QDs and H:Si QDs. Figure 13 shows the  $J$ – $V$  curves of the devices fabricated with Cl:Si QDs, O:Si QDs, and H:Si QDs. A low  $J_{SC}$  of 0.7 mA/cm<sup>2</sup> and a low PCE of only 0.15% were obtained for the hybrid solar cell based on Cl:Si QDs.

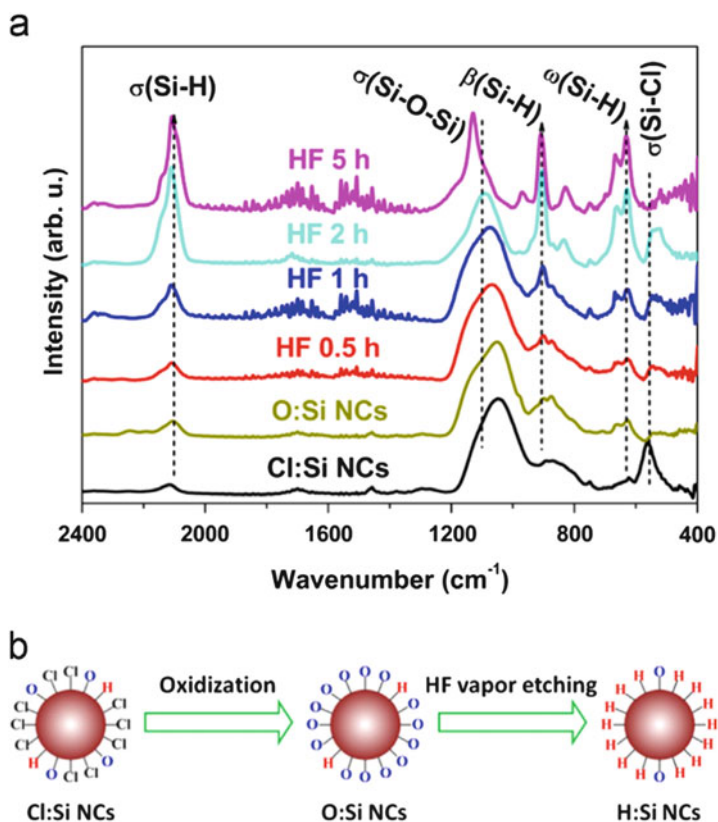
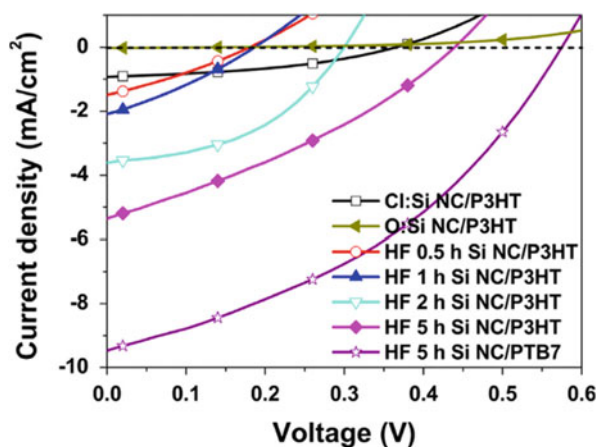


**Fig. 12** (a) FTIR spectra of as-produced Cl:Si QDs, O:Si QDs, and HF etched nanocrystals for 0.5, 1, 2, and 5 h, respectively. (b) Schematic depiction of Si QD surface evolution during treatment (Reprinted with permission from Ding et al. 2014a, Copyright 2014 Elsevier)

**Fig. 13** J-V curves of hybrid solar cells under 1 sun illumination (Reprinted with permission from Ding et al. 2014a, Copyright 2014 Elsevier)



The poor solar cell performance was induced by the recombination of carriers in the recombination centers, which were the most likely dangling bonds at the QD surface. PCE became nearly zero when Cl:Si QDs were severely oxidized. It was suggested that severe oxidation on the surface of Si QDs introduced thick oxide shells, which could block the carrier transport. After the oxide at the surface of Si QDs was etched by HF, the resulting H:Si QDs gave rise to the significant increase of PCE.  $J_{SC}$  increased to about 1.2 mA/cm<sup>2</sup> after 0.5 h etching. When the etching time of Si QDs further increased (1 h, 2 h, 5 h), both  $J_{SC}$  and  $V_{OC}$  increased. The hybrid solar cells based on Si QDs that were etched for 5 h exhibited the highest PCE of 0.5%, which was at least three times higher than that of the Cl:Si QD device. It is clear that Cl atoms should be removed from the surface of Cl:Si QDs to obtain good solar cell performance. The removal of Cl atoms might be facilely achieved by oxidizing the QD surface and then etching.

### Si QDs/PTB7 Solar Cells

As a kind of donor material, P3HT is widely used in hybrid solar cells because of its efficient light absorption and high hole mobility. However, it may not be the best choice in Si QD-based hybrid solar cells due to its wide bandgap of 2.0 eV. The absorption peak of P3HT is about ~530 nm, which limits the absorption of light in the long-wavelength region. Si QDs usually efficiently absorb light in the short-wavelength region. Although the absorption of Si QDs is complementary to that of P3HT, light with wavelengths longer than 650 nm cannot be well absorbed. Therefore, a donor material with a smaller bandgap in Si QD-based hybrid solar cells needs to be used to extend the solar cell response to longer-wavelength region.

Compared with P3HT, poly[[4,8-bis[(2-ethylhexyl)oxy] benzo[1,2-b:4,5-b]dithiophene-2,6-diyl][3-fluoro-2-[(2-ethylhexyl)carbonyl]-thieno[3,4-b]thiophenediyl]] (PTB7) is a better donor material because the bandgap of PTB7 is smaller than that of P3HT (1.8 eV vs 2.0 eV). Si QD/PTB7 blend films have complementary absorption in the wavelength range of 300–800 nm, as shown in Figure 14a (Ding et al. 2014b).

Figure 14b shows the molecular structures and corresponding energy levels of P3HT, PTB7, and Si QDs. As mentioned before, the alignment of the energy levels of P3HT and Si QDs leads to a type II structure, which is favorable for exciton dissociation at the interface of Si QDs/P3HT. A similar alignment is expected for the PTB7/Si QDs hybrid structure. However, the HOMO of PTB7 is approximately 0.15 eV lower than that of P3HT. This results in the enlarged difference between the HOMO level of PTB7 and the conduction band of Si QDs. Since  $V_{OC}$  is related to the difference between the CB of Si QDs and the HOMO of the polymer in the Si QDs/polymer system,  $V_{OC}$  was found to increase when PTB7 was used. Compared to the Si QD/P3HT devices, the Si QDs/PTB7 devices showed larger  $J_{SC}$ , consistent with the enhanced light absorption in the longer-wavelength region. Figure 15 illustrates the EQE curves of both the Si QD/P3HT and Si QD/PTB7 solar cells. The Si QD/P3HT solar cells showed photocurrent response up to ~650 nm with the maximum EQE of 50%, while the Si QD/PTB7 solar cell exhibited the photocurrent response up to 800 nm with the maximum EQE of 70%.

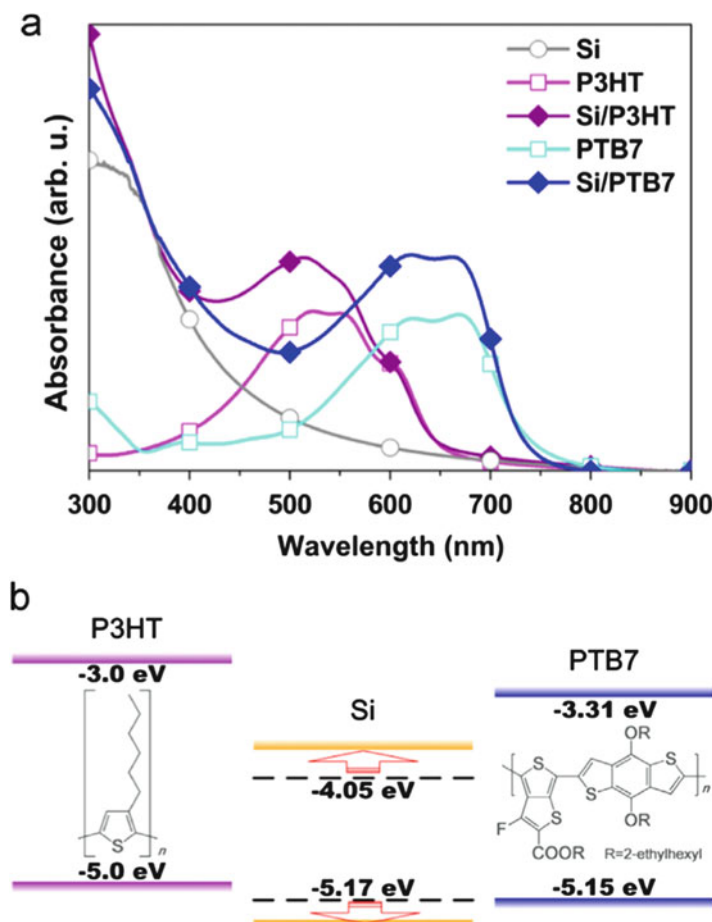


**Fig. 14** (a) Absorbance spectra of Si QDs, P3HT, PTB7, Si QD/P3HT blend, and Si QD/PTB7 blend films. (b) Chemical structures and energy level diagrams of Si QDs, P3HT and PTB7 (Reprinted with permission from Ding et al. 2014b, Copyright 2014 Elsevier)

Dangling bonds may exist at the surface of Si QDs, acting as carrier traps to deteriorate the solar cell performance. Ding et al. proposed to eliminate the dangling band at the surface of Si QDs by controlling the surface oxidation Ding et al. (2016). In their work, fresh Si QDs were oxidized in air for 0, 1, 12, 24, and 48 h, respectively. From the FTIR spectra shown in Figure 16a we can find that the intensity of the Si-O signal increased with the increase of oxidation time. However, Figure 16b shows that the electron spin resonance (ESR) signal related to the dangling bonds at the surface of Si QDs with a  $g$  factor of 2.006 decreased with the increase of oxidation time. Figure 16c demonstrates that the growth of the oxide at the QD surface was well correlated to the reduction of the dangling bonds at the QD surface.

**Fig. 15** Typical EQE spectra for Si QD/P3HT and Si QD/PTB7 devices (Reprinted with permission from Ding et al. 2014, Copyright 2014 Elsevier)

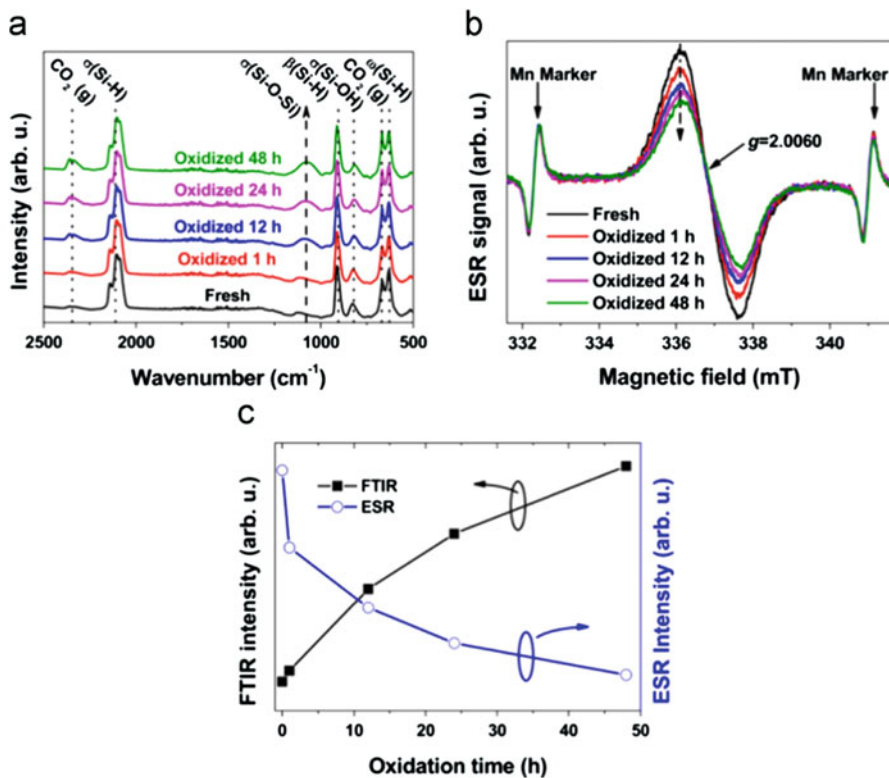
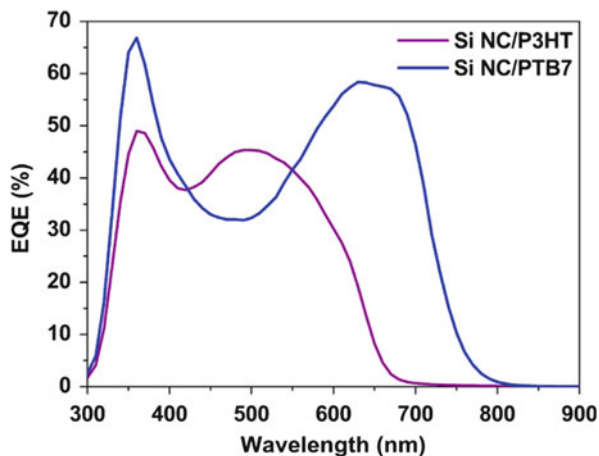


**Fig. 16** (a) FTIR and (b) ESR spectra of Si QDs oxidized for different time. (c) Si-O-related FTIR and dangling bond-related ESR intensities as the function of oxidation time (Reprinted with permission from Ding et al. 2014b, Copyright 2014 Elsevier)

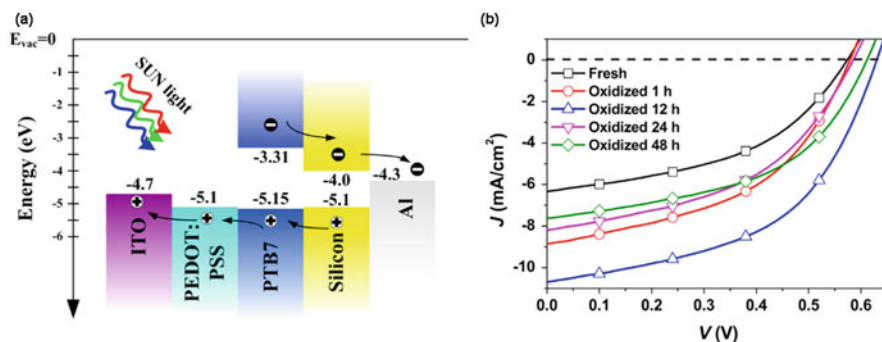


**Fig. 17** (a) Band alignment of Si QD/PTB7 hybrid solar cells. (b) Typical photo  $J$ - $V$  curves of solar cells fabricated with Si QDs oxidized for different time (Reprinted with permission from Ding et al. 2014b, Copyright 2014 Elsevier)

Figure 17a, b shows the band alignment and  $J$ - $V$  curves of Si QDs/PTB7 hybrid solar cells. The staggered band alignment of the type II Si QDs/PTB7 hybrid structure ensured efficient charge transport and collection. In all the devices  $FF$  and  $V_{OC}$  did not change with the oxidation time of Si QDs.  $FF$  and  $V_{OC}$  were always about 50% and 0.6 V, respectively. However,  $J_{SC}$  and PCE increased until the oxidation time was higher than 12 h. The average PCE was improved from 1.7% to 3.3%. The highest PCE of 3.6% was obtained after 12 h oxidation.

When the oxidation time of Si QDs in air was longer than 12 h,  $J_{SC}$  and PCE started decreasing. It was found that the mobility of the Si QDs film initially increased and then decreased with the increase of oxidation time, as shown in the Figure 18. The turning point was at  $\sim 12$  h. This implied that the too thick oxide at the QD surface was harmful to the charge transport of the Si QD/PTB7 solar cells, leading to the decrease of the solar cell performance.

### Si QDs/P3HT/PCBM Ternary Hybrid Solar Cells

Although all kinds of organic materials have been used together with Si QDs to form hybrid solar cells, the values of PCE have not reached those of classic organic solar cells. To further improve the performance of Si QD-based hybrid solar cells, Zhao et al. (2016) incorporated Si QDs into the classical bulk heterojunction organic solar cells based on P3HT and [6,6]-phenyl-C61-butyric acid methyl ester (PCBM) to fabricate the Si QDs/P3HT/PCBM ternary solar cells. In contrast to simply adding Si QDs into the P3HT:PCBM hybrid system (Kim et al. 2012), part of PCBM or P3HT was replaced with Si QDs. This led to the P3HT:(Si QDs) $_x$ :(PCBM) $_{1-x}$  or (P3HT) $_{1-y}$ :(Si QDs) $_y$ :PCBM ternary hybrid solar cells. Figure 19 shows the performance of the ternary solar cells with different weight fractions of Si QDs.

As shown in Figure 19a,  $J_{SC}$  initially increased and then decreased as  $x$  increased for P3HT:(Si QDs) $_x$ :(PCBM) $_{1-x}$  solar cells. The highest  $J_{SC}$  (16.15 mA/cm $^2$ ) appeared when  $x$  was 0.05. This maximum  $J_{SC}$  was significantly larger than that of the P3HT:PCBM solar cell. However,  $V_{OC}$  monotonically decreased from 0.59 to



**Fig. 18** Dependence of the carrier mobility of the Si QD film on the oxidation time of Si QDs (Reprinted with permission from Ding et al. 2014b, Copyright 2014 Elsevier)

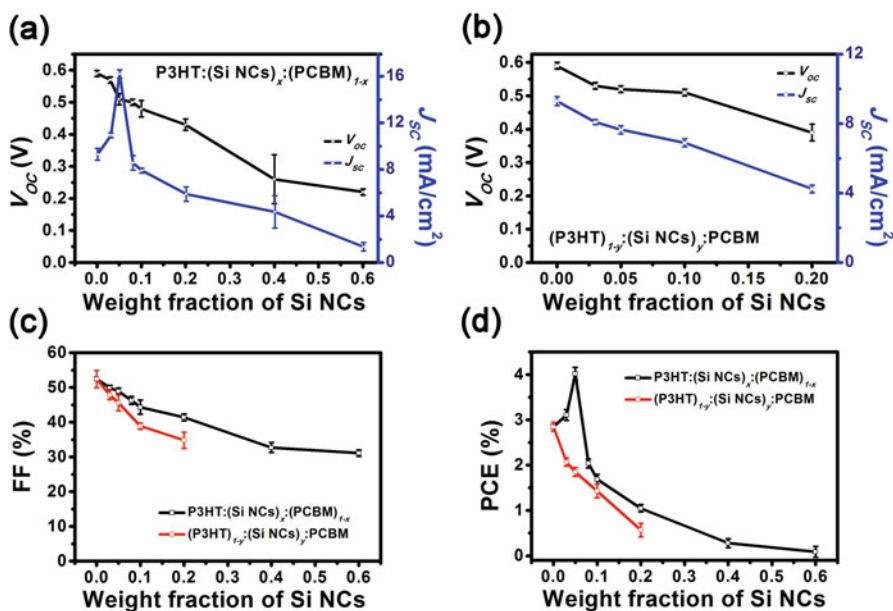
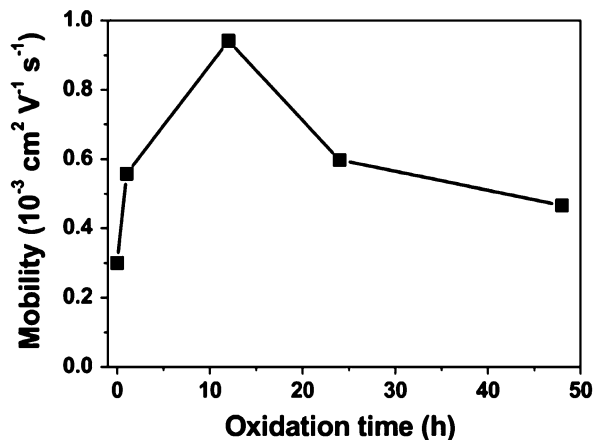


**Fig. 19** Dependence of  $J_{SC}$  and  $V_{OC}$  on (a)  $x$  and (b)  $y$ . Dependence of (c)  $FF$  and (d)  $PCE$  on  $x$  and  $y$ . Error bars in (a–d) correspond to a confidence of 95% (Reprinted with permission from Zhao et al. 2016, Copyright 2016 Elsevier)

0.22 V when  $x$  increased up to 0.6. For  $(\text{P3HT})_{1-y}:(\text{Si QDs})_y:\text{PCBM}$  ternary hybrid solar cells, it was found that both  $J_{SC}$  and  $V_{OC}$  decreased with the increase of  $y$  (Figure 19b). Figure 19c shows that  $FF$  decreased with the increase of the weight fraction of Si QDs for both  $\text{P3HT}:(\text{Si QDs})_x:(\text{PCBM})_{1-x}$  and  $(\text{P3HT})_{1-y}:(\text{Si QDs})_y:\text{PCBM}$  solar cells. Interestingly, the trend of the change of  $PCE$  was similar to that of  $J_{SC}$  when the fraction of Si QDs varied. This indicated the change of  $J_{SC}$  was mainly

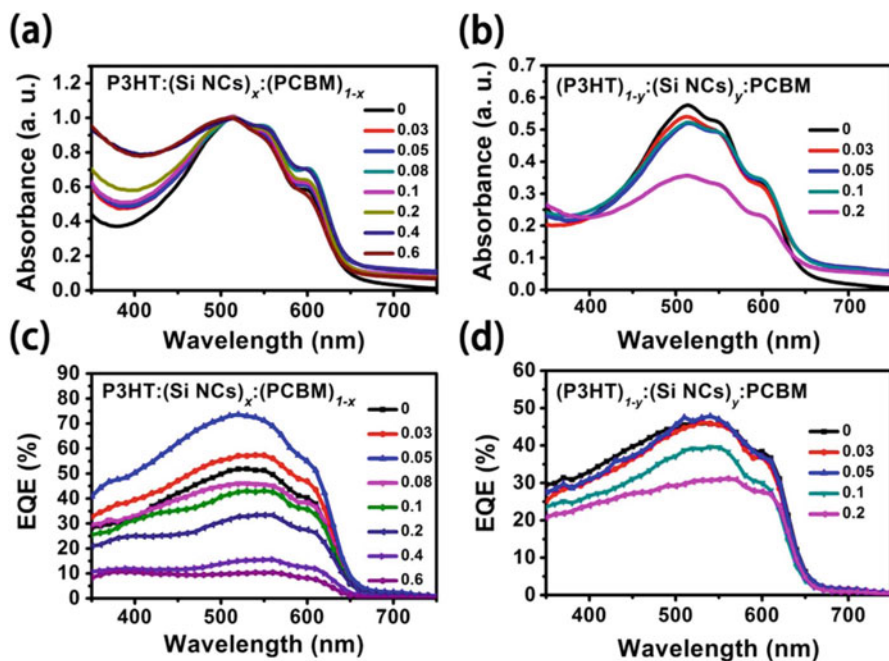


**Fig. 20** UV-vis absorption spectra of (a) P3HT:(Si QDs)<sub>x</sub>:(PCBM)<sub>1-x</sub> blends and (b) (P3HT)<sub>1-y</sub>:(Si QDs)<sub>y</sub>:PCBM blends. External quantum efficiency (EQE) of (c) P3HT:(Si QDs)<sub>x</sub>:(PCBM)<sub>1-x</sub> solar cells and (d) (P3HT)<sub>1-y</sub>:(Si QDs)<sub>y</sub>:PCBM solar cells (Reprinted with permission from Zhao et al. 2016, Copyright 2016 Elsevier)

responsible for the variation of PCE. It is worthy to point out that the highest PCE of 4.11% was obtained for P3HT:(Si QDs)<sub>x</sub>:(PCBM)<sub>1-x</sub> ternary hybrid solar cells when  $x$  was 0.05. The difference in the dependence of the PCE on the weight fraction of Si QDs between P3HT:(Si QDs)<sub>x</sub>:(PCBM)<sub>1-x</sub> and (P3HT)<sub>1-y</sub>:(Si QDs)<sub>y</sub>:PCBM solar cells implied that the weight fraction of Si QDs in the whole mixture could not solely determine the solar cell performance (Figure 20).

It was clear that the original P3HT:PCBM blend only efficiently absorb light in the wavelength region from 450 to 600 nm. When  $x$  increased, the absorption of the P3HT:(Si QDs)<sub>x</sub>:(PCBM)<sub>1-x</sub> blend in the short-wavelength region (<450 nm) increased. As  $x$  was not larger than 0.05, EQE increased with the increase of  $x$ . EQE increased not only in the short-wavelength region (<450 nm) but also in the long-wavelength region (450–600 nm). The Si QDs/P3HT/PCBM ternary hybrid structure had the cascade energy alignment, which might improve the carrier separation and transport and decrease the energy loss during the carrier separation and transport. In the wavelength region of 350–500 nm, the enhanced optical absorption should also lead to the increase of EQE. After  $x$  increased beyond 0.05, EQE decreased with the increase of  $x$  in the whole wavelength region. It was believed that structural deterioration became serious when  $x$  was large. For (P3HT)<sub>1-y</sub>:



(Si QDs)<sub>y</sub>:PCBM solar cells, EQE always decreased with the increase of  $y$  in the whole wavelength region. This was consistent with the fact that P3HT was mainly responsible for the optical absorption in the P3HT:PCBM blend. When the amount of P3HT decreased (i.e.,  $y$  increased), the optical absorption decreased, resulting in the decrease of EQE. In addition, when Si QDs directly replaced P3HT in (P3HT)<sub>1-y</sub>:(Si QDs)<sub>y</sub>:PCBM solar cells, the ratios of the weight of P3HT to that of Si QDs were smaller than those for P3HT:(Si QDs)<sub>x</sub>:(PCBM)<sub>1-x</sub> solar cells at the same values of  $x$  and  $y$ . Therefore, the crystallization of P3HT and nanostructure of active layer might be seriously affected by the excessive fraction of Si QDs. The maximum PCE of 4.11% was obtained for P3HT:(Si QDs)<sub>x</sub>:(PCBM)<sub>1-x</sub> solar cells when  $x$  was 0.05. The PCE of 4.11% corresponded to an increase of 40% with respect to that of the original P3HT:PCBM solar cell.

### Si QDs and Carbon Nanostructures Solar Cells

Švrček et al. (2010) prepared stable assemblies of Si QDs coupled with fullerenes (C<sub>60</sub>) without any additional surfactant or catalyst. The assemblies of Si QDs and C<sub>60</sub> were used as the active layers to fabricate heterojunction solar cells. The solar cell structure is shown in the inset of Figure 21a. The EQE of the Si QDs/C<sub>60</sub> solar cell in the short-wavelength region was quite high due to the strong optical absorption of Si QDs in the short-wavelength region (Figure 21a). Švrček et al. compared Si QDs produced by the fragmentation of bulk Si in water and those in ethanol. It was found that the EQE of the solar cell based on Si QDs produced in water was higher than that of the solar cell based on Si QDs produced in ethanol. A self-assembly process was thought to only occur to the fragmentation of bulk Si in water, while the fragmentation of bulk Si in ethanol tended to produce well-separated large spherical aggregates with an average diameter of 300 nm. The self-assembled networks of Si QDs more facilitated the charge transport than the well-separated large spherical aggregates of Si QDs. Hence, the EQE of the solar cell based on Si QDs produced in water was clearly higher than that of the solar cell based on Si QDs produced in ethanol. The solar cell based on Si QDs produced in water had the EQE of over 1.4% in the short-wavelength region and the EQE of up to ~0.06% in the wavelength region of 550–700 nm, as shown in Figure 21a. Figure 21b shows the band diagram of the hybrid Si QD/C<sub>60</sub> solar cell structure. The type II energy-level alignment between Si QDs and C<sub>60</sub> facilitated the charge separation. After the solar cell absorbed photons, excitons were generated and then dissociated at the Si QD/C<sub>60</sub> interface. Electrons transferred through C<sub>60</sub> to reach the cathode, while holes transferred through Si QDs to reach the anode.

Švrček et al. have also fabricated bulk-heterojunction solar cells by using *n*-type/*p*-type Si QDs and single-walled carbon nanotubes (SWCNTs) with an average diameter of ~0.83 nm (Švrček et al. 2011). Both *n*- and *p*-type of Si QDs were produced by electrochemical etching of silicon wafers and subsequent mechanical pulverization. Sedimentation of Si QDs in ethanol for 30 min was employed to eliminate large agglomerates before the mixing of Si QDs with SWCNTs in toluene. The mixture was spray-cast on glass coated with ITO/PEDOT:PSS. Finally, a ~100 nm thick Al electrode was deposited to complete the solar cell structure,

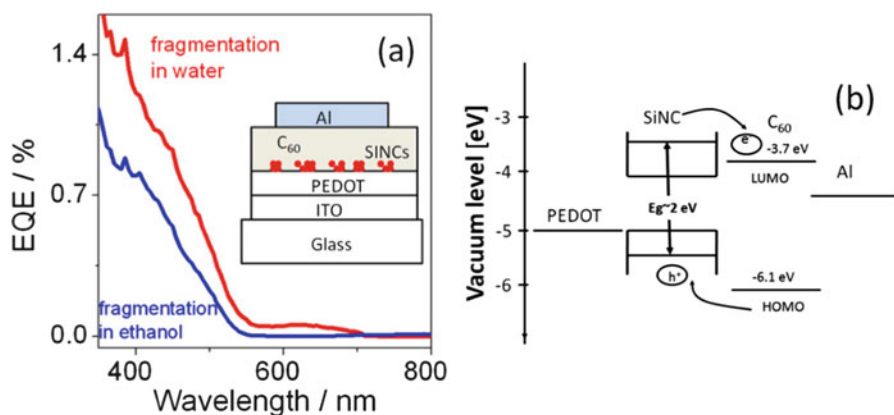


**Fig. 21** (a) EQE of the Si QD/C<sub>60</sub> hybrid solar cells. Si QDs were produced either in water or in ethanol. The inset shows the Si QD/C<sub>60</sub> hybrid solar cell structure. (b) Band diagram of the Si QD/C<sub>60</sub> hybrid solar cell (Reprinted with permission from Švrček et al. 2010, Copyright 2010 IOP Publishing Ltd)

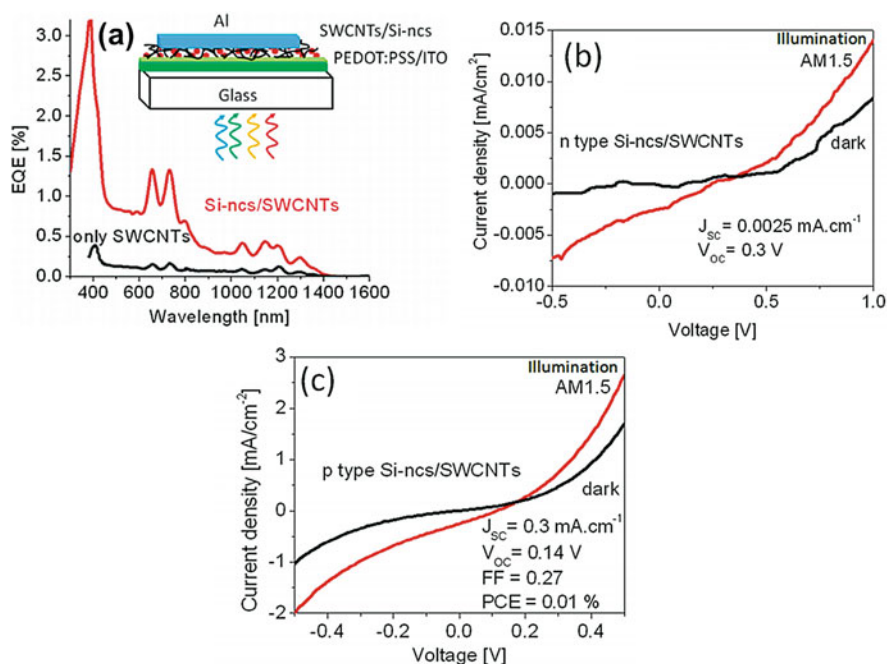


**Fig. 22** (a) Schematic view and EQE curves of the devices. The I–V characteristics in the dark and under AM 1.5 illumination of solar cells based on semiconducting SWCNTs and (b) n-type and (c) p-type Si QDs, respectively (Reprinted with permission from Švrček et al. 2011, Copyright 2011 American Chemical Society)

which is shown in the inset of Figure 22a. Figure 22a shows the EQE curves of *p*-type Si QDs/SWCNTs and SWCNTs-only solar cells. The EQE of the *p*-type Si QDs/SWCNTs solar cell was larger than that of the SWCNTs-only solar cell, especially in the short-wavelength region. The  $I$ - $V$  characteristics of the *n*-type Si QDs/SWCNTs and *p*-type Si QDs/SWCNTs solar cells are presented in Figure 22b, c, respectively. Both devices showed good rectifying characteristics. However, the current of the *p*-type Si QDs/SWCNTs solar cell was much higher than that of the *n*-type Si QDs/SWCNTs solar cell. This meant that *p*-type Si QDs were more suitable to combine with SWCNTs than *n*-type ones due to the better electrical coupling between *p*-type Si QDs and SWCNTs. This might originate from the better alignment of the energy levels between the *p*-type Si QDs and SWCNTs. The device with the *p*-type Si QDs/SWCNTs structure showed good optical absorption over a broad spectral range (300–1,400 nm). Under AM 1.5 illumination, the  $V_{OC}$ ,  $I_{SC}$ ,  $FF$ , and PCE of the device were 0.14 V, 0.3 mA/cm<sup>2</sup>, 0.25, and 0.01%, respectively.

### Si QD-Sensitized Solar Cells

In 1991, Gratzel's group reported a low-cost, high efficiency solar cell based on dye-sensitized TiO<sub>2</sub> films for the first time (Regan and Gratzel 1991). In the past decade, there has been interest in the use of QDs to sensitize TiO<sub>2</sub> films in the solar cell structures, leading to the so-called QD-sensitized solar cells (QDSSCs) (Chang et al. 2013; Li et al. 2011, 2012; Xu et al. 2012; Lin et al. 2013; Luo et al. 2013; Pan et al. 2014).

Wang et al. (2013) fabricated a Si QD-sensitized solar cell by using 1-dodecene hydrosilylated Si QDs. A TiO<sub>2</sub>-nanorod film was first fabricated on fluorinated tin oxide (FTO) with hydrochloric acid, deionized water, and tetra-*n*-butyl titanate through a hydrothermal process. The TiO<sub>2</sub>-nanorod film was then immersed in the solution of 1-dodecene hydrosilylated Si QDs for 96 h, leading to the attachment of Si QDs to the TiO<sub>2</sub>-nanorod film. The Si QD-absorbed TiO<sub>2</sub>-nanorod film was subsequently heated at 450 °C for 30 min. Figure 23a schematically shows the structure of the solar cell based on the Si QD-sensitized TiO<sub>2</sub>-nanorod film. The  $I$ - $V$  characteristics of the Si-QD-sensitized solar cell are shown in Figure 23b. The PCE of the solar cell was 0.1%. Such a low PCE was mainly due to the limited absorption of sunlight. Both TiO<sub>2</sub> and Si QDs could only effectively absorb short-wavelength light.

Kim et al. (2010) carried out surface modification for Si QDs to obtain carboxyl-terminated Si QDs. They used these Si QDs together with the dye of N719 to sensitize TiO<sub>2</sub> films in their solar cell structures. The solar cell performance under the standard illumination was shown in Table 1. Compared to the traditional dye-sensitized solar cell (DSSC) only with the dye of N719, the photovoltaic performance of the solar cell containing both N719 and Si QDs was significantly improved. Figure 24a, b showed the  $I$ - $V$  curves and IPCE curves of the solar cells only with the dye of N719 and with both the dye of N719 and Si QDs. Kim et al. attributed the improved solar cell performance to the connection of Si QDs and the dye of N719. The  $J_{SC}$  increase was due to both the direct sensitization of Si QDs and the indirect sensitization of the dye of N719 anchored at the surface of Si QDs. The

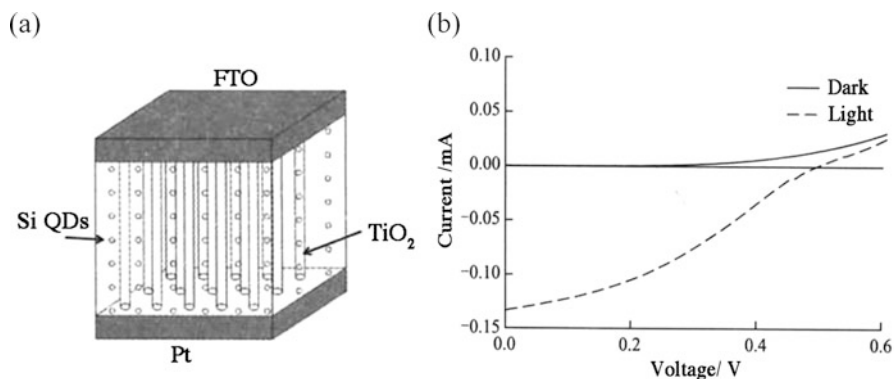


**Fig. 23** (a) Schematic diagram of a Si QDs sensitized solar cell. (b) Current-voltage characteristics of the Si QDs sensitized solar cell in the *dark* and AM1.5 illumination (Reprinted with permission from Wang et al. 2013, Copyright 2013 China Association for Science and Technology)

**Table 1** Photovoltaic parameters of DSSCs treated and untreated with carboxyl-terminated Si QDs at two different TiO<sub>2</sub> film thicknesses (Reprinted with permission from Kim et al. 2010, Copyright 2010 American Chemical Society)

Thickness ( $\mu\text{m}$ )	Si-COOH	$J_{\text{sc}}$ ( $\text{mA cm}^{-2}$ )	$V_{\text{oc}}$ (V)	FF (%)	$\eta$ (%)
$4 \pm 0.4$	Without	$7.97 \pm 0.22$	$0.67 \pm 0.01$	$67 \pm 3$	$3.6 \pm 0.2$
	With	$8.82 \pm 0.22$	$0.70 \pm 0.01$	$72 \pm 3$	$4.4 \pm 0.2$
$10 \pm 0.4$	Without	$12.9 \pm 0.22$	$0.69 \pm 0.01$	$58 \pm 3$	$5.2 \pm 0.2$
	With	$13.8 \pm 0.22$	$0.71 \pm 0.01$	$61 \pm 3$	$6.1 \pm 0.2$

incident photon to current efficiency (IPCE) increased in the entire visible range after the incorporation of Si QDs, indicating that Si QDs significantly enhanced the optical absorption of the dye of N719.

## Summary

Given the nontoxicity and abundance of Si and the solution-based processing, colloidal Si QDs are potentially suitable for the fabrication of low-cost and high-performance solar cells. Significant progress has been made on the use of colloidal Si QDs in all kinds of solar cell structures. However, the relatively weak optical absorption of Si QDs in the long-wavelength region and the poor charge transport of Si-QD films refrain the development of high-efficiency solar cells in which Si QDs play a central role. It has been recently demonstrated that doping can effectively tune the electronic and optical properties of Si QDs. The optical absorption of Si QDs may be extended to the long-wavelength region after doping. Doping may significantly improve the charge transport of Si-QD films. The continuous development of the surface manipulation of Si QDs should help further minimize the density

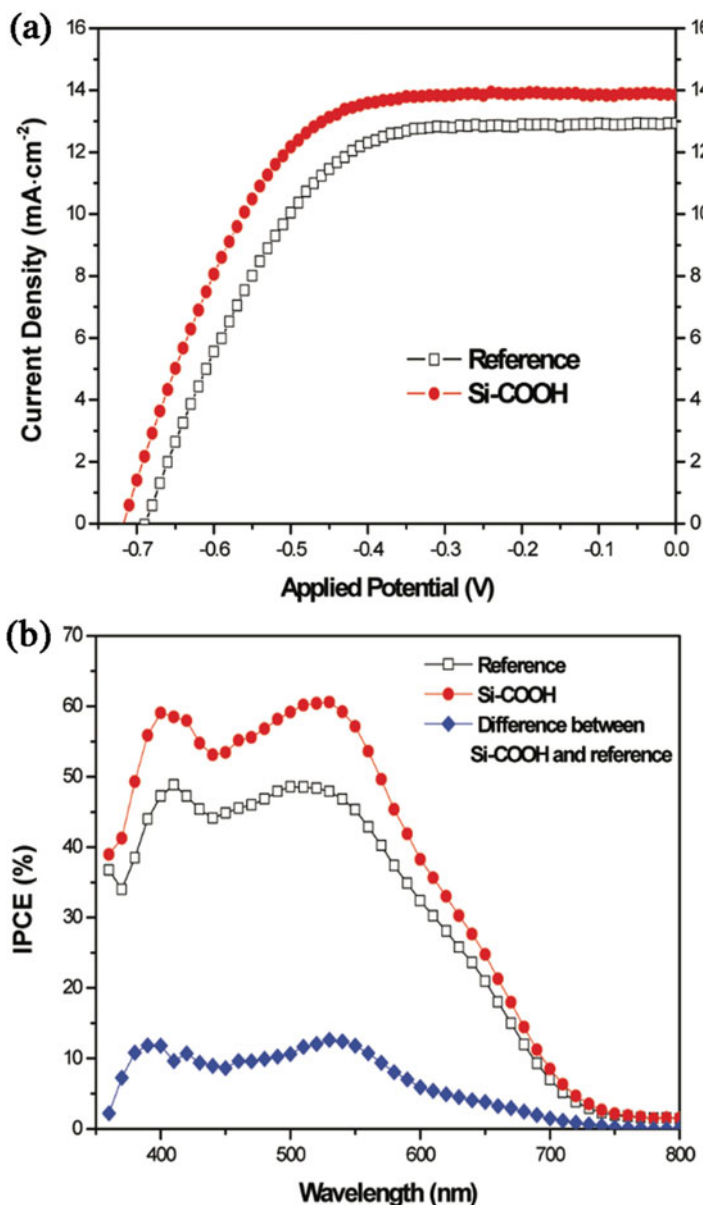


**Fig. 24** (a)  $J$ - $V$  curves of solar cells consisting of  $\text{TiO}_2$  films treated (solid circles) and untreated (open squares) with carboxyl-terminated Si QDs. (b) IPCE spectra of solar cells treated (solid circles) and untreated (open squares) with carboxyl-terminated Si QDs and the difference (solid diamonds) between the two spectra (Reprinted with permission from Kim et al. 2010, Copyright 2010. American Chemical Society)

of defects at the QD surface and facilitate the charge transport between Si QDs. All the improvements of the Si-QD materials greatly contribute to the design and fabrication of Si-QD solar cells. It may be envisioned that exciting development of both Si-QD solar cells and hybrid solar cells based on Si QDs with low cost and high efficiency will be realized in the future.

---

## References

- R. Anthony, U. Kortshagen, *Phys. Rev. B* **80**, 115407 (2009)
- E. Arici, S. Sariciftci, D. Meissner, *Adv. Funct. Mater.* **13**, 165 (2003)
- W. J. E. Beek, M. M. Wienk, R. A. J. Janssen, *Adv. Funct. Mater.* **16**, 1112 (2006)
- G. Belomoin, J. Therrien, A. Smith, S. Rao, H.N. Wagner, L. Mitas, *Appl. Phys. Lett.* **80**, 841 (2002)
- R. A. Bley, S. M. Kauzlarich, *J. Am. Chem. Soc.* **118**, 12461 (1996)
- C. Bostedt, T. van Buuren, T. M. Willey, N. Franco, L. J. Terminello, C. Heske, T. Möller, *Appl. Phys. Lett.* **84**, 4056 (2004)
- A. M. P. Botas, R. A. S. Ferreira, R. N. Pereira, R. J. Anthony, T. Moura, D. J. Rowe, U. Kortshagen, *J. Phys. Chem. C* **118**, 10375 (2014)
- R. Boukherroub, S. Morin, D. D. M. Wayner, F. Bensebaa, G. Sproule, J. Baribeau, D. Lockwood, *Chem. Mater.* **12**, 2002 (2011)
- T. Bronger, P. H. Wöbkenberg, J. Wördenweber, S. Muthmann, U. W. Paetzold, V. Smirnov, S. Traut, Ü. Dagkaldiran, S. Wieber, M. Cölle, A. P. Schwab, O. Wunnicke, M. Patz, M. Trocha, U. Rau, R. Carius, *Adv. Mater. Interface* **4**, n/a (2014)
- J. Buriak, *Chem. Mater.* **26**, 763 (2013)
- T.V. Buuren, L.N. Dinh, L.L. Chase, W.J. Siekhaus, L.J. Terminello, *Phys. Rev. Lett.* **30**, 3803 (1998)
- J. Chang, J. Lin, L. Su, C. Chang, *ACS Appl. Mater. Interfaces* **5**, 8740 (2013)
- D. Cui, J. Xu, T. Zhu, G. Paradee, S. Gerhold, *Appl. Phys. Lett.* **88**, 183111 (2006)
- A. Cullis, L. Canham, G. Calcott, *J. Appl. Phys.* **82**, 909 (1997)
- M. Dasog, Z. Yang, S. Regli, T. Atkins, A. Faramus, M. Singh, E. Muthuswamy, S. Kauzlarich, R. Tilley, J. G. C. Veinot, *ACS Nano* **7**, 2676 (2013)
- M. Dasog, G. Reyes, L.V. Titova, F. A. Hegmann, J. G. V. Veinot, *ACS Nano* **8**, 9646 (2014)
- Y. Ding, R. Gresback, Q. Liu, S. Zhou, X. Pi, T. Nozaki, *Nano Energy* **9**, 25 (2014a)
- Y. Ding, M. Sugaya, Q. Liu, S. Zhou, T. Nozaki, *Nano Energy* **10**, 322 (2014b)
- Y. Ding, M. Sugaya, S. Zhou, Z. Ni, X. Pi, T. Nozaki, *ACS Photon.* **3**, 415 (2016)
- K. Dohnalová, T. Gregorkiewicz, K. Kúsová, *J. Phys. Condens. Matter* **26**, 173201 (2014)
- M. Fujii, S. Hayashi, K. Yamamoto, *J. Appl. Phys.* **83**, 7953 (1998)
- M. Fujii, Y. Yamaguchi, Y. Takase, K. Ninomiya, S. Hayashi, *Appl. Phys. Lett.* **85**, 1158 (2004)
- Y. Gao, S. Zhou, Y. Zhang, C. Dong, X. Pi, D. Yang, *J. Mater. Sci. Technol.* **29**, 652 (2013)
- N. Greenham, X. Peng, A. P. Alivisatos, *Phys. Rev. B* **54**, 17628 (1996)
- R. Gresback, Y. Murakami, Y. Ding, R. Yamada, K. Okazaki, T. Nozaki, *Langmuir* **29**, 1802 (2013)
- S. Gunes, K. Fritz, H. Neugebauer, N. Sariciftci, S. Kumar, G. Scholes, *Sol. Energy Mater. Sol. Cells* **91**, 420 (2007)
- X. Guo, N. Zhou, S. Lou, J. Smith, D. Tice, J. Hennek, R. Ortiz, J. Navarrete, S. Li, J. Strzalka, L. Chen, R. Chang, A. Facchetti, T.J. Marks, *Nature Photon.* **7**, 825 (2013)
- A. Gupta, H. Wiggers, *Phys. E.* **41**, 1010 (2009)
- C. Hessel, D. Reid, M. Panthani, J. Wei, H. Fujii, V. Akhavan, D. Kortgel, *Chem. Mater.* **24**, 393 (2012)
- Y. Hori, S. Kano, H. Sugimoto, K. Imakita, M. Fujii, *Nano Lett.* **16**, 2615 (2016)
- A. Hryciw, J. Laforge, C. Blois, M. Glover, A. Meldrum, *Adv. Mater.* **7**, 845 (2005)

- F. Hua, M. Swihart, E. Ruckenstein, *Langmuir* **21**, 6054 (2005)
- D. Jurbergs, E. Rogojina, L. Mangolini, U. Kortshagen, *Appl. Phys. Lett.* **88**, 233116 (2006)
- J. Kelly, J. G. C. Veinot, *ACS Nano* **4**, 4645 (2010)
- J. Kelly, J. G. C. Veinot, E. Alberta, *ACS Nano* **4**, 2002 (2010)
- J. Kelly, A. Shukaliak, M. Fleischauer, J. G. C. Veinot, *J. Am. Chem. Soc.* **133**, 4645 (2011)
- R. Khelifi, D. Mathiot, R. Gupta, D. Muller, M. Roussel, S. Duguay, *Appl. Phys. Lett.* **102**, 13116 (2013)
- Y. Kim et al., *Chem. Mater.* **22**, 207 (2010)
- K. Kim, J. Lee, M. Swihart, M. Yang, *Appl. Phys. Express* **5**, 22302 (2012)
- J. Knipping, H. Wiggers, B. Rellinghaus, P. Roth, D. Konjhozic, C. Meierb, *J. Nanosci. Nanotechnol.* **4**, 1039 (2004)
- U. Kortshagen, *J. Phys. D. Appl. Phys.* **42**, 113001 (2009)
- U. Kortshagen, R. M. Sankaran, R. N. Pereira, S. L. Girshick, J. J. Wu, E. S. Aydil, *Chem. Rev.* **116**, 11061 (2016)
- C. Kwong, W. Choy, P. Chui, K. Cheng, W. Chan, *Nanotechnology* **15**, 1156 (2004)
- C. S. Lee, W. Yin, A. P. Holt, J. Sangoro, A. P. Sokolov, M. D. Dadmun, *Adv. Funct. Mater.* **25**, 5848 (2015)
- X. Li, Y. He, S. Talukdar, M. Swihart, *Langmuir* **19**, 8490 (2003)
- G. Li, V. Shrotriya, J. Huang, Y. Yao, T. Moriarty, K. Emery, Y. Yang, *Nat. Mater.* **4**, 864 (2005)
- T. Li, Y. Lee, H. Teng, *J. Mater. Chem.* **21**, 5089 (2011)
- T. Li, Y. Lee, H. Teng, *Energy Environ. Sci.* **5**, 5315 (2012)
- H. Liao, C. Tsao, T. Lin, M. Jao, C. Chuang, S. Chang, Y. Huang, Y. Shao, C. Chen, C. Su, U. Jeng, Y. Chen, W. Su, *ACS Nano* **6**, 1657 (2012)
- C. Lin, C. Teng, T. Li, Y. Lee, H. Teng, *J. Mater. Chem. A* **1**, 1155 (2013)
- C. Liu, Z. C. Holman, U. Kortshagen, *Nano Lett.* **9**, 449 (2009)
- C. Liu, Z. C. Holman, U. Kortshagen, *Adv. Funct. Mater.* **20**, 2157 (2010)
- Z. Liu, Y. Sun, J. Yuan, H. Wei, X. Huang, L. Han, W. Wang, H. Wang, W. Ma, *Adv. Mater.* **25**, 5772 (2013)
- X. Liu, Y. Zhang, T. Yu, X. Qiao, R. Gresback, X. Pi, D. Yang, *Part. Part. Syst. Charact.* **33**, 44 (2015)
- T. Lopez, L. Mangolini, *Nanoscale* **6**, 1286 (2014)
- P. Lu, W. Mu, J. Xu, X. Zhang, W. Zhang, W. Li, L. Xu, K. Chen, *Sci. Rep.* **6**, 1 (2016)
- J. Luo, H. Wei, Q. Huang, X. Hu, H. Zhao, R. Yu, D. Li, Y. Luo, Q. Meng, *Chem. Commun.* **49**, 3881 (2013)
- Y. Ma, X. Chen, X. Pi, D. Yang, *J. Phys. Chem. C* **115**, 12822 (2011)
- L. Mangolini, *J. Vac. Sci. Technol. B* **31**, 020801–020801 (2013)
- L. Mangolini, U. Kortshagen, *Adv. Mater.* **19**, 2513 (2007)
- L. Mangolini, E. Thimsen, U. Kortshagen, *Nano Lett.* **5**, 655 (2005)
- B. F. P. McVey, R. D. Tilley, *Acc. Chem. Res.* **47**, 3045 (2014)
- O. Nayfeh, A. Rao, J. Therrien, M. Nayfeh, *IEEE Photon. Technol. Lett.* **16**, 1927 (2004)
- J. Nelles, D. Sendor, A. Ebberts, F.M. Petrat, H. Wiggers, C. Schulz, U. Simon, *Colloid Polym. Sci.* **285**, 729 (2007)
- Z. Ni, X. Pi, M. Ali, S. Zhou, T. Nozaki, D. Yang, *J. Phys. D* **48**, 314006 (2015)
- Z. Ni, X. Pi, S. Zhou, T. Nozaki, B. Grandidier, D. Yang, *Adv. Optical Mater.* **4**, 700 (2016)
- M. Ostraat, J. Blauwe, M. Green, L. Bell, H. Atwater, R. Flagan, *J. Electrochem. Soc.* **148**, G265 (2001)
- Z. Pan, I. Sero, Q. Shen, H. Zhang, Y. Li, K. Zhao, J. Wang, X. Zhong, J. Bisquert, *J. Am. Chem. Soc.* **136**, 9203 (2014)
- N. Park, T. Kim, S. Park, *Appl. Phys. Lett.* **78**, 2825 (2001)
- K. Pettigrew, Q. Liu, P. Power, S. Kauzlarich, *Chem. Mater.* **15**, 4005 (2003)
- X. Pi, R. Liptak, S. Campbell, U. Kortshagen, *Appl. Phys. Lett.* **91**, 083112 (2007)
- X. Pi, R. Liptak, J. Nowak, N. Wells, C. Carter, S. Campbell, U. Kortshagen, *Nanotechnology* **19**, 245603 (2008)

- X. Pi, X. Chen, D. Yang, *J. Phys. Chem. C* **115**, 9838 (2011)
- X. Pi, L. Zhang, D.R. Yang, *J. Phys. Chem. C* **116**, 21240 (2012)
- X. Pi, T. Yu, D. Yang, *Part. Part. Syst. Charact.* **31**, 751 (2014)
- T. Purkait, M. Iqbal, M. Wahl, K. Gottschling, C. Gonzalez, M. Islam, J. Veinot, *J. Am. Chem. Soc.* **136**, 17914 (2014)
- B. Regan, M. Gratzel, *Nature* **353**, 737 (1991)
- P. Reiss, M. Carrière, C. Lincheneau, L. Vaure, S. Tamang, *Chem. Rev.* **116**, 10731 (2016)
- S. Ren, L. Chang, S. K. Lim, J. Zhao, M. Smith, N. Zhao, V. Bulovic, M. Bawendi, S. Gradecak, *Nano Lett.* **11**, 3998 (2011)
- I. Sandu, P. Moreau, D. Guyomard, L. R. Brousse, *Solid State Ionics* **178**, 1297 (2007)
- F. Sangghaleh, I. Sychugov, Z. Yang, J. G. C. Veinot, J. Linnros, *ACS Nano* **9**, 7097 (2015)
- R. Sankaran, D. Holunga, R. Flagan, K. Giapis, *Nano Lett.* **5**, 527 (2005)
- M. Scharber, D. Mühlbacher, M. Koppe, P. Denk, C. Waldauf, A. Heeger, C. Brabec, *Adv. Mater.* **18**, 789 (2006)
- T. Sonthheimer, D. Amkreutz, K. Schulz, P. Wöbkenberg, C. Guenther, V. Bakumov, J. Erz, C. Mader, S. Traut, F. Ruske, M. Weizman, A. Schnegg, M. Patz, M. Trocha, O. Wunnicke, B. Rech, *Adv. Mater. Interfaces* **1**, 1300046 (2014)
- H. Sugimoto, M. Fujii, K. Imakita, S. Hayashi, K. Akamatsu, *J. Phys. Chem. C* **116**, 19696 (2012)
- B. Sun, A. Findikoglu, M. Sykora, D. Werder, V. Klimov, *Nano Lett.* **9**, 1235 (2009)
- V. Švrček, I. Pelant, J. Rehspringer, P. Gilliot, D. Ohlmann, O. Crguét, B. Hönerlage, T. Chvojka, J. Valenta, J. Dian, *Mater. Sci. Eng. C* **19**, 233 (2002)
- V. Švrček, A. Slaoui, J. Muller, *Thin Solid Films* **451**, 384 (2004)
- V. Švrček, D. Mariotti, Y. Shibata, M. Kondo, *J. Phys. D. Appl. Phys.* **43**, 1646 (2010)
- V. Švrček, S. Cook, S. Kazaoui, M. Kondo, *J. Phys. Chem. Lett.* **2**, 1646 (2011)
- I. Sychugov, J. Valenta, K. Mitsuishi, J. Linnros, *Phys. Rev. B* **86**, 075311 (2012)
- R. Wang, X. Pi, D. Yang, *Acta Energetica Solaris Sin.* **34**, 2228 (2013)
- J.H. Warner, H.R. Dunlop, R.D. Tilley, *J. Phys. Chem. B* **109**, 19064 (2005)
- J. Wendy, U. Huynh, A. Alivisatos, *Science* **295**, 2425 (2002)
- L. Wheeler, N. Anderson, P. Palomaki, J. Blackburn, J. Johnson, N. Neale, *Chem. Mater.* **27**, 6869 (2015)
- M. Wolkin, J. Jorne, P. Fauchet, *Phys. Rev. Lett.* **82**, 197 (1999)
- I. Wurfl, X. Hao, A. Gentle, D. H. Kim, G. Conibeer, M. Green, *Appl. Phys. Lett.* **95**, 153506 (2009)
- G. Xu, S. Ji, C. Miao, G. Liu, C. Ye, *J. Mater. Chem.* **22**, 4890 (2012)
- D. Xue, J. Wang, Y. Wang, S. Xin, Y. Guo, L. Wan, *Adv. Mater.* **23**, 3704 (2011)
- J. Yang, R. Liptak, D. Rowea, J. Wu, J. Casey, D. Witker, S.A. Campbell, U. Kortshagen, *Appl. Surf. Sci.* **323**, 54 (2014)
- T. Yu, F. Wang, Y. Xu, L. Ma, X. Pi, D. Yang, *Adv. Mater.* **28**, 4912 (2016)
- M. Zacharias, J. Heitmann, R. Scholz, U. Kahler, M. Schmidt, J. Bläsing, *Appl. Phys. Lett.* **80**, 661 (2002)
- S. Zhao, X. Pi, C. Mercier, Z. Yuan, B. Sun, D. Yang, *Nano Energy* **26**, 305 (2016)
- S. Zhou, X. Pi, Z. Ni, Y. Ding, Y. Jiang, C. Jin, C. Delerue, D. Yang, T. Nozaki, *ACS Nano* **9**, 378 (2015)
- S. Zhou, Z. Ni, Y. Ding, M. Sugaya, X. Pi, T. Nozaki, *ACS Photon.* **3**, 415 (2016)
- L. Zuo, S. Zhang, H. Li, H. Chen, *Adv. Mater.* **27**, 43 (2015)



# Index

## A

Absorption coefficient, 658  
Advanced cast method, 265  
Agglomeration of silicon particles, 99  
All-nc-Si-based solar cell, 863, 875  
Aluminum induced crystallization (AIC), 763, 765, 770, 773, 782, 784  
Argon gas flow rate, 447  
Argon gas pressure, 447–449  
Artificial grain boundaries, in bulk Si crystals, 226  
Atmospheric pressure chemical vapor deposition (APCVD), 766  
Atomic force microscopy (AFM), 699–700, 727

## B

Bandgap profiling, 681  
Band-tail states, 656  
B doped ZnO (BZO), 731  
Boltzmann constant, 549  
Boron removal, slag treatment, 114–116  
Boundary conditions, 446  
Boussinesq approximation, 442  
Burgers vector, 544, 546, 553, 554  
By-product, comprehensive utilization of, 47, 55, 63, 64

## C

Carbon, 22–24  
Carbon impurity, in crystalline silicon, 439  
  argon gas flow, models for, 442–443  
  argon gas flow rate, effect of, 447  
  argon gas pressure, effect of, 447–449  
  carbon incorporation, mechanism of, 440  
  crucible cover design, 449–450  
  crucible cover material design, 451–456

  distribution of impurities, 446  
  global heat transfer, models for, 441–442  
  impurity transport, models for, 443–446  
  silica crucible and graphite susceptor, reaction control between, 456–459  
Carrier lifetime detection, 24–29  
Cast furnace, 250–258  
Casting, 176, 177, 187, 190  
Cast method, 194, 197, 198, 203, 205, 208, 210, 212  
Charge transfer model, 671  
Chemical vapor deposition (CVD), 765, 767  
  reactor, 38, 47, 65, 67  
Chlorination process, 41  
Chromium, 511  
Classic directional solidification process, 614  
Cleaning, 312, 314, 317, 325  
  procedures, 331  
  sequences, 333  
  of silicon surfaces, 324  
  solution, 327  
Cleavage, 271, 304  
Cobalt, 512  
Coincidence site lattice (CSL) grain boundaries, 222, 223, 226  
Coincidence site lattice (CSL) model, 594  
Cold wall reactor, 97–98  
Colloidal silicon quantum dots (Si QDs), 934  
  and carbon nanostructures solar cells, 951  
  electronic properties, 936  
  optical properties, 937–938  
  and P3HT/PCBM ternary hybrid solar cells, 948–951  
  and poly (3-hexylthiophene) solar cells, 940  
  preparation, 934–936  
  and PTB7 solar cells, 945–948  
Conductivity  
  hot probe, thermoelectric conductivity type test method, 17–18

- Conductivity (*cont.*)  
 rectifier conductivity type test method, 18
- Constant photocurrent method (CPM), 705
- Constrained crystallization principle, 848
- Contamination, wafer, 385–387
- Conversion efficiency, 261
- Coolants, 393
- Copper, 510
- Cover material, 449, 451–456
- Crucible cover  
 design, 449–450  
 material design, 451–456
- Crystalline evolution, 695, 698, 699, 708, 709
- Crystalline silicon  
 carbon impurity in (*see* Carbon impurity, in crystalline silicon)  
 dislocations (*see* Dislocations, crystalline silicon)
- Crystal/melt interface, 195, 198, 201
- Czochralski (CZ) method, 217
- Czochralski (Cz) processes, 438
- Czochralski silicon (CZ-Si), 401, 404, 408, 413, 415, 419, 421, 425, 427, 429  
 continuous growth, 153  
 crystal puller, 131  
 dislocation-free growth, 137  
 dopant distribution inhomogeneity, 144  
 germanium-doped crystal growth, 157  
 impurity segregation effect in, 142  
 light-induced-degradation, 148  
 magnetic field assisted growth, 151  
 melt flow, 140  
 N doping in CZ-Si silicon growth, 470–471  
 N impurity on mechanical properties, 476–477  
 N-O complexes, 471–474  
 oxygen control, 150  
 oxygen impurity, 146  
 oxygen precipitates, 475  
 pulling, 135  
 square ingot growth, 156  
 thermal control, 138  
 thermal donors, 474–475
- D**
- Dangling bonds, 641, 652, 670–672, 688, 946
- Dark conductivity, 664
- Debye length, 645
- Deep-level transient-spectroscopy (DLTS), 576
- Defect(s), 134, 148  
 B–O, 167  
 engineering (*see* SMART)  
 light-induced degradation, 167  
 radiation-induced, 163  
 slow- and fast-forming, 148  
 VO, 166
- Dendrite growth, 194, 195, 197, 198, 201, 203, 207, 208, 211
- Dendritic casting method, 625
- Diamond cubic (DC) structure, 543
- Diamond wire, 285, 286, 297, 302, 303, 374, 380
- Dichlorosilane (DCS), 55
- Directional solidification (DS), 175, 176, 590  
 fine grain structures without seeding  
 on Si feedstock, 630–633  
 fine grain structures with seeding on Si feedstock, 625–630  
 quasi-mono technology, 618–625  
 without seed crystals, 613–618
- Dislocation, 208, 210, 212, 213, 220, 222, 228, 229  
 clusters, 176, 179, 182, 187, 190  
 density, 241
- Dislocation-free Si, 551, 553
- Dislocation generation, 221  
 grain boundary microstructure,  
 influence of, 221–224  
 stress distribution, influence of, 223–225
- Dislocations, crystalline silicon  
 brittle-to-ductile transition, 571–572  
 critical stress, for dislocation generation, 558–560  
 crystal structure, 543–544  
 dislocation behavior, in multi-crystalline Si, 579–580  
 dislocation dynamics, in deformation, 555–557  
 dislocation immobilization, 561–563  
 dislocation-related deep states, 576–577  
 dislocation-related shallow states, 577–578  
 dislocation structures, 544–546  
 dislocation velocity, 548–550, 564–567  
 efficiency and electrical properties, of Si solar cells, 580–581  
 electrical characters, 573–574  
 electronic structures, 574–575  
 fracture toughness, 570–571  
 Hirth-Lothe kink diffusion model, 553–555  
 hydrogen-enhanced dislocation glides, 569–570  
 plastic deformation and yield strength, 550–553  
 recombination at dislocations, 576

- recombination-enhanced dislocation
  - glides, 567–569
  - shuffle- /glide-set of dislocations, 557–558
  - Suzuki effect, 563–564
- Drude model, 938
  
- E**
- Electron backscattered diffraction (EBSD), 780, 781
- Electron beam back scatter diffraction (EBSD), 605–606
- Electron-beam evaporation (EBE), 771, 773
- Electron beam induced conductivity (EBIC), 780
- Electron beam induced current (EBIC), 609
- Electron spin resonance (ESR), Si QDs, 946
- Energy band diagram, Si QDs/P3HT solar cell, 941
- Epitaxial growth, 760, 763, 764, 766, 768, 770, 771, 773, 774, 784
- Etching, 312, 313
  - anodic, 317
  - chemical, 317
  - dry, 312
  - electroless, 317
  - silicon, 313
- Etch-pit density (EPD), 252
- Eulerian-Eulerian model, 92
- Extended defects, 496, 498, 512
  - metal interaction with, 520–528
- External quantum efficiency (EQE), 427, 428, 715, 725, 728, 730, 735, 737, 742, 746, 748, 749
  
- F**
- F, 295
- Face-centered-cubic (fcc) lattices, 544
- Facet plane, 196, 199, 200
- Finite-difference time-domain (FDTD), 779
- Finite element calculations, 383
- Fixed abrasive(s), 366
  - sawing, 284, 287, 297, 302, 306
- Flexible solar laminates, 685
- Floating zone (FZ) method, 226
- Float zone, 13–15, 66
- Float zone silicon (FZ-Si), 404
- Fluidized bed reactor (FBR), 73, 627
  - bed pressure drop, 75–76
  - Geldart classification, 75
  - heat transfer, 76–77
  - industrial applications, 77–79
  - MGS conversion to polysilicon, 80
  - minimum bubbling velocity, 74
  - minimum fluidization gas velocity, 74
  - polysilicon production, 79
  - slugging beds, 76
- Fourier transform infrared (FTIR) spectra
  - B-doped Si NCs, 938
  - Si QDs with Cl, O and H, 943
- Fourier transform infrared spectroscopy (FTIR), 402, 403, 407, 412, 422, 432
- Fourth-order Runge-Kutta scheme, 442
- Fracture strength, 382–385
- Full width at half maximum (FWHM), 782
- Functional grain boundaries, 225, 620
  
- G**
- Gas-phase approaches, 934
- Geometrically necessary dislocations (GNDs), 781
- Gettering, 176, 182, 183
  - classification, 529
  - external, 497
  - intrinsic, 497
  - metal impurities, 528–533
  - relaxation, 529
  - segregation, 530
- Global simulation of carbon impurity, *see* Carbon impurity, in crystalline silicon
- Glow discharge, 643, 644, 646, 650–651
- Gold, 513
- Graded-sized nc-Si, 847, 861, 864, 872, 874
- Grain boundaries, 185
  - characterization, 600
  - decoration with impurity atoms, 596–598
  - definition, 591
  - directional solidification (*see* Directional solidification) and dislocations, 599
  - electronic material properties, 607–609
  - energy, 596–597
  - impact on electronic properties, 598
  - optical grain detection and analysis, 601–605
  - orientation mapping, 605–607
  - properties of, 596–599
  - types of, 593–595
- Grain detector, 607
- Granular silicon, 79, 88, 96, 102

**H**

- Hasen–Alexander–Sumino model, 225
- Heterogeneous nucleation, 613
- Heterojunction interdigitated back-contact (HJ-IBC) technology, 767
- High efficiency solar cells, 170
- High-performance multi-crystalline silicon, 175, 179
- High-purity Si
  - dislocation velocity, 548–550
  - plastic deformation and yield strength, 550–553
- High temperature vapor phase epitaxy, 766
- Hirth–Lothe kink diffusion model, 553–555
- Hot wire chemical vapor deposition (HWCVD), 768–770
- Hydrochlorination, 63
- Hydrogenated amorphous silicon (a-Si:H), 694, 695, 697, 699, 701, 710, 713, 714, 719, 720, 722, 725, 732, 733, 735, 737, 740, 744, 745, 747–751
  - absorption coefficients, 658–660
  - atomic structure model, 656
  - conductivity, 669–670
  - dark conductivity, 664–667
  - DC-PECVD, 643–646
  - how wire CVD, 652–654
  - infrared absorption, 661
  - microwave PECVD, 651
  - multi-junction solar cell, 682–685
  - n-i-p* single-junction solar cell, 679
  - photoconductivity, 668–669
  - photoluminescence, 660
  - p-i-n* single-junction solar cell, 677–678
  - Raman spectra, 663–664
  - RF PECVD, 646
  - single-junction solar cell, 675–677
  - Staebler–Wronski effect (*see* Staebler–Wronski effect)
  - VHF PECVD, 648
- Hydrogenated microcrystalline silicon ( $\mu\text{-Si:H}$ )
  - early stage, 694
  - electronic properties of, 701–704
  - optical properties of, 704–708
  - in solar cells (*see* Solar cells,  $\mu\text{-Si:H}$ )
  - structure properties of, 695–701
- Hydrogenated microcrystalline silicon germanium ( $\mu\text{-SiGe:H}$ ), 736
- Hydrogen chloride (HCL), preparation of, 39–42
- Hydrogen collision model, 671

- Hydrogen-enhanced dislocation glides, 569–570
- Hydrogen passivation, 497, 533–538

**I**

- Impurity, 695, 708, 714–719, 732, 751, 752
  - concentrations, 142
  - oxygen, 146
  - segregation coefficients, 144
- Impurity effects on dislocation activities, crystalline silicon, *see* Dislocations, crystalline silicon
- Incubation phase, 801
- Indentation, 372, 376–378
- Infrared (IR) absorption, 661–663
- Infrared laser scattering tomography (IR-LST), 411
- Inkjet printing of Si-QD ink, 939
- In situ observation, 194, 196, 199, 200
- Interstitial oxygen, 19–21
- Interstitial oxygen, in silicon
  - diffusivity and solubility, 401–402
  - interstitial oxygen concentration, measurement of, 402
  - oxygen dimers, 403–404
  - in solar silicon materials, 404

**K**

- Kikuchi diffraction pattern, 605
- Knoop test, 376

**L**

- Large angle grain boundaries, 593, 595, 602, 625
- Large area uniformity, 654
- Large diameter, 241
- Laue scanner method, 606–607
- LaWave<sup>®</sup> method, 368
- Lifetime, 177, 180, 182, 184, 187, 429, 431, 433, 497, 653, 668, 671
  - of charge carriers, 408–409, 423–426
  - on excitation level, 508
  - killer, 538
  - maps, 507
  - in solar cell, 532
- Lift-off and transfer of poly-Si thin films, 774
- Light beam induced current (LBIC), 581
- Light-induced-degradation (LID)
  - Czochralski silicon, 148
  - Ge-doped CZ silicon crystals, 166

- Light management, 864
- Light trapping, 695, 725–735, 740, 743, 744, 752
- effect, 868, 870, 872
  - structure, 759, 761, 772, 776, 778, 780, 784
  - technology, for poly-Si thin film solar cells, 775
- Liquid phase crystallization (LPC), 760, 764–766, 773, 780, 782, 784, 787
- Localized surface plasmon resonance, 937
- Local quantum efficiency, 581
- Loose abrasive, 274
- sawing, 276, 285, 297, 302
- Low cost silicon wafers, 153
- Low pressure chemical vapor deposition (LP-CVD), 731, 766
- Low-temperature region, 236
- M**
- Manganese, 514
- Mechanical strength, 161
- Melt growth, 236
- See also* Noncontact crucible (NOC) method
- Metal assisted chemical etching (MACE), 776, 777, 889
- Metal induced crystallization (MIC), 762
- Metal interaction, with extended defects, 520–528
- Metallic impurities and surface metallic contamination, 29–33
- Metallurgical grade silicon (MGS), 72, 80
- secondary refining of, 112
  - smelting of, 110–111
- Meyer-Nedel rule, 665
- Microcrystalline silicon ( $\mu\text{-Si}$ ), 796
- Microstructure factor, 662, 802
- Microwave detected photoconductivity (MDP), 608
- Microwave PECVD, 651
- Minority carrier lifetime, 257
- Mobility, 664–667
- Moderate/low temperature vapor phase epitaxy, 767
- Modified EMA model, 852
- Mono-like Si growth method
- advantages and disadvantages, 219–220
  - functional grain boundaries, 225–228
  - large rectangular seed crystals, 232
  - mushroom-type interface growth, 232
  - seed growth, 217–218
  - SMART, 228
  - using seed partitions, 231
  - without seed joints, 232
  - with special grain boundaries, 230
- Mott-CFO model, 657
- Multi-crystalline silicon (mc-Si), 179, 404, 409, 417, 418, 429, 431, 433, 590, 592
- dislocation behavior in, 579–580
  - growth in ambient nitrogen, 485–490
  - silicon nitride precipitates (*see* Silicon nitride precipitates)
  - soluble nitrogen, 478–481
- Multi-junction, 722, 725, 734, 737, 738, 744, 747
- thin film, 695
- Multiphase flow with interphase exchange (MFX), 93
- Multiple trapping, 666
- Multi-scale modeling, 94
- Multi wire sawing, 271, 303, 307
- Mushroom-type interface growth, 232
- N**
- Nanocrystalline silicon, 807, 885
- Nanostructured silicon, 893, 928
- Navier-Stokes equations, 442
- Nc-Si:H solar cells, 798
- Nc-SiOx:H solar cells, 742, 745, 746
- Neutron activation method, 29
- New donors (NDs), 405, 408
- n-i-p* solar cells, 715, 717, 725, 735, 740, 747, 749, 752
- Nitrogen doping, 464
- Noncontact crucible (NOC) method, 236
- applications, 261–264
  - characteristics and merits, 241
  - conversion efficiency, 261
  - furnace design, 238–241
  - growth mechanisms, 236–238
  - growth rate of Si ingots, 242–247
- Nonthermal plasma synthesis, 934
- Non-wetting, 210
- Nucleation, 427, 429, 433
- curves, 416–417
  - of oxide precipitates, 413–416
- O**
- Oxide precipitates, 401, 403, 406, 408, 410, 417, 422, 429, 431, 433
- charge carriers, lifetime of, 423–426
  - detection of, 411–413
  - nucleation of, 413–416

- Oxygen precipitation  
 boron, 431  
 carbon, 429  
 charge carriers, lifetime of, 423–426  
 detection of oxide precipitates, 411–413  
 hydrogen, 432  
 nitrogen, 431  
 nucleation curves, 416–417  
 nucleation of oxide precipitates, 413–416  
 numerical simulation of, 417–419  
 solar cells, performance of, 426–428  
 vacancies and oxygen in silicon, interaction of, 421–423  
 vacancy concentration, in solar silicon, 419–421
- P**
- Particle(s), 380  
 Particle-in-cell method, 93  
 Paschen curve, 644  
 Passivated emitter and rear contact (PERC), 430  
 PECVD, *see* Plasma enhanced chemical vapor deposition (PECVD)  
 Peierls potential, 544, 553, 555  
 Photo-carrier recombination processes, 660  
 Photoconductivity, 805  
 Photoluminescence (PL), 411, 608, 660–661  
 spectra of Si QDs, 937  
 Photovoltaics, 130, 147, 880, 892, 895, 924, 928  
 Physical vapor deposition (PVD), 765, 771  
*p-i-n* solar cells, 715, 716, 725, 728, 732, 735, 737, 740, 743, 745, 747, 749, 752  
 Plasma-assisted VLS growth, 898  
 Plasma enhanced chemical vapor deposition (PECVD), 641, 694, 695, 709, 739, 751, 761, 762, 765, 770–771, 882, 897  
 direct current, 643  
 microwave, 651–652  
 radio frequency, 646–647  
 RF PECVD, 738  
 very high frequency, 648–651  
 VHF PECVD, 738, 740, 752  
 Polycrystalline silicon (poly-Si) thin film solar cells  
 absorber thickness, 785  
 fabrication processes, 786  
 junction type, 785  
 lift-off and transfer of, 774–775  
 light trapping technology, 775–780  
 LPC, 764, 784, 785  
 main processes, 785  
 maximum efficiency, 785  
 quality characterization of, 780–784  
 seed layer techniques, 773–774  
 SPC, 761–763  
 VPD, 766–773  
 Polymorphous silicon thin film, solar cells, 882–888  
 Polysilicon, 38, 79, 86–87  
 ambient air test method, 35  
 atomic carbon content, 22–24  
 carrier lifetime, 24–29  
 conductivity, 17–19  
 donors and acceptors test methods, 16–17  
 float-zone method for characterization, 13–15  
 high pure water test method, 35  
 high purity gas test method, 35  
 interstitial oxygen, 19–21  
 metal impurity *vs.* TCS quality, 43  
 metallic impurities and surface metallic contamination, 29–33  
 metallurgical grade silicon test methods, 34  
 packaging material test method, 35  
 production and materials  
 characterization, 13  
 requirement in solar applications, 13  
 resistivity, 19  
 trichlorosilane, 34  
 Purification, silicon, 121  
 Purities removal, 110
- Q**
- Quantum efficiencies (QE), 717, 718  
 Quantum size effect, 846  
 Quasi-mono method, 216  
 Quasi-mono technology, 618
- R**
- Radial junction performance, tilting on, 918–923  
 Radial junction solar cells, 888, 894, 896, 898, 905, 907, 909, 911, 913, 918, 919, 922, 925, 926  
 Radial p-n junction solar cells, 890–892  
 Radio frequency-plasma enhanced chemical vapor deposition (RF-PECVD), 770, 771, 774  
 Raman scattering, 781  
 Raman spectroscopy, 696–698, 800  
 Random grain boundaries, 634  
 Rapid thermal anneal (RTA) process, 761

- Real time spectroscopic ellipsometry (RTSE), 701
- Recombination-enhanced dislocation glides (REDG), 567–569
- Recombination tunnel-junction (RTJ), 683
- Recycling, 270, 275, 280, 297, 298, 302, 303, 306
- Refining
  - metallurgical grade silicon, 112–116
  - plasma, 120–121
  - solvent, 116–117
  - vacuum, 117–119
- Residual stress, 237
- Resistivity, 19
- Resonant absorption, in radial junction units, 913, 914, 917
- Ribbon grown on substrate (RGS), 410
- Rigorous coupled-wave analysis (RCWA), 779
- Roughness, 363–367
- S**
- Scanning electron microscopy (SEM), 730, 731, 733, 734
- Scanning infrared reflection explorer (SIREX) method, 369
- Scanning TEM (STEM), 411
- Scratching, 378–382
- Seed cast, 216
- Seed layer technique, 763, 773
- Seed manipulation for artificially controlled defects technique (SMART), 228–229
- Segregation theory, 142
- Self-interstitials, 407, 413, 419, 420, 431
- Self-seeding, 613
- Shockley partial dislocations, 544, 545, 554, 557, 575
- Shockley-Queisser (S-Q) detailed-balance model, 796
- Si-based tandem solar cell, 845
- Siemens (SIE) process, 38, 39, 58, 60, 67, 81, 627
  - advantages, 82
  - vs. fluidized bed reactor, 83–85
  - operational difficulties, 82
- Silane based fluidized bed reactor
  - agglomeration of silicon particle, 99
  - chemical reactions, 87
  - designs for heating, 97–99
  - distributor and jet nozzles, 96–97
  - feed gas to, 95
  - homogeneous, heterogenous and scavenging reactions, 87–89
  - modeling, 89–95
  - preheater, feed gas, 96
  - reactor dimensions, pressure, 99
  - research and development, 103–106
  - safety issues, 103
  - silicon deposition removal on reactor wall, 102
  - silicon particle size distribution, 100–101
  - silicon powder formation and handling, 101
- Silica crucible and graphite susceptor, carbon impurities
  - chemical reaction model, 457–458
  - crucible reaction, effect of, 458–459
  - origin of, 456–457
- Silicon, 194, 196, 198, 199
  - atoms, 501
  - intrinsic, 500
  - n-type, 530
  - recycling, 303
  - self-interstitials, 502
  - transition metal point defects in, 498
  - wafers, 270, 274, 283, 350, 385
- Silicon-based radicals, 810
- Silicon carbide (SiC) particles, 438, 451, 456
- Silicon nanowires (SiNWs)
  - characteristics, 880
  - in CVD system, 893–896
  - etching formation, 889–891
  - solar cells, 888–928
- Silicon nitride precipitates
  - electric properties of cell performance, 484–485
  - formation, 482–484
  - wafering of mc-Si bricks, 483–484
- Silver, 513
- Si nanowires (Si NWs), 867, 869, 872
- Single crystalline Si ingots, growth method for, *see* Mono-like Si growth method
- Si/SiC multilayers, 847, 849, 851, 853, 855
- Si single crystals, 247
- Size-controllable nc-Si material, 846
- Size-controllable nc-Si/SiC multilayers, 859
- Size-dependent photovoltaic properties, 855–864
- Slurry, 274, 276, 278, 280, 286, 287, 291, 293, 297, 298, 307, 363, 390
  - sawing, 274
  - SiC, 391–393
- Small angle boundaries, 221, 223
- Small angle grain boundary (SAGB), 593, 611, 619
- Small angle X-ray scattering (SAXS) measurements, 715

- SMART-approach, 625
- Smooth anti-reflective three-dimensional (SMART) texture, 780
- Solar cell(s), 146, 148, 150, 168, 258–261, 845  
hetero-junction, 851, 855, 856, 860  
Si QDs and carbon nanostructures, 951–952  
Si QDs/P3HT, 940–944  
Si QDs/P3HT/PCBM ternary hybrid, 948  
Si QDs/PTB7, 945  
Si QDs-sensitized, 953–955  
Si-wafer-based, 937–940  
standard, 846  
structure, 846  
*See also* Czochralski silicon
- Solar cells,  $\mu\text{-Si:H}$   
a-Si:H, 747  
crystalline evolution and hydrogen dilution profile, 709–714  
doped layer, 740–744  
highest efficiency single junction, 746–747  
high rate deposition, 737–740  
impurity issue and controlling, 714  
interface layers, 744–746  
light induced metastability, 719–725  
light trapping, 725  
microcrystalline silicon germanium alloy, 735–737
- Solar grade silicon, 110
- Solidification, purification by, 123–124
- Solid phase crystallization (SPC), 760, 761  
MIC, 762–763  
thermal, 761–762
- Split seeds, 621
- Square-shaped single ingots, 248
- Staebler-Wronski effect, 670–671  
charge transfer model, 671  
hydrogen collision model, 671  
light induced structure changes, 672  
Si-Si weak-bond breaking model, 671
- STC hydrogenation, 38, 60, 60–64, 61
- Stokes shift, 661
- Structured wires, 281, 283, 287, 306, 365–366, 373, 390
- Submerged electric arc furnace, 110
- Subsurface damage (SSD), 367–376
- Suzuki effect, 563–564
- T**
- Tamman temperature, 100
- Thermal donors (TDs)  
charge carriers, lifetime of, 408–409  
detection and measurement of, 407–408  
nature and types of, 405–407  
solar cell manufacturing, new donors in, 409–410
- Thermal solid phase crystallization, 761
- Thickness variation, 361
- Thin film, 641, 646, 648, 684, 689  
 $\mu\text{-Si:H}$  (*see* Hydrogenated microcrystalline silicon ( $\mu\text{-Si:H}$ ))
- Third generation technology, 845
- Time-of-flight (TOF) measurements, 704
- Titanium, 512
- Total variation diminishing (TVD), 442
- Transition metals  
diffusion of, 500–505  
electrical properties in Si, 505–514  
on solar cell efficiency, 514–520  
solubility of, 497–500
- Transmission electron microscopy (TEM), 411, 698–699
- Transparent conductive oxide (TCO), 728, 731, 752
- Transverse optical (TO) mode, 800
- Trichlorosilane (TCS)  
decomposition and reduction, 47–50  
distillation and purification system, 38, 42, 43  
synthesis, 38–42, 67  
test methods, 34
- Trichlorosilane based FB process, 86
- Twin boundary(ies), 194, 199, 202, 205, 594, 609, 615, 629
- Two-phase model, 89
- U**
- Ultraviolet-visible-near-infrared (UV-Vis-NIR) spectrophotometer, 804
- Undercooling, 208, 213
- Unidirectional solidification furnace, 439, 441, 444, 459, 461
- Urbach energy, 659
- V**
- Vacancy, 407, 413, 414, 416  
interaction of, 421–423  
solar silicon, concentration in, 419–421
- Vapor-liquid-solid (VLS) mechanism, 893
- Vapor phase deposition (VPD)  
high temperature, 766–767  
moderate/low temperature, 767–771  
physical vapor deposition, 771–773



Vent gas recovery, 38, 44, 45, 52, 57, 59, 63  
Vertical Bridgeman method, 217

**W**

Wafering, 270, 272, 303, 304, 306  
Wet-chemical treatment, 314, 316  
Wire saw process, 66

**X**

X-ray scattering (XRD), 696, 709

**Z**

Zigzag faceted interface, 195, 199, 200  
Zinc, 514